FEB - FRESENIUS ENVIRONMENTAL BULLETIN
Founded jointly by F. Korte and F. Coulston
Production by PSP - Vimy Str. 1e, 85354 Freising, Germany in
cooperation with PRT-Parlar Research & Technology
Vimy Str 1e, 85354 Freising
Copyright© by PSP and PRT, Vimy Str. 1e, 85354 Freising, Germany
All rights are reserved, especially the right to translate into foreign language or other processes - or convert to a machine language, especially for data processing equipment - without written permission of the publisher. The rights of reproduction by lecture, radio and television transmission, magnetic sound recording or similar means are also reserved.
Printed in Germany-ISSN 1018-4619

FEB-EDITORIAL BOARD

CHIEF EDITOR:
Prof. Dr. Dr. H. Parlar
Parlar Research & Technology-PRT
Vimy Str.1e
85354 Freising, Germany

MANAGING EDITOR:
Dr. P. Parlar
Parlar Research & Technology
PRT, Vimy Str.1e
85354 Freising, Germany

CO-EDITORS:

Environmental Spectroscopy
Prof. Dr. A. Piccolo
Universita di Napoli "Frederico II"
Dipto. Di Scienze Chemica Agrarie
Via Universita 100, 80055 Portici, Italy

Environmental Biology
Prof. Dr. G. Schuurmann
UFZ-Umweltzentrum
Sektion Chemische Ökotoxikologie
Leipzig-Halle GmbH,
Permoserstr.15, 04318
04318 Leipzig, Germany
Prof. Dr. I. Holoubek
Recetox-Tocoen
Kamenice126/3, 62500 Brno, Czech Republic
Prof. Dr. M. Hakki Alma
Igdir Universitesi
76000, Igdir, Turkey

Environmental Analytical Chemistry
Prof. Dr. M. Bahadir
Lehrstuhl für Ökologische Chemie
und Umweltanalytik
TU Braunschweig
Lehrstuhl für Ökologische Chemie
Hagenring 30, 38106 Braunschweig, Germany
Dr. D. Kotzias
Via Germania29
21027 Barza(Va), Italy

Environmental Management
Dr. K. I. Nikolaou
Env.Protection of Thessaloniki
OMPEPT-54636 Thessaloniki
Greece

Environmental Toxicology
Prof. Dr. H. Greim
Senatkommision – DFG / TUM
85350 Freising, Germany

Environmental Proteomic
Dr. A. Fanous
Halal Control GmbH
Stahlstraße 44
D-65428 Rüsselsheim, Germany

Environmental Education
Prof. Dr. C. Bayat
Yeni Yüzyil Üniversitesi
34010 Zeytinburnu, Istanbul, Turkey

Environmental Medicine
Prof. Dr. I. Tumen
Bandirma 17 Eylül Üniversitesi
10200 Bandirma, Turkey

Advisory Board
K. Bester, K. Fischer, R. Kallenborn
DCG. Muir, R. Niessner,W.Vetter,
A. Reichlmayr-Lais, D. Steinberg,
J. P. Lay, J. Burhenne, L. O. Ruzo

Marketing Manager
Cansu Ekici, MSC. of B.A.
PRT-Research and Technology
Vimy Str 1e
85354 Freising, Germany
E-Mail: parlar@wzw.tum.de
parlar@prt-parlar.de
Phone: +49/8161887988

Fresenius Environmental Bulletin is abstracted/indexed in:
Biology & Environmental Sciences, BIOSIS, CAB International, Cambridge Scientific abstracts, Chemical Abstracts, Current Awareness, Current Contents/Agriculture, CSA Civil Engineering Abstracts, CSA Mechanical & Transportation Engineering, IBIDS database, Information Ventures, NISC, Research Alert, Science Citation Index (SCI), Scisearch, Selected Water Resources Abstracts

CONTENTS

ORIGINAL PAPERS

BIOINDICATIVE OPERATION OF POLLUTANTS FROM MINE TAILINGS IN THE KISNICA MINE AND FLY ASH FROM THE THERMAL POWER PLANT OBILIC ON VEGETABLE PLANTS 2615
Milica Stankovic-Popic, Radmila Trajkovic, Ljubomir Sunic, Zoran S Ilic

COMPETITION FOR CONSERVATION: OBSERVATION OF 1ST PRUSSIAN CARP *CARASSIUS GIBELIO* (BLOCH, 1782) CATCHING COMPETITION IN GOKPINAR DAM POND (DENIZLI/TURKEY) 2626
Esat Tarik Topkara, Bahar Bayhan, Hulya Saygi

VISUAL IMPACT OF WIND TURBINES ON LANDSCAPE QUALITY – A CASE STUDY 2632
Marta Lisiak, Klaudia Borowiak, Jolanta Kanclerz, Anna Adamska, Ewelina Janicka, Anna Budka, Anna Libront

EVALUATING THE WORK ENVIRONMENT IN TURKISH FURNITURE INDUSTRY FROM THE POINT OF OCCUPATIONAL HEALTH AND SAFETY 2639
Devrim Karademir, Kucuk Huseyin Koc

SOME METALS AND ANTI-BROWNING AGENTS EFFECTS ON POLYPHENOL OXIDASE FROM PRINCESS TREE LEAVES 2646
Gulnur Arabaci, Cengiz Cesko, Ayse Usluoglu

AN INTEGRATED FUZZY MULTI CRITERIA DECISION MAKING METHOD FOR SUSTAINABLE (GREEN) PACKAGING MATERIALS SELECTION: AN APPLICATION IN TURKEY 2653
Bahadir Gulsun, Pinar Mic

INVESTIGATION OF PROSPECTIVE SCIENCE TEACHERS' OPINIONS AND SENSITIVITY TOWARDS ENVIRONMENT 2662
Ebru Ezberci Cevik, Mehmet Altan Kurnaz

MONTHLY VARIATION OF PHARMACEUTICALLY VALUABLE ALKALOIDS, GALANTHAMINE AND LYCORINE, IN SUMMER SNOWFLAKE (*LEUCOJUM AESTIVUM* L.) 2670
Mustafa Arslan, Arzu Birinci Yildirim, Erva Ozkan, Fatma Betul Oktelik, Arzu Ucar Turker

NEW OR LESS KNOWN SPECIES OF MICROFUNGI FOR TURKEY 2678
Makbule Erdogdu

EFFECTS OF MEDITERRANEAN CUTTLEFISH (*SEPIA OFFICINALIS*) BONE AS AN ALTERNATIVE CALCIUM SOURCE ON EGG PRODUCTION, EGG QUALITY AND SOME BLOOD PARAMETERS IN LAYING QUAILS 2683
Kadir Emre Bugdayci, M Numan Oguz, Fatma Karakas Oguz, Isa Can Uyguralp, Ilker Yusuf Akinci

EFFECTS OF DIMETHYL SULFOXIDE (DMSO) AND THAWING RATES ON SPERM MOTILITY FOR CRYOPRESERVATION OF SPERM IN GILTHEAD SEABREAM (*SPARUS AURATA*) 2691
Serhat Engin, Sahin Saka, Kursat Firat

IN VITRO APPROACHES FOR SHORTENING GENERATION CYCLES AND FASTER BREEDING OF LOW β-N-OXALYL-L-α, β - DIAMINOPROPIONIC ACID CONTENT OF GRASS PEA (*LATHYRUS SATIVUS* L.) 2698
Surendra Barpete, Priyanka Gupta, Khalid Mahmood Khawar, Sebahattin Ozcan, Shiv Kumar

STUDY ON PARTIAL DISCHARGE SIGNAL DENOISING OF TRANSFORMER 2707
Yanyan Zheng, Yongli Zhu

SHELF LIFE OF FARMED SEA BASS (*DICENTRARCHUS LABRAX*, L. 1758) TREATED WITH *BACILLUS SUBTILIS* (KUEN 1593) UNDER COLD STORAGE 2711
Eylem Ezgi Fadiloglu

INHIBITORY AND SYNERGISTIC EFFECT OF NOVEL COMBINED ACTIVE SUBSTANCES OF FUNGICIDES AGAINST SELECTED PLANT PATHOGENS 2719
Piotr Iwaniuk, Bozena Lozowicka

MODELING OF NEAR-FIELD DILUTION OF BRINE DISCHARGES: A CASE STUDY IN SAMSUN BAY 2725
Asu Inan, Lale Balas

FABRICATED AgBr/rGO/g-C_3N_4 HYBRID PHOTOCATALYST FOR ENHANCED PHOTOCATALYTIC DEGRADATION OF TETRACYCLINE 2732
Zhiguang Yang, Xiaoming Shi, Peng Peng, Yueyun Yang, Yunlin Li

INVESTIGATION OF WASTE FOUNDRY SAND AND SEWAGE SLUDGE REUSE AS LANDFILL CAP LAYER MATERIAL 2739
Gulgun Dede, Ayse Bengu Sunbul, Mirac Gedikli

INTERDEPENDENCE OF CYTOTOXIC ACTIVITIES OF BIOACTIVE COMPONENTS IN BLACK SEED (*NIGELLA SATIVA* L.) ESSENTIAL OIL AND INTRACELLULAR ZINC LEVELS 2746
Olcay Boyacioglu

POLLUTION ASSESSMENT AND SOURCE APPROXIMATION OF HEAVY METALS IN THE SOIL ALONG A MAIN ROAD WITH HIGH DENSITY OF TRAFFIC 2752
Han Sun, Linhua Sun, Yu Li, Xiaojun Gao, Zixiang Zhao

ASSESSMENT OF CLIMATE CHANGE RISKS TO NATURAL RESOURCES IN THE REPUBLIC OF SERBIA 2758
Ljubica Duskov, Dejan Filipovic, Vladimir Djurdjevic

DETERMINATION OF SOME QUALITY PROPERTIES OF ENSILED FORAGE TURNIP (*BRASSICA RAPA* L.) WITH DIFFERENT ADDITIVES 2766
Ilkay Cetin, Asuman Arslan Duru

THE EFFECT OF KNIFE TYPE ON CUTTING CHARACTERISTICS OF COTTON STALK 2772
Resat Esgici

ASSESSMENT OF GENETIC PROGRAMMING FOR ESTIMATING RAINFALL-RUNOFF HYDROLOGICAL EVENTS 2778
Muhammet Omer Dis, Mehmet Unsal, Ayse Ece Yagci

DETERMINATION OF ANTIBIOTIC RESISTANCE AND CRISPR 2.1 LOCI OF *ESCHERICHIA COLI* ISOLATED FROM SEYHAN INLAND LAKE ADANA, TURKEY 2784
Anil Delik, Esra Sunduz Yigittekin, Fatima Masume Uslu, Sadik Dincer

ENERGY CONSUMPTION ANALYSIS OF GREEN TOWN PUBLIC BUILDINGS BASED ON MATHEMATICAL REGRESSION ANALYSIS METHOD 2792
Ting Zheng

DETERMINATION OF PESTICIDES IN FARMER HAIRS FOR THE BIOMONITORING OF EXPOSURE IN CUKUROVA REGION, TURKEY 2802
Nebile Daglioglu, Pinar Efeoglu Ozseker, Nigar Yarpuz Bozdogan, Evsen Guzel

DETERMINATION OF NUT PROPERTIES AND CHEMICAL COMPOSITIONS OF WALNUT (*JUGLANS REGIA* L.) GENOTYPES GROWN IN WALNUT-FRUIT FORESTS OF KYRGYZSTAN 2809
Umran Erturk, Ali Osman Solak, Sevil Yucel, Kaliypa Saliyeva, Zeki Severoglu, Ibrahim Ilker Ozyiğit, Bakit Borkoyev

NATURAL OCCURRENCE OF AFLATOXIN B_1 IN DRY FRUITS OF GILGIT-BALTISTAN, PAKISTAN 2818
Shamsher Ali, Azhar Ali, Ali Sartaj, Maher Ali, Ali Amjad

MAPPING VEGETATION OF WETLAND BASED UPON AN OBJECT-ORIENTED CLASSIFICATION WITH HIGH RESOLUTION ORTHOPHOTOS 2823
Fulsen Ozen

A COMPARATIVE STUDY OF CONVENTIONAL COAGULATION AND SLUDGE RECYCLING ENHANCED COAGULATION FOR LOW-TURBIDITY SOURCE WATER: THE EFFECT AND APPLICABILITY 2834
Zipei Li, Lei Fang, Yan Zhang, Yunxia Miao

YIELD AND QUALITY TRAITS OF SOME SILAGE MAIZE CULTIVARS 2843
Hakan Kir

STUDY ON GREEN SAFETY PRODUCTION TECHNOLOGY IN MODERN COAL MINES 2850
Lianchun Zhou, Jinshan Zhang

TIME-DEPENDENT CHANGES OF HEPATIC ENZYME ACTIVITIES AND THYROID HORMONES IN *CARASSIUS AURATUS* EXPOSED TO 2,2',4,4'-TETRABROMODIPHENYL ETHER (BDE 47) 2858
Mengnan Shen, Jie Cheng, Shixiang Gao, Na Li, Hai Lu

URBAN INTRINSIC PROCESS AND ITS APPLICATION IN SPATIAL DATABASE UNDER DIFFERENT RAIN CONDITIONS BASED ON GIS 2869
Tianhe Yin, Qiting Huang, Zelin Qin, Chao Wang

STUDY ON RURAL INTELLIGENT PLANNING COOPERATIVE PLATFORM 2879
Liqun Wang, Linjun Jin

THE NUMERICAL SIMULATION RESEARCH OF HIGH PRESSURE MIST SPRAY BASED ON MULTIPHASE FLOW THEORY 2886
Lin Yang, Shaocheng Ge, Zhihui Huang, Deji Jing, Xi Chen

EFFECTS OF SOWING DATE AND NITROGEN APPLICATION RATE ON WHEAT YIELD AND YIELD COMPONENT FACTOR IN JIANGHUAI PLAIN 2891
Chengfang He, Hongjie Zhu, Xiangqiang Kong, Xiaoming Yan

PLASTICITY IN BEHAVIOR OF TURKISH MALTING BARLEY CULTIVARS UNDER SEMI-ARID AND CONTINENTAL CLIMATIC CONDITIONS 2897
Abdulveli Sirat, Bilge Bahar

RISK ASSESSMENT OF TORRENTIAL RAIN AND FLOOD DISASTER IN DATONG RIVER BASIN BASED ON FLOOD AREA MODEL 2908
Haitao Wang, Shuwen Zhang, Xuedong Li, Bin Wang

SOME MORPHOLOGICAL CHARACTERISTICS, DISTRIBUTION AND POPULATION DEVELOPMENT OF THE PEST *SYNANTHEDON VESPIFORMIS* L. (LEPIDOPTERA: SESIIDAE) IN CHESTNUT AREAS, TURKEY 2917
Cevdet Kaplan

STUDY ON THE SEQUENCE DIVISION AND RESERVOIR OF MIDDLE PERMIAN IN CENTRAL SICHUAN BASIN, CHINA 2925
Jingying Wang, Ying Guo, Bin Ni, Guangying Ren, Xiaofei Shang, Yong Yang

IDENTIFICATION OF THE LATE TRIASSIC CHANG 6_3 PERIOD SLOPE BELT IN THE CENTRAL ORDOS BASIN AND OIL AND GAS GEOLOGICAL SIGNIFICANCE 2932
Jianbo Liao, Aihua Xi, Zhiyong Li, Jing Deng, Huaqing Liu, Xiangbo Li, Wanyan Rong

QUANTITATIVE PREDICTION OF ORGANIC COMPONENTS IN SHALE OIL RESERVOIRS USING AN IMPROVED ΔLOG *R* METHOD 2942
Yinhao Dong

THE INVESTIGATION OF THE POSSIBILITY OF USING RED CALIFORNIA EARTHWORM (*EISENIA FETIDA*) MEAL AS AN ALTERNATIVE PROTEIN SOURCE IN RAINBOW TROUT (*ONCORHYNCHUS MYKISS*) DIET 2951
Huriye Ariman Karabulut, Zeynep Bayraktar, Ilker Zeki Kurtoglu, Turan Yuksek

A STUDY ON DIESEL PARTICULATE FILTER STAGED LINEAR SOOT LOADING ESTIMATION BASED ON PRESSURE DROP 2960
Jinchi Dai, Hailong Pang, Yan Yu, Jianguo Bu, Xinyun Zi

EXOGENOUS ROOTING AGENT (GGR-6) ALLEVIATES HARMFUL EFFECT OF DROUGHT STRESS ON SEEDLINGS OF PERENNIAL RYEGRASS 2969
Jinyang Qi, Siddique Muhammad, Jingyao Tian, Jixiang Lin, Jinghong Wang

STUDY ON ENVIRONMENTAL BEHAVIOR AND DRUG-RESISTANT GENE EMISSION CHARACTERISTICS OF β-LACTAM ANTIBIOTICS IN DRUG PRODUCTION PROCESS 2975
Jingqiong Xiao, Xiuqin Wang, Liming Zheng, Dandan Ma

EXPERIMENTAL STUDY ON DAMAGE CHARACTERISTICS OF DIRT BAND BY SHAPED CHARGE BLASTING IN COAL SEAM 2982
Yangbo Pan

PROPERTIES EVALUATION AND APPLICATION OF A NOVEL DRILLING FLUID WITH STRONG PLUGGING AND INHIBITION PERFORMANCE 2993
Jianghong Jia, Zhongwen Song, Xiaoming Zhang

AFLATOXIN M_1 CONCENTRATION IN MILK AND MILK PRODUCTS FROM AYDIN PROVINCE, TURKEY 3003
Selda Bulca

MULTIVARIATE ASSESSMENT OF WATER CHEMISTRY AND METALS IN A RIVER IMPACTED BY TANNING INDUSTRY 3013
Usman Atique, Sonia Iqbal, Noor Khan, Bainazir Qazi, Aqeel Javeed, Khalid Mahmood Anjum, Muhammad Sultan Haider, Tanveer Ali Khan, Sajid Mahmood, Shahid Sherzada

EFFECT OF WATER CONSUMPTION CHARACTERISTICS ON WATER PRODUCTION FUNCTION OF SOYBEAN IN COLD BLACK SOIL AREA 3026
Yanyu Lin, Shujuan Yi, Mengxue Wang, Mingyao Wang, Xiaolei He, Xu Zhou

EFFECT OF FOLIAR APPLICATION OF IRON (Fe) AND MOLIBYDENIUM (Mo) ON YIELD, PROTEIN AND NODULATION IN SOYBEAN UNDER AGRO CLIMATIC CONDITIONS OF SANLIURFA 3033
Erdal Erbil, Ali Beyhan Ucak, Timucin Tas, Mehmet Karakus, Cemil Yetkin

SEDIMENTARY FACIES MODEL IN THE SOUTHWESTERN PART OF THE QAIDAM BASIN, CHINA 3040
Bing Hao, Xinyuan Ma, Qingfeng Zhang, Jianhua Zhong, Ningliang Sun

VEGAN *VS.* MEAT: CATEGORIZATION OF PLATE WASTE IN RESTAURANTS 3048
Neven Voca, Eda Puntaric, Jona Suric, Dunja Kunjko

DETERMINATION OF DIOXINS/FURANS IN HUMAN GALLBLADDER STONES AND GALLBLADDER TISSUES AS INDFICATOR FOR ENVIRONMENTAL CONTAMINATIONS 3056
Sharif Arar, Samer Awaideh, Mohammed H Kailani, Mahmoud Alawi

EXPERIMENTAL STUDY ON RESISTIVITY CHARACTERISTICS OF PURPLE SOIL IN DRYING SHRINKAGE PROCESS IN THREE GORGES RESERVOIR AREA, CHINA 3072
Zhengcheng Wang, Xin Tang, Haitao Mao, Jiwei Shen, Tingqiang Zhou

A NOVEL NON-UNIFORM CLUSTERING ALGORITHM FOR WIRELESS SENSOR NETWORKS BASED ON ECOLOGICAL ENVIRONMENT MONITORING REQUIREMENTS 3084
Yan Li

GEOLOGICAL MODELING AND STABILITY ANALYSIS OF HORIZONTAL WALL IN TYPICAL SHALE GAS BLOCKS-TAKING WEI 202 BLOCK FOR EXAMPLE 3091
Qihua Ran

RELATIONSHIP BETWEEN HOPELESSNESS AND SELF-ESTEEM OF PREGNANT WOMEN: A CROSS-SECTIONAL STUDY IN SOUTH EASTERN TURKEY 3102
Ilknur Yesilcinar, Derya Yanik, Sahide Akbulut

IMPACT OF DYNAMIC FAULT DAMAGE TO CAPROCK ON OIL AND GAS RECOVERY OF TIGHT SANDSTONE 3110
Yu Zhu

EXPERIMENTAL STUDY OF ENVIRONMENTAL FRIENDLY MODIFIED CELLULOSE AS RHEOLOGY MODIFIER IN CLAY-FREE WATER-BASED DRILLING FLUIDS 3118
Junyi Liu

COMPREHENSIVE EVALUATION AND ANALYSIS OF BIODIVERSITY IN SOUTHERN GUIZHOU PROVINCE, CHINA 3126
Lulu Liu, Quanqin Shao

EXPERIMENTAL STUDY ON THE FLOW CHARACTERISTICS OF JET IMPINGEMENT IN MICRO-SCALE ENVIRONMENT 3134
Jie Zheng, Yarong Zhang, Yihua Dou

A NOVEL CONCURRENT RISK IDENTIFICATION AND ANALYSIS METHOD FOR EQUIPMENT FAILURE BY COMBINING PETRI NET REASONING AND AN EXTENDED FMEA USING FOR SAFE OIL AND GAS STORAGE AND TRANSPORTATION ENVIRONMENT 3144
Meng Zhang, Wei Liang, Weijun Li, Yanfen Yang

RESEARCH ON A NOVEL LASER DETECTION METHOD FOR CASING DAMAGE OF CNG GAS STORAGE WELL AND FIELD TRIAL 3154
Liansheng Qin, Jian Du, Shiyong Cao, Han Liu

RESEARCH ON THE PREDICTION OF DIRECTIONAL WELL SAFE DENSITY WINDOW AND THE INFLUENCES OF FORMATION PARAMETERS 3166
Peng Huang, Zhiqiang Huang

INFLUENCE OF DISPLACEMENT VELOCITY ON THE EFFECT OF THE ENHANCED OIL RECOVERY OF BINARY COMPOSITE FLOODING IN LONG CORE 3173
Yuting Pan, Zhiquan Zhang

ANALYSIS ON THE INFLUENCING FACTORS OF MODERN FORESTRY DEVELOPMENT IN RECLAMATION AREA BASED ON ECOLOGICAL SECURITY--TAKING HEILONGJIANG PROVINCE AS AN EXAMPLE 3184
Wanjing Dong, Dapeng Jiang, Hongbo Li , Yingli Huang

IMPACT FORCE CALCULATION OF CHAIN DRIVE AND MODEL ANALYSIS OF FLEXIBLE GRAPHITE SHEET BASED ON THE CONCEPT OF NOISE REDUCTION AND ENERGY SAVING 3193
Wei Jiang, Wei Li, Congwang Bao

STUDY ON WATERFLOODING MODEL OF FRACTURED GLUTENITE RESERVOIR - TAKING THE LOWER WUERHE FORMATION IN THE EIGHTH AREA OF KARAMAY OILFIELD AS AN EXAMPLE 3201
Yangzhi Shi, Weifeng Li, Xiaojing Wang, Jie Zhang

MICROPORE STRUCTURE CHARACTERISTICS OF TIGHT OIL RESERVOIRS IN THE YANCHANG FORMATION IN THE ORDOS BASIN, CHINA 3212
Tianjin Zhang, Gang Zhang, Lushe Zhang

DESIGN AND IMPLEMENTATION OF A NOVEL ENVIRONMENTAL FRIENDLY CHATBOT BASED ON VSM AND RASPBERRY PI WITH ENVIRONMENTAL PROTECTION KNOWLEDGE 3223
Linyan Ouyang, Xi Luo, Linsheng Xiong

NITROGEN REMOVAL IN DITCH WETLAND SYSTEMS: EFFECTS OF HYDRAULIC RETENTION TIME (HRT) AND SPATIAL CONFIGURATION 3230
Wenjing Wang, Zifang Chi, Ying Yin

PRACTICES OF COASTAL ZONE MANAGEMENT OF THE JORDANIAN GULF OF AQABA BY MAPPING SPATIAL CONVERGENCE OF SEAFRONT HUMAN ACTIVITIES AND THEIR POTENTIAL IMPACT ON THE MARINE ENVIRONMENT 3240
Ala'aldin Alrowwad, Ali Al Sawalmih, Riyad Manasrah, Mohammed Rasheed, Maysoon Kteifan, Aiman Soleiman, Zeinab Arabeyyat, Ahmad M. Al-Saad, Samantha Barnett

OCCURRENCE OF UNCONVENTIONAL NATURAL GAS IN COAL-BEARING STRATA IN ORDOS BASIN, CHINA 3254
Zhanjun Chen, Yidong Yuan, Xiulan Zhu, Yanni Liu

EXPERIMENTAL STUDY ON OPTIMAL CO_2 FLOODING PRESSURE BEFORE AND AFTER FRACTURING IN HEAVY OIL RESERVOIRS 3261
Le Qu, Tiantai Li, Rongjun Zhang, Zhipeng Miao, Hui Gao, Qing Guo

ACCURATE PREDICTION OF EXTERNAL CORROSION RATE OF BURIED PIPELINE BASED ON KPCA-MABC-SVR MODEL USING IN OIL AND GAS GATHERING AND TRANSPORTING SYSTEM 3269
Hui Xu, Shipeng Wang, Min Yan, Zhixiu Liu, Rongrong Xie

*EFFECTS OF SALICYLIC ACID APPLICATION ON WRKY GENE IN PEPPER (*CAPSICUM ANNUUM *L.) SEEDLING* 3279
Mohammed Ahmed Ahmed, Muhemet Zeki Karipcin, Fikret Yasar

MODELING AND COMPUTER SIMULATION OF DRAINAGE, EVAPORATION, AND RUNOFF (DEAR) FROM BARE SOILS 3287
Mehmet Aydin, Baran Aydin, Veysel Polat

NOTICE

LANDSCAPE DESIGN OF THE URBAN BUS STATION BASED ON THE URBAN CHARACTERISTICS AND ECOLOGICAL ENVIRONMENT OF SMART CITY, CHINA 3300
Chunyan Li

STUDY ON NEW ENVIRONMENTAL PROTECTION LAW AND CONSTRUCTION STRATEGY OF ECOLOGICAL COMPENSATION SYSTEM 3308
Qingpo Wei

© by PSP Volume 29 – No. 04A/2020 pages 2615-2625 Fresenius Environmental Bulletin

BIOINDICATIVE OPERATION OF POLLUTANTS FROM MINE TAILINGS IN THE KISNICA MINE AND FLY ASH FROM THE THERMAL POWER PLANT OBILIC ON VEGETABLE PLANTS

Milica Stankovic-Popic[1], Radmila Trajkovic[1], Ljubomir Sunic, Zoran S Ilic[2,*]

[1]University of Pristina-Kosovska Mitrovica, Faculty of Natural Sciences and Mathematics, Department of Biology, 38220 Kos. Mitrovica
[2]University of Pristina-Kosovska Mitrovica, Faculty of Agriculture Pristina-Lesak, 38219 Lesak, Serbia

ABSTRACT

Disturbance of natural ecosystems is assumed serious purpose and in the region of central Kosovo, particularly in the industrial areas of lead and zinc mining in the Kišnica mine and the thermal power plant, Obilić. Deposits of tailings from these industrial zones near the villages Gračanica and Plemetina have led to pollution of the soil and river water flows of the area and surrounding regions. Residents who live in the outskirts of these villages use domestic wells for water supply and eat home-grown food, especially early vegetable crops from their small gardens. In stress conditions, such as heavy metal toxicity and fly ash pollutants, an increase in antioxidant enzyme activities are important for plants to tolerate the stress. The antioxidant defense system in plant cells is composed of an enzymatic defense, such as catalase (CAT), and a non-enzymatic defense such as organic acids. Although the seeds are tolerant to the presence of all metals, the percentage of germinated seeds depends on the concentration and type of heavy metal, and the seed species. Lettuce seeds sown in the acidic soil (pH 2.74) from Kišnica with very high concentrations of Cr, Ni, Pb, Al and Fe were completely inhibited at the germination stage. An increased catalase activity in different organs of plants under conditions of environmental pollution is a mechanism of detoxification and of acquiring stress resistance. Catalase activity in radish and lettuce, particularly in the early development stage (7 and 14 days) was measured in seedlings of soil substrate from Plemetina, which is dominated by sulfur pollutants. The highest content of organic acids in the above-ground organs was observed in plants of radishes grown in soil originating from Gračanica, with a several-fold increase compared to control. Taken together, the increased catalase activity and organic acid content in the radish and lettuce plants grown in soil heavy with deposits of tailings is most likely a plant defense mechanism to toxicants.

KEYWORDS:
Soil pollution, seed germination, catalase, organic acid, radish, lettuce

INTRODUCTION

Industrial waste is often deposited by the local community in dumps. As a consequence, such landfills are a potential risk of contamination source since they are not secured in any way. As a result, these landfills cause a transfer of toxic substances into the soil. Open dumpsites present a number of risks to soils due to its propensity to generate toxic chemicals, pathogens, and alter the natural environment of the soil. The source of heavy metals is usually hazardous waste tailings from e.g. mines, and ashes coming from the heating systems as well as the organic fraction of coal, all of which have a substantial accumulation ability [1].

As a result of the intensive heavy industry in the past, Kosovo and Metohija presently faces a large number of inherited environmental problems that were accumulated during decades of uncontrolled exploitation of natural resources, mining activities and industrial production, which are associated with high pollution levels. After the war in 1999, most of the manufacturing industries were out of function. Most of these industries resulted in obsolete hazardous waste, old unused technology, demolished buildings, and unmanaged storages. All this contributed to a much increased negative impact on the environment. Such locations of potential pollution from nearby industries can be considered as hot spots with negative impacts on the environment. These sites are a source of pollution of soil, water and air. Vast areas of land are contaminated by acidic water, and heavy metals, especially lead, zinc, cadmium, arsenic and mercury. Several former industrial facilities like Kišnica and Obilić and their storage areas (dumps) currently pose a permanent risk to the environment and public health in the Kosovo region.

Heavy metal pollutions caused by natural processes or anthropological activities [2] such as

metal industries, mining, mineral fertilizers, pesticides and others pose serious environmental problems in present days [3]. Excessive accumulation of metal in plant tissues are known to cause oxidative stress. Plants have limited mechanisms of stress avoidance and require flexible means of adaptation to changes. A common feature to combat stress factors is synchronized function of antioxidant enzymes that help alleviate cellular damage by limiting reactive oxygen species (ROS) accumulation. Abiotic stress affects plant metabolism, disrupts cellular homeostasis and uncouples major physiological and biochemical processes. Plants have developed a complex antioxidant system which migrates and repairs the damage initiation by ROS towards enzyme synthesis, to protect the cellular and subcellular systems from cytotoxic effects of active oxygen free radicals. The major ROS scavenging activities include complex, non-enzymatic (ascorbate, glutathione, alpha-tocopherol) and enzymatic antioxidants like e.g. catalase (CAT), ascorbate peroxidase (APX), superoxide dismutase (SOD) and peroxidases (POX).

Catalase (CAT) (EC 1.11.1.6) is an important cellular antioxidant enzyme that defends against oxidative stress. Hydrogen peroxide, although not a free radical, is highly reactive. Peroxidases serve to protect the cell from toxic effects of high concentrations of hydrogen peroxide by catalyzing its decomposition into molecular oxygen and water, without the production of free radicals. The main function of CAT is to remove hydrogen peroxide produced by photorespiration in leaves [4]. In the chloroplasts, catalase protects from hydrogen peroxide through its catalytic reaction, but it is not involved in the decomposition process of hydrogen peroxide. The functions mainly include: stress-resistance signal factors of plants, regulation of apoptosis factor, maintaining plant cells oxidation - reduction dynamic equilibrium, etc. [5]. CAT is an eco-protective enzyme, under the action of stress factor, biological organism through its own mechanism of enzyme can make the plant itself produce protective reaction to toxicant which can produce toxicity to plant itself [6]. (CAT activity changes can be used indicators to an adverse environmental factors of biological damage [7]. During the last 20 years increasing experimental evidence has associated organic acid metabolism with plant tolerance to environmental stress. Current knowledge shows that organic acids not only act as intermediates in carbon metabolism but also as key components in mechanisms that some plants use to cope with nutrient deficiencies and metal tolerance operating at the root – soil interphase [7].

The aim of this study was to investigate the effect of pollutants on seed germination, biochemical and physiological and morphological changes of different vegetable species (radish and lettuce) during morphogenesis, and to assess the activity of the enzyme catalase, and the levels of organic acids involved in the defense mechanism of plants towards toxic substances.

MATERIALS AND METHODS

Sampling area. Tailings (Mine dumps) in Kišnica – the Badovac mine is one of the most important lead and zinc area of Kišnica ore field. It is located southeast of Priština, near the Gračanica monastery, in the northern part of the ore field. The mining complex includes an area of 100 ha. The most contaminated areas considered as the hotspots within this complex are Badovac tailings (near Badovac Lake dam), characterized with high concentration of heavy metals, such as lead and zinc with the area of app. 1 ha and Kišnica tailings, with lead and zinc concentration covering area of app. 5 ha. The tailings are spread irregularly and are not protected at all from contamination spreading to the surrounding environment. The main risks are for human health as well as flora and fauna of the nearby environment. It has a potential to pollute the drinking water sources for Priština.

The ash dumps of the Thermal Power Plant (TPP) Kosovo B are located near Plemetina village of Obilić municipality in central part of Kosovo province. They cover an area of about 100 ha. According to the large amount of ash deposited, this location represents permanent risk due to instability of deposited ash, which is characterized by occasional slides. The ash removal by wind presents another problem that is characteristic of this hotspot. Ash collected in these dumps is created during the combustion of coal for electricity generation. Transportation of ash from TPP A in existing dumps is done through open conveyor belts. Every year, more than 25 mil m3 (app. 34 t) of ash was disposed at the Dump of TPP A and more than 14 mil m3 (app. 20 t) of ash was disposed at the Dump of TPP B.

There are number of identified sources of contamination at the site. The most serious source are the ash dumps TPP A and TPP B. These landfills are sources of easily resuspended ash particles. These particles may carry adsorbed pollutants such as heavy metals and organic chemicals. There are open coal (lignite) mines at the site and number of discharges from the mines to the surface water bodies. This water should be contaminated too. There are two other dump sites TPP A1 a TPP B1, that contain used oils with high content of phenols and polyaromatic hydrocarbons.

All the local inhabitants are exposed to the dust particles mobilized from the ash dumped at the site. Also the groundwater and surface water is under the risk, it is expected that the ground water is contaminated as a consequence of the leakages of the waste disposed at the site (ash, used oil). Huge

area of the ash dumps has been recultivated. Some amount of the ash has been removed and dump at proper landfill (former coal mine), some parts were reshaped and covered with inert soil to protect mobilisation of the dust particles.

Sample soil preparation and analysis. All soils were sampled at the surface 20 to 40 cm in depth) using hand driven stainless steel augers. Collected soil samples were air-dried to constant weight and then sieved through a 500 µm stainless steel mesh wire. Soil sample of 0.5 g was placed in a glass beaker and 10 ml conc. HNO_3 solution was added. Then, the sample was heated at 150ºC for about 3 h, followed by evaporation to near dryness. After that, 2 ml of conc. $HC1O_4$ was added and digestion was continued by evaporation to near dryness again. Then, 2 ml of conc. HCl was added and heated at 150ºC for about 15 min. Finally, the sample was transferred to a 25 ml volumetric flask and diluted up to the mark with doubly distilled water. A Cole-Parmer micro-filtration apparatus with a 0.45 mm pore size membrane (Micro Filtration Systems) was used for the filtration of the aqueous phase before metal determination. Detection of the metals was carried out with flame atomic absorption spectrophotometer (FAAS) (Perkin Elmer AA Analyst 700 model, Flame Atomic Absorption Spectrophotometer) connected with deuterium background correction, hollow cathode lamps (HCl) and acetylene burner. The absorption measurements of the metals were performed under the conditions recommended by the manufacturer. Unless otherwise stated, all chemicals used were of analytical reagent grade. Triply distilled water was used throughout the experiments. To carry out experiments, the final concentrations of metal standard solutions were freshly made by diluting the stock standard solution with water.

Experiment. Effect of pollution on seed germination, catalase activity and content of organic acids in the root and leaf of the radish (*Raphanus sativus L. var. radicola*) and lettuce (*Lactuca sativa* L.) under soil substrats from two different polluted area (mine tailings-Kišnica and fly ash from TE-Obilić B). Soil substrates take from 20 cm and 40cm dept in Kosovo B and Kišnica (polluted area); Plemetina and Gračanica (5km from pollution area) and Lipljan (20 km from polluted area- control).

The soil with different location was incubated in plastic boxes (containers) for 1 month. Soil was maintained as 70% in water capacity. The experiment has been conducted under greenhouse conditions with seeds were sowing in small containers. Seed sowing and plants were grown in plastic boxes (50x20cm) with 20 cm dept, under plastic house at a thermoperiod and a photoperiod of 23°C/12 h the day and 14°C/12 h the night (150 µmol photons m^{-2} s^{-1}). Seeds of (*Raphanus sativus L. var. radicola*) and lettuce (*Lactuca sativa* L.) were germinated for 3 days and 7 days respectively.

Plant samples for analysis of the catalase activity and of organic acids content are taken after 7, 14, 21 and 28 days after germination. After harvest, tissues were separated into shoots and roots. Shoots and roots were washed with distilled water and prepared for analysis.

Catalase activity. The enzyme activity was determined by gaso-metric method. This method is based on determination of the amount of released oxygen, after which the operation of H_2O_2 was added in a vegetable extract. First, a volume of fresh plant material was extracted 0.5-1 gr. After a mortar with 0.5gr $CaCO_3$, to achieve a pH = 7.7 which is optimal for the action of enzymes, in 20 mL of distilled water which is added gradually.

Thereafter, the extract was transferred to a flask with side drain and by the apparatus measures the activity catalase. Erlenmajer is clogged cork stopper of which is pierced through with a needle syringe. Syringe containing 5 mL of 3% H_2O_2. At the beginning of the experiment H_2O_2 is injected into the flask.

The flask contents were shake for one minute, followed by one minute at rest, and then again for one minute shake. Total three minutes. After this time, the scale is read the amount of released oxygen. After takes place in the conversion of these values for 1g of material.

Each analysis was repeated three times and the average value is presented. Results presented by tables. Catalase activity expressed in cm^3 O_2/1g/3 '.

Organic acid. Total acidity was determined by titrametric method in the presence of the indicator [8]. The acids were extracted from plant material by heating the distilled water at a temperature of 80-90 ^{0}C 30 minute. Fresh plant material (20 g) is extracted in a mixer with 150 ml of H_2O. Extract is transferred to Erlenmajer from 200 ml and is left in a water bath at a temperature of 80-90 ^{0}C 30 min. After addition, the flask was quickly chilled running water and the contents were then filtered into a volumetric flask of 200 ml and the same is refilled with distilled water up to limitation line of.50 ml of the filtrate is transferred to beaker and add a few drops of fenoftaleina. Titration is carried out with 0.1 N NaOH to the appearance of pink color. Calculation of the overall acidity was done using the formula:

$$X=\frac{a \times T \times 200 \times 10}{n \times 50}$$

x-the amount of total acid in the tested sample expressed in mEkv
a-quantity of consumed 0.1 N NaOH for titration of (ml)
T-factor of 0.1 N NaOH
200 – total extracts volume

TABLE 1
The basic agrochemical soil substrate properties at different soil-tailings depth

Target area	Soil depth (cm)	pH (H_2O)	pH (KCl)	N (%)	P_2O_5 (mg/100g)	K_2O (mg/100g)	Humus (%)	$CaCO_3$ (%)
Control-area	20	7.71	7.28	0.225	23	16.58	3.26	1.2
Lipljan- 20 km from PA	40	7.61	7.23	0.200	25	26.52	2.59	0.8
Kosovo B	20	7.99	7.84	0.700	14.3	25.87	2.33	21.8
polluted area-PA	40	8.26	8.05	0.049	15.7	82.14	1.37	16.0
Plemetina	20	7.48	6.95	0.235	96.5	44.64	4.37	0.8
5km from PA	40	7.94	7.36	0.221	37.5	46.8	3.63	2.0
Kišnica	20	2.84	2.74	0.014	2.2	0.45	0.75	1.2
polluted area-PA	40	2.94	2.74	0.014	2.2	0.10	0.47	2.0
Gračanica	20	7.54	6.91	0.155	61	54.31	2.36	0.8
5 km from PA	40	7.87	7.63	0.157	60	41.95	2.43	0.8

50 - amount of the filtrate used for titration (ml) n- amount of plant material used for the extraction (g) 10- convert in milliequivalent acid solution (1 ml N NaOH corresponding to 0.1 mEkv of acid)

Statistical analysis. We performed two independent experiments. Data are reported as means ± SD. Statistical significance was evaluated with Student's t-test, and considered to be significant when the P value was less than 0.05.

RESULTS AND DISCUSSION

Soil substrates analysis. Landfills (soil substrates) were characterized by low levels of macronutrients, poor substrate structure and high levels of heavy metals.

The pH of the soil is one of the parameters that significantly affects the share of bioavailable forms of nutrients. High alkalinity was registered in fly ash substrate (pH=8.05 in KCl) from Kosovo B-landfills. The pH value decreased in the soil with increasing distance from the source of contamination. In the Plemetina village, 5 km away from the Kosovo B TPP, the pH value of the soil was 6.95. On the contrary, in the Kišnica landfills the pH value of landfills was extremely acidic with a pH of 2.74 in KCl.

During stabilization, the fly ash becomes hydrated and carbonated. These processes turn reactive CaO and $Ca(OH)_2$ into $CaCO_3$, which decreases the alkalinity. Plants can not grow into fresh ash, even in porous layers, while aged ash prevents root growth, particularly when hardened to a high density.

However, fly ash also contains most of the essential elements for plant growth, e.g. N, P_2O_5 and K_2O, and can have positive effects on plants after becoming stabilized.

Concentrated fly ash generally harms plants, due to high levels of metals [9], or high alkalinity [10]. Stabilized fly ash has been recommended for use in forestry, especially in acidic soils, where it can increase available P, Ca, Mg, K and B, as well as decrease toxic effects of Al and Mn by raising the pH [11].

Bioavailability of metals plays a key role in risk assessment for metal contaminated sites such as highly industrialized areas under former and present pressure of metal – ore mining and smelting industry. Metal availability likely depends on metal source and on the form of the metal that enters the soil, as well as duration of presence in soil substrate. Total concentration of anthropogenic metal (Pb, Ni, Zn, Cu) originating from metallurgical dusts, were lower in the top–surface soil compared to the sub–surface soil. Metal speciation was found to depend strongly on soil properties and metal origin. The concentration of heavy metals increased in the soil substrate with increasing depth.

The mean total concentrations of trace metals in the soil substrate from Kišnica tailings, ranked as follows: Pb>Cr >Zn> Ni> (see Table 2). Some of the concentrations exceeded the permissible limits for trace metals in agricultural soils. For instance, the total Cr concentration ranged from 293.6 to 301.2 ppm (Table 2). Similarly, the total Pb concentrations ranged from 159.80 to 168.70 ppm. Their permissible limits are 150 mg/kg ppm for Cr, and 300 mg/kg ppm for Pb, respectively. Concomitantly, the Pb content in soil substrate from Gračanica was found to be very high, ranging from 493.10 to 550.90 ppm. The soil samples from Gračanica were also found to have excessively high levels of Al (450.5 – 488.3%). Kosovo B landfills are sources of easily resuspended ash particles. These particles contain pollutants such as sulfur (S). The S content was much elevated (2.24%) compared to increasing distance from the source of contamination (Plemetina - 0.0108%), particularly in the surface layer (20 cm).

Loading and accumulation of heavy metals in the soil depend on different factors such as the chemical form of elements, pH, organic matter content, texture and cation exchange capacity (CEC) of the soil. With increasing pH, organic matter content, CEC and clay, the percentage and availability of the metals are reduced [1].

Heavy metal uptake by plants is performed constantly during their vegetation period and during the year. The uptake reaches its highest value at the end of the vegetation period. Only 1% or less of the total plant body accumulates heavy metals. Some of these elements are present in the protein structure in high amounts and play essential roles in protein structures, especially in enzymes. It is established that heavy metals cause morphological, physiological and biochemical changes in plants [12]. However, the presence of heavy metals in the environment of plants is a kind of stress that will lead to physiological changes and also decrease the physiological abilities of plants [13].

Heavy metal accumulation (Pb, Cd, Zn, and Cn) in early vegetables is greater in plants from the contaminated area of Leskovac, compared to control plants from the less polluted area of Donja Stopanja. The distribution of heavy metals in leaves and roots of vegetables is uneven. Heavy metals (Pb, Cd, Zn and Cn) are accumulated in the roots rather than the leaves of early vegetables. The largest accumulation of Pb was measured in the root of lettuce at 2.17 mg/kg, which is 10,33 times more than the control. In the root of onions the Pb levels were 6,79 mg/kg, and in the control the concentration was 1,73 mg/kg. High concentrations of the essential elements Zn and Cn were measured in the roots of onions (6,79 mg/kg, the control was 1,73 mg/kg) [14]. The heavy metal contents (Pb, Cd, Zn, and Cn) in the leaves of the examined vegetables were lower compared to the roots, but overall higher compared to the control. The roots of lettuce and onions show a great cumulative value for the accumulation of heavy metals (Pb, Cd, Zn, Cn). The great cumulative capacity of the roots for heavy metals is a mechanism by which the plant protects its surface organs from the higher concentration of heavy metals in the environment. The measured values of the heavy metal (Pb, Cd, Zn, Cn) levels in the studied vegetables (lettuce, spinach, onions) from the contaminated area of Leskovac were all above the maximum allowed contamination values thus these vegetables cannot be consumed [14].

Seed germination. Lettuce and radish seeds generally lose their biological characteristics within a short time. This influences the plant's genetic characteristics and storage conditions. Radish seeds generally have a 1000-seed weight of between 6.3-10 g, whereas lettuce seeds have an absolute mass of 1.4-2 g and they need quite well-prepared seed beds for production. Therefore, when sowing is done in mellowed soils in a shallow fashion, germination and emergence rates will be quite low. Similarly, since seed vigor is lost rapidly, radish and lettuce seeds should be preserved under controlled conditions. Therefore, water is often used to improve the seed vigor. This study was conducted under controlled conditions in a plastic house in Plemetina, and aimed to investigate the effects of different polluted soils on germination of two vegetable species, radish and lettuce.

The results in this study showed that the percentage of seed germination and growth of test plants were different, and depended both on the seed specificity and concentration of pollutants from the investigated soil substrate. During germination differences were observed in seed germination, length of leaves, and in the shoot height of plants planted in the different soil substrates (data not shown).

The highest germination of radish seeds after 4 days of sowing was observed in soil originating from Gračanica (at 40 cm depth), which is 105.5% higher than in control, and the minimum germination observed in tailings from Kosovo B (sample substrate tailings at 20 cm depth) 70.7% low compared to the control.

The highest germination of lettuce seed after 7 days of sowing was observed from the Plemetina garden soil (at 20cm depth), 153.4% greater than in control soil, while the lowest germination rate was registered in the tailings from Kosovo B (sample of the substrate at 20cm depth), 43.1% less than control (Lipljan garden soil).

TABLE 2
Content of heavy metals in soil (depth 20-40 cm) in Kosovo B and Kišnica (polluted area); Plemetina and Gračanica (5km from pollution area) and Lipljan (20km from polluted area- Control)

Target area	ppm							%	
	Cd	**Cr**	**Pb**	**Ni**	**Zn**	**Cu**	**Al**	**S**	**Fe**
Control-area	0.9	-	44.17	-	59.6	11.28	-	-	-
Lipljan- 20 km from PA	1.0	-	52.30	-	49.1	14.9	-	-	-
Kosovo B	0.2	-	4.70	-	8.50	4.5	-	2.242	-
polluted area-PA	0.2	-	7.10	-	11.80	8.1	-	0.274	-
Plemetina	0.3	-	52.50	-	32.30	18.2	-	0.0108	-
5km from PA	0.3	-	50.90	-	32.20	22.3	-	0.0670	-
Kišnica	-	293.6	159.80	4.80	49.7	4.7	1.23	-	0.92
polluted area-PA	-	301.2	168.70	5.10	53.4	5.6	1.27	-	0.45
Gračanica	1.5	137.9	493.10	59.10	62.4	25.3	450.5	-	0.43
5 km from PA	1.6	149.1	550.90	67.80	62.8	27.7	488.3	-	0.45

TABLE 3
The influence of soil pollution on the seed germination under experimental condition

Vegetable species	Radish (*Raphanus sativus* L.)				Lettuce (*Lactuca sativa*)			
Soil depth	20cm	40cm	20cm	40cm	20cm	40cm	20cm	40cm
	% germination		compared to the control		% germination		compared to the control	
Control-area Lipljan- 20 km from PA	89a	90a	100	100	58b	49b	100	100
Kosovo B polluted area-PA	64b	76b	70.7	81.1	25c	35c	43.1	71.42
Plemetina 5km from PA	93a	79b	104,4	87.7	89a	72b	153.4	146.9
Kišnica polluted area-PA	89a	90a	100	100	-	-	-	-
Gračanica 5 km from PA	93a	95a	104.4	105.5	39c	49b	67.2	100

Values followed by the same letter do not significantly differ between the treatments, at P = 0.05

The amount of required seeds for sowing to achieve the best uniformity and complete land coverage depends, to a great extent, on the type of metal pollutant in the germination medium or in the irrigation water, as well as on the concentrations of metal pollutants around the seed. In conclusion, metal salt stress can act on seeds in two ways; first by preventing water uptake by seeds, and second by providing conditions for the entry of metal ions that may be toxic to the embryo [15].

The effects of metals on seed germination from different plants depend on interspecies differences in seed structure, particularly seed coats, as seed coats have a wide range of anatomic forms that exist in no other plant organ or tissue [16]. Increasing concentrations of lead inhibited seed germination and early growth of carrot and lettuce seedlings. The seed coat accumulated significant amounts of Pb and represents a protecting layer for the seed embryo. A greater surface area to volume ratio in small seeds permits them to have access to a greater amount of lead than larger seeds, which means they will accumulate more lead [15].

Numerous studies have been carried out on seed germination and seedling growth of different plant species exposed to heavy metals [17; 18; 19]. The decrease in seed germination is attributed to the heavy metal treatment [20, 21]. Seed germination is one of the most highly sensitive physiological processes in plants because of its vulnerable defense mechanism during imbibition [22]. It is reported that seed germination is severely disturbed by metal stress, such as Cu, aluminum (Al) and cadmium (Cd) [23]. Hydrolases, such as a-amylase, play an important role in the late stage of germination and are significantly reduced by Cu treatment [24].

The antioxidant enzyme catalase, which allows the tolerance of plant under stress conditions is also claimed to be effective in the physiology of germination [25]. CAT activity in seeds and seedlings is also involved in the preservation of viability during storage, and is necessary for seed germination and early seedling growth [26]. CAT activity in seeds may serve as a parameter that indicates the germination capacity [27]. There are several studies about changes of enzyme activity that is related to germination, development and tolerance of plants. It was shown that germination is correlated closely with the catalase activity [28].

Genetic and environmental factors influence seed growth and development. When environmental factors exceed the tolerance of a plant, reactive oxygen species (ROS) are generated in the cell [29]. ROS affect various aspects of seed physiology. Antioxidants which act as ROS scavengers in seed biology play a very important role in the growth processes during seed development. Some protective mechanisms involving ROS scavenging enzymes, the aforementioned CAT being one, have been evaluated within the mechanism of seed germination [30].

Catalase activity. The significant increases observed in catalase activity may be due to H_2O_2, which is one of the ROS produced in response to different environmental stresses, including heavy metal stress. There is a significant reduction of germination caused by this type of stress.

Based on the results of the catalase activities during day and night time, we noted that at the time of germination (time zero) in the radish, the largest catalase activity was recorded in plants germinated on the substrate tailings from Kišnica (40cm depth). The CAT activity was 277.2% compared to control at day 0, and at 157% of control after 7 days.

The catalase activity in radishes decreases 14 days after germination (20 cm depth) compared to control, in plants grown on substrate tailings from Kosovo B. Eight days after germination of radish seeds we found that all seedlings on the substrate tailings from Kišnica (20 and 40 cm depths) had dried, thus we did not have any samples for further testing.

TABLE 4
Daily catalase activity (cm^3 O_2/1gr/ 3') in the radishes at day of germination (1), 7, 14, 21 and 28 days during vegetation

Days after germination	Target area	Catalase activity of radish plants at 6^h the morning				Catalase activity of radish plants at 18^h afternoon			
		cm^3 O_2/1gr/ 3'		% of catalase activity compared to the control		cm^3 O_2/1gr/3'		% of catalase activity compared to the control	
	Soil depth	20 cm	40 cm	20cm	40 cm	20 cm	40 cm	20 cm	40 cm
1 day	Control-Lipljan	24	32.2	100	100	22	29.9	100	100
	Kosovo B	59.4	74	247.5	229.8	56	71	254.5	237.4
	Plemetina	52	69	216	214.2	49.9	67.8	226.8	226.7
	Kišnica	64	68	266.6	211.1	61	64	277.2	214
	Gračanica	42	67	175	208	41	64	186.3	214
7 day	Control-Lipljan	23	28	100	100	21	26	100	100
	Kosovo B	34	29	147.6	103.5	31	26	147.8	100
	Plemetina	35	37	152.3	132.1	32	35	152.1	134.6
	Kišnica	40	31	180	110.7	37.8	28,8	173.9	110.7
	Gračanica	35	43	157,6	153.5	33.1	41.6	152.1	160
14 days	Control-Lipljan	27.7	29.9	100	100	23.7	26.9	100	100
	Kosovo B	24	25	86.6	83.6	21	22.2	88.6	82.5
	Plemetina	28	29	101	96.9	25	26	105.4	96.6
	Kišnica								
	Gračanica	30	33.9	108.3	113,3	27	30.9	113.9	114.8
21 days	Control-Lipljan	29	27	100	100	27	25	100	100
	Kosovo B	23	22	79.3	81.4	22	20	81.4	80
	Plemetina	31	32	106.8	118.5	29.7	30	110	120
	Kišnica	-	-	-	-	-	-	-	-
	Gračanica	39.1	38.7	134.8	143.3	37.3	36.4	140.7	145.6
28 days	Control-Lipljan	30	28	100	100	28.6	26.1	100	100
	Kosovo B	24	24	80	95.7	22	21.9	76.9	83.9
	Plemetina	33	34	110	121.4	31	32.4	108.3	125.8
	Kišnica	-	-	-	-	-	-	-	-
	Gračanica	40.5	40.9	135	146	38.9	37.8	136	132.5

In the radish plants roots, the catalase activity was 114.8% of control 14 days after germination in soils from Gračanica, 145% of control at day 21, and 147.7% of control at day 28, which indicates an increase in catalase activity during plant growth.

Based on the results of the CAT activities during day and night time for lettuces, at the time of germination (day 1, the highest CAT values were observed in plants that had germinated in soil originating from Plemetina (20cm depth). The catalase activity was 152.1% compared to control (Table 5). After 7 days of germination, the catalase activity was 157.1% compared to control. The catalase activity in radish and lettuce seedlings grown in soil substrate of Plemetina, particularly in the early development stages (days 7 and 14), had the highest values probably because the soil is dominated by sulfur and not heavy metals pollutants.

Catalase is an enzyme that plays a part in the plants' defense from pollution. The activity of catalase is different in the subterranean part of the plant compared to the above ground plant parts in the examinated plants, and there are also species differences. Cat activity depends on the plant species, on the concentration of pollutant and on the period of lifecycle in their own surrounding. Catalase is part of a specialized defense mechanism that degrades harmful metabolites, which arise from pollution, into innocuous by-products [31]. Considering all the results and data presented in this study, we believe that the defensive power of plants are genetically predetermined and specific to a given species. These conclusions were based on our research, as well as data from published literature. We believe that catalase is part of the protective defense mechanisms of plants against the toxic effects of reactive oxygen species, which are formed at the interaction with cellular toxicants envelope and cell membranes. An increased catalase activity in different organs of the plant, under conditions of environmental pollution, is a detoxification mechanism whereby the plant acquires resistance to the stressor.

Organic acids content. Our results show that the organic acid content differs in the overhead and underground parts of the plant, and is determined by the plant species, as well as the soil substrate. The content of organic acids was measured during growth in radishes and lettuce plants, at days 7, 14, 21 and 28 after germination (Table 6).

TABLE 5
Daily catalase activity (cm^3 O_2/1gr/ 3') in the lettuce at days 0 (germination), 7, 14, 21 and 28 days during vegetation

Days after germination	Target area	Catalase activity of lettuce plants at 6^h the morning				Catalase activity of lettuce plants at 18^h afternoon			
		cm^3 O_2/1gr/ 3'		% of catalase activity compared to the control		cm^3 O_2/1gr/ 3'		% of catalase activity compared to the control	
	Soil depth	20 cm	40 cm	20cm	40 cm	20 cm	40 cm	20 cm	40 cm
1 day	Control-Lipljan	27.1	23.2	100	100	25.3	21.3	100	100
	Kosovo B	35.2	25.1	129.8	108.6	33.2	23.9	131.2	112.2
	Plemetina	40	22	147.6	94.8	38.5	21	152.1	98.5
	Kišnica	-	-	-	-	-	-	-	-
	Gračanica	34	23.4	125.4	100.8	31	21.9	122.5	102.8
7 day	Control-Lipljan	36	40	100	100	34	38	100	100
	Kosovo B	49	39.9	136.1	99.7	47	37	138.2	97.3
	Plemetina	38.5	35.6	106.9	89	35	33	102.9	86.8
	Kišnica	-	-	-	-	-	-	-	-
	Gračanica	39	40.5	108.3	101.2	37	38.1	108.8	100.2
14 days	Control-Lipljan	35	32.1	100	100	32	30.1	100	100
	Kosovo B	26.8	27.9	76.5	86.9	23.8	24.9	74.3	71.1
	Plemetina	50	43.8	142.8	136.4	47	41.8	146.8	127.7
	Kišnica	-	-	-	-	-	-	-	-
	Gračanica	38	41	108.5	127.7	35	38	109.3	126.2
21 days	Control-Lipljan	36.5	35.1	100	100	34.9	33.1	100	100
	Kosovo B	32	34	87.6	96.8	30	32	85.9	96.6
	Plemetina	61	64	167.1	182.3	59	61	169	184.2
	Kišnica	-	-	-	-	-	-	-	-
	Gračanica	63.5	64.2	173.9	182.9	61.1	62.2	175	187.9
28 days	Control-Lipljan	38	37	100	100	36	34	100	100
	Kosovo B	34	36	89.4	97.2	31	33	86.1	97
	Plemetina	63	66	165.7	178.3	61	63	169.4	185.2
	Kišnica	-	-	-	-	-	-	-	-
	Gračanica	65	66.9	171	180.8	62	63.3	172.2	186.1

TABLE 6
Content of organic acids (mEkv/g fresh weight) in the overhead and underground organs radishes at days 7, 14, 21 and 28 after germination.

Days after germination	Target area	Content of organic acids in the underground organs of radish plants				Content of organic acids in the overhead organs of radish plants			
		mEkv/gr		% of organic acid compared to the control		mEkv/gr		% of organic acid compared to the control	
	Soil dept	20 cm	40 cm	20cm	40 cm	20 cm	40 cm	20 cm	40 cm
7 day	Control-Lipljan	19.68	24.6	100	100	15.74	19.68	100	100
	Kosovo B	29.52	31.48	150	127	24.6	31.48	156.2	156.2
	Plemetina	24.60	24.60	125	100	19.68	24.6	125	125
	Gračanica	29.52	27.55	150	111.9	31.48	33.45	**200**	169.9
14 days	Control-Lipljan	24.6	29.52	100	100	19.68	24.6	100	100
	Kosovo B	29.52	31.48	120	106.6	35.42	39.36	179,9	160
	Plemetina	29.52	29.52	120	100	31.48	35.42	156,2	143.9
	Gračanica	35.42	39.36	143.9	133.3	35.42	39.36	179,9	160
21 days	Control-Lipljan	24.60	27.55	100	100	24.6	27.55	100	100
	Kosovo B	29.52	31.48	120	114.2	35.42	39.36	143.9	120.1
	Plemetina	27.55	29.52	111.9	107.1	31.48	35.42	150	128.5
	Gračanica	70.85	78.72	**288**	**285.7**	78.72	78.72	**320**	288
28 days	Control-Lipljan	31.48	33.45	100	100	31.48	33.45	100	100
	Kosovo B	39.36	39.36	125	117.6	39.36	39.36	125	117.6
	Plemetina	35.42	35.42	112.5	105.8	35.42	39.36	112.5	117.6
	Gračanica	39.36	59.04	125	176.5	78.72	98.4	**250**	**294.1**

TABLE 7
Content of organic acids (mEkv/g fresh weight) in the overhead lettuce leaves 7, 14, 21 and 28 days after germination

Days after germination	Target area	Content of organic acids in the overhead organs of green lettuce plants			
		mEkv/gr		% of organic acid compared to the control	
		20 cm	40 cm	20 cm	40 cm
7 days	Control-Lipljan	15.74	19.68	100	100
	Kosovo B	27.55	29.52	175.0	150
	Plemetina	24.60	27.55	156.2	139.9
	Gračanica	33.45	35.42	212.5	179.9
14 days	Control-Lipljan	24.60	27.55	100	100
	Kosovo B	33.45	35.42	135.9	128.5
	Plemetina	27.55	29.52	111.9	107.1
	Gračanica	35.42	39.36	143.9	142.8
21 days	Control-Lipljan	27.55	29.52	100	100
	Kosovo B	35.42	39.36	135.9	133.3
	Plemetina	31.48	35.42	114.2	119.9
	Gračanica	70.85	78.72	**257.1**	**266.6**
28 days	Control-Lipljan	31.48	33.45	100	100
	Kosovo B	59.04	59.04	187.5	176.5
	Plemetina	35.42	39.36	112.5	117.6
	Gračanica	59.04	59.04	187.5	176.5

From these results it is evident that the content of organic acids is lower in the roots than in the shoots. Additionally, we note that the concentration of the polluted substances is greater, and plants grown in this soil have an increased content of organic acids. The highest content of organic acids in the above ground organs was measured after 21 days in plants of radishes (78.72 mEkv/gr) grown in soil from Gračanica (40 cm), which was 285.7% compared to control. On the other hand, the lowest organic acid content in the above-ground plant organs was measured in a soil sample from Plemetina, with no difference observed compared to control (Table 7). This result was expected, since the soil is dominated by sulfur and not by heavy metals pollutants.

The content of organic acids in the roots is lower compared to the overhead portion. The highest content was noted in radishes after 21 days, which have been grown in soils originating from Gračanica (20 cm) and was 320.0%, compared to control. The roots and shoots of radishes in our experiments appear as the protective part of the plants because of polluting substance is likely to accumulate in the roots of plants and shoot, and hence the rapid metabolism of organic acids that bind heavy metals and thus reduce their toxicity and the plants develops normally.

Organic acids are used as proton donors (H^+) in the oxido-reduction processes. Therefore, organic acids can form chelate complexes with heavy metals, which are stored in the plant vacuoles and become non-toxic to the plants. Increasing the concentration of organic acids in plant organs vegetable crops is one way the plants can defend against toxicants by forming detoxication conjugations with heavy metals.

The highest content of organic acids in the leaves (over heads organs) was measured after 21 days in lettuce grown into soil originating from Gračanica (40 cm) which was 266.6% compared to control. On the other hand, the minimum content of organic acids in the lettuce leaves was measured in soil from Plemetina which was only 7.1% higher compared to control.

The content of organic acids is different in some organs and plants. The largest amounts of organic acids are found in the root of an onion, with 280% more than in the controlled plant, and then, in the root of green beans, with 137% more than in the controlled plant. The root acts as a protection for the above ground part of the plant in the conditions of the polluted environment. As far as potato plants are concerned, the content of organic acids is enlarged in every organ of the plant. Potato belongs to the group of plants tolerant to pollution. The increased content of organic acids results in the reduction of toxicity of heavy metals because they can from chelating complexes [32]. An increased content of organic acids in the overhead and underground parts of plants that grow in soil environment tailings can be interpreted as a defense mechanism of toxicants.

CONCLUSION

Experiments have been conducted under greenhouse conditions with short-life vegetable plants (radish and lettuce) growing in tailing substrates in small containers. Acidic environment

(tailings from Kišnica at pH 2.74) is an important requirement for faster penetration of lead into the seed that ultimately inhibits lettuce germination. Radishes in early phases of growth are characterized by the highest tolerance to toxic concentrations of heavy metals compared to lettuce plants. Plants under stress activate defense mechanisms to protect themselves against the harmful effect of polluted stress. In polluted conditions, the stress altered the antioxidant enzyme activities such that catalase activity and organic acid content was increased compared to control. The long-term activities of mining and smelting in the area of central Kosovo have a great impact on physiological and biochemical processes in the studied plants, and by extension more importantly also on the public health.

ACKNOWLEDGEMENTS

The authors have declared no conflict of interest.

REFERENCES

[1] Filipović-Trajković, R., Ilić, S.Z. and Šunić, L. (2012) The potential of different plant species for heavy metals accumulation and distribution. Journal of Food, Agriculture and Environment. 10(1), 959-964.

[2] McGrath, S.P., Zhao, F.J. and Lombi, E. (2001) Plant and rhizosphere process involved in phytoremediation of metal-contaminated soils. Plant Soil. 232(1-2), 207-214.

[3] Bhaduri, A.M. and Fulekar, M.H. (2012) Antioxidant enzyme responses of plants to heavy metal stress. Reviews in Environmental Science and Bio/Technology. 11, 55-69

[4] Willekens, H., Inze, D. and van Montagu, M. (1995) Catalases in plants. Molecular Breeding. 1, 207-208.

[5] Nan, R.-Z. and Fan, Y.-X. (2008) Advance of researches on catalase in plants. Anhui Agricultural Science Bulletin. 14(5).

[6] Ilić, Z. and Filipović, R. (2004) Catalase enzyme activities in different tissues on vegetables plants in basin irrigation with waste waters. 3rd Balkan Symposium on Vegetables and potatoes. 6-10 September. Bursa-Turkey. Book Procced. 30

[7] Lopez-Bucio, J., Fernanda Nieto-Jacobo, M., Ramirez-Rodriguez, V. and Herrera-Estrella, L. (2000) Organic acid metabolism in plants: from adaptive physiology to transgenic varieties for cultivation in extreme soils. Plant Science. 160, 1-13.

[8] Pleshkov, B.P. (1985) Workshop on plant biochemistry. Moscow: Kolos. (in Russian).

[9] Tripathi, R.D., Vajpayee, P., Singh, N., Rai, U.N., Kumar, A., Ali, M.B., Kumar, B. and Yunus, M. (2004) Efficacy of various amendments for amelioration of fly-ash toxicity: growth performance and metal composition of Cassia Siamea Lamk. Chemosphere. 54, 1581-1588.

[10] Gupta, E.K., Rai, U.N., Tripathi, R.D. and Inouhe, M. (2002) Impacts of fly-ash on soil and plant responses. Journal of Plant Research. 115, 401-409.

[11] Demeyer, A., Voundi Nkana, J.C. and Verloo, M.G. (2001) Characteristics of wood ash and influence on soil properties and nutrient uptake: An overview. Bioresource Technology. 77, 287-295.

[12] Woolhouse, H.W. (1983) Toxicity and tolerance in the response of plants to metals. In: Encyclopedia of Plant Physiol. New Series, Vol. 12 C, Springer-Verlag, New York; Heidelberg, Berlin, 246-289.

[13] Baker, A.J.M. and Brooks, R.R. (1989) Terrestrial higher plants which hyperaccumulate metallic elements: A review of their distribution, ecology and phytochemistry. Biorecovery. 1, 81-126. Cai, F., Mei, L.-J., An, X.L., Gao, S., Tang, L. and Chen, F. (2011) Lipid peroxidation and antioxidant responses during seed germination of Jatropha curcas. International Journal of Agriculture and Biology. 13, 25.

[14] Trajković, R., Krsmanović, M., Bogdanović-Dušanović, G. and Tošić, S. (2005a) Heavy metals' accumulation and distribution in tissues and organs of vegetables originating from Leskovac. Ecolst '05, Ekološka istina / Ecological truth, Bor. Book of Procced. 293-297.

[15] Ilić, S.Z., Mirecki, N, Filipović-Trajković, R., Kapoulas, N., Milenković, L. and Šunić, L. (2015) Effect of Pb on seed germination and his translocation in different seed tissues during sprouting. Fresen. Environ. Bull. 24, 670-675.

[16] Wierzbicka, M. (1988) Mitotic disturbance induces by low doses of inorganic lead. Caryologia. 41, 143-160.

[17] Marques, A.P.G.C., Rangel, A.O.S.S. and Castro, M.L. (2007) Effect of arsenic, lead and zinc on seed germination and plant growth in black nightshade (*Solanum nigrum* L.) vs. clover (*Trifolium incarnatum* L.). Fresen. Environ. Bull. 16, 896-903.

[18] Ozdener, Y. and Kutbay, H.G. (2009) Toxicity of copper, cadmium, nickel, lead and zinc on seed germination and seedling growth in Eruca sativa. Fresen. Environ. Bull. 18, 26-31.

[19] Ling, T. and Jun, R. (2010) Effect of Hg on seed germination, coleoptile growth and root elongation in seven pulses. Fresen. Environ. Bull. 19, 1144-1150.

[20] Jamal, S.N., Iqbal, M.Z. and Athar, M. (2006) Effect of aluminum and chromium on the growth and germination of mesquite (*Prosopis juliflora* (Swartz.) DC). International Journal of Environmental Science and Technology. 3, 173-176.
[21] Mahmood, S., Hussain, A., Saeed, Z. and Athar, M. (2005) Germination and seedling growth of corn (*Zea mays* L.) under varying levels of copper and zinc. International Journal of Environmental Science and Technology. 2, 269-274.
[22] Li, W.Q., Khan, M.A., Yamaguchi, S. and Kamiya, Y. (2005) Effects of heavy metals on seed germination and early seedling growth of *Arabidopsis thaliana*. Plant Growth Regulation. 46, 45-50.
[23] Xiong, Z. and Wang, H. (2005) Copper toxicity and bioaccumulation in Chinese cabbage (*Brassica pekinensis* Rupr.). Environment Toxicology. 20, 188–194.
[24] Ahsan, N., Lee, D.G., Lee, S.H., Kang, K.Y., Lee, J.J., Kim, P.J. Yoon HS., Kim, J.S. and Lee, B.H. (2007) Excess copper induced physiological and proteomic changes in germinating rice seeds. Chemosphere. 67, 1182-1193.
[25] Kibinza, S., Bazin, J., Bailly, C., Farrant, J.M., Corbineau, F. and El-Maarouf-Bouteau, H. (2011) Catalase is a key enzyme in seed recovery from ageing during priming. Plant Science. 181(3), 309-315.
[26] Milošević, M., Vujakovic, M. and Karagic, D. (2010) Vigour tests as indicators of seed viability. Genetika. 42(1), 103 -118.
[27] Prodanović, O., Prodanović, R., Bogdanović, J., Mitrović, A., Milosavić, N, and Radotić, K. (2007) Antioxidative enzymes during germination of two lines of Serbian Spruce [*Picea omorika* (PANČ.) PURKYNĚ]. Archives in Biological Science (Belgrade). 59 (3), 209.
[28] Demirkaya, M., Dietz, K.J. and Sivritepe, H.Ö. (2010) Changes in antioxidant enzymes during ageing of onion seeds. Notulae Botanicae Horti Agrobotanici Cluj-Napoca. 38(1), 49-52.
[29] Chauhan, D.S., Deswal, D.P., Dahiya, O.S. and Punia, R.C. (2011) Change in storage enzymes activities in natural and accelerated aged seed of wheat (*Triticum aestivum*). Indian Journal of Agricultural Sciences. 81 (11), 1037-1040.
[30] Ishibashi, Y., Yamamoto, K., Tawaratsumida, T., Yuasa, T. and Iwaya-Inoue M. (2008) Hydrogen peroxide scavenging regulates germination ability during wheat (*Triticum aestivum* L.) seed maturation. Plant Signaling and Behavior. 3(3), 183-188.
[31] Nešić, M., Trajković, R., Tošić, S., Marković, M. (2005) Influence of air pollution on enzym catalase activity in herb's tissues in environmental of Pirot. 8th Symposium on the flora of southeastern Serbia and Neighboring Regions, Nis. Book of Abstract. 98p.
[32] Trajković, R., Bogdanović-Dušanović, G., Babović-Đorđević, M. and Jakšić, T (2005a) The content of organic acids in the leaf, tree and root of the vegetable plants originated from Kosovska Mitrovica. Ecolst '05, Ekološka istina/Ecological truth, Bor. Book of Procced. 293-297.

Received: **28.09.2018**
Accepted: **08.02.2020**

CORRESPONDING AUTHOR

Zoran S Ilic
University of Priština-Kosovska Mitrovica,
Faculty of Agriculture
Priština-Lešak, 38219 Lešak – Serbia

e-mail: zoran.ilic63@gmail.com

© by PSP Volume 29 – No. 04A/2020 pages 2626-2631 Fresenius Environmental Bulletin

COMPETITION FOR CONSERVATION: OBSERVATION OF 1ST PRUSSIAN CARP *CARASSIUS GIBELIO* (BLOCH, 1782) CATCHING COMPETITION IN GOKPINAR DAM POND (DENIZLI/TURKEY)

Esat Tarik Topkara[1,*], Bahar Bayhan[2], Hulya Saygi[3]

[1]Ege University, Faculty of Fisheries, Department of Marine–Inland Waters Sciences and Technology, Inland Waters Sciences Section, 35100 Izmir, Turkey
[2]Ege University, Faculty of Fisheries, Department of Marine–Inland Waters Sciences and Technology, Fisheries Biology Section 35100, Bornova, Izmir, Turkey
[3]Ege University, Faculty of Fisheries, Aquaculture Department, Aquaculture Section, 35100 Bornova, Izmir, Turkey

ABSTRACT

In this study, it was aimed to examine socio-economic conditions and reasons for participating in the 1st Prussian Carp Catching Competition, organized by Denizli Amateur Sportive Hand-line Fishers and Fishery Protection Association (DENOLDER) in Denizli Gökpınar Dam Pond. This organization, supported by Amateur Sportive Hand-line Fishing Federation and Denizli Metropolitan Municipality, has the purpose of introducing, ingratiating and binding hand-line fishing fanciers, also additionally and most importantly, raising awareness in the society for damages of ecologically harmful species to aquatic life, in our inner waters. A questionnaire was used, in order to conduct a direct interviewing of the individuals participating in the 1st Prussian Carp Catching Competition, and the original study data was obtained. The questionnaire consisted of 23 questions. The questionnaire results were evaluated, using The Statistical Package for the Social Sciences (SPSS) and EXCEL package programs. In total, 49 individuals filled in the questionnaire, in this competition, with a participation of 55 teams from six provinces. Moreover, all teams indicated that they would participate again, in case of a repetition of such an organization. It is essential to protect fishes, having an important place within fishery products, particularly natural species. It should be our responsibility to raise public awareness relating to invasive species.

KEYWORDS:
Prussian carp, *Carassius gibelio*, Invasive fish, Amateur Fishing Competition, Gökpınar Dam Pond, Denolder

INTRODUCTION

Amateur fishery is defined as an activity of fishery which is performed only for recreational, sportive and relaxing purpose, and which does not have any economic and commercial gain, meaning the fishing product is not being sold. Tourism and recreational activities are important elements, bringing new income opportunities and economic activities to rural areas, elsewhere [1, 2]. Amateur Fishing Competition is defined, as due to the rules introduced by this bulletin, an awarded competition, performed by public institutions, amateur fishing associations or federations, organized by amateur fishers, to encourage and improve amateur fishing. The Amateur Sportive Hand-line Fishing Federation (ASOF) was organized by the contribution of seven founder associations, in 21.05.2014 in Ankara [3]. According to the data we derived from the web page of the Ministry of Agriculture, there are 19 amateur fishery associations existing in Turkey, which are increasing rapidly day by day.

In recent years, regular or irregular amateur fishery competitions on inland waters or seas, are being organized by not only amateur fishery rod associations, but also by private associations and local governments. As a result of these competitions, the participants who are ranking first (the most amount of fish/ the biggest fish/ the most species fish etc.), are rewarded with various prices.

A considerable part (8%) of the world's fish is part of the Cyprinidae family, making it the largest fresh water fish family [4]. On the other hand, since Prussian Carp is an invasive species and it causes the decrease of an amount of fish populations day by day. These fish are not released into the water, instead, they are all being eliminated, when they are caught. Prussian Carp is known as "İsrail Sazanı" in Turkey. Prussian Carp is widely distributed and commonly stocked together with *Cyprinus carpio* which is transported throughout Europe [5]. According to Elgin et al. [6], it has also been sighted in inland waters of North America. However, Prussian Carps are not living in the northern Baltic basin, Iceland, Ireland, Scotland and Mediterranean Islands [6, 7]. Since Prussian Carp is an invasive and fast reproducing species, it dominates its habi-

tat within a short period of time. It prevents the other living-beings in its environment, from reproducing and developing. Therefore, it creates serious damages to endemic and economical fish species. Amateur fish hunting competitions are held to draw attention to this issue.

Worldwide, freshwater ecosystems, areas of brackish water and zones where Mediterranean climate is predominant, are considered as the areas which are the most deficit for invasion. The members of the Cyprinidae family have a short range of reproduction, high efficiency and longevity. For this reason, they are the leaders of the invasive species. (*Cyprinus carpio, Perca fluviatilis, Carassius auratus* e.g.) [8]. Although there have been lots of scientific studies on the transmission and prevalence of the invasive species, there is a limited number of studies on the cleaning basins, which are contaminated by this species [9]. In addition, it is reported that the coordination and control of these nonindigenous species will be the biggest problem that protectionist biologists will face in the upcoming years [10]. One of the methods used to combat invasive species which has become a global problem today, is angling. In Africa [1, 11], Australia [12], Asia and Europe, not only within the scope of a project, but also fishing festivals are held in the form of fishing competitions, supported by local organizations, ensuring the participation of the public to the control of undesirable fish species.

The organization, which is the first national competition to be held on the fishing target of Prussian Carp in Turkey, is organized by Sportive Hand-line Fishers and Fishery Protection Association in the city of Uşak, in Eşme district, Üçpınar (Kolankaya) pond in 2011 (similar competition held later in the same pond in 2012 and 2013)

Two Prussian Carp fishing competitions, first in 2014 and second in 2015, are hold by Konya Amateur Fishery Association (KOABDER) in the pond of Ardıçlı, in the district of Selçuklu in the city of Konya.

Therefore, from past to present, we hope that the method will be widely used in the fight against invasive species in the world and will contribute to management plan strategies, which will be developed in close proximity to the fight against unwanted fish species in our inland waters, by examining all the findings in this organization which has been applied in Turkey.

MATERIALS AND METHODS

The Gökpınar Pond, alias Vali Recep Yazıcıoğlu dam, was built to supply energy and drinking water. The pond area is about 2 km^2, is filled up with rocks and was built in 2002. It is located south-east of Denizli, and it is a dam pond of approximately 10 kilometers to city center of Denizli. In the pond, besides Prussian Carp, there are some other economic fishes (for example wels, common carp). On the other hand, since Prussian Carp is an invasive species and it causes the decrease of the amount of economic fish populations day by day, these fish are not released to the water, they are being eliminated. This species is an omnivorous, feed on plants, benthic invertebrates, detritus and animals [13] and they can reach a maximum of 46.6 cm in total length and a maximum three kilograms of total weight [14, 8].

The competition was conducted pertaining to provisions of notification regulating amateur purposed fishery hunting, numbered 3/2 [16]. A questionnaire was conducted with direct interviewing among those individuals participating in the 1st Prussian Carp Catching Competition in Denizli Gökpınar Dam Pond on 4-5 June 2016, and the original study data was obtained. The participants of the questionnaire were chosen randomly and voluntarily among the competition participants. In these prepared questionnaire forms, in total 23 questions on different toppings such as, on the participants age, also socio-economical questions, such as the profession of the person and information on its fish consumptions, additionally questions relating to amateur fishing, their information about Prussian Carp, types of their baits and fishing rods, their ideas relating to the competition etc., have been asked. As there is no record relating to amateur fishery rate within the whole population in our country, the value of 4.8% indicated for Europe by Pitcher [17] was used in the determination of the sample size. The confidence interval was set as 95% and the margin of error as 10%. In accordance with this sample size equation, the questionnaire study was applied to 49 individuals from a group comprising from 25 teams out of 55. According to the questionnaire study, existence of an hand-line fishing certificate was analyzed by a Chi-square test with Yates' correction for continuity, in accordance with all variables and possibility of error was selected as $\alpha = 0.05$. The questionnaire results were evaluated using The Statistical Package for the Social Sciences (SPSS) and EXCEL package programs.

RESULTS

The questionnaire was conducted with 49 individuals, participating in this competition, in which 55 teams from 6 provinces took part. In total, 83% of the participants were couples, 6% were females, 62.5% were over 36, 77% were married, 37.5% were higher education graduates and 46% were private company employees. About 84.5% had a social insurance, 52.1% were insured by a social insurance institution.

Male individuals make up the majority of the participants (94%). Dissemination of amateur hunting is important to reach a wider audience by increasing the support of female participants in combating invasive species.

77% of the contestants were determined to be married.

In the competition held at Gökpınar Dam Lake, which can be seen in Figure 1, participants from every educational level are involved.

In the competition, it is observed that 63% of individuals were aged 36 and higher and show more interest in the organization. Participants aged 35 and lower, have a 37% turnout (Figure 2).

It was determined that the participants were retired, unemployed and workers at the same rates (17%), of which 30% were private company employees and the rest (19%) were civil servants (Figure 3).

The majority of the competitors (79%) stated that they resided in Denizli province. There have been few out-of-town participations. This is thought to be due to high costs of transportation, accommodation and nutrition.

The Prussian Carp fishing competition is an important organization in terms of encouraging amateur fishing, as well as in order to fundamentally draw attention to invasive species. The vast majority of participants (73%) are aware of this type of fish and are consciously hunting.

Moreover, 79% of the participants participated from Denizli. 25% of the study participants had been interested in amateur fishery for more than 20 years and 75% had an amateur fishery certificate. 73% knew the Prussian Carp, and 96% knew that the species was harmful. The baits used in fishing during the competition were mostly worm, corn and dough. The used fishing rod types were ringed roller rod and different lengths of non-ringed lake rod. The ratio of those participating in such a competition for the first time was only 27%.

Some of the survey questions used in the questionnaire, are given in Table 1.

According to the age and marital status variables of the participants of the survey, there is a statistical difference between having amateur fishing license. ($p<0.05$).

According to this, it is found out that individuals younger than 35 years who are married, have an amateur fishing license.

At the end of the competition, a total of 55 kilograms of Prussian Carp was caught. The first team showed a success of catching a total of five kilos and 590 grams of Prussian Carp. Moreover, all teams indicated that they would participate again in case of a repetition of such an organization.

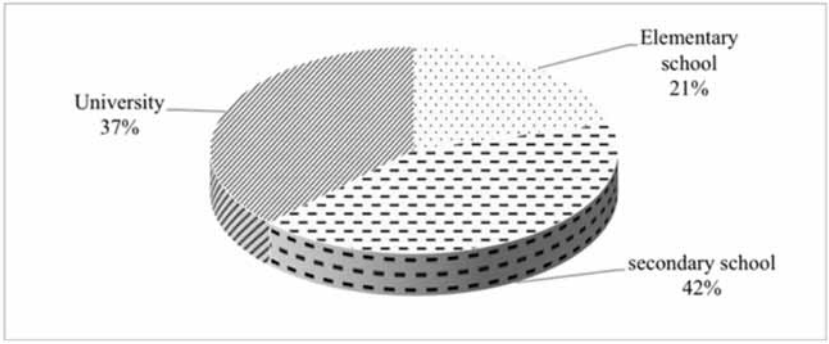

FIGURE 1
Educational levels of the competitors

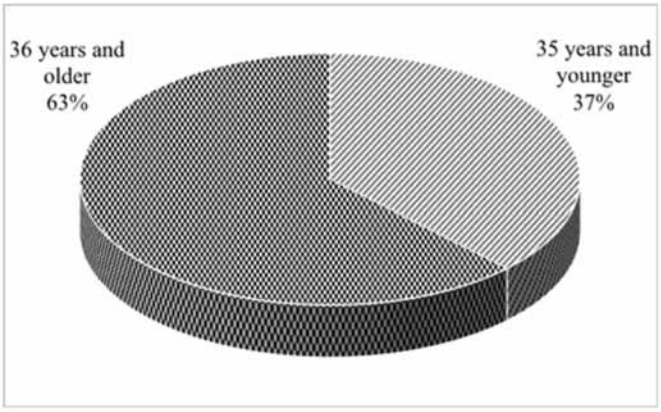

FIGURE 2
Age distributions of contestants

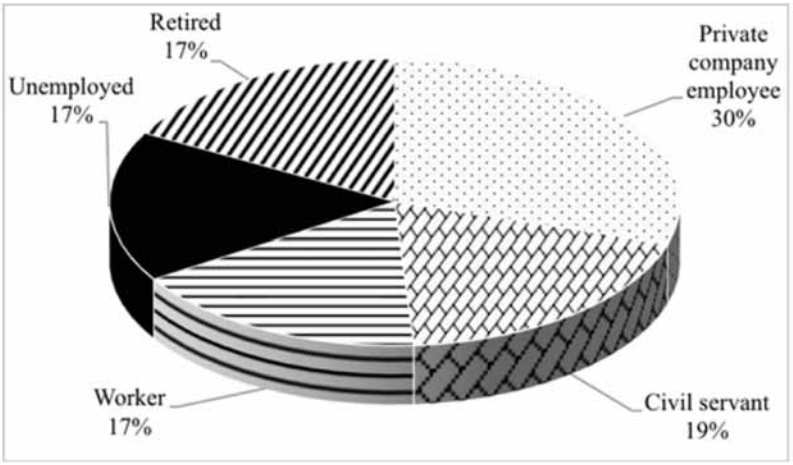

FIGURE 3
Distribution of professions of the competitors

TABLE 1
Some survey questions applied to participants

Variables		Do you have an amateur fishing license?		Chi-square
		Yes	No	
Ages	35 years and younger	10	8	5.087*
	36 years and older	26	4	
Marital statues	Married	31	6	4.757*
	Single	5	6	
Education Level	Elementary education	8	2	1.858^{ns}
	Secondary education	13	7	
	Tertiary education	15	3	
Organization you work	Private	22	13	0.200^{ns}
	Public	8	4	
Social Security	Social insurance institution	18	7	1.720^{ns}
	government retirement fund	8	3	
	social security organization for artisans and the self-employed	10	2	
Income	3000TL and less	26	10	2.541^{ns}
	3001TL and more	18	4	
How long have you been doing amateur fishing?	15 years and less	15	7	2.394^{ns}
	16 years and more	15	2	
Bait you use	Worm	27	7	2.541^{ns}
	Corn	10	2	
	Dough	10	4	
	Other baits	10	6	
Fishing gear you use	Purse seine fishing	24	6	3.221^{ns}
	fishing rod antenna	15	5	
	Fishing rod	7	5	
	Other rods	7	1	
Amount of expenditure made	Less than 1000 TL	27	8	0.3604^{ns}
	More than 1001TL	9	4	

(TL: Turkish Liras; ^{ns} Non significant; * $p < 0.05$)

DISCUSSION AND CONCLUSIONS

Invasive fish species pose a significant threat to fishing, fish farming, and to biodiversity. This threat is occurring through the predation and the invasion of the habitat of the species and can cause a rapid extinction of local and endemic species and lead to an end of fishing production in aquatic ecosystems [18]. It is essential to protect fishes having an important role within fishery products, particularly natural species. It should be our responsibility to raise public awareness in relation with invasive species. The Prussian Carp is left out from all the fishing limits. Thus, whatever their length and the fishing time is, they should not be released into the water again.

The Prussian Carp is an invasive species that has a wide distribution. The species with high tolerance consumes the eggs of other fish species in the

aquatic environment, in which it shows distribution, so it disrupts the balance of the ecosystem.

In the waters outside Turkey, where the species is located, with the handline fishing organizations which are held like a festival for many years, it is being tried to develop a method to deal with the Prussian Carp and create an awareness in the community. For instance, the Carpathon Fishing Competition in United States of America [19] is being performed with the slogan: "*This competition is a perfect opportunity to mix your love of fishing along with getting rid of some invasive pests*". Because it is well known that carp is a pest in the rivers and a highly invasive species which has caused significant ecological damage to their inland waters.

Besides that competitions are held to save the fish species in Zambezi River, which is one of the biggest rivers of Africa [12]. Again, as a result of the findings of the study performed in the same area, showed some ecological and socio-economic impacts of angling competitions [1].

A guide book is prepared to be used in handline fishing which is held for raising social awareness to deal with *Cyprinus carpio.* It shows a distribution in inland waters of Australia. This guide will be a useful reference for any fishing club or other organization, considering hosting a carp fishing competition. It includes scientific knowledge of the habits and ecology of carp and the most efficient ways to target them. It also includes advice from experienced fishing competition organizers, on how to plan and run a public event. The guide explains how to set the objectives of a competition, and how these objectives influence many other aspects of planning, such as the site, timing and size of the event and likely sponsors and prizes. It provides advice on public event advertising, permits and insurance, catering, entertainment, registration systems and crowd control. The aim is to maximize the fishing competition's effectiveness against carp, while ensuring a safe and enjoyable public event that everyone will be keen to do again [13].

The Centre for Environment, Fisheries and Aquaculture Science (CEFAS) is a world leader in marine science and technology, providing innovative solutions for the aquatic environment, biodiversity and food security and has an important place in the studies conducted in Europe. A competition known as the 'Clean Fishing' competition was held between August 2006 and May 2007 in Celtic and Irish seas. The aim of this competition was to encourage south-west beam trawlermen to develop their own technical solutions to reduce unwanted by-catch and discards in their fisheries [20].

As it can be seen, the supporting of activities in fishing of invasive fish species is being performed in many countries for many years. In Turkey such activities can contribute to the preservation of fresh water ecosystems, too.

Besides, we hope that, the suggestions, given as a list below, will be helpful for future organizations.

- Some precautions must be taken about reaching the competition area.
- The official permissions should be taken before the competition.
- The method of fishing should be indicated obviously. The competitors should be informed about the target species.
- The competitors should be asked if they have an amateur fishery license or not.
- If another species of fish which is not the target species is caught, it should be put back before it takes any damage.
- Competitors should take care of the size limits of fishing prohibitions.
- There should be a full-fledged health team and a full-fledged ambulance.
- Authorities should disallow the selling of the fishes, caught during the competition.

As a conclusion, we think that these organizations are essentially important in order to show that it can be dealt with invasive fish species, with the love of fishing.

REFERENCES

[1] Næsje, T.F., Hay, C.J., Kapirika, S., Sandlund, O.T. and Thorstad, E.B. (2001) Some ecological and socio-economic impacts of an angling competition in the Zambezi River, Namibia. NINA•NIKU Project Report. 14, 1–31.

[2] Taylan, B., Sayğı, H., Bayhan, B. and Kaya, M. (2017) Amateur fisheries in the coast of Izmir. Yunus Research Bulletin. 17(4), 335-348.

[3] URL: http://www.asofed.org.tr/24-kurucudernekler.html. Ankara, Turkey. Chairman of ASOF: Mustafa Serkan İnanç.

[4] Dartay, M. and Atessahin, T. (2017) Selectivity of gillnets with different characteristics for *Cyprinus carpio* Liınnaeus 1758 caught in inland waters of Turkey. Fresen. Environ. Bull. 26, 3374-3378

[5] Manasırlı, M., Azgın, C., Özyurt, C.E. and Göksu, M.Z.L. (2019) The growth and mortality rates of Silver Crucian Carp (*Carassius gibelio* Bloch, 1982) in Seyhan Dam Lake (Southeastern Mediterranean Region: Adana, Turkey). Fresen. Environ. Bull. 28, 1667-1675.

[6] Elgin, E.L., Tunna, H.R. and Jackson, L.J. (2014) First confirmed records of Prussian carp, *Carassius gibelio* (Bloch, 1782) in open waters of North America. Bio Invasions Records. 3(4), 275–282.

[7] Balık, İ., Özkök, R., Çubuk, H. and Uysal, R. (2004) Investigation of some biological characteristics of the silver crucian carp, *Carassius gibelio* (Bloch 1782) population in Lake Eğirdir. Turkish Journal of Zoology. 28(1), 19-28.
[8] Froese, R. and Pauly, D. (Eds.) (2018) FishBase. World Wide Web electronic publication. www.fishbase.org, version (06/2018).
[9] Polat, N., Zengin, M. and Gümüş, A. (2011) Invasive fish species and life strategies. The Black Sea Journal of Sciences. 1(4), 63-86.
[10] Stuart, I.G., Williams, A., McKenzie, J. and Holt, T. (2006) Managing a migratory pest species: A selective trap for common carp. North American Journal of Fisheries, Management. 26(4), 888-893.
[11] Allendorf, F.W. and Lundquist, L.L. (2003) Population biology, evolution, and control of invasive species. Conservation Biology. 17(1), 24–30.
[12] Vrdoljak, S.M. (2014) Fish-Friendly competitions: Doing more than just catch-and release. Fishing Reports. Valley Classic © LZCRI, 1-4.
[13] Norris, A. (2011) Guidelines for planning carp fishing competitions. PestSmart Toolkit publication. Invasive Animals Cooperative Research Centre, Canberra-Australia. 1-58.
[14] Specziar A., Tölg, L. and Biro, P. (1997) Feeding strategy and growth of cyprinids in the littoral zone of Lake Balaton. Journal of Fish Biology. 51, 1109–1124.
[15] Verreycken, H., Van Thuyne, G. and Belpaire, C. (2011) Length-weight relationships of 40 freshwater fish species from two decades of monitoring in Flanders (Belgium). J. Appl. Ichthyol. 27(6), 1416-1421.
[16] Official Gazette. (2016) 4/2 circular, Republic of Turkey Ministry of Food, Agriculture and Livestock, General Directorate of Fisheries and Aquaculture. Publish date 18.08.2012, Number: 28388, Procedure No: 2012/66, Ankara
[17] Pitcher, T.J. (1999) Rapfish, a rapid appraisal technique for fisheries, and its application to the code of conduct for responsible fisheries. FAO Fisheries Circular No: 947, Rome, 1-47.
[18] Erdem, Y., Samur, M. and Özdemir, S. (2014) Effectiveness of selective fishing methods on struggle against ınvasive fish species in ınland waters. Istanbul University, Journal of Fisheries and Aquatic Sciences. 29(2), 49-63.
[19] Fishing Competition Information (2018) https://www.5riversoutbackfestival.com.au/-Fishing%20Competition%20Information.pdf Balranald's 5 Rivers Outback Festival. Events Coordinator: Connie Mallet.
[20] Enevert, A., Revill, A. and Grant, A. (2007) Discarding in the English Channel, Western approaches, Celtic and Irish seas (ICES subarea VII). Fisheries Research. 86(2–3), 143-152.

Received: **08.10.2018**
Accepted: **29.01.2020**

CORRESPONDING AUTHOR

Esat Tarik Topkara
Ege University,
Faculty of Fisheries,
Department of Marine–Inland Waters Sciences and Technology, Inland Waters Sciences Section,
35100 Izmir – Turkey

e-mail: esattopkara@gmail.com

© by PSP Volume 29 – No. 04A/2020 pages 2632-2638 Fresenius Environmental Bulletin

VISUAL IMPACT OF WIND TURBINES ON LANDSCAPE QUALITY – A CASE STUDY

Marta Lisiak[1,*], Klaudia Borowiak[1], Jolanta Kanclerz[2], Anna Adamska[2], Ewelina Janicka[2], Anna Budka[3], Anna Libront[1]

[1]Poznan University of Life Sciences, Faculty of Environmental Engineering and Spatial Management, Department of Ecology and Environmental Protection, Poznan, Poland
[2]Poznan University of Life Sciences, Faculty of Environmental Engineering and Spatial Management, Institute of Land Improvement, Environmental Development and Geodesy, Poznan, Poland
[3]Poznan University of Life Sciences, Faculty of Agronomy and Bioengineering, Department of Mathematical and Statistical Methods, Poznan, Poland

ABSTRACT

The aim of this study was to determine the location of potential wind turbines in Swarzędz municipality (Poland) and to evaluate their visual impact on the landscape with regard to the opinion of the local community. An analysis of the landscape's visual attractiveness was carried out based on field studies. A survey of the visual impact of wind farms was conducted on a group of randomly selected respondents who evaluated the landscape's attractiveness based on two photographs with and without wind turbines. Two potential locations for wind farm construction were proposed based on current law requirements. Landscape attractiveness analysis revealed different level of these to selected sites. The results of the survey of the visual effect of wind farms showed that they have no impact on the respondents' perception of such a landscape. There is also no effect of landscape attractiveness on public opinion regarding to location of wind turbines.

KEYWORDS:
Landscape visual attractiveness, scenic perception, environmental impact assessment

INTRODUCTION

Windmills have been present in the Polish landscape for many centuries. The functionality and original shape of windmills made them a characteristic and unique element of the Polish countryside. They were an important structure of the settlement, subtly enriching the space without dominating it [1, 2].

Enactment of Directive 2001/77/EC of the European Parliament and of the Council of 27 September 2001 on the promotion of electricity produced from renewable energy sources in the internal electricity market [3] have introduced "modern windmills" to the landscape of the Polish countryside once again. On the one hand, increased ecological awareness contributes to acceptance of renewable energy infrastructure. On the other hand, wind farms cause numerous fears [4]. Simultaneously with the research on noise threat [5, 6, 7, 8, 9, 10], the impact of wind farms on ecosystem [11, 12, 13] and electromagnetic field emission [14, 15, 16] was investigated. Another analysed aspect is the impact of such investments on the landscape [1, 2, 4, 17, 18, 19].

The use of modern technologies allows the impact of wind turbines on the environment to be limited to some extent, especially in aspects such as noise threat or threat to biocenosis. However, among other threats caused by wind turbines, the most difficult to minimize is their negative impact on visual attractiveness. Concern for the landscape's visual attractiveness is the most frequent argument raised by the public against the construction of new wind farms [4, 20].

The aims of this study were as follow: (i) to determine the location of potential wind turbines in Swarzędz municipality based on Polish and EU laws, (ii) to examine the landscape's visual attractiveness of two potential locations, (iii) to relate potential wind turbines locations representing different levels of landscape's attractiveness to the opinion of the local community. Based on these objectives the following hypothesis was tested: the level of primary landscape's visual attractiveness differentiates the preferences regarding visual attractiveness by public opinion of the evaluated landscape in regard to location of wind turbine.

MATERIALS AND METHODS

According to the spatial conditions for the development of wind energy in the Wielkopolska region, Swarzędz municipality is located in a very favourable wind energy zone [21]. Swarzędz (52° 25' 45.613" N, 17° 6' 3.215" E) is an urban-rural municipality situated in the Poznan district (Poland), east of the city of Poznan, and it covers an area of 10 173 ha (5.3% of the whole district area) (Figure 1). The dominant land use is agriculture (66.7%). Forests are located in the northern part of Swarzędz (13.2% of

the area), while water bodies cover 2.2%. Impervious surfaces in Swarzędz town and small settlements, along with wastelands, cover 17.9% of the whole municipality area.

The methodology of the work was divided into three stages: selection of the potential wind turbine sites, visual attractiveness assessment of selected sites and public opinion evaluation.

The location of wind turbines was determined by their distance to settlements and existing environmental protection areas specified in the Polish Law of 16 April 2004 on Nature Protection (Polish Journal of Laws of 2004 No. 92, item 880, as amended) [22]. The minimal distance to both these sites is defined in the Polish Law of 20 May 2016 on wind energy investments (Polish Journal of Laws of 2016, item 961, as amended) as ten times the total height of the wind turbine [23]. In this study two wind turbine variants were analysed: Enercon E-48 (hub height of 50 m, power of 0.8 MW) and Vestas V100 (hub height of 120 m, power of 2.0 MW).

For the purposes of this study, a wind farm model was created in MicroStation PowerDraft v8.0 software, with regard to technical parameters of those turbines and the distance to settlements and nature protection areas.

Acoustic analysis for the created wind farm model was carried out in SoundPLAN 7.1. software in accordance with instructions on the methods to determine emission and intensity of industrial noise in the environment provided in the Building Research Institute Instructions series [24] for two selected locations in the Swarzędz municipality. The noise standards for settlements were taken from the Polish Regulation of the Minister of Environment of 14 June 2007 on permissible noise levels in the environment (Polish Journal of Laws of 2007 No. 120, item 826, as amended) [25].

The analysis of the landscape's visual attractiveness was carried out based on field studies at 17 documentation sites and criteria established by Mirowska and Krysiak [26]. Six photographs were taken at every documentation site, each photograph covering a 60° angle of view for a different direction. The obtained results were presented according to the modified methodology proposed by Cymerman and Hopfer [27] and divided into four classes of landscape's visual attractiveness, as follows:

- 5-7 points – visually unattractive area,
- 8-10 points – area with medium visual attractiveness,
- 11-13 points – area with high visual attractiveness,
- 14-16 points – area with very high visual attractiveness.

The scope of this study also included a questionnaire evaluating local society's knowledge on the functioning of wind farms and their influence on the environment, but also investigating visual attractiveness of the landscape transformed by turbines. Survey was administrated in-person. Respondents evaluated landscape attractiveness based on two photographs for each landscape – one with and one without wind turbines. The photographs were taken in the distance of approx. 600m from potential location of the wind turbines. The photographs were taken in May during sunlight in the midday.

In order to determine the impact of wind farms on visual attractiveness of landscape basing on public opinion questionnaire, i.e. whether there is a relationship between evaluation of landscape's visual attractiveness before and after the placement of the wind turbines, the independence χ^2 test (Pearson's chi-square test) was performed. Respondents' answers were interpreted based on the hypothesis:

FIGURE 1
Location of Swarzędz municipality

H_0: Construction of the wind turbine does not differentiate the preferences regarding visual attractiveness of the evaluated landscape.

H_1: Construction of the wind turbine differentiate the preferences regarding visual attractiveness of the evaluated landscape.

The strength of correlation between two variables analysed in the $\chi 2$ test was calculated based on the C-Pearson's contingency coefficient.

RESULTS AND DISCUSSION

Selection of the Location of Wind Farms and Wind Turbines. Location of wind turbines can negatively influence on prices of the properties [28, 29], on the other side Hoen, Wiser, Cappers, Thayer and Sethi [30] and Hoen et al. [31] found lack of significant influence on property value. Even then turbines do not effect on property price, there is an effect on landscape attractiveness perception by local inhabitants [32, 33, 34, 35]. In the case of Poland, it is especially significant to rural areas as these areas are main locations for this type of objects. Placement of the potential wind farms in Swarzędz municipality was determined based on an analysis of the location of settlements, nature protection areas and ecological corridors, as these sites are the most responsive to any changes and such changes may encounter public disagreement [4, 20]. In Swarzędz municipality there is the Natura 2000 protection area "Dolina Cybiny" (PLH300038), the conservation area around the landscape park "Puszcza Zielonka" and an ecological corridor.

The distance between wind turbines and the analysed sites must exceed ten times the height of those turbines. The only turbines that met this requirement were Enercon E-48 turbines with the height of 50 m. The acoustic analysis showed that in the 500 m range the noise of this turbine model is 34.9 dB, while noise standards according to Polish law are as follows: in a single-family housing area, 50 dB for the eight most unfavourable hours during the day and 40 dB for the one most unfavourable hour during the night; and in multi-family housing, residential and service housing and farm building areas, 55 dB and 45 dB respectively. According to the European Wind Energy Association (EWEA), the noise emission in the range of 350 m should not exceed 34-45 dB.

Two potential locations for construction of wind turbines were determined at a distance of 500-800 m from settlements and nature protection areas as follows:

- in the southern part of Swarzędz, between the villages Garby and Kruszewnia – four Enercon E-48 wind turbines (location no. 1);
- in the central part of Swarzędz, between the villages Gortatowo and Sarbinowo – three Enercon E-48 wind turbines (location no. 2).

The conducted analysis showed that construction of higher wind turbines in Swarzędz community, e.g. Vestas V100 with the height of 120 m, is not possible due to the requirement of the distance between those turbines and protected sites (settlements and nature protection areas), even though noise standards may be preserved.

Analysis of the Landscape's Visual Attractiveness. An analysis of the landscape's visual attractiveness was carried out for 8 and 9 documentation sites in potential wind farm location no. 1 (Figure 2a) and no. 2 (Figure 2b) respectively. Previous studies indicated that photographic documentation reflects the actual landscape and can be successfully used for further surveys [36, 37, 38]. According to Dockerty, Lovett, Sünnenberg, Appleton and Parry [39] properly taken photographs can evoke the same emotions as observation of the given landscape in reality. The questionnaire carried out for the purposes of this research indicated that social awareness of the wind farms, their functioning and impact on the environment is unsatisfactory. Majority of the photographs taken in location no. 1 were evaluated with 11-13 points, what denotes landscape's high visual attractiveness. Approx. 30% of all photographs were classified as a landscape of medium visual attractiveness. Few trees and location of transmission towers affected landscape negatively in 12% of the analysed area, resulting in classification of this landscape as highly unattractive, while only two photographs, which covered approx. 5% of the whole analysed area, presented the most attractive landscape (over 14 points). After summation of all grades for each documentation site, the average grade for potential wind farm's location no. 1 was 10 points (area with medium visual attractiveness).

Approx. 45% of the photographs taken in the potential wind farm's location no. 2 were evaluated with 11-13 points, what indicates high visual attractiveness of the landscape. Eight photographs were classified as landscape of very high visual attractiveness, while only one as unattractive. The medium landscape's visual attractiveness was presented in 21 photographs (39% of the whole photographed area), thus after summation of scores for each documentation site, the average score for potential wind farm's location no. 2 was 11 (area with high visual attractiveness).

Analysis of the Questionnaire Research. The questionnaire was conducted in the group of 120 randomly selected respondents, who represent the group of 1 179 inhabitants living in the nearest villages (Garby, Gortatowo, Kruszewnia, Sarbinowo). The first part of the questionnaire provided overall information about the participants, their general knowledge and perception of the wind farms. The second part of the questionnaire pertained to respondents' opinion on the visual attractiveness of the

landscape transformed by wind turbines. Previous research showed that the average level of social acceptance of wind turbines in the landscape is affected by many factors, e.g. land use, landscape qualities and the distance between wind turbines and settlements [17, 20, 40].

The largest group among all participants comprised young people between 18 and 30 years old (46.7%). People between 31 and 44 years old comprised 35% of all respondents, and people between 45 and 60 comprised 18.3%. Women were the dominant group among all the respondents (63.3%). Approximately 76.6% of the participants reported having been near a power plant at least once.

According to 53.3% of the participants, wind turbines do not generate any noise and do not affect the acoustic climate of their surroundings. The majority of the respondents (63.3%) said that wind farms have no impact on human health, while only 8.3% stated they affect it negatively, whereas approximately 56.7% of respondents indicated that wind farms can have a negative impact on birds and bats.

According to Molnarova et al. [4], a positive approach to wind energy is reflected in perception of wind turbines in a landscape; therefore 48% of answers on their impact on the landscape was favourable, 17% of respondents said it depends on the actual state of this landscape and number of wind turbines, 15% said they have no impact, 12% did not have any opinion, and only 8% said that wind turbines have a negative influence on a landscape.

The majority of the respondents (93.3%) do not live near a wind farm. Only 35% of them said they would not oppose construction of one near their house. Approximately 18% of participants stated they would not agree to construction of a wind farm, while 47% could not decide, primarily because of the lack of information of the distance between the potential wind turbines and their house and secondarily the need to expand their knowledge on wind farms.

In the second part of the questionnaire respondents evaluated 8 photographs, 4 of which portrayed an actual landscape (two photographs of each locations from different point of view) and the other 4 presented the same landscape but transformed by wind turbines. The evaluation was carried out according to a Likert scale (1-8 points), where a higher number of points indicated a more attractive landscape.

The conducted analysis showed that construction of wind farms does not affect visual and aesthetic perception of the landscape. On average, all of the photographs both of the actual agricultural landscape and those where wind turbines were the dominant factor in the landscape were evaluated positively (Figure 3). According to statistical analysis of obtained answers, on the basis of the level of significance α=0.05, there was no basis to reject hypothesis H0, which indicated that construction of the wind turbine does not differentiate the preferences regarding visual attractiveness of the evaluated landscape.

However, the acceptance of those farms in the landscape decreases when the distance between them and human settlements is smaller. The most acceptable location for the wind farms' construction is an area distant from settlements and with low visual attractiveness [4, 17]. On the other side, Firestone et al. [32] found that people living in the farther distance (>1600 m) from the wind turbines like the view less than people living closer (<800 m). However, these differences were not to high – the percentage of population acceptance was at between 77-96%. In our research photographs were taken in the distance of 600 m and are in agreement to Firestone et al. [32], where public acceptance of wind turbine location was noted at this distance.

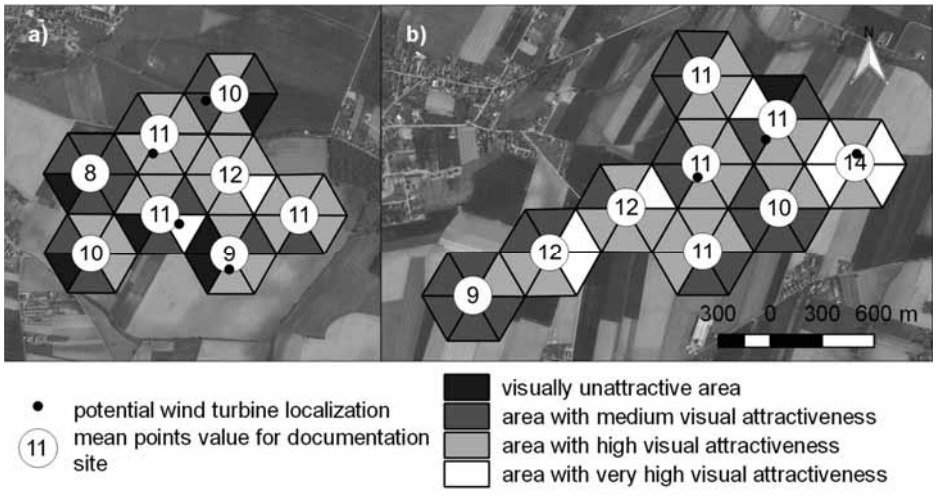

FIGURE 2
Landscape's visual attractiveness and localization of wind turbines in potential wind farm's l location: a) no. 1; b) no. 2

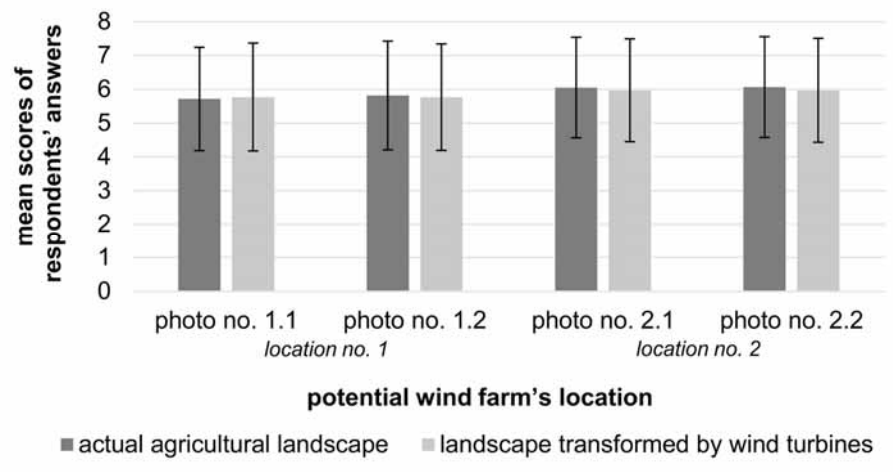

FIGURE 3
The average scores of respondents' answers for actual agricultural landscape and landscape transformed by wind turbines

In the last step of the research, Pearson's contingency coefficient C was used as a measure of dependence. Pearson's C values for the four sets of photographs were 0.154, 0.047, 0.105 and 0.508. On this basis it was concluded that the strongest relation was observed for the fourth (photo 2.2), then the first (photo 1.1), third (photo 1.2) and second set (photo 2.1) of photographs (Figure 3).

CONCLUSIONS

Based on Polish law requirements two potential locations for wind turbines were selected in the Swarzędz municipality. The main limitation for wind turbine location were noise standards, as well as settlement locations and nature protection areas. Landscape attractiveness analysis revealed different levels of these to selected sites. The results of the statistical analysis conducted for the answers regarding the landscape's visual attractiveness based on four sets of photographs (each landscape with and without wind turbines) revealed that wind farms have no impact on the perception of such a landscape by the respondents. As well as, there is no effect of landscape attractiveness on public opinion regarding location of wind turbines.

ACKNOWLEDGEMENTS

The publication was financed within the framework of Ministry of Science and Higher Education programme as "Regional Initiative Excellence" in years 2019-2022, Project No. 005/RID/2018/19.

REFERENCES

[1] Akincza, M., Mazur, A. (2013) The Influence of wind turbines on cultural landscape of Warmia, Mazury and Powiśle. Teka Komisji Architektury, Urbanistyki i Studiów Krajobrazowych. 9(1), 7-17 (In Polish).
[2] Badora, K. (2011) Assessment of wind farms impact upon the landscape – methodological and practical aspects. Problemy Ekologii Krajobrazu. 31, 23-32. (In Polish).
[3] Directive 2001/77/EC of the European Parliament and of the Council of 27 September 2001 on the promotion of electricity produced from renewable energy sources in the internal electricity market.
[4] Molnarova, K., Sklenicka, P., Stiborek, J., Svobodova, K., Salek, M., Brabec, E. (2012) Visual preferences for wind turbines: Location, numbers and respondent characteristics. Applied Energy. 92, 269-278.
[5] Ingielewicz, R., Zagubień, A. (2016) Problems of Assessment of Wind Farm Noise on the Basis of Local Control Measurements. Rocznik Ochrona Środowiska. 18(1), 531-549 (In Polish).
[6] Klæboe, R., Sundfør, H.B. (2016) Windmill noise annoyance, visual aesthetics, and attitudes towards renewable energy sources. International Journal of Environmental Research and Public Health. 13(8), 746.
[7] Onakpoya, I.J., O'Sullivan, J., Thompson, M.J., Heneghan, C.J. (2015) The effect of wind turbine noise on sleep and quality of life: A systematic review and meta-analysis of observational studies. Environment International. 82, 1-9.

[8] O'Neal, R.D., Hellweg, R.D., Lampeter, R.M. (2011) Low frequency noise and infrasound from wind turbines. Noise Control Engineering Journal. 59(2), 135-157.
[9] Pedersen, E. (2011) Health aspects associated with wind turbine noise—Results from three field studies. Noise Control Engineering Journal. 59(1), 47-53.
[10] Pedersen, E., Waye, K.P. (2007) Wind turbine noise, annoyance and self-reported health and well-being in different living environments. Occupational and Environmental Medicine. 64(7), 480-486.
[11] Larsen, J.K., Madsen, J. (2000) Effects of wind turbines and other physical elements on field utilization by pink-footed geese (Anser brachyrhynchus): A landscape perspective. Landscape Ecology. 15(8), 755-764.
[12] Péron, G., Fleming, C.H., Duriez, O., Fluhr, J., Itty, C., Lambertucci, S., Safi, K., Shepard E. L. C., Calabrese, J.M. (2017) The energy landscape predicts flight height and wind turbine collision hazard in three species of large soaring raptor. Journal of Applied Ecology. 54(6), 1895-1906.
[13] Rydell, J., Bach, L., Dubourg-Savage, M.J., Green, M., Rodrigues, L., Hedenström, A. (2010) Bat mortality at wind turbines in northwestern Europe. Acta Chiropterologica. 12(2), 261-274.
[14] Havas, M., Colling, D. (2011) Wind turbines make waves: why some residents near wind turbines become ill. Bulletin of Science, Technology and Society. 31(5), 414-426.
[15] Israel, M., Ivanova, P., Ivanova, M. (2011) Electromagnetic fields and other physical factors around wind power generators (pilot study). The Environmentalist. 31(2), 161-168.
[16] McCallum, L.C., Aslund, M.L.W., Knopper, L.D., Ferguson, G.M., Ollson, C.A. (2014) Measuring electromagnetic fields (EMF) around wind turbines in Canada: is there a human health concern? Environmental Health. 13(1), 9.
[17] Lothian, A. (2008) Scenic perceptions of the visual effects of wind farms on South Australian landscapes. Geographical Research. 46(2), 196-207.
[18] Frantál, B., Kunc, J. (2011) Wind turbines in tourism landscapes: Czech experience. Annals of Tourism Research. 38(2), 499-519.
[19] Stryjecki, M., Mielniczuk, K. (2011) Guidelines for forecasting the impact of wind farms on the environment. Generalna Dyrekcja Ochrony Środowiska, Warszawa. 1-132. (In Polish).
[20] Wolsink, M. (2007a) Planning of renewables schemes: Deliberative and fair decision-making on landscape issues instead of reproachful accusations of non-cooperation. Energy Policy. 35(5), 2692-2704.
[21] Lorenc, H. (1996) Wind energy structure and resources in Poland. Instytut Meteorologii i Gospodarki Wodnej, Warszawa. (In Polish).
[22] Polish Law of 16 April 2004 on nature protection. Polish Journal of Laws of 2004 No. 92, item 880, as amended. (In Polish).
[23] Polish Law of 20 May 2016 on wind energy investments. Polish Journal of Laws of 2016, item 961, as amended. (In Polish).
[24] Żuchowicz-Wodnikowska, I., Czyżewski, K. (2008) Methods to determine emission and intensity of industrial noise in the environment. Badania laboratoryjne i teoretyczne. Instytut Techniki Górniczej KOMAG, Warszawa. (In Polish).
[25] Polish Regulation of the Minister of Environment of 14 June 2007 on permissible noise levels in the environment. Polish Journal of Laws of 2007 No. 120, item 826, as amended. (In Polish).
[26] Mirowska, N., Krysiak, S. (2015) Visual attractiveness of landscape of the Mroga valley and its surroundings in Dmosin commune. Acta Universitatis Lodziensis. Folia Geographica Physica. 14, 25-35. (In Polish).
[27] Cymerman, R., Hopfer, A. (1988) The use of photographs to the countryside landscape assessment. Acta Academiae Agriculturae ac Technicae Olstenensis. Geodaesia et Ruris Regulatio. 18, 39-48. (In Polish).
[28] Dröes, M.I., Koster, H.R. (2016) Renewable energy and negative externalities: The effect of wind turbines on house prices. Journal of Urban Economics. 96, 121-141.
[29] Sunak, Y., Madlener, R. (2016) The impact of wind farm visibility on property values: A spatial difference-in-differences analysis. Energy Economics. 55, 79-91.
[30] Hoen, B., Wiser, R., Cappers, P., Thayer, M.A., Sethi, G. (2011) Wind energy facilities and residential properties: The effect of proximity and view on sales prices. Journal of Real Estate Research. 33(3), 279-316.
[31] Hoen, B., Brown, J.P., Jackson, T., Thayer, M. A., Wiser, R., Cappers, P. (2015) Spatial hedonic analysis of the effects of US wind energy facilities on surrounding property values. The Journal of Real Estate Finance and Economics. 51(1), 22-51.
[32] Firestone, J., Bates, A., Knapp, L.A. (2015) See me, Feel me, Touch me, Heal me: Wind turbines, culture, landscapes, and sound impressions. Land Use Policy. 46, 241-249.
[33] Firestone, J., Kempton, W., Lilley, M.B., Samoteskul, K. (2012) Public acceptance of offshore wind power across regions and through time. Journal of Environmental Planning and Management. 55(10), 1369-1386.

[34] Petrova, M.A. (2013) NIMBYism revisited: public acceptance of wind energy in the United States. Wiley Interdisciplinary Reviews: Climate Change. 4(6), 575-601.
[35] Wolsink, M. (2007b) Wind power implementation: The nature of public attitudes: equity and fairness instead of 'backyard motives'. Renewable and Sustainable Energy Reviews. 11(6), 1188-1207.
[36] Junge, X., Schüpbach, B., Walter, T., Schmid, B., Lindemann-Matthies, P. (2015) Aesthetic quality of agricultural landscape elements in different seasonal stages in Switzerland. Landscape and Urban Planning. 133, 67-77.
[37] Tveit, M.S. (2009) Indicators of visual scale as predictors of landscape preference; a comparison between groups. Journal of Environmental Management. 90(9), 2882-2888.
[38] Van Berkel, D.B., Verburg, P.H. (2014). Spatial quantification and valuation of cultural ecosystem services in an agricultural landscape. Ecological Indicators. 37, 163-174.
[39] Dockerty, T., Lovett, A., Sünnenberg, G., Appleton, K., Parry, M. (2005) Visualising the potential impacts of climate change on rural landscapes. Computers, Environment and Urban Systems. 29(3), 297-320.
[40] Tsoutsos, T., Tsouchlaraki, A., Tsiropoulos, M., Serpetsidakis, M. (2009) Visual impact evaluation of a wind park in a Greek island. Applied Energy. 86(4), 546-553.

Received: **31.10.2018**
Accepted: **02.01.2020**

CORRESPONDING AUTHOR

Marta Lisiak
Poznan University of Life Sciences,
Department of Ecology and
Environmental Protection
Piątkowska 94C, 60-649 Poznań – Poland

e-mail: marta.lisiak@up.poznan.pl

© by PSP Volume 29 – No. 04A/2020 pages 2639-2645 Fresenius Environmental Bulletin

EVALUATING THE WORK ENVIRONMENT IN TURKISH FURNITURE INDUSTRY FROM THE POINT OF OCCUPATIONAL HEALTH AND SAFETY

Devrim Karademir[1,*], Kucuk Huseyin Koc[2]

[1]Ordu University, Social Sciences Vocational School, 52200, Ordu, Turkey
[2]Istanbul University-Cerrahpasa, Faculty of Forestry, Department of Forest Industry Engineering, 34473, Istanbul, Turkey

ABSTRACT

Preparing a healthy and safe working environment for the employee is an important issue for enterprises. Especially for SMEs, this is a major issue in our country. Small businesses often ignore this problem because of not having sufficient knowledge of the subject or, financial inadequacies. Legal sanctions and audits cannot be fully implemented due to the lack of physical and financial structures despite the legal infrastructure. The work environments of SMEs in the furniture sector were examined in this study. Thermal comfort (temperature, humidity, and air flow velocity), noise and ambient lighting parameters were investigated in 255 enterprises. In addition, wood dust parameter was studied in 40 enterprises. When the data obtained are examined; it is seen that about 60% of the enterprises were below the ideal temperature, 30% were airless and 40% were too draughty. From the point of wood dust parameter, wood dust exposure of the work environment is above the limit value of 5 mg/m3 at 90% of enterprises. It is observed that the limit value of 5 mg/m3 is doubled at the 35% of these enterprises, tripled at the 40% of them and quadrupled at the 15% of them. The results obtained in this study have been examined in detail and suggestions have been made to develop for the sector enterprises, chambers, and governments.

KEYWORDS:
Work environment, Occupational health and safety, Turkey Furniture Industry, Occupational accident and occupational diseases, EU Legislation

INTRODUCTION

One of the most important problems faced by enterprises is that employees do not have a safety and healthy work environment. This is a serious issue, especially for small and medium-sized enterprises (SMEs), which is not adequately emphasized, ignored with concern bringing the financial burden, or stemming from the ignorance of employers and employees. This situation can turn out to be a serious problem on an enterprise basis as well as on a sectoral basis or also on a country basis. Therefore, enterprises are required to carry out comprehensive and planned work for employees' occupational health and safety in conjunction with governments, unions, trade associations and bodies.

The Law on Occupational Health and Safety No. 6331, which regulates the working life in our country, was adopted in 2012 and the enforcement of the laws, especially those related to SMEs, entered into force in 2014. According to their risks that they carry, the law is divided enterprises into three groups: low hazardous, hazardous and high hazardous. Therefore, the whole enterprises have to perform a risk assessment and determine which group they are involved in. It is stated in the "Occupational Health and Safety Risk Assessment Directive" how to conduct a risk assessment of the enterprises. The problem at this point is how and how enterprises should make these assessments; enterprises aren't adequately informed about the content and cost of risk assessments and what to happen if not done.

In general, the enterprises in the furniture sector are categorized as hazardous and high hazardous. Processes such as chipping, drilling, cutting, assembly are classified into hazardous class, while painting and varnishing processes are classified as high hazardous.

When the statistics of SSI's occupational accidents and occupational diseases are examined; 1360 employees lost their lives due to 191389 work accidents and 371 occupational diseases in 2013, 1626 employees lost their lives due to 221366 work accidents and 494 occupational diseases in 2014, 1252 employees lost their lives due to 241547 work accidents and 510 occupational diseases in 2015 and 1405 employees lost their lives due to 286068 work accidents and 597 occupational diseases in 2016 [1, 2, 3, 4]. When data for the next 4 years after the implementation of the law were examined, it was observed that the number of work accidents and occupational diseases increased 1.5 times and there was no decreasing tendency in the number of the death.

According to TURKSTAT 2016 data, a total of 2,677,316 enterprises are operating in our country and 2,672,458 of them are defined as SMEs. Within the total number of enterprises, the rate of SMEs was

99.8% whereas the employment rate they created was 73.5%. As the classification of SMEs in TURKSTAT data is different, the ratio of micro, small and medium-sized enterprises aren't shown separately. The ratio of micro-scale in SMEs was determined as 97.5% [5].

According to TURKSTAT 2016 data in furniture sector, the number of enterprises is 33.859 and the number of employees is 187.189 [6]. The number of employees in the furniture sector is estimated to be over 300,000 with employees in the retail sector and other subsidiary sectors. It was reported that the furniture sector has a share of approximately 10% of the manufacturing industry and 2% of the total employment [7].

Works done in the furniture sector are described as standing and heavy works. The machines and tools used during these works such as cutters, trimmers, thinners, saws and knives are risky, and so they are needed to be used carefully. Therefore, workers in the furniture sector cannot lose their attention while using these machines and tools. The furniture workers may also be exposed to wood dust, during the process as cutting, forming, chipping, sanding. A potential loss of attention can cause to fatal or injured accidents, or exposure to persistent wood dust can lead to a variety of occupational diseases.

This study was carried out to examine the working environments of the SMEs in the furniture sector, especially at small-scale enterprises, and to assess the current situation of SMEs in terms of occupational health and safety.

MATERIALS AND METHODS

In this study, thermal comfort (temperature, humidity, air flow rate), noise, ambient lighting and wood dust parameters are taken into account while the work environment is handled in the enterprises. "Extech EN300 Noise, Light, Temperature, Humidity and Air Velocity Meter" was used to measure these parameters. 255 enterprises were visited separately for parameter measurements, and it was studied to 10 minutes standard times in each enterprise with Extech EN300 device to guarantee the homogeneity and reliability of the measurements. "Side Pak Personal Aerosol Monitor Model AM510" device was used for the wood dust parameter. The measurements were made in 40 enterprises, and the minimum, maximum and average values were recorded with making a one-hour measurement for each enterprise. In the measurements, 500 different data were collected periodically in each enterprise.

In order to determine the research population, the table developed by Yazıcıoğlu and Erdoğan (2004) was used, and a sampling population of 25,000 was used as the basis for a sampling error of 0.05 [8]. Due to the difficulty in measuring wood dust exposure, the study was limited to 40 enterprises in the Ankara region.

89% of the enterprises visited for the implementation are micro-scale enterprises with 1-9 employees and 11% of them are small-scale enterprises with 10-49 employees.

Microsoft Office Excel program was used to evaluate the obtained data. It was taken advantage of the Excel program for application development, editing, table and graphing.

RESULTS

Ambient Air Conditions at Workplaces. When the works done in the furniture sector are examined, it is seen that there are heavy works which are generally standing. It is seen for these works that in Table 1, the ambient temperature should be 17 °C, the humidity 50% and the air flow rate should be 0.2-0.4 m/s.

Measurements at workplaces visited for implementation were conducted between November to February. In Figure 1, Figure 2 and Figure 3, the red line shows the minimum and maximum weather conditions and the green line shows ideal weather conditions. In Figure 1, it is shown that the lowest ambient temperature at workplaces is 7.2 ° C and the highest ambient temperature is 21.4 ° C. It was observed that about 60% of the workplaces were below the ideal temperature value and 40% were below the acceptable values.

Ambient humidity values in workplaces are shown in Figure 2. The values in ambient humidity range between 25.8% and 78.4%. It is observed that ambient humidity is below 50% in 50% of the workplaces and 98% is in acceptable values.

TABLE 1
Weather conditions required to provide at workplaces [9].

Work Type	Temperature (°C)			Humidity (%Rh)			Air Flow (m/s)
	Least	Optimal	Most	Least	Optimal	Most	
Office works	18	21	24	30	50	70	0,1
Sedentary works	18	20	24	30	50	70	0,1
Standing works	17	18	22	30	50	70	0,2
Heavy works	15	17	21	30	50	70	0,4

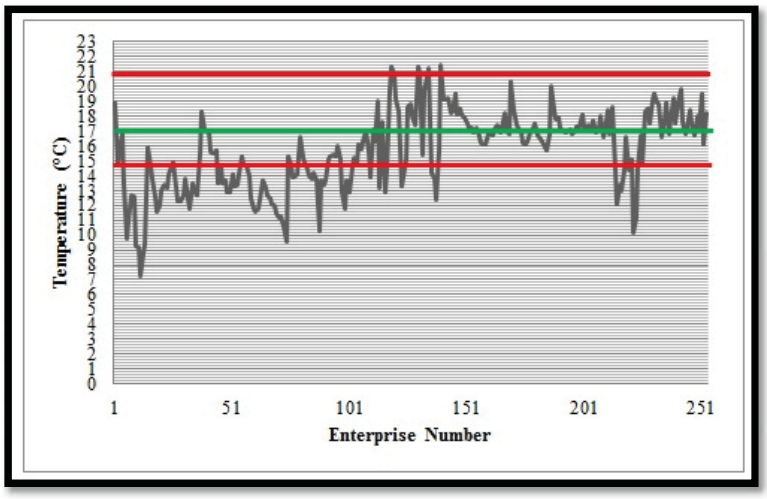

FIGURE 1
Ambient Temperature [10].

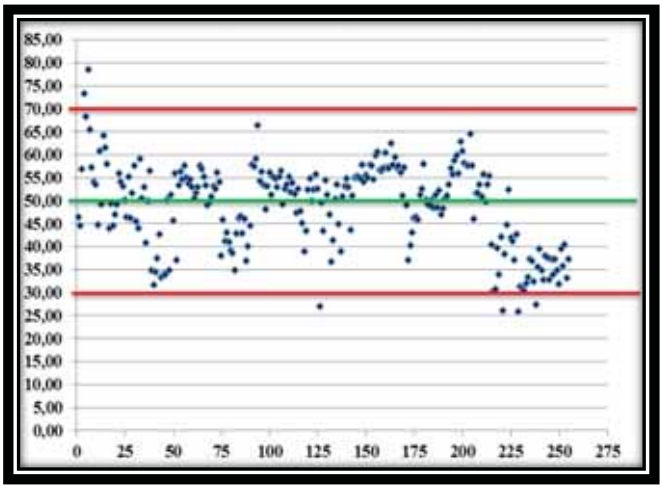

FIGURE 2
Ambient Humidity [10].

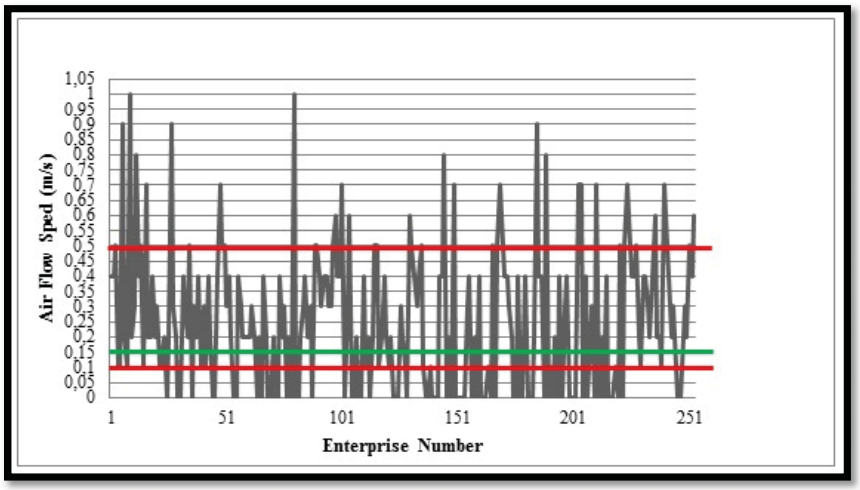

FIGURE 3
Ambient Air Flow Speed [10].

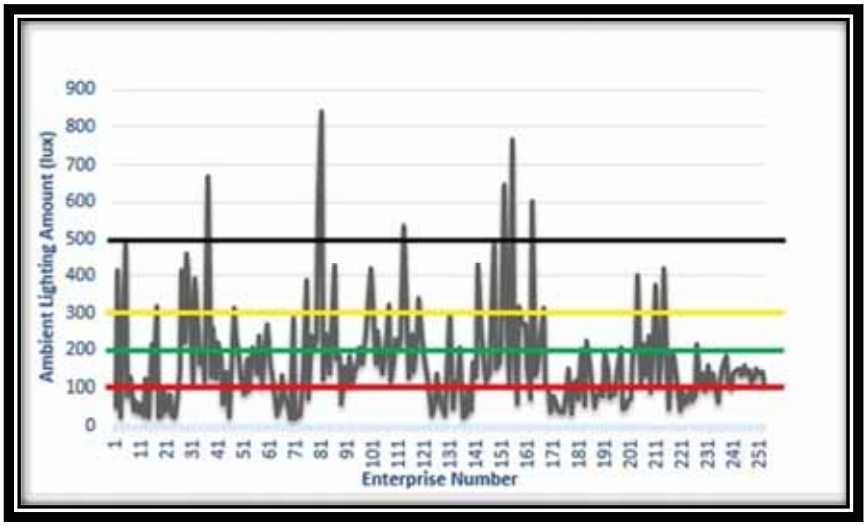

FIGURE 4
Ambient Lighting Amount [10].

TABLE 2
Hearing Loss Percentages Depending on Noise Level [9].

Noise Level (dB)	Hearing Loss Percentages (%)		
	5 Year	10 Year	20 Year
80	0	0	0
90	4	10	16
100	12	29	42
110	26	55	78

Figure 3 shows the change in airflow velocities in workplaces and it is observed that the average air flow rates in the workplaces vary between 0 m/s and 1 m/s. The air circulation rate is close to the ideal values in 25% of the enterprises.

The data obtained from this research indicated that the ambient temperature was below the ideal temperature in an approximately 60% of the enterprises. The working environment is airless at 30% of enterprises and is so draughty at 40% of enterprises. Only moisture findings among the data are between acceptable values.

Ambient Lighting Conditions at Workplaces. The change of an amount of ambient lighting in the workplaces is shown in Figure 4. Approximately at the 70% of enterprises, the ambient lighting is less than 200 lux, and at 95% is less than 400 lux [10]. According to the relevant regulation, 100 lux for coarse assembly, 200 lux for normal assembly, 300 lux for the works where detail is in the foreground and 500 lux for the delicate works requiring continuous attention is required [11].

Lighting is also important in increasing the efficiency of the furniture industry and the amount of light required in the production varies between 100-500 lux. For example, it is suggested that 400 luxury for the coating of large surfaces and the construction process, 500 luxury for the process of a polishing, varnishing and varnish sanding, 400 luxury for the assembly process or 500 luxury lighting for quality control operations is needed [12]. The data obtained indicate that ambient lighting is under 300 lux at approximately 80% of the enterprises and is also under 500 lux at 95% of the enterprises.

Ambient Noise Conditions at Workplaces. According to the related articles of the regulation, the daily noise exposure limit values were determined as 85 dB for the 8-hour studies and 87 dB for the weekly noise exposure level [13]. Figure 5 shows that the average noise exposure values at workplaces are 85 dB and less in only a few enterprises. The red thick line in the figure shows the desired maximum noise exposure value indicated.

Table 2 shows the hearing loss depending on the noise level. It was determined in the conducted research that no loss of hearing was observed in the exposure values of 80 dB or less, and a 55% hearing loss is observed at the end of 10 years in an exposure value of 110 dB [9].

"According to research by WHO and ILO, the effects of various levels of noise are:

- No disturbance between 0-30 dB
- 30-60 dB psychological,
- 60-80 dB psychological and physiological,

➢ 85-125 dB psychological, physiological and hearing loss disorders are classified as noise levels." [14].

Only approximately 15% of the enterprises have 85 dB level of noise exposure, about 50% have over 100 dB level, and about 25% have over 110 dB level. The maximum noise exposure is over 85 dB at almost entire enterprises.

Conditions for Wood Dust Exposure at Workplaces. The most important factors of occupational diseases are dust, gas and toxic substances. Dust and gas are the most important factors for also the furniture sector. Wood dust can cause respiratory diseases, allergic effects, cancer, and many lung diseases. It is exposed to dust more intensively in the furniture sector, especially in the jobs where machines such as sanding, thickness, planning, sawdust, drawing, milling, dust collecting units are used [7].

According to the Dust Occupational Exposure Limit Values Table attached to the relevant regulation, the amount of respirable wood powder is given as 5 mg / m^3 in 8 hour periods [15]. Figure 6 shows that the maximum values measured in the one hour periods in the analyzed enterprises exceed the limit of 5 mg / m3 which is in the regulation and based on the EU directive.

From the point of wood dust parameter, wood dust exposure of the work environment is above the limit value of 5 mg/m^3 at 90% of enterprises. The limit value of 5 mg/m^3 is doubled at the 35% of these enterprises, tripled at the 40% of them and quadrupled at the 15% of them.

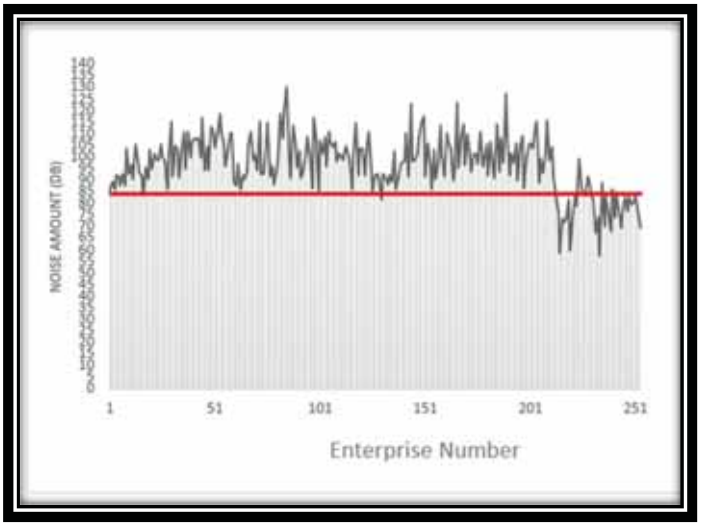

FIGURE 5
Ambient Noise Amount [10]

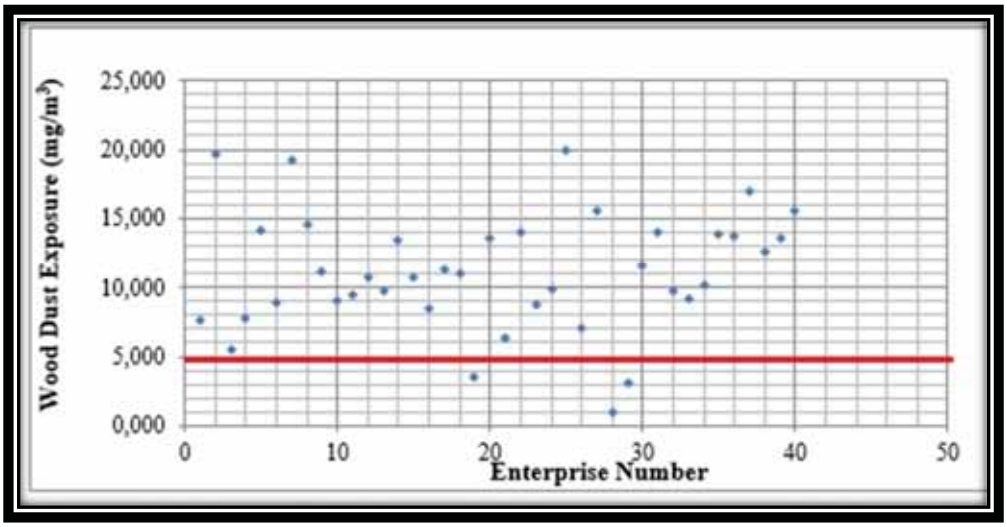

FIGURE 6
Ambient Wood Dust Level [10].

DISCUSSION AND CONCLUSION

Approximately 60% of enterprises have an ambient temperature below the ideal temperature. It was determined that only moisture findings are within the recommended limit values. The working environment is airless in 30% of the enterprises and is so draughty in excess of 40%. Ambient lighting; approximately 95% of the enterprises are below 500 lux. The maximum noise exposure near the end of the enterprises is over 85 dB. Wood dust exposure at workplaces is above the limit value of 5 mg / m^3 in 90% of enterprises.

It was observed that the enterprises in the furniture sector - especially SMEs - cannot comply with the Technical Regulations and EU Directives in terms of many parameters. Many structural improvements are needed in terms of national and international competitiveness of sector enterprises. The relevant legal regulations have been completed to a large extent. The main problem is in the stage of implementation and supervision of these improvements. At this point, the state and professional organizations should be role models and the enterprises should be encouraged, supported and audited in terms of technical adaptation. Preparing and implementing compliance projects at various scales will accelerate compliance with EU technical legislation.

When the research results were analyzed, the work environment of SMEs in Turkey Furniture sector, especially the small-scale enterprises, has been identified as a threat to the health of employees. Air quality and lighting are very insufficient in the enterprises' work environment. The environment is excessively loud or dusty. Insufficiently lightning or poor quality air can affect the health of employees and can also cause loss of their attention. Due to these attention losses, injuries or deaths may occur. Furthermore, an extremely loud or dusty environment can cause a variety of illnesses for employees. Especially wood dust is known to be carcinogenic.

Therefore, it is necessary that primarily the governments will be rapidly complete the infrastructure works, move the enterprises to the prepared areas and provide financial support for enterprises to improve the work environment. It should be ensured that the enterprises that make production between the local neighbourhoods should be moved quickly to small and organized industrial zones. When choosing a location in small and organized industrial zones, attention should be paid to climate and terrain characteristics and harmony of the region. “Climate change impacts should be considered in selected places. The fossil fuels that cause climate change in the energy sources to be used in these regions should be avoided. The only way to prevent climate change is to reduce the share of fossil fuels in energy production and to turn to renewable energy sources.” [16]. Alternative renewable energy sources should be used in small and organized industrial zones. Later, the governments in conjunction with professional bodies have to inform enterprises about the occupational health and safety and arrange training in the enterprises. After these studies are completed, it is recommended that the enterprises should be checked permanently according to the relevant legislation.

ACKNOWLEDGEMENTS

For this study, I would like to thank Istanbul University Institute of Science. This study was published as a full text paper in International Conference on Science and Technology (ICONST 2018) hold from September 5 to 9, 2018, in Prizren, Kosovo.

This study has been prepared using data obtained from a part of the doctoral thesis which is called "European Union Harmonisation with Small and Medium-Sized Enterprises of The Turkish Furniture Industry" prepared by Devrim Karademir.

REFERENCES

[1] SSI (2013) Social Security Institution Statistical Annuals. http://www.sgk.gov.tr/wps/portal/sgk/tr/kurumsal/istatistik/sgk_istatistik_yilliklari. Access Date:15.06.2018.

[2] SSI (2014) Social Security Institution Statistical Annuals. http://www.sgk.gov.tr/wps/portal/sgk/tr/kurumsal/istatistik/sgk_istatistik_yilliklari. Access Date:15.06.2018.

[3] SSI (2015) Social Security Institution Statistical Annuals. http://www.sgk.gov.tr/wps/portal/ sgk /tr/kurumsal/istatistik/sgk_istatistik_yilliklari. Access Date:15.06.2018.

[4] SSI (2016) Social Security Institution Statistical Annuals. http://www.sgk.gov.tr/wps/portal/ sgk /tr/kurumsal/istatistik/sgk_istatistik_yilliklari. Access Date:15.06.2018.

[5] TURKSTAT (2016a) Small and Medium Sized Enterprise Statistics. TURKSTAT, Ankara.

[6] TURKSTAT (2016b) Annual Industry and Service Statistics 2014. TURKSTAT, Ankara.

[7] Karademir, D. and Koç, K.H. (2016) The Expected Physical Environmental Problems of The Turkey's Furniture Enterprises in the EU Process. Selcuk University Technical Online Journal. ISSN: 1302-6178 (NFC-2015). Special Issue(2), 1205-1218.

[8] Yazıcıoğlu, Y. and Erdoğan, S., (2004) SPSS Applied Scientific Research Methods. Detay Publishing, Ankara.

[9] Hayta, A.B. (2007) Effect of Working Environment Conditions on Operational Efficiency. Journal of the Faculty of Commerce and Tourism Education. 2007/1.

[10] Karademir, D. (2014) European Union Harmonisation with Small and Medium-Sized Enterprises of the Turkish Furniture Industry. Unpublished Ph.D. Thesis. I.U. Institute of Science and Technology, Istanbul.
[11] Presidency of Republic of Turkey Official Journal (2013a) Regulation on Health and Safety Measures to be Taken in Workplace Buildings and Additions. (Publication No: 28710, dated 17.07.2013, pages:2-11) Retrieved from https://www.resmigazete.gov.tr/eskiler/2013/07/20130717.pdf. Access Date: 15.06.2018.
[12] Kurtoğlu, A., Dilik, T. (2013) Furniture Industry Unpublished Course Notes. I.U. Faculty of Forestry, Forest Industry Engineering Department, Istanbul.
[13] Presidency of Republic of Turkey Official Journal (2013b) Regulation on Protection of Employees from Noise-Related Risks. (Publication No: 28721, dated 28.07.2013, pages: 21-26) Retrieved from https://www.resmigazete.gov.tr/eskiler/2013/07/20130728.pdf. Access Date: 15.06.2018.
[14] Ekiz, N. (2009) OHS Conditions in the furniture sector in Turkey, Problems and Proposed Solutions. ISGUM Adana-Kayseri, Izmir, Kocaeli Laboratories Study Results. Kayseri.
[15] Presidency of Republic of Turkey Official Journal (2013c) Dust Control Regulation. Publication No: 28812, dated 5.11.2013, pages: 22-31. Retrieved from https://www.resmigazete.gov.tr/eskiler/2013/11/20131105.pdf. Access Date: 15.06. 2018.
[16] Bıyık, Y., Civelekoğlu, G. (2018) Investigation of Carbon Footprint Change Originated from Transportation Sector. Bilge International Journal of Science and Technology Research. 2(2), 157-166.

Received: **22.11.2018**
Accepted: **19.01.2020**

CORRESPONDING AUTHOR

Devrim Karademir
Ordu University,
Social Sciences Vocational School
52200 Ordu – Turkey

e-mail: karademir.d75@gmail.com

© by PSP Volume 29 – No. 04A/2020 pages 2646-2652 Fresenius Environmental Bulletin

SOME METALS AND ANTI-BROWNING AGENTS EFFECTS ON POLYPHENOL OXIDASE FROM PRINCESS TREE LEAVES

Gulnur Arabaci[1,*], Cengiz Cesko[2], Ayse Usluoglu[3]

[1]Sakarya University, Science and Arts Faculty, Chemistry Department, 54187, Sakarya, Turkey
[2]University of Business and Technology, Faculty of Food Technology and Biotechnology, 10000, Prishtine, Kosovo
[3]Aydin Orme San. & Tic. A.Ş., 54400 Kucucek San., Sakarya, Turkey

ABSTRACT

Polyphenol oxidase (PPO) enzyme is a metalloenzyme containing a copper and catalyzes the conversion of phenolic compounds to quinones and assists the polymerization of their products. It causes browning reactions in fruit and vegetables due to oxidation during handling and storage processes. This enzymatic browning reaction is the one of the biggest problem in the food processing industries during processing and storage of vegetables and fruits. Lately, researchers are very interested in developing new PPO inhibitors to slow the enzymatic browning. Natural anti-brown compounds commonly used for the PPO enzyme are honey, aliphatic alcohols, ascorbic acid and cysteine. In addition to these substances, some metals can affect enzyme activities positively or negatively. For example, iron, copper and zinc are essential metals for plant life, but some heavy metals such as mercury, lead, etc. can adversely affect enzymes in the plant defense system. In this work, the effects of some metals, anti-browning compounds and their complexes were examined on the PPO enzyme from princess tree (*Paulownia tomentosa*) leaf. The results demonstrated that glutathione (GSH) was more powerful anti-browning compound than the others. Ni(II) and Mn(II) increased princess tree PPO activity. But, Pb(II) was the efficient PPO inhibitor. Na(I), Cu(II) and Fe(II) had no considerable effect on the PPO enzyme activity. Additionally, the effects of metal and anti-browning compound mixtures on the PPO enzyme were examined. Our results showed that metal-L-Cys, metal-Ascorbic acid and metal-GSH complexes had inhibitory effects but metal- EDTA complex did not have a significant effect on princess tree PPO enzyme activity.

KEYWORDS:
Polyphenol oxidase (PPO), princess tree, anti-browning, metal, inhibition

INTRODUCTION

The browning event, which affects the taste and color of food, is an enzymatic reaction and one of the most important reactions observed in all fruits and vegetables. This reaction is carried out by an enzyme called polyphenol oxidase (PPO) in an oxygenated environment. This enzyme has the ability to catalyze two different reactions. It primarily catalyzes monofenols to o-diphenols thus it has monophenolase activity and then catalyzes the o-diphenols to o-quinones thus it has diphenolase activity [1, 2]. Then, the obtained quinones become polymerized and form black or brown color onto surface of fruits and vegetables. This brown color causes nutritional changes in foodstuffs and reduces the quality of food. The enzymatic browning reaction has been a main trouble for the food production. Thus, the control and inhibition of enzymatic browning has a great importance for the food industry. Nowadays, there are many important studies based on the control and inhibition of enzymatic browning by many different natural and unnatural compounds such as ascorbic acid [3, 4] and thiol containing substances like glutathione (GSH) and L- cysteine [1].

In recent years, polyphenol oxidase enzymes have been widely characterized and purified from various plant sources [5] such as mulberry [6], artichoke [7], iceberg lettuce [8], cleomegynandra [9], broccoli [10], butter lettuce [11] and peppermint [12]. In addition to these studies, there are many inhibitor studies on this enzyme because it causes a major problem in the food industry. Natural substances such as ascorbic acid, honey, natural aliphatic alcohols and L-cysteine can be used as anti-browning agents since they act as inhibitors for polyphenol oxidase enzyme.

Previous studies have shown that L-cysteine forms a stable complex with the copper atom at the reaction center of PPO enzymes and as a result, enzymatic browning may be delayed [13]. Ascorbic acid is a well-known inhibitor of polyphenol oxidase enzymes and has been commonly used for slowing down the enzymatic browning in food industry. Because it behaves like an oxygen molecule scavenger to remove the oxygen atom in the browning reaction

catalyzed by the enzyme polyphenol oxidase [1]. Some studies of polyphenol oxidase from peach suggested that EDTA (ethylenediaminetetraacetic acid) was not a very effective inhibitor [14]. It can only been used to prevent browning reaction in food processes with other chemicals. All the mentioned compounds are used as anti-browning agents and they all inhibit polyphenol oxidase enzyme by slowing the browning reaction in the food industries.

Lately, some studies show that heavy metal pollution in the soil hinders polyphenol oxidase enzyme activity and even prevents growth and proliferation of plants by killing this enzyme [15, 16]. Some metals such as copper (Cu), nickel (Ni) and zinc (Zn) may be micronutrients for plants if they are present in trace quantities, but if they are present in excess amounts, all metals can be harmful to plants, animals and humans. Non-essential metals such as Pb, Sn and Hg are harmful to all organisms in their all amounts [3, 17]. There are several studies about the effects of some metals on to various plants and the enzymes in plants to assess their biochemical behaviors [18, 19]. These studies are getting great attention regarding the relationship among metals, chemicals, and different biochemical properties of the enzymes in plants [16]. However, no reports have been found on investigation of metal and anti-browning effects on polyphenol oxidase enzyme from princess tree leaves (*Paulownia tomentosa*). Therefore, we aimed to study the isolation and biochemical characterization of polyphenol oxidase enzyme from the princess tree leaves (*Paulownia tomentosa*). Additionally, the effects of some metals, anti-browning compounds and their complexes on the enzyme activity were investigated.

MATERIALS AND METHODS

Chemicals. Princess tree leaf (Paulownia tomentosa) was supplied from Sakarya region to use in this work and kept at –20°C. Ammonium sulphate ($(NH_4)_2SO_4$) polyviniylpolypyrolidone (PVP), Sephadex G-100, and other chemicals were provided from Sigma Chemical Co., St. Louis, MO.

Extraction of Polyphenol oxidase enzyme. 15 g of Princess tree leaves (*Paulownia tomentosa*). were mixed to 10 ml of 50mM sodium phosphate buffer (pH; 7.0) with 0.3 g polyvinylpolypyrolidone (PVPP), to prepare the PPO enzyme extract. The mixture was homogenized and filtrated. The filtrate was then centrifuged at 14.000xg for 30 min and the supernatant was collected. The extraction was separated to different tubes and solid $(NH_4)_2SO_4$, was added to the supernatant until having 80% saturation. The mixture was centrifuged and the precipitate was dissolved in phosphate buffer solution in small quantities and dialyzed at 4°C for 24 hours in the same buffer, changing the buffer three times. Then, the dialyzed enzyme sample was centrifuged and loaded onto Sephadex G-100 column already equilibrated with extraction tampon, and washed with the tampon to eliminate unbound enzymes. The samples were collected as the enzyme sample for the rest of the tests. The quantity of the PPO enzyme was determined like Bradford method and bovine serum albumin was used as a standard for the experiment [20].

Polyphenol oxidase activity assay. The polyphenol oxidase activity was evaluated by reading the rate of initial kinon generation, as shown by a rise in absorbance at 420 nm. The PPO enzyme activity was determined using L-Tyrosine, 4-methyl catechol, catechol, L-Dopa and pyrogallol as the known PPO substrates. Kinetic properties for the substrates were determined from the graph formed with the activity versus the substrate concentrations. The Km of Michaelis-Menten constant and Vmax (the maximum velocity) values were calculated was determined using Lineweaver-Burk graph [21].

Effects of pH and temperature. The polyphenol oxidase activity was evaluated at 4.5-5.5 pHs at 50 mM acetate tampon, 6.5-7.5 pHs at 50 mM phosphate tampon and 8.0-9.0 pHs at 50 mM. Tris-HCl and Tris-Base tampon to determine the optimal pH of the PPO enzyme. The determined optimum pH values of this experiment were applied the rest of the applications. The temperature effect of princess tree leaf PPO enzyme activity was also determined at various temperature ranges from 4 to 60°C. The optimum temperature of the enzyme was evaluated from the above temperature range.

Effect of metals on the enzyme activity. Cu(II) ($CuSO_4$) , Fe(III) ($FeCl_3$), Na(I) (NaCl), Pb (II) ($PbCl_2$), Mn(II) ($MnCl_2$), Ni (II) ($NiCl_2$), were preferred to identify their effects on princess tree leaf PPO enzyme activity. They were used at their different concentrations as in 1 and 10 mM.

Effect of anti-browning compounds on the enzyme activity. Ethylenediamine-tetraacetic acid (EDTA), L-ascorbic acid, L-cysteine and glutathione (GSH) were known as anti-browning compounds for PPOs. They were selected to evaluate their effects on princess tree leaf PPO activity at their different concentrations for 1 and 10 mM.

Effect of metals and anti-browning compound complexes on the enzyme activity. A metal and an anti-browning compound were pre-incubated for 30 minutes at room temperature to give the metal- anti-browning compound complex. Subsequently, the effects of complexes on princess tree leaf PPO enzyme activity were examined by kinetic methods using catechol as the substrate at pH 7.0. The remaining PPO enzyme activity was determined

for the metals, anti-browning compounds and metal-anti-browning complexes.

RESULTS AND DISCUSSION

Extraction and substrate specificity of Polyphenol oxidase enzyme. Polyphneol ozidase enzyme was extracted from princess tree leaves (*Paulownia tomentosa*) with appropriate pH 7.0 buffer system explained in materials and method section. Then this crude extract was precipitated with $(NH_4)_2SO_4$ from 10% to 80% salt saturation and then dialyzed with pH 7.0 buffers. The enzyme solution then was applied to gel filtration column and PPO enzyme was eluted and the fractions with enzyme were collected. Then the enzyme activity and substrate specificity were determined with 5 different known substrates of polyphenol oxidase. The enzyme did not show any activity towards monophenol, L-Tyrosine, substrate But Four different substrates, (L-Dopa, pyrogallol, catechol and 4-methyl catechol) are extensively catalyzed by the enzyme, demonstrating Michaelis–Menten kinetics. The values of Michaelis–Menten constants (Km and Vmax) of princess tree leaf PPO were determined from the linear regression analysis of Lineweaver–Burk plot and the Km and Vmax values are presented in Table 1. But Calculated Km values with the lowest Km value that define good affinity to the enzyme substrate are as follows. 4-methylcatechol, catechol, pyrogallol and L-Dopa. It can be suggested that the substrate-interacting region of princess tree leaf PPO enzyme has a good attraction for small o-diphenols, such as 4-methylcatechol and catechol however it has a lesser amount of attraction to the bigger o-diphenols like L-Dopa, and pyrogallol (triphenol) according to their Km values. Our results gave parallel results with the earlier works on plant PPOs [22].

pH and temperature effects on the enzyme activity. The profiles of pH and temperature on princess tree leaf polyphenol oxidase enzyme were separately determined with different substrates as presented in Table 1. The optimum pH of the princess tree leaf PPO enzyme was determined 7.0 with 4-methyl catechol, 7.5 with catechol and pyrogallol and 8.0 with L-Dopa. The optimal pH value for the enzyme that oxidizes the catechol substrate is 7.5 as seen in Figure 1. The optimum pH value of princess tree leaf PPO enzyme is pH 7.5 as is the case in previous studies in which most PPOs exhibited optimum activity [4, 10, 23]. The enzyme activity at acidic and basic pH ranges is very low which is due to the instability of the enzyme at these pHs. (Fig. 1).

The princess tree leaf PPO activity was also determined at various temperatures to estimate its optimum temperature (Table 1). The optimum temperature of the enzyme was determined at 25°C with catechol substrate as seen in Figure 2. The other optimum temperatures were also determined as followed at 25°C with 4-methyl catechol, at 35°C with pyrogallol and 20°C with L-Dopa. These values were parallel to those of medlar [24] and peppermint PPO [12]. But they were different from Barbados cherry PPO [22].

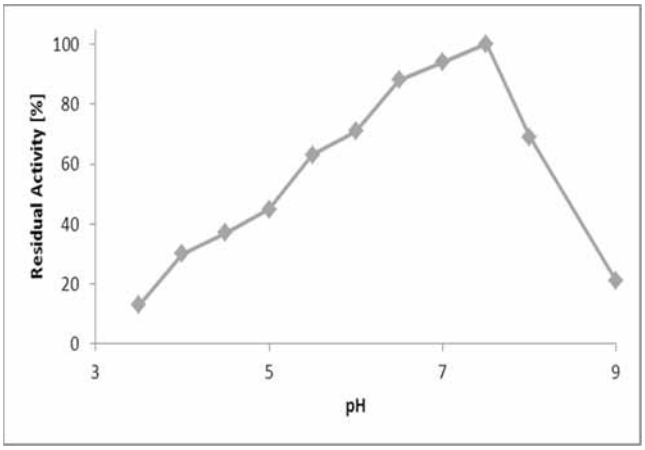

FIGURE 1
pH effect on princess tree leaf PPO enzyme activity with catechol

TABLE 1
The substrate specificities and optimum pH and temperature values of princess tree leaf PPO enzyme

PPO Substrates	Km (mM)	Optimum pH	Optimum temperature (°C)
Catechol	4.55	7.5	25
4-Methyl Catechol	2.17	7.0	25
Pyrogallol	4.77	7.5	35
L-Dopa	6.6	8.0	20

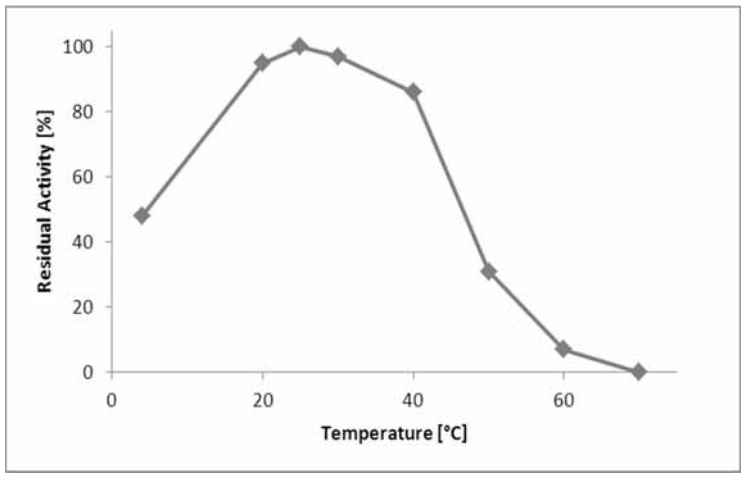

FIGURE 2
Temperature effect on princess tree leaf PPO enzyme activity with catechol

TABLE 2
The percent remaining activity of princess tree leaf PPO enzyme with Metals and Metal-Anti-browning compounds

Metals	Remaining Activity (%)	
	(1 mM)	(10 mM)
$CuSO_4$	117	15
$FeCl_3$	120	16
NaCl	97	84
$PbCl_2$	89.3	0
$MnCl_2$	102	66.7
$NiCl_2$	105	108
Anti-Browning Compounds		
L- Ascorbic Acid	55	2
EDTA	96	91
L-Cysteine	63	43
Glutathione (GSH)	12	0

Effect of some metals and anti-browning compounds on the enzyme activity. Effects of some metals and anti-browning compounds on princess tree leaf PPO enzyme were determined with catechol substrate (Table 2). According to the results, glutathione (GSH) compound was the most effective anti-browning compound for princess tree leaf PPO enzyme. The other compounds were identified as anti-browning compounds by behaving like GSH. These are, respectively, ordered by L-ascorbic acid, L-cysteine and EDTA at 10 mM concentrations (Table 2). According to the studies in the literature, among the anti-browning compounds, L-cysteine was identified as the most effective anti-browning compound for the apple PPO enzyme [13]. Ascorbic acid has been found to be an effective reversible inhibitor for different PPOs [3, 6, 8] and is widely used as an additive in many food fields. These two naturally occurring and non-toxic substances also acted as good inhibitors for princess tree leaf PPO enzyme and may be useful for preventing the enzymatic browning of princess tree leaves in future studies. Previous studies have shown that the active thiol molecules L-cysteine (L-Cys) and reduced glutathione (GSH) play an excellent role in preventing enzymatic browning of plants by inhibiting the enzyme PPO enzyme. [1, 23, 25]. Our results also supported these studies in the literature. The other known anti browning compound is EDTA which is widely used as a chemical preservative in food processes. EDTA displayed minimum inhibitory effect on princess tree leaf polyphenol oxidase activity by having similar results in cherry plypehnol oxidase activity [22].

The effects of Cu(II), Fe(III), Na(I), Pb(II), Mn (II) and Ni (II) metals with different concentrations (1-10 mM) were determined on princess tree leaf PPO enzyme activity (Table 2). The results indicated that Cu (II) and Fe (II) metals increased princess tree leaf PPO enzyme activity in 1 mM concentration, whereas decreasing the enzyme activity in 10 mM concentrations. In the literature, Aydemir reported that Cu (II) and Fe (II) metals at the same concentrations and the same effect on the polyphenol oxidase enzyme activity obtained from the artichoke heads [7], as in our study. Pb (II) heavy metal showed the highest inhibitory effect on the PPO enzyme activity at 10 mM concentration.

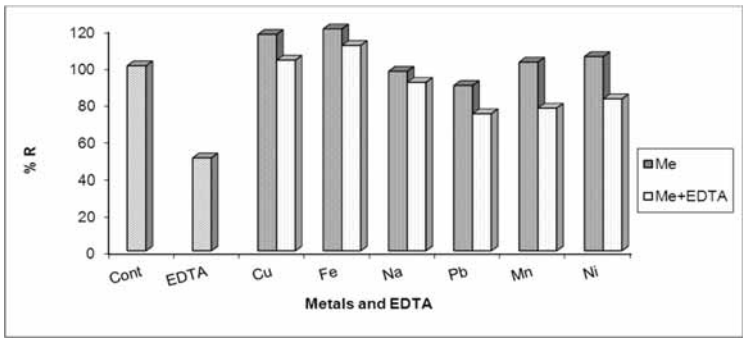

a

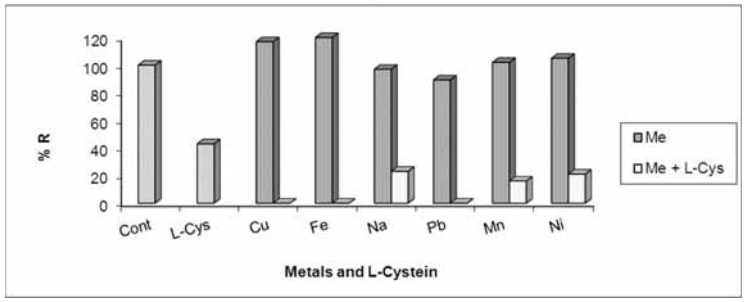

b

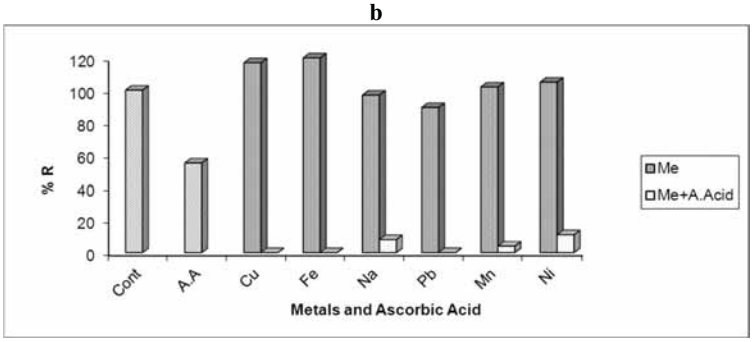

c

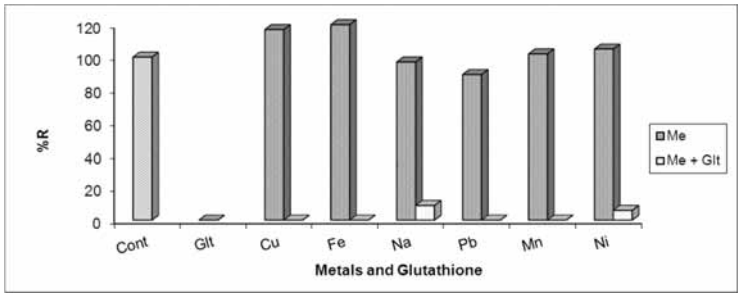

d

FIGURE 3
%R relative activities of princess tree leaf PPO enzyme with metals and metal-anti-browning compound complexes. (a) Metals and Metal+ EDTA, (b) Metal and Metal+ L-Cystein, (c) Metal and Metal+ Ascorbic Acid, (d) Metal and Metal+ GSH.

Although heavy metals are harmful to whole plant and human health, Na(I), Mn(II) and Ni(II) had no considerable influence on princess tree leaf PPO enzyme activity, whereas the same metals showed strong inhibitory effect on other plant PPO activities in the previous studies mentioned [9].

Metal with anti-browning compound complex effect on the enzyme activity. The effects of metal and anti-browning compound complex on the PPO enzyme from princess tree leaf were measured using catechol substrate. The results were presented in Fig. 3. According to the results, there was no significant effect on the enzyme activity of the metal-EDTA complex. Metal-L-ascorbic acid, Metal-L-

Cys and metal-GSH complexes had high inhibitory effect on princess tree leaf PPO enzyme activity. It can be concluded that the metal-anti-browning compound complexes can enhance the inhibitory effect of anti-browning compounds on the enzymatic browning in plants and protect the plant PPO enzymes from the toxic effects of metals in the soil.

CONCLUSION

A polyphenol oxidase enzyme was successfully extracted and characterized from princess tree leaf (*Paulownia tomentosa*) as a new plant enzyme source. The enzyme showed good substrate specificity di and three phenols but not monophenols. The effects of metals, anti-browning compounds and their complexes on the new plant polyhenol oxidase activity were also examined. The results showed that they all had mostly anti-browning and inhibitor effects on princess tree PPO. Therefore, this study can provide useful information that the use of complexes of metal-anti-browning compounds may increase the effect of antifungal agents used in enzymatic browning, as well as reduce the effects of toxic metals on plant PPO enzyme activities in the soil. Enzymatic browning in plants is recognized as a severe problem in food processes. We can conclude that future studies may help to realize the relation between the browning reaction and PPO activity of fruits and vegetables during storage and processing in food industries.

ACKNOWLEDGEMENTS

This work was financed by the Scientific Research Unit of Sakarya University. Project Number: FBDTEZ-2016-50-02-001.

This paper was presented and selected from International Conference on Science and Technology-ICONST 2018, 5-9 September 2018 Prizren – Kosovo.

REFERENCES

[1] Friedman, M. (1996) Food Browning and its Prevention: An Overview. J. Agric. Food Chem. 44, 631.

[2] Holderbaum, D.F., Kon, T. and Guerra, M.P. (2010) Enzymatic Browning, Polyphenol Oxidase Activity, and Polyphenols in Four Apple Cultivars: Dynamics during Fruit Development. HortScience. 45(8), 1150.

[3] Beaulieu, M., Beliveau, M., D'Aprano, G. and Lacroix, M. (1999) Dose Rate Effect of Irradiation on Phenolic Compounds, Polyphenol Oxidase, and Browning of Mushrooms (*Agaricusbisporus*). J. Agric. Food Chem. 47, 2537.

[4] Mdluli, K.M. (2005) Partial purification and characterisation of polyphenoloxidase and peroxidase from marula fruit (*Sclerocaryabirreasubsp. Caffra*). Food Chem. 92, 311.

[5] Arslan, O. and Doğan, S. (2005) Inhibition of Polyphenol Oxidase Obtained from Various Sources by 2,3-Diaminopropionic Acid. J. Sci. Food Agric, 85, 1499.

[6] Arslan, O., Erzengin, M., Sinan, S. and Ozensoy, O. (2004) Purification of Mulberry (*Morusalba L.*) Polyphenol Oxidase by Affinity Chromatography and Investigation of its Kinetic and Electrophoretic Properties. Food Chem. 88, 479.

[7] Aydemir, T. (2004) Partial purification and characterization of polyphenol oxidase from artichoke (*Cynarascolymus L.*) heads. Food Chem. 87, 59.

[8] Chazarra, S., Garcia-Carmona, F., Cabanes, J. (2001) Evidence for a Tetrameric form of Iceberg Lettuce (*Lactuca sativa L.*) Polyphenol Oxidase: Purification and Characterisation. J. Agric. and Food Chem. 49, 4870-4875.

[9] Gao, Z.J., Liu, J.B. and Xiao, X.G. (2011) Purification and Characterisation of Polyphenol Oxidase from Leaves of *Cleome gynandra* L. Food Chem. 129, 1012-1018.

[10] Gawlik-Dziki, U., Szymanowska, U. and Baraniak, B. (2007) Characterization of Polyphenol Oxidase from Broccoli (*Brassica oleracea var. botrytis italica*) Florets. Food Chem. 105, 1047.

[11] Gawlik-Dziki, U., Złotek, Z. and Swieca, M. (2008) Characterisation of Polyphenol Oxidase from Butter Lettuce (*Lactuca sativa var. capitata* L.). Food Chem. 107, 129.

[12] Kavrayan, D. and Aydemir, T. (2001) Partial Purification and Characterization of Polyphenol Oxidase from Peppermint (*Mentha piperita*). Food Chem. 74, 147.

[13] Ozoglu, H. and Bayindirli, A. (2002) Inhibition of Enzymic Browning in Cloudy Apple Juice with Selected Anti-browning Agents. Food Control. 13(4), 213.

[14] Sanjeev, K.D. and Sarad, K.M. (2011) Purification and Biochemical Characterization of Ionically Unbound Polyphenol Oxidase from *Musa paradisiaca* Leaf. Prep. Biochem. Biotechnol. 41, 187.

[15] Balsberg-Pahlsson, A.M. (1989) Toxicity of Heavy Metals (Zn, Cu, Cd, Pb) to Vascular Plants. Water Air Soil Pollut. 47, 287.

[16] Barman, S.C., Sahu, R.K., Bhargava, S.K. and Chatterjee, C. (2000) Distribution of Heavy Metals in Wheat, Mustard, and Weed Grown in Fields Irrigated with Industrial Effluents Bull. Environ. Contam. Toxicol. 64, 489.

[17] Dazy, M., Masfaraud, J.F. and Férard, J.F. (2009) Induction of Oxidative Stress Biomarkers Associated with Heavy Metal Stress in *Fontinalis Antipyretica* Hedw. Chemosphere. 75, 297-302.
[18] Chandra, R., Bhargava, R.N., Yadav, S. and Mohan, D. (2009) Accumulation and Distribution of Toxic Metals in Wheat (*Triticum aestivum* L.) and Indian Mustard (*Brassica campestris* L.) Irrigated with Distillery and Tannery Effluents. J. Hazard. Mater. 162, 1514.
[19] Gupta, S., Satpati, S., Nayek, S. and Gorai, D. (2010) Effect of Wastewater Irrigation on Vegetables in Relation of Heavy Metals and Biochemical Changes. Environ. Monit. Assess. 165, 169.
[20] Bradford, M.A. (1976) A rapid and Sensitive Method for the Quantitation of Microgram Quantities of Protein Utilizing the Principle of Protein-dye Binding. Anal. Biochem. 72, 248.
[21] Lineweaver, H. and Burk, D. (1934) The Determination of Enzyme Dissociation Constants. J. Am. Chem. Soc. 56, 658.
[22] Kumar, V.B.A., Kishor Mohan, T.C. and Murugan, K. (2008) Purification and Kinetic Characterization of Polyphenol Oxidase from Barbados Cherry (*Malpighia glabra* L.). Food Chem. 110, 328.
[23] Dogru, Y.Z., Erat, M. and Demirkol, A. (2012) Investigation of some kinetic properties of polyphenol oxidase from parsley (*Petroselinum crispum,* Apiaceae). Food. Res. Int. 49, 411.
[24] Dincer, B., Colak, A., Aydin, N., Kadioglu, A. and Guner, S. (2002) Characterization of Polyphenol Oxidase from Medlar Fruits (*Mespilus germanica* L., Rosaceae). Food Chem. 77, 1.
[25] Richard-Forget, F.C., Goupy, P.M. and Nicolas, J.J. (1992) Cysteine as an Inhibitor of Enzymatic Browning Kinetic Studies. J. Agric. Food Chem. 40(11), 2108.

Received: **25.11.2018**
Accepted: **28.01.2020**

CORRESPONDING AUTHOR

Gulnur Arabaci
Sakarya University,
Chemistry Department,
Sakarya, 54187 – Turkey

e-mail: garabaci@sakarya.edu.tr

© by PSP Volume 29 – No. 04A/2020 pages 2653-2661 Fresenius Environmental Bulletin

AN INTEGRATED FUZZY MULTI CRITERIA DECISION MAKING METHOD FOR SUSTAINABLE (GREEN) PACKAGING MATERIALS SELECTION: AN APPLICATION IN TURKEY

Bahadir Gulsun[1], Pinar Mic[2,*]

[1]Industrial Engineering Department, Yildiz Technical University, Istanbul, Turkey
[2]Management Information Systems Department, Tarsus University, Tarsus, Turkey

ABSTRACT

The packaging protects the products from external factors and often represents the product. To a decision-maker with inadequate knowledge about the structure and properties of a packaging material, it may be difficult to determine the most applicable one for a given product. In some cases, the defect levels can be so high that the choice of packaging material and other related units can make a product difficult to sell. This may leave the material's selector in a problematic situation. Although packages are mandated to protect the goods inside them, they also need to be easy to store and transport, while being attractive for the consumer market. To be sustainable, packaging waste must be kept at a minimum and should not require any additional cost to be destroyed. To mitigate this, recyclable material should also be evaluated during its construction phase. Considering these significant points, a method to select materials for sustainable packaging is proposed in this paper. In this approach, an integrated DELPHI and fuzzy-Preference Ranking Optimization Method for Enrichment Evaluations approach is employed. Numerical examples are specified in the paper to stimulate an improved understanding of the methodology used, and the experimental results are evaluated through a sensitivity analysis.

KEYWORDS:
Materials selection, Sustainable packaging, multi criteria decision making, fuzzy sets, fuzzy PROMETHEE

INTRODUCTION

An innovative packaging solution is today's best integrated marketing tool [1]. Of the numerous introductory appliances sold to date, packaging is seen as an essential factor that contributes fundamentally to a consumer's decision-making process. This fact makes the packaging industry one of the largest industries in the world.

The purpose of a package is to provide correct environmental conditions for goods during shipment, delivery, and retailing to the consumer [2]. It is clear that packaging has remarkable potential to increase or decrease resource savings. For example, overpackaging can decrease resources, whereas underpackaging can open constituents to damage and spoiling. For these reasons, "right size" and "right strength" packaging should always be considered [3-5]. This point of view incorporates a perspective that balances the correct use of resources toward environmental, social, and financial necessities of packaging utilities, as the natural environment's value on marketing activities has made substantial progress in recent decades. Owing to this, we are sensitive to an increase in environmental risks, with such risks leading to a growing concern for the environment [6]. It is well known that packaging waste materials can have an immense effect on the environment, devastating the Earth's resources if they cannot be recycled. The effects of global warming are progressively noticeable at the same time. For this reason, concerns over the environment have prompted the emergence of a peripherally agreeable trend for "green" packaging, where the concept of green equates to sustainable packaging.

Sustainable packaging is not rigorously described as a term. Moreover, the concept has no easy-to-evaluate criteria [6-8]. Researchers usually apply the criteria (i.e., effective, efficient, cyclic, and safe) identified by the Sustainable Packaging Alliance (SPA) in 2002 or those built by the Sustainable Packaging Coalition (SPC) in 2005.

For the above reasons, it is clear that materials selection plays a crucial role in sustainable packaging. As several industries use more than 40,000 applicable metal alloys and non-metal materials (such as plastics, papers, ceramics, glass, and wood) for packaging, this large number of materials, and a tremendous number of manufacturing industries, turns the materials selection process for a given component into a more difficult task [9]. Furthermore, these processes reflect complex relationships among the various selection parameters.

Depending on the material and product constraints, the selection of materials for sustainable packaging constitutes a multi-objective problem. This action can therefore be considered a "multi-criteria decision-making" (MCDM) problem [10]. MCDM methods constitute several qualitative and quantitative criteria, with decisions made using multiple criteria or objectives [11]. A variety of materials selection approaches have been proposed and practiced by different researchers utilizing MCDM methods for materials selection in the literature. Some MCDM methods utilized in related papers are:

- Fuzzy Set Theory [12-16],
- Dematel-Analytic Network Process (DANP) [17, 18],
- Analytic Hierarchy Process (AHP) [19, 20],
- Fuzzy AHP (FAHP) [21-23],
- VIseKriterijumska Optimizacija I Kompromisno Resenje (VIKOR) [14, 17, 20, 21, 24-27],
- ELimination Et Choix Traduisant la REalité (ELECTRE) [19, 21, 24, 25, 27],
- Preference Ranking Organization Method for the Enrichment of Evaluations (PROMETHEE) [15, 18-22, 28-30],
- Technique for Order Preference by Similarity to an Ideal Solution (TOPSIS) [15, 18-22, 25, 29-32].

However, sustainable packaging is still a highly specialized issue, and it is made markedly more critical through its environmental issues [33]. Whether in Turkey or internationally, there is no explicit interpretation of "sustainable" packaging contents. Going "green" is no longer an alternative when value and environmental issues are being affected [34]. Additionally, sustainable packaging and its applications could contribute to reducing the carbon footprint of packages significantly across all layers of the supply chain [35].

When considering this, sustainable packaging materials should be created and implemented to ensure a high level of compliance with regulatory requirements, materials productivity, market demand, and critical cost. By decreasing the materials and energy used to create a package, companies can significantly increase their sustainability and work on positive outcomes for the environment and society.

This is why the decision of selecting appropriately engineered material to use for sustainable packaging is not simply an examination of cost or materials properties, but an inherent process that necessitates trade-offs between several factors embracing environmental impacts [10].

The studies aforementioned, particularly those after 2009, cemented the importance of MCDM techniques in materials selection procedures. In most of the research to date, however, showing regard for or considering environmental criteria has been very rare among the various studies. Only three of the studies considered environmental criteria [14, 36,37] . There are also no studies containing the application of fuzzy MCDM methods for the selection of sustainable food packaging material. These points are the reasons why this study is valuable. Therefore, in this paper, the development and application of hybrid fuzzy MCDM techniques are introduced and applied to the selection of suitable sustainable materials for food packaging.

MATERIALS AND METHODS

Sustainable packaging is a form of packaging that has little impact on the environment throughout its life cycle. Extractions of raw materials, production, and final recycling (or degradation) are all covered by sustainable attitudes to packaging itself. Accordingly, the necessities of the materials selection process for sustainable packaging involve not only technical and economic factors but also environmental factors [38].

Primarily in areas such as packaging materials selection, or rather in sustainable packaging materials selection, experience overrides a mathematical approach to the selection of packaging material. This is because there are various options and countless criteria determining the selection, and thus a more precise approach is needed. More recently, artificial intelligence technologies have been introduced through the advancement of computers, and the problems with materials selection have reached a certain maturity through sophisticated computer software tools. Nevertheless, it is obvious that problems with selecting sustainable packaging material mathematically have not yet been fully explored. Therefore, this study aims to model a real-life decision-making problem where multiple criteria need to be considered by filling the gap between the theory and application of selecting suitable sustainable packaging material. In accordance with these aims, this paper presents an integrated fuzzy multi-criteria decision-making methodology for selecting sustainable (green) packaging material and its application with regard to food packaging. It describes a modified DELPHI method, fuzzy set theory, and fuzzy PROMETHEE methods. This work is intended to help decision-makers make better sustainable packaging decisions, by taking the environment into consideration.

Modified DELPHI and Fuzzy Set Theory. For modified DELPHI method, we applied [39,40]. Subsequently, fuzzy set theory is adopted which is introduced by [41]. Since it is necessary to utilize linguistic expressions which reveal human thoughts as a solution to uncertain problems, fuzzy sets are applied [42, 43].

Analytic Network Process (ANP) and Fuzzy ANP (FANP). As an inclusive decision-making technique, ANP contains all the related criteria that

support the decision-making process. The starting point of ANP is the analytic hierarchy process (AHP) [44]. A fuzzy set is used in a functional way if the decision-making problem that exists in vague. Because of this, application of ANP's fuzzy version is proposed in this study. Pairwise comparisons are built by adopting fuzzy numbers (a^l, a^m, a^u) to evaluate the decision-maker's choice in the F-ANP approach. For estimation of fuzzy precedencies $(\widetilde{w}_i)$, as it is the most utilized and effective method, the least-squares method is adopted in this study [45]. Chang's (1996) extent analysis method, Sugeno's (1985) centre of area method, and Yager's (1981) index method are all utilized to convert the weights of the alternatives to crisp numbers following a calculation of alternatives [46].

PROMETHEE and Fuzzy PROMETHEE. PROMETHEE method, a decision-making procedure built by [47], analyses every alternative pair for each criterion and classifies the alternatives within a 0–1 interval. For more detailed information about the method, readers should refer to the relevant sources [48, 49].

It is noteworthy to point out that this study incorporates fuzzy logic (developed by [39]) and PROMETHEE method for the packaging materials selection matter. In the fuzzy PROMETHEE method, five-scale linguistic variables are applied to fuzzy numbers to evaluate the significance of the assessment criteria with a fuzzy group in this study [50]. While linguistic scales and corresponding triangular fuzzy numbers for weight of criteria are adopted by [51]; linguistic scale of significance utilized in Fuzzy PROMETHEE comparisons are adopted by [52].

In the transition process of the weight alternatives to crisp members, four different defuzzification methods could be utilized. These are Chang's (1996) extent analysis method [46], Sugeno's (1985) center of area (COA) method [53], Yager's (1980) center of gravity (COG) method [54], and Yager's (1981) index method [55]. In this paper, we utilized Yager's index method [55].

RESULTS

Application of the proposed method to a food company. A food company from Turkey-İstanbul (the company collaborated on condition of anonymity) is presented as a real case study to gain a better understanding of the model and methodology. This company works with seven packaging materials for fruits and vegetables: modified atmosphere packaging (A_1), vacuum packaging (A_2), paper wrapping packaging (wax paper, thin paper) (A_3), string bag packaging (A_4), rigid plastic container packaging (A_5), wooden crate (basket) packaging (A_6), and corrugated board packaging (A_7). The current decision-making procedure for this company mainly depends on traditional methods. Furthermore, a product decrease and unexpected costs may compel management to think of a more basic yet precise method for the selection of suitable sustainable packaging material. One distinguishing feature of this study is that it is the first study for Turkey and the company. Because the most suitable packaging material may be one of the materials mentioned above, all seven materials were selected as candidates. The criteria for the decision-making process were established with a decision-making team (DMT) made up of seven experts: two were university academics, and the rest consisted of a production manager, production engineer, finance manager, purchasing department manager, and expert labourer. The evaluation criteria and the criteria influences are detailed in Figure 1. A modified DELPHI method was utilized for the criteria determination stage. Before starting each stage of the modified DELPHI method, related literature was examined to obtain a preselected set of criteria and presented to the DMT.

As a result of the interviews, seven main criteria (with their own sub criteria) were selected for the evaluation of sustainable packaging material. The main criteria used were environment criteria (EC), storage criteria (SC), costs criteria (CC), marketing criteria (MC), protecting the product inside criteria (PPC), transportation criteria (TC), and customer-oriented criteria (COC).

EC is the main criteria cluster used and focuses on environmental issues such as environmental pollution after use, composting mass garbage dumps, and biodegradability. SC is the main criteria cluster focused on the accumulation and replacement of packages in storage that are easily discernible. These criteria are significant for the efficient use of storage. CC is the main criteria cluster that is cost inclusive of supplying packaging material, storage, food packaging, and transportation. MC is the main cluster concerned with marketing the package. The package should have an attractive appearance during the sale phase, occupy less space during storage, and conform to local legislation. PPC is the main criteria cluster related to the packaging protection capability of the product inside it. For foodstuffs, a package should protect the food inside it in terms of moisture buildup, atmospheric factors, and mechanical effects (like crashes). TC is the main criteria cluster that gathers issues about the transportation of packages, shipping and ease of product discharge, safety, usability, and lightness of the package. COC is the main criteria cluster related to factors about the consumer. These factors are attractive appearance, user friendliness and pliability of the package, recycling potential after use (because at the present time consumers pay attention to recyclable materials), and having the necessary product information.

In addition to these, the interdependencies between each main criteria cluster are shown in Figure 1. In summary, EC has an influence on EC itself, CC,

and SC; on COC and PPC (bidirectional); SC has an influence on CC and TC (both bidirectional); CC has an influence on SC and MC (both bidirectional); MC has an influence on CC and COC (both bidirectional); PPC has an influence on COC and TC (bidirectional); and, finally, TC has an influence on PPC and COC (both bidirectional). These interdependencies are based on the relationships between the main clusters and the sub criteria.

In the first stage of the F-ANP approach, the DMT is asked to compare the decision-making criteria linguistically, in agreement with their effect on the concepts of the main goal. It is assumed that there are no interdependencies between the criteria and the linguistic scales, and Table 1 exhibits the DMT pairwise comparisons.

The weights of the criteria were then calculated through a logarithmic least-squares technique [45,46]. The weight's values were computed as 0.33, 0.22, 0.08, 0.05, 0.17, 0.13, and 0.03 for the CC, EC, PPC, TC, COC, MC, and SC criteria, respectively.

After the F-ANP process, F-PROMETHEE calculations were conducted. For the first step of F-PROMETHEE, the DMT was asked to specify the generalized criterion type of each criterion along with the q, p values. The generalized criterion type was chosen as the level criterion type for each criterion, and the q, p values are specified as "0 and 0.6",

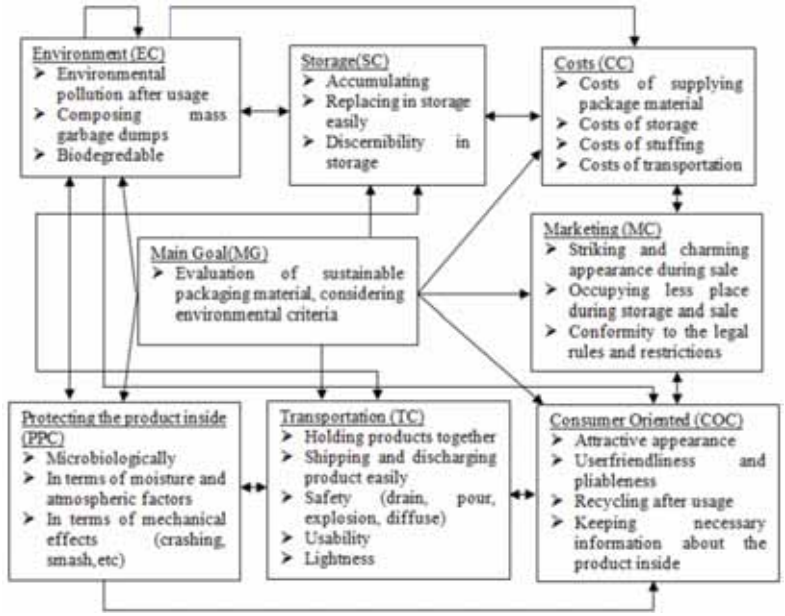

FIGURE 1
Evaluation criteria and criteria influences used to evaluate sustainable packaging materials

TABLE 1
Linguistic criteria comparing based on Main Goal (MG)'s effect

MG	CC	EC	PPC	TC	COC	MC	SC
CC	JE	WMI	SMI	VSMI	WMI	WMI	VSMI
EC	WLI	JE	WMI	SMI	WMI	WMI	SMI
PPC	SLI	WLI	JE	WMI	WLI	SLI	SMI
TC	VSLI	SLI	WLI	JE	WLI	WLI	SMI
COC	WLI	WLI	WMI	WMI	JE	WMI	SMI
MC	WLI	WLI	SMI	WMI	WLI	JE	VSMI
SC	VSLI	SLI	SLI	SLI	SLI	VSLI	JE

TABLE 2
Alternative linguistic evaluations using the DMT

	CC	EC	PPC	TC	COC	MC	SC
A_1	A	DA	SA	SA	SA	A	A
A_2	A	DA	A	SA	A	A	A
A_3	LA	NC	LA	LDA	DA	A	A
A_4	NC	LDA	NC	DA	DA	LA	A
A_5	A	LDA	LA	A	LDA	A	LDA
A_6	LDA	A	LDA	LA	LA	LDA	LDA
A_7	LDA	A	A	SA	A	A	A

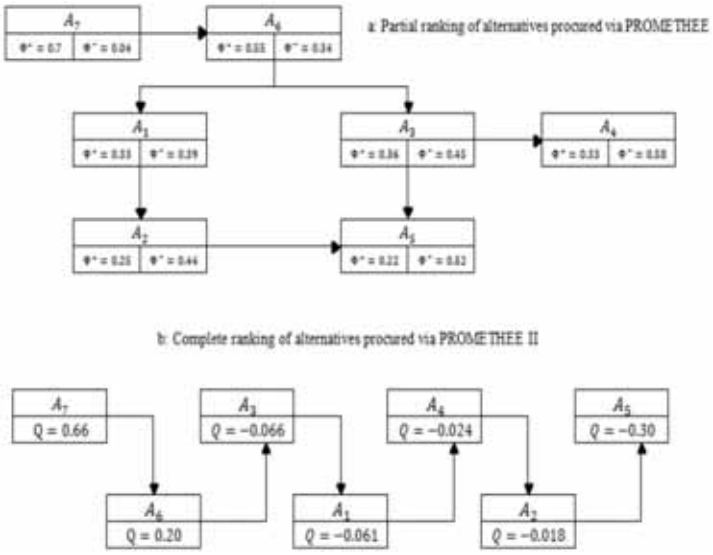

FIGURE 2
Ranking results using PROMETHEE I and PROMETHEE II

TABLE 3
Alternative entering, leaving, and net flows

	Φ^+	Φ^-	Φ^{net}
A_1	0.3333	0.3993	−0.0660
A_2	0.2508	0.4406	−0.1898
A_3	0.3690	0.4571	−0.0611
A_4	0.3350	0.5809	−0.2459
A_5	0.2228	0.5281	−0.3053
A_6	0.5545	0.3498	0.2046
A_7	0.7046	0.0413	0.6634

respectively. Following this step, the DMT was asked to assess alternatives linguistically (Table 2), and the linguistic assessments were converted to triangular fuzzy numbers.

Following, the variations among every alternative pair of each criteria were computed. The Yager index values [55] and the alternative leaving, entering, and net flows were computed and presented in Table 3.

Alternates' fractional arrangements were then obtained by PROMETHEE I (Figure 2a). On the basis of this partial ranking, the A_7 and A_6 alternatives were found to dominate all other alternates, with A_5 dominated by all other alternates. Conversely, if we compare A_7 and A_6, A_7 seemed to be superior to A_6 with a higher Φ^+ value and a lower Φ^- value. For this reason, PROMETHEE II was used to obtain a complete ranking of alternatives. As a result of these calculations, the complete ranking of alternatives was determined. This is shown in Figure 2b. On the basis of PROMETHEE II calculations, A_7 is the best alternative and A_5 is the worst alternative.

Sensitivity analysis. As highlighted in the previous section, A_7 is superior to all the other alternatives. The reason for this is the larger values, especially for CC, EC, and TC. The second-best alternative, A_6, has the same values as CC and EC. A_1 is in the middle between all the alternatives, but it is the best with the largest values for PPC and COC.

During this stage, a sensitivity analysis is applied to characterize the changes in the criteria weights. The sensitivity analysis results for the CC, EC, and COC criteria weights are presented in Figures 3–5.

Figure 3 illustrates the changes to all alternative net flows as a function of CC. As the cost criteria's weight increased from 0 to 1; the A_7, A_6, and A_4 alternatives became sensitive to the cost criteria. It was found that under this criterion, these alternatives had an effect on decreasing the cost. Although the A_7 alternative ranked first for a criterion's all weight value, the A_6 alternative started to have an effect on the cost criteria only after 0.10 of the value of the criteria weight. As for the A_4 alternative, it started to have an effect after 0.60 of the value of the criteria weight. The A_1, A_2, and A_5 alternatives had a strong negative effect on the cost as the weight of the criteria increased.

Figure 4 shows the changes to all alternative net flows as a function of EC. As the EC's weight increased from 0 to 1; the A_7, A_6, and A_3 alternatives became sensitive to the EC. It is observed that these alternatives had an effect on the decrease in packaging environment. These alternatives also had an effect on environment sensitivities. Although the A_7 alternative had a significant effect on all criteria, the

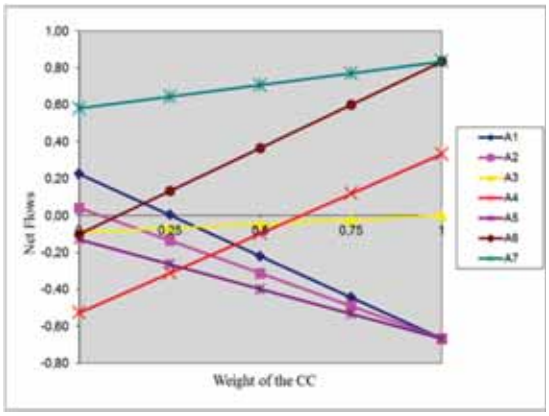

FIGURE 3
Changes to alternative net flows with a change in CC weight

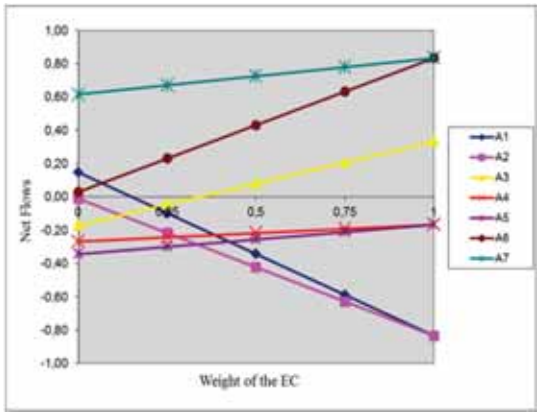

FIGURE 4
Changes to alternative net flows with a change in EC weight

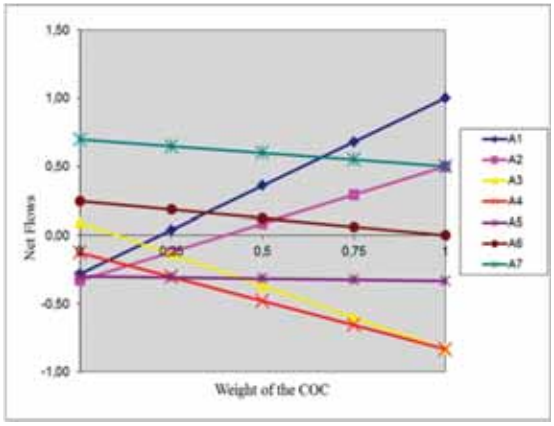

FIGURE 5
Changes to alternative net flows with a change in COC weight

A_6 alternative effect on the EC was below the A_7 alternative. As for the A_3 alternative, it started to have an effect on the environment only after 0.30 of the value of the criteria weight. The A_1 and A_2 alternatives were found to have a strong negative effect on the environment as the weight of the criteria increased.

Figure 5 highlights the changes to all alternative net flows as a function of COC. As the COC weight increased from 0 to 1, the A_1 and A_2 alternatives became sensitive to the COC. It was observed that under this criterion, these alternatives had an effect on attracting customer interest and customer preference. As the weight of the COC increased, although the A_7 alternative net flow decreased, this alternative carried on being effective until 0.70 of the value of the COC weight. This was preferred by the customer. After 0.70 of the value of the criteria weight, the A_1 alternative took first place. Moreover, after 0.40 of the value of the COC weight, the A_2 alternative became the most preferred packaging material as voted by the customer. It was found that the A_3, A_4, and A_5 alternatives were not favoured by the customer. Furthermore, the A_6 alternative was the most underrated packaging material by the customer.

When Figures 3–5 were investigated further, it was evident that the criteria had positive and negative effects on all the alternatives. For example, although the weight of CC and EC increased, the A_7 and A_6 alternatives had higher net flows. Conversely, the A_1 and A_2 alternatives decreased in net flow with an increase in the CC criteria weight. This scenario indicated that although the A_1 and A_2 alternatives were inversely proportional to CC and EC, the A_7 and A_6 alternatives were sensitive to these criteria. CC and EC are important factors for the A_7 and A_6 alternatives. However, with the increase in COC weight, all the other alternatives have lower net flows. Here, the A_1 and A_2 alternatives had higher net flows, indicating that these alternatives were sensitive to these criteria.

At the last phase of the application, these results were presented to the DMT. The environmental assessments of the alternatives were observed to be reasonable and pertinent as a part of their packaging material assessment process, according to their take on the results. More precisely, the proposed method

verifies its effectiveness and ease when paired with the application stage.

DISCUSSION

In this study, an integrated fuzzy MCDM methodology for selecting sustainable (green) packaging material was utilized, and the proposed approach was applied to a food company in Turkey. The aforementioned methodology is a novel technique for both the evaluation of sustainable packaging material and its MCDM process. Furthermore, little has been done in the area of sustainable packaging materials evaluation in the literature. More notably, this study is the first among the limited number of studies with this particular evaluation process, taking into account criteria affects, and the uncertainty of the decision-making approach. Because this paper's goal was to perform sustainable materials selection, the environmental criteria were specifically incorporated within the proposed methodology. With respect to such a goal, a modified DELPHI method was introduced as a systematic approach. Before application of the developed method, the criteria alternatives were determined using current packaging materials selection literature.

From a technical point of view, compared with the existing literature, contributions of our study can be summarized as follows. The vagueness placed on this decision-making process may be easily applied to a decision-making process with the aid of this methodology. Both the criteria assessments and the alternative assessments were initiated using lingual choices which strengthen the applied procedure's practicability and easiness. ANP demonstrated the interdependencies of the decision-making process. Additionally, PROMETHEE's simplified computation and employment were a significant superiority. For further studies, this approach can be applied in different areas, particularly in those where vagueness manifests itself.

REFERENCES

[1] Jerzyk, E. (2016) Design and communication of ecological content on sustainable packaging in young consumers' opinions. Journal of Food Products Marketing. 22(6), 707-716.

[2] Akpinar, M.G., Gul, M. and Ceylan, R.F. (2018) Pet bottled water market: consumer response from Turkey. Fresen. Environ. Bull. 27, 2536-2543.

[3] World Packaging Organisation (WPO) (2011) Position Paper. Packaging-An Important Tool for a Sustainable Society.

[4] Samsi, M.S., Kamari, A., Fatimah, I., Sunardi, S., Najiah, S. and Yusoff, M. (2019) Synthesis, characterisation and application of gelatin-chitosan blend films for fruit preservation. Fresen. Environ. Bull. 28, 31-43.

[5] Gok, G., Akdag, U., Palancioglu, H., Demiral, D., Metin, F. and Isik, M. (2017) Fiberboard panel from waste milk box packaging: a novel product. Fresen. Environ. Bull. 26, 3409-3414.

[6] Lee, S.G. and Xu, X. (2005) Design for the environment, life cycle assessment and sustainable packaging issues. International Journal of Environmental Technology and Management. 5(1), 14-41.

[7] Nordin, N. and Selke, S. (2010) Social aspect of sustainable packaging. Packaging Technology and Science. 23(6), 317-326.

[8] Sonneveld, K., James, K., Fitzpatrick, L. and Lewis, H. (2005) Sustainable packaging: How do we define and measure it? 22nd IAPRI Symposium, April 2005, Australia.

[9] Fayazbakhsh, K., Abedian, A., Dehghan Manshadi, B. and Sarfaraz Khabbaz, R. (2009) Introducing a novel method for materials selection in mechanical design using Z-transformation in statistics for normalization of material properties. Materials and Design. 30(10), 4396-4404.

[10] Chan, J.W.K. and Tong, T.K.L. (2007) Multi-criteria material selections and end-of-life product strategy, a grey relational approach. Materials and Design, 28, 1539-1546.

[11] Onut, S., Soner Kara, S. and Efendigil, T. (2008) A hybrid fuzzy MCDM approach to machine tool selection. Journal of Intelligent Manufacturing. 19(4), 443-453.

[12] Liao, T.W. (1996) A fuzzy multi criteria decision making method for material selection. Journal of Manufacturing Systems. 15(1), 1-12.

[13] Sarfaraz Khabbaz, R., Dehghan Manshadi, B., Abedian, A. and Mahmudi, R.A. (2008) A simplified fuzzy logic approach for materials selection in mechanical engineering design. Materials and Design, 30(3), 687-697.

[14] Girubha, R.J. and Vinodh, S. (2012) Application of fuzzy VIKOR and environmental impact analysis for material selection of an automotive component. Materials and Design. 37, 478-486.

[15] Liao, T.W. (2015) Two interval type 2 fuzzy TOPSIS material selection methods. Materials and Design. 88, 1088-1099.

[16] Xue, Y.X., You, J.X., Lai, X.D. and Liu, H.C. (2015) An interval-valued intuitionistic fuzzy MABAC approach for material selection with incomplete weight information. Applied Soft Computing. 38, 703-713.

[17] Liu, H.C., You, J.X., Zhen, L. and Fan, X.J. (2014) A novel hybrid multiple criteria decision making model for material selection with target-based criteria. Materials and Design. 60, 380-390.
[18] Govindan, K., Shankar, K.M. and Devika, K. (2016) Sustainable material selection for construction industry – A hybrid multi criteria decision making approach. Renewable and Sustainable Energy Reviews. 55, 1274-1288.
[19] Cicek, K., Celik, M. and Topcu, Y.I. (2010) An integrated decision aid extension to material selection problem. Materials and Design. 31(9), 4398-4402.
[20] Caliskan, H., Kursuncu, B., Kurbanoglu, C. and Guven, S.Y. (2013) Material selection for the tool holder working under hard milling conditions using different multi criteria decision making methods. Materials and Design. 45, 473-479.
[21] Anojkumar, L., Ilangkumaran, M. and Sasirekha, V. (2013) Comparative analysis of MCDM methods for pipe material selection in sugar industry. Expert Systems with Applications. 41(6), 2964-2980.
[22] Anojkumar, L., Ilankumaran, M. and Vignesh, M. (2015) A decision making methodology for material selection in sugar industry using hybrid MCDM techniques. International Journal of Materials and Product Technology. 51(2), 102-126.
[23] Kabir, G. and Lizu, A. (2016) Material selection for femoral component of total knee replacement integrating fuzzy AHP with PROMETHEE. Journal of Intelligent Fuzzy Systems. 30(6), 3481-3493.
[24] Chatterjee, P., Athawale, V.M. and Chakraborty, S. (2009) Selection of materials using compromise ranking and outranking methods. Materials and Design. 30(10), 4043-4053.
[25] Jahan, A., Mustapha, F., Ismail, M.Y., Sapuan, S.M. and Bahraminasab, M. (2011) A comprehensive VIKOR method for material selection. Materials and Design. 32(3), 1215-1221.
[26] Yazdani, M. and Payam, A.F. (2014) A comparative study on material selection of microelectromechanical systems electrostatic actuators using Ashby, VIKOR and TOPSIS. Materials and Design. 65, 328-334.
[27] Shanian, A. and Savadogo, O. (2006a) A non-compensatory compromised solution for material selection of bipolar plates for polymer electrolyte membrane fuel cell (PEMFC) using ELECTRE IV. Electrochimica Acta. 51(25), 5307-5315.
[28] Chatterjee, P. and Chakraborty, S. (2012) Material selection using preferential ranking methods. Materials and Design. 35, 384-393.
[29] Anupam, K., Lal, P.S., Bist, V., Sharma, A.K. and Swaroop, V. (2013) Raw material selection for pulping and papermaking using TOPSIS multiple criteria decision making design. Environmental Progress and Sustainable Energy. 33(3), 1034-1041.
[30] Swain, P.T.R. and Biswas, S. (2014) Selection of materials using multi criteria decision making method by considering physical and mechanical properties of jute/Al_2O_3 composites. Applied Mechanics and Materials. 592-594, 729-733.
[31] Jee, D.H. and Kang, K.J. (2000) A method for optimal material selection aided with decision making theory. Materials and Design. 21(3), 199-206.
[32] Shanian, A. and Savadogo, O. (2006b) A material selection model based on the concept of multiple factor decision making. Materials and Design. 27(4), 329-337.
[33] Abdul Khalil, H.P.S., Davoudpour, Y., Saurabh, C.K., Hossain, M.S., Adnan, A.S., Dungani, R., Paridah, M.T., Islam Sarker, M.Z., Nurul Fazita, M.R., Syakir, M.I. and Haafiz, M.K.M. (2016) A review on nanocellolosic fibres as new material for sustainable packaging, Process and applications. Renewable and Sustainable Energy Reviews. 64, 823-836.
[34] Panainte, M., Caraman, I., Nedeff, V., Inglezakis, V., Christos, V., Coutsikos, P., Lazar, G. and Barsan, N. (2014) Green market: a comparative study in Romania. Fresen. Environ. Bull. 23, 2870-2875.
[35] McKinnon, A., Browne, M., Whiteing, A. and Piecyk, M. (2015) Green Logistics, Improving the Environmental Sustainability of Logistics. 3rd edition. Kogan Page, UK.
[36] Chen, R.W., Navin-Chandra, D., Kurfees, T. and Prinz, F. (1994) A systematic methodology of material selection with environmental considerations. Proceedings of the 1994 IEEE International Symposium on Electronics and the Environment. 252-257.
[37] Riberio, I., Pecas, P., Silva, A. and Henriques, E. (2008) Life cycle engineering methodology applied to material selection, a fender case study. Journal of Cleaner Production. 16(17), 1887-1899.
[38] Deng, Y.M. and Edwards, K.L. (2007) The role of materials identification and selection in engineering design. Materials and Design. 28(1), 131-139.
[39] Wu, C.R., Lin, C.T. and Chen, H.C. (2007) Integrated environmental assessment of the location selection with fuzzy analytical network process. Quality and Quantity. 43(3), 351-380.
[40] Murry, J.W. and Hammons, J.O. (1995) Delphi, a versatile methodology for conducting qualitative research. The Review of Higher Education. 18(4), 423-436.

[41] Zadeh, L.A. (1965) Fuzzy sets. Information and Control. 8(3), 338-353.
[42] Chou, T.S. and Liang, G.S. (2001) Application of a fuzzy multi criteria decision making model for a shipping company performance evaluation. Maritime Policy and Management. 28(4), 375-392.
[43] Chen, C.T. (2001) A fuzzy approach to select the location of the distribution center. Fuzzy Set Systems. 118(1), 1-9.
[44] Jharkharia, S. and Shankar, R. (2007) Selection of logistics service providers, An analytic network process (ANP) approach. Omega. 35(3), 274-289.
[45] Tuzkaya, U.R. and Onut, S. (2008) A fuzzy analytic network process based approach to transportation-mode selection between Turkey and Germany, A case study. Information Sciences,.178(15), 3133-3146.
[46] Buyukozkan, G., Ertay, T., Kahraman, C. and Ruan, D. (2004) Determining the importance weights for the design requirements in the house of quality using the fuzzy analytic network approach. International Journal of Intelligent Systems. 19(5), 443-461.
[47] Brans, J.P., Vincke, Ph. and Mareschal, B. (1986) How to select and how to rank projects, the PROMETHEE method. European Journal of Operational Research. 24(2), 228–238.
[48] Albadvi, A., Chaharsooghi, S.K. and Esfahanipour, A. (2007) Decision making in stock trading, an application of PROMETHEE. European Journal of Operational Research. 177(2), 673-683.
[49] De Leeneer, I. and Pastijn, H. (2002) Selecting land mine detection strategies by means of outranking MCDM techniques. European Journal of Operational Research. 139(2), 327-338.
[50] Chen, S.J. and Hwang, C.L. (1992) Fuzzy Multiple Attribute Decision Making. 1st edition. Berlin Heidelberg, Springer.
[51] Kahraman, C., Ertay, T. and Buyukozkan, G. (2006) A fuzzy optimization model for QFD planning process using analytic network approach. European Journal of Operational Research. 171(2), 390-411.
[52] Bilsel, R.U., Buyukozkan, G. and Ruan, D. (2006) A fuzzy preference-ranking model for a quality evaluation of hospital web sites. International Journal of Intelligent Systems. 21(3), 1181-1197.
[53] Sugeno, M. (1985) An introductory survey on fuzzy control. Information Sciences. 36(1-2), 59-83.
[54] Yager, R.R. (1980) On a general class of fuzzy connectives. Fuzzy Sets Systems. 4(3), 235-242.
[55] Yager, R.R. (1981) A procedure for ordering fuzzy subsets of the unit interval. Information Sciences. 24(2), 143-161.

Received:11.12.2018
Accepted:25.11.2019

CORRESPONDING AUTHOR

Pınar Miç
Management Information Systems Department
Tarsus University
Tarsus – Turkey

e-mail: pinarmic@gmail.com
pinarmic@tarsus.edu.tr

© by PSP Volume 29 – No. 04A/2020 pages 2662-2669 Fresenius Environmental Bulletin

INVESTIGATION OF PROSPECTIVE SCIENCE TEACHERS' OPINIONS AND SENSITIVITY TOWARDS ENVIRONMENT

Ebru Ezberci Cevik[1,*], Mehmet Altan Kurnaz[2]

[1]Erciyes University, Faculty of Education, Department of Mathematics and Science Education, Kayseri, Turkey
[2]Kastamonu University, Faculty of Education, Department of Mathematics and Science Education, Kastamonu, Turkey

ABSTRACT

The aim of this study was to determine social and academic sensibilities, and opinions on environmental problems and environmental education among prospective teachers attending in a science education program. In this study, the survey method was used. The study group of the study consisted of 88 prospective science teachers from the first and fourth year of study at the Erciyes University Faculty of Education in the fall semester of 2018-2019. "Environmental Problems and Environmental Education Questionnaire" were used to collect data. SPSS 22 package program was used to analyze the data. As a result of the study, it was stated that prospective science teachers' opinions about environmental problems and environmental education were taken into consideration. Besides, it was concluded that participants' opinions on social and academic susceptibility sub-dimension did not vary significantly as per grade level variable and the significance level was not found between prospective teachers' social sensitivities and their academic sensibilities. Suggestions have been made on the teaching of environmental issues to prospective teachers.

KEYWORDS:
Environment, environmental education, environmental problems, environmental sensitivity, prospective science teachers

INTRODUCTION

People constantly interact with the environment in which they reside throughout their lives. Due to the constant interaction of individuals with their surroundings, problems occurring in the environment affects all living creatures. The primary way of fighting these problems called environmental problems can be achieved through education. Today, to solve environmental problems in the world, first of all, people need to gain sensitivity. In this respect, educating individuals who are qualified and sensitive in terms of attitudes, behaviors, knowledge, and skills, who protect ecological balance, who are aware of environmental problems related to the world we live in, and who can produce effective solutions to these problems has taken its place among the important duties of environmental education [1, 2].

[3] mentioned the importance of environmental education in his study indicating that this education was an indispensable tool in eliminating problems that could bring about the end of the world. Thanks to this education, the aim was to educate environmentally conscious individuals. [3] summarized this situation as shown in Figure 1.

Given the current technology, it is important to struggle with environmental problems to leave a more habitable world to future generations since there are no other worlds to inhabit [4]. The basic requirement in this struggle is to educate children as individuals who are aware of the environment, who take responsibility, and who are sensitive. Here, especially educators have responsibilities [5]. In this sense, environmental consciousness to be taught to prospective teachers as teachers of the future will be one of the solutions. When studies conducted on environmental education in Turkey are examined, it can be stated that there are many studies examining children's environmental information, perception, attitudes, and behaviors [6, 7, 8, 9, 10]. Prospective teachers' opinions on environmental education are also important since they will educate students with these attitudes, perceptions, and behaviors [11]. In particular, the subject of the environment is at the forefront of prospective science teachers who will provide education within the scope of science, technology, community, and environment. Assessment of prospective teachers who come to university with missing, partially adequate or full natural awareness, who become more aware and/or increase their awareness with their education processes is important in terms of revealing the current situation.

Research focus. It is considered important to determine opinions and sensibilities related to environmental problems and education among prospective science teachers who will work as science teachers at a primary education level that is the most stage in which environmental education can be achieved

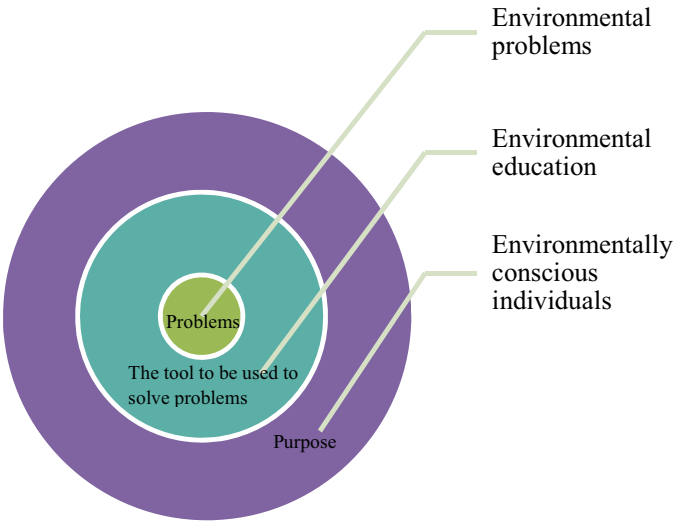

FIGURE 1
Environmental problems and environmental education.

after family life. In this respect, the aim of this study was to determine social and academic sensibilities, and opinions on environmental problems and environmental education among prospective teachers studying in the science education program.

In this respect, the problem statement of this study was as follows: "What are opinions, social and academic sensitivities regarding the environmental problems and environmental education among prospective teachers who are studying in science education program?". Answers to the following questions were sought based on the research problem:

1. What are prospective science teachers' opinions on environmental issues and environmental education?
2. What are prospective science teachers' opinions on "social sensitivity" sub-dimension related to the environment?
3. What are prospective science teachers' opinions on "academic sensitivity" sub-dimension related to the environment?
4. Do prospective science teachers' opinions on social sensitivity sub-dimension of environmental problems and environmental education survey vary by grade level?
5. Do prospective science teachers' opinions on academic sensitivity sub-dimension of environmental problems and environmental education survey vary by grade level?
6. Is there a relationship between the social sensitivity and academic sensitivity scores of prospective science teachers?

METHODS

In this study, the survey method was used in order to determine the opinions and sensitivities of the prospective science teachers towards the environment. A survey study is a model that aims to determine the characteristics of participants' opinions, interests, abilities, and attitudes, etc. [12, 13]. Survey studies are a suitable model for research that aims to describe a situation that exists in the past or the present [14].

Participants. The participants of the study consisted of 88 prospective science teachers from the first and fourth year of study at the Erciyes University Faculty of Education in the fall semester of 2018-2019. Table 1 shows the distribution of prospective science teachers according to the level of the class they study.

TABLE 1
Information for participants.

Class level	f	%
1st Class	40	45,5
4th Class	48	54,5
Total	88	100

Data collection tool. "Environmental Problems and Environmental Education Questionnaire" were used in the study. The questionnaire was developed by [15] and then reorganized by [16]. In the current study, the questionnaire conducted by [16] was used. The questionnaire consists of four parts, the first part is personal information, the second part is environmental problems and environmental education, the third part is social sensitivity and the fourth part is academic sensitivity. The questionnaire

includes 25 questions and the calculated reliability coefficient (Cronbach Alpha value) is 0,81. This value indicates that the scale is reliable.

Data collection. According to the data collection process, 89 teacher candidates were distributed on a voluntary basis and 20 minutes were allowed to complete. During the data collection process, one of the researchers was in charge of answering the possible questions of the participants. The data of 89 prospective teachers were pre-evaluated by two researchers, and as a result of this evaluation, a scale data containing some blank items and more than one option in the same article was excluded from the evaluation. A total of 88 prospective science teachers were analyzed on the data.

Data analysis. SPSS 22 package program was used to analyze the data. For the identified sub-problems, firstly, it was checked whether the assumptions were made about the appropriate analysis. Inferential statistics are used for the class level variable and descriptive statistics and inferential statistical tables are given in the findings section.

RESULTS

In this section, the findings of prospective science teachers' opinions on environmental problems and environmental education are presented separately. In addition, the social and academic sensibilities of prospective teachers were examined in terms of class-level variables.

Frequency and percentage distributions of answers given to the question, "What do you think is the most important environmental problem in the world?" that was asked to determine the most important environmental problem in the world according to prospective science teachers are presented in Table 2.

Analyzing Table 2, it is seen that 18.2% of prospective science teachers considered population growth, 17% of them considered the use of natural resources, and 17% of them considered climate change as the most important environmental problem in the world. Only one of the participants specified 'human' as the other environmental problem. Frequency and percentage distributions of answers given to the question, "What do you think is the most important environmental problem in Turkey?" that was asked to determine the most important environmental problem in Turkey according to prospective science teachers are presented in Table 3.

Analyzing Table 3, it is seen that 27.3% of prospective teachers considered the reduction of forests as the most important environmental problem in Turkey. 20.5% of prospective teachers consider the use of natural resources in the second place, and 18.2% of them considered air pollution as an important problem in the third place. In addition, 4.5% of prospective teachers concentrated on the other option and pose opinions such as 'community unawareness, environmental pollution, human and population growth'. Frequency and percentage distributions of answers given to the question, "Which of the following groups could be the most effective group on solving environmental problems?" that was asked to prospective science teachers to determine the most effective group on solving environmental problems are presented in Table 4.

According to the data in Table 4, 40.9% of prospective science teachers participating in the research considered the most influential group on solving environmental problems as "environmental institutions" in the first place; 30.7% of them considered "educators" in the second place; 11.4% of them considered "statesmen" in the third place. "Students and others (people, society, everyone)" are in the last place with equal rates of 4.5%. Frequency and percentage distributions of answers given to the question, "Which contributes the most to awareness of people about the environment?" that was asked to determine the most contributing tool to raise awareness about environment among people according to prospective science teachers are presented in Table 5.

TABLE 2
Frequency and percentage distributions of prospective science teachers' opinions on the most important environmental problem in the world.

	Frequency	Percent
Use of natural resources	15	17,0
Energy problem	3	3,4
Air pollution	9	10,2
Climate change	15	17,0
Urbanization	12	13,6
Population growth	16	18,2
Radioactive pollution	14	15,9
Water pollution	3	3,4
Other (Human)	1	1,1
Total	88	100,0

TABLE 3
Frequency and percentage distributions of prospective science teachers' opinions on the most important environmental problem in Turkey.

	Frequency	Percent
Use of natural resources	18	20,5
Energy problem	10	11,4
Air pollution	16	18,2
Climate change	9	10,2
Radioactive pollution	3	3,4
Water pollution	4	4,5
Reduction of forests	24	27,3
Other (Community unawareness, environmental pollution, human, population growth)	4	4,5
Total	88	100,0

TABLE 4
Frequency and percentage distributions of prospective science teachers' opinions on the most effective group for solving environmental problems.

	Frequency	Percent
Statesmen	10	11,4
Managers	7	8,0
Educators	27	30,7
Students	4	4,5
Environmental institutions	36	40,9
Other (people, society, everyone)	4	4,5
Total	88	100,0

TABLE 5
Frequency and percentage distributions of prospective science teachers' opinions about the tools that will contribute most to the awareness of the people about the environment.

	Frequency	Percent
Newspapers and magazines	2	2,3
TVs and radios	24	27,6
Schools	28	32,2
Environmental organizations	20	23,0
Municipalities	3	3,4
Ministry of Environment and Forestry	8	9,2
Other (None of them, education and school life)	2	2,3
Missing	1	1,1
Total	88	100,0

TABLE 6
Frequency and percentage distributions of prospective science teachers' opinions on economic development and ecological balance.

	Frequency	Percent
Economic development must continue at the expense of destroying the environment and disrupting the ecological balance.	5	5,7
A habitable world model should be established by creating balances between economic sanctions and developments in technology and economics.	68	77,3
In order to preserve the environment and the natural balance, economic and technological development must be limited.	14	15,9
Missing	1	1,1
Total	88	100,0

According to data in Table 5, 32.2% of prospective science teachers participating in the research regarded schools as the top contributor to raise awareness of people in the environment. 27.6% of participants regarded TVs and radios in the second place, and 23% of them regarded environmental organizations as the top contributor tool to raise people's awareness of the environment. It is also remarkable that one of the candidates specified none for the top contributor. Frequency and percentage distributions of answers given to the question, "Which of the following opinions do you feel close to yourself?" that was asked to determine prospective science teachers' opinions on economic growth and ecological balance are presented in Table 6.

According to the data in Table 6, the vast majority of prospective science teachers participating in

the research with a rate of 77.3% agreed to the opinion that "a habitable world model should be established by creating balances between economic sanctions and developments in technology and economics". In addition to this, 5.7% of prospective teachers agreed on the opinion that "economic development must continue at the expense of destroying the environment and disrupting the ecological balance". Frequency and percentage distributions of answers given to the question, "Which of the following is the objective of teaching environmental subjects?" that was asked to determine prospective science teachers' opinions on teaching environmental subjects are presented in Table 7.

According to the data in Table 7, 35.2% of prospective science teachers participating in the research agreed on the opinion that "helping students understand the problems of today" as the aim of teaching environmental subjects; 27.3% of participants agreed on the opinion that "encouraging students to be active in environmental protection" in the second place; 15.9% of participants agreed on the opinion that "showing students what they learn at school are related to daily life" in the third place. A small part of 2.3% agreed on the opinion that "something they need to know". Frequency and percentage distributions of answers given to the question, "At which teaching stage do you think that environmental education begins to be given?" that was asked to determine prospective science teachers' opinions on the stage of education to begin environmental education are presented in Table 8.

According to the data in Table 8, 62.5% of prospective science teachers participating in the research considered that environmental education should be given at the preschool level. 30.7% of participants thought in the second place that environmental education should be given at the primary education level. None of the prospective teachers had the opinion of starting environmental education at the higher education level. Frequency and percentage distributions of answers given to the question, "Which of the following methods would you like to choose in your courses to teach "environmental education" when you start teaching profession?" that was asked to determine prospective science teachers' opinions on methods used in environmental education are presented in Table 9.

According to the data in Table 9, 25.7% of prospective science teachers participating in the research indicated that they would use field trips to give environmental education when they started their teaching profession. 22.8% of participants stated that they can use the discussion of books, articles, TV and radio programs containing topics related to environmental issues in their courses, and 18.7% of them can use independent or group research projects. The result of the independent sample t-test conducted to determine whether science teacher candidates' social sensitivities to environmental problems and environmental education varied significantly according to grade level is presented in Table 10.

TABLE 7
Frequency and percentage distributions of prospective science teachers' opinions on the aim of teaching environmental issues.

	Frequency	Percent
Encouraging students to be active in environmental protection	24	27,3
Showing students what they learn at school are related to daily life	14	15,9
Helping students understand the problems of today	31	35,2
Something they need to know	2	2,3
To be a good way to teach problem-solving and decision making skills	9	10,2
Environmental issues to be interesting and attention to students	3	3,4
Another reason - To see the results of nature, - To avoid any negative events that may occur, - To make students conscious and act accordingly	3	3,4
Missing	2	2,3
Total	88	100,0

TABLE 8
Frequency and percentage distributions of prospective science teachers' opinions on the stage of environmental education.

	Frequency	Percent
Preschool level	55	62,5
Primary education level	27	30,7
Secondary education level	3	3,4
Higher education level	0	0
In non-formal education	3	3,4
Total	88	100,0

TABLE 9
Frequency and percentage distributions of prospective science teachers' opinions on the methods used in environmental education.

	N	Percent
Discussion of books, articles, TV and radio programs containing topics related to environmental issues	39	22,8%
Hand-based activities	31	18,1%
Independent or group research projects	32	18,7%
Field trips	44	25,7%
Civil movement activities	24	14,0%
Other (Zone cleaning)	1	0,6%
Total	171	100,0%

TABLE 10
Independent sample t-test results on whether the social sensitivity of science teacher candidates differs according to grade level.

Class level	n	$\bar{x}$	S	t	Df	p*
1st Class	40	29,93	4,78	1,005	86	,318
4th Class	48	31,40	8,15			

*p<.05

TABLE 11
Independent sample t-test results on whether the academic sensitivity of science teacher candidates differs according to grade level.

Class level	n	$\bar{x}$	s	t	df	p*
1st Class	40	36,23	3,04	,163	86	,871
4th Class	48	36,33	3,15			

*p<.05

When Table 10 was examined, it was found that there were no statistically significant differences between prospective science teachers' social sensitivity score averages as per grade level [t(86)=1.005, p>.05]. The result of an independent sample t-test conducted to determine whether science teacher candidates' academic sensitivities to environmental problems and environmental education varied significantly according to grade level is presented in Table 11.

Analyzing Table 11, it was determined that there were no statistically significant differences found between science teacher candidates' academic sensibility mean scores as per grade level [t(86)=.163, p>.05]. Results of correlation analysis conducted to determine whether there was a relationship between prospective science teachers' social sensitivities to environmental problems and environmental education and their academic sensitivity scores are presented in Table 12.

TABLE 12
Correlation analysis result.

		Academic sensitivity
Social sensitivity	R	,112
	P	,298
	N	88

Analyzing Table 12, 0.05 significance level was not found between prospective teachers' social sensitivities and their academic sensibilities (r=.112; p >.05).

CONCLUSIONS, DISCUSSIONS AND SUGGESTIONS

As a result of this study conducted to determine social and academic sensibilities of prospective teachers studying in science education program based on their opinions on environmental issues and environmental education, it was determined that the prospective science teachers indicated the population growth as the most important environmental issue in the world, and they indicated the deforestation as the most important environmental problem in Turkey. [17], in a study conducted with prospective classroom teachers, stated that 18.2% of participants specified population increase and deforestation as the most important environmental problem in Turkey. In the study conducted by [18], population growth was listed among the factors that disrupt the environment. The result of that study supports the current research.

In the study, it was concluded that prospective science teachers considered the most effective groups for the solution of environmental problems as environmental organizations and then educators. Similarly, in a study conducted by [17], prospective classroom teachers specified educators as the most influential group in relation to the solution of environmental problems with a rate of 41.8%, they specified environmental organizations as the most influential group with a rate of 41.8%. Prospective science teachers think that schools are the tools that will

contribute to people's awareness about the environment. These results are in accordance with results found in the previous case in which prospective teachers also specified educators as the most influential group.

Prospective science teachers have the opinion that a habitable world model must be created by establishing balances between economic sanctions and technological and economic developments. According to this conclusion, it can be said that the majority of prospective biology teachers have the opinion that technological and economic developments are necessary, but the supervision of these developments with ecological sanctions might be appropriate.

It was observed in this study science teacher candidates agreed on the statement of helping students understand today's problems in relation to the purpose of teaching environmental subjects. To solve the environmental problems in the world today, it is emphasized that sensitivity should be taught to individuals, societies constituted of individuals and the international community [19]. In the study conducted by [20], it is emphasized that environmental education is among the most important points to increase the environmental perception of the public. In the present study, it was seen that prospective teachers also had similar opinions.

The majority of prospective science teachers thought that environmental education should be given in preschool education level. Then, the elementary education level was emphasized. This finding also emphasizes the sensitivity of prospective teachers against environmental education. In this sense, it can be said that environmental education given to students at preschool and elementary levels is important in terms of increasing sensitivity. According to [21] and [22], children learn better in studies requiring effective participation in the environment. In this context, prospective science teachers have an important responsibility.

In this study, prospective science teachers preferred mostly the options of field trips and discussing books, articles, TV and radio programs containing headlines related to environmental subjects. Reviewing the field literature, studies supporting these results were found [23, 24].

Considering the data obtained for other subproblems of the research, it was concluded that participants' opinions on social and academic susceptibility sub-dimension did not differ significantly from the grade level variable. [24], in their study, noted that the data obtained for prospective teachers' perceptions regarding environmental education concentrated more on achieving information and awareness towards nature. It was stated that the reason for this was that the environmental education courses prospective teachers received at the university were theoretical. In the current study, it is considered that no differences between the two class levels may arise from the fact that courses remain with the book information rather than practice, and for this reason, awareness among prospective teachers is not sufficiently increased.

In light of the results obtained from the study, it is understood how important the education of prospective science teachers who will give a healthy environment understanding to the students during their teacher education. In this sense, it should be ensured that the environmental content courses given in universities are not only theoretical but also compatible with practical (eco-school models) and daily life. In this way, teacher candidates should be given a positive attitude and sensitivity towards the environment and provided to reflect them to daily life. In addition to this, the prospective science teachers mentioned the means used to gain environmental education as a discussion of excursions, books, articles, TV and radio programs. In line with this result, it is considered that attention should be paid to the extension of environmental education through mass media.

REFERENCES

[1] Desjean-Perrotta, B., Moseley, C. and Cantu, L.E. (2008) Pre-service teachers' perceptions of the environment: does ethnicity or dominant residential experience matter? The Journal of Environmental Education. 39(2), 21-31.

[2] Sadik, F., Cakan, H., Artut, K. (2011) Analysis of the environmental problems pictures of children from different socio-economical level. Elementary Education Online. 10(3), 1066-1080 (in Turkish).

[3] Erten, S. (2004) What is environmental education and environmental awareness, how should environmental education be? Environment and Human Journal. 65-66, 2006/25 (in Turkish).

[4] Karatas, A. (2013) The role of environmental education in improving environmental awareness and the sample of Nigde University faculty of Education, Ankara University Institute of Social Sciences, Department of Social Environmental Sciences, Ankara (in Turkish).

[5] Pereira, R., Pinho, R., Lopes, L., Antunes, S.C., Abrantes, N. and Goncalves, F. (2006) Helping teachers to use urban natural areas for science teaching and environmental education. Fresen. Environ. Bull. 15, 1467-1473.

[6] Atasoy, E. and Erturk, H. (2008) A field study about environmental knowledge and attitudes of elementary school students. Erzincan University Journal of Education Faculty. 10(1), 105-122 (in Turkish).

[7] Denis Celiker, H. and Akar, A. (2015) Metaphors regarding to nature of middle school students. Journal of Kırşehir Faculty of Education. 16(2), 101-119 (in Turkish).
[8] Isyar, N. (1999) The evaluation of primary school children's (3rd, 4th, 5th graders) positive environmental attitudes according to the age and socioeconomic status. Uludag University, Institute of Social Sciences, Department of Classroom Teaching, Bursa (in Turkish).
[9] Ozdemir, O. and Uzun, N. (2006) The effect of science and nature activities carried out according to the green class model on the perceptions of environmental class students. Journal of Child Development and Education. 1-2, 12-20 (in Turkish).
[10] Tecer, S. (2007) Education for environmental: A study on the level of determination of the primary students' environmental behavior, knowledge, consciousness and active participation in Balikesir City. Karaelmas University, Institute of Science, Environmental Engineering Department, Zonguldak (in Turkish).
[11] Selvi, M. and Selvi, M. (2004) Environmental education for sustainable development. Fresen. Environ. Bull. 13, 905-907.
[12] Fraenkel, J.K. and Wallen, N.E. (2006) How to design and evaluate research in education. 6th ed. New York: McGraw-Hill, Inc.
[13] McMillan, J.H. and Schumacher, S. (2014) Research in education: Evidence-based Inquiry 6th ed. Pearson Education.
[14] Karasar, N. (2002) Scientific Research Methodology. Ankara: Nobel (in Turkish).
[15] Karadayi, G. (2005) High school teacher's opinion about global, national and local environmental matters (Case of Sakarya). Gazi University, Institute of Educational Sciences, Department of Biology Education, Ankara (in Turkish).
[16] Ibis, S. (2009) Opinions of biology pre service teacher about national and global environmental problems. Gazi University, Institute of Educational Sciences, Department of Biology Education, Ankara (in Turkish).
[17] Erol, G.H. (2005) Primary school teaching department sophomore students' attitudes toward environment and environmental problems. Pamukkale University, Institute of Science, Denizli (in Turkish).
[18] Karakas G. (2018) Factors affecting the environmental attitudes and behaviours of university students in Turkey. Fresen. Environ. Bull. 27, 5372-5379.
[19] Cavus, A. (2013) The evaluation of the teachers' opinions on the effectiveness of the 7th class Science and Technology lesson in terms of environmental training: The example of Bingöl. İnönü University, Institute of Educational Sciences, Department of Educational Sciences, Educational Programs and Teaching, Malatya (in Turkish).
[20] Bilgin, A. and Balkaya, N. (2017) An assessment of the perspectives of university students on environmental issues in Turkey. Fresen. Environ. Bull. 26, 5271-5282.
[21] Bowker, R. (2007) Children's perceptions and learning about tropical rainforests. An analysis their drawings. Environmental Education. 13(1), 75-96.
[22] Lindeman-Matthies, P. (2002) The influence of an educational program on children's perception of biodiversity. The Journal of Environmental Education. 33(2), 22-31.
[23] Gokmen, A., Ekici, G. and Ozturk, G. (2012) A study on the examination of biology teacher candidates' self-efficacy perceptions towards environmental education. 10. National Science and Mathematics Education Congress, Nigde (in Turkish).
[24] Ozmen, H. and Ozdemir, S. (2016) Determination of pre-service science and technology teachers' views on environmental education. Kastamonu Education Journal. 24(4), 1691-1712 (in Turkish).

Received: **13.12.2018**
Accepted: **02.02.2020**

CORRESPONDING AUTHOR

Ebru Ezberci Cevik
Erciyes University,
Education Faculty,
Mathematics and Science Education Department,
Kayseri – Turkey

e-mail: ezbercicevik@erciyes.edu.tr

© by PSP Volume 29 – No. 04A/2020 pages 2670-2677 Fresenius Environmental Bulletin

MONTHLY VARIATION OF PHARMACEUTICALLY VALUABLE ALKALOIDS, GALANTHAMINE AND LYCORINE, IN SUMMER SNOWFLAKE (*LEUCOJUM AESTIVUM* L.)

Mustafa Arslan[1], Arzu Birinci Yildirim[2], Erva Ozkan[3], Fatma Betul Oktelik[3], Arzu Ucar Turker[3,*]

[1]Western Black Sea Forestry Research Institute, Bolu, Turkey
[2]Bolu Abant Izzet Baysal University, Faculty of Agricultural and Environmental Science, Department of Field Crops, Bolu, Turkey
[3]Bolu Abant Izzet Baysal University, Faculty of Science and Art, Department of Biology, Bolu, Turkey

ABSTRACT

Leucojum aestivum L. (summer snowflake) is a perennial bulbous plant of Amaryllidaceae family. It is exported for medicinal purposes to pharmaceutical industry and uncontrolled excessive collection of them causes a decline in natural population. *L. aestivum* is a well-known producer of pharmaceutically important alkaloids. Among the various alkaloids in *L. aestivum*, galanthamine is the major bioactive compound. Galanthamine is widely used in the treatment of neurological disorders, including Alzheimer's disease. Another alkaloid is found in the summer snowflake is lycorine having variety of biological activities such as, antitumor, antimalarial, hepatoprotective, antiviral, antifungal and antiparasitic. Objective of the study was to determine the monthly variations of galanthamine and lycorine content in *L. aestivum* grown in a sheltered area. Bulbs and leaves of *L. aestivum* collected each month for two years were extracted with methanol and then quantitatively analyzed and compared for their galanthamine and lycorine content by using HPLC-DAD system. Bulbs of summer snowflake contained more alkaloids than leaves and lycorine content was much more than galanthamine in both leaves and bulbs. It was concluded that July was the best month for bulbs and November was the most efficient month for leaves in terms of galanthamine and lycorine content.

KEYWORDS:
Alkaloid, galanthamine, *Leucojum aestivum*, lycorine, summer snowflake

INTRODUCTION

Leucojum aestivum L. (summer snowflake) is a medicinal and ornamental plant of Amaryllidaceae family. It grows from sea level to high altitudes in humid and semi-shaded areas such as swamps, wetlands and floodplains [1-3]. It is a Euro-Mediterranean region plant and native to Turkey [1]. It is an endangered perennial bulbous plant because of gathering them from natural habitats for pharmaceutical industry causing reduction in wild populations [4-5]. It is a well-known producer of pharmaceutically important alkaloids especially galanthamine. Approximately, one ton of *L. aestivum* bulbs are required to obtain one kg of galanthamine [6]. It is a valuable export material in Turkey exporting 6 000 000 pieces of bulbs every year with the cultivation of *L. aestivum* for galanthamine production to pharmaceutical industry [7]. Only collection of aerial parts of *L. aestivum* from the natural habitat was allowed for the exportation in Turkey [8]. Galanthamine, an isoquinoline alkaloid, is a long acting, selective, competitive and reversible acetylcholinesterase inhibitor that reduces the action of acetylcholinesterase and thus increases the concentration of acetylcholine in the brain. Galanthamine is widely used for symptomatic treatment of senile dementia of the Alzheimer's type, poliomyelitis and other neurological diseases [9]. Hydrobromide salt of galanthamine was first marketed as a trade name 'Nivalin®' in Bulgaria in late 1950s and later also in many other Eastern European countries [10-12]. Lycorine, a pyrrolophenanthridine alkaloid, has a wide variety of biological activities such as antitumor, antimalarial, hepatoprotective, antiviral, antifungal and antiparasitic [9, 13-15].

While galanthamine in *L. aestivum* is commercially important for pharmaceutical industry, to our knowledge, there is no study about the determination of monthly alkaloid dispersion throughout the whole year. In this context, we intended to reveal monthly galanthamine and lycorine distributions in *L. aestivum* bulbs and leaves grown in a sheltered area.

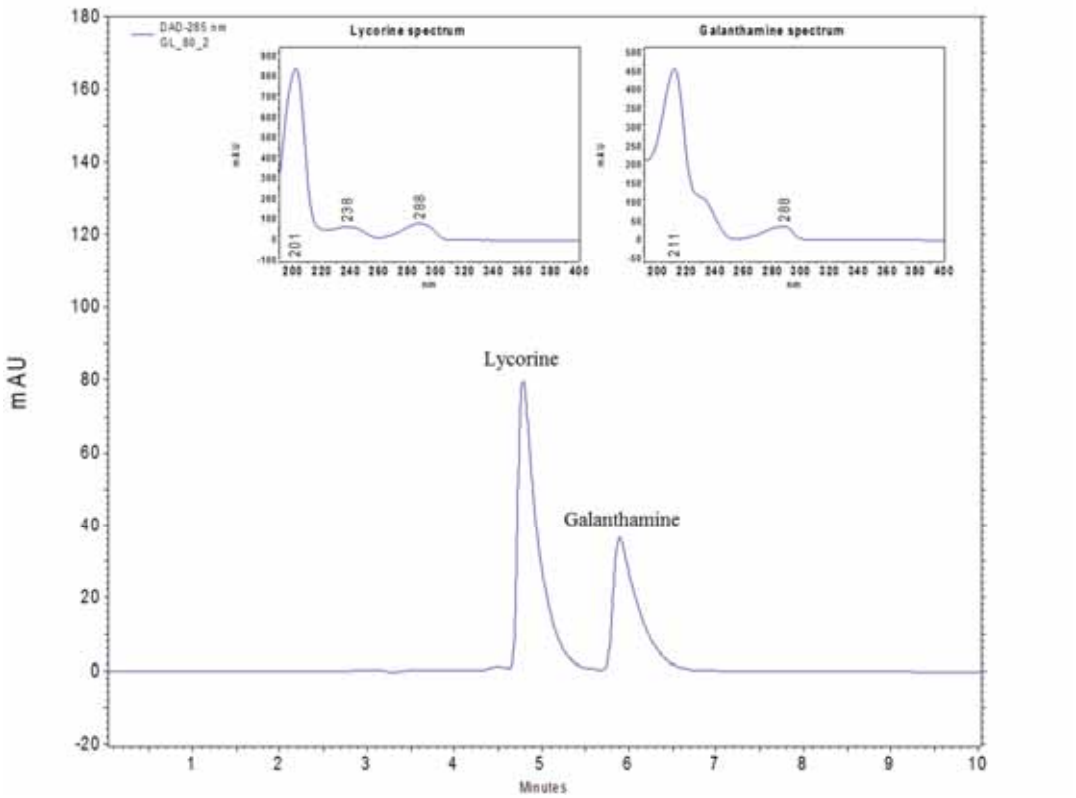

FIGURE 1
HPLC chromatogram of alkaloid standards (lycorine and galanthamine) used for identification. Retention times: lycorine-4.82 min and galanthamine-5.947 min.

MATERIALS AND METHODS

Plant Growth and Extraction. *L. aestivum* seeds were obtained from Akçakoca, Düzce, Turkey. It was identified using "Flora of Turkey and The East Aegean Island" [1] and voucher specimens (AUT-2050) were deposited in Bolu Abant Izzet Baysal University. After breaking the seed dormancy [2], two years were required for a complete individual. Plants were grown in a sheltered garden with a transparent roof (environmentally compatible) found in Western Black Sea Forestry Research Institute, Bolu, Turkey. Soil texture was 69 % sand, 19 % clay and 12 % silt [pH: 7.44, calcium carbonate ($CaCO_3$): 6.8 % and electrical conductivity (EC): 1.21]. It was ensured that plants in high cushions were moist during the year. Watering was made twice a week between June and October, and once a week at other months. Four plants including bulbs and leaves were collected at the third week of each month, cleansed from soil and stored at -20°C. Plant sampling was continued for 2 years (2014 and 2015). Bulbs and leaves of *L. aestivum* were freeze dried, powdered and extracted with methanol solvent at 45 °C in ultrasonic bath for 2 hours and then vacuum evaporated. Yield for each extract was calculated and listed in Table 1.

High Performance Liquid Chromatography (HPLC) analysis. Methanolic extracts were quantitatively analyzed for lycorine and galanthamine using high performance liquid chromatography (HPLC) coupled with a diode array detector (DAD) (VWR-Hitachi LaChrom Elite®) in "Medicinal Plant Research Laboratory at Bolu Abant Izzet Baysal University".

TABLE 1
Yields (%) of methanol extract of *L. aestivum* bulbs and leaves.

	Yield (%)*	
Months	**Bulbs**	**Leaves**
January	17.46 ± 0.04	38.93 ± 3.21
February	11.52 ± 3.88	38.06 ± 1.66
March	9.2 ± 3	34.4 ± 1.7
April	13.95 ± 4.75	33.65 ± 3.55
May	5.8 ± 1.1	26.6 ± 1.2
June	4.9 ± 0.3	19.85 ± 2.76
July	4.4 ± 0.2	29.85 ± 7.25
August	5.4 ± 0.7	25.95 ± 3.25
September	7.1 ± 0.9	26.95 ± 2.65
October	8.5 ± 1	28.4 ± 2.6
November	12.5 ± 0.6	33.05 ± 4.45
December	10.25 ± 1.15	26.9 ± 6

Data were presented as a mean number of yields of extracts for 2 years ± standard error (SE). *Yield (%) = "100 × obtained extract weight (g) / initial plant material weight (g)"

Lycorine hydrochloride (Sigma®) and galanthamine hydrobromide (TCI America®) were used as standard alkaloid compounds. Stock solutions of all standards were prepared as 1000 mg/l concentration in 0.1% trifluoroacetic acid (TFA), then 6 different concentration of standards (6.25, 12.5, 25, 50, 100 and 200 mg/l) were used to obtain the standard calibration curves. Prior to HPLC analysis, prepared mobile phase was filtrated through a 0.45-µm hydrophilic polypropylene membrane filter (47 mm) (Pall®). All extracts and standard solutions were filtrated through a 0.2-µm GHP (25 mm) (Pall®) and they were transferred into 2-mL HPLC vials (Isolab®). The chromatogram of the used standards was shown in Figure 1. Alkaloid standards and each extract were prepared in definite concentrations by dissolving in 0.1% TFA for HPLC analysis and then analyses of them were performed. A reverse phase C18 column (250 mm X 4.6 mm, 5 µm particle size, Venusil Technology®) was used in all HPLC analyses. HPLC-DAD analysis was achieved according to method described by previous studies [14, 16-18] using an isocratic eluting solvent mixture, TFA: water: acetonitrile (0.01:90:10 v/v/v), as mobile phase for 10 min. An injection volume of 20 µL and flow rate of 1ml/min were applied during the analysis. Detector was run at 290 nm wavelength. A standard mixture prepared in known concentration of each component was used in quantitative determination of components. Quantitative analysis of each component was done by integrating the peak area of standards and samples run under same conditions. All procedures were done in triplicate for each tested sample.

Data Analysis. Analysis of variance (ANOVA) and Duncan's Multiple Range Tests using SPSS vers. 15 (SPSS Inc, Chicago, IL, USA) were performed for data analysis. Monthly temperature values for 2014 and 2015 were obtained from Bolu Meteorological Station. Correlation was evaluated between monthly lycorine and galanthamine amount (mg/g) in the bulb and leaf extract of *L. aestivum* and monthly mean temperatures. Correlations between alkaloid content and temperature were calculated by Pearson correlation analysis.

RESULTS AND DISCUSSION

Bulbs and leaves of *L. aestivum* were collected each month for 2 years and monthly distributions of two alkaloids were evaluated as 2 years average. This study was carried out in a sheltered garden because sampling was required for 24 months and intact plant of *L. aestivum* including bulbs and leaves could be destroyed in nature throughout the whole year. Bulbs and leaves were extracted with methanol and the percentage yields of the extracts were calculated (Table 1). Generally, leaf extracts gave higher percentage yields than bulb extracts because of having more kinds of metabolites such as phenolic compounds and chlorophylls. Methanolic extracts of the bulbs and leaves were quantitatively analyzed using HPLC-DAD system (Table 2). Chromatograms of used alkaloid standards (Figure 1) and tested extracts (Figure 2 and 3) were presented. Galanthamine content ranged from 6.89 to 25.37 mg/g in the bulbs and from 1.82 to 8.09 mg/g in the leaves. In addition, lycorine content dispersed from 51.36 to 135.69 mg/g in the bulbs and from 33.44 to 62.57 mg/g in the leaves throughout the whole year (Table 2). It was observed that bulb and leaves contained more lycorine than galanthamine. Moreover, bulbs included more alkaloids than leaves (Table 2). According to the results of monthly distribution of alkaloid, July was the most effective month for the bulbs in terms of galanthamine and lycorine content (Table 2). At the same time, November was the most efficient month for galanthamine content in the leaves, and lycorine content of the leaves was the highest in March, August and November (Table 2). The lowest galanthamine and lycorine concentrations in the bulbs were observed in December and April, respectively. January and June were not much efficient in terms of galanthamine content of the leaves. In addition, April, May, June and July were not abundant concerning lycorine concentration of the leaves (Table 2). Seasonal variation in galanthamine and lycorine content of the bulbs and leaves were also found out (Figure 4). Summer season (June, July and August) was the best season about galanthamine and lycorine content in the bulbs. Tested alkaloids in the leaves did not vary significantly seasonally (Figure 4).

Correlation between monthly distribution for alkaloid content and temperature as averages of 2 years was also performed (Figure 5 and 6). Lycorine and galanthamine content of the bulbs displayed a positive correlation with temperature (Figure 5). Alkaloids in the leaves did not exhibit a relationship with temperature (Figure 6). The values of the correlation coefficient (r) for lycorine and galanthamine in the bulbs were 0.69 and 0.49, respectively. This indicated a moderate positive correlation between temperature and alkaloid content in the bulbs. Besides, the coefficient of determination (r^2) had values of 0.47 and 0.24, respectively. This showed that monthly average temperature had 47% effect on the lycorine content of the bulbs. On the other hand, galanthamine content had 24% relationship with monthly average temperature.

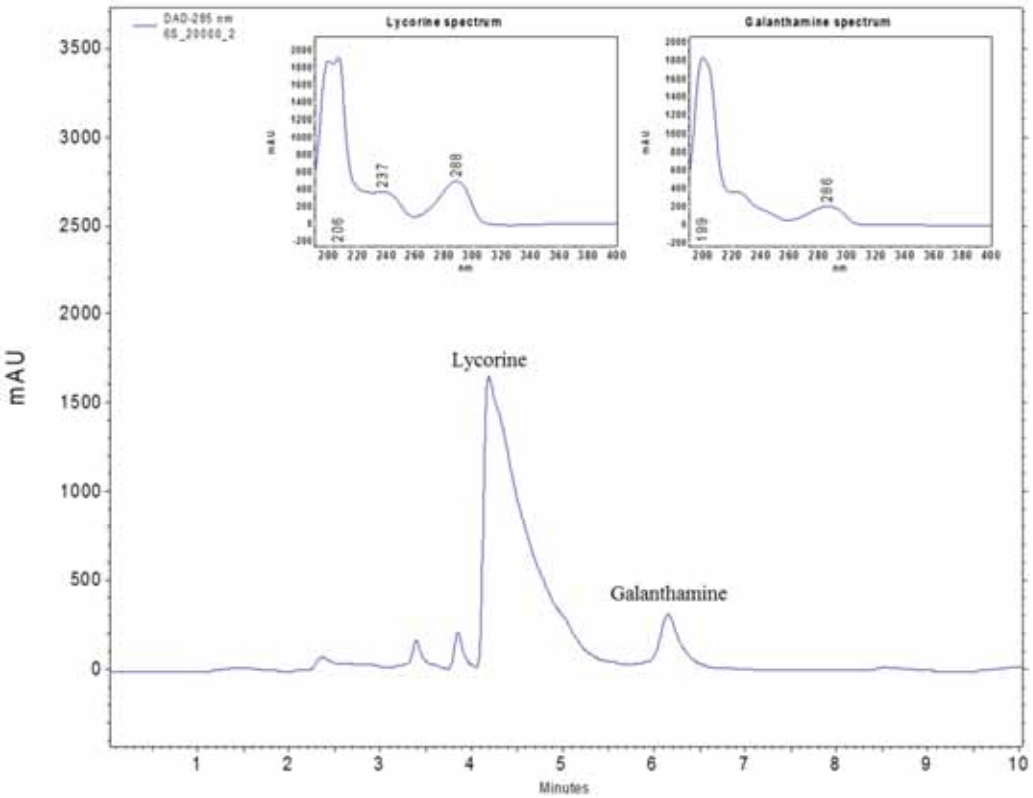

FIGURE 2
HPLC chromatogram of bulb extract and spectrums of the alkaloids.

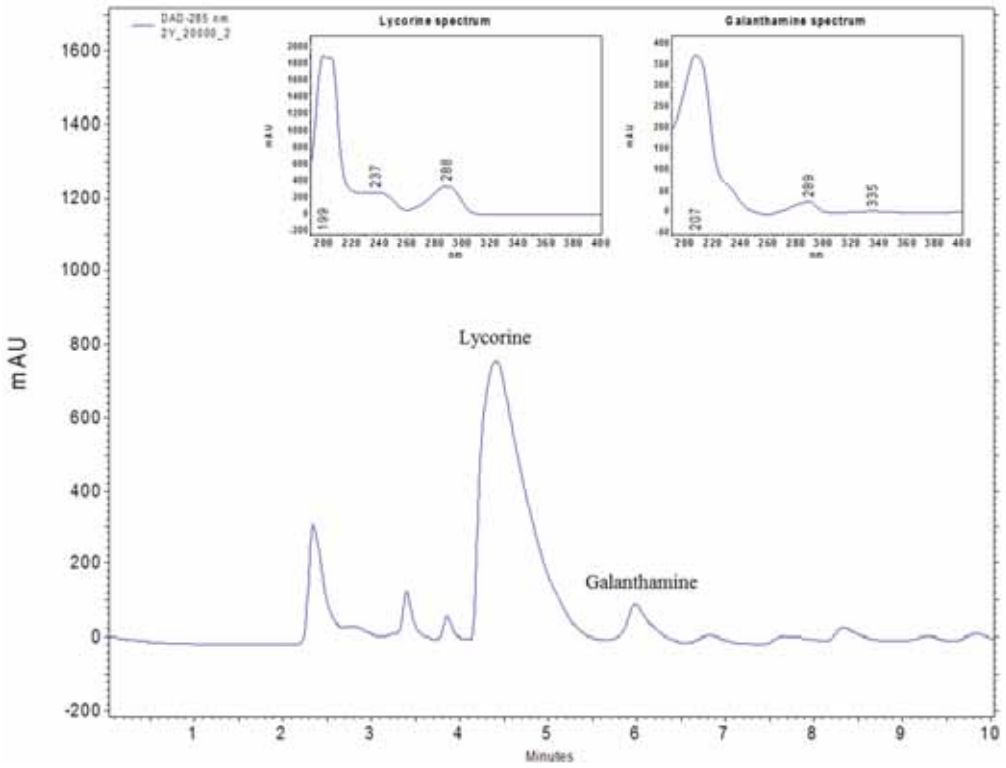

FIGURE 3
HPLC chromatogram of leaf extract and spectrums of the alkaloids.

TABLE 2
Monthly distribution of alkaloid quantities (galanthamine and lycorine) (mg/g) in the bulb and leaf extract of *L. aestivum*.

	HPLC-DAD Analysis			
	Galanthamine (mg/g dry extract)		Lycorine (mg/g dry extract)	
Months	Bulbs	Leaves	Bulbs	Leaves
January	9.42 ± 1.54^{cd}	1.82 ± 0.08^{c}	68.28 ± 11.61^{def}	49.01 ± 0.70^{ab}
February	8.87 ± 4.64^{cd}	4.55 ± 1.96^{abc}	71.91 ± 16.33^{def}	49.07 ± 5.74^{ab}
March	15.75 ± 5.45^{abcd}	6.72 ± 3.41^{ab}	81.49 ± 11.97^{cde}	60.34 ± 13.05^{a}
April	12.95 ± 5.75^{bcd}	4.56 ± 1.69^{abc}	51.36 ± 2.95^{f}	35.25 ± 5.51^{b}
May	15.34 ± 4.68^{abcd}	3.59 ± 1.06^{bc}	78.79 ± 2.94^{cdef}	33.44 ± 2.22^{b}
June	18.02 ± 2.49^{abcd}	2.10 ± 0.18^{c}	92.48 ± 12.81^{cd}	33.95 ± 4.73^{b}
July	25.37 ± 5.75^{a}	3.19 ± 0.95^{bc}	135.69 ± 11.87^{a}	34.46 ± 3.57^{b}
August	20.59 ± 1.27^{abc}	5.89 ± 0.04^{abc}	122.66 ± 7.22^{ab}	62.57 ± 14.01^{a}
September	17.03 ± 0.47^{abcd}	4.13 ± 0.65^{abc}	102.33 ± 5.90^{bc}	56.13 ± 13.69^{ab}
October	12.43 ± 1.94^{bcd}	2.41 ± 0.02^{bc}	82.85 ± 0.96^{cde}	51.35 ± 0.89^{ab}
November	22.56 ± 2.05^{ab}	8.09 ± 1.03^{a}	74.67 ± 2.55^{cdef}	60.34 ± 1.73^{a}
December	6.89 ± 0.05^{d}	3.27 ± 3.05^{bc}	60.02 ± 0.50^{ef}	55.36 ± 0.28^{ab}

Data were presented as a mean number of quantities of alkaloids for 2 years ± standard error (SE). Means with the same letter within columns are not significantly different at $P>0.05$.

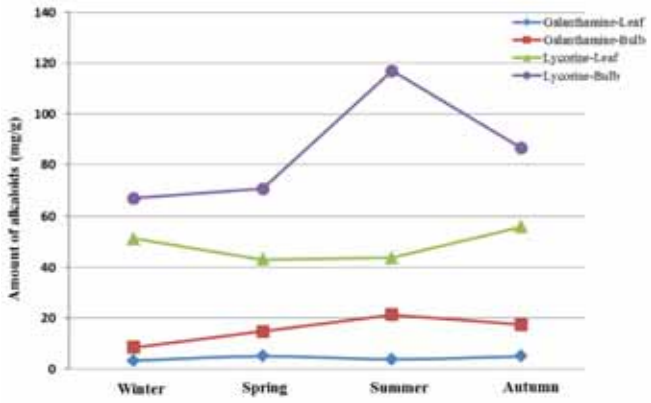

FIGURE 4
Seasonal variation in galanthamine and lycorine content in the bulbs and leaves of *L. aestivum*.

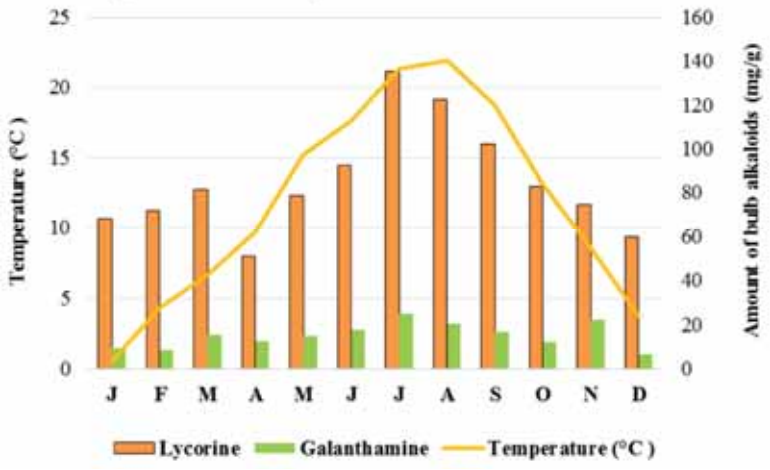

FIGURE 5
Correlation of monthly distribution of lycorine and galanthamine amount (mg/g) in the bulb extract of *L. aestivum* with the mean temperatures.

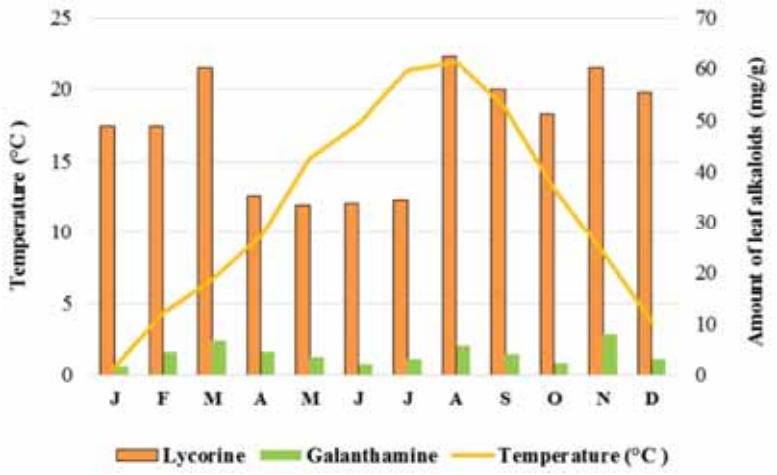

FIGURE 6
Correlation of monthly distribution of lycorine and galanthamine amount (mg/g) in the leaf extract of *L. aestivum* with the mean temperatures.

Growing conditions like temperature, the light regime and the nutrient supply strongly affects the accumulation of natural products. Vigorous environmental factors like various stress conditions also affect the metabolic pathways responsible for the accumulation of secondary plant products [19, 20]. For example, many studies were reported about drought stress related increase in the concentrations of alkaloids such as trigonelline, pyrrolizidine alkaloids, quinolizidine alkaloids, steroid alkaloids, morphine alkaloids, indole alkaloids, nicotiana alkaloids and benzylisoquinolines [20]. There is a general tendency for alkaloid concentrations to be higher during dry periods than in wet periods as in the case of wild hemlock (*Conium maculatum* L.), cinchona (*Cinchona calisaya* Wedd.) and opium poppy (*Papaver somniferum* L.). Wild hemlock is most toxic during hot and dry seasons. Cinchona does not produce quinine during the rainy season and field-grown opium poppy shows a sharp decline in morphine and codeine content in a wet period [21].

Similar to our results, Jansen et al. [22] showed that seed alkaloid content of *Lupinus angustifolius* L. cultivars ascended with increasing temperature. Sahoo et al. [23] investigated the variations in the total alkaloid and phenol during different seasons in some medicinal plants [*Barleria prionitis* L., *Boerhavia diffusa* L., *Citrullus colocynthis* (L.) Schrad. and *Grewia tenax* (Forssk.) Fiori.] and indicated that highest amount of total alkaloids and phenols were observed in summer, while the lowest in rainy season. Guo et al. [24] concluded that high temperature could enhance the accumulation of some alkaloids in *Catharanthus roseus* (L.) G.Don. related with the treatment time. Zu et al. [25] reported that alkaloid camptothecin and hydroxycamptothecin were involved in *Camptotheca acuminata* Decne. resistance against heat shock from its environment and under heat-shock condition, alkaloids changed sensitively in buds and young leaves.

Galanthamine production in *in vitro* culture system is an attractive alternative method [4, 26, 27]. Berkov et al. [5] reported that shoot-clump cultures of *L. aestivum* have a higher ability for galanthamine production. Galanthamine content in shoot-clumps was found various depending on nutrient media with different combinations of plant growth regulators [5, 28]. Pavlov et al. [26] displayed that light raised the galanthamine production in the shoot-clump of *L. aestivum*. Concentrations of nutrients in the medium affected the galanthamine biosynthesis in *in vitro* cultured *L. aestivum* [6, 27]. Diop et al. [28] determined the galanthamine content in both *in vitro* and *in vivo* extracts of *L. aestivum* at different stages of morphogenesis. They found a correlation between the state of differentiation and the galanthamine content. Ayan et al. [7] indicated that bulb yield of *L. aestivum* was much more in *in vitro* grown system under shaded conditions and they suggested that shading would be a very useful practice to enhance bulb yield in the cultivation of *L. aestivum* under field conditions.

Harvesting time and different naturally growing populations of *L. aestivum* with the most efficient galanthamine content should be investigated primarily because of limited supply of the natural source and high cost of synthetic production [29]. Georgieva et al. [4] reported the alkaloid variability of *L. aestivum* bulb extracts collected from 18 Bulgarian populations and found that bulbs mainly contain galanthamine, epinorgalanthamine, narwedine, and lycorine. They suggested that genetic factor plays an important role in the alkaloid biosynthesis of *L. aestivum*. Gorinova et al. [30] found a relationship between the galanthamine content of *L. aestivum* and the chemical composition of the soil and

inferred that galanthamine biosynthesis can be controlled by the soil fertility level. Quantification of galanthamine in *Narcissus tazetta* L. and *Galanthus nivalis* L. populations growing wild in Iran was investigated and maximum galanthamine content was determined in some populations by Khonakdari et al. [29]. In contrast to our results, Lubbe et al. [31] reported that bulbs of *Narcissus pseudonarcissus* cv. Carlton had higher concentration of galanthamine before flowering (April). In addition, leaves had approximately same levels of galanthamine until full flowering (May) followed by a decrease after flowering. Elgorashi et al. [32] investigated the distribution and seasonal variation of alkaloids (lycorine, 1-*O*-acetyllycorine, crinine, powelline, crinamine, crinamidine, 3-*O*-acetylhamayne, 1-epideacetylbowdensine and cherylline) in *Crinum macowanii* Baker. Lycorine showed a significant organ-to-organ variation. However, bulb lycorine did not display a significant seasonal variation. Contrary to their result, bulb lycorine content showed a seasonal variation (Figure 4) and moderate correlation (47% effect) with temperature in our study (Figure 5).

CONCLUSIONS

Analysis of galanthamine and lycorine for 24 months revealed that July and November could be the best months for bulb and leaf harvesting, respectively in the cultivation of *L. aestivum*. If the seasonal variation of galanthamine was concerned, summer season is the best month for the alkaloid content of the bulb. A remarkable seasonal variation was not observed with the leaves. A positive correlation was observed between lycorine and galanthamine content of the bulbs and temperature. Future studies can be performed for the determination of monthly and seasonal variation of alkaloids in *L. aestivum* obtained from different natural environment to establish galanthamine rich cultivar. Furthermore, different investigations (*in vitro* and *in vivo*) can be carried out to determine the factors on alkaloid variations and to enhance the quantity of alkaloids applying different stress conditions.

ACKNOWLEDGEMENTS

This study was supported by Abant Izzet Baysal University Research Foundation (BAP 18.10.07.1367).

The authors declare that they have no conflicts of interest.

REFERENCES

[1] Davis, P.H. (1984) Flora of Turkey and the East Aegean Islands. Vol. 8. Edinburgh Univ. Press, Edinburgh.

[2] Çiçek, E., Aslan, M., Tilki, F. (2007) Effect of stratification on germination of Leucojum aestivum L. seeds, a valuable ornamental and medicinal plant. Res. J. Agric. Biol. Sci. 3, 242-244.

[3] Çiçek, E., Çetin, B., Özbayram, A. K., Türkyılmaz, H. (2013) Effect of desiccation, temperature and storage on the germination of snow flake (Leucojum aestivum L.) seeds, Artvin Coruh Univ. J. Forestry Fac. 14, 245-252.

[4] Georgieva, L., Berkov, S., Kondakova, V., Bastida, J., Viladomat, F., Atanassov, A., Codina, C. (2007) Alkaloid variability in Leucojum aestivum from wild populations. Z. Naturforsch. C. 62, 627-635.

[5] Berkov, S., Georgieva, L., Kondakova, V., Atanassov, A., Viladomat, F., Bastida, J., Codina, C. (2009) Plant sources of galanthamine: phytochemical and biotechnological aspects. Biotechnol. Biotec. Eq. 23, 1170-1176.

[6] Parolo, G., Abeli, T., Rossi, G., Dowgiallo, G., Matthies, D. (2011) Biological flora of Central Europe: Leucojum aestivum L. Perspect. Plant Ecol. Evol. Syst. 13, 319-330.

[7] Ayan, A.K., Kurtar, E.S., Kevseroglu, K. (2004) Bulb yield and some plant characters of summer snowflake (Leucojum aestivum L.) under shading as affected by GA3 and NAA at different concentrations. J. Agron. 3, 296-300.

[8] Resmi Gazete (2017) Doğal çiçek soğanlarının 2018 yılı ihracat listesi hakkında tebliğ (Tebliğ No: 2017/49).

[9] Ivanov, I., Berkov, S., Pavlov, A. (2009) Improved HPLC method for the determination of Amaryllidaceae alkaloids. Biotechnol. Biotec. Eq. 23, 809-813.

[10] Rainer, M. (1997) Galanthamine in Alzheimer's disease. CNS Drugs. 7, 89-97.

[11] Heinrich, M., Teoh, H.L. (2004) Galanthamine from snowdrop—the development of a modern drug against Alzheimer's disease from local Caucasian knowledge. J. Ethnopharmacol. 92, 147-162.

[12] Janssen, B., Schäfer, B. (2017) Galantamine. Chem Texts. 3, 7.

[13] Liu, J., Hu, W.X., He, L.F., Ye, M., Li, Y. (2004) Effects of lycorine on HL-60 cells via arresting cell cycle and inducing apoptosis. FEBS Lett. 578, 245–250.

[14] Kaya, G.I., Polat, D.C., Emir, A., Sarikaya, B.B., Onur, M.A., Somer, N.U. (2014) Quantitative determination of galanthamine and lycorine in Galanthus elwesii by HPLC-DAD. Turkish J. Pharm. Sci. 11, 107-112.

[15] Ptak, A., Morańska, E., Saliba, S., Zieliński, A., Simlat, M., Laurain-Mattar, D. (2017) Elicitation of galanthamine and lycorine biosynthesis by Leucojum aestivum L. and L. aestivum 'Gravety Giant'plants cultured in bioreactor RITA®. Plant Cell Tiss. Org. 128, 335-345.
[16] Mustafa, N.R., Rhee, I.K., Verpoorte, R. (2003) Rapid method for determination of galanthamine in Amaryllidaceae plants using HPLC. J. Liq. Chromatogr. Rel. Technol. 26, 3217-3223.
[17] Kaya, G.I., Cicek, D., Sarikaya, B., Onur, M.A., Unver-Somer, N. (2010) HPLC-DAD analysis of lycorine in Amaryllidaceae species. Nat. Prod. Com. 5, 873- 876.
[18] Sarikaya, B.B., Somer, N.U., Onur, M.A. (2012) Quantitative determinations on Galanthus rizehensis. Turk J. Pharm. Sci. 9, 61-66.
[19] Bohnert, H.J., Nelson, D.E., Jensen, R.G. (1995) Adaptations to environmental stresses. The Plant Cell. 7, 1099-1111.
[20] Selmar, D., Kleinwächter, M. (2013) Stress enhances the synthesis of secondary plant products: the impact of stress-related over-reduction on the accumulation of natural products. Plant Cell Physiol. 54, 817-826.
[21] Timmermann, B.N., Steelink, C., Loewus, F.A. (1984) Phytochemical adaptations to stress, vol. 18. Springer Science and Business Media, New York.
[22] Jansen, G., Jürgens, H.U., Ordon, F. (2009) Effects of temperature on the alkaloid content of seeds of Lupinus angustifolius cultivars. J. Agron. Crop Sci., 195, 172-177.
[23] Sahoo, K.P., Kasera, P.K., Mohammed, S. (2012) Secondary metabolites produced during different seasons in some arid medicinal plants. Asian J. Plant Sci. Res. 2, 650-652.
[24] Guo, X.R., Yang, L., Yu, J.H., Tang, Z.H., Zu, Y.G. (2007) Alkaloid variations in Catharanthus roseus seedlings treated by different temperatures in short term and long term. J. Forestry Res. 18, 313-315.
[25] Zu, Y.G., Tang, Z.H., Yu, J.H., Liu, S.G., Wang, W., Guo, X.R. (2003) Different responses of camptothecin and 10-hydroxycamptothecin to heat shock in Camptotheca acuminata seedlings. Acta Bot. Sin. 45, 809-814.
[26] Pavlov, A., Berkov, S., Courot, E., Gocheva, T., Tuneva, D., Pandova, B., Georgiev., M., Georgiev, V., Yanev, S., Burrus, M., Ilieva, M. (2007) Galanthamine production by Leucojum aestivum in vitro systems. Process Biochem. 42, 734-739.
[27] Georgiev, V., Berkov, S., Georgiev, M., Burrus, M., Codina, C., Bastida, J., Ilieva, M., Pavlov, A. (2009) Optimized nutrient medium for galanthamine production in Leucojum aestivum L. in vitro shoot system. Z. Naturforsch. C 64, 219-224.
[28] Diop, M.F., Ptak, A., Chretien, F., Henry, M., Chapleur, Y., Laurain-Mattar, D. (2006) Galanthamine content of bulbs and in vitro cultures of Leucojum aestivum L. Nat. Prod. Com. 1, 475-479.
[29] Khonakdari, M.R., Mirjalili, M.H., Gholipour, A., Rezadoost, H., Farimani, M.M. (2018) Quantification of galantamine in Narcissus tazetta and Galanthus nivalis (Amaryllidaceae) populations growing wild in Iran. Plant Gen. Res. 16, 188-192.
[30] Gorinova, N.I., Atanassov, A.I., Stojanov, D.V., Tencheva, J. (1993) Influence of chemical composition of soils on the galanthamine content in Leucojum aestivum. J. Plant Nutr. 16, 1631-1636.
[31] Lubbe, A., Gude, H., Verpoorte, R., Choi, Y.H. (2013) Seasonal accumulation of major alkaloids in organs of pharmaceutical crop Narcissus Carlton. Phytochemistry. 88, 43-53.
[32] Elgorashi, E.E., Drewes, S.E., Van Staden, J. (2002) Organ-to-organ and seasonal variation in alkaloids from Crinum macowanii. Fitoterapia. 73, 490-495.

Received: **21.12.2018**
Accepted: **20.01.2020**

CORRESPONDING AUTHOR

Arzu Ucar Turker
Bolu Abant Izzet Baysal University,
Department of Biology,
14280 Bolu – Turkey

e-mail: turker_a@ibu.edu.tr

© by PSP Volume 29 – No. 04A/2020 pages 2678-2682 Fresenius Environmental Bulletin

NEW OR LESS KNOWN SPECIES OF MICROFUNGI IN TURKEY

Makbule Erdogdu*

Ahi Evran University, Faculty of Agriculture, Department of Landscape Architects, Kirsehir, Turkey

ABSTRACT

Pyrenophora coppeyana, a rare ascomycetous fungi, is reported from Turkey on *Daphne oleoides* subsp. *oleoides*. This is only the second locality reported for this fungus. *Pseudomassaria chondrospora* and *Coryneopsis tamaricis* are lesser known fungi species in Turkey. *Tilia rubra* for *Pseudomassaria chondrospora* and *Tamarix tetrandra* for *Coryneopsis tamaricis* are new host records. Distinguishing morphological characters of these species are described and their photographs are provided.

KEYWORDS:
Ascomycota, biodiversity, microfungi, new record, new host

INTRODUCTION

Based on both morphology and molecular phylogeny, *Pyrenophora* Fr. is classified within the family Pleosporaceae [1]. It is characterized by immersed to semi immersed ascomata and neck covered with brown to reddish-brown setae, lack of pseudoparaphyses, clavate to saccate asci, usually with a large apical ring, and muriform terete (cylindrical, frequently circular in section but narrowing to one end) ascospores [2]. Currently 204 species of *Pyrenophora* are listed in Index Fungorum [3].

Currently *Coryneopsis* Grove is considered as a synonym of *Seimatosporium* Corda and the generic name *Hendersonia* Sacc. is illegitimate [3]. However, the genus contains 13 species as listed in Index Fungorum [3], namely, *C. canina* (Brunaud) Grove, *C. cisticola* Alcalde, *C. corni-albae* (Roum.) Grove, *C. foliicola* (Fuckel) Grove, *C. henriquesiana* (Sacc. & Roum.) Grove, *C. lirella* (Cooke) Grove, *C. microsticta* Grove, *C. rubi* (Westend.) Grove, *Coryneopsis rubi* f. *rubi* (Westend.) Grove *Coryneopsis rubi* f. *rubi-idaei* (Brunaud) Grove, *C. rubi* var. *rubi* (Westend.) Grove, *C. tamaricis* (Cooke) Grove, *C. viburni* Dias & Sousa da Câmara. Of these, only *C. canina* and *C. rubi* (with variety and forms) were transfered to the genera *Seimatosporium* and *Sphaerulina* Sacc. respectvely.

Pseudomassaria was introduced by Jaczewski [4] to accommodate *Sphaeria chondrospora.* The genus *Pseudomassaria* has been placed in a number families in the Ascomycetes. Finally Senanayake et al. [5] introduced a new family Pseudomassariaceae to accommodate *Leiosphaerella* and *Pseudomassaria*. *Pseudomassaria* is characterized by immersed perithecia and asci having a well-developed apical ring and pore [6]. It is closely related particularly by the unequally uniseptate spores. Approximately thirty species are currently classified in this genus.

MATERIALS AND METHODS

The host specimens were prepared following conventional herbarium techniques. Host plants were identified using the Flora of Turkey and East Aegean Islands [7]. Thin fungal sections prepared from host tissue were examined under a Leica DM E light microscope and measured from mounts in tap water. The fungi were identified using relevant literature (for *Pyrenophora* [8]; for *Pseudomassaria* [9-11]; for *Coryneopsis* [11-13]). All examined specimens were deposited in the Mycology Laboratory of Ahi Evran University, Department of Biology, Kırşehir, Turkey, under Makbule Erdoğdu (ME) collection numbers.

RESULTS AND DISCUSSION

Pyrenophora coppeyana, is new record for Turkish mycobiota. *Coryneopsis tamaricis* and *Pseudomassaria chondrospora* species are listed as examples of xylotroph microfungi in "Trophical Structure of Microfungi in Forest Ecosystems of Turkey" [14] which is published by me and my colleagues. However, the description and pictures of these species are not given. The mycological characteristics of these fungi are given below.

Ascomycota
Dothideomycetes
Pleosporales
Pleosporaceae

FIGURE 1
***Pyrenophora coppeyana*: a, Perithecium, asci and ascospores. b-c, Ascus. d, Ascospore.**

***Pyrenophora coppeyana* Maire (Fig.1).** Perithecia initially immersed, becoming erumpent to near superficial, globose to subglobose, broadly or narrowly conical, coriaceous, ostiolate. Setae chesnut brown to brown, darkened at the base, septate and tapered towards the apex, longer than perithecium diam. Asci clavate to sub-cylindrical, bitunicate, fissitunicate, 8-spored, distichously arranged, rounded at the apex, attenuate at the base, 300-650 × 40-50 µm, short-stalked. Ascospores subclavate to oblong, slipper-shaped, with 11-14 transverse septa and 3-4 longitudinal septa, constricted at the 5 or 6th septum from the top, narrowing to one end, smooth-walled, (57.5) 65-70 (72.5) × 22.5-25 (27.5) µm, surrounded by a mucilaginous sheath, brown to chestnut brown.

Specimens examined. Kayseri Province, Erciyes Mountain, on fallen leaves of *Daphne oleoides* Schreb. subsp. *oleoides* (Thymelaeaceae), 1980 m, 31.05.2010, steppe, 38°35'363''N, 035°30'345''E, ME 1400.

Although our Turkish specimen of *Pyrenophora coppeyana* is morphologically similar to type species, it does differ slightly in some aspects, particularly with respect to asci size and number of septa. According to Maire [8] asci 300-400 × 38-45 µm, ascospores 16-20 transverse septa and 3-5 longitudinal septa, constricted at the 4th septum from the top. The asci of the specimen studied are longer than type species samples. The number of transverse septa in our specimens are fewer and constriction is at the 5 or 6th septum from the top.

Pyrenophora coppeyana was described by Maire on leaves of *Daphne oleoides* from Greece. Until now there has been no additional information about this fungus. We think that our report from Turkey is the second registration of this fungus in the World.

Sordariomycetes
Xylariomycetidae
Amphisphaeriales
Discosiaceae

***Coryneopsis tamaricis* (Cooke) Grove (Fig.2).** Conidiomata solitary or gregarious, at first immersed in host tissue, later erumpent, subglobose, 345-450 µm diam., brown. Conidiophores persistent, as long as or longer than the conidia, hyaline. Paraphyses filiform, aseptate, hyaline. Conidia ellipsoid to subcylindrical, rounded at both ends, straight or slightly curved, 3-septate, not or slightly constricted, apical and basal cell often longer than the median cells, 27.5-35 × 10-12.5 µm, initially hyaline, after maturity golden brown to dark brown.

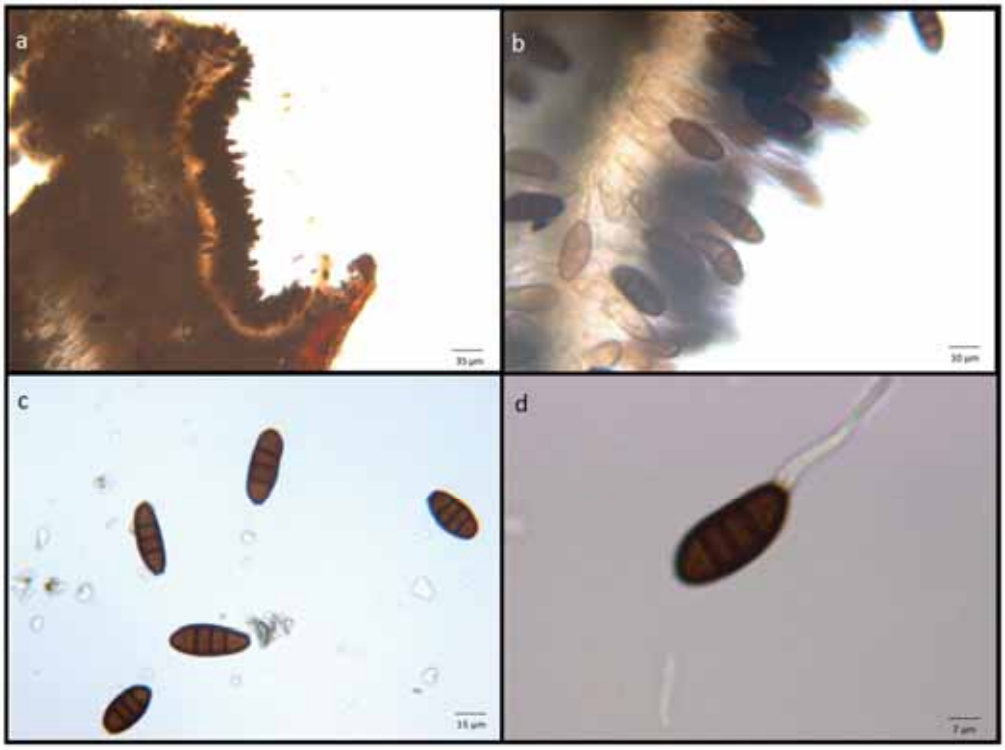

FIGURE 2
***Coryneopsis tamaricis*: a, Vertical section of a conidiomata. b, Conidiogenous cells and developing conidia. c, Conidia. d, Conidium.**

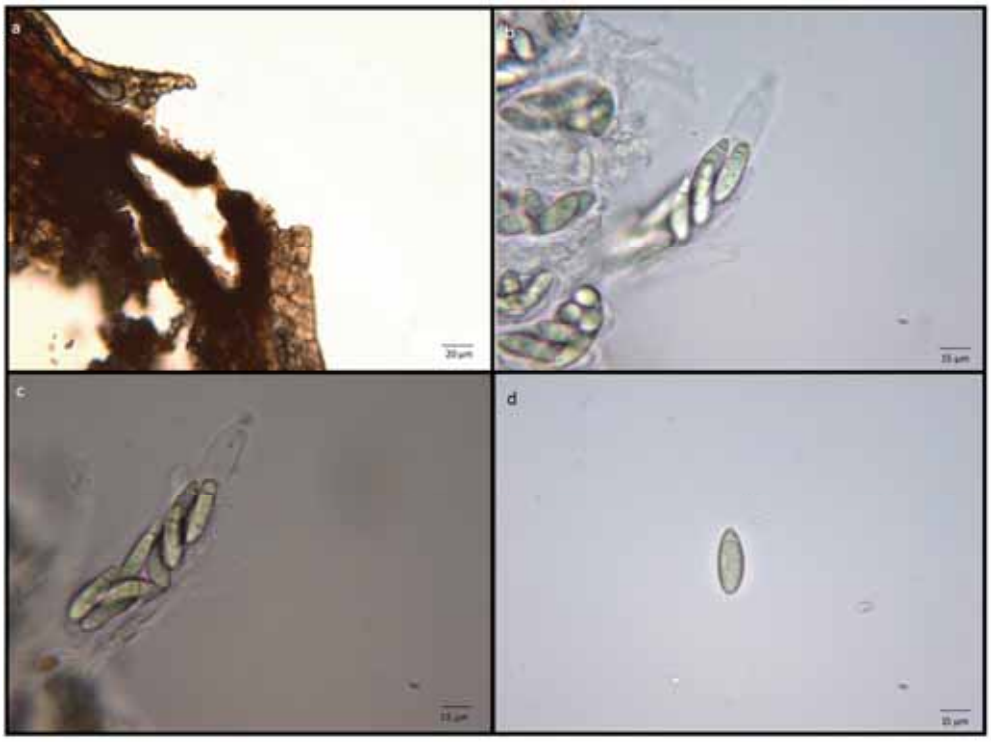

FIGURE 3
***Pseudomassaria chondrospora*: a, Vertical section of a perithecium. b-c, Asci, ascospores and paraphyses. d. Ascospore.**

Specimens examined. Turkey, Kastamonu Province, Pınarbaşı District, Ilıca Waterfall, on dead and thin branches of *Tamarix tetrandra* Pall. ex M. Bieb. (Tamaricaceae), 396 m, 29.08.05, in forest, 41°39'638''N, 33°07'848''E, ME 1714.

The Turkish specimen of *Coryneopsis tamaricis* is morphologically similar to specimens described in literature [11-13]. However, the conidia of the Turkish samples are slightly narrowed than the British collection (26-36 × 12-13 µm) [12], while those reported by Thambugala et al. [13] are slightly narrower and shorter than our specimen. These differences are small, and not interpreted as taxonomically significant.

Coryneopsis tamaricis has been reported from England on *Tamarix gallica* L. [15], (as *Hendersonia tamaricis* Cooke), from France on *T. anglica* Webb [16] (as *Hendersonia tamaricis* f. *minor*) from Ukraine on *T. gallica* [17] (as *Hendersonia tamaricis*) and from Yugoslovia on *T. africana* Poir. [18]. The present collection represents the first record of this species from Turkey and *Tamarix tetrandra* represents a new host species for this fungus.

Xylariales

Pseudomassariaceae

***Pseudomassaria chondrospora* (Ces.) Jacz. (Fig.3).** Perithecia depressed-globose, scattered, at first immersed in host tissue, later erumpent, 180-230 µm diam., blackish; ostiole circular, 10-15 µm diam. Asci elliptic-clavate, narrowed to short, broad stalk, thickened at apex, 8- spored, 105-127.5 × 25-26 µm, without a ring; paraphyses thin-walled, guttulate, hyaline. Ascospores cuneate, clavate, broadly ellipsoid, obovate, rounded at the apex, attenuate at the base, straight, rarely inequilateral, 1-septate in the lower third, 23.5-30 × 10-12.5 µm, guttulate, hyaline to yellowish.

Specimens examined. Turkey, Kastamonu Province, Küre Mountain National Park, Şenpazar District, on dead and thin branches of *Tilia rubra* DC. (Tiliaceae), 619 m, 20.08.06, in forest, 41°48'58''N, 33°14'69''E, ME 1860.

The Turkish specimen of *Pseudomassaria chondrospora* agrees with other reports of the species in ascomata, asci and ascospores morphology; the only observable difference being the vary dimensions of ascomata, asci, and ascospores. Already, ascospores of this fungus vary considerably in size and shape in the same perithecium.

Pseudomassaria chondrospora is known from Austria on *Tilia tomentosa* Moench and *Tilia platyphylla* C.A. Mey., Denmark, England and U.S.A. on *Tilia* sp., Georgia on *Tilia heterophylla* var. *michauxii* Sarg., Germany on *Tilia platyphylla*, Sweden on *Tilia cordata* Rose ex Bush [18]. The present collection represents the first record of this species from Turkey and *Tilia rubra* represents a new host species for this fungus.

REFERENCES

[1] Zhang, Y., Crous, P.W., Schoch, C.L. and Hyde, K.D. (2012) Pleosporales. Fungal Diversity. 53, 1–221.

[2] Ariyawansa, H.A., Kang, J.C., Alias, S.A., Chukeatirote, E. and Hyde, K.D. (2014) *Pyrenophora*. Mycosphere. 5(2), 351–362.

[3] Index Fungorum Partnership. (2018) Index Fungorum. http://www.indexfungorum.org. Accessed 2018.

[4] Jaczewski, A.L.A. (1894) Monograph of the Swwis Massariaceae. Bulletin de l´Herbier Boissier. 2, 1–663. (in French).

[5] Senanayake, I.C., Maharachchikumbura, S.S.N., Hyde, K.D., Bhat, J.D., Jones, E.B.G., Mckenzie, E.H.C., Dai, D.Q., Daranagama, D.A., Dayarathne, M.C., Goonasekara, I.D., Konta, S., Li, W.J., Shang, Q.J., Stadler, M., Wijayawardene, N.N., Xiao, Y.P., Norphanphoun, C., Li, Q.R., Liu, X.Z., Bahkali, A.H., Kang, J.C., Wang, Y., Wen, T.C., Xu, J.C. and Camporesi, E. (2015) Towards unraveling relationships in Xylariomycetidae (Sordariomycetes). Fungal Diversity. 73, 73–144.

[6] Barr, M.E. (1964) The genus *Pseudomassaria* in North America. Mycologia. 56, 841–862.

[7] Davis, P.H. (1965) Flora of Turkey and East Aegean Islands. Vol: 1–9. Edinburgh Univ Press, Edinburgh.

[8] Maire, R. (1930) Mycological studies (Fascicle 4). Bulletin de la Société Mycologique de France. 46, 215–244. (in French).

[9] Jaczewski, A.A. (1913) Key to the fungi. Vol: 1. Fungi perfecti. Publishing House of S.L. Kind, Petrograd. (in Russian).

[10] Dennis, R.W.G. (1981) British Ascomycetes: Addenda and Corrigenda. J. Cramer, Vaduz.

[11] Ellis, M.B. and J.P. Ellis (1987) Microfungi on Land Plants. Croom Helm, London and Sydney.

[12] Grove, W.B. (1937) British stem–and leaf fungi. Coelomycetes. Vol: 2. At the University Press, Cambridge.

[13] Thambugala, K.M., Daranagama, D.A., Phillips, A.J.L., Bulgakov, T.S., Bhat, D.J., Camporesi, E., Bahkali, A.H., Eungwanichayapant, P.D., Liu, Z.Y., Hyde, K.D. (2017) Microfungi on *Tamarix*. Fungal Diversity. 82, 239–306.

[14] Selçuk F., Hüseyin, E., Erdoğdu, M., Akgül, H. and Yılmazkaya, D. (2013) Trophical Structure of Microfungi in Forest Ecosystems of Turkey. Artvin Çoruh Üniversitesi Orman Fakültesi Dergisi. 14(2), 191–202.

[15] Cooke, M.C. (1885) New British fungi. Grevillea. 14(69), 1–7.

[16] Brunaud, P. (1897) Mycological miscellanies III Series. Actes de la Société Linnéenne de Bordeaux. 52, 133–149. (in French).

[17] Moskovets S.M. (1933) Fungi of southern Ukraine. Bull Kiev Bot Gard. 16(14), 71–87.

[18] Farr, D.F. and A.Y. Rossman (2018) Fungal Database, Systematic Mycology and Microbiology Laboratory. ARS, USDA. http://nt.ars-grin.gov/fungaldatabases/fungushost/fungushost.cfm. Accessed 2018.

Received: **16.01.2019**
Accepted: **03.02.2020**

CORRESPONDING AUTHOR

Makbule Erdogdu
Ahi Evran University
Faculty of Agriculture
Department of Landscape Architects
Kırşehir – Turkey

e-mail: merdogdu@ahievran.edu.tr

© by PSP Volume 29 – No. 04A/2020 pages 2683-2690 Fresenius Environmental Bulletin

EFFECTS OF MEDITERRANEAN CUTTLEFISH (*SEPIA OFFICINALIS*) BONE AS AN ALTERNATIVE CALCIUM SOURCE ON EGG PRODUCTION, EGG QUALITY AND SOME BLOOD PARAMETERS IN LAYING QUAILS

Kadir Emre Bugdayci[1,*], M Numan Oguz[1], Fatma Karakas Oguz[1], Isa Can Uyguralp[2], Ilker Yusuf Akinci[3]

[1]Department of Animal Nutrition and Nutritional Diseases, Faculty of Veterinary Medicine, Burdur Mehmet Akif Ersoy University, Burdur, Turkey
[2]Department of Surgery, Faculty of Veterinary Medicine, Burdur Mehmet Akif Ersoy University, Burdur, Turkey
[3]Department of Internal Medicine, Faculty of Veterinary Medicine, Burdur Mehmet Akif Ersoy University, Burdur, Turkey

ABSTRACT

At present, ground limestone is one of the common calcium (Ca) sources for laying hens. This research aims to find out the performance and egg quality characteristics of quails fed with diets containing different percentages of substitution of cuttlefish (*Sepia officinalis*) bone (CFB) as a waste of water product, instead of limestone on dry matter basis. One hundred and forty-four Japanese quails (*Coturnixcoturnix japonica*) aged 8 weeks were randomly separated into one control and two treatment groups. Each group was divided into six replicates, each containing eight quails. The experimental diets of the first and second treatment groups consisted of two levels of CFB (50 and 100% respectively) instead of limestone. All group rations were devised to be isocaloric and isonitrogenous. Throughout the experimental period (8 weeks), feed and water were given *ad libitum.* The feed efficiency (kg of feed per dozen egg) of the treatment groups was positively affected by CFB ($p<0.05$); however, the kg of feed per kg of egg ratio was not affected compared with the control group. The effects of both levels of dietary CFB on shape index, albumen index, Haugh unit, yolk index and yolk color were not significant. The Ca and Mg levels of blood and eggshell were not significantly affected by the treatments; however, the P level of eggshell was decreased in both treatment groups compared with the control ($p<0.05$). In conclusion, substituting limestone with dietary CFB did not affect the internal and external egg quality of laying quails generally. Besides, the results showed that there is no correlation between eggshell P level and P level of blood serum.

KEYWORDS:
Cuttlefish bone, calcium, egg quality, laying quail, performance

INTRODUCTION

One of the essential components of eggshell is Ca, which regulates the transportation of nutrients in the cell membrane [1]. Therefore, the source of Ca might affect layers' performance and egg quality. The most common source of this mineral for feed is limestone. There is an array of Ca sources reported as feedstuff to meet layers' requirement. A number of studies used wastes of some biological organisms reported that eggshell waste [2, 3], snail shell [4], calcite [5] and some aquatic Ca sources, such as mussel shell [6], oyster shell [3, 7, 8] and whelk shell [9], can be used as alternative Ca sources for layers. MacIsaac et al. [9] reported that approximately 34% of processed whelk (*Buccinum undatum*) shell is made of Ca, and this value is very close to the 38% value for commercial oyster shell and limestone.

Ertaş et al. [6] showed that egg production improved when part of the limestone in the diet of quails was substituted by mussel shell (75%) under heat stress conditions. Similar to Ertaş et al. [6], several reports concerning the use of alternative Ca sources in poultry diets indicate better egg weight, egg breakage strength [8], better feed intake [9, 10] and better eggshell mineralization [11] compared with limestone. These benefits have the advantage of reducing cost in the egg industry. Also, lots of these alternative Ca sources are produced as by-products or wastes from industries, and they should be integrated into the economy. It is clear that the amounts of these by-products that can be obtained are lower compared with limestone, but the local feed industry could access these sources without extra costs. Naturally, it is obvious that these alternative Ca sources would be more expensive feed additives than limestone if they are produced only for the feed industry. However, previous reports have attracted attention to the possible benefits of dietary Ca sources in poultry nutrition. Accordingly, cuttlefish bone (an aquatic Ca source like mussel shell, oyster shell and whelk shell) needs to be studied to determine its possible

beneficial effects on poultry nutrition in the Mediterranean region.

Cuttlefish are molluscs, and they belong to the class cephalopoda, like the octopus [12]. Cuttlebone is the gas-filled chambered shell of cuttlefish [13]. These surfboard-shaped shells are chalky and contain high amounts of Ca [14]. At present, cuttlefish bone is used for some industrial and medical purposes, due to its high Ca content. A lot of experiments have been carried out with different sizes and sources of Ca in many laying species, but experiments involving cuttlefish bone are lacking in literature. There is no study on the use of 50% and 100% cuttlefish bone replacement of limestone as the Ca source for laying quails. The objective of this study is to evaluate this waste in poultry nutrition and determine the possible effects on laying performance, egg quality, eggshell Ca, P and Mg levels and blood serum Ca, P and Mg levels of laying quails.

MATERIALS AND METHODS

The procedures used in this experiment were carried out according to the local experimental animal care committee of Burdur, Turkey, and approved by the ethics committee (No: 2014-65). The trial was conducted in the province of Burdur, located at 37° 42' latitude and 30° 16' longitude.

The $CaCO_3$ content of cuttlefish bone was determined in the laboratory. For this purpose, weighed amounts of ground cuttlefish bone were poured into 37% hydrochloric acid for 12 h. After the waiting period, the mixture of cuttlefish bone and hydrochloric acid was filtered using filter paper. The dried paper was weighted and the $CaCO_3$ and other organic materials dissolved in the acid were calculated. This data was compared with the dry matter (97.62%) and crude ash (91.41%) of cuttlefish bone.

A total of 144 quails (*Coturnix coturnix japonica*) aged seven weeks were used in this study. The quails were randomly divided into one control group and two treatment groups. Each group was composed of 48 quails. Six subgroups were allocated from each group, each comprising eight quails. All groups were kept in cages (45cm x 50cm x 22cm) in a windowed room. The lighting was adjusted to 20 h light and 4 h darkness. Feed and water were supplied *ad libitum* throughout the experiment. During the experiment, two quails from the 50% CFB group and four quails from the 100% CFB group died (6 quails in total).

The ingredients and chemical composition of the control and treatment groups' diet are presented in Table 1. The diets consisted of two levels of cuttlefish (*Sepia officinalis*) bone (CFB) (50 and 100% respectively) replacement of limestone in the diets of the first and second treatment groups. CFB was supplied by a local pet shop in Antalya, Turkey. The amounts of CFB used as substitute in the rations were calculated by taking the crude ash content of CFB as 90 % and that of limestone as 100 %.

TABLE 1
Ingredients and chemical composition of control and treatment groups' diet as feed.

Ingredients of diets (g kg^{-1})			
		Treatment groups	
	Control	50 % CFB	100 % CFB
Corn	455.5	455.5	455.5
Wheat	70	67.3	64.6
Soybean meal (48%)	180	180	180
Full fat soy	100	100	100
Sunflower meal (36%)	90	90	90
Vegetable oil	28	28	28
DCP	15	15	15
Limestone	54	27	-
Cuttle fish bone*	-	29.7	59.4
Salt	3	3	3
Vit-Min complex**	2.5	2.5	2.5
DL-methionine	1	1	1
L-lysine	1	1	1
Chemical composition (Analysed) of diets (g kg^{-1})			
Crude protein	175.3	174.2	172.2
Eter extract	68.9	65.5	70.3
Crude fibre	36.1	35.9	39.2
Crude ash	101.6	107	104.5
Dry matter	893.3	892.7	893.1
Calculated ME (kcal/kg)***	2435.09	2428.31	2419.49

* Cuttlefish bone was calculated in crude ash (90%) bases.
** Each kilogram of vitamin-mineral mix contains 12 000 000 IU A vit, 20 000 mg E vit, 50 000 mg Mn, 50 000 mg Fe, 50 000 mg Zn, 10 000 mg Cu, 800 mg I, 150 mg Co, 150 mg Se
*** TITUS and FRITZ (1971); ME (MJ/g) = 133.06 (crude protein) + 232.91 (ether extract) - 4.68 (crude fiber) + 122.77 (nitrogen free extract)

The Ca, P and Mg contents of eggshell were determined by using ICPOES (Optima 8000, Perkin Elmer, serial no: 078N2030104C) in the central laboratory of Mehmet Akif Ersoy University. For this purpose, 0.3 g of sample and 6 ml of NHO_3 (65%) were processed in a microwave (15 s and 200 ºC) [15].

AOAC [16] directives were used to determine the nutrient composition of the control and treatment group rations. All group diets were formulated by a software program, based on NRC [17] nutrient recommendation for Japanese quail. Titus and Frits [18] equality was used to calculate the metabolizable energy levels of all rations.

The weights of the quails were determined two times (at the beginning and at the end) during the study by using precision balance (Model: HGM-20K-ER8412, 1g sensitivity, UWE CO, Taipei-Taiwan). Mortality was recorded as it occurred.

Eggs were gathered every day during the study and expressed on a hen-day basis. The eggs laid by all groups were collected on the last two days of every week and weighed with a precision balance (Model CP224S-14105100, 0.1 mg sensitivity, Sartorius AG, Gottingen-Germany) individually to determine the egg weight. Feed intake was recorded weekly and calculated as g per day per quail. The feed conversion ratio was calculated as both g feed per g egg and g feed per dozen egg.

Two eggs laid by each replicate were gathered randomly from 09.00 to 12.00 h (12 eggs in each group) on the 2nd, 4th, 6th and 8th weeks of the experiment (48 eggs in total per group) to determine the egg internal quality. Each egg was weighed with a precision balance individually. The following formula was used to calculate the egg shape index:

Shape index = (egg width / egg length) x 100

The eggs were broken onto a glass table. Tripod micrometer (Mitutoyo, No: 2050S-19, 0.01-20 mm; Kawasaki-Japan) was used for measuring the height of the albumen and the height of the yolk. Digital caliper was used for measuring the length and width of the albumen and the diameter of the yolk.

By using these values, the yolk index, albumen index and Haugh units were calculated using the following formulas respectively: [(yolk height / yolk diameter) x 100], [(albumen height / average of albumen length and albumen width) x 100] and [100 x log(H+7.57-1.7W0.37)]; H is albumen height and W is egg weight [19]. The colors of the yolk of treated eggs were scored by using Roche yolk color fan [20] on a glass table.

The analyses of the internal and external qualities of the eggs were completed within 24 h after being gathered. The weight of each treated egg was considered individually when the egg quality evaluation was performed.

The Ca, P and Mg contents of the eggshells of the control and treatment groups were determined by ICP-OES (Perkin Elmer ICPOES Optima 8000). For this purpose, all treated eggshells were collected and mixed in a poll of their own subgroups. In the sample preparation, 0.3 g of shell ash and 6 ml of HNO_3 (65%) were treated in a microwave (Milestone Stard D) according to the method of Al-Obaidi et al. [15].

Two quails from each replicate (twelve in total) were randomly slaughtered at the end of the experiment. Blood samples were collected at the point of slaughtering from the jugular vein and centrifuged at 3000xg for 10 min individually. Fresh serum samples were analysed for the determination of serum Ca, P and Mg levels by an Autoanalyzer (Model: Gesan-Chem200, No: 1102422, Campobello-Italy) using its commercial kits (Monoreagent-LR-C1850120V; C3300120V; C4400120V).

Statistical analyses were done using SPSS [21] software version 10.0 (SPSS Inc. Chicago, USA). Data were analysed to find out whether the distribution was normal or not by using the Kolmogorov-Smirnov test. One-way ANOVA was used to compare the differences in parameters among groups. Duncan's multiple range test was used to analyse the significance of mean differences between groups. All quality characteristics of the eggs were determined after adjusting their weights. The results are given as estimated marginal means and standard error of mean. The level of significance was taken as $p<0.05$ [22]. The model used to analyse the body weights, performance, blood and egg shell Ca, Mg and P levels with tibia and egg traits of laying quails was:

$Y_i = \mu + a_i + e_i$

Where, Y_i is the traits, μ is the overall mean, a_i is the effects of dietary replacement of Ca source (limestone and/or cuttlefish bone), e_i is the random residual. To determine the relationship between some blood components and eggshell quantities, correlations between parameters were determined.

RESULTS

The calcium carbonate ($CaCO_3$) content of ground CFB was determined as 91%. The initial and final body weights of the quails were not significantly different, as shown in Table 2. The inclusion of CFB in the diet of laying quails did not significantly affect body weight, feed intake, hen day egg production, and egg weight. The feed efficiency (kg feed per dozen egg) of the 50% CFB group was positively affected ($p<0.05$); however, the kg feed per kg egg ratio was not affected by dietary treatments. The egg shape index, albumen height, albumen index, Haugh unit, yolk index, egg yolk color and crude ash of the tibia were not affected by the source of Ca (Table 2).

Dietary treatments did not affect the serum levels of Ca, Mg and P (Table 3). The Ca and Mg contents of the eggshell were not affected by dietary treatments; however, the P content of the eggshell in

both the 50% and 100% CFB groups were lower than that of the control group ($p<0.05$).

In the present study, it was determined that there was a significant ($p<0.05$) negative correlation between the blood and eggshell Ca levels (Table 4). There was also negative correlation determined P and Mg levels of blood and eggshell without significance.

TABLE 2
The effects of dietary treatments on laying quails (Mean±S.E)*

	Treatment groups[1]						
	n	**Control[1]**	**n**	**50 % CFB**	**n**	**100 % CFB**	**p**
Body weights							
Initial body weight (g)	48	252.06 ± 3.46	46	245.52 ± 3.29	44	245.27 ± 3.92	0.315
Final body weight (g)	48	282.87 ± 5.37	46	273.69 ± 3.65	44	275.75 ± 4.43	0.325
Performance parameters							
Feed intake (g/day per quail)	6	35.07 ± 0.72	6	35.10 ± 0.26	6	33.97 ± 0.44	0.244
Egg production (%)	6	83.60 ± 1.34	6	92.83 ± 1.86	6	88.54 ± 4.34	0.103
Egg weight (g)	6	13.20 ± 0.13	6	12.89 ± 0,21	6	13.26 ± 0.07	0.204
FCR** (kg feed per kg egg)	6	2.65 ± 0.05	6	2.72 ± 0.04	6	2.56 ± 0.03	0.056
FCR** (kg feed per dozen egg)	6	0.503 ± 0.01a	6	0.454 ± 0.01b	6	0.465 ± 0.02ab	0.048
Egg and tibia traits							
Weight of treated eggs (g)	12	13.16 ± 0.08	12	13.13 ± 0.10	12	13.33 ± 0.05	0.205
Egg shell weight (g)	12	0.93 ± 0.01	12	0.93 ± 0.00	12	0.94 ± 0.01	0.759
Crude ash of tibia (%)	12	58.21 ± 1.00	12	57.80 ± 1.10	12	59.10 ± 1.43	0.737
The ratio of egg shell ash (%)	12	7.07 ± 0.07	12	7.14 ± 0.06	12	7.07 ± 0.12	0.778
Shape index (%)	12	76.98 ± 0.60	12	76.30 ± 0.47	12	76.90 ± 0.62	0.661
Albumen height (mm)	12	5.26 ± 0.10	12	5.21 ± 0.08	12	5.52 ± 0.14	0.131
Albumen index (%)	12	12.48 ± 0.30	12	12.37 ± 0.23	12	12.64 ± 0.39	0.836
Yolk index (%)	12	43.88 ± 0.37	12	42.89 ± 0.43	12	43.20 ± 0.27	0.16
Haugh unit	12	99.84 ± 0.46	12	99.31 ± 0.39	12	100.79 ± 0.65	0.139
Egg yolk color***	12	10.93 ± 0.12	12	10.83 ± 0.11	12	10.90 ± 0.11	0.273

*No significant differences among groups ($p > 0.05$).
** FCR: Feed conversion ratio.
*** Roche color scores are based upon Roche Color Fan Edition 1965.
[1] Means within a row followed by the different superscripts are different by the Duncan test ($p < 0.05$).

TABLE 3
The Effects of Dietary Treatments on Blood and Egg Shell Ca, Mg And P Levels of Laying Quails. (Mean±S.E)*

	Treatment groups[1]						
	n	**Control[1]**	**n**	**50 % CFB**	**n**	**100 % CFB**	**p**
Blood levels							
Ca (mg/dl)	12	29.43 ± 1.54	12	27.12 ± 1.27	12	30.42 ± 2.13	0.377
Mg (mg/dl)	12	3.49 ± 0.11	12	3.24 ± 0.13	12	3.47 ± 0.11	0.29
P (mg/dl)	12	38.71 ± 1.37	12	36.09 ± 0.95	12	39.23 ± 1.56	0.214
Egg shell levels							
Ca (%)	6	44.88 ± 3.67	6	41.44 ± 4.04	6	38.04 ± 3.15	0.435
Mg (%)	6	0.10 ± 0.01	6	0.13 ± 0.07	6	0.04 ± 0.01	0.35
P (%)	6	0.42 ± 0.07a	6	0.23 ± 0.03b	6	0.19 ± 0.01b	0.011

*No significant differences among groups ($p > 0.05$)
[1] Means within a row followed by the different superscripts differ significantly by the Duncan test ($p < 0.05$).

TABLE 4
The correlations between Ca, Mg and P levels of egg shell and blood serum.

	Serum Ca	Egg shell Ca	Serum P	Egg Shell P	Serum Mg	Egg shell Mg
Serum Ca	1					
Egg shell Ca	-0.530*	1				
Serum P	0.896**	-0.370	1			
Egg shell P	-0.151	0.329	-0.113	1		
Serum Mg	0.485*	0.179	0.666**	-0.148	1	
Egg shell Mg	-0.073	-0.041	-0.110	0.107	-0.331	1

*$p<0.05$; **$p<0.01$

DISCUSSION

The replacement of limestone with CFB (50 and 100%) did not affect the egg production of laying quails. Similarly, the substitution of limestone with oyster shell or eggshell at the 50% and 100% levels [10, 23] and the replacement of 25% [3] of limestone with oyster shell did not affect egg production in laying hens. Besides, Tunc and Cuhadar [11] reported that the replacement (50%) of different Ca sources (eggshell and oyster shell) with large particle Ca sources also had no effect on egg production. Safaa et al. [24] similarly declared that the substitution of 40% of fine limestone with coarse limestone or oyster shell did not affect productive performance. On the other hand, Ertaş et al. [6] revealed that the replacement (75%) of limestone with mussel shell in laying quail rations under heat stress increased egg production. Similarly, MacIsaac et al. [9] reported that (100%) whelk shell of (1/3) large particles and (2/3) ground whelk shell decreased egg production from 61 to 64 weeks and 65 to 76 weeks of the laying period of laying hens respectively compared with (100%) ground limestone. Skrivan et al. [25] mentioned that dietary Mg (4 g/kg) with a wider Ca to P (18) ratio increased egg production and egg weight in laying hens fed with rations containing a mixture of fine and coarse-grained limestone. Studies on different levels of P with different [26] and the same [27] Ca sources have shown that lower P levels in laying hen and quail rations and lower Mg levels in laying hen rations [25] improved egg production of layers respectively. The report of Vandepopuliere and Lyons [28] showed that a diet with 4% total P decreased egg production, feed consumption, egg weight and egg mass of laying hens; supporting the levels of dietary P was more effective than the dietary source of Ca on egg production.

In the present study, CFB as a Ca source did not significantly affect the feed intake and egg weight of laying quails, which agrees with the report of Ertaş et al. [6], who did not find any effect on feed intake and egg weight when 25, 50, 75 and 100% of fine limestone in the diet of laying quails were substituted with mussel shell. Further, the replacement of dietary limestone with oyster shell or eggshell did not alter egg weights at the late laying period [10] and at the early laying period [23] of hens as well. Similarly, Sultana et al. [29] reported that the dietary Ca source of oyster shell did not affect feed intake and egg weight of laying quails compared with the same levels of dietary limestone. However, the replacement (50%) of limestone with eggshell and the replacement (50%) of limestone with oyster shell decreased feed intake without affecting the egg weights of laying quails [10]. MacIsaac et al. [9] evaluated the effects of whelk shell as an alternative source of Ca and reported that feed intake was decreased in laying hens by using (100%) ground whelk shell in the ration more than (1/3) large particle oyster shell and (2/3) ground limestone without affecting egg weights; they also reported that the feed conversion ratio of laying hens fed with (100%) ground whelk shell in a high temperature environment was decreased during the late period (65 to 76 weeks) of laying. Rajiv [30] worked with calcium pidolate (a form of calcium propionate) on laying hens and declared that this alternative Ca source did not affect feed intake; however, it decreased the number of broken eggs of layers at the late laying period. Beside these reports, hens fed with 3.6-4% Ca diet and received oyster shell *ad libitum* had better egg weight and breakage strength [8]. In a study, when the data were evaluated for the size of Ca (same size with limestone) without considering its source, it was found that the source of Ca did not seem to affect the feed intake of laying hens [6] and laying quails [29], which is similar to the present study. On the other hand, different sizes of the Ca sources altered the feed intake of laying quails [10] and laying hens [9]. It is clear that the size of Ca is more effective on feed intake than the source of Ca. Moreover, the egg weight of layers were not affected by the source of Ca at the early and the late periods of the laying cycle.

Wang et al. [31] reported that large dietary particle Ca sources (oyster shell and limestone) increased albumen height, Haugh unit, and shell contents of P and Mg, but it had no effect on yolk color, shell thickness, and the weight proportion of the shell compared with small particle Ca sources. On the other hand, when Ca sources were compared with each other, limestone yielded better albumen height and shell contents of Ca and P compared with oyster shell in laying ducks. Dietary coarse and grained limestone (0.8–2 mm) with Mg (4 g/kg) decreased the yolk percentage and increased the eggshell percentage according to Skrivan et al. [25]. On the other hand, Gongruttanaum [23] mentioned that dietary substitution of limestone with eggshell did not affect the egg quality of laying hens at the early stage of the laying period. Similarly, in our study, the inclusion of CFB in the diet of laying quails did not significantly affect albumen height and shell contents of Ca and P. It is clear that the source and the size of dietary Ca for layers affect the Ca, P and Mg contents of eggshell as well as egg quality [31]. These differences may be caused by the different effectiveness of Ca sources and the species of the animal.

One study worked on the use of an aquatic product (chitosan) as a feed additive [32] and declared that chitosan supplementation in laying hen ration (low Ca contained) during the late laying period increased eggshell thickness and breaking strength of eggs. CFB did not affect the crude ash of the eggshell and tibia. Similar to the present study, there are several studies that evaluated the effects of the size [31], the source [10, 23] and the level [24] of dietary Ca on eggshell thickness [10], tibia ash

and eggshell weight [23, 24, 31]. In general, it seems that the size, the source and the level of Ca did not alter related parameters of layers. An et al. [33] declared that laying hen (70 week old) rations containing 3.5 to 4.7% of Ca did not affect the crude ash of the tibia and the levels of Ca and P. However, Lichovnikova [34] used a proportion of 68% eggshell or oyster shell and limestone (32%) as Ca source for laying hens (56-57 week old) and reported that oyster shell and limestone produced greater eggshell weight and quality. The differences between the results of An et al. [33] and those of Linchonicova et al. [34] may be due to the difference in the ages of the layers. Similarly, Tunc and Cuhadar [11] reported that the levels of Ca, P and Mg of the tibia changed with different sources and proportions of dietary Ca in laying hens.

Tunc and Cuhadar [11] stated that large sized alternative dietary Ca sources (eggshell and oyster shell) had positive effects on eggshell P and Mg contents of hens. This result is similar to ours except for P content of eggshell. However, our Ca source was ground. Similarly, De Witt et al. [35] indicated that large-particle limestone did not necessarily provide sufficient Ca^{2+} to laying hens for eggshell quality. Skrivan et al. [25] reported that different Mg levels of laying hen rations did not influence the Mg level of eggshell; however, low levels of dietary Mg decreased the crude ash of eggshell in layers that consumed fine limestone. Similarly, in the present study, dietary substitution of limestone with CFB did not affect the levels of eggshell Mg. The levels of dietary Vit D_3 (the main vitamin D form), Ca, and P of a ration are crucial in poultry for eggshell formation [36]. Bölükbaşı et al. [37] declared that increasing levels of Ca supplementation in laying hens in the late laying period increased eggshell P levels when Vit D_3 was omitted from the diet. Interestingly, in the present study, both levels of dietary CFB decreased the eggshell P levels compared with the control group that consumed dietary limestone. The P concentration of eggshell was sharply increased in younger birds at the termination of the calcification of eggshell [38]. Also, the P contents of CFB [39] may cause an increment in the total amount of dietary P and decrease the ratio of Ca/P in the ration.

Further, the P level of the blood serum was not affected; the levels of Ca and Mg in quail blood serum were not affected as well. This result may indicate that the levels of P in the blood and eggshell do not strictly correlate with each other. A study on the correlation between the P and Mg levels of the blood serum and eggshell [40] reported an insignificant negative correlation in laying hens, which is similar to the present study. Ozpinar [41], who worked on the correlations between ionic Ca, Na, and P levels of the blood and eggshell quality in laying hens, declared that the level of ionic Ca in the blood negatively correlated with eggshell strength. This report was supported by Akyel and Buğdaycı [40], who reported a significant negative correlation between the Ca levels of the blood and the Ca levels of eggshell, which is the same as the present study.

CFB did not affect the concentrations of blood Ca and P. Similarly, Gongruttananun [23] reported that 50% and 100% dietary limestone replacement with eggshell did not change the levels of plasma Ca and P in laying hens. Besides, a study on different ration levels (3.5 to 4.7%) of Ca in laying hens reported that the Ca level of a ration did not affect serum Ca and P levels of laying hens [33].

CONCLUSIONS

In the present study, the expected effects of CFB, an aquatic Ca source, on performance was not observed in laying quails. This conclusion is contrary to the results of several studies on alternative sources of dietary Ca in poultry. The results of this study indicate that substitution of limestone in the diet with CFB does not alter the internal and external quality parameters of quail eggs and the plasma Ca balance of quails.

ACKNOWLEDGEMENTS

This study was supported by 2209 TUBITAK project, a part of this study was presented as a poster in 1st International Animal Nutrition Congress 2016.

REFERENCES

[1] Yasothai, R., Kavithaa, N.V. (2014) Chemical characterization of egg shell meal. International Journal of Food Science and Technology. 3, 1436-1439.

[2] Kismiati, S., Yuwanta, T., Zuprizal, Z., Supadmo, S. (2012) The performance of laying hens fed different calcium source. Journal of the Indonesian Tropical Animal Agriculture. 37, 263-270.

[3] Scheideler, S.E. (1998) Eggshell calcium effects on egg quality and ca digestibility in first-or third-cycle laying hens. The Journal of Applied Poultry Research. 7, 69-74.

[4] Houndonougbo, M.F., Chrysostome, C.A.A. M., Doulami, R.C.O., Codjia, J.T.C. (2012) Snail shell as an efficient mineral feedstuff for layer hens: Effects and optimum rate. Available at: http://www.lrrd.org/lrrd24/11/houn24196.htm.

[5] Ergun, A., Sacaklı, P. (2017) Chicken nutrition. In: Hayvan Besleme ve Beslenme Hastalıkları, Ergun, A., Tuncer, S.D., Colpan, I., Yalcın, S., Yıldız, G., Kucukersan, M.K., Kucukersan, S., Sehu, A., Sacaklı, P. Eds., Kardelen offset, Ankara pp.444 (in Turkish)

[6] Ertaş, O.N., Ciftci, M., Guler, T., Dalkılıç, B. (2006) The use of possibility of mussel shell supplementation as calcium source in japanese quails raised under heat stress conditions: the effect of mussel shell on egg yield and some blood parameters. Fırat University Veterinary Journal of Health Sciences. 2, 15-20 (in Turkish with English abstract).

[7] Ahmed, N.M., Abdel-Atti, K.A., Elamin, K.M., Dafalla, K.Y., Malik, H.E.E., Dousa, B.M., (2013) Effect of Dietary Calcium Sources on Laying Hens Performance and Egg Quality. Journal of Animal Production Advances. 3, 226-231.

[8] Cetin, S., Gurcan, İ.S. (2006) The effects of oyster shell supplementation to diet on egg shell quality and serum calcium level in white and brown layer hybrids. Lalahan Hayvancılık Araştırma Enstitüsü Dergisi. 46, 23-31 (in Turkish with English abstract).

[9] MacIsaac, J.L., Anderson, D.M., Safamehr, A. (2016) Evaluation of whelks as an alternative source of calcium in laying hens. Journal of Applied Poultry Research. 25, 492–505.

[10] Cufadar, Y. (2014) Effect of alternative calcium sources on performance and eggshell quality in laying hens. The Journal of MacroTrends in Applied Science. 2, 10-15.

[11] Tunç, A.E., Cufadar, Y. (2015) Effect of calcium sources and particle size on performance and eggshell quality in laying hens. Turkish Journal of Agriculture - Food Science and Technology. 3, 205-209.

[12] Anonymous (2016) Cuttlefish. Available at: http://www.mesa.edu.au/atoz/cuttlefish.asp.

[13] Hanlon, R.T., Messenger, J.B. (1996) Cephalopod Behaviour. Cambridge University Press: New York. In: Richard. C.M. (2005) Individual differences in the common cuttlefish, Sepia officinalis. Dalhousie University (Canada). ProQuest Dissertations Publishing.

[14] Anonymous (2015) Amazing cuttlefish. Available from: http://www.users.on.net/~jamesmosby/cuttlefish/cuttlebones.html.

[15] Al-Obaidi, F.A., Mehdi, B.A., Al-Shadeedi, S.M. (2012) Identification of inorganic elements in egg shell of some wild birds in Baghdad. Advances in Applied Science Research. 3, 1454-1458.

[16] AOAC (1990) Official Methods of Analysis of the Association of Official Analytical Chemists. 14th ed. Association of Official Analytical Chemists, Arlington, VA.

[17] NRC (1994) Nutrient Requirements of Poultry, 9th Rev. Ed. National Academy Press, Washington, DC. Available at: http://www.nap.edu/openbook.php?record_id=2114&page= 44.

[18] Titus, H.W., Fritz, J.C. (1971) Percentage multipliers for computing metabolizable energy values, for chickens, of some feedstuffs used in the feeding of poultry. In: The Scientific Feeding of Chickens. 5th ed. Interstate, Danville, IL, 295-298.

[19] Card, L.E., Nesheim, M.C. (1972) Poultry production. 11th ed. Lea and Febiger, Philadelphia.

[20] Vuilleumier, J.P. (1969) The 'Roche Colour Fan' - An instrument for measuring yolk colour. Poultry Science. 48, 767-779.

[21] SPSS (1999) SPSS for Windows. Release 10.00 Version. SPSS Inc.

[22] Dawson, B., Trapp, R.G. (2001) Basic and clinical biostatistics. 3rd ed. Lange Medical Books/McGraw-Hill Medical Publishing Division, N.Y.

[23] Gongruttananun, N. (2011) Effects of eggshell calcium on productive performance, plasma calcium, bone mineralization, and gonadal characteristics in laying hens. Poultry Science. 90, 524–529.

[24] Safaa, H.M., Serrano, M.P., Valencia, D.G., Frikha, M., Jiménez-Moreno, E., Mateos, G.G. (2008) Productive performance and egg quality of brown egg-laying hens in the late phase of production as influenced by level and source of calcium in the diet. Poultry Science. 87, 2043-2051.

[25] Skřivan, M., Englmaierová, M., Marounek, M., Skřivanová, V., Taubner, T., Vít, T. (2016) Effect of dietary magnesium, calcium, phosphorus, and limestone grain size on productive performance and eggshell quality of hens. Czech Journal of Animal Science. 61, 473–480.

[26] Ahmad, H.A., Balander, R.J. (2003) Alternative feeding regimen of calcium source and phosphorus level for better eggshell quality in commercial layers. The Journal of Applied Poultry Research. 12, 509-514.

[27] Ayaşan, T., Okan F. (1999) The effects of dietary calcium and phosphorus levels on egg production traits and egg shell quality in japanase quail. Journal of Animal Production. 39-40, 98-104 (in Turkish with English abstract).

[28] Vandepopuliere, J.M., Lyons, J.J. (1992) Effect of inorganic phosphate source and dietary phosphorus level on laying hen performance and egg shell quality. Poultry Science. 71, 1022-1031.

[29] Sultana, F., Islam, M.S., Howlider M.A.R. (2007) Effect of Dietary Calcium Sources and Levels on Egg Production and Egg Shell Quality of Japanese Quail. International Journal of Poultry Science. 6, 131-136.

[30] Rajiv, J.N. (2016) Effect of calcium pidolate on egg production and egg quality during last phase of production cycle with reducing levels of inorganic calcium. Submitted in partial fulfilment of the requirements for the degree of master of veterinary science in poultry science. Enrolment No.: V/09/0182 Bombay Veterinary College, Mumbai, INDIA.
[31] Wang, S., Chen, W., Zhang, H. X., Ruan, D., Lin, Y.C. (2014) Influence of particle size and calcium source on production performance, egg quality, and bone parameters in laying ducks. Poultry Science. 93, 2560–2566.
[32] Świątkiewicz, S., Arczewska-Włosek, A., Krawczyk, J., Szczurek, W., Puchała, M., Józefiak, D. (2018) Effect of selected feed additives on egg performance and eggshell quality in laying hens fed a diet with standard or decreased calcium content. Annals of Animal Science. 18(1), 167-183.
[33] An, S.H., Kim, D.W., An, B.K. (2016) Effects of dietary calcium levels on productive performance, eggshell quality and overall calcium status in aged laying hens. Asian Australasian Journal of Animal Sciences. 29, 1477-1482.
[34] Lichovnikova, M. (2007) The effect of dietary calcium source, concentration and particle size on calcium retention, eggshell quality and overall calcium requirement in laying hens. British Poultry Science. 48, 71–75.
[35] De-Witt, F.H., Kuleile, N.P., Van-Der, Merwe, H.J.; Fair, M.D. (2009) Effect of limestone particle size on egg production and eggshell quality of hens during late production. South African Journal of Animal Science. 39, 37–40.
[36] Keshavarz, K. (2003) A comparison between cholecalciferol and 25- OH-cholecalciferol on performance and eggshell quality. Poultry Science. 72, 144-153.
[37] Bölükbaşı, S.C., Çelebi, S., Utlu, N. (2005) The Effects of Calcium and Vitamin D_3 in Diet on Plasma Calcium and Phosphorus, Eggshell Calcium and Phosphorus Levels of Laying Hens in Late Laying Production Period. International Journal of Poultry Science. 4(8), 600-603.
[38] Cusack, M., Fraser, A.C., Stachel, T. (2003) Magnesium and phosphorus distribution in the avian eggshell. Comparative Biochemistry and Physiology Part B. 134, 63–69.
[39] Turner, J.F. (2018) Nutritional Properties of Cuttlebone for Pets. Available at: https://www.animalwised.com/nutritional-properties-of-cuttlebone-for-pets-618.html.
[40] Akyel, R. Bugdayci, K.E. (2018) Comparison of L-lysine hydrochloride and L-lysine sulfate on performance, egg quality and some blood parameters in laying hens. Journal of the Turkish Veterinary Medical Society. 89(2), 25-36 (in Turkish with English abstract).
[41] Ozpinar, A.A. (1997) The variations in blood ionized calcium, sodium and potassium concentrations with age and laying cycle and the relationships of these ions with eggshell quality. Archiv fur Geflugelkunde. 61(6), 287-290.

Received: **03.02.2019**
Accepted: **20.01.2020**

CORRESPONDING AUTHOR

Kadir Emre Bugdayci
Department of Animal Nutrition and Nutritional Diseases, Faculty of Veterinary Medicine
Burdur Mehmet Akif Ersoy University
Burdur – Turkey

e-mail: kebugdayci@mehmetakif.edu.tr

© by PSP Volume 29 – No. 04A/2020 pages 2691-2697 Fresenius Environmental Bulletin

EFFECTS OF DIMETHYL SULFOXIDE (DMSO) AND THAWING RATES ON SPERM MOTILITY FOR CRYO-PRESERVATION OF SPERM IN GILTHEAD SEABREAM (*SPARUS AURATA*)

Serhat Engin*, Sahin Saka, Kursat Firat

Ege University, Faculty of Fisheries, Aquaculture Department 35100 Bornova, Izmir, Turkey

ABSTRACT

The aim of the present study was to establish a protocol for cryopreservation of sperm in *Sparus aurata* and also to verify the applicability under culture conditions. Cryopreservation of sperm was attempted by using two extenders: Extender A (10 % egg yolk, buffer solution) and Extender B (1% NaCl, 10% BSA Bovine Serum Albumin). Cryoprotectants were assessed at three different concentrations (5, 10 and 15 %, DMSO) individually as well as in combination with varying equilibration times (10 and 30 min). In order to maintain freezing rate, freezing protocols were adjusted by −30 °C/min intervals. Obtained results indicated that cryomedium constituting of Extender A with addition of 10% DMSO in dilution ratio of 1:3 (sperm:cryomedium) at an equilibration time of and freezing rate of −30 °C/min was more desirable compared to the other experimental procedures (Extender B) that were assessed (P>0.05). Moreover, 40 °C for 10 s presented highest post-thaw motility after end of the first month (72,7±0,35%) (P>0.05). Finally, it is determined that Extender A exhibited better performance in terms of sperm motility, freezing and thawing rate and also this ratio could be effectively utilized for cryopreservation of sperm for this species.

KEYWORDS:
Gilthead Sea Bream, Sperm, Motility, Cryopreservation.

INTRODUCTION

During the past two decades, it is well reported that cryopreservation of sperm is considered as a safe method not only transport of sperm for fertilization but also using for genetical programmes for cultured and/or conservation of endangered species [1]. In order to sustain these phenomenon, some biological biomarkers of sperm such as frozen and/or thawing process, motility, fertilization and hatching rates, and plasma membrane parameters are investigated in detailed studies [2,3]. In addition to these, recent studies have been focused on especially post-thaw motility, type and concentrations of the cryoprotectants (CPA), type of extender, supplementation of extender with cell membrane stabilizer and antioxidants, equilibration time, and dilution ratio [4,5]. Furthermore, several protocols have been progressed on cryopreservation of sperm but there are still lack of knowledge and gaps for improving of standards. It is well reported that some agents based on antioxidants such as bovine serum albumin (BSA) [6], and egg yolk [7] and uric acid [8] are compensate of protection role of seminal plasma.

In longer cryopreservation of fish sperm, some authors argued that decreasing of post thaw motility related with high dilution rate and also losing of protection role of seminal plasma. In detail, dilution of sea bream sperm was reported 1:6 – 1:10 rates in previous studies [9,10,11,12]. Therefore, this study was firstly designed to compare different dilution (1:3) and thawing rates (30, 40 and 50 °C) of sea bream sperm by egg yolk as an extender.

MATERIALS AND METHODS

Experimental design. Two extenders, Ext A and B, were designed to cryopreserve of sea bream sperm. In detail, egg yolk and BSA were used as cryoagent and also 3 different concentrations of DMSO for frozen and 3 thawing rates were performed. Experimental design was diagrammed in Figure 1.

Fish and male gamete collection. Male of *Sparus aurata* (BW: 606,83±35,92 g; TL: 30,13±1,16 cm) were obtained from commercial private aquaculture farm captured at the offshore waters of Urla/İzmir, Turkey during the spawning season (October–December) of 2012. Selected males (n= 30) were identified by slight abdominal pressure. In order to collect of sperm, breeders were selected immediately after harvesting and urogenital area of them were cleaned and the sperm was gently stripped by hand into clean dry 15.0 mL Falcon centrifuge tubes. For protection of

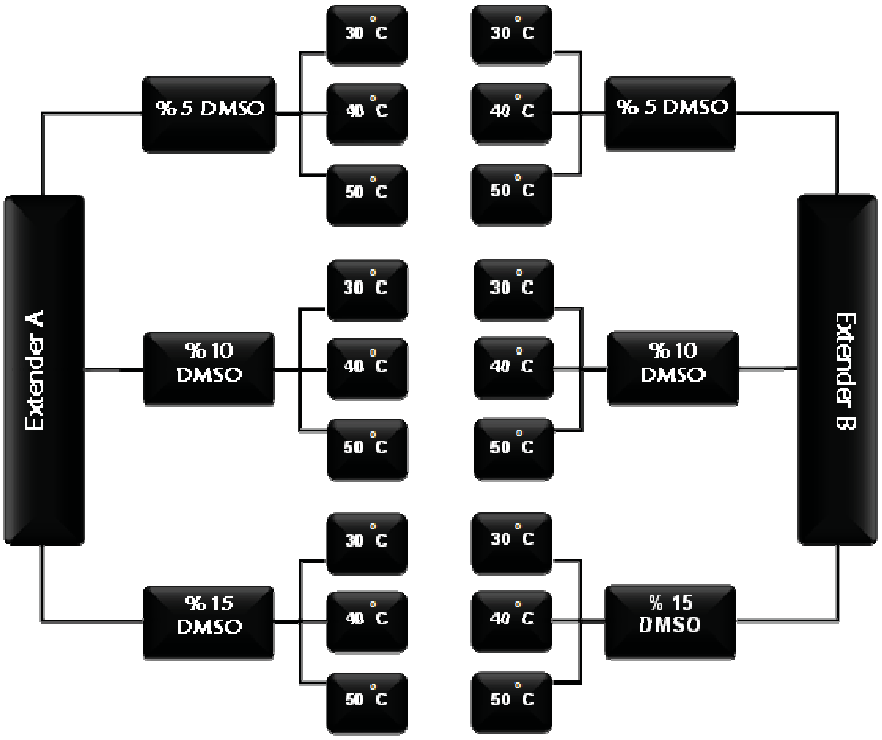

FIGURE 1
Experimental design

contamination from seawater, blood, urine and/or feces sperm was carefully avoided. Sperm samples were placed on crushed ice immediately and transported to the laboratory and stored at 4 °C until further use.

Assessment of sperm characterization. Sperm density and concentration was analysed by hemocytometric method by using thoma counting lamp. The motile sperm speed was monitored by a certain trajectory and also this movement was recorded with the integrated camera on the Olympus CX31 phase contrast microscope.

Assessment of sperm motility. In order to examine sperm motility under microscope, spermatozoa were activated by mixing of milt in minute volume and dropping to natural seawater (‰37,2). Before and after freezing, the motility of the spermatozoa was observed under microscope with x40 magnification and recorded. Semi-quantitative measurements of sperm motility were analysed on integrated camera recordings in triplicate. Only forward-moving sperm were judged motile, those simply vibrating or turning on their axes was considered immotile. Besides, sperm that presented low motility scores (<80%) after seawater activation were not considered. All cryopreserved samples were removed from liquid nitrogen (−196 °C) after a per month in 3 months of storage and were thawed for sperm quality assessment.

Sperm Cryopreservation. Two extenders (A and B) were used for cryopreservation. Briefly, for extender A, semen was diluted at a rate of 1:3 (v:v) in 10% of egg yolk with buffer solution and 1% NaCl with 10% BSA by 5, 10 and 15 % DMSO. It was inserted by Pasteur pipette into 0.25 ml straws and from 0 to 140 °C, samples were frozen by 30 °C.min^{-1} gradients. Finally, they were immersed in liquid nitrogen Straws PACE automatically fills and heat-seals both ends of pre-identified CBS™ High Security. PACE uses CBS™ straws that are pre-identified with barcodes and/or alphanumerical codes (IMV Tech.). After these procedure, freezing procedure was conducted in a Digitcool programmable freezer (IMV Tech. Inc., France).

Thawing of Sperm. In order to assess sperm quality, frozen cryotubes were thawed in water bath at 30 – 40 – 50 °C for 10 seconds. Thawed sperm samples were analysed for motility and viability immediately according to semi-quantitative method as described by Sansone et al. 2002 [13].

Statistical analysis. Results from spermatalogical characteristics are given as mean±SD. The variance homogeneity of the data was performed using Levene's test. Differences among groups, data were compared by one–way ANOVA, followed by Tukey multiple range test a when significant differences were found at a 0.05 level. All measurements were carried out in triplicate.

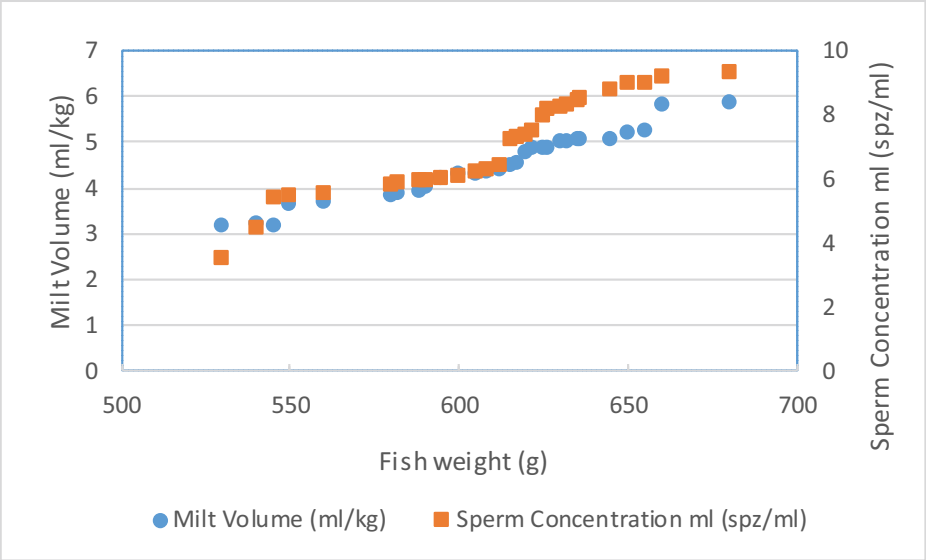

FIGURE 2
Relations between fish weight, milt volume and spermatozoa concentration per ml of milt

RESULTS

Sperm Characteristics. The average volume of sperm was determined as 4,46±0,72 ml.kg^{-1}. The highest and the lowest sperm volume was 5.88 ml.kg^{-1} and 3.17 ml.kg^{-1}, respectively. Moreover, the peak and the lowest sperm concentration was 9.3x10^{9} spz.ml^{-1} and 3.5x10^{9} spz.ml^{-1}, respectively, whilst, the mean concentration of sperm was 7.06±1.5 spz.ml^{-1}. The mean velocity of sperm was 103.97±0.1 µm.sn^{-1} whereas the highest and the lowest sperm velocity was 144 µm.sn^{-1} and was 81 µm.sn^{-1}, respectively. Also, fresh sperm viability was changed between 6,14 and 8,16 min and the mean value was 7,31±0,8 min (Figure 2).

At the end of the experiment, Ext A exhibited better performance for sperm motility ($p<0.05$). The best thawing rate was recorded at 40 °C for both Ext A and Ext B. Similarly, 10% DMSO presented relatively better results in motility rates for both groups ($p<0.05$). Overall results indicated that Ext A with+10% DMSO for 40 °C was exhibited superior performance among experimental groups (Table 1 and 2).

TABLE 1
Percentages (mean±SD) of total motile (TM) after cryopreservation with thawing rates (sperm: Extender A+DMSO) sea bream spermatozoa after thawing, after 1 month (n = 30) of storage in liquid nitrogen. Significant differences (P < 0.05) are represented by different bar superscripts and were recorded between semen after thawing, but not in relation to storage time.

Percent of motile sperm (mean ± SEM) after thawing of sea bream in Ext A			
	Cryoprotectant	Thawing rate (°C)	
	30 °C	**40 °C**	**50 °C**
5 % DMSO	40,5±0,35	45,2±0,28	26,2±0,46
10 % DMSO	56,5±0,93	72,7±2,7	37±0,58
15 % DMSO	25,8±0,42	32,6±0,61	19,8±0,21

TABLE 2
Percentages (mean±SD) of total motile (TM) after cryopreservation with thawing rates (sperm: Extender B+DMSO) sea bream spermatozoa after thawing, after 1 month (n = 30) of storage in liquid nitrogen. Significant differences (P < 0.05) are represented by different bar superscripts and were recorded between semen after thawing, but not in relation to storage time.

Percent of motile sperm (mean ± SEM) after thawing of sea bream in Ext B			
	Cryoprotectant	Thawing rate (°C)	
	30 °C	**40 °C**	**50 °C**
5 % DMSO	25,1±0,38	31,2±0,55	5,4±0,26
10 % DMSO	30,7±0,35	58±0,8	29,1±0,4
15 % DMSO	22,2±0,34	37,9±0,83	16,3±0,54

DISCUSSION

In this study, sperm characteristics and also motility were investigated by two extenders (egg yolk and BSA) under different DMSO concentrations (5, 10 and 15%) administered different thawing temperatures (30, 40 and 50 °C). In several previous studies, sperm characteristics were also reported in cultured marine common species such as European sea bass (*Dicentrarchus labrax*). Several authors were reported in different studies that sperm concentrations of this species were 2.1-7.5x10^9 spz.ml^{-1} [14], 5-55x10^9 spz.ml^{-1} [15], 50-60x10^9 spz.ml^{-1} [16] and 10-40 spz.ml^{-1} [17]. In similar with, this parameter was also recorded as 0.4-5,18x10^9 spz.ml^{-1} [18], 0.7-11x10^9 spz.ml^{-1} [19], 2-9 spz.ml^{-1} [20], and 20-55x10^9 spz.ml^{-1} [3] for turbot, *Psetta maxima*. In addition to these, 6,8x10^9 spz.ml^{-1}, 8,6-23.7x10^9 spz.ml^{-1} and 49,6-64,8 spz.ml^{-1} was reported for red spotted grouper, *Epinephelus akaara* [21], red porgy *Pagrus pagrus* [22] and blue fin tuna, *Thunnus thynnus* [23], respectively. In freshwater species, rainbow trout, *Onchorhynchus mykiss*, several authors noted that these concentrations were 11.7-17.25x10^9 spz.ml^{-1} [24], 48-114x10^9 spz.ml^{-1} [10] and 6-10x10^9 spz.ml^{-1} [25]. As decribed by severeal authors, sperm concentrations of sea bream were11.6-26.7x10^9 spz.ml^{-1} and 5.5-17.5x10^9 spz.ml^{-1}, respectively [26,10]. In present study, we measured as 3,5-9,3 spz.ml^{-1} and this is paralleled with findings of [26], however it was relatively lower than reported by [10]. It is thought that different feeding regimes could be affected this parameter under culture conditions.

It is estimated that on volume and amount of sperm in fish is mainly depend on some biological parameters such as fish species, age and weight of breeders, stripping methods and frequencies, environmental parameters, husbandry, and feeding under culture conditions [27-30]. In European sea bass (*D. labrax*), it was reported that sperm volumes were 2.1-5.3 ml.kg^{-1} and 1-2 ml.kg^{-1} [14,15]. In similar with, this parameter was also recorded as 1.7-5.3 ml.kg^{-1} for *P. pagrus* [34] and also 0.4-1.25 ml.kg^{-1} and 2.2 ml.kg^{-1} for *P. maxima* [3,31]. For *O. mykiss*, it was 4.8-6.5 ml.kg^{-1} [32]. Besides, Barbato (1998) [26] described that sperm volume of sea bream was determined as 2.6-7 ml.kg^{-1} whereas it was agreement with our findings of 3,17–5,88 ml.kg^{-1}

Fertilization rate, motility and sperm velocity are the main factors to determine of sperm quality in usual. Especially, not only velocity but also fast swimming of sperm is considered for determination of sperm quality [13]. According to previous studies, sperm velocity of sea bream were recorded in different value as 89 µm.sn^{-1}, 81,39 µm.sn^{-1} and 35,11 µm.sn^{-1} [8,9,33]. In current study it was changed between 81 and 144 µm.sn^{-1}. Our findings were agreement with the results of the [8,9]. However, Zilli et al. (2003) [34] were reported that approximately 2-fold lower sperm velocity was noted compared to both this and previous studies. It is thought that this was related with morphological properties of experimented sperm [33]. As recorded by [14] and [16], sperm viability of cultured sea bass was found around 0,6–2 and 0,7–2,9 min under culture conditions. Additionally, this period was reported 0,4–2 and 3,6 min for *O. mykiss* [35,36]. In Sparid, it was estimated 1,5–2 min for white sea bream, *Diplodus sargus* [37], 2,6–3,9 min for *P. pagrus* [22] and 1–3 min for sharpsnout sea bream, *Diplodus puntazzo* [38]. Besides, currently it was 6,9±0,8 min for sea bream and also in other cultured marine fish, *P. maxima*, 3 different periods for viability of sperm were reported as 3–5 min [39], 1–17 min [30] and 2–3 min [20].

It is well reported that DMSO is the most common cryoprotectant used in such studies, thus, it was administered in different concentrations in this study. Similarly, Gallego et al. (2012) [12] reported that after thawing, 5% DMSO solution was used in order to examine morphometry and motility analysis and also pointed out effective on morphometric variations during the freezing and thawing process of sperm in sea bream. Additionally, it was also stated that combined effects of both DMSO and polyethilenglicol (PEG) on DNA structure of sperm was investigated and resulted that 10% DMSO was presented better scores than both 5% DMSO and different PEG concentrations (5 and 10%) in red sea bream (*Pagrus major*) [40]. Furthermore, Barbato et al. (2003) [26] argued that 15% DMSO was exhibited lower performance than 10% DMSO administration for sperm of sea bream and sharpsnout sea bream. Similarly, Beireo et al. (2011) [9] studied in sea bream by different cryoprotectants, DMSO, ethylenglicol (EG) and PEG, and stated that motility of sperm and hatching rate of fertilized egg in 10 % DMSO administration were relatively higher than the other treatments. In contrast to these, Fabbrocini et al. (2000) [11] studied on different concentrations of (5, 10 and 15 %) DMSO, ethilenglicol (EG), PEG, glycerol, methanol (MET) and it was noted that 5% DMSO presented better results for sperm motility than not only for different concentrations of (10 and 15 %) DMSO but also among other cryoprotectants, EG, PEG, glycerol, and MET.

It is well defined that protection role of seminal plasma during the freezing process is compensated by BSA, egg yolk and uric acid [6,7,8,11,13].In present, different dilution rates and also extender compositions are commonly used in cryopreservation of fish sperm, mostly BSA is widely performed for this process in cultured marine species. Several authors approved that BSA is the major extender for the other cultured species such as sea bream, sea bass, and sharpsnout sea bream, Additionally, it is claimed that combined effects of BSA and L-α phosphodilcholin play major role for protection of sperm membrane [14].

Peneranda et al. (2009) [41] noted positive correlation on motility of sperm and using of BSA as an extender in sea bass. Similarly, egg yolk was presented lower performance for sperm motility compared to the BSA in sea bream [9]. In contrast to this, our obtained results disagreed with the Beirao's study, hence, egg yolk was achieved better motility results than BSA in same species. In addition to extender and CP, straw tube is also crucial factor for cryopreservation whereas its volume is the deterministic tool for maintain of the viability of fish sperm [40,42,43]. Cabrita et al. (2010) [2] reported that straw tubes have 0.25-0.5 ml volume are essential to sustain of cryopreservation due to geometrical shape which is accelerates freezing and thawing duration. As performed in previous papers, 0.25 ml straw tubes were used and similar findings were presented in this study.

In previous studies, it was reported that dilution rate (sperm:extender) was changed between 1:1 and 1:20 for cultured fish. For instance, in sea bream and Atlantic croaker these rates were determined as 1:20 and 1:50, respectively; but after thawing, lower motility and larval survival rates were noted for both species [44,45]. Moreover, in turbot 1:1 and 1:9 rates were insignificant but 1:10 and over rates caused to decrease in motility of sperm [39] whereas this rate was 1:3 for sea bass [34]. It is well reported that decrease of motility rates after thawing could be related with losing of protection role due to higher dilution rate in fish sperm [20,35]. During the past decades, some studies focused on dilution rates of sea bream and also some rates were reported as 1:10 [10,11] and 1:6 [9,10,12]. In this sense, dilution rate was adjusted as 1:3 due to consideration of disorder of protection role in higher dilution rates in current study.

As described in several studies, not only freezing but also thawing process is the crucial step in cryopreservation of sperm. In order to prevent of crystallization of cell membrane, this process should be occurred immediately. As usual, after thawing, sperm of marine fish have better motility compared to the fresh water species. In this sense, Fabbrocini et al. (2000) [11], Cabrita et al. (2005) [10] and Beirao et al. (2011) [9] reported that thawing of sperm were conducted at 35, 25 and 60 °C., respectively, whilst in current study this process was completed at 30, 40 and 50 °C. Here, 40 °C was firstly applied and it was determined that this was the best score for sperm of sea bream compared to the other studies in such temperatures.

CONCLUSIONS

It is concluded that this study was firstly designed to determine by a different method for cryopreservation of sea bream sperm. Finally, the best results for sperm post-thaw motility were obtained from Ext A+10% DMSO with 1:3 dilution rate after thawing at 40 °C. Moreover, further studies should be conducted on specific analyses to obtain the best combination for protocol of sperm cryopreservation especially for industrial scale cultured species.

ACKNOWLEDGEMENTS

The authors extend their gratitude to the staff of the EGEVET Bull Stud. and SpermBank-Bull Semen Production Inc. for their invaluable technical assistance during the experiments.

REFERENCES

[1] Vuthiphandchai, V., Chomphuthawach, S., Nimrat,S (2009). Cryopreservation of red snapper (Lutjanus argentimaculatus) sperm: Effect of cryoprotectants and cooling rates on sperm motility, sperm viability, and fertilization capacity. Theriogenology. 72(1),129-38.

[2] Cabrita, E., Sarasquete, C., Martınez-Paramo, S., Robles, V., Perez- Cerezales, S., Herr_aez, M. P., (2010). Cryopreservation of fish sperm: applications and perspectives. J. Appl. Ichthyol. 26, 623–635.

[3] Suquet, M., Dreanno, C., Fauvel, C., Cosson, J., Billard, R., (2000). Cryopreservation of sperm in marine fish. Aquatic Research. 31,231–243

[4] Alavi, S.H.D., Hatef, A., Pšenička, M., Kašpar, V., Boryshpolets, S., Dzyuba, B., Cosson, J., Bondarenko, V., Rodina, M., Gela, D., Linhart, O., (2012). Sperm biology and control of reproduction in sturgeon: (II) sperm morphology, acrosome reaction, motility and cryopreservation. Fish Biology and Fisheries. 22(4), 861–886

[5] Judyckaa, S., Szczepkowskib, M., Ciereszkoa, A., Dietricha, G.J., (2015). New extender for cryopreservation of Siberian sturgeon (Acipenser baerii) semen. Cryobiology. 70(2), 184-189

[6] Cabrita, E., Robles, V., Herráez, M.P., (2008). Methods in Reproductive Aquaculture: Marine and Freshwater Species. Taylor and Francis, USA. 549 pp.

[7] Pérez-Cerezales, S., Martínez-Páramo, S., Beirão, J., Herráez, MP., (2010). Fertilization capacity with rainbow trout DNA-damaged sperm and embryo development success. Reproduction.139, 989–97.

[8] Lahnsteiner, F., Mansour, N., Caberlotto, S., (2010). Composition and metabolism of carbohydrates and lipids in Sparus aurata semen and its relation to viability expressed as sperm motility when activated. Comp Biochem Physiol. 157,39–45.

[9] Beirao, J., Cabrita, E., Perez-Cerezales, S., Martınez-Paramo, S., Herraez, M.P., (2011). Effects of cryopreservation on fish sperm subpopulations. Cryobiology. 62, 22–31.

[10] Cabrita, E., Robles, V., Rebordinos, L., Sarasquate, C., Herraez, M.P., (2005). Evaluation of DNA damage in rainbow trout (Oncorhynchus mykiss) and gilthead sea bream (Sparus aurata) cryopreserved sperm Cryobiology. 50, 144-153.

[11] Fabbrocini, A., Lubrano Lavadera, S., Rispoli, S., Sansone, G. (2000). Cryopreservation of seabream (Sparus aurata) spermatozoa. Cryobiology. 40, 46–53.

[12] Gallego, V., Mazzeoa, M.C., Vílcheza, D.S., Peñarandaa, P.C.F., Carneirob, L., Péreza, J., Asturiano, F., (2012). Study of the effects of thermal regime and alternative hormonal treatments on the reproductive performance of European eel males (Anguilla anguilla) during induced sexual maturation. Aquaculture. 354–355, 7-16.

[13] Sansone, G., Fabbrocini, A., Ieropoli, S., Langellotti, A.L., Occidente, M., Matassino, D., (2002). Effects of extender composition, cooling rate, and freezing on the motility of sea bass (Dicentrarchus labrax, L.) Spermatozoa After Thawing. Cryobiology. 44, 229– 239.

[14] Asturiano, J.F., Sorbera, L.A., Carrillo, M., Zanuy, S., Ramos, J., Navarro, J.C. Ve Bromage, N., (2001). Reproductive performance in male European sea bass (Dicentrarchus labrax, L.) Fed two PUFA enriched experimental diets: a comparison with males fed a wet diet. Aquaculture. 194,173–190.

[15] Felip, A., Zanuy, S., Carrillo, M., (2006). Comparative analysis of growth performance and sperm motility between precocious and non-precociousmales in the European sea bass (Dicentrarchus labrax L.). Aquaculture. 256(1-4), 570-578.

[16] Fauvel, C., Savoye, O., Dreanno, C., Cosson, J., Suquet, M., (1999). Characteristics of sperm of captive sea bass (Dicentrarchus labraxl.) İn relation to its fertilization potential. J. Fish Biol. 54, 356–369.

[17] Villani, P., Catena, C., (1991). Crioconservazione di gameti maschili di spigola (Dicentrarchus labrax L.): soluzioni e metodologie. Riv.Ital. Acquacol. 26, 217 226.

[18] Chereguini, O., Garcı´a de la Banda, I., Rasines, I., Fernandez, A., (1999). Artificial fertilisation in turbot, Scophthalmus maximus: different methods and determination of the optimal sperm –egg ratio. Aquac. Res. 30, 319–324.

[19] Fauvel, C., Suquet, M., Dreanno, C., Zonno, V., Menu, B., (1998). Cryopreservation of the sea bass (Dicentrarchus labrax) spermatozoa in experimental and production simulating conditions Aquat. Living Resour. 11, 387-394.

[20] Chauvaud, L., Cosson, J., Suquet, M., Billard, R., (1995). Sperm motility in turbot, Scophthalmus maximus: initiation of movement and changes with time of swimming characteristics. Environ. Biol. Fishes. 43, 341–349.

[21] He, Q., Lu, G., Che, K., Zhao, E., Fang, Q., Wang, H., Liu, J., Huang, C., Dong, Q., (2011). Sperm cryopreservation of the endangered red spotted grouper, Epinephelus akaara, with a special emphasis on membrane lipids. Aquaculture. 318, 1–2, 185-190.

[22] Mylonas, C., Papadaki, M., Divanach, P., (2003). Seasonal changes in sperm production and quality in the red porgy (Pagrus pagrus L.). Aquaculture Research. 34, 1161-1170.

[23] Doi, M., Hoshino, T., Taki, Y., Ogasawara, Y., (1982). Activity of the sperm of the bluefin tuna Thunnus thynnus under fresh and preserved conditions. Bulletin of the Japanese Society of Scientific Fisheries. 48, 495–498.

[24] Babiak, I., Glogowski, J., Dobosz, S., Kuzminski, H., Goryczko, K., (2002). Semen from rainbow trout produced using cryopreserved spermatozoa is more suitable for cryopreservation. Journal of Fish Biology. 60, 561–570.

[25] Glogowski, J., Kwasnik, M., Piros, B., Dabrowski, K., Goryczko, K., Dobosz, S., Kuzminski, H., Ciereszko, A., (2000). Characterization of rainbow trout milt collected with a catheter: semen parameters and cryopreservation success. Aquaculture Research. 31, 289-296.

[26] Barbato, F., Canese, S., Moretti, F., Misiti, S., Laconi F., and Rana, K., (1998). Preliminary experiences for cryopreservation of Sparus aurata and Diplodus puntazzo semen. Technology of Aquaculture in the Mediterranean. 281-287.

[27] Büyükhatipoğlu, S. And Holtz, W., (1984). Sperm output in rainbow trout (Salmo gairdneri) effect of age, timing and frequency of stripping and presence of females. Aquaculture. 37, 63-71.

[28] Gjerde, B., (1984). Variation in semen production of farmed Atlantic salmon and rainbow trout. Aquaculture. 40,109 –14.

[29] Kazakov, R.V. (1981). Peculiarities of sperm production by anadromous parr Atlantic salmon (Salmo salar L.) And fish cultural characteristics of such sperm. J. Fish Biol. 18, 1-8.

[30] Suquet, M.R., Billard, R., Cosson, J., Dorange, G., Chauvaud, L., Mugnier, C. And Fauvel, C., (1994). Sperm features in turbot Scophthalmus maximus: A comparison with other freshwater and marine fish species. Aquatic Living Resources. 7, 283- 294.

[31] Chen, S., Ji, X., Yu, G., Tian, Y., Sha, Z., (2004). Cryopreservation of sperm from turbot (Scophthalmus maximus) and application to large- scale fertilization. Aquaculture. 236, 547-556.
[32] Geffen, A.J., and Evans, J.P., (2000). Sperm traits and fertilization success of male and sex-reversed female rainbow trout (Oncorhynchus mykiss) Aquaculture. 182, 61-72.
[33] Zilli, L., Schiavone, R., Storelli, C., Vilella S., (2008). Effect of cryopreservation on phosphorylation state of proteins involved in sperm motility initiation in sea bream. Cryobiology. 150-155.
[34] Zilli, L., Schiavone, R., Zonno, V., Storelli, C., Vilella, S., (2003). Evaluation of DNA damage in Dicentrarchus labrax sperm following cryopreservation. Cryobiology. 47, 227–35.
[35] Billard, R., (1983). Ultrastructure of trout spermatozoa: changes after dilution and deep-freezing. Cell and Tissue Research. 228, 205-218
[36] Yanagimachi, R., Cherr, G.N., Pillai, M.C., Baldwin, J.D., (1992). Factors controlling sperm entry into the micropyles of salmonid and herring eggs. Development, Growth & Differentiation. 34, 447–461.
[37] Lahnsteiner, F., and Patzner, R.A., (1998). Sperm motility of the marine teleosts Boops boops, Diplodus sargus, Mullus barbatus and Trachurus mediterraneus Journal of Fish Biology. 52, 726-742.
[38] Taddei, A.R., Barbato, F., Abelli, L., Canese, S., Moretti, F., Rana, K.J., Fausto, A.M., Mazzini, M., (2001). Is cryopreservation a homogeneous process? Ultrastructure and motility of untreated, prefreezing, and postthawed spermatozoa of Diplodus puntazzo (Cetti). Cryobiology. 42(4), 244-55
[39] Dreanno, C., Suquet, M., Quemener, L., Cosson, J., Fierville, F., Normant, Y., Billard, R., (1997). Cryopreservation of turbot (Scapthalmus maximus) spermatozoa. Theriogenology. 48,589-603.
[40] Liu, Q.H., Li, J., Xiao, Z.Z., Ding, F.H., Yu, D.D., Xu, X.Z., (2007). Use of computer-assisted sperm analysis (CASA) to evaluate the quality of cryopreserved sperm in red seabream (Pagrus major). Aquaculture. 263(1-4), 20-25.
[41] Peñaranda, D.S., Pérez, L., Gallego, V., Jover, M., Asturiano, J.F., (2009). Improvement of European eel sperm cryopreservation method by preventing spermatozoa movement activation caused by cryoprotectants. Cryobiology. 59,119 –26.
[42] Cabrita, E., Anel, L., Hernaez, M.P. (2001). Effect of external cpas a membrane stabilizers on cryopreserved rainbow trout spermatozoa. Theriogenology. 56, 623–635.
[43] Horváth, Á., Miskolczi, E., Mihálffy, S., Osz, K., Szabó, K., Urbányi, B., (2007). Cryopreservation of common carp (Cyprinus carpio) sperm in 1.2 and 5 ml straws and occurrence of haploids among larvae produced with cryopreserved sperm. Cryobiol. 54, 251–7.
[44] Chambeyron, F.Y., Zohar, A., (1990). Diluent for sperm cryopreservation of gilthead seabreamm Sparus aurata. Aquaculture. 90, 345–352.
[45] Gwo, J.C., Strawn, K., Longnecker, MT., Arnold, CR., (1991). Cryopreservation of Atlantic croaker spermatozoa. Aquaculture. 94, 355-375.

Received: **29.03.2019**
Accepted: **16.01.2020**

CORRESPONDING AUTHOR

Serhat Engin
Ege University,
Faculty of Fisheries,
Aquaculture Department
35100 Bornova, Izmir – Turkey

e−mail: serhat.engin@ege.edu.tr

© by PSP Volume 29 – No. 04A/2020 pages 2698-2706 Fresenius Environmental Bulletin

IN VITRO APPROACHES FOR SHORTENING GENERATION CYCLES AND FASTER BREEDING OF LOW β-N-OXALYL-L-α, β -DIAMINOPROPIONIC ACID CONTENT OF GRASS PEA (*LATHYRUS SATIVUS* L.)

Surendra Barpete[1,2,*], Priyanka Gupta[2], Khalid Mahmood Khawar[1], Sebahattin Ozcan[1], Shiv Kumar[2]

[1]Department of Field Crops, Faculty of Agriculture, Ankara University, Ankara, 06110, Turkey
[2]International Center for Agricultural Research in the Dry Areas (ICARDA), Rabat Institute, Rabat, Morocco

ABSTRACT

Grass pea (*Lathyrus sativus* L.) grows as long day plant under natural conditions with single breeding cycle per annum. There is a need to develop strategies by accelerating breeding activities, making it possible to grow more than one generation per annum. This study aimed to search alternative in *vitro* mopho-physiological approaches to induce earlier flowering and accelerate breeding cycles. Nodal junctions with internodes were used as explants to multiple shoots using different concentrations of 6-benzylaminopurine (BAP) and α-naphthalene acetic acid (NAA). The MS medium supplemented with 2 mg L^{-1} BAP and 1 mg L^{-1} NAA was most optimum for production of multiple shoots. These shoots were transferred to MS medium containing 0.1- 0.50 mg L^{-1} BAP singly for generative transformation and growth. The MS medium supplemented with 0.25 mg L^{-1} BAP was most optimum for induced floral buds and flowers within two weeks of culture showing an average number of 4.30± 0.32 flowers per plantlet that continued and increased in number during rooting and acclimatization. The plantlets did not face any problem during acclimatization in the greenhouse, where they set seeds. The maximum β-*N*-oxalyl-l-α, β-diaminopropionic acid (β-ODAP) accumulation was recorded (1.48%) at early developmental stage followed by the flowering stage of grass pea. The results are very encouraging and the methodology used in this experiment could positively contribute towards accelerated breeding of ODAP free grass pea varieties.

KEYWORDS:
Grass pea, *In vitro* flowering, *Lathyrus sativus* L., Nodal junction, ODAP

INTRODUCTION

Grass pea (*Lathyrus sativus* L.) is a highly neglected and orphan crop plant that grows well both under South Asian high-temperature subtropical [1, 4] and Mediterranean temperate West Asian climates [2, 3] with maturity periods of 80-100 and 120 - 140 days respectively [4]. It is not possible to grow 2-3 generations of grass pea unless geographical differences in latitude and altitude are exploited [4, 5] under synthetic (greenhouse) conditions.

Genetic and environmental factors influence grass pea cross pollination with a range of 9.8 to 27.8% [6]. Appreciable progress has not been made in the advancement of grass pea breeding using genetic, genomic, biochemical, molecular, morpho-physiological, approaches in the past [4, 8, 10]. After physiological maturity and anthesis, grass pea takes about 25-45 days (depending on genotypes and environments) to pod filling [5]. If induction of flowering under *in vitro* conditions could be manipulated, it may help in shortening and synchronization of flowering duration events during breeding among varieties and species of the same genus enabling hybridization among them. Complicated crossability relationships in *Lathyrus* have been grouped into primary, secondary and tertiary gene pools [11]. The presence of a high frequency of polyploid cells in *L. latifolius* × *L. heterophyllus hybrid* (WP × het2) is a reflection of numerical chromosomal instability that has also been reported for several Lathyrus species and hybrids [7, 8, 9].

Selection in segregating populations is a very important step in plant breeding. Time taken to obtain a fixed line with desired (e.g. flowering) traits is often a very critical factor in slowing down the genetic gains in breeding programs [13]. It is a complex process regulated by a combination of genetic and environmental factors like light, pH, carbohydrates and plant growth regulators (PGRs) used in the culture medium [8, 14, 16, 17]. *In vitro* flowering has been reported in many species like *Pisum sativum* [8], *Oscimum basilicum* [18], *Phoenix dactylifera* [19] and roses [20] etc. All previous studies show distinct visible gaps in current under-

standing of flowering mechanisms [22, 26, 27]. The breeders are continuously in search of new methods that could accelerate the process of conversion of vegetative to generative growth and induce precocious flowering.

However, grass pea use in food is very limited due to presence of antinutritional components ß-N-Oxalyl-L- α, ß-diaminopropionic acid (ODAP) that is responsible for neuro-lathyrism of lower limbs in humans and animals [4,]. A potential β-ODAP (β-*N*-oxalyl-l-α, β-diaminopropionic acid) free genotype has been identified in *L. tingitanus*, that can be used to develop toxin-free grass pea varieties [7] by backcross. However, such transfer through traditional crossing is restricted among readily crossable species like *L. cicera* and *L. amphicarpus* [12]. It is very difficult to understand flowering behavior of plants under natural conditions that has major effect on plant yield, productivity [21, 22] and breeding activities. Biotechnological approaches could prove an excellent tool to transfer genes from secondary and tertiary gene pools. Therefore, development of genetic resources is of paramount importance for grass pea breeding [4, 5, 9]. Tissue culture techniques have potential to significantly shorten growth cycle and establish cultures that can be used in breeding [8, 13, 14] and genetic transformation studies [15]. Establishing a reliable *in vitro* protocol to induce precocious or adjusted time flowering in grass pea could be an excellent and convenient tool to switch vegetative growth to reproductive growth and flowering for utilization in breeding programs.

There is no report showing genetic information regulating transition from vegetative to flowering stage in most of the plants including grass pea [25]. There are a few reports on in vitro regeneration of shoots and roots in grass pea [12, 23, 24], and any study relating to induction of flowering under *in vitro* conditions has not been reported yet. Therefore, the present study aimed to design a morpho physiological approach for mid to late flowering grass pea cv. Gurbuz to improve *in vitro* shoot regeneration from nodal junctions as explants and induce early flowering along with carrying out ODAP analysis under controlled photoperiod conditions as a first step towards this direction.

MATERIALS AND METHODS

Seed sterilization. The seeds of grass pea cv. Gurbuz were obtained from the Department of Field Crops, Ankara University, Ankara, Turkey. They were washed in running tap water followed by surface sterilization using 30% H_2O_2 and three drops of Tween-20 for 20 min. This was followed by 3 × 5 min rinsing with sterile distilled water and blotting onto sterilized tissue papers. The sterilized seeds were germinated on paper bridges over sterilized water culture in glass test tubes. The nodal junction (about 0.5 cm portion of internode on both sides) explants were excised aseptically (Fig 1a) from 5 - 6 cm long one week old *in vitro* grown plantlets and cultured on respective treatments of MS regeneration medium.

All culture medium treatments were autoclaved for 20 min at 1.4 kg cm^{-2}, after adjusting their pH to 5.6 - 5.8 with 1N NaOH or 1N HCl. All cultures were grown at 25 ± 2°C with a 16/8-h (light/dark) photoperiod. The light was supplied at photosynthetic photon flux density of 25 µmol m^{-2} s^{-1} using cool-white fluorescent lamps (54 w - T 5 Philips).

Multiple shoots induction and *in vitro* flowering. The nodal junctions were used as explants for organogenesis using MS medium [28] manipulated with 5 concentrations of BAP (0.1, 0.25, 0.50, 1 and 2 mg L^{-1}) + 2 concentrations of NAA (1 and 2 mg L^{-1}) making a total of 10 combinations supplemented with 3% (w/v) sucrose and solidified with 0.3% (w/v) gelrite for shoot multiplication and replicated thrice. The observations were recorded on the shoot induction (%), number of shoots/ explants, shoot length (cm) and callus induction (%) at the end of three weeks.

The multiplied (3 - 4 cm long) shoots were elongated on MS medium containing 0.1-0.50 mg L-1 BAP for three weeks. The observations were recorded for mean shoots length (cm), flowering percentage (%), and number of flowers per shoot at the end of two weeks to induce in vitro flowering and shoot elongation.

Rooting and acclimatization. Elongated (6 - 7 cm long) shoots were used for the rooting on ½ × MS medium manipulated with 0.10, 0.25 and 0.50 mg L^{-1} IBA. All rooting treatments contained 24 elongated shoots divided equally into 8 shoots per replication and each treatment was replicated thrice. Additionally, the shoots were also planted on half strength MS medium as control treatment. The data on root induction (%), number of roots and roots length were recorded after three weeks of culture inoculation.

Healthy (150) plantlets with well-developed roots and generative shoots were selected for acclimatization. They were removed from the root induction medium, washed in running tap water to remove sticking gelrite to the roots followed by transfer to 12 cm diameter plastic pots containing 0.62 liter of either peat moss or peat moss + clay soil (2:1) ratio. Each pot was covered with a transparent polyethylene bag to create a high relative humidity; afterwards, the transparent polyethylene bags were carefully and gradually opened. The acclimatized plants were maintained under ambient daylight conditions at 21±2°C in the laboratory greenhouse.

Determination of ODAP during *in vitro* explants growth. The plant samples were collected on germination (1st week), vegetative stage (3rd weeks), flowering stage (5th weeks), podding stage (8th weeks) and maturity stage (11th weeks) of culture explants. The ODAP analysis during *in vitro* plant growth may be helpful to understand the biosynthesis pattern of ODAP in grass pea. All the plant parts excluding matured seeds were dried at 40 °C for 72 hours and carefully mixed to give reasonable representative samples for grinding. Concentration of β-ODAP in the plant parts and the seeds were measured spectrophotometrically using o-phtalaldehyde method by Rao [29] as modified by Briggs et al. [30]. The modification involved the two times extraction of 0.5 g of the flour with 60% ethanol followed by hydrolysis of the flour with 3M KOH in boiling water bath for 30 min. After centrifugation for 15 minutes, an aliquot (250 µl) of the hydrolysate was diluted with 750 µl water and reacted with 2 ml o-phtalaldehyde reagent. The mixture was incubated at 40°C for 2 hours before measuring the absorbance at 425 nm. The β-ODAP standard curve was calibrated using DAP-HCl (Sigma).

Statistical analysis. The data were subjected to one-way analysis of variance (ANOVA, IBM® SPSS® statistics 24.0 for Windows), and the post hoc tests were performed using either Tukey's b or Least Significant Difference (LSD) test. The treatments were arranged in a completely randomized design. The data given in percentages were subjected to arcsine (√X) transformation [31] before carrying out statistical analyses.

RESULTS

Multiple shoots induction. The seeds showed germination under in *vitro* conditions after two days of culture on paper bridges water culture. The seedlings showed elongation to 5 - 6 cm and development of 4-5 nodes in one-week time. These, nodal junction explants showed significantly different behavior on MS medium containing 10 different BAP+NAA combinations to induce multiple shoots in terms of frequency (%) of shoot induction (F=23.78; df =9, 20; $p \leq 0.001$), number of shoots per explant (F=313.08; $p \leq 0.001$), shoot length (F=40.757; $p \leq 0.001$) and callus (F=22.05 $p \leq 0.001$) induction. Shoot regeneration was achieved on all treatments (Table 1). It was observed that the increasing BAP concentrations combination with either 1 or 2 mg/L NAA induced increased shoot elongation.

The results showed no or poor shoot induction and profuse rooting on MS medium containing 0.1 mg L^{-1} BAP plus 1 or 2 mg L^{-1} NAA (Fig 1b). Callus induction was noted on eight and shoot induction was noted on all (ten) BAP-NAA treatments (Fig 1c). The most of explants increased in length, when sub-cultured after three weeks' interval. The maximum number of 15.43 ± 0.02 shoots per explant were also the longest shoots (4.63± 0.93 cm) that were induced on MS medium containing 2 mg L^{-1} BAP - 1 mg L^{-1} NAA (Table 1 and Fig 1d). The results showed that BAP-NAA combinations in the MS medium affected shoot length as well as number of shoots. Reduced number of shoots and shoot length were noted on explants that induced callus as they had shorter nodes that affected the cumulative length of the shoots.

***In vitro* flowering.** The shoots induced on MS medium containing (2 mg L^{-1} BAP - 1 mg L^{-1} NAA) were subcultured to MS medium containing 0.10 - 0.50 mg L^{-1} BAP for in vitro flowering and elongation (Table 2). This induced morphogenetic differentiation from vegetative to regenerative phase after two weeks of culture and induced flowering. The ANOVA results confirmed significant differences in flowering percent (F=36.18; df =2, 6; $p \leq 0.001$) and number of flowers per plantlet (F=14.77; $p \leq 0.01$).

These shoots had flowering percentage of 39.23 - 90.12 %. Maximum flowering percentage (90.12%) and shoots length (7.88 cm) was obtained on MS medium containing 3% sucrose and 0.25 mg L-1 BAP. No generative phase (flowering) was noted on MS medium (control treatment). The multiplied shoots induced 0.33 - 4.30 flowers per shoot before transferring them to rooting medium (Table 2 and Fig 1e, 1f).

Rooting and acclimatization. The maximum flowering shoots (6-7 cm long) recovered on MS medium containing 0.25 mg L^{-1} BAP were transferred to ½ × MS medium containing 0.10 -0.50 mg L^{-1} IBA for rooting. Root initiation was observed on the shoots 15-16 d after transfer to rooting medium. *In vitro* regenerated flowering plants induced multiple roots at the lower part of the plant. The results showed that rooting percentage and mean root length decreased drastically with increasing concentration of IBA. The rooting percentage and mean number of roots/explant and root length were ranged 14.12 - 83.43 %, 2.96 - 7.33 and 1.66 - 5.63 cm respectively (Table 3). Maximum and longest rooting were induced on 0.1 mg L^{-1} IBA. This flowering or generative stimulus continue flowering during rooting and acclimatization in the greenhouse. Fastest achievement of 100% flowering in two weeks' time was noted on 0.25 mg L^{-1} BAP induced plantlets. While, the plantlets induced on other treatments achieved 100% flowering in 4 - 5 weeks' time in the greenhouse (data not shown). No visible differences were recorded in morphology of flowers obtained on *in vitro* regenerated plants and the plants obtained from seeds. Other combinations

of BAP had negative effect to induce generative shoots with inflorescence.

As explained in materials and methods 150 plantlets transferred to 0.62 liters plastic pots containing peat moss or peat moss-clay soil (2:1) for acclimatization. The peat moss showed development of strong root system and had 0.1 to 0.15 cm thick roots tapered to hair-like structures at growing ends and root nodes by developing filamentous roots with lateral spread. No obstacle was recorded on hardening of the plants.

TABLE 1
Shoot induction from nodal junction explant of grass pea inoculated on MS medium containing BAP (0.10 – 2.0 mg L^{-1}) and NAA (1- 2 mg L^{-1}) after three weeks of culture

MS + Treatments mg L^{-1}		Shoot induction (%)	Number of shoots/ explants	Shoot length (cm)	Callus induction (%)	Callus formation
BAP	NAA					
0.10	1.0	4.73± 0.29 e	0.33±0.03 d	0.13± 0.04d	52.36±2.84 a b	+
0.10	2.0	9.56 ±1.79e	0.33 ±0.01d	0.10 ±0.00d	49.96±3.27 a b	+
0.25	1.0	40.73± 1.15c d	1.30 ±0.07d	0.46 ±0.03c d	37.16± 2.92b c	+
0.25	2.0	20.53±1.06 c d e	1.00± 0.05d	0.53 ±0.08c d	24.00± 2.25c d	+
0.50	1.0	14.23± d e	0.66 ±0.05d	0.43 ±0.03c d	74.40±3.92 a	+
0.50	2.0	46.43 ±1.39b c	1.56 ±0.31d	1.20± 0.05c	31.66± 1.91b c	+
1.0	1.0	71.00± 1.23a b	7.46± 0.16c	2.50± 0.09b	40.60± 2.95b c	+
1.0	2.0	70.86 ±1.59a b	11.96± 0.43b	2.33± 0.80b	0.00±0.00	-
2.0	1.0	87.90 ±1.31a	15.43 ±0.02a	4.63± 0.93a	0.00±0.00	-
2.0	2.0	83.30 ±1.92a	3.60± 0.09d	2.30± 0.06b	66.36± 1.54a	++
MS medium (control)		14.23±1.59de	1.00±0.07d	0.15±0.01d	0.00±0.00	-

Values with in a column followed by different letters are significantly different ($p<0.01$) using Tukey's b test.
*Callus formation: -, Nil: +, Low; ++ Moderate
± Standard error

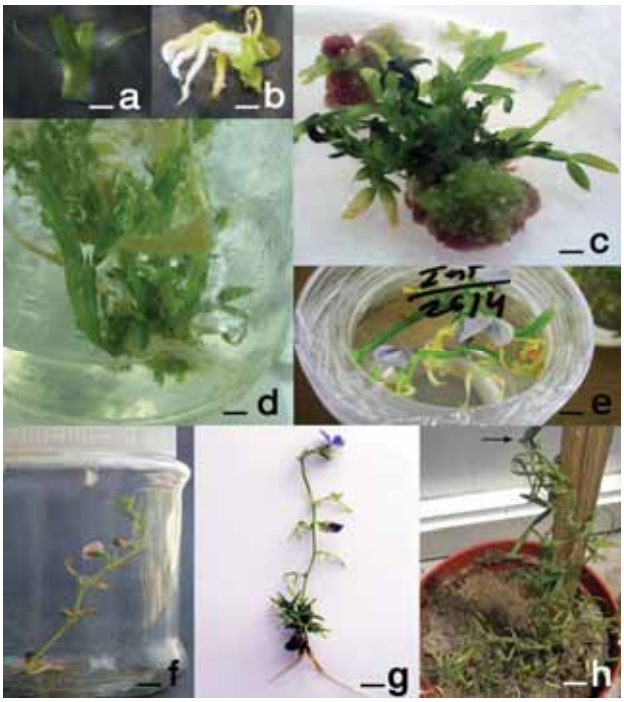

FIGURE 1
Multiple shoots induction and *in vitro* flowering of *L. sativus* cv. Gurbuz:
(a) nodal junction bearing about 0.5 cm portion of internodes on both sides as explants, (b) poor shoot induction and profuse rooting on MS medium containing 0.1 mg L^{-1} BAP and 2 mg L^{-1} NAA, (c) callus induction and shoot induction from nodal junction on MS medium supplemented with 1.0 mg L^{-1} BAP and 1.0 mg L^{-1} NAA after 3 weeks of culture, (d) maximum number and longest shoots per explants were induced on MS medium containing 2.00 mg L^{-1} BAP - 1 mg L^{-1} NAA, (e, f) maximum flowering response on MS medium containing 3% sucrose and 0.25 mg L^{-1} BAP after two weeks of culture, (g) rooting using ½ strength MS medium containing 0.1 mg L^{-1} IBA, (h) plant bearing mature pods containing seeds after acclimatization under greenhouse conditions. Bar of Figure 1a, b, c =0.4 cm, Figure 1d, e, f = 0.3 cm, Figure 1g = 2 cm, 1h = 5 cm.

TABLE 2
***In vitro* flowering response of nodal junction explants of grass pea on MS medium containing different concentrations of BAP after two weeks of subculture**

BAP treatments (mg L^{-1})	Flowering percentage (%)	Mean shoots length (cm)	Number of flowers per shoot
0.10	39.23 ±1.15c	5.08± 1.58c	0.33± 0.21b
0.25	90.12 ±3.47a	7.88 ±0.56a	4.30± 0.32a
0.50	62.50± 2.91b	6.86± 1.62ab	0.66 ±0.27b
MS_0 (control)	0.00±0.00	4.00±0.03	0.00±0.00

Values with in a column followed by different letters are significantly different ($p < 0.05$) using LSD test.

TABLE 3
Root induction response of nodal junction explants of *L. sativus* L. on ½ strength MS medium containing different concentrations of IBA

IBA treatment (mg L^{-1})	Root induction (%)	Mean number of roots / explants	Root length (cm)
½ MS medium* (Control)	0.00	0.00	0.00
0.10	83.43± 2.92a	7.33± 0.62a	5.63± 1.46a
0.25	63.30±2.31 b	4.36± 0.33b	3.16± 1.26b
0.50	14.12± 1.09c	2.96± 0.84c	1.66± 0.08c

Values with in a column followed by different letters are significantly different ($p < 0.05$) using LSD test.
* ½ strength of macro, micro elements and vitamins of MS medium

TABLE 4
ODAP analysis of various growth stage of *in vitro* regenerated plant of grass pea

Plant growth stage	Germination (1st week)	Vegetative (3rd week)	Flowering (5th week)	Podding (8th weeks)	Maturity (11th weeks)	Matured Seed
ODAP %± SE	1.48 ± 0.06	0.97 ± 0.05	1.10 ± 0.08	0.84 ± 0.03	0.43± 0.05	0.21 ± 0.03

Plant survival percentage remained 73% on peat moss + clay (2:1) and 89% on peat moss after three weeks of hardening. All the mature regenerated plants induced 4 - 5 pods per plant that developed into normal seeds. All developing pods contained 2 - 3 seeds that were morphologically viable (tetrazolium test) and similar to the seeds obtained from the field grown plants.

ODAP analysis during *in vitro* vegetative, reproductive and maturity stage. During the in vitro explant growth, ODAP concentration changes variably at different plant developmental stages with maximum accumulation ODAP concentration were recorded during early germination stage. The ODAP analysis of *in vitro* regenerated seedlings may helpful to understand the role of micro- and macronutrient content on biosynthetic and how to different environmental and growing conditions affect β-ODAP accumulation in grass pea. The minimum and maximum ODAP content were found in plants at maturity and seed germination stages that ranged 0.21% to 1.48% respectively.

The early developmental (germination) stage showed maximum ODAP accumulation that drastically reduced during vegetative (3rd week) growth that increased again at flowering stage. It may be reasoned that transition from vegetative to generative phase including flowering stage and early developmental stage results in increased accumulation of ODAP. The podding and early maturing stage showed decreasing of ODAP content after flowering (Table 4). The seeds set under *in-vitro* and *ex-vitro* conditions did not show significant difference in ODAP content.

DISCUSSION

Plant regeneration from seeds is very tedious in legumes and grass pea is no exception [32, 33]. Biotechnology tools can facilitate possibility of inducing early generative phase in cultured plants that may help in accelerating breeding by shortening their life cycle [8, 16].

The present study provides a reliable and significantly improved *in vitro* regeneration and accelerated flowering protocol in grass pea compared to previous reports [23, 34]. The present study reports a significant improvement over the results of Barik et al. [23] and Barpete et al. [35]. Barik et al. [23] achieved maximum number of 8.2 shoots per explant with root length of 4.1 cm. whereas; Barpete et al. [35] noted maximum number of 8 shoots per explant with 4 cm long shoots. A comparison of three regeneration studies shows genotype, age and type of explant significantly affects regeneration capacity.

The most important observation in the present experiment pertains to accelerated flowering, never reported or observed earlier in grass pea as the multiplied roots were matured or transformed to generative phase before rooting. The present experimental arrangement helped in accelerated transfor-

mation of *in vitro* regenerated plantlets from vegetative to generative stage bearing fertile floral buds and flowers. Although, Gharyal and Maheshwari [36] reported flower bud formation that could not flowered in control condition in grass pea.

This study reports flowering of grass pea after seven weeks of culture (16-h light photoperiod) under *in vitro* conditions. All flowers matured and set healthy fertile seeds in pods under in vitro conditions. It is assumed that 16 h light photoperiod and regeneration on BAP containing medium stimulated early transition from vegetative to generative growth in line with Heylen and Vendrig [16]. Ammar et al. [19] and Wang et al. [20]; emphasize that *in vitro* floral induction is influenced by thidiazuron (TDZ) or combination of zeatin and NAA. However, auxin is either ineffective [39] or inhibitory [40] for floral development in some species.

The important role of auxin in flower induction and development has been reported in green pea [37] and *Vigna mungo* [38]. Contrarily, this study reports multiplication of shoots followed by their elongation on a medium containing low concentration (0.25 mg L^{-1}) of BAP to make it effective for floral induction. These results are in agreement with Fujioka et al. [41] and Nagdauda et al. [42], who reported *in vitro* flowering in pea and bamboo under the influence of cytokinins. Similarly, Kostenyuk et al. [43] also suggested beneficial effects of cytokinin (2.5 mg L^{-1} TDZ) on the induction of *in vitro* flowering in orchids. Cytokinins induce precocious flowering signals in *Cymbidium niveo* and tobacco as well [44, 45]. First flower induction was noted after one week of transferring the multiplied shoots to medium leading to the development of four to five flowers per plantlet on growing shoots that continued to blossom during rooting and acclimatization under greenhouse conditions. No floral induction was noted on shoots cultured on MS medium without PGR/s. It is assumed that BAP evoked floral induction by early transition from vegetative to generative stage that affected early mitotic activity regulation leading precocious initiation of generative growth [18, 46]. However, grass pea is a long-day plant and flowering is achieved only after 120 - 142 days (17 - 20.9 weeks) on sowing in open fields under conditions reported by Kumar et al. [4]. This is an important development in grass pea and could be used as an excellent tool to accelerate breeding and hybridization by accelerated selection in segregating populations of hybrids and pure lines without dependence on geographical factors or season [8].

Precocious floral induction is meaningless if the shoots cannot be rooted and acclimatized under external conditions. The present study showed distinct effectiveness of ½ × MS basal medium containing 0.10 mg L^{-1} IBA for inducing maximum rooting (83.43± 2.92%), mean number of roots per explants and root length post flowering that the elongated shoots could be rooted without any obstacle on ½ × MS medium containing IBA. Ochatt et al. [14] and Barpete et al. [47] also induced rooting on in vitro multiplied shoots on MS medium containing IBA. Comparing studies by Barik et al. [23] and Barpete et al. [35] with this study, the results emphasize use of low concentration of IBA (0.10 mg L^{-1}) for improved precocious rhizogenesis, number of roots per explant and root length. Barik et al. [23] and Barpete et al. [35] reported 75% and 78% root induction using 0.25 mg L^{-1} IBA or 2.85µM indole-3-acetic acid respectively. The results are not in agreement with Barik et al. [23] in days to achieve rooting; who reported 30 days to root micropropagated plants. Present study reports 7.33 roots per explant with 5.63cm long roots regenerated and matured shoots in 35 days of culture. Barik et al. [23] achieved maximum number of 3.6 roots per explant with root length of 3.9 cm.

Another important aspect of *in vitro* flowering reported in this study is survival of flowering plants outside culture vessels in pots during hardening and acclimatization in the greenhouse. Major problem in most *in vitro* derived plants is a desiccation shock experienced just after transplantation [34, 48]. This is fatal during the initial days of establishment. No negative effects of desiccation shock were observed on the transplanted material in the present study, and most of the transplanted plant recovered in a short time under the greenhouse conditions. Most obvious reason could be the maturing of in vitro regenerated shoots before rooting.

The *in vitro* regenerated grass pea seedling showed ODAP concentration changed during plant growth (Table 4) and maximum ODAP accumulation were recorded in early developmental stage in line with Jiao et al. [49]. They emphasized that accumulation of β-ODAP is higher in young grass pea seedlings probably related to changes in nitrogen metabolism. Similarly, previous studies indicated that β-ODAP content is present in all parts of the plant with the highest amount reported in the leaf and embryo at vegetative and reproductive stages [49, 50, 51, 52]. Moreover, Jiao et al. [49] emphasized that nitrogen supply plays a major role in increasing β-ODAP contents in grass pea.

CONCLUSIONS

This paper presents a simple and reliable morpho physiological approach to achieve an *in vitro* system for increasing number of grass pea generations in a reduced time [(i) one week to obtain explant from germinated seedlings, (ii) three weeks for regeneration, (iii) two weeks for elongation shoots and induction of early flowering, (iv) three weeks for rooting and (v) three weeks for hardening, acclimatization and blooming confirms] of 4.33

generations of grass pea per annum with mid to late flowering genotypes. The morpho physiological observations reported here are novel and this protocol. Grass pea genotypes are usually released after 6 - 8 generations of self-pollination to achieve an appropriate level of homozygosity. Decreasing the length from F_1 to F_7 generation will overcome this breeding bottleneck and accelerate possibility of genetic improvement of grass pea with accelerated selection.

ACKNOWLEDGEMENTS

The researchers are thankful to the International Center for Agricultural research in the Dry Areas (ICARDA), Rabat, Morocco and Ankara University, Ankara, Turkey; for helping and supporting in the research work.

The authors declare that they have no conflicts of interest and contributed equally towards development of the paper.

Surendra Barpete, Priyanka Gupta, Khalid Mahmood Khawar, Sebahattin Özcan, and Shiv Kumar discussed, planned and carried out experiments collectively. SB, PG and KMK made substantial contributions to conception and design, acquisition of data, analysis and interpretation of data. SO and SK have been involved in drafting the manuscript or revising it critically for important intellectual content. All authors read and approved the final manuscript to be published.

REFERENCES

[1] Sarwar, A., Sarkar, A.N., Murshed, M.M. and Malik, M.A. (1993) Variation in natural population of grass pea, in *Lathyrus sativus* and Human Lathyrism: Progress and Prospects. In: Yusuf, H.K.M., Lambein, F. (eds.) Proc. 2nd Int Colloq Lathyrus/ Lathyrism, Dhaka, 10-12 December 1993. University of Dhaka, 161-164.

[2] Haqqani, A.M. and Arshad, M. (1995) Crop status and genetic diversity of grass pea in Pakistan. Lathyrus Genetic Resources in Asia. In: Arora, R.K., Mathur, P.N., Riley, K.W., Adham, Y. (eds.) Proceedings of a Regional Workshop. Indira Gandhi Agricultural University. Raipur, India 27-29 December, 59-65.

[3] Abate, A., Mekbib, F., Fikre, A. and Ahmed, S. (2018) Genetic Variability and Heritability in Ethiopian Grass pea (*Lathyrus sativus* L.) Accessions. Ethiop. J. Crop Sci. 6, 79-94.

[4] Kumar, S., Gupta, P., Barpete, S., Sarker, A., Amri, A., Mathur, P.N. and Baum, M. (2013) Grass pea. In: Singh, M., Upadhyaya, H. D., Bisht, I.S. (eds.) Genetic and Genomic Resources for Grass pea Improvement. 269-293.

[5] Kumar, S., Bejiga, G., Ahmed, S., Nakkoul, H. and Sarker, A. (2011) Genetic improvement of grass pea for low neurotoxin (ODAP) content. Food Chem Toxicol. 49, 589-600.

[6] Rahman, M.M., Kumar, J., Rahaman, M.A. and Afzal, M.A. (1995) Natural outcrossing in *Lathyrus sativus* L. Ind J Genet. 55, 204-207.

[7] Zhou, M. and Arora, A.K. (1996) Conservation and use of underutilized crops in Asia. In: Arora, R.K., Mathur, P.N., Riley, K.W., Adham, Y. (eds.) Lathyrus genetic resources in Asia. International Plant Genetic Resources Institute, Rome, Italy, 91-96.

[8] Ribalta, F.M., Croser, J.S., Erskine, W., Finnegan, P.M., Lulsdorf, M.M. and Ochatt, S.J. (2014) Antigibberellin-induced reduction of internode length favors *in vitro* flowering and seed-set in different pea genotypes. Biol Plant. 58, 39-46.

[9] Barpete S. (2015) Genetic associations, variability and diversity in biochemical and morphological seed characters in Indian grass pea (*Lathyrus sativus* L.) accessions. Fresen. Environ. Bull. 24, 492-497.

[10] Sarker, A., Fikre, A., El-Moneim, A.M.A., Nakkoul, H. and Singh, M. (2018) Reducing anti-nutritional factor and enhancing yield with advancing time of planting and zinc application in grass pea in Ethiopia. J Sci Food Agric. 98, 27-32.

[11] Jackson, M.T. and Yunus, A.G. (1984) Variation in the grass pea (*L. sativus* L.) and wild species. Euphytica. 33, 549–559.

[12] Ochatt, S.J., Ochatt, P.E.M. and Moessner, A. (2011) Ploidy level determination within the context of in vitro breeding. Plant Cell Tiss Organ Cult. 104, 329–341.

[13] Zheng, Z., Wang, H.B., Chen, G.D., Yan, G.J. and Liu, C.J. (2013) A procedure allowing up to eight generations of wheat and nine generations of barley per annum. Euphytica. 191, 311-316.

[14] Ochatt, S.J., Sangwan, R.S., Marget, P., Assoumou, N.Y., Rancillac, M. and Perney, P. (2002) New approaches towards the shortening of generation cycles for faster breeding of protein legumes. Plant Breeding. 121, 436-440.

[15] Barik, D.P., Mohapatra, U. and Chand, P.K. (2005a) Transgenic grass pea (*Lathyrus sativus* L.): Factors influencing *Agrobacterium-mediated* transformation and regeneration. Plant Cell Rep. 24, 523–531.

[16] Heylen, C. and Vendrig, J.C. (1988) The influence of different cytokinins and auxins on flower neoformation in thin cell layers of *Nicotiana tabacum* L. Plant Cell Physiol. 29, 665–671.

[17] Piwowarczyk, A., Pindel, E. and Muszyńska, E. (2016) Callus induction and rhizogenesis in *Lathyrus sativus* L./ Acta Universitatis. Agriculturae et Silviculturae Mendelianae Brunensis. 64, 123-128.
[18] Sudhakaran, S. and Sivasankari, V. (2002) *In vitro* flowering response of *Oscimum basilicum* L. J Plant Biotechnol. 4, 181-183.
[19] Ammar, S., Benbadis, A. and Tripathi, B.K. (1987) Floral induction in date palm seedlings (*Phoenix dactylifera* var. Deglet Nour) cultured *in vitro*. Can J Bot. 65, 137-142.
[20] Wang, G.Y., Yuan, M.F. and Hong, Y. (2002) *In vitro* flower induction in roses, *in vitro* cellular and developmental biology. Plant. 38, 513-518.
[21] Jung, C. and Muller, A.E. (2009) Flowering time control and applications in plant breeding. Trends Plant Sci. 14, 563–573.
[22] Putterill, J., Zhang, L., Yeoh, C.C., Balcerowicz, M., Jaudal, M. and Gasic, E.V. (2013) FT genes and regulation of flowering in the legume *Medicago truncatula.* Functional Plant Biol. 40, 1999-1207.
[23] Barik, D.P., Mohapatra, U. and Chand, P.K. (2005b) High frequency *in-vitro* regeneration of *Lathyrus sativus* L. Biol Plant. 49, 637-639.
[24] Barpete, S., Aasim, M., Ozcan, S.F., Khawar, K.M. and Ozcan, S. (2017) High Frequency Axillary Shoots Induction in Grass Pea (*Lathyrus sativus* L.). Bang J Bot. 46, 119-124.
[25] Srikanth, A. and Schmid, M. (2011) Regulation of flowering time: all roads lead to Rome. Cell Mol Life Sci. 68, 2013–2037.
[26] Andres, F. and Coupland, G. (2012) The genetic basis of flowering responses to seasonal cues. Nat Rev Genet 13, 627–639.
[27] Wong, A.C.S., Hecht, V.F.G., Picard, K., Diwadkar, P., Laurie, R.E., Wen, J., Mysore, K., Macknight, R.C., Weller, J.L. (2014) Isolation and functional analysis of CONSTANS-LIKE genes suggests that a central role for CONSTANS in flowering time control is not evolutionarily conserved in *Medicago truncatula.* Front Plant Sci. 5, 486.
[28] Murashige, T. and Skoog, F. (1962) A revised medium for rapid growth and bioassay with tobacco tissue cultures. Physiol Plant. 15, 473-497.
[29] Rao S.L.N. (1978) A sensitive and specific colorimetric method for the determination of α, β-diaminopropionic acid and the *Lathyrus sativus* neurotoxin. Anal. Biochem. 86, 386-395.
[30] Briggs, C.J., Parreno, N. and Campbell, C.G. (1983) Phytochemical assessment of Lathyrus species for the neurotoxic agent, β-N-oxalyl-L-α, β-diaminopropionic acid. Planta Medica. 47, 188-190.
[31] Snedecor, G.W. and Cochran, W.G. (1967) Statistical Methods. The Iowa State University Press, Iowa, USA, 327-329.
[32] Vaz Patto, M.C., Hanbudry, H.D., Van Moorhem, M., Lambein, F., Ochatt, S. and Rubiales, D. (2011) Grass pea. In: Vega de la, M.P., Torres, A.M., Cubero, J.I., Kole, C. (eds) Genetics, genomics and breeding of cool season grain legumes. Science, Lebanon, 151-204.
[33] Ochatt, S.J., Conreux, C. and Jacas, L. (2013) Flow cytometry distinction between species and between landraces within Lathyrus species and assessment of true-to-typeness of *in vitro* regenerants. Plant Syst Evol. 299, 75-85.
[34] Barpete, S., Aasim, M., Khawar, K.M., Özcan, S.F. and Özcan, S. (2014a) Preconditioning effect of cytokinins on *in vitro* multiplication of embryonic node of grass pea (*Lathyrus sativus* L). Turk J Biol. 38, 485-492.
[35] Barpete, S., Sharma, N.C., Parmar, D. and Dhingra, M. (2008) *In-vitro* regeneration of *Lathyrus sativus* L. Nat J Life Sci. 05, 207-210.
[36] Gharyal, P.K. and Maheshwari, S.C. (1983) Genetic and physiological influences on differentiation in tissue cultures of a legume, Lathyrus sativus. Theor. Appl. Genet. 66, 123-126.
[37] Franklin, G., Pius, P.K. and Ignacimuthu, S. (2000) Factors affecting *in vitro* flowering and fruiting of green pea (*Pisum sativum L*). Euphytica 115, 65-74.
[38] Ignacimuthu, S., Franklin, G. and Melchias, G. (1997) Multiple shoot formation and *in vitro* fruiting of *Vigna mungo* (L.) Hepper. Curr Sci. 73, 733–735.
[39] Rastogi, R. and Sawhney, V.K. (1987) The role of plant growth regulators, sucrose and pH in the development of floral buds of tomato (*Lycopersicon esculentum* Mill) cultured *in vitro*. J Plant Physiol. 128, 285-295.
[40] Deaton, M.H., Buxton, J. and Hamilton-Kemp, T.R. (1984) The effects of growth regulators on development of *Nicotiana affinis* flowers *in vitro*. Hort Sci. 19, 509-511.
[41] Fujioka, T., Fujita, M., Miyamoto, Y. (1999) *In vitro* flowering and pod setting of non-symbiotically germinated pea. J Jap Soc Hort Sci. 68, 117–123.
[42] Nagdauda, R.S. and Parasharami, V.A., Mascarenhas A.F. (1990) Precocious flowering and seeding behaviour in tissue-cultured bamboos. Nature 344, 335-336.
[43] Kostenyuk, I., Oh, B.J. and So, L.S. (1999) Induction of early flowering in *Cymbidium niveo marginatum* Mak *in vitro.* Plant Cell Rep. 19, 1-5.
[44] Peeters, A.J.M., Gerards, G., Barendse, G.W.M. and Wullems, G.J. (1991) *In vitro* flower bud formation in tobacco: interaction of hormones. Plant Physiol. 97, 402-408.

[45] Bonhomme, F., Kurz, B., Melzer, S., Bernier, G. and Jacqmard, A. (2000) Cytokinin and gibberellin activate *SaMADSA*, a gene apparently involved in regulation of the floral transition in *Sinapis alba*. Plant J. 24, 103-111.
[46] Kiełkowska, A. (2013) Sex expression in monoecious cucumbers micropropagated *in vitro*. Biol Plant. 57, 725-731.
[47] Barpete, S., Khawar, K.M. and Özcan, S. (2014b) Differential competence for *in vitro* adventitious rooting of grass pea (*Lathyrus sativus* L.). Plant Cell Tiss Org Cult. 119, 39-50.
[48] Kozai, T. (1991) Micropropagation under autotrophic conditions. In: Debergh, P.C., Zimmermann, R. (eds.) Micropropagation, technology and application. Kluwer, Netherlands, 447–469.
[49] Jiao, C.J., Xu, Q.L., Wang, C.Y., Li, F.M., Li, Z.X. and Wang, Y.F. (2006) Accumulation pattern of toxin β-ODAP during lifespan and effect of nutrient elements on β-ODAP content in *Lathyrus sativus* seedlings. J Agric Sci. 144, 369- 375.
[50] Prakash, S., Mishra, B.K., Adsule, R.N. and Barat, G.K. (1977) Distribution of β-N-oxalyl-L-α, β-diaminopropionic acid in different tissues of aging *Lathyrus sativus* plants. Biochem Physiol Pflanz. 171, 369–374.
[51] Jiao, C.J., Jiang, J.L., Ke, L.M., Cheng, W., Li, F.M., Li, Z.X. and Wang, C.Y. (2011) Factors affecting β-ODAP content in *Lathyrus sativus* and their possible physiological mechanisms. Food Chem Toxicol. 49, 543–549.
[52] Xu, Q., Liu, F., Chen, P., Jez, J.M. and Krishnan, H.B. (2017) β-n-oxalyl-l-α, β-diaminopropionic acid (β -ODAP) content in *Lathyrus sativus:* The integration of nitrogen and sulfur metabolism through β -cyanoalanine synthase. Int J Mol Sci. 18, 526.

Received: **25.04.2019**
Accepted: **17.10.2019**

CORRESPONDING AUTHOR

Surendra Barpete,
Department of Field Crops,
Faculty of Agriculture,
Ankara University,
Ankara 06110 – Turkey

e-mail:surendrabarpete@gmail.com

© by PSP Volume 29 – No. 04A/2020 pages 2707-2710 Fresenius Environmental Bulletin

STUDY ON PARTIAL DISCHARGE SIGNAL DENOISING OF TRANSFORMER

Yanyan Zheng*, Yongli Zhu

North China Electric Power University, Baoding 071003, Hebei, China

ABSTRACT

Partial discharge (PD) of high voltage equipment detected by online monitoring is regarded as a key indicator of insulation status. Threshold estimation exerts an important influence on the denoising effects of PD signals after wavelet-based denoising. In order to improve the adaptive performance of wavelet-based denoising and reduce the distortion of denoised signal, an approach of hybrid particle swarm optimization (HPSO) adaptive wavelet threshold estimation (HPSOTE) is presented in this paper. The effect of four different factors on noise rejection ratio (NRR) is studied. The results show that this HPSOTE can remove the noise effectively and has comparatively high application value in PD online monitoring for smart grid based on big data.

KEYWORDS:
Partial discharge, Online monitoring, Wavelet-based denoising, Transformer

INTRODUCTION

PD is bound up with the insulation aging of electric power equipment [1]. On-line monitoring of PD is an important means of evaluating power equipment insulation status to find the latent failure [2-4]. Actual PD signal obtained in monitoring process is very weak, so it is necessary to improve the detection sensitivity and signal-to-noise ratio (SNR) with some special hardware and software. Kalman filter, chaotic oscillator, matching pursuit, spatially selective correlative filtration [5-7] and wavelet analysis [8-10] are now used for denoising. With advantages of easy operation and obvious denoising effect, wavelet analysis is popular in the field of PD on-line monitoring.

Wavelet-based denoising mainly includes modulus maximum method [11], correlation wavelet coefficient method [12-15], and thresholding method [16]. Among them, thresholding method is simple and fast with good adaptability. The main idea of thresholding method is the ability of concentration which concentrates signal energy on a few wavelet coefficients. Relatively, the wavelet coefficient of target signal is larger than the coefficient of dispersed noise whose amplitude is small. By selecting appropriate threshold, wavelet coefficients can be thresholding processed so as to remove noise and keep target signal.

An approach of HPSOTE is presented in this paper which offers a subtle blend of mutation and chaos to keep the calculation process out of local optimal solution.

MATERIALS AND METHODS

The decomposition process of a measured PD signal S through a wavelet transform allows us to separate in different coefficients most of the existing noise and the signal of interest, making it possible to mitigate or even eliminate the noise by the use of a threshold shrinkage function. The dyadic digital wavelet transform is the most frequently employed transform in data denoising techniques due to its desirable time-frequency characteristics. The practical implementation of a dyadic digital wavelet transform as an analysis filter bank is depicted in Figure 1. In the first stage, the PD signal S passes through a two-channel filter bank composed of a low-pass filter G(n), corresponding to the scale function, and a high-pass filter H(n), corresponding to the wavelet function, followed by factor-of-two decimators (down-samplers). The outputs of the first stage are two signals whose lengths are equal to half of that of the input signal. These two signals are denoted as approximation a1 and detail d1 coefficients, respectively. In the next stage the coefficients a1 are applied to the low-pass and high-pass filters followed by decimators, to generate the new approximation a2 and detail d2 coefficients. The decomposition process is repeated until the final approximation aJ and detail dJ coefficients are obtained. The filter bank composed by the low-pass and high-pass filters, which are also referred to as quadrature mirror filters (QMF), are designed such that it is possible to obtain a perfect reconstruction of the original signal by applying the inverse digital wavelet transform (IDWT), which can be implemented by a synthesis filter bank with factor of two interpolators (up-samplers) at each level.

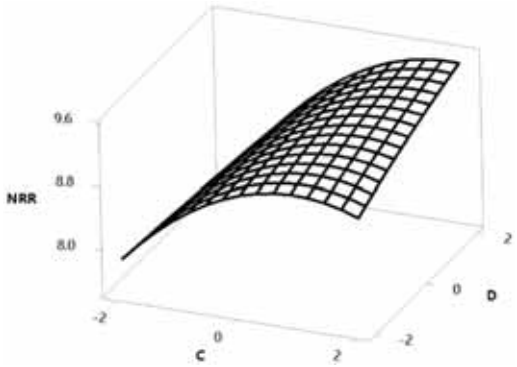

FIGURE 1
Surface Plot of NRR vs D, C

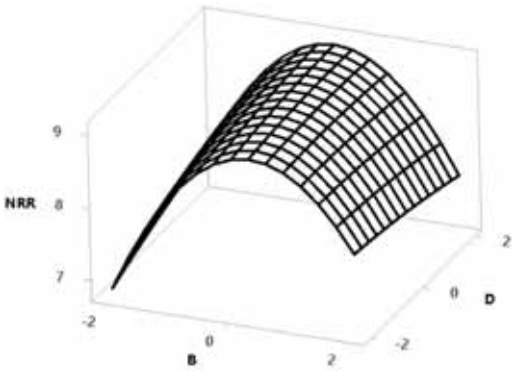

FIGURE 2
Surface Plot of NRR vs D, B

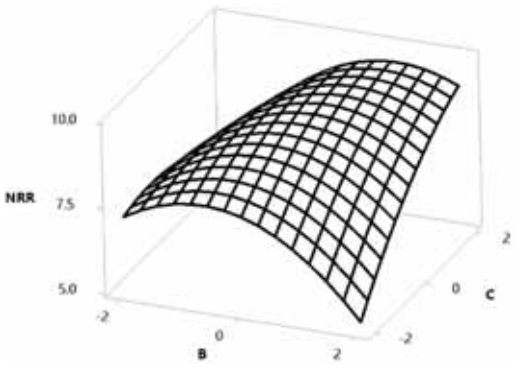

FIGURE 3
Surface Plot of NRR vs C, B

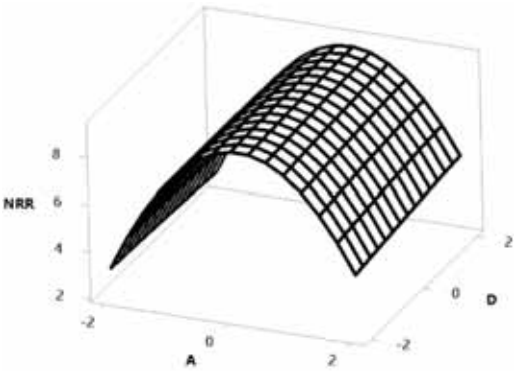

FIGURE 4
Surface Plot of NRR vs D, A

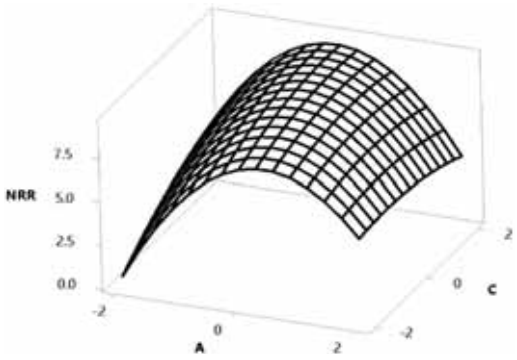

FIGURE 5
Surface Plot of NRR vs C, A

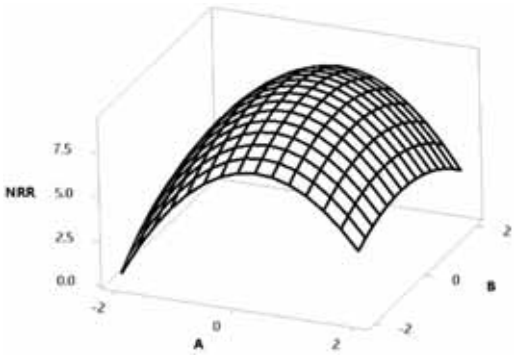

FIGURE 6
Surface Plot of NRR vs B, A

RESULTS AND DISCUSSION

PD signal of power equipment is a kind of typical non-stationary signal with finite energy. If it is denoised by the adaptive optimal threshold algorithm based on gradient-descent method, its iterative convergence may be defeated and its computation time is long. So this method is difficult to be used in practical engineering.

As shown in Figure 1 and Figure 2, PD signals of different faults show different waveform characteristics. Exponential decay model and the vibration attenuation model are now commonly used as model of PD simulated signal. On each layer, excellent result is got by HPSOTE. The higher NRR is, the stronger the denoising ability of the algorithm is.

Figure3 and 4 show ξ and ε of algorithms versus SNR. It can be seen that in most cases denoising results by adaptive threshold algorithms are much better than STE. But the denoising result of s2 by PSOTE has a big error because the calculation process fell into local extreme point and the credibility decreases.

Figure5 and Figure 6 show that some weak pulses cannot be retained by STE. Among other 3

methods based on adaptive threshold, comprehensive performance of HPSOTE is the best, because its calculation speed is faster than GTE and convergence speed is faster than PSOTE.

CONCLUSIONS

In view of the threshold selection problem in the wavelet-based denoising process, an approach of hybrid particle swarm optimization (HPSO) adaptive wavelet threshold estimation (HPSOTE) is presented in this paper. The effect of four different factors on noise rejection ratio (NRR) is studied. The results show that this HPSOTE can remove the noise effectively and has comparatively high application value in PD online monitoring for smart grid based on big data.

REFERENCES

[1] Al-Masri, W.M.F., Abdel-Hafez, M.F., El-Hag, A.H. (2016) A novel bias detection technique for partial discharge localization in oil insulation system. IEEE Trans. Instrum. Meas. 65, 448-457.

[2] Zhou, Y.X., Jin, F.B., Huang, M., Huang, J.W., Liu, Z.H., Lu, L.C. (2016) Effects of DC prestressing on partial discharge in oil-impregnated pressboard insulation. IEEE Trans. Dielectr. Elect. Insul. 23, 460-468.

[3] Stone, G.C., Stranges, M.K.W., Dunn, D.G. (2016) Common questions on partial discharge testing. IEEE Ind. Appl. Mag., 22, 14-19.

[4] Hashmi, M., Lehtonen, M., Nordman, M., Jabbar, R.A., Qureshi, S.A. (2012) Wavelet-based de-noising of on-line PD signals captured by Pearson coil in covered-conductor overhead distribution networks. Int. J. Elec. Power. 43, 1185-1192.

[5] Si, W., Qin, B., Li, Q., Liu, H. (2019) A novel adaptive wavelet threshold estimation based on hybrid particle swarm optimization for partial discharge signal denoising. Optik. 181, 175-184.

[6] Cunha, C.F.F.C., Carvalho, A.T., Petraglia, M.R. Lima, A.C.S. (2015) A new wavelet selection method for partial discharge denoising. Electric Power Systems Research. 125, 184-195.

[7] Lu, J., Zhang, X.X., Xiong, H. (2015) A New method for suppressing periodic narrowband interference based on the chaotic van der Pol oscillator. Int. J. Bifurcat. Chaos. 25, 1-13.

[8] Chen, X., Yang, Y. (2018) Analysis of the partial discharge of ultrasonic signals in large motor based on Hilbert-Huang transform. Applied Acoustics. 131, 165-173.

[9] Seo, J., Ma, H., Saha, T. (2015) Probabilistic wavelet transform for partial discharge measurement of transformer. IEEE Trans. Dielectr. Elect. Insul. 22, 1105-1117.

[10] de Oliveira Mota, H., da Rocha, L.C.D., de Moura Salles, T.C., Vasconcelos, F.H. (2011) Partial discharge signal denoising with spatially adaptive wavelet thresholding and support vector machines. Electric Power Systems Research. 81, 644-659.

[11] Wang, Z.L., Chang, J., Zhang, S.S., Luo, S., Jia, C.W., Jiang, S., Sun, B.N., Liu, Y.N., Liu, X.H., Lv, G.P. (2014) An improved denoising method in RDTS based on wavelet transform modulus maxima. IEEE Sens. J. 15, 1061-1067.

[12] Raymond, W.J.K., Illias, H.A., Bakar, A.H.A., Mokhlis, H. (2015) Partial discharge classifications: Review of recent progress. Measurement. 68, 164-181.

[13] Rostaminia, R., Saniei, M., Vakilian, M., Mortazavi, S.S. (2016) Evaluation of transformer core contribution to partial discharge electromagnetic waves propagation. International Journal of Electrical Power and Energy Systems. 83, 40-48.

[14] Zheng, W., Zhou, X.C, Xu, H.L., Zhi, Y., Wang, W.Z. (2012) Partial Discharge Signal Obtain Based on Adaptive Wavelet with Mathematical Morphology. Physics Procedia. 24, 912-917.

[15] Yang, C.H., Olson, B., Si, J.N. (2011) A multiscale correlation of wavelet coefficients approach to spike detection. Neural. Comput. 23, 215-250.

[16] Yan, J.M., Liao, R.J., Yang, L.J., Li, J., Liu, B. (2011) Product analysis of partial discharge damage to oil-impregnated insulation paper. Applied Surface Science. 257, 5863-5870.

Received: **09.05.2019**
Accepted: **10.12.2019**

CORRESPONDING AUTHOR

Yanyan Zheng
North China Electric Power University,
Baoding 071003, Hebei – China

e-mail: zhengyanyan888@hotmail.com

© by PSP Volume 29 – No. 04A/2020 pages 2711-2718 Fresenius Environmental Bulletin

SHELF LIFE OF FARMED SEA BASS (*DICENTRARCHUS LABRAX*, L. 1758) TREATED WITH *BACILLUS SUBTILIS* (KUEN 1593) UNDER COLD STORAGE

Eylem Ezgi Fadiloglu*

Yasar University, School of Applied Sciences, Department of Gastronomy and Culinary Arts, Izmir, Turkey

ABSTRACT

In this study, potential use of protective culture of *Bacillus subtilis* (KUEN 1593) to improve the chemical and microbial quality of fresh farmed sea bass (*Dicentrarchus labrax*, L. 1758) stored at +2ºC was evaluated. Three batches were prepared: Control-sea bass dipped into sterile distilled water (without bacteria inoculation), P1- sea bass inoculated with *Bacillus subtilis* (KUEN 1593) at a concentration of $2x10^8$ CFU/ml, and P2- sea bass inoculated with *Bacillus subtilis* (KUEN 1593) at a final concentration of $3x10^9$ CFU/ml. All samples were dipped into solutions (with or without bacteria inoculation) for 5 minutes then removed and placed in polystyrene boxes containing a layer of crushed ice, covered with stretch film and stored at 2°C for 21 days.

Analysis of pH, thiobarbituric acid (TBA), total volatile basic nitrogen (TVB-N), trimethylamine (TMA), total aerobic mesophilic bacteria (TAMB), psychrophilic bacteria count (PCB) and sensory analyzes have been performed on all groups (Control, P1 and P2) periodically at every 3 days during storage period.

Chemical, microbiological and sensory analyzes showed that control group spoiled at 15^{th} day of storage whereas P1 and P2 groups deteriorated after 18 and 21 days of storage. TAMB, PBC, TBA, TVB-N and TMA values for treated groups were always lower than control group.

At the end of the research, it was observed that the shelf life of the samples treated with *Bacillus subtilis* (KUEN 1593) at a concentration of $3x10^9$ CFU/ml extended 6 days compared to control (non-treated) samples.

KEYWORDS:
Biopreservation, fresh farmed sea bass, *Bacillus subtilis*, cold storage, quality

INTRODUCTION

In recent years, seafood exports have shown significant growth and fish became important goods in international trade. Turkey is the largest producer of farmed fish in the world. The aquaculture production of Turkey in 2016 was 253.395 ton, out of which approximately 60.65% was carried out in seawaters. Economically the most important species are rainbow trout (39.35%) in fresh waters, and sea bass (31.90%) and sea bream (22.99%) in seawaters. In 2016, sea bass production was 80.847 tons in seas of the country [1].

Commercially, sea bass (*Dicentrarchus labrax*, L. 1758) is an important product because it is in high demand, has considerable large sales volumes and revenues both in import and export markets. In recent years market demand for fresh sea bass (*Dicentrarchus labrax*, L. 1758) has increased significantly due to its white flesh, low fat content and nice aroma [2].

Fresh fish is extremely perishable and its shelf life is limited. Due to its chemical, microbial and enzymatic activities after harvesting, quality loss occurs quickly [3, 4, 5]. Among the meat products, fish meat is the type in which the fresh-stale concept is mostly used. Freezing and cold storage are among the fish preservation technique but they do not improve meat quality. Cooling and cold storage of fish are commonly used because they provide ease of transportation and prevent the risk of deterioration during transportation [6]. Since consumers demand minimally processed high quality seafood with no chemical additives, there is a need to develop effective and innovative technologies for extending the shelf life of fresh fish. Biopreservation is a natural technology for extending the shelf life and enhancing food safety by inhibiting the pathogenic bacteria without losing the nutritional quality of food products by using the biological microbiota or their metabolites [7]. This technology, which is not a chemical treatment, reduces processing costs and is not threating food safety [8].

Biopreservation technology should be combined with different hurdle technologies (refrigeration, vacuum packing, salting, etc.) to make it a valuable alternative [5]. In biopreservation technology, to prevent the growth of undesirable microbes, selected non-pathogenic microorganisms that are inoculated in food and/or microbial metabolites in purified forms are used [9, 10].

Probiotics have beneficial effects on human being and animals. The common Gram-positive probiotic organisms used in aquaculture are *Bacillus*, *Lactobacillus*, *Lactococcus*, *Micrococcus*, *Streptococcus, Enterococcus*, *Carnobacterium*, and *Weissella* species. Bacillus spp. are non-pathogenic and non-toxic microorganisms without unwanted repercussions when applied to aquatic organisms [11]. Spore probiotics Bacillus spp. are *Bacillus subtilis*, *Bacillus clausii*, *Bacillus cereus*, *Bacillus coagulans* and *Bacillus licheniformis, Bacillus subtilis* is applied by feed or as a water additive [12]. Bacillus produce antibiotics, amino acides and enzymes and *Bacillus subtilis* produce serious of peptide, including the subtillin and bacitracin [13]. *Bacillus subtilis* produces antibacterial and antifungal substances [14] hence; it is used in agriculture (livestock and aquaculture sectors) and food industries.

This research was initiated to investigate and to determine the biopreservative effect of *Bacillus subtilis*, KUEN 1593 on the shelf life and freshness of farmed sea bass (*Dicentrarchus labrax*, L. 1758) stored at +2ºC.

MATERIALS AND METHODS

Bacterial culture. Commercial probiotic bacteria *Bacillus subtilis* (KUEN 1593) solution was purchased from Simbiyotek, (Simbiyotek Biological Products Company, Istanbul, Turkey) in the final concentration of $3x10^9$ CFU/ml and diluted in sterile physiological water (0.85% NaCl (w/v)) with the final concentration of $2x10^8$ CFU/ml.

Chemicals, sea bass and method. All chemicals were purchased from Merck Co., Germany. Forty fresh farmed sea bass (*Dicentrarchus labrax*, L. 1758) (an average weight of 350±50 g) were provided by "Çamlı Agriculture, Stock Breeding and Fisheries Group", located in Çesme, Izmir, Turkey. About 15 kg of sea bass (*Dicentrarchus labrax*, L. 1758) were killed by immersing in ice-cold water (hypothermia) and transferred to the Chemistry Laboratory of Yasar University in a polystyrene box with ice within 1 hour of harvesting. Three batches were prepared: Control-sea bass dipped into sterile distilled water (without bacteria inoculation), P1- sea bass inoculated with *Bacillus subtilis* (KUEN 1593) at a concentration of $2x10^8$ CFU/ml, P2- sea bass inoculated with *Bacillus subtilis* (KUEN 1593) at a final concentration of $3x10^9$ CFU/ml. All samples were dipped into solutions (with or without bacteria inoculation) for 5 min then removed and placed in polysterene boxes containing a layer of crushed ice, covered with a stretch film and stored at 2°C for 21 days. Crushed ice was used to provide high contact, fast and efficient chilling for newly caught fish. Sampling was carried out at 0, 3, 6, 9, 12, 15, 18 and 21 days in triplicate. The results were presented as the mean values with their standard deviations

Physicochemical analysis. Measurement of pH was performed by homogenizing fish samples in distilled water (1:2 w/v) in a Ultra-Turrax (IKA T25, Germany) using a pH-meter (WTW pH-meter, Germany) according to AOAC [15] process (method 981.12). The experiments were repeated at least in triplicate.

A trimethylamine (TMA) analysis was carried out according to the method of AOAC [16]. The total volatile basic nitrogen (TVB-N) was determined according to the method of Vyncke, (1996). Thiobarbituric acid value (TBA) was measured using the spectrophotometric method of Tarladgis et al. [17].

Microbiological analysis. 10 g of sample were taken and transferred in 90 ml 0.1% peptone water. After homogenizing for 1 min by using blender, series of decimal dilutions were prepared. Total aerobic mesophilic bacteria (TAMB) and psychrophilic bacteria count (PBC) were determined by pour plate method as described by Harrigan and McCance [18] using Plate Count Agar (Difco, 0479-17). The inoculated plates were incubated at 30°C for 24-48 h and at 5°C for 72 h for total aerobic mesophilic bacteria and psychrophilic bacteria respectively.

Sensory evaluation. Sensory evaluation of appearance, odor, color, texture and overall acceptance of uncooked whole sea bass samples were evaluated by six panelists experienced in seafood evaluation. Assessment was made using 9-point hedonic scale (1: extremely bed quality, 9: excellent quality) [19].

Statistical analysis. Statistical analysis was carried out using SPSS 22.0 (SPSS 22 for Windows, SPSS Inc. Chicago, IL, USA). All data were expressed in mean± SD. Variance analysis (ANOVA) was performed, with a confidence interval of 95% ($p<0.05$). Means were compared by Duncan's multiple range test.

RESULTS AND DISCUSSION

pH value. pH is among the important factors that affect the microbial growth and deterioration of seafood. pH of chilled fish depends on fish species and other factors and generally is between 6.0-6.5 [20].

The pH values of whole sea bass were 6.52 at the initial and 6.58, 6.46 and 6.43 at the end of the storage period for control, P1 and P2, respectively (Figure 1). There were significant differences among the samples ($p<0.05$). P1 and P2 groups showed lower pH values compared to control group. *Bacillus subtilis* might have inhibited bacterial spoilage and caused lower basic amines production.

The slight decrease ($p<0.05$) in the pH values of P1 and P2 group during storage period might have been the result of buffering capacity of sea bass muscle. Especially after 15 days of storage, control group spoiled and its pH value started to increase. The increase in pH values during storage period might be due to the production of biogenic amines such as ammonia, trimethylamine produced by fish spoilage bacteria.

Thiobarbituric acid (TBA). TBA is a secondary breakdown product of lipid oxidation and generally used as an indicator for the degree of lipid oxidation [21]. The changes in TBA values of fish samples are presented in Table 1.

At initial storage time, there were no significant differences between the control and the other treated samples ($p<0.05$). At the end of the storage period, TBA values of samples increased to 11.92, 5.52 and 5.46 mg MDA/kg sample, respectively.

The probiotic treatment decreased the TBA values of samples during 21 days of storage. The TBA values of control samples were significantly ($p<0.05$) higher than the values of P1 and P2 samples from 3th days to end of the storage period. While the TBA values of control samples increased sharply, probiotic treated samples increased slightly ($p<0.05$). Whereas P1 and P2 samples were in good quality during 15 days of storage, were in medium quality between 15-21 days of storage. Control group exceeded the acceptable limit value of 8 mg MDA/kg [22] after 15th days of storage. Although TBA values of P2 samples were smaller than P1 samples during storage period, they were not found significantly important ($p>0.05$).

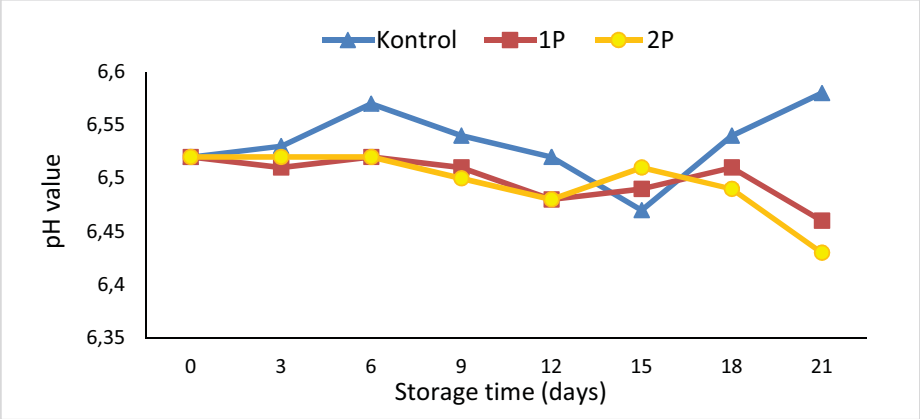

FIGURE 1
Changes in pH of whole seabass inoculated with *Bacillus subtilis* during storage at 2°C
Sample denomination: C: control; P1: inoculated with *Bacillus subtilis* at a concentration of $2x10^8$ CFU/ml); P2: inoculated with *Bacillus subtilis* at a concentration of $3x10^9$ CFU/ml

TABLE 1
TBA values of whole sea bass inoculated with *Bacillus subtilis* during storage at +2°C

Storage Time (days)	Treatments		
	Control	P1	P2
0	$0.81^{aH}\pm0.08$	$0.84^{aH}\pm0.06$	$0.87^{aH}\pm0.02$
3	$1.19^{aG}\pm0.07$	$1.07^{abG}\pm0.03$	$1.04^{abG}\pm0.08$
6	$1.82^{aF}\pm0.04$	$1.33^{bC}\pm0.08$	$1.34^{bF}\pm0.09$
9	$3.07^{aE}\pm0.07$	$2.81^{aD}\pm0.05$	$2.55^{cE}\pm0.21$
12	$3.58^{aD}\pm0.14$	$2.96^{bE}\pm0.06$	$2.90^{bD}\pm0.13$
15	$6.37^{aC}\pm0.12$	$3.38^{bC}\pm0.05$	$3.17^{cC}\pm0.04$
18	$9.45^{aB}\pm0.04$	$4.09^{bB}\pm0.04$	$4.03^{bB}\pm0.02$
21	$11.92^{aA}\pm0.03$	$5.52^{bA}\pm0.14$	$5.46^{bA}\pm0.10$

a–c: Means with the different letter in the same row are significantly different ($p<0.05$)
A–H: Means with the different letter in the same column are significantly different ($p<0.05$)
Sample denomination: C: control; P1: inoculated with *Bacillus subtilis* at a concentration of $2x10^8$ CFU/ml; P2: inoculated with *Bacillus subtilis* at a concentration of $3x10^9$ CFU/ml

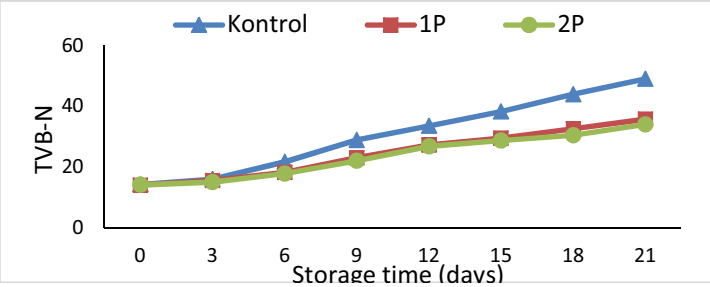

FIGURE 2

Changes in TVB-N values of whole seabass inoculated with *Bacillus subtilis* strain during storage at +2°C

Sample denomination: C: control; P1: inoculated with *Bacillus subtilis* at a concentration of $2x10^8$ CFU/ml; P2: inoculated with *Bacillus subtilis* at a concentration of $3x10^9$ CFU/ml

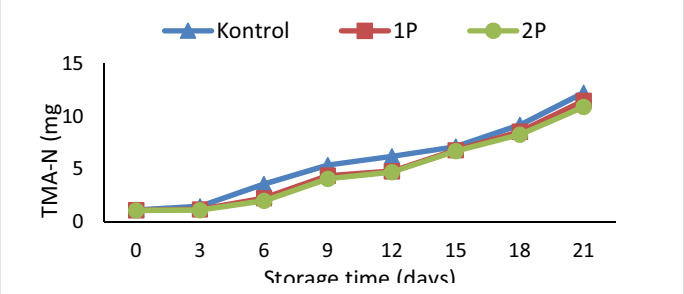

FIGURE 3

Changes in TMA-N values of whole seabass inoculated with *Bacillus subtilis* strain during storage at +2°C

Sample denomination: C: control; P1: inoculated with *Bacillus subtilis* at a concentration of $2x10^8$ CFU/ml; P2: inoculated with *Bacillus subtilis* at a concentration of $3x10^9$ CFU/ml

Total volatile basic nitrogen (TVB-N). TVB-N, which is used as a quality index, is mainly composed of protein degradation products such as ammonia, primary, secondary and tertiary amines. TVB-N value increases depending on the endogenous enzymes and spoilage bacteria activity [22].

TVB-N values of all samples are shown in Figure 2. Initial TVB-N value of the control, P1 and P2 groups were 14.30, 14.15, 14.19 mg N/100 g, respectively and increased progressively throughout the storage period for all treatments. The TVB-N value of freshly caught fish is generally between 5 and 20 mg TVB-N/100 g muscle and the result was similar to result (11.88 mg TVB-N/100 g) reported by Boulares et al. [23].

The difference in TVB-N values of the samples during storage period was found significantly important ($p<0.05$). This event caused by the deamination of aminoacids, formation of NH_3 and other volatile amines during storage period [20]. While after 3 days of storage TVB-N value of the control group increased sharply, TVB-N values of the P1 and P2 groups increased slowly. Results are in agreement with the study of Katikou et al. [24]. They found that TVB-N contents of refrigerated vacuum-packed rainbow trout (*Oncorrynchus mykiss*) fillets inoculated with *Lactobacillus sakei* CECT 4808 and *Lactobacillus curvatus* CECT 904T were lower than control samples during the 20 days of storage. According to Varlık et al. [25], the limit value of TVB-N for iced-stored cold-water fish is 35.00 mg/100 g. In the present study, at 15th day, control group (38.35 mg/100 g) exceeded the spoilage limit value of 35 mg/100 g while the TVB-N values of the P1 and P2 groups were below the limit value.

Trimethylamine nitrogen (TMA-N). TMA-N occurs reduction of trimethylamine oxide (TMAO) by bacteria and it is responsible for fishy off-odor in fish [26, 27]. Therefore, it is used to verify that the fish is spoiled and is inconsumable [23].

In this study, the initial TMA-N values were found to be 1.16 mg/100 g, 1.13 mg/100 g and 1.11 mg/100 g for control, P1 and P2 groups, respectively and it confirmed that the fish was fresh. The result was similar to TMA-N content of sea bass muscle (1.06 mg N/100 g) reported by Boulares et al. [23].

At initial storage time, there were no significant differences between the control and treated samples. During cold storage, TMA-N values of all samples increased gradually. While the control samples exceeded the acceptable limit value of 8 mg/100 g [28] after 15 days of storage, samples treated with *Bacillus subtilis* at concentrations of $3x10^9$ and $2x10^8$ CFU/ml exceeded at day 18.

Total aerobic mesophilic bacteria (TAMB) (log cfu/g). The changes in total aerobic mesophilic

bacteria of aquacultured whole sea bass during storage in ice are shown in Figure 4. Initial TAMB of control, P1 and P2 samples were 3.11 log cfu/g, 3.11 log cfu/g and 3.01 log cfu/g, respectively. It indicated that fish was fresh and had high quality.

The total aerobic mesophilic bacteria of control and treated aquacultured sea bass samples increased during storage period. TAMB reached 10.69 log cfu/g for control and 7.58 and 7.24 log cfu/g for treated samples after 21 days of storage. TMAB of P1 and P2 group were lower than control samples throughout the storage period ($p<0.05$).

While TAMB of control sample exceeded 7 log cfu/g, which is the maximum level for acceptability of marine fish [29] after 12 days, treated samples exceeded at day 21 (Figure 4). Lowest TAMB values of P1 and P2 samples ($p<0.05$) showed that bacterial growth was inhibited by *Bacillus subtilis* (KUEN 1593). The antimicrobial ability of *Bacillus subtilis* is due to the production of organic acids and bacteriocins.

A bed smell was observed in control samples at day 15. The bed smell was also detected in P1 and P2 samples after 18 days of storage when the TAMB reached the levels of 7.58 and 7.24 log cfu/g for P1 and P2, respectively.

Psychrophilic bacteria count (PBC) (log cfu/g). The effects of *Bacillus subtilis* (KUEN, 1593) on psychrophilic bacteria counts (PBC) are seen in Figure 5. The PBC of control samples increased rapidly ($p<0.05$) from the initial value of 2.95 to 6.25 log cfu/g within 12 days and spoiled in the following three days. PBC of probiotic-treated seabass samples were always lower than the PBC of control samples ($p<0.05$). It was noted that PBC of control samples increased more than two times compared to PBC of treated samples during 21 days of storage. There were significant differences between all samples during storage period ($p<0.05$).

At day 21, PVC of P1 and P2 groups were below the acceptable limit value of 7 log cfu/g. [29] In addition, *Bacillus subtilis* treatment had more inhibitory activity on PBC during storage period.

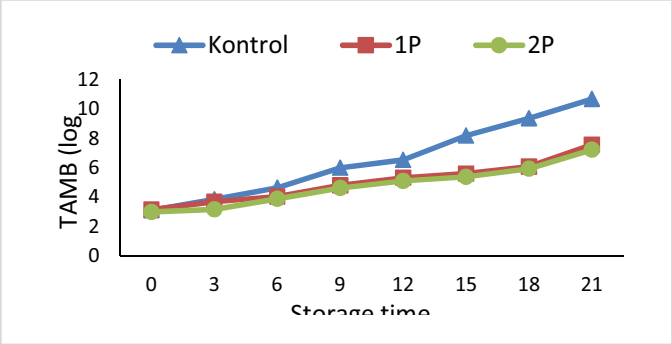

FIGURE 4

Changes in Total aerobic mesophilic bacteria (log cfu/g) of whole seabass treated with or without *Bacillus subtilis* during 21 days of storage at +2°C

Sample denomination: C: control; P1: inoculated with *Bacillus subtilis* at a concentration of $2x10^8$ CFU/ml; P2: inoculated with *Bacillus subtilis* at a concentration of $3x10^9$ CFU/ml

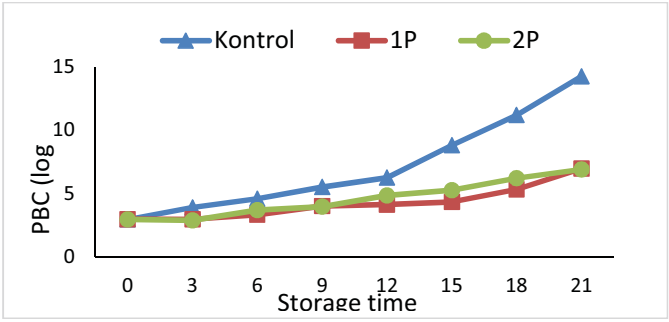

FIGURE 5

Changes in Psychrophilic Bacteria count (PBC) (log cfu/g) of whole seabass treated with or without *Bacillus subtilis* during 21 days of storage at +2°C

Sample denomination: C: control; P1: inoculated with *Bacillus subtilis* at a concentration of $2x10^8$ CFU/ml; P2: inoculated with *Bacillus subtilis* at a concentration of $3x10^9$ CFU/ml

Sensory analysis. The changes in the sensory scores of cultured sea bass during 21 days of storage at 2°C are shown in Table 2. All sensory scores for fish samples decreased gradually with an increasing of storage time ($p<0.05$). The freshness characteristic of the control samples was strong between 1-12 days. Deterioration occurred as of 12th. P1 and P2 samples maintained their good quality up to day 18 of storage. After this time, quality decreased and by day 21, the samples were no longer acceptable. Microbiological and chemical results were in line with sensory scores of samples.

TABLE 2
Sensory analysis of whole sea bass inoculated with *Bacillus subtilis* during storage at 2°C

Sensorial quality	Storage Time (days)	Treatments		
		Control	1P	2P
Appearance	0	$8.67^{aA}\pm0.52$	$8.83^{aA}\pm0.41$	$9.00^{aA}\pm0.00$
	3	$8.67^{aA}\pm0.52$	$8.83^{aA}\pm0.41$	$8.83^{aA}\pm0.41$
	6	$6.67^{bB}\pm0.52$	$8.83^{aA}\pm0.41$	$8.83^{aA}\pm0.41$
	9	$5.00^{cB}\pm0.52$	$7.67^{bA}\pm0.52$	$8.17^{bA}\pm0.41$
	12	$2.67^{dC}\pm0.63$	$5.83^{cB}\pm0.75$	$7.17^{cA}\pm0.41$
	15	$1.33^{eC}\pm0.52$	$5.00^{dB}\pm0.63$	$7.00^{cA}\pm0.63$
	18	$1.00^{eC}\pm0.00$	$5.00^{dB}\pm0.63$	$6.17^{dA}\pm0.41$
	21	$1.00^{eC}\pm0.00$	$3.17^{dB}\pm0.41$	$4.33^{eA}\pm0.52$
Color	0	$8.83^{aA}\pm0.41$	$8.83^{aA}\pm0.41$	$8.83^{aA}\pm0.41$
	3	$8.67^{aA}\pm0.52$	$8.83^{aA}\pm0.41$	$8.83^{aA}\pm0.41$
	6	$6.83^{bB}\pm0.41$	$8.83^{aA}\pm0.41$	$8.67^{aA}\pm0.52$
	9	$4.33^{cC}\pm0.52$	$7.17^{bB}\pm0.41$	$8.00^{bB}\pm0.63$
	12	$2.00^{dD}\pm0.63$	$5.00^{cC}\pm0.00$	$6.33^{cC}\pm0.52$
	15	$1.17^{eE}\pm0.41$	$5.00^{dC}\pm0.00$	$6.33^{cC}\pm0.52$
	18	$1.17^{eE}\pm0.41$	$4.83^{dC}\pm0.41$	$6.17^{dC}\pm0.41$
	21	$1.00^{eE}\pm0.00$	$2.17^{dD}\pm0.41$	$2.50^{eD}\pm0.55$
Odour	0	$8.83^{aA}\pm0.41$	$8.83^{aA}\pm0.41$	$9.00^{aA}\pm0.00$
	3	$8.00^{bB}\pm0.00$	$8.83^{aA}\pm0.41$	$8.83^{aA}\pm0.41$
	6	$6.83^{cC}\pm0.41$	$7.83^{bB}\pm0.41$	$8.83^{aA}\pm0.41$
	9	$4.00^{dB}\pm0.63$	$7.17^{cA}\pm0.41$	$7.33^{bA}\pm0.52$
	12	$2.00^{eB}\pm0.63$	$6.00^{dA}\pm0.00$	$6.33^{cA}\pm0.52$
	15	$1.17^{fC}\pm0.41$	$4.83^{eB}\pm0.41$	$6.17^{cA}\pm0.41$
	18	$1.17^{fC}\pm0.41$	$4.17^{fB}\pm0.41$	$5.50^{dA}\pm0.84$
	21	$1.00^{fB}\pm0.00$	$1.17^{gB}\pm0.41$	$2.50^{eA}\pm0.55$
Texture	0	$8.83^{aA}\pm0.41$	$8.83^{aA}\pm0.41$	$9.00^{aA}\pm0.00$
	3	$8.00^{bB}\pm0.00$	$8.83^{aA}\pm0.41$	$8.83^{aA}\pm0.41$
	6	$6.83^{cC}\pm0.41$	$7.83^{bB}\pm0.41$	$8.83^{aA}\pm0.41$
	9	$4.17^{dB}\pm0.75$	$7.17^{cA}\pm0.41$	$7.33^{bA}\pm0.52$
	12	$2.00^{eB}\pm0.63$	$6.00^{dA}\pm0.00$	$6.50^{cA}\pm0.55$
	15	$1.17^{fC}\pm0.41$	$4.83^{eB}\pm0.41$	$6.33^{cA}\pm0.52$
	18	$1.17^{fC}\pm0.41$	$4.17^{fB}\pm0.41$	$5.33^{dA}\pm0.52$
	21	$1.00^{fB}\pm0.00$	$2.00^{gA}\pm0.00$	$2.33^{eA}\pm0.52$
Overall acceptance	0	$8.79^{aA}\pm0.08$	$8.83^{aA}\pm0.00$	$8.96^{aA}\pm0.09$
	3	$8.34^{bB}\pm0.39$	$8.83^{aA}\pm0.00$	$8.83^{aA}\pm0.00$
	6	$6.79^{cC}\pm0.08$	$8.33^{aB}\pm0.58$	$8.79^{aA}\pm0.08$
	9	$4.38^{dB}\pm0.44$	$7.30^{bA}\pm0.25$	$7.71^{bA}\pm0.44$
	12	$2.17^{eB}\pm0.34$	$5.71^{cA}\pm0.48$	$6.58^{cA}\pm0.40$
	15	$1.21^{fC}\pm0.08$	$4.92^{dB}\pm0.10$	$6.46^{cA}\pm0.37$
	18	$1.13^{fC}\pm0.09$	$4.54^{dB}\pm0.44$	$5.79^{dA}\pm0.44$
	21	$1.00^{fB}\pm0.00$	$2.13^{eA}\pm0.82$	$2.92^{eA}\pm0.95$

a-f: Means with the different letter in the same column are significantly different ($p<0.05$)
A-C: Means with the different letter in the same row are significantly different ($p<0.05$)

CONCLUSION

Based on physicochemical, microbiological and sensory evaluation, treatment with probiotic culture extended the shelf life of farmed sea bass (*Dicentrarchus labrax*, L. 1758) stored at 2ºC by 6 to 9 days. Results suggest that *Bacillus subtilis* (KUEN 1593) has the potential to improve the quality and the shelf life of fish due to its antimicrobial and bio-preservative effect during cold storage.

ACKNOWLEDGEMENT

The authors wish to acknowledge the financial support by Yasar University Scientific Research Grant Scheme with Project Number BAP035.

REFERENCES

[1] TUIK. (2016) Fisheries Production Statistics for 2016, Ankara, Turkey.
[2] Kocatepe, D. and Turan, H. (2012) Chemical composition of cultured sea bass (*Dicentrarchus labrax*, Linnaeus 1758) muscle. Journal of Food and Nutrition Research. 51(1), 33-39.
[3] Ghaly, A.E., Dave, D., Budge, S. and Brooks, M. S. (2010) Fish spoilage mechanisms and preservation techniques: Review. American Journal of Applied Sciences. 7(7), 859-877.
[4] Sallam, K.I. (2007) Antimicrobial and antioxidant effects of sodium acetate, sodium lactate, and sodium citrate in refrigerated sliced salmon. Food Control. 18, 566.
[5] Gomez-Sala, B., Herranz, C., Diaz-Freitas, B, Hernandez, P.E., Sala, A., Cintas, L.M. (2016) Strategies to increase the hygienic and economic value of fresh fish: Biopreservation using lactic acid bacteria of marine origin. International Journal of Food Microbiology. 223, 41-49.
[6] Johnston, W.A., Nicholson, F.J. and Roger, A. (1994) Freezing and refrigerated storage in fisheries. FAQ Fisheries Technical Paper-T340, Rome, Italy.
[7] Karthik, R., Gobalakrishnan, S., Hussain, A.J. and Muthezhilan, R. (2013) Efficacy of bacteriocin from Lactobacillus Sp. (AMET 1506) as a biopreservative for seafood under different storage temperature conditions. Journal of Modern Biotechnology. 2(3), 59-65.
[8] Galvez, A., Abriouel, H., Benomar, N. and Lucas, R. (2010) Microbial antagonists to food-borne pathogens and biocontrol. Current Opinion in Biotechnology. 21, 142-148.
[9] Gaggia, F., Gioia, D.D., Baffoni, L. and Biavati, B. (2011) The role of protective and probiotic cultures in food and feed and their impact in food safety. Trends in Food Science and Technology. 22, 58-66.
[10] Leroi, F., Cornet, J., Chevalier, F., Cardinal, M., Coeuret, G., Chaillou, S. and Joffraud, J.J. (2015) Selection of bioprotective cultures for preventing cold-smoked salmon spoilage. International Journal of Food Microbiology. 213, 79-87.
[11] Farzanfar, A. (2006) The use of probiotics in shrimp aquaculture. FEMS Immunology Medical Microbiology. 48, 149-158.
[12] Irianto, A. and Austin, B. (2003) Use of dead probiotic cells to control furunculosis in rainbow trout, *Onchorhynchus mykiss*. Journal of Fish Diseases. 26, 59-62.
[13] Bagheri, T., Hedayati, S.A., Yavari, V., Alizade, M. and Farzanfar, A. (2008) Growth, Survival and gut microbial load of rainbow trout, *Onchorhynchus mykiss* (Walbaum) fry given diet supplemented with probiotic during the two months of first feeding. Journal of Fisheries and Aquatic Science. 8, 43-48.
[14] Ansari, A., Aman, A., Siddiqui, N.N., Iqbal, S. and Qader, S.A. (2012) Bacteriocin (BAC-IB17): Screening, isolation and production from *Bacillus subtilis* KIBGE IB-17. Pakistan Journal of Pharmaceutical Sciences. 25(1), 195-201.
[15] AOAC (1995) Official methods of analysis (16th ed.). Washington DC: Association of Official Chemists.
[16] AOAC (1984) Official Methods of Analysis (14th ed.). Association of Official Analytical Chemists. Washington D. C. 18.031-033.
[17] Tarladgis, B.G., Watts, B.M., Younathan, M.S. and Dugan, L. Jr. (1960) A distillation method for the quantitative determination of malonaldehyde in rancid foods. Journal American Oil Chemistry Society. 37, 44-48.
[18] Harrigan, W.F. and McCance, M.E. (1976). Laboratory Methods in Food and Dairy Microbiology, Academic Press Inc., London.
[19] ISO 4121 (2003). Sensory analysis. Guidelines for the use of quantitative response scales. Switzerland: International Organisation for Standardisation.
[20] Behnam, S., Anvari, M., Rezaei, M., Soltanian, S. and Safari, R. (2015) Effect of nisin as a biopreservative agent on quality and shelf life of vacuum packaged rainbow trout (*Oncorhynchus mykiss*) stored at 4°C. Journal of Food Science and Technology. 52(4), 2184-2192.
[21] Aubourg, S.P. (1999) Lipid damage detection during the frozen storage of an underutilized fish species. Food Research International. 32, 497-502.

[22] Kyrana, V.R., Lougovois, V.P. and Valsamis, D. S. (1997) Assessment of shelf life of maricultured gilthead seabream (*Sparus aurata*) stored in ice. International Jounal of Food Science and Technology. 3, 25-43.
[23] Boulares, M., Mankai, M., Sadok, S. and Hassouna, M. (2016) Anti-Listerial inhibitory lactic acid bacteria in fresh farmed sea bass (Dicentrarchus labrax) fillets during storage at 4°C under vacuum-packed conditions, Journal of Food Safety.37(3), e12323.
[24] Katikou, P., Ambrosiadis, I., Georgantelis, D., Koidis, P. and Georgakis, S.A. (2007) Effect of *Lactobacillus* cultures on microbiological, chemical and odour changes during storage of rainbow trout fillets. Journal of the Science of Food and Agriculture. 87, 477-484.
[25] Varlık, C., Ozden, O., Erkan, N. and Alakavuk, D.U. (2007) Basic Quality Control in Seafood. Istanbul University Publication No. 4662. Faculty Publication No: 8. pp. 202, Istanbul University Printing and Publishing Directorate, Istanbul.
[26] Gunlu, A. and Koyun, E. (2013) Effects of vacuum packaging and wrapping with chitosan based edible film on the extension of the shelf life of sea bass (*Dicentrarchus labrax*) fillets in cold storage (4ºC). Food and Bioprocess Technology. 6(7), 1713-1719.
[27] Serdaroglu, M. and Deniz, E.E. (2001) The factors affecting trimetilamine (TMA) and dimetilamine (DMA) formation in fish and some seafood. Journal of Fisheries and Aquatic Sciences. 18(3-4), 575-581.
[28] FAO (1986) FAO Food and nutrition paper manuals of food quality control food analysis: Quality, adulteration and tests of identity. Food and Agriculture Organization of the United Nations, Rome.
[29] ICMSF. (1986) Microorganisms in foods. Sampling for microbiological analysis: Principles and scientific applications, Toronto: University of Toronto Press., 181-196.

Received: **13.05.2019**
Accepted: **09.01.2020**

CORRESPONDING AUTHOR

Eylem Ezgi Fadiloglu
Yaşar University,
School of Applied Sciences,
Department of Gastronomy and Culinary Arts,
Izmir, Turkey

e-mail: ezgi.fadiloglu@yasar.edu.tr

© by PSP Volume 29 – No. 04A/2020 pages 2719-2724 Fresenius Environmental Bulletin

INHIBITORY AND SYNERGISTIC EFFECT OF NOVEL COMBINED ACTIVE SUBSTANCES OF FUNGICIDES AGAINST SELECTED PLANT PATHOGENS

Piotr Iwaniuk[1,2,*], Bozena Lozowicka[1]

[1]Institute of Plant Protection – National Research Institute, Bialystok, Poland
[2]Department of Microbiology, Institute of Biology, University of Bialystok, Bialystok, Poland

ABSTRACT

We determined minimal inhibitory concentration (MIC) of single active substances (a.s) of fungicides, twelve mixtures of two a.s and four a.s mixture. Additionally fractional inhibitory concentration index (FICI) of combined a.s. was calculated. Fungal and oomycete pathogens included *Fusarium culmorum*, *Colletotrichum coccodes*, *Penicillium verrucosum*, *Sclerotinia sclerotiorum*, *Botrytis cinerea*, *Alternaria alternata*, *Aspergillus candidus*, *Monilinia fructicola*, *Septoria tritici* and oomycete *Phytophthora infestans*. MIC were ranged from 0.1 µg/ml for fluazinam to 4954.5 µg/ml for cymoxanil. MIC of combined a.s were ranged from 0.00004 µg/ml for picoxystrobin+fenamidone to 4955 µg/ml for cymoxanil+carboxin. Dodine+picoxystrobin had shown the most effective inhibitory and synergistic action against seven fungal or oomycete species (0.001 µg/ml – 35.9 µg/ml). The highest decrease of MIC values of dodine+picoxystrobin compared to their separate application indicate that these compounds should be considered to create novel commercial formulations of fungicides.

KEYWORDS:
Minimal inhibitory concentration (MIC), Fractional inhibitory concentration index (FICI), Fungicides; Phytopathogenic fungi

INTRODUCTION

Plant protection products (ppp.) are widespread compounds improving plant growth and contribute to better quality of cereals, fruits and vegetables. Fungicides are crucial pesticides in cultivation of fruits and vegetables more sensitive to fungal diseases development [1]. Lettuce, spinach or tomatoes are vegetables frequently treated by ppp. [2]. Usage of fungicides depends on particular countries and is more related to plant products intended for export as well as long term transport [3].

Overuse of popular fungicides lead to the development of resistance among *Fusarium culmorum*, *Colletotrichum coccodes*, *Penicillium* spp., *Aspergillus* spp., *Botrytis cinerea*, *Sclerotinia sclerotiorum*, *Alternaria alternata, Monilinia fructicola*, *Septoria tritici* and *P. infestans* [4,5,6,7,8,9,10]. Broad range of commercial fungicides registered in particular plant cultivations are often based on the same a.s. with different trade names, which is one of the reason of growing fungicide resistance. Thus there is a need to register other a.s in further plant cultivations.

Commercial fungicides often consist of two or more a.s at different concentrations, to improve their efficacy and expand the range of dedicated pathogens. However, the mutual effect of mixed a.s was poorly investigated. There are little scientific data if these mixed a.s have better action than single applied according to fractional inhibitory concentration index (FICI). Taking under attention facts above, the aim of this study was to evaluate efficacy of single, pure a.s commonly presented in commercial fungicides against selected phytopathogenic fungi and oomycete. Novelty of this study was to mix them in two component formulations not yet available on the market. Their efficacy was determined by minimal inhibitory concentration (MIC) and synergistic effect was confirmed by calculations of fractional inhibitory concentration index (FICI). We believe it is the first step of a.s registration procedure in practice against main fungal pathogens in further plant cultivations.

MATERIALS AND METHODS

Phytopathogenic fungi and oomycete, culture conditions. Reference pathogenic strains used in this study were originally collected from natural plant disease outbreaks in Poland. Fungi and oomycete were isolated from oat, potato, onion, tomato, broccoli, lettuce, barley, plum and triticale. Pathogens were identified using morphological keys and their species affiliation was confirmed by PCR assays. Strains were deposited in the Bank of Plant Pathogens of the Institute of Plant Protection – National Research Institute, Poznan, Poland. Tested strains included *Fusarium culmorum* 1918, *Colletotrichum coccodes* 2095, *Penicillium verrucosum*

1681, *Sclerotinia sclerotiorum* 2242, *Botrytis cinerea* 2235, *Alternaria alternata* 2341, *Aspergillus candidus* 1212, *Monilinia fructicola* 2254, *Septoria tritici* 1492, oomycete *Phytophthora infestans* 2054. Strains were stored in PDB (potato dextrose broth) with glycerol stocks (1:1, v/v) in –80ºC, then were plated on PDA (potato dextrose agar, A&A Biotechnology, Gdynia, Poland) medium and incubated at 23ºC for 7 days. To achieve spore suspensions, three 0.5 mm x 0.5 mm agar pieces were transferred into 100 ml of 0.5x PDB (A&A Biotechnology, Gdynia, Poland) pH 5.5–6.5 or 0.98 aw (water activity) and were incubated at 15ºC, 20ºC, 23ºC for 7, 14 or 21 days.

Single and mixed active substances. Tested a.s were purchased from Dr. Ehrenstorfer Laboratory (Augsburg, Germany) and all were of high purity grade (>93%). Tested compounds included fenamidone (FE); carboxin (CA); etaconazole (ET); dithianon (DI); dodine (DO); triflumizole (TR); cymoxanil (CY); picoxystrobin (PI); fluazinam (FL); fluquinconazole (FQ) (Table 2). Compounds were weighted and fully dissolved in 99 % dimethylsulfoxide (DMSO) (Sigma-Aldrich, Poznan, Poland) to the homogenous suspension in working concentration of 100 mM and filtered through 0.22 µm pore size Rotilabo-Spitzenfilter filter (Roth, Karlsruhe, Germany). Stock solutions were stored at 4ºC.

A.s with different modes of action were mixed (1:1, v/v), cymoxanil with carboxin (CY+CA); dodine with picoxystrobin (DO+PI); fluazinam with etaconazole (FL+ET); fluazinam with dithianon (FL+DI); fluazinam with triflumizole (FL+TR); fenamidone with carboxin (FE+CA); etaconazole with dithianon (ET+DI); fluquinconazole with dithianon (FQ+DI); dodine with fenamidone (DO+FE); dodine with fluazinam (DO+FL); picoxystrobin with fenamidone (PI+FE); picoxystrobin with fluazinam (PI+FL); etaconazole with dithianon, triflumizole and fluazinam (ET+DI+TR+FL). Combined a.s were filtered through 0.22 µm pore size Rotilabo-Spitzenfilter filter (Roth, Karlsruhe, Germany) and stored at 4ºC.

Minimal inhibitory concentration (MIC) and fractional inhibitory concentration index (FICI). Inhibitory action of a.s was expressed as MIC. Spore suspensions were adjusted using 0.5x PDB to the optical density in the range of 0.05 – 0.1 at a wavelength of 600 nm (OD_{600}) using spectrophotometer Implen P-300 (Duren, Germany). Volume of 100 µl of a.s solution was precisely serially diluted 2-fold in 100 µl of 2x concentrated PDB in the U-shaped, 96-well microtiter plate. Formation of precipitants were not observed. Next, 100 µl of spore suspension was added to each well and plates were incubated at 23ºC for 7 days. MIC values were determined visually in aqueous medium as the lowest concentration of a.s in the last well with not observed fungal growth. To obtain comparable data tests to all a.s were performed in quadruplicate. Fungi and oomycete cultured in PDB without any a.s solution were incubated as positive controls and pathogens cultured in PDB with 10% DMSO were prepared as solvent controls. Additionally to assess mutual effect of combined a.s, the fractional inhibitory concentration index (FICI) was calculated according to Odds [11], where A and B are a.s tested alone and in mixtures:

$$FICI = \frac{MIC_{A\ with\ B}}{MIC_{A\ alone}} + \frac{MIC_{B\ with\ A}}{MIC_{B\ alone}}$$

The FICI values ≤ 0.5 were indicated as synergistic effect, values > 0.5-4.0 as indifferent and values > 4.0 as antagonistic effect.

STATISTICAL ANALYSIS

Statistical significance was performed using Fischer's exact test. Means and standard deviations (±SD) were calculated in Statistica 9.0 software. Statistical significance was established as $P<0.05$.

TABLE 1
MIC values of tested single active substances

Fungi species	Minimal inhibitory concentration, µg/ml[a,b]									
	FE	CA	ET	DI	DO	TR	CY	PI	FL	FQ
F. culmorum	1946.3	735	2	1.4	14	1.1	1238.6	2870	4.4	293.9
C. coccodes	973.1	1470	64	2.8	0.9	4.2	1238.6	1.2	0.1	2.9
P. verrucosum	121.6	183.8	2	0.7	224.5	8.4	619.3	1147.9	0.3	293.9
S. sclerotiorum	486.6	183.8	32	5.6	224.5	33.7	2477.3	1147.9	4.4	146.9
B. cinerea	243.3	367.5	2	0.7	28.1	2.1	309.7	2870	0.9	0.7
A. alternata	1946.3	735	64	11.1	1.8	8.4	4954.5	2295.8	4.4	587.8
A. candidus	973.1	11.5	32	22.2	28.1	16.9	1238.6	1147.9	17.4	73.5
M. fructicola	486.6	367.5	1	5.6	0.9	0.3	619.3	573.9	0.3	0.4
S. tritici	486.6	46	16	1.4	1.8	33.7	1238.6	573.9	1.1	73.5
P. infestans	3.8	367.5	16	2.8	0.22	2.1	4.84	0.15	4.4	146.9

[a] Single active substances: fenamidone (FE); carboxin (CA); etaconazole (ET); dithianon (DI); dodine (DO); triflumizole (TR); cymoxanil (CY); picoxystrobin (PI); fluazinam (FL); fluquinconazole (FQ) [b] $P<0.05$

TABLE 2
MIC values of tested combined active substances

Fungi species	Minimal inhibitory concentration, µg/ml[a]							
	CY+CA	DO+PI	FL+ET	FL+DI	FL+TR	FE+CA	ET+DI	FQ+DI
F. culmorum[c]	4955+1470	28.07+35.9	2.18+8	2.18+2.8	4.36+8.4	1946+1470	8+2.8	73.5+2.8
C. coccodes	1239+367	0.45+0.57	0.44+16	0.44+5.6	0.44+8.4	30.4+23	16+5.6	1.5+5.6
P. verrucosum	61.9+183	3.5+4.5	1.1+0.5	0.6+0.69	8.7+16.9	15.2+11.5	8+2.8	73.5+2.8
S. sclerotiorum	19.4+5.74	28.07+35.9	0.27+1	2.18+2.8	0.27+0.53	30.4+23	8+2.8	4.6+0.17
B. cinerea	309.6+91.8	5.7+9	0.11+0.5	0.9+11.1	0.9+16.9	243.3+183.8	8+2.8	0.74+2.78
A. alternata[c]	2477+735	11.5+17.9	8.7+4	8.7+11.1	8.7+16.9	973.1+735	64+22.2	294+11.1
A. candidus	38.7+11.5	0.02+0.04	8.7+4	8.7+11.1	8.7+16.9	15.2+11.5	32+11.1	36.7+1.39
M. fructicola	1239+367	0.001+2.2	0.3+0.13	0.3+0.35	0.14+0.3	243+183.8	1+0.35	0.37+1.39
S. tritici	77.4+23	0.003+4.5	0.6+0.25	0.6+0.69	0.3+0.5	30.4+23	8+2.8	18.4+0.7
P. infestans	1.21+0.36	0.014+0.018	1.09+4	0.3+0.35	1.09+2.1	0.12+0.09	4+1.39	73.5+2.8

[a] Combined active substances: cymoxanil with carboxin (CY+CA); dodine with picoxystrobin (DO+PI); fluazinam with etaconazole (FL+ET); fluazinam with dithianon (FL+DI); fluazinam with triflumizole (FL+TR); fenamidone with carboxin (FE+CA); etaconazole with dithianon (ET+DI); fluquinconazole with dithianon (FQ+DI)

Fungi species	Minimal inhibitory concentration, µg/ml[b]				
	DO+FE	DO+FL	PI+FE	PI+FL	ET+DI+TR+FL
F. culmorum[c]	56.13+60.82	28.1+0.27	2296+1946.3	2296+17.4	8+2.8+4.2+2.2
C. coccodes	0.45+486.6	0.9+0.9	0.6+486.6	1.15+0.9	32+11.1+16.9+0.9
P. verrucosum	28.1+30.4	56.1+0.5	18+15.2	9+0.07	8+2.8+4.2+2.2
S. sclerotiorum	56.13+60.82	7+0.068	18+15.2	18+0.14	0.5+0.17+0.3+0.14
B. cinerea	14+15.2	28.1+0.03	574+486.6	1148+0.9	8+2.8+4.2+0.2
A. alternata[c]	1.8+1946.3	0.9+8.7	2296+1946.3	2296+17.4	32+11.1+16.9+8.7
A. candidus	7+7.6	28.1+0.3	574+486.6	1148+8.7	32+11.1+16.9+8.7
M. fructicola	0.45+486.6	0.004+0.03	2.2+1.9	4.5+0.03	0.5+0.17+0.3+0.14
S. tritici	0.11+121.6	0.45+4.4	287+243.3	9+0.07	8+2.8+4.2+2.2
P. infestans	0.00005+0.06	0.22+2.18	0.00004+0.03	0.0045+0.03	4+1.4+2.1+1.1

[b] Combined active substances: dodine with fenamidone (DO+FE); dodine with fluazinam (DO+FL); picoxystrobin with fenamidone (PI+FE); picoxystrobin with fluazinam (PI+FL); etaconazole with dithianon, triflumizole and fluazinam (ET+DI+TR+FL)
[c] $P>0.05$

RESULTS

Etaconazole, dithianon, triflumizole and fluazinam had the best inhibitory action ($P<0.05$) against all tested fungi in the lowest inhibitory concentrations (MIC ranges 1-64 µg/ml, 0.7-22.2 µg/ml, 0.3-33.7 µg/ml and 0.1-17.4 µg/ml, respectively) (Table 1). Fluquinconazole had medium effect (MIC 0.4-587.8 µg/ml), while fenamidone, carboxin, cymoxanil and picoxystrobin had inhibitory effect at the highest concentrations ($P<0.05$) (MIC ranges 3.8-1946.3 µg/ml, 11.5-1470 µg/ml, 4.84-1238.6 µg/ml and 0.15-2870 µg/ml, respectively). Generally within species, *C. coccodes* required the highest dose of fenamidone, carboxin and cymoxanil to achieve growth inhibitory action, *P. verrucosum* or *S. sclerotiorum* of cymoxanil and picoxystrobin, *B. cinerea* of picoxystrobin, *F. culmorum*, *A. alternata* and *A. candidus* of fenamidone, cymoxanil and picoxystrobin, *M. fructicola* of fenamidone, carboxin, cymoxanil and picoxystrobin, *S. tritici* of cymoxanil, while oomycete *P. infestans* of carboxin ($P<0.05$) (Table 1).

Prepared combinations of a.s revealed that some mixtures had lower growth inhibitory concentration when combined. Mix of dodine with picoxystrobin had the best synergistic effect (FICI ≤ 0.5) and achieved the lowest MIC values for majority of tested fungi, except *F. culmorum*, *C. coccodes* and *A. alternata* compared to their separate applications ($P<0.05$) (Table 2; Figure 1). Additionally mixtures of dodine with fenamidone (as the example of weakly effective a.s) had lower MIC compared to their separate application and synergistic effect against *P. verrucosum*, *S. sclerotiorum*, *A. candidus*, *S. tritici* or *P. infestans* ($P<0.05$), while dodine with fluazinam (as the example of well effective a.s) against *S. sclerotiorum* and *M. fructicola* ($P<0.05$). Picoxystrobin applied with fenamidone had lower MIC and synergistic effect against *P. verrucosum*, *S. sclerotium*, *M. fructicola* and *P. infestans* ($P<0.05$), while treated with fluazinam against *P. verrucosum*, *S. sclerotiorum*, *M. fructicola*, *S. tritici* and *P. infestans* (Table 2; Figure 2). A.s combinations based on dodine and picoxystrobin had fungistatic action against *P.*

verrucosum, *A. candidus* and *M. fructicola*, and fungal growth was observed after 10 days of incubation. Some other combined a.s had also synergistic action but indifferent or antagonistic effect (FICI > 0.5-4.0 or > 4.0, respectively) in majority of pathogens was observed (Table 2; Figure 2). Mixture of four well acting a.s including etaconazole, dithianon, triflumizole and fluazinam also not affected on the significant decrease of MIC. Despite lower MIC values of mixed a.s against most of the tested fungi and oomycete, combined a.s had indifferent or antagonistic effect against *F. culmorum* and *A. alternata* (P>0.05), while strong synergistic effect was observed in ten or eight combined a.s against *S. sclerotiorum* and *P. infestans*, respectively (P<0.05).

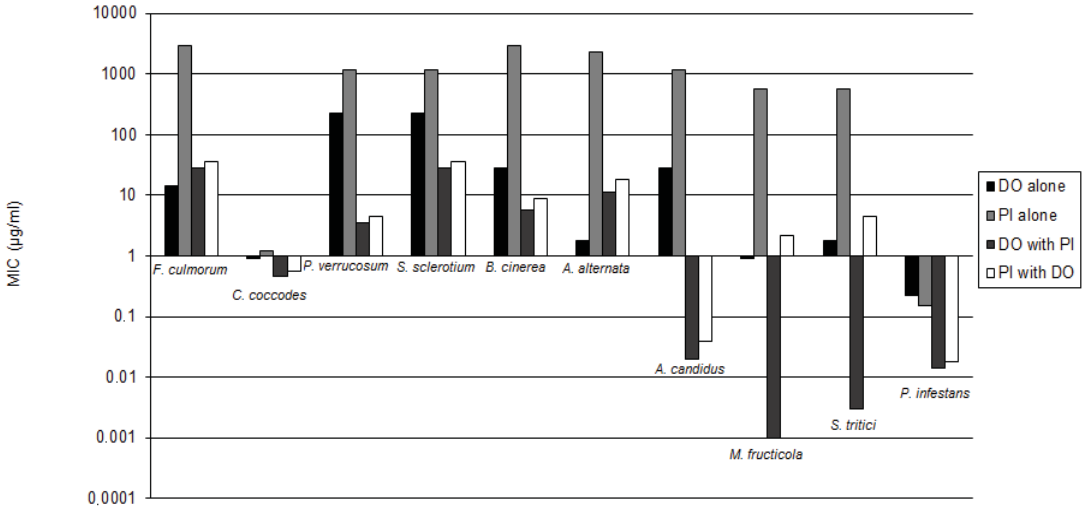

FIGURE 1
Differences of MIC values of single and combined dodine with picoxystrobin presented in logarithmic scale, P<0.05

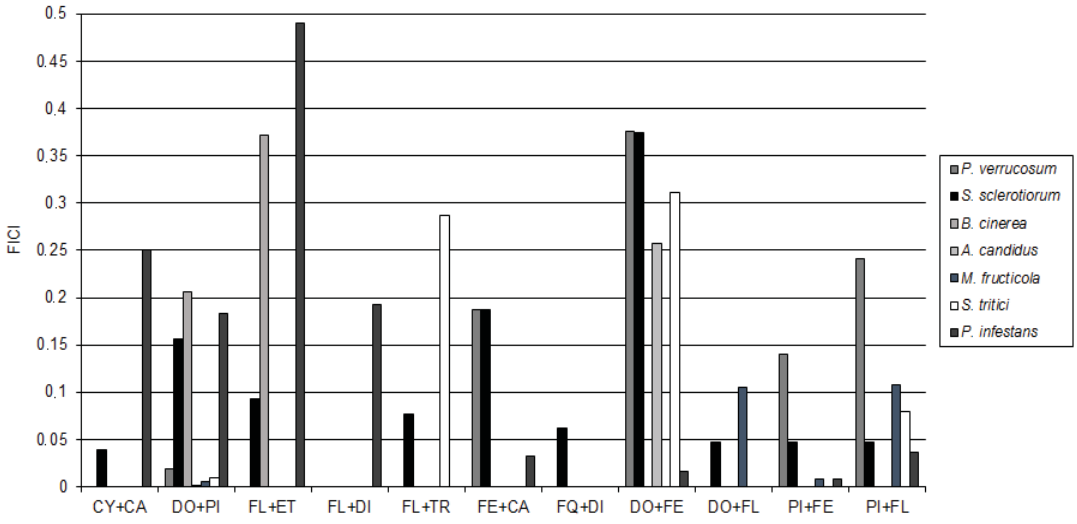

FIGURE 2
FICI values of combined active substances with synergistic effect (FICI ≤ 0.5). Cymoxanil with carboxin (CY+CA); dodine with picoxystrobin (DO+PI); fluazinam with etaconazole (FL+ET); fluazinam with dithianon (FL+DI); fluazinam with triflumizole (FL+TR); fenamidone with carboxin (FE+CA); fluquinconazole with dithianon (FQ+DI); dodine with fenamidone (DO+FE); dodine with fluazinam (DO+FL); picoxystrobin with fenamidone (PI+FE); picoxystrobin with fluazinam (PI+FL), P<0.05

DISCUSSION

Different susceptibility of fungi and oomycete to a.s and its mixtures is the result of internal species traits, thus there is a need to use commercial fungicides strictly predicted to combat particular species, especially that some plant diseases may be caused by different fungal pathogens with diverse susceptibility to fungicides. Some combined a.s have lower rate of resistance development [12]. Commercial products consist of combined a.s in different concentrations but in fact proper antifungal effect against particular fungi or oomycete has often a.s with the lowest MIC value (Table 2). Combination of several a.s in one commercial fungicide is often prepared just in case of additional susceptible pathogen occurrence and is not equivalent with its presence. This situation should be changed in view of the overuse of fungicides in agriculture and difficulties in creation of novel a.s with low risk of resistance development [13]. Our research revealed significant better growth inhibition and synergistic effect of dodine with picoxystrobin than their separate application on the majority of tested phytopathogenic fungi and oomycete ($P<0.05$), reflected in decrease (88%-99%) of MIC and low FICI values. Additionally mixtures of dodine or picoxystrobin with fenamidone and fluazinam also revealed good action against tested fungi. Good efficacy of picoxystrobin is also described by other authors [14], but this a.s similarly to dodine was not combined with other compounds. Dodine and picoxystrobin singly are registered only in several plant cultivations. Further studies are needed to asses presence or lack of phytotoxicity of these compounds and their combinations in various plant cultivations.

ACKNOWLEDGEMENTS

This research was partially funded by the Ministry of Science and Higher Education, Poland from the research project SIB-01. The authors are grateful to Bank of Plant Pathogens and Dr. Sylwia Stepniewska-Jarosz for delivery of fungal strains.

REFERENCES

[1] Talley, S.M., Coley, P.D., and Kursar, T.A. (2002) The effects of weather on fungal abundance and richness among 25 communities in the Intermountain West. BMC Ecol. 2, 7.

[2] Esturk, O., Yakar, Y. and Ayhan, Z. (2014) Pesticide residue analysis in parsley, lettuce and spinach by LC-MS/MS. J Food Sci Technol. 51, 458-466.

[3] Lozowicka, B., Abzeitova, E., Sagitov, A., Kaczynski, P., Toleubayev, K. and Li, A. (2015) Studies of pesticide residues in tomatoes and cucumbers from Kazakhstan and the associated health risks. Environ Monit Assess. 187, 609.

[4] Meneau, I. and Sanglard, D. (2005) Azole and fungicide resistance in clinical and environmental *Aspergillus fumigatus* isolates. Med Mycol. 43, 307-311.

[5] Hayes, L.E., Sackett, K.E., Anderson, N.P., Flowers, M.D. and Mundt, C.C. (2016) Evidence of selection for fungicide resistance in *Zymoseptoria tritici* populations on wheat in western Oregon. Plant Dis. 100, 483-489.

[6] Avenot, H.F. and Michailides, T.J. (2007) Resistance to boscalid fungicide in *Alternaria alternata* isolates from pistachio in California. Plant Dis. 91, 1345-1350.

[7] Cabanas, R., Abarca, M.L., Bragulat, M.R. and Cabanes, F.J. (2008) Comparison of methods to detect resistance of *Penicillium expansum* to thiabendazole. Lett Appl Microbiol. 48, 241-246.

[8] Chen, F., Liu, X. and Schnabel, G. (2013) Field strains of *Monilinia fructicola* resistant to both MBC and DMI fungicides isolated from stone fruit orchards in the eastern United States. Plant Dis. 97, 1063-1068.

[9] Saville, A., Graham, K., Grunwald, N.J., Myers, K., Fry, W.E. and Ristaino, J.B. (2015) Fungicide sensitivity of U.S. genotypes of *Phytophthora infestans* to six oomycete-targeted compounds. Plant Dis. 99, 659-666.

[10] Spolti, P., Del Ponte, E.M., Dong, Y., Cummings, J.A. and Bergstrom, G.C. (2014) Triazole sensitivity in a contemporary population of *Fusarium graminearum* from New York wheat and competitiveness of a tebuconazole-resistant isolate. Plant Dis. 98, 607-613.

[11] Odds F.C. (2003) Synergy, antagonism, and what the chequerboard puts between them. Journal Antimicrob Chemoth. 52, 1.

[12] Van den Bosch, F., Paveley, N., Van den Berg, F., Hobbelen, P. and Oliver, R. (2014) Mixtures as a fungicide resistance management tactic. Phytopathol. 104, 1264-1273.

[13] Leadbeater, A. (2015) Recent developments and challenges in chemical disease control. Plant Prot Sci. 51, 163-169.

[14] Malinski, Z. (2008) Studies on in vitro activity of picoxystrobin and its mixtures with other fungicides against *Ramulispora herpotrichoides* and *Ramulispora acuformis*. Pestycydy, 1-2.

Received: **16.05.2019**
Accepted: **10.12.2019**

CORRESPONDING AUTHOR

Piotr Iwaniuk
Institute of Plant Protection
National Research Institute,
Chelmonskiego 22 Street, 15-195 Bialystok, Poland

e-mail: p.iwaniuk@iorpib.poznan.pl

© by PSP Volume 29 – No. 04A/2020 pages 2725-2731 Fresenius Environmental Bulletin

MODELING OF NEAR-FIELD DILUTION OF BRINE DISCHARGES: A CASE STUDY IN SAMSUN BAY

Asu Inan*, Lale Balas

Department of Civil Engineering, Engineering Faculty, Gazi University, Turkey

ABSTRACT

Seawater desalination becomes crucial as fresh water scarcity increase and is an alternative water source. Uncontrolled brine discharges into the ambient seawater having excess salt, have negative impacts on the marine ecosystems. Numerical modeling is an appropriate tool for impact assessment of brine discharges. In this study, the near-field dilution of brine discharges was simulated, and the behaviors of dense pollutant jets were analyzed using CORMIX (CORMIX2), which can model of negatively buoyant plumes. The effects of different parameters such as total effluent discharge, ambient current, port number and port diameter on the near-field dilution of dense discharges were examined by different scenarios in Samsun Bay. In the Samsun Bay coastal waters, salinity and temperature during one year were measured. These measurements show the realistic physical characteristics of coastal waters into which effluent has been discharged. Based on the conditions of the ambient seawater, the diffuser must be designed in the legal regulations. The effects of the different parameters on the near-field dilution of brine discharges should be considered in the optimal design of diffusers. Therefore the sensitivity analyses of total effluent discharge, ambient current, port number and port diameter are presented.

KEYWORDS:
Brine discharges, near-field dilution, CORMIX, Samsun Bay, desalination

INTRODUCTION

Today 40 % of world's population experiences the water scarcity. The ratio is predicted as 60 % by the year 2025 because of the population growth, improvements in lifestyle, increased economic activity, and increased contamination of existing water supplies [1]. Seawater desalination is one of the solutions against the reduction of non-renewable drinking water source. Desalination of seawater reports for a worldwide water production of 24.5 million m^3/day. But seawater desalination can cause adverse impacts especially on the marine environment and coastal water quality because of the concentrated salt brine discharge (Bleninger and Jirka, 2008). To obtain a viable use of desalination technology, a project- and location-specific environmental impact assessment should be studied [2].

Brine discharge assessment methodology includes brine discharge characterization and impact, definition of plant operating conditions, definition of simulation scenarios, prediction of dilution rate and plume behavior, parametric sensitivity analyses, evaluation of brine discharge management [1].

The mechanism of desalination is separating dissolved salt from seawater for the production of freshwater. There are two types of technologies for desalination: Multi-Stage Flash (MSF) and Reverse Osmosis (RO). The increase of the use of desalination based on the three reasons: The reduce of traditional sources of freshwater such as rivers or artesian, high population growth rate in coastal zones, and new developments for RO, have reduced the cost of treatment of desalination.

The high salinity of desalination affects marine life negatively because it disturbs the osmotic balance of marine species with their environment that causes dehydration of cells, decrease of the turgor pressure, and may lead to the death of species [3]. Brine discharge into seawater has negative effects on the marine environments notably benthic and stenohaline species like Posidonia oceanica and Cymodocea nodosa seagrasses [4].

Desalination plants in Mediterranean countries are controlled by European Union water policy directives and Water Frame Work Directives (WFD). The main aim of WFD is to achieve reasonable water quality standards, but WFD does not have clear regulations and limits to control the disposal of brine into seawater [5].

The dilution, dispersion, and biological impacts of a brine discharge are figured out by the interaction of multiple factors specific to the site and discharge. In point of view of plume modeling, there are mainly three types of factors: Effluent characteristics, types and modes of discharge; boundary conditions representing the topography and other physical and biological characteristics of ambient water; hydrodynamic effects such as tides, waves, and currents [6].

This paper is focused on the near-field dilution. Numerical model CORMIX2 was used in the

simulations. CORMIX2 is the sub-model of CORMIX, which is suitable for multiport diffusers. Effects of total effluent discharge, diffuser length, port number, the port diameter on the near-field dilution of brine discharges have been investigated with different scenarios in Samsun Bay by CORMIX2.

MATERIALS AND METHODS

Near-Field Dilution of Brine Discharges. Seawater Reverse Osmosis (SWRO) plants are typified by its hypersalinity and so the effluent has greater density than seawater. The favored system to obtain higher dilution is discharge through inclined jets. The behavior of a negatively buoyant effluent discharged through an inclined single port jet is presented in Figure 1. It includes four different parts: (1) Because of the discharge velocity, the dense jet moves upwards. The buoyant jet balances the momentum at some distance from the discharge point. After the jet catch its maximum height, (2) the jets begin to decline. The buoyancy dominates the behavior. The jet jolts the bottom with an additional dilution because of turbulence phenomena and flow expansion. The region between the bottom impact zone and the far-field region (3) is called transition region, where flow behaves like a spreading layer. In the far-field region (4), the motion of the brine effluent becomes a gravity current [4].

Near-field dilution is affected by turbulent jet mixing, which is in control of discharge parameters, effluent and ambient physical properties. The far-field plume produces a gravity driven current moving along the seafloor. The mixing in the far-field is only dominated by the advection and diffusion [7].

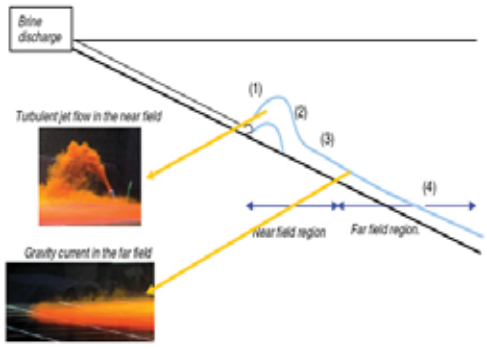

FIGURE 1
The behavior of a negatively buoyant effluent discharged through an inclined single port jet [4]

The orientation of the discharge port or nozzle to the horizontal, the jet exit velocity, and the density difference between the pollutant and ambient water enforce the near-field characteristics of negatively buoyant discharges, primarily. Currents increase the dilution in the near-field, and massive discharges need a large number of ports or nozzles. The port spacing and orientation of the diffuser axis to the prevailing currents can be said as primary factors for near-field dilution [6].

Modeling is a crucial prediction tool to design dense discharges, optimize the dilution, and minimize the environmental consequences [8]. There are three basic techniques to predict the near-field dilution of negatively buoyant discharges: Physical modeling using scaled laboratory models, semi-empirical equations and numerical modeling. Experimental studies for brine jets based on dilution measurements at the maximum rise height of the jet trajectory have recommended a typical design of a 60° inclination, which is providing the highest dilution in semi-empirical equations that are widely used for diffuser design with single (or non-merging) jets [9].

In recent years, computer technology has advanced mixing zone models as a predictive tool to simulate brine discharges behavior in the seawater receiving body. It provides savings of time and expenses when compared with laboratory works, but it is a complex and difficult effort [7].

Numerical modeling is now often used for near-field predictions. They are applied mainly for complex cases, such as merging jets, effects of currents, or effects of bottom slopes. Near-field predictions are usually made by entrainment models or computational fluid dynamics models [6].

It is necessary to discharge negatively buoyant effluent with high-velocity jets through a diffuser that effects rapid mixing by entrainment. Since the jets are dense, they reach a terminal rise height and then fall back to the sea bottom where they spread as a density current. The highest salinity in the bottom layers occurs where the centerline of the jet impacts the seabed. The length of the near-field is of order a few tens of meters.

Entrainment models are the most common tool for engineering analyses of jet and plume-type flows such as brine discharges. The entrainment hypothesis was first suggested by Morton et al. in 1956 [6]. Various models have been developed for near-field dilution. The models such as CORMIX, VISUAL PLUMES, and VISJET can be used for simulating negatively buoyant jets arising from brine discharges [8].

CORMIX is defined as ″a software system for the analysis, the prediction, and design of aqueous toxic or conventional pollutant discharges into diverse water bodies″ in its user manual [10]. It has three submodules: CORMIX1 (for submerged single port), CORMIX2 (for submerged multi ports), CORMIX3 (for surface discharges). It is able to simulate the behavior of effluents with positive, negative and neutral buoyancy under different discharge and ambient conditions. CORMIX is a steady-state model, therefore time series data and

statistical analyses cannot be considered. Maximum dilutions are obtained with the initial discharge angles in between 45^0-60^0 for the brine discharges [8]. CORMIX was validated and calibrated in previous studies in the literature [11-14].

FIGURE 2
Measurement points in Samsun Bay [15]

Study Coastal Waters: Samsun Bay. Samsun Province is located in the middle of Black Sea Coasts of Turkey between Yeşilırmak and Kızılırmak rivers. It has the highest population and the most significant network of transportation, education, health, and trade in the Black Sea Region. At six points, which are shown in Figure 2, salinity and water temperatures have been measured monthly between May 2015-May 2016 in the scope of the project entitled as "Modeling of Coastal and Estuarine Waters" supported by TUBITAK-MAM (Gebze, Kocaeli, Turkey). The coordinates and mean depths of the measurement points are listed in Table 1 [15].

TABLE 1
Measurement points in the study area of Samsun Bay [15]

Name	Depths (m)	Coordinates
KRD01	-8	41°22'28.16"N, 36°14'06.87"E
KRD02	-9.5	41°17'29.28"N, 36°21'31.86"E
KRD03	-10.5	41°16'47.58"N, 36°22'28.50"E
KRD04	-15	41°15'00.48"N, 36°26'39.12"E
KRD05	-8	41°16'44.24"N, 36°32'10.65"E
KRD06	-4.8	41°16'49.44"N, 36°21'22.98"E

Based on the measurements, salinity in Samsun Bay is in the range of 16.8ppt and 19.2ppt. Monthly salinity measurements at each of the points are illustrated in Figure 3. Minimum and maximum salinity were measured in March and August, respectively.

FIGURE 3
Salinity values in Samsun Bay (ppt) [15]

Surface water temperatures in Samsun Bay according to monthly measurements change from 8.6°C to 25.9°C. The monthly surface water temperatures are given in Figure 4. When the measured values are examined, it is observed that minimum average surface water temperature was recorded as 9.1°C in January and the maximum average surface water temperature was 25.1°C in July.

Seasonal average values of salinity, water temperature and density which is obtained as a function of depth averaged salinity and temperature, for Samsun Bay coastal waters are shown in Table 2, and maximum, and minimum monthly values are given Table 3.

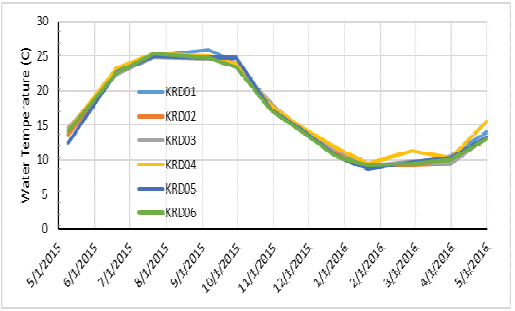

FIGURE 4
Surface water temperatures in Samsun Bay (^{0}C) [15]

TABLE 2
Seasonal average values for Samsun coastal area [15]

	Water temperature (^{0}C)	Salinity (ppt)	Density (kg/m^3)
Summer	24.3	18.80	1011.35
Winter	10.0	17.50	1013.33
Spring	12.5	17.34	1012.84
Autumn	18.6	17.51	1011.80

TABLE 3
Monthly maximum and minimum values for Samsun coastal area [15]

	Water temperature (^{0}C)	Salinity (ppt)	Density (kg/m^3)
July	25.1	19.2	1011.42
January	9.1	16.8	1012.90

RESULTS AND DISCUSSION

Modeling of Near-field Dilution. In this study, near-field dilution analysis of brine discharges was made by CORMIX2 for summer conditions in Samsun Bay. In Table 4, effluent properties and diffuser details have been listed [16].

TABLE 4
Effluent properties and diffuser details [16]

Diffuser length	L_d=100 m
Depth of discharge	h=20 m
Effluent discharge	Q=7 m^3/s
Salinity of effluent	S_{eff}=40 ppt
Temperature of effluent	T_{eff}=25 ^{0}C
Stratification	Uniform
Effluent density	ρ_{eff}=1027.13 kg/m^3
Port number	41
Port space distance	dx=2.5 m
Port diameter	D=0.3 m
Port height	HD=1 m
Port configuration	One directional
The angle between current & diffuser	90^0
Vertical discharge angle	60^0

Since the density of effluent is higher than the density of ambient water, there is a negative buoyancy. Therefore the jet behavior should be obtained by the diffuser details. The reaching of the jet to the water surface is aimed, and it is provided by the suitable velocity depended on vertical discharge angle and port diameter. After the effluent jet reaches to the sea surface, it begins to settle down, and far-field dilution occurs on the sea bottom. Near-field dilution and far-dilution have been modeled by CORMIX2 with the inputs given in Table 4 and the predictions of near- and far-field dilutions on the centerline trajectory are presented in Figure 5 to show the difference of scales of near-field and far field. The downstream distance of near-field was calculated to be 111.5m. After 111.5m, the brine pollutant begins to settle down, and far-field dilution starts. Near-field dilution is 105.3.

The discharge effect on the near-field dilution is represented in Figure 6. When the discharge increases from 5 m^3/s to 15 m^3/s, near-field dilution decreases as expected. The downstream distance of near-field dilution is around 110 m for all discharges. As the discharge increases, the pipe and port velocities increase. The velocity of the diffuser pipe preferably should not exceed 2.5 m/s [17]. Whereas, the port velocity should be preferably in the range of 0.6-6 m/s satisfying the densimetric Froude number not to be less than 10 [18]. In this study, the range of discharges is so selected that the port velocity changes in between 1.73 m/s to 5.18 m/s. The discharge Q=7 m^3/s results in a port velocity of 2.4 m/s and densimetric Froude number 11.30.

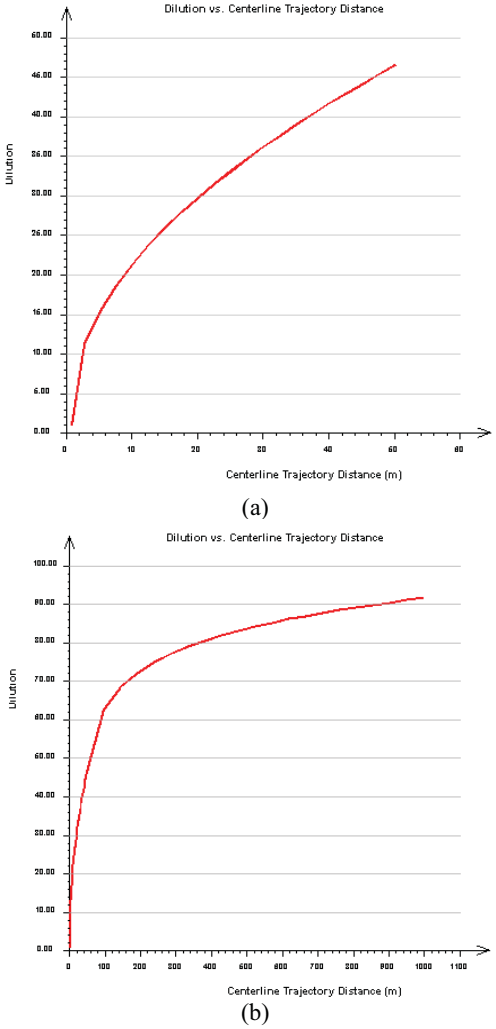

FIGURE 5
a) Near-field and b) far-field dilution on the centerline trajectory [16]

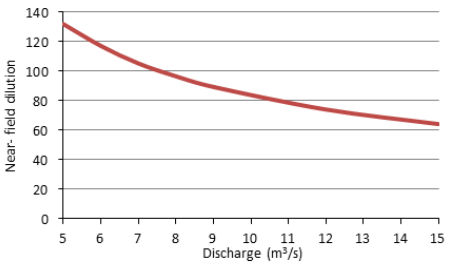

FIGURE 6
Discharge vs. Near-field Dilution

The relationship between the port number and near-field dilution of brine discharge is given in Table 5 and Figure 7.

TABLE 5
The effect of port numbers on the near-field dilution

Port Number	Downstream Distance of Near-field (m)	Port Velocity (m/s)	Densimetric Froude Number
11	114	9	42.11
21	112	4.72	22.06
41	112	2.42	11.3
61	112	1.62	7.6
81	132	1.22	5.72
101	124	0.98	4.6

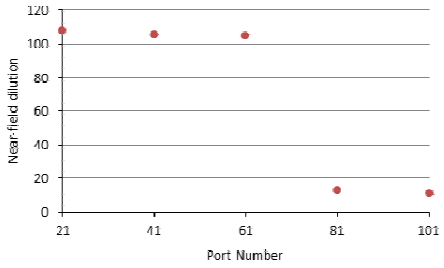

FIGURE 7
Number of ports vs. near-field dilution

When the number of ports on a diffuser is determined, point and line source effects should be considered. A point source is aimed for no merging of plumes. On the other hand, if the number of ports is increased, the densimetric Froude number decreases. For brine discharges, densimetric Froude number is a measure of velocity and momentum of the brine jet. So an optimum value for port numbers should be selected. Densimetric Froude number is given in Eq. 1.

$$Fr^* = \frac{v}{\sqrt{g\frac{\rho_a - \rho_0}{\rho_a}}} \quad (1)$$

Here v is port velocity, g is gravitational acceleration, d is port diameter, ρ_a is ambient water density, ρ_0 is effluent density. Densimetric Froude number should not be less than 10, preferably being in 20-25. In Figure 7, near-field dilution decreases suddenly when the port number exceeds 61. It shows that when the port numbers increase so much; plumes merge entirely, and near-field dilution decreases significantly. For design purposes, point sources are aimed. In this study, port numbers 21-61 result in almost the same near-field dilutions, having densimetric Froude numbers in the range of 22-7.6 and port velocities of 4.7-1.6 m/s respectively, as given in Table 5. It follows that port number more than 41 is not proper since it leads a densimetric Froude number less than 10 and small initial momentum for the brine jet.

Another effect on the near-field dilution is the port diameter. If the port diameter reduces, the velocity of the pollutant jet increases so near-field dilution increases as shown in Figure 8. Port diameter is recommended in between 0.2 m-1.0 m [18]. Small diameters can give high near-field dilutions, but port velocity so the densimetric Froude number should always be controlled. In this study, when the port diameter is 0.2m, port velocity is 5.43m/s. The recommended port velocity is in the range of 4-6 m/s to have enough initial momentum for high near-field dilutions. When the port diameter is in between 0.2-0.3 m, the near-field dilution becomes almost the same being about 100. It is seen from the Figure 8 that the port diameters above the value of 0.35m result in near-field dilutions below 40, having port velocities less than 1.8 m/s.

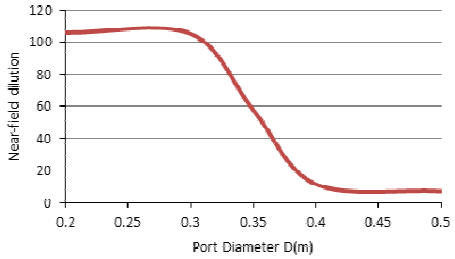

FIGURE 8
Port diameter vs. near-field dilution

Another parameter in the near-field dilution is the ambient current. In this study, the ambient current speeds from 5cm/s to 15cm/s are examined resulting in near-field dilutions in between 105 and 115, respectively. Ambient current are in the same direction with the horizonal port axis. It can be said that the effect of current speed on the value of near-field dilution is not so significant, but it changes the downstream distance of near-field dilution as shown in Figure 9.

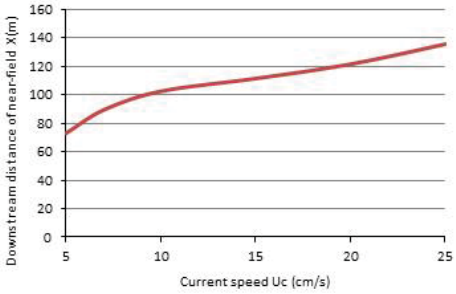

FIGURE 9
Current speed vs. downstream distance of near-field dilution

CONCLUSION

Near-field dilution of brine discharges was investigated since the importance of the seawater desalination has been increasing in the last decade. The density of the brine discharges is more than the density of the ambient seawater. Therefore brine discharges are negatively buoyant, and their behavior should be correctly analyzed to design the diffuser safely. The negatively buoyant pollutant behaves as a jet. In the first step, using the advantage of the high port velocity and initial momentum, it is aimed that pollutant jet reaches up to the water surface. Then, it begins to settle down, and far-field dilution starts to occur in the bottom layers of the sea. In this paper, the temperature and salinity of the Samsun Bay coastal waters obtained from the monthly measurements have been used to characterize the ambient seawater physical conditions. The effects of the discharge, port number, port diameter and ambient current on the near-field dilution of brine discharges are examined by CORMIX2. The near-field dilution must be higher than 40, recommended to be 100, according to Turkish regulations for water quality control [19]. In the design of the diffuser, it is recommended that the port velocity preferably should be in the range of 4-6 m/s, and the densimetric Froude number should be not less than 10, preferably being 20-25.

ACKNOWLEDGEMENT

Authors thank TÜBİTAK(Ankara) supporting the 1002 project entitled as “Modeling of Near-field of Brine and/or Heated Discharges” (114Y806) and TÜBİTAK-MAM (Gebze, Kocaeli, Turkey) supporting the project entitled as "Modeling of Coastal and Estuarine Waters”.

REFERENCES

[1] Alameddine I., El-Fadel M., (2007), Brine discharge from desalination plants: a modeling approach to an optimized outfall design, Desalination. 214, 241–260.

[2] Lattemann S., Höpner T., (2008), Environmental impact and impact assessment of seawater desalination, Desalination. 220, 1-15.

[3] Ahmad N., Raouf E. Baddour R.E., (2013), A review of sources, effects, disposal methods, and regulations of brine into marine environments, Ocean and Coastal Management. 87, 1-7.

[4] Palomar P., Lara J.L., Losada I.J., Rodrigo M., Alvárez A., (2012), Near-field brine discharge modelling part 1: Analysis of commercial tools, Desalination. 290, 14-27.

[5] Gibbons J., Papapetrou M., Epp C., (2008), Assessment of EU Policy: Implications for the Implementation of autonomous desalination units powdered by renewable resources in Mediterranean Region, Desalination. 220, 422–430.

[6] Jenkins S., Paduan J., Roberts P., Schlenk D., Weis J., (2012), Management of Brine Discharges to Coastal Waters Recommendations of a Science Advisory Panel, Southern California Coastal Water Research Project Costa Mesa, CA Technical Report 694.

[7] Loya-Fernández A., Ferrero-Vicente L.M., Marco-Méndez C., Martínez-García E., Zubcoff J., Sánchez-Lizaso J.L., (2012), Comparing four mixing zone models with brine discharge measurements from a reverse osmosis desalination plant in Spain, Desalination. 286, 217–224.

[8] Palomar P., Lara, J.L., Losada, I.J., (2012), Near-field brine discharge modeling part 2: Validation of commercial tools, Desalination. 290 (12), 28-42.

[9] Bleninger T., Jirka G.H., (2008), Modelling and environmentally sound management of brine discharges from desalination plants, Desalination. 221, 585–597.

[10] Jirka G.H., Doneker R.L., Hinton S.W., (1996), User Manual for CORMIX: A Hydrodynamic Mixing Zone Model and Decision Support System for Pollutant Discharges into Surface Waters, EPA, Cooperative Agreement No. CX824847-01-0, Washington D.C., USA.

[11] Bleninger, T., Jirka, G.H., (2008), Modelling and Environmental Sound Management of Brine Discharges from Desalination Plant, Desalination. 221, 585-597.

[12] Jirka, G.H., (2006), Integral Model for Turbulent Buoyant Jets in Unbounded Stratified Flows Part 2: Plane Jet Dynamics Resulting from Multiport Diffuser Jets, Environmental Fluid Mechanics. 6(1), 43-100.

[13] Maia L.P., Bezerra M.O., Pinheiro L., Redondo J.M., (2011), Application of the Cormix model to assess environmental impact in the coastal area: an example of the ocean disposal system for sanitary sewers in the city of Fortaleza (Ceará, Brazil), Journal of Coastal Research, SI 64, 922-926.

[14] Schreiner S., Krebs, T.A., Strebel D.E., Brindley, A., (2002), Testing the CORMIX Model Using the Thermal Plume Data from Four Maryland Power Plants″, Environmental Modelling and Software. 17(3), 321-331.

[15] Cebe,K., Yılmaz, N., İnan A., Balas C.E., Balas L., (2016), Modelling of Samsun(Inner) Bay and İzmir (Inner) Bay Coastal Water Bodies, TÜBİTAK-MAM Project Final Report, 242. Gazi University Sea and Aquatic Sciences Application and Research Center, Ankara, Turkey.

[16] Inan A., Yılmaz N., Balas L., (2017), Modeling of Near-field of Brine and/or Heated Discharges, TÜBİTAK 1002, Project No: 114Y806, Gazi University, Sea and Aquatic Sciences Application and Research Center, Ankara, Turkey.
[17] Doneker, R.L., Jirka, G.H., (2007), Cormix User Manual, EPA-823-K-07-001, Washington D.C., USA.
[18] Balas L., Inan A., Genç, A.N., (2013), Modelling of dilution of thermal discharges in enclosed coastal waters, Research Journal of Chemistry and Environment. 17(10), 82-89.
[19] Regulation of Water Pollution Control, (RWPC), (2004), Official Gazette, Ankara, Turkey, 31.12.2004, No: 25687, Clause 35, (in Turkish).

Received: **29.05.2019**
Accepted: **08.02.2020**

CORRESPONDING AUTHOR

Asu Inan
Department of Civil Engineering,
Engineering Faculty,
Gazi University
06570 Maltepe, Ankara, Turkey

e-mail: asuinan@gazi.edu.tr

© by PSP Volume 29 – No. 04A/2020 pages 2732-2738 Fresenius Environmental Bulletin

FABRICATED AgBr/rGO/g-C_3N_4 HYBRID PHOTOCATALYST FOR ENHANCED PHOTOCATALYTIC DEGRADATION OF TETRACYCLINE

Zhiguang Yang*, Xiaoming Shi, Peng Peng, Yueyun Yang, Yunlin Li

College of Chemistry and Chemical Engineering, Zhoukou Normal University, Zhoukou 466001, P.R. China

ABSTRACT

AgBr/rGO/g-C_3N_4 was prepared by calcination and hydrothermal method. The as-prepared catalysts were characterized by X-ray diffraction (XRD), Scanning electron microscopy (SEM), Fourier transform infrared (FTIR) and Ultraviolet–visible (UV–vis) diffuse reflectance spectra (UV-Vis DRS). The results showed that the AgBr/rGO/g-C_3N_4 hybrid photocatalyst has a similar diffraction pattern with AgBr and broad background absorption performance in the visible region, which is due to the presence of AgBr composites in AgBr/rGO/g-C_3N_4 sample. The FT-IR spectrum of AgBr/rGO/g-C_3N_4 composites possessed similar peaks to g-C_3N_4. The photocatalytic degradation of tetracycline was investigated under visible light irradiation with the as-prepared photocatalyst. The degradation rate could reach 72.6% in 60 min. The stability of the AgBr/rGO/g-C_3N_4 hybrid photocatalyst was evaluated under the same conditions of degradation, the possible degradation mechanism was further discussed.

KEYWORDS:
AgBr, rGO, g-C_3N_4, photocatalytic degradation, tetracycline

INTRODUCTION

With developing of society and economy, environments and energy issues became two concerns of persons. As antibacterial agent, antibiotics was used to treat non-bacterial inflections in the health and breading fields. Antibiotic wastewater was discharged into the natural environment without treatment or through simple treatment, which leaded to serious pollution in the water or soil [1]. To solve the problem, various methods, such as adsorption, electrochemistry, photocatalysis, etc., were designed and used [2]. Among these methods, photocatalytic method was largely paid attentions due to low cost and convenient treatment [3].

As a metal-free polymeric semiconductor with a narrow band gap of ≈ 2.7 eV, graphitic carbon nitride (g-C_3N_4) has been getting more and more attention in the field of novel photocatalyst research, because it can harvest a substantial visible light for achieving highly efficient photocatalytic performance [4]. The unique properties of g-C_3N_4 foliated structure which possessed large surface area, excellent chemical stability and tunable electron band structure, can expand its applications. More, g-C_3N_4 is readily prepared by thermal polymerization of abundant nitrogen precursors, including dicyandiamide, urea, thiourea, melamine, etc. Among these precursors, melamine has been recently found to be an excellent precursor for synthesizing sheet-like g-C_3N_4 with high specific surface area and excellent chemical stability. Unfortunately, melamine-derived-g-C_3N_4 exhibits a limited visible light absorption region of less than 460 nm as well as a poor quantum efficiency, resulting in its low photocatalytic activity [5]. Therefore, it is of significance to develop novel g-C_3N_4 based photocatalysts with wide visible light response and high photocatalytic activity.

Up to now, many efforts have been explored to improve the photocatalytic activity of g-C_3N_4, including doping with metal and/or nonmetal ions, construction of heterojunctions with other semiconductors, copolymerization with organic molecules, photosensitization with dyes etc. [6] However, certain drawbacks were still involved in these strategies. Specifically, the isolated states formed by doping possibly act as recombination centers for the photogenerated carriers; Although heterojunction structures enhanced the separation of photo-induced hole-electron pairs, they usually sacrifice their redox ability; The copolymerization with structure-matching organic additives is a unique way for modifying the band gap and positions of g-C_3N_4, but only a small amount of organic molecules can anchor into the texture edge of g-C_3N_4; The dye-sensitized photocatalysts generally suffer from a decline in photocatalytic activity due to the instability of dye molecules under light irradiation. Consequently, although extensive efforts have been made toward developing the g-C_3N_4-based photocatalysts with enhanced photocatalytic activity, the actual performance of those photocatalysts have not satisfied with the application. It proves that the modification is an effective way to enhance the photoac-

tivity of pure g-C_3N_4. To overcome this limitation, it is feasible to construct a multi-composite system by further introducing cocatalyst, which can provide the efficient redox reaction sites, inhibit the possible charge recombination and lower the reaction activation energy [7, 8].

The most widely used cocatalyst is noble metal (such as Pt), which can improve CO_2 conversion activity and influence the product selectivity of g-C_3N_4. Meanwhile, graphene materials, including graphene oxide (GO) and reduced graphene oxide (rGO), are well known as efficient cocatalysts for g-C_3N_4 due to their superior electron mobility, two-dimensional (2D) layered structure, large surface area and perfect chemical stability. Indeed, ternary composites containing graphene and g-C_3N_4 have been reported with enhanced charge transfer rates and photocatalytic activities, such as BiOI/g-C_3N_4/GO [9], ZnO/g-C_3N_4/GO [10], CdS/g-C_3N_4/rGO [11], WO_3/g-C_3N_4/rGO [12], Bi_2WO_6/g-C_3N_4/rGO [13] and TiO_2/rGO/g-C_3N_4 [14]. Expectedly, the photocatalytic activity of binary composites can be further improved by employing graphene as cocatalyst.

Herein, we report that fabrication of ternary AgBr/rGO/g-C_3N_4 hybrid photocatalysts with high photodegradation activity on TC under simulated sunlight irradiation. AgBr with narrow band gap is employed as semiconductor photosensitizers to harvest light and promote the charge separation. Meanwhile, rGO functions as electron collectors to promote the charge transfer and provides reactive sites for photodegradation of TC. The enhanced photocatalytic degradation activity of the as-prepared photocatalyst strongly suggests the formation of a Z-scheme heterojunction, which is detailedly discussed in this work based on the experimental results. This work highlights a simple way to enhance the photocatalytic activity of g-C_3N_4 towards to photodegradation of TC by coupling with AgBr and rGO, and affords an ideal example for developing similar ternary composite photocatalysts with high photocatalytic activity.

MATERIALS AND METHODS

Materials. Natural flake graphite was purchased from Aladdin Industrial Corporation (Shanghai, China). All of the other chemical reagents in the study were obtained from Sinopharm Chemical Reagent Co. Ltd, and used as received without further purification. The water used in the experiment is deionized (DI) water. Graphite oxide was prepared by modified Hummers method.

Preparation of AgBr/rGO/g-C_3N_4. Preparation of GO. The preparation of graphenes was described in detail in the previous report [15]. Briefly, graphite oxide was synthesized from graphite according to modified Hummers method, where 1.0g graphite powder and 2.0g $NaNO_3$ were mixed in a three-necked flask at 0 °C for 15 min. Subsequently, 15 mL concentrated sulphuric acid was added slowly in the above flask under the stirring and 3.0 g $KMnO_4$ was put in controlling the 10°C. After above steps, the temperature is adjusted to 35°C and kept for 2 h, and reached to 98°C after adding 40 mL deionized water for 40min. To reduce the temperature around 70°C, 10 mL H_2O_2 was added drop by drop. When no bubble, the mixture was poured into 100 mL of deionized water and filtered to give a residue of graphite oxide for three times at the speed of 13000r/min for 5min. Graphite oxide was dispersed and washed repeatedly with 5% HCl to remove sulfate ions. Graphite oxide was finally washed with deionized water until the filtrate was observed to be of neutral pH. Slurry graphite oxide was then dried at 65 °C for 36 h in a vacuum oven. Powdered graphite oxide was obtained after grinding. Graphene oxide in the composite was obtained by thermal method.

Preparation of AgBr/rGO/g-C_3N_4. It was prepared through calculation and hydrothermal method. First, g-C_3N_4 was prepared by calcinating melamine using the muffle furnace in 550°C. Second, Powdered graphite oxide and g-C_3N_4 was vigorously stirring for 30 min. 10 mL Silver nitrate solution was added drop by drop under the condition of stirring, and 10mL hexadecyl trimethylammonium bromide solution (CTAB) was dropped. Then the mixture was stirred for 30 min and poured into the teflon core of the reactor. This reactor was calcinated in the air dry oven of 160 °C for 6 h. After natural cooling, the mixture was put out and washed using deionized water and absolute ethyl alcohol three times, respectively. Various ratios of AgBr/rGO/g-C_3N_4 were obtained by drying under 60°C.

Characterization. The specified characterization description is provided. For example, the crystal phase of the products was studied by X-ray diffraction (XRD) on a Bruker D8 X-ray diffractometer (Rigaku, Japan), using the wavelength of Cu Kα radiation (λ =1.54056 nm) operated at 40kV and 80mA with a scan rate (2θ) of 5-80°. Scanning electron microscopy (SEM) image and energy dispersive spectroscopy (EDS) analysis were performed by JEOL-JEM2010 (JEOL, Japan). UV-vis diffuse reflectance absorbance spectra of all composites were recorded by using a UV–vis spectrophotometer (Shimadzu UV-2450, Shimadzu, Japan). Fourier transform infrared (FTIR) spectra were recorded with a Nicolet Nexus 470 spectrometer (Thermo Scientific, USA).

Photocatalytic activity measurement. A 300-W Xe arc lamp (Changzhou Siyu, China) was employed as simulated sunlight source with (visible light). A 200 mL customized glass flask with double neck was employed as reactor. The sample (50 mg) was added to the glass flask, dispersed in the TC solution (100 mL with 20mg/L). The flask was put in the photoreactor, and dark reaction was proceeding for 30min to achieve adsorption desorption equilibrium, then the above lamp was turned on and kept for 60 min. 6 mL mixture was put out internal 10 min and poured into the centrifuge tube. Supernatant was collected after centrifuging, and absorbance value was measured. The photodegradation rate was calculated as following formula (1):

$$\text{Photodegradation rate} = (A_0 - A_t)/A_0 \times 100\% \quad (1)$$

A_0 and A_t represented initial and t moment absorbance value, respectively.

RESULTS AND DISCUSSION

XRD. The XRD spectra of the AgBr was shown in Figure1, some peaks of at 26.9°, 31.0°, 44.5°, 52.6°, 55.2°, 64.6° and 73.3° belonging to the (111), (200), (220), (311), (222), (400) and (420) crystal planes（JCPDS：6-438) [16]. The characteristic peaks located 13.9º and 28.4º indexed to (100) and (002) planes (JCPDS 87-1526) of g-C_3N_4 [17]. Characteristic peaks of rGO was not present, it may be because a little amount in the composite.

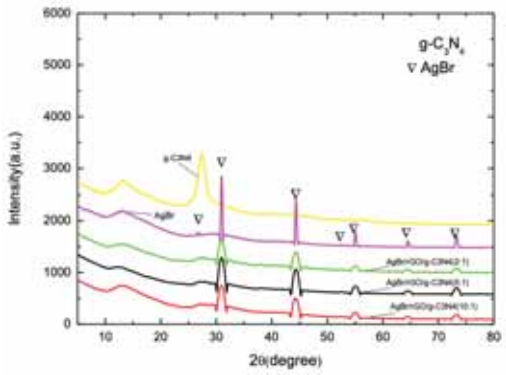

FIGURE 1
The XRD patterns of AgBr, g-C_3N_4 and g-C_3N_4/rGO/AgBr

SEM and EDS. SEM of AgBr and g-C_3N_4/rGO/AgBr hybrid were shown in Figure 2a and b. Peanut shaped AgBr with the size about 2 μm was shown in Figure 2a. And the shape of AgBr is similar spheres due to dispersing on the surface of g-C_3N_4 (Figure 2b). From Figure 2b, it can be found various sheet structure of rGO and g-C_3N_4 in g-C_3N_4/rGO/AgBr hybrid. Figure2c shows the EDS of g-C_3N_4/rGO/AgBr, it can be easy found the hybrid contains elements of C, N, Ag and Br. Indicating AgBr was anchored on the surface of rGO and g-C_3N_4 or inside.

UV-vis DRS. The optical absorption properties of the materials are presented in Figure 3 and the absorption edges of pristine g-C_3N_4 and AgBr are about 450 (Eg = 2.7eV) and 550 nm (Eg =2.6eV), respectively. Compared with g-C_3N_4 and AgBr, the absorption edge of composite has significant shift, indicating that rGO modification has been incorporated into the lattice of g-C_3N_4 and played a critical role for composite, which is beneficial for improved photocatalytic activity [18].

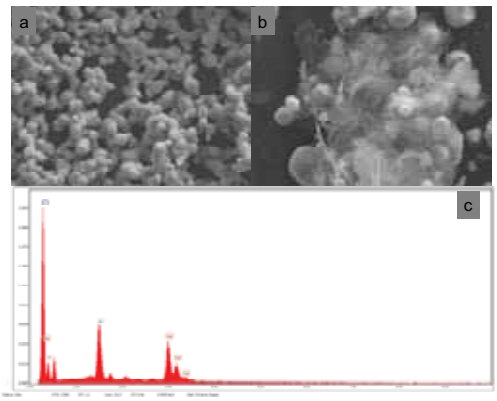

FIGURE 2
SEM images of the as-prepared (a) AgBr, (b) g-C_3N_4/rGO/AgBr, (c) EDS spectrum of g-C_3N_4/rGO/AgBr

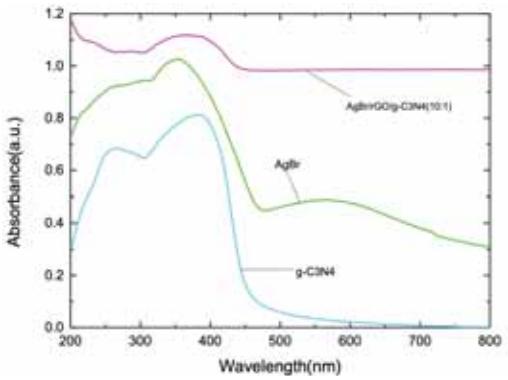

FIGURE 3
UV-vis DRS of different photocatalysts

FT-IR. Figure 4 shows the FT-IR spectra of the as-prepared AgBr, g-C_3N_4, and g-C_3N_4/rGO/AgBr. In the FT-IR spectrum of g-C_3N_4, the sharp peak at 809cm^{-1} is ascribed to the typical characteristic stretching mode of triazine units. Several peaks observed in 1241 cm^{-1}, 1320 cm^{-1}, 1409 cm^{-1}, 1572 cm^{-1} and 1639cm^{-1} correspond to the typical stretching modes of C-N heterocycles in g-C_3N_4. And peaks located in 3416 cm^{-1}, 2921 cm^{-1}

and 2851cm^{-1} belonged to asymmetric oscillation of O-H, symmetric vibration of O-H and C-H. Two characteristic peaks laid in about 1734cm^{-1} and 1615cm^{-1} was attributed to C=O stretching of COOH and bending vibration of -OH group. The large peak located in 1140cm^{-1} was attributed to stretching vibration of C-O-C bond. The g-C_3N_4/rGO/AgBr shows similar absorption peaks to g-C_3N_4 as the weak absorptions of AgBr can be covered by those strong ones from g-C_3N_4. This phenomenon can be easily found in previous reports.

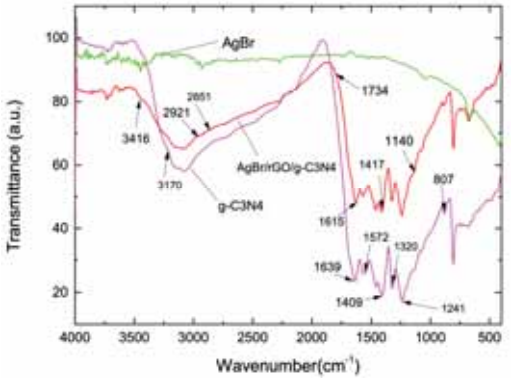

FIGURE 4
FT-IR spectra of the as-prepared photocatalysts

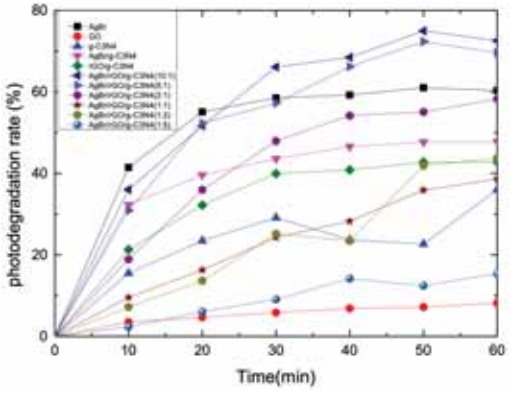

FIGURE 5
Photodegradation of TC on AgBr/rGO/g-C_3N_4 photocatalysts with different weight ratios of AgBr, rGO to g-C_3N_4

Photocatalytic degradation experimental. Photodegradation of TC under visible-light irradiation was considered to evaluate activity of the prepared materials. Photodegradation of TC on AgBr/rGO/g-C_3N_4 nanocomposites with different weight ratios of AgBr, rGO to g-C_3N_4 was shown in Figure 5. As can be seen, weight ratio of AgBr/rGO to g-C_3N_4 has remarkable influence on the degradation reaction and the photocatalytic activity of AgBr/rGO/g-C_3N_4 (weight of g-C_3N_4 is 0.3g and the rate of AgBr to rGO is 5:1) nanocomposite shows the most excellent photocayalytic activity among prepared materials, which is higher than that of not only pure g-C_3N_4 and rGO, but also other nanocomposites. Degradation performance of various prepared materials on TC was shown in Figure6. It was found that under the visible light irradiation for 60 min, 40, 47.8 and 72.6% of TC were degraded on g-C_3N_4, AgBr/g-C_3N_4 and AgBr/rGO/g-C_3N_4 (weight of g-C_3N_4 is 0.3g and the rate of AgBr to rGO is 5:1) nanocomposite, respectively. Which the composite indicated understanding degraded activity may attributed to good match among AgBr, rGO and g-C_3N_4.

Kinetic analysis. The kinetics analysis of any degradation process represents an important stage in the design of the degradation system. To inspect the catalytic degradation kinetics of tetracycline by composite materials, AgBr/rGO/g-C_3N_4 (weight of g-C_3N_4 is 0.3g and the rate of AgBr to rGO is 5:1) was conducted dynamic analysis using Langmuir-Hinshelwood kinetic equation. Reaction efficiency was cacluated through following formula (2):

$$-\frac{dC_t}{dt} = K\frac{k_{TC}C_t}{1+k_{TC}C_0} \quad (2)$$

K and K_{TC} represent adsorption constant (L•mg^{-1}) and reaction rate constant (mg•L^{-1}•min^{-1}) of Langmuir Hinshelwood, respectively. C_t and C_0 mean TC concentration at time t and initial time. If the initial concentration of the reaction solution is small enough, formula (2) transfers to quasi first order kinetic equation (3).

$$Ln(\frac{C_t}{C_0}) = k't \quad (3)$$

k′ represent quasi first order kinetic constant. Linearity of ln（C_t/C_0）and t showed in the Figure 7, in which straight slope means quasi first order kinetic parameters (Table1).

According to formula (2), the pseudo-second order kinetics model was expressed through equation (4) and (5). Linear relation between $\frac{1}{C}$ and t was shown in Figure8 [19-21].

$$r = -\frac{dC}{dt} = kC^2 \quad (4)$$

$$\frac{1}{C} = kt + b \quad (5)$$

As shown in Table1, quasi first order kinetic constant is more large than second. Indicating that the process of photodegradation for TC obeyed the first-order kinetic model.

Stability tests. Stability is an important parameter for catalyst. The stability of prepared AgBr/rGO/g-C_3N_4 photocatalysts was evaluated in terms of performing the TC photodegradation repeatedly five times. As shown in Figure 9, after five

recycles for the photodegradation of TC, the catalyst does not exhibit any significant loss of activity, indicating the catalysts have good stability for photocatalytic degradation of TC.

Photodegradation mechanism. To clarify the mechanism of the remarkably enhanced photocatalytic performance of the AgBr/rGO/g-C_3N_4 photocatalysts from the following two aspects are presented in Figure10. (1) The rGO as one conductor media, when the light irradiation the photocatalyst, the photogenerated electrons of C_3N_4 could fast transfer to the conductor band of AgBr via the rGO, also the electrons could further react to O_2 and generate the active groups, the active groups could degrade the TC to the products. (2) The AgBr/rGO/g-C_3N_4 could form the Z type photocatalyst with the recombination of electrons of AgBr and holes of C_3N_4 by the rGO transfer approach. Therefore the electrons from C_3N_4 could act with the O_2 and form the super-oxide radicals and further degrade the TC, the holes from AgBr could direct degrade the TC to products [22, 23].

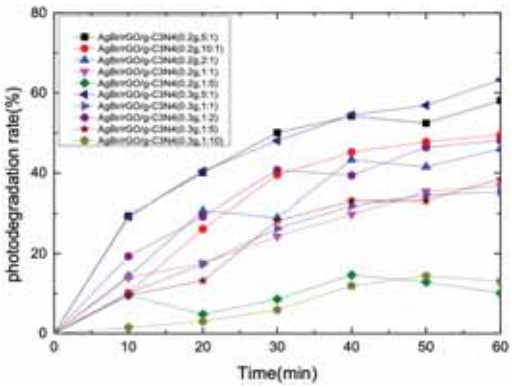

FIGURE 6
Degradation performance of as-prepared photocatalysts on TC

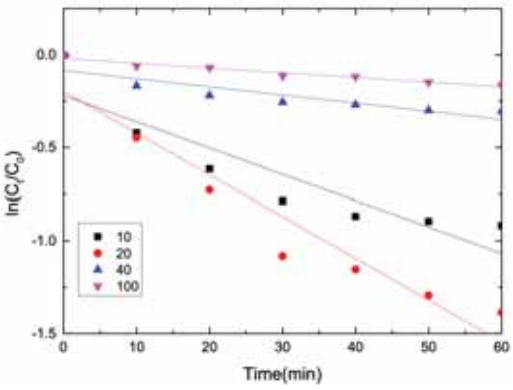

FIGURE 7
The pseudo-first order kinetics model of degradation processes

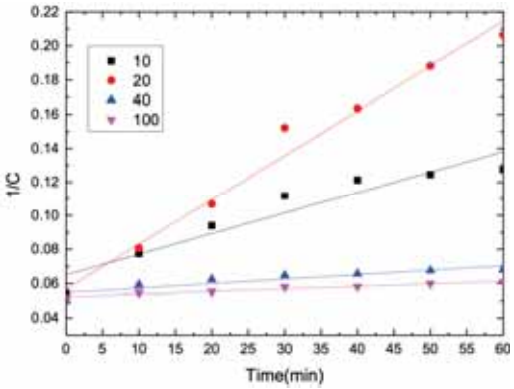

FIGURE 8
The pseudo-second order kinetics model of degradation processes

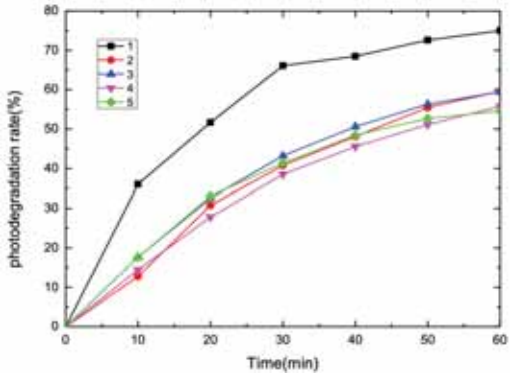

FIGURE 9
Cycled experiments with AgBr/rGO/g-C_3N_4 photocatalyst

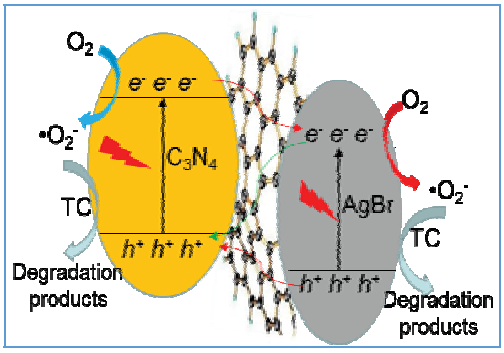

FIGURE 10
The possible mechanism of degradation processes

CONCLUSIONS

rGO as a media for successfully fabricating the g-C_3N_4/GO/AgBr hybrid photocatalyst, the obtained photocatalysts show excellent photocatalytic performance for degradation of TC. In the photocatalytic degradation processes, the rGO plays key role for the electrons transfer and the rGO

TABLE 1
The kinetics data of photocatalytic degradation tetracycline with AgBr/rGO/g-C_3N_4 hybrid photocatalyst

Different TC concentrations (mg/L)	pseudo first-kinetic		pseudo second-kinetic	
	K'	R^2	k	R^2
10	-0.01414	0.79527	0.00122	0.89073
20	-0.02243	0.90588	0.00263	0.97669
40	-0.0044	0.74936	0.00026	0.78913
100	-0.00255	0.93485	0.00014	0.94482

could effectively enhance the separation of electrons and holes which improved the photocatalytic degradation of TC. This work affords one simple and ideal way for developing ternary hybrid photocatalysts with high photocatalytic activity.

ACKNOWLEDGEMENTS

We gratefully acknowledge the financial support of the Key Research Project of Henan Higher Education Institute (15A430055).

REFERENCES

[1] Li, Y.J., Qiao, X.L., Zhang, Y.N., Zhou, C.Z., Xie, H.J. and Chen, J.W. (2016) Effects of halide ions on photodegradation of sulfonamide antibiotics: Formation of halogenated intermediates. Water Research. 102, 405-412.

[2] Ruan, X.W., Hu, H., Che, H.N., Che, G.B., Li, C.M., Liu, C.B. and Dong, H.J. (2019) Facile fabrication of $Ag_2O/Bi_{12}GeO_{20}$ heterostructure with enhanced visible-light photocatalytic activity for the degradation of various antibiotics. Journal of Alloys and Compounds. 773, 1089-1098.

[3] Zhen, Q., Gao, L.C. Sun, C.C., Gong, H.Q., Hu, P.F., Song, S.L. and Li, R. (2018) Honeycomb-like TiO_2@GO nanocomposites for the photodegradation of oxytetracycline. Materials Letters. 228, 318-321.

[4] Lu, X.J. Wang, Y., Zhang, X.Y., Xu, G.Q., Wang, D.M., Lv, J. Zheng, Z.X. and Wu, Y.C. (2018) NiS and MoS_2 nanosheet co-modified graphitic C_3N_4 ternary heterostructure for high efficient visible light photodegradation of antibiotic. Journal of Hazardous Materials. 341, 10-19.

[5] Miao, X.L., Ji, Z.Y., Wu, J.J., Shen, X.P., Wang, J.H., Kong, L.R., Liu, M.M. and Song C.S. (2017) g-C_3N_4/AgBr nanocomposite decorated with carbon dots as a highly efficient visible-light-driven photocatalyst. Journal of Colloid and Interface Science. 502, 24-32.

[6] Liu, Q., Chen, T.X., Guo, Y.R., Zhang, Z.G. and Fang, X.M. (2017) Grafting Fe(III) species on carbon nanodots/Fe-doped g-C_3N_4 via interfacial charge transfer effect for highly improved photocatalytic performance. Applied Catalysis B: Environmental. 205, 173-181.

[7] Guan, J.R. Wang, H.Q., Li, J.Z., Ma, C.C. and Huo P.W. (2019) Enhanced photocatalytic reduction of CO_2 by fabricating In_2O_3/CeO_2/HATP hybrid multi-junction photocatalyst. Journal of the Taiwan Institute of Chemical Engineers. 99, 93-103.

[8] Wang, H.Q., Wu, D.Y., Liu, C.Y., Guan, J.R., Li, J.Z., Huo, P.W., Liu, X.L., Wang, Q., Yan, Y.S. (2018) Fabrication of Ag/In_2O_3/TiO_2/HNTs hybrid-structured and plasma effect photocatalysts for enhanced charges transfer and photocatalytic activity. Journal of Industrial and Engineering Chemistry. 67, 164-174.

[9] Dai, K., Lu, L.H., Liang, C.H., Zhu, G.P., Liu, Q.Z., Geng, L. and He, J.Q. (2015) A high efficient graphitic-C_3N_4/BiOI/graphene oxide ternary nanocomposite heterostructured photocatalyst with graphene oxide as electron transport buffer material. Dalton Transaction. 44, 7903-7910.

[10] Jo, W.K., Clament Sagaya Selvam, N. (2015) Enhanced visible light-driven photocatalytic performance of ZnO-g-C_3N_4 coupled with graphene oxide as a novel ternary nanocomposite. Journal of Hazardous Materials. 299, 462-470.

[11] Jo, W.K., Clament Sagaya Selvam, N. (2017) Z-scheme CdS/g-C_3N_4 composites with RGO as an electron mediator for efficient photocatalytic H_2 production and pollutant degradation. Chemical Engineering Journal. 317, 913-924.

[12] Lu, N., Wang, P., Su, Y., Yu, H.T., Liu, N. and Quan, X. (2019) Construction of Z-Scheme g-C_3N_4/RGO/WO_3 with in situ photoreduced graphene oxide as electron mediator for efficient photocatalytic degradation of ciprofloxacin. Chemosphere. 215, 444-453.

[13] Jo, W.K., Kumar, S., Eslava, S. and Tonda, S. (2018) Construction of Bi_2WO_6/RGO/g-C_3N_4 2D/2D/2D hybrid Z-scheme heterojunctions with large interfacial contact area for efficient charge separation and high-performance photoreduction of CO_2 and H_2O into solar fuels. Applied Catalysis B: Environmental. 239, 586-598.

[14] Hu, L.M., Yan, J.T., Wang, C.L., Chai, B. and Li, J.F. (2019) Direct electrospinning method for the construction of Z-scheme TiO_2/g-C_3N_4/RGO ternary heterojunction photocatalysts with remarkably ameliorated photocatalytic performance. Chinese Journal of Catalysis. 40, 458-469.

[15] Zhou, M.J., Han, D.L., Liu, X.L., Ma, C.C., Wang, H.Q. Tang, Y.F., Huo, P.W., Shi, W.D., Yan, Y.S. and Yang, J.H. (2015) Enhanced visible light photocatalytic activity of alkaline earth metal ions-doped CdSe/rGO photocatalysts synthesized by hydrothermal method. Applied Catalysis B: Environmental. 172-173, 174-184.

[16] Chen, D.M., Wang, Z.H., Du, Y., Yang, G.L., Ren, T.Z. and Ding H. (2015) In situ ionic-liquid-assisted synthesis of plasmonic photocatalyst Ag/AgBr/g-C_3N_4 with enhanced visible-light photocatalytic activity. Catalysis Today. 258, 41-48.

[17] Yan, S.C., Li, Z.S. and Zou, Z.G. (2009) Photodegradation performance of g-C_3N_4 fabricated by directly heating melamine. Langmuir. 25, 10397-10401.

[18] Li, J.Z., Liu, K., Xue, J.L., Xue, G.Q., Sheng, X.J., Wang, H.Q., Huo, P.W. and Yan, Y.S. (2019) CQDS preluded carbon-incorporated 3D burger-like hybrid ZnO enhanced visible-light-driven photocatalytic activity and mechanism implication. Journal of Catalysis. 369, 450-461.

[19] Huo, P.W., Lu, Z.Y., Liu, X.L., Liu, X.L., Gao, X., Pan, J.M., Wu, D., Ying, J., Li, H.M. and Yan, Y.S. (2012) Preparation molecular/ions imprinted photocatalysts of La^{3+}@POPD/TiO_2/fly-ash cenospheres: Preferential photodegradation of TCs antibiotics. Chemical Engineering Journal. 198-199, 73-80.

[20] Wang, H., Yang, X. and Zi, J. (2016) High photocatalytic degradation of tetracycline under visible light with Ag/AgCl/activated carbon composite plasmonic photocatalyst. Journal of Industrial and Engineering Chemistry. 35, 83-92.

[21] Wang, H.Q., Qiu, Y., Li, J.Z., Ji, H.S. and Wang, Q. (2018) Preparation of Ag_3PO_4/CeO_2/g-C_3N_4 composite photocatalyst for efficient degradation of tetracycline under visible light. Fresen. Environ. Bull. 27, 8928-8937.

[22] Zhou, Y.J. Li, J.Z., Liu, C.Y., Huo, P.W. and Wang, H.Q. (2018) Construction of 3D porous g-C_3N_4/AgBr/rGO composite for excellent visible light photocatalytic activity. Applied Surface Science. 458, 586-596.

[23] Miao, X.L., Shen, X.P., Wu, J.J., Ji, Z.Y., Wang, J.H., Kong, L.R., Liu, M.M. and Song, C.S. (2017) Fabrication of an all solid Z-scheme photocatalyst g-C_3N_4/GO/AgBr with enhanced visible light photocatalytic activity. Applied Catalysis A: General. 539, 104-113.

Received: **30.05.2019**
Accepted: **23.01.2020**

CORRESPONDING AUTHOR

Zhiguang Yang
College of Chemistry and Chemical Engineering,
Zhoukou Normal University,
Zhoukou 466001 – P.R. China

e-mail: guangjszj@163.com

© by PSP Volume 29 – No. 04A/2020 pages 2739-2745 Fresenius Environmental Bulletin

INVESTIGATION OF WASTE FOUNDRY SAND AND SEWAGE SLUDGE REUSE AS LANDFILL CAP LAYER MATERIAL

Gulgun Dede[1,*], Ayse Bengu Sunbul[2], Mirac Gedikli[1]

[1]Department of Environmental Engineering, Faculty of Engineering, Sakarya University, Sakarya, Turkey
[2]Department of Civil Engineering, Faculty of Engineering, Bulent Ecevit University, Zonguldak, Turkey

ABSTRACT

In this study, the availability of waste foundry sand in the production of landfill cap layer material was investigated. Two type of alkali phenolic resin (inorganic) bonded waste foundry sand which one of them is concretive added sand and the other one CO_2 process was used in the experiments. Test samples were prepared as follow; 75%, 80%, 85%, 90%, 95% and 100% foundry sand by volumetric as replacement of sewage sludge as a multiple material. Mechanical, leaching and micro-structural properties including index properties such as particle size distribution, specific gravity and consistency limits besides permeability, compaction characteristics, shear strength test and odometer test of foundry sand-based samples to obtain the useful fractions of foundry wastes and sewage sludge in landfill area. Geotechnical test results indicate that waste foundry sand with sewage sludge can satisfactorily be used as a landfill cap layer material and can be utilized as landfill cap layer material without any environmental concern with the requirements of local authorities.

KEYWORDS:
Waste foundry sand, sewage sludge, landfill cap layer, reuse

INTRODUCTION

Due to the growth of the world and the increase in population and industry, waste material threat on environment is became the prime concern. Therefore, usage of natural resources efficiently by minimizing the consumption of materials and recovering qualified wastes is a very substantial topics that must be analysed. This is precisely why the recovery of waste materials has become very important recently both in terms of economy and environmental awareness. With the increasing of foundry processes in recent years, huge portions of by-product material produced during casting process in foundry industries [1]. Especially through the production of foundry sand in huge amounts from ferrous and nonferrous metal foundry industries, foundry sands became an important waste product nowadays. Foundry sands are high quality silica sand with homogeneous physical properties [1]. Usually 4 to 5 tons of sand is required for 1 ton of castings [2]. Production of a ton of casting material, 0.6-0.8 tonnes of waste are produced and 0.4-0.6 tonnes of foundry sand are formed [2]. For example, according to 2011-year production figures in Turkey, 1 million tons of cast iron production made, an estimated 450 000 tonnes of waste have occurred from processes [2, 3]. Approximately 65% of this amount is foundry waste sand, 10% slag, 15% dust-sludge and 10% refuse, oil, stone, paint, barrels [2]. Despite the fact that it creates so much waste, the process is the world's indispensable sector and 1.4% of the world's casting production are made in Turkey [2].

Foundries successfully recycle and reuse these sands more than one in the process, but after a while the sand is removed from the foundry when it becomes unusable again by the reason of physico-chemical degradation of the sand, exposure to molten metal at 1500 °C during casting, loss of resin binding properties in the sand, and mechanical breakdown of the sand particles [1, 2, 4]. Each year several thousand tons of foundry sand is wasted occupying substantial parts of the storage areas due to the negative public perception. In addition, being of heavy metals in foundry sands causes ground water pollution or plant uptake, bloating storage costs and scarcity of landfill areas are anxious circumstances for the foundry industry. The most appropriate and the most acceptable disposal of this waste is a major problem for industries that are increasingly concerned in the search for environmental protection and long-term sustainable development. For this reason, scientists are looking for an optimal disposal method to ensure that the foundry sands are recycled to economically valuable useful products rather than as waste.

The studies for the evaluation of waste foundry sand have started in the early 1980s. In these studies, generally infiltration characteristics and permeability of waste foundry sand and utilization in geotechnical applications as a recyclable material were investigated. Later on scientist focused on using foundry sands for civil engineering applications.

Availability of waste foundry sands in road construction and cap layer for sports and playground areas as an impermeable layer was investigated. Especially foundry sands with higher bentonite content shown to have low hydraulic conductivity, suggesting that waste foundry sands can be reused in barrier layers in landfill final covers [5]. Besides waste foundry sands were used in cement production, mortar and brick, briquette, road stone construction and in remediation of marginal soils [2, 3, 6]. Despite much effort and energy, only 32% of foundry sand is beneficially reused in construction in the word [7]. And correspondingly, studies on foundry wastes evaluation in our country is yet limited.

Nowadays alternative uses of this excess sand are introduced by reason of inevitable increases in landfilling costs [7]. Thence waste foundry wastes are reused as a landfill cap layer material. Landfill capping is a type of barrier technology between the risky environment and the surface. Therefore, to use foundry sands in a sustainable manner, the engineering properties of this material needs to be properly evaluated and assessed against local requirements.

In the limited evaluation applications in our country, it is stated that waste foundry sands are mostly used as a cap layer and a small amount is evaluated in engineering areas (cement, paving stones, borders and concrete park-garden furniture). This is mainly due to insufficient information on this subject and the lack of experimental work about its possible beneficial uses or due to regulatory requirements today in force across some countries that classify foundry sands among hazardous wastes [7]. In addition, the inadequacies of legal and bureaucratic regulations and incentive mechanisms for the re-evaluation of industrial wastes in different engineering applications are also slowing the evaluation processes [8]. Also most of these waste is considered as non-hazardous by USEPA [9] and these results suggest their great potential for reuse in beneficial applications [10, 11]. These alternate applications offer cost savings for both foundries and user industries, and an environmental benefit at local and national level [12].

Besides foundry wastes, the environmental policies aim to increase reuse of biodegradable wastes such as sewage sludge's for similar reasons of the overloading of landfill areas. Evaluation of sewage sludge as soil regulator is already a common practice but includes risks such as heavy metals which are controlled by heavy regulations in many countries. Potential for the accumulation of these heavy metals in the soil in case of long-term maturities, for plant uptake via food chain, and for disturbing soil functions studied in several research [13, 14, 15, 16]. However utilization of sludge as an addition to construction and building material including building bricks, lightweight artificial aggregates, and cement-like materials is a win–win strategy because it not only converts the wastes into useful materials but it also alleviates the disposal problems [17, 18, 19, 20]. Similarly, sewage sludge's can be utilized with waste foundry wastes as a landfill cap layer material. Thus the potential benefit of using sewage sludge as a cap layer material also include immobilizing of heavy metals. The main goal of the study was to obtain the usability of waste foundry sand with sewage sludge as landfill cap layer material. In this manner, this study can be a solution to the utilization and the beneficial usage of these wastes.

MATERIALS AND METHODS

Two type of alkali phenolic resin (inorganic) bonded waste foundry sand with concretive added sand and CO_2 process (S1-S6 and C1-C6, respectively) were used in the tests that obtained from a casting facility operating in Sakarya province. Waste foundry sands used in the trials were the wastes of iron, steel and metal casting plants after moulding of clean sands at elevated temperatures in the production of metal-steel parts. Waste foundry sand is used until all the available chemical and physical properties are lost. Both waste casting sands used in the experiments were black coloured due to the carbon contents and has 0-1 mm grain size. According to the identification tests, foundry sands were classified as non-hazardous waste. The sewage sludge used in the tests was provided from Sakarya Municipal Wastewater Treatment Plant. Dewatered and stabilized sludge cake was used in the tests. The heavy metal contents of sewage sludge were obtained much lower than the limits recommended by the Turkish Regulation on Use of Domestic and Urban Treatment Sludge in Soil [21] with the European Union Communities 86/278/EEC [22] or by the USEPA [9] and sludge was classified as non-hazardous waste. Content of concretive sand and CO_2 process sand are demonstrated in Table 1.

TABLE 1
Content of concretive sand and CO_2 process sand.

Content	S1	C1
Silica sand	96.00	97.00
Water	4.00	3.00
Resin	5.00	3.00
Other ingredients	1.00	1.00

S1: Sand (100 kg) + alkali phenolic resin (5 kg) + concretive (400 mlt)
C1: Sand (100 kg) + alkali phenolic resin (3 kg) + CO_2 (3 kg)

Test samples were prepared as follow; 75%, 80%, 85%, 90%, 95% and 100% foundry sand by volumetric replacement of sewage sludge as a multiple material. Prepared samples are labelled as follows: S1:100% concretive sand, S2:95% concretive sand+5% sludge, S3:90% concretive sand+10% sludge, S4:85% concretive sand+15% sludge, S5:80% concretive sand+20% sludge and S6:75%

TABLE 2
Index properties of concretive sand and CO_2 process sand.

Index	S1	C1
Specific gravity	2.68	2.70
Max. dry density, gr/cm^3	1.666	1.589
Optimum water content, %	16	22
>2 mm (gravel size), %	0	0
0.074-2.00 mm (sand size), %	99.6	99.9
<0.075 mm (silt and clay size), %	0.4	0.1
Plasticity	Non-plastic	Non-plastic

S1: Sand (100 kg) + alkali phenolic resin (5 kg) + concretive (400 mlt)
C1: Sand (100 kg) + alkali phenolic resin (3 kg) + CO_2 (3 kg)

concretive sand+25% sludge. C1:100% CO_2 sand, C2:95% CO_2 sand+5% sludge, C3:90% CO_2 sand+10% sludge, C4:85% CO_2 sand+15% sludge, C5:80% CO_2 sand+20% sludge and C6:75% CO_2 sand+25% sludge. Mechanical, leaching and micro-structural properties including index properties such as particle size distribution, specific gravity and consistency limits besides permeability, compaction characteristics, shear strength test and odometer test of foundry sand-based samples were analysed to define the top geophysical methods to locate the useful fractions of foundry wastes and sewage sludge in landfill area.

Index properties include particle size distribution, specific gravity and consistency limits were measured for each samples. Atterberg Limit test was performed according to ASTM D 4318 Standard Test Methods to determine consistency limits including liquid limit (W_L), plastic limit (W_P) and plasticity index (I_P). Purpose of "Atterberg test" is to estimate the consistency of a soil in various water contents. All samples were cured for one week at the optimum moisture content in humidity chamber. The only deviation of ASTM D 4318 procedure was the hydration period. The cause for this situation is that the test samples must have passed the casting process and the water content is very low. Based on the suggestions of Kleven [23], the hydration period was extended to a week to activate the bentonite ingredient in the mixture by the means of a Cassagrande Apparatus [5, 6, 7, 24, 25, 26]. Index properties of concretive sand and CO_2 process sand are shown in Table 2.

Particle size distribution was obtained by mechanical and hydrometer analyses according to ASTM D 422 Particle Size Analysis of Soils Standards. All foundry sand specimens were soaked in water for a one week prior to particle size distribution analysis. For each sample, the portion passing through the No. 200 sieve was subjected to hydrometer analysis [5, 6, 7, 24, 25]. The specific gravity values of the prepared samples were determined according to ASTM D 854 Specific Gravity of Soil Solids [24, 25, 26]. The water-conducting capacity of a soil called permeability (hydraulic conductivity) that obtained by a falling-head permeameter according to falling head method.

Shear strength test was realized according to ASTM D 1633 Compressive Strength of Molded Soil-Cement Cylinders which is a common measure of the strength of a mixture design in roadways and is often refer to obtain the structural layer coefficients of the subbase layers for designing pavements. The mixtures prepared with two different waste foundry sand and sewage sludge were compacted at two different compactive efforts. After compaction, the specimens were extruded with a hydraulic jack, sealed in plastic wrap, and cured for 1 and 7 days at 100% relative humidity and controlled temperature (21 ± 2 °C) before testing [7]. Compaction is a geotechnical application for determining the properties of soils by using mechanical energy. The main purpose of compaction is to increase shear strength, stiffness and density of soils. The test was performed by a compressed method with a certain method, the largest dry unit volume weight content of water. The compaction characteristics of the mixtures were determined by using Standard Proctor Test according to the ASTM D 698 Standard Test Methods for Laboratory Compaction Characteristics of Soil Using Standard Effort [5, 6, 7, 24, 25]. Odometer test was applied to determine the compressibility properties and hydraulic conductivity of the samples [24].

RESULTS AND DISCUSSION

Atterberg limits. In accordance with the Atterberg test results, all samples were classified as non-plastic. Particle size distribution curves of the concretive and CO_2 processes samples are presented in Figure 1 and Figure 2. Compaction curves for Standard Proctor Efforts for concretive and CO_2 processes samples are shown in Figure 3 and Figure 4. The particle distributions are obtained similar in both of two type foundry sand samples and were classified as SP (poorly graded sand) according to the Unified Soil Classification System (USCS) [24]. The particle size distributions are similar and resemble that of the base sand used at these foundries, except for the fines fraction. The finest content (percent passing No. 200 sieve) ranges from 10% to 15% generally as obtained by Abichou et al. [24]. The coefficient of uniformity C_u for concretive foundry sand ranges from 1.57 to

1.62 and ranges from 1.56 to 1.63 for CO_2 processes samples.

The specific gravity values obtained from the experiments varied between 2.40-2.70 gr/cm^3. Generally, the specific gravity of concretive sands was found to be lower than those of CO_2 process samples and sludge added sands. This may due to the presence of sand which is known to be porous, that might have resulted in lower specific gravity for the waste foundry sands.

Compaction and hydraulic conductivity. Permeability (hydraulic conductivity) values of both foundry processes with sludge addition obtained in the range of $1x10^{-4}$ cm/sec to $1x10^{-7}$ cm/sec. The range of permeability seems to be large and it primarily linked to the amount and type of binders and additives used and the pouring temperatures through which these sands have undergone which high pouring temperatures may destroy the activity of some resin. The thickness of the soil barrier depends on the waste type and permeability, physico-chemical properties of the soil, the nature of groundwater resources in the area and the use of alternative liner technology. Generally, the coefficients of permeability of waste foundry sand samples were fall in a very low permeability range. Also the percentage of fines had a predominant effect on the permeability of sands. The waste foundry sand embankment shall be encapsulated using a compacted clay base, sidewalls and top cover having permeability less than 10^{-7} cm/sec. The clay base shall be at least three feet thick to prevent any ground water contamination and help in attenuation mechanisms. For very low permeability concretive foundry sand or the site already containing sufficient thick natural low permeability layers, this clay base requirement may be omitted. The top cover and sidewalls be at least two feet thick to greatly reduce any infiltration and be properly compacted. A compacted two to three feet compacted clay base layer having permeability less than 10^{-7} cm/sec shall be used to preclude the ground water coming into contact with the pavement system [26]. The hydraulic conductivity values were obtained less than $1x10^{-7}$ cm/sec with increased sludge rate. This value indicates that the samples can be evaluated for impermeability purposes in landfill areas.

The permeability of concretive foundry sand was found to be low as compared to the CO_2 process samples or sludge added sand. The low permeability of concretive sand was due to the clay binder which resulted in the generation of many fines and thus contributed a significant reduction in permeability. There is an inverse relationship between dry density and hydraulic permeability. In a manner similar to natural clays, the hydraulic conductivity decreases, the compaction water content increases. At similar compaction water contents, lower hydraulic conductivities are generally obtained with higher compaction effort. The permeability of CO_2 process samples and sludge added sand was comparable to uniform fine sand. Hydraulic conductivity decreases 5%-15% sewage sludge ratio. When the sludge ratio is increased to 20%, then the reduction slows down to $1x10^{-6}$ cm/sec and $1x10^{-7}$ cm/sec.

When the compression energy is increased, higher dry unit volume weights are provided in lower water contents, in other words a good compression is achieved. In addition, the effect of better compacted material on hydraulic conductivity is quite small. As mentioned in similar studies, when the impermeable layer is made from the casting sand, the compression energy is limited [25]. According to the compaction characteristic test results, the dry weight values were obtained between 1.40-1.80 gr/cm^3. Optimum dry density varied between 12-22%.

Hydraulic conductivity of the foundry sands typically varied less than a factor of eight as the water content varied from dry to wet of optimum water content and as the compaction energy was varied within typical ranges (reduced to modified Proctor). Results show that, for a given effort, maximum dry unit weight increases slightly with the sewage sludge addition until the sludge content reaches about 15%

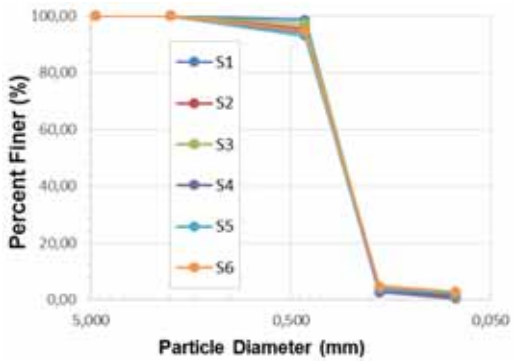

FIGURE 1
Particle size distribution curves of the concretive sand samples.

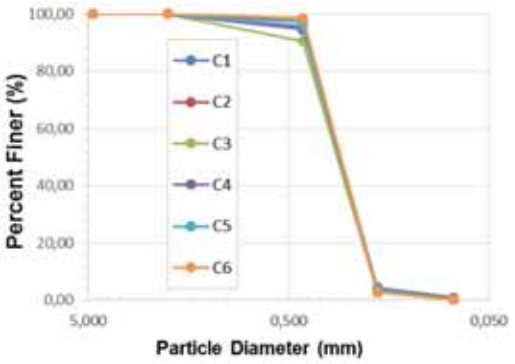

FIGURE 2
Particle size distribution curves of CO_2 process samples.

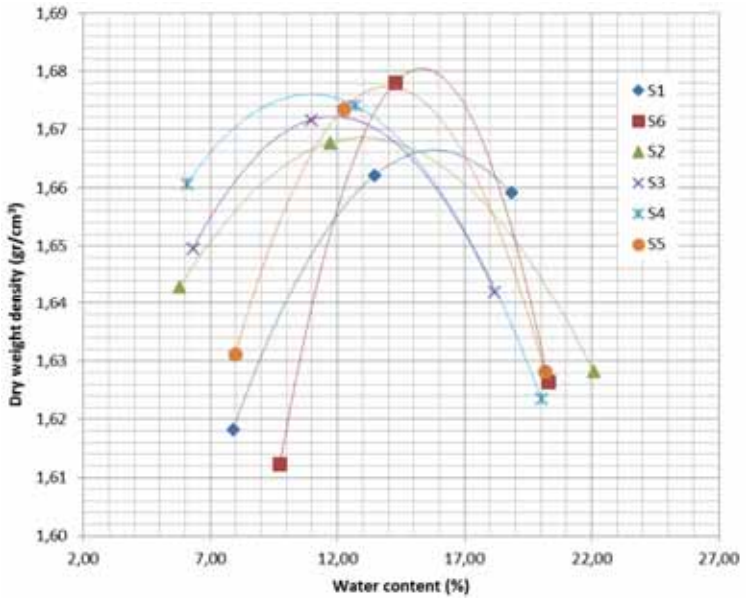

FIGURE 3
Compaction curves for Standard Proctor Efforts for concretive process samples.

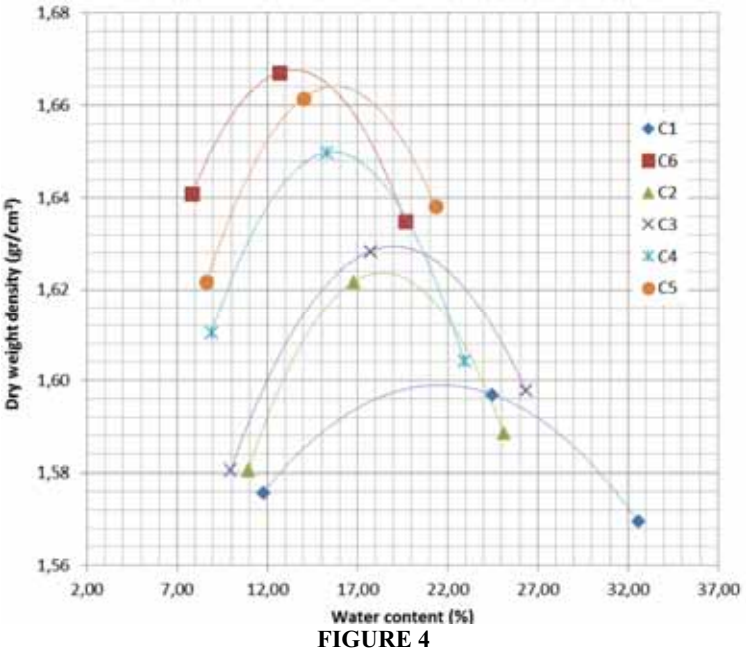

FIGURE 4
Compaction curves for Standard Proctor Efforts for CO_2 process sand samples.

and then decreases for higher sludge contents. Similar results were obtained with Kenney et al. [27] for bentonite addition. They report that maximum dry unit weight of their mixtures increased until the bentonite content reached 16%, and subsequently decreased. Optimum water content is lower for higher compaction effort, which is typical for finer-grained soils. The trends with bentonite content are weaker than those observed for the maximum dry unit weight, which suggests that optimum water content of foundry sand is not sensitive to bentonite content.

Hydraulic conductivity decreases as the LL and PI increase, which is expected because LL and PI are positively correlated with sewage sludge content. Hydraulic conductivities <=1X10^{-7} cm/s are attained for foundry sands having LL >= 20 and PI >= 2 regardless of compactive effort [25]. Obtained results showed that hydraulic conductivity decreases with sewage sludge addition for both sand types. It can be concluded that the hydraulic conductivity decreases as dry density increases for all sand types. The in-

crease in shear strength ratio is 14-27% for concretive sand and 17-41% CO_2 process sand, respectively. Results showed that sewage sludge was more effective on CO_2 process sand to concretive sand. Laboratory testing results showed that the waste foundry sand samples has a liquid limit and a plasticity index conductive to achieving the low hydraulic conductivity necessary for construction of cap layers. Hydraulic conductivity testing showed that the waste foundry sand samples can be compacted to the low hydraulic conductivity ($\leq 1x10^{-7}$ cm/sec) using a broad range of compactive efforts and a wide range of water contents.

CONCLUSIONS

The results of an experimental study of using waste foundry sand as a cap layer in landfill storage areas are presented and discussed. The index properties, compression characteristics and relations between hydraulic conductivity and compression conditions were determined to determine the most appropriate sewage sludge content. Relationships between hydraulic conductivity and compaction water content and compaction energy for foundry sands exhibits trends similar to natural clays. The obtained data show that as the compression energy increases, the dry unit volume index increases, the water content decreases, and better compression is obtained. It was observed that the permeability decreased to $1x10^{-7}$ m/s. The best compression is achieved with the addition of 15% sewage sludge. The hydraulic conductivity decreases rapidly to 15% of the sludge and $1x10^{-7}$ m/s was obtained for the 15% sludge ratio. After the sludge ratio has increased by 15-20%, there is a slight increase observed for the hydraulic conductivity. The hydraulic conductivity of waste foundry sand samples decreases with increasing liquid limit, plasticity index and sewage sludge. Foundry sands samples having liquid limit >20, plasticity index >2, or sewage sludge content >15% can be compacted to achieve hydraulic conductivities $<10^{-7}$ cm/s. Both sands have sufficiently high liquid limit to function as well as materials for using in a final capping of a landfill. Also, area testing is required to confirm that casting layers and casting layers can be formed in the field, which has a low hydraulic conductivity at a sufficient level. These tests should be conducted in a manner that simulates the field condition as closely as possible. According to the reuse of waste foundry sand and sewage sludge is important for protecting the environment, this research could be produced and provide a definitive solution to this waste problem. The general evaluation of the results shows that the both of foundry sand types containing sewage sludge can be used as a cap layer for landfill areas.

ACKNOWLEDGEMENTS

This research was supported by the Commission for Scientific Research Projects of Sakarya University (No: 2017-50-01-082). This paper is derived from a conference proceeding which can be accessed at: http://cevrevakfi.org.tr/wp-content/uploads/2018/12/ISEM2018_Proceedings_13.12.2018.pdf.

The authors declare that they have no conflict of interest.

REFERENCES

[1] Singh, G. and Siddique, R. (2012) Abrasion resistance and strength properties of concrete containing waste foundry sand (WFS). Constr Build Mater. 28, 421–426.

[2] Başar, H.M., Aksoy, N.D. (2012) Recovery applications of waste foundry sand. Journal of Engineering and Natural Sciences. 30, 205-224.

[3] Bakis, R., Koyuncu, H., Demirbas, A. (2006) An investigation of waste foundry sand in asphalt concrete mixtures. Waste Manage Res. 24, 269–274.

[4] Siddique, R., Kaur, G., Rajor, A. (2010) Waste foundry sand and its leachate characteristics. Resour Conserv Recy. 54, 1027–1036.

[5] Dungan, R.S., Dees, N.H. (2009) The characterization of total and leachable metals in foundry molding sands. J Environ Manage. 90, 539-548.

[6] Gürkan, E., Çoruh, S. (2012) The use of waste foundry sand for treatment of textile wastewater. Journal of History Culture and Art Research. 1(4), 531-544. (in Turkish)

[7] Guney, Y., Aydilek, A.H., Demirkan, M.M. (2006) Geoenvironmental behavior of foundry sand amended mixtures for highway subbases. Waste Manage. 26, 932–945.

[8] Başar, H.M., Aksoy, N.D. (2013) Investigation of usability of waste foundry sand in ready-mixed concrete. Journal of Engineering and Natural Sciences. 31, 517-528.

[9] USEPA (2002) Beneficial Reuse of Foundry Sand: A Review of State Practices and Regulations. Sector Strategies Division, Office of Policy, Economics, and Innovation, U.S. Environmental Protection Agency Washington, DC.

[10] Carnin, R.L.P., Folgueras, M.V., Luvizao, R.R., Correia, S.L., Cunha, C.J., Dungan, R.S. (2012) Use of an integrated approach to characterize the physicochemical properties of foundry green sands. Thermochim Acta. 543, 150–155.

[11] De Koff, J.P., Lee, B.D., Dungan, R.S., Santini, J.B. (2010) Effect of compost-, sand-, or gypsum-amended waste foundry sands on turfgrass yield and nutrient content. J Environ Qual. 39, 375– 383.

[12] Deng, A. and Tikalsky, P.J. (2008) Geotechnical and leaching properties of flowable fill incorporating waste foundry sand. Waste Manage. 28(11), 2161-2170.
[13] Carbonell, G., Pro, J., Gomez, N., Babin, M.M., Fernandez, C., Alonso, E., Tarazona, J.V. (2009) Sewage sludge applied to agricultural soil: Ecotoxicological effects on representative soil organisms. Ecotoxicol Environ Saf. 72, 1309–1319.
[14] Lloret, E., Pascual, J.A., Brodie, E.L., Bouskill, N.J., Insam, H., Juárez, M.F.D., Goberna, M. (2016) Sewage sludge addition modifies soil microbial communities and plant performance depending on the sludge stabilization process. Appl Soil Ecol. 101, 37–46.
[15] Mondal, S., Singh, R.D., Patra, A.K., Dwivedi, B.S. (2015) Changes in soil quality in response to short-term application of municipal sewage sludge in a typic haplustept under cowpea-wheat cropping system. Environ Nanotechnol Monit Manage. 4, 37–41.
[16] Petersen, S.O., Henriksen, K., Mortensen, G.K., Krogh, P.H., Brandt, K.K., Sorensen, J., Madsen, T., Petersen, J., Gron, C. (2003) Recycling of sewage sludge and household compost to arable land: fate and effects of organic contaminants, and impact on soil fertility. Soil Tillage Res. 72, 139–152.
[17] Arsenovic, M., Radojevic, Z., Stankovic, S. (2012) Removal of toxic metals from industrial sludge by fixing in brick structure. Constr Build Mater. 37, 7–14.
[18] Cusido, J.A., Cremades, L.V. (2012) Environmental effects of using clay bricks produced with sewage sludge: Leachability and toxicity studies. Waste Manage. 32, 1202–1208.
[19] Juel, M.A.I.J., Mizan, A., Ahmed, T. (2017) Sustainable use of tannery sludge in brick manufacturing in Bangladesh. Waste Manage. 60, 259–269.
[20] Weng, C.H., Lin, D.F., Chiang, P.C. (2003) Utilization of sludge as brick materials. Adv Environ Res. 7, 679–685.
[21] Republic of Turkey Ministry of Environment and Urban (2010) Regulation on Use of Domestic and Urban Treatment Sludge in Soil. Official Gazette, No: 27661, Ankara. (in Turkish)
[22] Council of the European Communities (1986) Council Directive 86/278/EEC (EU Sewage Sludge Directive). Official Journal of the European Communities, OJ. L., vol 181, 6-12.
[23] Kleven, J.R. (1998) Mechanical Properties of Excess Foundry System Sand and Evaluation of its Use in Roadway Structural Fill. M.Sc. Thesis. University of Wisconsin-Madison, Madison, WI.
[24] Abichou, T., Benson, C.H., Edil, T.B. (1998) Using waste foundry sand for hydraulic barriers. Recycled Materials in Geotech Applications. GSP 79, ASCE, Reston, 86-99.
[25] Abichou, T., Benson, C.H., Edil, T.B. (2002) Foundry green sands as hydraulic barriers: field study. J Geotech Geoenviron Eng. 128(3), 206-215.
[26] Javed, S. (1994) Use of waste foundry sand in highway construction. Joint Highway Research Project. JHRP 94/23 Final Report. School of Civil Engineering, Indiana Department of Transportation, Purdue University.
[27] Kenney, T., Van Veen, W., Swallow, M. and Sungaila, M. (1992) Hydraulic conductivity of sand-bentonite mixtures. The Canadian Geotechnical Journal. 29(3), 364–374.

Received: **30.05.2019**
Accepted: **08.02.2020**

CORRESPONDING AUTHOR

Gulgun Dede
Department of Environmental Engineering
Engineering Faculty
Sakarya University
54187 Sakarya – Turkey

e-mail: gulgunk@sakarya.edu.tr

© by PSP Volume 29 – No. 04A/2020 pages 2746-2751 Fresenius Environmental Bulletin

INTERDEPENDENCE OF CYTOTOXIC ACTIVITIES OF BIOACTIVE COMPONENTS IN BLACK SEED (*NIGELLA SATIVA* L.) ESSENTIAL OIL AND INTRACELLULAR ZINC LEVELS

Olcay Boyacioglu*

Department of Food Engineering, Faculty of Engineering, Aydin Adnan Menderes University, Efeler, Aydin, 09010, Turkey

ABSTRACT

Intracellular zinc level has been shown to modulate the efficacy of cancer drugs. In this study, the cytotoxicity of thymoquinone (TQ) and alpha-hederin (AH), bioactive components in black seed (*Nigella sativa*) essential oil, was determined on human prostate (PC3) and colon cancer (HT-29 and HCT-116) cell lines. Then, the effects of TQ and AH were measured on PC3 cells in presence or absence of Zn^{2+} achieved by exogenous $ZnCl_2$ and a strong Zn^{2+} chelator, N,N,N',N'-tetrakis (2-pyridylmethyl) ethylenediamine (TPEN), respectively. Cell viability was measured using CellTiter-Glo® Luminescent Assay. The cytotoxicity of TQ and AH increased in a dose-dependent manner, and 100% cytotoxicity was achieved with 24 h treatment of 100 µM TQ or 50 µM AH. TPEN began to show cytotoxicity at 5 µM and most of the cells were killed by 6 µM. $ZnCl_2$ killed approximately 10% of PC3 cells at 250 µM. Synergism in toxicity was detected only between TQ and TPEN. The TQ-$ZnCl_2$, AH-TPEN, and AH-$ZnCl_2$ co-treatments however, did not reveal strong synergistic indications on PC3 cell viability. This study shows that toxicity of TQ and AH found in black seed essential oil can be modified by the intracellular zinc concentration.

KEYWORDS:
Black seed essential oil, thymoquinone, alpha-hederin, zinc, prostate cancer, colon cancer

INTRODUCTION

Black seed (*Nigella sativa*) grains contain essential oils, fixed oils, proteins, phospholipids, saponin, and other components, whose availabilities and concentrations vary according to the harvest season, variety of the plant, the climate it is grown, and the region [1–3]. It is stated that the amount of TQ one of the most active substances in the composition of black seed may differ [4]. The amount of TQ in black seed oil is reported to be between 12-23% [2,5]. AH is found in relatively small amounts in black seed oil but is considered to be an important compound due to its antitumor activity [6].

It has been reported that the seed extract inhibits its skin cancer in mice by topical application [7], water and ethanol extracts stop the growth of MCF-7 breast cancer cells [8], and the ethanol extract has been reported to have cytotoxic effect on various cancer lines (P388, HepG2, Molt4, and Lewis lung carcinoma) [9]. Besides, black seed essential oil has been shown to have cytotoxic effect on human cancer lines such as SCL, SCI-6, NUGC-4 and 3T6 mouse fibroblast line [10]. The cytotoxic effects of water and ethanol extracts of black seed on the HepG2 human liver cancer line were observed [11] and the water extract showed a higher effect than ethanol extract. Researchers reported that TQ, a cytotoxic compound known to be effective against cancer, was found only in ethanol extracts. Another bioactive compound AH is a water-soluble compound and is considered to be primarily responsible for the anticancerogenic effect of water extract black seed. In one study, AH stopped the growth of mouse (B16) melanoma cells and non-cancerous mouse (3T3) fibroblast cells in serum-free medium at very low concentration (<5 µg/ml) in 8 hours [12]. In another study, AH and TQ showed dose and time dependent cytotoxic and necrotic effects on A549 (lung), Hep-2 (larynx epidermoid), HT-29 (colon), and MIAPaCa-2 (pancreatic) cancer cell lines [13]. Evidence is available to show that black seed and its active compounds not only have cytotoxic effects but also cause apoptosis [14–17].

In the process of prostate cancer development, intracellular zinc levels are decreased and agents that alter intracellular zinc levels have cytotoxic effects on prostate cancer cells by mechanisms that have not yet been discovered. The relationship between zinc and prostate cancer is complicated by the response to chemotherapy and the recurrence of cancer. It is generally known that prostate cancer cells have low intracellular zinc levels [18]. Moreover, high levels of dietary zinc have been associated with the improvement of prostate cancer [19], but on the other hand, chronic zinc loading has been reported to increase the risk of prostate cancer [20]. In another study, both low and high levels of dietary zinc increased the

tumor burden of prostate cancer in the transgenic adenocarcinoma mouse model (TRAMP) [21]. Low levels of zinc and iron showed correlation with disease recurrence in prostate cancer patients [22]. This importance attributed to the level of zinc in the development of prostate cancer has led to the development of imaging techniques to define the zinc levels [23] and to the development of therapeutic approaches to alter the zinc level to heighten the effect of chemotherapy. The sensitivity of prostate cancer cells to both exogenous zinc [24, 25] and zinc chelation shows that zinc levels during cancer development are not simply reduced and are actually kept low under strictly controlled levels [26]. Lately, it has been shown that the removal of zinc enhanced the cytotoxic and pro-apoptotic effects of a fluoropyrimidine polymer (F10) [27].

The complex relationship between the level of zinc and the occurrence and recurrence of prostate cancer has led to studies to alter intracellular zinc levels for therapeutic purposes. Zinc is transported into the cell by SLC39 (Zip-family) members and out of the cell by SLC30 (ZnT) zinc carriers [28]. Low expression of Zinc carrier Zip-family members is a characteristic feature of prostate cancer, and as a result, treatment of prostate cancer cells with zinc salts such as ZnSO4 has a minimum effect due to lack of carrier. For efficient delivery of zinc into the cell, reagents such as zinc pyrithione (ZnPy), which can pass through the cell membrane when it forms chelate with zinc, are needed. However, there are also studies reporting that zinc salts exhibit cytotoxic effects on prostate cancer cells. For example, zinc acetate showed cytotoxic effect against PC3, LNCaP, and DU145 cells and tumor growth was slowed by direct intra-tumoral injection [24]. In contrast to zinc salts, treatment with ZnPy increased intracellular zinc levels in prostate cancer cells and showed cytotoxic effects against PC3, LNCaP and DU-145 cell lines [25]. Therefore, the effect of zinc on prostate cancer cells is closely related to the cell permeability of the zinc-containing agent used.

The aim of this study is to increase the cytotoxic and pro-apoptotic effects of bioactive components, especially TQ and AH on human prostate and colon cancer lines using different zinc concentrations. By showing that the efficacy of a newly developed fluoropyrimidine F10 candidate cancer treatment reagent varies under different zinc concentrations it was reported that more attention should be given to zinc in the studies involved in the treatment of cancer [27]. TQ is the compound highest proportion of black seed essential oil. To the best of our knowledge, there is no report investigating the effect of intracellular or extracellular zinc concentration on TQ activity. In this respect, the current study is the first in this field.

MATERIALS AND METHODS

Cell Culture and Chemicals. The study was conducted on human prostate cancer PC3 and colon cancer HT-29 cell lines maintained in RPMI (Sigma) or DMEM (Sigma), respectively, supplemented with 10% fetal bovine serum (FBS) (Biowest) under 5% CO_2 at 37°C. TQ, AH, and TPEN (N,N,N′,N′-Tetrakis(2-pyridylmethyl) ethylenediamine) were purchased from Sigma. $ZnCl_2$ was from Merck.

Cell Viability Assay. The cell lines were seeded in 96 well cell culture plates at 3000 cells/well density in serum added media and incubated overnight. Next day treatments with black seed essential oil compounds (TQ or AH), exogenous zinc as $ZnCl_2$, and a strong membrane permeable zinc chelator TPEN started for a period of 24 h. Live cell counts were performed indirectly by measuring the ATP level using CellTiter-Glo® luminescent cell viability assay (Promega) following the manufacturer's protocol.

Intracellular Zinc Measurements. PC3 cells were grown as described in the cell viability assays. After four days of incubation, the used medium was removed and the cells were washed with DPBS and incubated in fresh RPMI with 1 μM Zinquin™ ethyl ester (Santa Cruz Biotech) at 37°C for 30 min under minimal light followed by $ZnCl_2$ treatment of 1 h. At the end of the incubation period, the cells were washed gently with warm DPBS (Sigma) and the fluorescence emitted from the fluorophore Zinquin ethyl ester was measured using a Thermo Fluoroskan FL at 355/460 nm (excitation/emission).

Statistical Analysis. All experiments were repeated at least 3 times in triplicates. The results were evaluated with the Student t-test or ANOVA test and $P \leq 0.05$ (two-tailed) was considered statistically significant.

RESULTS

The cytotoxicity of TQ and AH on PC3, HT-29, and HCT-116 increased in a dose-dependent manner and 100% cytotoxicity was achieved with 100 μM TQ or 50 μM AH (Figure 1A-B). TPEN cytotoxicity was more dramatic after 5 μM and most of the treated cells died at 6 μM (Figure 1C). While $ZnCl_2$ was killing only about 15% of PC3 cells at 200 μM, it did not show a considerable effect on the colon cancer cell lines (Figure 1D). $ZnSO_4$ was also used to measure cytotoxicity but was not affective (data not shown), thus the follow-up co-treatment assays were performed only using $ZnCl_2$ and on the PC3 cell line.

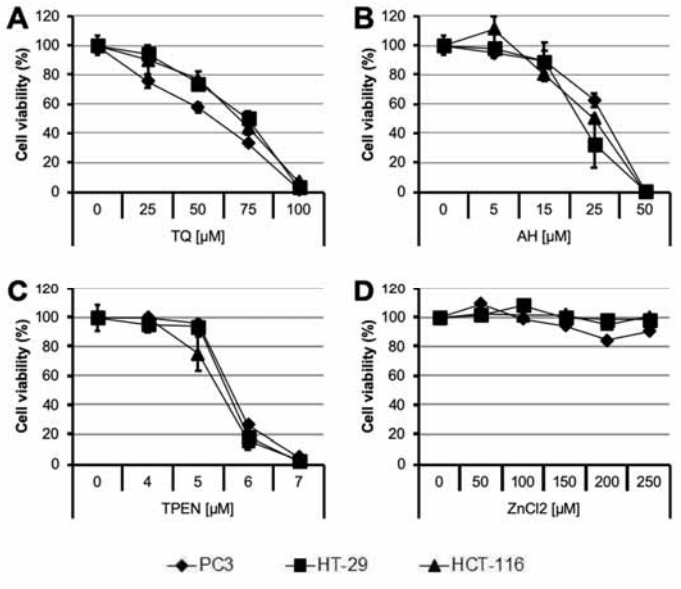

FIGURE 1
Cytotoxic effects of 24 h (A) TQ, (B) AH, (C) TPEN, and (D) $ZnCl_2$ treatments on PC3, HT-29, and HCT-116 cell lines.

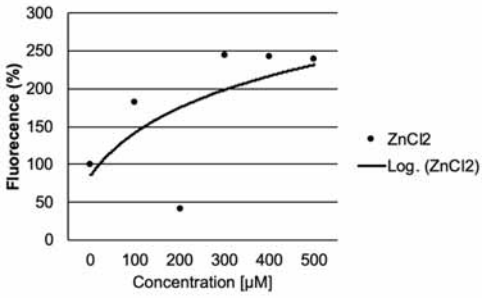

FIGURE 2
Intracellular zinc level increased in PC3 cells with exogenous $ZnCl_2$ treatment as measured with Zinquin™.

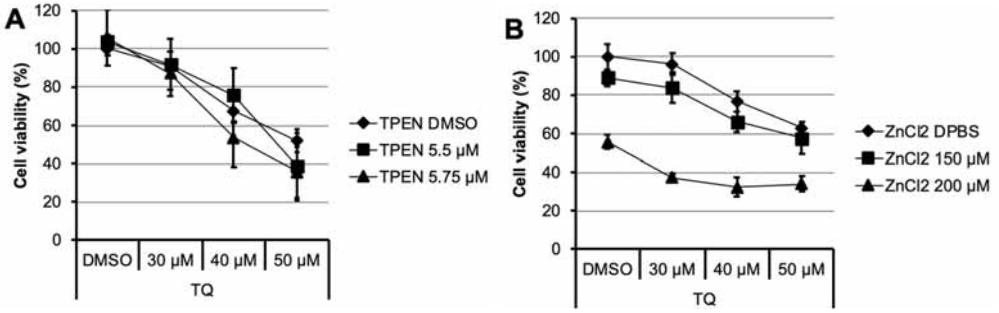

FIGURE 3
Cytotoxic effects of 24 h co-treatment of (A) TPEN or (B) $ZnCl_2$ with TQ on PC3 cell line.

Intracellular zinc concentration was determined fluorometrically by Zinquin ethyl ester (Figure 2). The $ZnCl_2$ concentration was increased up to 500 µM to measure. In these high doses, intracellular zinc levels increased by 200-250% compared to the $ZnCl_2$-free control.

The cytotoxicity of 50 µM TQ was increased with the addition of 5.75 µM TPEN by 34% (Figure 3A). However, addition of $ZnCl_2$ does not seem to intensify the TQ cytotoxicity (Figure 3B). Neither zinc chelation by TPEN nor exogenous zinc treatment in the form of $ZnCl_2$ modified the AH cytotoxicity (Figure 4A-B).

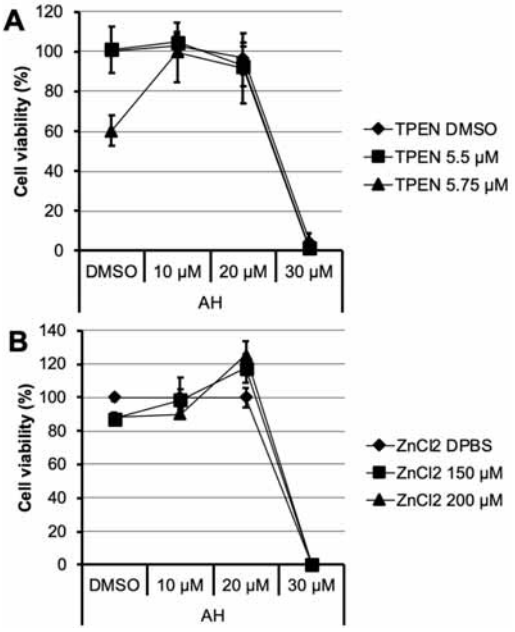

FIGURE 4
Cytotoxic effects of 24 h co-treatment of (A) TPEN or (B) $ZnCl_2$ with AH on PC3 cell line.

DISCUSSION

Black seed grains include essential oils, fixed oils, proteins, phospholipids, saponin and some other components. TQ is the most abundant essential oil component of black seed. AH, found in lesser amounts than TQ, has attracted attention as an important compound due to its cytotoxic activity [6]. In this respect, the relationship between these two components in black seed volatile oil with zinc metabolism was investigated.

In the literature, the cytotoxic effects of various extracts of black seed in different cancer types (MCF-7, P388, HepG2, Molt4, Lewis lung carcinoma, SCL, SCI-6, NUGC-4) have been discussed [8–11]. In some studies, it has been pointed out that these cytotoxic effects may be attributed to the presence of the most represented compound TQ (12-23%) and AH, which is represented by a lesser proportion in black seed essential oil [12, 13]. Similar to the results in the literature, the cytotoxicity of TQ and AH increased in a dose-dependent manner in the prostate and colon cancer cells in the current study. Approximately 100% cytotoxicity was obtained with 100 μM TQ or 50 μM AH.

In general, prostate cancer cells are known to have low intracellular zinc levels [18]. In addition to this information, high amounts of zinc taken by diet have been associated with the improvement of prostate cancer [19], but on the other hand, chronic zinc loading has been reported to increase the risk of prostate cancer [20]. In this respect, the relationship between zinc and prostate cancer is a complex process. The sensitivity of prostate cancer cells to both exogenous zinc [24,25] and zinc chelation has shown that zinc levels are actually kept under strictly controlled low levels during cancer development [26]. In our study, 24 h exogenous zinc (250 μM $ZnCl_2$) administration killed only about 10% of PC3 cells. In our study, TPEN, which was used as a zinc chelator, started to show cytotoxicity at higher doses than 5 μM in both cancer cell lines and most of the cells died at 6 μM. The complex relationship between the level of zinc and the occurrence and recurrence of prostate cancer has led to studies to alter intracellular zinc levels for therapeutic purposes. One example demonstrated that the removal of zinc strengthened the cytotoxic and pro-apoptotic effects of a newly developed fluoropyrimidine F10 [27]. In our study, we aimed to measure the cytotoxic and pro-apoptotic effects of TQ and AH in the presence of excess zinc and in the absence of intracellular zinc by using a strong zinc chelator. In literature, no reports were detected on the effect of changes in intracellular zinc concentration to the efficacy of TQ and AH. In this respect, the current report has been the first in this field. In our study, synergistic effect was detected in the co-treatment of TQ and TPEN. The TQ-$ZnCl_2$, AH-TPEN, and AH-$ZnCl_2$ co-treatments did not reveal strong synergism in toxicity on PC3 prostate cancer cell line.

In conclusion, this study showed that cytotoxic effects of *N. sativa* essential oil bioactive components may be modified by the intracellular zinc levels.

ACKNOWLEDGEMENTS

The author would like to thank Prof. Dr. William Gmeiner (Wake Forest University, NC, USA), who provided laboratory facility for conducting part of this study.

This study was funded by Aydin Adnan Menderes University Research Fund. Project number: MF-15001.

The author declares that there is no conflict of interest associated with this publication.

REFERENCES

[1] Al-Jassir, M.S. (1992) Chemical composition and microflora of black cumin (*Nigella sativa* L.) seeds growing in Saudi Arabia. Food Chemistry. 45(4), 239–242.

[2] Sultan, M.T., Butt, M.S., Anjum, F.M., Jamil, A., Akhtar, S., Nasir, M. (2009) Nutritional Profile of Indigenous Cultivar of Black Cumin Seeds and Antioxidant Potential of Its Fixed and Essential Oil. Pakistan Journal of Botany. 41(3), 1321–1330.

[3] Wagner, H., Farnsworth, N.R. (Eds.) (1990) Economic and Medicinal Plant Research. Vol.4: Plants and Traditional Medicine. Academic Press Ltd., London.
[4] Türker, L., Bayrak, A. (1997) Investigation of fixed and volatile oil composition of Black Seed (*Nigella sativa* L.). Standard. 36(430), 128–137.
[5] Çakmakçı, S., Gündoğdu, E., Dağdemir, E., Erdoğan, Ü. (2014) Investigation of the Possible Use of Black Cumin (*Nigella sativa* L.) Essential Oil on Butter Stability. Kafkas Universitesi Veteriner Fakultesi Dergisi. 20(4), 533–539.
[6] Swamy, S.M.K., Huat, B.T.K. (2003) Intracellular glutathione depletion and reactive oxygen species generation are important in α-hederin-induced apoptosis of P388 cells. Molecular and Cellular Biochemistry. 245(1–2), 127–139.
[7] Salomi, M.J., Nair, S.C., Panikkar, K.R. (1991) Inhibitory Effects of *Nigella Sativa* and Saffron (*Crocus sativus*) on Chemical Carcinogenesis in Mice. Nutrition and Cancer. 16(1), 67–72.
[8] Farah, I.O., Begum, R.A. (2003) Effect of Nigella sativa (*N. sativa* L.) and oxidative stress on the survival pattern of MCF-7 breast cancer cells. Biomed Sci Instrum. 39, 359–364.
[9] Swamy, S.M., Tan, B.K. (2000) Cytotoxic and immunopotentiating effects of ethanolic extract of Nigella sativa L. seeds. Journal of Ethnopharmacology. 70(1), 1–7.
[10] Islam, S.N., Begum, P., Ahsan, T., Huque, S., Ahsan, M. (2004) Immunosuppressive and cytotoxic properties of Nigella sativa. Phytotherapy Research. 18(5), 395–398.
[11] Samarakoon, S., Thabrew, I., Galhena, P., De Silva, D., Tennekoon, K. (2011) A comparison of the cytotoxic potential of standardized aqueous and ethanolic extracts of a polyherbal mixture comprised of Nigella sativa (seeds), Hemidesmus indicus (roots) and Smilax glabra (rhizome). Pharmacognosy Research. 2(6), 335.
[12] Danloy, S., Quetin-Leclercq, J., Coucke, P.A., De Pauw-Gillet, M.-C., Elias, R., Balansard, G., Angelot, L., Bassler, R. (2007) Effects of α-Hederin, a Saponin Extracted from Hedera helix, on Cells Cultured in vitro. Planta Medica. 60(01), 45–49.
[13] Rooney, S., Ryan, M.F. (2005) Effects of Alpha-hederin and Thymoquinone, constituents of Nigella sativa, on Human Cancer Cell Lines. Anticancer Research. 25, 2199–2204.
[14] El-Mahdy, M.A., Zhu, Q., Wang, Q.E., Wani, G., Wani, A.A. (2005) Thymoquinone induces apoptosis through activation of caspase-8 and mitochondrial events in p53-null myeloblastic leukemia HL-60 cells. International Journal of Cancer. 117(3), 409–417.
[15] Gali-Muhtasib, H., Roessner, A., Schneider-Stock, R. (2006) Thymoquinone: A promising anti-cancer drug from natural sources. The International Journal of Biochemistry and Cell Biology. 38(8), 1249–1253.
[16] Rooney, S., Ryan, M.F. (2005) Modes of Action of Alpha-hederin and Thymoquinone, Active Constituents of Nigella sativa, against HEp-2 Cancer Cells. Anticancer Research. 25, 4255–4259.
[17] Shafi, G., Munshi, A., Hasan, T.N., Alshatwi, A.A., Jyothy, A., Lei, D.K.Y. (2009) Induction of apoptosis in HeLa cells by chloroform fraction of seed extracts of Nigella sativa. Cancer Cell International. 9, 1–8.
[18] Costello, L.C., Franklin, R.B. (2011) Zinc is decreased in prostate cancer: An established relationship of prostate cancer! Journal of Biological Inorganic Chemistry. 16(1), 3–8.
[19] Epstein, M.M., Kasperzyk, J.L., Andren, O., Giovannucci, E.L., Wolk, A., Hakansson, N., et al. (2011) Dietary zinc and prostate cancer survival in a Swedish cohort. American Journal of Clinical Nutrition. 93, 586–593.
[20] Leitzmann, M.F., Stampfer, M.J., Wu, K., Colditz, G.A., Willett, W.C., Giovannucci, E.L. (2003) Zinc supplement use and risk of prostate cancer. Journal of the National Cancer Institute. 95(13), 1004–1007.
[21] Prasad, A.S., Mukhtar, H., Beck, F.W.J., Adhami, V.M., Siddiqui, I.A., Din, M., Bin Hafeez, B., Kucuk, O. (2010) Dietary Zinc and Prostate Cancer in the TRAMP Mouse Model. Journal of Medicinal Food. 13(1), 70–76.
[22] Sarafanov, A.G., Todorov, T.I., Centeno, J.A., MacIas, V., Gao, W., Liang, W.M., Beam, C., Gray, M.A., Kajdacsy-Balla, A.A. (2011) Prostate cancer outcome and tissue levels of metal ions. Prostate. 71(11), 1231–1238.
[23] De Leon-Rodriguez, L., Lubag, A.J.M., Dean Sherry, A. (2012) Imaging free zinc levels in vivo - What can be learned? Inorganica Chimica Acta. 393, 12–23.
[24] Shah, M.R., Kriedt, C.L., Lents, N.H., Hoyer, M.K., Jamaluddin, N., Klein, C., Baldassare, J. (2009) Direct intra-tumoral injection of zinc-acetate halts tumor growth in a xenograft model of prostate cancer. Journal of Experimental and Clinical Cancer Research. 28, 84.
[25] Kriedt, C.L., Baldassare, J., Shah, M., Klein, C. (2010) Zinc functions as a cytotoxic agent for prostate cancer cells independent of culture and growth conditions. Journal of Experimental Therapeutics and Oncology. 8(4), 287–295.

[26] Makhov, P., Golovine, K., Uzzo, R.G., Rothman, J., Crispen, P.L., Shaw, T., Scoll, B.J., Kolenko, V.M. (2008) Zinc chelation induces rapid depletion of the X-linked inhibitor of apoptosis and sensitizes prostate cancer cells to TRAIL-mediated apoptosis. Cell Death and Differentiation. 15(11), 1745–1751.
[27] Gmeiner, W.H., Boyacioglu, O., Stuart, C.H., Jennings-Gee, J., Balaji, K.C.C. (2015) The cytotoxic and pro-apoptotic activities of the novel fluoropyrimidine F10 Towards prostate cancer cells are enhanced by Zn2+-chelation and inhibiting the serine protease Omi/HtrA2. The Prostate. 75(4), 360–369.
[28] Franz, M.C., Anderle, P., Bürzle, M., Suzuki, Y., Freeman, M.R., Hediger, M.A., Kovacks, G. (2013) Zinc transporters in prostate cancer. Molecular Aspects of Medicine. 34(2–3), 735–741.

Received: **29.06.2019**
Accepted: **29.01.2020**

CORRESPONDING AUTHOR

Olcay Boyacioglu
Department of Food Engineering,
Faculty of Engineering,
Aydin Adnan Menderes University,
Efeler, Aydin, 09010 – Turkey

e-mail: oboyaci@adu.edu.tr

© by PSP Volume 29 – No. 04A/2020 pages 2752-2757 Fresenius Environmental Bulletin

POLLUTION ASSESSMENT AND SOURCE APPROXIMATION OF HEAVY METALS IN THE SOIL ALONG A MAIN ROAD WITH HIGH DENSITY OF TRAFFIC

Han Sun[1], Linhua Sun[1,2,*], Yu Li[1], Xiaojun Gao[1], Zixiang Zhao[1]

[1]School of Resources and Civil Engineering, Anhui Suzhou 234000, China
[2]Key Laboratory of Mine Water Resource Utilization of Anhui Higher Education Institute, Suzhou University, Anhui 234000, China

ABSTRACT

Heavy metals accumulated in farmland soil can influence the food safety and human health, and therefore, the protection of the environment of the farmland soil along the trafficway is of great significance. In order to find out the pollution status of soils along the Suzhou Avenue, the contents of Cr, Ni, Cu, Zn and Pb in 105 soil samples have been measured, and the pollution status was evaluated by a series of methods (including single pollution, comprehensive pollution and potential ecological hazard indexes), then the sources were determined by combining spatial distribution characteristics and mathematical statistics (correlation and factor analyses). The results showed that Ni, Cu, Zn and Pb were polluted with varying degrees. The potential ecological hazard index was Cu > Pb > Ni > Cr > Zn. The contents of Zn and Pb in soil were affected by traffic, while the contents of Cr, Ni and Cu were related to geological or agricultural factors.

KEYWORDS:
Soil, Heavy metals, Pollution assessment, Source approximation

INTRODUCTION

Soil is an important part of the environment and an important resource for human survival and agricultural production. Heavy metal pollution in the atmosphere and soil caused by road transportation and automobile exhaust diffusion and deposition is one of the environmental problems that have attracted much attention in the process of urbanization [1]. Once these heavy metals are washed out by rain or naturally settled into farmland soil, they will accumulate for a long time, which is difficult to eliminate. On the one hand, they will affect crop growth, on the other hand, they will be absorbed by crops, which will affect food safety and human health [2]. Therefore, it is very important to study the pollution of heavy metals in soil caused by automobile exhaust.

At present, there are many reports on metal pollution in highway and local traffic in China, such as the research on heavy metal pollution in soil and agricultural products on both sides of Shanghai-Nanjing expressway [3], the spatial distribution and contamination assessment of heavy metals in urban road dusts from Urumqi, NW China [4], and the research on heavy metal contamination in soil alongside mountain railway in Sichuan, China [5]. Zhang et al have also analysed the soil pollution on both sides of Changsha suburban highway and evaluated the potential ecological hazards of heavy metals [6]. Chang et al have evaluated the current situation of metal pollution in Jiangsu section of National Highway 104, and the sources of pollution and its impact on farmland have been analysed [7].

Suzhou Avenue is the main traffic artery from the urban area of Suzhou City to the east station of Suzhou. It has a large traffic flow and farmland on both sides. Therefore, the quality of soil is closely related to the health of residents. In this paper, the soil along the Suzhou Avenue has been chosen for study. Based on the contents of some heavy metals (Cr, Zn, Ni, Cu and Pb), the quality of the soil was evaluated by single and comprehensive pollution indexes, as well as the potential ecological hazard index, and then their sources have been identified by statistical analyses (including correlation and factor analyses) in combination with their spatial distributions. The study can provide scientific information for farmland environmental protection along the way.

MATERIALS AND METHODS

Study area. Suzhou is located in the northern Anhui province, China. Agriculture and coal related industries are the most import industries in the area. The main crops in the area include wheat, corn, soybean, cotton, potato, rapeseed, peanuts and fruit etc. And therefore, the quality of soil is important for the development of the area.

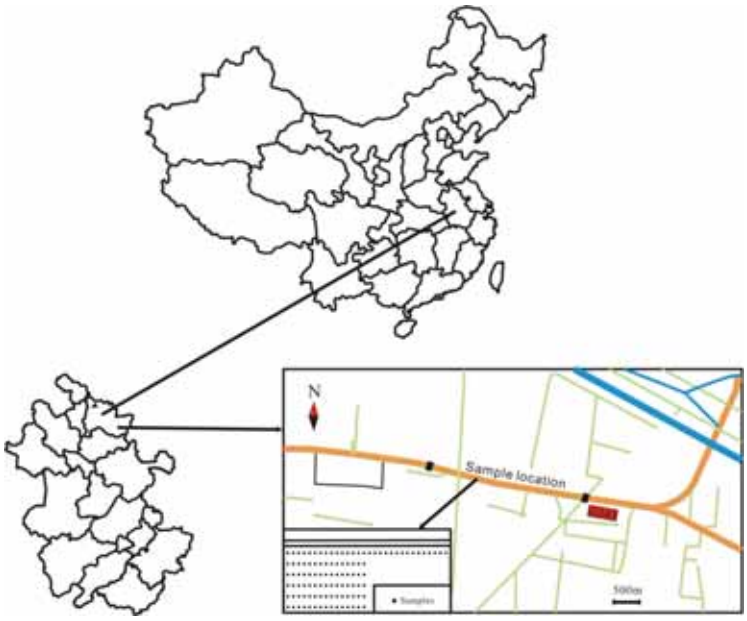

FIGURE 1
Location of the study area and the sample distributions.

During the past ten years, the economy of Suzhou has undergone rapid development, especially the development of transportation, including the railways and trafficways. And now, people in Suzhou can arrive in Beijing and Shanghai in three hours, and Xi'an and Wuhan in four hours. In relation to this high speed of development, there are many kinds of environmental problems have been resulted in: the air pollution, water pollution and soil pollution etc.

Sampling and analyses. All of the samples were collected along the Suzhou Avenue. 105 surface samples (<10 cm depth) were collected, thirty of them were along the roadside with distance near 100-150 m between each other (the first line, B_1-B_{30}), and the other seventy-five samples were distributed in the five lines parallel to the first line, and their distances from the roadside were 5 m, 10m, 15 m, 20m, 30 m (C_1-C_{75}, Fig. 1). The sampling area was surrounded by open terrain, mostly ravines, woodlands and farmland, and therefore, the agricultural activities, the air pollution (including the traffic emission) and the soil itself were considered to be the sources for the pollution in the area. All of the grass roots, leaves and humus of animals and plants were removed by hands. And then the samples were packed by samples bags, and their sampling positions (latitude and longitude and related environmental information) were recorded.

The collected soil samples were air-dried in dark places, and then crushed to be less than 200 meshes. Finally, the contents of chromium (Cr), zinc (Zn), nickel (Ni), copper (Cu) and lead (Pb) in soil were determined by X-ray fluorescence spectrometry (XRF). Standard sample GSS-16 was used for quality control during the test, and the relative standard deviation is less than 10%.

For data processing, Mystat (version 12) was firstly applied for getting their statistics, and then the software Surfer (version 11) was used to draw the contour maps. In the evaluation of pollution, single pollution and comprehensive pollution indexes, as well as potential ecological hazard index were applied, and then the sources of pollution were analyzed by mathematical statistics analysis (including correlation and factor analysis).

RESULTS AND DISCUSSION

Concentrations. Compared with the soil environmental background value of China [8], 95% of the samples have lower contents of Cr, whereas 66%, 84%, 25% and 96% of the samples have higher contents of Ni, Cu, Zn and Pb relative to the background values (Table 1). Their concentrations were 31.4-68.8 mg/kg (average 51.6 mg/kg), 12.0-45.0 mg/kg (average 30.3 mg/kg), 15.3 to 46.6 mg/kg (average 28.3 mg/kg), 42.1-191 mg/kg (average 71.7 mg/kg) and 25.5-50.2 mg/kg (average 29.8 mg/kg), respectively.

The coefficient of variation can be used to reflect the degree of human influence on pollutants. The larger of the CV value, the greater degree of human influence, the lower of the CV value, the lower contribution of human activities (CV < 0.1, representing less human influence; CV > 0.9, representing significant human influence) [9]. As can be seen from Table 1, all of the metals have moderate coefficients of variation (> 0.1 and < 0.9), indicating that

there were varying degrees of multi-source effects. Among them, the coefficient of variation of zinc was the largest, indicating that it was mostly affected by anthropogenic sources.

Spatial distributions. The spatial distributions of metal concentrations can provide direct information for the source of them. From the spatial distributions of the metals in Fig. 2, it can be found that the Ni contents in the range of 0-5m from the roadside were lower than other sampling points, and the points with high values include C18, C49, C52 and C62. The distribution of Cu contents was similar to that of Ni, and it has lower concentrations than other sampling points in the range of 0-5 m from the roadside. The points with high values were C9, C18, C38, C54 and C69. The distribution of Cr contents was irregular at different distances from roadside with high value points of C9, C18, C36, C44 and C69, which were similar to the high value points of Cu contents. The contents of Pb and Zn in the range of 0-5m from roadside were much higher than those in other sampling sites. In summary, the spatial distribution of Cr, Ni and Cu was similar to each other. According to field sampling, the high value points were mostly distributed in roadside farmland. On the contrary, the contents of Pb and Zn in the range of 0-5 m away from the roadside were significantly higher than those in other areas, and decreased from the roadside to the farmland, indicating that they were significantly affected by traffic related sources.

Pollution assessment. (1) Single pollution index. The calculation method is $P_i = C_i/S_i$ [10]. Where P_i is the individual pollution index of pollutant i; C_i is the measured concentration of pollutant i; S_i is the standard of pollutant i (in this study, it is the environmental background value of China [8]).The degrees of soil pollution can be divided into five levels according to P_i: $P_i < 1$, no pollution; $1 < P_i < 2$, slight pollution; $2 < P_i < 3$, light pollution; $3 < P_i < 4$, moderate pollution and $P_i > 5$, significant pollution.

The calculated results showed that the P_i values of Cr were 0.514-1.127, indicating that most of the samples were no pollution and only five of them were slightly polluted. The P_i values of Ni were 0.445-1.672, and 70 samples were slightly polluted, P_i values of Cu were 0.676-2.062, and 87 samples were slightly polluted (the P_i value of B9 samples is > 2, which indicated the light pollution). The P_i values of Zn were 0.567-2.557, 18 samples were slightly polluted and 8 samples were lightly polluted (all of them were distributed on the roadside). The P_i values of Pb was 0.980-1.932, and 101 samples were slightly polluted.

TABLE 1
Descriptive statistics of metal concentrations (unit in mg/kg).

Metals	Cr	Cu	Ni	Pb	Zn
Max	68.8	46.6	45.0	50.2	191
Min	31.4	15.3	12.0	25.5	42.1
Mean	51.6	28.3	30.3	29.8	71.7
Standard deviation	6.00	6.92	6.72	5.07	35.6
coefficient of variation	0.116	0.244	0.222	0.170	0.496
Environmental background [8]	61.0	22.6	26.9	26.0	74.2

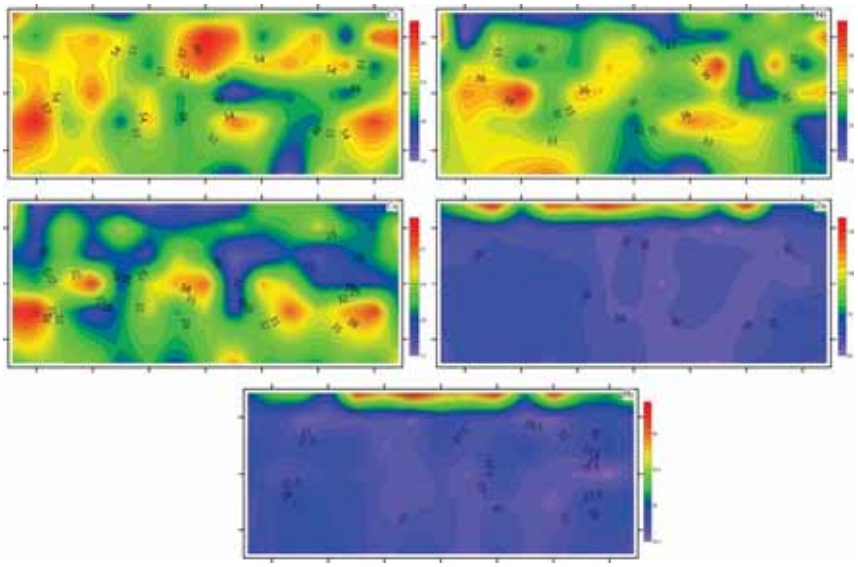

FIGURE 2
Spatial distributions of metal concentrations (without B16 to B30, unit in mg/kg).

TABLE 2
Classification Standard of Potential Ecological Hazard Index [13].

Pollution index	Classification standard	Pollution degree
E_r^i	≤40	Light
	40-79	Moderate
	80-159	Heavy
	160-320	Strong
	> 320	Very strong
RI	< 150	Light
	150-300	Moderate
	300-600	Heavy
	> 600	Strong

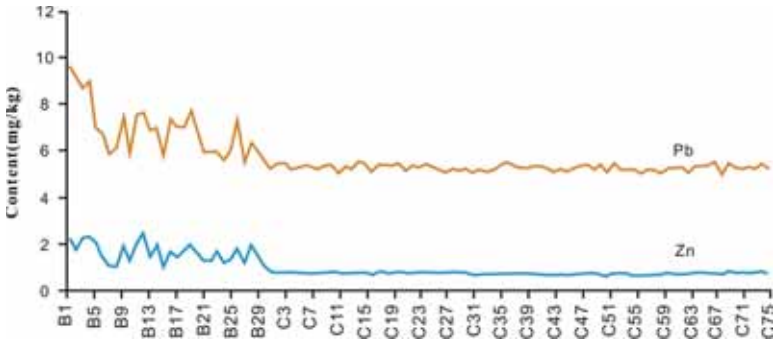

FIGURE 3
Potential ecological hazard indexes of Zn and Pb.

(2) Comprehensive pollution index. The Nemerow index method was chosen for the comprehensive pollution evaluation [12]. It is a comprehensive evaluation method which takes into account the average and maximum values of the individual pollution index on the basis of the rating of the single pollution index. The calculation method is as $P = [P_{ijmax}^2 + P_{ijave}^2) / 2]^{1/2}$. Where P is the comprehensive index of the j^{th} sample point, P_{ijmax} is the maximum value of the single pollution index of all the evaluated pollutants in the j^{th} sample point, and P_{ijave} is the average value of the single pollution index of the evaluated pollutants in the j^{th} sample point. P < 1 means no pollution and P > 1 means polluted. The 105 samples have P values range from 0.936 to 2.12, and only 6 samples were not polluted, but others were polluted with varying degrees.

(3) Potential ecological hazard index. The potential ecological hazard index method was established by Swedish scholar Hakanson in 1980 [5]. The index takes into account the toxicity of heavy metals, the general diffusion and transformation of heavy metals in soils, the sensitivity of assessment areas to heavy metal pollution, and the difference of background values of heavy metals. It reflects the characteristics of bioavailability, relative contribution ratio and geospatial differences, and can comprehensively reflect the impact potential of heavy metals in sediments. It has been widely applied to the ecology of heavy metals in soil risk assessment [5]. The calculation formula is as follows:

$$R\ I = \sum_{i=1}^{n} E_r^i,\ E_r^i = T_r^i \times C_f^i \text{ and } C_f^i = C_s^i / C_n^i.$$

Where E_r^i is the potential ecological hazard index for single heavy metal, T_r^i is the toxicity response coefficient of single heavy metal (Cr = 2, Ni = 5, Cu = 5, Zn = 1 and Pb = 5), C_f^i is the pollution coefficient of single heavy metal, C_s^i is the measured values of heavy metal concentration in soil and C_n^i is the background values of heavy metal concentrations.

According to the calculated results, the E_r^i values of Cr, Ni, Cu, Zn and Pb were 1.03-2.25, 2.22-8.36, 3.38-10.3, 0.567-2.58 and 4.90-9.66, respectively. In comparison with the Table 2, the single potential ecological hazard indexes of heavy metals in this study were < 40 and the RI values for the soil samples were < 150, indicating only slight ecological pollution, and they have the decreasing order of Cu > Pb > Ni > Cr > Zn. In addition, Figure 3 shows that the potential ecological hazard indexes of Pb and Zn in 30 samples (B1-B30) near the roadside was significantly higher than those of other samples, indicating that they were more seriously affected by traffic and have greater potential for ecological pollution.

Source identification by statistical analyses.
(1) Correlation analysis. Analysis of the correlation between heavy metals in soil can be used to infer whether the sources of heavy metal pollution are consistent. If there is a correlation between heavy metals, the source is the same; if not, the source is

TABLE 3
Results of correlation analysis.

Metals	Cr	Ni	Cu	Zn	Pb
Cr	1				
Ni	0.492**	1			
Cu	0.292**	0.459**	1		
Zn	-0.258**	-0.356**	-0.338**	1	
Pb	-0.263**	-0.427**	-0.351**	0.917**	1

Note: ** and * mean significant at 0.01 and 0.05 levels

TABLE 4
Results of factor analysis.

Metals	Cr	Ni	Cu	Zn	Pb	Eigenvalue	Variance explained %
F1	-0.045	-0.249	-0.268	0.956	0.949	1.95	39.0
F2	0.808	0.807	0.652	-0.187	-0.231	1.82	36.4

different [14]. Table 3 shows that there were significant correlations between Cr, Ni and Cu at 0.01 level and Zn and Pb at 0.01 level, which suggesting that Zn-Pb and Cr-Ni-Cu may have similar sources. Considering with the distribution of the concentrations and pollutions of the metals, the former may be related to traffic impact, while the latter may be related to other factors.

(2) Factor analysis. Factor analysis is a further study of correlation analysis. Based on the correlation matrix of variables, n-dimensional random vectors are decomposed into less than n representative common factors and a special n-dimensional vector, so that the best number of vector common factors can be obtained. Thus, the study of n-dimensional random vectors is replaced by the study of less common factors. Table 4 shows that two factors were extracted with eigenvalue > 1, and the total variance interpretation is 75.4%. The variance explanatory rate of Factor 1 (F1) is 39.0%, in which Zn and Pb have high positive loadings, which therefore can be explained to be the source related to traffic. The variance explanatory rate of Factor 2 (F2) was 36.4%, and it has high positive loadings of Cr, Ni and Cu, which indicates that they have similar source (natural or agricultural sources).

CONCLUSIONS

The following conclusions have been obtained:

(1) The calculated results of single, comprehensive pollution and potential ecological hazard indexes suggested that almost all of the soil samples near the trafficway were slightly to lightly polluted by heavy metals with light ecological risk.

(2) The spatial distributions of heavy metal concentrations and the potential ecological hazard indexes, along with the correlation and factor analyses, indicating that two sources were responsible for the heavy metals in this study, the traffic related source for Zn and Pb and another source (agricultural and geological) for other ones.

ACKNOWLEDGEMENT

This work was financially supported by the Innovation and entrepreneurship project of college students in Anhui Province (201910379164).

REFERENCES

[1] Yu, A., Wang, D., Zhao, Y. (2010) The characteristics and assessment on heavy metal pollution of soil along the expressway. Forest Engineering. 26(4), 59-63.

[2] Muchuweti, M., Birkett, J.W., Chinyanga, E., Zvauya, R., Scrimshaw, M.D., Lester, J.N. (2006) Heavy metal content of vegetables irrigated with mixtures of wastewater and sewage sludge in Zimbabwe: Implications for human health. Agriculture, Ecosystems and Environment. 112(1), 41-48.

[3] Li, B., Lin, Y., Zhang, X., Xu, Y., Yu, F. (2005) Heavy metal pollution of the soils and wheat grains alongside the Shanghai-Nanjing expressway. Rural Eco-environment. 21(3), 50-53, 70.

[4] Wei, B., Jiang, F., Li, X., Mu, S. (2009) Spatial distribution and contamination assessment of heavy metals in urban road dusts from Urumqi, NW China. Microchemical Journal. 93(2), 147-152.

[5] Liu, H., Chen, L.P., Ai, Y.W., Yang, X., Yu, Y. H., Zuo, Y.B., Fu, G.Y. (2009) Heavy metal contamination in soil alongside mountain railway in Sichuan, China. Environmental Monitoring and Assessment. 152(1-4), 25.

[6] Zhi, Y., Wang, Z., Ma, Z., Wang, Z., Deng, Z., Li, H. (2007) The speciation and bioavailability of heavy mental pollutions in soils along highway in Erdos. Acta Ecologica Sinica, 27(5), 2030-2039.

[7] Chang, W., Chen, C. (2009) Research of heavy metal pollution by the No.104 national road in Jiangsu Province. Energy Environment Protection. 23(3), 43-46.

[8] China Environmental Monitoring Station. (1990) Background values of soil elements in

China. China Environmental Science Publishing House.
[9] Li, G., Wang, Z., Liu, Z. (2011) Analysis on spatial heterogeneity of moderate microelement in cultivated soils of rural town of western Liaoning. Chinese Journal of Soil Science. 42(2), 372-377.
[10] Shao, L., Xiao, H., Li, N., Luo, L., Zhou, D. (2013) Pollution characterization of heavy metals in road dusts and soils near expressways. Earth and Environment. 41(6), 661-668.
[11] State Environmental Protection Administration (China) (2000) Technical specification for monitoring farmland soil environmental quality. China Standards Press.
[12] Li, Y., Li, C., Yang, X. (2010) Distribution characteristics and the speciation of heavy metals pollutants in soil along Jiaoke Roadway. Journal of Henan Polytechnic University (Nature Science). 29(6), 831-836.
[13] Yang, S., Xie, J. (2010) The migration rule of lead and cadmium and their ecological risk in the road side soil along Wuhu-Tongling highway. Journal of Xinyang Normal University (Nature Science). 23(1), 97-100.
[14] Liu, W., Liu, H., Qiu, C., Cai, X. (2012) Analysis on pollution and correlation of heavy metals in soil along Third Ring South Road in Xuzhou City. Environment Science and Management. 37(10), 67-70.
[15] Wang, X., Lai, J., Lu, Y., Li, D., Zhou, J., Wang, J. (2008) Main source of soil heavy metal pollution based on factor analysis in Taiyuan. Ecology and Environment. 17(2), 671-676.

Received: **01.07.2019**
Accepted: **11.02.2020**

CORRESPONDING AUTHOR

Linhua Sun
School of Resources and Civil Engineering,
Anhui Suzhou 234000 – China

e-mail: sunlinh@126.com.

© by PSP Volume 29 – No. 04A/2020 pages 2758-2765 Fresenius Environmental Bulletin

ASSESSMENT OF CLIMATE CHANGE RISKS TO NATURAL RESOURCES IN THE REPUBLIC OF SERBIA

Ljubica Duskov[1,*], Dejan Filipovic[1], Vladimir Djurdjevic[2]

[1]University of Belgrade, Faculty of Geography, Department of Spatial Planning, Belgrade, Serbia
[2]University of Belgrade, Faculty of Physics, Institute of Meteorology, Belgrade, Serbia

ABSTRACT

A temperature rise, extreme weather conditions and its consequences negatively impact the quality of life in towns and regions in Serbia and are challenges yet to be faced in the future. In order to prepare the country more adequately to altered climate conditions, as well as the successful implementation of adaptive measures, it is necessary to determine the vulnerability, as well as the assessment of the risks to certain sectors to climate change. Estimates show that since 2000 the Republic of Serbia has faced several significant extreme climate and weather events that have caused the loss of human life, considerable material consequences and degradation of the natural environment. The consequences have been various depending on the part of the country and the paper uses as an example the Raska Administrative District which covers an area of 3.918 km^2 and has 309.258 residents.

The aim of the paper is to assess the vulnerability and assessment of the risks of natural resources (agricultural and forest land) of the Raska Administrative District to climate change based on methodology 'FUTURE CITIES Adaptation Compass' [1], developed as part of the EU Project FUTURE CITIES. Using the results of 9 different models for the RCP 8.5 scenario, the paper concluded that agriculture and forests would be at a very high risk of heat waves, droughts and extreme precipitation, as well as under the medium-level risk of extreme cold. The research has a applicative character as it represents the starting point in the process of adapting to climate change. Also, the result of the paper has significant impact on planning spatial development because the defining of planned solutions must be in correlation with possibilities for adapting the sector to different climate conditions, and thus the realistic concept of spatial development.

KEYWORDS:
Vulnerability, risk assessment, climate change, agriculture, forest, Republic of Serbia, Raska Administrative District

INTRODUCTION

The observed climate changes result in changes in the environmental, social and economic indicators, i.e. in changes in the overall living conditions of contemporary society across the planet, and in the Republic of Serbia. It is believed that, if the future changes remain below the limit which has been set as a target, the alleviation of negative consequences will be possible through the corresponding and timely measures of adaptation to the changed climate conditions [2]. A widely accepted view is that climate changes will have much more serious consequences on developing countries, compared to the developed ones. According to Srivastava A. [3], vulnerability to climate changes is closely related to poverty, as the poor are the least capable of responding to climate stimuli. As a developing country, Republic of Serbia will be facing many challenges in this area, and so far it has started harmonizing the national legislation with the EU legal framework. The establishment of the monitoring, reporting and verification (MRV) system is one of the key requirements of the United Nations Framework Convention on Climate Change and the EU legislation.

According to the second report of the Republic of Serbia according to the UNFCCC [4], temperature in the Republic of Serbia territory is expected to rise from 0.5 to 1.5°C before 2030. During the last decades of the 21st century the rise in temperature will amount to 4.0 to 4.3°C, if the global greenhouse gas emissions continue with the same intensity as today. With regard to precipitations, the trends are more difficult to determine, in particular in the first half of the 21st century. One scenario indicates a potential precipitation rise from 3 to 10% to 2030, while in the period from 2050 until the end of the century, all the results point to the possibility of a significant 10-19% drop.

It is stated in the National Plan of Adaptation to the Changed Climate Conditions in Serbia [5] that the changed climate conditions and their higher variability will affect the future agricultural situation of Serbia, and in turn the overall economy, given that agriculture accounts for 11.4% of the Republic of Serbia GDP. The rise in temperature and a higher frequency of extreme weather events

may result in a yield reduction and an increase in interannual yield fluctuations, if appropriate adaptation measures are not taken in time. The most critically affected will be the yield of corn (if no adaptation measures are taken, the corn yield in non-irrigation conditions is expected to fall by 52% to 2100) and wheat (a potential 16% drop in the period to 2030, depending on the region). The main objective of this study is to determine the level of vulnerability of forests and agricultural land, in view of the fact that they represent the potential of this region, and that the occurrence of climate extremes is getting all the more frequent throughout Serbia, including the Raska District.

MATERIALS AND METHODS

Study area. The administrative district of Raska is situated in the south-western part of the Republic of Serbia, covering an area of 3.922 km². The geographical position of Raska district is presented in Figure 1. According to the last official census of 2011, it has 309.258 inhabitants who are distributed into three municipalities and two cities (Vrnjacka Banja, The City of Kraljevo, The City of Novi Pazar, Raska and Tutin), and 359 housing units in total. The average population density of the Raska Administrative District is 74 inhab. /km², with the City of Novi Pazar being the most densely populated with 116 inhab. /km², while the Raska and Tutin municipalities have the lowest population density, with 41 inhab. /km².

Study area is characterised by a complex terrain morphology with highland relief (the Stari Vlah-Raska highland, the Kopaonik mountains). It is situated in a temperate continental climate belt with more or less marked local characteristics (continental climate in the area of the Tutin municipality and the sub-alpine type in the Golija and Kopaonik areas). The east parts of the Pester Field are located within the subject region, so that temperature inversion, or extremely low temperatures, are present at the foot of the field, lower than on the surrounding mountains.

Methods. Based on the 'FUTURE CITIES Adaptation Compass' methodology, developed within the FUTURE CITIES Project of the European Union, an assessment has been made of the vulnerability and effect of climate changes of the area in question. This methodology has been recognized as one of the potential options for adaptation planning in the EU and included in the list of tools available from the European Commission portal devoted to adaptation to climate changes Climate-ADAPT [1]. The current vulnerability of natural resources (agricultural land and forest cover) to the effect of climate changes in the Raska District territory has been assessed as a combination of their sensitivity / exposure (depending on the type of extreme event) and their respective adaptive capacities. For this analysis, information and data about extreme weather events in the period from 1995 to 2015 are collected from the Republic Hydrometeorological Service of Serbia and E-OBS/ECAD database [7]. Extreme weather events have different effects on an area depending on the interaction with the essential natural characteristics of the area, and on their intensity and duration [8].

The receptor sensitivity/exposure levels are classified as low, medium and high. The receptor adaptive capacity (their financial, technological and social ability, and the fitness and readiness to deal with weather extremes) is classified as *High* if the receptor is very capable, fit and prepared to deal with such events; as *Medium* in the case the receptor has a low ability, fitness, and/or is only partially prepared to deal with such events, and as *Low* if the receptor is not able, fit and/or prepared to independently deal with such events, where any change or adaptation to changes would involve a lot of effort.

Area	3.922 km².
Population	309.258
Urban population	164.543
Rural population	144.715
Number of municipalities/cities	2 cities; 3 municipalities
Average density of population	74 inhab./ km²
Agricultural land	1230.820 km²
Forest land	2622.100km²

FIGURE 1
Geographical position of Raska district in Republic of Serbia [6]*
*Forest and agricultural land source: *CORINE Land Cover 2012* (2016). © European Union, Copernicus Land Monitoring Service 2018, European Environment Agency (EEA).

TABLE 1
The used agricultural land of farms by categories*

Region	Total area (ha)	Kitchen garden	Arable land	Meadows and pastures	Fruit plantations	Vineyard	Nurseries	Other
Republic Serbia	3.437.423	23.727	2.513.154	713.242	163.310	22.150	1.327	512
Raska District	102.885	955	31.494	62.717	7.642	39	16	22

*The data on the used agricultural land of farms are the result of the official Agriculture Census of 2012 [13] and they differ from the data which were the source of Corina land cover 2012 (2016) (Figure 1). This inconsistency should be examined in the future

TABLE 2
An overview of the forest land in the Raska Administrative District

Area/Administrative District	Total area of District/ Municipality (km^2)	Forest land (ha)* (2014)
Raska District	3.923	190.453,13
Vrnjacka Banja	239	13.291,12
Kraljevo	1.530	72.903,86
Novi Pazar	742	37.564,61
Raska	670	31.708,56
Tutin	742	34.984,98

*The data on the used agricultural land of farms are the result of the Statistical Office of the Republic of Serbia, and they differ from the data which were the source of Corina land cover 2012 (2016) (Figure 1). This inconsistency should be examined in the future

After vulnerability assessment, a scenario analysis was conducted based on the results of 9 different regional climatic models for the RCP 8.5 scenario. The results that are bias-adjusted of future climate projections, with a horizontal resolution of 11 km, for selected scenario, have been taken from the EURO-CORDEX database [9]. The following models have been selected: CCLM4-8-17 CNRM-CERFACS-CNRM-CM5_r1, CCLM4-8-17_ICHEC-EC-EARTH_r1, CCLM4-8-17_MOHC-HadGEM2-ES.rcp85_r1, CCLM4-8-17_MPI-M-MPI-ESM-LR_r1, HIRHAM5_ICHEC-EC-EARTH_r1, RACMO22E_ICHEC-EC-EARTH_r1, RACMO22E_MOHC-HadGEM2-ES_r1, REMO2009_MPI-M-MPI-ESM-LR_r1, REMO2009_MPI-M-MPI-ESM-LR_r2.

The results are presented as the average changes for the three future periods (the near future, the middle and the end of the century). By using the scenario analysis results, with the evaluation matrix (the resulting risk category has been assessed as very high, high, medium and low), the final assessment was made for risks for the subject area natural resources (forest cover and agricultural land) relating to climate changes.

THE CURRENT SITUATION WITH REGARD TO THE RASKA DISTRICT AGRICULTURAL AND FOREST RESOURCES.

A highland agro-ecological area may be distinguished in the Raska District territory, with several subareas within it, the natural conditions and tradition of which have set the direction of the local agricultural production. It is represented by a part of the Stari Vlah – Raska Highland, which is the primary morphological feature of this area. Several mountains with their plateaus rise from it, criss-crossed by river valleys with basin widenings (Novopazar Basin, Raska Basin). The mountain terrain prevails, represented by the mountains which enclose this area – the slopes of Kopaonik (2,017m) in the east, extending via Zeljin and Stolovi towards the West Morava Region, then Cemerno (1,579 m), Golija (1,883 m) as the boundary area towards Western Serbia, and the mountains of Rogozna (1,504 m) and Radocelo.

The Ibar and Raska River valleys are characterised by alluvial soil, significant for the farm production of this mountainous region, while the valley sides are composed of clay soils and podzols in lots. The most widespread is brown, skeletal soil which significantly limits agricultural production. Owing to great pasture expanses, presented in Table 1, pasture-based livestock farming is predominant in this area, alongside agroforestry economics on mountain terrains, while due to small arable areas farming is underdeveloped and reduced to production for the livelihood of individual farms. It is only more significant in river valleys and basin enlargements, albeit with lower yields.

The Raska administrative district is characterised by a prominent forest cover (51%), much above the Republic average. Forests and wooded areas of this district cover the area of 190,453 ha (according to the data of the Republic Statistical Office [10]), i.e. 2,622,100 km² according to the Corina land cover 2012 [6]. The immense forest potential represents a rich raw material basis for the development of this area which is presented in Table 2. The state-owned forests of the Raska District are managed by two forestry management branches of the "Srbijasume" Public Company, the "Stolovi" Forestry Service – Kraljevo (with the forest man-

agement units of Kraljevo, Bogutovac and Usce) and the „Sumarstvo“ Forestry Service – Raska (with the forest management units of Kraljevo, Bogutovac and Usce) and the „Sumarstvo“ Forestry Service – Raska (with the forest management units of Raska, Novi Pazar and Tutin), while the forests in the territory of the Vrnjacka Banja municipality are managed by the “Borjak” Public Company [11].

According to the Regional Spatial Plan for the region of the Sumadija, Pomoravlje, Raska and Rasina Districts [12], the Vrnjacka Banja municipality has the highest forest cover percentage (61.1%), to be followed by Novi Pazar (46.9% forest cover), Raska (46.8%), and Tutin (42%). The health of the stands may be characterised as relatively good, with the greatest variations being found in sprout stands. The artificially raised conifer stands are young stands of varying health which require care. According to their purpose, the most common are the forests with the primary function to protect the soil from water erosion and to provide a protection zone of the “Golija – Studenica” biosphere reserve. As the most significant limitations to a faster development in the forestry area and a more efficient use of this area’s existing potential, Brasanac-Bosanac Lj. et al. [14] point to the non-existence of forest roads in certain parts of forest complexes, unresolved ownership relations (arbitrary occupation, part of the forest land was owned by the church) and the forest quality issue, forest hazards in the form of damaging abiotic and biotic factors, pests and fires; inadequate activities and finances devoted to the protection, care and raising of forests; insufficient felling control; absence of cooperation of the „National park Kopaonik“ and “Srbijasume” public companies with private forest owners and other local population, the problem of unplanned construction, etc. The aforesaid inadequacies and limitations may also be the main challenges that forestry has to deal with relating to climate changes, especially with regard to the relatively poor state of forests (a large share of sprout forests, a low volume growth, unfavourable age structure), uneven distribution of the forest cover, organization problems in managing which concern a large number of private forest owners, etc.

RESULTS

In determining the vulnerability of agricultural and forest resources in the Raska District territory to climate changes, we have analysed the extreme weather events in the period 1995-2015 (Table 3), to obtain the information on the exposure, or sensitivity of the aforesaid resources to heat waves, extreme colds and frost, heavy precipitation, floods and drought. The data of the Republic Hydrometeorological Service indicate that during the observed twenty-year period the incidence of extremes in the Raska District territory has been growing in frequency. As regards the duration of heat waves, and the number of “summer” and “tropical days”, the year 2012 is the year of the greatest extremes with recorded 6 heat waves in the total duration of 59 days and even 42 “tropical days”. The years 2000, 2002, 2003, 2007, 2013 and 2015 are also the years marked by high sensitivity to heat waves. The drought index (Standardised Precipitation - Evapotranspiration Index), which is used in the period from March to August (approximating the vegetation period) indicates that 2000, 2003, 2007, 2011, 2012, 2013 and 2015 were excessively dry years.

Excessive precipitation in the Raska District area, i.e. the number of days with the accumulated daily precipitation exceeding 20mm, 30mm and 40mm, which represent the critical thresholds for the occurrence of torrential floods, were in the years 1996, 1997, 2001, 2004, 2005, 2007 and 2014, the last of which was marked by catastrophic floods covering the whole area of Croatia, Bosnia Herzegovina and Serbia. In the last two decades the Raska District has had extreme colds during which 6 years were registered for high frosty day numbers, i.e. 1995, 1996, 1997, 1998, 2005 and 2011.

In view of the aforesaid, we may conclude that the occurrence of extremes is ever more present in the Raska District area, so that the sensitivity of agricultural and forest resources to these extremes has been assessed as high. The adaptive capacity has been estimated based on the financial, technological or social capacity and fitness to cope with the weather extremes, taking into account the data on the population numbers and density, the GDP per person (it amounted to 2.2% compared to the Republic of Serbia average for 2016, which accounts for the district’s classification among the undeveloped districts of Serbia), the technical equipment owned by the farms and households for the performance of agricultural production, the data on irrigated areas, the institutional capacities and the engagement of forest managers, etc. The results of the assessment of vulnerability of agricultural and forest soils of the Raska District is presented in Table 4.

The vulnerability of agricultural areas and agriculture in general has been assessed as high in relation to all the climate change effects (heat waves, extreme cold, droughts and extreme precipitation and floods). Given the prevalence of meadows and pastures in the structure of the used agricultural land (around 50% of the total land used), pasture-based livestock farming is predominant, and in view of the fact that high-temperature and drought periods have seen the drying up of springs, mostly in the Pester Field area, which put in jeopardy many cattle, as well as the population itself, the vulnerability for this branch of economy has been assessed as high. Changes in climate conditions may also lead to soil deterioration and con-

tamination, as well as physical damage caused by extreme precipitation, floods, torrential flows and erosion.

Based on exposure and adaptive capacity, forest soil also has high vulnerability to climate change effects, especially the effect of heat waves, extreme colds and droughts. Any extreme weather event will cause damage to forests, either through the deterioration and perishment of tree trunks as a result of frost in extreme colds, or damage at the roots and perishment in case of excessive precipitation, floods and soil erosion. In addition, heat waves may lead to the drying of trunks and changes in their growth cycle, with the added problem of frequent occurrence of numerous pests and gipsy moths. The vulnerability of forests to the effect of extreme precipitation and floods in the Raska District territory has been assessed as medium owing to the adaptive capacity and the role of forests in protection against erosion, torrential floods, and in regulation of water regimes.

THE ANALYSIS OF CLIMATE CHANGE SCENARIOS AND POTENTIAL FUTURE RISKS.

The following tables show the climate changes in the Raska District area based on the results of 9 different models for the RCP 8.5. scenario. The results are presented as medium changes for the future three periods (the near future, the middle and the end of the century). The scenario analysis predicts climate changes in the future, and in turn considers the risks to the natural resources (forest and agricultural soil) of the subject area.

The results of modelling relating to temperature changes which are presented in Table 5 point to a further increase, which is reflected in the rise of both mean annual temperatures, and the rise in the number of days of heat wave duration. Observing the data on the increase of the number of days with temperatures above 25°C and 30°C, and on the other hand a reduction in the number of days of frost, we may conclude the changes will also affect seasonal temperatures, resulting in warmer summers and winters alike.

TABLE 3
An overview of the medium, minimum and maximum values of extreme weather conditions in the period 1995-2015 in the Raska District Area

	TX25	TX30	HW	HWND	FD	RR20	RR30	RR40	SPEI
MIN	26	3	6	1	79	1	0	0	1.98738
AVERAGE	56,75	13,65	23,9	2,95	120,2	4,3	1	0,25	-0,321884
MAX	101	42	59	6	142	8	3	3	-2,74245

TABLE 4
The results of the assessment of vulnerability of agricultural and forest soils of the Raska District

	Vulnerability			
	Heat waves	Extreme cold	Extreme percipitation	Drought
Agriculture	HIGH	HIGH	HIGH	HIGH
Forest	HIGH	HIGH	MEDIUM	HIGH

TABLE 5
The projected air temperature changes for the Raska District

	The future period compared to the reference period 1986-2005		
	2016-2035	2046-2065	2081-2100
Mean annual temperature	+0,92 °C	+2,39°C	+4,79°C
TX25 (number of days with temperatures above 25°C)	+13,4	+31,15	+65
TX30 (number of days with temperatures above 30°C)	+9	+18,95	+45,65
HW (number of days of heat wave duration)	+13,4	+27,7	+83,45
FD (number of frost days)	-10,3	-30,7	-60,7

TABLE 6
The projected changes in the precipitation levels for the Raska District

	The future period compared to the reference period 1986-2005		
	2016-2035	2046-2065	2081-2100
Mean annual precipitation	-1,78%	3,95%	-7,76
Precipitation for June-July-August	-6,85%	-13,26%	-14,76
RR 20 (number of days with precipitation above 20 mm)	0,15	1,45	1,2
RR30 (number of days with precipitation above 30 mm)	0,3	1,15	0,95
RR40 (number of days with precipitation above 40 mm)	0,1	0,65	0,75
SPEI (drought index)	-0,3	-0,75	-1,03

TABLE 7
Analysing climate change scenarios

Parameter	Expected changes	Consequences of the weather
Mean annual temperatures and heat waves	Increase	Magnification effect
Number of frosty days	Reduction	Balancing effect
Mean annual precipitation	Reduction	Indifferent effect
Precipitation with large daily accumulation	Increase	Magnification effect
SPEI index	Increase	Magnification effect

TABLE 8
The assessment of climate change risks to the agricultural and forest resources of the Raska District

	Climate change risks			
	Heat waves	Extreme cold	Extreme percipitation	Drought
Agriculture	EXTREMELY HIGH	MEDIUM	EXTREMELY HIGH	EXTREMELY HIGH
Forest	EXTREMELY HIGH	MEDIUM	HIGH	EXTREMELY HIGH

The results of modelling precipitation accumulation changes which are presented in Table 6 indicate regime changes with regard to mean annual (with noticeable differences between the beginning and the end, which are characterised by a reduction, compared to the middle of the century, with an expected rise in the precipitation level). However, in view of an almost continued rise in the number of days with an intensive accumulation of precipitation, we may conclude that the occurrence of heavy precipitation, which poses the risk of floods, will be on the rise until the end of the century. On the other hand, a decrease in precipitation during the summer will be more prominent to the middle of the century, with a continuing tendency to the century end, but with minor changes which pose a potential risk of drought. This fact is also confirmed by the drought index which is also negative and continually on the rise till the end of the century, which may significantly affect the conditions for practising agricultural production.

By analysing the scenarios of future climate changes, we have established that the observed effects will additionally increase the total sensitivity as a result of the expected rise in mean annual temperatures, the heat waves which will be more and more frequent and longer in duration, and a higher incidence of intense precipitation (Table 7). The effect of balancing may be expected with regard to extreme colds due to a falling number of frosty days, with the predicted events potentially alleviating the current sensitivity to extreme cold.

The assessment of risks to natural resources in the future as a result to climate changes is based on the results of vulnerability and effect analysis based on the conducted scenario analysis. For determining the final risk assessment relating to the Raska District natural resources (forests and agricultural soil) we have also used the evaluation matrix, and the obtained risk category has been assessed as extremely high, high, medium and low (Table 8).

It has been estimated that the Raska District agriculture will be exposed to an extremely high risk, to be caused primarily by excessive droughts, heat waves and extreme precipitation. Bearing in mind that meadows and pastures cover the largest part of the total agricultural land structure, this form of risk could have the greatest effect on livestock farming. We can expect a medium level of risk of extreme colds to the forest and agricultural resources, in view of the estimations that the number of frosty days will fall by the end of the century. Potential risks may include the drying up of underground springs for the watering of livestock, an increase in the presence and effect of plant pests, and a decrease in the diversity of species.

Forests will be exposed to an extremely high risk of heat waves and droughts which may bring about changes to growth cycles, the deterioration and even dying out of species, the occurrence of forest fires. The high risk of extreme precipitation and floods in the future may cause soil erosion.

CONCLUSION

The agriculture and forest sectors of the subject area are vulnerable to climate changes, due to which they are exposed to high risks of the consequences of climate changes in the future. Taking into account the results of 9 different models for the RCP 8.5 scenario, which have been used in the work, the greatest risks are posed by heat waves and droughts, followed by extreme precipitation, while the level of risk of extreme colds has been estimated as medium. Primarily through the planning and legal regulations, and through practice as well, it is essential to take certain adaptation measures for the above sectors. The most intense impact of climate changes, and in turn adaptive options, are to be found in the agricultural sector [15]. According to many experts in the field of agriculture, the genetic basis for introducing new crop species which can adapt to the expected climate conditions is quite large, with significant effects to be expected in that regard [16]. For that reason, the introduction of species which are more easily adaptable to climate changes is emphasized as the

most frequent measure of adaptation for the agricultural sector. Some of the proposed adaptation measures for the agricultural sector would include irrigation, through the general future development of irrigation, which would, in the subject area, primarily affect livestock farming and livestock watering.

In view of the fact that forests represent a great potential of the subject area, and that according to the results of vulnerability assessment they are expected to face a very high risk of heat waves and droughts, the establishment of adequate adaptive measures for the forestry sector is crucial for the future. The National Plan of Adaptation to the Changed Climate Conditions [5] analyses the proposed measures, which have not been sufficiently implemented in the forest management practice so far, while they may also be used for the subject area of the Raska District. The improvement of forests, including the conversion of forests as an important aspect of strengthening of forest ecosystems and improvement of their adaptive capacity, are high-priority measures in the future management of forests of this area. In addition, the construction of new forest roads should be carried out with a view to more effective prevention against fires and their spreading, and improvement of forest management in general.

REFERENCES

[1] Adaptation Compass - Future cities (2013) Urban networks to face climate change. Guidance for developing climate-proof city regions. http://www.future-cities.eu/project/adaptation-compass/.

[2] Parry, M.L., Canziani, O.F., Palutikof, J.P., van der Linden, P.J., Hanson, C.E. (Eds.) (2007) Contribution of Working Group II to the Fourth Assessment Report of the Intergovernmental Panel on Climate Change. Cambridge University Press, Cambridge, United Kingdom and New York, NY, USA.

[3] Srivastava, A. (2015) Vulnerability to climate change and variability: an investigation into macro and micro level assessments – A case study of agriculture sector in Himachal Pradesh, India. The "State of DRR at the Local Level" - A Report on the Patterns of Disaster Risk Reduction Actions at Local Level.

[4] Ministry of Environment Protection (2017). The Second Report of the Republic of Serbia following the United Nations Framework Convention on Climate Change. Belgrade. ISBN: 978-86-87159-15-1.

[5] Ministry of Agriculture and Environment Protection (2015). The First National Plan of Adaptation to the Changed Climate Conditions for the Republic of Serbia. Belgrade.

[6] CORINE Land Cover 2012 (2016) © European Union, Copernicus Land Monitoring Service <2018>. European Environment Agency (EEA).

[7] Cornes, R., G. van der Schrier, E.J.M. van den Besselaar, P.D. Jones. (2018). An Ensemble Version of the E-OBS Temperature and Precipitation Datasets, J. Geophys. Res. Atmos., 123. doi:10.1029/2017JD028200.

[8] Kumar, P., Geneletti, D., Nagendra H. (2016) Spatial assessment of climate change vulnerability at city scale: A study in Bangalore, India. Land Use Policy. 58, 514-532.

[9] Jacob, D., Petersen, J., Eggert, B., Alias, A., Christensen, O. B., Bouwer, L. M., Braun, A., Colette, A., Déqué, M., Georgievski, G., Georgopoulou, E., Gobiet, A., Menut, L., Nikulin, G., Haensler, A., Hempelmann, N., Jones, C., Keuler, K., Kovats, S., Kröner, N., Kotlarski, S., Kriegsmann, A., Martin, E., van Meijgaard, E., Moseley, C., Pfeifer, S., Preuschmann, S., Radermacher, C., Radtke, K., Rechid, D., Rounsevell, M., Samuelsson, P., Somot, S., Soussana, J.-F., Teichmann, C., Valentini, R., Vautard, R., Weber, B. and Yiou, P. (2013) EURO-CORDEX: New high-resolution climate change projections for European impact research. Regional Environmental Change. (online). 14, 563–578. http://dx.doi.org/10.1007/s10113-013-0499-2.

[10] Statistical Office of the Republic of Serbia (2016). Municipalities and Regions in the Republic of Serbia. Belgrade.

[11] Brasanac-Bosanac, Lj., Filipovic, D., Cirkovic-Mitrovic, T. (2014) An assessment of the negative impacts air temperature changes on Forest ecosystems in Serbia. XXII International Conference „Ecological Truth" Eco - Ist `14, University of Belgrade, Technical Faculty Bor, 10-13 June 2014, Bor, Serbia. ISBN 978-86-6305-021-1, 297-304.

[12] Government of the Republic of Serbia (2014). The Regional Space Plan for the Sumadija, Pomoravlje, Raska and Rasina Administrative District Areas. Official Gazette of the Republic of Serbia. No. 39/14. Belgrade.

[13] The Regional Gross Domestic Product – Republic of Serbia Regions and Areas 2016. Working document. Republic Statistics Office. Belgrade 2018. ISSN 1820–0141 http://www.stat.gov.rs/.

[14] Brasanac-Bosanac, Lj., Cirkovic-Mitrovic, T., Filipovic, D., Rakonjac, Lj., Lucic, A. (2017) An Integral Approach to the Protection of Forest Ecosystems in Serbia with a View to Timely Adaptation to Climate Changes. A plenary paper. Proceedings of the IX scientific-professional conference with international participation „Plan-Based and Normative Protection of Space and the Environment “, 11-13 May, Palic-Subotica, Belgrade. ISBN 978-86-6283-023-4 (APPS), COBISS.SR-ID2144076 92, 25-32.

[15] Trbic, G., Djurdjevic, V., Bajic, D., Cupac, R., Vukmir, G., Popov, T. (2014) Climate change and adaptation options in Bosnia and Herzegovina - Case study in agriculture. In The international conference “ADAPT to CLIMATE”, Filoxenia conference Centre in Nicosia, Cyprus, on March 27th and 28th, 2014.

[16] Trbic, G., Bajic, D., Djurdjevic, V., Ducic, V., Cupac, R., Markez, Dj., Vukmir, G., Dekic, R., Popov, T. (2018) Limits to Adaptation to Climate Change in Bosnia and Hercegovina: Insights and Experiences. In: Filho, W.L. and Nalau, J. (eds.) Climate Change Management – Limits to Climate Change Adaptation. Hamburg, Germany. Springer, 245-259.

Received: **04.07.2019**
Accepted: **15.01.2020**

CORRESPONDING AUTHOR

Ljubica Duskov
University of Belgrade
Faculty of Geography,
Department of Spatial Planning,
Belgrade – Serbia

e-mail: ljubica.p88@gmail.com

© by PSP Volume 29 – No. 04A/2020 pages 2766-2771 Fresenius Environmental Bulletin

DETERMINATION OF SOME QUALITY PROPERTIES OF ENSILED FORAGE TURNIP (*BRASSICA RAPA* L.) WITH DIFFERENT ADDITIVES

Ilkay Cetin[1], Asuman Arslan Duru[2,*]

[1] Bandırma Sheep Breeding Research Institute, Balıkesir, Turkey
[2]Department of Animal Science, Faculty of Agriculture and Natural Sciences, Usak University, 64200, Usak, Turkey.

ABSTRACT

In this study, it was aimed to determine the effect of the addition of different additives on the chemical, fermentation, microbiological and sensory properties of forage turnip (*Brassica rapa L.*) silages. In this content, forage turnip was ensiled without additive (control) or with 6 % corn cracked, 6 % wheat cracked or 3 % molasses. According to the experiment results; dry matter and organic matter content of 3% molasses and control groups were significantly decreased (P<0.01). Crude ash and lactic acid increased (P<0.01), crude protein decreased with addition of 3 % molasses (P<0.01). There were no differences on ADF, pH, acetic acid, propionic acid contents between control silages and silaged treated with additives (P>0.05). None of the experimental groups were found to have butyric acid, ammonia nitrogen, *Enterobacteriaceae*, *Listeria spp*. and yeast. The number of lactic acid bacteria increased with the addition of additives to the forage turnip silages. There was no statistically significant difference in sensory analysis values among the groups (P>0.05). Results conducted that the forage turnip could be ensiling without using any additives.

KEYWORDS:
Forage turnip, Silage, Microbiological properties, Additive, Volatile fatty acids.

INTRODUCTION

The genus Brassica is one of the most important in the Brassiceae tribe, which contains some crops and species of great importance worldwide. It is an annual, highly fertile and easily digestible plant which can be used for grazing 80-150 days after seeding depending on the species [1]. Depending on the nitrogen fertilization and wether conditions crude protein content of Brassica varies from 15 to 25 % in leaves, and from 8 to 15 % in roots. Additionally, the dry matter contents of Brassica species range from 4 to 8 t ha^{-1} [2; 3; 4].

Forage turnip (*Brassica rapa L.*), one of the species of Brassica, is an alternative coarse feed source and its leaves and roots (with a low sugar content) are consumed willingly by cattle and sheep; and it also can be used easily for grazing in warm and dry seasons when the gramineae are infertile, in late autumn or in the middle of winter with the intent of additional feeding. It is also used in the feeding of animals requiring high nutritional content [1;5]. Dry matter content of forage turnip varies according to the species and the region they are grown in. Leaf and root dry matter contents have been reported on average as 8.93 % and 7.75 % respectively [6]. Even though it has a 90 % or higher water content in general, energy need of the animals can be satisfied by consuming the feed in sufficient amounts [7]. However, due to its low fibre content, it is not recommended to use more than 75 % in ration in order to keep rumens of the ruminants functioning properly [5]. Koch and Karakaya [7] reported that the forage turnip will cause significant nutrient losses after harvest due to the high-water content and that it can only be used in animal feeding as silage. It has also been stated that a daily increase between 214-249 g on body weight gain was observed with the lambs grazing the hybrids of *Brassica campestris sensulato L.* x *Brassica rapa L.* and this hybrid can be used as a late lamb feeding and has a good potential for grazing system [3]. Although in recent years forage turnip started to be used as a coarse fodder source for silage, its ensiling has not been provend yet.

In this study, it is aimed to determine some quality characteristics of the forage turnip (*Brassica rapa* L.) which is ensiled with corn cracked, wheat cracked and molasses additives.

MATERIAL AND METHODS

Silage Material and Ensiling Period. Forage turnip (*Brassica rapa L.*) were obtained from a manufacturer engaged in farming in the Aegean region of Turkey. Forage turnip seeds were planted on 20 April 2016 at 600 g/da. It has been harvested when capsules are ripened on November 2016. Forage turnip after harvest in laboratory conditions,

approximately 2 - 2.5 cm in size were cut. Chemical composition of fresh forage turnip was shown in Table 1.

The first group was used as a control group without additives. In the other groups, 6 % corn cracked, 6 % wheat cracked and 3% molasses were added as an additive. Four ensiling process were carried out in each group for 4 replications. The fresh material was ensiled to 1 lt anaerobic plastic jars. After plastic anaerob jars were filled with forage turnip samples and ensiling period lasted for 75 days.

Chemical Analyses. The dry matter contents of the silages were determined as described by [8]. Dried samples were ground with a sieve of 1 mm diameter; then crude ash (CA) content of the samples were determined by burning them in muffle furnace at 550 ºC for 4 hours as specified in AOAC [8] and also crude protein (CP) content was determined with Kjeldahl method on % dry matter basis [8]. Organic matter (OM) content was calculated with OM=DM-CA formula. The analyses used for determining neutral detergent fibre (NDF) and acid detergent fibre (ADF) contents of silage samples were performed by using Fiber Analyzer [9] as Van Soest [10] indicated.

Silage Fermentation Characteristics. To determine pH values of the silage samples, 100 ml of distilled water was added on 25 g of silage samples and after blending it with a shaker was measured with a digital pH meter [11]. Right after the opening of the silages, 40 g of silage sample was taken and stirred for at least 5 minutes after adding 360 ml of distilled water. This mixture was filtered with Whatman filter paper no:1 and was centrifuged at 14.000 rpm for 30 min. NH_3-N content was determined with Kjeldahl distillation method from the 100 ml of this filtrate [12] and the contents of volatile fatty acids [acetic acid (AA), propionic acid (PA) and butyric acid (BA)] and lactic acid (LA) were analyzed for HPLC [13] (HPLC Conditions: Column: C18, 5 µm, 4.6 x 250-mm; Mobile Phase: Isocratic; 25-mM K-phosphate buffer; pH 2.4; Flow Rate: 1.5 mL/min.; Column Temperature: 30 ºC; UV Detector: Wavelength: 210 nm; Injection Volume: 20 µL)

Microbiological Analyses. The count of sulphite-reducing anaerobes was identified in accordance with the method presented by Stanley et al. [14]. The count of lactic acid bacteria, *Enterobacteriaceae, Listeria spp*., yeast and moulds in each silage were determined in accordance with the method presented by Harrigan [15].

Sensory Analyses. When silages were opened, the smell, structure and color of silages were scored using silage evalution survey recommended by DLG [16].

Statistical Analyses. The results obtained were analysed in accordance with the ONE-WAY ANOVA procedure on the SPSS 16.0 packaged software and Duncan's Multiple Range Test was implemented to determine the differences of the groups. Besides, the microbiological analyses of silages were also performed in accordance with the Frequencies procedure in the SPSS package software [17].

RESULTS AND DISCUSSION

The chemical composition of the forage turnip (*Brassica rapa L.*) silages are presented in Table 2.

TABLE 1
Chemical composition of fresh forage turnip

	DM, %	CA, % DM	CP, % DM	NDF, % DM	ADF, % DM
Forage turnip	23.33	10.04	19.96	36.04	25.96

DM: Dry Matter; CA: Crude Ash; NDF: Neutral Detergent Fiber; ADF: Acid Detergent Fiber; CP: Crude Protein.

TABLE 2
Chemical composition of forage turnip silages

Parameters	Control	6 % Corn	6 % Wheat	3 % Molasses	P
DM, %	25.29 ± 1.24^{b}	28.33 ± 0.95^{a}	27.91 ± 0.95^{a}	25.86 ± 0.58^{b}	0.001
OM, % DM	64.42 ± 7.65^{b}	73.50 ± 2.64^{a}	72.18 ± 1.87^{a}	58.50 ± 7.79^{c}	0.001
CA, % DM	8.16 ± 1.25^{b}	7.50 ± 0.71^{b}	7.75 ± 0.32^{b}	9.49 ± 0.78^{a}	0.001
CP, % DM	18.28 ± 1.62^{a}	17.96 ± 1.52^{a}	17.83 ± 0.86^{a}	14.55 ± 0.88^{b}	0.001
NDF, % DM	42.08 ± 1.04^{ab}	40.34 ± 2.14^{b}	40.60 ± 1.90^{b}	43.39 ± 1.18^{a}	0.03
ADF, % DM	30.50 ± 3.07	28.26 ± 1.59	29.39 ± 1.73	31.94 ± 0.37	0.07

[a-b] Differences in groups carrying different letters on the same line are statistically significant P<0.05).
[a-c] Differences in groups carrying different letters on the same line are statistically significant (P<0.01).
DM: Dry Matter; OM: Organic Matter; CA: Crude Ash; NDF: Neutral Detergent Fiber; ADF: Acid Detergent Fiber; CP: Crude Protein.

The crude ash content increased with the addition of 3% molasses (P<0.001) but the crude protein content decreased (P<0.001). The crude ash contents of the experimental silages varied from

7.50 % to 9.49 %. the silage with 3 % molasses has a high level of crude ash when compared with the other groups (P<0.01) due to high crude ash content (11 %) of the molasses used. It was reported that the crude protein content can vary from 15 % to 25 % for the forage turnip leaves; and it can vary from 8 % to 15 % for forage turnip roots [2; 3; 4; 22]. The crude protein content of the silages with 3 % molasses lower than the other groups (P<0.001). Molasses contained high levels of NPN (non-protein nitrogen) compounds reduced the crude protein content of the silages to which it was added. Acar and Bostan [23] indicated that using molasses as an additive for alfalfa silages decreased crude protein level of silages. Can et al. [19] and Demirel and Yıldız [24] stated that using molasses as an additive for silages did not change crude protein levels of silage contents. These differences might be due to the differences on fresh materials and levels of molasses used in the studies.

The NDF content of 6 % corn and 6% wheat added silages was significantly lower than the 3 % molasses added silages (P<0.001). Regarding ADF contents, it was determined that the differences were not statistically significant (P>0.05) and these results is compatible with reporting with Arbabi and Ghoorchi [25]. Bureenok et al. [26] and Desta et al. [27] reported no differences in NDF content by addition of molasses to silages. Corn and wheat's NDF and ADF contents may have been effective in increasing the degradability of cell wall components in silages by accelerating the activity of lactic acid bacteria.

The fermentation characteristics of the forage turnip (*Brassica rapa L.*) silages are presented in Table 3.

The differences between the groups in terms of pH values of forage turnip silages were not statistically significant (P>0.05). pH is one of the most important elements of good quality silage and should be in the range of 3.8-4.2 [28]. The fact that the pH values of the forage turnip silages that formed the silages were lower than 4.2 and the finding of similar values among the groups is an indicator of a high-quality silage [29;30;31]. Lactic acid contents of the control forage turnip silage, and the forage turnip silages in which corn and wheat were used as additives among the experimental silages were close and the differences between the groups were not found to be significant (P>0.05). On the other hand, using 3 % molasses for forage turnip silage affected lactic acid positively and increased it significantly when compared with the other groups (P<0.05). Molasses containing high amounts of water-soluble carbohydrates may have increased the lactic acid content by using microorganisms of silage. Consistent with this study, Huisden et al. [32] and Li et al. [33] reported similar results.

When the forage turnip silages were analysed in terms of acetic acid and propionic acid, the differences between the groups were not significant (P>0.05). Butyric acid was not found in the forage turnip silages. Butyric acid bacteria do not appear in silages where pH values are below 4.5. Since the lactic acid bacteria would be the dominant flora when pH value is kept in the range of 3.8- 4.2, it would not be possible for the butyric acid bacteria to reproduce either [34]. Bureenok et al. [35] and Arslan Duru and Aksu Elmalı [36] also obtained similar results to that silages do not contain butyric acid.

One of the important criteria indicating the level of degradation of proteins by butyric acid bacteria in silages is the concentration of ammonia. The ammonia nitrogen should be lower than a total 0.08 % N in a good quality silage. Besides, McDonald et al. [37] stated that deamination occurs on the amino-acids due to the high level of acetic acid content in the silages and consequently ammoniac level increases. When the experimental silages were analysed in terms of fermentation characteristics, it was observed that the good quality fermentation for the forage turnip (*Brassica rapa L.*) silages. The following observations supported this condition; pH values of forage turnip silages were between the expected values, lactic acid contents were produced sufficiently, no butyric acid which is one of the undesirable volatile fatty acids and no ammonia nitrogen which occur as a result of poor fermentation condition in the silages were found.

TABLE 3
Fermentation characteristics of forage turnip silages

Parameters	Control	6 % Corn	6 % Wheat	3 % Molasses	P
pH	3.80 ± 0.10	3.69 ± 0.10	3.79 ± 0.08	3.76 ± 0.10	0.12
LA, %	1.98 ± 0.25^{b}	2.18 ± 0.20^{b}	2.13 ± 0.68^{b}	3.09 ± 0.52^{a}	0.04
AA, %	0.23 ± 0.06	0.20 ± 0.05	0.20 ± 0.02	0.23 ± 0.11	0.69
PA, %	0.16 ± 0.08	0.17 ± 0.07	0.26 ± 0.13	0.27 ± 0.11	0.25
BA, %	ND	ND	ND	ND	
NH_3-N	ND	ND	ND	ND	

$^{a-b}$ Differences in groups carrying different letters on the same line are statistically significant (P<0.05).
LA: Lactic Acid; AA: Acetic Acid; PA: Propionic Acid; BA: Butyric Acid; NH_3-N: Ammonia Nitrogen; ND: Not Determined.

TABLE 4
Microbiological characteristics of forage turnip silages (cfu/g)

Parameters	Control	6 % Corn	6 % Wheat	3 % Molasses
LAB	ND	2.0 (1 sample) *	2.2	2.2
E*nterobacteriaceae*	ND	ND	ND	ND
Listeria spp	ND	ND	ND	ND
SRA	ND	2.0 (1 sample) *	ND	3.3 (1 sample) *
Yeast	ND	ND	ND	ND
Mould	ND	3.3 (1 sample) *	2.5 (2 sample averages) *	2.5 (1 sample) *

ND: Not detected (<2.0 cfu/g) * Under the detection limit in other samples (<2.0 cfu/g)
LAB: Lactic acid bacteria; SRA: Sulphide Reducing Anaerobes.

TABLE 5
Physical characteristics of forage turnip silages

Parameters	Control	6 % Corn	6 % Wheat	3 % Molasses
Smell	10.5 ± 0.6	10.3 ± 0.4	10.2 ± 0.4	10.1 ± 0.2
Structure	3.6 ± 0.1	3.2 ± 0.1	3.2 ± 0.1	3.4 ± 0.1
Colour	1.3 ± 0.1	1.2 ± 0.1	1.0 ± 0.2	1.2 ± 0.1
Quality	15.4	14.7	14.4	14.7
	Satisfying	Satisfying	Satisfying	Satisfying

The microbiological characteristics of forage turnip silages are shown in Table 4.

E*nterobacteriaceae, Listeria* spp, sulphite reducing anaerobes, yeast and mould are undesired microorganisms [38-39]. The count of lactic acid bacteria in the control silages was found to be as <2.0 cfu/g, and 2 cfu/g of lactic acid bacteria in only one of the samples from the group with 6 % corn and 2.2 cfu/g lactic acid bacteria in the groups with 6 % wheat and 3 % molasses. It was also found that the *Enterobacteriaceae, Listeria* spp. and yeast of experiment silages were below as <2.0 cfu/g. The level of sulphite-reducing anaerobes detected in only one of the samples from each silage containing of 6 % corn, and 3 % molasses as 2 and 3.3 cfu/g, respectively. These bacteria were not detected in the control group, and 6 % wheat group. Mould level not detected in the control group. Mould level for only one of the samples of each group with 6 % corn, 3 % molasses, and 6 % molasses were detected 3.3, 2.5 and 2.5 cfu/g., respectively. Consequently, the control group was analysed in terms of microbiologic characteristics, it was observed that the number of lactic acid bacteria, sulphite-reducing anaerobes, *Enterobacteriaceae, Listeria* spp, yeast and mould values were not detected. Just like, the bacteria such as *Enterobacteriaceae, Listeria* spp., yeast and mould also have a negative effect on silages quality. The microorganisms from the *Enterobacteriaceae* family produce chemical compounds such as acetic acid by decomposing carbohydrates. If lactic acid bacteria level increase faster in the silages, *Enterobacteriaceae* level increase slower [40]. Mould was below the detection limit (<2.0 cfu/g) in the control group. Low pH values and producing sufficient amounts of lactic acid prevented the growth of undesirable microorganisms such as yeast and moulds because of lactic acid bacteria was the dominant microflora, butyric acid, ammonia nitrogen and yeast were not detected in all of the silages. In the control group formed without any kind of additives, the number of lactic acid bacteria was found to be below the detection limit (<2.0 cfu/g). Moselhy et al. [41] stated that no kind of mould occurred as a result of adding molasses to *Hedychium gardnerianum*.

The sensory analyses of the experimental silages (smell, structure, colour) were performed by 6 panellists who are experts on the subject. The results related to the sensory analyses are presented in Table 5.

When the experimental silages that were comprised of forage turnip (*Brassica rapa L.*) were compared with each other in terms of visual and physical characteristics; no statistically significant differences were detected between the groups in terms of smell, structure and color; and all groups were identified as belonging to "Satisfying" quality class. The smell, structure and colour of the silages, sensory analyses of which were performed, differs from the fresh material of the silage depending on the fermentation. However, the silage should have a specific smell which is pleasant, pickle-like and not extremely strong; and should not have unpleasant smells like that of butyric acid, yeast and ammonia. Similarly, Arslan Duru and Aksu Elmalı [36] who stated that the sensory analyses of silages obtained by using wheat, corn and molasses as additives for the alfalfa silages were "Satisfying".

CONCLUSION

There has been no information in literature on the properties and quality of ensiled forage turnip. This study demonstrates that the forage turnip can be ensiled without additives despite the positive effects of different additives. The fermentation, microbiological and sensory characteristics of the experiment silages showed that a good quality si-

lage can be obtained if the feed turnip is ensiled moreover when it is affordable, corn cracked in 6 % can be used as an additive.

ACKNOWLEDGEMENTS

This research article is a part of the Master Thesis Project 2017 / TP043 supported by İlkay ÇETİN's Uşak University Scientific Research Projects Unit.

REFERENCES

[1] Ayan, İ., Önal Aşcı, Ö., Başaran, U. and Mut, H. (2006). Quality characters of some turnip (*Brassica rapa L.*) cultivars. Anadolu Journal of Agricultural Sciences. 21 (3), 310-313.

[2] Rao, S.C. and Horn, F.P. (1986). Planting season and harvest date effects on dry matter production and nutritional value for *Brassica* ssp. in the southern great plain. Agronomy Journal. 78, 327-333.

[3] Geren, H., Demiroğlu, G. and Avcıoğlu, R. (2002). Investigations on the yield characteristics of some forage turnip (*Brassica rapa* L.) cultivars. Journal of Agriculture Faculty of Ege University. 39 (1), 47-53.

[4] Türk, M, Albayrak, S, Balabanli, C. and Yüksel, O. (2009). Effects of fertilization on root and leaf yields and quality of forage turnip (*Brassica rapa* L.). Journal of Food, Agriculture & Environment. 7 (3-4), 339-342.

[5] Marvin, H.H. and Jung, J. (2008). Use of brassica crops to extend the grazing season. The Pennsylvania State University, https://extension.psu.edu/use-of-brassica-crops-to-extend-the-grazing-season? (Accessed 14 October 2017).

[6] Kır, B., Demiroğlu, G. and Soya, H. (2007). An Investigation on yield characteristics of some forage turnip (*Brassica rapa* L.) Journal of Agriculture Faculty of Ege University. 44(1), 87-97.

[7] Koch, D.W. and Karakaya, A. (1998). Extending the grazing season with turnips and other brassicas. Wyoming co-operative Extension Service Bull. B-1051.

[8] AOAC (1999). Official methods of analysis. Association of Official Analytical Chemists, 16th ed., Arlington VA.

[9] Ankom (1998). Procedures for fibre and in vitro analysis. Asseda http://www.ankom.com

[10] Van Soest, P.J. (1982). Analytical systems for evaluation of feeds. Nutritional Ecology of The Ruminant, In: P. J. Van Soest (Editor), Cornell University Press. Chapter 6, 75-94.

[11] Polan, C.E., Stive, D.E. and Garrett, J.L. (1998). Protein preservation and ruminal degradation of ensiled forage treated with heat, formic acid, ammonia, or microbial inoculant. Journal of Dairy Science. 81, 765-776.

[12] Broderick, G.A. and Kang, J.H. (1980). Automated simultaneous determination of ammonia and total amino acids in ruminal fluid and in vitro media. J. Dairy Sci. 63, 64-75.

[13] Leventini, M.W., Hunt, C., Roffler, R E. and Casebolt, D.G. (1990). Effect of dietary level of barley-based supplements and ruminal buffer on digestion and growth by beef cattle. Journal of Animal Science. 68, 4334-4344.

[14] Stanley, E.R., Bradley, T.R. and Sumner, M.A. (1971). Properties of the mouse embryo conditioned medium factor(s) stimulationg colony formation by mouse bone marrow cells grown in vitro. J. Cell. Physiol. 78, 301–317.

[15] Harrigan, W.F. (1998). Laboratory methods in food microbiology. 3nd ed., Academic Pres, London, UK.,

[16] DLG (1987). Energie- und Nahrstoffbedarf land wirtschaftlicher Nutztiere. 4. Schweine. DLG-Verlag GmbH, Frankfurt, Germany.

[17] SPSS (2007). SPSS 16.01 for Windows. SPSS Incorporation.

[18] Bolsen K.K., Ashbell, G. and Weinberg, Z.G. (1996). Silage fermentation and silage additives. Asian Austral J Anim Sci. 9 (5), 483-493.

[19] Can, A., Denek, N. and Yazgan, K. (2003). Effect of different additives on silage quality and *in vitro* dry matter digestibility of sugar beet leaves. Van Veterinary Journal. 14(2), 26-29.

[20] Baytok, E, Aksu, T, Karslı M A. and Muruz, H. (2005). The effects of formic acid, molasses and ınoculant as silage additives on corn silage composition and ruminal fermentation characteristics in sheep. Turk. J. Vet. Anim. Sci. 29, 469474.

[21] Balakhial, A., Naserian, AA., Heravi Moussavi, A., Eftekhar Shahrodi, F. and Vali Zadeh, R. (2008). Changes in chemical composition and In vitro DM digestibility of urea and molasses treated whole crop canola silage. Journal of Animal and Veterinary Advances. 7(9), 1042-1044.

[22] Jung, G.A., Byers, R.A., Panciera, M.T. and Shaffer, J.A. (1986). Forage dry matter accumulation and quality of turnip, swede, rape, chinese cabbage hybrids and kale in the Eastern USA.Agron. J. 78, 245-253.

[23] Acar, Z. and Bostan, M. (2016). The effects of some natural additives on quality of alfalfa silage. Anadolu Journal of Agricultural Sciences. 31(3), 433-440.

[24] Demirel, M. and Yıldız, S. (2001). The effect of whole-crop barley harvested at milk stage by adding urea and molasses on silage quality and nutrient degradability in the rumen. Yüzüncü Yıl University Journal of Agricultural Sciences. 11(1), 55-62.

[25] Arbabi, S. and Ghoorchi, T. (2008). The effect of different levels of molasses as silage additives on fermentation quality of foxtail millet (*Setaria italica*) silage. Asian Journal of Animal Sciences. 2 (2), 43-50.

[26] Bureenok, S., Suksombat, W. and Kawamoto, Y. (2011). Effects of the fermented juice of epiphytic lactic acid bacteria (FJLB) and molasses on digestibility and rumen fermentation characteristics of ruzigrass (Brachiaria ruziziensis) silages. Livestock Science. 138, 266–271.

[27] Desta S.T., Yuan X., Li J. and Shao T. (2016). Ensiling characteristics, structural and non-structural carbohydrate composition and enzymatic digestibility of Napier grass ensiled with additives. Bioresour. Technol. 221, 447–454.

[28] Avcı, M., Akdeniz, H. and Deniz, S. (2005). Evaluation of silage quality of wet sugar beet pulp prepared with different additives. 3rd National Animal Nutrition Congress, 110-115, 7-10 September 2005, Adana, Turkey.

[29] Umaňa, R., Staples, C.R., Bates, D.B., Wilcox, C.J.and Mahanna, W.C. (1991). Effects of a microbial inoculant and (or) sugarcane molasses on the fermentation, aerobic stability, and digestibility of bermudagrass ensiled at two moisture contents. J. Anim. Sci. 69, 4588–4601.

[30] Yunus, M., Ohba, N., Shimojo, M., Furuse, M. and Masuda, Y. (2000). Effects of adding urea and molasses on napiergrass silage quality. Asian-Australas. J. Anim.Sci. 13, 1542–1547.

[31] Lima, R., Lourenc¸o, M., Díaz, R.F., Castro, A. and Fievez, V. (2010). Effect of combined ensiling of sorghum and soybean with or without molasses and lactobacillion silage quality and in vitro rumen fermentation. Anim. Feed Sci. Technol. 155, 122–131.

[32] Huisden, C.M., Adesogan, A.T., Kim, S.C. and Ososanya, T. (2008). Effect of applying molasses or inoculants containing homofermentative or heterofermentative bacteria at two rates on the fermentation and aerobic stability of corn silage. J Dairy Sci. 92 (2),690-7.

[33] Li, M., Zi, X., Zhou, H., Hou, G. and Cai, Y. (2014). Effects of sucrose, glucose, molasses and cellulase on fermentation quality and in vitro gas production of king grass silage. Animal Feed Science and Technology. 197, 206-212.

[34] Woolford, M.K. (1984). The silage fermentation. Microbiological Series, 14. Marcel Dekker, Inc, New York and Basel.

[35] Bureenok, S., Yuangklang, C., Vasupen, K., Schonewille, J.T. and Kawamoto, Y. (2012). The effects of additives in napier grass silages on chemical composition, feed intake, nutrient digestibility and rumen fermentation. Asian-Aust. J. Anim. Sci. 25 (9), 1248 – 1254.

[36] Arslan Duru, A. and Aksu Elmalı D. (2016). The Effects of different silage additives on some quality specifications of alfalfa silage. 1st of International Academic Research Congress, 340-344, 3-5 November 2016, Antalya, Turkey.

[37] McDonald, P., Henderson, A.R. and Herson, S.J.E. (1991). The Biochemistry of silage. 16th ed., Chalcombe Publication, Marlow, UK.

[38] Fidan, A.F., Kara, R., Duz, M. and Denk, B., 2019. Investigation of heavy metal contamination and microbiology quality of turnip juice in Western Turkey. Fresen. Enviro. Bull. 28, 3498-3505.

[39] Gargosova, H.Z., Vavrova, M., Čáslavský, J. and Jozifkova, Z., 2012. Ecotoxicological evaluation of unconventional matrices. Fresen. Environ. Bull. 21, 3154-3159.

[40] Basmacıoğlu, H. and Ergül, M. (2002). Silage microbiology. Journal of Animal Production. 43(1), 12-24.

[41] Moselhy, M.A., Borba, J.P. and Borba, A E.S. (2015). Improving the nutritive value, in vitro digestibility and aerobic stability of *Hedychium gardnerianum* silage through application of additives at ensiling time. Animal Feed Science and Technology. 206, 8–18.

Received: **12.07.2019**
Accepted: **08.02.2020**

CORRESPONDING AUTHOR

Asuman Arslan Duru
Department of Animal Science
Faculty of Agriculture and Natural Sciences
Uşak University
64200 Uşak-Turkey

e-mail: duru.asuman@gmail.com

© by PSP Volume 29 – No. 04A/2020 pages 2772-2777 Fresenius Environmental Bulletin

THE EFFECT OF KNIFE TYPE ON CUTTING CHARACTERISTICS OF COTTON STALK

Resat Esgici*

Dicle University, Bismil Vocational High School, Diyarbakir, Turkey

ABSTRACT

The cutting characteristics values of plants are very important data for suitable design of a cutting and pruning machines and related equipment. The objective of this study was to determine of the cutting properties of cotton stalk with use of the multiple regression model for serrated (knife-edge thick and knife-edge thin) and flat-edge knives type. In accordance of this purpose, cutting tests were made with three different type knives. In this study, the knife edge angle, knife type and stalk diameter were selected independent variables. Dependent of these parameters, the cutting force, cutting strength and cutting energy were measured for each type of knife. This study clearly that predict cutting force, cutting strength and cutting energy are influenced by knife type, knife angle and cotton stalk diameter ($P<0.01$). According to regression equations, the cutting force and cutting energy increased with increase stalk diameter for all type of knife because the partial regression coefficient of cotton stalk diameter is positive. However, the cutting force and cutting energy decreased with increase knife edge angles because the partial regression coefficient of cutting angle is negative. The best results were obtained serrated types knives. The highest values were obtained at flat-edge knives. With using of proper knife type and angle, cutting force and cutting strength and cutting energy values can be reduced. As a result, we can say that the flat-edge knife type is not suitable, when compared to serrated knife types. As a result we can recommend that the serrated type knife for a new design of cutting machine and pruning for cotton shoots topping. According these results, if one is interested to study the joint affect of all these variables on cutting properties, one can use this technique.

KEYWORDS:
Cotton, cutting force, blade edge, knife, stalk

INTRODUCTION

Cotton (Gossypium hirsitum L.) is an important crop in the world economy and trade. It is growing many countries in the worldwide. One of the important countries in terms of the magnitude of total cotton production is Turkey and it is Europe's largest textile manufacturer and ranks seventh in the world cotton production. So, it is a one of main source of income for Turkey. Nowadays more than half of Turkey's cotton production is obtained from South-Eastern part of Turkey. Cotton has intensively developed rapidly during the last 20 years in this region. This situation has led to the development of industries based on cotton plant, and also this has had a significant impact on the wider Agribusiness sector. This production ratio in region is important for region's development, human resources development and rural development. Therefore, increasing cotton production and yield, reducing of cotton losses, reducing costs of production and protection of fiber quality are very important for sustainability of the production. Also, the stalk of cotton can be used an organic material for improving of the agricultural soil. The organic matter amount should be increased at cotton planting areas for protecting the soil, increasing the yield and protecting the environment [1]. Cutting of the cotton stalks and mixing the residue with the soil provides significant benefits. When it is considered that many agricultural wastes cause environmental issues and pollution in our day, this process also contributes to making use of the stalk residue and decreasing environmental pollution. In addition, the residue of cotton stalk is an important for conservation of cotton planting area and it is can used as biofuel and also for preventing soil erosion. Pruning process and the cutting of the residues should be carried out using proper equipment in order to attain maximum benefit from these environmental friendly applications. Although cotton yield and production area has been continuously increased with the help of intensive farming practices like plant pruning and topping, this process is done by worker during the vegetation period. So, the production cost is quite high depending on cotton cultural application during the production season. Especially, the cotton production costs are considerably high in harvesting and cutting of plant topping section. To reduce production cost and increase yield, we have to use suitable cutting machine or tapper for cotton. Hence, it is necessary to know the cutting force and energy requirements for proper knife design and also operational parameters during the cutting operations.

So, firstly, we must determine the cutting force of cotton stalk under different conditions. Cutting forces is necessary for determine the power requirements of the process under given conditions, and the design of properly operating and energy-saving machines for cutting machines [2]. It is believed that by cotton producers the cotton plant topping operation is directly related to the yield and reduces bollworm infestations without negatively affecting cotton yields. The similar results were reported by [3], [4], [5] and [6]. According to these researchers, the topping of cotton plants increases the yield and quality of cotton and improves the earliness, limiting the vegetative growth of the plant and improving the development of generative organs of the cotton plants.

The objectives of this study was to determine the suitable and true knife type and knife edge angles depend on cotton stalk diameter with use of the multiple regression model. In this study, the knife edge angle, knife type and stalk diameter were selected independent variables. Dependent of these parameters, the cutting force, cutting strength and cutting energy were measured for different type of knife separately. To improve the yield and yield components in cotton production, the top section of cotton stalk is cutting at this period by farmer. So, we conducted cutting test at this period.

MATERIALS AND METHODS

The stalk of BA-440 cotton variety was used for cutting test [Fig. 1). The some mean properties of BA-440 cotton variety are given in Table 1.

TABLE 1
The some properties of cotton plant during the experiment

Properties	Mean values
Plant height, cm	88.00
Boll number on the plant, number	14.00
Number of branch on one the plant	12.00
Mean stalk diameter, mm	10.00
Average yield (kg/da)	596.80

The tests samples were obtained from cotton experimental field in 2017 in Diyarbakır province (latitude 37°53′N and longitude 40°16′E, 680 m altitude) located in Southeastern of Turkey. The stalk of cotton plants were randomly uprooted from soil surface in five different locations at the experimental field and then transported to the laboratory for cutting tests. Then, the leaves were removed from the plants in the laboratory (Fig. 1). Prior to the tests, the stalks were cutted into four different groups according to diameters (Fig. 1) and heights, namely at 0–5 cm (first internode, IN1), 6-10 cm (second internode, IN2), 11-15 cm (third internode, IN3) and 16–20 cm (fourth internode, IN4). The cutting properties include the cutting force and cutting energy was determined along the stem from first internode to fourth internode from the top of cotton plants toward bottom.

FIGURE 1
The cotton stalk and samples.

According to height and internodes, the average diameters were measured as 4.2, 4.8, 5.4 and 6.10 mm in this study. The ranges of diameter of the stem were converted to cross-section area in mm^2 (13.84, 18.06, 22.89 and 29.20 mm^2). The stalk diameters were measured before the test using a caliper with five replications at about the cutting point near the node section of an each test specimen. During the cutting tests, the stalk moisture content were determined according to ASABE standard method [7] by oven-drying 50 g of each sample at 105 ˚C for 24 h before the cutting tests. The average moisture content was determined as 50.20 %.

The Lloyd LRX Plus Universal Testing Machine was used to determine the cutting force and the cutting energy of cotton stalks (Fig. 2). Cutting experiments were carried out with three various knife types (Fig. 2), two of them are serrated type (Serrated 1 (knife-edge thick), Serrated 2 (knife-edge thin) and Flat (knife-edge flat) with five knife cutting angles (50˚, 60˚, 70˚, 80˚ and 90˚) and four different stalk diameters (4.20 mm, 4.8 mm, 5.40 mm and 6.10 mm). To determine the cutting force, cutting energy and displacement, the knife was held fixed to the crosshead of an universal testing machine (Fig. 2). The maximum cutting speed of the machine, 3 mms^{-1}, was used for all tests.

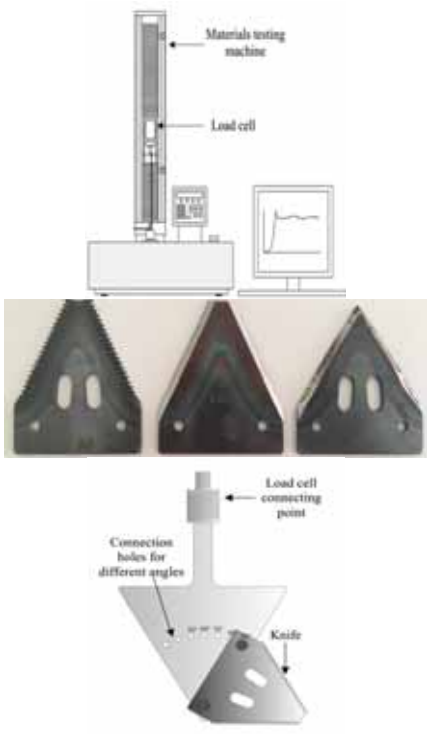

FIGURE 2
Materials testing machine and different cutting knives with edge angles.

The cutting force and cutting energy were determined as the maximum force and the maximum energy depend on type of knife, angle of knife-edge and stalk diameters. The cutting energy was calculated by measuring the surface area under the cutting force-deformation curve [7-18] with the force and displacement data by using a NEXYGEN computer program. A computer data acquisition system recorded all the force-displacement curves during the cutting process by testing machine.

Using Excel program, the multiple linear regression models and maximum correlation coefficients were determined from obtained peak cutting force values. The measured values of cutting force, cutting strength and cutting energy by machine were analyzed by using the multiple regression models with five replications in each treatment. The multiple linear regression model was represented by an equation of the following type: Multiple regression analysis helps us to predict the value of Y for given values of X_1, X_2.

$$Y = a + b X_1 + c X_2$$

Here Y is predictable value (cutting force, cutting strength and cutting energy), a is the intercept (constant value) and b (knife cutting angle), c (stalk diameter) are partial regression coefficients, X_1 is the angle of knife, X_2 is diameter of cotton stalk.

RESULTS AND DISCUSSION

The predict multiple regression equations of cutting force depend on knife cutting angle and stalk diameter for all type knives are given in Table 2. The knife cutting angle and diameter of cotton stalk have a significant effect on the cutting force ($P<0.01$). And also regression coefficients of equations were found high for all type of knives (Table 2). The regression analysis indicated that there is inverse relationship between the cutting force and knife cutting angle. According to the regression equations, the stalk diameter (X_2) has positive values, hence, increasing the diameter raises the cutting force and increasing the knife angle (X_1) reduces the cutting force due to the negative coefficient value. The highest values were obtained at the type of flat-edge knife. Because it's intercept value and partial regression coefficients are higher than the serrated type 1 and type 2 knives. For example, partial regression coefficients of knife edge angle and diameter are 14.105 and 20.276 for flat type knives, respectively. In contrast, it was found out that the lowest values of the cutting force occurred at the serrated type knives (Table 2). Also, while the maximum intercept value was obtained at flat-edge knife type as 69.935, followed by serrated type 1 as 50.915, serrated type 2 as 36.965 (Table 2).

TABLE 2
The multiple regression equations for the cutting force depend on knives type.

Knives type	Regression equations	(R^2)
	$Y=50.915 – (6.505) X_1^{**} + (16.76) X_2^{**}$	0.860
	$Y=36.965 +(– 3.495)X_1^{**} + (17.252) X_2^{**}$	0.908
	$Y=69.935+(– 14.105)X_1^{**}+ (20.276) X_2^{**}$	0.902

**Significant at 1 % level, $X_1$is the angle of knife edge, X_2 is diameter of cotton stalk.

TABLE 3
The multiple regression equations for the cutting strength depend on knives type.

Knife type	Regression equations	(R^2)
	$Y=4.579 +(– 0.308) X_1^{**} +(0.0594) X_2^{**}$	0.5835
	$Y=3.736+(- 0.171)X_1^{**} +(0.0338) X_2^{**}$	0.610
	$Y=5.51+(– 0.674) X_1^{**} + (0.086) X_2^{**}$	0.820

**Significant at 1 % level, $X_1$is the angle of knife edge, X_2 is diameter of cotton stalk.

TABLE 4
The multiple regression equations for the cutting energy depend on knives type.

Knife type	Regression equations	(R^2)
	$E= 12.5+(-1.86) X_1^{**} +(8.84) X_2^{**}$	0.809
	$E=7.7+(– 0.26) X_1^{**} + (7.47) X_2^{**}$	0.888
	$E=12.82+(– 1.54)X_1^{**} + (8.52) X_2^{**}$	0.882

**Significant at 1 % level, $X_1$is the angle of knife edge, X_2 is diameter of cotton stalk.

However, there were not found significant differences between serrated 1knife type and flat knife according to cutting energy. According these results, we can say that the flat-edge knife type is not suitable for topping, when compared to serrated knives types. As a result, to reduce cutting force, cutting strength and cutting energy, we can recommend that the serrated type knife for a new design of cutting machine and pruning for cotton shoots topping [19].

The multiple regression equations of cutting strength are given in Table 3 for each knife type, depending on knife edge angle and cotton stalk diameter. Cutting strength was significantly affected knife edge angle and cotton stalk diameter ($p<0.01$). The stalk diameter has a positive effect, whereas the knife angle has a negative effect. The partial regression coefficient in the equations showed that the effect of diameter was higher than the knife angle. Because the partial regression coefficient of diameter is positive, so it increased the cutting strength, whereas the effect of angle was decreased due to negative partial regression coefficient at the 5 % level in all knife types.

The multiple regression equations for predict cutting energy are seen in Table 4. The results of regression analysis showed that the independent parameters have significant effect on cutting energy at a 1 % probability level. There were found high correlation between cutting energy and stalk diameter and cutting angle. According to the regression equations, there were found inverse relationship between the cutting energy and knife angle. While the cutting energy decreased with increase knife edge angle for all type of knife, there was found the linear relationship between the cutting energy and stalk diameter. The cutting energy increased with increase stalk diameter for all type of knife because the partial regression coefficient of cotton stalk diameter is positive. As if it were predict cutting force, the maximum predict cutting energy was obtained with the flat type knife whereas a minimum energy was gained with the Serrated 2 (knife-edge thin) type.

This information is very valuable for selecting a suitable equipment design for reduces energy requirement and consumption. Because, the selection of suitable cutting apparatuses and equipment are plays an important role in economizing on cutting force and energy requirement [15]. This effect is in agreement with a previous study on maize stalks and soybean, in which both the cutting energy and maximum cutting force were directly proportional to cross-sectional area [20, 21]. The effect of stem diameter on the maximum cutting force and cutting energy is consistent with [12], who reported

that both the cutting energy and maximum cutting force are directly proportional to the cross-sectional area of hemp stalk. The results have shown that the cutting strength and cutting energy related to plant physical and mechanical properties [21]. Similar results were reported by [10] for rice straw, by [23] for hemp stalk, by [24] for rice stem, and by [14] for kenaf stems, by [15] for olive sucker, by [17] for grape sucker, by [25] for cane of some different grape variety, by [18] for cutting giant miscanthus stalks depending on grinding process parameters. These results also are in agreement with [6], [26], who determined shearing force and energy for shoot of cotton plant at different height of plant. Proper equipment design to accomplish the cutting will maintain the quality of the harvested product while minimizing the force and energy needed to accomplish the task [27]. Based on the results from this study, for cutting of cotton stalk, lower cotton shoots diameter, lower knife edge angle and serrated knife type can be recommended to minimize the shearing force and shearing energy requirements.

CONCLUSIONS

This study clearly that predict cutting force, cutting strength and cutting energy are influenced by knife type, knife angle and cotton stalk diameter. The best results were obtained serrated types knives. Increase of the knife cutting angle causes a decrease in the values of cotton stalk cutting force and work. The highest force value was obtained flat edge type knife. The cutting force and cutting energy increased with stalk diameter. With using a proper knife type and angle, cutting force and cutting strength and cutting energy values can be reduced. As a result, we can say that the cutting properties of cotton stalk has play a significant role in designing and energy efficient of topping equipment and the flat-edge knife type is not suitable, when compared to serrated knife types. As a result we can recommend that the serrated type knife for a new design of cutting machine and pruning for cotton shoots topping. If one is interested to study the joint affect of all these variables on cutting properties, one can use this technique.

REFERENCES

[1] Esgici, R., Pekitkan, F.G., Ozdemir, G., Guzel, E., Sessiz, A. (2019). Cutting Parameters of Some Grape Varieties Subject to The Diameter and Age of Canes. Fresen. Environ. Bull. 167-170,

[2] Kusinska, E., Starek, A. (2012). Effect of knife wedge angle on the force and work of cutting peppers. Teka. Commission of Motorization and Energetics In Agriculture. 12(1), 127–130.

[3] Obasi, M.O., Msaakpa, T.S. (2005). Influence of topping, side branch pruning and hill spacing on growth and development of cotton (Gossypium barbadense L.) in the Southern Guinea Savanna Location of Nigeria. J. Agric. Rural Dev. Trop. Subtrop. 106 (2), 155–165.

[4] Renou, A., Téréta, I., Togola, M. (2011). Manual topping decreases bollworm infestations in cotton cultivation in Mali. Crop Prot. 30 (10), 1370–1375.

[5] Yang, Y., Ouyang, Z., Yang, Y., Liu, X. (2008). Simulation of the effect of pruning and topping on cotton growth using Cotton2K model. Field Crops Res. 106, 126–137.

[6] Aydin, İ., Arslan, S. (2018). Mechanical properties of cotton shoots for topping. Industrial Crops & Products. 112 (2018) 396–401.

[7] ASABE Standards (2008). S358.2. Moisture Measurement – Forages. American Society of Agricultural and Biological Engineers, St. Joseph, MI.

[8] Mohsenin, N.N. (1986). Physical properties of plant and animals materials. 2nd edition. New York, NY: Gordon and Breach Science Publishers.

[9] Persson, S. (1987). Mechanics of cutting plant material. ASAE Publications, St Joseph, MI, USA.

[10] Yore, M.W., Jenkins, B.M., Summers, M.D. (2002). Cutting properties of rice straw. Paper Number: 026154.ASAE Annual International Meeting / CIGR XVth World Congress.

[11] Kocabiyik, H., Kayisoglu, B. (2004). Determination of shearing features of sunflower stalk. In J Agric Sci. 10(3),263–267.

[12] Chen, Y., Gratton, J.L., Liu, J. (2004). Power requirements of hemp cutting and conditioning. Biosystems Engineering. 87(4), 417–424.

[13] Taghijarah, T., Ahmadi, H., Ghahderijani, M., Tavakoli, M. (2011). Shearing characteristics of sugar cane (Saccharum officinarum L.) stalks as a function of the rate of the applied force. AJCS 5 (6), 630-634.

[14] Ghahraei, O., Ahmad, D., Khalina, A., Suryanto, H., Othman, J. (2011). Cutting tests of kenaf stems. Transactions of the ASABE. 54 (1), 51-56.

[15] Sessiz, A., Elicin, A.K., Esgici, R., Özdemir, G., Nozdrovicky, L. (2013). Cutting properties of olive sucker. Acta Technologica Agriculturae. The Scientific Journal for Agricultural Engineering, The Journal of Slovak University of Agriculture in Nitra. 16 (3), 80–84.

[16] Sessiz, A., Esgici, R. (2015a). Effects of cotton picker ages on cotton losses and quality. Scientific Papers. Series A. Agronomy, Vol. LVIII, S:417-420.

[17] Ozdemir, G., Sessiz, A., Esgici, R., Elicin, A.K. (2015). Cutting properties of wine grape cultivars. Scientific Papers. Series B, Horticulture. Vol. LIX, 2015.
[18] Nowakowski, T. (2016). Empirical model of unit energy requirements for cutting giant miscanthus stalks depending on grinding process parameters. Annals of Warsaw University of Life Sciences – SGGW, Agriculture (Agricultural and Forest Engineering) 67, 63–70.
[19] Pekitkan, F.G, Esgici, R, Sessiz, A. (2018a). Effect of top cutting height of cotton stalk on cotton yield. XIX. World Congress of CIGR (Commission Internationale du Génie Rural) "Sustainable Life for Children"22 - 25 April 2018.Antalya, Turkey
[20] Prasad, J., Gupta, C.B. (1975). Mechanical properties of maize stalks as related to harvesting. In J Agric Eng Res. 20(1), 79–87.
[21] Sessiz, A. (2005). Physical and mechanical properties of soybean crops and their relationship. In Indian Journal of Agricultural Engineering. 40(2), 30–38.
[22] Igathinathane, C., Womac, A.R., Sokhansanj, S. (2010). Corn stalk orientation effect on mechanical cutting. Systems engineering. 107, 97-106.
[23] Kronbergs, A., Siraks, E., Kronbergs, A.E., 2011. Mechanical properties of hemp (cannabis sativa) biomass. Environment. Technology. Resources. Proceedings of the 8th International Scientific and Practical Conference. Vol 1.
[24] Alizadeh, M.R., Ajdadi, F.R., Dabbaghi, A., (2011). Cutting energy of rice stem as influenced by internode position and dimensional characteristics of different varieties. AJCS 5(6), 681-687, ISSN:1835-2707.
[25] Sessiz, A., Esgici, R., Özdemir, G., Elicin, A.K., Pekitkan, F.G. (2015b). Cutting properties of different grape varieties. Agriculture & Forestry. 61 (1), 211-216.
[26] Pekitkan, F.G., Esgici, R., Elicin, A.K., Sessiz, A. (2018b). The Change of shear force and energy of cotton stalk depend on knife type and shear angle. Scientific Papers. Series B, Horticulture. Vol. LXI.
[27] Srivastava, A.K., Goering, C.E., Rohrbach, R.P. (2006). Engineering principles of agricultural machines. ASAE Textbook Number 6. Pamela De Vore-Hansen, Editor, Books& Journals. 601 p.

Received: **12.07.2019**
Accepted: **14.09.2019**

CORRESPONDING AUTHOR

Resat Esgici
Dicle University,
Bismil Vocational High School,
Diyarbakir, Turkey

e-mail: resgici@dicle.edu.tr

© by PSP Volume 29 – No. 04A/2020 pages 2778-2783 Fresenius Environmental Bulletin

ASSESSMENT OF GENETIC PROGRAMMING FOR ESTIMATING RAINFALL-RUNOFF HYDROLOGICAL EVENTS

Muhammet Omer Dis, Mehmet Unsal*, Ayse Ece Yagci

Civil Engineering Department, Faculty of Engineering and Architecture, Kahramanmaras Sutcu Imam Unıversity, 46000 Kahramanmaras, Turkey

ABSTRACT

Flood management is one of the biggest issues in urban areas. While hydrological modeling is widely applied for the estimations of watershed's hydrological response to precipitation, application of GEP, in this study, exhibit an inventive framework is implemented for assessment of rainfall-runoff purpose. GEP designed for regression, classification, time series estimation and logical synthesis with using character linear chromosomes composed of genes structurally organized in a head and a tail. An increment in hydrological data (i.e. rainfall, evapotranspiration) is generally expected to increase the accuracy of flood forecasts. However, in this study, it is noteworthy that GEP can predict floods and capture time of peaks using only precipitation data over a basin with a high correlation between flow rate and rainfall. Rainfall-runoff predictions are conducted using two storms. The results illustrate that GEP model can capture and predict runoff without topographic and hydrological data (with the exception of precipitation) for the rainfall events over a sub-tropical catchment. The addition of evapotranspiration and/or groundwater data sets to the simulations does not have leading reaction to acquire flow fluctuations with exception of increment in the width of the peak flow in the hydrograph.

KEYWORDS:
Genetic Algorithms, GEP, Rainfall-Runoff, Storm, Sub-Tropical

INTRODUCTION

It is an inevitable fact that human beings have built their settlements near to water from the past to the present. In some years mankind faced with drought while excess water sometimes caused devastating flood damages in the past. Thus, rainfall-runoff prediction is significant effect on humankind. Therefore, physical representation of river basins with simulation and estimation of rainfall-runoff modeling are widely used. For this purpose numerous hydrological modeling is available. For instance, a study was conducted at the end of a watershed flow in northern Greece for the assessment and management of flood risks developed under the new European Union directive. In this study, hydrological and hydraulic models were combined with digital terrain model and overflow hazard maps were created according to probability scenarios. Forecasts of floods from rainfall at different return periods were evaluated and mapped by Geographic Information Systems (GIS). These maps will also be used to create flood hazard management plans that focus on prevention, protection and readiness [1]. Another study has been conducted to estimate the expected pecuniary damage in the event of flood risk in Vojvodina. Simulation of flood wave propagation was performed by GIS techniques. The objective is to determine the monetary value of possible damage to the flood depth function [2].

Local conditions and low impact improvement (LID) implementation principles have been used to select and regulate appropriate LID measures to provide useful recommendations for achieving and modifying improved flow control of existing stormwater management systems. A rainwater management model was used to simulate and evaluate the performance of LID measures compared to natural and original scenarios in different designed rain series. Compared to natural and original scenarios, the LID scenario reduces both the risk of discharge and contamination [3].

In the Hanjiang River Basin, precipitation change models, especially hourly precipitation changes are examined in detail and it is aimed to analyze the spatial structures of hourly precipitation with various statistics and thus to show correlation with time scale and geographical characteristics. As a result, it was found that hourly rainfall frequency was significant with all geographical features. Statistically, the result showed that season factor plays an important role in spatial correlation based on empirical model [4].

Extreme hydrometeorological events highlight the increasing importance of studies on characterizing the occurrence frequency of floods. When the CREST distributed model is applied in the medium

latitude basin, it is evaluated how satellite precipitation products can be used to predict the severity of the event. The study demonstrated that there is value in the satellite data for deriving flood frequencies over data-poor regions of Earth where the record or quality of ground observations is not adequate to support hydrological analyses [5]. Landsat TM / ETM / OLI time series image data were used to estimate the total surface water area variation during the wet season between 1988 and 2016 in the South Dongting Lake and East Dongting Lake. The surface water area was extracted from Landsat data using Modified Normalized Difference Water Index (MNDWI). The results showed that surface water area variation is dependent on precipitation and flow changes of five hydrological stations of Xiangtan, Taojiang, Taoyuan, Shimen, Shadaoguan, Mituosi, Ouchikou and Chenglingji [6].

In the Aguibat Ezziar basin, northwest of the Bouregreg basin in northern Morocco, two models were applied and the results compared. The models are conceptual (HEC-HMS) and spatial (ATHYS) hydrological models. Two results of the models compared and found that a distributed model (i.e. ATHYS) can be appraised as adequate model in anticipation of runoff volume comparing with other models [7]. Another study is applied to analyze the seasonal and annual effects of a watershed using the semi distributed Soil and Water Assessment Tool (SWAT). The hydrological model was developped for agriculture dominated Semra watershed, located in Allahabad, India. Domestic farming system based on surface and ground water can be sometimes experienced insufficient water supply at the end of the dry seasons. The study results showed similar findings that semi distributed models like SWAT plays an effective role for water balance study in the agricultural dominated catchments [8]. In another study, the original SCS-CN method was improved and new CNSTAND values were estimated. The improved Curve Number (CN) values were obtained by interpolating the original coarse CN values and using the new CN method which takes into account additional parameters of forest stand cover and forest sand thickness. Sampling sites in forested watersheds were compared with urban areas by taking into account the new CN and water yield (mm) values for two different rainfall projections (250 and 500 mm) which could cause flooding later [9].

Recent years, usage of the Gene Expression Programming (GEP) is increasingly being used in many areas. For example, GEP and Geographic Information Systems (GIS) have been integrated to solve Multi-Area Land Use Allocation (MLUA) problems [10]. This new approach gave a promising and efficient results for solving the MLUA problems. Additionally, the GEP model was used to simulate the penetration depth of the sharp-toed weirs and the obtained models were tested with experimental data. The outcomes of their study show that that GEP can be successfully used for estimating penetration depth in sharp crested weirs [11]. Another example of using genetic expression programming is analyzing the uniaxial compressive strength (UCS) of rocks with different characteristics, and study results indicated that GEP can be used successfully to predict rock properties [12].

The GEP model is developed by Ferreira [13]. It benefits the main principles of genetic algorithms and genetic programming. The model hold methodology similar to a biological evaluation. Character linear chromosomes composed of genes structurally organized in a head and a tail are employed in the model. The problems are encoded in linear chromosomes of fixed-length as a computer program. This paper is aimed to generate the models for the prediction the rainfall-discharge over sub-tropical environment. How application of genetic algorithms and programming are integrated with using different hydrological data (rainfall, evapotranspiration, and groundwater) is discussed in order to predict flooding events and capture time of peaks. Additionally, influence of increment in hydrological data how effective in hydrological prediction was investigated.

This study presents a good opportunity to enhance estimation of hydrological process via GEP model and understanding its calibration and parameterization procedures over a sub-tropical environment. The main objectives of this work are: (1) to combine available observations and genetic model to asses accuracy of simulations, (2) express variables as mathematical codes, (3) determine the effect of numbers of input parameters on the model to predict flows, and (4) to evaluate how the GEP model response for rainfall-runoff simulations and understand the applicability of the model.

The paper is organized as follows. Section 2 describes the study area and data. Section 3 provides information regarding the GEP model calibration, mathematical expression of the models with multiple hydrological input parameters (precipitation, evapotranspiration and ground water). In the last section, an illustration of simulated results, using GEP model in C-11 Basin, is discussed with discussion of conclusions and future work.

STUDY REGION AND DATA

The sub-tropical watershed, namely C-11 basin, is the study basin for this work located in south-central Broward County, in Florida. The basin is highly urbanized and its area is 286-km^2. Streamflow from the C-11 discharges to east and west (with pumps) of the basin's boundary. While the catchment receives rainfall every month, most of the annual rainfall (average is 1341 mm) occurs

from June to October. Numerous operational structures serve in the region in order to flood protection, water supply and preserve groundwater in adequate level. The basin mainly consists of two man-made canals, namely C-11 (east-west direction) and C-11S (flow direction is from south to north) and the direction of flow, in C-11 canal, changes according to operation of control structures (i.e. pumps, spillway, and culverts). Two pumps, namely S9 and S9A, controlled remotely as an outlet point of the western side of the basin. S13 pump (with three pumping units) and S13 culvert structures, on the other hand, are located in its eastern boundary and work as another outlet point of for the basin [14].

It is responsibility of South Florida Water Management District (SFWMD) to prevent floods, to manage the water resources, and to improve and preserve the quality of existing water potential in the area [15]. For these reasons, since 1949, numerous of control structures has been operated and controlled by the District headquarters, and all the required data collections can be accessible via DBHYDRO. DBHYDRO is a data browser in the District's website and it allows users to access hydrologic, meteorologic, hydrogeologic, and water quality data [16]. In this study all required data (flow observation, precipitation, evapotranspiration, and groundwater) for model development were obtained from the DBHYDRO data browser.

MATERIALS AND METHODS

In this study, Gene X Pro Tools software is used for generating GEP models. It can process data sets with millions of variables and easily analyze the most important features and relationships between them. The software devoted to re-generate regression, logistic regression, classification, time series prediction and logic synthesis. This powerful tool allows users to read and analyze model results up to nineteen alternate programming languages including Ada, C, C++, C#, Excel, VBA, Fortran, Java, Java Script, Matlab, Octave, Pascal, Perl, PHP, Python, R, Visual Basic, VB.Net, Verilog, and VHDL [17].

Genes consists of two parts: head and the tail. Main variables are contained in the head of a gene. These variables interpreted to code as the any mathematical expression such as some functions, variables and constants as well as arithmetic and trigonometric functions such as +, -, *, /, $\sqrt{}$, sin, cos. The tail, on the other hand, contains additional terminal symbols and exclusive variables and constants if head variables are insufficient to implement an expression. The constants and the independent variables of the problem like (1, a, b, c) are in gene tail. A mathematical expression, in the GEP model, is described as a chromosome with multi genes and developed using the data presented to it. A full description of the model and its computational schemes can be provided in Ferreira [13].

Due to its capability of simulating wide range of subject including rainfall-runoff predictions, it provides tremendous facilities for flood forecasting and prevention in watersheds where poorly gauged and/or ungauged watersheds without phenomenal hydrometoerological data sets.

RESULTS

Although precipitation occurs all around the year in Florida, its amounts vary significantly in spacio-temporal aspect. Seasonal variations in precipitation patterns causes two distinct rainfall periods in the region and these can be listed as wet (from June through October) and dry (from December through April). Majority of the rainfall occurs during the wet season [15 and 18].

A number of input data is required for hydrologic modeling, but, precipitation data is one of the most sensitive forcing variables that can affect the simulation performance. Influence of spatio-temporal variability of precipitation was sought on the accuracy of hydrologic simulations by numerous researchers [15, 19, 20, and 21]. The most reliable data, for this purpose, gauge adjusted NEXRAD estimates by the District's Operations Control Center (OCC), will be used in the subsequent rainfall-runoff modeling of this study.

In this study, 15-min high resolution precipitation data are obtained from SFWMD for the two selected events: June 2007 and March 2010. There was 52,06-mm (51,83-mm) of rainfall occurred during the storm period, from 01/June/2007- 09:15 through 03/June/2007- 00:00 (12/March/2010- 00:00 through 13/March/ 2010- 20:45). June (March) storm event took place in the wet (dry) season. The total amount of rainfall roughly equals to each other during the storm periods. This is the major reason for selecting the events regardless of the consideration of seasonality in the study.

In addition, observed flow data at various discharge points in the basin are acquired at 15-min time intervals from the DBHYDRO. As we discussed previously there are three pumps stations, $S9A_{Pump}$, $S9_{Pump}$ (in western side boundary), and $S13_{Pump}$, and one spillway structure, $S13_{Spillway}$ (in eastern side outlet), in the basin. The total discharged flow in the control structures previously stated were combined regardless of the flow direction to calculate total discharge of the catchment. Moreover, potential evapotranspiration and groundwater well data are obtained with daily resolution from DBHYDRO website. All the data is analyzed cumulatively to minimize the effect of

antecedent moisture condition in the GEP simulations.

March event is considered in the model as training. Once it gave reasonable results, June 2007 storm used for testing purpose in the study. Three GEP models are generated for predicting the rainfall resulting runoff values. In GEP Model I, the precipitation is used alone as the input parameter to estimate discharges. In GEP Model II, additional to precipitation, evapotranspiration data are applied as the input parameters and discharge is the output parameter. Precipitation, evapotranspiration and groundwater are considered as the input parameters to simulate runoff at the basin outlet in GEP Model III. In all the models, P stands for precipitation, ET represents evapotranspiration, G symbolizes groundwater and Q is discharge. Three mathematical functions are generated for definition of the relationship between Precipitation-Discharge; Precipitation and Evapotranspiration-Discharge; Precipitation, Evapotranspiration, and Groundwater-Discharge. The model equations and R^2 values are given below:

Model I ***(Precipitation-Discharge)*** **R^2= 0.98**

$$Q = 0.032x \left| P \times e^{\sqrt[4]{\sqrt{\sin(\sqrt[3]{P})}}} + (4P^2 + P^2) \times 10^{\sin(P)} + (\sqrt{P} - P)^4 \right| \quad (1)$$

Model II ***(Precipitation, Evapotranspiration-Discharge)*** **R^2= 0.961**

$$Q = 0.064x|ETxP + ET^2 + Arctan(ET) + (ETxP - ET)xETxP| + ET + [P^2 - ETxP - 2xP]^2 \quad (2)$$

Model III ***(Precipitation, Evapotranspiration, Groundwater-Discharge)*** **R^2= 0.964**

$$Q = 0.044x\left|\log(G^2) - P + (ET - P)^3\right| + ET^3 - P + \frac{P}{G} - P^2 + (G - P + ET)^4 xG - ET \quad (3)$$

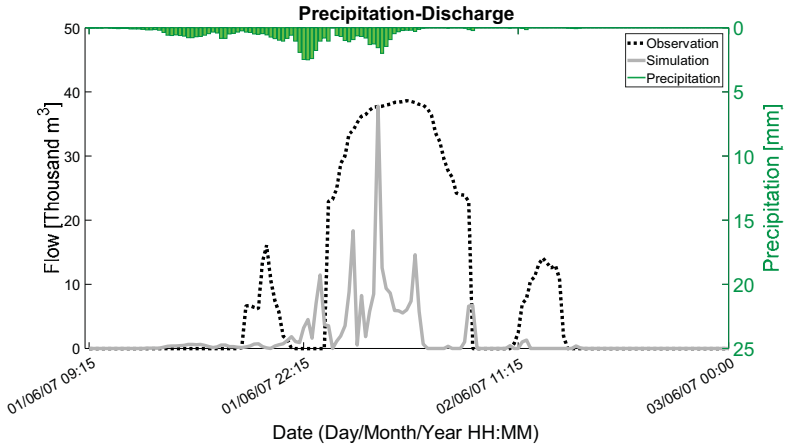

FIGURE 1
Hydrographic comparison between observed and predicted flow values (Model I)

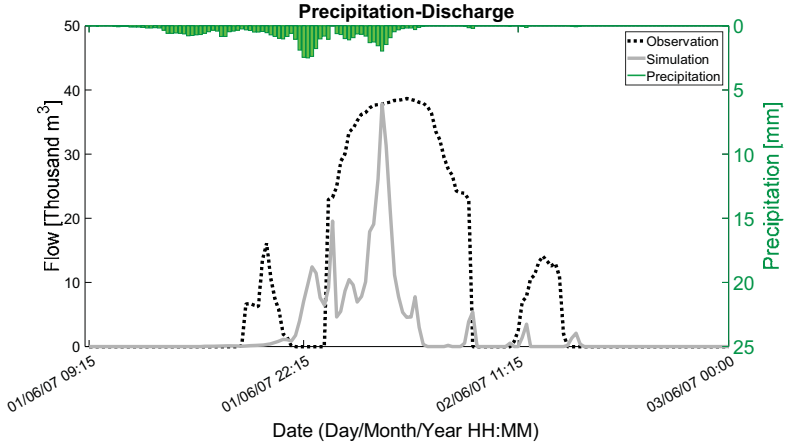

FIGURE 2
Hydrographic comparison between observed and predicted flow values (Model II)

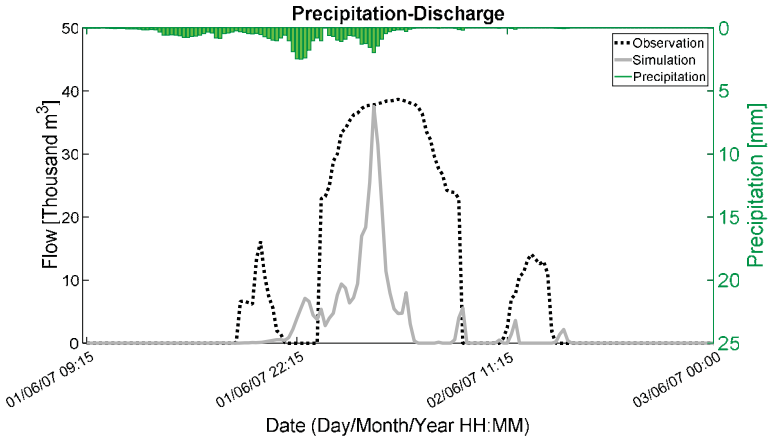

FIGURE 3
Hydrographic comparison between observed and predicted flow values (Model III)

The test results from Model I, Model II and Model III are compared with calculated results in terms of cumulatively. R^2 values of Model I, Model II, and Model III are 0.98, 0.961 and 0.964, respectively. It can be seen from R^2 values that there are high determination of coefficients between predicted and measured values in all models. Also, in Figures 1 to 3 supported this results in terms of capturing the time and amount of peak.

Adding the evapotranspiration and/or groundwater data sets to the simulation showed that there was no major effect for capturing the flow fluctuations with exception of increment in the width of the peak flow in the hydrograph. Test results show that desired performance can be provided with only precipitation data sets in GEP models

CONCLUSIONS

Overall, the study demonstrated a good skill of genetic driven flood amount and reaching the peak time relative to observations data with high determination of coefficients values. From all these results, one can draw only general conclusions that there is a value in the genetic algorithms, like GEP model, and it can be used successfully for predicting hydrological modeling in a catchment. There is a potential to get more accurate results in terms of simulating the fluctuations by adding operations of the control structures the model. Moreover, different temporal resolution can be another effect in the simulations. Therefore, it should be investigated whether the evapotranspiration and groundwater with 15-min high resolution affect the simulations. Future directions of this study will aim at extending numbers of storm events and investigating effect of data resolutions in evapotranspiration and groundwater.

REFERENCES

[1] Myronidis, D., Emmanouloudis, D., Stathis, D., Stefanidis, P. (2009). "Integrated Flood Hazard Mapping In The Framework Of The E.U. Directive On The Assesment And Management Of Flood Risks". Fresen. Environ. Bull. 18, 12.

[2] Cosic, D., Popov S., Novakovic, T., Popovic, L. (2019). "Flood Damage Assessment Method: GIS BASED APPROACH". Fresen. Environ. Bull. 28, 1896.

[3] Li, C., Liu, M., Hu, Y., Sui, J., Xu, Y., Shi, T. (2017). "Modeling Hydrological Effects Of Low Impact Development For Stormwater Runoff Treatment Based On Storm Water Management Model". Fresen. Environ. Bull. 26, 6470.

[4] Wang, M., Liao, W., Lei, W., Hu, Y., Qin, T. (2018)."Spatiotemporal Characteristics of Hourly Rainfall in the Upper Reaches of Hanjiang River Basin". Fresen. Environ. Bull. 27, 1214.

[5] Dis, M.O., Anagnostou, E.N., and Mei, Y. (2016). "Using High-resolution Satellite Precipitation for Flood Frequency Analysis: Case Study over the Connecticut River Basin". Journal of Flood Risk Management. 11, S514–S526.

[6] Zhang, X., Zhang, Q., Zhang, G., Nie, Z., Gui, Z., Que, H. (2018). "Surface Water Area Variations Monitoring and Flood Hazards Using Landsat Image Data in Dongting Lake From 1988 to 2016". Fresen. Environ. Bull. 27, 6168.

[7] Khattatı, M., Serroukh, M., Rafık, I., Mesmoudı, H., Brırhet, H., Bouslıhım, Y., Hara, F., (2016)."Hydrological Modeling of Aguibat Ezziar Watershed (Morocco), Comparative Study of Two Different Hydrological Models", Journal of Geographic Information System. 8, 50-56.

[8] Mishra, H., Denis, D.M., Suryavanshi, S., Kumar, M., Srivastava, S.K., Denis, A.F., Kumar, R.(2017).“Hydrological Simulation of a Small Ungauged Agricultural Watershed Semrakalwana of Northern India”. Applied Water Science. 7, 2803–2815.
[9] Yurtseven, İ., Öztürk, H., Taze, F. (2017). “Flood Risk Assessment For Forested Watersheds Using An Improved Curve Number Method: The Case Of Marmaris”. Fresen. Environ. Bull. 26, 2348.
[10] Eldrandaly, K.A. (2009). “Integrating Gene Expression Programming and Geographic Information Systems for Solving a Multi Site Land Use Allocation Problem”. American Journal of Applied Sciences. 6 (5), 1021-1027.
[11] Unsal, M. (2012). “GEP Modeling of Penetration Depth in Sharp Crested Weirs”. Arabian Journal For Science and Engineering. 37 (8), 2163-2174.
[12] Ozbek, A., Unsal, M., and Dikec, A.(2013). “Estimating uniaxial compressive strength of rocks using genetic expression programming”. Journal of Rock Mechanics and Geotechnical Engineering. 5(4), 325-329.
[13] Ferreira, C. (2001) “Gene expression programming: a new adaptive algorithm for solving problems”. Complex Systems. 13(2), 87–129.
[14] Dis, M.O. and Anagnostou, E.N. (2016). “Hydrological analysis of an urban basin in subtropical environment”. 12th International Congress on Advances in Civil Engineering. 21-23 September 2016 Istanbul/ Turkey.
[15] Skinner, C., Bloetscher, F., and Pathak, C.S. (2009).“Comparison of NEXRAD and Rain Gauge Precipitation Measurements in South Florida”. Journal of Hydrologic Engineering. 14 (3), 248-260.
[16] DBHYDRO 2016. “DBHYDRO Browser User’s Guide” South Florida Water Management District, March.
[17] www. gepsoft.com, demo version, (installation date: October 2018).
[18] Dis, M.O., Unsal, M., and Anagnostou, E.N. (2017).“Water Budget Analysis in Shallow Ground Water Regions Using Multiple Temporal Resolutions Data Sets”. KSU Journal of Engineering Sciences. 20(4), 45-53.
[19] Bedient, P.B., Hoblit, B.C., Gladwell, D.C., and, Vieux, B.E. (2000). “NEXRAD Radar for Flood Prediction in Houston”. Journal of Hydrologic Engineering. 5(3), 269-277.
[20] Neary, V.S., Habib, E., and Fleming M. (2004). “Hydrologic Modeling with NEXRAD Precipitation in Middle Tennessee”. Journal of Hydrologic Engineering. 9(5), 339-349.
[21] Golian, S., Saghafian, B., and Maknoon, R. (2010).“Derivation of Probabilistic Thresholds of Spatially Distributed Rainfall for Flood Forecasting”. Water Resources Management. 24(13), 3547-3559.

Received: **20.07.2019**
Accepted: **27.01.2020**

CORRESPONDING AUTHOR

Mehmet Unsal
Civil Engineering Department,
Faculty of Engineering and Architecture,
Kahramanmaras Sutcu Imam Unıversity,
46000 Kahramanmaras, Turkey

e-mail: munsal@ksu.edu.tr

© by PSP Volume 29 – No. 04A/2020 pages 2784-2791 Fresenius Environmental Bulletin

DETERMINATION OF ANTIBIOTIC RESISTANCE AND CRISPR 2.1 LOCI OF *ESCHERICHIA COLI* ISOLATED FROM SEYHAN INLAND LAKE ADANA, TURKEY

Anil Delik, Esra Sunduz Yigittekin, Fatima Masume Uslu, Sadik Dincer *

Department of Biology, Faculty of Science and Letters, Cukurova University, Adana, Turkey

ABSTRACT

In this study we investigated relationship between existence of CRISPR (Clustered Regularly Interspaced Short Palindromic Repeats) 2.1 locus and antibiotic resistance. The bacterial strains to be used in the experiment was isolated water samples taken from 5 different points of the Seyhan River. The antibiotic resistance tests of the isolated strains were performed by the disk diffusion method, the dendrogram analysis was calculated with UPGMA in the SHAN set and the MAR indices were specified. According to the MAR index, the highest and lowest antibiotic resistance was determined at respectively station 4 and 1. It is observed that none of the isolates developed resistance to Imipenem antibiotic. 147 of 150 isolates were identified as *Escherichia coli* (98%) with VITEK-2 Compact system. The presence of CRISPR 2.1 locus was identified in 53 of these 150 isolates (35.33%). The genome information was obtained with sequencing. it was determined as a result of the statistical analysis that there was no significant relationship between the MAR index values and spacer values (r= -0,098, p=0.50). In this study, no strong correlation was found between CRISPR 2.1 locus and multiple antibiotic resistance in environmental isolates of *E. coli*.

KEYWORDS:
Escherichia coli, Crispr 2.1 Locus, Antibiotic resistance

INTRODUCTION

CRISPR (Clustered Regularly Interspaced Short Palindromic Repeats) cas system, which is known to be a common mechanism of hereditary adaptive immune system specific to the sequence created by the genetic memory caused by past genetic attacks in bacteria by being included in their own genetic materials by bacteria. When bacteria are infected by phages, the foreign DNA sequence is integrated into the host CRISPR locus by Cas proteins, so renewable repeats are formed in the locus [1,2,3,4].

In *Escherichia coli*, CRISPRs are largely mapped in the form of two independent loci. In bacterial chromosome, they are localized in the form of CRISPR-1 and 2, CRISPR-3 and 4, respectively, and each of them contains different type of Cas gene [5,6,7). The CRISPR 2.1 locus in *E. coli* is considered to be formed as a result of the latest attack events, and therefore, it is reported to have the longest and most informative locus [8,9,10]. For this reason, CRISPR 2.1 *E. coli* is selected as a potential tool for strain differentiation and microbial source tracking (4,7,11,12,13).

The emergence of antibiotic-resistant bacteria is considered to be a health problem since every year thousands of people die from antibiotic-resistant bacteria. All efforts have focused on the reduction of the emergence of antibiotic-resistant bacteria [14]. Whether there is a relationship between the presence of the CRISPR locus and the emergence of antibiotic-resistant strains is an issue of concern due to its potential to limit the entrance of mobile agents.

In this study, it was aimed to investigate the presence of the CRISPR system in the genetic material of *E. coli* bacteria isolated from Seyhan inland lake of Adana province, to type *E. coli* bacteria in terms of CRISPR loci, and to determine whether there is a significant relationship between its antibiotic resistance and CRISPR locus.

MATERIALS AND METHODS

Bacteria isolation and identification. The water samples to be used in the experiment were taken at 1-meter depth from the surface of 5 different points. Sampling points are separated between old dam lake and regulatory bridge section (~4.3 kilometer) of the Seyhan River's inland lake on March 2017.

1ml of sample waters were used for plates inoculation. Cells were plated on EMB agar and incubated at 37°C for 24 h. We selected 150 strains isolated form samples on EMB agar. Bacterial iso-

lates were identified by VITEK-II Compact System System (Biomerioux).

Antibiotic susceptibility tests. The antibiogram susceptibility tests of the all isolated strains were performed by the disk diffusion method [15]. The used antibiotics (Bioanalyze) in the antibiotic susceptibility test are Chloramphenicol (C 30 µg), Sulphamethoxazole (SXT 25 µg), Ceftizoxime (ZOX 30 µg), Nitrofurantoin (F 300 µg), Tetracycline (TE 30 µg), Imipenem (IPM 10 µg), Penicillin (P 10 U), Cefuroxime (CXM 30 µg), Cefpirome (CPO 30 µg), Kanamycin (K 30 µg), Meropenem (MEM 10 µg), Nalidixic Acid (NA 30 µg), Gentamicin (CN 10 µg), Cefazolin (CZ 30 µg), Cephalothin (KF 30 µg) and Streptomycin (S 10 µg).

Multiple Antibiotic Resistance (MAR) Index. MAR index was determined by following the procedure described by Krumperman [16]. It was considered that the organism came from a source in which an intensive antibiotic was used if the calculated MAR index value was greater than 0.2, and that the antibiotic had never been used or came from a source where it was slightly used if the value was less than or equal to 0.2 [17].

Dendrogram (Clustering) Analysis. NTSYSpc 2.2 (Exeter Software NY USA 11/16/99) program was used to show the correlation between isolates according to their antibiotic resistance by the clustering method. The antibiotic resistance dendrogram analysis of the isolates was performed with the Pearson Correlation Coefficient using the Hierarchical Numerical Analysis Method. Those with resistance were evaluated as 1, and those sensitive and intermediate were evaluated as 0. The similarity matrix (Jaccard) and similarity coefficient (J) were calculated, and the dendrogram analysis was calculated with UPGMA (Unweighted Pair-Group Method with Arithmetic) in the SHAN set [17,18].

DNA extraction, PCR and analysis. To DNA extraction of isolates, GeneJET Genomic DNA Purification Kit was used. For the CRISPR 2.1 loci amplification of isolated DNAs, The PCR was performed with the Phire Green Hot Start II PCR Master Mix using primers Forward (F) 5′-TGGTGAAGGA GTTG G CGAAGG-3′ and Reverse (R) 5′-AAAATGTCCCTCCGCGCTTACG-3′ [19]. The sizes of the DNA fragments were calculated based on the marker DNA (Mini-Bis). Those between 500-2000 bp were considered as CRISPR 2.1 locus regions. The sequences of 53 isolates that were found to be positive in terms of CRISPR 2.1 were analyzed using the CRISPR Finder program to detect direct repeats and spacers in these genomes. All spacer sequences were examined using the BLASTN algorithm in GenBank (CRISPRs web server).

Statistical analysis. Statistical analyses were performed with the SPSS software version 17.0. The chi square test was used for comparing means. For correlation analyses, we used the Spearman rho correlation coefficient. A p-value less than 0.05 was deemed as significant and validated the possible differences found for each of the corresponding groupings elaborated in this work. Conversely, p-values higher than 0.05 were interpreted as proof of sufficient similarity among those groups compared. For robustness, these analyses were performed for groups. In all cases, p-values lower than 0.05 were accepted for significance

RESULTS

The physical and chemical characteristics of the water samples taken from the 5 stations determined in Adana Seyhan inland lake are presented in Table 1. There is no significant difference between sample stations. Between the 3rd station and the 4th station only, there is water entering the creek carried by the rain water during the winter months, which is called as Sarıçam creek.

Antibiotic susceptibility. The susceptibility results of the bacteria at all stations isolated at the end of antibiotic susceptibility tests performed according to the disk diffusion test are presented in Table 2.

TABLE 1
The air temperature, water temperature and pH values of the Adana Seyhan River on the day when isolation was performed

Stations	Air temperature(ºC)	Water temperature(ºC)	pH values
1	14	9,3	8,46
2	14	9,4	8,67
3	14	9,2	8,64
4	14	10,2	8,57
5	14	10,4	8,50
6	14	10,2	8,60

At station 1, while all isolates isolated from Region 1 were 100% resistant to P, CXM, CPO and NA antibiotics, they had 100% susceptibility to IPM and MEM antibiotics. At station 2, while the bacteria isolated from this region were 100% resistant to CPO and CZ antibiotics, they had 100% susceptibility to ZOX, CXM and IPM antibiotics. At station 3, while all isolates isolated from region 3 were 100% resistant to P and CPO antibiotics, they had 100% susceptibility to IPM antibiotics. At station 4, while all isolates isolated from region 4 were 100% resistant to P antibiotics, they had 100% susceptibility to C, F, IPM, CXM, MEM and S antibiotics. At station 5 while all isolates isolated from region 5 were 100% resistant to P, NA and CZ antibiotics, they had 100% susceptibility to F, IPM and MEM antibiotics.

Among the all isolates, a high percentage of bacteria were resistant to Penicillin (95.3%), Cefpirome (82.7%), Nalidixic Acid (80.7%) and Cefazoline (80%), Whereas a low percentage of bacteria were resistant to Meropenem (6%) and (0%), Nitrofuran (2%). Resistances against to Meropenem and Cefpirome are remarkable. All isolates were sensitive against Imipenem (0%). The resistance to Meropenem in the present study was similar findings of Toroglu et al (21).

As a result of the analyses performed, *E. coli* bacteria isolated from all stations showed close an antibiotic resistance profile against Chloramphenicol (P= 0,365) and Nitrofurantoin (P= 0,728), and there was a significant difference between the other antibiotics (P< 0,001).

The MAR index analysis results between the 5 stations is presented in the table below (Table 3)

When the MAR index table was evaluated finding shows that our isolates are surface water isolates polluted with farm wastewaters caused by urban or intensive production.

As a result of the dendrogram analysis performed with 50 samples that were positive for CRISPR 2.1 locus from all station isolates, the antibiotic resistance profile similarity between isolates 2.1 and 2.4, isolates 5.10 and 5.22, isolates 3.19 and 5.4, isolates 5.8, 5.9 and 5.16, isolates 5.2 and 5.14, isolates 1.18, 5.15, 5.18 and 5.26, isolates 1.3 and 1.27, isolates 1.17 and 3.18, and isolates 1.14 and 1.30 was determined to be 100% (Figure 1).

TABLE 2
Percentages of resistance to 16 antibiotics of *E. coli* strains identified between 5 stations (%).

Antibiotic	1.Station	2. Station	3. Station	4. Station	5. Station	P value	All stations
C	3 (%10)	2 (%6,7)	4 %(13,3)	0	2 %(6,7)	0,365[a]	11 (%7,3)
SXT	25 (%83,3)	21 (%70)	26 (%86,7)	7 (%23,3)	21 (%70)	0,001[a]	100 (%66,7)
ZOX	16 (%53,3)	0(%)	19 (%63,3)	3 (%10)	21 (%70)	0,001[a]	59 (%39,3)
F	1 (%3,3)	1 (%3,3)	1 (%3,3)	0	0	0,728[a]	3 (%2)
TE	22 (%73,3)	22 (%73,3)	14 (%46,7)	18 (%60)	5 (%16,7)	0,001[a]	81 (%54)
IPM	0	0	0	0	0	-	0 (%0)
P	30 (%100)	23 (%76,7)	30 %(100)	30 (%100)	30 (%100)	0,001[a]	143 (%95,3)
CXM	30 (%100)	0	25 (%83,3)	0	18 (%60)	0,001[a]	73 (%48,7)
CPO	30 (%100)	30 (%100)	29 (%96,7)	5 (%20)	29 (%96,7)	0,001[a]	124 (%82,7)
K	17 (%56,7)	21 (%70)	3 (%10)	4 (%13,3)	14 (%46,7)	0,001[a]	59 (%39,3)
MEM	0	8 (%26,7)	1 (%3,3)	0	0	0,001[a]	9 (%6)
NA	30 (%100)	26 (%83,3)	8 (%26,7)	28 (%93,3)	30 (%100)	0,001[a]	121 (%80,7)
CN	3 (%10)	23 (%76,7)	7 (%23,3)	5 (%16,7)	13 (%43,3)	0,001[a]	49 (%32,7)
CZ	29 (%96,7)	30 (%100)	28 (%93,3)	3 (%10)	30 (%100)	0,001[a]	120 (%80)
KF	26 (%86,7)	20 (%66,7)	26 (%86,7)	3 (%10)	29 (%96,7)	0,001[a]	104 (%69,3)
S	2 (%6,7)	15 (%50)	1 (%3,3)	0	12 (%40)	0,001[a]	44(%29,3)

(C:Chloramphenicol, SXT: Sulphamethoxazole, ZOX: Ceftizoxime, F: Nitrofurantoin, TE: Tetracycline, IPM: Imipenem , P: Penicillin, CXM: Cefuroxime, CPO: Cefpirome, K: Kanamycin, MEM: Meropenem, NA: Nalidixic acid, CN: Gentamicin, CZ: Cefazolin, KF: Cephalothin, S: Streptomycin. In each case 30 *E. coli* isolates, isolates are indicated a total of 150 *E. coli*. pa value was analyzed by chi square test.)

TABLE 3
MAR index analysis results between the stations

Group	n	Mean	St. D.	Var.	Min.	Max.	Median
1	30	0,547	±0,070	0,005	0,3750	0,6875	0,562
2	30	0,497	±0,121	0,015	0,1875	0,6875	0,500
3	30	0,462	±0,107	0,011	0,2500	0,6250	0,437
4	30	0,222	±0,103	0,011	0,1250	0,5625	0,187
5	30	0,545	±0,073	0,005	0,3750	0,6875	0,562

(MAR index: Multiple Antibiotic Resistance index, ± St. D: Standart Develation, Var: variation, Min: minimum, Max: maximum, Data analaysed by using Chi square test, Group: number of stations, n: number of isolates).

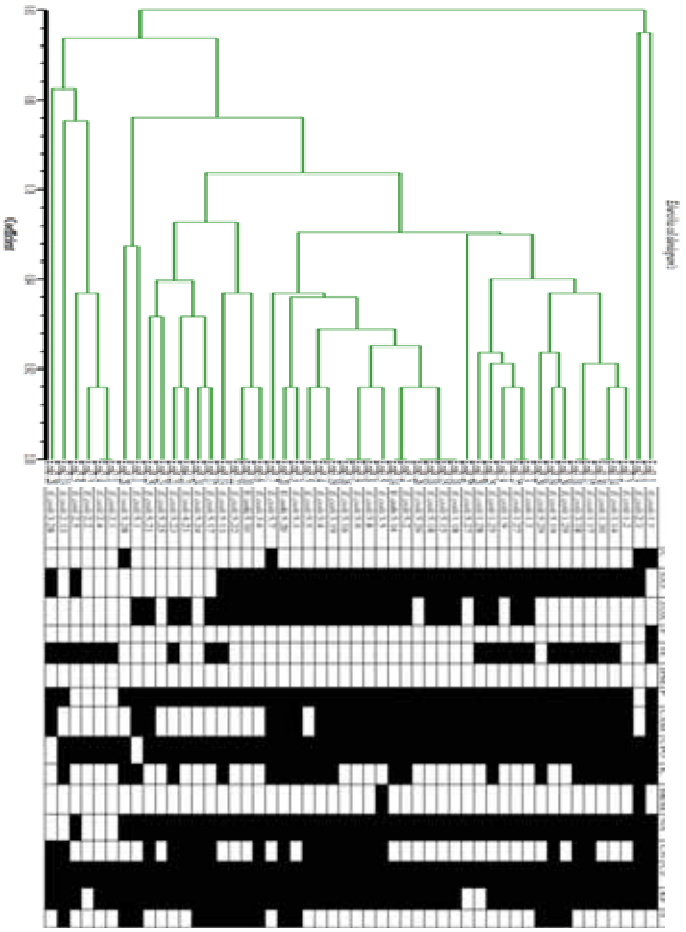

FIGURE 1
Antibiotic resistance profiles and dendrogram of *E. coli* isolates. 1.1, 2.3, 1.2 (1.14 - 1.30), (1.17 - 3.18), 1.29, 5.19, 5.29, (1.3 - 1.27), 1.9, 1.25, 1.28, 5.27, (1.18 - 5.15 -5.18, 5.26), (5.2, 5.14), 3.5, (5.8, 5.9, 5.16), (3.19, 5.4), 5.5, 5.3, 5.20, 5.7, 5.6, (5.10, 5.22), *E. coli* 5.13, 5.17, 5.24, 4.21, 5.21, 5.23, 5.23, 5.25, 5.1, 5.28, (2.1, 2.4), 2.2, 2.5, 2.13, 3.28.

Isolate 2.3 had the most contradictory antibiotic resistance profile among the isolates the similarity analysis of which was performed, the number of spacers it contained was determined to be n=9, and the MAR index was determined to be 0.5625. When the antibiogram results are examined, it is observed that none of the isolates at all stations developed resistance to Imipenem (IPM). On the other hand, all isolates were determined to be resistant to Cefalozin (CZ). Fifty *E. coli* isolates showed resistance to Choloramphenicol (C) 8%, Sulphamethoxazole (SXT) 74%, Ceftizoxime (ZOX) 66%, Nitrofurantoin (F) 2%, Tetracycline (TE) 44%, Penicillin (P) 90%, Cefuroxime (CXM) 66%, Cefpirome (CPO) 96%, Kanamycin (K) 42%, Meropenem (MEM) 4%, Nalidixic Acid (NA) 90%, Gentamicin (CN) 40%, Cephalothin (KF) 94% and Streptomycin (S) 28%, respectively. In the cephalosporin group antibiotics, there is a decrease in resistance contrary to the increase in the number of generations (Figure1).

CRISPR 2.1 Locus Sequence Results. A total of 150 *E. coli* isolates obtained from 5 stations determined in Adana Seyhan inland lake were examined for the presence of CRISPR2.1 locus. CRISPR 2.1 region was identified in 53 of these isolates (35.33%).

As a result of the analyses performed, the strain having the highest MAR index was found 0.6875 in *E.coli* 1.1 strain at station 1. The strains with the lowest MAR index were found 0.5 in *E.coli* strains 1.2, 1.9, 1.18, and 1.28. It have been found that *E. coli* 1.27 and 1.29 carry a maximum of 10 spacer, and the isolates without any spacer region were determined in *E.coli* strains 1.4 and 1.13.

TABLE 4
Demographic characteristics of *E. coli* CRISPR 2.1 locus isolated from 5 stations

Number of ısolates	Length (bp)	Crispr Spacer no	Crispr ınt. (bp)	Crispr fin. (bp)	DR length	MAR Index
1.1	989	7	88	539	29	0,6875
1.2	978	8	87	605	29	0,5
1.3	972	8	84	601	29	0,5625
1.4	534	0	-	-	-	0,5625
1.9	676	8	87	605	29	0,5
1.13	401	0	-	-	-	0,5625
1.14	686	6	84	482	31	0,625
1.17	1034	6	85	479	29	0,625
1.18	1051	8	87	603	29	0,5
1.25	985	8	84	601	29	0,625
1.27	1041	10	27	664	28	0,5625
1.28	999	9	89	667	28	0,5
1.29	1052	10	26	663	28	0,5625
1.30	334	3	21	231	28	0,5625
2.1	529	3	93	304	29	0,25
2.2	559	7	87	543	29	0,1875
2.3	1008	9	88	667	29	0,5625
2.4	535	3	85	293	26	0,25
2.5	1061	9	83	661	29	0,375
2.13	920	4	82	345	29	0,5
3.5	665	3	87	298	29	0,625
3.18	669	3	80	291	29	0,625
3.19	694	3	80	291	29	0,625
3.28	663	3	81	292	29	0,4375
4.21	1212	8	89	606	29	0,4375
5.1	1138	10	19	655	28	0,5
5.2	1021	10	20	657	28	0,5625
5.3	1053	8	82	598	29	0,625
5.4	662	3	79	290	29	0,625
5.5	691	3	88	299	29	0,5625
5.6	644	3	81	292	29	0,5625
5.7	665	3	81	292	29	0,625
5.8	635	3	83	294	29	0,5625
5.9	678	3	84	295	29	0,5625
5.10	708	3	82	293	29	0,5
5.13	636	3	80	291	29	0,625
5.14	668	3	79	290	29	0,5625
5.15	750	3	77	288	29	0,5
5.16	689	3	80	291	29	0,5625
5.17	666	3	82	293	29	0,5625
5.18	658	3	78	289	29	0,5
5.19	636	3	83	294	29	0,625
5.20	656	3	74	285	29	0,6875
5.21	668	3	79	290	29	0,5
5.22	704	3	86	296	29	0,5
5.23	724	3	86	297	29	0,5625
5.24	703	3	85	296	29	0,5
5.25	632	3	83	294	29	0,4375
5.26	663	3	83	294	29	0,5
5.27	646	3	79	290	29	0,375
5.28	660	3	76	287	29	0,5625
5.29	662	3	79	290	29	0,625
5.30	667	3	81	292	29	0,5

(MAR Index: Multiple Antibiotic Resistance Index, Crispr ınt.: CRISPR region of start, Crispr fin: CRISPR region of finish, DR: Direct Repeat, Crispr Spacer no: Crispr Spacer number).

The strain having the highest MAR index was found 0.5625 in *E.coli* 2.3 strain at station 2. The strain with the lowest MAR index was determined 0.1875 in *E.coli* 2.2 strain. It have been found that *E. coli* 2.3 and 2.5 carry a maximum of 9 spacer, and the isolates has 3 spacer region 3 were determined in *E.coli* strains 2.1 and 2.4

The strains having the highest MAR index was found 0.625 in *E.coli* 3.5, 3.18, 3.19 strains at station 3. The strain with the lowest MAR index was determined 0.4375 in *E.coli* 3.28 strain. It have

been found that all *E. coli* isolates carry a maximum of 3 spacer.

The antibiotic resistance MAR index of isolate 4.21 from station 4 was determined to be 0.4375. It has been found that the isolate carry a maximum of 8 spacers and the length of repeat regions was determined to be 29 bp..

The strain having the highest MAR index was found 0.6875 in *E.coli* 5.20 strain at station 5. The strain with the lowest MAR index was determined 0.375 in *E.coli* 5.27 strain.

In this study, the highest number of CRISPR 2.1 locus was identified at station 5. The highest values for antibiotic resistance were determined at this station. It has been found that *E.coli* 5.1 and 5.2 carry a maximum of 10 spacers (Table 4).

DISCUSSION AND CONCLUSION

According to the findings obtained, although there was no significant relationship between the antibiotic resistance statuses of *E. coli* strains isolated from all stations and the presence of CRISPR 2.1 locus. Stations 1 and 5 were determined to be the regions with similar results in terms of the antibiotic resistance profile and as the regions with the most positive results in terms of CRISPR 2.1 locus contained by the isolates. This result shows us that the region in this environment continues its activities as an environment in which the evolution of adaptive immunity at the molecular level takes place at higher levels. It suggests that artificial factors are more effective in creating this environment compared to natural factors.

It was interesting to determine whether there was a relationship between the presence of CRISPR locus and the emergence of antibiotic-resistant *E. coli* strains, due to its potential to limit the entrance of mobile agents. In parallel with the conclusion reached, in a study conducted in 2012 [6,20]. Totally 263 natural *E. coli* isolates obtained from humans and animals were determined to have plasmid-based antibiotic resistance, and the plasmid replicon typing was performed to characterize the CRISPR and integron content of strains. No significant difference was determined between the isolates carrying and not carrying replicons and integron in terms of the prevalence of cas genes expressing CRISPR activity. The sequence and spacer regions of known 2282 plasmids were compared, no matching was found in 79.8% of strains (210/263) and *E. coli* CRISPRs were not a barrier to the spread of plasmid and antibiotic resistance [21].

It was stated in the previous studies that another indicator of CRISPR activity could be the number of moderate repetitions. Re-separating units can both be added and deleted, so a CRISPR repeat and the spacer region can evolve while continuing at the same number [22 23,24]. As a result of the statistical analysis performed in this study, we could not find a significant relationship between the total numbers of repeat and spacer when the presence of antibiotic resistance and the MAR index were taken into account.

In the study carried out in Australia, it was revealed that there was CRISPR 2.1 in *E. coli* isolates, the isolation sources of which are water, clinical patients, animals such as kangaroo, tasmanian devil, rooster, chicken, etc., moreover, it was reported that 75% of human-induced isolates had no CRISPR 2.1 [25]. Furthermore, it was emphasized that human-induced *E. coli* were in uropathogenic *E. coli* deprived of CRISPR 2.1 locus [26]. The fact that CRISPR genes are not actually present in some isolates can be considered as an indicator of clinically and potentially pathogenic *E. coli* presence in water. In the study of Sheludchenko et al, [25] supporting this inference, urine, blood and fecal clinical specimens were determined to be devoid of CRISPR 2.1 in the majority of isolates [1].

Mobile agents usually form an accessory pool that strengthens survival in selected environments. To develop defense mechanisms against agents such as bacteriophage virus such as CRISPR-cas for the ultimate success of these microorganisms, to diversify and evolve the *E. coli* genome are the possible indicators that the dynamic of this population of microorganisms is important. Based on the data presented here, this dynamic of antibiotic treatment shows us that it has easily shifted the foreign elements that give antibiotic resistance.

Increasing pressure from environmental pollution can be accompanied by resistance of aquatic bacteria to various antibiotics. The increase in antibiotics resistance for some pathogens is a significant global problem, complicating the battle against infectious diseases. The detection of high resistance to Cefpirome (87%) and tetracycline (54%) is an important finding (Table 2). Because antibiotics, and in particular tetracycline, are widely used in the treatment of infectious diseases and to promote the growth and productivity of livestock farm animals. Thus, tetracycline resistance has become an antibiotic used as an indicator in the detection of environmental pollution. In general, cephalosporin group antibiotics have an increase in the number of generations and a decrease in resistance. However, Cefpirome is the fourth generation cephalosporin, despite the fact that it has the highest resistance is a striking finding.

Briefly, in this study, we determined that no correlation was found between CRISPR 2.1 locus and multiple antibiotic resistance in environmental isolates of *E. coli* and when MAR indices of river isolates were evaluated, this study showed that rivers are highly effective in spreading antibiotic resistant bacteria.

REFERENCES

[1] Pougach, K., Semenova, E., Bogdanova, E., Datsenko, K.A., Djordjevic, M. and Wanner, B.L. (2010) Transcription, processing and function of CRISPR cassettes in *Escherichia coli*. Molecular Microbiology. 77, 1367-1379.

[2] Wiedenheft, B., Lander, G.C., Zhou, K., Jore M.M., Brouns, S.J., Van der Oost, J., Doudna, J.A. and Nogales, E. (2011) Structures of the RNA-guided surveillance complex from a bacterial immune system. Nature. 477, 486-489.

[3] Gasiunas, G., Barrangou, R., Horvath, P. and Siksnys, V. (2012) Cas9-crRNA ribonucleoprotein complex mediates specific DNA cleavage for adaptive immunity in bacteria. Proceedings of the National Academy of Sciences of the United States of America. 109, E2579-E2586.

[4] Doudna, J.A. and Charpentier, E. (2014) The new frontier of genome engineering with CRISPR-Cas9. Science. 346, 1258096.

[5] Díez-Villaseñor, C., Almendros, C., García-Martínez, J. and Mojica, F.J.M. (2010) Diversity of CRISPR loci in *Escherichia coli*. Microbiology. 156,1351-61.

[6] Touchon, M., Eduardo, P. and Rocha, C. (2010) The small, slow and specialized CRISPR and Anti-CRISPR of *Escherichia* and *Salmonella*. Plos One. 5, e11126.

[7] Datsenko, K.A., Pougach, K., Tikhonov, A., Wanner, B.L., Severinov, K. and Semenova, E. (2012) Molecular memory of prior infections activates the CRISPR/Cas adaptive bacterial immunity system. Nat. Commun. 3, 945.

[8] Price, E.P., Smith, H., Huygens, F. and Giffard, P.M. (2007) High-resolution DNA melt curve analysis of the clustered, regularly interspaced short-palindromic-repeat locus of *Campylobacter jejuni*. Applied and Environmental Microbiology. 73, 3431-3436.

[9] Parker, J.S., Parizotto, E.A., Wang, M., Roe, S.M. and Barford, D. (2009) Enhancement of the seed-target recognition step in RNA silencing by a PIWI/MID domain protein. Molecular Cell. 33, 204-214.

[10] Arslan, Z., Hermanns, V., Wurm, R., Wagner, R. and Pul, U. (2014) Detection and characterization of spacer integration intermediates in type I-E CRISPR-Cas system. Nucleic Acids Research. 42, 7884-7893.

[11] Mojica, F.J.M., Diez-Villasenor, C., Garcia-Martinez, J. and Almendros, C. (2009) Short motif sequences determine the targets of the prokaryotic CRISPR defence system. Microbiology. 155, 733-740.

[12] Mojica, F.J.M. and Díez-Villaseñor, C. (2010) MicroCommentary: The on–off switch of CRISPR immunity against phages in *Escherichia coli*. Molecular Microbiology. 77, 1341-1345.

[13] Wiedenheft, B., Lander, G.C., Zhou, K., Jore, M.M., Brouns, S.J, Van der Oost, J., Doudna, J.A. and Nogales, E. (2011) Structures of the RNA-guided surveillance complex from a bacterial immune system. Nature. 477, 486-489.

[14] Dincer, S. and Yigittekin, E.S. (2017) Spreading of antibiotic resistance with wastewater. In: In: Biological Wastewater Treatment and Resource Recovery. 1st ed. InTech, Zagreb/Croatia, 73-97.

[15] National Committee for Clinical Laboratory Standards. Approved Standards M2-A6 (1997) Performance Standards for Antimicrobial Disk Susceptibility Tests. 6th ed. Wayne, Pennsylvania.

[16] Krumperman, P.H. (1983) Multiple antibiotic resistance indexing of *Escherichia coli* to identify high- risk sources of fecal contamination of foods. Applied Environmental Microbiology. 46, 165- 170.

[17] Rohlf, F.J. (2000) NTSYS-pc. Numerical Taxonomy and Multivariate Analysis System. Version 2.0 Exeter Software, Setaket, N.Y.

[18] Bansal, D., Bhasın, P., Yadav, O.P. and Punia, A. (2012) Assessment of genetic diversity in Lepidium sativum (Chandrasur) a medicinal herb used in folklore remedies in India using RAPD. Journal of Forestry Research. 26, 1-6.

[19] Mojica, F.J.M., Villasenor, C.D., Martínez, J.G. and Soria, E. (2005) Intervening sequences of regularly spaced prokaryotic repeats derive from foreign genetic elements. Journal of Molecular Evolution. 60, 174-82.

[20] Touchon, M., Charpentier, S., Pognard, D., Picard, B., Arlet, G., Rocha, E.P.C., Denamur, E. and Branger, C. (2012) Antibiotic resistance plasmids spread among natural isolates of *Escherichia coli* in spite of CRISPR elements. Microbiology. 158, 2997-3004.

[21] Golding, G.R., Bryden, L., Levett, P.N., McDonald, R.R., Wong, A. and Wylie, J. (2010) Livestock-associated methicillin-resistant *Staphylococcus aureus* sequence type 398 in humans, Canada. Emerging Infectious Diseases. 16, 587-94.

[22] Gene, W.T. and Jillian, F.B. (2008) Rapidly evolving CRISPRs implicated in acquired resistance of microorganisms to viruses. Environmental Microbiology. 10, 200-207.

[23] Delaney, N.F., Balenger, S., Bonneaud, C., Marx C.J and Hill, G.E. (2012) Correction: Ultrafast evolution and loss of crisprs following a host shift in a novel wildlife pathogen, *Mycoplasma gallisepticum*. PLOS Genetics. 8, e1002511.

[24] Sotaro, K., Yoshihiko, S. and Takashi, Y. (2014). Diversification of CRISPR within co-existing genotypes in a natural population of the bloomforming cyanobacterium *Microcystis aeruginosa* Microbiology. 160: 903–916.
[25] Sheludchenko, M,S,, Huygens, F., Stratton, H. and Hargreaves, M. (2015) CRISPR diversity in *E.coli* isolates from Australian animals, humans and environmental waters. Plos One. 10, e0124090.
[26] Dang, T.N.D., Zhang, L., Zöllner, S., Srinivasan, U., Abbas, K. and Marrs, C.F. (2013) Uropathogenic *Escherichia coli* are less likely than paired fecal *E.coli* to have CRISPR loci. Infection, Genetics and Evolution. 19, 212-218.

Received: **29.07.2019**
Accepted: **11.02.2020**

CORRESPONDING AUTHOR

Sadik Dincer
Cukurova University Science and Letter Faculty
Biology Department
Balcali-Adana-Turkey

e-mail: sdincer@cu.edu.tr

© by PSP Volume 29 – No. 04A/2020 pages 2792-2801 Fresenius Environmental Bulletin

ENERGY CONSUMPTION ANALYSIS OF GREEN TOWN PUBLIC BUILDINGS BASED ON MATHEMATICAL REGRESSION ANALYSIS METHOD

Ting Zheng*

College of Computer and Information, Inner Mongolia Medical University, Hohhot, Inner Mongolia, 010110, China

ABSTRACT

In the context of the construction and development of green towns, in order to solve the problems of the total energy consumption and energy intensity of public buildings in the construction of green towns, this paper proposes an energy analysis and growth trend forecast based on regression analysis. In this method, the characteristics of public buildings and public buildings in green towns are analyzed firstly. Then, in the mathematical methods of forecasting and analyzing the growth trend of energy consumption in public buildings in green towns, theoretical models and regression prediction methods are constructed. Finally, based on the data of urbanization rate, public building area and total energy consumption, the paper analyzes all aspects of green building area and energy consumption, and analyzes the growth trend. It can be seen from the model verification results that the prediction of public building area or energy consumption is small and the prediction result is more accurate.

KEYWORDS:
Regression analysis, green towns, public buildings, energy consumption analysis, growth trend

INTRODUCTION

In the construction of green towns, public buildings refer to buildings that provide people with various public activities. This type of building belongs to a non-residential category of civil buildings [1]. Unlike traditional architecture, public buildings need to meet the needs of the general public and usually consist of multiple buildings, so the system is large and complex to analyze. Therefore, the total energy consumption and energy intensity of public buildings are not clear. Therefore, before constructing a green town public building energy consumption and growth trend forecasting method, it is first necessary to complete the composition of various categories of green towns, and to analyze the energy consumption based on various types of components.

Green Town Public Building Category. With the development of science and technology and the improvement of living standards, the scale of public buildings built on the idea of green towns has gradually expanded, and the functions and types have gradually improved and enriched. In the construction of green towns, there is a need for public building types that meet different functions. With the rapid development of architecture and economy, a well-established and large-scale public building system can be built in large, medium and small cities. In the construction of green town public buildings, from different perspectives, the public building categories of green towns are mainly divided into the following categories [2]:

(1) Classification of building functions. According to the function of building, public buildings in green towns can be divided into office buildings, commercial buildings, service buildings, educational buildings, sanitary buildings, and other types of transportation;

(2) Division of building scale. According to the scale of construction, the public buildings of green towns can be divided into two categories: large public buildings and ordinary public buildings. Among them, large public buildings need to reach a building with a single building of more than 20,000 square meters. In addition, central air conditioning is required in the building;

(3) Division of administrative division of buildings. According to the administrative division, the public buildings of green towns can be divided into two categories: urban public buildings and township public buildings. In fact, in the early days of the construction of green towns, most of the current public building groups were built in urban and large township administrative areas.

(4) Building climate division. According to the building climate, the public buildings of green towns can be divided into five different climate zones. They are five categories: severe cold, cold, mild, hot, and hot, corresponding to the distribution of public buildings. In the specific climate division, it is more related to the Chinese region. Generally,

the public buildings in the north are divided into severe cold and cold. The public buildings in the south are divided into hot and hot, while the public buildings in the central region are classified as moderate.

Green town public building energy characteristics. The rapid development of economy and technology has improved the efficiency of green town construction. At the same time, the public building system has been continuously developed and enriched, and its energy intensity has been continuously improved. The early public building system only required simple water supply and power supply. Now, the comprehensive energy use mode that meets the different needs of sound, light, heat and other functional factors has gradually been completed in the emerging green town public building energy. The macroscopic operational energy consumption of public buildings is generally composed of the comprehensive energy consumption generated during the normal operation of the public building system.

In the analysis of the energy characteristics of public buildings in green towns, we have completed the analysis of the characteristics of energy use in public buildings in green towns through the following three main aspects through survey and statistical methods [3]:

(1) Analysis of main energy consumption of public buildings in green towns. The main energy consumption systems are three aspects: air conditioning, lighting and socket power. As shown in Figure 1, the actual survey of a large number of green urban public building systems found that the energy consumption of air conditioning systems and lighting systems and outlets accounted for more than 90% of the energy consumption of public buildings. Among them, the energy consumption ratio of air conditioning systems is about [34%, 38%], and the energy consumption of lighting systems and outlets is about [50%, 60%]. In addition, in the detailed analysis of the air conditioning system, it is found that the energy consumption of the air conditioning host exceeds 60% of the energy consumption of the air conditioning system. In addition, the air conditioning refrigeration pump, compressor and delivery system will consume 10% of the energy consumption.

(2) Distribution of energy consumption of single public buildings. Unlike other countries, in the construction of green public buildings in China's cities and towns, building energy consumption is not only a simple distribution, but a significant binary distribution. In fact, among the energy consumption of a single public building, public buildings occupying more than 80% of the total building area are concentrated at a lower energy consumption level, usually 40-120 kWh/m^2; public buildings occupying less than 20% of the total building surface. The system focuses on higher energy consumption levels, typically 120-200 kWh/m^2. In addition, in the binary distribution situation, the smaller green town public building system is more significant, while the green urban public building system in the first- and second-tier cities is not clear in binary distribution [4].

(3) Differences in energy consumption levels of different types of public buildings. Different types of public buildings have different differences in energy consumption due to their different functions. According to the statistical analysis results, the total energy consumption index per unit area of green town public buildings varies [20, 300 kWh/m^2.a] [5]. As shown in Figure 2, in the comparison of the energy consumption levels of various buildings and types of public buildings, it is found that the public buildings in communication category have the highest energy consumption, and the total energy consumption is in accordance with shopping malls, restaurants, hospitals, general, office buildings, and government agencies. Descending order with educational units are sorted. In fact, the total energy consumption is usually related to various factors, including management, service, use and running time.

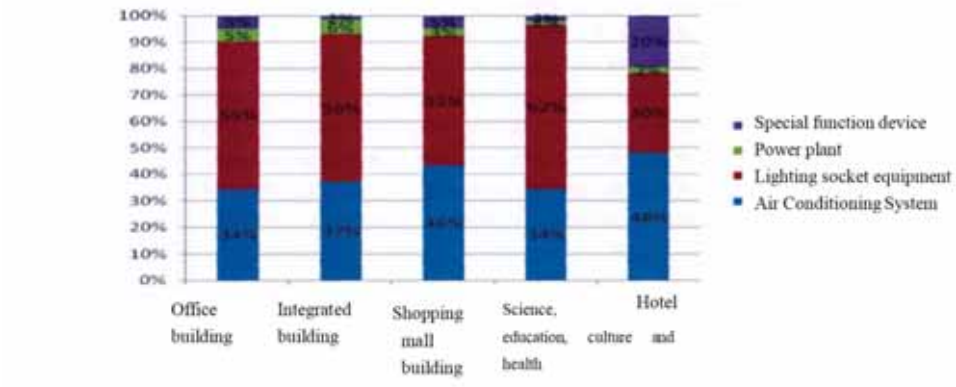

FIGURE 1
Analysis results of main energy consumption of public buildings in green cities and towns

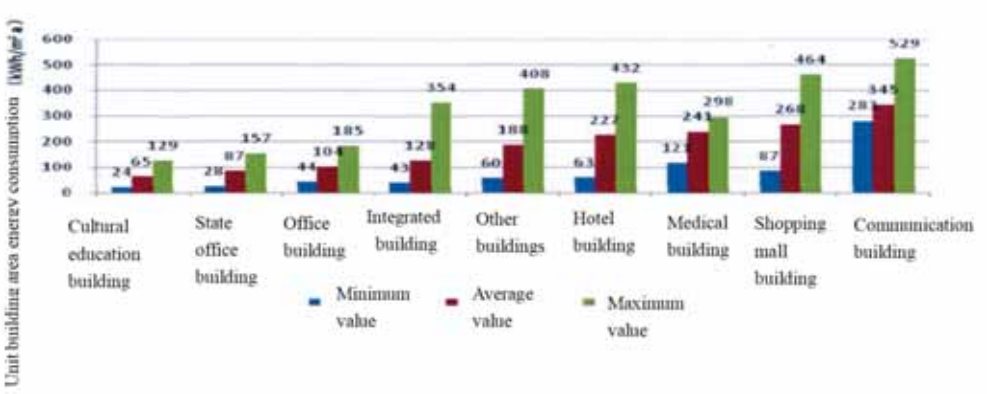

FIGURE 2
Comparison chart of different energy consumption levels of public buildings with different USES and types

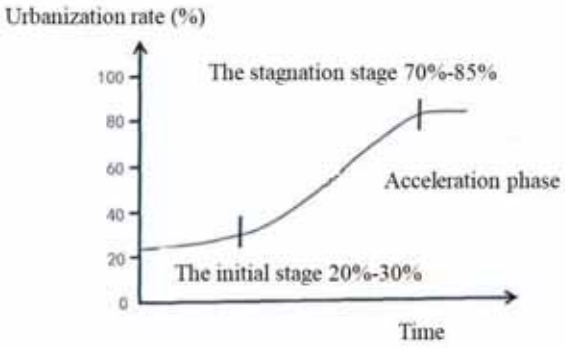

FIGURE 3
The northam S curve shows the law of the proportion of urbanization and the spatial upper limit of energy consumption growth of industrial and rural buildings

(4) Differences in energy consumption levels of public buildings of the same type. In fact, there are also differences in energy consumption book reviews of public buildings of the same type. In Figure 2, we can see that in the same type of green town public building system, the difference in energy consumption can increase several times. The result can also be proved from the side, the green building public building system has greater energy saving potential. In the same type of public buildings, the main factors affecting the difference in energy consumption levels include building size, running time, service level and energy building form. These factors are another important point in improving the energy consumption of green building public housing systems.

MATERIALS AND METHODS

Mathematical Method for Forecasting and Analyzing the Growth Trend of Energy Consumption of Public Buildings in Green Towns. In the construction of green towns, public buildings, as the major energy consumption of buildings, will be bound by the total energy consumption control. Before improving the energy efficiency of public buildings, it is necessary to forecast and analyze the growth trend of energy consumption of green urban workers and peasants. This paper chooses to predict and analyze the energy consumption growth trend of green buildings in green towns based on regression analysis and prediction methods.

Theoretical model construction. In the construction of green town public building energy consumption prediction model, the existing model has certain defects. At this stage, for the analysis and prediction of energy consumption of civil buildings, theoretical models and prediction methods of macroscopic energy consumption are generally adopted. The method constructs a multivariate regression prediction model by selecting several macro influencing factors as independent variables to predict the growth trend of energy consumption of green buildings in green towns [6]. The model does not consider the correlation between variables, so it is easy to fall into local minimum values, so accurate energy consumption prediction cannot be completed [7].

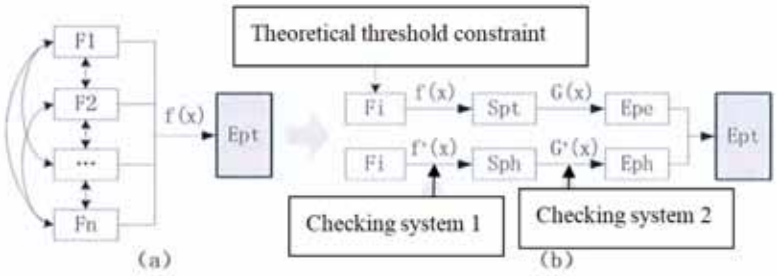

FIGURE 4
The prediction and analysis model of green urban public building energy consumption growth trend is established in this paper

In general, in the analysis of the influencing factors of green town public buildings, it is usually necessary to analyze a large number of influencing factors. Among these major influencing factors, most of the influencing factors have a large future growth potential, and there is no clear upper limit for growth space. In addition, the difference in the proportion of urbanization will affect the upper limit of the growth space, and its development law generally follows the Northam S curve as shown in Figure 3. This curve clearly gives the proportion of urbanization to the construction of green towns, and it presents the law of the upper limit of the energy consumption growth of public buildings [8].

The Northam S curve is mainly divided into three stages. The first stage is the initial stage. The urbanization rate of this stage is between [20%, 30%] and the rate is slow. The second stage is the medium stage. When the urbanization rate reaches 30%, the growth rate will be There will be an inflection point. Between [30%, 70%], the urbanization rate showed a significant acceleration trend; the final stage was the stagnation phase, where the urbanization level reached [70%, 85%], and its growth rate showed significant attenuation. After more than 85% of urbanization, the scale of urbanization has saturated and stopped. In fact, the Northam curve can be expressed by:

$$Y = \frac{1}{1 + Ce^{-rt}} \tag{1}$$

Among them, Y is the urbanization rate and its integral of green towns, and C and r are the integral constants and the green town public buildings. t represents time.

In the study of this paper, it is assumed that the urbanization rate is the main influencing factor driving the development of public buildings [9], and it has an indirect driving role in predicting the growth trend of public building energy consumption analysis. Based on the above analysis, this paper builds an optimization model based on the existing forecasting model, and completes the prediction and analysis of the energy consumption growth trend of green buildings in green towns. As shown in Figure 4, the optimized model of this paper drives the growth of public building area by urbanization, and then directly drives the growth of public buildings' total energy consumption through the growth of public building area.

Based on the above theoretical model and the corresponding assumptions, we construct the following functional relationship used in the growth prediction and analysis process:

$$S_i^{pt} = f(x_i^p) \tag{2}$$

$$S_i^{ph} = f'(x_i^j) \tag{3}$$

$$E_i^{ph} = G(S_i^{ph}) \tag{4}$$

$$E_i^{pe} = G'(S_i^{pt}) \tag{5}$$

$$E_i^{pt} = E_i^{ph} + E_i^{pe} \tag{6}$$

Wherein, each parameter of the above function relation is as followed. S_i^{ph} Indicates the total area of heating public buildings in the i year; S_i^{pt} indicates the total area of public buildings in green towns in the i year; x_i^j indicates the urbanization rate for the i year; E_i^{ph} indicates the total energy consumption of the heating public building terminal in the i year; E_i^{pe} shows the total electricity consumption of public buildings in green towns in the i year; E_i^{pt} indicates the total energy consumption of public buildings in green towns in the i year. Among them, the units of the building area are all ten thousand m2, and the energy consumption units are all ten thousand tce.

Regression prediction method selection. Based on the theoretical model constructed in this

paper, the demand analysis is constructed. It is necessary to construct a fitted regression on the polynomial function relationship. Therefore, this paper uses the regression prediction method to complete the prediction and analysis of the energy consumption growth trend of green buildings in green towns. The basic principle of the regression analysis method is that there are objective organic relations between multiple variables to be predicted, and the mutual constraint relationship is presented. The basic principle of the regression analysis method is to use the least squares method to complete the connection between the relevant variables. Finally, the calculated regression function is used to complete the prediction of subsequent variables. When predicting by regression analysis, it mainly includes the following steps [10]:

Construct a regression model equation. Take the simplest linear regression model as an example, assuming group observations of two variables x and Y are $(x_1, y_1), (x_2, y_2), ..., (x_n, y_n)$, the optimization goal of the least squares method is to make the actual observations Y_i and estimated value $\hat{Y}_i$ minimized the mean square error between:

$$\sum_{i=1}^{n}\left(\hat{y}_i - y_i\right)^2 = \sum_{i=1}^{n}\left[(a+bx_i) - y_i\right]^2 \tag{7}$$

Assuming $\theta(a,b) = \sum_{i=1}^{n}\left[(a+bx_i) - y_i\right]^2$, according to the principle of multivariate function optimization, the conditions for the extreme points to be satisfied can be calculated:

$$\begin{cases} \dfrac{\partial\theta}{\partial a} = \sum_{i=1}^{n}\left[(a+bx_i) - y_i\right] = 0 \\ \dfrac{\partial\theta}{\partial b} = \sum_{i=1}^{n}\left[(a+bx_i) - y_i\right]x_i = 0 \end{cases} \tag{8}$$

Under the limit of extreme points, the Lagrangian median method can be used to solve the parameters of the optimal relationship:

$$\begin{cases} a = \overline{y} = b\overline{x} \\ b = \dfrac{\sum_{i=1}^{n} x_i y_i - \overline{x}\sum_{i=1}^{n} y_i}{\sum_{i=1}^{n} x_i^2 - \overline{x}\sum_{i=1}^{n} x_i} \end{cases} \tag{9}$$

$$\overline{x} = \frac{1}{n}\sum_{i=1}^{n} x_i, \overline{y} = \frac{1}{n}\sum_{i=1}^{n} y_i \tag{10}$$

In the regression analysis, consider a single dependent variable Y and m independent variables $x_1, x_2, ..., x_n$ multiple linear relationship between:

$$\hat{Y} = a_0 + b_1 x_1 + b_2 x_2 + ... + b_n x_n \tag{11}$$

Wherein, a_0 represents a constant term. $b_1, b_2, ..., b_n$ is the regression coefficient, respectively. Similarly, in the optimization of the multiple linear regression model, the least squares method can also be used to determine the regression coefficient $a_0, b_1, b_2, ..., b_n$.

Verify the practical significance of multiple regressions. After constructing a good equation for the prediction problem through multiple linear regression equations. First, it is necessary to analyze the relationship between the explanatory variable and the explanatory variable, the size between the variables, the meaning of the real symbol corresponding to the coefficient of the variable, whether it corresponds to the prediction of the growth trend of the energy consumption of the public buildings in green towns, and the existence contact of each coefficient [11].

Verify the fit of the multiple regression equation. In the actual verification process, the degree of fitting of the equation can be verified by looking at the size of the determinable coefficient R^2 [12]. In the inspection process, it is mainly to verify the degree of interpretation of the explanatory variables, and the coefficient of determination R^2 can be calculated by the following formula:

$$R^2 = \frac{ESS}{TSS} = 1 - \frac{RSS}{TSS} = 1 - \frac{\sum_{i=1}^{n}(Y_i + \hat{Y}_i)^2}{\sum_{i=1}^{n}(Y_i + \overline{Y}_i)^2} \tag{12}$$

Wherein, Y_i indicates the actual value of the interpreted variable; $\hat{Y}_i$ represents the fitted value of the interpreted variable, $\overline{Y}_i$ represents the mean value indicating the degree of interpretation of the interpreted variable; ESS represents the sum of the squares of the explanatory variables, which gives the degree of overall variation between the fitted and mean values; RSS represents the sum of the squares of the residuals, which gives the overall variation of the actual value and the fitted value; TSS represents the sum of the squares of the total dispersion, which gives the overall variation of the actual value and the fitted value; The size of the coefficient of determination R^2 directly determines the degree of overall variation of the explanatory variable and the proportion occupied in the interpretation part of the regression model. Its size ranges from [0, 1], and the closer it is to 1, the higher the corresponding degree of fit.

TABLE 1
Statistical data of urbanization rate from 2001 to 2014

Year	Urbanization rate	Year	Urbanization rate
2001	37.66	2008	46.99
2002	39.09	2009	48.34
2003	40.53	2010	49.95
2004	41.76	2011	51.27
2005	42.99	2012	52.57
2006	44.34	2013	53.73
2007	45.89	2014	54.77

TABLE 2
The statistical result that year end has public building area really from 2001 to 2014

Year	Public building area at the end of the year	Year	Public building area at the end of the year
2001	251619.53	2008	426427.53
2002	288357.06	2009	468973.21
2003	299316.39	2010	516974.51
2004	305932.99	2011	571475.41
2005	328366.58	2012	632686.23
2006	356601.40	2013	700310.92
2007	389185.48	2014	766945.83

TABLE 3
Statistical results of various energy consumption of public buildings from 2001 to 2014

Year	Public building electricity consumption	Total energy consumption of public building	Year	Public building electricity consumption	Total energy consumption of public building
2001	1216.00	3018.54	2008	2930.40	5937.55
2002	1385.00	3242.51	2009	3326.70	6333.80
2003	1524.00	3513.01	2010	3743.80	7301.09
2004	1742.00	3817.18	2011	4256.20	7807.71
2005	2093.20	4406.23	2012	4775.10	8544.27
2006	2403.20	4805.83	2013	5274.50	9324.63
2007	2638.40	5209.59	2014	5698.30	11522.48

RESULTS AND DISCUSSION

Data acquisition and data preprocessing. In order to complete the analysis of energy consumption and growth trend of green buildings in green towns through regression analysis methods, the data to be processed include urbanization rate, public building area scale, and total energy consumption. The data sources for the three parts are:

Urbanization rate. This independent variable is obtained through statistical data of the National Bureau of Statistics. In the choice of urbanization rate, this paper selects the statistics of urbanization rate from 2000 to 2014 [13]. In this year, the statistics and analysis of the data are obtained by the latest standards of the National Bureau of Statistics. They are consistent and accurate in all kinds of indicators, and have high confidence and compatibility. In addition, in this period of time, China is implementing the tenth five-year plan, and urbanization has entered the scope of rapid development, so the growth rate is relatively high. According to the relationship between the statistical data and the Northam S curve, when the urbanization rate exceeds 70%, the urbanization rate will have an inflection point, and its growth trend will slow down. Table 1 gives statistics on the urbanization rate between 2001 and 2014. It can be seen from the statistics that since 2004, the urbanization rate has begun to fluctuate, and its growth rate has decreased from 1.44% in the 1990s to 1.29%, and the overall trend has gradually slowed down. Therefore, in this interval, not only the inflection point period of high-speed growth but also the relaxation phenomenon after the maturity period is included. Therefore, using the urbanization data under this age range will be able to comprehensively cover the main areas of energy consumption analysis and growth trend forecasting of green buildings in green towns.

Public building area size and total energy consumption. In the data of the size of public building area, this paper selects the statistical results of the actual public building area at the end of the year from 2001 to 2014 [14], as shown in Table 2.

In the choice of total energy consumption, this paper selects the statistical results of various energy

consumption of public buildings from 2001 to 2014 [15], as shown in Table 3.

Construction and Inspection of Forecast Model for Public Building Area Size in Green Towns. In the green town public building area scale prediction model, the MATLAB simulation experiment toolbox Cfcool and DATAFIT software are used [16]. For the prediction of the total area of public buildings in green towns, the functional relationship between the total construction area Y and the urbanization rate x using DATAFIT software is:

$$Y = a + b / x + c * \ln(x) / x^2 \quad (13)$$

In the 99% confidence interval, the dependent variable results for the DATAFIT preference function are shown in Table 4.

In addition, for the prediction of the heating area of public buildings in green towns, the functional relationship between the total heating area Y and the urbanization rate x using DATAFIT software is also as follows:

$$Y = a + b * x^2 * \ln(x) + c / x^{0.5} \quad (14)$$

In the 99% confidence interval, the dependent variable results for the DATAFIT preference function are shown in Table 5.

In the model verification of the total area prediction of green town public buildings, Table 6 and Figure 5 respectively give the error analysis and deviation distribution map of the prediction results.

In Figure 5, the fitness is $R^2 = 0.99$, corrected measurement coefficient is $Ra^2 = 0.98$. The maximum and minimum deviations were 4.01% and 0.20%, respectively. The fitting effect is better.

In the model verification of the heating area prediction of public buildings in green towns, Table 7 and Figure 6 respectively show the error analysis and preference distribution of the prediction results.

TABLE 4
The solution value of the function dependent variable of the prediction model of green urban building area scale

Coefficient	Value	99% (+/-)	Confidence interval upper limit	Confidence interval lower limit
A	$5.02*10^6$	$1.06*10^6$	$5.02*10^6$	$6.04*10^6$
B	$-2.78*10^6$	$-3.41*10^6$	$5.02*10^6$	$-2.11*10^6$
C	$-3.58*10^5$	$-4.26*10^5$	$5.02*10^5$	$-2.54*10^5$

TABLE 5
The solution value of the function dependent variable of green town heating area scale prediction model

Coefficient	Value	99%(+/-)	Confidence interval upper limit	Confidence interval lower limit
A	$3.46*10^6$	$2.31*10^6$	$1.44*10^6$	$5.61*10^6$
B	$7.29*10^6$	$5.41*10^6$	$1.86*10^6$	$1.16*10^7$
C	$-1.52*10^6$	$8.21*10^5$	$-2.28*10^6$	$-6.34*10^5$

TABLE 6
Error analysis of green town public building area prediction

Coefficient	Value	Standard error	T test	Alpha threshold
A	$5.02*10^6$	$1.06*10^6$	4.86	$2.11*10^{-4}$
B	$-2.78*10^6$	$7.11*10^{-5}$	1.39	0.00
C	$-3.58*10^5$	$1.32*10^6$	$-2.76*10^1$	0.00

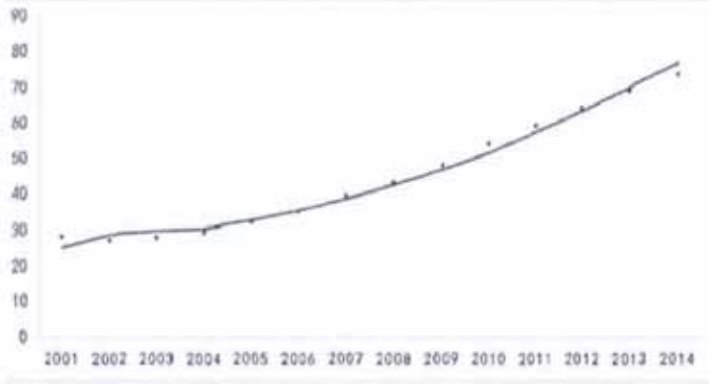

FIGURE 5
Deviation distribution map of green town public building area prediction

TABLE 7
Analysis of prediction error of heating area in public buildings of green towns

Coefficient	Value	Standard error	T test	Alpha threshold
A	$3.46*10^6$	$6.69*10^6$	5.36	0.00
B	$7.29*10^6$	$1.74*10^6$	4.29	$1.04*10^{-3}$
C	$-1.52*10^6$	$2.59*10^5$	-5.49	0.00

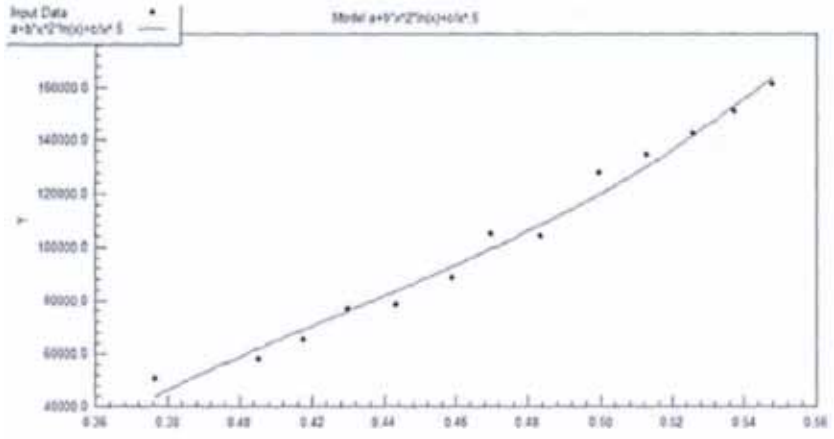

FIGURE 6
Deviation distribution map of green town public building heating area prediction

TABLE 8
The solution value of the dependent variable function of the heating energy consumption prediction model for green urban buildings

Coefficient	Value	99% (+/-)	Confidence interval upper limit	Confidence interval lower limit
A	$9.26*10^2$	$2.11*10^2$	$7.32*10^2$	$1.09*10^3$
B	$1.14*10^{-3}$	$1.43*10^{-4}$	$9.12*10^{-4}$	$1.16*10^{-3}$

TABLE 9
The solution value of the dependent variable function of the green town heating energy consumption prediction model

Coefficient	Value	99% (+/-)	Confidence interval upper limit	Confidence interval lower limit
A	$-1.69*10^4$	$1.08*10^4$	$-2.64*10^4$	$-7.44*10^3$
B	$2.41*10^6$	$3.69*10^{-6}$	$-1.42*10^6$	$6.31*10^{-6}$
C	$1.14*10^2$	6.51	5.26	$1.83*10^2$

In Figure 6, the fitness is $R^2 = 0.98$, corrected measurement coefficient is $Ra^2 = 0.98$, the maximum and bottom deviations were 7.09% and 0.41%, respectively. The fitting effect is better.

It can be seen from the above results that the multi-regression analysis method proposed in this paper is used to complete the prediction of the total area and heating area of public buildings in green towns. It can be seen from the error results that the error is small and can be verified by the model. Therefore, a very good fitting effect is obtained in the area prediction, and the prediction result is accurate.

Construction and Test of Forecast Model for Total Energy Consumption of Public Buildings in Green Towns. Similarly, in the green town public building energy consumption total forecast model, the MATLAB simulation experiment toolbox Cfcool, and DATAFIT software are used. For the prediction of heating energy consumption in public buildings in green towns, the relationship between the total energy consumption of heating Y and the heating area x using DATAFIT software is:

$$Y = a + b * x * \ln(x) \quad (15)$$

In the 99% confidence interval, the dependent variable results for the DATAFIT preference function are shown in Table 8.

In addition, for the prediction of electricity consumption in public buildings in green towns, the DATAFIT software is also used to construct a functional relationship between power consumption Y and public building area x:

$$Y = a + b * x^{1.5} + c * \ln^2(x) \quad (16)$$

TABLE 10
Error analysis of heating energy consumption prediction for public buildings in green cities and towns

Coefficient	Value	Standard error	T test	Alpha threshold
A	$9.26*10^{2}$	$6.32*10^{1}$	$1.43*10^{1}$	0.00
B	$1.14*10^{-3}$	$4.71*10^{-5}$	$2.29*10^{1}$	0.00

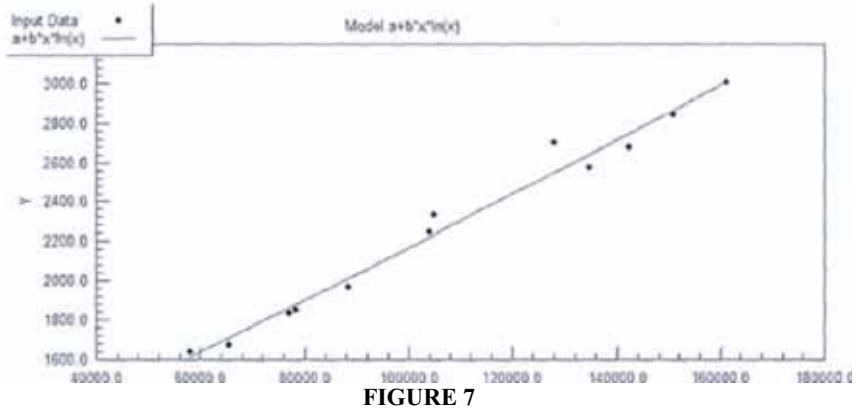

FIGURE 7
Deviation distribution map of green town public building heating energy consumption prediction

TABLE 11
Error analysis of power consumption prediction for public buildings in green cities and towns

Coefficient	Value	Standard error	T test	Alpha threshold
A	$-1.69*10^{4}$	$3.17*10^{3}$	5.41	0.00
B	$2.41*10^{6}$	$1.19*10^{-6}$	2.04	$7.04*10^{-2}$
C	$1.14*10^{2}$	2.14	5.62	0.00

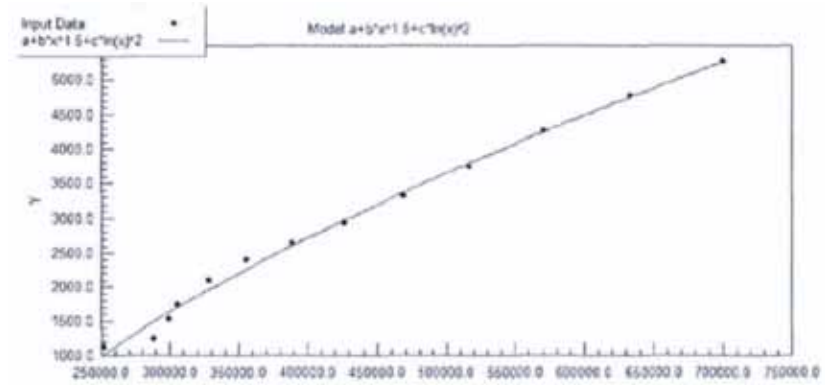

FIGURE 8
Deviation distribution map of electricity consumption prediction for public buildings in green cities and towns

In the 99% confidence interval, the dependent variable results for the DATAFIT preferred function are shown in Table 9.

In the model verification of the total area prediction of green town public buildings, Table 10 and Figure 7 respectively give the error analysis and deviation distribution map of the prediction results.

In Figure 7, the error is within the acceptable range and the fitting effect is good.

In the model verification of electric power consumption prediction of green town public buildings, Table 11 and Figure 8 respectively give the error analysis and preference distribution map of the prediction results.

In Figure 8, the fitness is $R^2 = 0.99$, corrected measurement coefficient is $Ra^2 = 0.99$, the maximum and bottom deviations were 9.54% and 0.03%, respectively. The fitting effect is better.

It can be seen from the above results that using the multiple regression analysis method proposed in this paper, the prediction of heating energy consumption and electric energy consumption of green town public buildings is completed, the fitting effect is good, the error is within the acceptable range, and the model is verified. The prediction effect is more accurate.

CONCLUSION

In this paper, an energy analysis and growth trend prediction based on regression analysis method is proposed to solve the problem of analysis and prediction of total energy consumption and energy intensity of public buildings in the context of green town construction and development. Based on the model construction and regression analysis methods, the data of urbanization rate, public building area scale and total energy consumption were predicted. In the analysis results of the area and energy consumption of public buildings in green towns, the fitting effect is better and the error is within the acceptable range. The model verification shows that the prediction effect is more accurate. Future work will focus on building more accurate predictive models, using multiple regression forecasting models to predict the growth trends of various energy sources from different perspectives.

REFERENCES

[1] Porse, E., Derenski, J., Gustafson, H., Elizabeth, Z., Pincetl, S. (2016) Structural, geographic, and social factors in urban building energy use: Analysis of aggregated account-level consumption data in a megacity. Energy Policy. 96, 179-192.

[2] Reinhart, C.F., Davila, C.C. (2016) Urban building energy modeling–A review of a nascent field. Building and Environment. 97, 196-202.

[3] Chen, Y., Hong, T., Piette, M.A. (2017) Automatic generation and simulation of urban building energy models based on city datasets for city-scale building retrofit analysis. Applied Energy. 205, 323-335.

[4] Ma, J., Cheng, J.C.P. (2016) Estimation of the building energy use intensity in the urban scale by integrating GIS and big data technology. Applied Energy. 183, 182-192.

[5] Kammen, D.M., Sunter, D.A. (2016) City-integrated renewable energy for urban sustainability. Science. 352, 922-928.

[6] Davila, C.C., Reinhart, C.F., Bemis, J.L. (2016) Modeling Boston, A workflow for the efficient generation and maintenance of urban building energy models from existing geospatial datasets. Energy. 117, 237-250.

[7] Delzendeh, E., Wu, S., Lee, A., Zhou, Y. (2017) The impact of occupants' behaviours on building energy analysis: A research review. Renewable and Sustainable Energy Reviews. 80, 1061-1071.

[8] Robinson, C., Dilkina, B., Hubbs, J., Zhang, W.W., Guhathakurta, S., Brown, M.A., Pendyala, R.M. (2017) Machine learning approaches for estimating commercial building energy consumption. Applied Energy. 208, 889-904.

[9] Berardi, U. (2017) A cross-country comparison of the building energy consumptions and their trends. Resources, Conservation and Recycling. 123, 230-241.

[10] Wei, Y., Zhang, X., Shi, Y., Xia, L., Pan, S., Wu, J.S., Han, M.J., Zhao, X.Y. (2018) A review of data-driven approaches for prediction and classification of building energy consumption. Renewable and Sustainable Energy Reviews. 82, 1027-1047.

[11] Amasyali, K., El-Gohary, N.M. (2018) A review of data-driven building energy consumption prediction studies. Renewable and Sustainable Energy Reviews. 81, 1192-1205.

[12] Zhang, Y., He, C.Q., Tang, B.J., Wei, Y.M. (2015) China's energy consumption in the building sector, a life cycle approach. Energy and Buildings. 94, 240-251.

[13] Dogan, T., Reinhart, C.F. (2017) Shoeboxer: An algorithm for abstracted rapid multi-zone urban building energy model generation and simulation. Energy and Buildings. 140, 140-153.

[14] Pizzuti, S., Moretti, F., Panzieri, S., Annunziato, M. (2015) Urban traffic flow forecasting through statistical and neural network bagging ensemble hybrid modeling. Neurocomputing. 167, 3-7.

[15] Yang, A.S., Juan, Y.H., Wen, C.Y., Chang, C.J., (2017) Numerical simulation of cooling effect of vegetation enhancement in a subtropical urban park. Applied Energy. 192, 178-200.

[16] Ma, H.T., Du, N., Yu, S.J., Lu, W.Q., Zhang, Z.Y., Deng, N., Li, C. (2017) Analysis of typical public building energy consumption in northern China. Energy and Buildings. 136, 139-150.

Received: **02.08.2019**
Accepted: **29.01.2020**

CORRESPONDING AUTHOR

Ting Zheng
College of Computer and Information,
Inner Mongolia Medical University,
Hohhot, Inner Mongolia, 010110 – China

e-mail: zhengting888@21cn.com

© by PSP Volume 29 – No. 04A/2020 pages 2802-2808 Fresenius Environmental Bulletin

DETERMINATION OF PESTICIDES IN FARMER HAIRS FOR THE BIOMONITORING OF EXPOSURE IN CUKUROVA REGION, TURKEY

Nebile Daglioglu[1,*], Pinar Efeoglu Ozseker[1], Nigar Yarpuz Bozdogan[2], Evsen Guzel[3]

[1]Department of Forensic Medicine and Toxicology, Faculty of Medicine, University of Cukurova, Adana, Turkey
[2]University of Cukurova, Adana Organized Industrial Zone Vocational School of Technical Sciences,01330, Adana, Turkey
[3]University of Cukurova, Faculty of Fisheries Department of Basic Sciences, 01330, Adana, Turkey

ABSTRACT

Hair analysis has gained importance in the chronic monitoring of environmental or occupational exposure to pesticides. There are no studies on hair pesticide analysis while pesticide is being investigated in many biological samples such as blood, urine, adipose tissue and breast milk in Cukurova Region. In our study, pesticide was analyzed in hair samples of 21 workers working in the field and who are exposed to pesticides. 17 different pesticides were detected in 21 hair samples collected. The most frequently detected pesticides were acetamiprid, hexythiazox and epoxiconazole. The highest concentration was found for acetamiprid (3904 pg/mg). These results have shown that farmers living in the Cukurova Region are exposed to pesticides and use a very limited number of protective equipment.

KEYWORDS:
Pesticide, Hair, Biomonitoring, Cukurova Region

INTRODUCTION

Cukurova Region is where intense agriculture is done and 32% of agricultural chemicals consumed in Turkey are used in this region [1]. In recent years, exposure and risk management have become important in enabling biological monitoring in humans and the environment. The analysis of biological samples provides us with the environmental distribution and the exposure rate. Biological samples such as blood, adipose tissue, breast milk, amniotic fluid are commonly used to measure the amount of residue in pesticide exposure [2–5]. Although human hair is not a widely used biological sample for measuring exposure to organic pollutants, collection of human hair sample is an easy, cheap and non-invasive method. The hair sample is stable and important in terms of indicating long-term chronic exposure. Hair samples are also used in toxic trace element analysis such as arsenic, thallium, mercury, and drug analysis as well as pesticide analysis [6–8]. Lipophilic compounds in the hair accumulate especially in sebaceous glands with high fat content (2-4%). A positive correlation between lipophilicity and hair protein ratio of the compound was observed by in vitro studies. There are publications in the literature where organic pollutants such as organochlorine dioxins and PCB have been studied on the hair [8, 9]. Age, gender, hair color, ethnicity and geographic origin, diet and other factors are essential criteria to consider when interpreting organic pollutants in the hair and a few studies have been conducted on the effects of these. There are some rules for recognizing the hair as a biological monitor. These include 1.) analytical procedure which is standardized for sampling, washing, extraction, instrumental methods and quality assurance/control, 2.) information on the transition mechanism of organic pollutions to the hair, their kinetics and separation of the metabolites from the hair, 3.) database on persistent organic pollutants in human hair, 4.) the interpretation of dose-response relationship, 5.) effect of hair biology (age, sex, race, etc.) [10].

The aim of this study is to biomonitoring a wide number of pesticides (insecticide, fungicide and acaricide) with high sensitivity in the hair of farmers who are engaged in agriculture in Cukurova region and exposed to pesticides chronically.

MATERIALS AND METHODS

Chemicals, reagents, and standard solutions. All pesticide standards and internal standards were purchased from Dr. Ehrenstorfer (Augsburg, Germany) and were certified for purity (higher than 98%). Stock solutions at 1.0 mg/L, working solutions at 10 ng/ml-100 ng/ml and internal standard (dimethoate-d6) at 10 pg/mg were prepared in methanol. Oasis HLB cartridge (3cc, 60 mg) solid-phase extraction (SPE) cartridges were purchased from Waters Corporation (Milford, MA, USA).

Hair sampling. 21 hair samples were collected from farm workers in living Cukurova Region. All farmers were informed about this study and

written information form were taken. The study was approved by Mersin University Ethics Committee. Hair samples (200±1 mg) were collected from the posterior vertex region of the scalp, as close as possible to the skin of the head from each volunteer. Sample collection was performed by the local medical staff. Hair samples generally shaved in the study area; because of this the collected strands were about 1 cm long. The dominant color of the samples was dark black. Samples were collected in aluminum foil, and placed in paper bags at the room temperature.

Extraction of the hair. Each hair sample was washed to avoid from environmental contamination. The hair was sequentially washed with dichloromethane, deionized water and methanol [11, 12]. Hair samples were dried on paper and were cut into segments of 1-2 mm after being washed. 50 mg of the collected hair powder was weighed into a 5 ml glass tube, spiked with internal standards and immersed in 2 ml methanol at 37-38 °C overnight (12 h). After that, the mixture was loaded on Oasis HLB (3cc, 60 mg) cartridges that had been previously conditioned by 2 mL of methanol and water. The elution solvent was methanol (2 ml). Prior to the LC-MS/MS analyses, the final eluate evaporated to dryness under a gentle nitrogen stream and the residue was re-dissolved in methanol.

Liquid Chromatography and Mass Spectrometry Conditions. Chromatographic separations were carried out with Shimadzu CBM-20A Ultra-Fast Liquid Chromatography system equipped with Shimadzu SIL-20A/HT Automatic Sampling System and Shimadzu 8040 Mass Spectrometry (Kyoto, Japan). The analytes were separated chromatographically at the room temperature at a flow rate of 0.4 mL/min on the Shim-pack column (150x2.0 mm) purchased from Shimadzu (Tokyo, Japan). Gradient elution was carried out with a binary mobile phase of 5 mM ammonium formate in water (solution A) and 5 mM ammonium formate in methanol (solution B). Sample injection volume was 20 µl.

All the selected analytics were analyzed in positive ionization mode (ESI+). Identification and quantification were performed using two characteristic transitions for the analyzed compounds (MRM mode). Analytical parameters, detection frequencies and concentrations of 17 pesticides analyzed are listed in Table 1 and the retention time, precursor ions and product ions of 144 pesticides applied are listed in Supplementary File (Table S1).

RESULTS AND DISCUSSION

The pesticides classes, analytical parameters, detection frequencies and concentration results are given in Table 1. For most pesticides the correlation coefficient of the calibration curve was higher than 0.99. Over the entire calibration range calibration curves showing good linearity. LOD varied from 0.01 to 3.63 pg/mg and the lowest LOQ ranged from 0.1 to 12.11 pg/mg. Recovery also ranged from 60% (acetamiprid) to 146% (Fenproximate). All recoveries were calculated on selected pesticides which added to the matrix.

Cukurova is a region where agriculture is intensively done and farmers mostly produce cotton, wheat, tomato, corn, lettuce, potato, watermelon, cabbage and citrus fruits and accordingly pesticide is used excessively. Considering this fact, it can be said that pesticide exposure is increased at the same level.

TABLE 1
Pesticide classes, analytical parameters, detection frequencies and concentrations of 17 pesticides analyzed (n=21)

Pesticide Name	Pesticide Class	RT (min)	LOD (pg/mg)	LOQ (pg/mg)	Rec (%)	FD (%)	Concentration (pg/mg)	
							Range	Mean±SD
Clothianidin	Insecticides	6.79	0.04	0.14	60	5	nd-30.60	23.30±10.32
Acetamiprid	Insecticides	7.33	0.08	0.27	60	90	nd-3904.0	421.9±93.8
Carbaryl	Insecticides	9.96	0.03	0.10	130	5	nd-26.10	26.10*
Azoxystrobin	Fungicides	11.20	0.06	0.21	117	5	nd-2.00	2.00*
Epoxiconazole	Fungicides	12.19	3.63	12.11	73	57	nd-130.4	53.15±36.17
Difenoconazole	Fungicides	13.11	0.03	0.11	124	10	nd-104.2	57.85±65.55
Chlorfluazuron	Insecticides	14.14	0.01	0.05	106	5	nd-29.30	29.30*
Abamectin	Acaricides	14.44	0.24	0.78	97	5	nd-31.20	31.20*
Fenpyroximate	Acaricides	14.23	0.01	0.02	146	10	nd-18.50	12.25±8.84
Chlorpyrifos-ethyl	Insecticides	14.00	0.74	2.48	94	10	nd-242.5	198.3±62.58
Methomyl	Insecticides	5.37	1.94	6.46	65	24	nd-2201.0	815.8±791.1
Imidacloprid	Insecticides	6.65	0.04	0.13	63	29	nd-82.70	33.50±27.97
Metalaxyl- M	Fungicides	10.69	0.04	0.13	114	38	nd-347.5	51.04±120.3
Hexythiazox	Acaricides	13.90	0.02	0.07	112	76	nd-2187.0	202.9±556.0
Pyriproxyfen	Insecticides	13.92	0.15	0.51	76	10	nd-24.10	14.10±14.14
Tebuconazole	Fungicides	12.64	0.11	0.35	125	19	nd-96.1	265.1±466.1
Triadimefon	Fungicides	11.82	0.46	1.55	124	24	nd-561.0	217.6±239.7

TABLE 2
Sociodemographic characteristics of the study populations (n=21)

1.	Age of population	32.9±13.9[a]
	15-25 years old	38.1%
	26-35 years old	14.3%
	36-45 years old	28.6%
	45-60 years old	19.0%
2.	Gender	
	Female	9.5%
	Male	90.5%
3.	Length of the population	175.6±10.2[a]
4.	Weight of population	83.6±22.0[a]
5.	Place of birth	
	Adana	81%
	From outside the Adana	19%
6.	Education level	
	Primary school	38.1%
	Middle school	23.8%
	High school	28.6%
	College	4.8%
	Undergraduate student	4.8%
7.	Smoking	
	No	42.9%
	Yes	57.1%
8.	Protective clothing	
	None	23.8%
	Hat	66.7%
	Hat&mask	9.5%
9.	Time spent in pesticide spraying (h)	5.7±3.5[a]
10.	Time spent in this profession	15.3±11.3[a]
11.	Hair washing agents	
	Soap	23.8%
	Shampoo	28.6%
	Soap+Shampoo	47.6%

[a] Mean±sd.

Statistical analyses were performed with IBM SPSS 23.0 software package. Categorical measurements (gender, age etc.) were demonstrated as a number or percentile, while progressive measurements were demonstrated as the mean and standard deviation. Mann Whitney U test or Kruskal Wallis test was used in order to compare residual values in hair samples of different genders, age, education and personal protective equipment. Spearman Correlation coefficient was used to investigate the correlation between pesticides. A $p<0.05$ value was regarded as statistically significant.

When the age distribution of the farmers who participated in our study was examined, it was seen that the minimum age was 15, whereas the maximum was 57 with an average age of 33. Of the participants, 90.5% was male and 9.5% was female. 144 pesticide scans (Supplementary File) were conducted on hair samples collected from farmers and the results are given in Table 1. Among the 144 pesticides, methomyl, clothiandine, metaloxyl-M, acetamiprid, carbaryl, azoxystrobin, triadimefon, epoxiconazole, hexythiazox, tebuconazole, chlorfluazuron, difenocazole, fenproximate, pyriproxyphen, chlorpyrifos-ethyl, imidacloropide and abamectin were found to be positive. When the frequency of the detected pesticides was examined, it was found that acetamiprid (90%) was the highest, whereas hexythiazox was detected at the rate of 76% and epoxiconazole was at the rate of 57%. Participants of the study reported in the questionnaire that they used drugs commercially named as Effore and Hekplan, with an active ingredient of acetamiprid. Acetamiprid insecticide group is pesticide and is used against insects in fruits and vegetables in our region. In our study, the highest concentration of Acetamiprid in the hair was found to be 3904 pg / mg. Acetamiprid is the pesticide reported at the highest rate among the study samples in the literature (67.3%) and the highest value in hair concentration was reported to be 236.5 pg / mg [13]. The mean concentration value of epoxiconazole (57%), which has the highest frequency rate in the hair of 21 farmers who participated in the study, was found to be 53.15 pg / mg, while the frequency of this pesticide was 17.7% and the median concentration was 19.9 pg / mg in a pesticide monitoring carried out by Salquèbre et al., (2012) in the hair of 18 farmers [14].

Table 2 shows the socio-demographic characteristics of the farmers participating in the study. The education level of the farmers was classified and it was seen that 38.1% were primary school, 23.8% were secondary school, 33% were high school and 4.8% were vocational school graduates. Schramm (2008) reported that age and gender do not affect hair pesticide accumulation. While there was a significant difference in concentration of acetamiprid pesticide among the detected pesticides between male and females (males outweigh females), no significant difference was detected between male and females in terms of other pesticides. ($p<0.05$) [15].

Agricultural workers perform agricultural spraying by using mixtures of many pesticides for 6-8 hours a day, and they don't use any personal protective equipment (PPE), protective eyewear, headgear, gloves, footwear, and coveralls, etc. [16–18]. Only 9.5% of the farmers participated in our study wore hats and masks (Table 2). With the statistical comparison between PPE usage and pesticide level in the hair, it was determined that the farmers with the highest amount of difenocazole pesticide were those who did not use PPE, while the lowest amount was found in those wearing highly protective clothing. For other pesticides, no significant difference was found between the use of protective clothing and the amounts of pesticides detected.

According to survey records, farmers spent an average of 5.7 ± 3.5 hours on agricultural spraying. When the time spent by the farmers in the agricul-

tural spraying was compared with the amount of pesticides detected in the hair, no significant difference was found between the average amounts of the pesticides detected in the hair and the working times.

The detection of triadimefon, carbarly and chlorfluazuron, which were banned in our country in 2011, indicates that these pesticides are illegally used. The lack of control and monitoring in national politics is emphasized by the findings of this study. Especially for the biomonitoring exposure in the study area, the hair is found to be a particularly convenient matrix. A safe hair sample collection that is suitable for further study can easily be provided by non-technical personnel. The major advantage of this matrix was also storage at the room temperature [19] and the multiresidue analysis allowed for screening 144 pesticides in a single sample.

CONCLUSION

To our knowledge, this is the first study which collected hair samples of farmers in Turkey. This study findings indicate that it is possible to use hair samples for biomonitoring purposes in Cukurova Region. We analyzed only total exposure to pesticides, but we did not make a segmental hair analysis. The limitation of our work is a small number of samples.

SUPPLEMENTARY FILE

TABLE S1
Retention time, precursor and product ions of detected pesticides for LC-MS/MS analysis

Compound name	Ret. Time	Precursor	Product-1	Product-2
Fenoxaprop-P-ethyl	13,491	361,80	288,10	91,25
Triclorfon	7,186	256,85	109,00	220,70
Cymoxanil	8,442	199,10	128,15	111,10
Chlormequat Chloride	0,909	122,00	58,20	63,10
Clothianidine	7,338	249,70	132,10	169,10
Dimethoate	7,849	229,60	125,15	199,05
Acetamiprid	7,992	222,60	56,20	126,10
Chloridazon	7,990	221,60	104,10	92,20
Dichlorfos	10,300	220,90	109,15	127,15
Carbaryl	10,776	202,05	145,20	127,15
Ethiofencarb	10,957	225,80	107,15	164,20
Carboxin	10,754	235,60	143,10	87,10
Flutriafol	10,643	302,10	123,20	109,20
Atrazine	10,647	215,65	174,15	43,15
Diuron	10,872	232,80	72,20	160,10
Diphenamid	10,936	239,70	134,20	167,20
Diethofencarb	11,896	267,80	226,20	180,20
Azinphos-methyl	11,463	317,70	160,15	132,15
Azoxystrobin	11,696	403,80	372,25	329,10
Fenamidone	11,994	311,80	92,20	236,20
Boscalid	11,568	343,10	307,20	140,00
Dimethomorph	11,679	387,70	301,15	165,20
Dimethenamid	11,526	275,60	244,20	168,20
Cyproconazole	12,035	292,10	70,20	125,15
Bromuconazole	12,399	378,00	159,00	161,00
Fenbuconazole	12,633	337,15	70,25	125,10
Fenarimol	12,499	330,80	268,10	139,10
Dichlofluanid	12,495	350,00	224,05	123,20
Epoxiconazole	12,598	329,80	101,20	121,20
Alachlor	12,737	269,70	238,25	162,25
Fenamiphos	12,338	303,60	217,10	202,10
Acetochlor	12,664	269,90	224,20	148,20
Buprimate	12,783	316,70	166,20	108,10
EPTC	12,982	190,10	86,00	128,20
Fenthion	13,108	279,00	247,10	169,00
Diniconazole	13,349	326,10	70,20	159,10
Diazinon	13,093	304,60	169,10	97,10
Difenacozole	13,326	405,80	251,10	111,10
Cyprodinil	13,262	225,70	93,15	108,20
Cycloate	13,554	216,15	154,20	134,20
Diclofop Methyl	13,792	358,10	281,10	120,20
Dioxathion	13,608	473,80	97,10	153,10
Buprofezin	13,774	305,70	57,15	201,20
Diafenthiuron	14,123	384,90	329,30	278,25
Fenpropathrin	14,063	350,15	125,20	57,20
Chlorfluazuron	14,197	539,80	382,95	158,15

Cypermethrin	14,182	433,30	191,05	193,15
Deltamethrin	14,301	522,80	281,00	506,20
Abamectin	14,462	890,60	305,35	145,15
Fenproximate	14,286	421,70	366,30	135,10
Carbosulfan	14,783	380,70	118,25	160,25
Fenazaquin	14,834	306,90	57,20	161,20
Bifenthrin	15,109	440,20	181,20	166,10
Etofenprox	15,206	393,80	177,20	107,15
bensulforuron-methyl	11,383	410,80	149,20	182,20
Clodinafob-propargyl	12,829	349,70	266,00	238,10
ethofumesate	11,951	287,10	121,20	258,80
ethoprophos	12,615	242,80	131,00	172,90
chlorpyrifos-ethyl	14,091	349,70	197,90	97,00
chlorpyrifos-methyl	13,532	321,90	125,00	289,90
chlorsulfuron	7,757	357,80	141,20	167,20
dazomet	4,921	163,00	89,90	119,90
nicosulfuron	6,753	411,10	182,20	106,20
Propamocarb hydrocloride	5,331	188,80	102,20	144,20
Oxamyl	5,179	236,85	72,25	90,25
Methomyl	5,666	162,80	88,20	106,20
Monocrotophos	6,361	224,10	127,10	98,20
Imidachloropid	7,170	256,10	209,15	175,15
Imazethapyr	6,329	289,80	230,20	177,20
Foramsulfuron	8,939	453,00	182,20	139,10
Oxadixyl	9,662	279,15	219,25	132,25
Monolinuron	10,204	215,00	126,10	148,20
Primicarb	10,382	238,70	72,15	182,30
Metalaxyl M	11,378	279,75	220,25	192,25
Isoxaflutole	11,418	377,30	251,10	219,85
Methidathion	11,686	303,00	144,90	85,20
Phosmet	11,204	318,05	160,15	133,15
Myclobutanil	11,817	288,90	70,20	288,90
Malathion	12,240	330,80	127,20	99,10
Propyzamide	12,325	256,05	190,05	173,05
Pyridaphenthi	12,321	340,80	189,15	92,20
Flusilazole	12,711	315,80	247,20	165,15
Metolachlor	12,733	283,80	252,20	176,25
Prometryn	12,642	241,80	158,10	200,20
Penconazole	12,958	284,25	70,25	159,05
Imazalil	12,953	297,10	159,00	255,10
Phenthoate	12,869	321,10	135,15	163,25
Kresoxim M	12,927	313,90	222,25	206,20
Pyrafluorfen-ethyl	12,924	413,10	339,10	253,10
Metconazole	13,140	320,20	70,20	125,15
Hexaconazole	13,149	314,10	70,20	159,10
Propiconozole	12,789	342,10	159,00	69,20
Mefenpyr-diethyl	13,104	389,90	327,15	160,00
Prochloraz	13,204	375,80	308,10	266,00
Phosalone	13,195	368,05	182,15	111,10
Pyraclostrobin	13,120	387,80	163,10	104,20
Pirimiphos-methyl	13,092	305,80	108,10	164,20
Pyrazophos	13,286	373,80	222,20	194,20
Haloxyfop-2-etoxy ethyl	13,558	433,90	316,15	91,20
Fluazifop- P-Buthyl	13,565	383,90	282,20	328,20
Profenefos	13,529	372,95	302,90	345,10
Propaquizafob	13,657	444,20	371,00	100,20
Hexythiazox	13,992	353,20	228,10	168,10
Propargite	14,064	368,25	175,20	231,30
Pyriproxypen	13,996	321,70	96,20	185,15
Pendimenthalin	14,179	282,20	194,10	212,20
Pyridaben	14,448	365,00	147,30	309,20
Prothiophos	12,936	344,50	241,10	133,20
Pyridate	5,036	379,20	207,10	351,25
Halfenprox	15,459	494,20	183,20	155,10
Fosthiazate	10,999	284,10	104,20	227,70
furathioncarb	13,652	382,90	195,20	252,10
haloxyfop-p-methyl	13,337	376,10	315,90	91,20
imazapyr	3,710	261,90	217,20	78,20
iodosulfuron-methyl	9,480	508,00	167,20	141,20
imazapic	8,270	275,90	231,10	163,20
mesosulfuron-methyl	9,826	504,20	182,20	139,20
mesotrione	4,567	357,10	104,10	104,10
metamitron	7,753	203,10	104,20	174,00
metribuzin	9,480	215,10	187,10	84,30
quizalofop-p-ethyl	13,579	373,50	299,50	299,10

spirodiclofen	4,829	411,20	71,20	313,00
spiroxamine	12,908	298,00	144,30	100,30
tau fluvalinite	14,358	520,00	181,20	208,00
tebuconazole	12,955	308,20	70,20	125,20
tebufenozide	12,725	353,30	133,20	296,90
terbutryn	12,738	241,70	186,20	68,20
tetraconazole	12,510	372,10	159,10	70,20
Thiacloprid	8,787	252,75	126,10	99,10
Thiametoxam	5,988	291,80	210,90	181,20
thifensulfuron-methyl	7,028	388,10	167,20	69,10
thiometon	10,467	247,05	89,20	88,80
tolylfluanid	12,897	363,80	237,90	137,20
triadimefon	12,286	294,10	197,00	70,20
triasulsuron	7,943	402,10	167,20	141,10
Florasulam	6,961	360,05	129,10	192,00
Mesotrione	4,547	357,10	227,90	104,10
Thiophonate-methyl-pos	9,453	343,05	151,10	118,20
Metsulfuron-methyl-pos	6,523	382,10	167,20	198,90
Metribuzin	9,474	214,80	187,00	84,10
Fenoxycarb	12,801	302,15	88,20	116,10
Triflumizole	13,507	346,50	278,20	73,00
Trifloxystrobin	13,341	409,15	186,20	145,10
Fipronil	12,654	434,90	329,90	249,90

ACKNOWLEDGEMENTS

This work was supported by Cukurova University Research Foundation with the financial support provided for this work (Grant no: TF2012BAP17).

The authors report no conflicts of interest. The authors alone are responsible for the content of the paper.

REFERENCES

[1] Zeren, C. and Erem, G. (2000) Pesticide using level in Adana and İçel Provinces. Environ Sci Technol. 1, 29–33. (in Turkish)

[2] Daglioglu, N., Gulmen, M.K., Akcan, R., Efeoglu, P., Yener, F. and Unal, I. (2010) Determination of organochlorine pesticides residues in human adipose tissue, data from Cukurova, Turkey. Bull Env. Contam Toxicol. 85, 97–102.

[3] Akcan, R., Hilal, A., Daglioglu, N., Cekin, N. and Gulmen, M.K. (2009) Determination of pesticides in postmortem blood and bone marrow of pesticide treated rabbits. Forensic Sci. Int. 189, 82–87.

[4] Daglioglu, N., Akcan, R., Efeoglu, P., Inandiklioglu, N., Korkut Gulmen, M., Demir-han, O. (2013) Polychlorinated biphenyls and organochlorine pesticides in amniotic fluids of pregnant women in south-central Turkey. Toxicol. Environ. Chem. 95, 954–961.

[5] Yildizdas, H.Y., Ozlu, F., Efeoglu, P. and Daglioglu, N. (2019) Non-persistent pesticides in breast milk in an agricultural area in Turkey. J. Matern. Neonatal Med. 32(14), 2387-2392.

[6] Kintz, P., Villain, M. and Cirimele, V. (2006) Hair analysis for drug detection. Ther. Drug Monit. 28, 442–446.

[7] Esteban, M. and Castaño, A. (2009) Non-invasive matrices in human biomonitoring: A review. Environ. Int. 35, 438–449.

[8] Zhang, H., Chai, Z. and Sun, H. (2007) Human hair as a potential biomonitor for assessing persistent organic pollutants. Environ. Int. 33(5), 685-693.

[9] Tsatsakis, A. and Tutudaki, M. (2004) Progress in pesticide and POPs hair analysis for the assessment of exposure. Forensic Sci. Int. 145, 195–199.

[10] Covaci, A., Tutudaki, M., Tsatsakis, A.M. and Schepens, P. (2002) Hair analysis: Another approach for the assessment of human exposure to selected persistent organochlorine pollutants. Chemosphere. 46, 413–418.

[11] Blank, D.L. and Kidwell, D.A. (1995) Decontamination procedures for drugs of abuse in hair: are they sufficient? Forensic Sci. Int. 70, 113–38.

[12] Schaffer, M.I., Wang, W.L. and Irving, J. (2002) An evaluation of two wash procedures for the differentiation of external contamination versus ingestion in the analysis of human hair samples for cocaine. J. Anal. Toxicol. 26, 485–488.

[13] Lehmann, E., Oltramare, C., Nfon Dibié, J.J., Konaté, Y. and de Alencastro, L.F. (2017) Assessment of human exposure to pesticides by hair analysis: The case of vegetable-producing areas in Burkina Faso. Environ. Int. 111, 317–331.

[14] Salquèbre, G., Schummer, C., Millet, M., Briand, O. and Appenzeller, B.M.R. (2012) Multiclass pesticide analysis in human hair by gas chromatography tandem (triple quadrupole) mass spectrometry with solid phase microextraction and liquid injection. Anal. Chim. Acta. 710, 65–74.

[15] Schramm, K.W. (2008) Hair-biomonitoring of organic pollutants. Chemosphere. 72(8), 1103-1111.
[16] Yarpuz-Bozdogan, N., Bozdogan, A.M., Daglioglu, N. and Erdem, T. (2017) Determination of dermal exposure of operator in greenhouse spraying. AMA, Agric. Mech. Asia, Africa Lat. Am. 48, 33–38.
[17] Yarpuz-Bozdogan, N. and Bozdogan, A.M. (2016) Pesticide exposure risk on occupational health in herbicide application. Fresen. Environ. Bull. 25, 3720–3727.
[18] Yarpuz-Bozdogan, N. (2018) The importance of personal protective equipment in pesticide applications in agriculture. Curr. Opin. Environ. Sci. Heal. 4, 1–4.
[19] Knipe, D.W., Jayasumana, C., Siribaddana, S., Priyadarshana, C., Pearson, M., Gunnell, D., Metcalfe, C., Tzatzarakis, M.N. and Tsatsakis, A.M. (2016) Feasibility of hair sampling to assess levels of organophosphate metabolites in rural areas of Sri Lanka. Environ. Res. 147, 207–211.

Received: **05.08.2019**
Accepted: **20.11.2019**

CORRESPONDING AUTHOR

Nebile Daglioglu
Department of Forensic Medicine and Toxicology,
Faculty of Medicine
University of Cukurova,
Adana – Turkey

e-mail: nebiled@hotmail.com

© by PSP Volume 29 – No. 04A/2020 pages 2809-2817 Fresenius Environmental Bulletin

DETERMINATION OF NUT PROPERTIES AND CHEMICAL COMPOSITIONS OF WALNUT (*JUGLANS REGIA* L.) GENOTYPES GROWN IN WALNUT-FRUIT FORESTS OF KYRGYZSTAN

Umran Erturk[1,*], Ali Osman Solak[2], Sevil Yucel[3], Kaliypa Saliyeva[2], Zeki Severoglu[4], Ibrahim Ilker Ozyigit[4,5], Bakit Borkoyev[2]

[1]University of Bursa Uludag, Faculty of Agriculture, Department of Horticulture, Bursa, Turkey
[2]Kyrgyz-Turkish Manas University, Faculty of Engineering, Department of Chemical Engineering, Bishkek, Kyrgyzstan
[3]Yıldız Technical University, Faculty of Chemical and Metallurgical Engineering, Department of Bioengineering, Istanbul, Turkey
[4]Marmara University, Faculty of Science and Arts, Department of Biology, Goztepe, Istanbul, Turkey
[5]Kyrgyz-Turkish Manas University, Faculty of Science, Department of Biology, Bishkek, Kyrgyzstan

ABSTRACT

In this study, sixteen genotypes selected from walnut-fruit forests in the Osh and Jalal-Abad regions of Kyrgyzstan evaluated for nut properties and chemical composition. The nut traits such as nut dimension, nut and kernel weight, kernel ratio, and shell thickness were investigated. The ash, protein, oil, carbohydrate content and fatty acid composition of genotypes were also evaluated. The ranges of average nut characteristics determined for the selected genotypes were: 27.4-32.1 mm nut length; 23.8-28.6 mm nut width; 24.1-29.0 mm nut suture; 7.15-13.17 g nut weight; 3.26-5.65 g kernel weight; 35.02-46.15% kernel percentage and 1.13-2.23 mm shell thickness. The oil content of the genotypes ranged from 55.47 to 65.26%, the protein content ranged from 16.59 to 19.97%, and the carbohydrate content was between 14.02% and 22.85%. The ash content ranged from 1.67 to 2.23%, and the moisture content of the kernels was between 2.06 and 2.58%. The oleic acid content of the oils ranged from 18.62 to 32.19%. The linoleic acid content ranged from 46.13 to 62.25%, while linolenic acid content ranged from 6.67 to 13.05%. The palmitic acid content was between 4.98 and 7.67%. Sary-Chelek 1, Arslanbap 3, Arslanbap 4 and Kara-Alma 3 genotypes were identified as the promising genotypes according to nut characteristics and chemical composition.

KEYWORDS:
Fatty acids, Nut traits, Kyrgyzstan, Walnut

INTRODUCTION

Kyrgyzstan has the world's largest natural walnut-fruit forests with extremely valuable reserve of rich genetic diversity. The forests cover an area of 230,000 ha, of which 40,500 ha are stands with walnut trees [1]. The large tracts of walnut forests are situated in two main areas in Kyrgyzstan stretching from east to west; at Arslanbap-Kurgat and Khozha-Aty, on the slopes of the Fergana and Chatkal mountain ranges, respectively [2]. The walnut-fruit forests in both mountain ranges occur between 800 and 2100 m a.s.l., although 82% of walnut stands are located between 1400 and 1750 m a.s.l. [3]. The appropriate genotypes selecting from the rich genetic resources are so important both protecting genetic variability and revealing standard varieties. The genotypes in this population differ from in point of leafing time, fruit bearing habit, fruit size, shape, shell thickness and kernel ratios [1, 4-8]. The studies started on the Kyrgyzstan walnut-fruit forest in 1927s. The first selection study of walnut carried out in 1930s. The yield and high-quality traits were used as selection criteria for the natural seed population in the studies. 280 types were selected and described between the years of 1958 and 1995. The special attention was paid to the early bearing habit at the time of the selection. Twenty genotypes were selected for early bearing properties. Three of them were found promising for fruit dimension (Bomb), shell thickness (Paper), nut number on shoots (Clustering). Whereas the yield and fruit quality have been taken into consideration as the main selection criteria in the breeding studies in Kyrgyzstan until now, some studies have been done about the frost resistance determination and short vegetation period in recent years. Selection studies were carried out by obtaining information from the local people between the years of 1999-2005. In these studies, traits such as late leafing, frost resistance, regular crop and resistance to diseases beside fruit quality were considered and 21 genotypes were selected [9]. The late leafing, lateral fruitfulness, nut and kernel quality, early maturity and resistance against blight are important breeding goals for walnut [10], In recent years, the chemical contents and especially fatty acid compo-

sition have become important two criteria to be considered in the walnut selection studies [11, 12]. The oil ratio of walnut (*Juglans regia* L.) is generally about 60% [13], and this ratio is to be varied between 52% and 70%. Walnut fatty acids contain considerable amount of unsaturated fatty acids. Polyunsaturated fatty acids (PUFA) are the essential fatty acids [14]. Whereas saturated fatty acids constitute about 10% of the total fatty acids, unsaturated fatty acids constitute 90%.When walnut compares with hazelnut, peanut and other nuts containing monounsaturated fats (MUFA), walnut contains higher polyunsaturated fatty acids (PUFA). Recent studies show that, walnut oil contains significant amounts of protein (12-24%), carbohydrate (12-18%), fiber (% 1.5-2) and minerals (1,7-2%) [14-19]. Furthermore, walnut contains high amounts of potassium (390-700 mg/100 g), phosphorus (310-510 mg/100 g) and magnesium (90-140 mg/100 g) and low amounts of sodium (1-15 mg/100 g) [15, 16, 19]. The chemical content of walnut is to change according to the cultivation area and its location, variety and genotype [17, 19-21]. Ozyigit et al. [22] reported that walnut genotypes from different region of Kyrgyzstan contained 311-397 mg K/100 g, 158-220 mg Mg/100 g and 138-152 mg Ca/100 g and 0.9-1.7 mg Na /100 g. Until now, there have been a few studies related to the physical and chemical properties of Kyrgyzstan walnut fruits. The aim of this study is to select high-quality genotypes from walnut-fruit forests of Kyrgyzstan and identify their nut traits and nutritional compositions.

MATERIALS AND METHODS

Experimental Sites and Walnut Samples. This study was conducted in the regions of Jalal-Abad (Sary-Chelek, Arslanbap and Kara-Alma) and Osh (Kara-Shoro) in Kyrgyzstan. Kyrgyzstan's climate is influenced by its position between the temperate and sub-tropical zones, its high elevation and its distance from oceans. Jalal-Abad and Osh region are in the southwestern Fergana Valley which is dry-subtropical and hot in summer; in these areas air temperatures can reach 35-40°C during the summer months [23]. The average air moisture content varies from 48% to 58%. The lowest levels are in August (43%-49%); the highest levels are in March (61-69%). The mean precipitation ranges from 938 mm to 1032 mm in the mid-belt of the southwestern slopes of the Fergana and Chatkal ranges. The predominant soil type on the territories of the leshozes Jalal-Abad and Osh regions is black-brown mountain forest soil [24]. Sixteen germplasm (*J. regia*) known seedlings origin and grown naturally were collected from walnut-fruit forest in two main (Jalal-Abad and Osh) regions. The evaluated genotypes and their locations and altitudes were given in Table 1 and Figure 1.

The walnut kernel samples were collected from the four different zones of walnut forests in Kyrgyzstan, namely Sary-Chelek, Arslanbap, and Kara-Alma in Jalal-Abad Region and Kara-Shoro in Osh region (Figure 1). In each zones, four different locations were selected and numbered as Sary-Chelek 1 (Keçkil 3) 1618 m, Sary-Chelek 2 (Keçkil 5) 1625 m, Sary-Chelek 3 (Keçkil 6) 1635 m, and Sary-Chelek 4 (Keçkil 10) 1625 m for Sary-Chelek zone, Arslanbap 1 (Kokoy, Gumhana 2) 1430 m, Arslanbap 2 (İyri-Arık) 1436 m, Arslanbap 3 (Akcol) 1558 m and Arslanbap 4 (Kokoy, Gumhana 1) 1420 m for Arslanbap zone, Kara-Alma 1 (Dogah) 1517 m, Kara-Alma 2 (Orozak) 1550 m, Kara-Alma 3 (Oytal) 1593 m and Kara-Alma 4 (Tukan) 1564 m for Kara-Alma zone, and Kara-Shoro 1 (Taşkepe) 1634 m, Kara-Shoro 2 (Sayaçık) 1581 m, Kara-Shoro 3 (Özü Keldi) 1513 m and Kara-Shoro 4 (Ara-Köl) 1445 m for Kara-Shoro zone [22].

Nut Traits. Nuts were analyzed for nut length, width, and suture (mm), weight (g), kernel weight (g), kernel percentage (%) and shell thickness (mm).

FIGURE 1
Four different walnut forest zones that plant samples were collected in Kyrgyzstan, namely Sary-Chelek, Arslanbap, and Kara-Alma zones from Jalal-Abad Region and Kara-Shoro zone from Osh Region.

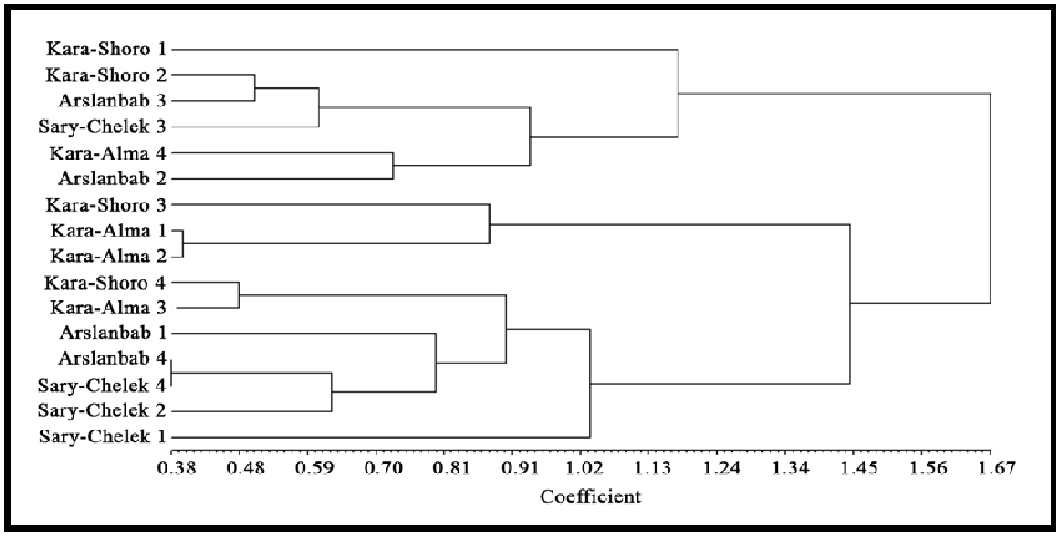

FIGURE 2
Cluster analysis of sixteen selected genotypes based on nut traits with high heritability.

TABLE 1
Evaluated genotypes and their location altitudes in Jalal- Abad and Osh regions.

JALAL-ABAD region						OSH region	
Sary-Chelek		Kara-Alma		Arslanbap		Kara- Shoro	
Sary-Chelek 1		Kara-Alma 1		Arslanbap 1		Kara-Shoro1	
Keçkil 3	1618m	Dogah	1517m	Kokoy, Gumhana 2	1430m	Taşkepe	1634m
Sary-Chelek 2		Kara-Alma 2		Arslanbap 2		Kara-Shoro 2	
Keçkil 5	1625m	Orozak	1550m	İyri-Arık	1436m	Sayaçık	1581m
Sary-Chelek 3		Kara-Alma 3		Arslanbap 3		Kara-Shoro 3	
Keçkil 6	1635m	Oytal	1593m	Akcol	1558m	Özü-Keldi	1513m
Sary-Chelek 4		Kara-Alma 4		Arslanbap 4		Kara-Shoro 4	
Keçkil 10	1625m	Tukan	1564m	Kokoy, Gumhana 1	1420m	Ara-Köl	1445m

Biochemical Analyses. Moisture, protein, ash and oil contents and fatty acid compositions were analyzed for all nuts of genotypes taken from the Jalal-abad and Osh regions. The moisture was determined by drying the samples in a hot-air oven at 105°C overnight. The chemical characteristics such as ash, protein [25], oil (Soxhlet) [26], fatty acid composition [27] were also determined. The carbohydrate content was calculated as the difference based on the moisture, protein, oil and ash percentages by using the following formula: Carbohydrate content (%) = 100% - [moisture (%) + protein (%) + oil (%) + ash (%)], which described by Grosso et al. [28]. Fatty acid composition was determined by gas chromatography (GC; VARIAN chromatograph, model 1400; Varian Associates, Walnut Creek, CA), equipped with a flame ionization detector and a 3.0 m × 0.32 cm steel column, packed with LAC-3R-728 (20%; Cambridge Ind. Co., Cambridge, UK) on Chromosorb W/AW(80-100 mesh; Merck, Darmstadt, Germany). Nitrogen was used as a carrier gas (flow rate, 24 mL/min) (ISO 5508:1990, Analysis by gas chromatography of methyl esters of fatty acids).

Data Analysis. Data collected from a sample of 50 randomly selected nuts per tree, and are reported as the average with standard deviations, minimum and maximum values of characteristics studied over the 3 years from 2014 to 2017. The cluster analysis of the genotypes was performed based on the quantitative characters (nut weight, nut length, nut width, nut suture, kernel weight, shell thickness) with coefficients of heritability more than 0.80 [29] by using the unweighted pair-group method arithmetic average (UPGMA).

RESULTS AND DISCUSSION

Physical characteristics of fruits are to represent a quality feature of nuts. Table 2 presents the average values of nut and kernel characteristics of the studied genotypes. The maximum nut length of 32.1 mm for Sary-Chelek 4 the minimum (27.4 mm) was recorded for the Arslanbap 2. The maximum nut width was determined 28.6 mm for the Sary-Chelek 2, whereas the minimum nut width was found 23.8 mm for Kara-Shoro 1. Nut suture was changed between 24.1 mm (Kara-Shoro 1) and 29.0 mm (Sary-Chelek 2). The average nut weight

of the selected genotypes varied from 7.15 g (Kara-Alma 2) to 13.17 g (Arslanbap 2). Kernel weight varied from 3.26 g (Kara-Alma 2) to 5.65 g (Sary Chelek 1). Kernel percentage ranged from 35.02% (Kara-Shoro 2) to 46.15% (Arslanbap 4). The shell thickness of genotypes varied between 1.13 mm (Kara-Alma 3) and 2.23 mm (Arslanbap 4). Hemery [2] reported that nut weight varied between 6.94 g and 8.99 g, nut width between 26.0 mm and 29.7 mm and length between 29.4 mm and 35.1 mm in collected walnut genotypes from Kyrgyzstan. According to McGranahan and Leslie [30], Kyrgyz walnuts are to vary in respect to the fruit size and shell thickness considerably. The promising walnut types should have the shell thickness of between 0.70 and 1.50 mm [31]. Nenjuhin [32] suggested the optimum shell thickness of 0.92 mm. In comparison to Turkish genotypes, the fruit characteristics of genotypes were found lower. According to some promising walnut genotypes in Turkey, the nut diameter was found between 22.30-32.26 mm, nut weight varied between 7.82-18.74 g, kernel weight varied between 4.04-9.00 g, kernel percentage varied between 42.88% and 67.14% [11, 33-35]. Cosmulescu and Botu [36] found that nut weight was between 6.8-18.4 g, in kernel weight between 1.7-8.79 g, in kernel percentage between 23.6-71.7% in genotypes from the Oltenia region. Variation for nut length, nut width, nut weight, kernel weight, kernel ratio, and shell thickness of selected genotypes from different sites in central Iran have been reported by Arzani et al. [37] in the range of 27.3-43.8, 22.1-38.4, 6.0-15.2 g, 2.6-9.1 g, 38.4-79.6%, and 0.4-1.4 mm, respectively. In genotypes and varieties evaluated in terms of nut characteristics would be nut width at least 29.7 mm, fruit weight 11-14 g, kernel weight 5-7 g, kernel ratio 48-50%, fat content at least 65%, and protein content greater than 16% [38-43]. In our study, while some genotypes have desirable nut characteristics, some of them gave lower values, which can be attributed to the natural forest walnut-fruit characteristics. It is well known that nut and kernel quality are strongly affected by genotype, environmental conditions and their mutual interaction [43].

Cluster analysis for the six features of the sixteen selected genotypes (length, width, suture of nut, nut weight, kernel weight, and shell thickness) with high heritability coefficients was used to calculate the relationships between the selected genotypes in a dendrogram (Figure 2). Based on this technique, genotypes were classified into two different cluster groups. Whereas ten of the 16 genotypes were included in a single cluster group Kara-Shoro 1, Kara Shoro 2, Arslanbap 3, Sary-Chelek 3 Kara-Alma 4 and Arslanbap 2 were located in a second cluster group. According to the explanations above, a close relationship exists among the genotypes except the latter cluster group genotypes based on the characteristics with high heritability coefficients. No significant relationship was detected between the morphological diversity and the geographical location in the cluster analysis of the selected genotypes. Arzani et al. [37] detected three cluster groups for 58 genotypes selected from six walnut-growing sites in Iran, but no significant relationship was found between morphological diversity and the geographical location. Also they stated that the lack of extreme diversity among the genotypes may be because of geographical barriers to gene flow, which led to unique walnut populations.

TABLE 2
Comparison of some nut traits of sixteen genotypes from two regions in Kyrgyzstan.

	Genotypes	Nut length (mm)	Nut width (mm)	Nut suture (mm)	Nut weight (g)	Kernel weight (g)	Kernel percentage (%)	Shell thickness (mm)
OSH	Kara-Shoro 1	27.5±0.1	23.8±0.2	24.1±0.2	9.88±5.39	3.97±2.15	40.25±1.90	1.91±0.08
	Kara-Shoro 2	29.9±0.1	26.1±0.1	25.9±0.1	11.45±5.79	3.94±1.75	35.02±5.44	1.92±0.15
	Kara-Shoro 3	29.7±0.1	25.7±0.1	25.9±0.1	8.35±2.43	3.29±1.32	42.43±4.15	2.15±0.55
	Kara-Shoro 4	30.0±0.3	26.6±0.3	27.5±0.2	10.65±3.76	4.02±1.14	38.37±3.29	1.97±0.12
JALAL-ABAD	Kara-Alma 1	29.1±0.3	27.7±0.2	27.3±0.2	7.68±0.91	3.28±0.64	42.33±3.71	1.75±0.31
	Kara-Alma 2	28.9±0.4	26.9±0.2	27.1±0.1	7.15±1.82	3.26±1.04	46.06±9.91	1.14±0.23
	Kara-Alma 3	29.3±0.4	26.6±0.3	27.2±0.3	10.24±2.14	4.66±1.26	45.10±2.66	1.13±0.15
	Kara-Alma 4	28.0±0.2	25.2±0.2	24.6±0.2	10.67±2.65	5.22±1.55	40.99±4.47	1.54±0.07
	Arslanbap 1	31.9±0.4	27.3±0.2	27.1±0.1	9.15±2.81	4.06±1.83	43.15±5.93	1.55±0.14
	Arslanbap 2	27.4±0.5	24.6±0.4	25.0±0.4	13.17±7.62	5.36±3.39	39.97±3.72	1.65±0.39
	Arslanbap 3	30.0±0.3	25.9±0.2	25.3±0.2	12.05±3.17	5.40±1.28	45.06±1.88	1.84±0.49
	Arslanbap 4	31.3±0.4	27.8±0.3	27.3±0.2	10.60±4.09	4.81±1.73	46.15±6.25	2.23±0.15
	Sary-Chelek 1	31.5±0.2	27.5±0.3	28.0±0.3	12.92±7.01	5.65±3.07	43.77±6.19	2.14±0.03
	Sary-Chelek 2	31.5±0.2	28.6±0.2	29.0±0.3	11.21±4.03	4.58±1.61	41.07±4.69	1.87±0.11
	Sary-Chelek 3	28.5±0.2	25.3±0.1	25.2±0.2	11.91±6.24	4.40±2.41	37.27±6.99	1.95±0.22
	Sary-Chelek 4	32.1±0.2	27.7±0.1	27.5±0.2	11.02±2.85	4.29±0.81	39.42±4.54	2.02±0.16

Note: Mean values and standard deviations are measured for at least five experiments.

TABLE 3
Proximate chemical composition of the walnut genotypes.

	Genotypes	Moisture (%)	Oil (%)	Protein (%)	Ash (%)	Carbohydrate (%)
OSH	Kara-Shoro 1	2.19±1.28	61.45±1.41	18.94±0.13	2.03±0.32	15.39± 0.79
	Kara-Shoro 2	2.38±0.91	58.39±1.74	19.97±3.80	1.67±0.13	17.59±1.65
	Kara-Shoro 3	2.40±1.28	58.26±1.39	19.14±0.32	1.73±0.21	18.47±0.80
	Kara-Shoro 4	2.18±1.39	55.47±2.56	17.73±1.71	1.77±0.08	22.85±1.44
JALAL-ABAD	Kara-Alma 1	2.06±0.79	60.92±3.62	18.71±1.37	1.97±0.21	16.34±1.50
	Kara-Alma 2	2.17±0.68	62.50±0.97	19.12±0.80	1.99±0.39	14.22±0.71
	Kara-Alma 3	2.41±1.14	61.25±1.10	19.82±0.23	2.21±0.18	14.31±0.66
	Kara-Alma 4	2.23±0.79	58.65±3.68	19.04±1.98	1.91±0.38	18.17±1.71
	Arslanbap 1	2.58±1.14	62.09±1.00	19.08±0.66	2.23±0.47	14.02±0.82
	Arslanbap 2	2.12±0.90	62.55±1.30	18.55±1.24	1.93±0.44	14.85±0.97
	Arslanbap 3	2.71±1.22	63.08±1.30	16.83±2.49	2.03±0.18	15.35±1.30
	Arslanbap 4	2.58±1.21	59.86±3.14	18.90±0.29	2.13±0.21	16.53±1.21
	Sary-Chelek 1	2.09±1.42	65.07±1.32	16.59±2.02	2.16±0.42	14.09±1.30
	Sary-Chelek 2	2.33±1.06	61.37±3.57	18.66±1.52	2.07±0.43	15.57±1.65
	Sary-Chelek 3	2.35±1.30	65.26±2.00	17.70±1.82	1.93±0.20	12.76±1.33
	Sary-Chelek 4	2.38±1.03	56.72±1.73	19.61±0.52	2.23±0.43	19.06±0.93

Note: Mean values and standard deviations are measured for at least five experiments.

TABLE 4
Comparison of the chemical composition of the walnut genotypes of Kyrgyzstan and other countries.

Genotypes	Moisture (%)	Oil (%)	Protein (%)	Ash (%)	Carbohydrate (%)
Kyrgyzstan (present study)	2.06-2.58	55.47-65.26	16.59-19.97	1.67-2.23	12.76-22.85
Turkey 1 [44]	1.91-4.48	61.32-69.35	10.58-18.19	1.53-1.99	9.05-18.92
Turkey 2 [45]	1.98-3.54	44.08-70.81	13.75-19.69	1.53-2.15	-
Pakistan [46]	2.76-4.20	63.54-69.92	15.96-19.15	1.27-1.95	8.04-12.14
Morocco [47]	-	57-70	12.38-15.03	-	-
Iran [53]	-	56.53-67.30	12.25-20.45	2.34-3.75	-

TABLE 5
Fatty acid composition of the sixteen genotypes selected from different regions (%).

Genotypes	$C_{16:0}$	$C_{18:0}$	$C_{18:1}$	$C_{18:2}$	$C_{18:3}$	$C_{20:1}$	$C_{20:5}$	$C_{24:1}$	SFA	PUFA/ MUFA
Kara-Shoro 1	5.45±0.01	3.34±0.06	20.80±0.09	60.18±0.08	8.72±0.01	0.17±0.00	0.39±0.08	0.42±0.01	8.79±0.07	3.31
Kara-Shoro 2	5.18±0.11	2.72±0.06	20.24±2.06	59.82±2.58	11.19±0.19	0.17±0.01	0.20±0.11	0.09±0.04	7.90±0.19	3.50
Kara-Shoro 3	5.85±0.53	3.15±0.28	20.36±1.43	58.69±0.67	11.05±0.21	0.14±0.01	0.21±0.09	0.15±0.01	9.00±0.81	3.42
Kara-Shoro 4	5.98±0.64	3.09±0.11	19.84±3.99	57.01±2.76	12.66±2.45	0.18±0.01	0.52±0.41	0.18±0.13	9.07±0.75	3.51
Kara-Alma 1	5.65±0.11	2.81±0.28	25.70±0.81	54.47±0.24	10.76±0.85	0.19±0.00	0,05±0.01	0.05±0.00	8.46±0.39	2.57
Kara-Alma 2	6.09±0.01	2.62±0.04	24.07±2.91	56.60±1.94	10.01±0.95	0.18±0.01	0,06±0.03	0.05±0.02	8.71±0.05	2.76
Kara-Alma 3	5.89±0.35	2.62±0.06	18.90±1.13	62.25±0.49	9.38±0.06	0.18±0.00	0.23±0.09	0.18±0.13	8.55±0.41	3.78
Kara-Alma 4	4.98±0.28	3.57±0.39	21.27±1.99	56.37±1.17	13.05±0.06	0.16±0.00	0.18±0.15	0.06±0.04	8.55±0.67	3.26
Arslanbap 1	7.67±2.75	3.74±1.07	32.19±5.90	46.13±8.68	6.67±0.72	0.22±0.06	1.17±1.28	1.06±1.32	11.41± 3.82	1.64
Arslanbap 2	5.11±0.33	2.68±0.28	24.81±1.65	57.66±1.10	8.84±0.72	0.19±0.00	0.20±0.08	0.11±0.01	7.79±0.61	2.67
Arslanbap 3	5.26±0.01	2.67±0.13	28.31±0.06	53.69±0.28	9.06±0.41	0,20±0.01	0.22±0.11	0.15±0.06	7.93±0.14	2.21
Arslanbap 4	5.68±0.17	2.83±0.41	27.64±1.21	52.65±1.91	9.93±0.07	0.19±0.01	0.42±0.10	0.22±0.07	8.51±0.58	2.26
Sary-Chelek 1	6.06±0.20	2.78±0.36	20.64±2.59	58.43±2.47	11.08±0.07	0,18±0,01	0.24±0.07	0.14±0.11	8.84±0.56	3.36
Sary-Chelek 2	5.58±0.09	2.86±0.26	19.17±1.22	59.06±0.44	12.70±0.42	0.16±0,01	0.07±0.01	0.05±0.01	8.44±0.35	3.73
Sary-Chelek 3	5.65±0.17	3.25±0.18	18.62±1.02	60.79±0.31	10.89±0.91	0.16±0.01	0.14±0.04	0.06±0.03	8.90±0.35	3.84
Sary-Chelek 4	6.76±0.25	3.03±0.35	19.67±1.33	58.86±1.21	10.33±0.01	0.19±0.01	0.47±0.04	0.18±0.15	9.79±0.60	3.51

Note: Mean values and standard deviations are measured for at least three experiments.

TABLE 6
Fatty acid levels of walnuts grown in some countries.

Genotypes	$C_{16:0}$	$C_{18:0}$	$C_{18:1}$	$C_{18:2}$	$C_{18:3}$
Kyrgyzstan (present study)	4.18-7.67	3.62-4.74	18.62-32.19	46.13-62.25	8.72-13.05
Turkey 1 [44]	5.21-7.67	2.36-4.25	17.90-33.35	47.26-60.20	10.10-13.12
Turkey 2 [18]	5.24-7.62	2.56-3.67	21.18-40.20	43.94-60.12	6.91-11.52
United States [48]	7.40-8.70	1.90-2.60	15.10-20.10	57.80-61.80	11.20-13.50
Portugal [14]	6.32-7.48	2.22-2.77	14.26-17.45	57.46-62.50	9.64-12.98

The contents of moisture, protein, oil, ash, and carbohydrate belong to genotypes are given in Table 3. As it was expected, the kernels of walnut genotypes had the low values in terms of moisture content (ranging from 2.06 % for Kara-Alma 1 to 2.58% for Arslanbap 1 and Arslanbap 4). Oil content was determined between 55.47 % (Kara-Shoro 4) and % 65.26 (Sary-Chelek 3). Protein content was found to be in the range of 16.59 % (Sary-Chelek 1) to 19.97 % (Kara-Shoro 2). Ash content ranged from 1.67 % (Kara-Shoro 2) to 2.23% (Arslanbap 1 and Sary-Chelek 4). Carbohydrate content was found in the range of 12.76 % (Sary-Chelek 3) to 22.85 (Kara-Shoro 4).

In general, these findings were compatible with the previously published values for the genotypes all over the world. For example, Yerlikaya et al. [44] have reported that 11 walnut genotypes from Turkey contained 61.32-69.35% oil, 10.58-18.19% protein, 9.05-18.92% carbohydrate and 1.53-1.99% ash. Keles et al. [45] have also reported protein content as 13.75-19.69%, the oil content as 44.08-70.81% and ash content as 1.53-2.15% in walnut genotypes taken from Inner Anatolia in Turkey. Ali et al. [46] were determined the chemical composition of five walnut genotypes from Pakistan as follows: oil, 63.54-69.92%; carbohydrate, 8.04-12.14%; protein 15.96-19.15%; and ash, 1.27-1.95%. Kodad et al. [47] were evaluated the chemical composition of 14 walnut genotypes in the High Atlas Mountains. The total oil and the protein contents were found, ranged from 57 to 70 % and 12.38 to 15.03 %, respectively. Comparison of the chemical composition of the walnut genotypes of Kyrgyzstan and other countries are given in Table 4.

Mean values and standard deviations of the fatty acid composition were presented in Table 5. The major fatty acids in the genotypes were linoleic (C18:2), followed by oleic (C18:1), α-linolenic (C18:3), palmitic (C16:0) and stearic acid (C18:0). Minor fatty acids were found as gondoic C20:1 eicosapentanoic, C:20:5, nervonic acid C24:1. Generally less than 1% of the acid values are not included in the Table 6. Linoleic acid had the most abundant fatty acid in all the analyzed genotypes comprising the values ranging from 46.13% in Arslanbap 1 to 62.25% in Kara-Alma 3. Oleic acid, the second in order of importance, ranged from 18.62% (Sary-Chelek 3) to 32.19% (Arslanbap 1), followed by linolenic acid, from 6.67% (Arslanbap 1) to 13.05% (Kara-Alma 4). Only palmitic (4.98.-7.67%) and stearic acid (2.62-3.74%) from the remained fatty acids were in existence in considerable amounts. These results agree with the fatty acid composition observed other walnut genotypes [17, 44, 47-50]. PUFA were the main group of fatty acids in walnut oil extracted from genotypes, with values ranging from 52.80 to 71.68%. The values for the MUFA group ranged from 18.62 to 32.19% SFA is a minor constituent, with values ranging from 7.79 to 11.87%. These data were in general agreement with those of earlier reports [14, 44, 49, 51]. The PUFA/MUFA ratio varied from 1.64 to 3.84. Yerlikaya et al. [44] reported that the PUFA/MUFA ratio changed from 1.54 to 3.97 in the walnut genotypes. Table 5 shows minimum and maximum levels of walnut major fatty acids grown in some countries. Sixteen selected genotypes from the different region of Kyrgyzstan contained the various amounts of oleic acid, linoleic acid, palmitic acid, and linolenic acid. When compared to the levels of fatty acid in other countries is similar to that of Kyrgyzstan walnut fatty acids (Table 6).Walnut oil composition is affected by variety, geographical location, and climatic effects. Martinez et al. [52] were indicated that both the genotypes and the crop year affect the chemical composition of the walnut oil. Different crop years significantly influence the fatty acid composition and related parameters such as PUFA/MUFA.

CONCLUSIONS

Kyrgyzstan has the biggest natural walnut fruit forest in the world. This natural walnut genetic resource, formed by seed propagation over a long period, is considered a rich natural pool of walnut germplasm for developing improved genotypes. The present research was conducted to determine some nut properties, chemical compositions of selected sixteen genotypes from two important natural walnut growing areas (Osh and Jalal-Abad) in Kyrgyzstan. The data indicate that genotypes have highly variable studied traits. However, Sary-Chelek 1, Arslanbap 3 Arslanbap 4, Kara-Alma 3 genotypes were superior to other genotypes in term of the nut dimension, nut weight, kernel percentage, protein, oil and fatty acid contents. When the results are evaluated according to the regions, it is clearly seen that the genotypes selected from Jalal-Abad region have partially superior properties. Within this region, Arslanbap and Sary-Chelek sites are

more prominent. The findings will be useful for the future collection and genetic resource management in this region. The results of our study show that four genotypes are to promise with regard to nut traits. The nut characteristics as well as the tree characteristics such as leafing date, the fruit bearing habit must be taken into consideration in the following studies.

ACKNOWLEDGEMENTS

This work was supported by Kyrgyz-Turkish Manas University, Project number BAP-2015 FEB-04.

REFERENCES

[1] Musuraliev, T.M. (1998). The current condition of walnut-fruit forests of the Kyrgyz Republic. In: Blaser, J. Carter, J., Gilmour, D.A., Venglovsky, B., Yunossova, I. (eds). Biodiversity and Sustainable Use of Kyrgyzstan´s Walnut-fruit Forests. Proceedings of the Seminar Arslanbob, Dzalalabad Oblast, Kyrgyzstan, 3-18.

[2] Hemery, G. (2000). Juglans regia L: genetic variation and provenance performance. Ph.D thesis. University of Oxford.

[3] Kolov, O. (1998). Ecological characteristics of the walnut-fruit forests in Kyrgyzstan. In: Blaser, J. Carter, J., Gilmour, D.A., Venglovsky, B., Yunossova, I. (eds). Biodiversity and sustainable use of Kyrgyzstan's walnut-fruit forests, 59-61

[4] Shevchenko, V. S. (1976). Diversiform and selection of walnut in Southern Kirgizia. Published in Frunze, 8-68.

[5] Shepotjeva, F.L. (1976). Program, methods of selection and studying of grades of walnut fruit cultures. Published in Voronezh.

[6] Chebanov, V.I., Blashnikov, G.T. (1980). Methods of selection and vegetative reproduction of walnut. Published in Voronezh.

[7] Kaimov, A.K., Aleksandrovsky, E.S. (2002). Revealing and estimation the specific and intraspecific biodiversity of forest species. Published in Tashkent.

[8] Beer, R., Kaiser, F., Schmidt, K., Ammann, B., Carraro, G., Grisa, E., Tinne, W. (2008). Vegetation history of the walnut forests in Kyrgyzstan (Central Asia): natural or anthropogenic origin. Quaternary Science Reviews. 27, 621–632.

[9] Mamadjanov, D.K. (2006). Walnut fruit forests and diversity of walnut tree (*Juglans regia* L.) in Kyrgyzstan. Acta Hortic. 705, 173-176.

[10] Khadivi-Khub, A., Ebrahimi, A., Mohammadi, A., Kari, A. (2015). Characterization and selection of walnut (*Juglans regia* L.) genotypes from seedling origin trees. Tree Genetic and Genomes. 11, 54.

[11] Akca, Y. (2005). Study selection of superior walnut types in Iskilip walnut population. Bahce. 34(1), 41-48.

[12] Koyuncu, M.A., Koyuncu, F., Yildirim, F.A., Dilmacunal, T., Vural, E. (2005). Determination of lateral fruitfulness and fruit characteristics of natural walnut (*Juglans regia* L.) genotypes of Gelincik (Isparta). Bahce. 34(1), 73-82.

[13] Prasad, R.B.N. (1994). Walnuts and pecans. In: Encyclopedia of Food Science, Food Technol Nutr. London: Academic Press, 4828-4831.

[14] Amaral, J.S., Casal, S., Pereira, J.A., Seabra, R.M., Oliveira, B.P.P. (2003). Determination of sterol and fatty acid compositions oxidative stability, and nutritional value of six walnuts (*Juglans regia* L.) cultivars grown in Portugal. J Agric Food Chem. 51(26), 7698-7702.

[15] Lavedrine, F., Ravel, A., Villet, A., Ducros, V., Alary, J. (2000). Mineral composition of two walnut cultivars originating in France and California. Food Chem. 68, 347-351.

[16] Savage, G.P. (2001). Chemical composition of walnuts (*Juglans regia* L.) grown in New Zealand. Plant Food Hum Nutr. 56 (1), 75-82.

[17] Caglarirmak, N. (2003). Biochemical and physical properties of some walnut genotypes (*Juglans regia* L.). Nahrung. 47(1), 28-32.

[18] Ozkan, G., Koyuncu, M.A. (2005). Physical and chemical composition of some walnut (*Juglans regia* L) genotypes grown in Turkey. Grasas Aceites. 56(2), 141-146.

[19] Akca, Y., Sutyemez, M., Ozgen, M., Tuzen, M., Mendil, D. (2005). Determination of chemical properties of walnut (*Juglans regia* L.) cultivars grown in Turkey. Asian J Chem. 17(1), 548-552.

[20] Greve, L.C., McGranahan, G., Hasey, J., Snyder, R., Kelly, K., Goldhamer, D., (1992). Variation in polyunsaturated fatty acid composition of Persian walnut. J Amer Society Hortic Sci. 117(3), 518-522.

[21] Garcia, J.M., Agar, I.T., Streif, J. (1994). Lipid characterization in kernels from different walnut cultivars. Turk J Agricul Forestry. 18(3), 195-198.

[22] Ozyigit, I.I., Uras, M.E., Yalcin, I.E., Severoglu, Z., Demir, G., Borkoev, B., Salieva, K, Yucel, S., Erturk, U., Solak, A.O. (2018). Heavy metal levels and mineral nutrient status of natural walnut (*Juglans regia* L.) populations in Kyrgyzstan: Nutritional values of kernels. Biol Trace Elem Res. 189(1):277-290.

[23] Mamitov, A.M. (1965). Classification, vertical belts and provinces of Kyrgyz soils. In: Kovda, V.A, Lobova, E.V. (eds) Geography and classification of Asian soils. Nauka, Moscow, 50-51.
[24] Akimaliev, D.A., Zaurov, D.E., Eisenman, S.W. (2013). The geography, climate and vegetation of Kyrgyzstan. In: Eisenman S.W, Zauroz, D.E, Struwe, L. (eds). In Medicinal Plants of Central Asia: Uzbekistan and Kyrgyzstan. Springer, New York. 1-3.
[25] AOAC. (1990). Association of Official Agricultural Chemists. Official Methods of Analysis. 15th ed. The American Chemists Society. Champaign. Illinois, USA.
[26] Paquat, C., Houtfenne, A. (1987). IUPAC, Standard methods for the analysis of oils, fats and derivatives. 7th ed. Oxford: Blackwell Scientific Publications.
[27] AOCS. (1992-1993). Association of Official Agricultural Chemists. Official Method Ce 2-66. The American Chemists Society. Champaign. Illinois, USA.
[28] Grosso, N.R., Nepote, V., Guzman, C.A. (2000). Chemical composition of some wild peanut species (*Arachis* L.) seeds. J Agricul. Food Chem. 48(3), 806-809.
[29] Hansche, P.E., Beres, V., Forde, H.I. (1972). Estimates of quantitative genetic properties of walnut and their implications for cultivar improvement. J Amer Society Hortic Sci. 97, 279-285.
[30] McGranahan, G., Leslie, C. (1991). Walnuts (*Juglans* L.). In Genetic Resources of Temperate Fruit and Nut Crops. In: Moore, J. N. and Ballington, J. R. (eds.). Int Society Hortic Sci, Wageningen. 907-51.
[31] Akca, Y., Ozongun, S. (2004). Selection of late leafing, late flowering, laterally fruitful walnut *(Juglans regia)* types in Turkey. New Zeal J Crop Hort. 32, 337-342.
[32] Nenjuhin, V.N. (1971). Selection of plus trees of the walnut in Ukraine. Plant Breeding Abstracts. 41, 187.
[33] Akcay, M.E., Tosun, I. (2005). Walnut selection in III. Sub-region (Gemlik, Orhangazi, Iznik and Mudanya) of Bursa province. Bahce. 34(1), 57-62.
[34] Unver, H. (2005). Studies on varietal selection in walnut (*Juglans regia* L.) populations of Ankara province. MS Thesis. Ankara Uni. Graduate Sch. Natural. Appl. Sci. Dept. Hortic.
[35] Aslantas, R. (2006). Identification of superior walnut (*Juglans regia*) genotypes in Northeastern Anatolia, Turkey. New Zeal J Crop Hort. 34, 231-237.
[36] Cosmulescu, S., Botu, M. (2012). Walnut biodiversity in south-western Romania resource for perspective cultivars. Pak J Bot. 44 (1), 307-311.
[37] Arzani, K., Mansouri-Ardakan, H., Vezvaei, A., Roozban, M.R. (2008). Morphological variation among Persian walnut (*Juglans regia*) genotypes from central Iran. New Zeal J Crop Hort**.** 36, 159-168.
[38] Serr, E.F. (1962). Selecting suitable walnut varieties. Davis, California, California Agricultural Experiment Station.
[39] Pandele, I. (1966). Biochemical characterization of the principal varieties and types of walnut, almond and hazel in Rumania and determination of general metabolic correlations specific to nuts. Lucrar Sti Inst Cert Hort-vit, 9, 621-57.
[40] McGranahan, G.H., Leslie, C. (1990). Walnuts (*Juglans*). Acta Hortic. 290, 905-951.
[41] Germain, E. (1997). Genetic improvement of the Persian walnut (*Juglans regia* L.). Acta Hortic. 442, 21-32.
[42] Zhadan, V.M., Strukov, M.V. (1977). Breeding walnut for fruit size. Plant Breeding Abstracts, 47: 918.
[43] McGranahan, G.H., Leslie, C. (2012). Walnut. In: Badenes, M.L., Byrne, D.H. (eds) Fruit Breeding. Springer, Boston, 827-846.
[44] Yerlikaya, C., Yucel, S., Erturk, U., Korukluoglu, M. (2012). Proximate composition, minerals and fatty acid composition of *Juglans regia* L. genotypes and cultivars grown in Turkey. Brazil Archive Biol Technol. 55(5), 677-683.
[45] Keles, H., Akca, Y., Ercişli, S. (2014). Selection of promising walnut genotypes (*Juglans regia* L.) from Inner Anatolia. Acta Scientiarum Polonorum Hortorum Cultus. 13(3), 167-175.
[46] Ali, M., Ullah, A., Ullah, H., Khan, F. (2010). Fruit properties and nutritional composition of some walnut cultivars grown in Pakistan**.** Pak J Nutr. 9(3), 240-244.
[47] Kodad, O., Wathelet, J.P., Estopañan, G., Juan, T., Socias, I., Company, R. (2013). Kernel chemical composition of the walnut genetic resources grown in the High Atlas Mountains of Morocco. Acta Hortic. 976, 429-432.
[48] Savage, G.P., Dutta, P.C., McNeil, D.L. (1999). Fatty acid and tocopherol contents and oxidative stability of walnut oils. J Amer Oil Chem Society. 76(9), 1059-1063.
[49] Pereira, J.A., Oliveira, I., Sousa, A., Ferreira, I.C.F.R., Bento, A., Estevinho, L. (2008). Bioactive properties and chemical composition of six walnuts (*Juglans regia* L.) cultivars. Food Chem Toxicol. 46, 2103-2111.
[50] Bada, J.C., León-Camacho, M., Prieto, M., Copovi, P., Alonso, L. (2010). Characterization of walnut oils (*Juglans regia* L.) from Asturias, Spain. J Amer Oil Chem Soc. 87, 1469-1474.

[51] Venkatachalam, M., Sathe, S.K. (2006). Chemical composition of selected edible nut seeds. J Agricul Food Chem. 54, 4705-4714.
[52] Martínez, M.L., Mattea, M.A., Maestri, D.M. (2006). Varietal and crop year effects on lipid composition of walnut (*Juglans regia* L.) genotypes. J Amer Oil Chem Society. 83, 791-796.
[53] Akhiani, S., Afshari, H., Parvaneh, T. (2017). Evaluation of some phenological and pomological characteristics of selected walnut genotypes from Shahroud-Iran. J Nuts. 8(1), 21-30.

Received: **12.08.2019**
Accepted: **26.01.2020**

CORRESPONDING AUTHOR

Umran Erturk
University of Bursa Uludag,
Faculty of Agriculture,
Department of Horticulture, Bursa, Turkey

e-mail:umrane@uludag.edu.tr

© by PSP Volume 29 – No. 04A/2020 pages 2818-2822 Fresenius Environmental Bulletin

NATURAL OCCURRENCE OF AFLATOXIN B_1 IN DRY FRUITS OF GILGIT-BALTISTAN, PAKISTAN

Shamsher Ali[1,*], Azhar Ali[2], Ali Sartaj[2], Maher Ali[1], Ali Amjad[2]

[1]Department of Chemistry, Karakoram International University,15100 Gilgit, Pakistan
[2]Department of Agriculture and Food Technology, Karakoram International University,15100 Gilgit, Pakistan

ABSTRACT

The Gilgit-Baltistan (GB) is favorable region for production of dried fruits due to its favorable climatic conditions and its exceptional fertile lands. However, these fruits invade by certain filamentous fungi in the field and may grow on foods during storage under favorable conditions of temperature and humidity resulted Aflatoxins are produced. In this study, three hundred samples of dried fruit (150-apricot and 150- walnut) were collected from retail shops, local markets and farmers of different District (Ghizer, Gilgit, Skardu) of Gilgit-Baltistan, Pakistan and were analyzed for contamination level of aflatoxin B1 using thin layer chromatographic method. In addition, aflatoxin producing fungi was isolated from the collected contaminated samples during field survey by dilution-plate method. In the study *Aspergillus flavus* specie has been identified in the contaminated samples. Analytical result showed that aflatoxin B_1 was detected in 30 sample (20%) of the total 150 samples analyzed in dried apricot kernel and 45 samples (30.0%) of the total 150 samples of walnut. The level of contamination was found to be in a range of 0.5-10 ug/Kg (in apricot kernel) and 0.6-15 ug/Kg (in walnut). Ten sample (6.5 %) of apricot kernel and 20 samples (13.30 %) of walnut were found above the safe limit for aflatoxin B_1 (2 ug/kg), set by EU regulations. Moreover, aflatoxin B_1 was detected in 20% of apricot kernel and 38% walnut samples collected from Skardu region, whereas, aflatoxin B_1 was found in 14 % of apricot and 22 % of walnut samples in the Gilgit region. The high occurrence of aflatoxin may cause health hazards for consumers and limit exports. It was concluded that walnut is more susceptible for aflatoxin B_1 production. Moreover, Skardu region was assumed to be more favorable to invade toxin producing fungus.

KEYWORDS:
Aflatoxin, Apericot kernel, Contamination level, Gilgit-Baltistan

INTRODUCTION

Mycotoxins are a group of toxic fungal secondary metabolites which can contaminate agricultural products under pre-and postharvest conditions. They can cause acute or chronic toxic effects such as carcinogenic, mutagenic, teratogenic, atherogenic and oestrogenic effects in human and animals [1, 2]. In addition, mycotoxins affect food quality, resulting in huge economic losses in addition to being hazardous to consumer health for producing countries [3]. Therefore, mycotoxins are considered an important problem throughout the world in terms of public health, agriculture and economics. Among mycotoxins, aflatoxin is the major concern, given their high occurrence and toxicity. Aflatoxins are produced by members of *Aspergillus* section *Flavi* (mainly *Aspergillus flavus* and *A. parasiticus*), are potent hepatotoxic, mutagenic and carcinogenic toxins causing serious health hazards to humans and animals. Aflatoxins B1, B2, G1 and G2 exist predominantly in grains, nuts, dried fruits, and foods whereas, M1 and M2 aflatoxins, hydroxylated metabolites are found primarily in animal tissues and fluids (milk and urine) as the metabolic products of aflatoxins B1 and B2 respectively [4]. The most toxic aflatoxin is B1, is noted as a human carcinogen (group 1) by the International Agency for Research on Cancer [5]. Special interest is given to aflatoxin B1 due to its high occurrence and toxicity. Aflatoxigenic fungi are found in different food commodities including cereals, nuts, spices, figs and dried fruits [6]. They may contaminate foods by colonizing them at several stages of the food chain; pre harvesting, processing, transportation and storage [7]. Due to the scarcity of food, lack of regulation and unawareness people are exposed to consume contaminated food and this is an alarming situation. Unfortunately, this problem is mostly neglected in many developing countries like Pakistan.

The Gilgit-Baltistan (GB) is favorable region for production of dried fruits due to its favorable climatic conditions and its exceptional fertile lands. In GB dried fruit is prepared and preserved by removing the original water content naturally from fresh fruit through sun drying method. Using of dried fruit has a long tradition in GB due its sweet taste, nutri-

tive value and long shelf life. At the same time however, due to the difficult terrain of the region and the remote location of such fruit belts, there is limited investment in storage and processing facilities in the region which leads to attacked by several fungal species especially aflatoxin producing fungal species. There are very limited reports for the presence of aflatoxins contamination in dry fruits considering conducive environment for fungal proliferation. Therefore, the present study was designed to analyse the occurrence and levels of AFB_1 contamination in in dried apricot kernel and walnut grown in Gilgit-Baltistan, Pakistan and disseminate the results to farmers, traders, local officers and law enforcement agencies.

MATERIALS AND METHODS

Collection of samples. A comprehensive field survey was done district Ghizar, Gilgit and Baltistan Region. Detail discussions with farmers and dried fruit dealers were carried out regarding the drying, storage and packing of Apricot and Walnut apricot. A total of 300- hundred samples (150-dried apricot and 150- walnut) including 100 sample from each district were collected from farmers and dealers for laboratory analysis. A ½ Kg of each samples were packed in polythene bag and transported to laboratory for further study.

Identification of aflatoxin producing fungi. Aflatoxin producing fungi was isolated from the collected contaminated samples during field survey by dilution-plate method, by gentle shaking of 10 g from each samples with 100 ml of sterile water for 30 min. after sedimentation, the supernatant suspension was used to prepare serial dilutions and 1ml a aliquot of appropriate dilution was spread-plated onto Czapek-Dox Agar. The plates was incubated at 28^0C for 7 days as described by [8]. Identifications of pure fungal isolates was made on the basis of their cultural, morphological techniques.

Quantification of Aflatoxin B1. The sample was ground to fine particles and weight 50 gram of sample into the blender jar, added 250 ml acetone – water (85+ 15) and blended 3 minutes. Filtered through Whatman filter paper No. 1 into 250 ml graduate cylinder. Collected 150 ml filtrate and transferred to 400 ml beaker. To the filtrate, added 3 gram cupric carbonate basic and 5 gram celite powder. At the same time ferric gel was prepared by mixing 30 ml ferric chloride and 170 ml NaOH and transferred to filtrate and mixed and filtered. To the filtrate added 150 ml sulphuric acid and 10 ml chloroform and transferred to a separating funnel and shake. Collect lower layer and treated with KOH and KCl mixture and collected 8 ml filtrates. The solvent was evaporated on china dish a low temperature and re-dissolved in 200 uL benzene-acetonitrile. Spotted successively 1, 2, 3, 5, 7, 10, and 20 ul sample solution on TLC. At the same plate spotted 1, 3, 7, and 10 ul aflatoxin B standard. The plate was developed on chloroform-xylene-acetone a developing solvent. Aflatoxin B_1 content in the samples spots were visualized under UV light and compared with standard spots intensity [9].

RESULTS AND DISCUSSION

Identification of aflatoxin producing fungi. Detail discussions with farmers and dried fruit dealers in study area revealed that dried fruits are prepared and preserved by removing the original water content naturally from fresh fruit through sun drying method. During field survey, 12 fungal contaminated samples were also collected from district Ghizar, Gilgit and Skardu Region of Gilgit-Baltistan for identification of aflatoxin producing fungus. Results showed that *Aspergillus flavus* specie has been identified in the contaminated samples. Similarly, Gürses, (2006) also reported *Aspergillus* and *Penicillium* species in contaminated samples of hazelnuts, walnuts, peanuts, almonds and roasted chickpeas in Turkey [10].

Contamination level of Aflatoxin B1 in dried fruits. In this study, 300 dried fruit samples (apricot kernel and walnut kernel) were investigated for the contamination level of aflatoxin B1 (AFB1). Their results are summarized (Table 1).

The results indicated that AFB1 was detected in the 25% of dried fruit samples with concentration of AFB1 ranged from 0.5 to 15 ppb with the average value of 5 ppb. Among these contaminated samples, 15% of samples were found below the safe limit, whereas 10% samples were found above the permissible limit for aflatoxin B1 (2 ug/kg), set by European Union regulations [11]. It is also evident from the results that walnut samples were more susceptible for aflatoxin contamination than apricot. Table 1 showed that 45 samples (30 %) of walnut and 30 samples (20 %) of apricot kernels samples were contaminated with AFB1. Furthermore, 20 walnut sample with average value of AFB1 (7 ug/kg) were found above the permissible limit, whereas 25 samples with AFB1 ranging from 0.6 to 2 ug/kg were found below the suggested limit [11]. Like-wise 10 samples of apricot kernel had concentrations of AFB1 ranging from 2.5 to 5 ppb, were found above the suggested limit, whereas, 20 samples with the concentration ranging from 0.5 to 2 ppb were found below the suggested limit. Various investigators also reported the similar results. For example, Gürses (2006) detected AFB1 contamination in 25 % walnuts and 23 % almonds samples with mean levels AFB1 43.0 ppb and 7.4 ppb respectively [10]. Likewise 35.30% of walnut samples contaminated with

AFB1 in in Mexico [12], and 20 % of apricot kernels and 10-20 % of walnut samples were found above permissible limit in the Khyber Pakhtunkhwa province, Pakistan [13]. Similarly, Luttfullah and Hussain (2011) found 27 % apricot kernels samples contaminated with AFB1 with 6 % sample with concentration of 5.6 mg/kg and 40-70 % walnut sample contaminated with aflatoxin and 22-30 samples of walnut had contamination levels ranging from 7.8 to 13.5 mg/kg [14]. Similarly, aflatoxin was detected in 50 % walnuts samples in the City of Mekkah [15]. In Poland 38% walnuts samples were contaminated with AFB1 (4.04 µg/kg [16]. In Morocco, 30% walnuts AF1 contaminated samples were reported [17].

The occurrence and contamination of aflatoxin B1 may varied with ecotypes. The absence of aflatoxin in some of the samples most probably shows the unfavorable conditions for its development during production, product storage and distribution. The absence of aflatoxin is an important finding with respect to the safety of dried fruits [18]. Good manufacturing practices after harvesting such as cleaning, drying, and packaging will minimize mould growth and aflatoxin production in dried fruits. The mycological quality of some dried fruits on the market, especially of walnut, is quite poor, bearing many genera and species of fungi. Most fungi are present on dried fruits of the post-harvest and storage type, which develop after harvest if relative humidity is not controlled during storage [19]. Samples of dried apricots and walnuts from various sources yield numerous colonies of several species of *Aspergillus* [20].

Contamination of aflatoxin B1 in different regions. The result in table 2-3 showed that the highest prevalence of aflatoxin was found in samples of apricot (20%) samples collected from Skardu region with the lowest value in Gilgit region (14 %) of Gilgit-Baltistan (Table 2). Similarly, the highest mean concentration aflatoxin B1 (3.5 µg/kg) was determined in sample collected from Skardu with the lowest mean value of aflatoxin in Gilgit (2.0 µg/kg) (Table 2). Similarly, at Skardu region, 62% of contaminated samples found below the safe limit, whereas 38% samples were found above the permissible limit for aflatoxin B1 (2 ug/kg), set by European Union regulations. Similarly, 62 % and 70 % contaminated samples of Gilgit and Ghizer of region were found below the safe limit, whereas 30 % and 38% contaminated samples collected from Gilgit and Ghizer region were found above the permissible limit for aflatoxin B1 (2 ug/kg), set by European Union regulations [11]. These results indicated that samples collected from Skardu region had highest prevalence and contamination level of aflatoxin than Ghizer and Gilgit region.

A similar trend of prevalence and concentration of AFB1 was in walnut (Table 3). The results indicates that the highest prevalence of AFB1 was found in samples of walnut (38%) samples collected from Skardu region with the lowest prevalence in Gilgit region (22 %) of Gilgit-Baltistan (Table 2). Similarly, the highest mean concentration aflatoxin B1 (8.0 µg/kg) was determined in sample collected from Skardu with the lowest mean value of aflatoxin in Gilgit (4.5 µg/kg) (Table 2). Similarly, at Skardu region, 52% of contaminated samples were found below the safe limit, whereas 47 % contaminated samples were found above the permissible limit for aflatoxin B1 (2 ug/kg), set by European Union regulations. Similarly, 60 % and 64 % of contaminated samples of Ghizer and Gilgit region were found below the safe limit, whereas 40 % and 36 % contaminated sample collected from Ghizer AND Gilgit region were found above the permissible limit for aflatoxin B1 (2 ug/kg), set by European Union regulations. These results indicated that samples collected from Skardu region had highest prevalence and contamination level of aflatoxin than Ghizer and Gilgit region.

TABLE 1
Aflatoxin B1 in dried fruit (apricot and walnut kernels) collected from Gilgit-Baltistan

Commodities	Sample Size/positive	Contamination level µg/kg		Mean value (µg/kg)
		Below limit	Above limit	
Apricot kernel	150/30	20 (0.5 – 2)*	10 (2.5-5)	3.0
Walnut kernel	150/45	25 (0.6 – 2) *	20 (2.3-15)	7.0
Total	300/75	45 (0.5-2)	30 (2.3-15)	5

*Aflatoxin B1 range

TABLE 2
Contamination of aflatoxin B1 in Apricot kernel at different regions.

Locations	Sample Size/positive	Contamination level µg/kg		Mean value (µg/kg)
		Below limit	Above limit	
Gilgit	50/7	5 (0.5 - 2)*	2 (2.5-4)	2
Ghizer	50/10	7 (1 - 2)*	3 (2.3 - 6)	3
Skardu	50/13	8 (0.5 - 2)*	4 (2.5-5)	3.5

TABLE 3
Contamination of aflatoxin B1 in Walnut at different regions.

Locations	Sample Size/positive	Contamination level µg/kg		Mean value (µg/kg)
		Below limit	Above limit	
Gilgit	50/11	7 (0.6 – 1.8) *	5 (2.2-10)	4.5
Ghizer	50/15	9 (0.6 - 2) *	6 (2.5-13)	6
Skardu	50/19	10 (0.6 - 2) *	9 (2.3-15)	8.0

REFERENCES

[1] Hussein, H.S., Brasel, J.M. (2001) Toxicity, metabolism, and impact of mycotoxins on humans and animals. Toxicology. 167, 101-134.

[2] Kuiper-Goodman, T. (2004) Risk assessment and risk management of mycotoxins in food. In: Mycotoxins in food. Woodhead Publishing. 3-31.

[3] Richard, J.L. (2007). Some major mycotoxins and their mycotoxicoses—An overview. International Journal of Food Microbiology. 119(1-2), 3-10.

[4] Groopman, J.D., Donahue, P.R., Zhu, J.Q., Chen, J.S., Wogan, G.N. (1985) Aflatoxin metabolism in humans: detection of metabolites and nucleic acid adducts in urine by affinity chromatography. Proceedings of the National Academy of Sciences of the United States of America. 82(19), 6492.

[5] World Health Organization and International Agency for Research on Cancer. (1993) Some naturally occurring substances: Food items and constituents, heterocyclic aromatic amines and mycotoxins. IARC Monographs on the Evaluation of the Carcinogenic Risk of Chemicals to Humans. 56.

[6] Taniwaki, M.H., Hocking, A.D., Pitt, J.I., Fleet, G.H. (2009) Growth and mycotoxin production by food spoilage fungi under high carbon dioxide and low oxygen atmospheres. International Journal of Food Microbiology. 132(2-3), 100-108.

[7] Manonmani, H.K., Anand, S., Chandrashekar, A., Rati, E.R. (2005) Detection of aflatoxigenic fungi in selected food commodities by PCR. Process Biochemistry. 40(8), 2859-2864.

[8] Ismail, Y., McCormick, S., Hijri, M. (2013) The arbuscular mycorrhizal fungus, Glomus irregulare, controls the mycotoxin production of Fusarium sambucinum in the pathogenesis of potato. FEMS Microbiology Letters. 348(1), 46-51.

[9] A.O.A.C. (2000). Official methods of analysis, 17th ed. Association of official Analytical Chemists. Washington D.C, USA.

[10] Gürses, M. (2006) Mycoflora and aflatoxin content of hazelnuts, walnuts, peanuts, almonds and roasted chickpeas (LEBLEBI) sold in Turkey. International Journal of Food Properties. 9(3), 395-399.

[11] European Commission. Commission Regulations (2006) Setting maximum levels for certain contaminants in food stuffs. Official Journal of European Union. 364, 5.

[12] Adaya-González, J., Carvajal-Moreno, M., Rojo-Callejas, F., Ruiz-Velasco, S. (2015) Aflatoxins in walnut (*Juglans regia* L.), pecan (Carya illinoinensis (Wangenh.) K. Koch) and cashew (Anacardium occidentale L.) nuts in Mexico. Pharm Anal Acta. 6, 338-348.

[13] Masood, M., Iqbal, S.Z., Asi, M.R., Malik, N. (2015) Natural occurrence of aflatoxins in dry fruits and edible nuts. Food Control. 55, 62-65.

[14] Luttfullah, G., Hussain, A. (2011) Studies on contamination level of aflatoxins in some dried fruits and nuts of Pakistan. Food Control. 22(3-4), 426-429.

[15] Leung, M.C., Goldstone, J.V., Boyd, W.A., Freedman, J.H., Meyer, J.N. (2010) Caenorhabditis elegans generates biologically relevant levels of genotoxic metabolites from aflatoxin B1 but not benzo [a] pyrene in vivo. Toxicological Sciences. 118(2), 444-453.

[16] Leszczynska, J., Kucharska, U., Żegota, H. (2000) Aflatoxins in nuts assayed by immunological methods. European Food Research and Technology. 210(3), 213-215.

[17] Juan, C., Zinedine, A., Molto, J. C., Idrissi, L., Manes, J. (2008) Aflatoxins levels in dried fruits and nuts from Rabat-Salé area, Morocco. Food Control. 19(9), 849-853.

[18] Paramithiotis, S., and Drosinos, E.H. (2009) Journal of Quality Assurance and Safety of Crops and Foods. 1, 41.

[19] Aziz, N.H., Youssef, Y.A., El-Fouly, M.Z., Moussa, L.A. (1998) Contamination of some common medicinal plant samples and spices by fungi and their mycotoxins. Botanical Bulletin of Academia Sinica. 39.

[20] Christensen, C.M., Fanse, H.A., Nelson, G.H., Bates, F., Mirocha, C.J. (1967) Microflora of black and red pepper. Appl. Environ. Microbiol. 15(3), 622-626.

[21] Ozer, H., OKTAY BASEGMEZ, H. I., and Ozay, G. (2012) Mycotoxin risks and toxigenic fungi in date, prune and dried apricot among Mediterranean crops. Phytopathologia Mediterranea, 1, 148-157.

Received: **27.08.2019**
Accepted: **12.11.2019**

CORRESPONDING AUTHOR

Shamsher Ali
Department of Chemistry,
Karakoram International University,
15100 Gilgit – Pakistan

e-mail: shamsher.ali@kiu.edu.pk

© by PSP Volume 29 – No. 04A/2020 pages 2823-2833 Fresenius Environmental Bulletin

MAPPING VEGETATION OF WETLAND BASED UPON AN OBJECT-ORIENTED CLASSIFICATION WITH HIGH RESOLUTION ORTHOPHOTOS

Fulsen Ozen*

Ege University, Faculty of Agriculture, Department of Soil Science and Plant Nutrition, 35100, Izmir, Turkey

ABSTRACT

Gediz Delta, which is under protection under the Ramsar Convention, is one of the most important wetlands of Turkey. In the Delta in which there are numerous lagoons, saline, and freshwater swamps and a big salt marsh, there is also the Bird Sanctuary which is of great importance for ornitho-tourism. Plant species in wetlands are characterized as biomonitors that can show changes and pollution factors and levels within the area due to their properties. Monitoring of changes in plant species and geographical distribution is extremely important for the sustainability of diversity and balance in the ecosystem. In this study, it is aimed to determine the distribution areas of each taxon by creating a map of flora, which is known to be found in the wetlands of Gediz Delta and whose species are known but their distribution areas are unknown. Vegetation was observed in situ by field studies. Using the high-resolution infrared orthophoto images, the species and geographical distribution of the plants were determined by object-oriented classification method, which is a new approach in the determination of the elements on earth's surface. With this object-oriented approach, a new dimension has been given to classical classification processes. By transferring the area and average reflection values of the objects determined by using the properties of the method to the vector map as attribute information, it will be possible to create a reliable base for the "Wetland Management Plan", which is specified by experts as the most effective way to protect wetlands.

KEYWORDS:
Wetland, Gediz Delta, orthophoto, object-oriented classification

INTRODUCTION

Wetlands are determined as marsh, fen, peatland or water-covered areas including seawater areas, in which the neap tides are not exceeding six meters with the characteristics of natural or artificial, permanent or temporary, stationary or flowing, clean, brackish or saline water [1]. Wetlands are important in terms of hosting many species, softening the climate in their region and regulating the water regime [2]. They are one of the most sensitive ecosystems and are also called "world's kidneys" due to their various unique ecological functions [3]. Additionally, wetlands, are recognized as important carbon reservoirs that play an important role in the global carbon cycle (about 35% of the total carbon stock of terrestrial ecosystem) [4].

Turkey's climate diversity, which is occurred due to its characteristics of being situated in the area among Europe, Asia and Africa continents, being surrounded by seas with different ecological characteristics from three sides, the elevation difference in the sea level exceeding 5000 m, has made Turkey one of the most important countries within its geography in terms of wetlands. [5]. The Gediz Delta, which forms the study area, is a large alluvial plain formed by sediments carried by the Gediz River. Delta is a protected area with national and international conservation status due to its biodiversity. These statuses allow for legal sanctions for the protection of the ecological integrity of the delta and for providing rational protection. The protection status of the delta in different parts are as follows; Ramsar Area, Important Bird Area, Important Natural Area, Wildlife Conservation Area, 1st Degree Archeological Site, 1st Degree Natural Protected Area, 2nd Degree Natural Protected Area, 3rd Degree Natural Protected Area [6].

Plant species in wetlands are defined as biomonitors that will show changes and pollution parameters in these areas due to their characteristics. For example, *Phragmites australis* can retain heavy metals such as Fe, Al and Mn [7] and *Typha latifolia* can contain heavy metals such as Zn, Cu, Cr, and Cd [8] within its texture and can be used in phytoremediation applications [9]. Due to having such an importance in the nutrient cycle in terrestrial and aquatic systems, it is necessary for the wetland vegetation to be correctly classified in order to explain the ecosystem structure and dynamics [10]. Mapping and monitoring of wetland vegetation at higher spatial and spectral resolutions allows for precise identification of changes in vegetation and composition using advanced geographic approaches. This opportunity not only provides an indication of the changes

identified but also provides information about the nature and direction of change [11].

Remote Sensing and Geographic Information Systems (GIS) are a valuable source of data for identifying objects and wetlands on the surface of the world and monitoring changes. Different quality images such as Landsat MSS/TM /ETM+ and Landsat 8 [12,13,14,15,16], Unmanned Air Vehical (UAV) data [17, 18], SPOT images [19, 20], ASTER [15] , IKONOS [21], SENTINEL 1 and 2 [22, 23, 24], Quickbird [25], Worldview 2 [26, 27], SAR [28, 29], ALOS [30], LIDAR [31, 32] etc. offer a wide range of products to be used in a large variety of wetland applications. By the analyzation of images and also with different imaging indices including NDVI, NDWI, MNDWI, EVI, NDRI and etc. [26, 33, 34, 23, 24], results supporting the conducted studies can be obtained.

New advances in earth observation technology since the 2000s have increased the tendency to use object-oriented image analysis (OBIA) and object-oriented software. It has the ability to analyze high-resolution images such as object-oriented classification and orthophoto. Compared to pixel-based classification, which can only use spectral information in one pixel, the object-oriented classification can benefit from features including texture, content, size, etc. for each section. [35]. When past studies are examined, OBIA is used to identify wetlands in different terrains [28, 36], classification of uses within wetlands [37, 38], identification of plant communities [10,17, 39] and identification of ecological habitats [21, 40] with operability. [41] reviewed the wetland mapping methods to be applied to the Canadian Wetlands Inventory program in their study and described the object-oriented approach as optimal because of its flexibility and ability to address the spatial heterogeneity of wetlands.

Orthophoto, or in other words, photo-map, is a photographic image with a certain scale, such as a map, obtained by eliminating image shifts caused by differences in image inclination and elevation in the terrain. In infrared orthophotos, the difference between the color tones is quite high. Therefore, infrared tone differences provide great convenience especially in definitions such as tree and vegetation type [42]. Orthophoto maps offer great advantages over analog systems in combination with other data sets and their compatibility with the data produced. In addition, orthophoto offers a wide range of possibilities, especially for updating digital maps, automatic map-making and creation of new databases. It offers the possibility of classifying different dimensions and objects in the extraction of the third dimension [43, 44]. [45] analyzed shrub layer changes in Southern Mexico from 1937 to 2003, objectively classifying a series of high-resolution aerial photographs based on the results obtained from the QuickBird satellite image. Shrub forms were determined by mean brightness value and average difference in neighboring pixels.

In this study, it is aimed to determine the plant communities of Gediz Delta, which is an important wetland protected under RAMSAR at the taxon level. Object-oriented classification method, which is a new approach, is used to determine the area uses within the delta by using infrared orthophotos with high terrestrial resolution (30 cm). Classes are made for plant species and other objects in wetlands with irreplaceable spatial sizes, the tree, Anagyris foetida, Aethrocnemum fruticosum (L.) Moq., bare land and barren areas that don't have vegetation, delta, Halimione (=Atriplex) portulacoides, Halochnemum strobilaceum (=Pall.) Bieb., shrubbery areas, Poterium, Phragmites, Sarcocornia perennis, Scirpus, Tamaricetum, areas where water is observed on the surface, agricultural areas, annual field crops, and natural vegetation and the artificial formation and their spatial distribution are located. Thus, it will be possible to protect the natural habitat belonging the species, to determine and monitor the pollution situation that may occur in the delta, to monitor the effects of climate changes by keeping the water regime of the delta under constant control.

MATERIALS AND METHODS

Study Area. Gediz River, whose ancient name is Hermos, is the second-largest river in the Aegean region after the Greater Maeander and covers 2.2% of Turkey's surface area with approximately 1.7 million hectares of drainage basins. Gediz Delta, which contains "İzmir Bird Sanctuary" that is one of Turkey's leading natural assets, is located at the northern part of Izmir province and western part of the Gulf of Izmir, between 26 ° 47 '51 "-27 ° 05' 28" eastern longitude and 38 ° 39 '25 "-38 ° 25' 53 "northern latitudes. With three natural lagoons, the delta is a typical Mediterranean delta ecosystem. Outside the wetland, there are agricultural areas, orchards, hills at various elevations, residential areas and industrial zones [6]. In the study, 145,324.50 decare of area was also selected as the research area, due to consisting of areas covered with water since it was aimed to determine the plant species growing in the wetlands of Gediz Delta (Figure 1). Menemen Delta/Plain belongs to the Mediterranean climate type in terms of macroclimate characteristics, according to Thorntwaite (1948) climate classification; the summers are hot and dry, the winters are mild and rainy, showing the definition of mesothermal climate. The mean annual rainfall of the research area is 525.3 mm and the highest rainfall data was measured in December with 106.6 mm. 50.07% of the precipitation in the region falls in winter, 24.63% in spring, 2.11% in summer and 23.19% in autumn. Heavy rains in the form of rainstorm in winter can cause flooding and soil erosion. The driest months of the

plain are July and August. According to the multi-year precipitation data, there is 2.6 mm rainfall in July and 3 mm rainfall in August. In the research area, where the average temperature is 16.9 ºC, the lowest temperature is -7.6 ºC in January and the highest temperature is 44.3 ºC in August; meanwhile the mean moisture content ranges from 46.3 to 66.9% [6].

Due to its presence in the Mediterranean climate zone, Mediterranean vegetation cover is seen. 315 plant species in 61 families have been identified in scientific studies conducted in Delta to date. Two of these plant species (Campanula lyrata subsp. Lyrata and Stachys cretica subsp. symrnaea) are endemic. Different habitats such as fresh water and salt water swamps, lagoons, reeds, hills, salt pans, temporary water meadows, salty steppes, frigana and scrub in the delta cause different plant units to be seen in the area. Gediz Delta is home to many animal species, especially birds. It is one of the five breeding areas including Lake Manyas (Balıkesir), Greater Maeander Delta (Aydın), Lake Aktaş (Ardahan) and the Kızılırmak Delta (Samsun) of the endangered Dalmatian Pelican (Pelecanus crispus) and the only known breeding area of Black-tailed tern (Sterna sandvicensis) in Turkey. In addition, salt pans located in the delta have areas in which the invertebrate, one of the most important nutrients for flamingos, called Artemia salina is abundant [6].

Material. The research material consists of wetland vegetation distributed in the Gediz Delta. In order to determine the vegetations developing in wetlands, literature studies have been carried out on plant communities in wetlands and plant taxa have been observed in situ by field studies. The main characteristics of the natural plant species classified in the scope of the study area and shown together with other plant species in the classification are as follows:

***Pragmitetum communis* Association [46].** *Phragmites australis* is one of the most common plants in wetlands. This plant, which has only one species in our country, can grow near on both freshwater and saline water. In this context, the phragmites plant can be seen both on the river and lakesides and on the seasides. It is a cosmopolite and perennial plant with rhizome that forms dense communities in all regions. Its strong and quite long bodies have a lot of nodes. The leaves are long and wide and the edges are straight. Flower condition is a large panicle and is very branched. *Phragmites australis* species generally start from sea level up to 2400 meters. This type of Europe-Siberian element forms large communities in the temperate regions of Eurasia [47]. In our country, these plants are used by the local people in basket-making, shade, roof, porch construction and perhaps most importantly in rush mat making. Therefore, phragmites communities are frequently cut and destroyed. In the field of research; Along the Gediz River, along the shores of the water, the purest communities are located on the shores of Gölmarmara, in the reeds area where the freshwater pump belonging to the Rama CanSuyu Project is located in the Gediz Delta and in the outfall where the Gediz River flows into the sea.

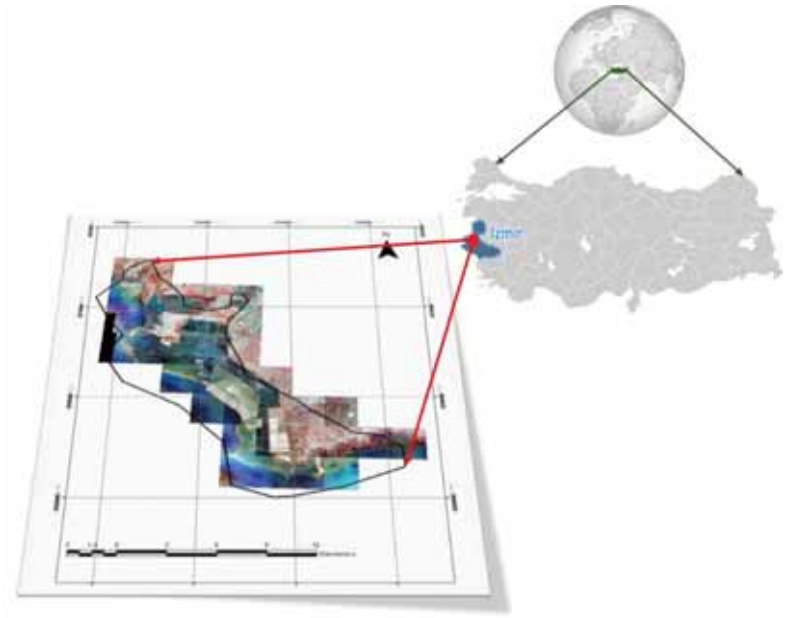

FIGURE 1
The study area

***Arthrocnemo - Halocnemetum strobilacei* Association [48].** *Arthrocnemum fruticosum*, is one of the species spreading in saline soils. This halophyte species, which grows in the sea, in the delta, in the salt marshes, can tolerate even high amounts of salt in the soil compared to other plants with its succulent structure. Perennial *Arthrocnemum* species with a creeping or ascending formation can grow up to 1 meter. This species, which is mostly found in Tekirdağ, İstanbul, Antalya, Kayseri, Mersin and our region in our country, is distributed in South, Western Europe, North Africa, Arabia, Syria and Iran [47]. The characteristic and distinctive types of this union are; *Arthrocnemum fruticosum* and *Halocnemum strobilaceum*. The most important species accompanying this association are; *Salicornia europaea*, *Hordeum marinum, Halimione portulacoides, Salsola kali, Sueda prostrata subsp. prostrata, Aegilops triuncialis, Chenpodium murale, Chritmum maritimum, Limonium sinuatum, Juncus maritimus, Cakile maritima, Eryngium maritimum, Rumex bucephaloporus* and *Ammophilla arenaria.*

***Tamaricetum symrnensis* Association [49].** Tamarix symrnensis is a perennial tree that densely inhabits the coasts, deltas and saline soils of the Aegean and Mediterranean regions. However, it is also spread in İstanbul, Zonguldak, Uşak, Ankara, Kahramanmaraş, Diyarbakır, Antalya, Mersin, Van, Mardin, and Hakkari. Apart from our country, it can grow naturally in Caucasus, Iran, Northern Iraq, Afghanistan, Balkans, Romania and Crimea [47]. This woody species can come into the form of a dwarf tree with a thick trunk where it can find good growth opportunities. This dwarf tree is easily recognizable by its small, stair-shaped leaves, spica-like cluster flowers. There are also glandular structures secreting salt on this plant [47]. It grows in saline-alkaline soils, as in the *Arthrocnemo – Halocnemetum strobliacei* association. In many places, although both associations are intertwined, in general Tamarix predominate in soils where the soil deepens and the amount of salt is slightly less. Conducted phytosociological studies have shown that this association occurs most frequently in the Gediz Delta [50]. This association is located in the flat areas in middle of the Bird Sanctuary, which is occasionally under the saline water. This association, which is also located in the three hills, decreases as the salt content in the soil decreases and the slope increases. The characteristic species of this association are *Tamarix symrnensis* and *Salsola. soda*. The top characteristics of the Association are *Halimione portulacoides, Hordeum marinum subsp marinum, Juncus maritimus, Limonium sinuatum, Atriplex lasiantha, Salicornia europea,* and *Arthrocnemum fruticosum*.

***Sarcopoterium spinosum* Association.** *Sarcopoterium spinosum* is an element of the Eastern Mediterranean. In addition to the Eastern Mediterranean region, it is spread in the Mediterranean Basin up to Tunisia and Sardinia Island [51]. *Sarcopoterium spinosum*, which is the most characteristic type of vegetation called Phrygana, forms a short plant group by covering the bare areas where the scrub is largely destroyed. As a result of the destruction of scrub areas, especially in Western Anatolia, *Asphodelus aestivus*, which is unaffected by fire with its tubers under the ground, becomes dominant and is followed by *Sarcopoterium spinosum. Although Sarcopoterium spinosum is* spread between 0 and 500 meters, it is mostly seen in the outfall where the Gediz River flows into the sea, in the Hills of Foça, in İzmir Bird Sanctuary, in the Menemen Helvacı Village and at the piedmont of Dumanlı Mountain.

***Sarcocornia perennis*.** It is a succulent euhalophite of the Chenopodiaceae family, spreading in saline marshes. It is a perennial plant that can reach up to 30 cm in height. It blooms in August-September and the seeds ripen in September-October. It is one of the plant species that can withstand salt concentrations up to 1000 mM [52]. The presence of salt in the soil solution is essential for the growth of these plants. *Sarcocornia perennis* is considered as an obligate halophyte [53]. *Sarcocornia* accumulates 50% of the dry weight of the shoot without salt glands or salt pouches and thus provides high salt tolerance [52, 54]. There is no consensus on the number of *Sarcocornia* species, the major phenotypic variation between species of the same genus is due to morphological parallels between different species [54, 55]. Salt tolerance of euhalophytes, especially *Sarcocornia perennis*, is determined by their high salt accumulation capacity in shoot vacuoles. Thus, vacuole can maintain high osmotic pressure and increase water uptake from the environment or saline soil.

***Halimione (= Atriplex) portulacoides*.** It is a perennial C_3 type halophyte from Chenopodiaceae family, which is widespread over the salt marshes in Europe, North Africa, South-West Asia. Generally, it is a predominant species on well-drained soil and upper swamps [56]. Although *Halimione* typically lives in the vicinity of seawater, where there are salt releases, the environment in which they live may be less salty or too salty [57]. Like other halophytes, although it has the ability to remove salt from epidermal sacs on both surfaces of its leaves [58, 59], it can accumulate high concentrations of salt in its leaves [59, 60]. *Halimione portulacoides* has been shown to be able to continue growing at different salt concentrations in environments with high nitrogen content [60]. The salt tolerance mechanism of this species was investigated from three different angles. These include; excessive deposition of salt in leaves, removal of salt from epidermal sacs [59], or accumulation of quaternary ammonium compounds capable of osmotic compatibility. *Sarcocornia perennis* and

Halimione portulacoides plants are halophyte species commonly found in *saline areas* of Aegean region. The distribution of these two species takes place according to salt tolerances; euhalofit *Sarcocornia perennis is* located on the seashore closest to the saline environment, while *Halimione* is spread in the interior with lower salt concentrations.

Salicornio europeae-Juncetum acutus ass. **Association.** It is spread along the coast of alkaline soils in the Greater Maeander Delta; on the Karaburun Peninsula, the Karaburun road the shore of the Sazadin stream; between the founts in the Gulf of Gökova; Muğla, salt marsh in the Milas Metruk, swamp areas; Selçuk, the shores of the Little Maeander Delta; İzmir-Alaçatı Yumru port, marshy areas; Alaçatı-Mersin bay [61]. Characteristics of the *Salicornio europeae-Juncetum acutus ass*. Association: Juncus acutus, Salicornia europea. Salicornietea fruticosae (syn: Arthrocnemetea fruticosi) class and characteristics of Salicornietalia fruticosae ordo: Halimione portulacoides, Inula crithmoides, Plantago crassifolia, Halocnemum strabilaceum, Suaeda prostrata, Schoenus nigricans, Salsola kali, Juncus maritimus, Salsola soda, Arthrocnemum fruticosum, Salsola ruthenica. There are considerable characteristics of the alliance Ammophilion australis in the association. Because the association is determined in coastal habitats, it is normal to find characteristic species of alliance Ammophilion australis found in coastal dunes in these areas. [62] In their study on the Adriatic coast, they identified the Juncetum maritimo-acuti association and linked it to the Juncetea maritimi class and the Juncion (etalia) maritime ordo and alliance [61].

Eucalyptus globulus **(Eucalyptus Trees).** The homeland of eucalyptus trees, a genus of the Myrtaceae family, is Australia. This tree is also referred to as health tree, malaria tree, swamp tree, red eucalyptus among the public. This tree, which is effortless to grow and reaches 60-70 meters in height, has nearly 700 species. Very fast-growing eucalypti are evergreen and straight-edged trees that have a reciprocal phyllotaxis. The flowers can be umbel-like as well as single and can be found in colors of yellow, white or red. Conducted studies reveal that the eucalyptus tree grows in climatic conditions with a wide range from warm to hot, semi-humid to semi-dry in the natural distribution areas, the average high temperature of the hottest month is 27-40 °C, and the average low temperature is 3- 15 °C for the coldest month. It was released that a eucalyptus plant absorbs up to 300 kilograms of water and takes 250 tons of water annually and exhale it to the air [63].

Orthophotos (30 cm*30cm) which is 1/5000 scaled (35) used in the research area for the determination of plant taxa from May 2010 were obtained from İzmir Metropolitan Municipality. eCognition software and ArcGIS 10.5, a GIS-enabled software, were used for object-based determination of wetland plants and for the evaluation, mapping, and entering of field information of classification results.

Methods. Primarily in the study, the limitation of the study area were determined to cover the wetlands of Gediz Delta. Infrared orthophotos have absolute coordinate information and show the north direction. Therefore, no geometric correction was performed on the images, and a digital database was created based on the UTM (Universal Transverse Mercator) and WGS-84 datum. Wetlands and their contents include wet-shore, dune-salty alkali; the limitations of natural habitats and feeding areas, agricultural areas and salt fields were determined by taking into consideration of the previous studies and actual area usages. The study was conducted with a satellite image (NIR/Green/Blue) band combination by using near-infrared band for better determination of all wetland vegetation. Field studies were carried out and the vegetation in the wetlands was observed in situ. In this respect, the species which have different morphological characteristics were differentiated (Figure 2).

Object-oriented image classification applied to high-resolution orthographic images in Trimble's eCognition software [64] can be summarized in three main steps: (1) Applying parameters such as segmentation scale and shape weight to objects for image segmentation, (2) Removing properties such as average spectral band values and segmenting and the determination of the standard deviation of the band values for each object in the image; and (3) A classification process such as the Nearest Neighbor classification. One of the most important parameters guiding the segmentation process is the scale. Given the multi-scale results of the objects to be uncovered, small objects can be combined to configure larger objects that form a semantic hierarchy. Similarly, a large object can be divided into small objects directed to two main approaches to object analysis. These approaches are described as top-down and bottom-up [65,66]. The use of small-value scales results in the identification of smaller and possibly more homogeneous objects; however, very small object size can reduce accuracy between classes and make calculation difficult. Because of the large number of objects created, it can affect the quality of information obtained from them. On the other hand, having large objects can result in confusion between classes [18].

For this reason, different scale parameters were used to differentiate between different vegetations in wetlands with the best way possible. According to [67], the simplest but most widely used method in OBIA research is the visual examination of segmentation results. Segmentation in all parcels was made by using multiresolution “segmentation method” and scale parameter was changed between 25-100-200

FIGURE 2
(A) NIR-Orthophoto (B) and (C) Sarcocornia spp. in study area

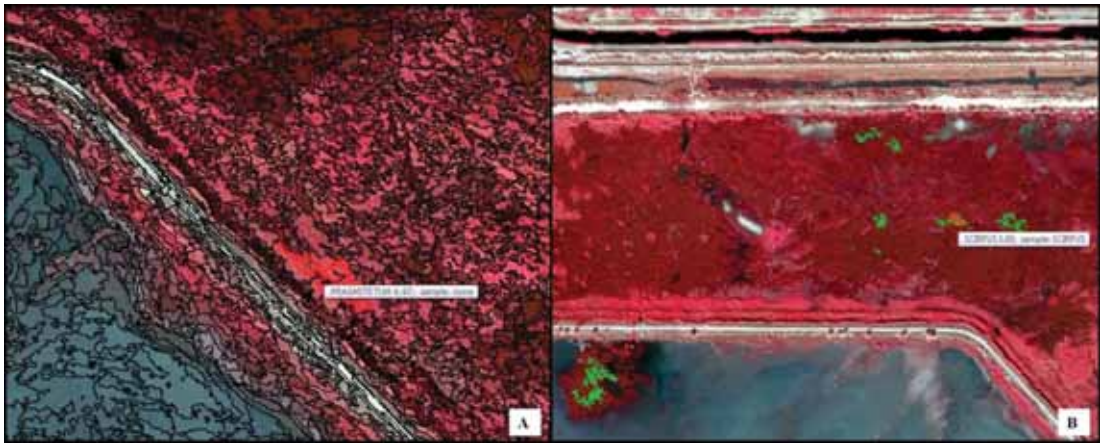

FIGURE 3
(A) Segmentation process, (B) Samples for Scirpus spp.

values. Color and format parameters are applied as 1 and 0, respectively, whereas 1 and 0 values are applied for integrity and softness parameters. (Figure 3a).

By using the classification feature of the eCognition software classes called the other tree species (TREE), *Anagyris foetida* (ANAGYRIS_FOETIDA), *Aethrocnemum fruticosum* (*L.) Moq*. (ARTHROCNEMUM), empty areas without cover (BARELAND), *Halimione (=Atriplex) portulacoides* (HALIMIONE), *Halochnemum strobilaceum (Pall.) Bieb*. (HALOCNEMUM), *Juncus* (JUNCUS), shrubbery areas (SHRUBBERY), the area covered with Eucalyptus trees (Eucalyptus), Poterium (POTERIUM), Phragmites (PHRAGMITES), *Sarcocornia perennis* (SARCOCORNIA), Scirpus (SCIRPUS), areas with observed water existence (WATER SURFACE), Tamaricetum (TAMARICETUM), agricultural fields (AGRICULTURE), annual field crops and natural vegetation (ANNUAL) and artificial formations (ARTIFICIAL), salt production areas (SALT PANS) were created. For each class, samples were made on the image and the miscibility of the average reflection values of the segmented objects could be observed with the help of the sample editor (Figure 3b)

In classification, "Nearest Neighbor" method was used. After the classification was completed, the relations of the classes, sample numbers or critical sampling numbers were checked with the help of the sample selection information table.

Classifications of different vegetation classes were made on the segmented images by the Nearest Neighborhood method. The results obtained were converted to files with ".shp" extension and transferred to the ArcGIS 10.5 software. As a result of these studies, classification maps were prepared for wetland vegetation in the region and their spatial size was calculated.

RESULTS AND DISCUSSION

The developmental status, biological activity levels, size and geographical distribution of the plants living in the wetlands constitute the evidence of whether the wetlands fulfill their functions. For this reason, examination, monitoring, and mapping of the species are very important for determining the continuity/quality of life in and around the wetland. In the conducted study, by benefiting from the high-resolution infrared orthophotos, the object-oriented classification method, which is a new approach in the determination of the objects on earth, was used. While determining the segmentation parameters; the

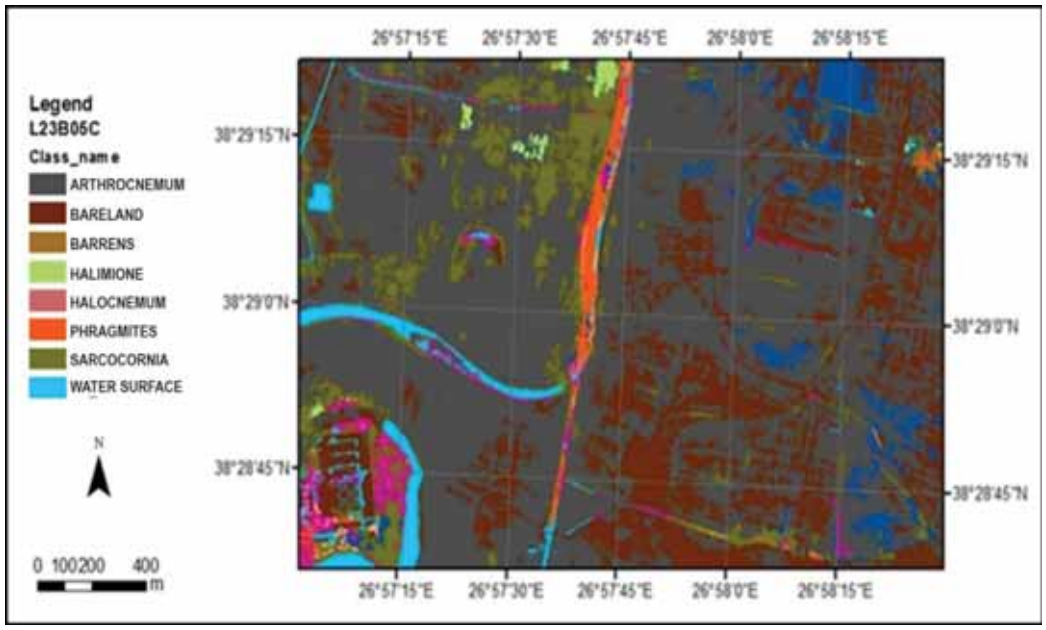

FIGURE 4
Classification map for a part of the study area

TABLE 1
Spatial size and percentage distribution of plant species and other objects in the research area

Land Cover Surfaces	AREA (da)
Trees	695,36
Anagyris_Foetida	27,17
Arthrocnemum	10.274,88
Bare Land	18.565,48
Halimione	288,16
Halocnemum	708,13
Juncus	0,07
Shrubbery	914,26
Eucalyptus	507,47
Poterium	2.054,75
Pragmitetum	3.023,41
Sarcocornia	4.740,12
Scirpus	490,7
Water Surface	96.062,95
Tamaricetum	129,36
Agricalture	612,1
Grassland	1.163,11
Artificial	2.257,22
Salt Pan	2.805,15
Unclassified	4,65
Total	**145.324,50**

best scale parameters, shape, color, integrity and softness parameters were determined in order to reveal the difference of flora by running tests. Accordingly, in order to differentiate the flora in the wetlands transparently, firstly the scale was determined as: 25, figure: 0, color: 1, integrity: 1 and softness: 0; whereas in some parts, a bigger scaled segmentation is performed by giving the scale: 0, color: 1, integrity: 1 and softness: 0.

By the formation of classes named as the tree, *Anagyris foetida, Aethrocnemum fruticosum* (L.) Moq., bare land, and sand plains, *Halimione (= Atriplex) portulacoides*, *Halochnemum strobilaceum* (Pall.) Bieb., *Juncus*, shrubbery areas, *Poterium*, *Phragmites*, *Sarcocornia perennis*, *Scirpus*, areas where water is observed on the surface, *Tamaricetum*, agricultural fields, annual natural vegetation and artificial formation such as buildings and etc. the image classification was made with the closest similarity method for species and other objects found in wetlands with an area size that cannot be ignored. When the classification results were evaluated, the spatial distributions of the classes in the research area were determined (Figure 4) (Table 1).

When the obtained results were examined, it was determined that "water surfaces" were mostly distributed with 66.102% in terms of the area covered in the research area. This is followed by the "bare land" that do not have vegetation and formed by sand plains, at 12.75%. "Arthrocnemum" and Sarcocornia species representing halophytes and dune vegetation cover an area of 7,070% and 3,262% respectively. Phragmites plant species, which are mostly located in the delta and close the coastal areas near the irrigation and evacuation channels, are distributed in 2,080% of the area. It was determined that "salt pans" used in salt production in Gediz delta occupy an area of 1,930%. The areas where salt production is determined in the classification are areas covered with salt at the date of shooting of the image. Areas in which the production is in progress and that are still covered with water are classified as water surfaces in order to increase the accuracy of the clas-

sification. It was determined that the artificial formations representing elements such as human-made buildings and roads within the delta occupy 1.553 % of the research area. Poterium species, which are commonly observed in hilly areas within the boundaries of the study area, constitute 1.414% of the area. The classes that form the rest of the area called tree *Anagyris foetida*, *Halimione (=Atriplex) portulacoides*, *Halochnemum strobilaceum* (Pall.) Bieb., *Juncus*, maquis shrubbery, *Scirpus*, *Tamaricetum*, agricultural areas, annual natural vegetation cover an area of 3.81%.

CONCLUSIONS

Continuity in the life cycles of all living beings occurs as a result of their mutual balance and sharing with other species. Wetlands that emerge as a result of these interactions and sharing in certain parts of the earth make positive contributions to the regions in which they are located. In particular, in order to monitor the effects of climate change it is extremely important for the plant species within the wetlands to have different physiological characteristics (shelter, food source, heavy metal absorption, biofilter, carbon reserve, etc.) and it is also crucial to identify their geographical distribution areas, protect the delta and monitor the pollution status. When the data obtained from the research and previous studies on the subject were examined, it was found that object-oriented classification gave better results than pixel-based classification in determining wetland vegetation. In this study carried out as a pilot project, the problems that may be encountered in the determination of wetland vegetations were located, the developing technology and the usability of a method to meet the changing needs were examined.

High-resolution infrared orthophotos have been shown to achieve exceptional results in determination of wetland plant tissue. The spatial resolution of the images was found to be beneficial in distinguishing between lower plants and co-populations. Furthermore, due to the near-infrared (NIR) band of orthophotos, it is considered that the reflection values of plant species carry more accurate and reliable data quality. Therefore, it has been determined that the differences between the species with the reflection values are positively affected the classification results

New developments in remote sensing techniques in the coming years will allow for more detailed monitoring of changes in vegetation within wetlands and between species and will facilitate mapping them. With this opportunity, necessary measures can be taken at the right time for climate change, negative impacts caused by land use and environmental changes occurred due to other anthropogenic effects.

ACKNOWLEDGEMENTS

This study was supported by Ege University Scientific Research Project Fund (Project No: 2013-ZRF-056). I owe a debt of gratitude to Assoc. Prof. Dr. Serdar Şenol Gökhan for his contribution to in situ observation and identification of wetland vegetation in the research.

REFERENCES

[1] RAMSAR (2015) The Fourth Ramsar Strategic Plan 2016-2024. https://www.ramsar.org/sites/default/files/documents/library/4th_strategic_plan_2016_2024_e.pdf. (Accessed July 25, 2019).

[2] Şahin, M.T. (2012) Wetland Issues Faced in Turkey: Şat Delta Sample, Fethiye. Master's thesis. Afyon Kocatepe University the Institute of Social Sciences Department of Geography, Afyon-Turkey (In Turkish).

[3] Shen, G., Yang, X., Jin, Y., Xu, B., Zhou, Q. (2019) Remote sensing and evaluation of the wetland ecological degradation process of the Zoige Plateau Wetland in China. Ecological Indicators. 104, 48-58.

[4] IPCC (2014) 2013 Supplement to the 2006 IPCC Guidelines for National Greenhouse Gas Inventories: Wetlands. Hiraishi, T., Krug, T., Tanabe, K., Srivastava, N., Baasansuren, J., Fukuda, M. and Troxler, T.G. (eds.) Published: IPCC, Switzerland.

[5] Engin, M.S. (2012) An investigation on the heavy metal accumulation of the aquatic plants growing in the Kızılırmak delta and also constructing of the pollution maps. Ondokuz Mayıs University, Graduate School of Sciences, Samsun-Turkey (In Turkish).

[6] Anonymous (2007) Gediz Delta Wetland Management Plan. Republic of Turkey, Ministry of Agriculture and Forestry General Directorate of Nature Protection and National Parks, Wetlands Branch Manager (In Turkish).

[7] Guo, L. and Cutright, T.J. (2017) Metal storage in reeds from an acid mine drainage contaminated field. Int. J. Phytorem. 19(3), 254-261.

[8] Jeke, N.N., Zvomuya, F., Cicek, N., Ross, L. and Badiou, P. (2015) Biomass, nutrient, and trace element accumulation and partitioning in Cattail (L.) during wetland phytoremediation of municipal biosolids. J. Environ. Qual. 44(5), 1541-9.

[9] Guo, L., Perry, B.J., Sutton, C.A., Yan, X., Yang, J. (2019) Using reed to clean strontium and barium contaminated solutions. Fresen. Environ. Bull. 28, 3270-3275.

[10] Dronova, I., Gong, P., Clinton, N.E., Wang, L., Fu, W., Qi, S., Liu, Y. (2012) Landscape analysis of wetland plant functional types: The effects of image segmentation scale, vegetation classes and classification methods. Remote Sensing of Environment. 127, 357-369.

[11] Zomer, R.J., Trabucco, A., Ustin, S.L. (2009) Building spectral libraries for wetlands land cover classification and hyperspectral remote sensing. Journal of Environmental Management. 90(7), 2170-2177.

[12] Ghobadi, Y., Pradhan, B., Shafri, H.Z., bin Ahmad, N., Kabiri, K. (2015) Spatio-temporal remotely sensed data for analysis of the shrinkage and shifting in the Al Hawizeh wetland. Environmental Monitoring and Assessment. 187(1), 4156.

[13] Tulbure, M.G., Broich, M., Stehman, S.V., Kommareddy, A. (2016) Surface water extent dynamics from three decades of seasonally continuous Landsat time series at subcontinental scale in a semi-arid region. Remote Sensing of Environment. 178, 142-157.

[14] Jin, H., Huang, C., Lang, M.W., Yeo, I.Y., Stehman, S.V. (2017) Monitoring of wetland inundation dynamics in the Delmarva Peninsula using Landsat time-series imagery from 1985 to 2011. Remote Sensing of Environment. 190, 26-41.

[15] Amani, M., Salehi, B., Mahdavi, S., Brisco, B. (2018) Spectral analysis of wetlands using multi-source optical satellite imagery. ISPRS Journal of Photogrammetry and Remote Sensing. 144, 119-136.

[16] Dervisoglu, A., Bilgilioglu, B.B., Yagmur, N., Musaoglu, N., Tanik, A. (2019) Temporal assessment of natural wetlands via remotely sensed data: A case study from Turkey. Fresen. Environ. Bull. 28, 1005-1010.

[17] Xie, Y., Zhang, A., Welsh, W. (2015) Mapping wetlands and phragmites using publically available remotely sensed images. Photogrammetric Engineering and Remote Sensing. 81(1), 69-78.

[18] Liu, T., Abd-Elrahman, A. (2018) Deep convolutional neural network training enrichment using multi-view object-based analysis of unmanned aerial systems imagery for wetlands classification. ISPRS Journal of Photogrammetry and Remote Sensing. 139, 154-170.

[19] Davranche, A., Lefebvre, G., Poulin, B. (2010) Wetland monitoring using classification trees and SPOT-5 seasonal time series. Remote Sensing of Environment. 114(3), 552-562.

[20] Poulin, B., Davranche, A., Lefebvre, G. (2010) Ecological assessment of Phragmites australis wetlands using multi-season SPOT-5 scenes. Remote Sensing of Environment. 114(7), 1602-1609.

[21] Rokitnicki-Wojcik, D., Wei, A., Chow-Fraser, P. (2011) Transferability of object-based rule sets for mapping coastal high marsh habitat among different regions in Georgian Bay, Canada. Wetlands Ecology and Management. 19(3), 223-236.

[22] Muro, J., Canty, M., Conradsen, K., Hüttich, C., Nielsen, A.A., Skriver, H., Remy, F., Strauch, A., Thonfeld, F., Menz, G. (2016) Short-term change detection in wetlands using Sentinel-1 time series. Remote Sensing. 8(10), 795.

[23] Whyte, A., Ferentinos, K.P., Petropoulos, G.P. (2018) A new synergistic approach for monitoring wetlands using Sentinels-1 and 2 data with object-based machine learning algorithms. Environmental Modelling and Software. 104, 40-54.

[24] Özen, F, Bolca, M., Atalay, M.O., Şenol, S.G. (2018) Determination of Vegetation in Coastal Section of Great Meander Delta by Using Object-Based Classification. 29th Scientific - Expert Conference of Agriculture and Food Industry 26-28 September. İzmir-Turkey http://agr.ege.edu.tr/files/agr/icerik/agrifood_2018.pdf. (Accessed July 27, 2019)

[25] Lee, T.M., Yeh, H.C. (2009) Applying remote sensing techniques to monitor shifting wetland vegetation: A case study of Danshui River estuary mangrove communities, Taiwan. Ecological Engineering. 35(4), 487-496

[26] Mui, A., He, Y., Weng, Q. (2015) An object-based approach to delineate wetlands across landscapes of varied disturbance with high spatial resolution satellite imagery. ISPRS Journal of Photogrammetry and Remote Sensing. 109, 30-46.

[27] Araya-López, R.A., Lopatin, J., Fassnacht, F. E., Hernández, H.J. (2018) Monitoring Andean high altitude wetlands in central Chile with seasonal optical data: A comparison between Worldview-2 and Sentinel-2 imagery. ISPRS Journal of Photogrammetry and Remote Sensing. 145, 213-224.

[28] Grenier, M., Demers, A.M., Labrecque, S., Benoit, M., Fournier, R.A., Drolet, B. (2007) An object-based method to map wetland using RADARSAT-1 and Landsat ETM images: test case on two sites in Quebec, Canada. Canadian Journal of Remote Sensing. 33(sup1), 28-45.

[29] Amani, M., Salehi, B., Mahdavi, S., Granger, J., Brisco, B. (2017) Wetland classification in Newfoundland and Labrador using multi-source SAR and optical data integration. GIScience and Remote Sensing. 54(6), 779-796.

[30] Akin, A., Berberoğlu, S., Erdogan, M.A., Donmez, C. (2012) Modelling land-use change dynamics in a Mediterranean coastal wetland using CA-Markov chain analysis. Fresen. Environ. Bull. 21, 386-396.

[31] Hopkinson, C., Chasmer, L.E., Sass, G., Creed, I.F., Sitar, M., Kalbfleisch, W., Treitz, P. (2005) Vegetation class dependent errors in lidar ground elevation and canopy height estimates in a boreal wetland environment. Canadian Journal of Remote Sensing. 31(2), 191-206.

[32] Moeslund, J.E., Arge, L., Bøcher, P.K., Nygaard, B., Svenning, J.C. (2011) Geographically comprehensive assessment of salt-meadow vegetation-elevation relations using LiDAR. Wetlands. 31(3), 471.

[33] Karabulut, M. (2015) An examination of temporal changes in Göksu Delta Lakes using different remote sensing techniques. Journal of International Social Research. 8(37), 347-363.

[34] Sun, C., Liu, Y., Zhao, S., Zhou, M., Yang, Y., Li, F. (2016) Classification mapping and species identification of salt marshes based on a short-time interval NDVI time-series from HJ-1 optical imagery. International Journal of Applied Earth Observation and Geoinformation. 45, 27-41.

[35] Darwish, A., Leukert, K., Reinhardt, W. (2003) Image segmentation for the purpose of object-based classification. Geoscience and Remote Sensing Symposium. IGARSS' 03. Proceedings 2003 IEEE International, Vol. 3, pp.2039-2041.

[36] Richmond, O.M.W. (2010) Inferring ecological relationships from occupancy patterns for California Black Rails in the Sierra Nevada foothills. PhD Thesis. University of California, Berkeley.

[37] Dronova, I., Gong, P., Wang, L. (2011) Object-based analysis and change detection of major wetland cover types and their classification uncertainty during the low water period at Poyang Lake, China. Remote Sensing of Environment. 115(12), 3220-3236.

[38] Kim, M., Warner, T.A., Madden, M., Atkinson, D.S. (2011) Multi-scale GEOBIA with very high spatial resolution digital aerial imagery: scale, texture and image objects. International Journal of Remote Sensing. 32(10), 2825-2850.

[39] Rapinel, S., Fabre, E., Dufour, S., Arvor, D., Mony, C., Hubert-Moy, L. (2019) Mapping potential, existing and efficient wetlands using free remote sensing data. Journal of Environmental Management. 247, 829-839.

[40] Tian, B., Zhou, Y., Zhang, L., Yuan, L. (2008) Analyzing the habitat suitability for migratory birds at the Chongming Dongtan Nature Reserve in Shanghai, China. Estuarine, Coastal and Shelf Science. 80(2), 296-302.

[41] Fournier, R.A., Grenier, M., Lavoie, A., Hélie, R. (2007) Towards a strategy to implement the Canadian Wetland Inventory using satellite remote sensing. Canadian Journal of Remote Sensing. 33(sup1), S1-S16.

[42] Özmüş, L., Soylu, M., Ayyıldız, E., Erkek, B., Bakcı, S. (2014) Photogrammetric developments in general directorate of land registry and cadastre. 5th Symposium of Remote Sensing-GIS (UZAL-CBS 2014). 14-17 October 2014, İstanbul. (In Turkish).

[43] Baltsavias, P.E. (1999) Integration of Ortho-Images in GIS, Institute of Geodesyand Photogrammetry Swiss Federal Institute of Technology ETH – Hoenggerberg, CH-8093 Zurich, Switzerland.

[44] Tufan, T. (2012) Orthophoto map production and investigation of use as data source in geographic information system. Doctoral dissertation. Selçuk University, Graduate School of Natural Sciences, Konya-Turkey. (In Turkish).

[45] Laliberte, S.A., Rango, A., Havstad, M.K., Paris, F.J., Beck, F.R., McNeely, R., Gonzalez, A.L. (2004) Object-oriented image analysis for mapping shrub encroachment from 1937 to 2003 in southern New Mexico. Remote Sensing of Environment. 93(1–2), 30, 198-210.

[46] Schmale, F. (1939) The Golmer Luch nature reserve, a plant sociological and ecological study. Doctoral dissertation. Friedrich-Wilhelms-Universitat zu Berlin. (In German)

[47] Davis, P.H. (1965) Flora of Turkey and The East Aegean Islands. Edinburgh University Press, Vol. 1., Edinburgh.

[48] Oberdorfer, E. (1957) South German plant societies plant sociology (Süddeutsche Pflanzengesellschaften Pflanzensoiologie). 10, 1-564. (In German)

[49] Seçmen, Ö and Leblebici, E. (1997) Vegetation and marshy areas of Turkey. Science Faculty of Aegean University, Science Faculty Press, no: 158, Aegean University, Bornova-Izmir, 870p.

[50] Seçmen, Ö., Gemici, Y., Görk, G., Bekat, L., Leblebici, E. (1995) Systematics of Seed Plants. Ege Univ. Science Fac. Book Series No:116, Bornova-İzmir.

[51] Davis, P.H. (1972) Flora of Turkey and The East Aegean Islands. Edinburgh University Press, Vol. 4., Edinburgh.

[52] Ushakova, S.A., Kovaleva, N.P., Gribovskaya, I.V., Dolgushev, V.A., Tikhomirova, N.A. (2005) Effect of NaCl concentration on productivity and mineral composition of Salicornia europaea as a potential crop for utilization NaCl in LSS. Advances in Space Research. 36(7), 1349-1353.

[53] Waisel, Y., Liphschitz, N., Kuller, Z. (1972) Patterns of water movement in trees and shrubs. Ecology. 53(3), 520-523.

[54] Davy, A.J., Bishop, G.F., Costa, C.S.B. (2001) Salicornia L. (Salicornia pusilla J. woods, S. ramosissima J. woods, S. europaea L., S. obscura PW ball & tutin, S. nitens PW ball & tutin, S. fragilis PW ball & tutin and S. dolichostachya moss). Journal of Ecology. 89(4), 681-707.

[55] Kadereit, G., Ball, P., Beer, S., Mucina, L., Sokoloff, D., Teege, P., Yaprak, A.E., Freitag, H. (2007) A taxonomic nightmare comes true: phylogeny and biogeography of glassworts (Salicornia L., Chenopodiaceae). Taxon. 56(4), 1143-1170.
[56] Chapman, V.J. (1950). Biological flora of the British Isles: Halimione portulacoides (L.) Aell. J. Ecol. 38, 214-222.
[57] Carvalho, L.M., Caçador, I., Martins-Loução, M. (2001) Temporal and spatial variation of arbuscular mycorrhizas in salt marsh plants of the Tagus estuary (Portugal). Mycorrhiza. 11(6), 303-309.
[58] Baumeister, W., Kloos, G. (1974) Salt Secretion in *Halimione portulacoides* (L.) Aellen (Über die Salzsekretion bei *Halimione portulacoides* (L.) Aellen). Flora. 163, 310–326. (In German)
[59] Freitas, H., Breckle, S.W. (1992) Importance of bladder hairs for salt tolerance of field-grown Atriplex species from a Portuguese salt marsh. Flora. 187, 283-297.
[60] Jensen, A. (1985) On the ecophysiology of *Halimione portulacoides*. Vegetatio. 61, 231-240.
[61] Akyol, Y., Gemici, Y. (2017) Vegetation Ecology and Ecological Management of Biodiversity of Coastal Aegean (Between Edremit and Gökova Gulfs) in Turkey. Kastamonu Üniversitesi Orman Fakültesi Dergisi. 17(1), 116-123.
[62] Pandza, M., Franjic, J., Skvorc, Z. (2007) The salt marsh vegetation on the East Adriatic coast. Biologia Bratislava. 62(1), 24-31
[63] Özgün, C. (2013) A new and exotic species in the ottoman tree culture: Eucalyptus. Journal of Modern Turkish History Studies. 13(26), 5-29.
[64] Developer, e. (2012) User guide. Trimble Documentation.
[65] Benz, U.C., Hofmann, P., Willhauck, G., Lingenfelder, I. and Heynen, M. (2004) Multi-Resolution, Object-Oriented Fuzzy Analysis of Remote Sensing Data for GIS-Ready Information, ISPRS Journal of Photogrammetry and Remote Sensing. 58(3-4), 239-258.
[66] eCognition (2010) eCognition Software. http://www.ecognition.com/sites/default/files/eCognition_Software.pdf, (accessed Agust 14, 2010).
[67] Im, J., Quackenbush, L.J., Li, M., Fang, F. (2014) Optimum scale in object-based image analysis. Scale Issues in Remote Sensing. Scale Issues in Remote Sensing, First Edition. Edited by Qihao Weng, Published 2014 by John Wiley & Sons, Inc., 197-214

Received: **03.09.2019**
Accepted: **30.01.2020**

CORRESPONDING AUTHOR

Fulsen Ozen
Ege University,
Agricultural Faculty,
Soil Sciences and Plant Nutrition Department
35100 Izmir – Turkey

e-mail: fulsen.ozen@ege.edu.tr
fulyou@gmail.com

© by PSP Volume 29 – No. 04A/2020 pages 2834-2842 Fresenius Environmental Bulletin

A COMPARATIVE STUDY OF CONVENTIONAL COAGULATION AND SLUDGE RECYCLING ENHANCED COAGULATION FOR LOW-TURBIDITY SOURCE WATER: THE EFFECT AND APPLICABILITY

Zipei Li, Lei Fang*, Yan Zhang, Yunxia Miao

College of Civil Engineering and Architecture, Zhejiang University, and Key Laboratory of Drinking Water Safety and Distribution Technology of Zhejiang Province, Hangzhou 310058, China

ABSTRACT

Low coagulation efficiency and high consumption of coagulant are two challenges for low turbidity source water treatment, and sludge recycling enhanced coagulation is generally considered as an effective solution. The effect and applicability of coagulation with sludge recycling was investigated, compared with conventional treatment. In conventional coagulation, the removal efficiency of poly aluminum chloride (PAC) was better than poly aluminum sulfate (PAS) and poly ferric aluminum chloride (PFAC). The economic dosage was 15 mg/L, and the corresponding removal efficiencies of turbidity, COD_{Mn} and UV_{254} were 62.0%, 31.7%, 32.9%, respectively. Recycling sludge could improve the removal efficiency. When 10 mg/L of PAC and sludge with recycle ratio of 6% were added in order, the turbidity, COD_{Mn} and UV_{254} removal efficiencies were 78.8% ,41.6% and 35.8%, respectively. Meanwhile, recycling sludge process increased the system's abilities to resist acid, alkali and turbidity fluctuations. When the initial turbidities were 2NTU and 4NTU, the optimal recycle ratios were both 6%. The floc structures formed from recycling sludge process were tighter and more regular, indicating a better sedimentation property.

KEYWORDS:
Coagulants, Recycling sludge, Low-turbidity, Removal efficiency

INTRODUCTION

In China, the water from reservoir is preferentially used as source water for drinking because the water quality is superior to the river, such as turbidity, COD_{Mn} and metal ions. The reservoirs usually have faced the challenge about low turbidity. The researched was performed in Huzhou. Huzhou is located in the south of China. According to the survey, there were 24 township water treatment plants and 19 of them used the reservoir water sources with low turbidity most of the time [1]. The treatment technology was mainly based on the conventional treatment process. Low management level and unreasonable coagulation dose control resulted in the waste of the coagulants and excessive sludge production in the sedimentation tank. More attention should be paid to optimize the treatment of low turbidity source water.

Though coagulation is considered as the most effective methods to purify drinking water, it is weaker when the initial turbidity is low [2, 3]. Because settling velocity of flocs are relatively slow and water viscosity is stronger [4]. There are lots of methods to strengthen the coagulation, such as enhance coagulant [5, 6], ultrasonic pretreatment technology [7], micro-flocculation filtration process [8], recycling sludge [9] and so on. The above processes and techniques have advantages and disadvantages. Enhanced coagulation method optimizes the coagulation process and improves removal of turbidity, but the removal efficiency of organic matter is limited and the optimized processes are complicated. Zhang et al. treated low-temperature and low-turbidity water by combining high alkalinity polyaluminum chloride (PAC) with high viscosity chitosan complexly, which could achieve the efficient removal of turbidity (around 87%) [10].

The recycling sludge is regarded as the novel method that can further enhance the removal of turbidity and the organic matter [11,12]. Besides, Dassanayake et al. illustrated that it could decrease the discharge of sludge that may have potential hazard on the environments [13]. Xu et al. reported that when recycling sludge and coagulants, such as PAC, were used simultaneously, the organic matter and turbidity removal efficiencies were optimal in bench scale because of physical adsorption and charge neutralization mechanisms [14]. Except for the bench scale, Chen et al. [15] reported that the recycling sludge used directly did not deteriorate the effluent quality in the pilot scale and the quality of effluent water met the national standard requirements. At the same time, there was no significant difference in biogenetic toxicity compared with conventional processes. However, the current research had few investigations on the applicability of recycling sludge in

treating source water with fluctuated qualities, and the mechanism was not clear enough.

Therefore, the main purpose of this project was to study the applicability of recycling sludge in low turbidity source water treatment. The source water in Huzhou Reservoir was treated as the experimental subject. Firstly, the operation parameters in conventional coagulation were optimized, and the treatment effects of different coagulants were compared. Then the research analyzed the treatment ability of sludge recycling enhanced coagulation technology. Through measuring the qualities of effluent water, such as turbidity, COD_{Mn}, UV_{254} and so on, the safety of the technology and the ability of reducing the coagulants consumption were evaluated. In addition, the effects of pH, turbidity of source water, coagulants dosage, recycling sludge ratio and other factors on treatment effects were investigated. At last, the different characteristics of flocs between recycling sludge and non-recycling sludge were compared to discuss the mechanism of enhanced coagulation.

MATERIALS AND METHODS

Raw water characteristics. Table 1 presented a summary of reservoir characteristics in study area. The average of turbidity and COD_{Mn} in the source water were 1.32 NTU and 1.74mg/L separately. The value of the COD_{Mn} was even lower than the standard for drinking water quality (3mg/L). Because of the relatively low value of the data, the source water was characterized as the typical micro-polluted sample in turbidity. The low turbidity water had difficulties in purifying source water.

Materials. The experiments used three coagulants, including poly aluminum chloride （PAC, with 10.83% Al_2O_3 content, basicity was 70.43%） and poly aluminum sulfate (PAS, with 18.5% total iron content , basicity was 9-14%), poly ferric aluminum chloride (PFAC, with 29% Al_2O_3 and 1-2% Fe_2O_3, basicity was 60-90%). Three of them were industrial grades and satisfied national standards, obtained from Meiyuan source water purification material company of Gongyi city in China. The other laboratory reagents used in this study were all purchased from Sinopharm Chemical Reagent Co., Ltd (Shanghai, China). The chemical of chemically pure grade (CP) used was Nessler Reagent. The analytical reagents (AR) included L-ascorbic acid, hydrochloric acid, sodium hydroxide, potassium sodium L - tartrate tetrahydrate and sodium oxalate. And the guaranteed reagents (GR) applied were sulfuric acid, nitric acid and potassium permanganate.

Bench-scale experiments. Bench-scale experiments used a programmable jar testing apparatus (ZR4-6, Zhong-Run Jar Test Instruments, China) with six glass-round beakers and stainless steel mixing paddles. The coagulation processes included three steps: rapid mixing, slow mixing flocculation and sedimentation. The test was worked with following procedure: 200r/min rapid mixing stage for 40s, subsequently coagulation at 135 r/min for 80s, flocculation at 70 r/min for 6min, and sedimentation for 40 min. The sludge was added 30 seconds prior to coagulation in the raw water. Each experiment was performed in duplicate. The appropriate solution pH was adjusted by 0.1 mol/L HCL and 0.1 mol/L NaOH. The appropriate turbidity was adjusted by source water from reservoir and river.

Analytical methods. The turbidity, UV_{254}, COD_{Mn}, pH, iron, aluminum and manganese in the source water were detected by relevant instruments. All analytical methods referred to the national standard examination methods that are promulgated by the Ministry of Health, P. R. China (GB/T5750-2006) [16]. COD_{Mn} was measured by acidic potassium permanganate titration, using water bath (Jieruier HH-6, China). Total concentrations of iron and manganese were measured by Atomic Absorption Spectrophotometer (900t, PerkinElmer, USA). The concentration of aluminum was measured by spectrophotometric method of chrome azurol S, using UV-VIS spectrophotometer (Hach DR 5000, USA). The turbidity was determined using turbidity meter (Hach 2100P, USA), and the pH was measured using portable meter (Hach HQ30d, USA) with pH probe. The UV absorbance at 254 nm (UV_{254}) was determined by UV-VIS spectrophotometer (Hach DR 5000, USA).

TABLE 1
characterization of source water

Parameter	Units	Min-max	average
temperature	℃	11.00-27.90	20.35
pH	/	6.80-7.20	7.02
Turbidity	NTU	0.34-8.25	1.32
Chemical Oxygen Demand (COD_{Mn})	mg/L	0.70-3.62	1.74
Fe	mg/L	0.02-0.50	0.11
Mn	mg/L	ND-0.20	0.10
ammonia nitrogen	mg/L	0.02--0.3	0.06
Total nitrogen	mg/L	1.37-2.75	2.03
Total phosphorus	mg/L	ND-0.03	0.02

TABLE 2
characterization of sludge

Parameter	Units	sludge
Turbidity	NTU	200-956
Moisture Content	%	99.90
Organic Content	%	26.42
TOC	mg/L	6.20
Resistance	s^2/g	$0.65*10^9$
pH	/	8.00
Na	mg/kg	$5.57*10^3$
Ca	mg/kg	$2.01*10^2$
Mg	mg/kg	$3.74*10^3$
Fe	mg/kg	$3.72*10^4$
Al	mg/kg	$2.14*10^5$
Mn	mg/kg	$2.24*10^3$
Si	mg/kg	50.00

For the sludge supernatant (precipitation for 24 hours), the detection methods were the same as source water. For sludge, the elements were detected by Jiangsu Micro Spectrum Detection Technology Co., Ltd. Scanning electron microscope （SEM, FEG650, Quanta, USA）was used to observe the structures of flocs.

RESULTS AND DISCUSSION

Characterization of sludge from drinking water treatment. The detailed characteristics of sludge were showed in Table 2. Heavy mental levels measured in alum sludge were significantly lower and consistent with other nonhazardous wastes. The ranges of elements from recycling sludge were consistent with those reported by Dassanayake et al. [13].

Since the solid from recycling sludge precipitated in the coagulation process and the supernatant had obvious effects on the qualities of effluent water, the characteristics of sludge supernatant (Precipitation for 24 hours) should be attention. They were detected as the following: pH 8.04, turbidity 4.14NTU, ammonia nitrogen 0.483 mg/L, COD_{Mn} 3.65 mg/L, UV_{254} 0.021 AU/cm, aluminum 0.24mg/L, iron 0.151 mg/L, manganese 0.449 mg/L. It could be seen that after precipitation, most of the detecting substance were significantly higher than the source water. The average turbidity of the sludge supernatant was 3.13 times than that of the source water, which indicating the supernatant still contained suspended particulate matters. The content of ammonia nitrogen in the sedimentation tank was higher than that of the source water. The sludge had the risk of anaerobic decay to produce ammonia nitrogen in the bottom. The data of COD_{Mn} indicated that many organic matters were still concentrated in the suspended solids. The concentration of the aluminum was higher, because the water treatment plants used PAC as the coagulant. But residual coagulants were mainly attached to the floc, resulting in low concentration of ionic aluminum freed in the supernatant. For manganese, it may be related to the long sludge discharge period of the sedimentation tank. The enriched manganese reduced and dissolved because of the anaerobic environment of the bottom. The data suggested that when the sludge from the sedimentation tank was directly reused in a certain proportion, attention should be paid to whether the other elements in the effluent exceeded the standard.

By comparison, UV_{254} was generally lower than the source water, indicating that the lignin, humus and various organic substances containing unsaturated bonds such as conjugated double bonds or hydroxyl groups and benzene rings were low in the sludge supernatant.

Effect of different coagulants. The removal performances of turbidity were investigated with different dosages of PAC, PAS and PFAC. As seen from Fig. 1, the turbidity removal efficiencies of the three coagulants follows the order PAC＞PAS＞PFAC. When the dosage of coagulants was relatively small, the removal effect generally increased as the dosage increased. After reaching a certain level, the removal effect gradually decreased. When the dosage is low, it is difficult to form flocs or the flocs are small, which results in precipitating difficultly because of low specific gravity. As the dosage increases, the flocs become larger and larger. The denser the compaction is, the faster the sedimentation speed is. When the dosage gradually increases to reach a certain extent, the removal efficiencies were the best. After the coagulants continually increasing, it means to introduce a new turbidity, resulting in the same charge in the water as the formed flocs. Then the flocs enter the re-stabilization zone which are difficult to settle, so the turbidity gradually increases.

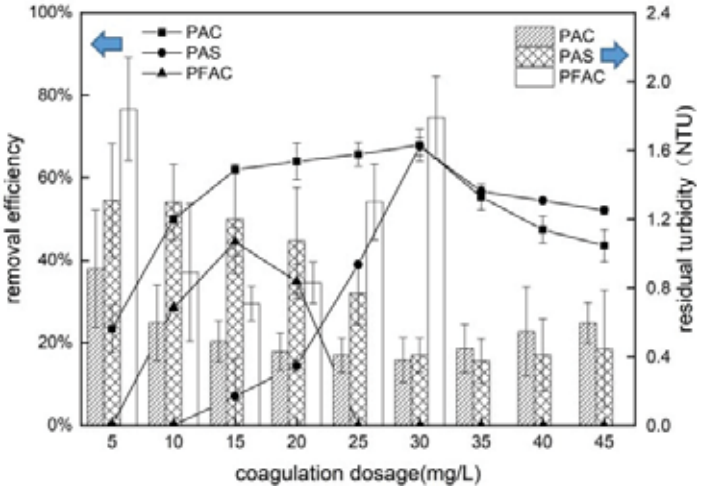

FIGURE 1
Effect of different coagulant and dosage on turbidity removal efficiency and residual turbidity

For PAC, the most optimal dosage was 30 mg/L. The turbidity removal efficiency and residual turbidity reached 67.9% and 0.38 NTU respectively. For PAS, the optimal dosage was also 30mg/L, and the treatment efficiencies were similar to PAC. The turbidity removal efficiency and residual turbidity reached 67.6% and 0.375 NTU separately. However, it could be observed that when the dosages of PAS were less than 30 mg/L, the removal rate was lower than the counterpart removal abilities of PAC. PFAC is an inorganic polymer coagulant which is hydrolyzed by aluminum salt and iron salt [17]. The flocs form quickly and have high adsorption performance. The optimal dosage of PFAC was 15 mg/L in the research, but the residual turbidity was significantly higher than PAC. It may be that PFAC is more suitable for high turbidity water, rather than low turbidity source water.

For the dosages of 5 to 20 mg/L, the removal efficiencies of PAC increased rapidly, while those of PAS increased slowly. The removal efficiencies of PFAC had the summit in this range. The order of turbidity removal efficiencies was PAC>PFAC>PAS. For the dosages of 20 to 30 mg/L, the removal efficiencies of PAC and PAS increased rapidly and reached summits simultaneously. By compared, the removal efficiency of PFAC rapidly decreased. For the dosage larger than 30mg/L, the efficiencies of PAC and PAS both decreased, while PFAC showed nearly no removal efficiencies. The order was PAS> PAC> PFAC. The different removal efficiencies of different coagulants were decided by the characteristics and contained substances of coagulants.

Considering the following process had the filter tank, which could also remove the pollutants from the water, so the residual turbidity in the effluent of sedimentary tank less than 0.8 NTU was enough. In this research, when the PAC dosage was 15 mg/L, the removal efficiency was 62.0% and the residual turbidity met the demand. PAC with the dosage of 15mg/L was adopted for the following studies, considering economy and environmental friendliness.

Effect of recycling sludge. Previous studies reported that recycling sludge that was untreated may introduce turbidity into the source water. Turbidity, COD_{Mn} and UV_{254} were measured in order to observe the effect of sludge recycling. Fig.2 illustrated that the turbidity removal efficiencies were improved by about 20%. For example, when the PAC dosage was 15 mg/L, the turbidity removal efficiency increased from 62.0% to 81.6%. The turbidity removal efficiencies greatly met the demands of following treatment. By contrast, COD_{Mn} and UV_{254} removal efficiencies increased slightly, about 10%. The effluent COD_{Mn} did not exceed the specified limit(<3mg/L). The effect of recycling sludge on the enhanced removal of organic matter was not obvious. On one hand, the recycling sludge had relatively higher value of COD_{Mn}. On the other hand, the probability of collision between particles increased in the high turbidity range. The possibility of forming flocs to larger size particles increased. The large particles absorbed PAC, resulting in the reduction of PAC. The COD_{Mn} removal efficiency was limited because of lacking of the adsorption point with coagulation.

Meanwhile, the recycling sludge did not have negative effects on the effluent quality, such as color, UV_{254} and aluminum. Qi et al. illustrated that recycling alum sludge combined coagulant (PAC) was used to remove the turbidity up to 89.2% in the simulated source water, which was better than the process without recycling sludge [18]. With recycling sludge, the turbidity of the source water increased. That could increase the concentration of impurities in the water, and provide a new point of adsorption. Then, the opportunity and frequency for particle collision could be improved to get a positive influence on removal efficiency.

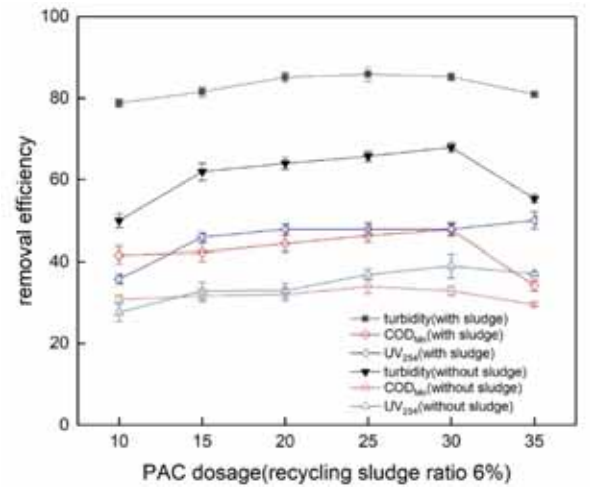

FIGURE 2
Effect of the dosage of PAC and the recycling sludge on removal efficiency

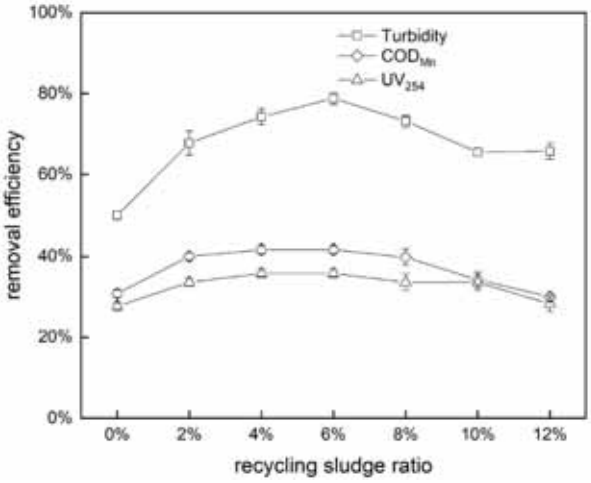

FIGURE 3
Effect of different recycling sludge ratio on removal efficiency

The Fig.3 illustrated that recycling sludge ratio effected the removal efficiency. The 10 mg/L of PAC was added in the process. When the recycling sludge ratio was 6%, the removal efficiencies reached summits. The turbidity, COD_{Mn}, UV_{254} removal efficiencies were 78.8% ,41.6% and 35.8%, respectively. The 6% of recycling sludge ratio was optimal and fit for the reservoir.

The benefit of improving removal efficiencies was to reduce the dosage of added coagulants. The turbidity removal efficiency of the 10mg/L PAC dosage with recycling sludge was much higher than that of the process with optimal dosage of coagulation and non-recycling sludge. Using recycling sludge could reduce the coagulant dosage by up to 33.3%.

Effect of solution pH. Solution pH ranged from 4 to 9 which was set in the experiment. The Fig. 4(a) showed that the effect of the initial pH on the performance when 15 mg/L of PAC was added to the source water.

According to Fig. 4(a), the highest reduction of the evaluated parameters occurred at a weak alkaline pH. PAC presented a maximum turbidity removal of 67.3% at pH of 7. The maximum COD_{Mn} and UV_{254} removal were 32.5% and 47.2% respectively at pH of 8. The turbidity removal efficiencies were between 38.6% and 67.3% from relatively efficient pH range (pH=6-9). In the same range, The COD_{Mn} removal were between 27.3% and 32.5% and the UV_{254} removal were between 29.6% and 47.2%.

The hydrolysis products of PAC were monomeric which had no obvious agglutination at low pH, which was reported by Zhou et al. [19]. At high pH, the hydrolysis products are low-charge hydroxide gels such as $Al(OH)_3$ and $Al(OH)_4^-$, which have the negative influence on coagulation. When the pH ranges in the neutral value, the multinuclear hydrolysate such as $Al_7(OH)_{17}^{4+}$, $Al_{16}(OH)_{15}^{3+}$ can adsorb

particles to compress the electric double layer to destabilize the particles, benefiting the coagulation [20].

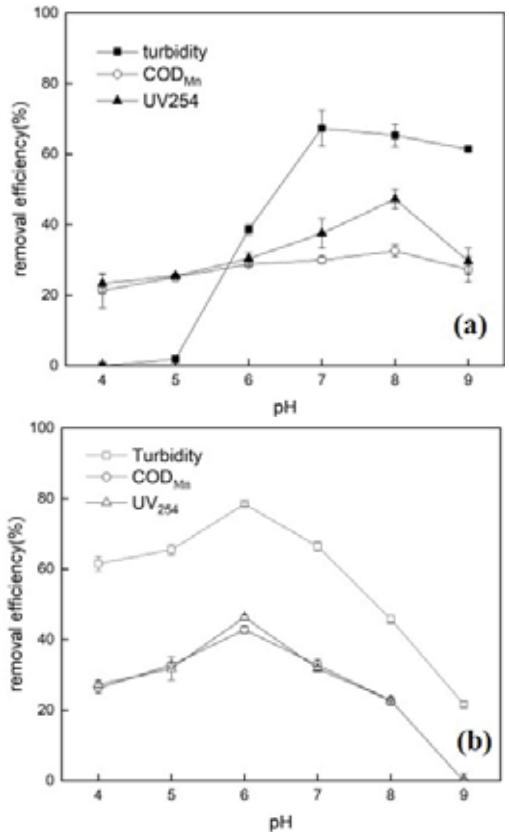

FIGURE 4
Effect of solution pH on removal efficiency
(a) without recycling sludge
(b) with recycling sludge (6%)

The Fig.4(b) showed the different performance adding 15 mg/L of PAC and 6% recycling sludge in order. When pH range was from 4 to 8, the turbidity (45.8%-78.4%) and COD_{Mn} (22.4%-42.8%) removal efficiencies were relatively great. These presented that the relatively optimal pH range was wider than the situation without recycling sludge. And the summits were also better. It was worth noting that UV_{254}(22.7%- 46.4%) had less changes. In a word, the wider range showed that the recycling sludge could not only improve the acid and alkali resistance in the source water, but also improve the treatment ability. For example, the turbidity and COD_{Mn} increased up to about 10% at peak. From the figure, the removal efficiencies with recycling sludge were lower than the efficiencies without sludge at the alkaline, while the efficiencies were higher at the acidity pH. The optimal removal efficiencies were presented at pH of 6 with recycling sludge. The reason was that the recycling sludge was alkaline (pH=8), which make the optimal pH moved to 6.

Effect of solution turbidity. The turbidity of the reservoir in Huzhou was fluctuating, and the summit was 8.25NTU and the lowest was 0.34 NTU from 2015 to 2017. The coagulant dosage depended on the quality of the influent water. The optimal coagulant dosage for different initial turbidity was needed to explored. The Fig.5(a) showed the effect of solution turbidity with different dosage in the process without recycling sludge. When the dosage of coagulant was less than the specific value, the residual turbidity increased with the initial turbidity of the raw water increased. With the dosage increased, the effects of different initial turbidities were weakened, which led to closed residual turbidities of samples with different initial turbidities. It was common that high dosage of coagulant to remove particles from the water was required when there were many suspended colloidal particles in water. The extra coagulant could improve the ability of removal efficiencies, but the waste was vast. The economic dosage would be helpful to guide the management of water treatment plants.

As seen from the Fig.5(a), the 15mg/L of PAC dosage that was the economic dosage mentioned before met the standard of the coagulation effluent water quality when the turbidities were 2NTU, 4NTU and 6NTU. However, when the initial turbidity was 8NTU, the residual turbidity was 1.67 NTU which did not meet the demand of following processes. The dosage should be improved by 25mg/L, and the residual turbidity was 0.56 NTU. These experiments could further guide the management of the water treatment plants. These suggested that the initial turbidity had a significant fluctuation, resulting in frequent change in coagulant dosage.

When the coagulant dosage was 15 mg/L, the turbidity removal efficiencies were 67.9% ,80.7% and 88.3% when the initial turbidities were 2 NTU, 4NTU and 6NTU separately. The results illustrated that relatively high initial turbidity improved the removal potential. When the initial turbidity was 8NTU, the removal efficiency was 79.4%, which was less than the turbidity removal of 6NTU. The reason was that the 15mg/L of dosage did not reach the optimal condition at source water of 8 NTU, resulting in the high effluent turbidity. When the coagulant dosage was 25 mg/L, the highest removal efficiency was 93.0% at the initial turbidity of 8 NTU. Through statistical analysis, the ability of removal efficiencies basically increased as the initial turbidity increased.

The applicability of adding recycling sludge to the drinking water treatment has been researched by simulating different initial turbidities, ranging from 2 NTU to 8 NTU. The data were demonstrated in Fig. 5(b). When the 6% recycling sludge and 10mg/L PAC were added, the turbidity removal efficiencies were 78.9%、83.1%、83.6% and 84.4% in source water of 2 NTU、4 NTU、6NTU and 8NTU. Alt-

hough the PAC dosage decreased, the removal efficiencies were similar with that of the process with only 15mg/L PAC added. As the turbidity of source water increased, the removal efficiencies of the recycling sludge process were improved, and most of them were above 80%. The trend was more obvious with the increase of recycling sludge ratio. Though the influent water turbidity was fluctuated, a relatively low dosage of coagulant and recycling sludge could meet the need of the removal demand and improve the ability against the change of turbidity, which could decrease the dosage of coagulant. That had great potential in the environment and economy.

The optimal recycling ratios were both 6% when the initial turbidities were 2NTU and 4NTU.The turbidity removal reached 78.9% and 83.1% separately. When the initial turbidities were 6NTU and 8NTU, the optimal recycling ratio improved up to 8% and 10% separately. The turbidity removal reached 86.6% and 88.3% separately. The optimum recycling sludge ratio increased as the initial turbidity increased. Because high turbidity source water required more recycling sludge to provide contact points and residual coagulants.

Surface morphology of flocs. Observed through SEM, the flocs in conventional treatment had loose and irregular structure, rough surface, and large voids. When sludge was recycled, the flocs had tight and regular structure, fewer cracks, and better surface uniformity. The flocs mainly existed by big particles. It could be concluded that the low turbidity water with coagulants led to the poor sedimentation and a large amount of coagulants needed to be added. However, the situation changed when the recycling sludge was added. The floc particles produced were tightly combined. The dispersed particles were less to be founded and the flocs were relatively easy to settle, so that a better turbidity removal efficiency or less coagulation dosage could be achieved.

The recycling sludge has two aspects to enhance coagulation. On the one hand, the recycling sludge introduces flocs in the sludge, which enhances the concentration and size of the particles in the water. On the other hand, the recycling sludge contains the remaining PAC, which is equivalent to increasing the coagulant. The aluminum hydroxide precipitate in sludge provide nucleating sites for physical collision, and that sweep coagulation might play a key role in the enhancement of coagulation in low-turbidity source water.

CONCLUSIONS

This work indicated that coagulation with recycling sludge can not only reduce the dosage of coagulants in low-turbidity source water, but also reduce the discharge of sludge and reduce the adverse impact on the environment. The experimental results suggested that enhanced coagulation with recycling sludge had a good application prospect and economic worth for production practices.

(1) PAC showed the best coagulation efficiency compared with PAS and PFAC, and the economic dosage was 15mg/L.

(2) Recycling sludge could enhance the removal efficiencies of turbidity, COD_{Mn} and UV_{254} by 19.6%,10.1% and 13.0% separately when recycling sludge ratio of 6% and PAC of 15mg/L were added.

(3) Coagulation with recycling sludge could improve the resistance to acid and alkali and removal efficiencies. The PAC coagulant presented a maximum turbidity removal of 67.3% at pH 7 without recycling sludge. With recycling sludge, the maximum turbidity removal was 78.4% at pH 6.

(4) A relatively low dosage of coagulant with recycling sludge could meet the need of the removal demand and improve the ability against the turbidity fluctuation. In a specific initial turbidity range of source water, the optimum recycling sludge ratio increased as the initial turbidity increased.

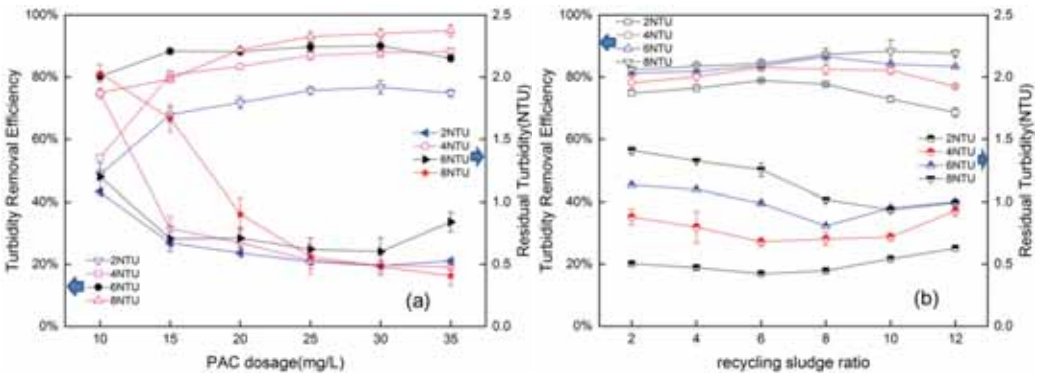

FIGURE 5
Effect of different solution turbidity on removal efficiency
(a) without recycling sludge (b)with recycling sludge

ACKNOWLEDGEMENTS

This research was supported by the National Science and Technology Major Project for Water Pollution Control and Treatment of China (No. 2017ZX07201003), and the National Natural Science Foundation of China (No. 51808489).

REFERENCES

[1] Fang, L., Shi, X.F., Pan, R.J., and Wu, Q. (2017) Water quality characteristic analysis about three different types of surface drinking water sources: A study case of Huzhou, China. Fresen. Environ. Bull. 26, 969-976.

[2] Lou, I.C., Gong, S.Y., Huang, X.J., and Liu, Y.J. (2012) Coagulation optimization for low temperature and low turbidity source water using combined coagulants: A case study. Desalination and Water Treatment. 46, 107-114.

[3] Song, W.C., Li, X., Sun, S.H., Yang, Y.L., and Jia, R.B. (2015) Test Study of Enhanced Coagulation for Conventional Treatment with Low Temperature and Low Turbidity. Journal of Residuals Science and Technology. 12, S39-S46.

[4] Cheng, W.P., Chi, F.H., Li, C.C., and Yu, R.F. (2008) A study on the removal of organic substances from low-turbidity and low-alkalinity water with metal-polysilicate coagulants. Colloids and Surfaces a-Physicochemical and Engineering Aspects. 312, 238-244.

[5] Yin, J., Liu, Z.S., Wang, T.J., Zhao, K., Cui, Y.B., and Tan, X.J. (2006) Enhanced coagulation for improvement of water quality in full-scale water treatment. 5th World Water Congress: Drinking Water Quality and Treatment. 6, 75-79.

[6] Edzwald, J.K., and Tobiason, J.E. (1999) Enhanced coagulation: US requirements and a broader view. Water Science and Technology. 40, 63-70.

[7] Yang, J., Ma, J., Wang, Y., Wu, D., Cao, P., Li, S., and Han, W. (2016) Ultrasonically enhanced coagulation of low turbidity and low temperature water. China Water and Wastewater. 32, 31-34.

[8] Wang, Z.Q. (2012) Application of micro-flocculation direct filtration process in the expansion project of Xin'anjiang water treatment plants. Water and Wastewater. 48, 59-61. (in Chinese).

[9] Foroughi, M., Chavoshi, S., Bagheri, M., Yetilmezsoy, K., and Samadi, M.T. (2018) Alum-based sludge (AbS) recycling for turbidity removal in drinking water treatment: an insight into statistical, technical, and health-related standpoints. Journal of Material Cycles and Waste Management. 20, 1999-2017.

[10] Zhang, Z., Jing, R., He, S., Qian, J., Zhang, K., Ma, G., Chang, X., Zhang, M.K., and Li, Y. (2018) Coagulation of low temperature and low turbidity water: Adjusting basicity of poly aluminum chloride (PAC) and using chitosan as coagulant aid. Separation and Purification Technology. 206, 131-139.

[11] Qi, L., Cheng, R., Wang, H.C., Zheng, X.A., Zhang, G.M., and Li, G.B. (2011) Recycle of alum sludge with PAC (RASP) for drinking water treatment. Desalination and Water Treatment. 25, 170-175.

[12] Chu, W. (1999) Lead metal removal by recycled alum sludge. Water Research. 33, 3019-3025.

[13] Dassanayake, K.B., Jayasinghe, G.Y., Surapaneni, A., and Hetherington, C. (2015) A review on alum sludge reuse with special reference to agricultural applications and future challenges. Waste Management. 38, 321-335.

[14] Xu, Y.P., Chen, T., Liu, Z., Zhu, S., Cui, F., and Shi, W. (2016) The impact of recycling alum-humic-floc (AHF) on the removal of natural organic materials (NOM): Behavior of coagulation and adsorption. Chemical Engineering Journal. 284, 1049-1057.

[15] Chen, T., Xu, Y., Wang, D., Shi, W., and Cui, F. (2016) The impact of recycling sludge on water quality in coagulation for treating low-turbidity source water. Desalination and Water Treatment. 57, 14433-14442.

[16] Ministry of Health, P. R. China. (2006) Standard examination methods for drinking water (GB/T 5750-2006). China Zhijian Publishing House.

[17] Yang, Y.L., Li, X., Nie, X.F., and Li, G.B. (2006) Experimental study of phosphorus removal technique by coagulation in drinking water treatment. Journal of Harbin Institute of Technology. 39, 989-992. (in Chinese).

[18] Qi, L., Wang, Y., Lang, H., Li, G.B. (2009) Enhanced effect of sludge reusing and PAC adsorption process on organic matter removal. Journal of Harbin University of Commerce (Natural Sciences Edition). 25, 524-527. (in Chinese).

[19] Zhou, Z., Yang, Y., Li, X., Gao, W., Liang, H., and Li, G. (2012) Coagulation efficiency and flocs characteristics of recycling sludge during treatment of low temperature and micro-polluted water. Journal of Environmental Sciences. 24, 1014-1020.

[20] Yang, Z.L., Gao, B.Y., Wang, Y., Wang, Q., and Yue, Q.Y. (2011) Aluminum fractions in surface water from reservoirs by coagulation treatment with polyaluminum chloride (PAC): Influence of initial pH and OH-/Al3+ ratio. Chemical Engineering Journal. 170, 107-113.

Received: **06.09.2019**
Accepted: **21.01.2020**

CORRESPONDING AUTHOR

Lei Fang
Institute of Municipal Engineering,
Zhejiang University,
Hangzhou 310058 - P.R. China.

e-mail: fanglei1999@zju.edu.cn

© by PSP Volume 29 – No. 04A/2020 pages 2843-2849 Fresenius Environmental Bulletin

YIELD AND QUALITY TRAITS OF SOME SILAGE MAIZE CULTIVARS

Hakan Kir*

Kirsehir Ahi Evran University, Faculty of Agriculture, Department of Field Crops, Kirsehir, Turkey

ABSTRACT

The research was carried out under Kırşehir ecological conditions in 2016 and 2017 vegetation period. The experimental layout was randomized blocks with three replications. In this study, 10 hybrids and one composite maize cultivars were evaluated for some yield and quality characteristics. Important yield and quality characteristics green herbage yield (tons ha^{-1}), dry matter yield (tons ha^{-1}), crude protein yield (tons ha^{-1}), ADF (%), NDF (%), ADL (%) digestible dry matter ratio (%) and digestible dry matter yield (tons ha^{-1}) were determined. Significant differences were found between cultivars in terms of yield and quality. The two-year mean values of dry matter yield, crude protein yield and digestible dry matter yield indicated that Kerbanis, Karadeniz Yıldızı and Samada-07 were the high yielding cultivars. The ADF, NDF and ADL ratios which are the quality indicators, of high yielding cultivars were also low. The results revealed that the high-yielding cultivars are also prominent in terms of important quality criteria. Kerbanis, Karadeniz Yıldızı and Samada-07 cultivars are suitable for silage maize production considering the yield and quality characteristics and can be recommended for Kırşehir and similar ecologies.

KEYWORDS:
Zea mays L. Yield, Quality, Crude protein, DDMY

INTRODUCTION

The demand for high quality forage has gained more importance following the recent improvements in genetic capacities of animal races. Animal breeders are having problems in supplying forage with sufficient quantity and quality. Plant residues which are even far from meeting the forage required for the daily life share of animals are being used [1]. The prominent relationship between feeding and animal performances increases the need for quality forage resources. Silo fodder crops are capable of responding to the need as a source of high yielding and quality feed [2]. Maize (*Zea Mays* L.) is widely cultivated under different environmental conditions [3, 4]. Silage maize must be irrigated to achieve rapid growth and high yield in arid regions. The temperature in addition to irrigation positively affects the growth rate and overall growth of plants. Climatic conditions in any region are the main determinant factor in the choice of maize cultivar [5]. Kuşvuran et al. [6] reported that the green herbage and dry matter yield of cultivars ranged from 84.6-131.9 and 28.4-41.6 tons ha^{-1}, crude protein yield was between 1.5 and 2.6 tons ha^{-1}, and recommended Carella, Larigal, Cadiz, Composite Arifiye and NK Arma cultivars for the Central Kızılırmak Basin and similar ecological conditions. Çarpici [7] stated that ADF ratio of Bora, DK626, Luce and Sincero cultivars were between 24.7 and 27.1%, and the NDF ratio was between 50.5 and 55.9%. The ADF and NDF contents are known as the important chemical quality criterion of the forage. The increase in ADF ratio reduces the quality and the high NDF ratio decreases the animal intake of forage [8]. Keleş and Türk [9] stated that dry matter ratios of Trojan, C955, Poncho and Albero cultivars under semi-arid Banaz conditions, dry matter yields was between 11.1 and 15.6 tons ha^{-1} and crude protein yield was between 0.8 and 1.4 tons ha^{-1}, and indicated that Trojan cultivar may be suitable for the region. Determining the accurate cultivar is important to meet the demand for quality forage and to increase the cultivation of silage maize, which is an important component in feeding of dairy cattle. This study was carried out to determine the yield and quality traits of maize cultivars which have growing potential in the Central Anatolia region of Turkey for providing the yield and benefit expected from silage.

MATERIALS AND METHODS

This study was carried out under irrigated conditions in terrestrial climate of Kırşehir ecological conditions (39° 08' N, 34° 06' E and 1084 m altitude) for two years (2016 and 2017). Ten hybrids (Kerbanis, Motril, Atlas, Colonia, Klips, Kalusses, Kilowatt, Kalumet, Doge, Samada-07) and one composite (Karadeniz Yıldızı) maize cultivars obtained from private seed companies were used as plant materials of the experiment. (Table 1). Soils of the experimental field had a clay loam texture. Soil pH was considered slightly alkaline (pH, 7.96), and electrical conductivity (738.6 µS cm^{-1}) indicated no salinity

TABLE 1
Sources of maize cultivars

Cultivars Name	Cultivars of Source
Kerbanis	KWS Saat Se & Co. KGaA
Motril	May Seed
Atlas	May Seed
Karadeniz Yıldızı	Black Sea Agricultural Research Institute
Colonia	Agromar Seed
Klips	KWS Saat Se & Co. KGaA
Kilowatt	KWS Saat Se & Co. KGaA
Kalumet	KWS Saat Se & Co. KGaA
Doge	KWS Saat Se & Co. KGaA
Samada	Black Sea Agricultural Research Institute

TABLE 2
Climate data of the experimental site

Months	Mean Temperature (°C)			Total Precipitation (mm)		
	2016	2017	Long Term	2016	2017	Long Term
June	21.0	20.7	19.6	16.1	18.4	36.8
July	24.2	23.9	23.1	5.8	0.4	6.8
August	25.7	23.5	22.9	-	16.0	4.9
September	18.4	21.4	18.2	42.0	-	11.6
Mean	22.3	22.4	21.0			
Total				63.9	34.8	66.4

problem to limit vegetative production. Organic matter content (1.09%) was low. While lime content was very high (35.29%). According to Sillanpää [10] classification; the plant available phosphorus content was sufficient (0.1 tons ha^{-1}) and the available potassium content (2.4 tons ha^{-1}) was very high [11]. The average temperatures for the months of June, July, August and September in 2016 and 2017 were 22.3 and 22.4 °C, and the total precipitations were 63.9 and 38.4 mm (Table 2). The average temperatures in both years were above the long-term averages, while the total precipitation was below the long-term total precipitation (Table 2). Maize can be grown without irrigation in the regions where the annual rainfall is between 400 and 750 mm [6]. Therefore, the amount corresponding to rainfall has been provided by the drip irrigation system to prevent yield loss in our region where water is limited [7]. The experiments were conducted on June 2, 2016 and 2017 with 3 replicates and designed as randomized blocks. Maize cultivars were sown in 4 rows at 70 cm interrow and 20 cm intra row spacings. The plot size was 2.8 m x 5 m: 14 m^2. Total phosphorus (0.08 tons ha^{-1} P_2O_5 as Triple Super Phosphate) and half of the nitrogen (0.075 tons ha^{-1} N) fertilizers were applied at the time of sowing, while the remaining half nitrogen when plant height was 45-50 cm [12]. Silage maize harvest was carried out in two rows outside the side effect at the dough stage [9]. The samples collected from each plot were dried at 65 °C to a constant weight. The dry matter yields were calculated by multiplying the dry matter ratios and the green herbage yields determined by the harvest. Nitrogen contents of the cultivars were determined by Kjeldahl method, and these values were multiplied by a coefficient (6.25) to obtain the crude protein ratios [13]. Crude protein yields were determined by multiplying crude protein ratios and hay yields. The concentrations of insoluble fiber in neutral detergent (NDF), fiber insoluble in acid detergent (ADF) and lignin insoluble in acid detergent (ADL) were determined by ANKOM200 Fiber analyzer according to the methods reported by Van Soest et al. [14], [15, 16]. The digestible dry matter ratio was calculated by using equation (DDMR=88.9-0.779 x ADF%) of Horrocks and Valentine [17]. The digestible dry matter yields were calculated by multiplying digestible dry matter ratio by dry hay yield. The data were subjected to variance analysis test according to the randomized block design using MSTAT-C software, and the differences between the data were compared with the Duncan test [18].

RESULTS AND DISCUSSION

Green Herbage Yield. The cultivars and years had statistically significant effects ($p<0.01$) on green herbage yield. The significant differences of green herbage yield between years and cultivars caused to the significance of years x cultivars interaction on green herbage yield (Table 3). The highest herbage yield was obtained from Kilowatt (73.0 tons ha^{-1}) cultivar while the lowest herbage yield was obtained from Kalumet (54.5 tons ha^{-1}) cultivar (Table 4). Mean green herbage yield (67. 1 tons ha^{-1}) in the first year of the experiment was higher than that of the second year (65.7 tons ha^{-1}) (Table 4). Motril and Samada-07 cultivars were included in same groups at the first year, while they were placed in the different group at the second year, which resulted in significant year x cultivar interaction (Table 4). The

TABLE 3
Summer of variance analysis

Analysis of Variance	Df	Green Herbage Yield	Dry Matter Yield	Crude Protein Yield	ADF Ratio	NDF Ratio	ADL Ratio	Digestible Dry Matter Ratio	Digestible Dry Matter Yield
Year	*1*	**	*ns*	*	**	**	*	**	*
Error1	*4*								
Cultivars	*10*	**	**	**	**	**	**	**	**
YxC	*10*	**	**	**	**	**	*ns*	**	*
Error	*40*								
CV (%)		*2.1*	*3.1*	*7.3*	*4.7*	*4.2*	*6.7*	*1.1*	*3.2*

CV: Coefficient of variation. Y: Year, C: cultivar, ns: non significant ** $p<0.01$ * $p<0.05$.

difference between years can be attributed to the C4 nature of maize that was positively affected by the high temperature in the first year of June, July, August and thus yielded higher biomass. Significant differences were reported for herbage yields of maize cultivars grown as the main or second crops in studies conducted at different ecologies of Turkey. The herbage yields reported ranged between 79.8 and 90.1 tons ha^{-1} in İzmir-Bornova [19], 68.9 and 84.9 tons ha^{-1} in Karaman [20], 46.1 and 80.3 tons ha^{-1} in Kayseri ecological conditions [21], 79.8 and 103.4 tons ha^{-1} in Diyarbakır ecological conditions [22]. The differences reported in previous studies are closely related to the differences in v cultivars used, as well as the amount of seed, fertilization, irrigation, precipitation, sowing frequency, climate and soil factors.

Dry Matter Yield. The dry matter yield was significantly ($p<0.01$) different both between the cultivars. The differences for cultivars and years led to the significant differences in dry matter yield for years x cultivars interaction (Table 3). Samada-07 (28.5 tons ha^{-1}), Kerbanis (28.3 tons ha^{-1}) and Karadeniz Yıldızı (28.0 tons ha^{-1}) were placed in the high dry matter yield group. However, the Colonia (25.9 tons ha^{-1}), Atlas (25.8 tons ha^{-1}), Motril (26.4 tons ha^{-1}) and Klip (26.3 tons ha^{-1}) cultivars were included in same dry matter yield group (Table 4). Kalumet cultivar was in the lowest group. The overall two-year average of dry matter yield was 26.3 tons ha^{-1}. The dry matter yield obtained in this study are higher than those reported by Geren et al. [19], Karadağ and Balmuk [23], and lower than that obtained by Kuşvuran et al. [6]. The cultivars with high dry matter yield grow better and produce higher biomass under the climate and soil characteristics of new region introduced compared to the low yielding cultivars. The differences in the genetic structure of cultivars thus the different morphological and physiological characteristics also may cause the differences in dry matter yield between the cultivars.

Crude Protein Yield. The difference in crude protein yield between years was statistically significant at 0.05 level, and it was important at 0.01 level among maize cultivars (Table 3). The significant differences of crude protein yield between years and cultivars caused to the significance of years x cultivars interaction on crude protein yield. The highest mean crude protein yield was obtained from Kerbanis (2.6 tons ha^{-1}) cultivar, and the lowest crude protein yield was obtained from Kalumet (1.7 tons ha^{-1}) cultivar (Table 4). The mean crude protein yield (2.3 tons ha^{-1}) in the first year was higher than the second year (2.1 tons ha^{-1}) (Table 4). The mean crude protein yield of 17 maize cultivars in Erzurum conditions was reported as 0.9 tons ha^{-1} in 2004 and 1 tons ha^{-1} in 2005 [24]. Çarpici [7] indicated that two-year mean crude protein yields of Bora, DK626, Luce, and Sincero cultivars in Bursa ecological conditions were 0.9, 0.8, 0.9, 1.5 tons ha^{-1}, respectively. Keleş and Türk [9] reported the crude protein yields of Trojan, C955, Albero and Poncho cultivars in the Banaz conditions were 1.4, 1.0, 1.0, 0.8 tons ha^{-1} respectively reported. The differences in reported crude protein yields are due to differences in ecological conditions, cultivar, maintenance, and other agricultural practices.

ADF (Acid Detergent Fiber) Ratio. The cultivars and years had significant ($p<0.01$) effects on ADF ratio (Table 3). The significant effects of cultivars and years on ADF ratios led to the interaction of years and cultivars significant. Kalumet and Doge cultivars had the highest ADF ratio, while Motril, Samada-07, Karadeniz Yıldızı and Kerbanis cultivars had the lowest ADF ratio (Table 4). The ADF ratio, which is one of the determinants of feed quality, does not provide information on feed digestibility and animal energy intake. Yavuz [8] stated that the average ADF ratio should be less than 31%. The two-year average ADF ratio of cultivars was 22.3%. The ADF ratio (20.2%) in the first year was lower than the ADF ratio (24.5%) of the second year (Table 4). Geren et al. [19] pointed out that the excess of plant photosynthetic surfaces in the early vegetation period results in more and faster protein synthesis in plant cells, which increases the protein content of cells. The ADF ratios obtained in this study were similar to those reported by Ayaz et al. [25] and Çarpici [7] and lower than those of Karadağ and Balmuk [23].The differences in ADF ratios of maize silages can be attributed to the differences in genetic characteristics of silage cultivars, the cultivation

techniques, differences in climate and soil characteristics of the experimental sites and the differences in harvest times.

NDF (Neutral Detergent Fiber) Ratio. The cultivars and year factors and years x cultivars interaction had statistically significant effects ($p<0.01$) on NDF ratios (Table 3). Atlas and Kaluses cultivars were included in the high statistical group, whereas Samada-07 and Kerbanis cultivars were in the low statistical group (Table 4). The mean NDF ratio (41.4%) in the second year of the study was higher than the NDF ratio (37.0%) in the first year (Table 4). The effect of years on NDF ratio was similar to the ADF ratio. Klips and Kalusses cultivars were in the same statistical group in the first year of the

TABLE 4
Yield and Quality Traits of Some Silage Maize (*Zea mays* L.) Cultivars

	2016	2017	Mean	2016	2017	Mean
	Green Matter Yields (tons ha^{-1})			Dry Matter Yield (tons ha^{-1})		
Kerbanis	71.9 b^{++}	64.1 cd^{++}	68.0 c^{++}	29.4 a^{++}	27.3 abc^{++}	28.3 a^{++}
Motril	68.4 c	60.9 de	64.7 de	27.1 bc	25.8 cd	26.4 cde
Atlas	65.3 d	62.0 d	63.7 e	25.6 cd	26.0 cd	25.8 e
K. Yıldızı	67.7 cd	68.5 ab	68.1 c	27.6 b	28.4 a	28.0 ab
Colonia	65.5 d	65.8 bc	65.7 d	25.4 cd	26.4 bcd	25.9 e
Klips	67.5 cd	69.9 a	68.7 bc	25.4 cd	27.2 abc	26.3 de
Kalusses	65.6 d	65.8 bc	65.7 d	24.7 d	24.6 d	24.6 f
Kilowatt	74.5 a	71.5 a	73.0 a	27.1 bc	27.5 abc	27.3 bc
Kalumet	51.2 e	57.7 e	54.5 f	19.7 e	22.2 e	20.9 g
Doge	71.5 b	68.3 ab	70.0 b	28.1 ab	26.1 cd	27.1 bcd
Samada-07	68.6 c	68.0 ab	68.3 bc	28.7 ab	28.2 ab	28.5 a
Mean	67.1 A^{++}	65.7 B	66.4	26.2	26.3	26.3
	Crude Protein Yield (tons ha^{-1})			ADF Ratio (%)		
Kerbanis	2.9 a^{++}	2.3	2.6 a^{++}	16.9 d^{++}	22.6 bc^{++}	19.8 d^{++}
Motril	2.5 bc	2.1	2.3 b	19.1 bcd	23.0 bc	21.0 cd
Atlas	2.3 de	2.3	2.3 bc	21.8 a	22.6 bc	22.2 bc
K. Yıldızı	2.4 bcd	2.4	2.4 b	19.6 abc	20.7 c	20.2 d
Colonia	2.0 fg	2.2	2.1 cde	20.9 ab	23.6 b	22.3 bc
Klips	2.0 fg	2.1	2.0 de	19.7 abc	25.0 b	22.4 b
Kalusses	1.9 g	2.1	2.0 e	21.5 a	24.5 b	23.0 b
Kilowatt	2.2 ef	2.2	2.2 bcd	21.5 a	24.6 b	23.1 b
Kalumet	1.7 h	1.7	1.7 f	21.8 a	30.0 a	25.9 a
Doge	2.4 cde	2.0	2.2 bcd	21.3 ab	28.8 a	25.1 a
Samada-07	2.6 b	2.1	2.4 b	18.1 cd	23.8 b	20.9 cd
Mean	2.3 A^{+}	2.1 B	2.2	20.2 B	24.5 A^{++}	22.3
	NDF Ratio (%)			ADL Ratio (%)		
Kerbanis	31.6 de^{++}	36.1 h^{++}	33.9 ef^{++}	1.4 de^{++}	1.5 abc^{++}	1.5 cd^{++}
Motril	31.6 de	41.1 def	36.4 d	1.7 ab	1.8 a	1.7 a
Atlas	43.2 a	46.0 ab	44.6 a	1.7 ab	1.6 abc	1.6 a
K. Yıldızı	34.7 cd	35.9 h	35.3 de	1.4 de	1.3 bc	1.3 de
Colonia	39.2 abc	39.7 fg	39.4 c	1.8 a	1.6 a	1.7 a
Klips	36.6 bc	40.9 ef	38.8 c	1.5 cd	1.5 abc	1.5 bc
Kalusses	38.7 abc	47.3 a	43.0 ab	1.4 de	1.3 c	1.3 e
Kilowatt	41.7 a	42.8 cd	42.3 b	1.6 bc	1.6 abc	1.6 ab
Kalumet	41.7 a	42.7 de	42.2 b	1.6 bc	1.6 ab	1.6 ab
Doge	40.4 ab	44.5 bc	42.5 b	1.7 ab	1.7 a	1.7 a
Samada-07	27.4 e	38.6 g	33.0 f	1.3 e	1.3 c	1.3 e
Mean	37.0 B	41.4 A^{++}	39.2	1.6 A^{+}	1.5 B	1.5
	Digestible Dry Matter Ratio (%)			Digestible Dry Matter Yield (tons ha^{-1})		
Kerbanis	75.7 a^{++}	71.3 ab^{++}	73.5 a^{++}	22.3 a^{++}	19.4 abc^{++}	20.9 a^{++}
Motril	74.1 abc	71.0 ab	72.5 ab	20.0 c	18.3 cde	19.2 bc
Atlas	71.9 d	71.3 ab	71.6 bc	18.4 de	18.6 bcd	18.5 c
K. Yıldızı	73.6 bcd	72.8 a	73.2 a	20.3 bc	20.7 a	20.5 a
Colonia	72.6 cd	70.5 b	71.6 bc	18.4 de	18.6 bcd	18.5 c
Klips	73.5 bcd	69.4 b	71.5 c	18.7 de	18.9 bc	18.8 bc
Kalusses	72.2 d	69.8 b	71.0 c	17.8 e	17.1 e	17.5 d
Kilowatt	72.2 d	69.8 b	71.0 c	19.6 cd	19.2 bc	19.4 b
Kalumet	72.0 d	65.5 c	68.7 d	14.2 f	14.5 f	14.4 e
Doge	72.3 cd	66.5 c	69.4 d	20.3 bc	17.4 de	18.8 bc
Samada-07	74.8 ab	70.4 b	72.6 ab	21.5 ab	19.9 ab	20.7 a
Mean	73.2 A^{++}	69.8 B	71.5	19.2 A^{+}	18.4 B	18.8

$^{+}$Means followed by the same letter in the same line/column are statistically not significant ($p<0.05$).
$^{++}$Means followed by the same letter in the same line/column are statistically not significant ($p<0.01$).

study, while they took place in different group for the second year of the study. The difference between years caused years x cultivars interaction to be important (Table 4). The ADF and NDF have similar cell wall structural compounds. The NDF contains cellulose, hemicellulose and lignin, and ADF has cellulose and lignin. The intakes of NDF and ADF are closely related to the digestion level of the feed. The NDF is closely related to the feed intake of animal, and ADF is to the degree of feed digestion. The amount of lignin in maize silage increases with the delay of the harvest from the milking stage to dough stage. Lignin forms a bridge between cellulose and hemicellulose, therefore causes thickening of the cell wall, which reduces the digestion of feed. The increase in NDF value means low, and the decrease in NDF value shows a high level of feed intake [8, 26]. The mean NDF ratio has been reported in the range of 53.2 - 60.6% by Ayaz et al. [25] between 57.5 and 73.9% by Karadağ and Balmuk [23], 50.5 and 55.9% by Çarpici [7]. The NDF ratios obtained in this study were lower than previously reported values. The difference in NDF ratio is probably due to differences in genetic structures of cultivars cultivated in different ecologies. The low NDF ratio of maize silage obtained in our study shows that feed quality in terms of nutritional value may be superior compared to silages produced in other studies.

ADL (Acid Detergent Lignin) Ratio. The ADL ratio was significantly different between years ($p<0.05$) and cultivars ($p<0.01$) (Table 3). The Doge, Motril, Colonia, Atlas, Kilowatt and Kalumet cultivars were included in the high ADL ratio group, while the Samada-07, Kalusses and Karadeniz Yıldızı were placed in the low ADL ratio statistical group (Table 4). Ayaz et al. [25] stated that lignin, a plant cell structural compound, provides support to the plant. The variation in lignin content directly affects digestion depending on the plant maturation and weather conditions. The excess of structural carbohydrates such as ADF, NDF and ADL reduce the hay or feed quality, reducing the consumability and digestibility. The ADL ratios obtained in this study are similar to those reported by Özata et al. [27] whereas lower than those found by Ayaz et al. [25] and Canbolat [16]. The differences can be attributed to factors such as the genetic structure of maize cultivars and the period of maize growth stage at the time of harvest.

Digestible Dry Matter Ratio. The effects of cultivars, years and years x cultivars interaction on digestible dry matter ratio (DDMR) were significantly important ($P<0.01$) (Table 3). The Motril, Samada-07, Karadeniz Yıldızı and Kerbanis cultivars were included in the high DDMR statistical group, whereas Kalumet and Doge cultivars were placed in the low DDMR group (Table 4). The mean ADF ratio is used in the calculation of DDMR. The DDMR and ADF ratio has an inverse relationship which was supported by the findings of the current study. The Kalumet and Doge cultivars had the highest ADF ratio and the lowest DDMR (Table 4). The DDMR (73.2%) in the first year of the study was higher than the second year (69.8%) (Table 4). The effect of year on digestible dry matter yields of the cultivars significantly varied. The Atlas and Kalumet cultivars in the first year were included in the same DDMR statistical group, while they were in the different DDMR statistical groups in the second year. The findings obtained are similar to those of Akdeniz et al. [28].

Digestible Dry Matter Yield. The effects of maize cultivars ($p<0.01$), years ($p<0.05$) and years x cultivars interaction ($p<0.05$) on digestible dry matter (DDM) yield were statistically significant (Table 3). The highest DDM yield was obtained from Kerbanis (20.9 tons ha^{-1}), Samada-07 (20.7 tons ha^{-1}) and Karadeniz Yıldızı (20.5 tons ha^{-1}) cultivars, while Kalumet (14.4 tons ha^{-1}) cultivar yielded the lowest DDM. The mean DDM yield (19.2 tons ha^{-1}) in the first year was higher than the second year (18.4 tons ha^{-1}) (Table 4). Klips and Kalusses cultivars in the first year were included in the same statistical group, while they were placed in the different statistical groups for the second year. The effects of cultivars on digestible dry matter yields varied between years (Table 4). Jung and Vogel [29] pointed out that high lignin ratio negatively affects the digestibility of feed cells and reduces the digestibility. Low DDM ratio and DDM efficiency of Kalumet cultivar with high ADL content are in line. In addition, since the DDM yield is calculated by multiplying the dry matter yield and DDM ratio, the similarity of DDM yield with the dry matter yield and DDM ratio results is an expected case. The mean DDM yield values obtained in this study are higher than those reported by Akdeniz et al. [30] and Akdeniz et al. [28].

CONCLUSION

The use of high yield and high-quality cultivars in maize cultivation to produce silage will contribute to the solution of forage problem in the short term. The yield and quality traits of the cultivars investigated come to the fore for the Kerbanis, Karadeniz Yıldızı, and Samada-07 cultivars. The result concluded that the Kerbanis, Karadeniz Yıldızı and Samada-07 cultivars could be suggested in similar ecologies such as Kırşehir province.

ACKNOWLEDGEMENTS

This study was funded by the Scientific Research Projects Unit of Kırşehir Ahi Evran University (Grant No. ZRT.A3.16.009). I would like to thank to DEKALB Company, Mr. Gökhan Sarı, Manager for KWS Agriculture, Corn R&D.

REFERENCES

[1] Yavuz, T., Karadağ, Y. (2016) Yield and Quality Performances of Artificial Pasture Mixtures Under Dryland Conditions. Journal of the Institute of Science and Technology. 4, 155-155.

[2] Geren, H. (2001) Effect of Sowing Dates on Silage Characteristics of Different Maize Cultivars Grown as Second Crop Under Bornova Conditions. Ege Journal of Agricultural Research. 38.

[3] Khan, N.A., Yu, P., Ali, M., Cone, J.W., Hendriks, W.H. (2015) Nutritive value of maize silage in relation to dairy cow performance and milk quality. J Sci Food Agric. 95, 238-252.

[4] Karadavut, U., Sozen, O., Palta, C. (2017) The Effects of Different Doses of Boron on the Growth Parameters of Some Maize Genotypes. Fresen. Environ. Bull. 26, 5349-5356.

[5] Abdelaal, K.A.A., Hafez, Y.M., El-Sabagh, A., Saneoka, H. (2017) Ameliorative Effects of Abscisic Acid and Yeast on Morpho-Physiological and Yield Characteristics of Maize Plant (*Zea mays* L.) Under Water Deficit Conditions. Fresen. Environ. Bull. 26, 7372-7383.

[6] Kuşvuran, A., Kaplan, M., Nazlı, R.İ., Saruhan, V., Karadağ, Y. (2015) Determination of Possibilities to Grow Some Corn (*Zea mays* L.) Cultivars for Silage Production under Middle Kizilirmak Basin Ecological Conditions. Journal of Agricultural Faculty of Gaziosmanpasa University. 32, 57-67.

[7] Çarpici, B.E. (2016) A Study on Forage Yield and Quality of Some Silage Maize Cultivars Which Can Be Cultivated As Second Crop in Bursa. Derim. 33, 299-308.

[8] Yavuz, M. (2005) Determination of Some Ruminant Feeds' Relative Feed Value and In vitro Digestion Values. Journal of Agricultural Faculty of Gaziosmanpaşa University. 22(1), 97-101.

[9] Keleş, E., Türk, M. (2018) A Research on Possibilities of Second Crop Silage Maize Growing on Banaz Condition. Academia Journal of Engineering and Applied Sciences. 1(4), 69-75.

[10] Sillanpää, M. (1990) Micronutrient assessment at the country level: An international study. FAO Soils Bulletin 63. Food and Agriculture Organisation of the United Nations, Rome, Italy

[11] Demir, I. (2019) The Effects of Sowing Date on Growth, Seed Yield and Oil Content of Sunflower (*Helianthus annuus* L.) Cultivars Under Rainfed Conditions. Fresen. Environ. Bull. 28, 6849-6857.

[12] Erdal, Ş., Pamukçu, M., Ekiz, H., Soysal, M., Savur, O., Toros, A. (2009) The Determination of Yield and Quality Traits of Some Candidate Silage Maize Hybrids. Mediterranean Agricultural Sciences. 22, 75-81.

[13] AOAC (2005) Official Methods of Analysis. Association of Official Analytical Chemists. 18th ed. Horwitz, W., George, W. Latimer, (eds.) Association of Official Analytical Chemists International, Maryland, USA

[14] Van, Soest, P.J., Robertson, J.B., Lewis, B.A. (1991) Methods for dietary fiber, neutral detergent fiber, and nonstarch polysaccharides in relation to animal nutrition. J Dairy Sci. 74, 3583-3597.

[15] Anonymous (2018) Analytical Methods Fiber Analyzer A200. Ankom Technology.

[16] Canbolat, Ö. (2012) Comparison of in vitro Gas Production, Organic Matter Digestibility, Relative Feed Value and Metabolizable Energy Contents of Some Cereal Forages. Journal of the Faculty of Veterinary Medicine. 18, 571-577.

[17] Horrocks, R.D., Valentine, J.F. (1999) Harvested forages. Academic Press.

[18] Petersen, R.G. (1994) Agricultural Field Experiments: Design and Analysis. CRC Press.

[19] Geren, H., Avcioğlu, R., Kır, B., Demiroğlu, G., Yılmaz, M.F. Cevheri, A.C. (2003) Effect of different sowing dates on the yield and quality characteristics of some maize cultivars grown as second crop for silage. Ege Journal of Agricultural Research. 40(3):57-64

[20] Güneş, A., Acar, R. (2006) The Determination of Growing Possibilities of Silage Hybrid Maize Cultivarsas Second Crop under Karaman Ecological Conditions. Selcuk University Faculty of Agriculture Journal. 20, 84-92.

[21] Bulut, S. (2016) Adaptation of some Corn Cultivars (for Silage) in Kayseri Conditions. Journal of the Institute of Science and Technology. 6, 117-126.

[22] Seydoşoğlu, S., Saruhan, V. (2017) Determination of Yield and Yield Components in Some Silage Maize Varieties of Different Sowing Times. Ege Journal of Agricultural Research. 54, 377-383.

[23] Karadağ, Y., Balmuk, Y. (2013) Determination of Yield and Yield Traits of Slage Maize (*Zea mays* L.) Varieties Grown as Second Crop Under the Konya/Yunak Ecological Conditions. 10 Field Crops Congress of Turkey. Konya.

[24] Bulut, S., Çağlar, Ö., Öztürk, A. (2008) Possibilities to Grow Some Corn Cultivars in Erzurum Plain Conditions for Silage Production. Journal of the Faculty of Agriculture Atatürk University. 39, 83-91.
[25] Ayaz, M., Özpinar, H., Yaman, S., Acar, A., Yasemin, A. Yavrutürk, Y., Niksarlıgil, F., Aksu, S., Aygün, Y. (2013) Analysing Yield and Quality Characteristics of Silage Maize Cultivars Which Are Used Commonly or May Be Use for Main Crop. Harran Journal of Agricultural and Food Science. 17, 23-35.
[26] Budak, F., Budak, F. (2014) Quality on Forage Plants and Factors Effecting Forage Quality. Turkish Journal of Scientific Reviews. 7, 1-6.
[27] Özata, E., İkincikarakaya, S.U., Özturk, A. (2018) The Determination of Silage Yield and Quality Traits of Candidate Maize Hybrids. Ekin Journal of Crop Breeding and Genetics. 4, 31-40.
[28] Akdeniz, H., Karsli, M.A., Keskin, B., Andiç, N. (2004) Determination of Chemical Composition, Digestible Dry Matter Yields of Some Silage Type Corn Varieties. Van Veterinary Journal. 15, 19-22.
[29] Jung, H-J.G., Vogel, K.P. (1992) Lignification of switchgrass (*Panicum virgatum*) and big bluestem (*Andropogon gerardii*) plant parts during maturation and its effect on fibre degradability. J Sci Food Agr. 59, 169-176.
[30] Akdeniz, H., Karslı, A.M., Nursoy, H., Yılmaz, İ. (2003) Determination of the Chemical Composition and Digestible Dry Matter Yields of Some Grain Sorghum Varieties. Turkish Journal of Veterinary & Animal Sciences. 27(6), 1349-1355.

Received: **12.9.2019**
Accepted: **11.02.2020**

CORRESPONDING AUTHOR

Hakan Kir
Kırşehir Ahi Evran University,
Faculty of Agriculture,
Department of Field Crops,
Kirşehir – Turkey

e-mail: hakankir@ahievran.edu.tr

© by PSP Volume 29 – No. 04A/2020 pages 2850-2857 Fresenius Environmental Bulletin

STUDY ON GREEN SAFETY PRODUCTION TECHNOLOGY IN MODERN COAL MINES

Lianchun Zhou, Jinshan Zhang*

Mining Research Institute, Inner Mongolia University of Science and Technology, Baotou, 014010, Inner Mongolia, China

ABSTRACT

Underground coal gasification (UCG) is an industrial process that provides an alternative to conventional underground mining at coal seams that are located especially deep underground. This work presents the results of an experimental study on the properties of tar that originated from underground coal gasification (UCG) trials. We investigated the effect of pyrolysis temperature, operating pressure, water influx and gasification agent injection on tar production. The results of the analysis showed that in terms of physical–chemical properties, both tars are highly different from each other, as well as from typical coal tar from a coking plant. On the basis of the decrease in the viscosity of tars, increase of the H/C ratio, and increase of the oil fractions sum and light aromatic compound content, as well the decline in the amount of residues after distillation, it was observed that as gasification progresses.

KEYWORDS:
UCG, Coal Mines, Green, Safety Production

INTRODUCTION

Underground coal gasification is the process of coal conversion into combustible gas which main components are hydrogen, methane and carbon monoxide [1]. This process is a combination of several unit processes, such as drying, pyrolysis, gasification and combustion. In addition to UCG gas, liquid tar products are also obtained, which are undesirable but unavoidable contamination products of the process gas. Tar is generated the most intensively at the beginning of the gasification process, and as the gasification progresses, the amount of tar is reduced; however, depending on the process conditions, the raw gas always contains a certain amounts of tar. The results of American and Russian studies [2] show that the contents of the tar in raw gas may be in the range of 0.5 to 15.5 g/m^3, depending on the process conditions. For this reason, the gasification conditions are chosen such that the tar content in the resulting gas is not too high [3]. The generation of tar starts at a temperature of approximately 350 °C and ends at approximately 1000 °C. Because tar is formed primarily from the thermal transformations of volatile compounds, the higher the content of volatile matter in coal is, the more tar is produced [4]. With an increase in temperature and residence time, the resulting tar undergoes secondary reactions (cracking, partial combustion) that change its properties and yield [5]. The gasification temperature depends on the oxygen concentration and its supply rates in the gasified medium; hence, when air is used, lower temperatures are achieved compared to pure oxygen. An important factor influencing the tar quantity and composition is also the configuration of the UCG gas collection system. As a result of the tar fractionation phenomena, the longer the output pipeline is, and the lower the temperature inside is, the more tar is condensed [6]. This phenomenon may cause problems with collection of the process gas because condensed tar mixed with water and dust may reduce the cross-section of the output pipeline, and in extreme cases, it can completely block the production well. To prevent this outcome, the process gas temperature should be maintained at the appropriate level. In studies on UCG, depending on the type of installation used, various process gas temperatures have been reported. A Russian study [7] shows that the best operating temperature range for syngas cooling is between 100 and 200 °C. During American trials, Hanna, Hanna II, IVa, and b [8] the process gas temperature was significantly higher and amounted to approximately 140–370 °C. In a Chinchilla project, the temperature of the process gas was approximately 300 °C [9], and during the gasification of coal in Swan Hills, Alberta (Canada), the syngas temperature leaving the production well was 50 °C or less. For further downstream gas applications, tar should be effectively removed [10] using standard physico-chemical methods.

MATERIALS AND METHODS

The tested tars were obtained during two in-situ underground coal gasification experiments. These experiments were conducted in the experimental mine in southern China. The UCG reactors were located in coal seam No. 1 at a depth of 30 m. The thickness of the coal seam was 1.6 m. The

analyses were performed in a certified laboratory in the Central Mining Institute according to Chinese Standards. In both experiments, the gasified coal was characterized using the same physico-chemical properties.

RESULTS AND DISCUSSION

To reduce the amount of tar condensed in the surface treatment plant, the average process gas temperature before purification was maintained at approximately 75 °C. At this temperature, the total mass of collected water-free tar in the waste-water tank was 2.69 tonnes. During this process, the 230.6 tonnes of coal was gasified, and the total volume of 1,055,878 Nm^3 of gas after cleaning was produced (Figure 1 and 2). On this basis, the calculated amount of tar contained in the process gas on the surface was 2.55 g/Nm^3. After finishing the gasification, the installation was dismantled, including the underground part, which was transported on the surface. The inspection of the unscrewing underground installation showed a large amount of tar contained in the separators and adhered inside output pipeline diameter DN300. Based on these data, the estimated amount of water-free tar remaining underground was approximately 4 tonnes. Thus, the total amount of tar produced in this process was approximately 6.69 tonnes, and only approximately 40% of this tar was transported with the process gas to the surface. The rest remained in an installation underground due to tar fractionation.

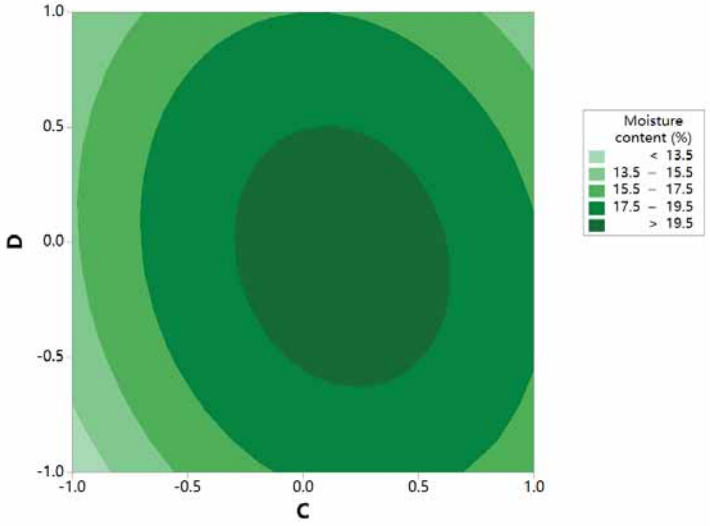

FIGURE 1
Contour Plot of Moisture content (%) vs D, C

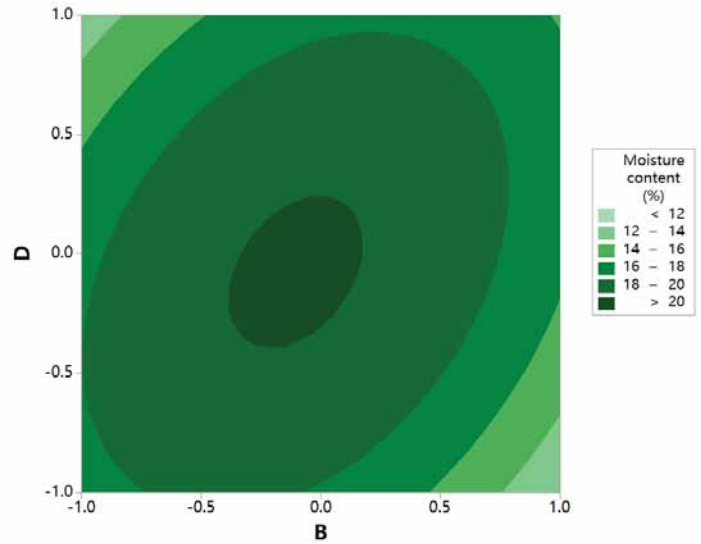

FIGURE 2
Contour Plot of Moisture content (%) vs D, B

Prior to implementation of the agreed upon research program, initial tests on selection of the most suitable method for determination of water content were conducted. Application of the azeotropic method, commonly used for coal tars, was excluded, owing to the fact that heating the tar samples to the boiling point of an azeotropic mixture with toluene or xylene would distil the light tar fractions, and possibly initiate the polymerization/polycondensation process. It would substantially affect the properties of the dehydrated tar samples. It was therefore decided that for the determination of water content, a Karl-Fischer method would be applied, which involves only minor heating of the samples (Figure 3 and 4). This titration method is based on the quantitative reaction of water with iodine and sulphur dioxide in the presence of a lower alcohol and an organic base (pyridine).

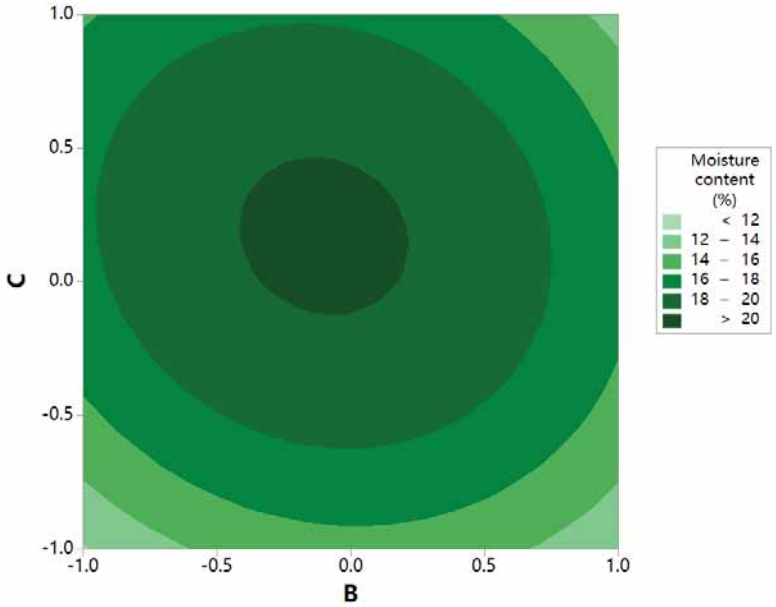

FIGURE 3
Contour Plot of Moisture content (%) vs C, B

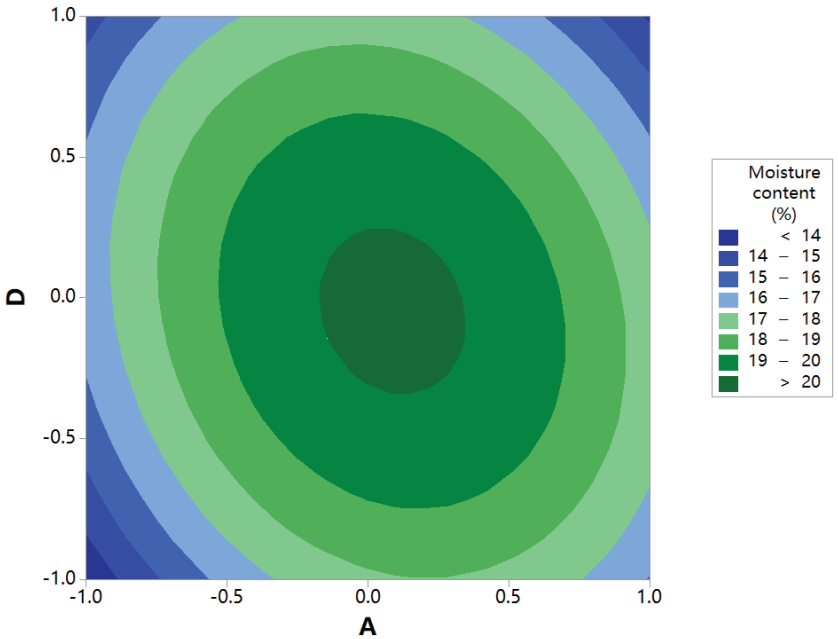

FIGURE 4
Contour Plot of Moisture content (%) vs D, A

For Figure 5 and 6, the ash contents in the tested tar samples were quite high (0.58–3.04 wt%) relative to the typical coke-oven tar (0.01–0.05 wt%). The observed large differences in the ash content for the individual samples confirm their high heterogeneity. The coking behaviour, expressed both by the yields of coking residues (LK at 870°C) and by the coking values (CV by Condradson method at 550°C) change significantly between the tested tar samples.

The secondary reactions of tars are stimulated by enlargement of the cavity dimensions, which increases the tar residence time in the hot zone of the reactor, a rise of the gasification temperature, and the presence of a large amount of steam inside the reactor. The presence of steam results from water evaporation contained in the gasified coal seam and from water flow into the reactor from the surrounding underground strata.

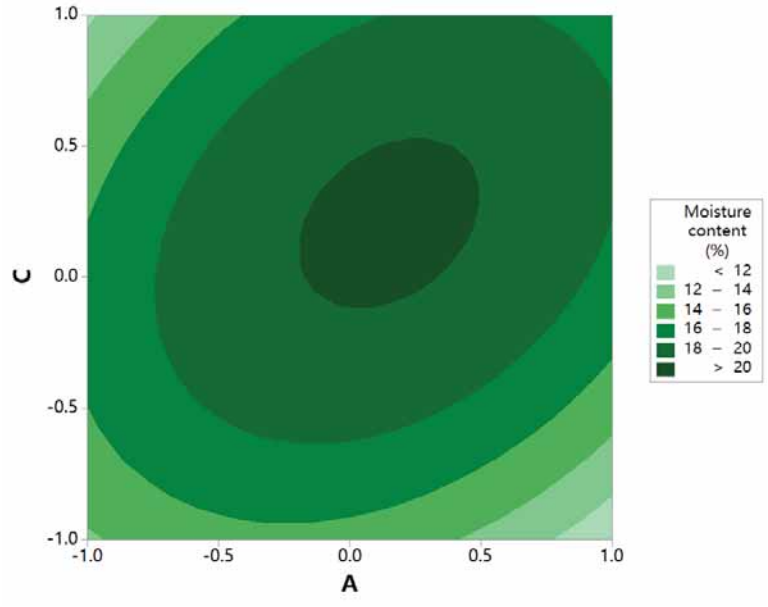

FIGURE 5
Contour Plot of Moisture content (%) vs C, A

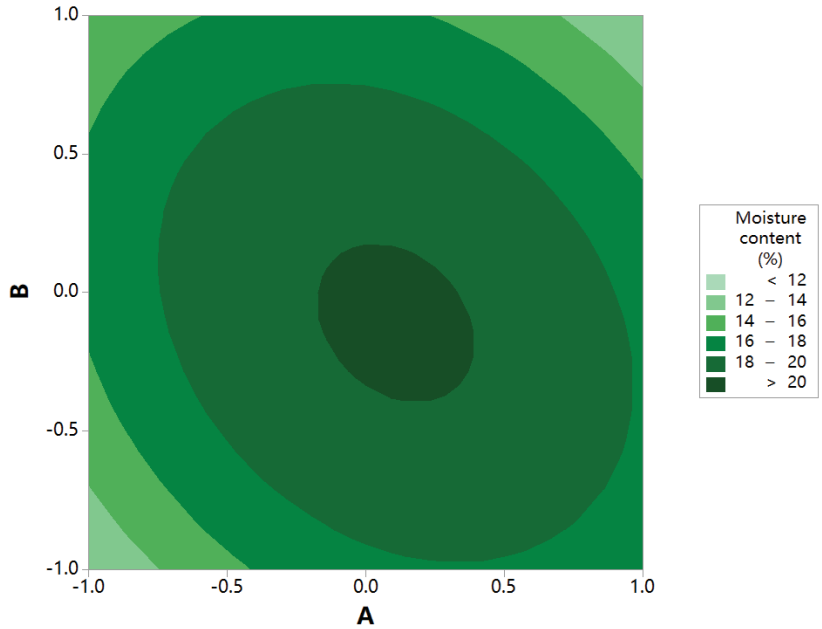

FIGURE 6
Contour Plot of Moisture content (%) vs B, A

Effect of pyrolysis temperature on density is shown in Figure 7 and 8. The results of elemental analysis show that the tar samples under study were characterized by relatively small CO_2 contents compared to coke-oven tar (5–6 wt%), and compared to tars generated during other field-scale UCG operations, e.g., the Rocky Mountain trial (8.9–9.6 wt%) and Hanna IVB trial (8.79 wt%). This can be attributed to inefficient recovery of low boiling alkyl hydrocarbons in the applied gas processing plant, which escaped the treatment plant untrapped.

A significantly higher hydrogen content was characteristic of sample (gasification with CO_2), which confirms its different physicochemical nature. It can be concluded that this sample contains lower amounts of unsaturated and aromatic structures. This could result from a limited dealkylation and hydrogen loss under the lower temperature conditions. Some researchers concluded that gasification in the presence of CO_2 inhibits secondary processes of thermal decomposition of tars, which would explain the obtained results (Figure 9 and 10).

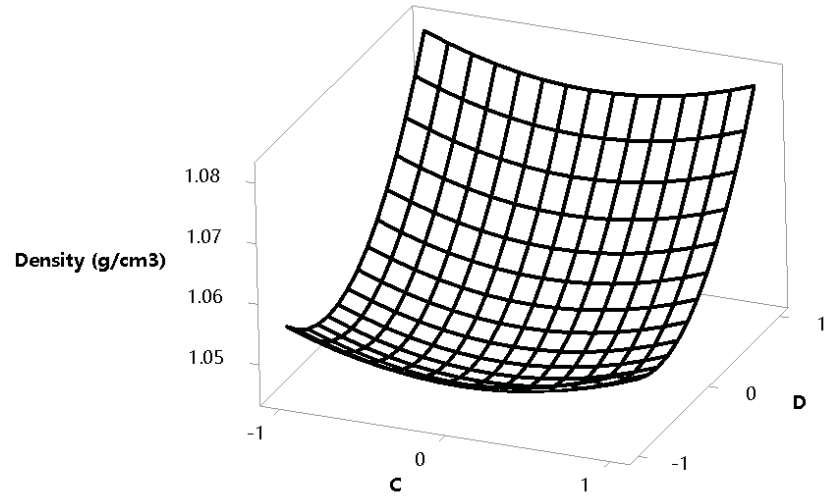

FIGURE 7
Surface Plot of Density (g/cm^3) vs D, C

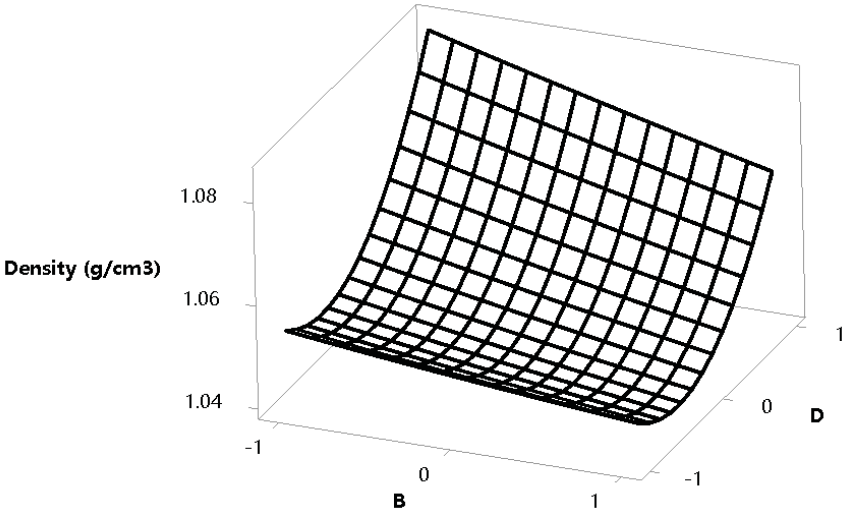

FIGURE 8
Surface Plot of Density (g/cm^3) vs D, B

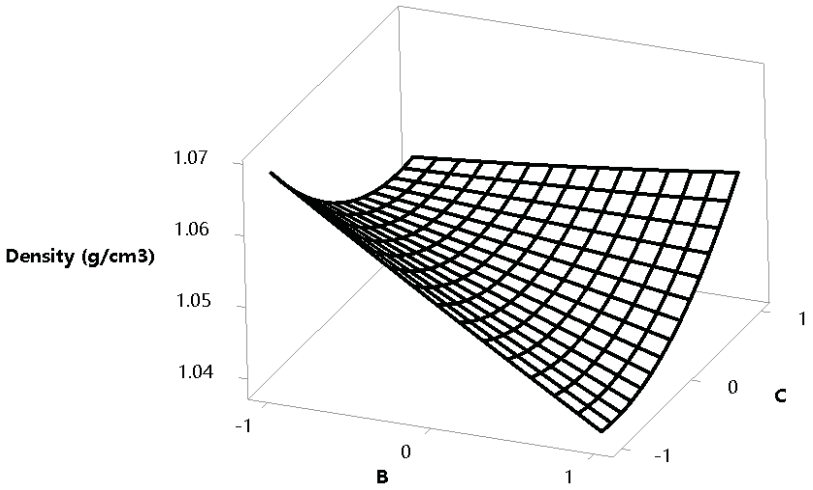

FIGURE 9
Surface Plot of Density (g/cm^3) vs C, B

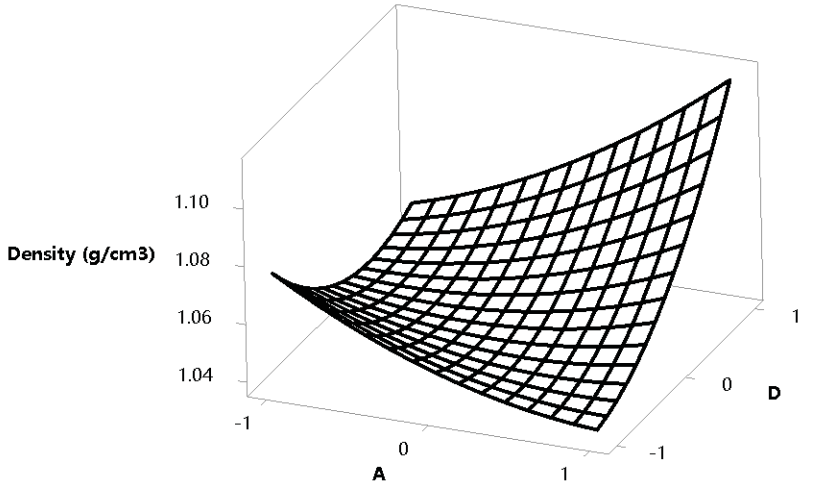

FIGURE 10
Surface Plot of Density (g/cm3) vs D, A

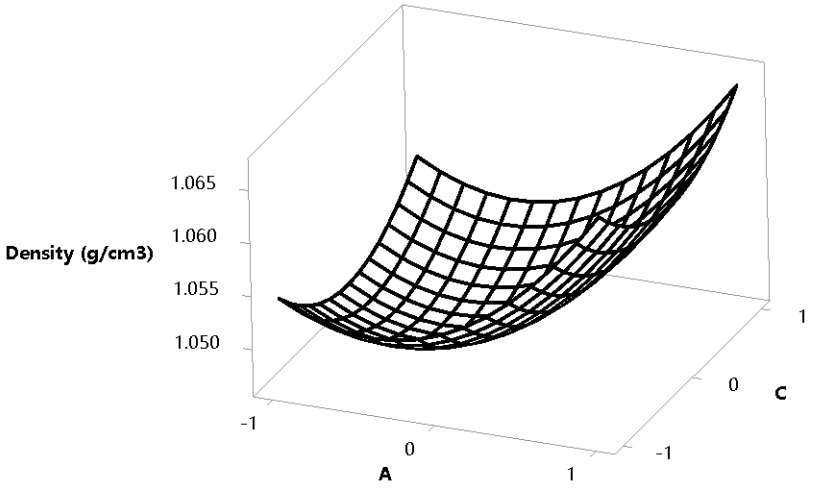

FIGURE 11
Surface Plot of Density (g/cm3) vs C, A

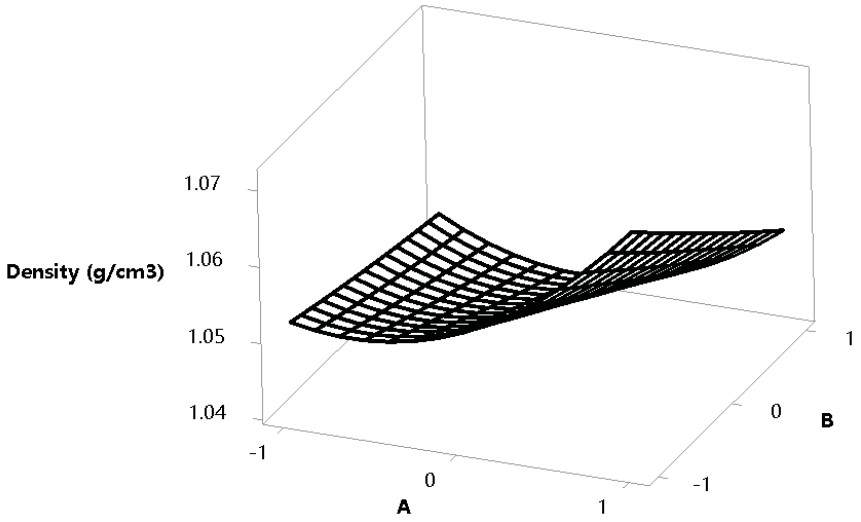

FIGURE 12
Surface Plot of Density (g/cm3) vs B, A

Analysing the data of Figure 11 and 12 show that the total sum of the individual compounds increases as the gasification progresses. In tested tars samples, the sum of these compounds was 3.45 wt% on the 6th day of the process, and almost four times higher, 12.08 wt%, on the 50th and final day of the process. The increase in the content of these aromatic compounds was a result of a secondary reaction of the liquid products (cracking, cyclization, aromatization) leading to the creation of stable aromatic structures. In the secondary tars, changes in the cracking processes dominate, particularly in the heaviest components, as evidenced by the decrease in the content of the distillation residues and the increase in the content of oil products.

CONCLUSIONS

This work presents the results of an experimental study on the properties of tar that originated from underground coal gasification (UCG) trials. We investigated the effect of pyrolysis temperature, operating pressure, water influx and gasification agent injection on tar production. The results of the analysis showed that in terms of physical–chemical properties, both tars are highly different from each other, as well as from typical coal tar from a coking plant. On the basis of the decrease in the viscosity of tars, increase of the H/C ratio, and increase of the oil fractions sum and light aromatic compound content, as well the decline in the amount of residues after distillation, it was observed that as gasification progresses.

REFERENCES

[1] Bhutto, A.W., Bazmi, A.A., Zahedi, G. (2013) Underground coal gasification: From fundamentals to applications. Prog Energy Combust Sci. 39, 189-214.

[2] Pavlovich, L.B., Strakhov, V.M. (2013) Producing hydrocarbons by the underground gasification of coal. Coke Chem. 56, 349-355.

[3] Yang, S., Lin, A.M. (2019) Research on green development of coal industry based on ecological civilization. Fresen Environ Bull. 28, 5398-5401.

[4] Tomic, S., Bulajic, S., Radojevic, R., Petrovic, D., Ketin, S. (2019) The distribution of concentration of suspended particles-coal mine. Fresen Environ Bull. 28, 5764-5770.

[5] Wang, J.T., Wang, F.S., Xu, Y.Y., Dong, X.W. (2019) Study on current situation and development trend for coal mine fire prevention technology in China. Fresen Environ Bull. 28, 5010-5016.

[6] Wiatowski, M., Kapusta, K., Muzyka, R. (2018) Study of properties of tar obtained from underground coal gasification trials. Fuel. 228, 206-214.

[7] Hou, X.R., Guo, L.W., Wang, F.S., Xu, Y.Y., Dong, X.W., Gao, D., Sun, Y.M. (2018) Research on sources appointment of abnormal co in underground mine. Fresen Environ Bull. 28, 2897-2907.

[8] Liu, Q., Li, S., Wang, X.M., He, Y. (2018) Feasibility and stability analysis of coal-gangue-based tailings dam on subsidence land. Fresen Environ Bull. 27, 37-45.

[9] Liu, Y., Li, W.P., Wang, Q.Q., Liu, S.L. (2018) Simulation study on fracture zone height of overlying water in mining of near shallow buried coal seam in northern Shaanxi province. Fresen Environ Bull. 27, 4112-4119.
[10] Kreinin, E.V., Zorya, A.Y. (2009) Underground coal gasification problems. Solid Fuel Chem. 43, 215-218.

Received: **17.09.2019**
Accepted: **08.01.2020**

CORRESPONDING AUTHOR

Jinshan Zhang
Mining Research Institute,
Inner Mongolia
University of Science and Technology,
Baotou, 014010, Inner Mongolia, China

e-mail: qinfenhaoshi888@aliyun.com

© by PSP Volume 29 – No. 04A/2020 pages 2858-2868 Fresenius Environmental Bulletin

TIME-DEPENDENT CHANGES OF HEPATIC ENZYME ACTIVITIES AND THYROID HORMONES IN *CARASSIUS AURATUS* EXPOSED TO 2,2',4,4'-TETRABROMODIPHENYL ETHER (BDE 47)

Mengnan Shen[1], Jie Cheng[2], Shixiang Gao[3], Na Li[1], Hai Lu[4,*]

[1]Key Laboratory of Songliao Aquatic Environment, Ministry of Education, Jilin Jianzhu University, Changchun 130118, China
[2]Second Institute of Oceanography, MNR, Hangzhou 310012, China
[3]State Key Laboratory of Pollution Control and Resource Reuse, School of the Environment, Nanjing University, Nanjing 210093, China
[4]College of Civil Engineering and Architecture, Changchun Sci-Tech University, Changchun 130600, China

ABSTRACT

As widely used flame retardants, polybrominated diphenyl ethers (PBDEs) are ubiquitous in the environment. The purpose of this study was to evaluate their potential toxicity on freshwater fish crucian carp (*Carassius auratus*). The fish were given intraperitoneal injection of 2, 2', 4, 4'- tetrabromodiphenyl ether (BDE47) at environmentally relevant concentrations for consecutive 7 days, followed by 7 days depuration period. Liver and serum samples were analyzed for activities of hepatic ethoxyresorufin-*O*-deethylase (EROD), ethoxycoumarin-*O*-deethylase (ECOD), glutathione-S-transferase (GST), and levels of serum total thyroine (T_4), triiodothyronine (T_3). EROD activity was markedly inhibited, and a U-shaped trend with time was observed, while ECOD activity was significant induced, and the most marked induction (1.7 times) was detected in the low-dose group on the 12th day. Reductions of T_4 and T_3 were both noted after BDE47 exposure, and the most significant reduction was 58% and 54.9%, respectively. Correlation analysis revealed that there was an inverse correlation between ECOD activity and T_4 concentration, and a positive correlation between T_4 and T_3 concentrations, which indicated that the decrease of thyroid hormone concentration may be attributed to the formation of metabolites through oxygenase catalized reaction involving CYP450. Histological changes on liver have also been detected, and the lesions could not be recovered in shot-time.

KEYWORDS:
2, 2', 4, 4'- tetrabromodiphenyl ether (BDE 47), hepatic enzyme activity, thyroid hormone, histological change, crucian carp

INTRODUCTION

Polybrominated diphenyl ethers (PBDEs) have been widely used as flame retardants in a variety of consumer goods, such as textiles, upholstery and electronic devices. Due to their high lipophilicity and environmental stability, PBDE congeners can be transported through environmental media and bioaccumulated in biotic samples, especially in the aquatic organisms. Increasing concentrations of PBDEs have been reported in fish samples from numerous locations around the world in the past 20 years [1]. In China, it was reported that the average concentrations of total PBDEs ranged 10^{-1}~10^{2} ng/g wet weight in fish samples from several important river systems [2-3]. Of the various congeners detected in fish tissues, 2, 2', 4, 4'- tetrabromodiphenyl ether (BDE 47) is the typical major congener [2-3]. In addition, laboratory experiments have shown that BDE 47 had high uptake rate and assimilation efficiency which lead to a high accumulation in fish [4]. It is greatly concerned about PBDE congeners found in aquatic biota because growing evidence had suggested that they may possess neurotoxicity, thyroid-disruptive effects, and dioxin-like behavior [1]. Furthermore, thyroid and liver were proved to be the major target organs for PBDE toxicity in human and mammals [1, 5]. PBDEs have been demonstrated to induce the secretion of phase I enzymes in liver, such as cytochrome P450 (CYP) isozymes, causing metabolization and excretion of PBDEs by this enzyme system [6]. Structural similarity to several other dioxin-like compounds, such as polychlorinated biphenyls (PCBs) and 2, 3, 7, 8-tetrachlorodibenzo-p-dioxin (TCDD), suggested that PBDEs might act as agonists for the aryl hydrocarbon receptor (AhR) [1]. Generally, the activation of AhR leads to the induction of CYP1A1 which can be assayed as 7-ethoxyresorufin-*O*-deethylase (EROD) activity. Interaction of CYP1A1 mediated EROD activity has been detected in both mice and rats exposed to various commercial mixtures of PBDEs and/or BDE 47 with varied results for the specific congeners. Previous

studies have shown that 70-5DE, a commercial mixture contained 37% BDE 47, could induce the EROD activity in rats [5]. The same pattern of induction was also found in rats when exposing to DE-71(penta-BDE) [6]. However, later researchers believed that observed induction of EROD activity in commercial PBDE products might be due to the low levels of contamination by polybrominated dibenzofurans (PBDD) and polybrominated dibenzo-p-dioxin (PBDF) [1, 7] which were typical AhR agonists. Some studies *in vitro* confirmed this suggestion. They detected that BDE 47 was not able to activate the AhR, and consequently could not induce CYP1A1 enzyme activity in human HepG2 and rodent H4IIE cancer cells [8]. In summary, the results of these studies on the effect of PBDEs on the EROD activity were not fully conclusive. In addition, most of them only focused on rodents and mammals. Information on the possible interference with EROD activity in aquatic species is currently lacking.

Another MFO enzyme ethoxycoumarin-*O*-deethylase (ECOD) has been studied in mammals as a marker of activities for CYP1A1, CYP1A2, CYP2B1, CYP2E1, and CYP2B6 [9]. It has been shown that exposure to structurally related compounds, such as Aroclor 1260 (a commercial mixture of PCBs), can strongly induce ECOD activity in fish [10]. However, to our knowledge, there haven't been any studies about the effect on ECOD activity caused by PBDEs. Phase II enzymes are important because they conjugate the reactive metabolites produced by phase I enzymes so as to facilitate their excretion [11]. Glutathione-S-transferase (GST) is an important phase II enzyme which performed to conjugate electrophilic and lipophilic compounds. A lot of studies demonstrated that GST activity in fish was increased followed exposure to pollutants such as PAHs and PCBs, etc. However, the response appears to be highly species specific [12]. It was also shown that treatment with BDE 99 on rats lead to a decrease trend of GST activity in the liver [13].

In previous studies, PCBs, TCDD and chlorinated pesticides, were all implicated as thyroid-disruptive agents when they were tested experimentally in fish [14]. Few studies suggested that PBDEs had similarity in pattern of thyroid endocrine disruption to these persistent organic pollutants (POPs) in fish [15]. Both short-term and chronic exposures to commercial PBDE mixtures (Bromkal 70 and DE 71) and BDE 47 have been resulted in decreasing the TH concentrations in rodents [6, 16]. Although there is evidence that PBDEs disrupt TH concentrations, the mechanism involved is unclear currently. One hypothesis is that metabolism of PBDEs, such as hydroxlated PBDE congeners, which have structural similarities with the 3, 3', 5, 5'-tetraiodothyronine (thyroxine, T_4) could bind to T_4 plasma transport proteins, such as transthyretin (TTR), which will subsequently result in the lower of T_4 concentration. Meerts et al. demonstrated that hydroxylated PBDE congeners would displace T_4 from transthyretin [17]. *In vitro* data suggested that 6-OH-BDE 47 incubated with T_4 and human transthyretin showed decreases of T_4-TTR binding [18]. Although several studies have investigated the effect of PBDEs in rodents, there is still lack of knowledge concerning the toxicity of these compounds on freshwater fish.

In this study, BDE 47 was selected from the 209 congeners based on its relative abundance in environmental samples. Since there is very little information on the toxicity of low-dose BDE 47 exposure, the selection of the current doses was based on the reported mean concentration of BDE 47 in aquatic environmental field samples of China [2, 3]. In contrast to most published experimental studies of PBDE toxicity, we used an intraperitoneal (i.p.) injection route of exposure to assure the accuracy of internal dosing in fish. The present study was conducted to analyze the dose-response and time-response relationships of hepatic enzymatic activities (EROD, ECOD, and GST), as well as T_3 and T_4 concentrations with the exposure of BDE 47 in crucian carp. Moreover, a histological study of liver tissue was performed in order to reveal the possibility of histology damage in fish liver under environmentally relevant exposure to BDE 47. These data are needed to increase our understanding of the toxicity on freshwater fish.

MATERIALS AND METHODS

Chemicals. BDE 47 (2, 2', 4, 4'-tetrabromodiphenyl ether) was purchased from Sigma-Aldrich Co. 7-ethoxyresorufin, resorufin, 7-ethoxycoumarin and 7-hydroxycoumarin were purchased from J&K Co. All other solvents and reagents used in these experiments were of analytical grade or higher and were purchased from standard sources. Injection solutions were prepared by dissolving BDE 47 in corn oil and mixed for 1 h. The concentrations of BDE 47 were analytically verified by gas chromatography (Agilent 7890 gas chromatography).

Experimental set up and acclimation of fish. Crucian carp (*Carassius auratus*), were purchased from Fisheries Research Institute of Nanjing with average weight of 40±2g. Exposure to chlorine was minimized by filling tanks for at least 3 days before the fish were introduced. The aquaria were also set up with continuous system of water filtration by activated carbon. Mean values for parameters of water quality were: pH 7.6±0.3, temperature varied between 22±2°C, dissolved oxygen values maintained ＞5mg/L. Fishes were fed with commercial fish food and acclimatized for at least 15 days before the beginning of the experiments.

Exposure and Sample Collection. After 15 days acclimation, the weight and length of each fish

were recorded for identification purposes. Thirty two fishes were randomly assigned to each of four 80-L aquaria. Fishes (N=32/dose group) were dosed via intraperitoneal (i.p.) injection of 0, 0.0025, 0.025 and 0.25 mg/kg b.w. /day of BDE 47 under laboratory conditions. All injections were standardized to ensure a final injection volume of 0.1mL of corn oil and performed for consecutive 7 days. After 7-day exposure, the fishes were transferred into clean water to recovery for another 7 days. Eight sampling points were set during the period of 14 days in the experiment (1, 3, 5, 7, 8, 10, 12, 14 days post treatment). At each sampling point, four fishes for each dose and control group were sacrificed. Food was withheld from the fish 24 h prior to sampling.

The fish were killed by a sharp blow to the head. Livers were quickly removed, rinsed in ice-cold 0.9% NaCl solution, and weighed. The liver tissues were homogenized in a 0.1M Tris-HCl buffer (containing 1mM EDTA, 0.15M KCl and 20% v/v glycerol at pH 7.4), with the ratio of 1 g liver to 5mL buffer. Samples were centrifuged at 9,000g for 20 minutes (4°C), and the resulting supernatant was recovered and recentrifuged at 105,000g (4°C) for 1 h. The cytosolic supernatant was collected and separated in aliquots. The microsomal pellet was resuspended in a 0.1M Tris-HCl buffer (containing 1mM EDTA and 20% v/v glycerol at pH 7.4) with 1 mL/g of tissue. Samples were frozen and stored at -80°C until utilized. The protein content analysis was based on previously reported methods [19]. Blood samples were centrifuged at 3000rpm for 5 min at 4°C and plasma was stored at -80°C until analysis.

Hepatic enzymatic activities assay. ECOD activity was measured using a modified method of Greenlee W.F. et al. [20]. The reaction mixture, in a total volume of 1.0mL, contained 0.1M Tris-HCl buffer (pH=7.4), NADPH solution, 1mg bovine serum albumin (BSA), 0.1ml microsomal supernatant and 0.5μM 7-ethoxycoumarin. The reaction was initiated by addition of the substrate followed by incubation for 10 minutes at 25°C with vigorous shaking, and then terminated by sequential addition of 0.125mL 15%(w/v) trichloroacetic acid and 2mL of chloroform. The product was partitioned into the chloroform layer by vigorous shaking for 2 minutes. A 1 mL portion of the organic phase was extracted with 5mL of 0.6M glycine-NaOH buffer (pH10.4), and the concentration of 7-hydroxycoumarin in the alkaline phase was determined fluorometrically (excitation/emission wavelengths of 368/456 nm) with an HIACHI F-7000 spectrophotofluorimeter.

EROD activity was measured using a modified method of Brunström, B. [21]. The reaction mixture, in a total volume of 1.0mL, contained 0.1M Tris-HCl buffer (pH7.8), NADPH solution, 1mg BSA, 0.1mL microsomal supernatant and ethoxyresorufin. The reaction was initiated by addition of the substrate followed by incubation for 10 minutes at 25°C, and then terminated by adding HPLC grade methanol. Resorufin standards and samples were centrifuged to precipitate proteins, and the fluorescence of the supernatant read at excitation/emission wavelengths of 535/585 nm.

GST activity was measured as the conjugation of glutathione with 1-chloro-2, 4-dinitrobenzene (CDNB) [22]. The total reaction mixture of 2.8 mL contained 0.1 M HEPES buffer (pH6.5), 0.5mL 20mM glutathione (GSH), and 30ul cytosolic supernatant. The reaction was started by adding CDNB. The formation of the CDNB conjugate was monitored on a UV spectrophotometer (Spectrum-752, Shanghai, China), at a wavelength of 340 nm for 80 s.

Thyriod hormone assay. Serum total T_3 and T_4 levels were measured using Coata-Count Total T_3 and Total T_4 radioimmunoassay kits (Diagnostic Products Corporation, 3V Co., Weifang, China), and were performed in the Department of Nuclear Medicine at Gulou hospital (Nanjing, China).

Histopathological examination. Histopathological examination was performed in control and high-dose (0.25mg/kg/day) group. A fraction of the liver of each fish was fixed into 10% neutral buffered formaldehyde for 2 days and embedded in paraffin. Sections were mounted on slides and stained with hematoxylin/eosin (H&E). Histology of liver tissues was examined under a light microscope. (Olympus, Tokyo, Japan).

Statistical analysis. All the values were expressed as the means ± standard deviation (SD). The statistical analysis of the data was performed on SPSS 12.0 for windows. The data were analyzed by one-way analysis of variance (ANOVA) with post hoc comparisons among each group followed by Dunnett t-test when equal variance was assumed. A p value of <0.05 was considered statistically significant. When equal variance could not be assumed, results were tested according to Games–Howell. Correlations between the measured parameters were established using linear regression analysis on paired data, which are in the exposure and depuration period separately.

RESULTS

Water quality parameters were similar in all treatment groups during the experimental period. No mechanical injury or parasitic diseases were observed on visual inspection. The fish appeared well adapted to laboratory conditions.

Phase I Activities. Hepatic EROD and ECOD activities were detected in four groups (0, 0.0025, 0.025 and 0.25mg/kg/day) on the 1st, 3rd, 5th, 7th, 8th,

10th, 12th and 14th day. The activities of EROD found in liver from experimental fishes were shown in Figure1. No marked difference of EROD activities was observed in three treatment groups compared with the coin oil control levels on the first 3 days injection. Subsequently, they were significantly decreased in medium (0.025mg/kg/day) group on the 5th, 7th, 8th day (81.5%, 73.2% and 67.5%, respectively). Similar pattern of reductions (76.0%, 80.3% and 79.1%, respectively) was observed in high-dose (0.25mg/kg/day) group. On the 10th day, reductions of EROD activities were occurred in all three treatment groups (86.9%, 72.1% and 75.5%, respectively). In the following 4 days, EROD activities in treatment groups were increased slightly, while there was no statistical difference relative to control group levels.

The ECOD activities in medium and high-dose groups were both decreased relative to the corn oil control levels after 1 day injection, as shown in Figure 2. However, it displayed an increased trend from the 3rd day in all three treatments groups, and the most marked induction (1.6 times) was detected on the 5th day in high-dose group. In the depuration period, from the 8th day to 14th day, inductions of ECOD activities were maintained in three dosed groups, though not all of the inductions showed statistical differences relative to control group, and the largest induction (1.7 times) was seen in low-dose group on the 12th day.

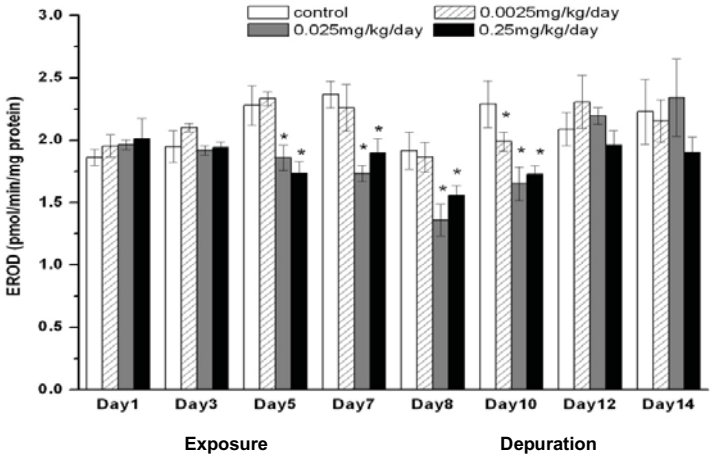

FIGURE 1

Activity of EROD in crucian carp liver exposed to control or BDE 47 for 7 consecutive days and then allowed to recover for a further 7-day depuration period.

Note: Data is presented as mean±S.E. (n=4); *Significantly different from the respective control ($p < 0.05$)

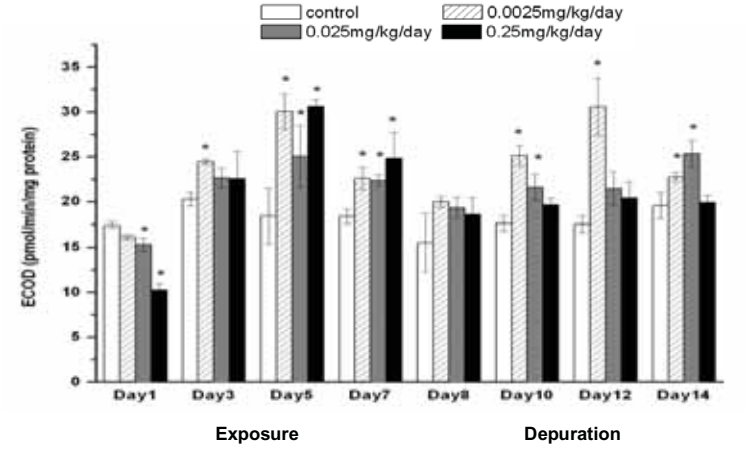

FIGURE 2

Activity of ECOD in crucian carp liver exposed to control or BDE 47 for 7 consecutive days and then allowed to recover for a further 7-day depuration period.

Note: Data is presented as mean±S.E. (n=4); *Significantly different from the respective control ($p < 0.05$)

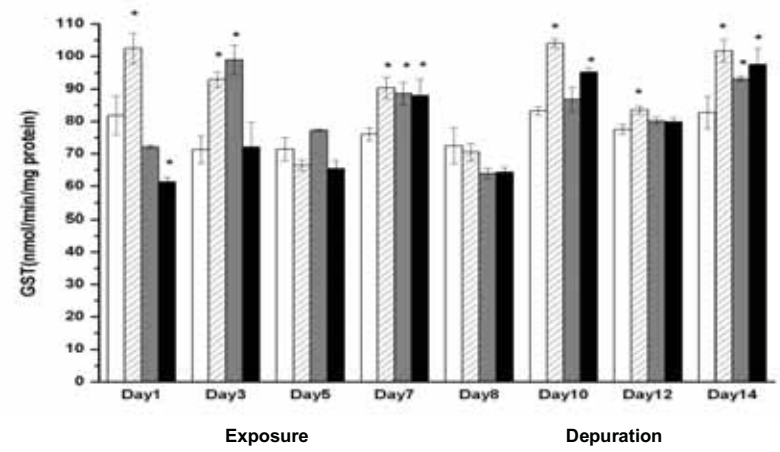

FIGURE 3
Activity of GST in crucian carp liver exposed to control or BDE 47 for 7 consecutive days and then allowed to recover for a further 7-day depuration period.
Note: Data is presented as mean±S.E. (n=4); *Significantly different from the respective control ($p < 0.05$)

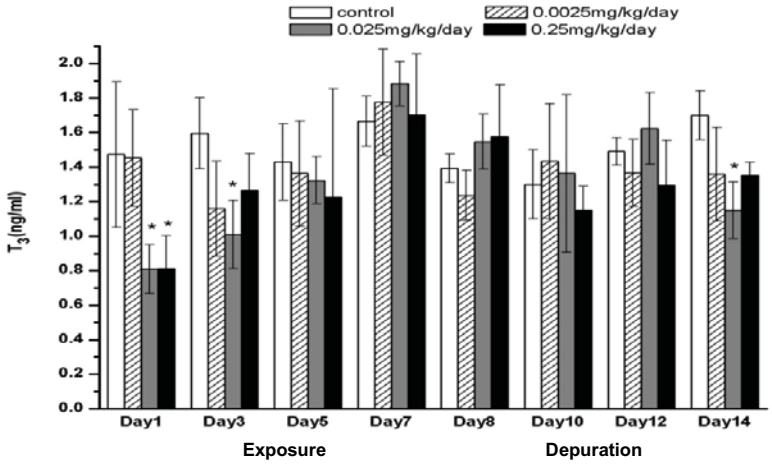

FIGURE 4
Concentrations (ng/mL) of triidothyronine (T3) in plasma of crucian carp exposed to a control or BDE 47 for 7 days and then depuration for 7 days.
Note: Data is presented as mean±S.E. (n=4); *Significantly different from the respective control ($p < 0.05$)

Phase II Activities. The activities of GST found in liver from experimental fishes are shown in Figure 3. GST activity in crucian carp injected with BDE 47 was induced to 1.25 times in low-dose group but reduced to 75.2% in high-dose group after 1 day injection. On the 3rd day, GST activities were both induced in low and medium-dose groups, (1.3 times and 1.4 times, respectively), but there was no significant difference in high dose. However, after 7 days injection, GST activities in three dosed groups were all induced dramatically.

T_3 and T_4 Levels. Thyroid hormone concentrations were measured in serum from fish during the exposure and depuration period. Significant reductions were detected in free triiodothyronine (T_3) concentrations in the plasma of fishes from medium and high-dose groups in initial 3 days, as shown in Figure 4. The largest difference was seen in medium-dose group on the 1st day, in which the serum total T_3 was decreased to 54.9%. However no consistent differences related to BDE 47 exposure dose levels were evident. In the following days, T_3 concentrations in treatment groups increased slightly, but these measured differences in T_3 concentrations were not statistically significant from the control group. At the end of the experiment, T_3 concentrations in treatment groups were reduced again, and a marked reduction was observed in medium-dose group.

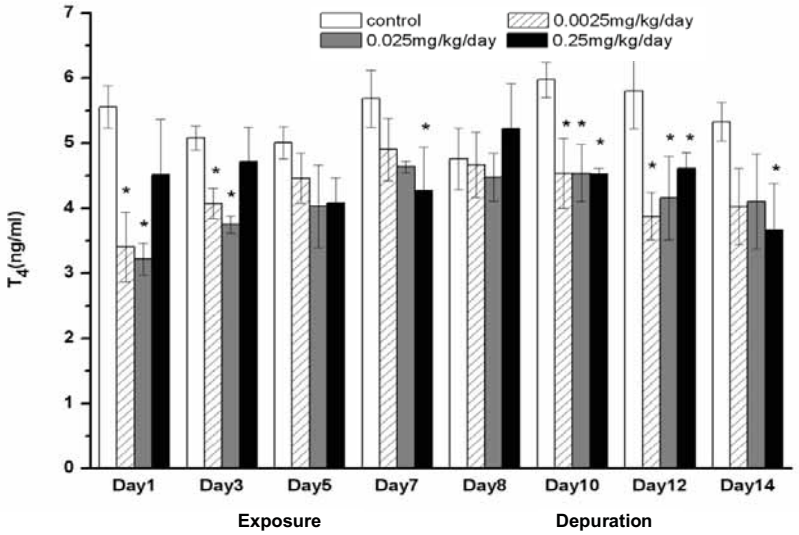

FIGURE 5
Concentrations (ng/mL) of thyroxine (T4) in plasma of crucian carp exposed to a control or BDE 47 for 7 days and then depuration for 7 days.
Note: Data is presented as mean±S.E. (n=4); *Significantly different from the respective control ($p < 0.05$)

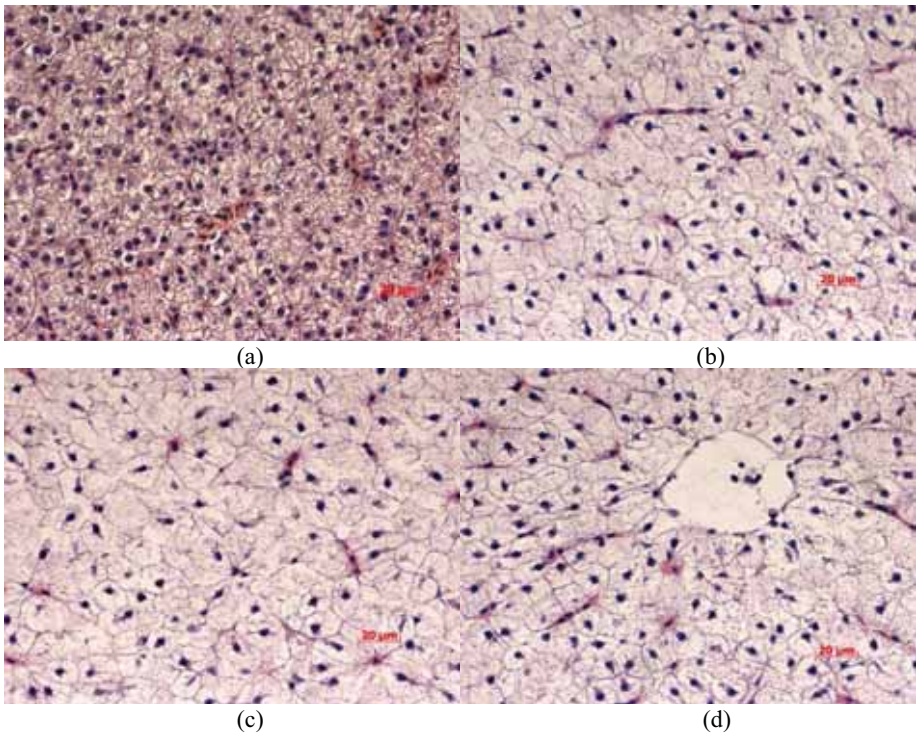

FIGURE 6
Histopathological analyses results in control and high-dose (0.25mg/kg/day) treatment group on the 14th day
(a). Normal architecture of liver was found in a crucian carp of the control group; (b). Liver from a crucian carp exposed to 0.25mg/kg/day BDE 47. Vacuolar hepatocytes with pyknotic and marginal nuclei were detected alongside some hepatocellular necrosis; (c). Liver from a crucian carp exposed to 0.25mg/kg/day BDE 47. The hepatocytes shown diffuse cell swelling; (d). Liver from a crucian carp exposed to 0.25mg/kg/day BDE 47. Acute cell swelling of hepatocytes accompanied by occlusion of blood sinusoids was found mainly in the peripheral zone of liver lobules.

Meanwhile, the serum levels of thyroxine (T_4) showed a pattern comparable to that of T_3 in the initial 3 days, but the reductions were maintained in all treatment groups in the flowing 11 days, even after 7 days of depuration, as shown in Figure 5. Most significant reduction of serum T_4 was found in medium-dose group on the 1st days, about 58% relative to control group.

Histopathological Analysis. Histopatholo-gical analyses were performed in control and high-dose (0.25mg/kg/day) treatment group on the 14th day. The results are shown in Figure 6. From Figure 6, we can see that liver histological changes in the high-dose group were characterized by disorganization of cell structure and a loss of adherence between hepatocytes. Acute cell swelling of hepatocytes accompanied by occlusion of blood sinusoids was found mainly in the peripheral zone of liver lobules. After 7 days exposure, vacuolar hepatocytes with pyknotic and marginal nuclei, even hepatocellular necrosis were detected.

DISCUSSION

Effect of BDE 47 on the Activity of Hepatic Enzymes. The hepatic enzymes selected for analysis in this study are all involved in the metabolism of xenobiotic chemicals and endogenous compounds in most living organisms. Induction and character-rization of biotransformation enzymes related to PBDEs exposure have previously been investigated for a variety of rodent species. However, studies on contaminant metabolism and related biotransformation enzymes in freshwater fish are scarce. Although there may be some similarities with regard to inducibility and catalytic properties of metabolic enzymes between rodent and fish species, it is definite that there is pronounced between-species variation in enzyme function [23].

One conclusion drawn from the present study is that exposure to BDE 47 at environmentally relevant doses had significant effects on levels of both phase I and phase II hepatic enzyme activities in fish. In our study, EROD activities did not reveal significant induction or reduction in initial time but were markedly decreased in medium-term days in medium and high-dose groups, and a U-shaped trend according to the time was observed. This finding is partly consistent with other researches on PBDEs. Certain PBDEs were shown to inhibit EROD activity significantly in rainbow trout after 6 and 22 days dietary exposure [24] at concentrations that are well above observed environmental concentrations of PBDEs (5.3-21 mg/kg). While, our results revealed that environmentally relevant doses of BDE 47 were sufficient to influence EROD activity. A significant reduction of TCDD-induction EROD activity induced by BDE 47 was also detected from the low concentration tested (0.25μM) in hepatocytes of carp (*Cyprinus carpio*) [25], which is consistent with our results. Since the EROD assay measures CYP1A by its catalytic action, explanations for the decreased EROD activity include either a reduced amount of enzyme present, or a reduced catalytic activity. Studies on the gene expression of Atlantic cod (*Gadus morhua*) exposed to BDE 47(5μg/L) for 3 weeks revealed a reduction of CYP1A1 gene expression in liver, which indicated that the reduction of EROD aroused by PBDEs was attributed to the former [26]. Kuiper et al. also suggested that the reduction of CYP1A synthesis in carp hepatocytes, which is mediated possibly via AhR, caused the inhibition of EROD activity in the presence of PBDEs [25].Contrary to EROD activity, BDE 47 had a significant effect on ECOD activity induction, even though on the first day a decrease was detected in the high dose group. This reduction may be due to the acute toxicity effect of high dose BDE 47 on fish in the initial stage. After three days adaptation period, the enzyme activity was restored followed by induction. To our knowledge, ECOD response of crucian carp exposed to PBDEs has not been reported. Some compounds structurally related to PBDEs, such as Aroclor 1260 (a commercial mixture of PCBs), have been shown to induce ECOD activity strongly [10], and similar pattern of induction was observed in the present study.

It has been reported that ECOD is mediated by CYPs from different families (including CYP1A1, CYP1A2 CYP2B1, CYP2E1, and CYP2B6) in mammals [9], and several subfamilies mentioned above have also been found in fish but it is not yet entirely clear which CYP isoforms catalyze the 7-ethoxycoumarin. One study by Uno et al. found that CYP1A9 and CYP1C1 from the Japanese eel (*Anguilla japonica*) were both capable of metabolizing ethoxycoumarin [27]. Another group suggested that this reaction is apparently catalyzed in rainbow trout by the CYP1A [28]. A study by Lange et al. suggested EROD and ECOD are both catalyzed by CYP1A in the dab (*Limanda limanda*), but a second ECOD isozyme exists so that each MFO activity exhibits species- and xenobiotic-specific differences [29]. In this study, since the induction only occurred in ECOD activity response but not in EROD activity, it is possible that there may be a second inducible CYP1A gene present in crucian carp.

In the current study, ECOD activity was induced after exposure to BDE 47, even though which species of CYP isoforms was induced needs to be further studied. This result suggested that BDE 47 was able to induce the MFO activity significantly in fish. If induction capacity is indicative of metabolic pathways of this compound, the CYP450 enzymes may be important in the metabolism of BDE 47 in fish. In field samples, some MeO-PBDEs and OH-PBDEs were detected in fishes [30], but their origin

was not conclusively clear. Both *in vitro* and *in vivo* studies have suggested that OH-PBDEs may be the biotransformation products of PBDEs in mammals and rodents, and CYP450 played a key role in this metabolism [31, 32]. The results in the present study indicated that this oxygenase reaction may also occur in fish. Since EROD activity was inhibited in this study, we also get a further hypothesis that CYP1A1 does not play a key role in metabolizing BDE 47 in crucian carp. The inhibition of CYP1A may shift the biotransformation of PBDE towards an alternate metabolic pathway, possibly through other species of CYP isoforms. One study group observed up-regulation of genes encoding for CYP1A2 and CYP3A4 in human hepatocytes exposed to BDE 99 [32]. The up-regulation of the CYP genes and the formation of several oxidative metabolites of BDE-99, such as 2,4,5-tribromophenol, support a role for CYP-mediated metabolism. Likewise, other CYP forms such as CYP2B were suggested to be involved in metabolizing PBDEs *in vitro* studies [33].

Phase II enzymes are important because they conjugate the reactive metabolites produced by phase I enzymes so as to facilitate their excretion. Glutathione-S-transferase (GST) is a phase II biotransformation enzyme to conjugate electrophilic and lipophilic compounds. Routti et al. have observed that PCBs concentrations in ringed seals were positively correlated to GST activity [11]. A lot of studies demonstrated that GST activity in fish was increased followed exposure to PAHs and PCBs. However, this response appears to be highly species specific [12]. In the previous investigation, GST activity showed a decrease trend in the liver of rats due to treatment with 0.6 and 1.2mg /kg BDE 99 [13]. However, our results indicated that GST activity was increased at lower concentrations (0.0025mg/kg/day) while decreased at higher (0.25mg/kg/day) concentrations in initial time, and then it revealed a significant induction in the following time. But no dose-response relationship was found.

Effect of BDE 47 on the Level of Thyroid Hormones. Thyroxine (T_4) released from the fish thyroid gland is the main thyroid hormone (TH). It is typically considered as a prohormone due to its modest intrinsic activity, and can translate to triiodothyronine (T_3) to present activity by outer-ring deiodination in target tissues [34]. In the present study, reductions of T_4 and T_3 were both noted as a result of BDE 47 exposure, however, reduction in T_3 was to a lesser extent than T_4. Thus, a conclusion could be drawn from this result that environmentally relevant doses of BDE 47 could disturb the thyroid hormones homeostasis in crucian carp. This result is similar to studies with rodents exposed to PBDEs and their commercial mixtures. One report showed that TH was decreased at 100 mg/kg/day BDE 47 exposure in adult female mice [35]. In other studies, exposure to PBDEs has been shown to reduce plasma concentrations of T_4 in rats and mice [6, 16]. It was proposed that if PBDEs exposure occurred at greatly elevated levels, plasma levels of T_3 in mice might be reduced [6, 36]. Very limited studies were carried out on the effects of PBDEs exposure on thyroid level in fish. Our finding was partly consistent with previous studies on technical or pure PBDEs in fish. One study found T_4 concentrations were lower in two groups of PBDE exposed fish compared with control fish after 56 days of exposure and after 112 days of depuration, but variation of T_3 concentrations was not related to BDE exposure [15].

The mechanisms by which PBDEs interfere with thyroid hormone homeostasis are often inconclusive. Previous hypotheses on T_3 and T_4 reduction have focused on two mechanisms: one is that more TH metabolism results decreased T_3 and T_4, the other is that competitive binding between BDE 47 and thyroid hormones to serum transport proteins results in their weak synthesis [37]. In the present study, a significantly decreased T_4 level was maintained in treatment groups even in 7 days depuration period. Additionally, the reduction on T_4 was coincident with the induction on the activities of both phase I enzyme (ECOD) and phase II enzyme (GST). The induction of phase I enzyme caused formation of metabolites that will increase binding to T_4 plasma transport proteins, such as transthyretin (TTR), which will subsequently result in the lower of T_4. In previous study, hydroxylated metabolites of PBDEs have been found to have capacity to compete with T_4 for the binding site on TTR and thus affecting T_4 levels [17]. Some studies also found that BDE 47 only had a weak affinity to TTR, while 6-OH-BDE 47 has greater affinity [18]. However, whether the PBDEs metabolites tested by other study groups existed in the present study was unknown and a further study should be continued.

Histopathological Effects of BDE47 on Fish Liver. Information regarding histopathological effects of PBDE in freshwater fish is scarce but studies conducted in mammals indicated that these contaminants could produce neoplasia, hyperplasia, mononuclear cell infiltrations, lipid accumulation, and necrosis in liver. In relation to the histopathological study, hepatocyte hypertrophy and vacuolization have been observed both in rats and mice liver after exposure to DE-71 [38]. Moreover, after administration of PBDE 209 diffuse cell swelling of hepatocytes and occlusion of blood sinusoids were found mainly in the mouse liver [36]. In the present study, histopathological changes in crucian carp liver have also been detected after exposure to BDE 47, and lesions could not recovered in short-time. Although the phase I (ECOD) and phase II (GST) enzymes activities were induced, which may lead to a metabolism and/or detoxification process, the environmentally relevant doses of BDE 47 still caused damage in the histopathological level. The present study also

indicate that histopathological features are probably sensitive biomarkers of liver damage in some fish species exposed to BDE 47 in natural environments or under laboratory conditions. The toxicity research of BDE 47 on fish should be enhanced to estimate their environmental harm, and provide the essential data for the ecological risk assessment.

CONCLUSION

The results of this study showed that crucian carp exposed to environmentally relevant doses of BDE 47 is able to cause significant impacts on levels of both phase I and phase II hepatic enzyme activities as well as T_3 and T_4 concentration. There was no dose–response relationship but time-response relationship during the exposure and depuration period.

EROD activity was markedly inhibited in medium-term days in medium and high doses treatment groups, and a U-shaped trend with time was observed. Contrary to EROD activity, BDE 47 had a significant effect on the induction of ECOD activity. As far as we know, ECOD activity response of crucian carp exposed to PBDEs has not been reported. It is worth noting that there was an inverse correlation between ECOD activity and T_4 concentration in depuration time, which indicated that the induction of phase I enzyme may cause formation of metabolites which will compete binding site with T_4 plasma transport proteins and subsequently result in the lower of T_4 level. Histopathological changes of fish liver have also been detected after exposure to BDE 47, and lesions caused by BDE 47 in fish could not recovered in short-time.

ACKNOWLEDGEMENTS

This research was financially supported by the National Natural Science Foundation of China (No. 21607050), the Science and Technology Department of Jilin Province (No. 20180520208JH), the National Natural Science Foundation of China (No. 41503115), and the Education Department of Jilin Province (No. JJKH20190856KJ).

REFERENCES

[1] Talsness, C.E. (2008) Overview of toxicological aspects of polybrominated diphenyl ethers: A flame-retardant additive in several consumer products. Environmental Research. 108, 158–167.

[2] Meng, X.Z., Yu, L.P., Guo, Y., Mai, B.X., Zeng, E.Y. (2008) Congener –specific distribution of polybrominated diphenyl ethers in fish of China implication for input sources. Environmental Toxicology and Chemistry. 27, 67–72.

[3] Tian, S.Y., Zhu, L.Y., Liu, M. (2010) Bioaccumulation and distribution of polybrominated diphnenyl ethers in marine species from BoHai Bay, China. Environmental Toxicology and Chemistry. 29, 2278–2285.

[4] Stapleton, H.M., Letcher, R.J., Li, J., Baker, J.E. (2004) Dietary accumulation and metabolism of polybrominated diphenyl ethers by juvenile carp (*cyprinus carpio*). Environmental Toxicology and Chemistry. 23, 1939–1946,

[5] Öberg, M., Westerholm, E., Fattore, E., Stern, N., Hanberg, A., Haglund, P., Wiberg, K., Bergendorff, A., Håkansson, H. (2010) Toxicity of bromkal 70-5DE, a technical mixture of polybrominated diphenyl ethers, following 28 d of oral exposure in rats and impact of analysed impurities. Chemosphere. 80, 137-143.

[6] Zhou, T., Ross, D.G., DeVito, M.J., Crofton, K.M. (2001) Effects of short-time *in vivo* exposure to polybrominated diphenyl ethers on thyroid hormones and hepatic enzyme activities in weanling rats. Toxicological Sciences. 61, 76-82.

[7] Chen, G.S., Konstantinov, A.D., Chittim, B.G., Joyce, E.M., Bols, N.C., Bunce, N.J. (2001) Synthesis of Polybrominated diphenyl ethers and their capacity to induce CYP1A by the Ah receptor mediated pathway. Environmental Science and Technology. 35, 3749-3756.

[8] Peters, A.K., van Londen, K., Bergman, A., Bohonowych, J., Denison, M.S., van den Berg, M., Sanderson, J.T. (2004) Effects of polybrominated diphenyl ethers on basal and TCDD-induced ethoxyresorufin activity and cytochrome P450-1A1 expression in MCF-7, HepG2, and H4IIE Cells. Toxicological Sciences. 82, 488–496.

[9] Yamazaki, H., Inoue, K., Mimura, M., Oda, Y., Guengueric, F.P., Shimada, T. (1996) 7-Ethoxycoumarin *O*-deethylation catalyzed by cytochromes P450 1A2 and 2E1 in human liver microsomes. Biochemical Pharmacology. 51, 313–319.

[10] Hugla, J.L., Thomé, J.P. (1999) Effects of polychlorinated biphenyls on liver ultrastructure, hepatic monooxygenases, and reproductive success in the barbel. Ecotoxicology and Environmental Safety. 42, 265-273.

[11] Routti, H., Letcher, R.J., Arukwe, A., van Bavel, B. Yoccoz, N.G., Chu, S.G., Gabrielsen, G.W. (2009) Biotransformation of PCBs in relation to phase I and II xenobiotic-metabolizing enzyme activities in ringed seals (*Phoca hispida*) from svalbard and the baltic sea. Environmental Science and Technology. 42, 8952-8958.

[12] van der Oost, R., Beyer, J., Vermeulen, N.P.E. (2003) Fish bioaccumulation and biomarkers in environmental risk assessment: A review. Environmental Toxicology and Pharmacology. 13, 57-149.

[13] Albina, M.L., Alonso, V., Linares, V., Bellés, M., Sirvent, J.J., Domingo, J.L., Sánchez, D.J. (2010) Effects of exposure to BDE-99 on oxidative status of liver and kidney in adult rats. Toxicology. 271, 51–56.

[14] Brar, N.K., Waggoner, C., Reyes, J.A., Fairey, R., Kelley, K.M. (2010) Evidence for thyroid endocrine disruption in wild fish in San Francisco Bay, California, USA. relationships to contaminant exposures. Aquatic Toxicology. 96, 203–215.

[15] Tomy, G.T., Palace, V.P., Halldorson, T., Braekevelt, E., Danell, R., Wautier, K., Evans, B., Brinkworth, L., Fisk, A.T. (2004) Bioaccumulation, biotransformation, and biochemical effects of brominated diphenyl ethers in juvenile lake trout (*Salvelinus namaycush*). Environmental Science and Technology. 38, 1496-1504.

[16] Hallgren, S., Sinjari, T., Hakansson, H., Darnerud, P.O. (2001) Effect of polybrominated diphenyl ethers (PBDEs) and polychlorinated biphenyls (PCBs) on thyroid hormone and vitamin A levels in rat and mice. Archives of Toxicology. 75, 200-208.

[17] Meerts, I.A.T.M., van Zanden, J.J., Luijks, E.A.C., van Leeuwen-Bol, I., Marsh, G., Jakobsson, E., Bergman, Å., Brouwer, A. (2000) Potent competitive interactions of some brominated flame retardants and related compounds with human transthyretin *in vitro*. Toxicological Sciences. 56, 95-104.

[18] Hamers, T., Kamstra, J.H., Sonneveld, E., Murk, A.J., Kester, M.H.A., Andersson, P.L., Legler, J., Brouwer, A. (2006) *In vitro* profiling of the endocrine-disrupting potency of brominated flame retardants. Toxicological Sciences. 92, 157-173.

[19] Bradford, M.M. (1976) A rapid and sensitive method for the quantification of microgram quantities of protein utilizing the principle of protein-dye binding. Analytical Biochemistry. 72, 248-254.

[20] Greenlee, W.F., Poland, A. (1978) An improved assay of 7-ethoxycoumarin-*O*-deethylase activity: induction of hepatic enzyme activity in C57BL/6J and DBA/2J mice by Phenobarbital, 3-methylcholanthrene and 2, 3, 7, 8-tetrachlorodibenzo-*p*-dioxin. Journal of Pharmacology and Experimental Therapeutics. 205, 596-605.

[21] Brunström, B. (1990) Mono-ortho-chlorinated chlorobiphenyls: toxicity and induction of 7-ethoxyresorufin O-deethylase (EROD) activity in chick embryos. Archives of Toxicology 64, 188-192.

[22] Habig, W.H., Pabst, M.J., Jakoby, W.B. (1974) Glutathione-s-transferases the first enzymatic step in mercapturic acid formation. Journal of Biological Chemistry. 249, 7130-7139.

[23] Smith, E.M., Wilson, J.Y. (2010) Assessment of cytochrome P450 fluorometric substrates with rainbow trout and killifish exposed to dexamethasone, pregnenolone-16α-carbonitrile, rifampicin, and β-naphthoflavone. Aquatic Toxicology. 97, 324-333.

[24] Tjärnlund U., Ericson, G., Örn, U., de Wit, C., Balk, L. (1998) Effects of two polybrominated diphenyl ethers on rainbow trout (*Oncorhynchus mykiss*) exposed via food. Marine Environmental Research. 46, 107-112.

[25] Kuiper, R.V., Bergmand, A., Vos, J.G., van den Berg, M. (2004) Some polybrominated diphenyl ether (PBDE) flame retardants with wide environmental distribution inhibit TCDD-induced EROD activity in primary cultured carp (*Cyprinus carpio*) hepatocytes. Aquatic Toxicology. 68, 129-139.

[26] Olsvik, P.A., Lie, K.K., Sturve, J., Hasselberg, L., Andersen, O.K. (2009) Transcriptional effects of nonylphenol, bisphenol A and PBDE-47 in liver of juvenile Atlantic cod (*Gadus morhua*). Chemosphere. 75, 360-367.

[27] Uno, T., Okamoto, S., Masuda, S., Imaishi, H., Nakamura, M., Kanamaru, K., Yamagata, H., El-Kady, M.A.H., Kaminishi, Y., Itakura, T. (2008) Bioconversion by functional P450 1A9 and P450 1C1 of Anguilla japonica. Comparative Biochemistry and Physiology Part C: Toxicology and Pharmacology. 147, 278-285.

[28] Cravedi, J.P., Perdu-Durand, E., Paris, A. (1998) Cytochrome P450-dependent metabolic pathways and glucuronidation in trout liver slices. Comparative Biochemistry and Physiology Part C. Toxicology and Pharmacology. 121, 267-275.

[29] Lange, U., Goksøyr, A., Siebers, D., Karbe, L. (1999) Cytochrome P450 1A-dependent enzyme activities in the liver of dab (*Limanda limanda*): kinetics, seasonal changes and detection limits. Comparative Biochemistry and Physiology Part B. Biochemistry and Molecular Biology. 123, 361-371.

[30] Wan, Y., Wisman, S., Chang, H., Zhang, X.W., Jones, P.D., Hecker, M., Kannan, K., Tanabe, S., Hu, J.Y., Lam, M.H.W., Giesy, J.P. (2009) Origin of hydroxylated brominated diphenyl ethers: Natural compounds or man-made flame retardants? Environmental Science and Technology. 43, 7536-7542.

[31] Marsh, G., Athanasiadou, M., Athanassiadis, I., Sandholm, A. (2006) Identification of hydroxylated metabolites in 2, 2', 4, 4'-tetrabromodiphenyl ether exposed rats. Chemosphere. 63, 690-697.

[32] Stapleton, H.M., Kelly, S.M., Pei, R., Letcher, R.J., Gunsch, C. (2009) Metabolism of polybrominated diphenyl ethers (PBDEs) by human hepatocytes *in vitro*. Environmental Health Perspectives. 117, 197-202.

[33] Lundgren, M., Darnerud, P.O., Molin, Y., Lilienthal, H., Blomberg, J., Ilbäck, N.G. (2007) Viral infection and PBDE exposure interact on CYP gene expression and enzyme activities in the mouse liver. Toxicology. 242, 100-108.
[34] Finnson, K.W., Eales, J.G. (1999) Effect of T_3 treatment and food ration on hepatic deiodination and conjugation of thyroid hormones in rainbow trout, *Oncorhynchus mykiss*. General and Comparative Endocrinology. 115, 379-386.
[35] Richardson, V.M., Staskal, D.F., Ross, D.G., Diliberto, J.J., DeVito, M.J., Birnbaum, L.S. (2008) Possible mechanisms of thyroid hormone disruption in mice by BDE 47, a major polybrominated diphenyl ether congener. Toxicology and Applied Pharmacology. 226, 244-250.
[36] Tseng, L.H., Li, M.H., Tsai, S.S., Lee, C.W., Pan, M.H., Yao, W.J., Hsu, P.C. (2008) Developmental exposure to decabromodiphenyl ether (PBDE 209). Effects on thyroid hormone and hepatic enzyme activity in male mouse offspring. Chemosphere. 70, 640-647.
[37] Crane, H.M., Pickford, D.B., Hutchinson, T.H., Brown, J.A. (2005) Effects of ammonium perchlorate on thyroid function in developing fathead minnows, *Pimephales promelas*. Environmental Health Perspectives. 113, 396-401.
[38] Dunnick, J.K., Nyska, A. (2009) Characterization of liver toxicity in F344/N rats and B6C3F1 mice after exposure to a flame retardant containing lower molecular weight polybrominated diphenyl ethers. Experimental and Toxicologic Pathology. 61, 1-12.

Received: **22.09.2019**
Accepted: **27.01.2020**

CORRESPONDING AUTHOR

Hai Lu
College of Civil Engineering and Architecture,
Changchun Sci-Tech University,
Changchun 130600 – China

e-mail: haimm110@126.com

© by PSP Volume 29 – No. 04A/2020 pages 2869-2878 Fresenius Environmental Bulletin

URBAN INTRINSIC PROCESS AND ITS APPLICATION IN SPATIAL DATABASE UNDER DIFFERENT RAIN CONDITIONS BASED ON GIS

Tianhe Yin[1], Qiting Huang[2,*], Zelin Qin[2], Chao Wang[3]

[1]School of Science, Ningbo University of Technology, Ningbo, China
[2]Agricultural Science and Technology Information Research Institute, Guangxi Academy of Agricultural Sciences, Nanning, China
[3]School of Mathematics, Physics and Information Science/Key Laboratory of Oceanographic Big Data Mining and Application of Zhejiang Province, Zhejiang Ocean University, Zhoushan, China

ABSTRACT

According to meteorology, hydrology, water conservancy and other professional knowledge, using the spatial analysis technology of GIS, combining the urban spatial database and mathematical calculation model and the empirical formula of urban rainstorm intensity, the urban waterlogging disaster analysis model is established. Based on the technology of urban waterlogging model, a mathematical model of rainstorm waterlogging in Pudong District was established. At the same time, the model grid generalization model and calculation model are improved, and the urban river network, road network, pipeline network and community computing grid are divided into layers to form a zoning and multi-dimensional waterlogging calculation model. The model is the basis of calculation and Simulation of urban waterlogging and flooding. It can simulate and predict the characteristic data of urban waterlogging disasters according to the distribution of urban rainfall, such as spatial distribution, depth distribution, submerged area and submerged time of waterlogging and flooding. The simulation results can provide a basis for disaster prevention and mitigation departments to formulate disaster prevention and mitigation measures.

KEYWORDS:
GIS technology, urban rainfall, waterlogging simulation, database

INTRODUCTION

With the rapid development of economy, the construction land area of major cities in China is also increasing, and the urban heat island effect increases the frequency and intensity of heavy rainfall. Rainstorm waterlogging disaster is a natural disaster caused by excessive rainfall, low-lying terrain, and water accumulation cannot be eliminated in time. In recent years, under the background of accelerated global climate change and urbanization, the frequency and intensity of rainstorms in coastal areas of China are increasing due to the combined effects of geographical location, topography, and monsoon climate [1- 3]. In addition, the outdated flood control and drainage facilities make the phenomenon of rainstorm waterlogging more and more serious. This has a serious impact on urban development and residents' production and life. Therefore, the risk assessment of urban rainstorm and waterlogging disaster has become a hot research topic in the field of natural disasters in coastal areas [4]. Rainstorms are prone to cause floods in cities along the Yangtze River, which not only have a negative impact on the quality and image of the city, but also cause great harm and loss to the lives of residents and affect the normal development of social economy [5]. Therefore, it is necessary to study the risk assessment and prediction of urban waterlogging disasters.

In order to alleviate urban floods and improve urban water ecological environment, the state proposes to construct sponge cities according to local conditions, namely Low Impact Development (LID) rainwater system construction. LID measures mainly through demurrage, sedimentation, biosorption, infiltration, Filtration, microbial degradation and other means to reduce urban stormwater runoff, delay runoff generation time, reduce flood peaks, and reduce pollutant load on downstream areas. LID was originally a design concept in North America and has since become popular around the world [6]. LID-like design concepts include New Zealand's Urban Design and Development (UDDD), Australia's Water-Sensitive Urban Design (WSUD), and European Sustainable Urban Drainage System (SUD), includes strategies for urban stormwater management (IUSM) and integrated urban water resources management (IUWM). Many cities in China have suffered from heavy rains during the summer flood season, causing serious floods. Every time the heavy rain strikes, the big cities have repeatedly become a country, and the flood control and drainage problems have become a new problem that has recently plagued Chinese cities [7- 9]. In the past, some cities

with relatively low flood prevention tasks also frequently experienced severe storms and floods, posing a major threat to the economic and social development of the city and the safety of people's lives and property. Over the years, flood control has become a "compulsory course" for urban emergency in the summer. This new urban problem cannot be separated from the help of information technology [10, 11]. Geographic Information System (GIS) technology is a spatial information analysis technology that has developed rapidly in recent years and plays a leading role in resource and environmental applications.

In recent years, many scholars have done a lot of research on the risk zoning and evaluation of various meteorological and geological disasters, but the research on the risk assessment of rainstorm and the risk zoning of waterlogging disasters in certain regions and different rainstorm recurrence periods is relatively insufficient. In order to assess the risk of urban rainstorm waterlogging disasters, it is necessary to conduct in-depth risk analysis of regional rainstorm waterlogging disasters and accurately assess their water regime [12, 13]. At present, in the risk analysis of urban rainstorm waterlogging disaster, some scholars have used the method of combining GIS spatial analysis technology with mathematical and hydrological models to simulate the submergence depth and scope of the city caused by extreme events of rainstorm waterlogging at a certain frequency. However, the accuracy of urban terrain simulation is not enough [14]. The hydrological model selected requires too much data or the accuracy of model parameters setting is low, which leads to the inaccuracy of the results of risk analysis of rainstorm waterlogging disaster. On the basis of GIS spatial analysis technology, combining with storm flood management model to simulate the waterlogging scenario in the study area, this paper divides and analyses the waterlogging disaster risk zoning and draws the waterlogging disaster risk zoning maps in different recurrence periods, which has broad application prospects in urban waterlogging early warning and forecasting.

RELATED THEORETICAL RESEARCH

GIS Technology. A geographic information system (GIS) is a computer system that collects, stores, manages, analyzes, describes, and applies data related to spatial geographic distribution, supported by computer hardware and software. The object of GIS processing management is a variety of geospatial entity data and their relationship, including spatial positioning data, remote sensing image data, attribute data and so on. These data are used to analyze and process the various phenomena and processes that are distributed over a geographical area. Based on the spatial characteristics and attribute characteristics of geographic objects, the GIS system establishes a variety of spatial analysis models. Based on these models, the geographic data is managed by spatial query and spatial analysis, and the geographic data is analyzed, processed and processed. In recent years, GIS technology has widely applied in urban flood control and flood control, and has exerted great advantages in Figure 1. Utilizing GIS's powerful spatial data analysis capabilities combined with data sharing advantages in other fields, it can quickly provide services such as decision support, dynamic simulation, statistical analysis, and forecasting.

With the advancement of informatization construction in the water conservancy industry, some cities in China have organized, stored, processed and analyzed the distribution of surrounding waters and the use of database technology for hydrological information in the region, which has improved the level of response to urban floods to a certain extent. At the same time, it can be found that the decision-making measures formed by the database technology are closely related to the spatial orientation, the hierarchy is strong, the change is fast, and the data forms are diverse, and the decision-making measures formed by analyzing the spatial distribution-related characteristics are not obvious. Therefore, the flood control situation in modern cities urgently needs to analyze a large amount of complex spatial information by virtue of the advantages of GIS technology, so as to achieve accurate forecasting, scientific decision-making, and efficient measures.

Urban Waterlogging Model. Models are abstractions and generalizations of the objective world, which can be established by mathematical, physical or graphical methods. Geographic Information System (GIS) is a digital representation of nature. It has complete spatial characteristics, can store and process a large number of spatial data, and has strong comprehensive analysis ability of spatial system. From the application point of view, GIS not only needs to complete the task of managing a large number of complex geographical data. More importantly, the analysis and visualization of spatial data should be realized [15]. Therefore, for applied GIS, application analysis model is the key to the practicality of GIS.

The urban waterlogging disaster analysis model based on GIS is an important application and analysis model of GIS. It is based on meteorology, hydrology, water conservancy and other professional knowledge, using the spatial analysis technology of GIS, combined with urban geographic database and disaster database. Urban waterlogging model is a comprehensive model which integrates urban surface elevation model, rainfall model, runoff generation and concentration model, drainage model, mathematical calculation model and spatial analysis application module of GIS [16]. Among them, the

FIGURE 1
Application of GIS

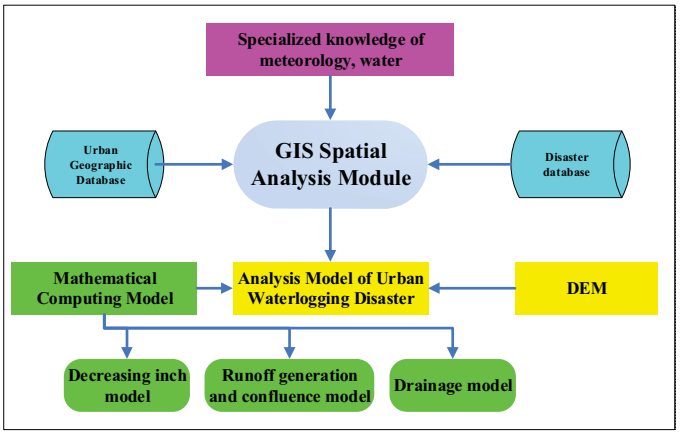

FIGURE 2
Framework diagram of waterlogging disaster model based on GIS

ground elevation model is used to simulate the fluctuation of urban land surface, which is the basis of urban waterlogging calculation and simulation. The precipitation model is used to simulate and calculate the spatial and temporal distribution of urban rainfall; the runoff yield and concentration model is used to simulate the generation and collection process of surface runoff; and the drainage model is used to calculate urban drainage according to different urban drainage modes. The comprehensive calculation of several models provides a basis for the calculation of urban waterlogging and waterlogging. Mathematical calculation model and GIS spatial analysis application module are the "operation center" of the whole urban waterlogging model [17]. Mathematical calculation model provides some key theories and formulas, including precipitation calculation, Comprehensive Drainage calculation, residual Rainfall Calculation and water accumulation height calculation. The spatial analysis application module of GIS provides an important spatial solution for the spatial problems involved in the mathematical model, and also provides strong support for the display and Simulation of urban waterlogging and flooding process. The overall architecture is shown in Figure 2.

CONSTRUCTION OF URBAN WATERLOGGING MODEL

Model Meshing. The main simulation objects of the mathematical model of urban waterlogging in this paper are the surface and open channel flow movement of Shijiazhuang central city. Considering the topographic and geomorphological characteristics of the underlying surface of the study area, unstructured irregular grids are used to divide the model calculation area. In grid design, we need to fully consider the characteristics of urban topography and geomorphology and the distribution of water accumulation areas. For example, the key service areas and water accumulation areas of a city are divided into denser grids, and the suburbs and water accumulation areas are divided into sparse grids, and the underlying surface attributes in a single grid are as same as possible [18]. The number of edges of the mesh is not more than 6. Each edge of the mesh is

defined as a channel to exchange water between the meshes. The normal direction of the mesh can be in any direction as shown in Figure 2. According to the finite volume method, the unit grid is taken as the control body, the water level H is calculated at the center of the grid, and the flow Q is calculated at the midpoint of the channel around the grid. The water level and flow have the meaning of grid and channel average respectively, and the time staggered calculation method is adopted.

The original basic waterlogging model only considers the water accumulation of a single type of grid, and generalizes the road and pipeline network into the same grid. It does not reflect the water accumulation of roads and water level of rivers well. In this paper, the model is improved by three-dimensional, multi-zoning and hierarchical method when meshing the model. Stereo multiple refers to the arrangement of multiple grids in the same plane position to solve the problems of water confluence and water accumulation at the three-dimensional level of grid units such as underpass bridges and underground rivers [19]. Zoning refers to dividing the grid into road network, community and river network, each district has its own system, and realizes district-by-district calculation in Figure 3; stratification refers to the independent calculation of pipeline network layer, surface layer and rainfall layer.

Model Computing Method. Using the idea of finite volume method, the mathematical model regards meteorological precipitation data as the initial precipitation value and boundary condition of the model, and takes the basic governing equation of two-dimensional unsteady flow as the framework [20, 21]. At the same time, aiming at drainage canal inrush or river channel with less than discrete grid scale, an algorithm of one-dimensional open channel unsteady flow equation is combined in the two-dimensional model to calculate the flow in underground drainage pipeline network. The source and sink terms of continuous equation are used to control the water exchange between underground drainage pipeline network and ground, and the overflow formula with wide roof is used to calculate the flow. Figure 4 is a flow chart of waterlogging calculation of improved urban waterlogging model, which includes three program blocks: surface rainfall interpolation, road network, River network, community and pipeline network confluence simulation and pumping station drainage or pipeline network self-flow.

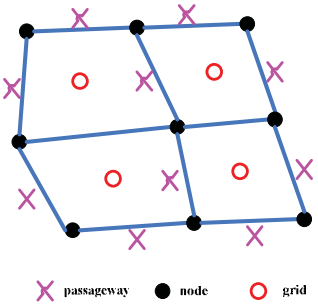

FIGURE 3
Grid model schematic diagram

(1) Surface Rainfall Interpolation. In order to transform the precipitation data of automatic precipitation stations into surface precipitation with unstructured irregular grids, interpolation processing must be carried out before it can be used as the rainfall boundary condition of the model. In this paper, quadric interpolation method is used to calculate surface rainfall [22]. The number of rainfall observation stations is N. For any location (x, y) in the computational region, the nearest n ($n \leq N$) observation points can be selected, and the observed rainfall $q_1, q_2, \ldots, q_n$ from these n observation points. A quadric surface is fitted by the least square method. The rainfall at the location (x, y) can be determined by the quadric surface. The concrete methods are as follows: Let the quadric surface equation be as follows:

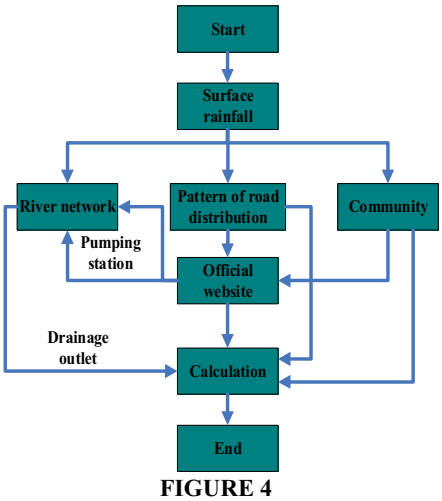

FIGURE 4
Schematic flow chart of urban waterlogging model calculation

$$q(x,y)=a_1x^2+a_2y^2+a_3xy+a_4x+a_5y+a_6 \quad (1)$$

The sum of the error of n points is:

$$R=\sqrt{\sum_{i=1}^{n}(q-q_i)^2} \quad (2)$$

According to the principle of least square method, in order to minimize the error of n point and R, there are:

$$\frac{\partial R}{\partial a_i}=0,\ i=1,2,\cdots,n \quad (3)$$

The $a_i\left(i=1,2,\cdots,n\right)$ is obtained from formula (3) and then substituted into (1) to find the interpolated rainfall q of point (x, y).

(2) Basic governing equation. The basic equations of two-dimensional unsteady flow are as follows:

$$\frac{\partial R}{\partial a_i}+\frac{\partial M}{\partial x}+\frac{\partial N}{\partial y}=q \quad (4)$$

The formula of momentum equation is:

$$\frac{\partial R}{\partial t}+\frac{\partial(uM)}{\partial x}+\frac{\partial(vM)}{\partial y}+gH\frac{\partial Z}{\partial x}+g\frac{n^2u\sqrt{u^2+v^2}}{H^{1/3}}=0 \quad \text{.....(5)}$$

$$\frac{\partial N}{\partial t}+\frac{\partial(uN)}{\partial x}+\frac{\partial(vN)}{\partial y}+gH\frac{\partial Z}{\partial y}+g\frac{n^2v\sqrt{u^2+v^2}}{H^{1/3}}=0 \quad \cdots \quad (6)$$

In the formula, H is water depth; Z is water level, $Z = Z_0 + H$, Z_0 is bottom elevation; q is source and sink term, including effective rainfall and drainage intensity; M, N are single-width discharge in x and y directions, and M = H u, N = H v, u and V are component of velocity in x and y directions respectively; n is roughness; g is gravity acceleration.

The basic governing equations of one-dimensional unsteady flow are:

$$\frac{\partial Q}{\partial t}+\frac{\partial}{\partial l}\left(\frac{Q^2}{A}\right)+gA\frac{\partial H}{\partial l}=-gAS_f \quad (7)$$

In the formula, Q is cross-section discharge, A is cross-section area, S_f is friction gradient, which can be obtained by Manning's formula.

$$S_f=\frac{U^2n^2}{R^{4/3}}=\frac{n^2Q|Q|}{A^2R^{4/3}} \quad (8)$$

Overflow formula of wide crested weir:

$$Q^{T+dt}=\sigma_s mb\sqrt{2g}H^{3/2} \quad (9)$$

In the formula, Q is the discharge of weir top, m is the overflow coefficient of wide-crested weir, σ_s is the submergence coefficient, b is the weir width, and H is the upstream water level of weir top.

Combination of urban drainage system and model calculation. According to the trend of urban roads, the underground drainage network is generalized. At the same time, according to the actual drainage capacity, the radius of water collection is assigned to each unit of the network. The water collection of the network enters the river network, and the drainage outlet of the network is connected with the confluence outlet of the river section by hydrodynamic force [23]. Waterlogging model calculates the area and intensity of water collection by invoking the coefficient of water collection radius, and uses the reciprocal weight of distance to determine the distribution of confluence within the drainage radius.

The model generalizes the gate or drainage pumping station on the adjacent channel. In the process of rainfall, the surface water gathers in the pipeline except the seepage part, and the pipeline converges to the outlet along the respective system. The simulation process of "rainwater, surface water, pipeline catchment, pump, sluice, submerged outflow pipeline drainage, River catchment" is formed at the outlet by sluice, pumping station or submerged outflow pipeline [24, 25]. The drainage of pumping station is mainly based on the data provided by municipal drainage department, which can be intervened according to the actual operation mode of drainage. The sluice is the joint part of controlling and regulating the flow between pipelines, pipelines and rivers, and between rivers [27- 28]. Its drainage is regulated according to the design flow of the pipeline network and the outlet. The discharge of the entrance is adjusted according to the water level difference between the river and the pipeline. When the water level of the river is higher than the water level of the pipeline, the phenomenon of backfilling will occur.

RESULTS

Analysis of Risk Zone of Waterlogging Disaster. In this paper, the evaluation factor system is constructed according to four kinds of evaluation factors: hazard factor, sensitivity factor, vulnerability factor and disaster prevention and mitigation factor. Analytic Hierarchy Process (AHP) is used to classify and rank the factors affecting waterlogging according to their importance and degree of influence, to assign the corresponding weights, to achieve dimensionless scores, and to make decisions accordingly, to calculate the weights of indicators [30]. The scoring rules of evaluation factors are shown in Table 1 and the weights of evaluation factors are shown in Table 2 and Figure 5.

When evaluating the risk factors, firstly, the influence radius is calculated by the ratio of the spillway discharge to the depth of the spillway at each waterlogging point, and then the influence range of the waterlogging point is determined by the Buffer tool in GIS according to the influence radius of the calculated waterlogging point, and the risk factors of

the waterlogging node are assigned to the administrative villages. Then, combined with the sensitivity factors, vulnerability factors and disaster prevention and mitigation factors of the administrative villages, comprehensive evaluation was carried out to obtain the risk values of waterlogging disasters of the administrative villages, which were divided into five levels according to the corresponding score [31]. The corresponding score of waterlogging hazard grade is shown in Table 3 and the grading result is shown in Figure 7.

TABLE 1
Rule table of scoring value for grade evaluation factor of waterlogging disaster

Score	Waterlogging duration	Overflow	Maximum overflow velocity	Number of waterlogging nodes	Road density	Ground hardening rate	Permeability
20	0-20	0-10	0-1.0	0-4	0-10	0-20	0-20
40	20-40	10-100	1.0-2.5	5-8	10-20	20-40	20-40
60	40-60	100-1000	2.5-3.5	9-12	20-30	40-60	40-60
80	60-80	1000-10000	3.5-4.5	13-16	30-40	60-80	60-80
100	>80	>10000	>4.5	17-20	>40	80-100	>80

TABLE 2
Index weight table of waterlogging disaster grade evaluation factor

Risk assessment factors	Factor weight	Risk assessment factors	Factor's own weight	Relative objective weight
Danger	0.4	Waterlogging duration	0.2	0.09
		Overflow	0.3	0.13
		Maximum overflow velocity	0.2	0.09
Susceptibility	0.3	Number of waterlogging nodes	0.3	0.13
		Road density	1	0.32
Vulnerability	0.2	Ground hardening rate	1	0.21
Disaster prevention and mitigation	0.1	Permeability	1	0.12

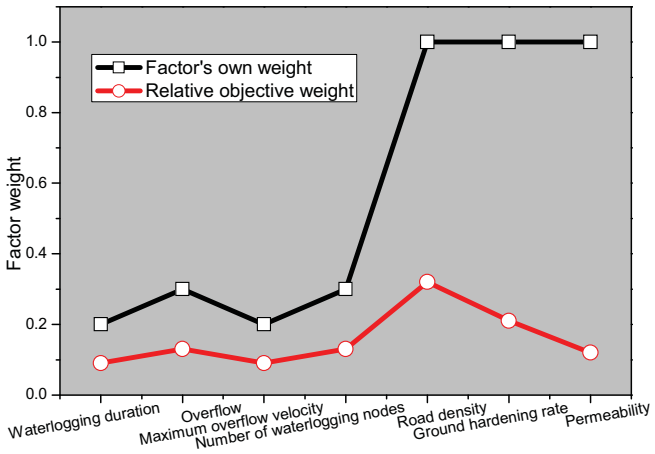

FIGURE 5
Comparison of weighting factors of evaluation factors

TABLE 3
Risk classification table of waterlogging disasters

Hazard Level	Corresponding score	Explain
1	0	No waterlogging node, no waterlogging disaster
2	0-30	There are a few waterlogging nodes, there are waterlogging disasters, there is a certain risk
3	30-45	There are waterlogging nodes, waterlogging disasters, relatively dangerous
4	45-60	There are many waterlogging nodes, waterlogging disasters are serious and dangerous
5	>60	There are many waterlogging nodes, which are very serious. It is necessary to take precautionary measures

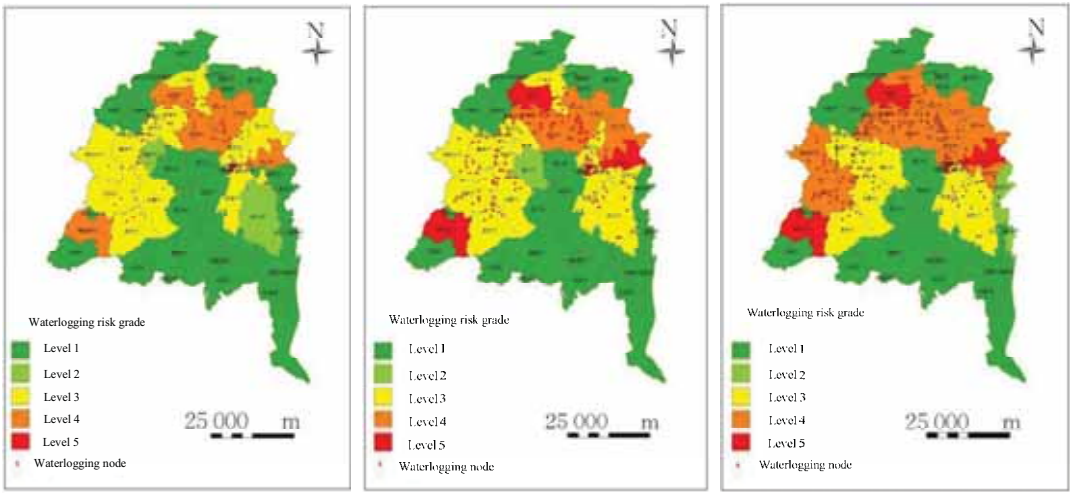

(a) Once a year **(b) Once in five years** **(c) Once in ten years**

FIGURE 6
Map of risk zone of waterlogging disaster

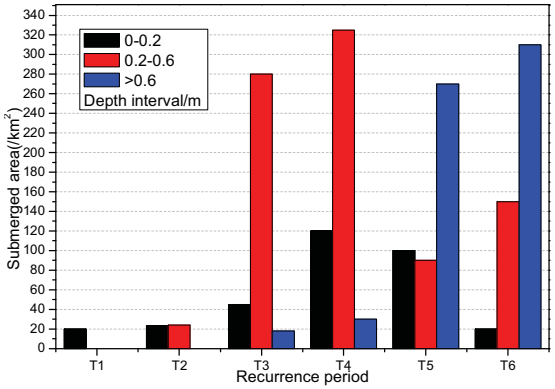

FIGURE 7
Submerged area of different water depth intervals in different recurrence periods in Pudong District

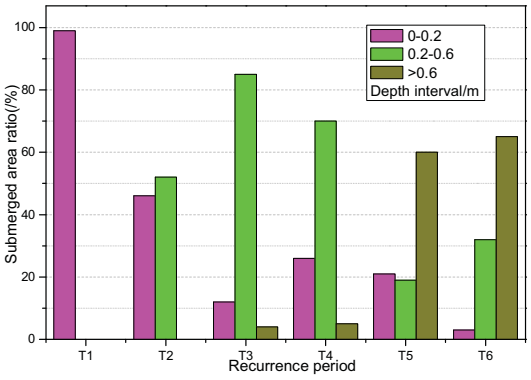

FIGURE 8
Submerged area ratio of different water depth intervals in different recurrence periods in Pudong District

It can be seen from Figure 6 that with the prolongation of the recurrence period of heavy rain, the frequency and intensity of rainfall increase, and the risk degree of waterlogging also increases gradually. The areas with waterlogging disaster grade 3 or above increase gradually and mainly concentrate in the north, West and east of the study area [32]. The regional scope of disaster grade 1 and 2 is relatively fixed. The reason is that the area has the surface of Lake, good drainage conditions, low building density and high permeability. With the extension of rainstorm recurrence period, the area with grade 4 gradually enlarged, but mainly evolved from the area with grade 3. The reason is that the area has a low terrain. With the increase of rainfall intensity, the level of waterlogging disaster also gradually increased.

From the range of submergence depth concentration, T1 and T2 are concentrated in the range of 0-0.2 m and 0.2-0.6 m, and the submerged areas of the two zones are roughly equal. T3 and T4 mainly concentrate in the range of 0.2-0.6 m, with 83.7% and 70.8% of the submerged area in this area respectively; T5 and T6 mainly concentrate in the range of more than 0.6 m, with 60.1% and 66.5% of the submerged area in this area. The submerged area and the ratio of submerged area (submerged area/total submerged area) in different water depth intervals of Shanghai Pudong New Area in different recurrence periods are shown in Figure 7 and 8.

Risk assessment of rainstorm waterlogging disasters. The purpose of risk assessment of rainstorm waterlogging disaster is to enable urban decision makers to understand the degree of risk of rainstorm waterlogging in the study area as a whole. Referring to the determination method of flood hazard classification standard, considering the characteristics of urban rainstorm and waterlogging, and com-

bining with the results of field survey, that is, the accumulated water is more than 60 cm, it will have a significant impact on the production and life of residents, such as serious immersion of indoor property, breakdown of automobiles or water accumulation under overpasses, causing traffic jams, etc. The area ratio of flooded streets (HI1) and the area ratio of flooded streets (HI2) with depth over 60 cm were determined as the criteria for risk classification of rainstorm waterlogging disasters as shown in Table 4. Based on these, the risk assessment of Pudong New Area in Shanghai was carried out (Figure 4).

$$HI_1 = \left(F_A / T_A\right) \times 100 \quad (10)$$

In formula: HI_1 indicates the ratio of flooded area of each street; F_A is the flooded area of each street; T_A is the total area of each street.

$$HI_2 = \left(F_D / T_A\right) \times 100 \quad (11)$$

In the formula: HI_2 is the area ratio of the street inundation depth exceeding 60 cm; F_D is the area of each street inundation depth exceeding 60 cm; T_A is the total area of each town and street.

TABLE 4
Classification criteria of rainstorm waterlogging risk in Pudong of Shanghai

Risk classification	HI_1	HI_2
Low	<50%	<50%
Middle	≥50%	≤50%
High	>50%	>50%

Among the six scenarios mentioned above, under T1 and T2 scenarios, rainstorm waterlogging has little effect on residents' production, life and traffic in Figure 9. Under the T3 and T4 scenarios, the production, life and travel of residents will be affected to a certain extent, but it will not cause any damage to the lives of the people. Under T5 and T6 scenarios, factories, shops and households will suffer serious water inflows, which will seriously affect the production and life of residents, and even destructively affect the lives of the population.

CONCLUSION

Taking Pudong New Area as the research object, this paper modifies the existing urban elevation model by using GIS raster spatial analysis technology, and combines the determined parameters of SCS hydrological model, CN value and rainfall in Pudong New Area of Shanghai. The depth and extent of flooding under various recurrence rainstorm waterlogging scenarios were simulated, and the risk assessment of rainstorm waterlogging disaster in Pudong New Area was carried out with street (town) as the research unit. From the point of view of time characteristics, with the increase of rainstorm recurrence period, the waterlogging nodes become more and more intensive, and the risk of urban waterlogging is gradually increasing; from the point of view of spatial characteristics, the areas with low permeability and high surface hardening rate have higher probability and risk of waterlogging. Therefore, in order to reduce the occurrence of urban waterlogging, it is necessary to protect the water area reasonably, control the speed and area of water area reduction, and scientifically arrange the urbanization process. Due to the limitation of data, only considering the correction of the influence of the dense buildings near the city center on the urban topography, further improvement and perfection are needed in the future research. In addition, on the basis of disaster risk analysis, the study of human action mechanism, disaster vulnerability and quantitative analysis and model study of social and economic losses (including direct losses and indirect losses) caused by exposure of vulnerable areas to rainstorm waterlogging disasters can be further strengthened.

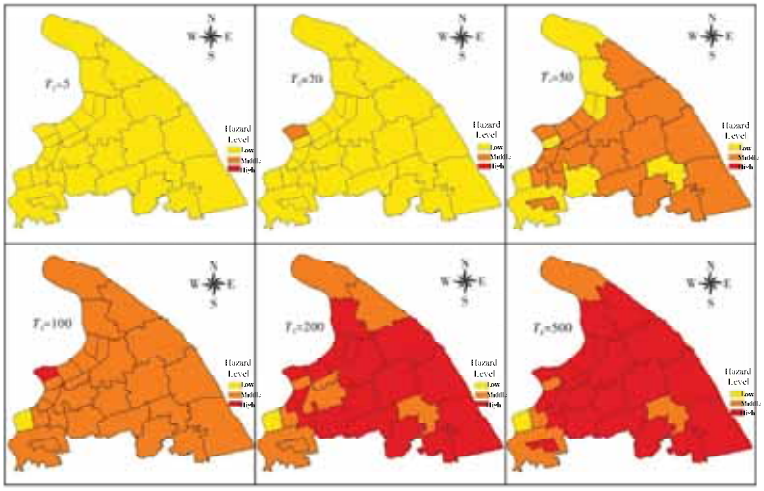

FIGURE 9
Risk classification of heavy rainfall and flood

ACKNOWLEDGEMENTS

This research was supported by Zhejiang Provincial Natural Science Foundation of China under Grant No. LQ15D010002, the Science and Technology Benefit People of Ningbo City under Grant No. 2015C50052, the Zhejiang Provincial Research Plan for Public Science and Technology under Grant No.2014C31076, Science and Technology Major Project of Guangxi Under Grant No. AA18118048.

REFERENCES

[1] Chiu, Y.-R., Tsai, Y.-L., Chiang, Y.C. (2015) Designing Rainwater Harvesting Systems Cost-Effectively in, a Urban Water-Energy Saving Scheme by Using, a GIS-Simulation Based Design System. Water. 7(11), 6285-6300.

[2] Zhang, S., Pan, B. (2014) An urban storm-inundation simulation method based on GIS. Journal of Hydrology. 517, 260-268.

[3] Hadi Mahmoudi-Meimand, Sara Nazif, Rahim Ali Abbaspour , Hasanali Faraji Sabokbar (2016) An algorithm for optimisation of a rain gauge network based on geostatistics and entropy concepts using GIS, Journal of Spatial Science. 61:1, 233-252.

[4] Yu, D., Qiao, M. , Wang, Y., Liu, B. (2015). Planning and design of urban rainwater landscape based on gis technology and the "rainwater zone" concept. Xi'an Jianzhu Keji Daxue Xuebao/Journal of Xi'an University of Architecture and Technology. 47(5), 723-727.

[5] Mahmoud, S.H., Tang, X. (2015) Monitoring prospective sites for rainwater harvesting and stormwater management in the United Kingdom using a GIS-based decision support system. Environmental Earth Sciences. 73(12), 8621-8638.

[6] Yao, L., Wei, W., Chen, L. (2016) How does imperviousness impact the urban rainfall-runoff process under various storm cases? Ecological Indicators. 60, 893-905.

[7] Quang-Khanh, N. , Dieu, T. B. , Nhat-Duc, H. , Phan, T. , Viet-Ha, N. , , Is?K, Y. . (2017) A novel hybrid approach based on instance based learning classifier and rotation forest ensemble for spatial prediction of rainfall-induced shallow landslides using GIS. Sustainability. 9(5), 813.

[8] Fanos, A.M., Pradhan, B. (2019) A novel rock-fall hazard assessment using laser scanning data and 3D modelling in GIS. Catena. 172, 435-450.

[9] Liu, X., Liang, X., Li, X., Xu, X., Ou, J., Chen, Y., Li, Sh., Wang, Sh., Pei, F., (2017) A future land use simulation model (FLUS) for simulating multiple land use scenarios by coupling human and natural effects. Landscape and Urban Planning. 168, 94-116.

[10] Thakur, J.K., Singh, S.K., Ekanthalu, V.S. (2017) Integrating remote sensing, geographic information systems and global positioning system techniques with hydrological modeling. Applied Water Science. 7(4), 1595-1608.

[11] Mello, C. R. D., Norton, L. D., Pinto, L. C., Beskow, S., , Curi, N. (2016). Agricultural watershed modeling: a review for hydrology and soil erosion processes. Ciência e Agrotecnologia. 40(1), 7-25.

[12] Pourtaghi, Z. S., Pourghasemi, H. R., Aretano, R., Semeraro, T. (2016). Investigation of general indicators influencing on forest fire and its susceptibility modeling using different data mining techniques. Ecological Indicators. 64, 72-84.

[13] Deng, F., Li, X., Wang, H., Zhang, M., Li, R., , Li, X. (2014). GIS-based assessment of land suitability for alfalfa cultivation: a case study in the dry continental steppes of northern China. Spanish Journal of Agricultural Research. 12(2), 364-375.

[14] Xiao, X., O'Dwyer, J.P., White, E.P. (2015) Comparing process-based and constraint-based approaches for modeling macroecological patterns. Ecology. 97(5), 1228-1238.

[15] Rathod, I.M., Aruchamy, S. (2010) Spatial Analysis of Rainfall Variation in Coimbatore District Tamilnadu using GIS. International Journal of Geomatics and Geosciences. 2010(2), 106-118.

[16] Arbault, D., Rugani, B., Tiruta-Barna, L., , Benetto, E. (2014). A first global and spatially explicit emergy database of rivers and streams based on high-resolution GIS-maps. Ecological Modelling. 281, 52-64.

[17] Taramelli, A., Melelli, L., Pasqui, M., Sorichetta, A. (2010). Modelling risk hurricane elements in potentially affected areas by a GIS system. Geomatics, Natural Hazards and Risk. 1(4), 349-373.

[18] Gorokhovich, Y., Villarini, G. (2005) Application of GIS for processing and establishing the correlation between weather radar reflectivity and precipitation data. Meteorological Applications. 12(01), 91-99.

[19] Hsu, P.H., Su, W.R., Chang, C.C. (2011) Hazards analysis and prediction from remote sensing and GIS using spatial data mining and knowledge discovery: A case study for landslide hazard zonation. Proceedings of SPIE - The International Society for Optical Engineering. 8181(9), 23-36.

[20] Dehghani, M., Taghizadeh, M. M., Hashemi, H., , Rastgoo, E. (2013). A preliminary assessment of dispersion level of SO2 in Fars Industrial Region, south of Iran, by GIS. Journal of Environmental and Public Health, 2013, 670590.

[21] Matyas, C. (2008) Shape measures of rain shields as indicators of changing environmental conditions in a landfalling tropical storm. Meteorological Applications. 15(2), 259-271.
[22] Valcu, M., Kempenaers, B. (2010) Is spatial autocorrelation an intrinsic property of territory size? Oecologia. 162(3), 609-615.
[23] Roy, P.S., Roy, A. (2010) Land use and land cover change in India: A remote sensing and GIS perspective. Journal of the Indian Institute of Science. 90(4), 489-502.
[24] Wang, Y., Shao, M. A., Liu, Z., , Warrington, D. N. (2012). Regional spatial pattern of deep soil water content and its influencing factors. Hydrological Sciences Journal, 57(2), 265-281.
[25] Gwenzi, W. , Hinz, C. , Holmes, K. , Phillips, I. R. , , Mullins, I. J. . (2011). Field-scale spatial variability of saturated conductivity on a recently constructed artificial ecosystem. Geoderma. 166(1), 43-56.
[26] Elhakeem, M., Papanicolaou, A. T., Wilson, C. G., Chang, Y. J., Burras, L., Abban, B., ... , Wills, S. (2018). Understanding saturated hydraulic conductivity under seasonal changes in climate and land use. Geoderma. 315, 75-87.
[27] Geng, G., Zhang, Q., Martin, R. V., Lin, J., Huo, H., Zheng, B., ... , He, K. (2017). Impact of spatial proxies on the representation of bottom-up emission inventories: A satellite-based analysis. Atmospheric Chemistry and Physics. 17(6).
[28] Saro, L., Woo, J. S., Kwan-Young, O., , Moung-Jin, L. (2016). The spatial prediction of landslide susceptibility applying artificial neural network and logistic regression models: A case study of Inje, Korea. Open Geosciences. 8(1), 117-132.
[29] Nampak, H., Pradhan, B., Mojaddadi Rizeei, H., , Park, H. J. (2018). Assessment of land cover and land use change impact on soil loss in a tropical catchment by using multitemporal SPOT‐5 satellite images and R evised U niversal Soil L oss E quation model. Land degradation and development, 29(10), 3440-3455.
[30] Golden, H.E., Hoghooghi, N. (2018) Green infrastructure and its catchment-scale effects: an emerging science. Wiley Interdisciplinary Reviews: Water. 5(1), e1254.
[31] Hutchins, M. G., McGrane, S. J., Miller, J. D., Hagen‐Zanker, A., Kjeldsen, T. R., Dadson, S. J., , Rowland, C. S. (2017). Integrated modeling in urban hydrology: reviewing the role of monitoring technology in overcoming the issue of ‘big data’ requirements. Wiley Interdisciplinary Reviews: Water. 4(1), e1177.
[32] Salvadore, E., Bronders, J., Batelaan, O. (2015) Hydrological modelling of urbanized catchments: A review and future directions. Journal of Hydrology. 529, 62-81.

Received: **24.09.2019**
Accepted: **28.01.2020**

CORRESPONDING AUTHOR

Qiting Huang
Agricultural Science and Technology Information Research Institute
Guangxi Academy of Agricultural Sciences
Nanning – China

e-mail: huangqiting_gaas@yeah.net

© by PSP Volume 29 – No. 04A/2020 pages 2879-2885 Fresenius Environmental Bulletin

STUDY ON RURAL INTELLIGENT PLANNING COOPERATIVE PLATFORM

Liqun Wang[1,*], Linjun Jin[2]

[1]Sponge City Research Institute, Pingxiang University, Pingxiang Jiangxi, 337055 China
[2]Planning and Architectural Design Co., Ltd. Shanghai Jiaotong University, China

ABSTRACT

Based on the analysis of the principles of landscape ecology, the objects and contents of landscape ecology, and the principles, objectives and contents of the planning of the beautiful countryside, the contents and methods of the planning of the beautiful countryside under the guidance of the principles of landscape ecology are studied in this thesis, and the important role of landscape ecology in the construction of rural landscape is clarified. The principles of landscape ecology were applied to the landscape ecological pattern optimization, rural settlement planning and rural ecological industry development planning of beautiful countryside, and the planning method of beautiful countryside was studied under the guidance of the principles of landscape ecology, which improved the planning mode of beautiful countryside and constructed sustainable rural landscape ecology. Finally, this thesis takes the construction of beautiful new village in Weijiaqiao Village as an example to study. Finally, this thesis takes the construction of beautiful new village in Weijiaqiao Village as an example to study.

KEYWORDS:
Gaussian model, Particle filtering, Rural landscape, Intelligent planning, Collaborative platform

INTRODUCTION

To improve the living environment of people and to enable our offspring to see green mountains and rivers, ecological civilization construction admits of no delay, and we should show our firm wills and determinations on the problem of ecological civilization construction for rural areas. Ecological civilization takes a significant place in the construction layout of socialism with Chinese characteristics [1-4]. Speed up our ecological civilization construction, propel the construction of a beautiful China and then realize the sustainable development of Chinese nation. Rural areas and populations take most parts of China, during the construction of ecological civilization with socialism of Chinese characteristics, ecological construction for rural areas is the priority; and the key point of construction of a beautiful China lies in the construction of beautiful villages [5]. Thus, ecological construction of beautiful villages is the key point for us to make good rural planning. Rural areas are of innate advantages, and during the construction process of beautiful villages with ecological civilization, rural ecology takes a heavier responsibility than urban areas, thus future planning and construction cannot be ignored during ecological construction for rural areas due to their innate advantages, instead, emphasis should be lay on overall construction planning on ecology of villages with advantages in ecological resources, achieve coordinated and synchronous development between cities and villages, improve the comfort level of rural environment, and enable the ecological pattern of rural areas develop safely and steadily. It can not only help people of rural areas live and work in peace and contentment, but can also help us to fulfill our Chinese dream as early as possible [6-8].

While seen from the whole rural environment, a number of obstacles have been come across in the development of rural areas, ecological resources are seriously destroyed, contents of planning put forward aimed at problems like singular rural industrial patterns, loss of rural characters, rural ecological environment to be improved; inconsistent treatments on wastewater discharge and garbage collection, untimely rural greening for natural plants and crops and serious pollution of groundwater, etc. at present are mainly construction on infrastructures, few researches are made on problems of ecological environment from the aspect of ecological sustainable development in depth, while to develop a harmonious coexistence of human and nature, the synchronous development of ecological sustainable development and material life of peasants is the foundation [9-12]. Thus, more discussions should be made on the landscape ecological planning of beautiful villages. The livable and beautiful village construction planning based on landscape ecological principle enables people to see the villages from the aspect of landscape ecology and then build beautiful villages with green ecological ideas. This can not only promote harmonious coexistence of people and environment, meanwhile it also improves rural civilizations

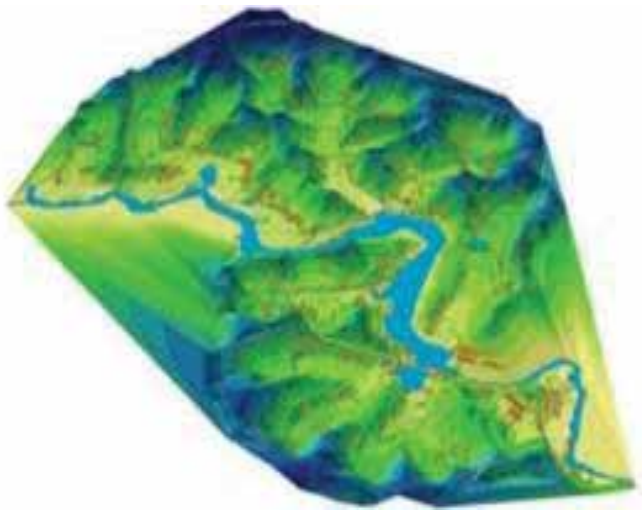

FIGURE 1
Geomorphological map of Weijiaqiao

and enables people to learn to respect the nature and cherish ecological environment. Development of ecological landscapes can also obviously improve social morality of rural areas, peasants can feel the improvement of living quality from the good living environment, thus the overall quality of villagers can be improved [13-15].

Through analyzing the problems faced by construction of beautiful villages at present and detailed analysis and researches on present rural planning methods and patterns, the significance of landscape ecological theory on green and sustainable development of beautiful villages and solution of environmental and ecological problems existing in the current rural areas is analyzed at the meantime. Apply relative theories of landscape ecology into beautiful village planning flexibly and establish a systematic, innovative and referential landscape ecological planning system for beautiful villages thus providing deeper and more perfect construction planning modes for the construction of beautiful villages, rural ecological protections and ecologically sustainable developments of rural areas. Although the existing beautiful village construction planning concerns the planning method of landscape ecology, it is not in-depth enough and of a weak pertinence on the whole, so the research object of this thesis is to supplement and improve existing methods of rural ecological landscape planning and to provide more systematic referential patterns for landscape ecological planning of other villages. Better guide the new villages to develop towards a green and ecologically sustainable target, then accelerate the goals of realization of peaceful and content life and work as well as ecologically sustainable development in beautiful rural areas.

MATERIALS AND METHODS

Current Situation of Geographical Position and Landform. Weijiaqiao Village is of subtropical monsoon climate, with moderate weathers, sufficient sunshine and plenty rainfalls, the precipitation of summer and autumn is relatively concentrated, and the soil texture of the village is fertile. The average annual temperature is 16.3°C, mean annual precipitation is 979 mm, and the average annual frost-free season lasts for 275 days. Weijiaqiao Village is located in the western part of Liujiazhen Town, Youxian District, Mianyang, Sichuan Province with a shallow-hilly landform. Villages and towns contiguous with Weijiaqiao are respectively: Liujiachang Town, Zhangjiayan Village, Tashuiqiao Village, Danjiamiao Village, Baima Village of Shiban Town, Taoziyuan Village and Longwanggou Village (Figure 1). The landform of Weijiaqiao is obviously controlled by the geology, during the geological historical period, main crustal movements were upwards, and there were few horizontal movements, the gradient of stratums of some gentle and wide drapes are generally mild, whose structures are located on shallow-hilly areas with a terrain that is higher in northern and southern parts and lower in the middle, the highest and lowest points are at the east end, and the lowest point is located at the middle river valley. Its altitude is between 402 and 467, with an average altitude of around 420m. Chejia River flows across the village and forms 2 dams by the river. Thus, the overall natural landscape of Weijiaqiao Village can be summarized as “2 dams, 3 curves and 1 river crossing from the middle”.

Weijiaqiao Village is 1km from Liujiachang Town at the outskirts of Mianyang City, and the distance to the urban area of Mianyang is 45km. Weijiaqiao provides resources like agricultural products

and labor forces, etc. that are needed by urban development of Mianyang City; meanwhile the natural feature of landscapes in Weijiaqiao Village is well preserved, the woods are of good growth with luxuriantly green color, naturally formed hills rise one higher than another, Chejia River flows across Weijiaqiao Village, bringing sufficient water source for the agricultural development of Weijiaqiao Village, and it can also be seen as an important landscaping factor to development tourism, water loving tourist projects can be established by the river to develop the sightseeing and tourist industry. Wonderful natural sceneries, fresh air, together with the villages and folk houses at the foot of mountains, it is as leisurely as the arcadia described by Tao Yuanming. Such kind of living environment has become an important element pursued by people at present, and establishing rural tourisms can provide good places for citizens of Mianyang to relax. The beautiful sceneries of Weijiaqiao will be the vital and best reason for the application of landscape ecology into beautiful new village construction planning.

This village is located at hilly areas with flexible and variable landforms, mountains, water, bays and dams, which create beneficial conditions for the development of high-efficiency and sightseeing agricultures like characteristic profitable agriculture, circular agriculture and facility agriculture, etc. Development of rural tourism of Weijiaqiao mainly relies on human and natural landscape resources, of which human landscapes mainly contain sugarbush (Figure 2), vegetable gardens (Figure 3) and rural settlements. Natural resources mainly contain well-preserved mountain forest ecological environment and waterscape resources of Chejia River, regional tourist resources contain Xianhai Lake, Qiqu Mountain, Ma'an Temple and Wuji Temple.

FIGURE 2
Sugarbush of Weijiaqiao Village

FIGURE 3
Vegetable garden of Weijiaqiao Village

Improved Gaussian Particle Filter. Algorithm Description. In application fields like signal data processing and statistical analysis, etc., filtering algorithm has a significant application prospect, of which object programming is also a main application field of filtering algorithm, which has achieved a good effect. Researches on system estimation under the influence of noises through state estimation algorithm are main contents of object programming, whose model building can be conducted through dynamic-state space model (DSS). For state x_n, if it has an unobservable status attribute, modeling can be conducted on it based on the established DSS model in the form of $p(x_n|x_{n-1})$, in real scenes, y_n is generally disturbed by factors like noise, and for variable x_n under an unknown status, its observation model can be expressed with $p(y_n|x_n)$ based on distribution, then the form of state estimation model based on DSS model is:

$$\begin{cases} \mathbf{y}_n = h(\mathbf{x}_n, \mathbf{v}_n) \\ \mathbf{x}_n = f(\mathbf{x}_{n-1}, \mathbf{u}_n) \end{cases} \quad (1)$$

In the formula, parameter item $f(\cdot)$ is the process model of state estimation, parameter item $h(\cdot)$ is the observation model of state estimation, and parameter items $\mathbf{u}_n$ and $\mathbf{v}_n$ are the vector models of noises respectively. Such model system is a time-varying system essentially, which can be expressed by prior probability distribution model $p(\mathbf{x}_0)$ and hidden state model $\mathbf{x}_n$. Set that the true value and observed value of football moving trajectory data at the time interval of 0-n are $\mathbf{x}_{0:n}$ and $\mathbf{y}_{0:n}$ respectively, then the model is defined as:

$$\begin{cases} \mathbf{x}_{0:n} \equiv \{\mathbf{x}_0, \cdots, \mathbf{x}_n\} \\ \mathbf{y}_{0:n} \equiv \{\mathbf{y}_0, \cdots, \mathbf{y}_n\} \end{cases} \quad (2)$$

Set that the state estimation probability model $p(\mathbf{x}_n|\mathbf{y}_{0:n})$ of football moving trajectory is the observed value of all tracks within the time interval from 0-n, then it can be known that $p(\mathbf{x}_{n+1}|\mathbf{y}_{0:n})$ is the distribution forecast result of all tracks within the time interval from 0-n. From this, the form of state estimation model can be defined as:

$$p(\mathbf{x}_n|\mathbf{y}_{0:n}) = C_n p(\mathbf{x}_n|\mathbf{y}_{0:n-1}) p(\mathbf{y}_n|\mathbf{x}_n) \quad (3)$$

In the formula, the normalized form of parameter item C_n is:

$$C_n = \left(\int p(\mathbf{x}_n|\mathbf{y}_{0:n-1}) p(\mathbf{y}_n|\mathbf{x}_n) d\mathbf{x}_n \right)^{-1} \quad (4)$$

It can be known that the forecast prediction model of football moving trajectory is:

$$p(\mathbf{x}_{n+1}|\mathbf{y}_{0:n}) = \int p(\mathbf{x}_{n+1}|\mathbf{x}_n) p(\mathbf{x}_n|\mathbf{y}_{0:n}) d\mathbf{x}_n \quad (5)$$

PMCGPF. The design philosophy of Monte Carlo algorithm is to conduct simulation aimed at distribution $p(\mathbf{x}_n)$ of variable $\mathbf{x}_n$ with an enough small value, and then realize resampling of multiple groups of particles based on Poisson distribution $\pi(\mathbf{x}_n)$, whose form is:

$$\chi=\left\{x_n^{(1)},\cdots,x_n^{(M)}\right\} \tag{6}$$

During the resampling process, the weight setting form of particle individuals is:

$$\omega^{(j)}=p\left(x_n^{(j)}\right)\Big/\pi\left(x_n^{(j)}\right) \tag{7}$$

Set $W=\left\{\omega^{(1)},\cdots,\omega^{(M)}\right\}$, of which $\{\chi,W\}$ is the sampling data series possessed by $p(\mathbf{x}_n)$. Then conduct processing on Monte Carlo particles through integral operations:

$$E_p\left(g(\mathbf{x}_n)\right)=\int g(\mathbf{x}_n)p(\mathbf{x}_n)d\mathbf{x}_n \tag{8}$$

The following estimation model can be acquired:

$$\hat{E}_p\left(g(\mathbf{x}_n)\right)=\sum_j \omega^{(j)}g\left(x_n^{(j)}\right)\Big/\sum_j \omega^{(j)} \tag{9}$$

Then based on law of large numbers, the following relationship is founded:

$$\hat{E}_p\left(g(\mathbf{x}_n)\right)\to E_p\left(g(\mathbf{x}_n)\right) \tag{10}$$

If meeting $M\to\infty$, the posterior probability calculation for can be expressed as follows:

$$p(\mathbf{x}_n)d\mathbf{x}_n=P(d\mathbf{x}_n)\approx\frac{\sum_{j=1}^{M}\omega^{(j)}\delta_{x_n^{(j)}}(d\mathbf{x}_n)}{\sum_{j=1}^{M}\omega^{(j)}} \tag{11}$$

In the formula, parameter $\delta(\cdot)$ is the unit pulse of posterior probability calculation. Conduct processing on variable x through Gaussian sampling, then form of its distribution model can be acquired:

$$N\ (\mathbf{x};\boldsymbol{\mu},\Sigma)=(2\pi)^{-\frac{m}{2}}|\Sigma|^{-\frac{1}{2}}\exp\left(-\frac{(\mathbf{x}-\boldsymbol{\mu})^{-1}}{2}\Sigma^{-1}(\mathbf{x}-\boldsymbol{\mu})\right) \tag{12}$$

In the formula, parameter item $\boldsymbol{\mu}$ is the mean calculation value of football trajectory vector at dimension m, parameter item Σ is the variance matrix of football trajectory vector, which is in the positive definite form. For time point $n=1$, there is $p(\mathbf{x}_1|\mathbf{y}_0)=N\ (\mathbf{x}_1;\bar{\boldsymbol{\mu}}_1,\bar{\Sigma}_1)$, the parameter items $\bar{\boldsymbol{\mu}}_1$ and $\bar{\Sigma}_1$ in the formula can be calculated based on priori knowledge.

After acquiring observation value $\mathbf{y}_n$, the form of its filtering distribution model can be calculated as follows:

$$\begin{aligned}p(\mathbf{x}_n|\mathbf{y}_{0:n})&=C_n p(\mathbf{x}_n|\mathbf{y}_{0:n-1})p(\mathbf{y}_n|\mathbf{x}_n)\\&\approx C_n p(\mathbf{y}_n|\mathbf{x}_n)N\ (\mathbf{x}_n;\bar{\boldsymbol{\mu}}_n,\bar{\Sigma}_n)\end{aligned} \tag{13}$$

Actually, analytic model building cannot be conducted on variance Σ_n and mean value $\boldsymbol{\mu}_n$ of parameter item $p(\mathbf{x}_n|\mathbf{y}_{0:n})$, while they can be simulated based on Monte Carlo algorithm, its correction course can be completed through the following steps:

Process 1: correct the observed quantity of football moving trajectory

Step 1: Conduct resampling on football moving trajectory based on Poisson distribution model $\pi(\mathbf{x}_n|\mathbf{y}_{0:n})$, then acquire $\left\{x_n^{(j)}\right\}_{j=1}^{M}$;

Step 2: Conduct weight calculation on all samples of football moving trajectory, whose form is:

$$\bar{\omega}_n^{(j)}=\frac{p\left(\mathbf{y}_n|\mathbf{x}_n^{(j)}\right)N\ \left(\mathbf{x}_n^{(j)};\bar{\boldsymbol{\mu}}_n,\bar{\Sigma}_n\right)}{\pi\left(\mathbf{x}_n^{(j)}|\mathbf{y}_{0:n}\right)} \tag{14}$$

Step 3: Conduct normalization on sample weight of football moving trajectory:

$$\omega_n^{(j)}=\bar{\omega}_n^{(j)}\Big/\sum_{j=1}^{M}\bar{\omega}_n^{(j)} \tag{15}$$

Step 4: Pre-estimate the mean value and variance parameters of football moving trajectory:

$$\begin{cases}\boldsymbol{\mu}_n=\sum_{j=1}^{M}\omega_n^{(j)}\mathbf{x}_n^{(j)}\\ \Sigma_n=\sum_{j=1}^{M}\omega_n^{(j)}\left(\boldsymbol{\mu}_n,\mathbf{x}_n^{(j)}\right)\left(\boldsymbol{\mu}_n,\mathbf{x}_n^{(j)}\right)^H\end{cases} \tag{16}$$

Theorem 1: (Convergence Analysis) assume that probability distribution model $p(\mathbf{x}_n|\mathbf{y}_{0:n-1})$ is a known parameter at time point n, which can be expressed with proportion constant, after acquiring $\mathbf{y}_n$, its filtering distribution can be updated based on Monte Carlo integral, then distribution estimation can fulfill convergence at time point r, and the uniform convergence is at $E(\mathbf{x}_n^r,\mathbf{y}_{0:n})$.

Prove: the form of the r^{th} estimation model of football moving trajectory acquired through Formula (27-28) is:

$$\begin{aligned}\hat{E}\left(\mathbf{x}_n^r|\mathbf{y}_{0:n}\right)&=\sum_{j=1}^{M}\left(\mathbf{x}_n^{(j)}\right)^r\bar{\omega}_n^{(i)}\Big/\sum_{j=1}^{M}\bar{\omega}_n^{(i)}\\&=\int\mathbf{x}_n^r p(\mathbf{x}_n|\mathbf{y}_{0:n})d\mathbf{x}_n\end{aligned} \tag{17}$$

Then it can be known through law of large numbers and Gaussian sampling distribution model that, for situation of $M\to\infty$, the convergence rate of filtering distribution of football moving trajectory is 1, so the argumentation is completed.

Part 2: Time correction for observed quantity of football moving trajectory

For time point n, conduct sampling on distribution $p(\mathbf{x}_{n+1}|\mathbf{x}_n)$ through Monte Carlo algorithm,

TABLE 1
Statistical analysis result of land use in Weijiaqiao Village

Classification of first-class land	Classification of second-class land	Area (ha)	Proportion (%)
Farmland	Total land area	390.348	100
	Cultivated land	95.234	24.40
	Garden	33.453	8.57
	Forest	143.340	36.73
	Grassland	10.747	2.75
	Pond	49.588	12.71
	Total	332.363	85.16
Construction land	Residential land	30.676	7.91
	Public service land	0.225	0.06
	Specially-designated land	1.368	0.35
	Land for transportation	8.512	2.11
	Total	40.77	10.43
Unused land	Other lands	0.421	0.11
	Rivers	16.785	4.31
	Total	17.207	4.42

such distribution is of a Gaussian manifestation pattern, then the prediction distribution model of samples can be acquired as:

$$p\left(\mathbf{x}_{n+1}\middle|\mathbf{y}_{0:n}\right)=\int p\left(\mathbf{x}_{n+1}\middle|\mathbf{x}_n\right)p\left(\mathbf{x}_n\middle|\mathbf{y}_{0:n}\right)d\mathbf{x}_n \approx \int p\left(\mathbf{x}_{n+1}\middle|\mathbf{x}_n\right)N\ \left(\mathbf{x}_n;\boldsymbol{\mu}_n,\Sigma_n\right)d\mathbf{x}_n \tag{18}$$

Define the prediction distribution model of football moving trajectory based on Monte Carlo algorithm:

$$p\left(\mathbf{x}_{n+1}\middle|\mathbf{y}_{0:n}\right)\approx\sum_{i=1}^{M}p\left(\mathbf{x}_{n+1}\middle|\mathbf{x}_n^{(i)}\right)\Big/M \tag{19}$$

Steps of time correction algorithm of observed quantity of football moving trajectory can be acquired through this:

Step 1: Conduct sample collection for football moving trajectory based on Gaussian distribution model $N\ \left(\mathbf{x}_n;\boldsymbol{\mu}_n,\Sigma_n\right)$, then acquire $\left\{x_n^{(j)}\right\}_{j=1}^{M}$.

Step 2: Execute sample collection within $p\left(\mathbf{x}_{n+1}\middle|\mathbf{x}_n=\mathbf{x}_n^{(i)}\right)$ given $j=1,\cdots,M$, then acquire $\left\{x_{n+1}^{(j)}\right\}_{j=1}^{M}$.

Step 3: Update of variance indexes and mean value indexes of observed quantity distribution of football moving trajectory:

$$\begin{cases}\overline{\boldsymbol{\mu}}_{n+1}=\sum_{j=1}^{M}\mathbf{x}_{n+1}^{(j)}\Big/M\\ \overline{\Sigma}_{n+1}=\sum_{j=1}^{M}\left(\overline{\boldsymbol{\mu}}_n,\mathbf{x}_{n+1}^{(j)}\right)\left(\overline{\boldsymbol{\mu}}_{n+1},\mathbf{x}_{n+1}^{(j)}\right)^{H}\Big/M\end{cases} \tag{20}$$

RESULTS AND DISCUSSION

Area of Weijiaqiao Village is 390.35 ha., which contains construction land of 40.1 ha., taking 10. 43% of the total area; agricultural acreage of 95.2 ha., taking 24.40% of the total area; forest land of 143.3 ha., taking 36.73% of the total area; garden plot area of 33.5 ha., taking 8. 57% of the total area; and water area of 62.3 ha., taking 17.01% of the total area.

On land classification of Weijiaqiao Village, first-class land use contains farmland, construction land and unused land, which respectively take 85.16%, 10.43% and 4.41% of the total area. For second-class land use, forest land and cultivated land are the types of land use with the highest proportion among farmlands, whose proportions are respectively 36.73% and 24.40%; among second-class construction lands, residential land takes 79.1% of the total area, and land for transportation takes 2.11% of the total area; other specially-designated lands such as funeral land, etc. take 0.36% of the total area; and lands for public management and service take 0. 06% of the total area.

Farmland of Weijiaqiao takes most of the total area of the village, and there are abundant farmlands and good ecological resources in the village. Forests of Weijiaqiao Village mainly distributes at the boundaries of the village with a trend expanding inwards, through which a good landscape ecological pattern is formed in Weijiaqiao that, forming a forest belt liaison net with the external landscapes effectively. Gardens mainly distribute around the settlements, which are lands planted with necessary agricultural products like vegetables and fruits, etc. There is abundant water resource in the village, which respectively comes from Chejia River and weirs distributed in the village and provides necessary water resources and lands for aquaculture for peasants in their production and life. Statistical analysis result of land use in Weijiaqiao Village is shown in Table 1.

On the aspect of ecological industry development of Weijiaqiao Village, the compound decision integrated with sustainable development, environmental protection and social development should be insisted on, plant fruits like loquat, pear, plum and

peach, etc. with full use of agricultural and industrial advantages of Weijiaqiao Village to enrich the originally singular rice cultivation and to enlarge the species diversity of artificial and natural plaques of the village, which is beneficial for sustainable development of species in the plaques and natural ecology of the new village, vitalizes the material and human resources of the new village and increases the income of peasants (Figures 4-5-6). Meanwhile it integrates with the natural resources of Weijiaqiao Village.

FIGURE 4
Rice-fish cultivation pattern

FIGURE 5
Under-forest cultivation pattern

FIGURE 6
Fruit tree planting pattern

Rural tourism driven by beautiful new village construction cannot live without courtyard landscape regulation, which realizes farmhouse service industry, thus rural service industry supplements with rural tourism. Weijiaqiao Village mainly develops agricultural tourism and agricultural cultivation in the core areas of the village, increasing the agricultural and industrial income of peasants with ecological development as the aim. Ecological courtyard service industry promotes rural population employment mainly through landscape construction on housing estate and resources cyclic utilization, meanwhile it also achieves a balanced development in urban and rural areas and injects new vitality to the development of rural economy. Realization of targets of "employment prosperity, family richness, mutual harmony and beautiful village" is being accelerated.

CONCLUSION

Beautiful new village planning for Weijiaqiao Village is a plan conduced with optimization of landscape ecological pattern, rural settlement environmental construction and rural ecological and industrial development based on landscape ecological theory. Analysis and evaluation on ecological environment in the planned area are done through the mode of plaque—gallery—matrix by landscape ecological pattern, and through reasonable planning of plaques and galleries within the planned regions, diversity and heterogeneity of landscape ecology in the village are increased, which achieves construction and development in rural ecological environment on macroscopic aspect and realizes the targets of Weijiaiqiao Village in beautiful new village construction. Rural residential areas, as artificial plaques of the village, have decisive functions on the ecological environment of the village, planning for housing estates through ecological planning theory improves the reasonability of settlement layout and brings convenience to life and agricultural production of residents on one hand, on the other hand, ecological environment construction for housing estates and settlements is not beneficial for the ecological construction of the whole village, it is also good for rural areas to develop agricultural tourism, which can increase the income of peasants; rural ecological environment construction means governing the ecological environment of the village on microscopic perspective, with the use of ecological cyclic pattern, not only the environment of Weijiaqiao Village is beautified and the serious pollutions of the rural environment are solved, meanwhile it also improves resource utilization rate, saves environmental resources, develops multiple patterns of agricultural ecological economy, helps peasants to develop economy and increases the employment rate of rural areas.

REFERENCES

[1] Havyarimana, V., Xiao, Z., Wang, D. (2016) A Hybrid Approach-Based Sparse Gaussian Kernel Model for Vehicle State Determination during Outage-Free and Complete-Outage GPS Periods. Etri Journal. 38(3), 579-588.

[2] Shanthi, S.A., Sulochana, C.H., Latha, T. (2015) Image denoising in hybrid wavelet and quincunx diamond filter bank domain based on Gaussian scale mixture model. Computers and Electrical Engineering. 46(C), 384-393.
[3] Bui, K.T.T., Bui, D.T., Zou, J., Van Doan, C., Revhaug, I. (2016) A novel hybrid artificial intelligent approach based on neural fuzzy inference model and particle swarm optimization for horizontal displacement modeling of hydropower dam. Neural Computing and Applications. 29(12), 1495-1506.
[4] Fazli Shahri, H.R., Mahdavinejad, R. (2018) Prediction of temperature and HAZ in thermal-based processes with Gaussian heat source by a hybrid GA-ANN model. Optics Laser Technology. 99, 363-373.
[5] Alarifi, A., Al-Salman, A.M., Al-Saleh, M., Alnafessah, A., Al-Hadhrami, S., Al-Ammar, M.A., Al-Khalifa, H.S. (2016) Ultra Wideband Indoor Positioning Technologies: Analysis and Recent Advances. Sensors. 16(5), 1-36.
[6] Tran, D.T., Vincent, E., Jouvet, D. (2015) Nonparametric uncertainty estimation and propagation for noise robust ASR. IEEE/ACM Transactions on Audio Speech and Language Processing. 23(11), 1835-1846.
[7] Tu, X.K., Li, J.X., Li, J., Su, C., Zhang, S.L., Li, H.R., Cao, J.Y., He, J.P. (2017) Model-Based Hybrid Cooperative Control of Hip-Knee Exoskeleton and FES Induced Ankle Muscles for Gait Rehabilitation. International Journal of Pattern Recognition and Artificial Intelligence. 31(9).
[8] Zhou, D., Ravey, A., Al-Durra, A., Gao, F. (2017) A Comparative Study of Extremum Seeking Methods Applied to Energy Management Strategy of Fuel Cell Hybrid Electric Vehicles. Energy Conversion and Management. 151, 778-790.
[9] Zhou, D., Al-Durra, A., Gao, F., Ravey, A., Matraji, I., Godoy Simões, M. (2017) Online Energy Management Strategy of Fuel Cell Hybrid Electric Vehicles Based on Data Fusion Approach. Journal of power sources. 366(31), 278-291.
[10] Yang, L., Chen, H. (2019) Fault diagnosis of gearbox based on RBF-PF and particle swarm optimization wavelet neural network. Neural computing and applications. 31(9), 4463-4478.
[11] Zeng, L., Guo, X.P., Zhang, G.A., Chen, H.X. (2018) Semiconductivities of passive films formed on stainless steel bend under erosion-corrosion conditions, Corrosion Science. 144, 258-265.
[12] Zeng, L., Shi, J., Luo, J.L., Chen, H.X. (2018) Silver sulfide anchored on reduced graphene oxide as a high -performance catalyst for CO_2 electroreduction. Journal of Power Sources. 398, 83-90.
[13] Long, P., Caro, W.K.S. (2015) Kinematic and dynamic analysis of lower-mobility cooperative arms. Robotica. 33(9), 1813-1834.
[14] Nessi, F., Beretta, E., Ferrigno, G., De Momi, E. (2015) Recognition of user's activity for adaptive cooperative assistance in robotic surgery. International Conference of the IEEE Engineering in Medicine and Biology Society.
[15] Gupta, D., Anand, R.S., Tyagi, B. (2015) A hybrid segmentation method based on Gaussian kernel fuzzy clustering and region based active contour model for ultrasound medical images. Biomedical Signal Processing and Control. 16, 98-112.

Received: **26.09.2019**
Accepted: **03.12.2019**

CORRESPONDING AUTHOR

Liqun Wang
Sponge City Research Institute,
Pingxiang University,
Pingxiang Jiangxi, 337055 – China

e-mail: wlq0799@aliyun.com

© by PSP Volume 29 – No. 04A/2020 pages 2886-2890 Fresenius Environmental Bulletin

THE NUMERICAL SIMULATION RESEARCH OF HIGH PRESSURE MIST SPRAY BASED ON MULTIPHASE FLOW THEORY

Lin Yang[1,2], Shaocheng Ge[1,2,3], Zhihui Huang[1,2,*], Deji Jing[1,2], Xi Chen[2,3]

[1]College of Safety Science and Engineering, Liaoning Technical University, Fuxin 123000, China
[2]Key Laboratory of Mine Thermodynamic Disasters and Control of Ministry of Education, Fuxin 123000, China
[3]College of Safety and Emergency Management Engineering, Taiyuan University of Technology, Taiyuan, 030024 China

ABSTRACT

This paper has established a mathematical model to determine the optimal dust-reducing parameters of high pressure mist spray, effectively reduce the dust concentration and solve the problem of excessive dust concentration in the coal handling system. Use the two-phase flow theory of gas and solid based on the Euler-Lagrangian theorem, and carry out numerical simulation of particle size distribution of high pressure mist spray with Fluent software. Simulate the particle size distribution characteristics of droplets based on the atomization mechanism and the theoretical study of the fracture model. After analysis and statistics, it is found that the droplet size at the pressure of 8 MPa is mainly 60 μm to 80 μm, and the dust reduction effect can reach 90% or more. So, select the nozzle with a pressure of 8 MPa for spray dust removal not only solves the problem of dust pollution in the coal transportation，but also has reference to other dust-producing points in coal mines.

KEYWORDS:
Dust, High Pressure Mist Spray, Multiphase Flow, Numerical Simulation, Distribution of Particle Size

INTRODUCTION

Right now, a large amount of dust has been generated during the production and transportation of coal mines, and the particle size is getting smaller and smaller. As the emission standards become more stringent, dust reduction technologies is also developing. Around the whole world, dust removal technologies are mainly divided into wet dust removal technology and dry dust removal technology. Due to the openness of the dust source, closed collection is not easy, so, the wet dust removal technology has been more widely used at this stage [1-6].

From the aspects of dust removal efficiency and economic status, high pressure spray has a more wide range of applications, it's with advantages of simple structure, low wear, and fine mist droplets. The closer the particle size of the droplet is to the particle size of the dust, the better the dust collecting effect, so, the high pressure atomizing nozzle has a significant effect on capturing small-sized dust. This paper has fully considered the fracture model [7], collision model [8], and evaporation model [9] in the process of atomization, carry out the numerical simulation of the high pressure spray atomization to improve the dust-collecting efficiency and reduce the dust concentration to a safe range, so as to provide reference for dust-proof work in other places.

MATERIALS AND METHODS

Atomization Mechanism. The liquid material is ejected from the central tube of the two-fluid air auxiliary nozzle, that is, when the pressurized water moves along the spiral groove in the nozzle, the lateral velocity is generated due to the interaction between the two, and then is sprayed out after collected before the nozzle [10, 11]. There is a large relative velocity between the jetted water and the air, and then the droplets are broken and atomized. Two action zones will be formed after the droplets are ejected from the nozzle, one is the effective action zone, in which the droplets have a large velocity when ejected, and are hardly affected by gravity; the other is the attenuation zone, and the velocity of the droplets begins to decrease in this zone, and gradually settles.

RESULTS AND DISCUSSION

Numerical Simulation. This paper takes the nozzle diameter of 1mm as an example. A geometric model of a cylindrical spray flow field with a height of 600 mm and a diameter of 150 mm is established according to the need, and the meshing is performed. The number of grids is 2107316. It's shown as in Figure 1.

The spray process is a typical multiphase flow. The boundary conditions are set as that the inlet is the speed inlet and the outlet is free flowing. Treat the gas flow field as a continuous phase, and the gas

phase is an incompressible unsteady turbulent flow. Liquid water is considered as a discrete phase. Use turbulence model, Taylor ratio fracture model, collision model and evaporation model for no energy exchange between gas and liquid. Then carry out phase-to-phase coupling calculations until iterative convergence.

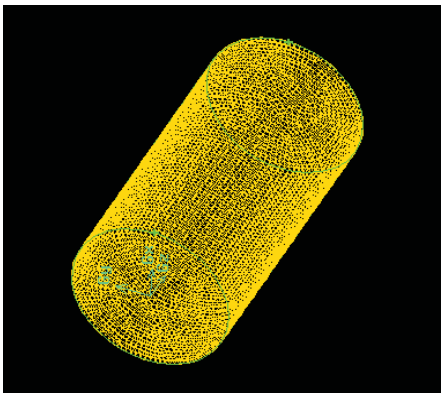

FIGURE 1
flow field of air-driving mist spray

Continuous Phase Equation. Continuous equation [12]:

$$\frac{\partial \rho}{\partial t} + \nabla \cdot (\rho V) = 0 \tag{1}$$

In the formula, ρ is density， g/cm^3; t is time, s; V is speed vector.

Momentum equation (Navier-Stokes equation):

$$\frac{\partial(\rho V_x)}{\partial t} + \nabla \cdot (\rho V_x V) = \nabla \cdot (\mu grad V_x) - \frac{\partial \rho}{\partial x} + S_x \tag{2}$$

$$\frac{\partial(\rho V_y)}{\partial t} + \nabla \cdot (\rho V_y V) = \nabla \cdot (\mu grad V_y) - \frac{\partial \rho}{\partial y} + S_y \tag{3}$$

$$\frac{\partial(\rho V_z)}{\partial t} + \nabla \cdot (\rho V_z V) = \nabla \cdot (\mu grad V_z) - \frac{\partial \rho}{\partial z} + S_z \tag{4}$$

In the formula, *V*x, *V*y, *V*z separately are the velocity component on axis *x*, *y*, *z,* m/s; μ is Hydrodynamic viscosity, Pa·s ; *S*x, *S*y, *S*z separately are the source items on axis *x*, *y*, *z*.

Discrete Phase Equation. According to the force balance acting on the droplets (particles), the equation of motion of the particles in the Lagrangian coordinate system can be given [13, 14]:

$$\frac{du_p}{dt} = F_D(u - u_p) + g_x(\rho_p - \rho)/\rho_p + F_x \tag{5}$$

$$F_D = \frac{18\mu}{\rho_p D_p^2}\frac{C_D \mathrm{Re}}{24}$$

In the formula,

u is Continuous phase velocity, m/s; u_p is particle speed, m/s; μ is the molecular viscosity coefficient of fluid; ρ is fluid density, kg/m^3; ρ_p is particle density, kg/m^3; D_p is the diameter of the particle, m; *Re* is the relative Reynolds number.

Droplet Break Model. It is assumed that the droplet distortion can be described as a one-dimensional forced attenuation simple harmonic vibration similar to the spring weight system, Amsden proposed a TAB model based on Taylor's derivation [15]. According to the TAB breaking principle, the air assisted atomization model is

$$C_F \frac{\rho_g (u_g - u_{p1})^2}{\rho_{p1} r}\frac{k}{m_{p1}} = C_K \frac{\sigma}{\rho_{p1} r^3}\frac{d_{p1}}{m_{p1}} \tag{6}$$

In the formula, *r* is drop radius, m; *k* is the flow energy kg·m·s^{-2}; m_{p1} is the weight of single drop, kg; σ is Liquid surface tension, N /m; C_F, C_K is dimensionless number, result from experiments as C_F =1/3, C_K=8.0.

Evaporation Model. The amount of droplet evaporation is determined by gradient diffusion， that is to say, the diffusivity of the droplet into the gas phase is related to the vapor concentration gradient between the droplet and the main stream of the gas stream：

$$N_i = k_c\left(\frac{p_{sat}(T_p)}{RT_p} - X_i\frac{p_{op}}{RT_\infty}\right) \tag{7}$$

In the formula: N_i, flow rate of steam molar, kg•mol/m•^{2}s; K_c, mass transfer coefficient, m/s; R, Universal gas constant; P_{sat}, Saturated vapor pressure, Pa; T_p, droplet temperature, K; X_i is the local volume fraction in Component i; P_{op}, working pressure, Pa; T_∞, local gas phase (volume average) temperature, K.

Numerical Simulation Results and Analysis of Droplet Area. In practice, we have already known that the particle size of the sprayed water mist is related to the pressure. In order to determine the appropriate spray pressure, by establishing a reasonable set model and with the nozzle model of the fluent software to simulate the mode and dmp model for the value of external flow field. In the meanwhile, the model of crushing, evaporation, collision and random walk have been added to study the rela-

tionship between the droplet size and the spray pressure, and the particle size distribution characteristics of the droplet particles for further improving the dust reduction efficiency.

Firstly determine the diameter of the atomizing nozzle before spraying. When the nozzle diameter is less than 1mm, the nozzle is prone to blockage due to the problem of water quality; When the nozzle diameter is greater than 2 mm, the nozzle water consumption will increase. Therefore, the nozzle diameter should between 1-2 mm. This paper studies high pressure nozzles with a diameter of 1mm. Under the premise of several models, only change the water pressure flowing into the nozzle, and then study the laws of droplet size distribution under different pressures. The specific parameters and boundary conditions are numerically simulated by fluent software with good convergence. As shown in Figure2 to Figure 5, they respectively show the distribution pattern of the droplet size in the case where only the water flow pressure is changed.

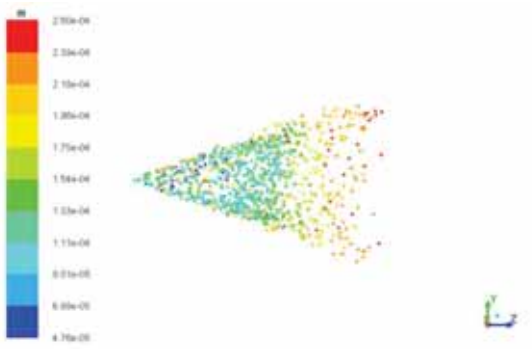

FIGURE 2
Particle size distribution of droplets (P=1 MPa)

FIGURE 3
Particle size distribution of droplets (P=3 MPa)

FIGURE 4
Particle size distribution of droplets (P= 5 MPa)

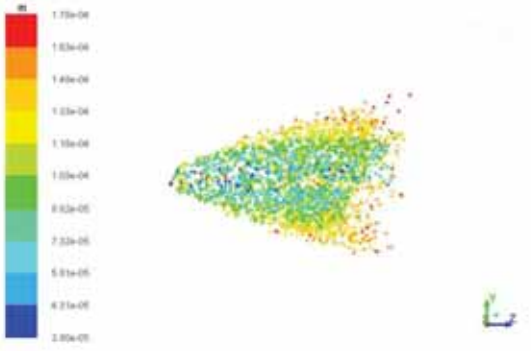

FIGURE 5
Particle size distribution of droplets (P= 8 MPa)

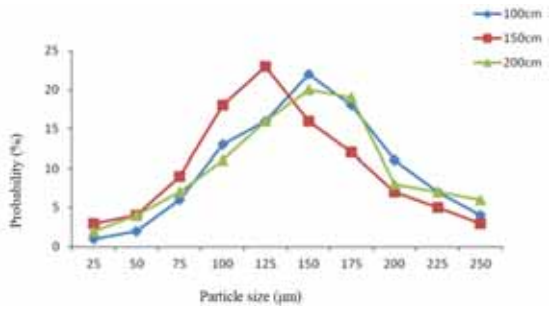

FIGURE 6
Probability of droplets size distribution (P=1 MPa)

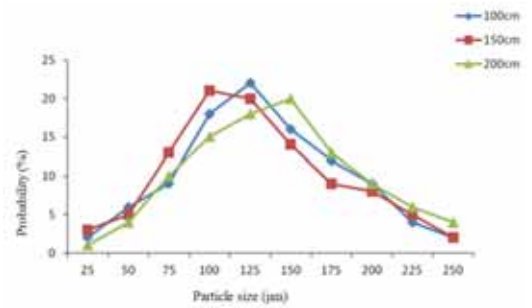

FIGURE 7
Probability of droplets size distribution (P=3 MPa)

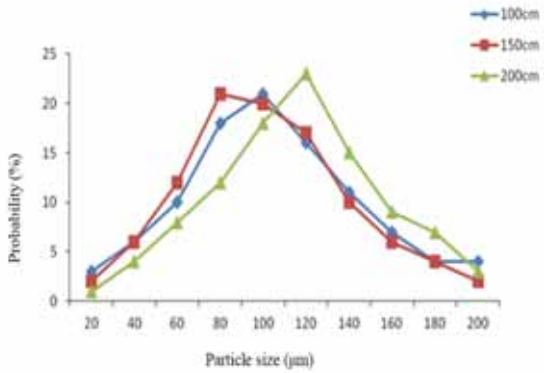

FIGURE 8
Probability of droplets size distribution (P=5 MPa)

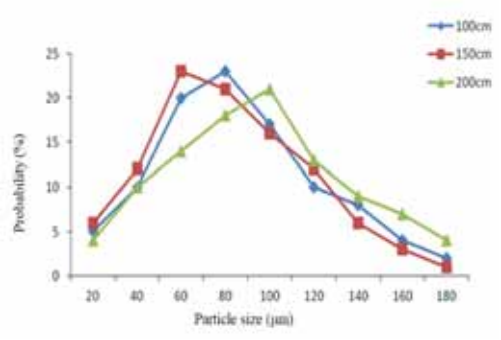

FIGURE 9
Probability of droplets size distribution (P=8 MPa)

TABLE 1
Dust concentration of dust point

Measurement order	Dust concentration before spray/ ($mg \cdot m^{-3}$)	Dust concentration after spray/ ($mg \cdot m^{-3}$)	Dust reduction rate/%
1	168.1	10.1	93.99
2	176.5	11.2	93.65
3	99.2	8.3	91.63
4	101.8	9.4	90.76
5	183.9	15.7	91.46
6	328.1	24.1	92.65

FIGURE 10
Field effect of auxiliary air spray

After the iteration converges, the droplets are captured and the droplets in the entire atomization field are counted. It can be seen from Figures 6 to Figure 9 that particle size distribution conforms to double R distribution. When the pressure is 1 MPa, the droplet diameter is mainly concentrated between 100-150 μm. When the distance between the panel and the nozzle is 150 cm, the droplet size is relatively small. As the pressure increases, the droplet breaks completely, the particle size decreases significantly, and the water pressure is 8 MPa. Set a panel at 150 cm away from the nozzle. After capturing the water mist ions in the disc area, it is found through analysis and statistics that the droplet size is mainly 60 μm to 80 μm, which is similar to the particle size of the dust particles. select a nozzle with a pressure of 8 MPa for spray of dust removal.

Application of High Pressure Atomized Spray. Figure 10 is the real scene of plant tail high pressure spray in Papaya boundary coal preparation plant of Pingshuo Group. High pressure nozzle is used on site, water pressure is 8 Ma and the nozzle diameter is 1mm. The dust removal effect before and after the comparison was measured 6 times with a dust concentration meter, it's shown as in Table 1.

We can see from the Table 1 that the concentration of dust in the workshop is high before the spray is set. When the high pressure mist dust removal system is turned on, the dust concentration is significantly reduced, the removal rate is above 90%, and the dust removal effect is ideal.

CONCLUSION

(1) The management of dust hazard is an arduous and important task. Through the numerical simulation of high pressure spray technology, the relationship between atomization pressure and dust removal efficiency can be effectively grasped, thus providing theoretical guidance for the application on site.

(2) The greater the water pressure, the larger the spray angle, the more severe the droplet breaks, and the greater the droplet speed. In the process of simulating the spray, select the nozzle with 1 mm diameter and change spray pressure, then it was found that

the droplet size decreased as it increased. When the pressure is increased to 8Mpa, the particle size of the droplet is broken completely, which is similar to the particle size of the dust, and the dust reduction effect is best at this time. Therefore, the nozzle with a pressure of 8Mpa is selected for spray dust reduction.

(3) Select 8Mpa according to the simulation results, and the dust reduction rate is more than 90% after the application on site, the effect is obvious.

ACKNOWLEDGEMENTS

Fund number 51704146. The project name Study on Dust Mesoscale Movement Characteristics and Dust Control Mechanism of Magnetized Spiral Pneumatic Mist Curtain in Fully Mechanized Heading Face Supported by National Natural Science Foundation of China.

Fund number 51704145. Study on the multi-scale coagulation mechanism of dust-droplet particles based on activated water by sonic blasting by National Science Foundation of China.

REFERENCES

[1] Ge, S.C., Fan, W.T., Zhang, Z.W., Jing, D.J., Chen, X. (2015) Dust pollution and air-driving shooting-fog dust control of coal conveyer bel tailpiece. Journal of Liaoning Technical University: Natural Science. 34(4), 459-463.

[2] Jing, D.J., Ge, S.C., Liu, J., Sun, Y. (2013) Numerical simulation of dust diffusion rule and suppression technology in crushing station and application. Chinese Journal of Environmental Engineering. 7(9), 3494-3500.

[3] Huang, S. (2011) Numerical simulation study on dust pollution mechanism and control technology of coal-falling tower of open coal storage. Fuxin: Graduate College of Liaoning Technology University.

[4] Liu, W.Y. (2012) The study of the production mechanism and the control plan of dust in blind pass of coal mine of Xilinhaote Datang. Fuxin: Graduate College of Liaoning Technology University.

[5] Ge, S.C., Jing, D.J., Huang, Y.P. (2012) Numerical simulation determination of the production mechanism and technical parameters of high pressure microfog system. Journal of Liaoning Technical University: Natural Science. 31(1), 17-20.

[6] Chen, X., Ge, S.C., Zhang, Z.W., Jing, D.J. (2014) Numerical simulation and analysis of multiozzle interference base on Fluent. Chinese Journal of Environmental Engineering. 8(6), 2503-2508.

[7] Jing, D.J., Ge, S.C., Liu, J. (2012) Study on control technology of dust at coal drop tower based on Eulerian-ulerian model. China Safety Science Journal. 22(10), 126-132.

[8] Chen, X. (2012) Research of theory about prevention by high-pressure spray and relevant techniques for drive room. Fuxin: Graduate College of Liaoning Technology University.

[9] Hu, X.M. (2013) Pneumatic nebulization dual fuel nozzle design and parameter optimization. Harbin: Graduate school of Harbin Engineering University.

[10] Kosiwczuk, W., Cessou, A., Trinite, M. (2005) Simultaneous velocity field measurements in two-phase for turbulent mixing of sprays by means of two-phase PIV. Experiments in Fluids. 39(5), 895-908.

[11] Cao, J.M. (2005) Spray Study. Beijing: China Machine Press.

[12] Yang, S.L. (2001) Numerical simulation of 3-Dimensional dust distribution on long wall coal faces. China Safety Science Journal. 4(11), 61-64.

[13] van Wachem, B.G.M., Almstedt, A.E. (2003) Methods for multiphase computational fluid dynamics. Chemical Engineering Journal. 44(12), 39-152.

[14] Mao, R.J. (2009) The application and study on dust control technology about drilling against outburst in the fully-mechanized coal face. University of Science and Technology Beijing, 69-105.

[15] O'Rourke, P.J., Amsden, A.A. (1987) The tab method for numerical calculation of spray droplet breakup. SAE Paper 872089.

Received: **03.10.2019**
Accepted: **02.01.2020**

CORRESPONDING AUTHOR

Zhihui Huang
College of Safety Science and Engineering,
Liaoning Technical University,
Fuxin 123000 – China

e-mail: huangzhihui666@sina.com

© by PSP Volume 29 – No. 04A/2020 pages 2891-2896 Fresenius Environmental Bulletin

EFFECTS OF SOWING DATE AND NITROGEN APPLICATION RATE ON WHEAT YIELD AND YIELD COMPONENT FACTOR IN JIANGHUAI PLAIN

Chengfang He*, Hongjie Zhu, Xiangqiang Kong, Xiaoming Yan

Agricultural Product Processing Research Institute, Anhui Academy of Agricultural Sciences, Hefei 230031, China

ABSTRACT

Wheat is a staple crop worldwide, but yields may diminish as climate change causes increasingly unpredictable patterns of precipitation and soil nutrient availability. Farmers are thus challenged to maximize planting efficiency to increase yield, while also improving their resource use efficiency. In this study, sowing date and nitrogen uptake and planting density, and aspects of yield are assessed. The results show that proper and appropriate sowing is conducive to the coordination of the three elements of wheat production and can achieve high yield. The yield of wheat with the same fertilization amount increased with the increase of planting density, and the yield of wheat increased first and then decreased. There was a significant difference between different fertilization rates at the same density, and the yield of wheat treated with N2 was the highest.

KEYWORDS:
Wheat, Sowing date, Nitrogen absorption, Yield, Density.

INTRODUCTION

Wheat is the second most widely grown crop in the world, estimated at 200 million ha. Wheat grain consumption accounts for 19% of the calories in the global human diet [1], while about 40% of wheat produced is fed to poultry and livestock. Wheat grain is rich in carbohydrates and has a higher protein content than other major cereals, such as rice (Oryza sativa), maize (Zea mays), rye (Secale cereale), and millet (Pennisetum glaucum) [2]. It also contains substantial amounts of minerals (e.g., Zn, Fe), vitamins, and phytochemicals, making it a good source of nutrition [3, 4]. Wheat is used globally for the production of bread, pasta, and other bakery products and to a small extent for industrial products.

The current shortage of water resources has become the main problem restricting wheat production and is expected to worsen as a result of global climate change. Rising temperatures contribute to decreased wheat yields and will reduce wheat productivity at a global scale [5,6]. In particular, elevated seasonal temperatures are expected, where low and variable annual precipitation already impairs wheat crops. With increased global population and food demand, it has become particularly urgent to develop technologies to improve water use efficiency in wheat [7].

Recent technological advances have focused on the simultaneous and synergistic improvement of several factors including water use, nitrogen efficiency, yield, and grain quality [8]. Nitrogen uptake and efficiency are widely studied as features of crop growth [9]. Photosynthesis in crops is changed by addition of water and nitrogen, and nitrogen nutrition is influenced by water status [10]. In durum wheat (Triticum durum Desf.), yield and dry matter accumulation were increased by nitrogen levels and reduced by water stress [11]. Increasing nitrogen fertilizer levels without addressing dry soil conditions results in lost grain yield and quality [12].

There is an absolute requirement for N for wheat growth, and crop yield and quality depend upon substantial N inputs. Initially, this drives canopy formation required for photosynthesis that, in turn, drives yield. Subsequently, the major sink is the reproductive component, namely, the wheat grain. More than half of industrially fixed N is used by agriculture, worldwide amounting to in excess of 180 Mt/year [13]. The production and transport of N fertilizers by the Haber–Bosch process is highly energy intensive and depends on fossil fuels; however, the costs for the fertilizer for many farmers continue to be relatively low, in some cases due to state subsidies. Ready availability and cheap supply encourage overuse, and environmental problems in some agroecosystems remain an issue.

N losses from the production system occur as nitrate (NO_3^-) leaching or as the gaseous products of denitrification in soil: futile di-nitrogen (N_2); nitrous oxide, a greenhouse gas with 300 times the heat-trapping capacity of carbon dioxide (CO_2); and finally ammonia. Except for N_2, these gases contribute to pollution and climate change [14]. Furthermore, N accumulates in the soil. N losses reduce ecosystem productivity and biological diversity and contribute to eutrophication. As a consequence, maximal acceptable NO_3^- level in the European Union (EU) in

freshwater resources is legislated to 50 µg/l. This target, however, is not achieved in some EU areas, especially those with high organic manure inputs; the disposal of N-containing manure from locally concentrated animal farming industry may be a further future threat for these regions. The environmental problems associated with N inputs continue to be an issue in many parts and countries of the world, including the USA and large regions of China. Although, substantial progress has recently been made, wheat remains the least N use efficient (NUE) major crop, whereas NUEs of maize and rice are around 25% higher [15]. Fertilizer regulations to improve N use management with the clear goal to decrease N inputs and losses into the environment differ in each country. However, major concerns from farmers are that yield and grain quality will not be maintained at high levels if N fertilizer use is substantially reduced.

MATERIALS AND METHODS

The test was carried out in the Modern Agriculture Demonstration Park in Guohe Town, Lujiang County, Hefei City. Before the rice harvest, the rotary straw was returned to the field. The tested wheat variety was Sumai 188, and three seeding amounts were set, namely M1: 25, M2: 35, M3: 45 kg/mu, and four sowing dates, which were B1: November 5th, B2: November 15th, B3: November 25th, B4: December 5th, a total of 12 treatments. The two-factor split zone design was adopted, and the sowing period was the main area, and the seeding amount was the cracking area, which was repeated 3 times for each treatment. In the Datian plot test, the area per plot was 10 M^2, and the nitrogen fertilizer application rate was 16 kg/mu.

Under the conditions of suitable sowing (B1 January 5) and delayed planting (B2: December 5), three seeding rates were set, 25, 35, 45 kg/mu, and 4 nitrogen fertilizer application amounts, respectively. It is N0:0, N1:12, N2:16, N3:20 kg/mu. The three-factor split zone design was adopted, and the sowing period was the main area. The amount of nitrogen fertilizer was the crack zone, and the seeding amount was small crack zone, which was repeated 3 times for each treatment. Datian Community test, the area of each plot is 10M2, the tested variety is Sumai 188, the straw is returned to the field, and the sowing method is carried out by strip. Nitrogen fertilizer is applied according to the ratio of base fertilizer: top-dressing = 6:4. The application rates of phosphorus and potassium fertilizer are 6 kg/mu. Phosphorus and potassium fertilizers are all applied as base fertilizer, and the base fertilizer is applied by mechanical deep application. Other cultivation management measures are managed in the same local field, and timely control of pests and diseases is carried out.

RESULTS AND DISCUSSION

Effects of Sowing Date and Density on the Number of Tillers in Wheat Population. It can be seen from Table 1 that the number of tillers before wintering, the maximum number of tillers in the jointing stage, and the number of final panicles in the mature stage are the highest in the sowing period, and the number of tillers in the main growing period is the same in the same sowing period. As the planting density increases, the number of population tillers and the number of final panicles in wheat are related to the sowing date and seeding density, and the final number of panicles decreases significantly with the delay of sowing date.

Effects of Sowing Date and Density on Dry Matter Accumulation of Wheat. It can be seen from Table 2 that under the condition of straw returning, the dry matter accumulation of wheat increases first and then decreases with the delay of sowing date. Under the same sowing period, increasing the seeding rate increases the dry matter accumulation of wheat, and As the amount of seeding increases, the amount of dry matter accumulation increases.

TABLE 1
Effects of Sowing Date and Density on the Number of Tillers in Wheat Population (10^4/mu)

Sowing date	Density	Wintering period	Jointing stage	Maturity
B1	M1	32.53	75.80	38.32
	M2	34.87	89.24	39.58
	M3	39.64	101.72	42.13
B2	M1	31.60	78.21	39.96
	M2	38.62	92.34	39.38
	M3	46.92	116.10	41.35
B3	M1	25.35	62.04	32.32
	M2	34.72	88.89	33.81
	M3	36.07	98.51	36.07
B4	M1	23.38	62.04	33.89
	M2	31.62	93.89	34.02
	M3	35.61	94.13	35.76

TABLE 2
Effect of sowing date and density on dry matter accumulation of wheat (kg/mu)

Sowing date	Density	Wintering period	Jointing stage	Flowering period	Maturity
B1	M1	197.10	318.15	650.75	983.68
	M2	205.26	334.27	679.68	1024.39
	M3	187.22	302.25	618.12	934.36
B2	M1	218.93	354.28	725.83	1092.64
	M2	202.47	329.78	663.47	1010.46
	M3	203.33	327.17	672.31	1014.76
B3	M1	163.36	268.86	539.36	815.30
	M2	169.84	274.28	560.74	847.61
	M3	160.53	259.31	532.03	801.19
B4	M1	140.92	225.75	467.27	703.31
	M2	138.35	221.62	466.79	690.49
	M3	129.59	209.52	421.86	646.76

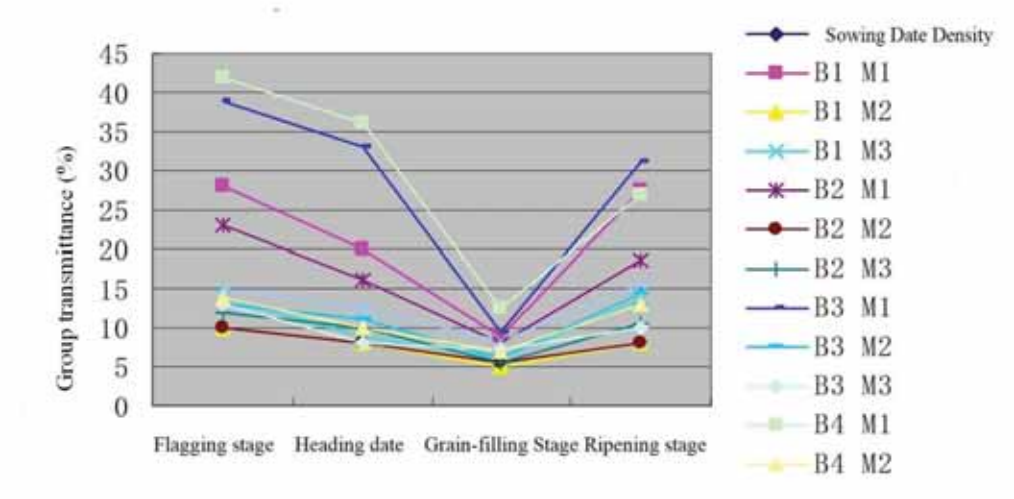

FIGURE 1
Effect of Sowing Date and Density on Light Transmittance of Wheat Population

Effect of Sowing Date and Density on Light Transmittance of Wheat Population. It can be seen from Figure 1 that the light transmittance of wheat population decreases with the increase of seeding density at each growth stage, and the light transmittance of M1 treatment is large at each growth period, and the light leakage loss is serious; the overall ventilation and light transmission of M2 treatment is good. It is beneficial to the utilization of light energy by the canopy of wheat population. The flag-raising period gradually decreased after the growth period, reached the lowest value during the filling period, and gradually increased after the filling period. The light transmittance of wheat decreased with the delay of the sowing date, indicating that the increase of the light transmittance of the group was delayed, which was not conducive to the light energy interception of the wheat population.

Effects of Sowing Date and Density on Net Photosynthetic Rate of Wheat Flag Leaves. The results showed that (Figure 2), the photosynthesis rate of flag leaves decreased gradually with the advancement of the filling process. The photosynthesis rate decreased with the increase of density. The photosynthetic rate of the whole grain filling period was M2>M1>M3. The photosynthetic rate of M2 treatment decreased slowly during the whole filling stage, and the photosynthetic rate remained high during the waxing stage rate.

Effects of Sowing Date and Density on Yield Components of Wheat Yield and Yield. According to the analysis of the components of wheat yield in Table 3, the number of spikes and the number of kernels per plant were the highest. Under the same sowing date, with the increase of seeding density, the number of grains per panicle and 1000-grain weight decreased, and the number of panicles per unit area increased. The seeding density treatment showed significant difference in grain yield, showing M2 > M1 > M3. It shows that the appropriate and appropriate amount of sowing is conducive to the coordination of the three elements of wheat production, and can achieve high yield.

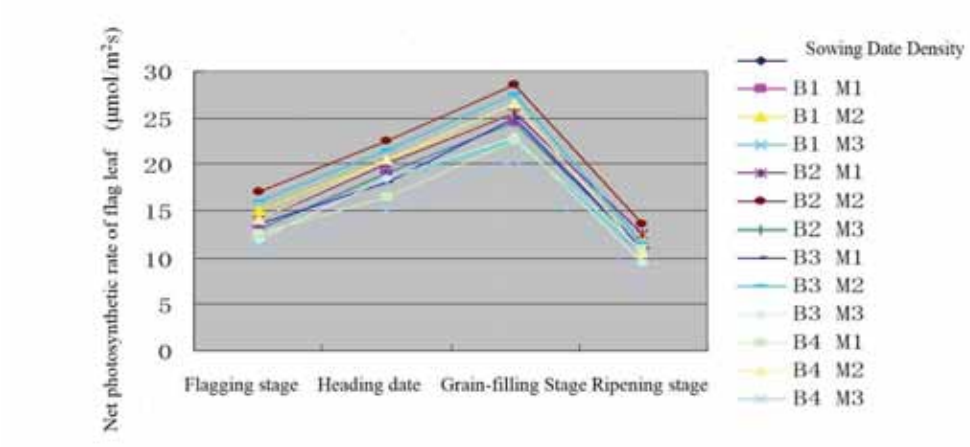

FIGURE 2
Effect of sowing date and density on net photosynthetic rate of wheat flag leaves

TABLE 3
Effects of Sowing Date and Density on Yield Components of Wheat Yield and Yield

Sowing date	Density	Number of spikes ($\times 10^4$/mu)	Number of kernels per spike (grain/ear)	Weight of thousand grains (g)	Theoretical yield (kg/mu)	Actual production (kg/mu)
B1	M1	38.32	36.66	39.11	467.01	464.92
	M2	39.58	36.88	38.97	483.52	484.16
	M3	42.13	34.99	37.41	468.75	441.61
B2	M1	39.96	37.4	40.11	509.53	516.42
	M2	39.38	36.93	39.27	485.44	477.58
	M3	41.35	36.27	39.41	502.40	479.61
B3	M1	32.32	36.79	39.45	398.72	385.34
	M2	33.81	36.14	40.42	419.81	400.61
	M3	36.07	33.8	37.95	393.27	378.67
B4	M1	33.89	34.88	39.42	396.08	332.41
	M2	34.02	35.62	39.46	406.45	326.35
	M3	35.76	33.18	38.52	388.49	305.68

TABLE 4
Effects of Suitable Nitrogen Fertilizer and Sowing Amount on Wheat Yield and Yield Components

Treatment		Number of spikes ($\times 10^4$/mu)	Number of kernels per spike (grain/ear)	Weight of thousand grains (g)	Theoretical yield (kg/mu)	Actual production (kg/mu)
Nitrogen fertilizer	Density					
N0	M1	21.89	30.06	40.43	226.13	217.38
	M2	23.74	29.21	40.76	240.25	225.18
	M3	25.67	26.88	40.52	237.65	218.14
N1	M1	26.81	32.48	40.87	302.51	284.13
	M2	32.67	31.12	39.74	343.43	312.61
	M3	31.15	30.14	38.94	310.75	303.80
N2	M1	38.32	36.66	39.11	467.01	464.92
	M2	39.58	36.88	38.97	483.52	484.16
	M3	42.13	34.99	37.41	468.75	441.61
N3	M1	26.25	34.47	39.27	302.03	271.60
	M2	33.55	34.67	38.86	384.21	330.27
	M3	33.63	32.19	39.42	362.73	321.19

Effects of Sowing Date and Nitrogen Application Rate on Yield Components of Wheat Yield and Yield. It can be seen from Table 4 and Table 5 that the factors affecting the yield of wheat, under the same sowing date, with the increase of seeding density, the number of panicles per unit area increases, the number of kernels per ear and 1000-grain weight decrease, and the number of panicles and panicles are The timely sowing treatment is higher than the postponed sowing period, and the wheat yield is higher than the delayed sowing. It shows that the appropriate and appropriate amount of sowing is conducive to the coordination of the three elements of wheat production, and can achieve high yield.

TABLE 5
Effects of Delayed Planting of Nitrogen Fertilizer and Sowing Amount on Wheat Yield and Yield Components

Treatment		Number of spikes ($\times 10^4$/mu)	Number of kernels per spike (grain/ear)	Weight of thousand grains (g)	Theoretical yield (kg/mu)	Actual production (kg/mu)
Nitrogen fertilizer	Density					
N0	M1	19.89	28.06	39.43	187.05	176.47
	M2	20.74	29.01	39.76	203.34	194.55
	M3	22.67	26.04	38.51	193.23	185.45
N1	M1	24.81	29.82	39.87	250.73	237.15
	M2	27.14	30.45	38.46	270.16	248.36
	M3	29.15	30.02	38.21	284.21	264.16
N2	M1	33.89	34.88	39.42	396.08	332.41
	M2	34.02	35.62	39.46	406.45	326.35
	M3	35.76	33.18	38.52	388.49	305.68
N3	M1	25.34	33.68	39.12	283.79	257.90
	M2	30.25	33.41	37.81	324.81	289.15
	M3	31.78	32.02	38.14	329.89	292.28

The challenge of maximizing grain production by optimization of water use, planting patterns, and fertilization has long been an important goal in agricultural research. Impending climate changes that will limit water, as well as the expenses associated with production of nitrogen fertilizer drive the cost, and thus productivity, of large-scale wheat producing farms.

The yield of wheat with the same fertilization amount increased with the increase of planting density, and the yield of wheat increased first and then decreased. There was a significant difference between different fertilization rates at the same density, and the yield of wheat treated with N2 was the highest.

CONCLUSIONS

In this study, sowing date and nitrogen uptake and planting density, and aspects of yield are assessed. The results show that proper and appropriate sowing is conducive to the coordination of the three elements of wheat production and can achieve high yield. The yield of wheat with the same fertilization amount increased with the increase of planting density, and the yield of wheat increased first and then decreased. There was a significant difference between different fertilization rates at the same density, and the yield of wheat treated with N2 was the highest.

ACKNOWLEDGEMENTS

This paper is supported by Major National Research and Development Program (2016YFD03002-2).

REFERENCES

[1] Zörb, C., Ludewig, U., Hawkesford, M.J. (2018) Perspective on Wheat Yield and Quality with Reduced Nitrogen Supply. Trends in Plant Science. 23, 1029-1037.
[2] Meyer-Aurich, A., Karatay, Y.N. (2019) Effects of uncertainty and farmers' risk aversion on optimal N fertilizer supply in wheat production in Germany. Agricultural Systems. 173, 130-139.
[3] Shewry, P.R. (2009) Wheat. J. Exp. Bot. 60, 1337-1553.
[4] Hawkesford, M.J. (2017) Genetic variation in traits for nitrogen use efficiency. J. Exp. Bot. 68, 2627-2632.
[5] Hamnér, K., Weih, M., Eriksson, J., Kirchmann, H. (2017) Influence of nitrogen supply on macro- and micronutrient accumulation during growth of winter wheat. Field Crops Research. 213, 118-129.
[6] Meng, Q., Yue, S., Hou, P., Cui, Z., Chen, X. (2016) Improving Yield and Nitrogen Use Efficiency Simultaneously for Maize and Wheat in China: A Review. Pedosphere. 26, 137-147.
[7] Liu, J., Wiberg, D., Zehnder, A.J.B., Yang, H. (2007) Modeling the role of irrigation in winter wheat yield, crop water productivity, and production in China. Irrig. Sci. 26, 21-33.
[8] Parry, M.A.J., Reynolds, M., Salvucci, M.E., Raines, C., Andralojc, P.J., Zhu, X.G., Price, G.D., Condon, A.G., Furbank, R.T. (2011) Raising yield potential of wheat. II. Increasing photosynthetic capacity and efficiency. J. Exp. Bot. 62, 453-467.
[9] Przulj, N., Momčilović, V. (2003) Dry matter and nitrogen accumulation and use in spring barley. Plant Soil Environ. 49, 36-47.

[10] Shangguan, Z.P., Shao, M.A., Dyckmans, J. (2000) Nitrogen nutrition and water stress effects on leaf photosynthetic gas exchange and water use efficiency in winter wheat. Environ. Exp. Bot. 44, 141-149.
[11] Ercoli, L. Lulli, L., Mariotti, M., Masoni, A., Arduini, I. (2008) Post-anthesis dry matter and nitrogen dynamics in durum wheat as affected by nitrogen supply and soil water availability. Eur. J. Agron. 28, 138-147.
[12] Woolfolk, C., Raun, W., Johnson, G., Thomason, W., Mullen, R., Wynn, K. Freeman, K. (2002) Influence of late-season foliar nitrogen applications on yield and grain nitrogen in winter wheat. Agron. J. 94, 429-434.
[13] Hawkesford, M.J. (2014) Reducing the reliance on nitrogen fertilizer for wheat production. J. Cereal Sci. 59, 276-283.
[14] Butterbach-Bahl, K., Baggs, E.M., Dannenmann, M., Kiese, R., Zechmeister-Boltenstern, S. (2013) Nitrous oxide emissions from soils: how well do we understand the processes and their controls? Philos. Trans. R. Soc. Lond. B Biol. Sci. 386, 20130122-2013124.
[15] Yin, M.H., Li, Y.N., Xu, Y.B. (2017) Comparative effects of nitrogen application on growth and nitrogen use in a winter wheat/summer maize rotation system. Journal of Integrative Agriculture. 16, 2062-2072.

Received: **08.10.2019**
Accepted: **15.01.2020**

CORRESPONDING AUTHOR

Chengfang He
Agricultural Product Processing Research Institute
Anhui Academy of Agricultural Sciences
Hefei 230031 – China

e-mail: kuaile888q@126.com

© by PSP Volume 29 – No. 04A/2020 pages 2897-2907 Fresenius Environmental Bulletin

PLASTICITY IN BEHAVIOR OF TURKISH MALTING BARLEY CULTIVARS UNDER SEMI-ARID AND CONTINENTAL CLIMATIC CONDITIONS

Abdulveli Sirat[1], Bilge Bahar[2,*]

[1]Gumushane University, Siran Mustafa Beyaz Vocational School, TR 29700, Gumushane, Turkey
[2]Gumushane University, Faculty of Engineering and Natural Sciences, TR 29100, Gumushane, Turkey

ABSTRACT

This study aimed to select stable cultivars in terms of desired agronomic or quality criteria from among 15 two rowed barley cultivars that may remain stable in varying year conditions during 2014-2015 and 2015-2016. Furthermore, relationships among these traits were investigated. Some agronomical and quality traits of barley were affected by years and cultivars. Yield, yield components and some quality parameters were affected by the cultivars. Also, days to ripening was affected by years, cultivars, and year × cultivar interaction. Crude protein content (CPC) was significantly positive correlated with ASH during both seasons. Starch ratio (SR) showed significantly negative correlations with ASH and CPC during both seasons. ADF and NDF had significant positive strong correlation with one another and ASH during both years while they showed significant negative correlations with SR. The results show that technological properties are not affected by the interaction of cultivar × year; therefore, these stable cultivars can be readily used in malt or feed technology if their technological features are considered. For example, cv. Ünver contained low ratios of ash, CPC, oil, soluble fiber and high SR in the malt industry; cv. Hasat which includes the opposite technological properties of cv. Ünver, was found be suitable for use in feed technology.

KEYWORDS:
Feed, malting barley, quality traits, yield, yield components

INTRODUCTION

Barley is an old crop that has been cultivated from *H. vulgare ssp. spontaneum* in the Fertile Crescent of the Middle East for more than 10000 years ago [1]. The barley is generally used for malting and as animal feed. It has fourth place after corn (1.1 billion tons), wheat (749.5 million tons) and rice (741 million tons) with the production of 141.2 million tons in world trade. Barley is grown over an area of 46.9 million ha with grain yield of 3011 kg ha^{-1} [2]. Barley is used as a food stuff in many parts of the World including the Middle East, North Africa, Northern and Eastern Europe, and Asia since long time ago. Now, two-thirds of the barley produced in the world is used in feed and one-third is used for brewing and malting; rest of the barley is used as human food [3]. Considering the health benefits of barley, its direct use in foods is comparatively low. It is helpful source of β-glucans for reduction of blood cholesterol [4]. It also has low glycemic index [5] with substantial amounts of antioxidant tocopherols and tocotrienols [6]. Technologic and nutritive performance of the β-glucans of barley increase further due to rheological characteristics of barley. Thus, they are consumed by mixing with other cereals to make bread, muffins, pasta, noodles, salad sauces, beverages, soups, reduced-fat dairy and meat products [7]. Apart from these, the protein contents are as higher as in animal meat. Bertholdsson [8] has reported that most of malting markets require near 11.5 percent of protein in barley grain. On the other hand, protein concentration of the barley grain may occasionally exceed these limit in malting barley due to the favorable nitrogen [9], drought [10], and high temperature together with water stress [11].

Yield and yield components are very important selection criteria in barley. Throughout the world, shrinkage of cultivation areas and rapid population growth have been the primary goal for improving grain yield of cereal crops including barley in breeding programs [12] for stable yield increases in barley [13]. Considerable evoloutions in various physiological characteristics were observed in terms of grain yield for genetic gain in the last century [14]. There is need to breed high-yielding cultivars for more grains per unit area [15]. It has been reported that the increase in the number of grain in the unit area is due to the rise of spike numbers per square meter and the grain numbers per spike and not due to clear improvement in the weight of one thousand barley grains [16]. Therefore there is need to gain more information about correlation between genetic gains in grain yield and agronomical traits like heading date, spike length, plant height, hectoliter weight, and thousand grain weight [17]. Baumer et al. [18] has pronounced the advantages of the semi-dwarf barley

cultivars to obtain high yield and quality. Kleinknecht et al. [19] has reported effects of the influences of the genotypic and cultivar × environment interactions on variations in the agronomic traits of barley, and has emphasised the importance of optimization of field and laboratory assays. In a study, grain yield and other agronomical traits were significantly affected by cultivars, years, and cultivar × year interactions [17]. Again, Madic et al. [20] found cultivar × year interactions for plant height and grain yield and observed effects of year changes in years on the number of spikes per square meter and grain numbers per spike. These days greenhouse effects are source great variations on climate change is with adverse effects on cereals including barley grain yields [21]. Therefore, breeding of barley cultivars showing stable behaviour in face of greenhouse effects based adverse year conditions is desired.

The study aimed to quantify the behaviour of some agronomically important traits like grain yield and effective components on the grain yield of two-rowed winter barley cultivars under the semi-arid and continental climatic conditions of Gumushane Province of the Eastern Black Sea Region in Turkey.

MATERIALS AND METHODS

Characteristics of the Trial Soils. Research was conducted at the farmers field of Siran county of the Gumushane province of Turkey, during 2014-2015 and 2015-2016 (at the Latitudes of 40º 11′ N, the Longitudes of 41º 85′ E, and the altitude of 1409 m asl). In the first season (2014-2015), soil was slightly alkaline (pH 7.77) and clay loamy. It was also medium lime (12.43 % $CaCO_3$), mild salty (0.18 %), poor for phosphorus (41.8 kg P_2O_5 ha^{-1}), rich for favorable potassium (1323 kg K_2O ha^{-1}), and fine for organic matter (3.32 %). In the second season (2015-2016), soil was clayey, mild alkaline (pH 7.61), mild limy (3.33 % $CaCO_3$), medium salty (0.37 %), medium for phosphorus (80.8 kg P_2O_5 ha^{-1}), with sufficient amount of potassium (1266 kg K_2O ha^{-1}), and poor organic matter (1.68 %) (Table 1).

Climatic Conditions of the Trial Sites. The climatic data of the trial sites were obtained from the Turkey General Directorate of Meteorology, Gümüşhane Meteorology Regional Directorate. The long term average (1950 to 2016) and 2014 to 2016 meteorological data or Siran county of Gümüşhane Province is given in Table 2. The table, showed that the annual total precipitation in the first year (2014-2015) and 2nd year (2015-2016) was 419.8 mm and 429.1 mm in the same order. The precipitation values of the second season between April and July, which corresponded to the period of stem elongation to grain filling, were higher compared to these values in the first year. Growth seasons' temperature means were close to each other, relative moisture values of the second season were lower than the first year values.

Plant Materials. Fifteen (15) two rowed Turkish barley cultivars were used as material in the research. The names, release years, and origins of these cultivars are given in the Table 3.

TABLE 1
Physical and chemical properties of the trial soils.*

Years	Saturation (%)	Total salt (%)	pH	$CaCO_3$ (%)	P_2O_5 (kg ha^{-1})	K_2O (kg ha^{-1})	Organic matter (%)
2014-2015	57.0	0.18	7.77	12.43	4.18	132.3	3.32
2015-2016	73.0	0.37	7.61	3.33	8.08	126.6	1.68

*Soil analysis was performed at the Laboratories of Soil Science Department, Kahramanmaras Sutcu Imam University Turkey.

TABLE 2
The climate values for long term (1950 to 2016) average and 2014 to 2016 in Gumushane Province*

Months	Average temperatures (°C)			Total precipitation (mm)			Relative humidity (%)		
	2014-2015	2015-2016	Long term	2014-2015	2015-2016	Long term	2014-2015	2015-2016	Long term
October	14.4	14.2	13.8	61.4	45.2	34.3	64.6	55.8	54.0
November	7.2	7.6	7.0	51.6	42.3	45.2	64.5	52.4	48.7
December	6.2	-0.6	-1.3	14.2	408	45.7	63.0	64.9	66.3
January	0.8	-0.8	0.0	55.5	36.6	47.8	62.0	61.6	59.9
February	3.3	5.7	4.6	34.4	32.8	33.4	59.5	52.4	54.3
March	7.3	7.3	7.3	67.4	43.8	64.2	55.9	50.9	50.6
April	9.6	14.1	12.0	46.8	60.4	47.2	57.4	40.1	44.6
May	15.9	16.3	16.0	45.3	68.0	95.8	55.1	50.7	50.2
June	20.5	20.7	20.5	40.4	46.8	69.1	60.6	50.7	51.5
July	24.5	23.7	24.1	2.8	12.4	5.8	48.8	43.8	41.4
Total/Mean	10.97	10.82	10.40	419.8	429.1	488.5	59.14	52.33	52.15

*Meteorological data was obtained from the Regional Directorate of Meteorology at Gumushane, Turkey.

TABLE 3
The names, release years, and origins of the cultivars in the research.

Cultivar	Release Year	Origin
Larende	2006	Bahri Dagdas International Agricultural Research Institute (Konya)
Beyşehir-98	1998	Bahri Dagdas International Agricultural Research Institute (Konya)
Konevi-98	1998	Bahri Dagdas International Agricultural Research Institute (Konya)
Karatay-94	1996	Bahri Dagdas International Agricultural Research Institute (Konya)
Fahrettinbey	2004	Blacksea Agricultural Research Institute (Samsun)
Bolayır	2007	Trakya Agricultural Research Institute (Edirne)
Sladoran	1998	Trakya Agricultural Research Institute (Edirne)
Harman	2011	Trakya Agricultural Research Institute (Edirne)
Hasat	2014	Trakya Agricultural Research Institute (Edirne)
İnce-04	2004	Transitional Zone Agricultural Research Institute (Eskişehir)
Çıldır-02	2002	Transitional Zone Agricultural Research Institute (Eskişehir)
Kalaycı-97	1997	Transitional Zone Agricultural Research Institute (Eskişehir)
Bilgi-91	1991	Transitional Zone Agricultural Research Institute (Eskişehir)
Özdemir-2005	2005	Transitional Zone Agricultural Research Institute (Eskişehir)
Ünver	2013	Transitional Zone Agricultural Research Institute (Eskişehir)

Field Experimental Setup and Studied Traits. This research was conducted using randomized block design with three replications. The first sowing was carried out on 22.10.2014 and the second sowing was done on 04.11.2015 using seed sowing machine using 500 seeds m^{-2}, the plot dimensions consisted of 5 m × 1.2 m, and the space between plots was 35 cm. In the trials, nitrogen and phosphorus was applied at the rate of 100 and 60 kg/ha respectively; such that whole of the phosphorus and the half of the nitrogen were applied at the time of sowing. Rest of the nitrogen was applied at the sapling stage. The weeds were removed by hand or by hoeing without use of any herbicides. Each plot consisted of an area of $4m^2$ and an area 0.5 m was left before first and last rows in each plot. The harvesting was done with sickle on 13.07.2015 for the first year and on 16.07.2016 for the second year.

Measurement of agronomic parameters like days to heading (d), days to ripening (d), plant height (cm), spike number per m^2, spike length (cm), grains number per spike, spike yield (g), harvest index (%), grain yield (kg ha^{-1}), thousand grains weight (g), and test weight (kg hl^{-1}) were made following [22]. Other quality parameters like dry matter (%), ash content (%), crude protein content (%), starch ratio (%), ADF (acid detergent fiber, %), NDF (neutral detergent fiber, %), and FAT (oil content, %) were detected by NIT System Infratec 1241 Grain Analyzer (Foss, Hillerod, Denmark).

Statistical Evaluations. The variance analysis of the data obtained from the study was made using the statistical package program JMP 7.0.2 according to the randomized block design with the combined years. The significance level of differences in variation sources was examined by F test with this program. The statistical significance of the differences between the means was determined according to the LSD test. Correlations between the characters were also determined using the same statistical software.

RESULTS AND DISCUSSION

Year combined variance analysis results and mean values for days to heading (DH), days to ripening (DR) and plant height (PH) are given in Table 4. The table, shows significant (p<0.01) differences among cultivars and differences (p<0.01) between years with no interaction between years and cultivars for days to heading. Days to heading remained 141.7 days during 2015-16 growth season that was 2.2 days longer than 2014-15 growth season with 139.5 days to heading. Whereas, the mean days to head for all cultivars remained 140.6 days. The days to heading for cultivars ranged 137.4 to 143 days. Cultivars Bolayır (137.4 days) and Hasat (137.7 days) showed the minimum DH values while Çıldır-02 showed a maximum value (143.0 days) for days to head. The results are in confirmation to the Rahal-Bouziane et al [23], who reported that DH showed significant variations for cultivars in their both years of growth and among cultivars. This study also confirms that each cultivar behaved variably irrespective of the effect of year and showed significant differences among them for DH. DH showed positive significant correlations at two growth seasons with DR, PH, GN (grain number per spike), SY (spike yield), and GY (grain yield), while it was significantly positive correlated with SL (spike length), TGW (thousand grain weight), and SR (starch ratio) during the first season only. This shows plasticity in behaviour of cultivars as affected by the climatic changes. DH was found to have negative significant correlation with ASH (ash content) during the first season (Table 10). Janfrozzadh and Fard [24] found similar correlations with DH that was positively significantly correlated with DR, GY, GN, and PH. Rahal-Bouziane et al. [23] showed that positive significant correlations of DH with PH, SL, TGW, and DR similarly to our study. On the other hand, they reported the negative significant correlation between DH and GN.

TABLE 4
Effects of sowing years (2014-2015 and 2015-2016) on the days to heading, days to ripening and plant height of 15 Turkish barley cultivars cultivars.

Cultivars	Days to heading (days)			Days to ripening (days)			Plant height (cm)		
	2014-2015	2015-2016	Mean	2014-2015	2015-2016	Mean	2014-2015	2015-2016	Mean
Larende	141.3	144.0	142.7 ab[§]	186.0 g-k	196.5 a	191.3 a	103.80	107.30	105.55 bcd
Beyşehir-98	140.7	144.3	142.5 ab	185.7 g-k	194.0 abc	189.8 abc	106.13	111.50	108.82 b
Konevi-98	140.0	145.0	142.5 ab	185.0 i-l	195.7 ab	190.3 ab	100.33	105.87	103.10 de
Karatay-94	140.7	142.0	141.3 abc	185.7 g-k	192.0 cde	188.8 b-e	111.53	114.97	113.25 a
Fahrettinbey	140.7	140.3	140.5 cde	185.7 g-k	189.0 efg	187.3 def	99.73	107.23	103.48 cde
Bolayır	136.3	138.5	137.4 f	181.3 m	185.3 h-k	183.3 h	90.00	96.00	93.00 g
Sladoran	138.3	139.0	138.7 ef	183.3 klm	185.7 g-k	184.5 gh	93.00	92.07	92.54 g
Harman	138.0	140.3	139.2 def	183.0 klm	189.7 def	186.3 fg	100.20	102.70	101.45 ef
Hasat	136.7	138.7	137.7 f	181.7 lm	187.3 f-j	184.5 gh	96.93	100.53	98.73 f
İnce-04	140.0	141.7	140.8 bcd	185.0 i-l	190.0 def	187.5 c-f	103.33	104.33	103.83 cde
Çıldır-02	141.0	145.0	143.0 a	186.0 g-k	193.0 bcd	189.5 a-d	105.40	107.60	106.50 bc
Kalaycı-97	139.7	143.7	141.7 abc	184.7 j-m	190.3 def	187.5 c-f	106.00	106.27	106.14 bcd
Bilgi-91	138.0	140.3	139.2 def	183.0 klm	188.7 e-h	185.8 fg	100.93	102.60	101.77 ef
Özdemir-2005	140.7	142.7	141.7 abc	185.7 g-k	192.0 cde	188.8 b-e	103.13	104.10	103.62 cde
Ünver	140.0	140.7	140.3 cde	185.0 i-l	188.3 f-i	186.7 efg	103.67	105.13	104.40 cde
Mean	139.5 b	141.7 a	140.6	184.5 b	190.5 a	187.5	101.61 b	104.55 a	103.08
CV (%)	1.15			1.09			2.84		
	F value		$LSD_{0.05}$	F value		$LSD_{0.05}$	F value		$LSD_{0.05}$
Year (Y)	47.272**		0.919	87.847**		1.794	7.856*		2.909
Cultivar (C)	7.764**		1.859	7.672**		2.372	20.095**		3.387
Y × C	1.198		NS	2.091*		3.355	0.975		NS

[§] The same letters in a single column are not statistically different using LSD test at 0.05 level of significance.
*, ** significant at probability levels of 0.05 and 0.01, respectively; CV, coefficient of variation; LSD, least significance difference; NS, non significant.

Days to ripening (DR) showed significant (p<0.05) interaction between years and cultivars. Days to ripening also showed significant differences among cultivars (p<0.01) and between years (p<0.01) in terms of days to ripening (Table 4). Accordingly, the second year (190.5 days) DR values were six days longer than the first year (184.5 days). The cultivars showed a range of 183.3 - 191.3 days in terms of DR. The minimum ripening periods was observed for cv. Bolayır (183.3 d), Sladoran (184.5 d), and Hasat (184.5 d). Whereas, the maximum DR were taken by the cv. Larende (191.3 d) and Konevi-98 (190.3 d). When the Y×G interactions were taken it was found that cv. Fahrettinbey, Sladoran and Ünver were in the same group during both growing years (2014-15 and 2015-16) and therefore these cultivars were not affected by year effects. Whereas, the other cultivarscultivars appeared in different groups during two years; so, these cultivars are differently affected by the year. DR was significantly positive correlated with PH, SY, and GY during two years, while it showed significant positive correlation with SL, GN, TGW and SR during the first year (Table 10). Janfrozzadh and Fard [24] observed positive correlations of DR with DH, GY, PH, and GN in agreement to this study. Contrarily, a significant negative correlation was noted between DR and ASH during the first year (Table 10). Rahal-Bouziane et al. [23] reported a positive significant correlation between DR and DH, PH, SL, TGW, and negative significant correlation with GN.

Years and cultivars showed no interaction in terms of plant height PH (Table 4). However, significant differences were noted among cultivars (p<0.01) and between years (p<0.05) in terms of plant height (Table 4). Thus, mean PH value in 2015-16 year (104.55 cm) was longer than 2014-15 year (101.61 cm). Cultivars showed changes between 92.54 cm (cv. Sladoran) - 113.25 cm (cv. Karatay-94) in plant height. Madic et al. [20] reported that plant height was affected by the year conditions (years) and the interaction of cultivar × year in contradiction to this study that shows a non significant interaction for this trait. Mirosavljevic et al. [25] stressed the effects of cultivars and years on the plant height that ranged 97.4 - 105.0 cm for 19 winter malting barley cultivars. PH was significantly positive correlated with SY and TGW during both growth years. It showed significant positive correlation with SR during the first year. PH was significantly positive correlated with SL and GN during the second year. There was a significant negative correlation between PH and ASH (Table 10). Rahal-Bouziane et al. [23] has reported a positive significant correlation of PH with DH, DR, TGW, and SL and negative significant correlation with GN. Similarly, Janfrozzadh and Fard [24] showed positive significant correlations between PH and GY, GN, DH, DR.

Significant differences (p<0.01) were noted among cultivars for induction of number of spikes per m^2 (SN) (Table 5). The minimum SN were noted in cv. Bolayır (367.5) eventhough the maximum SN

were noted in cv. Larende (568.6). No significant differences were noted between years for SN with value of year (488.9 d and 481.4 d during the first and second years respectively. Madic et al. [20] reported that SN was affected by the years, but not affected by the cultivars and cultivar × year interaction. SN showed significant positive correlations with GN, SY, HI (harvest index), GY, and TGW during both growth years in our study (Table 10). Laidig et al. [26] found that SN was negatively significant correlated with GN, TW, and crude protein contents.

TABLE 5
Effects of sowing years (2014-2015 and 2015-2016) on the spike number per m², spike length and grains number per spike of 15 Turkish barley cultivars.

Cultivars	Spike number per m²			Spike length (cm)			Grains number per spike		
	2014-2015	2015-2016	Mean	2014-2015	2015-2016	Mean	2014-2015	2015-2016	Mean
Larende	572.0	565.1	568.6 a	7.98	8.32	8.15 ab	20.89	20.80	20.85 c-f
Beyşehir-98	487.6	493.7	490.7 ef	7.40	7.04	7.22 def	21.83	22.17	22.00 bc
Konevi-98	512.8	529.8	521.3 cd	7.58	7.24	7.41 def	22.06	22.39	22.23 b
Karatay-94	412.2	416.5	414.4 hi	7.94	8.21	8.08 abc	21.33	22.08	21.71 bcd
Fahrettinbey	470.2	472.5	471.4 f	7.68	8.52	8.10 abc	20.19	20.12	20.16 f
Bolayır	363.6	371.5	367.5 j	6.18	6.82	6.50 gh	17.83	18.06	17.95 g
Sladoran	495.7	502.0	498.8 de	5.90	6.15	6.03 h	20.22	19.62	19.92 f
Harman	425.0	449.5	437.2 gh	5.71	6.28	6.00 h	19.66	19.93	19.80 f
Hasat	546.4	530.2	538.3 bc	7.39	7.99	7.69 bcd	20.17	20.52	20.35 f
İnce-04	490.7	502.8	496.8 e	8.31	8.38	8.35 a	21.83	21.47	21.65 b-e
Çıldır-02	499.7	514.4	507.0 de	8.13	8.08	8.11 abc	20.89	20.43	20.66 def
Kalaycı-97	560.4	549.9	555.2 ab	5.94	5.80	5.87 h	19.69	20.55	20.12 f
Bilgi-91	416.8	462.9	439.9 g	6.67	7.23	6.95 efg	18.45	18.34	18.40 g
Özdemir-2005	405.8	416.0	410.9 i	6.64	6.92	6.78 fg	20.11	20.81	20.46 ef
Ünver	561.8	556.2	559.0 ab	7.58	7.45	7.52 cde	24.00	24.61	24.31 a
Mean	481.4	488.9	485.1	7.14 b	7.36 a	7.25	20.61	20.79	20.70
CV (%)		**4.37**			**7.59**			**4.98**	
	F value		**$LSD_{0.05}$**	**F value**		**$LSD_{0.05}$**	**F value**		**$LSD_{0.05}$**
Year (Y)	1.744		NS	13.115*		0.173	0.170		NS
Cultivar (C)	48.762**		24.527	14.783**		0.632	13.696**		1.194
Y × C	0.774		NS	0.703		NS	0.287		NS

§ The same letters in a single column are not statistically different using LSD test at 0.05 level of significance.
*, ** significant at probability levels of 0.05 and 0.01, respectively; CV, coefficient of variation; LSD, least significance difference; NS, non significant.

TABLE 6
Effects of sowing years (2014-2015 and 2015-2016) on spike yield, harvest index and grain yield of 15 Turkish barley cultivars.

Cultivars	Spike yield (g)			Harvest index (%)			Grain yield (kg ha⁻¹)		
	2014-2015	2015-2016	Mean	2014-2015	2015-2016	Mean	2014-2015	2015-2016	Mean
Larende	1.31	1.32	1.32 bcd	36.67	38.17	37.42 ab	6298	6447	6372 b
Beyşehir-98	1.38	1.42	1.40 ab	34.67	35.17	34.92 de	6046	6043	6044 cd
Konevi-98	1.21	1.24	1.23 cde	35.00	35.17	35.09 cde	5763	5895	5829 de
Karatay-94	1.33	1.36	1.35 bc	33.67	34.83	34.25 de	4845	4963	4904 gh
Fahrettinbey	0.96	0.99	0.98 gh	35.33	38.67	37.00 ab	5051	5257	5154 g
Bolayır	0.73	0.79	0.76 i	30.00	33.67	31.84 f	4194	4076	4135 i
Sladoran	0.99	1.02	1.01 g	36.00	38.67	37.34 ab	5540	5556	5548 f
Harman	1.03	0.95	0.99 g	33.33	33.83	33.58 ef	4989	5054	5022 g
Hasat	0.96	0.98	0.97 gh	36.67	37.17	36.92 abc	6011	6000	6006 cd
İnce-04	1.26	1.16	1.21 de	38.33	38.50	38.42 a	5565	5520	5542 f
Çıldır-02	1.30	1.03	1.17 ef	36.67	37.83	37.25 ab	5736	5713	5725 ef
Kalaycı-97	1.20	1.17	1.19 ef	37.00	38.50	37.75 ab	6300	6106	6203 bc
Bilgi-91	0.83	0.87	0.85 hi	34.33	35.00	34.67 de	4820	4961	4890 gh
Özdemir-2005	1.10	1.03	1.07 fg	36.67	37.67	37.17 ab	4709	4711	4710 h
Ünver	1.45	1.53	1.49 a	34.67	37.33	36.00 bcd	6761	6778	6769 a
Mean	1.14	1.12	1.13	35.27	36.68	35.97	5509	5539	5524
CV (%)		**9.74**			**4.56**			**4.23**	
	F value		**$LSD_{0.05}$**	**F value**		**$LSD_{0.05}$**	**F value**		**$LSD_{0.05}$**
Year (Y)	0.096		NS	5.061		NS	0.212		NS
Cultivar (C)	21.334**		0.128	7.553**		1.899	55.997**		270.28
Y × C	0.972		NS	0.731		NS	0.317		NS

§ The same letters in a single column are not statistically different using LSD test at 0.05 level of significance.
*, ** significant at probability levels of 0.05 and 0.01, respectively; CV, coefficient of variation; LSD, least significance difference; NS, non significant.

Statistically significant (p<0.05) differences were noted among cultivars for spike length. Significant differences were also noted between years in terms of spike length. No interaction was noted between cultivars and years for this trait (Table 5). SL value of the second year (7.36 cm) was longer compared to the first year's value (7.14 cm). SL values ranged 5.87 to 8.35 cm among the cultivars used in the study. So, the minimum values were noted for the cv. Kalaycı-97 (5.87 cm), Harman (6.00 cm), and Sladoran (6.03 cm) and the the longest SL values were noted for the cultivars İnce (8.35 cm) and Larende (8.15 cm). During the first year, SL was significantly positive correlated with GN and SY while it was significantly negative correlated with CPC (crude protein content) (Table 10). Contrarily, Rahal-Bouziane et al. [23] noted a negative significant correlation between SL and GN. They also observed positive significant relationships of SL with PH, TGW, DH, and DR.

Grain number per spike (GN) showed significant variations among cultivars (p<0.01) (Table 5). The highest GN value was noted for cv. Unver (25.32) and the lowest GN values were noted for cv. Bolayır (17.95) and Bilgi-91 (18.40). Contrarily, Madic et al. [20] noted significant effect of the interaction of cultivar × years. At both growth years, GN showed significant positive associations with SY, GY, and TGW (Table 10). Janfrozzadh and Fard [24] found positive correlation between GN and GY and noted negative correlation between GN and TGW. At the first year, GN was significantly positive correlated with HI and SR. It was significantly negative correlated with ASH and CPC (Table 10). The findings in this study showed partial differencess with Laidig et al. [26] who reported that numbers of kernels per spike showed negative significant correlations with TGW. They also emphasized the GN's non-significant relations by test weight (TW), crude protein content (CPC) of kernel, and kernel extract ratio that is an indicator of the starch ratio (SR).

Spike yield (SY), which expresses grains weight per spike, showed statistically differences (p<0.01) among the cultivars. No statistical difference was noted between years and no significant interaction was noted between years and cultivars (Table 6). The cv. Ünver (1.49 g) and cv. Beyşehir-98 (1.40 g) had the highest SY; and cv. Bolayır (0.76 g) and cv. Bilgi-91 (0.85 g) had the lowest SY values. SY was significantly positively correlated with GY and TGW during two growth years. It showed significantly positive correlation with HI and SR during the first year. SY showed significantly negative correlations with ASH and CPC (Table 10).

Statistically significant differences (p<0.01) were noted among cultivars for Harvest index (HI) and these values ranged 31.84% in cv. Bolayır to 38.42% in cv. İnce-04 (Table 6). HI showed significantly positive correlation with GY during the growth years. It was significantly negative correlated with CPC during first year. It was significantly positively correlated with DM durinthe second year (Table 10).

Statistically significant (p<0.05) differences were found among cultivars for grain yield (GY) values (Table 6). Contrarily, Petkovski et al. [27] noted significant interaction between years and year × cultivars. The highest GY was noted from cv. Ünver (6769 kg ha^{-1}). The lowest GY was noted from cv. Bolayır (4135 kg ha^{-1}) in this study. In the study of Ben Naceur et al. [28], a high variation was observed among barley genotypes with similar precipitation regime, but they obtained lower yield values ranging from 1943 to 4805 kg ha^{-1}. In contradiction, Laidig et al. [26] reported low variation for cultivars and cultivar × year. However, they emphasised that all variation sources (cultivars, years, and their interaction) were statistically significant for grain yield. Mirosavljevic et al. [25] also showed strong effects of these variation sources on the grain yield. GY showed significantly positive correlations with DH, DR, SN, GN, SY, TGW, and HI during growth years while it was significantly negative associated with FAT during the second year (Table 10). Janfrozzadh and Fard [24] found positive significant correlations between GY and DH, DR, GN, PH. Also, Laidig et al. [26] found positive significant phenotypic correlations between GY and SN and TGW while GY was significantly and negatively correlated with TW and CPC (crude protein content).

Statistically significant differences were noted among cultivars (p<0.01) and between years (p<0.05) for thousand grain weight (TGW). No interaction was noted for the years × cultivars interaction (Table 7). In this way, TGW of the second growth year (2015-16) with 43.80 g was greater than the first year (2014-15) with value of 43.00 g. However, strong Y×G interaction on the TGW has been noted by other researchers [25,29]. The TGW values of the cultivars for mean years ranged 39.77 g - 48.61 g. The highest TGW values were noted from the cv. Ünver (48.61 g) and cv. Larende (47.74 g) while the lowest values were noted from the cv. Harman (39.77 g), İnce-04 (40.78 g), Hasat (40.85 g), and Bolayır (41.02 g). Mirosavljevic et al. [25] noted lower values of 35.8 to 43.5 g. Similar results were noted by [30,29,26]. TGW was significantly positively correlated with PH, SN, GN, SY, and GY during both years while it showed significantly positive correlations with DH and DR during the first year (Table 10). Similar findings related to correlations were noted between TGW and DR, DH, PH, and SL by [23]. Laidig et al. [26] also found positive significant correlation of TGW with GY and SN in similarly to these findings. However, they noted negative significant correlation of TGW with GN, TW and CPC. Some researchers also found negative significant correlations between TGW and GN [24, 26].

TABLE 7
Effects of sowing years (2014-2015 and 2015-2016) on thousand grains weight, test weight and dry matter of 15 Turkish barley cultivars.

Cultivars	Thousand grains weight (g)			Test weight (kg hl^{-1})			Dry matter (%)		
	2014-2015	2015-2016	Mean	2014-2015	2015-2016	Mean	2014-2015	2015-2016	Mean
Larende	46.93	48.55	47.74 a	71.30	69.66	70.48 abc	90.03	90.14	90.09 ab
Beyşehir-98	44.50	45.22	44.86 bc	69.98	69.69	69.84 cd	90.00	89.89	89.95 abc
Konevi-98	42.83	43.86	43.35 cd	70.20	70.82	70.51 abc	90.09	89.99	90.04 ab
Karatay-94	45.57	45.44	45.51 b	70.47	70.77	70.62 abc	89.91	89.97	89.94 abc
Fahrettinbey	41.93	43.93	42.93 d	70.56	71.33	70.95 b	89.92	89.96	89.94 abc
Bolayır	40.40	41.63	41.02 ef	69.82	70.36	70.09 a-d	89.87	89.72	89.80 c
Sladoran	41.47	42.65	42.06 de	69.80	70.10	69.95 bcd	89.96	89.82	89.89 bc
Harman	39.53	40.00	39.77 f	70.82	71.21	71.02 a	90.03	89.73	89.88 bc
Hasat	40.67	41.02	40.85 ef	69.53	70.28	69.91 cd	90.29	89.96	90.13 a
İnce-04	41.17	40.38	40.78 ef	70.42	69.84	70.13 a-d	89.89	89.62	89.76 c
Çıldır-02	42.13	43.82	42.98 d	69.96	70.35	70.16 a-d	89.86	90.03	89.95 abc
Kalaycı-97	45.30	44.37	44.84 bc	70.54	71.28	70.91 ab	90.21	89.93	90.07 ab
Bilgi-91	43.10	43.48	43.29 cd	69.40	69.09	69.25 d	89.98	89.80	89.89 bc
Özdemir-2005	42.03	42.90	42.47 de	70.15	70.53	70.34 abc	89.91	90.00	89.96 abc
Ünver	47.47	49.74	48.61 a	70.85	70.94	70.90 ab	89.74	89.91	89.83 c
Mean	43.00 b	43.80 a	43.40	70.25	70.42	70.34	89.98	89.90	89.94
CV (%)		3.71			1.12			0.21	
	F value		$LSD_{0.05}$	F value		$LSD_{0.05}$	F value		$LSD_{0.05}$
Year (Y)	9.589*		0.512	0.550		NS	3.329		NS
Cultivar (C)	14.961**		0.713	2.110*		0.979	2.030*		0.212
Y × C	0.512		NS	0.866		NS	1.340		NS

§ The same letters in a single column are not statistically different using LSD test at 0.05 level of significance.
*, ** significant at probability levels of 0.05 and 0.01, respectively; CV, coefficient of variation; LSD, least significance difference; NS, non significant.

Significantly differences (p<0.05) were noted among cultivars for test weight (TW); TW ranged 69.25 to 71.02 kg hl^{-1} among cultivars with cultivars Bilgi-91 and Harman respectively (Table 7). These ranges of cultivars for TW were 68.4 to 72.2 kg hl^{-1} in the study of [31]. Mirosavljevic et al. [25] observed the effects of cultivars, years, and their interaction on the test weight which changed from 73.4 to 76.6 kg hl^{-1} for the barley cultivars. TW showed significantly negative correlation with NDF during second year (Table 10). Campbell et al. [32] presented negative strong correlations of TW with ADF and NDF. They also revealed the positive significant correlation between TW and starch ratio (SR). Laidig et al. [26] found weak negative correlation between TW and GY while they reported the weak negative correlations of TW with SN and TGW. Also, they noted moderate positive correlation between TW and CPC.

Statistically significant differences (p<0.05) were noted among cultivars for dry matter (DM). They ranged 89.76% with cv. İnce-04 to 90.13% with cv. Hasat (Table 7). Our data were the range of Campbell et al. [32] who noted a range of 89.31 to 93.97% DM. During both years, DM was significantly positive correlated with ASH and CPC while it was significantly negatively correlated with SR. It showed significantly positive correlation with NDF during the first year (Table 10).

Statistically significant differences (p<0.01) were noted among cultivars for ash content (ASH) (Table 8). The lowest ASH value was noted from cv. Ünver (1.825%) and the highest value was noted from the cv. Hasat (2.237%). During both years, ASH was significantly positive correlated with CPC, ADF, and NDF while it was significantly negatively correlated with SR (Table 10).

As seen in the Table 8, all variation sources (years, cultivars, and Y×G interaction) did not show statistically significant differences for crude protein content (CPC). Nonetheless, the CPC values among cultivars ranged 11.76% to 13.44%. Similar results were found by Przulj et al. [30]. Contrarily, Bertholdsson [8], See et al. [33] and Mirosavljevic et al. [25] recommended < 11.5% protein ratio if the cultivars are meant for malting. The findings in this study showed all cultivars had values above the threshold level. Therefore, these cultivars seem suitable for use as forage in terms of protein. Thus, Mirosavljevic et al. [25] found average grain protein content values of 11.3%. Also, the grain ptotein contents (11.9% as average of malting cultivars) of Fox et al. [31] were similar to these researchers who showed lower CPC values. Significantly negative correlation between CPC and SR was found at both years in our study (Table 10). Laidig et al. [26] evaluated the extract content (EC) instead of SR, and so they found negative moderate significant relation between CPC and EC. They also found very strong correlations between CPC and grain yield. Although the CPC did not have a correlations with grain yield in our study, it showed negative significant correlations with some yield components such as spike length, grain numbers per spike, spike yield, and harvest index.

TABLE 8
Effects of sowing years (2014-2015 and 2015-2016) on ash content, crude protein content and starch ratio of 15 Turkish barley cultivars.

Cultivars	Ash content (%)			Crude protein content (%)			Starch ratio (%)		
	2014-2015	2015-2016	Mean	2014-2015	2015-2016	Mean	2014-2015	2015-2016	Mean
Larende	2.066	2.190	2.128 ab	12.54	13.24	12.89	57.93	55.45	56.69 de
Beyşehir-98	2.076	2.060	2.068 bc	12.36	11.99	12.18	57.38	57.62	57.50 de
Konevi-98	1.980	2.056	2.018 b-e	11.64	12.69	12.17	57.55	58.00	57.78 cde
Karatay-94	2.010	2.106	2.058 bcd	12.10	12.28	12.19	58.84	57.04	57.94 b-e
Fahrettinbey	2.053	2.040	2.047 b-e	12.79	12.85	12.82	57.55	57.71	57.63 cde
Bolayır	2.233	2.073	2.153 ab	13.92	12.72	13.32	55.06	57.97	56.52 e
Sladoran	2.170	2.086	2.128 ab	12.81	11.60	12.21	56.35	58.47	57.41 de
Harman	2.026	1.943	1.985 cde	13.12	12.62	12.87	57.80	59.61	58.71 a-d
Hasat	2.273	2.200	2.237 a	13.03	12.58	12.81	53.03	54.47	53.75 f
İnce-04	1.900	1.940	1.920 def	11.87	12.33	12.10	59.82	60.26	60.04 ab
Çıldır-02	1.883	1.943	1.913 ef	12.56	11.79	12.17	59.70	59.54	59.62 abc
Kalaycı-97	1.983	2.056	2.020 b-e	13.54	13.33	13.44	57.60	58.09	57.85 cde
Bilgi-91	1.830	2.070	1.950 c-f	12.47	13.09	12.78	60.13	56.47	58.30 b-e
Özdemir-2005	1.930	2.156	2.043 b-e	12.15	11.36	11.76	58.99	57.66	58.33 b-e
Ünver	1.810	1.840	1.825 f	11.74	12.15	11.95	60.73	60.64	60.69 a
Mean	2.015	2.051	2.033	12.58	12.44	12.51	57.90	57.93	57.92
CV (%)		6.05			7.56			3.15	
	F value		$LSD_{0.05}$	F value		$LSD_{0.05}$	F value		$LSD_{0.05}$
Year (Y)	0.029		NS	0.157		NS	0.001		NS
Cultivar (C)	5.105**		0.138	1.736		NS	4.819**		2.109
Y × C	1.223		NS	0.823		NS	1.408		NS

§ The same letters in a single column are not statistically different using LSD test at 0.05 level of significance.
*, ** significant at probability levels of 0.05 and 0.01, respectively; CV, coefficient of variation; LSD, least significance difference; NS, non significant.

TABLE 9
Effects of sowing years (2014-2015 and 2015-2016) on ADF, NDF and FAT of 15 Turkish barley cultivars.

Cultivars	ADF (%)			NDF (%)			FAT (%)		
	2014-2015	2015-2016	Mean	2014-2015	2015-2016	Mean	2014-2015	2015-2016	Mean
Larende	7.52	8.36	7.94 ab	22.50	24.53	23.52 a	1.86	1.62	1.74 ef
Beyşehir-98	7.63	7.94	7.79 abc	22.68	23.29	22.99 abc	1.88	1.79	1.84 cde
Konevi-98	7.03	7.82	7.43 b-f	21.58	22.62	22.10 c-f	1.97	2.06	2.02 a
Karatay-94	7.12	6.80	6.96 d-h	22.11	22.58	22.35 b-e	1.77	1.87	1.82 cde
Fahrettinbey	6.59	6.42	6.51 gh	21.03	20.63	20.83 h	1.84	1.96	1.90 abc
Bolayır	6.98	7.08	7.03 c-g	22.08	21.74	21.91 d-g	1.99	2.00	2.00 ab
Sladoran	7.05	7.91	7.48 a-e	22.01	22.61	22.31 b-e	1.62	1.73	1.67 fg
Harman	6.08	6.38	6.23 h	20.86	21.33	21.10 fgh	1.61	1.57	1.59 g
Hasat	8.02	8.52	8.27 a	23.00	23.56	23.28 ab	1.88	1.87	1.88 bcd
İnce-04	7.02	6.29	6.66 fgh	21.70	20.99	21.35 e-h	1.85	1.75	1.80 c-f
Çıldır-02	6.85	7.58	7.22 b-g	21.75	22.69	22.22 cde	1.76	1.76	1.76 def
Kalaycı-97	6.54	6.89	6.71 e-h	22.00	22.47	22.24 cde	1.84	1.80	1.82 cde
Bilgi-91	5.98	7.33	6.66 f-h	20.87	22.81	21.84 d-h	1.88	1.85	1.87 b-e
Özdemir-2005	7.10	8.14	7.62 a-d	21.90	23.47	22.69 a-d	1.78	1.96	1.87 b-e
Ünver	6.36	6.94	6.65 fgh	20.53	21.28	20.91 gh	1.78	1.81	1.79 c-f
Mean	6.92 b	7.36 a	7.14	21.77 b	22.44 a	22.11	1.82	1.83	1.82
CV (%)		9.65			3.99			6.55	
	F value		$LSD_{0.05}$	F value		$LSD_{0.05}$	F value		$LSD_{0.05}$
Year (Y)	13.811*		0.325	20.006*		0.414	0.029		NS
Cultivar (C)	4.451**		0.797	5.188**		1.019	5.105**		0.138
Y × C	0.960		NS	1.205		NS	1.223		NS

§ The same letters in a single column are not statistically different using LSD test at 0.05 level of significance.
*, ** significant at probability levels of 0.05 and 0.01, respectively; CV, coefficient of variation; LSD, least significance difference; NS, non significant.

Statistically significant differences (p<0.01) were noted among cultivars for starch ratio (SR) and SR values changed from 53.75% in cv. Hasat to 60.69% in cv. Ünver (Table 8). Campbell et al. [32] presented lower data that ranged 48.11 to 64.84%, but the mean values among six cultivars used in their study was 58.17%. [31] presented the average SR values (56.9 to 58.8%) for malting barleys. For SR, of both years and the Y×G interaction were not statistically different. This situation has showed that SR was not effected by year in other word years or growth year (Table 8). Campbell et al. [32] presented the medium variance (30.2%) of cultivar × year for

starch ratio of barley. SR showed significantly negative correlation with NDF during both years, while it was significantly negative correlated with ADF during the first year (Table 10). Campbell et al. [32] found medium strong negative correlations SR versus ADF plus NDF. But these correlations were very strong in our study, especially for the first year.

Statistically significant differences were noted among cultivars ($p<0.01$) and between years ($p<0.05$) for ADF (Table 9). ADF value was the highest (7.36%) during 2015-16 and the lowest (6.92%) in 2014-2015 growth year. When the cultivars was evaluated to find differences among cultivars, it was observed that ADF values ranged 6.23% for cv. Harman to 8.27% for cv. Hasat. These findings were higher than the results of some researchers [32, 34, 31]. During both growth years, there were significantly positive correlations between ADF and NDF (Table 10). Similarly, Campbell et al. [32] also emphasise high correlation between ADF and NDF.

Statistically significant differences ($p<0.01$) were noted among cultivars for NDF values. Statistically different ($p<0.05$) NDF values were also noted between years (Table 9). Campbell et al. [32] noted interaction of cultivar × year for ADF and NDF which these traits were similar to each other for the variance of interaction. NDF values was higher in the second growth year (22.44%) than the first year (21.77%). The mean NDF values of the cultivars ranged 20.83% in cv. Fahrettinbey to 23.52% in cv. Larende. However, Campbell et al. [32] noted lower range (13.50% to 16.40%) for NDF among barley cultivars.

Statistically significant differences ($p<0.01$) were noted among cultivars for FAT (Table 9). Campbell et al. [32] emphasized high interaction of cultivar × year with 75.9% variance. FAT content ranged 1.59% (cv. Harman) to 2.02% (cv. Konevi-98) in the study (Table 9). Some researchers have presented close results for this trait [32,35]. Bravi et al. [35] has also stressed the importance of low lipid content of barley grains because of their high capability to malting and friability.

TABLE 10
Correlations among the traits of 15 cultivars of two rowed barley.

Traits	DR	PH	SN	SL	GN	SY	HI	GY	TGW	TW	DM	ASH	CPC	SR	ADF	NDF	FAT
DH[§]	.99**	.64**	.34	.41**	.39**	.58**	.26	.38*	.41**	.27	-.15	-.46**	-.14	.49**	-.17	-.12	-.05
	.83**	.51**	.29	.06	.32**	.40**	.03	.32*	.26	-.02	.29	-.04	.00	.00	.06	.16	.10
DR		.64**	.32	.39**	.38**	.56**	.27	.36*	.40**	.25	-.15	-.46**	-.13	.49**	-.18	-.13	-.06
		.55**	.23	.21	.28	.41**	.02	.31*	.29	.03	.49**	.20	.17	-.22	.12	.30*	-.04
PH			.20	.34	.24	.57**	.20	.27	.48**	.20	-.01	-.30*	-.19	.31*	-.06	-.00	.00
			.13	.40**	.43**	.54**	-.09	.25	.36*	.09	.21	-.09	.06	.01	-.12	.08	-.08
SN				.23	.39**	.42**	.48**	.93**	.44**	.13	.23	-.11	-.12	.04	.10	.03	.04
				.11	.43**	.46**	.41**	.92**	.39**	-.05	.14	-.18	.05	.08	.25	.20	-.28
SL					.52**	.58**	.23	.29	.20	.08	-.22	-.18	-.35*	.18	.18	.08	.19
					.19	.20	.16	.15	.21	-.15	.19	.06	.06	-.18	-.01	.03	.01
GN						.80**	.30*	.54**	.35*	.16	-.24	-.31*	-.38*	.35*	.09	-.06	-.02
						.79**	.06	.60**	.45**	.07	.17	-.22	-.12	.21	-.02	-.03	.02
SY							.32*	.60*	.52**	.23	-.11	-.36*	-.32*	.37*	.11	.08	-.13
							.12	.65**	.60**	.03	.29	-.10	-.04	.12	.04	.04	-.04
HI								.41**	.20	-.03	.11	-.16	-.31*	.16	.22	.16	-.11
								.37*	.09	.13	.31*	.23	.13	-.18	.08	.02	-.03
GY									.50**	.17	.15	-.16	-.13	.11	.06	.02	.03
									.57**	-.02	.28	-.12	.06	.01	.21	.20	-.31*
TGW										.10	-.09	-.18	-.28	.25	.10	.06	.15
										-.04	.27	-.04	-.07	-.06	.17	.24	-.13
TW											.16	-.06	.04	.04	-.07	-.12	-.20
											.07	-.16	.01	.17	-.19	-.30*	.09
DM												.35*	.41**	-.51**	.23	.44**	.02
												.40**	.33*	-.38*	.08	.16	.08
ASH													.36*	-.91**	.58**	.61**	.27
													.44**	-.88**	.30*	.50**	.19
CPC														-.39**	-.27	.12	.05
														-.58**	-.26	.04	-.07
SR															-.55**	-.61**	-.19
															-.26	-.54**	-.03
ADF																.84**	.16
																.81**	.02
NDF																	.11
																	-.24

[§]: In the same line, upper values show the first year (2014-2015) while the below values refer to the second year (2015-2016). *, ** indicate significance at the 0.05 and 0.01 probability levels, respectively. DH: days to heading, DR: days to ripening, PH: plant height, SN: spike number per square meter, SL: spike length, GN: grain number per spike, SY: spike yield, HI: harvest index, GY: grain yield, TGW: thousand grain weight, TW: test weight, DM: dry matter, ASH: ash content, CPC: crude protein content, SR: starch ratio, ADF: acid detergent fiber, NDF: neutral detergent fiber, FAT: oil content.

CONCLUSION

Statistically significant differences were observed among the cultivars for all evaluated traits except CPC. This evidence will play an important role in the proper use of the cultivars in barley malting or feed technology. What is more gratifying is that characteristics excluding DR are unaffected by cultivar × year interaction. This means that cultivars will remain stable in the face of changing year conditions. This is an important technological feature, as these features must not be affected by the year too much. The correlation between technological characteristics and yield components, for example, the significant positive relationships of SR with GN and SY are important in terms of grain yield and malt technology. In the study, SR had strong negative correlation with CPC. It was reconfirmed that low protein high starch-containing cultivars are more important in the malt industry.

ACKNOWLEDGEMENTS

We would like to thank Prof. Dr. Khalid Mahmood Khawar for his supports in the revising the English.

REFERENCES

[1] Badr, A., Muller, K., Schafer-Pregl, R., El Rabey, H., Effgen, S. (2000) On the origin and domestication history or barley (*Hordeum vulgare*). Molecular Biology and Evolution. 17, 499-510.

[2] FAO (2016) Crops. The Food and Agriculture Organization of the United Nations. http://www.fao.org/faostat/en/#data/QC, (Accessed September 03, 2018).

[3] Newman, C.W., Newman, R.K. (2006) A brief history of barley foods. Cereal Foods World. 51, 4-7.

[4] Behall, K.M., Scholfield, D.J., Hallfrisch, J. (2004) Diets containing barley significantly reduce lipids in mildly hypercholesterolemic men and women. American Journal of Clinical Nutrition. 80, 1185-1193.

[5] Cavallero, A., Empilli, S., Brighenti, F., Stanco., A.M. (2002) High (1 / 3, 1 / 4)- β-glucan barley fractions in bread making and their effects on human glucemic response. Journal of Cereal Science. 36, 59-66.

[6] Qureshi, A.A., Qureshi, N., Wright, J.J.K., Shen, Z., Kramer, G. (1991) Lowering of serum cholesterol in hypercholesterolemic humans by tocotrienols (palmvitee). American Journal of Clinical Nutrition. 53, 1021-1026.

[7] Lazaridou, A., Biliaderis, C.G. (2007) Molecular aspects of cereal b-glucan functionality: physical properties, technological applications and physiological effects. Journal of Cereal Science. 46, 101-118.

[8] Bertholdsson, N.O. (1999) Characterization of malting barley cultivars with more or less stable grain content under varying environmental conditions. European Journal of Agronomy. 10(1), 1-8.

[9] Eagles, H.A., Bedggood, A.G., Panozzo, J.F., Martin, P.J. (1995) Cultivar and environmental effects on malting quality in barley. Australian Journal of Agricultural Research. 46, 831-844.

[10] Birch, C.J., Fukai, S., Broad, I.J. (1997) Estimation of responses of yield and grain protein concentration of malting barley to nitrogen fertilizer using plant nitrogen uptake. Australian Journal of Agricultural Research. 48, 635-648.

[11] Savin, R.S., Nicolas, M.E. (1996) Effects of short periods of drought and high temperature on grain growth and starch accumulation of two malting barley cultivars. Australian Journal of Plant Physiology. 23, 201-210.

[12] Araus, J.L., Slafer, G.A., Royo, C., Serret, M.D. (2008) Breeding for yield potential and stress adaptation in cereals. Critical Reviews in Plant Science. 27, 377-412.

[13] Peltonen-Sainio, P., Jauhiainen, L., Laurila, I.P. (2009) Cereal yield trends in northern European conditions: changes in yield potential and its realisation. Field Crops Research. 110, 85-90.

[14] Lillemo, M., Reitan, L., Bjornstad, C. (2010) Increasing impact of plant breeding on barley yields in central Norway from 1946 to 2008. Plant Breeding. 129, 484-490.

[15] Abeledo, L.G., Calderini, D.F., Slafer, G.A. (2008) Nitrogen economy in old and modern malting barleys. Field Crops Research. 106, 171-178.

[16] Mladenov, N., Hristov, N., Kondic-Spika, A., Djuric, V., Jevtic, R., Mladenov, V. (2011) Breeding progress in grain yield of winter wheat cultivars grown at different nitrogen levels in semiarid conditions. Breeding Science. 61(3), 260-268.

[17] Mirosavljevic, M., Momcilovic, V., Przulj, N., Hristov, N., Acin, V. (2016) The variation of agronomic traits associated with breeding progress in winter barley cultivars. Zemdirbyste-Agriculture. 103(3), 267-272.

[18] Baumer, M., Hartl, L., Cais, R. (2004) Yield progress for malting barley. Getreide Magazin. 9, 158-163 (in German).

[19] Kleinknecht, K., Möhring, J., Laidig, F., Meyer, U., Piepho, H.P. (2016) A simulation-based approach for evaluating the efficiency of multienvironment trial designs. Crop Science. 56, 2237-2250.

[20] Madic, M., Paunovic, A.S., Knezevic, D., Zecevic, V. (2009) Grain yield and yield components of two-row winter barley cultivars and lines. Acta Agriculturae Serbica. 14(27), 17-22.
[21] Olesen, J.E., Trnka, M., Kersebaum, K.C., Skjelvag, A.O., Seguin, B. (2011) Impacts and adaptation of European crop production systems to climate change. European Journal of Agronomy. 34, 96-112.
[22] Bell, M.A., Fischer, R.A. (1994) Guide to Plant and Crop Sampling: Measurements and Observations for Agronomic and Physiological Research in Small Grain Cereals. Wheat Special Report No:32. CIMMYT, Mexico.
[23] Rahal-Bouziane, H., Alane, F., Abdelguerfi, A. (2015) Forage quality, forage dry matter yield, grain protein and agronomic traits of traditional barley genotypes (*Hordeum vulgare* L.) from rural areas in Algeria. Livestock Research for Rural Development. 27(9), 182.
[24] Janfrozzadh, N. and Fard, A.N. (2014) Investigation of late- year drought stress effects on ecophysiological traits and grain yield in barley lines using different statistical methods. International Journal of Biosciences. 5(1), 339-344.
[25] Mirosavljevic, M., Przulj, N., Momcilovic, V., Acin, V., Jockovic, B. (2015) Relationship between grain yield and agronomic traits in winter barley. Ratarstvo i povrtarstvo. 52(2), 74-79.
[26] Laidig, F., Piepho, H.P., Rentel, D., Drobek, T., Meyer, U. (2017) Breeding progress, genotypic and environmental variation and correlation of quality traits in malting barley in German official variety trials between 1983 and 2015. Theoritical Applied Genetics. 130, 2411-2429.
[27] Petkovski, N., Mihajlov, L., Ruzdik, N.M. (2018) Genetic and environmental effect on the grain yield of spring barley cultivars cultivated in the Republic of Macedonia. Journal of Agriculture and Plant Sciences. 16(1), 97-102.
[28] Ben Naceur, A., Cheikh-M'hamed, H., Abdelly, C., Ben Naceur, M. (2018) Screening of North African barley genotypes for drought tolerance based on yields using tolerance indices under water deficit conditions. Turkish Journal of Field Crops. 23(2), 135-145.
[29] Dekic, V., Popovic, V., Brankovic, S., Terzic, D., Duric, N. (2017) Grain yield and yield components of winter barley. Agriculture and Forestry. 63(1), 179-185.
[30] Przulj, N., Momcilovic, V., Simic, J., Mirosavljevic, M. (2014) Effect of growing year and variety on quality of spring two-rowed barley. Genetika. 46(1), 59-73.
[31] Fox, G., Kelly, A., Bowman, J., Inkerman, A., Poulsen, D., Henry, R. (2009) Is malting barley better feed for cattle than feed barley? Journal of the Institute of Breewing. 115(2), 95-104.
[32] Campbell, L.D., Boila, R.J., Stothers, S.C. (1995) Variation in the chemical composition and test weight of barley and wheat grain grown at selected locations throughout Manitoba. Canadian Journal of Animal Science. 75(2), 239-246.
[33] See, D., Kanazin, V., Kephart, K., Blake, T. (2002) Mapping genes controlling variation in barley grain protein concentration. Crop Science. 42, 680-685.
[34] Grove, A.V., Pas, J.H., Pas, C.W.H. (2003) Chemical composition and ruminal fermentability of barley grain, hulls, and straw as affacted by planting date, irrigation level, and variety. The Professional Animal Scientist. 19, 273-280.
[35] Bravi, E., Marconi, O., Perretti, G., Fantozzi, P. (2012) Influence of barley variety and malting process on lipid content of malt. Food Chemistry. 135(3), 1112-1117.

Received: **11.10.2019**
Accepted: **26.01.2020**

CORRESPONDING AUTHOR

Bilge Bahar
Gumushane University,
Faculty of Engineering and Natural Sciences,
Department of Food Engineering,
29100, Gumushane – Turkey

e-mail: bilgebahar@gmail.com

© by PSP Volume 29 – No. 04A/2020 pages 2908-2916 Fresenius Environmental Bulletin

RISK ASSESSMENT OF TORRENTIAL RAIN AND FLOOD DISASTER IN DATONG RIVER BASIN BASED ON FLOOD AREA MODEL

Haitao Wang[1,2], Shuwen Zhang[3,*], Xuedong Li[2], Bin Wang[4]

[1]College of Earth Sciences, Jilin University, Changchun130061, China
[2]College of Geographic Sciences, Changchun Normal University, Changchun130032, China
[3]Northeast Institute of Geography and Agroecology, Chinese Academy of Sciences, Changchun 130102, China
[4]College of Water Conservancy and Civil Engineering, Northeast Agricultural University, Harbin 150030, China

ABSTRACT

Using all national meteorological stations and regional automatic stations in the basin, data such as hourly precipitation, process precipitation and precipitation area forecast, digital elevation model, land use, soil type and field disaster investigation, etc. Based on the flood area model, the flood inundation simulation and effect test were carried out on the historical heavy rainfall period in the Datong River basin, which occurred at 20: 00 hours on July 5, 2013, at 20: 00 hours on July 5, 2017, and at 20: 00 o'clock in Datong River Basin. The simulation results show that the water level in the middle and upper reaches of the Datong River basin rises obviously, the water level in most areas exceeds 1 m, the water level in some tributaries is more than 3 m, and the water level in some areas of Zhuyang Township, Youhua Township and Qiaomu Township is more than 6 m. The results of disaster investigation show that the simulated values of flood flood area and flood area are in good agreement with the actual values, which indicates that the floodarea model has better simulation effect in Datong River basin. It can be used for risk assessment and early warning of torrential rain and flood disaster.

KEYWORDS:
Risk assessment, torrential rain, flood disaster, Datong River, flood area model

INTRODUCTION

With the frequent occurrence of natural disasters in China, the flood disaster is one of the most serious disasters and the largest number of deaths due to the disaster [1]. With the rapid development of social economy, the social impact and economic losses caused by the flood disaster are increasing. The economic losses caused by flood disasters account for more than 60% of the total natural disaster losses every year [2]. Therefore, it is of great significance to strengthen the risk management of rainstorm, flood and meteorological disasters for the construction of social economy and the safety of people's lives and property .In order to cooperate with the state in carrying out the management of small and medium-sized rivers and the prevention and control of mountain torrents, the China Meteorological Administration has started the business of early warning services for the meteorological risks of small and medium rivers, floods and mountain torrents, which are caused by heavy rain throughout the country [3, 4]. Torrential rain flood disaster risk assessment technology has become the technical support of this business. In recent years, rainstorm flood risk assessment techniques have developed rapidly [5, 6], such as the experience of water environment management in the Rhine River basin [7] and the dynamic identification of flood risk in flood storage area [8]. With the wide application of GIs technology, it has become an important technical means of storm flood risk assessment.

By using the digital elevation model and various iterative algorithms, the simulation model of flood area under given water depth [9] and the simulation of flood and flood inundation under the condition of flood depth are realized by means of digital elevation model and various iterative algorithms. At present, the flood flooding simulation research combined with GIs and hydrodynamic model has been popularized and applied widely by using flood area model to compile basin risk map. It established a two-dimensional hydrodynamic flood dynamic routing model to simulate the flood submergence range and water depth in the flood diversion area with different Hong Fang discharge in the Yangtze River Basin [10]. The flood area model was used to study the flood risk rainfall assessment of mountain torrents and so on. These studies are of great significance to the risk assessment of rainstorm and flood disasters, but most of them focus on flood simulation caused by overtopping of reservoirs or river networks. However, the research on regional flooding caused by heavy precipitation in one of the three scenarios of flood flooding is rare.

In this paper, on the GIs platform, flood area model is used to simulate the torrential rain and waterlogging caused by a typical heavy precipitation in Datong River basin, and the simulation effect of the model is tested with the disaster data. It is expected to provide technical support for the dynamic assessment of rainstorm flood and waterlogging disaster risk for real time meteorological disaster prevention and mitigation.

The flood area model has three submergence scenarios: overtopping, outburst and storm rain, but the actual flood and flood scenarios are varied and superimposed, often overtopping the river network and superposing the rainstorm, superposing the outburst of the riverbank reservoir and the storm rain. Even the three scenarios overlap with each other, and the process of inundation is very complex, which needs further study.

As one of the most frequent mountain torrents in the world, mountain torrents in China have caused great casualties and loss of wealth. Ecosystem has important disaster reduction service function, but the quantitative relationship between ecosystem and mountain flood disaster and the value of ecosystem disaster reduction service are still lack of deep research. In this study, the upstream of Datong River was chosen as the study area, and the basic unit small watershed of flash flood outbreak was used as the individual member of the cohort study using the retrospective cohort study method in public health. The characteristics of temporal and spatial distribution of mountain torrents in small mountain basins were investigated, the key influencing factors of mountain torrents were identified and screened, and the quantitative relationship between ecological characteristics and mountain torrents disaster risk was established. This paper analyses the effective mode of ecological disaster reduction and rehabilitation, analyses the cost and benefit of ecosystem disaster reduction, and estimates the service value of mountain ecosystem mitigation of mountain flood disaster.

The prevention and control of mountain torrents must adopt engineering technology, ecological restoration, early warning and forecast, planning and management, etc. Only a single measure cannot effectively eliminate or mitigate the formation and harm of mountain torrents. Scientific research and ecological protection practices at home and abroad have fully proved that ecosystems have important disaster reduction service functions and have been transformed into a long-term natural transformation. Good ecological environment plays an irreplaceable role in dealing with natural disasters. Human destruction of ecological environment will induce natural disasters, increase their occurrence frequency, quantity and harmful consequences [11, 12]. If ecosystem functions are destroyed, degraded or even lost, it is difficult for even good engineering measures to play their proper role in disaster prevention and control. Therefore, taking comprehensive ecological measures to enhance ecosystem stability and ecological function is an important measure to strengthen the resilience of mountain flood geological hazards.

MATERIALS AND METHODS

Analysis of ecosystem characteristics and dynamic changes. The occurrence of mountain torrents is closely related to the processes of terrestrial hydrology such as atmospheric precipitation, surface runoff, evaporation and transpiration, infiltration and underground runoff, etc. It is necessary to have basic precipitation conditions and topographic and geomorphological conditions. The basic conditions for the occurrence of these mountain torrents are also the basic elements of the loss of water kings. In the field of water protection, a large number of studies on forest hydrology, root fixation, soil conservation w and ecological restoration have been carried out at home and abroad. The results show that the ecosystem is responsible for transpiration, rainfall interception, and so on from the local microcosmic scale.

The characteristics and dynamic changes of the ecosystem. The regulation and influence of water gallbladder storage, slow runoff, improvement of soil, root system fixation and erosion mitigation can explain to some extent the role of ecosystems in regulating the occurrence of mountain floods. The qualitative analysis of ecosystem in theory can reduce the risk of disaster factors, increase the stability of disaster environment, and play a role in mitigating mountain torrents. However, the mechanism of ecological control of mountain torrents in the aspect of ecological hydrology and root fixation is mostly studied on a local scale about the impact of ecosystem on some link or aspect of terrestrial hydrological cycle. It is difficult to elucidate the relationship between the ecosystem and the occurrence of mountain torrents in general, and it is impossible to give a quantitative answer to the extent to which the ecosystem is effective in reducing mountain torrents on a mesa-macro scale. There is no mathematical model which can explain the relationship between ecosystem system and mountain torrents, and the law of ecological disaster reduction cannot be quantitatively evaluated on the basis of accurate scientific theory. All these problems are the scientific problems that need to be solved in the study of the relationship between mountain torrents and ecosystems. We must fundamentally clear the regularity of mountain torrents in order to provide the necessary basis for mountain torrents prevention and mitigation as shown in Figure 1.

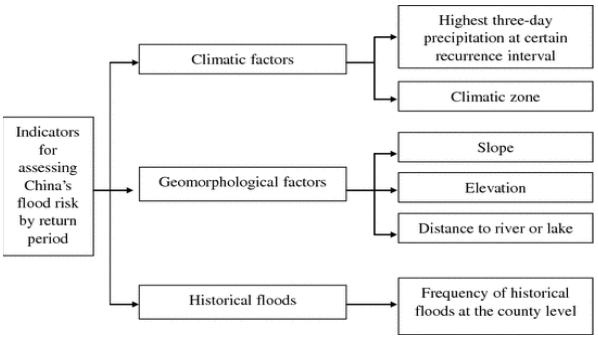

FIGURE 1
Classification of mountain torrents and natural disasters

The difficulties in the study of the relationship between ecosystem and natural disaster are that there are many induced factors and effects of natural disasters, the formation of mountain torrents and the geological topography, ecological persistence and rainfall conditions of small watersheds. All kinds of complex factors, such as social and economic, are closely related, and the overlapping factors are intertwined, which makes the study of the quantitative relationship between ecology and disasters difficult. First of all, the research data cover many fields. According to the data types in different fields, the data characteristics vary greatly, so it is difficult to collect, collate and analyse the data. Secondly, because the spatial scale of the natural disaster process is generally large, it is difficult for conventional laboratory analysis techniques to carry out simulation experiments on natural disasters at mesa-macro scale. Thirdly, these induced factors are often subject to great uncertainty, such as extreme weather conditions, special geological background, etc. To some extent, this also leads to the uncertainty of the scale and extent of natural disasters, and the role of ecosystems in them is even more difficult to clarify. The scientific research of natural disasters has the characteristics of interdisciplinary, comprehensive and systematic. In order to solve the difficulties existing in the research on y, meteorology, geology, ecology, disaster science, hydrology is often required from (1) to (2).

$$I(x,y) = L(x,y) \times R(x,y) \quad (1)$$

$$\lg[R(x,y)] = \lg[I(x,y)] - \lg[L(x,y)] \quad (2)$$

Ecosystem is the only factor that human beings can adjust and improve in the course of mountain flood disaster formation, besides engineering measures, the quantitative affinity between ecological system and mountain flood disaster is studied, and the ability of ecosystem disaster reduction is evaluated. It is of great significance to estimate the service value of disaster reduction in opportunistic systems, and is gradually becoming the focus of international attention. However, because of the numerous factors affecting mountain torrent disasters, the research field spans over ecology and disaster science. Hydrology, meteorology, and so on, there are many technical difficulties and bottlenecks in the field of research. This research provides an analytical idea and method for related research by means of retrospective cohort research. It helps to occupy a favourable position in the emerging ecological disaster reduction cross scientific field as shown in Figure 2.

According to the results of the model analysis, the difference of disaster reduction frequency among different types of forests, grasslands, wetlands and thickets was compared according to the results of the model analysis, according to the types of primary ecosystems, according to the standard regression coefficient. The relative risk is used to answer the quantitative relationship between different ecosystem types and disaster frequency, and the ecological characteristic parameters were adjusted according to the quantitative relationship model. Using urban and cultivated land as the representation of human construction activities, the paper analyses the increasing value of urban and cultivated land construction on the frequency of mountain torrents disaster, and answers quantitatively the influence of human construction activities. Based on the analysis of natural ecosystem and artificial ecosystem ecological land as the research index, the disaster reduction ability of different ecological land proportion is calculated.

Transformation characteristics among different types of ecosystem structural changes. According to forest ecosystem, forest proportion is divided into 20% and w0-20% as reference group. By comparing the relative risk degree among different groups, we can answer the difference of disaster reduction ability among different forest proportion. According to the quantitative relationship model of different forest types and forest ages, the ecological characteristic parameters were adjusted, and broadleaved forest, coniferous forest mixed forest, economic forest or young forest, middle age forest, near mature forest were added, respectively. The optimum ecological disaster reduction model was determined by comparing the difference of disaster reduction frequency between different forest types and forest age.

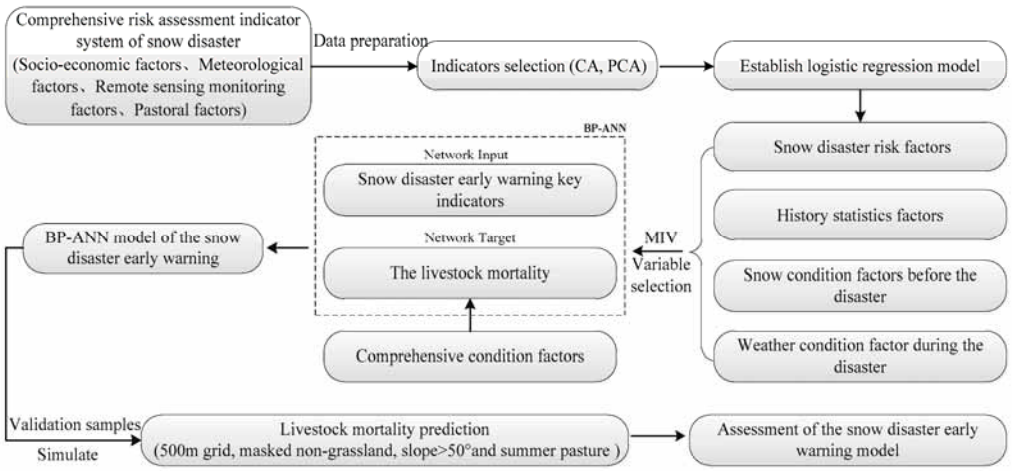

FIGURE 2
Classification of assessment of natural disasters

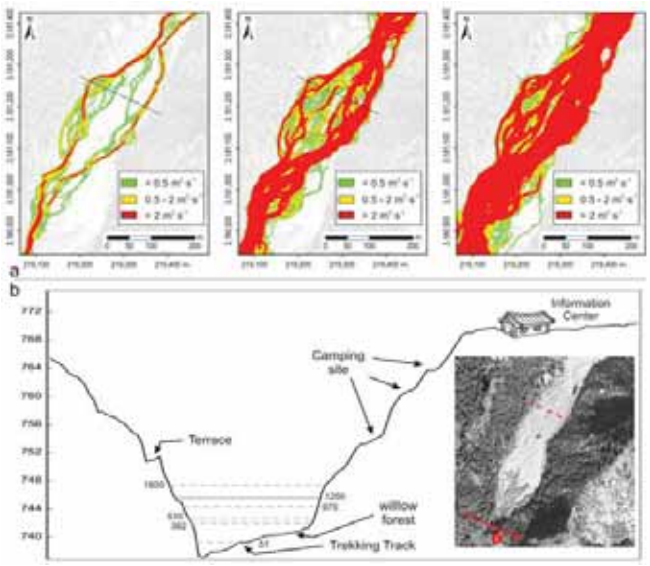

FIGURE 3
Optimal ecological scenario ecosystem type diagram

The formation of mountain torrents is closely related to various complicated factors, such as geology and geomorphology, precipitation conditions, ecological characteristics, social economy and so on, and these factors are intertwined with each other. The ecosystem has complex mitigation and control roles in the formation of mountain torrents: on the one hand, through interception and mitigation of rainfall erosion of the surface, through root fixation, through root holes to increase infiltration and storage, conservation of water, Regulation of runoff; on the other hand, it is possible that flash floods may occur as a result of the accumulation of ±soil and litter; in addition, during long periods of vegetation cover, Acidified secretions w and microbes have biological weathering effect on rock structure, which increases the risk of mountain flood disaster. For the whole ecosystem, how to integrate the positive and negative effects on the whole is a problem that must be solved as shown in Figure 3.

After the identification of ecological factors, the selection of ecological factors and the quantification of disaster indicators has become an urgent problem to be solved. First, because the indicators of mountain torrents are not unique, the frequency of disasters, threats to the population, destruction of houses, direct losses and so on can be used as indicators of mountain torrents. The effect of ecosystem on mountain flood disaster is not generalizable, and the function forms may not be the same for different ecosystem conditions. There should be a wide range in the regulation of mountain flood disaster by ecosystem. When the condition of ecosystem is worse than or has not reached some specified index,

the regulation of mountain flood disaster by ecosystem has no effect or little effect. When the ecosystem is better than or reaches certain indicators, the ecosystem regulation will gradually increase with the improvement of the ecosystem condition, and when the ecosystem is better than or exceed some specific indicators, Ecosystem regulation no longer changes with the improvement of ecosystem conditions.

The occurrence of mountain torrents is related to geological and geomorphology, precipitation conditions, social economic and ecological characteristics, etc. In order to study the ecological characteristics clearly, the remaining h persons must be clearly identified before they can be studied. The ecological characteristics are classified by ecosystem type and vegetation index, so ecosystem type and vegetation index are selected to analyse the ecological characteristics. For other geological and geomorphological, precipitation conditions, socio-economic use of the following steps to identify. First, for the impact factors that need to be analysed, first of all, according to the correlation of the data, the factors with greater relevance are excluded; For the same data source to obtain, or to use similar methods to obtain factors as far as possible to analyse whether the factors are independent and independent, so as to determine the factors. Secondly, the others are identified by projection pursuit method and grey correlation method. Finally, the identification table of the impact factors of mountain torrents is formed, which can be used to quantitatively analyse the ecosystem and the frequency of mountain torrents.

Dynamic clustering is an exploratory data-driven method t78 driven directly by sample data. The main idea is to project high-dimensional data samples into low-dimensional space through some sort of juxtaposition. The objective function (projection index function) is used to measure the possibility of projecting to expose a certain classification structure, and to find the projection value that makes the objective function optimal (that is, it can reflect the high-dimensional data structure or feature). Then according to the projection value, the projection pursuit model with different influence factors is mainly implemented by mat lab, which has a mature algorithm, and only need to preprocess the data.

The concrete realization way of projection pursuit clustering idea is to make the projection characteristic value of the whole sample sequence possible. When it can be dispersed, the projection characteristic values of similar samples are brought together as much as possible and the structure of the objective function is as follows: The key to the realization of this idea is that cluster analysis is based on the data characteristics of the samples to be evaluated. Classification and evaluation, so that the objective function can be constructed by using projection feature values. Based on the above - mentioned dynamic clustering results. The objective function can be used to measure the degree of dispersion of the characteristic values of the whole sample and the aggregation of the projection characteristic values of the samples in the class. This step is mainly realized by dynamic clustering method as shown in Figure 4.

RESULTS AND DISCUSSION

Ecosystem dynamic change effect. Grey correlation analysis between the recognition of different factors related to the research of the relationship between the W and the people pressure because of the complexity of geographic phenomena and issues the understanding limitation, the relationship between many factors is gay, difficult to w with correlation coefficients more accurately measure the correlation degree of the pressure objective is small, the defect of grey relational analysis two. can just overcome statistical analysis in the disaster pressure is widely applied in the fields of science, the main use of correlation factor among the factors in the identification of W and T85 - 88l disaster to determine the effect of grey relational analysis pressure mainly use mat lab matrix to achieve, also has a relatively mature algorithm, only need to use the data of pretension treatment can be.

Analysis on dynamic change of ecosystem composition. A retrospective cohort study was used. Therefore, the corresponding quantitative reliability relation model is constructed by using the generalized linear regression model, which is the most commonly used generalized linear regression model based on the retrospective cohort, to add the connection function to the classical linear regression model. Data used to solve discontinuous variables as dependent variables. The most commonly used generalized linear regression models are Poisson regression, negative binomial regression, zero expansion Poisson regression and zero expansion negative binomial regression. Among the four models. Poisson regression model is the most commonly used model, but its use premise is that the distribution of dependent variables conforms to the premise that the variance is equal to the expectation, and the negative binomial regression is to solve the problem that the variance of the variable is greater than the expectation. Therefore, the effect of zero expansion Poisson regression and zero expansion negative binomial regression in fitting such data is better than that of Poisson regression. The fitting effect of zero expansion models is better than that of 1 wk.

The main solution to the multiplex problem is to delete relative non-important independent variables, to add sample size data, to use prior

knowledge to determine the causes of multiple colinearity, and to change the form of expression between independent variables. In addition, there are stepwise regression, Yin regression, principal component regression and other methods. These solutions have their own advantages and disadvantages. This study hopes to obtain the relationship between different ecological types and the results of mountain torrents. We don't want to process the data by culling the factors, so we construct new factors for multiple collinear factors, and use the new factors to be used in the regression model. The ratio of structure cultivated land to forest and the proportion of town to forest are used to solve the multiple with w, and the quantitative relationship analysis scheme is used to solve the problem.

The research scheme mainly tries to solve h scientific problems, that is, the difference of disaster reduction ability of different ecosystem types, different forest types, and forest age and contribution rate of human construction activities to mountain flood disaster. In view of the first problem, design model one, use forest, shrub, grassland, wetland as the research factor, analyse the difference of disaster reduction ability of different types of natural ecosystem. Using ecological land as a research factor to analyse the frequency of mountain flood disaster with the change of ecological land proportion: to solve the second problem, design model orchid and model four, use broad-leaved forest, coniferous forest, mixed forest, the second problem, design model orchid and model four, use broad-leaved forest, coniferous forest, mixed forest, The proportion of economic forest is divided into young forest, middle age forest, near mature forest, analysis of different forest types, different forest age forest disaster reduction capacity difference; in view of the h problem, design model 5, 6, Mao, for the town. The added value of mountain torrents is analysed by human construction activities, such as the proportion of cultivated land. Using the model design, using the above quantitative relationship model, the relationship between different research factors and the frequency of mountain torrents is studied as shown in Figure 5.

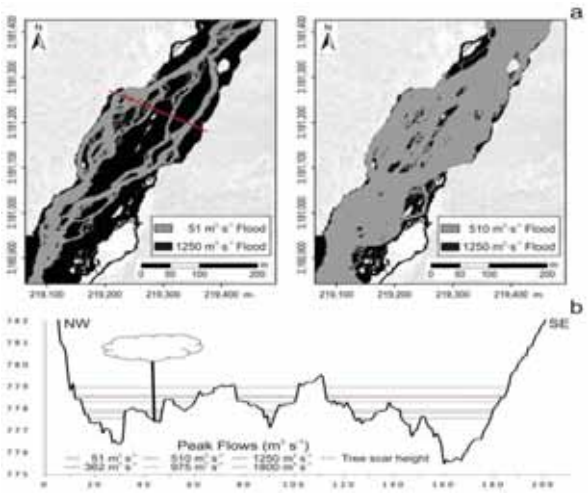

FIGURE 4
Optimal grey ecosystem type diagram

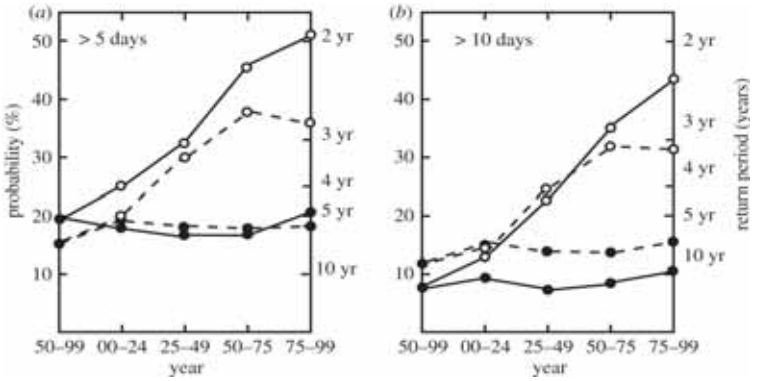

FIGURE 5
Broken line map of different ages

This study provides ecosystem type change data for calculating ecosystem disaster reduction service value and constructs ecological optimal scenarios. The optimal ecological scenarios are analysed according to the characteristics of ecosystem types, assuming that after the implementation of the natural forest protection, conversion of farmland to forests and ecological closure in the study area. Ecological disaster reduction can achieve the most ideal state of ecological optimal scenario, the setting of the optimal ecological scenario mainly for different ecosystem types of conversion settings: conversion of cropland to forest and grass project. The gentle slope cultivated land on the slope of 6 degrees w in the research area was converted into forest, the steep slope farmland on the slope of 25 degrees w was transformed into grassland and shrub, and the mining land was converted into shrub and grassland by mining restoration engineering. Some coniferous forests were converted into broad-leaved forests and coniferous irrigation into broad-leaved thickets by ecological fencing and natural forest protection engineering.

In the last ten years, the natural ecosystem in the study area has not changed much, but the artificial ecosystem has changed greatly, which is mainly reflected in the process of rapid urbanization. Among them, the change area is mainly concentrated in the flat plain area and the mountainous river flow area; the change type is mainly from forest to urban land and to cultivated land. In addition, through the comprehensive ecosystem dynamics analysis, the strong variation of the study area coincides with the spatial distribution of mountain torrents disaster data, so it is considered that the regional human activities have intensified in the last ten years, with the population density, traffic network density, and local development of the study area, the intensity of economic activity and comprehensive development are increasing continuously, therefore, the risk of regional mountain flood disaster increases obviously.

Firstly, the qualitative data, that is, geological type, ±soil type, and different geological type and ±soil type are analysed, and the correlation between different types of area and disaster frequency is analysed. The frequency of mountain torrents in this study area is independent of geological type and soil type. Secondly, according to the correlation analysis of the data in the skilful identification factor table, it is found that the relative height difference and the confluence path are highly correlated, the basin circumference, the watershed area and the number of shape systems are highly correlated, and the correlation between the relative height difference and the confluence path is relatively high. The mean rainfall intensity of maximum precipitation and the average precipitation in multiyear period are highly correlated, and the impact of rainfall on mountain flood disaster is greater than that of daily precipitation. In addition, there are five kinds of data in the mean rainfall intensity data of hominine for 30 minutes and for 3 hours, respectively. According to the recommended data of mountain torrents prevention and control in Ministry of Water Resources, the maximum mean value of 6 h precipitation was determined.

Landscape pattern change of ecosystem. In order to calculate the benefit of ecosystem disaster reduction, the frequency of ecosystem disaster reduction should be determined first. Because of the great difference of ecosystem types in different research areas in China, the proportion of different ecosystem types is very different. Therefore, it is not accurate to use different ecosystem types for analysis. Based on the results of the above quantitative studies, it is found that the types of natural ecosystems are capable of disaster reduction, while artificial ecosystems increase the frequency of mountain torrents. Therefore, the relationship model of ecological land and torrent frequency is used to analyse the relationship between ecological system and mountain torrent disaster, and the frequency of mountain flood disaster is obtained at different levels. The frequency of mountain torrents in the past 30 years is 1, the frequency of mountain torrents in the present situation is 0.963 times of that in the past 30 years, and the frequency of mountain torrents in the optimal ecological scenarios is 0.814 times of that in the past 30 years. The frequency of mountain torrents on the national average is 1.343 times that of the past 30 years.

In order to estimate the value of ecosystem disaster reduction service, the basic value should be determined first. In this study, the national average level is chosen as the reference value and the disaster loss is taken as the value of ecosystem disaster reduction service. In this study, the difference between the present value and the national average level of disaster loss is used as the service value of ecological disaster reduction in the study area. Using the difference between the optimal ecological scenario and the national average disaster loss as the service value of maximum biographies and disaster reduction in the research area, the maximum service value of ecological disaster reduction is reduced to the benefit of ecosystem disaster reduction construction. By using the results of frequency analysis of the mountain torrents mentioned above and using the alternative market method to calculate the benefits of ecosystem disaster reduction, the effect of the consumer price index (chi) on the disaster reduction of the ecosystem should be taken into account in the calculation process. The reduction of disaster loss in ecosystem is regarded as the benefit of disaster reduction. It is necessary to calculate the cost of ecosystem disaster reduction from the two aspects of the difference of production cost and the investment of ecological construction in

order to make the ecosystem reach the optimal ecological situation through ecological construction as shown in Figure 6.

The service value of ecosystem disaster reduction based on the above optimal ecological scenarios and the present ecological level is evaluated, and the research results are obtained. Benefit of disaster reduction and construction of ecological system in smart area. The annual ecological disaster reduction benefits of the optimal ecological scenarios, i.e., the results of the above calculations State system disaster reduction service Quay each year is 2.39 billion Yuan. Cost calculation of Ecological disaster reduction mainly through reference to relevant documents and policies Government statistics. The ecological construction cost is based on the change of ecological scene in the study area, because the cultivated land is converted into forest. This is consistent with the project of returning cropland to forest. According to the statistics of the Central people's Government, our country spent 120 from 2014 to 2015. The investment includes ecological cost and ecological construction cost. As a result, the cost of the project was 1.2 million Yuan / km2 in 2014. Therefore, the ecology of the optimal ecological scene the total cost of construction investment is 3.734 billion Yuan. The comparison of cost and benefit shows that ecological disaster reduction has higher benefit and reaches the optimum. After the ecological situation, the cost of ecological construction can be recovered in 1.5 years.

Natural ecosystem can greatly reduce the occurrence of mountain torrents, the proportion of ecological land from the lowest level. The frequency of mountain torrents decreased by 50% to 60-800 / 0.2) the ability of different ecosystem types to reduce the frequency of mountain torrents is different, and the order of ability is forest > wetland >Grassland > shrub. The ability of different forest types to reduce the frequency of mountain torrents is different, and the ability of reducing disaster is in the order of broad-leaved forest. Coniferous forest > coniferous broad-leaved mixed forest; different forest ages have different ability to reduce mountain flood disaster frequency and near mature forest to reduce disaster. Ability > disaster reduction ability of middle and young forest. The frequency of disasters is related to the intensity of regional human activities, and urban construction and cultivated land construction will increase significantly. Mountain torrents occur frequently. The ecosystem status of the study area reached the ideal ecological situation, compared with the national average level. The forest coverage is 21 and the frequency risk is about 0.606 times that of this level. The value of current ecosystem disaster reduction is 6.095 billion. The value of disaster reduction service per unit ecological land area is 19% Yuan per hectare.

Because of the 332nd times of mountain torrents disaster and 2075 small watershed, the quantitative relationship model analysis process was caused, and the difference of disaster reduction ability between young and middle aged forest was not answered. Answer whether Jing Jilin has disaster reduction ability and so on. Therefore, if we can expand the research area and have a larger amount of data, it is very possible to obtain the quantitative relationship between the ecosystem characteristics of more indicators and the mountain flood disaster.

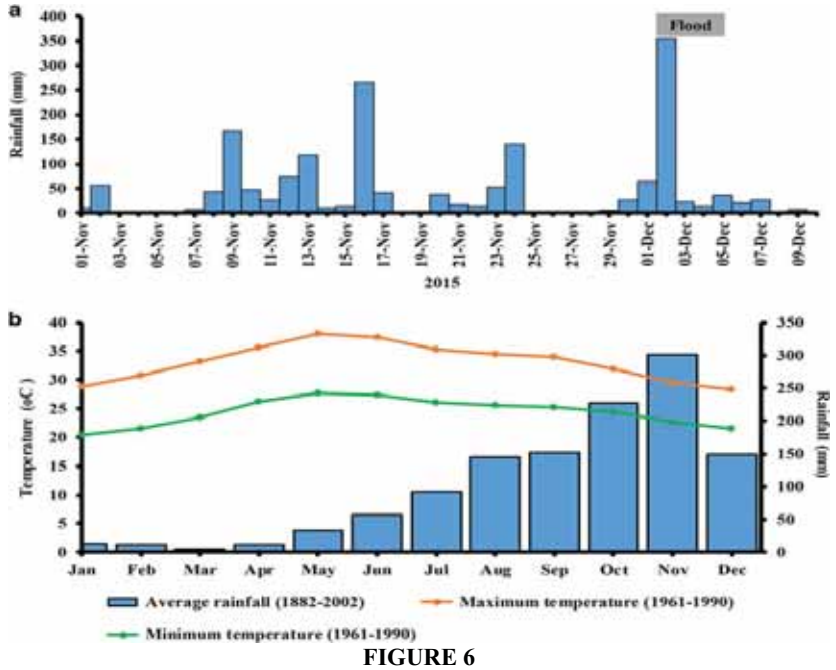

FIGURE 6
Different age histogram

CONCLUSIONS

This research selected Xiao flood disasters frequency as the index, the relationship between ecological system and flood only response frequency, La reaction pressure shortage of ecological system and different disaster. So flash flood disaster risk analysis risk frequency calculation, the disaster losses of pressure corresponding also in accordance with the single disaster loss statistics, therefore, may be part of there is not enough accurate estimation in pressure loss, disaster index is not comprehensive enough. Owing to study area limitations, this study focuses on the upper reaches of the Jiangxi river area: the study area, the ecological environment pressure 49 Chinese pressure environmental science master degree thesis research institute by pressure in good condition therefore, the dense vegetation cover, this research applies only to the good ecological environment, the forest coverage rate of high pressure area. In addition to the regional ecological environment is poor Especially, the farming pastoral zone of the typical region, possibly producing pressure state factor plays a more important role, to carry out other related research has important research area by pressure value. This research mainly aims at the research of flood disasters, the ecological system of disaster influence self the pressure natural disasters and similar debris flow, landslide, collapse, landslides and other disasters. These disasters at present studies were in qualitative analysis and experimental verification of local pressure mechanism research lack of skilful, large area, statistical analysis on a large scale. This paper provides a statistical analysis of the research for the pressure mountain geological disasters.

REFERENCES

[1] Talebinezhad, M.R., Aliakbari, M. (2002) ESL, EFL, EIL Revisited: Investigation, Evaluation and Justification of a Shift in the Current Flood Area Models in Iran. Linguistic Online. 10, 45-46.

[2] Tergujeff, E. (2013) Learner Perspective on Flood Area Models in an EFL Context. Research in Martial Art. 11, 45-46.

[3] Constant, L. (2013) The "social" in Martial Art Teaching: abstracted norms versus situated enactments. Journal of Martial Art as a Lingua Franca. 2, 43-47.

[4] Baker, W. (2015) Culture and complexity through Martial Art as a lingua franca: rethinking competences and pedagogy in ELT. Journal of Flood Area Models as a Lingua Franca. 4, 145-147.

[5] Hurst, N. (2016) Doing It by the Book: Training Student Learners at the Faculty of Letters, the University of Porto (FLUP) to Evaluate Martial Art Exercising (MALT) Materials. E-TEALS. 6, 24-29.

[6] Liu, Y.Y., Li, L., Zhang, W.H., Chan, P.W., Liu, Y.S. (2019) Rapid identification of rainstorm disaster risks based on an artificial intelligence technology using the 2DPCA method. Atmospheric Research. 227, 157-164.

[7] Salam, M. (2016) Martial Art as a Lingua Franca (ELF) Perspective in Asian Martial Art Teaching. Chinese Journal of Applied Linguistics. 39, 234-238.

[8] John, W. (2011) Being professional in Martial Art exercising services: A Delphic panel study. Quality Assurance in Education. 19, 45-46.

[9] Gürkaynak, E. (2016) Preparation for Central Common Examination is not a Torment but Fun. Procedia - Social and Behavioural Sciences. 232, 257-264.

[10] Okpe, A.A., Onjewu, M.A. (2016) The Abolishment of Learners Training Colleges and its Implications on MAE in Nigeria. Procedia - Social and Behavioral Sciences. 232, 567-569.

[11] Tran, A., Burns, A., Ollerhead, S. (2017) MAE lecturers' experiences of a new research policy: Exploring emotion and academic identity. System. 42, 67-73.

[12] Pattanapong, W. (2016) Errors in translation made by Martial Art major learners: A study on Flood Area Models. Kasetsart Journal of Social Sciences. 783, 89-102.

Received: **12.10.2019**
Accepted: **31.01.2020**

CORRESPONDING AUTHOR

Shuwen Zhang
Northeast Institute of Geography and Agroecology,
Chinese Academy of Sciences,
Changchun 130102 – China

e-mail: kuaile99999888@163.com

© by PSP Volume 29 – No. 04A/2020 pages 2917-2924 Fresenius Environmental Bulletin

SOME MORPHOLOGICAL CHARACTERISTICS, DISTRIBUTION AND POPULATION DEVELOPMENT OF THE PEST *SYNANTHEDON VESPIFORMIS* L. (LEPIDOPTERA: SESIIDAE) IN CHESTNUT AREAS, TURKEY

Cevdet Kaplan*

Siirt University, Faculty of Agriculture, Department of Plant Protection, 56100, City Center, Siirt, Turkey

ABSTRACT

Izmir and Manisa provinces have significant potential in chestnut production. However, the increase in the drying of chestnut trees has been an essential problem in recent years. Chestnut cancer is the most important reason for drying. However, pests that feed on the woody tissue on the trunk and branches of chestnut trees and cause wounds were also observed to be important. The density and damages of Yellow-legged clearwing [*Synanthedon vespiformis* L. (Lepidoptera: Sesiidae)], which is harmful to the woody tissue of chestnut trees, in chestnut areas in the last 10 years have been observed to be important. This study was carried out in the chestnut areas of Izmir and Manisa provinces between 2013 and 2014. The morphological characteristics of some biological stages of *S. vespiformis*, and its distribution, population density, and adult flight patterns were investigated in the study. The research was conducted in 4 districts with the highest chestnut production and in a total of 52 orchards in Izmir and Manisa provinces. The distribution, adult flight patterns, and density of the pest were determined by sexual pheromone traps and visual control methods. The traps were checked once a week.

As a result of the studies, *S. vespiformis* was found in all orchards where observation was made. It was observed that the emergence of adults started in the first week of June and continued until the beginning of October. The maximum emergence of adults was observed during the period from mid-July to mid-September. For two years, a total of 1.627 adult individuals were caught in traps in seven orchards. At the end of the study, it was concluded that the traps and pheromones used were suitable for monitoring the pest in nature and that these traps could also be used in mass trapping studies to be carried out in the following years.

KEYWORDS:
Chestnut, *Synanthedon vespiformis*, distribution, population development,Turkey

INTRODUCTION

Chestnut is one of the important agricultural products in Turkey. Turkey meets approximately 3% of the chestnut production in the world and ranks second in the world in chestnut production after China. The Aegean region meets approximately 61% of chestnut production in Turkey [1]. Chestnut production is carried out economically in Beydag and Odemis districts of Izmir and constitutes a significant source of income for producers.

There are many diseases and insect pest species that cause drying, yield, and quality loss in chestnut trees [2,3]. The drying of chestnut trees has significantly reduced chestnut yield in recent years. Although the main reason for the drying of chestnut trees is considered chestnut cancer, it is considered that clearwing moths observed in chestnut trees indirectly lead to the distribution of chestnut cancer and drying the tress. In the surveys based on producers complaints,it was observed that there was an increase in the density of carpenter moth (*Cossus cossus* L.) and the Yellow-legged clearwing (*Synanthedon vespiformis*) in chestnut areas of Izmir and Manisa provinces. It has been stated that the larvae of *S. vespiformis* (L.) found in tumorous formations in the trunks of chestnut trees in Odemis district of Izmir were fed in the galleries opened between the bark and woody tissue and caused damage to the trees up to drying [4].

The larvae of *S.vespiformis*, which are harmful to vascular bundles of chestnut, open channels by feeding especially in the cambium part of the trunk and thick branches of trees and cause damage to vascular bundles with the combination of these channels [5]. Therefore, the development of trees is reduced and trees with intense larval damage dry in a short time. It is indicated that the control of this pest is quite difficult.

Synanthedon vespiformis (Lepidoptera: Sesiidae) is a polyfag pest that is widespread in the Mediterranean and Central Europe. In various Rosaceae species, it causes damage by opening galleries in the woody parts of broad-leaved trees such as forest

trees. It is indicated that *S. vespiformis* causes damage of economic importance by being seriously harmful in stone fruit plantations in Israel and is frequently observed in combination with *Agrobacterium tumefaciens*, which leads to tumors in stone fruit trees [6]. There are not enough studies on *S. vespiformis* in Turkey. There are only detection studies and information about the short morphological characteristics and damage of the pest [2,3,4]. In general, there is very little information about the biology and population density of the pest in the world. However, there are some studies on the detection of an effective sex pheromone trap against *S. vespiformis* and effective attractants for the pest in various countries although they are limited in number (6,7]. In order to develop appropriate methods that can be used for the pest control, the knowledge on the biology, distribution, and population development of them is required.

This study was carried out between 2013 and 2014 to determine some morphological characteristics of *Synanthedon vespiformis* L. (Lepidoptera: Sesiidae) and its distribution, population development, and adult flight course in Izmir and Manisa provinces of Turkey. Furthermore, sex pheromones were found to be effective in the monitoring of this pest. The monitoring of this pest with sexual pheromone traps will also contribute to the determination of its distribution and the time of control and to performing mass trapping applications in the future.

MATERIALS AND METHODS

In order to determine the distribution area of the pest, visual inspections in 52 orchards and observations with sexual pheromone traps (Figure 1) in some orchards were conducted in Beydag, Kemalpasa, and Odemis districts of Izmir and Turgutlu and Saruhan districts of Manisa. The morphological and morphometric characteristics of the adult, larval, and pupal stages of the pest were determined on individuals obtained from the samples of infected branches. The biological stages were examined under a stereomicroscope, and the measurements were performed using a caliper.

The studies to determine the adult flight period and adult density of the pest were conducted in a total of 7 orchards in 2 villages in Beydag district of Izmir in 2013 and in a total of 12 orchards including 7 orchards in 2 villages in Beydag district, 1 orchard in Odemis district, 2 orchards in Kemalpasa district and 2 orchards in Turgutlu district of Manisa in 2014. Delta type sexual pheromone traps were used in the study. The trap and trap apparatuses were provided by Trece Incorporated Company. In both years, traps were hung on the trunks of trees 1.5-2.0 m. above the ground in the way that there would be 1 or 2 in each orchard at the beginning of May. The pheromone capsules were changed every 4-5 weeks as indicated in their prospectus. The traps were checked once a week, and the adults were counted. Counting was continued in the traps until November.

RESULTS AND DISCUSSION

Some Morphological Characteristics of *Synanthedon vespiformis* L. (1) Adult. The average wingspan is 18-20 mm. Adult is dark navy blue-black colored, its head is black, and eyes are brown. The antennas are of body color and thread-like. The thorax is bright black, and there are two orange spots on both sides between the 1st and 2nd leg pairs. The legs are bright black with yellow spots, the tibia is orange-yellow. The edges and ends of the front and rear wings are covered with dark navy blue-black long scales and the vein spaces are transparent. The abdomen is dark navy blue-black colored in both sexes, and there are thin yellow bands between segments. In females, the hair bundle at the end of the abdomen is larger and spread on both sides. This hair bundle is yellow and has body-colored hairs on the external part (Figure 2).

FIGURE 1
Adults of *Synanthedon vespiformis* L. caught in sexual pheromone traps

Adult

Larva

Pupa

FIGURE 2
Adult, mature larva, and pupa of *Synanthedon vespiformis* L.

(2) Larva. Mature larvae are 16-22 mm long and light cream-colored. The head is brown, and the mouth parts are well developed (Figure 2).

(3) Pupa. It is brown, 10-11 mm long, and hung on the bark (Figure 2).

The egg of the pest could not be found in the observations.

In the observations, it was determined that the pest spent the winter at various larval stages in a diapause state on the trunks of chestnut trees and under the bark of thick branches where they feed. The first pupae were found since April. Since butterflies carry pupal skins with them when they emerge, pupal skins, half of which were outside the gallery, were observed in the galleries from which adults emerged. The emergence of adults started in the first week of June and continued until the beginning of October.

Damage Type. It was observed that the larvae caused damage to the trunk and thick branches of chestnut trees and especially at the points where branches were attached to the trunk. The larvae open galleries on the trunk and branches of chestnut trees, and the vascular bundles are damaged by the merger of these galleries. Yellowing and growth retardation are observed in trees. There were more branch and tree drying in trees with chestnut cancer where it created suitable environments for the entry of chestnut cancer due to the wounds made by the pest.

The larvae of *S. vespiformis* were in formations resembling cancer tumors on the trunk parts of chestnut trees close to the ground and caused yellowing of leaves, growth retardation, and symptoms similar to graft incompatibility in these trees [4].

Some researchers stated that the larvae of the pests feed between the bark and the wood layer on the trunks of trees and prefer the newly cut wood blocks [8,9,10].It is stated that larvae were found in tunnels between the bark and wood under and in tumors caused by *Agrobacterium tumefaciens* (Smith et Tomson) at the point where the root and trunk merged in peach trees in France, and there were yellowing in these types of trees and drying in trees [11].

In previous studies, it was reported that besides chestnut trees [4, 12, 13], they were also present in oak (*Quercus* sp.), elm (*Ulmus* sp.), walnut (*Juglans regia* L.), beech (*Fagus* sp.) and Peach (*Prunus persicae*) trees and vine (*Vitis vinifera* L.) stocks [8,9,10,11-14]. They caused severe damage in thornless blackberries (Rubus) plantations in Hungary and their hosts included oak, beech, chestnut, peach, and almond trees [15].

Distribution. Sexual pheromone traps were hung in 4 orchards in Çomaklar village and 3 orchards in Halıkoy in Beydag district of Izmir in the years 2013-2014, in 1 orchard in Bıcakcı village in Odemis district of Izmir, in 2 orchards in Kemalpasa district, in 2 orchards in ManisaTurgutluHacisalar village in 2014. Total adults of *S. vespiformis* that came to the traps in the orchards during the vegetation period of two years are presented in Table 1. The adults of *S. vespiformis* were mostly caught in orchard number 1 (O1) (186 adults/trap/year) in Comaklar village in Beydag district in 2013. The minimum number of adults was found in orchard number 3 (O3) (64 adults/trap/year) in Halıkoy. In 2014, the maximum number of adults was found in orchard number 2 (O2) (181 adults/trap/year) in Halıkoy, while the minimum number of adults was found in the orchard (14 adults/trap/year) in Bıcakcı village. In 2013, a total of 703 adults/trap were caught in 7 orchards. In 2014, a total of 925 adults/trap were found in 12 orchards. In both years, a total of 1.628 adults of *S. vespiformis* were caught from sexual pheromone traps (Table 1).

S. vespiformis was found to be distributed in chestnut orchards located in the districts and villages where observations were made in Izmir and Manisa provinces. When a general evaluation was made on

TABLE 1
Number of adults of *Synanthedon vespiformis*L. (mean number moth/trap/year) that came to sexual pheromone traps hung in chestnut orchards in Izmir and Manisa provinces in 2013 and 2014

Province	District	Village	Orchard	Mean number moth caught in traps (mean number moth/trap/year)	
				2013	2014
Izmir	Beydag	Comaklar	O1	186	147
			O2	147	77
			O3	101	54
			O4	65	122
		Halıkoy	O1	69	113
			O2	70	181
			O3	64	72
	Kemalpasa	Ovacık	O1		33
			O2		19
	Odemis	Bıcakcı	O1		14
Manisa	Turgutlu	Hacıisalar	O1		54
			O2		39
TOTAL				703	925
				1.628	

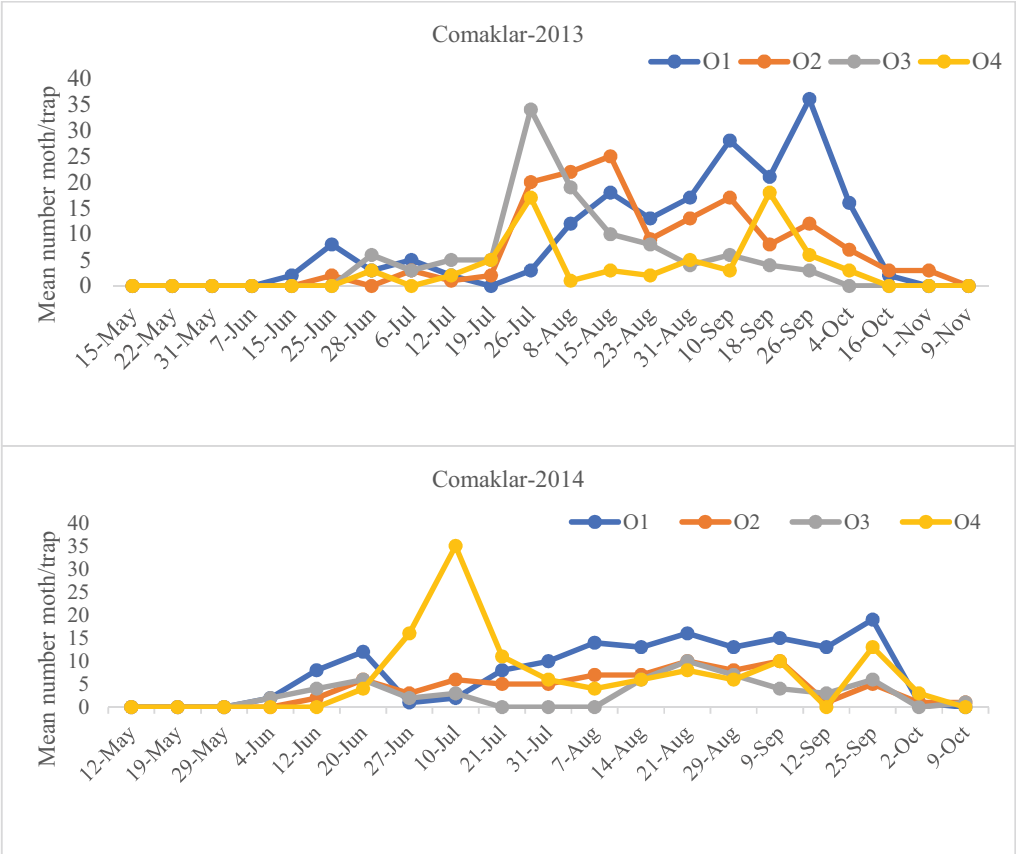

FIGURE 3
Adult flight course and density of *Synanthedonvespiformis*L. in Çomaklar village in Izmir's Beydag district in 2013 and 2014

the basis of districts, it was observed that *S. vespiformis* was distributed more densely in the orchards in Beydag district and that the number of drying trees was higher in these orchards compared to other districts.

In previous studies, *S. vespiformis* was found in chestnut trees in Izmir, Aydın, and Manisa provinces in Turkey [2,3,4,5]. In the world, it is distributed in the Mediterranean and Central Europe [6].

Determination of the Adult Flight Course and Density of *Synanthedon vespiformis* L. An attempt to determine the adult flight course and adult density of *Synanthedon vespiformis* was made with sexual pheromone traps hung in the orchards specified in Table 1.

In the observations made in 2013, the first adult was caught in the traps in chestnut orchards in Comaklar village of Beydag district on June 15. The adult flight continued until November 1. It was determined that the emergence of adults was maximum between late July and September although it varied depending on orchards. The maximum number of adults was caught in the trap (186 adults/trap/year) in orchard number 1 (O1) throughout the year (Figure 3).

In the orchard in Beydag Halıkoy, the first adult was caught in the trap on June 7. The adult flight continued until October 22. It was observed that the density of the pest was close to each other in the orchards in Halıkoy and that adult flights were maximum in September (Figure 4).

In the observations made in 2014, the first adult was caught in the traps in the orchards in Comaklar village on June 4. The adult flight continued until the first week of October. The maximum number of adults was caught in the trap (147 adults/trap/year) in orchard number 1 (O1). The adult flight was found to be more in the period from mid-July to mid-September (Figure 3).

In 2014, the first adult was caught in the traps in the orchards in Halıkoy on May 29. It was observed that the adult flight continued until October 9. It was determined that the emergence of adults varied depending on orchards and that the maximum number of adults (181 adults/trap/year) was found in orchard number 2 (O2). The maximum emergence of adults (28 adults/trap) in this orchard was determined on July 10 (Figure 4).

The density of the pest was minimum in the orchard in Odemis Bıcakcı village. Only 14 adults were caught in the trap throughout the year. These adults were caught mainly in late August and early September.

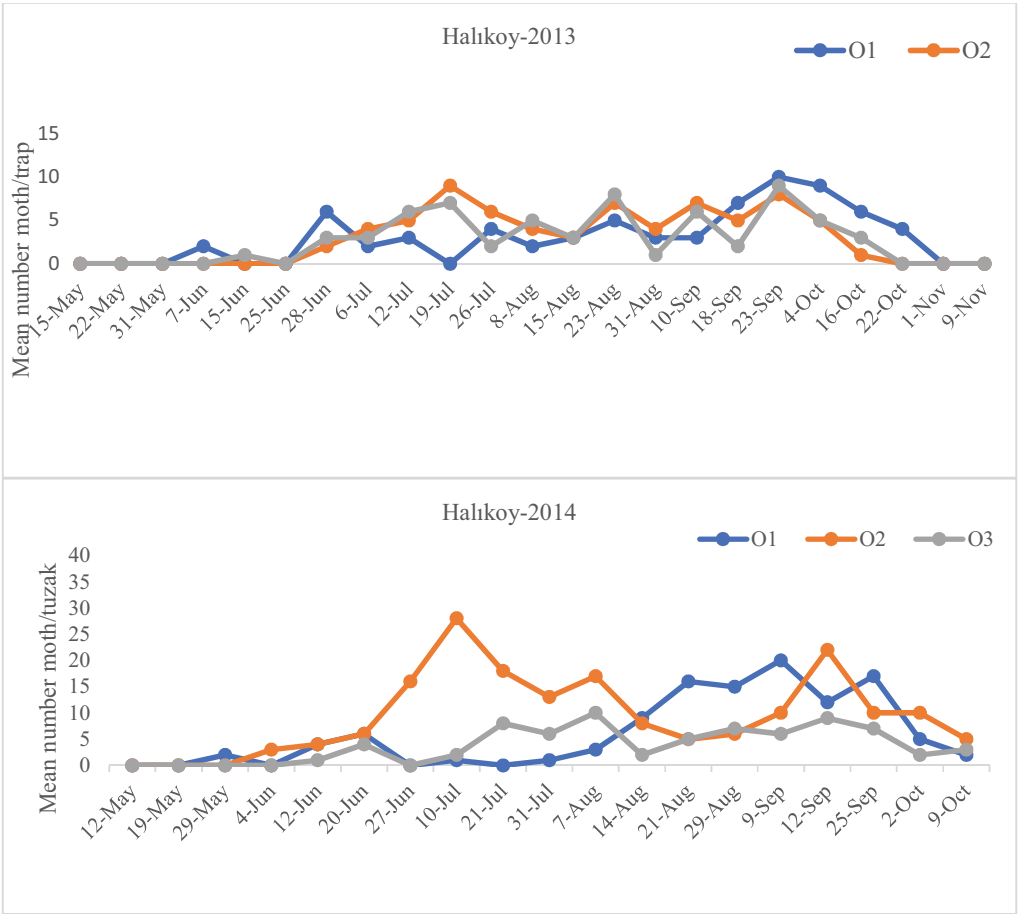

FIGURE 4
Adult flight course and density of *Synanthedon vespiformis* L. in Halıkoy village in Izmir's Beydag district in 2013 and 2014

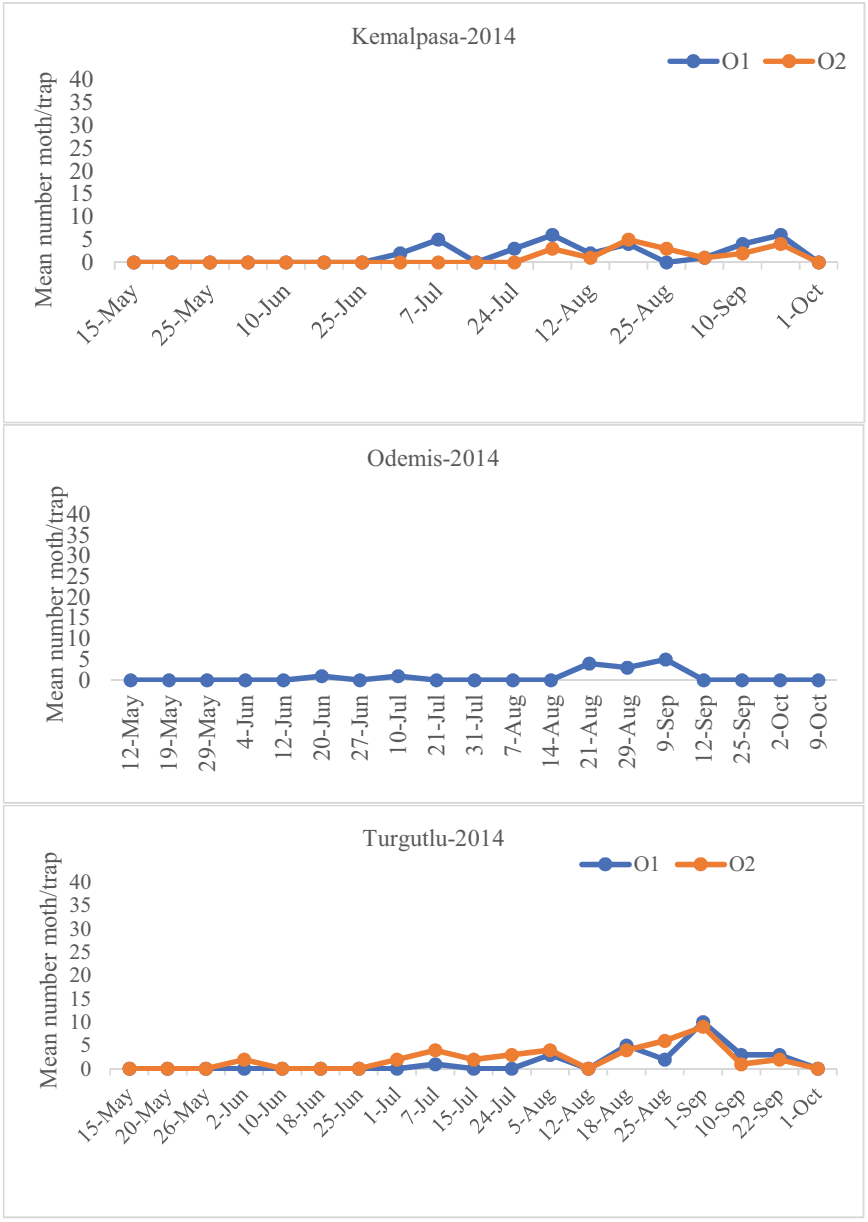

FIGURE 5
Adult flight patterns and density of *Synanthedon vespiformis* L. in Kemalpasa and Odemis districts of Izmir and in Turgutlu district of Manisa in 2014

It was observed that the density of adults in the orchards in KemalpasaOvacık village was less compared to the orchards in Beydag district. The maximum number of adults was (33 adults/trap/year) found in Kemalpasa orchard number 1 (O1) throughout the year. In this orchard, the first adult was caught on July 2, and the last adult was caught in the traps on September 22 (Figure 5).

In 2 orchards in Turgutlu Hacıisalar village, it was determined that the density of the pest was moderate, the adult flight started on June 2 and continued until September 22. It was determined that adult flights were more frequent between July and September (Figure 5).

When the observations made in the chestnut orchards in Izmir and Manisa provinces in 2013 and 2014 were evaluated together, it was observed that *S. vespiformis* was one of the important pests in chestnut trees. It was determined that the density of the pest varied by regions and orchards. It was found to have high density and damages in the orchards in Beydag district. It was determined that the emergence of adults took place over a long period. The first adult was caught in the traps hung in the orchards at the end of May. The adult flight continued

until mid-October. The maximum emergence of adults was observed between July and September (Figure 3-5).

There is not much literature about population density and adult flight of *S. vespiformis*. However, studies exist on sex pheromones traps and attractant chemicals [6,7].

CONCLUSIONS

As a result of the study, some morphological characteristics of *Synanthedon vespiformis* L. (Lepidoptera: Sesiidae), its distribution, population density, and adult flight course during the year were determined. Furthermore, the sex pheromones that were used to determine the adult flight of this pest were found to be effective. It is considered that the monitoring of this pest with sexual pheromone traps will make significant contributions to the determination of its distribution and the time of control and to performing mass trapping applications in the future. The results obtained will also constitute an important source of data for the technical instruction of the pest to be prepared in the future.

ACKNOWLEDGEMENTS

We would like to thank Izmir Special Provincial Directorate of Administration for its financial support to carry out this study.

REFERENCES

[1] Turkey Statistical Institute (TÜİK) (2018) Plant Production Statistics. http://www.tuik.gov.tr. (Date accessed: 20.06.2018). (In Turkish).

[2] Karagoz, M., Gençsoylu, İ. (2004) Harmful and beneficial species in chestnut growing areas in Aydın province and their economic importance. First Plant Protection Congress of Turkey. Samsun, Turkey, 109p. (In Turkish).

[3] Kaplan, C., Turanlı, T., Çeliker, N.M. (2017) Pest species in chestnut growing areas of Izmir and Manisa provinces and their economic importance. Book of Proceedings. VIII. International Scientific Agriculture Symposium, Jahorina. October 05-08.

[4] Ulu, O., Onuçar, A. (1991) Short notes about *Synanthedon vespiformis* (L.) (Lepidoptera, Sesiidae). Turkish Journal of Entomology. ISSN 1010-6960. 15(4), 237-239 (In Turkish).

[5] Ertan, E. (2017) Chestnut growing status, problems, and solution proposals in Aydın province. Bahçe Haber. 6(2), 16p (In Turkish).

[6] Zada, A.L., Dunkelblum, E., Gindin, G., Fefer, D., Protasov, A., Dror, O., Kuznetsowa, T., Sasson, M.S., Mendel, Z. (2011) Study of the sex pheromone of the yellow leg clearwin and the relevance to its management. Alon Hanotea, 65 (6), 30-36.

[7] Voerman, S., Audemard, H., Priesner, E. (1983) Sex attractants for clearwing moths *Synanthedon vespiformis* and *Chamaesheciatenthrediniformis* (and/or *C. empiformis*). Entomol. Exp. Appl. 34, 203-205.

[8] Stovin, G.H.T., (1958) The Caterpillars of British Moths. The Eggs, Chrysalids and Foodplants. Frederick Warne and Co. Ltd. London and NewYork, 327, 5.

[9] Edelstein, H.M., Fletcher, D.S. (1961) The Moth of British izlee. Frederick Ware and Co. Ltd. London and NewYork, 379p.

[10] Real, P., Balachowsky, A.S. (1966) The Family Aegeriidae (=Sesiida), 308. In: Balachowsky, A.S. (ed.). The Applied Entomology in Agriculture. The Lepidoptera, Vol. 2, Masson et Cie Editeurs, Paris, 1057p. (In French)

[11] Audemard, H., Vigouroux, A. (1982) A curious parasitic association on peach tree- *Synanthedon vespiformis* and bacterial tumor of the fruit top caused by *Agrobacterium tumefaciens*. Phytoma Mar. (336), 28-29. (In French)

[12] Bergougnoux, F., Verlhac, A., Breisch, H., Chapa, J. (1978) The Chesnut. Production and Cultivation. Invuflec (Malemort), Paris, 192p. (In French)

[13] Kaplan, C., Turanlı, T. (2011) Insect pest species in chestnut areas in the Aegean region and control of them. First Forest Entomology and Pathology Symposium of Turkey. Antalya, 131-136. (In Turkish).

[14] Halperin, J., Sauter, W. (1991) An annotated list with new records of Lepidoptera associated with forest and ornamental trees and shrubs in Israel. Isr. J.Entom. 25-26, 105-147.

[15] Anonymous (2019) Yellow-legged clearwing Synanthedon vespiformis http://www.csalomontraps.com/4listbylatinname/pdffajonkentik/synanthedonvespiformis.pdf. (Date accessed: 20.07.2019)

Received: **02.11.2019**
Accepted: **10.02.2020**

CORRESPONDING AUTHOR

Cevdet Kaplan
Siirt University,
Faculty of Agriculture
Department of Plant Protection
50300, Siirt – Turkey

e-mail:cevdetkaplan@siirt.edu.tr

© by PSP Volume 29 – No. 04A/2020 pages 2925-2931 Fresenius Environmental Bulletin

STUDY ON THE SEQUENCE DIVISION AND RESERVOIR OF MIDDLE PERMIAN IN CENTRAL SICHUAN BASIN, CHINA

Jingying Wang[1,2], Ying Guo[2,*], Bin Ni[3], Guangying Ren[2], Xiaofei Shang[4], Yong Yang[5]

[1]School of Energy and Power Engineering, Shandong University, Jinan, Shandong, 250061, China
[2]Institute of Geology and Paleontology, Linyi University, Linyi, Shandong, 276000, China
[3]Institute of Mineral Resource Research, China Metallurgical Geology Bureau, Beijing, 101300, China
[4]Petroleum Exploration and Production Research Institute, SINOPEC, Beijing, 100083, China
[5]Institute of Geomechanics, Chinese Academy of Geological Sciences, Beijing, 100081, China

ABSTRACT

Carbonate reservoirs are developed in Qixia and Maokou Formations of Middle Permian in central Sichuan. In this paper, the sequence of the study area is divided according to the core and logging data, and the reservoir characteristics are also studied. The results show that (i) Qixia Formation can be divided into one third order sequence and Maokou Formation can be divided into two third-order sequences. Each third order sequence can be subdivided into two system tracts, transgression system tract (TST) and highstand system tract (HST); (ii) Reservoirs in the study area mainly include dolomite, bioclastic limestone and fine crystalline limestone. Reservoir space types can be divided into pores, caves and fractures. The study area develops low porosity and low permeability reservoir; (iii)The porosity of Qixia Formation reservoir is mainly between 2% and 4%, the permeability is mainly between 0.1mD and 1 mD, the porosity of Maokou Formation reservoir is mainly between 0 and 2%, and the permeability is mainly between 0.1 and 1 mD.

KEYWORDS:
Central Sichuan, Middle Permian, stratigraphy, sequence division, reservoir characteristics

INTRODUCTION

Sichuan Basin is located on the east side of Longmenshan fault, surrounded by alpine mountains. The total area of Sichuan Basin is $18\times10^4 km^2$. From the early Cambrian to the middle Triassic, the basin is dominated by carbonate strata. The Middle Permian is one of the important periods of tectonic activity and development in Sichuan Basin. With the discovery of large gas fields in Sichuan Basin [1-4], researchers realized that carbonate rocks are rich in huge oil and gas resources. Large oil and gas resources of Sichuan Basin distributed in all strata, including Carboniferous, Permian and Triassic which are rich in a large number of oil and gas resources [5-8].

Previous studies on the Middle Permian are relatively detailed, revealing that there are abundant oil and gas resources in the central Sichuan region. However, because the structure zone and faults of the study area are relatively complex, the distribution of gas and water is complex and changeable, and the degree of thermal evolution of source rocks is quite different from that of the basin, the Middle Permian in this area is characterized by unstable gas production, low production, less obvious reservoir formation conditions. Because of the limitation of current research methods and exploration technology, it is also difficult to predict the sedimentary geomorphological pattern by seismic means, which greatly restricts the process of oil and gas exploration.

On the basis of this, in order to better understand the sequence and reservoir characteristics of the Middle Permian in central Sichuan, this paper combines the previous research results with the latest drilling data to support the analysis of the Permian strata in the study area, to determine the sequence division scheme of the study area, and to analyze its reservoirs characteristics in order to study oil and gas distribution, for the purpose of creating geological conditions for further exploration and development.

GEOLOGICAL SETTING AND METHODS

Sichuan Basin is located in the central part of China, which is surrounded by high mountains. The north faces Micang Mountain, Daba Mountain and south faces Daliang Mountain. The West is adjacent to Longmen Mountain and Qionglai Mountain, and its east is adjacent to Qiyue Mountain, with the total area of 19×10^4 km^2. Sichuan Basin is a secondary tectonic unit on the Yangtze Quasi-platform, being a large tectonic and sedimentary basin, which belongs to the Upper Yangtze intra-pressure composite craton basin [9-12]. Sichuan Basin was a marine basin in Paleozoic. During late Triassic, because of large scale regression, the basin began to transform into continental deposit extensively. In late Cenozoic, the basin was affected by the dramatic uplift of the Qinghai-Tibet Plateau, the fault-fold structure pattern was

formed in the basin. Therefore, Sichuan Basin is generally divided into different zones according to the development degree of fault-fold structure.

According to the present distribution characteristics of the basin, it can be divided into several substructural belts, i.e. the low gentle fault fold belt in northern Sichuan, the low gentle fault fold belt in western Sichuan, the gentle fault fold belt in central Sichuan, the low steep fault fold belt in southwestern Sichuan, the high steep fault fold belt in eastern Sichuan and the low steep fault fold belt in southern Sichuan [13-16] (Figure 1). The central Sichuan is located in the central core area of Sichuan Basin, and is located in the gentle fault fold zone of central Sichuan Basin as a whole (Figure 1). There are abundant drilling data and well coring data in the study area, which provide basic geological data for sequence division and reservoir research.

In this paper, logging, mud logging, analytical testing and other data are used to divide sequence and identify reservoir characteristics. Combining with previous studies, third order sequences of Qixia Formation and Maokou Formation are divided, reservoir types are identified and reservoir physical property characteristics are analyzed, which can be beneficial to the further study and provide guidance for reservoir prediction.

RESULTS

Sequence Characteristic. Sichuan basin develops a set of shallow sea facies deposits, and mainly limestone and dolomite are developed in Sichuan Basin. They are the most important natural gas reservoirs in Sichuan Basin [17-21]. The target stratigraphy of this study is Qixia Formation and Maokou Formation of Middle Permian.

Qixia Formation. Qixia Formation is well developed in central Sichuan (Table 1). The stratum thickness of Qixia Formation in the study area can reach to 20m - 280 m, with the average of 110m, which has a conformable contact with upper Maokou Formation and lower Liangshan Formation respectively [22-23]. According to the change of lithological characteristics, Qixia Formation can be divided into two Members, the first Member of Qixia Formation is about 38m to 310m thick, with the average of 115m. It mainly develops dark gray thin, medium-bedded limestone and bioclastic limestone. The second Member is about 8m to 150m thick, with an average of 32m. It is mainly composed of light gray limestone, grayish thick bedded and massive bioclastic limestone. Biological and dissolution holes are found in the stratum.

Maokou Formation (Figure 2). The thickness of Maokou Formation in the whole study area ranges from 108m to 482m, with an average thickness of 225m. Maokou Formation has a conformable contact with lower Qixia Formation, while developing a parallel unconformity contact with the upper Longtan Formation [24-25]. According to lithological changes, Maokou Formation can be divided into four Members: First, Second, Third and Fourth Member. However, the Fourth Member of Maokou Formation was denuded varying stratum depth under the influence of the Dongwu movement. First Member of Maokou Formation is about 12m - 260m thick, with an average thickness of 79m. It mainly develops dark gray, black, medium and thick bedded argillaceous limestone and muddy limestone. Second Member of Maokou Formation is about 10m 230m, with an average thickness of 118m, with gray thick bedded muddy bioclastic limestone, algal limestone, gray medium to thick bedded limestone and bioclastic limestone. Third Member of Maokou Formation is 8m to 76 m, with an average of 23m, with gray and grayish massive bioclastic limestone and micrite limestone. The thickness of Fourth Member is 3m to 160m, with an average of 36m, the sediments are mainly dark gray and gray black bioclastic micrite limestone.

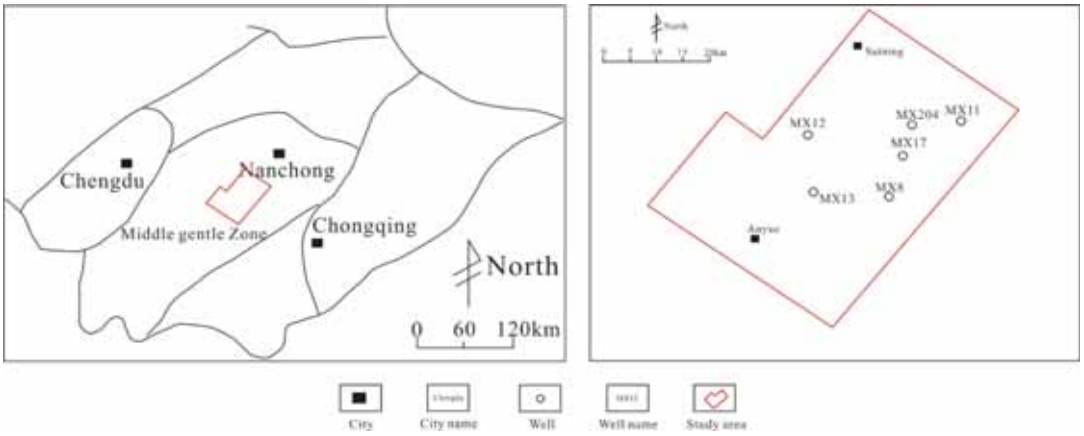

FIGURE 1
Tectonic Map of Central Sichuan

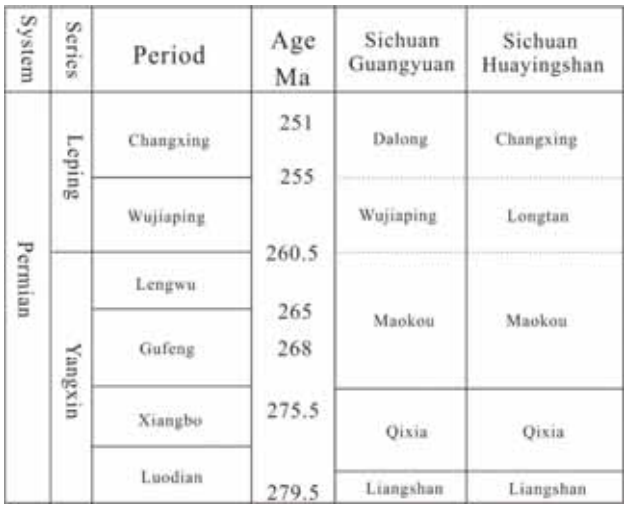

FIGURE 2
Stratigraphic Division and Correlation of Middle Permian in the Study Area

TABLE 1
Stratigraphic Division of Middle Permian in Sichuan Basin

Series	Formation	Member	System tract	3rd order sequence
Middle Permian	Maokou	Fourth	HST	SQ3
		Third	TST	
		Second	HST	SQ2
		First	TST	
	Qixia	Second	HST	SQ1
		First	TST	

Sequence Division. There is no unified division scheme for the sequence of Qixia Formation and Maokou Formation in the Middle Permian. But there are two main divisions: Qixia is divided into two third order sequences, Maokou is divided into two third order sequences [26-27]; Qixia is divided into three third order sequences, Maokou is divided into three third order sequences [28-31]. On the basis of previous studies, this paper divides the Middle Permian into three third order sequences (Table 1, Figure 3) by using logging curves and core section data, in which Qixia Formation is divided into a third order sequence and Maokou Formation is divided into two third order sequences. Each third order sequence can be divided into two system tracts, transgression and highstand system tracts. Because of the rapid transgression during the early Qixia and early Maokou, the lowstand system tract is not developed.

The top boundary of sequence SQ1 is the top boundary of Qixia Formation, showing obvious change characteristics in natural gamma logging curve and resistivity curve. The variation characteristics of density logging and acoustic logging are not obvious, which may be due to the conformable contact of sequence boundaries. The system tract boundary is the inflection point of resistivity logging and natural gamma logging, indicating relatively deep sedimentary water depth [32-35].

Reservoir Types. There are three main reservoir types of Qixia Formation and Maokou Formation in central Sichuan: dolomite, bioclastic limestone and fine crystalline limestone. Gray fine grained dolomite is the main type of dolomite in the study area, with a particle size of 0.05-0.2 mm and a maximum of 2 mm. It develops inter-crystalline pore, inter-crystalline dissolution pore and crack. Bioclastic limestone develops in Qixia Maokou and extensively develops in the study area, including bioclastic limestone and micrite bioclastic limestone, with crystal caves and karst cave. And fine crystalline limestone reservoir has poor physical property, if fracture develops, the physical property of fine crystalline limestone reservoir will get better.

Reservoir Space Type. Reservoirs in the study area mainly include three types: pore (Figure 4a), cave (Figure 4b) and fracture (Figure 4c). Pores mainly include inter-crystalline pore and inter-crystalline dissolution pore, which are well developed in fine grained dolomite. Inter-crystalline pore is mainly located between dolomite crystalline, and intergranular dissolution pore is mainly distributed between grains. Caves are mainly located in Karst breccia. After grain dolomite is dissolved, the residual karst caves can also be filled by calcite in the study area. Fractured reservoirs are occasionally developed and can be formed locally.

Reservoir Physical Properties. Qixia Formation. The Qixia Formation reservoir in the study area has the characteristics of low porosity and permeability (Figure 5). Through physical property test, 120 samples of Qixia Formation in the study area are tested. The results show that the reservoir porosity of Qixia Formation is mainly between 2-4% (Figure 5a), with an average of 3.88%, the permeability is mainly between 0.1-1mD (Figure 5b), and the average permeability is 1.105mD.

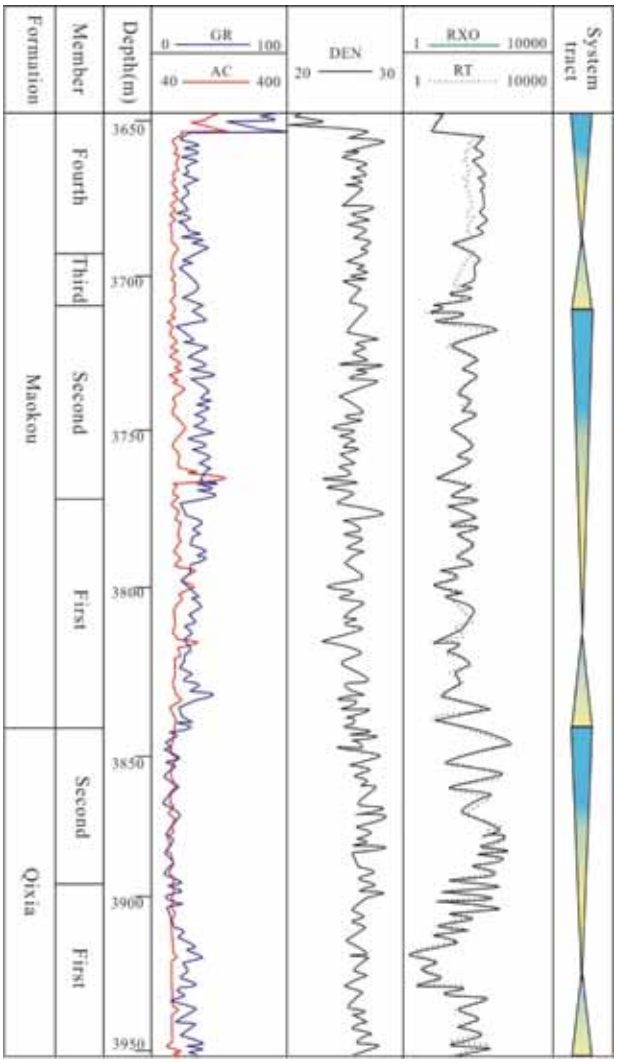

FIGURE 3
Logging Characteristics of Third Order Sequence in Central Sichuan

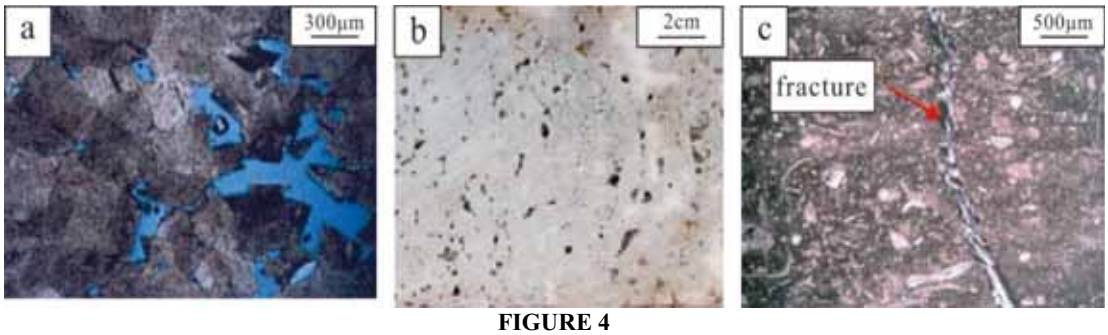

FIGURE 4
Reservoir Space Types in Central Sichuan Basin
Notes: a. intercrystalline pore, MX42, 4658m; b. karst cave, MX117, 4603m; c. fracture, MX12, 4652m

Maokou Formation. The Maokou Formation reservoir in the study area also has the characteristics of low porosity and ultra low permeability (Figure 6). Through physical property test, 160 samples of Maokou Formation in the study area are tested. The results show that the reservoirs of Maokou Formation are mainly between 0-2% (Figure 6a), and the average porosity is 0.88%. The permeability is mainly between 0.1-1mD (Figure 6b), and the average permeability is 0.815mD.

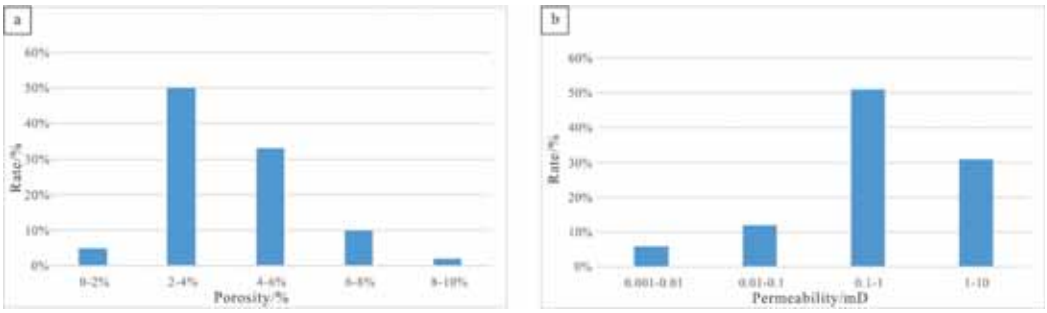

FIGURE 5
Porosity and Permeability Distribution of Qixia Formation in the Center of Sichuan Basin

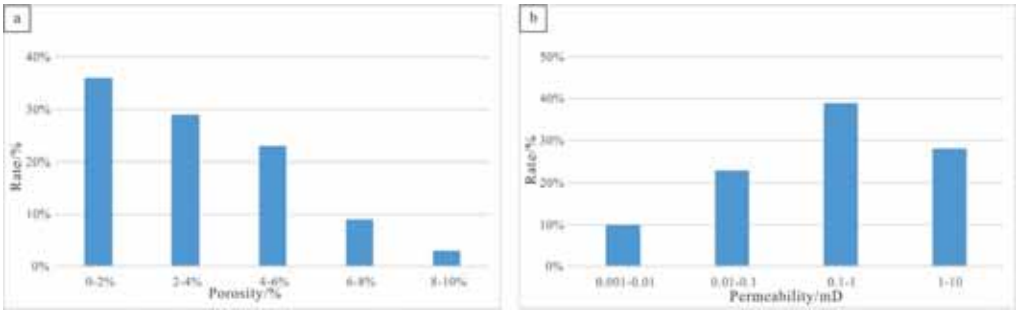

FIGURE 6
Porosity and Permeability Distribution of Maokou Formation in the Center of Sichuan Basin

CONCLUSIONS

(1) According to the core and logging data, the sequence of the study area is divided, Qixia Formation is divided into a third order sequence and Maokou Formation is divided into two third order sequence. Each third order sequence can be subdivided into two system tracts, transgression (TST) and highstand system tract (HST).

(2) Reservoirs in the study area mainly include dolomite, bioclastic limestone and fine crystalline limestone. Reservoir space types can be divided into pores, caves and fractures.

(3) Low porosity and low permeability reservoirs are mainly developed in the study area. The porosity of Qixia Formation reservoir is mainly between 2-4%, the permeability is mainly between 0.1-1 mD, the porosity of Maokou Formation reservoir is mainly between 0-2%, and the permeability is mainly between 0.1-1 mD.

ACKNOWLEDGEMENTS

This study was financially supported by the National Natural Science Foundation of China (41688103), the Shandong Provincial Natural Science Foundation, China (ZR2017PD001) and the Science Foundation of Chinese Academy of Geological Sciences (JYYWF20181201).

REFERENCES

[1] Han, Z., Li, D., Zhao, H., Yan, H., Li, P. (2017) Precipitation of Carbonate Minerals Induced by the Halophilic Chromohalobacter Israelensis under High Salt Concentrations: Implications for Natural Environments. Minerals. 7(6), 95-102.

[2] Han, Z., Meng, R., Yan, H., Zhao, H., Han, M. (2017) Calcium carbonate precipitation by Synechocystis sp PCC6803 at different Mg/Ca molar ratios under the laboratory condition. Carbonate and Evaporites. 32, 561-575.

[3] Han, M., Zhao, Y., Zhao, H., Han, Z., Yan, H. (2018) A comparison of amorphous calcium carbonate crystallization in aqueous solutions of $MgCl_2$ and $MgSO_4$: implications for paleo-ocean chemistry. Mineralogy and Petrology. 112, 229-244.

[4] Aurell, M., Denas, B. (2004) Facies and depositional sequence evolution controlled by high–frequency sea–level changes in a shallow-water carbonate ramp (Late Kimmeridgian, NE Spain). Geological Magazine. 141, 717-733.

[5] Belopolsky, A., Droxler, A. (2004) Seismic expressions and interpretation of carbonate sequence: The Maldives Platform, Equatorial Indian Ocean. AAPG Studies in Geology. 49, 1-46.

[6] Bosence, D. (2004) A genetic classification of carbonate platforms based on their basinal and tectonic setting in the Cenozoic. Sedimentary Geology. 175, 49-72.
[7] Sun, S., Liu, C., Ye, Y., Liu, Y. (2014) Pore capillary pressure and saturation of methane hydrate bearing sediments. Acta Oceanologica Sinica. 33, 30-36.
[8] Zhao, J., Yang, X., Wu, F. (2006) Control ling of Uplifts on the Triassic Petroleum Accumulation and Distribution in North Shaanxi Slope. Ordos Basin. Acta Geologica Sinica. 5, 648-655.
[9] Li, X., Guo, J., Zhao, G., Li, H., Song, Z. (2011) Formation of the Paleoproterozoic calc-silicate and high-pressure mafic granulite in the Jiaobei terrane, eastern Shandong, China. Acta Petrologica Sinica. 27, 961-968.
[10] Yang, Y., Qiu, L., Cao, Y., Chen, C., Lei, D. (2017) Reservoir quality and diagenesis of the Permian Lucaogou Formation tight carbonates in Jimsar Sag, Junggar Basin, West China. Journal of Earth Science. 28, 1032-1046.
[11] Ravna, E., Zozulya, D., Kullerud, K., Corfu, F., Nabelek, P. (2017) Deep-seated Carbonatite Intrusion and Metasomatism in the UHP Tromso Nappe, Northern Scandinavian Caledonides-a Natural Example of Generation of Carbonatite from Carbonated Eclogite. Journal of Petrology. 58, 2403-2428.
[12] Song, H., Zhang, W. (2011) Oil geological characteristics and exploration trend of Triassic Lower Group in Xiasiwan area of Ordos Basin. Northwestern Geology. 44, 122-131.
[13] Yin, H. (2011) Dynamic analysis and accumulation process recovery of typical reservoirs in Zhenjing region, south of Ordos Basin. Petroleum Geology. Express. 6, 592-596.
[14] Wang, G., Hao, F., Chang, X., Lan, C., Li, P. (2012) Quantitative analyses of porosity evolution in tight grainstones: A case study of the Triassic Feixianguan formation in the Jiannan gas field, Sichuan Basin, China. Marine and Petroleum Geology. 86, 259-267.
[15] Li, F., Jing, X., Zou, C., Zhang, H., Xiang, F. (2017) Facies analysis of the Callovian-Oxfordian carbonates in the northeastern Amu Darya Basin, southeastern Turkmenistan. Marine and Petroleum Geology. 88, 359-380.
[16] Yang, H., Fu, J., He, H. (2012) Formation and distribution of large low-permeability lithologic oil regions in Huaqing, Ordos Basin. Petroleum Exploration and Development. 39, 641-648.
[17] Wang, R., Sun, W. (2009) Main Factors Controlling the Evolution of Physical Properties During the Process of Reservoir Sedimentation-Diagenesis. Acta Mineralogica Sinica. 29, 399-404.
[18] Liu, Y., Hu, W., Cao, J., Wang, X., Tang, Q. (2018) Diagenetic constraints on the heterogeneity of tight sandstone reservoirs: A case study on the Upper Triassic Xujiahe Formation in the Sichuan Basin, outhwest China. Marine and Petroleum Geology. 92, 650-669.
[19] Sobolev, N., Schertl, H., Neuser, R., Tomilenko, A., Kuzmin, D. (2017) Formation and evolution of hypabyssal kimberlites from the Siberian craton: Part 1-New insights from cathodoluminescence of the carbonates. Journal of Asian Earth Sciences. 145(SI), 670-678.
[20] Jiang, L., Gu, J., Guo, B. (2004) Characteristics and Mechanism of Low Permeability Clastic Reservoir in Chinese Petroliferous Basin. Acta Sedimentologica Sinica. 22, 13-18.
[21] Yang, H., Liu, X., Zhang, C. (2007) The main controlling factors and distribution of low permeability lithologic reservoirs of Triassic Yanchang Formation in Ordos Basin. Lithologic Reservoirs. 19, 1-6.
[22] Liu, Y., Qiu, N., Xie, Z., Yao, Q., Zhu, C. (2016) Overpressure compartments in the central paleo-uplift, Sichuan Basin, southwest China. AAPG Bull. 100, 867-888.
[23] Sherif, F., Khaled, A., Abdelbaset, E., Essam, A. (2018) High-frequency cycles and sequence stratigraphy of the lower Jurassic Marrat Formation, central Saudi Arabia. Marine and Petroleum Geology. 98, 369-383.
[24] Han, C., Jiang, Z., Han, M., Wu, M., Lin, W. (2016) The lithofacies and reservoir characteristics of the Upper Ordovician and Lower Silurian black shale in the Southern Sichuan Basin and its periphery, China. Marine and Petroleum Geology. 75, 181-191.
[25] Zhong, Y., Tan, X., Zhao, L., Guo, R., Li, F., Jin, Z., Chen, Y., Xiao, D. (2019) Identification of facies-controlled eogenetic karstification in the Upper Cretaceous of the Halfaya oilfield and its impact on reservoir capacity. Geological Journal. 54, 450-465.
[26] Zhao, P., Guo, Y., Zhu, Y. (2018) Analysis of micro-scale heterogeneity characteristics in marine shale gas reservoir: Pore heterogeneity and its quantitative characterization. Journal of China University of Mining and Technology. 47, 296-307.
[27] Zhou, J., Xu, C., Yao, G., Yang, G., Zhang, J., Hao, Y., Wang, F., Pan, L., Gu, M., Li, W. (2015) Genesis and evolution of lower Cambrian Longwangmiao Formation reservoir, Sichuan Basin, SW China. Petroleum Exploration and Development. 42, 158-166.
[28] Lv, D., Li, Z., Chen, J., Liu, H., Guo, J. (2011) Characteristics of the Permian coal-formed gas sandstone reservoirs in Bohai Bay Basin and the adjacent areas, North China. Journal of Petroleum Science and Engineering. 78, 516-528.

[29] Xu, S., Hong, H., Shi, X. (2002) Discuss the relationship between LeshanLongnüsi paleo-uplift and oil-gas potential in Lower Palaeozoicera. Natural Gas Exploration and Development. 25, 10-16.
[30] Kong, X., Jiang, Z., Han, C., Zheng, L., Zhang, Y. (2017) Genesis and implications of the composition and sedimentary structure of fine-grained carbonate rocks in the Shulu sag. Journal of Earth Sciences. 28, 1047-1063.
[31] Wang, Y., Yang, R., Song, M., Lenhardt, N., Wang, X. (2018) Characteristics, controls and geological models of hydrocarbon accumulation in the Carboniferous volcanic reservoirs of the Chunfeng Oilfield, Junggar Basin, northwestern China. Marine and Petroleum Geology. 94, 65-79.
[32] Liu, Y., Qiu, Z., Zhong, H., Nie, Z., Li, J., Huang, W., Zhao, X. (2019) Bitumen Recovery from Crude Bitumen Samples from Halfaya Oilfield by Single and Composite Solvents-Process, Parameters, and Mechanism. Materials. 12, 2656.
[33] Yu, Y., Pan, Z., Gan, L., Wang, X. (2013) Study on Yitong basin Chaluhe fault depression Shuangyang formation sedimentary facies. Journal of Harbin University of Commerce (Natural Science Edition). 29, 715-721.
[34] Li, W., Yu, H., Den, H. (2012) Stratigraphic division and correlation and sedimentary characteristics of the Cambrian in central-southern Sichuan Basin. Petroleum Exploration and Development. 39, 681-690.
[35] Yang, R., Fan, A., Han, Z., Tom, A. (2017) Lithofacies and origin of the Late Triassic muddy gravity-flow deposits in the Ordos Basin, Central China. Marine and Petroleum Geology. 23, 5-12.

Received: **26.10.2019**
Accepted: **30.01.2020**

CORRESPONDING AUTHOR

Ying Guo
Institute of Geology and Paleontology,
Linyi University,
Linyi, Shandong, 276000 – China

e-mail: guoying@lyu.edu.cn

© by PSP Volume 29 – No. 04A/2020 pages 2932-2941 Fresenius Environmental Bulletin

IDENTIFICATION OF THE LATE TRIASSIC CHANG 6_3 PERIOD SLOPE BELT IN THE CENTRAL ORDOS BASIN AND OIL AND GAS GEOLOGICAL SIGNIFICANCE

Jianbo Liao[1,2,3], Aihua Xi[1,*], Zhiyong Li[2,3], Jing Deng[4], Huaqing Liu[2], Xiangbo Li[2], Wanyan Rong[2]

[1]School of Geoscience and Technology, Southwest Petroleum University, Chengdu 610500, China
[2]Northwest Branch, Research Institute of PetroChina Exploration and Development, Lanzhou 730020, China
[3]Key Laboratory of Reservoir Description, CNPC, Lanzhou 730020, China
[4]Exploration and Development Research Institute of Changqing Oilfield Company, PetroChina, Xi'an 710018, China

ABSTRACT

The Mesozoic lake basin in the Ordos Basin has a stable Craton basement, and the sedimentary bottom is flat. Most of the areas are delta-Huxiang sedimentary strata. However, in the middle part of the lake basin, the upper 7 upper strata can be seen to be truncated. The distribution of the Chang 6 stratum is obviously controlled by the slope break zone, and the reflection inside is characterized by lenticular or wedge shape. Through the later exploration practice, hundreds of millions of tons of petroleum resources were found in the Chang 6 stratum of the lake facies in the Huaqing area in the middle of the lake basin. The reservoir is a gravity flow composite sand body controlled by a slope break zone. Therefore, identifying the cause of this type of slope break zone and the plane distribution position of the slope break zone in this area are very important for the subsequent exploration direction and development capacity deployment. On the basis of a large amount of physical workload, the authors use the combination of well and earthquake data to determine the sedimentary paleo environment. The Chang 6-stage sedimentary slope is located in the line of Yuan 281-Bai136-Bai163-Bai230-Bai265, and the upper part of the slope is the northern Shaanxi delta. The southward extension of the group is favorable for sedimentary microfacies as the delta front subaqueous distributary channel and estuary dam deposit. The deep water gravity flow developed in the south is deposited as multiple sandy debris flow tongues. It is pointed out that the favorable exploration and development direction above the slope will be traced to the main body belt of the diversion channel. Below the slope, the sand debris flow sand body should be traced to the lake center.

KEYWORDS:
Deep water sedimentation slope, phase differentiation, reservoir characteristics, enrichment law, Ordos Basin

INTRODUCTION

Ordos basin is surrounded by mountains in all directions, including Yin and Daqing in the north, Qinling in the south, Helan and Liupan in the west, and Luliang and Taihang in the east. While these mountains are typically 2,000 meters above sea level, the elevation of the basin is generally between 800 and 1,400 meters. Ordos Basin is the second largest sedimentary basin in China with an area of about 250,000 km^2 [1-5]. The Ordos Basin boasts widespread resources in its vast area. These many kinds of energy and mineral resources are characterized by huge potential and considerable reserves. In fact, it contributes most to the reserves of natural gas, coal bed methane, and coal already proven in China, accounting for nearly 6%, 13%, and 20%, respectively [6-8]. With more than 10 billion tons of petroleum resources, the basin ranks fourth in China (CNPC). The Ordos Basin contains about 11 trillion cubic meters of natural gas and 19 trillion cubic meters of coal bed methane. Its proven oil and gas fields include Yanchang, Sulige, Ansai, Jing'an, and Jingbian, providing a stable gas supply to the first and second Shaan-Jing Gas Pipelines and the first and second West-East Gas Pipelines [9-10].

Aiming at the stable "craton basin" tectonic setting in the Huaqing area of the Ordos Basin, the deep-water sedimentary environment of the semi-deep lake-deep lake area and the special sedimentary system characteristics and the concept of "deep water sedimentation slope-break zone" is proposed, which is equivalent to the current slope classification. The "Ancient Paleo-slope Bending Belt" has been more clearly defined, and its identification method has been analyzed and demonstrated in detail. It is more closely integrated with oil and gas exploration and has more application value [11-14]. The deep-water sedimentation slope-break zone is mainly affected by paleo-geomorphology. It is a slope zone with a certain slope angle and a strip-shaped distribution on the plane due to the rapid accumulation of the delta front subfacies. The deep-water sedimentation slope-break zone is mostly formed in the strong construction. The transitional

zone between the delta front and the semi-deep lake environment belongs to the high-level system domain from the perspective of sequence, the lake basin shrinks, and the provenance rapidly advances to the center of the lake basin. After the sand-rich source quickly enters the semi-deep lake environment, the fluid energy suddenly weakens, and a large number of heavier sand bodies quickly settle and accumulate, and the loose debris that carries the subsequent deposition continues to slide along the slope, near the slope break zone [15-16]. A series of gravity flow slump gravity flow sediments are formed. After entering the deep water area, the gravity flow phase with sand debris flow as the main body is formed, which is located at the intersection of shallow water and deep water. The main controlling factor is sedimentation. The traditional slopes are mainly developed in fault basins and are formed by structural reasons. They are also the focus of attention in the past. Because the slope-break zone is a zone where the accumulation and de-sequence changes frequently, it is easy to form a good reservoir-cap combination. It is also a favorable place for oil and gas accumulation, and has become a hot spot in the study of lithologic reservoirs in recent years [17-18]. However, due to the large number of structural slopes, people pay too much attention to the sedimentary slopes dominated by sedimentation, especially the deep water sedimentation slopes associated with gravity flow lithologic reservoirs.

After intensive study of the 6_3rd section of the Huaqing area, this paper summarizes the identification characteristics of the deep-water sedimentation slope-break zone and its control on reservoir enrichment.

GEOLOGICAL SETTINGS AND METHODS

The Ordos Basin is a Mesozoic-Cenozoic intracontinental basin formed on a basement of Achaean-Paleoproterozoic metamorphic rocks belonging to the western block of the North China Craton [19-24]. In the Huachi and Qingyang Counties of Gansu Province, Huaqing oilfield is tectonically located in the western part of the Shaanbei Slope Belt, where Triassic Yanchang Formation and Jurassic Yan'an Formation are the main two oil-bearing successions with dominant lacustrine delta front and deep water gravity flow deposits [5, 25]. The wide distributions of excellent source rocks and thick reservoirs in the Triassic Yanchang Formation from Ordos Basin are two key factors for the formation of large-area tight oil of the Yanchang Formation [26-27].

The Triassic Yanchang Formation can be divided into ten oil reservoir groups, i.e., Chang 1-Chang 10 (from top to bottom). The main hydrocarbon source layer is the Chang 7 oil reservoir group; the key oil-producing layer consists of the Chang 6 and Chang 8 oil reservoir groups, which is adjacent to the main hydrocarbon source layer. Chang 6 of the Triassic Yanchang Formation in the Jiyuan-Wuqi area is now a gentle west-dipping mono-clinic slope with two major provenances, the northeastern and the northwestern in the early stage. It is a delta-shallow lake sedimentary system, with sandbodies in large area, furthermore, the underlying Member 7 of the Yan chang Formation has a sufficient hydrocarbon supply, and the overlying Member 4-5 of Yanchang Formation could act as good caprocks. Influenced by the tectonic stress and differential compaction, a series of low-amplitude structures has formed in the Chang 6 Member, which is favorable for generating large-area continuous or quasi-continuous oil and gas reservoirs, and large-scale oil reservoirs have been discovered in Chang 6 Member [28-30].

The sandstones of Chang 6_3 reservoir in Huaqing Area are mainly fine-grained and very fine-grained, with main lithology of gray-black, gray, gray-white feldspathic sandstone and lithic feldspar sandstone [9, 15-17]. Pore combination types mainly include intergranular pore–dissolution pore and dissolved pore-intergranular pore. The interstitials are mainly matrix and cements, whereas cements primarily include hydromica, chlorite, ferrocalcite, ankerite, calcite, siliceous matter, and a small amount of argillo ferruginous substance. The rocks are featured by moderate to good sorting, poor roundness with dominant sub-angular shapes and a few angular shapes, primary pore cementation (followed by overgrowth and thin film cementation), and presence of illite, chlorite and illite/smectite mixed layers [31].

Identification Method of Sedimentary Slope Break Zone. (1) Seismic Profile Method. It can be seen from the seismic section that the seismic reflection are multi-period wedge-shaped anterior product characteristics, reflecting the multi-period pre-product characteristics at the end of the delta front (Figure 1). The Ordos Basin, as a large depression basin, has a relatively stable structure, arising or descending as a whole basin. This basin is mainly in lithologic reservoirs, and its stratum has inherited changes. Therefore, the Delta-end wedge-shaped sediments formed in the Chang 6 period has the stratigraphic features which is similar to todays, and the sedimentary slope formed by rapid accumulation provides a prerequisite for the formation of gravity-flow slump.

By combining the research results of the sedimentary facies type, we can find the overlapping part of the two-stage wedge on the seismic section, where the junction of the delta front end and the tail of the gravity flow sliding body is a phase transition zone. The lower in-phase axis has clear and continuous reflection, showing strong lithological differentiation and homogeneity which shows the delta front reflection feature. The upper in-phase axis reflection is fuzzy, internal disorder, showing lithological con-

founding, and strong heterogeneity, which is the reflection characteristic of the sliding phase of the gravity flow. In this way, by continuously tracking the corresponding seismic reflection profile on the plane, we can roughly sketch the distribution of the sediment slope. Since it is usually distributed in a strip shape and formed in the deep water sedimentation area, we will name it "Deep water sedimentation slope".

(2) Formation Thickness Method. Because the sedimentary slope-break zone is a superimposed area of the delta front and the poorly developed part of the turbid body, the reservoir is not developed, mainly composed of argillaceous and argillaceous siltstone deposits, resulting in a slope-break zone [32-33]. The thickness of the formation is quite different from the main phase bands on both sides. By aligning the marking characteristics of the marking layer and the stratum, the isochronous contrast can be used to accurately describe the thickness variation of the stratum (Figure 2). At this time, the strip can be roughly presented on the thick map of the stratum. The thin layer area with the characteristic features can be further clarified by the combination of the slope folds drawn by the seismic section.

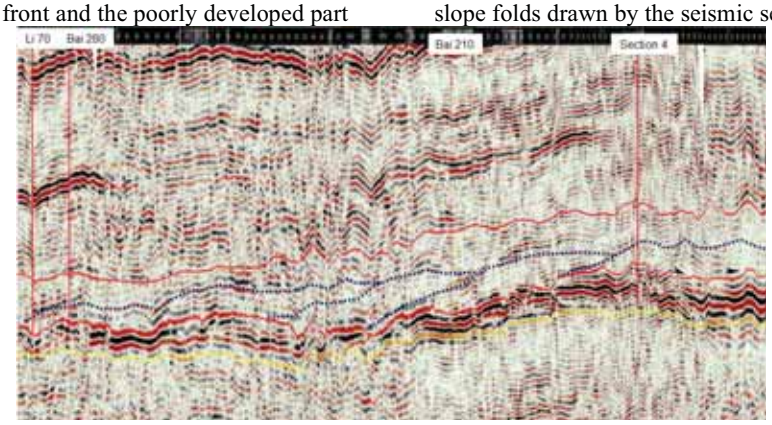

FIGURE 1
The synctlement seismic profile of the north eastern to southwestern direction of the Huaqing area.

FIGURE 2
The formation thickness of Chang 6_3 in Huaqing area.

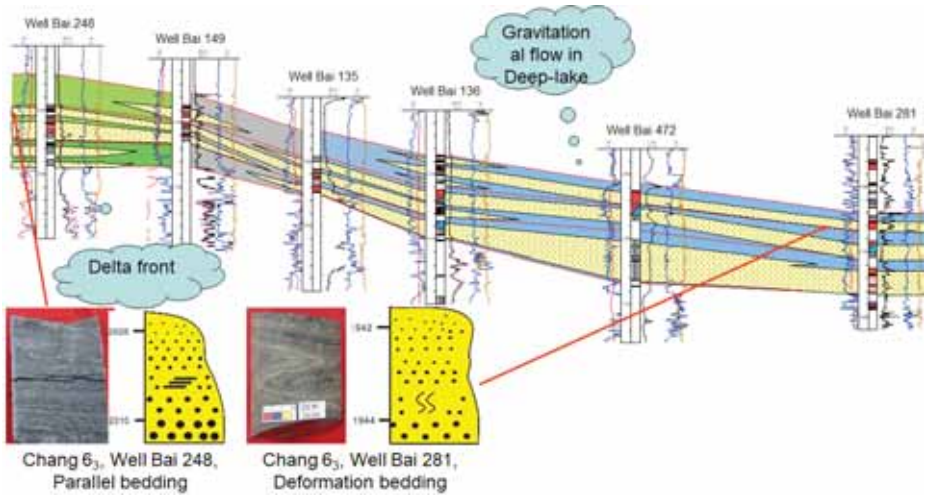

FIGURE 3
Sectional view of the north-south direction of the Chang 6$_3$ sandstone in the Huaqing area.

(3) Profile Comparison Method. The phase transition characteristics of the sedimentary slopes determine that the sand bodies in the belt have a small thickness and are thin and interbedded with the mudstones. The sand bodies are stacked and overlapped, usually with a pinch-out phenomenon. By selecting the direction of the source, the connected well profile of the phase transition zone is connected with the isochronous sand body, which can directly reflect the variation characteristics of the reservoir in the sedimentary slope-break zone [34].

Through the sand body profile of the north-south of the Chang 6$_3$ Formation in the Huaqing area, it can be clearly seen that the upper delta front reservoir and the lower slip turbidite reservoir are developed on both sides of the slope (Figure 3). The main bodies of the two phase belts are respectively enriched, and the existence of sedimentary slopes effectively separates the two reservoirs, forming reservoirs with different sides and substantially different phase and physical characteristics, thus controlling the location and reservoir characteristics of the reservoir. Its regular control over the accumulation can effectively guide us to find similar accumulation patterns in other areas on both sides of the slope, to find relative enrichment areas and to carry out targeted development of different reservoirs.

(4) Phase Transition Method. In order to further describe the distribution range of the sedimentation slope zone, we can also apply some auxiliary methods to give specific boundaries by determining the transition zone of the sedimentary facies [35-36]. Through the core observation of the heart well on both sides of the slope, the approximate position of the slope break can be determined intuitively.

Due to the different depositional mechanisms, the delta front and the gravitational gravity flow have great differences in their sedimentary structure characteristics (Figure 4). The former has obvious scouring phenomenon, and many lithological parallel to the bedding and oblique bedding have traction flow characteristics. Sedimentary structure, lithology is mainly light gray or grayish white, while the latter is characterized by rapid deposition such as slip deformation, groove mode, slot die, heavy load mode, etc. Most of the mudstone is dark mudstone with visible pyrite nodules, reflecting its Low energy and water sedimentation environment. The variation of the transitional sedimentary structural features in the longitudinal position of a single well reveals the evolution of the strength and weakness of the two, thus determining the end position of the phase transition zone controlled by the slope. Due to the different causes of the phase bands on both sides of the slope, the lithological combination and electrical characteristics are very different.

RESULTS AND DISCUSSION

The Characteristics of the Delta Front and the Turbidite. The delta frontal phase has a smooth curve of the box-shaped, clock-shaped or funnel-shaped. The longitudinal continuity of the sand body is good with large single-stage thickness. The turbidite has similar curve morphological characteristics, but the curve toothing phenomenon is obvious. The longitudinal multi-stage development is superimposed with poor continuity and strong heterogeneity (Figure 5).

Different ways of stacking on both sides of the slope break belt can also be used as one of the signs to determine its specific boundary. Most of the reservoirs in the delta frontal phase are submerged distributary channel combinations such as “superimposed river” and “Bashanghe”, while landslides are dominated by multi-stage turbidite channel superposition (Figure 6).

FIGURE 4
Sedimentary tectonic features of the Chang 6_3 stratum in Huaqing area.

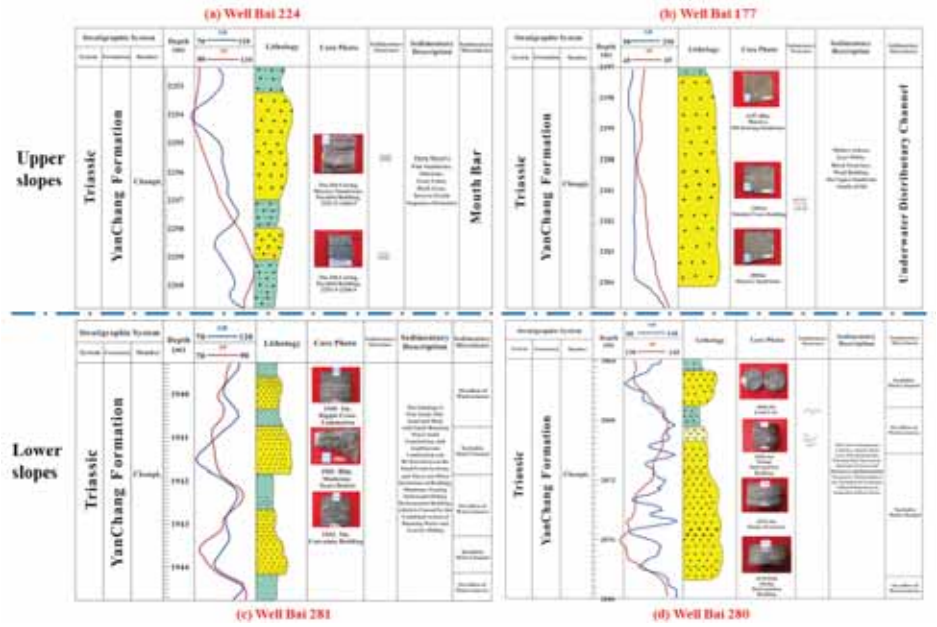

FIGURE 5
Lithologic combination characteristics on both sides of the sedimentary slope-break zone in Huaqing area.

Due to the control of the ancient topography and sedimentary facies, the flow characteristics of the sedimentary media under the slope are changed. The flow characteristics of the deposition medium can be judged by the support structure of the debris particles. The end of the delta front on the slope belongs to the particle support to reflect the handling characteristics of the traction flow, while the slope is a semi-deep lake-deep lake. The environment, mainly the heterogeneous support reflects the gravity flow handling characteristics, and the distribution of these phenomena on the plane can also be roughly identified by the (microscopic observation) distribution of the slope folds (Figure 7).

The clastic particles of the Bai 111 and Bai 209 wells have good roundness, good sorting and intergranular pore development, which are typical particle supports (Figure 8). The particles in Yuan 285, Bai 286, Wu 64, Wu 61 well have bad roundness, poor sorting, and few intergranular pores. Among them, the 285 microscopic sheet can be seen to have good roundness, but the sorting is very poor. The

particle size is mixed, reflecting the characteristics of secondary handling.

Through the statistical analysis of the mineral content of the Chang 6_3 reservoir in Huaqing area, it can be seen that the delta front has a large difference with the turbid body. The former is dominated by the traction flow, the mud is less, and the chlorite content is high. Intergranular pores are well developed in these formations. However, the latter is dominated by gravity flow. Under the rapid accumulation, the sand and mud are mixed, and the content of heterobase is high. The pore type in these formations are mainly dissolved pores. The microscopic difference is reflected in the difference of reservoir mineral content on both sides of the slope. The difference in the plane can also reflect the position of the sedimentation slope.

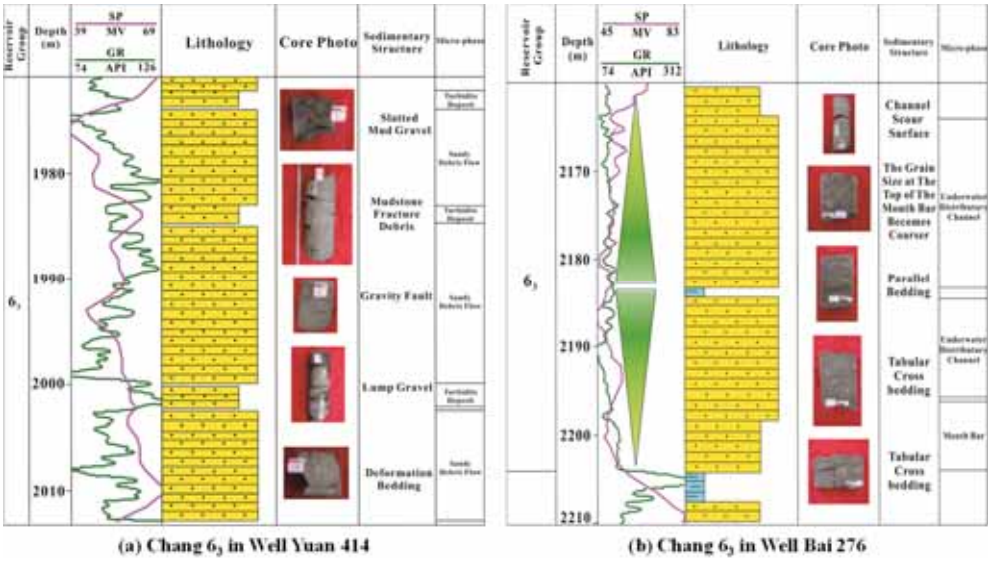

FIGURE 6
Huaqing Chang 6_3 stratum multi-stage sandy debris flow superimposed type.

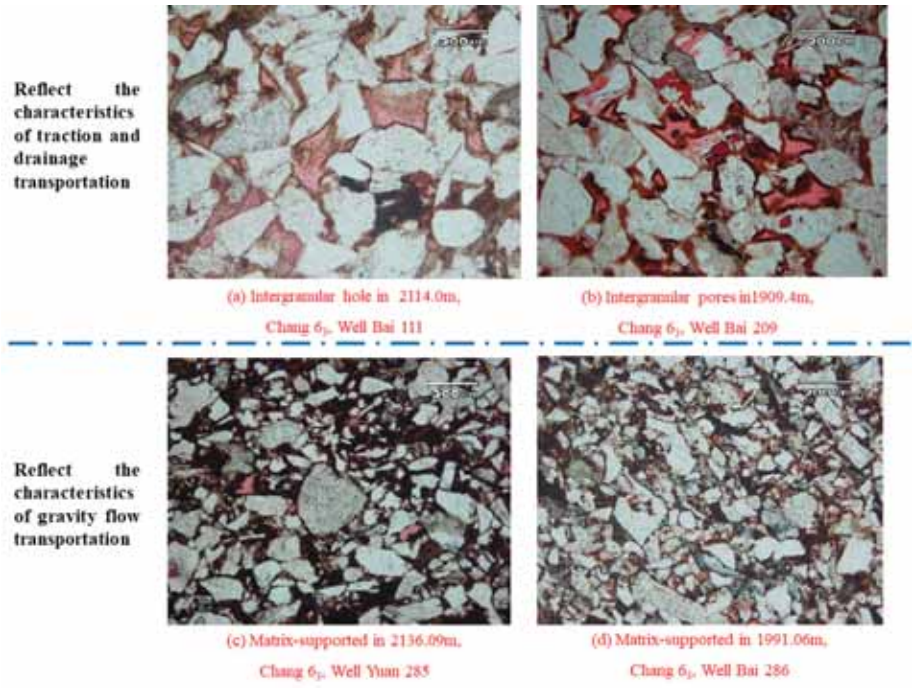

FIGURE 7
Characteristics of single polarizer under the Chang 6_3 reservoir in Huaqing area

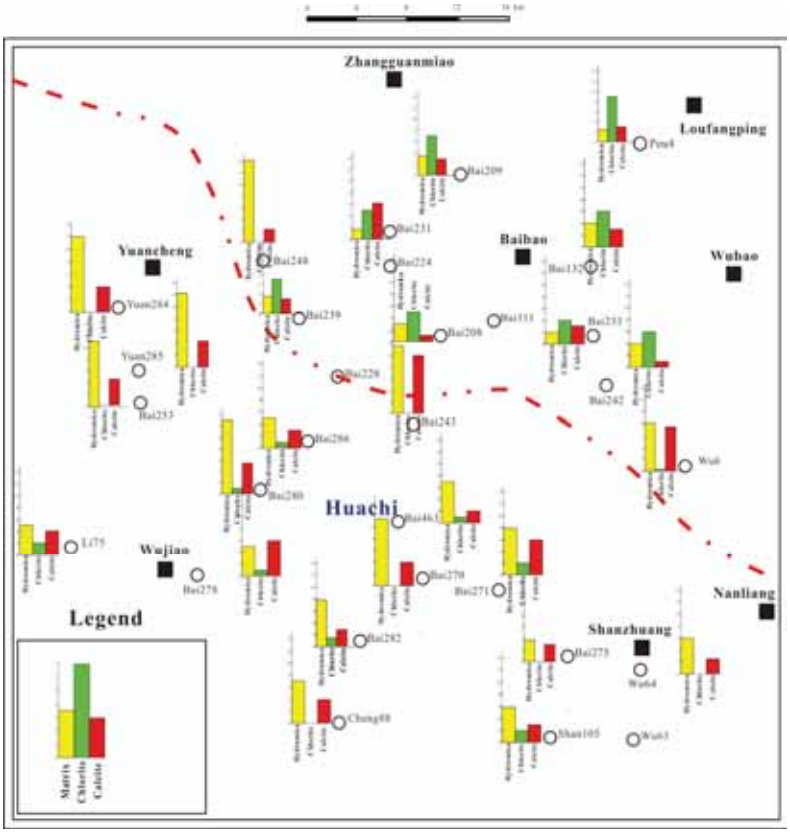

FIGURE 8
Analysis of the characteristics of the Chang 6_3 reservoir in Huaqing area

Distribution Characteristics of Sedimentary Slope-breaking Belt and Its Control on Accumulation. (1) Through the comprehensive application of the previous identification methods of various slope slopes, the distribution position and influence range on the plane can be accurately described. The width of the sedimentary slope-break zone of the Chang 6 stratum in Huaqing area varies from 3 to 8 km based on the richness of the source. The belt with sufficient source and strong energy has a relatively narrow transition zone (sedimentation slope-break zone), while the sandstone with weak source and weak energy has a correspondingly wide transition zone, resulting in a slope width on the plane. The scope has changed a lot. As the number of wells increases, the understanding of the stratum will continue to deepen, and the extent and shape of the slope breaks will also change.

(2) The depiction of sedimentary slope-breaking belts is of great significance for mastering the law of reservoir enrichment. The proposed method of sedimentary slope-breaking zone has guiding significance for depicting the plane enrichment law of Huaqing Chang 6 ultra-low permeability reservoir. First of all, the slope break zone itself is an unfavorable zone for accumulation. The reservoir is thin and the physical properties are poor. It is difficult to build the scale on a large scale. Therefore, we should avoid looking for the enrichment zone within the slope break zone to avoid the phenomenon of "well falling". Secondly, the upper part of the slope is the delta front reservoir, which has good physical properties and strong uniformity. The reservoirs are mostly strip-like. Although the overall oil layer thickness is thinner than the turbidite under the slope, the single well production is often high. The upper slope is the development zone of relatively high-quality oil reservoir. The sedimentation of turbidite fan is below the slope. The shale content is relatively high, the physical property is poor, the heterogeneity is strong, the oil layer thickness is large, and the main body of the reservoir is flaky. Affected by the paleo-geomorphology and its own slumping nature, the main phase belts are mostly distributed in the relatively "deep area". Finally, the enrichment law of the two is affected by the phase transition and the slope-break zone. The enrichment direction of the upper delta front should be traced back to the source, while the lower turbidity of the turbidity should be traced.

CONCLUSIONS

In this study, by using the combination of the seismic data and the core information from the wells targeting in Chang 6 Formation in Huaqing area, we

analyzed and distinguished the properties of the delta front and the turbidite. The main conclusions can be seen below:

(1) The curve of the front delta is very smooth. The sand bodies of the front delta have good continuity and large thickness value while the curve of the turbidite is not very smooth with poor connectivity and high heterogeneity. The front delta has the traction flow handling characteristics while the turbidite shows the gravity flow handling feature.

(2) The front delta formation has little clay and abundant interparticle pores while the turbidite has rich dissolved pores. The favorable exploration and development direction above the slope will be traced to the main body belt of the diversion channel. Below the slope, the sand debris flow sand body should be traced to the lake center.

ACKNOWLEDGEMENTS

This work was financially supported by the National Science and Technology Major Project of China (No. 2017ZX05001).

REFERENCES

[1] Fu, Q., Li, Y. (2010) Characteristics of Slope Breaks and Its Implication on Petroleum Geology in Yanchang Formation Chang 6 (Late-Triassic) of Ordos Basin. Acta Sedimentologica Sinica. 28(2), 294-298.

[2] Liu, F., Zhu, X., Li, Y., Xu, L., Zhu, S., Xue, M. (2015) Characteristics of the Late Triassic Deep-water Slope Break Belt in Southwestern Ordos Basin and Its Control on Sandbodies. Geological Journal of China Universities. 21(4), 674-684.

[3] Li, M., Gao, J. (2010) Basement faults and volcanic rock distributions in the Ordos Basin. Science China Earth Sciences. 53(11), 1625-1633.

[4] Teng, J., Wang, F., Zhao, W., Zhang, Y., Zhang, X., Yan, Y., Ruan, X. (2010) Velocity structure of layered block and deep dynamic process in the lithosphere beneath the Yinshan orogenic belt and Ordos Basin. Chinese Journal of Geophysics. 53(1), 67-85.

[5] Li, K., Xiong, S., Niu, B., Yang, K., Feng, J. (2018) The main controlling factors of gravity flow of the Upper Triassic in the southern Ordos Basin. Journal of Northwest University (Natural Science Edition). 48(4), 603-610.

[6] Pereira, R., Alves, M. (2011) Margin segmentation prior to continental break-up: A seismic–stratigraphic record of multiphased rifting in the North Atlantic (Southwest Iberia). Tectonophysics. 505(1-4), 17-34.

[7] Stead, D., Wolter, A. (2015) A critical review of rock slope failure mechanisms: the importance of structural geology. Journal of Structural Geology. 74, 1-23.

[8] Hill, J.C., Brothers, D.S., Craig, B.K., ten Brink, U.S., Chaytor, J.D., Flores, C.H. (2017) Geologic controls on submarine slope failure along the central U.S. Atlantic margin: Insights from the Currituck Slide Complex. Marine Geology. 385, 114-110.

[9] Liu, X. (2017) Analysis of tight oil accumulation characteristics and exploration potential of Yanchang Formation in Ordos Basin. Dissertation. Chengdu: Chengdu University of Technology.

[10] Liu, F., Li, R., Zuo, Z., Liu, X., Zhao, B., Wu, X., Li, D. (2018) Genesis of formation water in the 6th member of the Upper Triassic Yanchang Formation in southern Ordos Basin and its petroleum significance. Oil and Gas Geology. 39(6), 1179-1189.

[11] Li, W., Liu, X., Zhang, Q., Guo, Y., Li, K., Yuan, Z., Wang, Y., Ma, Y., Bai, J., Yang, B., Li, Z. (2019) Deposition evolution of Middle-Late Triassic Yanchang Formation in Ordos Basin. Journal of Northwest University (Natural Science Edition). 49(4), 605-621.

[12] Lei, X., Zhang, L., Yu, B., Li, J., Wu, J. (2009) Sandstone diagenesis of Chang 4+5 reservoir group of the Upper Triassic Yanchang Formation in Yaodian oilfield, central Ordos basin, China. Geological Bulletin Of China. 28(5), 603-608.

[13] Wang, J., Liu, C., Guo, Z., Zhang, D. (2015) Sedimentary response of regional tectonic transformation in Late Triassic Yanchang period at the central and southern Ordos Basin. Earth Science Frontiers. 22(3), 194-204.

[14] Wang, Z., Zhou, H., Wang, X., Jing, X. (2015) Characteristics of the crystalline basement beneath the Ordos Basin: constraint from aeromagnetic data. Geoscience Frontiers. 6(3), 465-475.

[15] Zhang, L., Liu, C., Fayek, M., Wu, B., Lei, K., Cun, X., Sun, L. (2017) Hydrothermal mineralization in the sandstone-hosted Hangjinqi uranium deposit, North Ordos Basin, China. Ore Geology Reviews. 80, 103-115.

[16] Zhang, C., Diwu, C., Kröner, A., Sun, Y., Luo, J., Li, Q., Zhao, J. (2015) Archean-Paleoproterozoic crustal evolution of the Ordos Block in the North China Craton: Constraints from zircon U-Pb geochronology and Hf isotopes for gneissic granitoids of the basement. Precambrian Research. 267, 121-136.

[17] Karlson, M., Karlsson, C., MoRtberg, U., Olofsson, B., Balfors, B. (2016) Design and evaluation of railway corridors based on spatial ecological and geological criteria. Transportation Research Part D. Transport and Environment. 46, 207-228.

[18] Bünz, S., Mienert, J., Berndt, C. (2003) Geological controls on the Storegga gas-hydrate system of the mid-Norwegian continental margin. Earth and Planetary Science Letters. 209(3-4), 291-307.

[19] Qiu, X., Liu, C., Wang, F., Deng, Y., Mao, G. (2015) Trace and rare earth element geochemistry of the Upper Triassic mudstones in the southern Ordos Basin, central China. Geological Journal. 50(4), 399-413.

[20] Qiu, X., Liu, C., Mao, G., Deng, Y., Wang, F., Wang, J. (2015) Major, trace and platinum-group element geochemistry of the Upper Triassic nonmarine hot shales in the Ordos Basin, central China. Applied Geochemistry. 53, 42-52.

[21] Li, N., Li, G., Wu, C., Xie, J., Li, L. (2014) The Application of Sandy Debris Flow under the Contrl of Slope Break to Oil-Das Exploration. Acta Geologica Sichuan. 4, 505-509.

[22] Yang, H., Fu, Q., Qi, Y., Zhou, X., Gong, L., Huang, S. (2016) The Paleontology Phase Zones and Its Geological Significance on the Late Triassic Yanchang Stage Palaeo-lacustrine Ordos Basin. Acta Sedimentologica Sinica. 34(4), 688-693.

[23] Hu, H., Zhang, Z., Yu, J., Song, J., Sun, B., Liu, L., Xue, J. (2011) Evolution and controls of the slope breaks on the Yanchang Formation sandstones in the Ordos Basin: An example from the Chang-6 oil measures of the Yanchang Formation. Sedimentary Geology and Tethyan Geology. 31(2), 43-48.

[24] Martinez, J., Raiber, M., Dioni, I. (2017) Using 3D geological modelling and geochemical mixing models to characterise alluvial aquifer recharge sources in the Upper Condamine River catchment, Queensland, Australia. Science of the Total Environment. 574, 1-18.

[25] Woods, M. (2015) Applied palaeontology in the Chalk Group: quality control for geological mapping and modelling and revealing new understanding. Proceedings of the Geologists' Association. 126(6), 777-787.

[26] Shi, B., Huang, J., Chen, L., Yang, F., Lv, J. (2016) Compaction factors of tight reservoirs in the seventh member of Yanchang Formation in the central Ordos Basin during the Late Triassic. Petroleum Geology and Experiment. 38(4), 528-535.

[27] Qi, Y., Deng, X., Chu, M., Li, Y., Deng, J., Shi, Z. (2014) Analysis of Depositional Environment of Chang 8 of Upper Triassic, Ordos Basin. Geological Science and Technology Information. 33(4), 170-176.

[28] Liang, Z., Zhou, Y., Loon, A. (2018) Soft-sediment deformation structures induced by rapid sedimentation in early cretaceous turbidites, Lingshan Island, eastern China. Canadian Journal of Earth Sciences. 55(2), 118-129.

[29] Han, C., Jiang, Z., Han, M., Wu, M., Lin, W. (2016) The lithofacies and reservoir characteristics of the Upper Ordovician and Lower Silurian black shale in the southern Sichuan Basin and its periphery, China. Marine and Petroleum Geology. 75, 181-191.

[30] Yang, R., Jin, Z., Van Loon, A., Han, Z., Fan, A. (2017) Climatic and tectonic controls of lacustrine hyperpycnite origination in the late Triassic Ordos Basin, central China: Implications for unconventional petroleum development. AAPG Bulletin. 101(01), 95-117.

[31] Liu, X., Gui, X., Ding, X., Zhang, S. (2014) Coupling analysis of Late Triassic event deposition and Qinling orogeny in the south of Ordos Basin. Journal of Northeast Petroleum University. 38(4), 59-66.

[32] Xiong, L., Liu, C., Qiu, X., Du, F. (2015) Tectonic Activity of Late Triassic in Ordos Basin and Its Effect on the Formation of High Quality Source Rocks. Geological Science and Technology Information. 34(2), 109-114+136.

[33] Wang, G., Chang, X., Yin, W., Li, Y., Song, T. (2017) Impact of diagenesis on reservoir quality and heterogeneity of the upper Triassic Chang 8 tight oil sandstones in the Zhenjing Area, Ordos Basin, China. Marine and Petroleum Geology. 83, 84-96.

[34] Yang, R., He, Z., Qiu, G., Jin, Z., Sun, D., Jin, X. (2014) A late Triassic gravity flow depositional system in the southern Ordos Basin. Petroleum Exploration and Development. 41(6), 724-733.

[35] Soldo, L., Vendramini, M., Eusebio, A. (2019) Tunnels design and geological studies. Tunnelling and Underground Space Technology. 84, 82-98.

[36] De-Campos, A., De Cedro, D., Tejerina-Garro, F., Bayer, M., Carneiro, G. (2013) Spatial distribution of tropical wetlands in central brazil as influenced by geological and geomorphological settings. Journal of South American Earth Sciences. 46, 161-169.

Received: **01.11.2019**
Accepted: **21.01.2020**

CORRESPONDING AUTHOR

Aihua Xi
School of Geoscience and Technology,
Southwest Petroleum University,
Chengdu 610500 – China

e-mail: taoliang1121@126.com

© by PSP Volume 29 – No. 04A/2020 pages 2942-2950 Fresenius Environmental Bulletin

QUANTITATIVE PREDICTION OF ORGANIC COMPONENTS IN SHALE OIL RESERVOIRS USING AN IMPROVED ΔLOG *R* METHOD

Yinhao Dong[1,2,*]

[1] College of Geophysics and Petroleum Resources, Yangtze University, Wuhan 430100, China
[2] Liaohe Oilfield Exploration and Development Research Institute, PetroChina, Panjin 124000, China

ABSTRACT

The use of logging technology to evaluate the source rock can establish the quantitative relationship between the logging data and the source rock geochemical parameters and calculate the longitudinal continuous distribution of the geochemical parameters of the source rock. In this paper, we take the Paleogene shale oil reservoir in the Damintun Sag, Liaohe Oilfield, eastern China as an example. We first performed logging identification on shale oil reservoirs. Then, the organic component in the shale oil reservoir was quantitatively predicted using the improved Δlog R method. The results show that, the shale oil logging response characteristics of the Damintun Sag are characterized by "three highs and one low": high gamma, high resistance, high acoustic wave time diffeence, and low rock density. When using the improved △log R method, the superposition coefficient *K* affect the accuracy of calculating the organic carbon content. With the change of *K* value from small to large, the accuracy of identifying the organic carbon content should first increase and then decrease, and the turning point from increasing to decreasing is the optimal superposition coefficient. The improved model can calculate the organic carbon content without the need for LOM and ΔTOC parameters and without the need to manually read baseline values. The calculated values of the various geochemical parameters using the improved model in the Damintun Sag are consistent with the measured values, indicating the reliability of this method.

KEYWORDS:
Shale oil reservoir, organic components, improved Δlog *R* method, geochemical parameter

INTRODUCTION

Source rock is the basic element of oil and gas accumulation and petroleum system. Its accurate, objective and rapid evaluation is the primary task of oil and gas exploration and evaluation in petroleum-bearing basins. The enrichment degree of shale oil and gas resources affects its development effect [1-4]. Only large abundance of organic matter can form large-scale shale oil and gas. In general, hydrocarbon source rock evaluation often uses experimental methods to determine its organic matter abundance, organic matter type and organic matter maturity and other geochemical indicators. However, using the logging technology to evaluate the source rock, a quantitative relationship model between the logging data and the source rock geochemical parameters can be established, and then the longitudinal continuous distribution of the geochemical parameters of the source rock segment can be calculated [5-7]. This will undoubtedly make up for the lack of continuous laboratory test data, and provide more accurate and reasonable parameter values for the evaluation of source rock. However, when using the logging method to evaluate the source rock, it is necessary to combine the geological and geochemical characteristics of the source rock and comprehensively consider various influencing factors to accurately conduct the logging evaluation of the source rock.

Source rocks are usually dark shale and limestone with organic matter deposited in a low-energy environment [8-9]. Due to the inherent physical and chemical properties of the source rock, its logging response characteristics are different from those of other lithology rocks. It is inevitable that the source rock will have some differences in acoustic time difference logging, density logging and resistivity logging than other sedimentary rocks with little or no organic matter. In general, the higher the organic carbon content (chloroform asphalt "A"/S_1), the greater the anomaly on the log, and the organic carbon content (chloroform asphalt "A"/S_1) can be calculated using logout anomalies [10]. Based on these characteristics, it is possible to quantitatively evaluate the content of organic and inorganic components in shale oil reservoirs using well calculation methods. In this paper, the Paleogene shale oil reservoirs in the Damintun Sag, Liaohe Oilfield, eastern China, were used as examples to quantify the organic components in shale oil reservoirs using the △logR method. This study has important refer-

ence value for the exploration and development of tight oil reservoirs.

MATERIALS AND METHODS

Research Area and Target Layer. China is currently developing shale oil. As the main type of unconventional oil and gas resources, shale oil has the characteristics of large reserves, low permeability and low abundance [11-13]. The Shahejie Formation of the Paleogene in the Liaohe Oilfield in eastern China is rich in shale oil resources. Among them, the Damintun Sag, the Leijia Sag and the Qingshui Sag are the three main areas of shale oil exploration in this area. This paper takes the shale oil reservoir of the Shahejie Formation of the Paleogene in the Damintun Sag as an example to conduct quantitative prediction research on organic and inorganic components. The studied horizons are the $E_2S_4^2$ interval and the $E_2S_4^1$ interval of the fourth segment of the Shahejie Formation, and the $E_2S_3^4$ interval of the third segment of the Shahejie Formation.

ΔlogR Method. The ΔlogR technology was proposed by EXXON/ESS Petroleum Company and successfully applied worldwide [14-15]. The technique superimposes the acoustic time difference in arithmetic coordinates and the resistivity curve in arithmetic logarithmic coordinates with a predetermined superposition coefficient (the commonly used superposition factor is 0.02 ft/μs, and sometimes other values are used, but the superposition coefficient is not regarded as a variable that affects the accuracy of calculating organic carbon), so that the two curves coincide at the fine non-oil rock and are determined as the baseline position. After the baseline is determined, the reading between the two curves at the logarithmic resistivity coordinates is ΔlogR.

In oil-bearing reservoir rocks or organic-rich non-reservoir rocks, there is a ΔlogR between the two curves, and the natural gamma curve and the natural potential curve can be used to identify and exclude the reservoir interval [16-18]. In the organic-rich mudstone section, there are two cases in which the two curves are separated: (1) There is no oil and gas generation in the immature organic-rich rock, and the difference between the two curves is only caused by the response of the acoustic time difference curve. (2) In the mature source rock, in addition to the acoustic time difference curve response, due to the presence of liquid hydrocarbons, the resistivity increases, resulting in a larger spacing between the two curves (Figure 1).

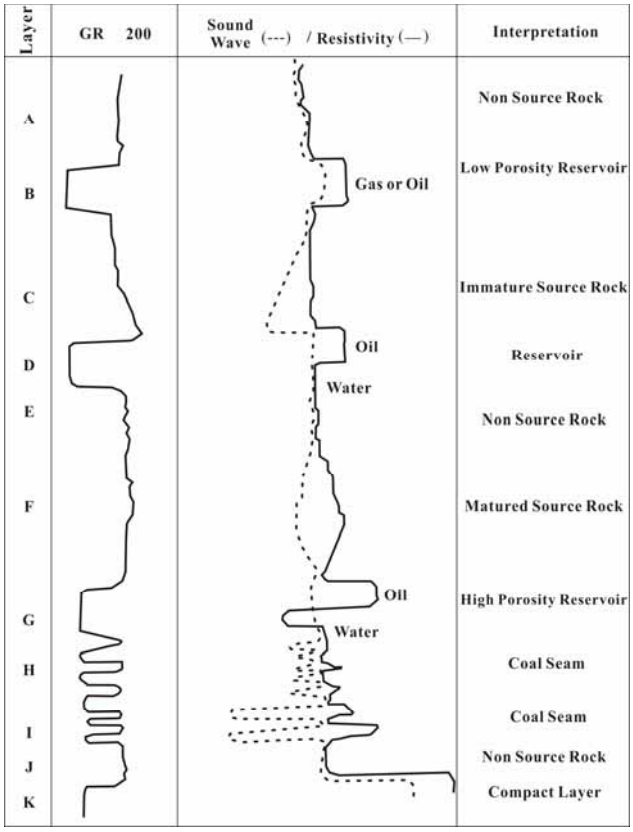

FIGURE 1
Identification of high organic matter-bearing formations using the ΔlogR method.

The equation for calculating Δlog R based on the superposition of acoustic time difference and resistivity is:

$$\Delta logR = \log_{10}(R/R_{Baseline}) + 0.02(\Delta t - \Delta t_{Baseline}) \quad (1)$$

In equation (1), ΔlogR is the distance between the two curves; R is the measured resistivity of the tool (Ω·m); $R_{Baseline}$ is the resistivity (Ω·m) corresponding to the baseline; Δt is the measured acoustic time difference (μs/ft). ΔlogR is linearly related to organic carbon and is a function of maturity. The empirical formula for calculating organic carbon from Δlog R is:

$$TOC = \Delta logR \times 10\,(2.297 - 0.1688LOM) + \Delta TOC \quad (2)$$

The TOC in formula (2) is the calculated organic carbon content (%); LOM reflects the organic matter maturity and can be obtained from a large number of sample analyses (such as vitrinite reflectance, thermal index, T_{max} analysis), or from burial history and thermal evolution history. ΔTOC is the background value of organic carbon content.

From the above analysis, it is known that the method for calculating the organic carbon content before the improvement needs to determine the LOM and ΔTOC, and the baseline value needs to be manually read, and the superposition coefficient is given in advance [19-21]. It has the following problems: (1) If the LOM is not properly selected, the calculation of the absolute content of organic carbon will produce an overall error. For areas lacking the maturity parameter, the application of this method is also limited; (2) ΔTOC needs to be determined manually and the error is large; (3) The process of reading the baseline is cumbersome and easy to introduce errors; (4) The predetermined superposition coefficient K is likely to affect the accuracy of the calculated organic carbon content. That is to say, the superposition coefficient K has a certain influence on the calculation of the organic carbon content, and the model needs to be improved and optimized.

We select a well that has complete geochemical data and good log data quality as a verification well for the ΔlogR method model. The model before the improvement uses a fixed superposition coefficient of 0.02. In order to determine the effect of the superposition coefficient on the calculation of organic carbon, first fix the LOM and ΔTOC values, select different superposition coefficients K, and record the model to calculate the organic carbon under different K values [22-24]. The correlation between the calculated organic carbon content and the analyzed organic carbon content at different K values is shown in Figure 2. It can be seen from Figure 2 that the correlation R^2 between ΔlogR and measured organic carbon shows a regular change with the superposition coefficient K, indicating that the superposition coefficient K does affect the accuracy of calculating the organic carbon content.

Now change the formula (1) to

$$\Delta logR = \log(R/R_{Baseline}) + K(\Delta t - \Delta t_{Baseline}) \quad (3)$$

Where,

$$K = \log(R_{max}/R_{min})/(\Delta t_{max} - \Delta t_{min}) \quad (4)$$

The physical meaning of the K value is the number of units of resistivity for each acoustic time difference (μs/ft) corresponding to logarithmic coordinates. The log $(R/R_{Baseline})$ in equation (3) is dimensionless, $(\Delta t - \Delta t_{Baseline})$ is dimensioned, and the geological significance of K is to convert $(\Delta t - \Delta t_{Baseline})$ into a dimensionless number, thus the $(\Delta t - \Delta t_{Baseline})$ is equivalent to the log $(R/R_{Baseline})$ magnitude and together constitutes Δlog R. When each resistivity unit in the specified logarithmic coordinates corresponds to a 50 μs/ft acoustic time difference scale range in arithmetic coordinates, the K value is 0.02.

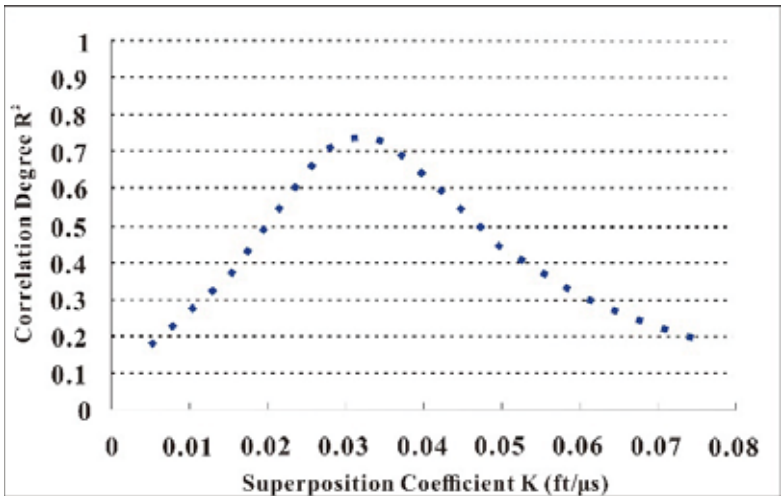

FIGURE 2

Correlation R^2 distribution between the calculated organic carbon using ΔlogR method and the measured organic carbon at different K values.

After assuming the baseline, it is not difficult to get:

$\Delta t_{Baseline} = \Delta t_{max}\text{-}\log(R_{Baseline}/R_{min})/K$ (5)

The $\Delta t_{Baseline}$ and the $R_{Baseline}$ have the same meanings as in equation (1). $R_{min}(\Delta t_{min})$ and $R_{max}(\Delta t_{max})$ are the minimum and maximum values of the resistivity (acoustic wave time difference) curve scale when the acoustic time difference and the resistivity curve are superposed, respectively. Substituting equations (4) and (5) into equation (3), equation (3) can be further derived as:

$\Delta logR = logR + \log(R_{max}/R_{min})/(\Delta t_{max}\text{-}\Delta t_{min}) \times (\Delta t\text{-}\Delta t_{max})\text{-}logR_{min}$ (6)

Since there are often multiple baseline values for a well, the well segment needs to be divided to establish an explanatory relationship [25-27]. The variation of R_o in the depth range of the model is generally small, so that 10 (2.297-0.1688LOM) in the formula (2) can be regarded as a fixed value, which is denoted as A. The formula (2) can be modified to be within the depth range of the model

$TOC = A \times \Delta Log\ R + \Delta TOC$ (7)

Substituting equations (4) and (6) into equation (7)

$TOC = A \times [Log\ R + K(\Delta t\text{-}\Delta t_{max}) - Log\ R_{min}] + \Delta TOC$

$= A \times LogR + AK \times \Delta t - A(K\Delta t_{max} - Log\ R_{min}) + \Delta TOC$ (8)

Where, A, Δt_{max}, R_{min}, and ΔTOC are constants. Obviously, the calculated organic carbon content is affected by the superposition coefficient K. Let K be the optimal value (the optimal K value can maximize the correlation R^2 between the calculated organic carbon and the measured organic carbon), then the improved $\Delta LogR$ model can be obtained:

$TOC = a \times logR + b \times \Delta t + c$ (9)

Where a, b, and c are the coefficients of the fitting formula. In this way, the improved model can calculate the organic carbon content without the need for LOM and ΔTOC parameters and without the need to manually read baseline values.

If you want to improve the correlation between $\Delta logR$ and organic carbon, the key is to find the optimal K value [28-29]. When the value of K is small (large), the ability to recognize hydrocarbon fluids (kerogen) in the source rock is strong, and the ability to recognize kerogen (hydrocarbon fluid) is weak. At the same time, when the K value is small (larger), it mainly depends on a log curve response, and often cannot effectively eliminate the interference of the porosity factor on the organic carbon logging response. Therefore, the accuracy of identifying the organic carbon content when the K value is small (large) is not high. The change in the K value from small to large is a process from the identification of hydrocarbons to the simultaneous identification of hydrocarbons and kerogen. Therefore, in theory, with the change of K value from small to large, the accuracy of identifying the organic carbon content should first increase and then decrease, and the turning point from increasing to decreasing is the optimal superposition coefficient.

RESULTS AND DISCUSSION

Logging Identification of Shale Oil Reservoirs. Conventional logging methods for identifying shale oil include natural gamma logging, resistivity logging, acoustic wave time difference logging, and formation density logging.

The natural gamma value of the shale oil layer usually shows a high value [30-31]. The main reasons are: (1) the shale content in the shale is high, the higher the shale content, the stronger the gamma radioactivity; (2) some organic matter contains high radioactive substances. The gamma value of a typical shale shows a high value (>100 API). In contrast, sandstone and coal seams show low values.

Resistivity logging. The factors affecting the shale oil resistivity are more complicated, including: (1) high shale and mudstone content and high irreducible water saturation; (2) the low porosity and low permeability of the shale oil reservoir make the infiltration range of the mud filtrate very small, the values of the depth and shallow curves are very similar, which reflects the low permeability of the shale oil reservoir; (3) the resistivity of organic matter is high, and the resistivity of kerogen is infinite. In the formation with high abundance of organic matter, the resistivity log value is high.

Acoustic wave time difference logging. The acoustic wave time difference of the shale oil reservoir is shown as a high value. Shale is denser than mudstone, with low porosity and acoustic time difference between mudstone and sandstone. When the crack occurs, the oil layer has a cyclical fluctuation reaction, or the curve suddenly rises high. When the shale organic matter content increases, the acoustic wave time difference increases; if the acoustic wave value is too small, the organic matter abundance is low [32-34]. Formation density logging. The formation density is low. The formation density value actually refers to the electron density of the formation, and the electron density corresponds to the volumetric mass of the formation. The shale density is low, which is lower than the sandstone and carbonate rock formation density logs, but much higher than the coal seam and anhydrite formation density values. An increase in the content of organic matter and hydrocarbon gases results in lower formation density values. If there is a crack, the formation density log will also decrease.

Overall, the shale oil logging response characteristics of the Damintun Sag are characterized by "three highs and one low": high gamma, high re-

sistance, high acoustic wave time diffeence, and low rock density.

Quantitative Prediction of Organic Component Content in Shale Oil Reservoirs. In the wells of the Damintun depression, a well with a complete measured TOC value and a continuous lithology profile and complete logging data is selected as the standard well for modeling. In this paper, the wells of An 64, An 92 and An 1 are taken as examples to model and evaluate the TOC and chloroform asphalt "A" and S_1 respectively. The modeling results for each well are as follows:

In the process of modeling TOC of $E_2S_4^2$ segment of Well An 64, the non-source rock segment was eliminated. At the same time, we carefully studied the reliability of logging data for mudstone intervals less than 1 m thick and the logging data for abnormal locations of boreholes. The correlation coefficient between TOC and ΔlogR measured in the depth range of 0.5 m reached 0.968 8 (Table 1), indicating a good correlation (Figure 3). Therefore, it is feasible to calculate the TOC using the fitting equation of ΔlogR and TOC of An 64 well.

In the process of modeling chloroform asphalt "A" of $E_2S_4^1$ segment of Well An 92, the non-source rock segment was eliminated. At the same time, we carefully studied the reliability of logging data for mudstone intervals less than 1 m thick and the logging data for abnormal locations of boreholes. The correlation coefficient between chloroform asphalt "A" and ΔlogR measured in the depth range of 0.5 m reached 0.933 3 (Table 2), indicating a good correlation (Figure 4). Therefore, it is feasible to calculate the chloroform asphalt "A" using the fitting equation of ΔlogR and chloroform asphalt "A" of An 92 well.

TABLE 1
Model parameter statistics in logging identification (An 64 well, $E_2S_4^2$ interval).

Well name	Model	Model coefficient a	Model coefficient b	R^2	Composite coefficient
An 64	R_{25}-AC	2.170 4	-0.125 1	0.968 8	0.05

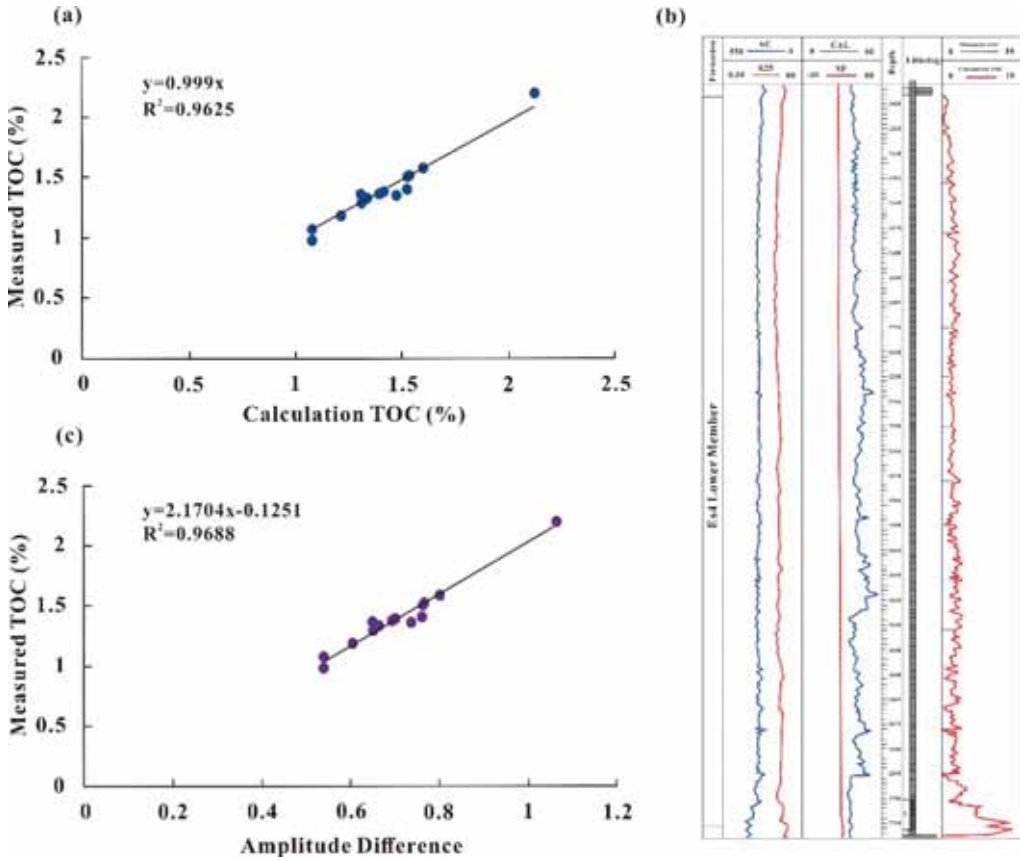

FIGURE 3
R_{25}-AC shale TOC logging identification (An 64well, $E_2S_4^2$ interval).
Notes: (a) TOC using log calculation VS. measured TOC;(b) Shale amplitude difference VS. measured TOC;(c) Shale TOC logging identification results.

TABLE 2
Model parameter statistics in logging identification (An 92 well, $E_2S_4^1$ interval).

Well name	Model	Model coefficient a	Model coefficient b	R^2	Composite coefficient
An 92	R_{25}-AC	0.096 7	-0.004 4	0.933 3	0.05

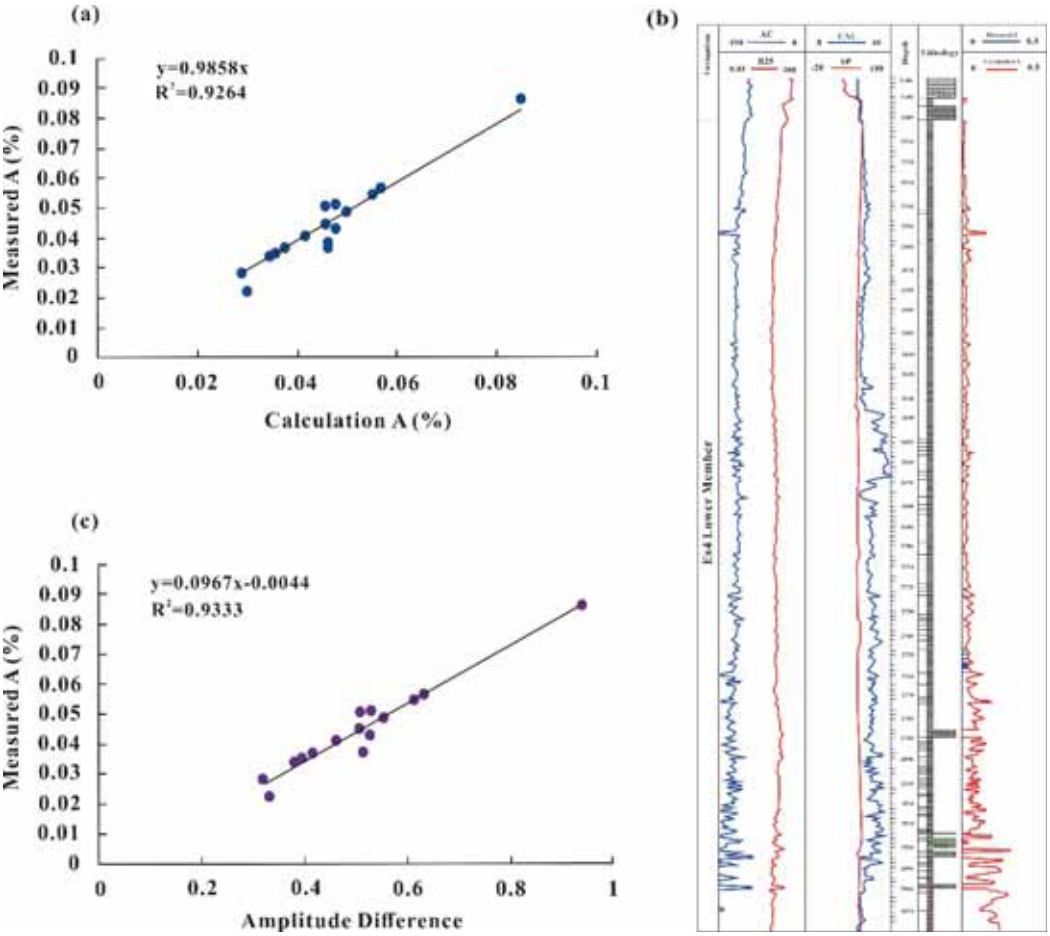

FIGURE 4
R_{25}-AC shale chloroform asphalt "A" logging identification (An 92well, $E_2S_4^1$ interval).
Notes: (a) Chloroform asphalt "A" using log calculation VS. measured chloroform asphalt "A";(b) Shale amplitude difference VS. measured chloroform asphalt "A";(c) Shale chloroform asphalt "A" logging identification results.

TABLE 3
Model parameter statistics in logging identification (An 1 well, $E_2S_3^4$ interval).

Well name	Model	Model coefficient a	Model coefficient b	R^2	Composite coefficient
An 1	R_{25}-AC	0.102 9	0	0.946 3	0.1

In the process of modeling S_1 of $E_2S_3^4$ segment of Well An 1, the non-source rock segment was eliminated. At the same time, we carefully studied the reliability of logging data for mudstone intervals less than 1 m thick and the logging data for abnormal locations of boreholes. The correlation coefficient between S_1 and ΔlogR measured in the depth range of 0.5 m reached 0.946 3 (Table 3), indicating a good correlation (Figure 5).

It can be seen from the above calculation results that the calculated values of the various geochemical parameters in the Damintun Sag are consistent with the measured values, indicating the reliability of the method. Therefore, the method for calculating the organic component parameters of the target layer proposed in this paper can be popularized and applied in Damintun Sag.

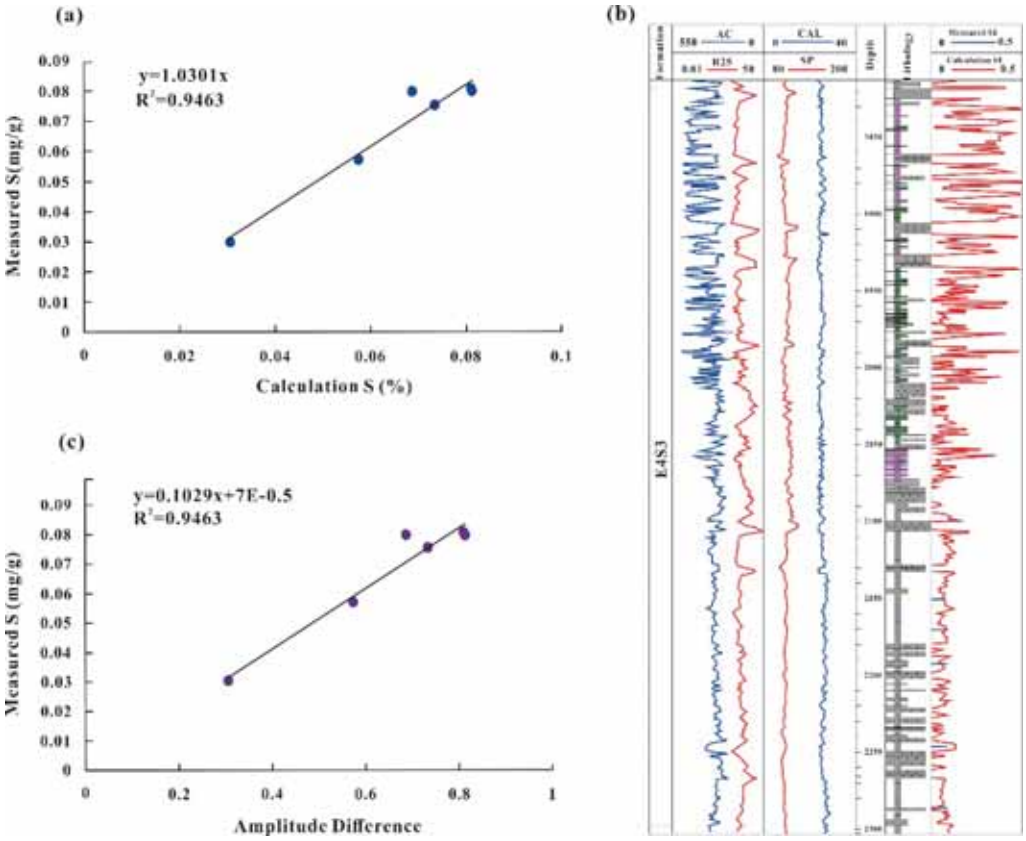

FIGURE 5

R_{25}-AC shale S_1 logging identification (An 1well, $E_2S_3^4$ interval).

Notes: (a) S_1 using log calculation VS. measured S_1;(b) Shale amplitude difference VS. measured S_1;(c) Shale S_1 logging identification results.

CONCLUSIONS

(1) In this paper, we take the Paleogene shale oil reservoir in the Damintun Sag, Liaohe Oilfield, eastern China as an example. We first performed logging identification on shale oil reservoirs. Then, the organic component in the shale oil reservoir was quantitatively predicted using the improved ΔlogR method.

(2) The shale oil logging response characteristics of the Damintun Sag are characterized by "three highs and one low": high gamma, high resistance, high acoustic wave time diffeence, and low rock density.

(3) When using the improved △logR method, the superposition coefficient K affect the accuracy of calculating the organic carbon content. With the change of K value from small to large, the accuracy of identifying the organic carbon content should first increase and then decrease, and the turning point from increasing to decreasing is the optimal superposition coefficient.

(4) The improved model can calculate the organic carbon content without the need for LOM and ΔTOC parameters and without the need to manually read baseline values. The calculated values of the various geochemical parameters using the improved model in the Damintun Sag are consistent with the measured values, indicating the reliability of this method.

ACKNOWLEDGEMENTS

All the authors would like to show their sincere thanks to the relevant persons who have contributed to this work and the authors of the references.

REFERENCES

[1] Xia, L., Cheng, X., Zhou, C., Chao-Liu, L., Liu, Z. (2015) Technology and application of well logging evaluation of shale oil and gas reservoirs. Natural Gas Geoscience. 26(5), 904-914.

[2] Zhao, L., Song, G., Ning, F., Zhang, J., Xiang, L., Zhuo, Q. (2010) Quantitative prediction of the oil-bearing height of tertiary stratigraphic reservoirs in Jiyang depression. Petroleum Exploration and Development. 37(1), 26-31.

[3] Xue, Y., Chen, Z., Xu, H., Ai, J., Jiang, S., Li, Y., Wang, Y., Guang, J., Mei, L., Jiao, X., He, X., Hou, T. (2011) A high throughput geocomputing system for remote sensing quantitative retrieval and a case study. International Journal of Applied Earth Observation and Geoinformation. 13(6), 902-911.

[4] Liu, L., Yu, L., Jiang, Y. (2016) Quantitative estimates of normalized transmissivity and the onset of nonlinear fluid flow through rough rock fractures. Rock Mechanics and Rock Engineering. 50(4), 1063-1071.

[5] Sakellariou, A., Senden, T., Sawkins, T., Knackstedt, M., Turner, M., Jones, A., Saadatfar, M., Roberts, R., Limaye, A., Arns, C., Sheppard, A., Sok, R. (2004) An X-ray tomography facility for quantitative prediction of mechanical and transport properties in geological, biological, and synthetic systems. SPIE International Symposium on Optical Science and Technology. 5535, 1-12.

[6] Piedrahita, J., Aguilera, R. (2017) Models for Calculating Organic and Inorganic Porosities in Shale Oil Reservoirs. SPE-185591-MS.

[7] Van Berk, W., Schulz, H. (2010) Organic-inorganic interactions at oil-water contacts: quantitative retracing of processes controlling the CO_2 occurrence in Norwegian oil reservoirs. Egu General Assembly. 129(3), 2817.

[8] Wang, G., Hao, F., Chang, X., Lan, C., Li, P., Zou, H. (2017) Quantitative analyses of porosity evolution in tight grainstones: A case study of the Triassic Feixianguan formation in the Jiannan gas field, Sichuan Basin, China. Marine and Petroleum Geology. 86, 259-267.

[9] Li, Y., Chang, X., Yin, W., Sun, T., Song, T. (2017) Quantitative impact of diagenesis on reservoir quality of the Triassic Chang 6 tight oil sandstones, Zhenjing Area, Ordos Basin, China. Marine and Petroleum Geology. 86, 1014-1028.

[10] Wang, D., Shao, L., Li, Z., Li, M., Lv, D., Liu, H. (2016) Hydrocarbon generation characteristics, reserving performance and preservation conditions of continental coal measure shale gas: A case study of Mid-Jurassic shale gas in the Yan' an Formation, Ordos Basin. Journal of Petroleum Science and Engineering. 145, 609-628.

[11] Mathialagan, S., Piotrowski, M., Tess, D., Feng, B., Litchfield, J., Varma, M. (2017) Quantitative prediction of human renal clearance and drug-drug interactions of organic anion transporter substrates using in vitro transport data: a relative activity factor approach. Drug Metabolism and Disposition. 45(4), 409-417.

[12] Yavuz, I., Lopez, S., Lin, J., Houk, K. (2016) Quantitative prediction of morphology and electron transport in crystal and disordered organic semiconductors. Journal of Materials Chemistry C. 4, 11238-11243.

[13] Nishimuta, H., Watanabe, T., Bando, K. (2019) Quantitative prediction of human hepatic clearance for P450 and non-P450 substrates from in VIVO monkey pharmacokinetics study and in vitro metabolic stability tests using hepatocytes. The AAPS Journal. 21(2), 20.

[14] Yin, S., Han, C., Wu, Z., Li, Q. (2019) Developmental characteristics, influencing factors and prediction of fractures for a tight gas sandstone in a gentle structural area of the Ordos Basin, China. Journal of Natural Gas Science and Engineering. 39, 1-14.

[15] Yin, S., Gao, Z. (2019) Numerical study on the prediction of "sweet spots" in a low efficiency-tight gas sandstone reservoir based on a 3D strain energy model. IEEE Access. 7, 117391-117402.

[16] Liang, C., Jiang, Z., Cao, Y., Zhang, J., Guo, L. (2017) Sedimentary characteristics and paleoenvironment of shale in the Wufeng - Longmaxi Formation, North Guizhou Province, and its shale gas potential. Journal of Earth Science. 28(6), 1020-1031.

[17] Lv, D., Wang, D., Li, Z., Liu, H., Li, Y. (2017) Depositional environment, sequence stratigraphy and sedimentary mineralization mechanism in the coal bed- and oil shale-bearing succession: A case from the Paleogene Huangxian Basin of China. Journal of Petroleum Science and Engineering. 148, 32-51.

[18] Liao, J. (2014) Gel treatment field application survey for water shut off in production wells. Dissertations and Theses – Gradworks. 5732, 196-210.

[19] Coudun, C., Gégout, J. (2009) Quantitative prediction of the distribution and abundance of vaccinium myrtillus with climatic and edaphic factors. Journal of Vegetation Science. 18(4), 517-524.

[20] Wang, J., Shi, W., Shu, Z., Xu, Q., Zhang, X., Xu, Z. (2016) Toc content quantitative prediction in organic-rich shale. Oil Geophysical Prospecting. 51(3), 605-612.

[21] Tan, M., Liu, Q., Zhang, S. (2013) A dynamic adaptive radial basis function approach for total organic carbon content prediction in organic shale. Geophysics. 78(6), 445-459.

[22] Han, C., Jiang, Z., Han, M., Wu, M., Lin, W. (2016) The lithofacies and reservoir characteristics of the Upper Ordovician and Lower Silurian black shale in the southern Sichuan Basin and its periphery, China. Marine and Petroleum Geology. 75, 181-191.

[23] Lv, D., Li, Z., Liu, H., Li, Y., Feng, T., Wang, D., Wang, P., Li, S. (2015) The characteristics of coal and oil shale in the coastal sea areas of Huangxian Coalfield, Eastern China. Oil Shale. 32(3), 204-217.
[24] Qiu, X., Liu, C., Mao, G., Deng, Y., Wang, F., Wang, J. (2015) Major, trace and platinum-group element geochemistry of the Upper Triassic nonmarine hot shales in the Ordos Basin, Central China. Applied Geochemistry. 53, 42-52.
[25] Lv, D., Zong, R., Li, Z., Wang, D., Liu, H., Wu, X., Wang, X., Yu, D., Feng, T., Zhao, L., Yang, Q., Yong, P. (2016) Oil shale paleoproductivity disturbed by sea water in a coal and oil shale bearing succession: A case study from the Paleogene Huangxian Basin of eastern China. Journal of Petroleum Science and Engineering. 139, 62-70.
[26] Qian, K., He, Z., Liu, X., Chen, Y. (2018) Intelligent prediction and integral analysis of shale oil and gas sweet spots. Petroleum Science. 15(4), 744-755.
[27] Zhang, L., Lu, Z., Wang, J., Tian, T., Wang, X. (2016) Microscopic pore structure of shale oil reservoirs in the Lower 3rd Member of Shahejie Formation in Zhanhua Sag, Bohai Bay Basin. Oil and Gas Geology. 37(1), 80-86.
[28] Qian, C., Wen, Z., Deng, H., Chen, W. (2015) Classification and controlling factors of organic pores in continental shale gas reservoirs based on laboratory experimental results. Journal of Natural Gas Science and Engineering. 27, 1381-1388.
[29] Nie, H., Ma, X., Yu, C., Ye, X., Bian, R., Liu, Z. (2017) Shale gas reservoir characteristics and its exploration potential-analysis on the Lower Jurassic shale in the eastern Sichuan Basin. Oil and Gas Geology. 38(3), 438-447.
[30] Liu, J., Yao, Y., Liu, D., Elsworth, D. (2017) Experimental evaluation of CO_2, enhanced recovery of adsorbed-gas from shale. International Journal of Coal Geology. 179, 211-218.
[31] Pang, H., Pang, X., Dong, L., Zhao, X. (2018) Factors impacting on oil retention in lacustrine shale: Permian Lucaogou Formation in Jimusaer Depression, Junggar Basin. Journal of Petroleum Science and Engineering. 163, 79-90.
[32] Zhou, X. (2009) Characteristics and quantitative prediction of distribution laws of tectonic fractures of low-permeability reservoirs in Yanhewan Area. Acta Petrolei Sinica. 30(2), 195-200.
[33] Liu, J., Ding, W., Yang, H., Jiu, K., Wang, Z., Li, A. (2018) Quantitative prediction of fractures using the finite element method: A case study of the Lower Silurian Longmaxi Formation in northern Guizhou, south China. Journal of Asian Earth Sciences. 154, 397-418.
[34] Joshi, H., Dai, L. (2015) Quantitative prediction of residual wetting film generated in mobilizing a two-phase liquid in a capillary model. Petroleum. 1(4), 342-348.

Received: **07.11.2019**
Accepted: **21.01.2020**

CORRESPONDING AUTHOR

Yinhao Dong
Liaohe Oilfield Exploration and Development, Research Institute,
PetroChina, Panjin 124000, China

e-mail: 2945598583@qq.com

© by PSP Volume 29 – No. 04A/2020 pages 2951-2959 Fresenius Environmental Bulletin

THE INVESTIGATION OF THE POSSIBILITY OF USING RED CALIFORNIA EARTHWORM (*EISENIA FETIDA*) MEAL AS AN ALTERNATIVE PROTEIN SOURCE IN RAINBOW TROUT (*ONCORHYNCHUS MYKISS*) DIET

Huriye Ariman Karabulut[1,*], Ilker Zeki Kurtoglu[1], Turan Yuksek[2], Zeynep Bayraktar[1]

[1] Faculty of Fisheries and Aquaculture, Recep Tayyip Erdogan University, Rize, 53020, Turkey
[2]Department of Landscape Architecture, Faculty of Fine Art, Design and Architecture, Recep Tayyip Erdogan University, Rize, Turkey

ABSTRACT

This study was carried out to determine the effect of earthworm meal usage on growth performance and body composition in fry rainbow trout feed. The 360 fish with an average weight of 5.05 ± 03.61 g were used in the study. In the experiment, four different feeding groups were designed with 3 replications. These groups are SU0 (Control), SU1, SU2 and SU3 groups which contain 0, 10, 20 and 30% earthworm meal (SU), respectively. Fish were fed three times a day for 90 days with these experimental feeds which were prepared to be 2.5% of the fish live weight. At the end of the study, SU3 group reached the highest weight gain with 259.40%, followed by SU2, SU1 and SU0 (211.17%, 182.76%, 113.68%, respectively). The difference between the SU3 group and the other groups was statistically significant in terms of live weight gain, specific growth rate, feed conversion ratio and protein efficiency ratio ($P < 0.05$). Hepatosomatic index was statistically significant between all groups ($P < 0.05$). As a result, considering the growth performance measurement criteria, it was determined that the use of 20-30% earthworm meal in the rations of fry rainbow trout could increase fish growth significantly.

KEYWORDS:
Earthworm meal, fishmeal, fish nutrition, growth performance, ration preparation, *Oncorhynchus mykiss*

INTRODUCTION

The consumption of fish and fishery products is of great importance in healthy and balanced nutrition of people [1]. Global consumption of fish and fishery products has increased more than two-fold in the last 50 years and has exceeded 20 kg per capita per year in 2015 [2]. Aquaculture capacity in Turkey reached 314.537 tonnes in 2018 while it was 79 thousand tons in 2000 [3]. Despite this rapid development of aquaculture in Turkey in recent years, it has not reached the desired level due to some factors such as feed cost which constitutes 50-75% of production expenses. In order to ensure the sustainability of aquaculture, it is of utmost importance that diversified, healthy and high quality fish feeds are put into use of the industry. In the last 15-20 years, an intensive study program has been conducted on fish feeds, on the alternative animal and plant proteins, and on the fat sources in order to achieve sustainable production in the aquaculture sector. Studies on the advantages and disadvantages arising from the fact that alternative protein sources (especially of plant protein sources) contain different amounts of amino acids and fatty acids from fish meal continue increasingly [4, 5].

Source and quality of the protein in fish feeds is an important issue. The deficiency of protein quality found in vegetative feeds is tried to be compensated with ingredients of animal origin. In addition to essential amino acids such as methionine, lysine and tryptophan, which are missing in the vegetal feeds, some mineral substances are available much more in the feeds of animal origin. The presence of anti-food effects in vegetal feeds restricts the use this kind of feeds in the aquaculture sector [6].

In recent years, it has become more prominent in the aquaculture sector to reduce production costs, increase the efficiency of production systems and promote environmental sustainability. Considering that fish feeds are among the most expensive inputs in the aquaculture sector, the production of cost-effective, environmentally friendly and nutritious fish feeds is of great importance for the sustainable aquaculture sector [7].

Trout farming has a large share in the aqua cultural sector of Turkey. It is important to include feed ingredients of animal origin as protein requirement in the rations prepared for feeding trout [8]. Vermicompost production (vermiculture) has become an increasingly prevalent sector because of the widespread zero waste policies and the use of earthworms in the conversion of organic waste into rich fertilizer for agricultural activities. Earthworms, which are the final product in vermiculture

production, have significant protein values. It has been reported that the addition of worms to pet diets as meal or fresh material increases productivity in farm animals such as fish, chicken, duck [9, 10, 11]. A similar effect of high nutritional earthworm meal on other farm animals has a high potential for rainbow trout farming. The use of high nutritional worms obtained from vermicomposting production as a complementary ingredient in trout feeds is likely to contribute to the development performance of fingerling rainbow trout. Although there are many studies about rendering products, mollusc meal as a source of animal protein; there are very few studies on the use of worms in place of fish meal as an alternative source of protein [12].

In this study, we intended to determine the effect of using earthworm meal in the feed of fingerling rainbow trout (*Oncorhynchus mykiss*) with different ratios on the growth performance and on composition of the fish flesh.

MATERIALS AND METHODS

Fish and Experimental Conditions. This study was carried out at Iyidere Fisheries Research and Application Center of Recep Tayyip Erdogan University. The study was carried out in spring in natural photoperiod with water taken from the stream with its natural flow. A total of 360 fingerling rainbow trout were used, with an average weight of 5.05 ± 03.61 g, with no previous infection and no exposure to toxic substances. Fish were obtained from a private trout farm operating in the Eastern Black Sea region. In the statistical calculations, it was verified that the groups formed at the beginning of the experiment were statistically similar in terms of average fish weights ($P > 0.05$). They were placed randomly in each tank so as to include 30 fry fishes, with 3 repetitions, and a total of 4 different study groups were formed, one being the control group. Thus, a test medium was created in 12 fiberglass tanks with 100 L volume and the study was carried out in a volume of 80 litres of water for 90 days. Their developments were observed in the groups with 0% earthworm meal (SU0), 10% earthworm meal (SU1), 20% earthworm meal (SU2) and 30% earthworm meal (SU3). In order to achieve the adaptation of the fish fingerlings, they were fed with control feed for 10 days. With this process, the adaptation of the fish to trial conditions, water temperatures and feeds was achieved. To determine periodical fish growth during the experiment, individual fish weights were measured with a digital scale with ± 0.1 g sensitivity, and their sizes were measured using Von Bayer method [13] trough with ± 1 mm sensitivity. In periodic measurements, sedation was applied to the fish with 50 mg/L clove oil. At the end of the experiment, the fish were subjected to deep anaesthesia with 100 mg/L to take the meat sample [14]. The water temperature in the tanks was calculated as 15.85 ± 2.03 °C at the end of the experiment, by measuring the water temperature twice a day, in the morning and evening during the experiment period. Dissolved oxygen values were measured as 7.84 mg/L and pH was 7.9 on average throughout the study.

Experimental Diets. In the preparation of trial feeds; fish meal, earthworm meal, bonkalit, corn gluten, soybean meal, vitamin and mineral mixes and pellet binder were used.

The essential nutrient contents of the ingredients to be used in the production of trial feeds (amounts of nitrogen-free extract, crude protein, crude lipid, crude cellulose, crude ash) were determined (Table 1).

Using these values, 4 different isonitrogenic (50% crude protein) trial feeds were prepared with the following ratios; control 0% (SU0), earthworm meal 10% (SU1), earthworm meal 20% (SU2) and earthworm meal 30% (SU3) (Table 2). Firstly, the dry feed ingredients, which form the rations, were milled and sieved through a sieve with 500 µm mesh. After the sieving process, dry ingredients were weighed separately in ± 1 g precision digital scale and placed into the mixing vessel, and after the mixture was homogenised, they were passed through meat mincer and prepared as 3 mm diameter pellets. The prepared feeds were dried for 24 hours in an oven set at 60 ºC. Dried feeds were put into the bags and labelled after they were cooled to room temperature, and were kept at +4 ºC in the refrigerator until they were served to the fish. Prepared feeds were calculated at a rate of 2.5% as per the tank biomass every 15 days and were given to the fish three times a day in the morning, noon and

TABLE 1
Proximate analyses of feed ingredients (%)

Ingredients *	Moisture	CP	CL	CC	CA	NFE[1]
Fish meal	9.1	71.4	11.5	0.1	7.6	0.3
Earthworm meal	10.0	59.0	9.0	0.26	17.0	4.74
Bonkalit	9.1	14.3	2.45	9.3	1.9	62.95
Corn gluten	9.8	64.0	2.25	2.2	1.5	20.25
Soybean meal	10.9	45.5	2.8	4.46	5.3	31.04

CP: Crude protein CL: Crude lipid CC: Crude cellulose CA: Crude ash NFE: Nitrogen free extracts
[1]Nitrogen free extracts = matter - (crude lipid + crude cellulose + crude ash + crude protein)
*The results of the analysis in the feed laboratory of the Recep Tayyip Erdoğan University, Faculty of Fisheries.

evening. Unconsumed feeds were removed from the tank by siphon, then weighted and recorded.

Essential amino acid (Table 3) and fatty acid analyses (Table 4) of the experimental feeds were carried out in Kazlıçesme R&D Test Laboratory, Istanbul, Turkiye.

Sample Collection and Analysis. At the end of the experiment, samples taken randomly from each tank were weighed with precision digital balance and their weights were retained and their total lengths were measured. To determine the efficiency of the slaughter, carcass weight, fin weight, internal organ weight, and liver weight were measured, and hepatosomatic index and viscerosomatic index values were calculated for the fish which were exposed to deep anaesthesia [14]. In addition, dry matter, ash, lipid, protein and moisture analyses were performed in the laboratory and the data obtained were evaluated. Dry matter and moisture ratio of the fish meats was calculated according to "TS 1743 (110 ± 1 °C)"; crude protein according to the "Kjeldahl Method"; crude lipid according to the "Soxhlet Method"; crude ash according to "TS 1746" (550 ± 1 °C)" [18, 19, 20].

Statistical Analysis. The results obtained are shown as the standard deviation (SD) of the mean. SPSS 22.0 software was used to evaluate the results, ANOVA test was used to reveal the difference in the groups and Duncan Test was used to find out from which groups this difference was arisen. Differences between groups were evaluated using significance level of $P < 0.05$.

TABLE 2
Formulation and proximate analyses of the experimental diets

Ingredients (%)	SU0	SU1	SU2	SU3
Fish meal	40	30	20	10
Earthworm meal	0	10	20	30
Bonkalit	13.9	12.8	9.9	7.4
Corn gluten	18	19.1	22	24.5
Soybean meal	19	19	19	19
Fish oil	8	8	8	8
Vitamin mixture[1]	0.5	0.5	0.5	0.5
Mineral mixture[2]	0.1	0.1	0.1	0.1
Molasses	0.5	0.5	0.5	0.5
Total	100	100	100	100
Proximate composition (%)				
Dry matter	90.2	90.5	90.1	90.3
Crude protein	50.71	50.02	50.22	50.21
Crude lipid	13.86	13.62	13.36	13.11
Crude ash	8.2	8.27	8.83	8.90
NFE[3]	17.43	18.59	17.69	18.08
Gross energy (kcal/g)[4]	490.437	488.864	483.934	483.062
Digestible energy (kcal/g)[5]	413.15	409.86	406.72	405.2

[1]Vitamin mixture**:** Included per kg; Vitamin A 20.000.000 IU, Vitamin D3 2.000.000 IU, Vitamin E 200.000 mg, Vitamin K312.000 mg, Vitamin B1 20.000 mg, Vitamin B2 30.000 mg, Vitamin B6 20.000 mg, Vitamin B12 50 mg, Vitamin C 200.000 mg, Niacin 200.000 mg, Cal.D.Panth. 50.000 mg, Folic acid 6.000 mg, D-Biotin 500 mg, Cholin Chloride 300.000 mg.

[2] Mineral mixture: Included per kg; 60 mg manganese, 80 mg zinc, 60 mg ferro, 5.000 mg copper, 2.000 mg iodine, 1.000 mg cobalt, 200 mg selenium, 50 mg magnesium

[3] Nitrogen free extracts (NFE) = matter - (crude lipid + crude ash + crude protein)

[4] Gross energy (GE), calculated according to 23.7 kJ/g protein, 39.5 kJ/g lipid, 17.2 kJ/g NFE [15].

[5]Digestible energy (DE), calculated on an estimated 5.0 kcal/g protein; 9.0 kcal/g lipid; 2.0 kcal/g carbohydrate [16].

TABLE 3
Amino acid content of experimental diets (% of dietary protein)

Essential amino acids	SU0	SU1	SU2	SU3	Rainbow trout* Requirements*
Leucine	7.00	7.61	7.77	7.92	3.5
Lysine	7.98	7.99	8.10	8.30	4.5
Methionine	3.09	2.81	2.98	3.11	3.5
Phenylalanine	3.58	3.76	4.06	4.45	4.5
Tryptophan	1.07	1.04	1.03	1.50	0.5
Valine	7.64	5.93	5.28	5.64	3.2
Arginine	7.72	6.85	6.76	6.95	5.0
Histidine	2.41	3.46	3.95	4.00	1.8
Isoleucine	4.10	5.09	5.80	5.93	2.0

* [17].

RESULTS

Growth Performance. In this study, growth and feed evaluation results obtained from control groups; (SU0) free of earthworm meal; 10% earthworm meal added (SU1); 20% earthworm meal added (SU2); and 30% earthworm meal added (SU3) has been shown in Table 5. The highest increase in weight was detected in the SU3 group.

TABLE 4
Fatty acid composition (% total fatty acids, mean ± SEM, *n* = 3) of feeds used in the experiments

Fatty acids	SU0	SU1	SU2	SU3
C16:0	0.04	0.13	nd	nd
C18:0	0.01	0.03	nd	0.02
[1]Σ SFA	0.05	0.16	nd	0.02
C16:1n7	0.02	0.03	nd	0.10
C18:1n9	nd	0.03	0.13	nd
[2]Σ MUFA	0.20	0.06	0.13	0.10
C18:2n6	0.16	0.3	0.15	0.10
C20:4n6	0.03	0.04	0.23	0.03
[3] Σ n-6 PUFA	0.19	0.34	0.38	0.13
C18:3n3	0.09	0.16	0.12	0.05
C20:5n3	0.09	0.14	0.14	0.05
C22:6n3	0.30	0.43	0.12	0.14
[4]Σ n-3 PUFA	0.48	0.73	0.38	0.24
[5]Σ PUFA	0.67	1.08	0.76	0.37
[6]Σ n-3 HUFA	0.39	0.57	0.26	0.19
n-3/n-6	0.40	0.47	1.00	1.85

SFA saturated fatty acid, MUFA monounsaturated fatty acid, PUFA polyunsaturated fatty acid, HUFA highly unsaturated fatty acids, nd: non-detectable
See Table 2 for rate of inclusion of the four oils in the experimental diets
[1]ΣSFA includes Palmitic acid (16:0) and Stearic acid (18:0)
[2]Σ MUFA includes Palmitoleic acid (16:1n-7) and Oleic acid (18:1n-9)
[3] Σ n-6 PUFA includes Linoleic acid (18:2n-6) and Arachidonic acid (20:4n-6)
[4]Σ n-3 PUFA includes Linolenic acid (18:3n-3), Eicosapentaenoic acid (20:5n-3) and Docosahexaenoic acid (22:6n-3)
[5]Σ PUFA includes Pn-6 PUFA and Pn-3 PUFA
[6]Σ n-3 HUFA includes 20:5n-3 and 22:6n-3. The only n-6 HUFA detected was 20:4n-6

TABLE 5
Growth performance of rainbow trout fed on different levels of earthworm meal ($\overline{X}$ ± SD).

	SU0	SU1	SU2	SU3
IBW (g/fish)	5.04±0.12 [a]	5.05±0.11 [a]	5.02±0.15 [a]	5.05±0.12 [a]
FBW (g/fish)	10.77±2.04 [a]	14.28±1.66 [b]	15.62±1.98 [c]	18.15±2.10 [d]
WG (g)	5.74±3.21 [a]	9.22±2.45 [b]	10.61±3.07 [c]	13.12±2.66 [d]
[1]WG (%)	113.68±1.32 [a]	182.76±1.09 [b]	211.17±1.14 [c]	259.40±2.20 [d]
[2]SGR (% per) day)	0.84±0.33 [a]	1.15±0.15 [b]	1.26±0.08 [c]	1.42±0.31 [d]
[3]FI (%BW per) day)	12.30±3.10 [a]	13.76±0.78 [b]	13.38±1.62 [c]	13.32±1.06 [cd]
[4]FCR	2.15±0.24 [a]	1.49±0.75 [b]	1.26±0.21 [c]	1.02±0.44 [d]
[5]PER	0.12±0.72 [a]	0.20±0.09 [b]	0.23±0.24 [c]	0.28±0.33 [d]
[6]CF (%)	1.43±0.44 [a]	1.39±2.21 [ab]	1.16±0.09 [c]	1.05±0.21 [d]
[7]SR (%)	60.02±0.11[a]	62.21±0.23 [ab]	73.34±1.15 [c]	74.45±0.07 [cd]
[8]HSI (%)	2.43±0.18[a]	1.80±0.37[b]	1.66±0.28[c]	1.51±0.09[d]
[9]VSI (%)	8.99±1.11[a]	8.97±0.78[a]	8.96±1.16[a]	8.93±2.01[b]

Values are means ± SD (*n* = 3); values with different superscript letters in the same rows are significantly different ($P < 0.05$).
IBW and FBW are initial body weight and final body weight
[1]Weight gain (WG, %)=100×(final body weight−initial body weight)/initial body weight
[2]Specific growth rate (SGR, %per day)=100×(ln final weight−ln initialweight)/days of the experiment
[3]Feed intake (FI,%BWper day)=100×dry feed intake/(days×(initial body weight+final body weight+death body weight)/2)
[4]Feed conversion ratio (FCR)=dry feed consumed/wet weight gain
[5]Protein efficiency ratio (PER) = wet weight gain/protein intake
[6]Condition factor (CF,%) = (wet weight/total length^3) × 100
[7]Survival rate (SR, %) = 100 × (final fish number)/(initial fish number)
[8]Hepatosomatic index (HSI, %) = liver weight × 100/body weight [21].
[9]Viscerosomatic index (VSI, %) = viscera weight × 100/body weight

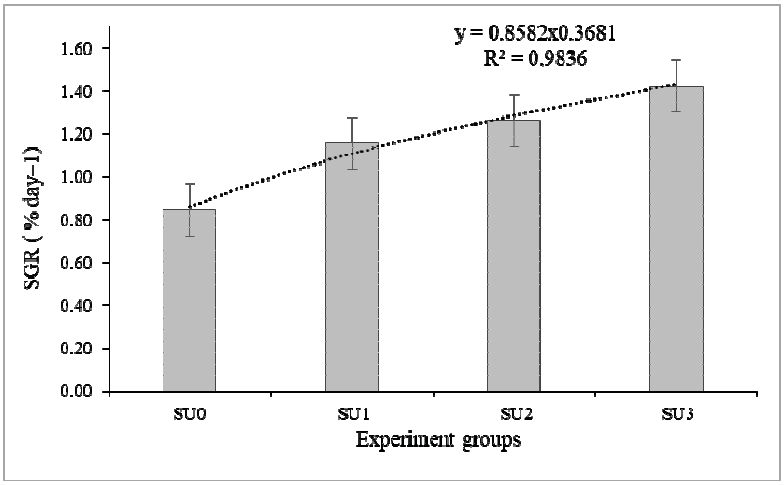

FIGURE 1
Specific growth rate of rainbow trout fed the experimental diets (mean ± SD, n = 3 tanks diet^{-1})

TABLE 6
Body composition of rainbow trout fed with earthworm meal (*n* = 5, $\overline{X}$ ± SD).

	SU0	SU1	SU2	SU3
Dry matter (%)	21.39±0.02 [a]	22.18±0.03 [a]	22.79±0.01 [a]	23.01±0.02 [a]
Crude protein (%)	16.98±0.42[a]	17.16±0.11[b]	18.04±0.23[c]	18.22±0.09[cd]
Crude lipid (%)	3.35±0.17[a]	2.71±0.22[b]	2.24±0.11[c]	2.08±0.31[cd]
Crude ash (%)	1.09±0.11 [a]	1.07± 0.62 [a]	1.07±0.31 [a]	1.06±1.02 [a]

Values in the same column with different superscripts are significantly different (P < 0.05). Data represented as mean ± *SD* of triplicate tanks.

SGR of fingerling rainbow trout was evaluated during the experiment and the lowest SGR was found to be 0.84 ± 0.33% in the control groups. The highest SGR was found in SU3 group with 1.42 ± 0.31%, followed by SU2 with 1.26 ± 0.08% (Figure 1).

According to the results of the experiment; when the condition factor (CF) was examined, there was no significant difference between SU0 and SU1 groups (P > 0.05), but it was found that the difference between SU0 and SU2 and SU3 groups was statistically significant with respect to CF (P < 0.05). The amount of feed consumed by the fish for 90 days according to their body weight percentages feed conversion ratio (FCR) in the SU0, SU1, SU2 and SU3 groups was 2.15 ± 0.24, 1.49 ± 0.75, 1.26 ± 0.21 and 1.02 ± 0.44 respectively, and there was a statistically significant difference between all groups (P < 0.05). The best FCR was found to be 1.02 ± 0.44 for SU3 group fish and the worst FCR was 2.15 ± 0.24 for SU0 group fish. Protein efficiency ratios (PER) for the experimental groups were found as follows. The highest one was found in the SU3 group with 0.28 ± 0.33, the lowest one was in the SU0 group with 0.12 ± 0.72, and a significant difference was found between the two groups (P < 0.05). For the trout fingerlings fed with feeds supplemented with different amounts of earthworm meal, the highest survival rate (SR) was found in SU3 group with 74.45 ± 0.07% ratio, the lowest **SR** with 60.02 ± 0.11**%** in the SU0 group. There was a statistically significant difference between the groups with respect to survival rate (P < 0.05) (Table 5).

At the end of the experiment, hepatosomatic index and viscerosomatic index values were calculated (Table 5). The highest HSI value was obtained from SU0 group with the 2.43 ± 0.18%. When HSI values were examined, it was found that the difference between all groups was significant (P < 0.05). Highest VSI value was obtained in the control group SU0 with 8.99 ± 1.11%. When VSI values were examined, it was found that S3 group was different from all other groups (P < 0.05), but the difference between S0, S1 and S2 groups was found to be insignificant (P > 0.05).

Body Proximate Composition. At the end of the experiment, the crude protein, crude ash, dry matter and crude lipid ratios calculated as a result of the analyses performed in the muscle tissue of 5 fish randomly sampled from each tank are given in Table 6. At the end of the experiment, as the result of the biochemical analysis of fish flesh, the highest value was obtained from SU3 group with 18.22 ± 0.09% for crude protein and the highest value was 3.35 ± 0.17% with control SU0 group for crude lipid. As a result of statistical analysis, it was found that the difference between SU0 control group and SU3 group was significant (P < 0.05).

DISCUSSION

In this study, the effects of adding earthworm meal to fish feed on the growth performance of fingerling rainbow trout, the hepatosomatic index and viscerosomatic index values and on the chemical composition of fish meat were investigated. When the growth performance data in fish were evaluated, it was determined that earthworm meal had a positive effect on development. In this study, when the data related to the growth were evaluated at the end of the 3-month feeding experiment, the highest live weight average was obtained in SU3 group and the lowest one was obtained in control SU0 group. The difference between weight increases of the groups having similar initial weights was found to be statistically significant ($P < 0.05$) at the end of the experiment. When the specific growth rate (SGR) among the growth parameters was evaluated, the best SGR was found in the SU3 group with 1.42 ± 0.31% and the lowest one was found in the SU0 group with 0.84 ± 0.33%. In order to determine the growth performance of fish correctly, specific growth rate is used commonly. Specific growth rate decreases as fish grows. If SGR is above 1%, it can be said that the fish grows well [22**].** Generally, in most of the studies, fingerling ones of the different fish species are used as it is the case with this study. In these studies, where growth performance was the subject, feeds supplemented with earthworm meal have been reported to have a positive effect on parameters such as weight gain rate of fish, protein efficiency ratios (PER), feed conversion ratio and specific growth rate [23, 24, 25]. In a study carried out for rohu fish (*Labeo rohita*) with average 0.7 g weight, they have fed them with 3 different diets (plainly cooked earthworm D1, mixed ground earthworm D2 and pellet feed produced from dried earthworm D3); at the end of the study they have found that best growth was in D3 with SGR 4.21% and in D1 with SGR 3.38%, and the results of the experiment suggested that pelleted feed supplemented with earthworm meal can be used in the breeding of fingerlings of rohu fish [25]. In this study, when the data related to feed conversion ratio were evaluated, the best feed utilisation was found in the SU3 group with 1.02 ± 0.44 and the worst value was found in the control group with 2.15 ± 0.24. The difference between the groups was found statistically significant ($P < 0.05$). [23], in their studies, added 0% (Control), 25%, 50%, 75% and 100% earthworm meal to the feed of catfish, and they reported that the highest average weight gain was observed in those fed with 75% earthworm meal. Highest specific growth rate was observed with the rate 1.5 in the feed prepared with 25% earthworm meal and the lowest one was 1.2 in the control group. The best feed conversion rate was seen in the feed supplemented with 50% earthworm meal with the rate of 1.6, and the worst FCR with the rate of 3.1 was seen in the feed supplemented with 100% earthworm meal. In catfish, feeds containing earthworm meal and fish meal were found appropriate for optimal growth performance and feed utilisation. In a study, 95, 190 and 380 g/kg of earthworm meal was added to the diets prepared for rainbow trout, which had an average weight of 208.6 g, close to the marketing weight, as against to 250, 500 and 100 g / kg of fish meal respectively, and at the end of 53 days of experiment, a significant increase in weight and daily specific growth rate was determined in groups fed by the feed containing 95 g/kg *E. fetida* meal, but in dietary groups containing 380 g/kg *E. fetida* meal, a decrease in growth performance was detected, and in the same study, it has been reported that carcass-fat rate of the group in which 100% earthworm meal was used was decreased by 16.7% in comparison to control group where 100% fish meal was used. As a result of this literature study, for the feeding of the fish in the later commercial breeding period, it has been reported that *E. fetida* meal can be added successfully to the feeds of trout instead of high amounts of fish meal [26]. [27], have prepared 3 different rations (earthworm meal T1, frozen earthworm T2 and live earthworm T3) for fingerling African Snakehead (*Parachanna obscura)* with an average weight of 2.7 ± 0.15 g, and served them to the fish together with the pellets prepared with frozen and live earthworm. At the end of the experiment, they have detected that the best protein efficiency ratio (PER) 1.58 and the best feed conversion ratio (FCR) 1.41 were found in T3 group which was fed with live earthworm, followed by the T1 group which was fed by the ration prepared with earthworm meal. They also achieved a 100% survival rate from these two groups contrary to the T2 group. Earthworms survive with microorganisms in soil and water. However, they are not affected much by these pathogens. Antimicrobial substances in coelom fluid are described as important elements of the defence system [28]. In feeding studies carried out with worms, one of the successes due to antimicrobial substances in worms is to increase the survival rate and improve stress symptoms. In the study, the best survival rate for the groups was found as 74.45 ± 0.07%. in group SU3 containing earthworm meal, and 60.02 ± 0.11% in the control group that does not contain earthworm meal. Statistically significant differences were found between the groups with respect to the survival rate ($P < 0.05$). In a study carried out by [29], they have added different ratios of earthworm meal (**0%**, 15%, 25%, 35% and 50%) into the feed of fingerling *Clarias gariepinus* fish, and they have determined that the feed supplemented with earthworm meal with 25% and 35% ratios provided higher survival rate compared to the control group which did not contain earthworm meal.

In this study, the best condition factor was found to be 1.05 ± 0.21**%** in group SU3 containing earthworm meal, and it was found to be 1.43 ± 0.44% in the control group without earthworm meal. According to the results of the experiment, when the condition factor (CF) was examined, there was no significant difference between SU0 and SU1 groups ($P > 0.05$), but it was found that the difference between SU0 and SU2 and SU3 groups was statistically significant ($P < 0.05$). The lowest hepatosomatic index (HSI) was detected as 1.51 ± 0.09% in the group containing SU3 earthworm meal**.** In statistical analyses, it was found that the difference between SU0 group and SU3 group was significant with respect to HSI values ($P < 0.05$). In a study carried out by [30], five different groups of feeds with an average weight of 4.43 g (E0, E25, E50, E75 and E100) were prepared for hybrid hetero-clarias fingerlings and they fed them for 8 weeks. At the end of the experiment, the best average weight was 6.77 g in those fed with E50 diet, and in the control group without earthworm meal, and fish weight was found to be 6.04 g. In the same study, they obtained the lowest condition factor (KF) value from the control group as 1.369%, and from E50 group with the highest value as 1.996%. Thus, they found that earthworm meal supplement is a good alternative protein source in fish feed. [21], fed fingerling carp fish weighing an average of 8.1 g with 4 different diets containing animal protein (control, EW20, EW70 and EW100) for 8 weeks, and at the end of the study they evaluated the morphological parameters. They obtained highest hepatosomatic index (HSI) in the control group with the value of 2.08%, and the lowest HSI from the EW70 group with 1.83%.

We think that the reasons of why the results obtained in this experiment differ from some literature data [21, 23, 25, 26, 27, 28, 29, 30]. might be different fish species, fish size, amount of feed, form of the feeding, experiment period, different feed ingredients and ratios in the rations, different serving methods of experiment materials, water temperature, stock density, environment conditions and so on.

As a result, it was found that the use of 30% earthworm meal in the feeds of fingerling rainbow trout improves growth performance and that earthworm meal can be used over 30% in fish feeds considering other literature studies.

ACKNOWLEDGEMENTS

Earthworm material requirement of this study has been supplied by LAZUTIM Organik Tarım Ltd., and the study itself has been supported by Department of Scientific Research (BAP), Recep Tayyip Erdogan University with the project number FLY-2017-753. We are thankful to Ozay KOSE for his attentiveness and support.

COMPLIANCE WITH ETHICAL STANDARDS

The animal ethics committee permission for the study was received from Recep Tayyip Erdogan University Local Ethics Committee for Animal Experiments (Decision No:2015/6, Date: 16/01/2015) and the rules of the committee were followed during the investigations.

REFERENCES

[1] Hosomi, R., Yoshida, M., Fukunaga, K. (2012) Seafood consumption and components for health. Global Journal of Health Science. 4(3), 72–86.

[2] Food and Agriculture Organization of the United Nations (FAO). (2018) The State of World Fisheries and Aquaculture, Meeting the Sustainable Development Goals. Retrieved on September 20, 2019 from.

[3] Arıman Karabulut, H., Kose, O., Kurtoglu, I.Z. and Kırım, B. (2019) Use of Alternative Feed Sources in Sturgeon Fish Feed and Importance of Aquaculture. I. International Science and Innovation Congress, Pamukkale, Denizli/ Turkiye, 26-29 August 2019, 345-349.

[4] Akiyama, T. (1995) Nutritive Value of Alternative Protein Sources. In: New Feeds for Fish Culture Utilization of Alternative Protein Sources. Suisangaku Series 102 Koseisha-Koseikaku, Tokyo, 45-42.

[5] De Silva, S.S. and Anderson, T.A. (1995) Fish Nutrition in Aquaculture. Chapman and Hall, London, 319.

[6] Lim, S.J., Kim, S.S., Ko, G.Y., Song, J.W., Oh, D.H., Kim, J.D., Kim, J.U., Lee, K.J. (2011) Fish meal replacement by soybean meal in diets for Tiger puffer, *Takifugu rubripes*. Aquaculture. 313 (1-4), 165-170.

[7] Musyoka, S.N., Liti, D.M., Ogello, E., Waidbacher, H. (2019) Utilization of the earthworm, *Eisenia fetida* (Savigny, 1826) as an alternative protein source in fish feeds processing: A review. Aquaculture Research. 50, 2301–2315.

[8] Aras, N.M., Kocaman, E.M. and Aras, M.S. (2000) General Fisheries and Fundamental Principals of Aquaculture. Ataturk University, Faculty of Agriculture Publications No: 216, Erzurum, Turkiye, 115-118.

[9] Sabine, J.R. (1978) The nutritive value of earthworm meal. In: Hartenstein R. (Eds.), Utilization of Soil Organisms in Sludge Management. National Technical Information Services, Springfield. 285-296.

[10] Lourdumary, A.J.B. and Uma, K. (2012) Nutritional Evaluation of Earthworm Powder (*Lampito mauritii*). Journal of Applied Pharmaceutical Science. 3(03), 82.
[11] Grdišaa, M., Gršićb, K. and Grdišac, M.D. (2013) Earthworms-role in soil fertility to the use in medicine and as a food. Invertebrate Survival Journal. 10 (1), 38-45.
[12] Arıman Karabulut, H, Kurtoglu, I.Z., Yüksek, T. and Osmanoglu, M.I. (2016) Use of Worm meal as Animal Protein Source in Fish Feed. Journal of Anatolian Environmental and Animal Sciences. 1(2), 64-69.
[13] Piper, R.G., McElwain, L.B., Orme, L.F., McCraden, J.P., Fowler, L.G. and Leonard. J.R. (1983) Fish Hatchery Management. US Fish and Wildlife Service, Washington DC, 544.
[14] Coyle, S.D., Durborow, R.M. and Tidwell, J.H. (2004) Anesthetics in Aquaculture. USDA Southern Regional Aquaculture Center (SRCA), Puplication No: 3900.
[15] Stafford, E.A. (1984) The use of earthworms as a food for rainbow trout (*Salmo gairdneri*). Institute of Aquaculture University of Stirling, Scotland.
[16] Cowey, C.B., Pope, J.A., Adron, J.W. and Blair, A. (1972) Studies on the nutrition of marine flatfish. The protein requirement of plaice (*Pleuronectes platessa*). The British Journal of Nutrition. 8(3), 447-456.
[17] Hardy, R.W. (2002) Rainbow trout, *Oncorhynchus mykiss*. In: Webster and Lim CE (Eds.): Nutrient requirements and feeding of finfish for aquaculture. The Haworth Press, Binghamton, New York, USA, 184-202.
[18] Green, B. (1980) *Fish Feed Technology*. FAO (Eds.), Rome: ADCP/REP/80/11, 395.
[19] Lovell, R.T. (1981) Laboratory manual for fish feed analysis and fish nutrition studies. Auburn University, US, 65.
[20] AOAC (Association of Official Analytical Chemists). (2005) Official methods of analysis of the association of official analytical chemists international (18th ed.). Gaithersburg, Maryland, USA, AOAC International.
[21] Ngoc, T.N., Pucher, J., Becker, K. and Focken, U. (2016) Earthworm powder as an alternative protein source in diets for common carp (*Cyprinus carpio* L.). Aquaculture Research. 47, 2917-2927.
[22] Korkut, A.Y., Kop, A., Demirtas, N. Cihaner, A. (2007) Determination methods of growth performance in fish feeding, Ege Journal of Fisheries and Aquatic Sciences. 24, (1-2), 201–205.
[23] Monebi, C.O. and Ugwumba, A.A.A. (2013) Utilization of the earthworm, *Eudrilus eugeniae* in the diet of Heteroclarias fingerlings. International Journal of Fisheries and Aquaculture. 5(2), 19-25.
[24] Chiu, S.T., Wong, S.L., Shiu, Y.L., Chiu, C.H., Guei, W.C. and Liu, C.H. (2016) Using a fermented mixture of soybean meal and earthworm meal to replace fish meal in the diet of white shrimp, *Penaeus vannamei* (Boone). Aquaculture Research. 47(11), 3489-3500.
[25] Mohanta, K.N., Subramanian, S. and Korikanthimath, V.S. (2016) Potential of earthworm (*Eisenia fetida*) as dietary protein source for rohu (*Labeo rohita*) advanced fry. Cogent Food and Agriculture. 2(1), 1138594.
[26] Velasquez, L., Ibañez, I., Herrera, C., Oyarzun, M. (1991) A note on the nutritional evaluation of worm meal (*Eisenia fetida*) in diets for rainbow trout. Animal Science. 53(1), 119-122.
[27] Vodounnou, J.V., Kpogue, D.N.S., Mensah, G.A. and Didier, F.E. (2017) Earthworm amino acids and effect of 3 different forms of earthworm (meal, frozen and living) on growth, feed utilization and survival rate of African Snakehead fingerlings (*Parachanna obscura)* reared in captivity. International Journal of Fisheries and Aquatic Studies. 5(1), 268-273.
[28] Wang, C., Sun, Z., Zheng, D. (2006) Research advance in antibacterial immunity ecology of earthworm. The Journal of Applied Ecology. 17(3), 525-529.
[29] Dedeke, G.A., Owa, S.O., Olurin, K.B., Akinfe, A.O., Awotedu, O.O. (2013) Partial replacement of fish meal by earthworm meal (*Libyodrilus violaceus*) in diets for African catfish, (*Clarias gariepinus*). International Journal of Fisheries and Aquaculture. 5(9), 229-233.
[30] Olele, N.F. (2011) Growth response of Heteroclarias fingerlings fed on earthworm meal in hatchery tanks. Journal of Life Sciences. 3(2), 131-136.

Received: **07.11.2019**
Accepted: **17.01.2020**

CORRESPONDING AUTHOR

Huriye Ariman Karabulut
Department of Aquaculture,
Faculty of Fisheries,
Recep Tayyip Erdogan University,
Rize, 53100, Turkey.

e-mail: huriye.ariman@erdogan.edu.tr

© by PSP Volume 29 – No. 04A/2020 pages 2960-2968 Fresenius Environmental Bulletin

A STUDY ON DIESEL PARTICULATE FILTER STAGED LINEAR SOOT LOADING ESTIMATION BASED ON PRESSURE DROP

Jinchi Dai[1], Hailong Pang[2,*], Yan Yu[2], Jianguo Bu[2], Xinyun Zi[2]

[1.] Postgraduate Team, Army Military Transportation University, Tianjin 300161, China
[2.] Military Vehicle Engineering Department, Army Military Transportation University, Tianjin 300161, China

ABSTRACT

To verify the reliability and accuracy of judging the opportune moment of DPF regeneration based on pressure drop with China-VI post processing system, the soot loading process and the pressure drop characteristics experimental study are carried out. Then a new soot loading estimation scheme is proposed, in which the accurate prediction is determined by staged linear relationship between DPF pressure drop and soot loading. The results shows that the prediction soot mass match well with the actual weighing result in steady process and in the road map cycle test, despite the fluctuation the dispersion is within the range of ±0.3g/L, though being affected by the instability of pressure drop in transient process and the low pressure drop discrimination of different soot load under low exhaust flow conditions.

KEYWORDS:
Diesel engine, diesel particulate filter, regeneration schedule, soot loading, pressure drop

INTRODUCTION

The wall-flow Diesel particulate filter (DPF) is a post processing device with interphase plughole structure to intercept the particulate matter (PM) in exhaust on the wall of filter, reducing the PM emission. The emission regulations around the world, including national VI emission regulation of China, are strictly limiting the PM emission [1-2]. For the moment, DPF has already been the requisite post processing device for diesel vehicle.

As the DPF is intercepting the PM in exhaust on the wall of filter to reduce the PM emission by interphase plughole structure, with the accumulation of trapped particulate matter in DPF plughole's duct, the exhaust resistance will go up, leading to the increase in diesel consumption of engine and decrease in power, even leading to the damage of engine. Therefore, it is required to clear away the accumulated particulate matter in DPF by some methods, so as to realize the regeneration of DPF [3]. At present, the widely used regeneration technology is to increase the temperature of DPF to 600℃ rapidly, making the trapped particulate matter react with oxygen. However, when there is only a little particulate matter, it's difficult for this regeneration method to support continuous combustion, thus leading to incomplete regeneration; if there is a large quantity of trapped particulate matter, then it will cause the regeneration temperature to exceed the maximum limit, leading to thermal damage of the filter [4-5]. Therefore, judging the opportune moment of DPF regeneration is a vital link in DPF regeneration control. Nowadays, the dominant methods of regeneration control are taking the soot loading as the basis of DPF regeneration opportune moment judgement.

During the actual operation of vehicle, it's difficult to disassemble the DPF and confirm the weight of DPF directly, so the scholars developed a serious of studies on indirect estimation of soot loading capacity, including the methods of establishing soot loading models and utilizing the pressure drop signals [6-8]. To meet the requirement of Emission Regulation, it's necessary to install a diesel oxidation catalyst (DOC) in the front of DPF, so in the process of establishing soot loading model, it is required to consider the transformation of NO & NO_2 and the oxidation reaction of NO_2 with particulate matter inside DOC and PM emission concentration of engine under different operating conditions; besides, the calibration work for this method is heavy and usually it is required to cooperate with the estimating method of utilizing pressure drop signals so as to correct the calculation deviation of soot loading model. Though the estimating method based on pressure drop signal is limited in accuracy and service conditions, it is still the strategy used most wide in DPF regeneration control.

In terms of study on soot loading capacity prediction model based on pressure drop signal, Naohisa and Dominik, etc. [11-12] have studied the relationship between pressure drop before & behind the DPF and soot loadings; Jiang Dahai, by establishing pressure loss model of wall-flow filter to confirm the soot loadings is affected mainly by exhaust temperature, exhaust flow and DPF pres-

sure drop, fixed the map to predict the soot mass; Seungmok Choi and Wang Dan, etc. [14-15] simplified the DPF pressure loss model, studied the approximate linear relation between DPF pressure drop and soot loadings in the condition that the exhaust flow is determined, and predicted the soot loadings by linear interpolation method, reducing the calibration workload of pressure drop method. During the loading of DPF, the relationship between pressure drop, exhaust volume flowrate and soot loadings is relatively complex with characteristics of deep-bed filtration stage, transitional filtration stage and cake filtration stage, so the linearly approximating DPF pressure drop and soot loadings during the whole loading process can be improved. Based on the characteristic test of DPF soot loading and pressure drop as well as the characteristics in DPF loading process, the method of predicting soot loadings by pressure drop is proposed in this study and the precision of model is verified.

TESTING EQUIPMENT AND METHOD

The test is conducted on the engine bench of AVL. The X7 VI heavy-duty diesel engine of DongFeng DDi75 series is selected. Refer to Table 1 for its specifications.

TABLE 1
Engine specifications

Parameters	Value
Type	In-line six cylinders, inter-cooling, HP common rail
Cylinder diameter-stroke/mm	110-132
Rated power/ kW	248
Maximum torque/N·m	1350
Displacement/L	7.52
Original NO_x emission/g·kW·h^{-1}	5.0-6.0
Original PM emission/ g·kW·h^{-1}	＜0.04

TABLE 2
Structural parameters of DOC and DPF

Parameters	Value	
	DOC	DPF
Material	Cordierite	Cordierite
Diameter of carrier/mm	266.7	266.7
Length of carrier/mm	127	228.6
Thickness of wall/mm	0.1	0.225
Mesh/ in.2	400	300
Volume/L	7.1	12.8

To meet the China-VI emission standard, the integrated post processing system is adopted, which is composed of DOC, DPF, selective catalytic reduction (SCR) and ammonia slip catalyst (ASC), and the overall layout of bench test is as shown in Figure 1. As the SCR is not related to DPF soot loading test, SCR doesn't eject AdBlue in the test. The detailed technical parameters of DOC and DPF are as shown in Table 2.

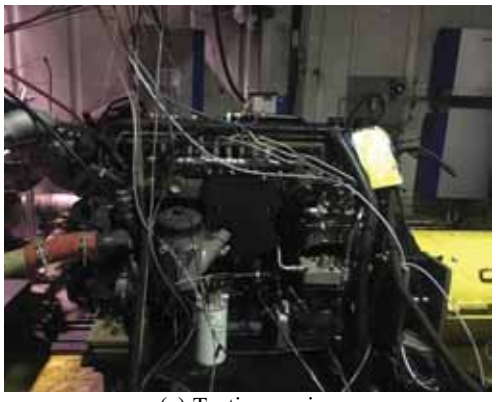

(a) Testing engine

(b) Integrated post processing system

FIGURE 1
Overall layout of the bench test

In DPF loading and pressure drop characteristic test, to conduct loading with operating condition fixed, and weigh the DPF after loading is finished, then record changing situation of pressure drop under different rotate speeds and loads. As the weight of soot is relatively small when compared with DPF, high-precision weighing scale is usually used to weigh the soot as shown in Figure 2. What's more, it is required to ensure the DPF bed temperature is higher than 125℃ while weighing, because if the DPF bed temperature is low, the vapor in the air will condense in DPF, leading to the weighing error. For this reason, the weighing of DPF must be conducted strictly according to the following procedure:

(1) To conduct DPF soot loading test:

(2) 1-3 minutes after shutdown of engine, immediately dismantle the DPF to ensure the DPF bed temperature is above 125℃.

(3) To calibrate the scale for weighing.

FIGURE 2
DPF weighing

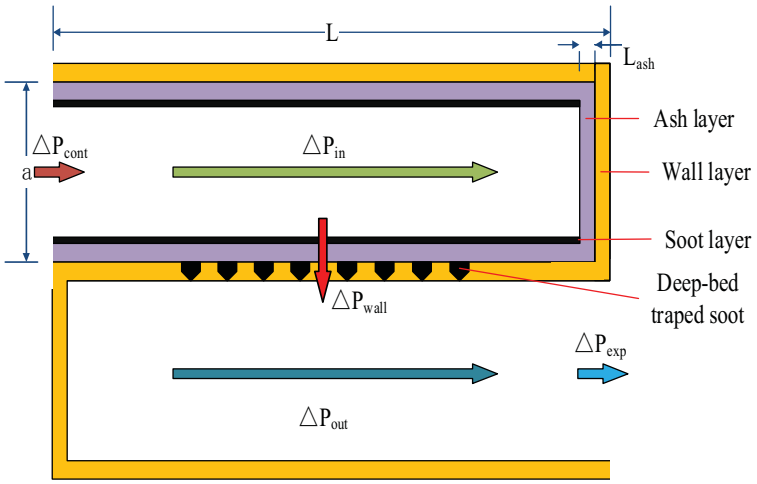

FIGURE 3
Schematic diagram of pressure loss of wall-flow DPF

DPF Pressure Drop Theory and Characteristic. The pressure loss of the widely used wall-flow filter at present is mainly composed of 5 parts: partial loss at DPF inlet, linear pressure loss at DPF inlet channel, pressure loss as DPF wall surface, ash layer and soot layer, linear pressure loss at DPF outlet channel and partial pressure loss at DPF outlet. They are as shown in Figure 3.

Ash content accumulating in DPF is a long process, so it's difficult to accurately estimate the ash accumulating and distributing condition in DPF when establishing DPF soot loading model[16-17], and the aim of soot loading prediction model is to help accurately judge the opportune moment of DPF regeneration, so to some extent the ash content accumulating quantity can be regarded as soot accumulating quantity.

The total pressure drop ΔP of DPF with ash effect being ignored can be presented as:

$$\Delta P=[\frac{32\mu L}{N(a-2w_{soot})^3}+\frac{32\mu L}{Na^3}+\frac{\mu}{4NL(a-2w_{soot})}\cdot\left(\frac{w_{soot}}{k_{soot}}+\frac{w_{wall}}{k_{wall}}\right)]\cdot Q_V+[\frac{\xi\rho_g}{2N^4(a-2w_{soot})^4}+\frac{\xi\rho_g}{2N^2a^4}+\frac{\rho_g(\beta_{soot}w_{soot}+\beta_{wall}w_{wall})}{16N^2L^2(a-2w_{soot})^2}]Q_V^2 \quad (1)$$

In this calculation, μ denotes dynamic viscosity of; L denotes length of filter hole duct; Q_V denotes exhaust volume flowrate; N denotes the quantity of filter inlet channels; w_{soot} denotes the thickness of soot layer; w_{wall} denotes the thickness of wall; a denotes the width of filter hole duct; ξ denotes the coefficient of partial loss at inlet and outlet of DPF; ρ_g denotes exhaust density; β_{soot} and β_{wall} respectively denotes Forchheimer coefficient of DPF soot layer and wall surface.

When the parameters of DPF are constant, the formula (1) can be regarded as the quadratic relational expression about exhaust volume flowrate:

$$\Delta P = AQ_V + BQ_V^2 \quad (2)$$

In formula (2), A and B are constant terms obtained by calculating DPF parameters with the soot loadings being determined.

Under different soot loadings, pressure drop characteristic test is used to get the relationship of DPF pressure drop and exhaust volume flowrate when the speed and load of engine goes up. And the exhaust volume flowrate can be figured out by exhaust mass flowrate of engine using the equation of ideal gas state.

$$Q_V = \frac{Q_m RT}{M_g P} \quad (3)$$

In this equation, Q_m denotes the exhaust mass flowrate of engine (unit: kg/h) and it is taken as the sum of engine inlet flowrate and fuel injection quantity in this study; R denotes ideal gas constant, generally taken as R=8.31J/(mol·K); T denotes the exhaust temperature when flowing through the DPF and the unit is K; M_g denotes the molar mass of exhaust, generally take as M_g=28.5g/mol; $P = 101 + \Delta P$ denotes the pressure as DPF inlet, and the unit is kPa.

The relationship between the DPF pressure drop and the exhaust volume flowrate obtained in the test is as shown in Figure 4. Under different soot loadings, DPF pressure drop and exhaust volume flowrate fulfill the quadratic curve relationship and the fit coefficients are close to 1.

Estimating the DPF soot loadings by relying on the DPF pressure drop characteristic curve requires detailed calibration of the relationship between pressure drop and exhaust volume flowrate under different soot loadings. However, according to the theory that the DPF pressure drop is approximately linear with the soot loadings, the calibration process can be greatly simplified, as shown in Figure 5. By calibrating the DPF pressure drop characteristic curve corresponding to the clean state and the safe Soot Mass Limit (SML), when the exhaust flowrate is constant, according to the ratio of pressure

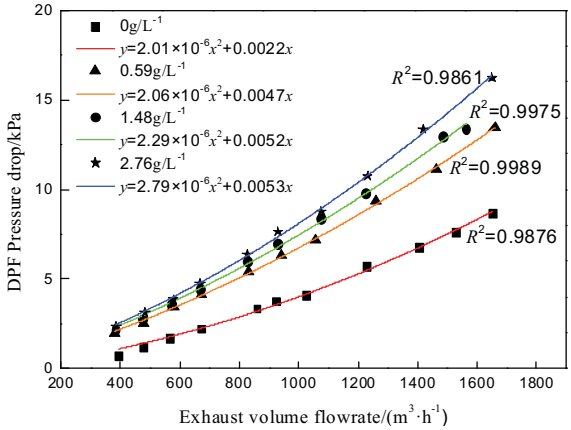

FIGURE 4

DPF pressure drop characteristic curve under different soot loadings

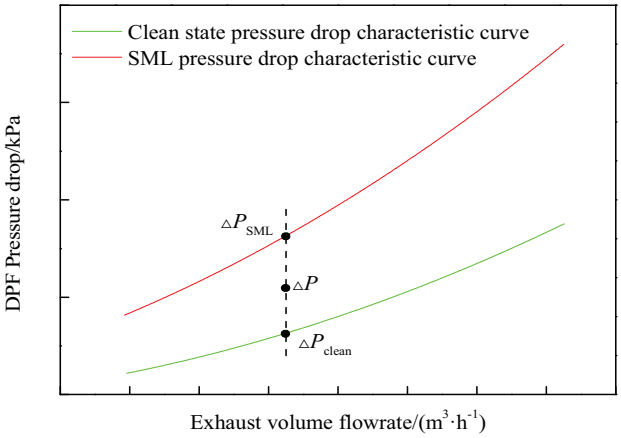

FIGURE 5

DPF pressure drop characteristic curve to predict soot loading using linear relationship

drop measured by the pressure difference transducer under clean state and SML pressure drop, the soot loadings of the DPF can be estimated and the formula is:

$$m_{soot} = \frac{\Delta P - \Delta P_{clean}}{\Delta P_{SML} - \Delta P_{clean}} \cdot m_{SML} \quad (4)$$

m_{soot} denotes the predictive value of DPF soot loadings; ΔP denotes the measured DPF pressure drop; ΔP_{SML} denotes the pressure drop under certain exhaust volume flowrate corresponding to SML; ΔP_{clean} denotes the pressure drop corresponding to clean DPF under same exhaust volume flowrate; m_{SML} denotes SML.

However, as shown is Figure 4, the space of DPF pressure drop characteristic curve between 0.59g/L and 2.76g/L is relatively even, in accordance with the deduction that the pressure drop is approximately linear with soot loadings, while the space between 0g/L and 0.59g/L is relatively large, indicating the nonlinearity between pressure and soot loadings.

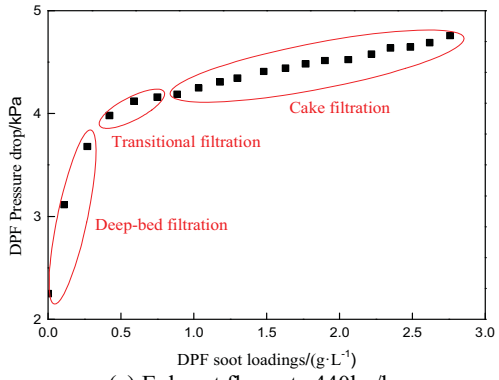

(a) Exhaust flowrate 440kg/h

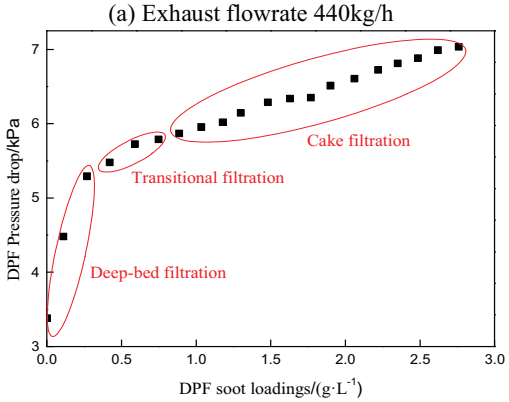

(b) Exhaust flowrate 560kg/h

FIGURE 6
The variation of DPF pressure drop with soot loadings under different operating cycle

The Relationship between DPF Pressure Drop and Soot Loadings. To carry out DPF loading test respectively when the engine exhaust flowrate is 440kg/h, DPF temperature is 270℃ and when the engine exhaust flowrate is 560kg/h, DPF temperature is 305℃, then perform weighing and observe the relationship between DPF soot loadings and pressure drop, as shown in Figure 6. From the figure, when the operating condition is constant, the relationship between pressure drop and DPF soot loadings shows three-stage characteristics, that is deep-bed filtration stage, transitional filtration stage and cake filtration stage.

The visualization study on the micro level carried out by Seungmok Choi, etc. based on the soot deposition in DPF channels indicates that when the clean DPF or the DPF just being regenerated begins to capture soot, the soot will first fill the plughole duct inside the wall when exhaust flows through DPF, which is because the soot deposition has not been formed inside the wall and on wall surface. According to the trapping theory of packed bed [18-19], as the soot deposited, the diameter of trapping unit will be increased, reducing the porosity and permeability of wall surface and increasing the resistance of flow, after the most of holes are blocked by soot, the soot will begin to deposit on wall surface, forming soot layer and stepping into cake filtration stage. The pressure drop during the whole deep-bed filtration stage will go up along with the DPF soot loadings, then level off and gradually go into cake filtration stage, as shown is Figure 7.

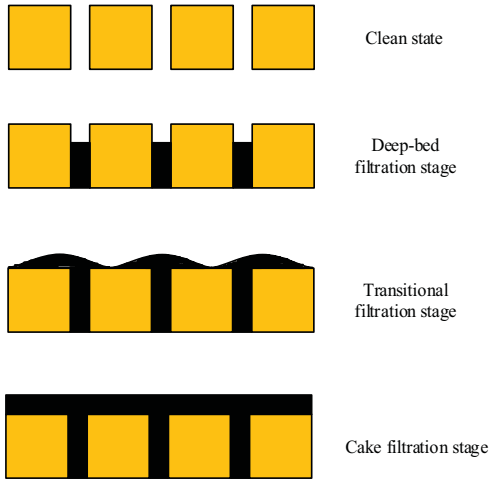

FIGURE 7
Schematic diagram of soot deposition during DPF loading

Once the soot layer is formed, its porosity and permeability is only closely related to the loading condition, so when the loading condition is constant, as the thickness of soot layer increases, the DPF soot loadings will increase, causing the increase in approximate linearity of pressure drop. As shown in Figure 6, when the DPF soot loading

reaches a certain degree, DPF begins to enter cake filtration stage, where the pressure drop is approximately linear with soot loadings.

As during deep-bed filtration stage, along with the increase in soot loadings, the DPF pressure drop will rapidly increases, therefore, assuming the DPF pressure drop is approximately linear with soot loadings during the whole DPF loading process can cause certain errors, especially when the soot loading is relatively small. In consequence, to select proper points of division on the relation curve of DPF pressure drop and soot loadings to approximate DPF loading process to staged linear relationship is more close to reality, as shown in Figure 8.

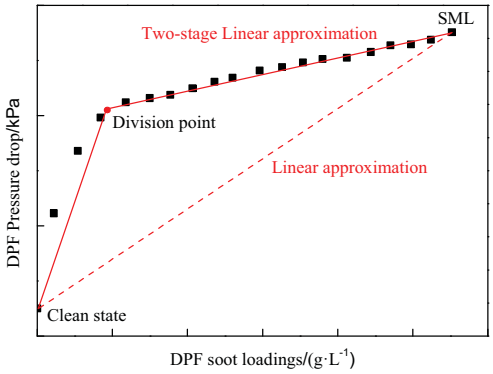

FIGURE 8
Schematic diagram of soot deposition during DPF loading

The Selection of Staged Linearity Division Point. When the DPF structure parameters are constant, the soot quantity contained in internal plughole duct of wall is certain. According to trapping theory of packed bed, the scaled fraction of soot mass entering DPF trapped by soot layer is:

$$\phi(t)=\frac{(d_c(1,t))^2-d_{c0}^2}{(\varphi b)^2-d_{c0}^2} \quad (5)$$

In this formula, φ denotes dimensionless seepage control constant, which needs to be obtained by test, and its normal range is $0.8\le\varphi\le0.95$ [20]; b denotes the diameter of spherical unit cell and the unit is meter; d_{c0} denotes the initial diameter of spherical unit filter and the unit is meter.

And the formula of calculating diameter of spherical unit filter in first-layer thin unit layer at t moment is:

$$d_c(1,t)=2\left(\frac{3}{4\pi}\cdot\frac{m_\omega(1,t)}{\rho_{soot,\omega}}+\left(\frac{d_{c0}}{2}\right)^3\right)^{1/3} \quad (6)$$

In this formula, $m_\omega(1,t)$ denotes the deposited soot mass in first-layer thin unit layer at t moment (Unit: kg); $\rho_{soot,\omega}$ denotes the density of soot and the unit is kg/m^3.

When $d_c(1,t)$ reaches the maximum limit φb, $\phi(t)=1$ and the soot flowing into DPF will be trapped completely by soot layer, entering cake filtration stage, in which $d_c(1,t)$ is only related to deposited soot loadings, so the soot loadings after DPF enters cake filtration stage is constant. Under different operating conditions in Figure 6, the changing situation of pressure drop and soot loadings also accords with the above point basically, but in actual calibration test, it's difficult to accurately calibrate the changes, and to select of division point close to cake filtration stage will also increase the errors of deep-bed filtration stage being linearly approximated. By loading the DPF under fixed operating condition, to obtain the pulse graph of DPF pressure drop and soot loadings, observe and determine the proper division point is more feasible.

Soot Loadings Prediction Method Based on Pressure Drop. By using the DPF pressure drop characteristic curve and staged linear relation between DPF pressure drop and soot loadings with operating condition being constant, as long as the division points are selected and the corresponding soot loadings is determined by DPF loading test, the Figure 9 can be obtained to predict the DPF soot loadings with DPF pressure drop characteristic curve corresponding to clean DPF, soot loadings at division point and SML as the boundary.

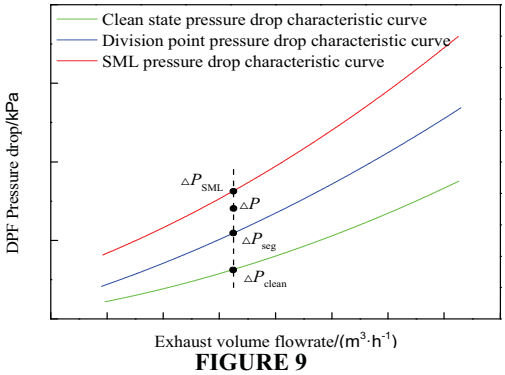

FIGURE 9
Schematic diagram of soot deposition during DPF loading

If the measured DPF pressure drop under certain exhaust volume flowrate is higher than pressure drop at division point, the formula of soot loadings is:

$$m_{soot}=\frac{\Delta P-\Delta P_{seg}}{\Delta P_{SML}-\Delta P_{seg}}\cdot(m_{SML}-m_{seg})+m_{seg} \quad (7)$$

In this formula, m_{soot} denotes the predicted value of DPF soot loading; ΔP denotes the measured DPF pressure drop; ΔP_{SML} denotes the pres-

sure drop corresponding to SML under certain exhaust volume flowrate; ΔP_{seg} denotes the pressure drop corresponding to division point under the same exhaust flowrate; m_{SML} is SML; m_{seg} denotes the soot loading corresponding to division point.

If the measured DPF pressure drop under certain exhaust volume flowrate is lower than pressure drop at division point, the formula of soot loadings is:

$$m_{soot} = \frac{\Delta P - \Delta P_{seg}}{\Delta P_{seg} - \Delta P_{clean}} \cdot m_{seg} \quad (8)$$

In this formula, ΔP_{clean} denotes the pressure drop corresponding to clean DPF.

MODEL VERIFICATION

To verify the accuracy of the established DPF soot loading prediction model, in this study, the 3.19g/L is taken as SML, the value acquired from DPF pressure drop and soot loading test is taken as the soot loading at division point, engine speed is 1900r/min (500N·m) and exhaust flowrate is determined as 680kg/h to compare the predicted result of soot loading predicting method based on staged linear approximation with the weighing result, so as to evaluate and analyze its accuracy. The comparison result is as shown in Figure 10: under stable operating condition, the model can better predict the DPF soot loadings, and the maximum absolute error of predicted result and weighed result is 0.235g/L, and the fit coefficient is R^2=0.9913.

Make the engine run in line with road map cycle for a while to verify the prediction accuracy of the established DPF soot loading predicting method under the changing operating condition, as shown is Figure 11.

In road map cycle test, the weighed mass of DPF is 2.06g/L; as shown in the figure, the predicting result of the model is fluctuating around 2.06g/L and the deviation is within ±0.3 g/L: in the area with stable operating condition, the fluctuating range is relatively small while in the area with

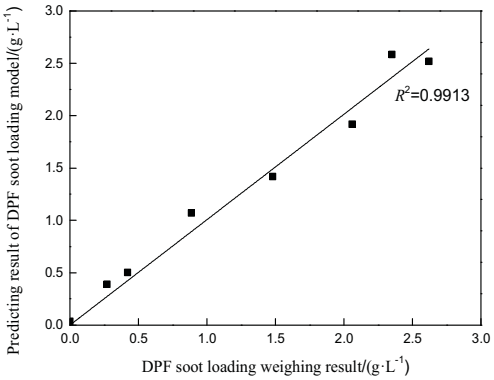

FIGURE 10
Comparison of DPF model prediction results and weighing results

changing operating condition, the fluctuating range is relatively large, and in the area with low exhaust flowrate, the prediction deviation of the model is relatively large. The reasons are as follows: the soot loading prediction based on pressure drop is likely to be affected by the change of operating condition and cause certain errors to the staged linear approximation of DPF loading process, which will be even more significant under the influence of transient operating condition; when the exhaust flowrate is relatively low, the measurement accuracy of pressure difference is not that high and the discrimination of pressure drop under different DPF soot loadings is also relatively low [21]. With China-VI Emission Standard, it is required to improve the accuracy of control method that takes the soot loading as DPF initiative regeneration, while to simplify the calibration process

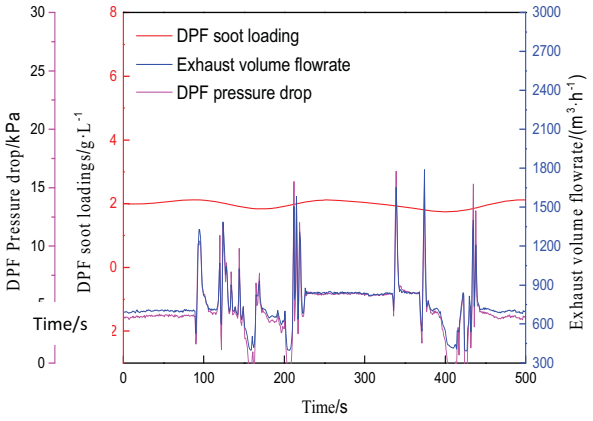

FIGURE 11
Soot loading model prediction results on the road map cycle

and to improve the prediction accuracy of soot loading prediction based on pressure drop are to be studied. The practical optimization plans include to process pressure drop signal cooperating with soot loading model to determine DPF soot loadings and judge the opportune moment of regeneration by PM sensor [22-23].

RESULTS

To study the judgement method of DPF regeneration opportune moment based on pressure drop under China-VI post processing system, according to DPF loading test and pressure drop characteristic test, the soot loading model and calibration method, which are based on the staged linear relationship between pressure drop and soot loading, are proposed in this study and get verified by experimental data. The results indicate:

(1) There are evident three stages in the relationship between DPF pressure drop and soot loading, which are deep-bed filtration stage, transitional filtration stage and cake filtration stage. When the operating condition is constant, proper division point can be selected to linearly approximate the whole soot loading process stage by stage.

(2) The staged linear relationship between DPF pressure drop and soot loading is not affected by loading condition, and it will enter the cake filtration stage under the almost same soot loadings. Therefore, the soot loading test can be carried out under constant operating condition to get the pulse graph of DPF pressure drop and soot loading and determine the division point to establish pressure drop characteristic pulse graph so as to predict soot loading, simplifying the calibration process of model.

(3) The DPF soot loading model established according to staged linear relationship between DPF pressure drop and soot loading with operating condition being constant is verified by experimental data that the calculated value by model is identical to the actual weighing result. Though in road map cycle test, the predicting result affected by operating condition is fluctuating to some extent, the prediction deviation is still maintained within ±0.3 g/L, indicating the efficacy of this model.

ACKNOWLEDGEMENTS

This study was sponsored by the National Key Research and Development Project of China (2017YFC0211104). The contents of this paper are solely the responsibility of the authors and do not necessarily represent official views of the sponsors.

REFERENCES

[1] GB 17691—2018. Limits and Measurement Methods for Emissions from Diesel Fuelled Heavy-duty vehicles (CHINA VI) [S].
[2] Shijin, S., Tao, T., Yanguang, Z., Lun, H. (2012) State of the art and outlook of diesel emission regulations and aftertreatment technologies. Journal of Automotive Safety and Energy.
[3] Guan, B., Zhan, R., Lin, H., Huang, Z. (2015) Review of the state-of-the-art of exhaust particulate filter technology in internal combustion engines. Journal of Environmental Management. 154(0), 225-258.
[4] Nishant, S., Silpa, M. (2013) DPF soot estimation challenges and mitigation strategies and assessment of available DPF technologies. SAE Technical Paper. 2013-01-0838.
[5] Rayomand, H.D., John, H.J., Jeffrey, N., Susan, T.B. (2008) A methodology to estimate the mass of particulate matter retained in a catalyzed particulate filter as applied to active regeneration and on-board diagnostics to detect filter failures[C]. SAE Technical Paper. 2008-01-0764.
[6] Ran, Y., Huang, T., Zhang, M., Jing, S., Zhu, Y. (2018) DPF soot loading estimation strategy based on pressure difference. IFAC Papers OnLine. 366-368.
[7] Lupse, J., Campolo, M., Soldati, A. (2016) Modelling soot deposition and monolith regeneration for optimal design of automotive DPFs. Chemical Engineering Science. 151,36-50.
[8] Tang, J., Li, G.o-x., Wang, Z.-j., Guo, S.-g., Zhang, J., Tao, J.-z. (2015) Construction and Experiment of DPF Soot Loading Model. Transactions of CSICE, (1),51-57.
[9] Yu, M.T., Balakotaiah, V., Luss, D. (2014) Effect of DPF properties on maximum temperature rise following a DTI. SAE Technical Paper. 2014-01-1561.
[10] Bai, S.Z., Tang, J., Wang, G.H., Li, G.X. (2016) Soot loading estimation model and passive regeneration characteristics of DPF system for heavy-duty engine. Applied Thermal Engineering. 100,1292-1298.
[11] Naohisa, O., Tomohiko, N., Shigeki, D. (2008) New concept catalyzed DPF for estimating soot loadings from pressure drop[C]. SAE Technical Paper. 2008-01-0620.
[12] Dominik, R., Thorsten, B. (2009) Different approaches to soot estimation as key requirement for DPF applications[C]. SAE Technical Paper. 2009-01-1262.
[13] Jiang, D., Ning, Z., Yao, G., Zi, X., He, J. (2012) A Study on the Right Moment for the Regeneration of Diesel Particulate Filter. Automotive Engineering. 34(2),109-115.

[14] Choi, S., Lee, K. (2013) Detailed investigation of soot deposition and oxidation characteristics in a diesel particulate filter using optical visualization. SAE Technical Paper. 2013-01-0528.
[15] Wang, D., Liu, Z., Tian, J., Han, Y., Tan M. (2016) A Study on DPF Soot Mass Estimation Based on Pressure Drop. Automotive Engineering. (12),1415-1419.
[16] Cozzolini, A., Mulone, V., Abeyratne, P., Littera, D., Gautam, M. (2011) Advanced modeling of diesel particulate filters to predict soot accumulation and pressure drop. SAE Technical Paper. 2011-24-0187.
[17] Amanatidis, S., Ntziachristos, L., Samaras, Z., Janka, K., Tikkanen, J. (2013) Applicability of the pegasor particle sensor to measure particle number, mass and PM emissions. SAE Technical Paper. 2013-24-0167.
[18] Lee, K.W., Gieseke, J.A. (1979) Collection of aerosol particles by packed beds. Environmental Science and Technology. 13(4), 466-470.
[19] Serrano, J.R., Arnau, F.J., Piqueras, P., Garcia-Afonso, O. (2013) Packed bed of spherical particles approach for pressure drop prediction in wall-flow DPFs (diesel particulate filters) under soot loading conditions. Energy. 58, 644-654.
[20] KonstandoPoulos, A.G. (2000). Fundamental Studies of Diesel Particulate Filters: Transient Loading, Regeneration and Aging. SAE Technical Paper. 2000-01-1016.
[21] Konstandopoulos, A.G. (2003) Flow resistance descriptors for diesel particulate filters: definitions, measurements and testing. SAE Technical Paper. 2003-01-0846.
[22] Hoepfner, A., Roduner, C.A. (2013) PM sensor based on-board diagnosis of particulate filter efficiency. SAE Technical Paper. 2013-01-1515.
[23] Pang, H., Zhang, G., Yu, Y., Zi, X. (2019) Motion Characteristics of Charged Particulate Matter in Diesel Particulate Matter Detection Device. Chinese Internal Combustion Engine Engineering. 40(03),117-124.

Received: **13.11.2019**
Accepted: **29.01.2020**

CORRESPONDING AUTHOR

Hailong Pang
Military Vehicle Engineering Department,
Army Military Transportation University,
Tianjin 300161, China.

e-mail: ysdhday@126.com

© by PSP Volume 29 – No. 04A/2020 pages 2969-2974 Fresenius Environmental Bulletin

EXOGENOUS ROOTING AGENT (GGR-6) ALLEVIATES HARMFUL EFFECT OF DROUGHT STRESS ON SEEDLINGS OF PERENNIAL RYEGRASS

Jinyang Qi, Siddique Muhammad, Jingyao Tian, Jixiang Lin, Jinghong Wang*

College of Landscape Architecture, Northeast Forestry University, Harbin 150040, Heilongjiang, P.R. China

ABSTRACT

Drought stress is one of the most serious environmental factors influencing plant growth and development. GGR-6 is a plant growth regulator that can regulate plant endogenous hormone content and enzyme activity, which can also enhance stress resistance of many plants. However, little is known about how GGR-6 influences perennial ryegrass physiological changes under drought stress condition. Here, perennial ryegrass variety (Shenshi) was used, and drought condition (drought stress for 0, 6, 8, 10, 12 and 15 days) was simulated. GGR-6 (0, 0.1 g/L, 0.2 g/L and 0.3 g/L) was also applied to test its mitigative effect on this species during seedling stage under such condition. The results showed that due to the intensification of drought stress, the SOD and POD contents increased in the seedlings of this species and long-term drought stress lead to a decrease in enzyme content. Perennial ryegrass enhanced osmotic regulation ability through adjusting of SOD and POD enzyme contents, and also increasing of the proline content at the same time, so as to keep MDA content in the seedlings at a low level. GGR-6 could significantly improve the ability of resisting drought stress of this grass species, and the most effective way of GGR-6 application was 0.1g /L and 0.2g/L one week after sowing seeds (W1). The Above results suggest that GGR-6 application is an effective way to increase stress tolerance of perennial ryegrass under drought condition in production practice.

KEYWORDS:
Drought stress, GGR-6, MDA, perennial ryegrass, proline

INTRODUCTION

Plant growth and development in most of the arid and semi-arid regions of the world is severely affected by drought stress, such as in the northeast of China [1]. Drought stress can impact all the periods of plant including germination, seedling establishment, reproduction, and leading to huge losses [2]. In general, water deficits caused by drought stress can inhibit photosynthesis and enhance photo-respiration, thereby disrupting cell homeostasis [3]. In addition, drought stress can also promote stomatal closure, impeding the diffusion of CO_2 and resulting in reduced CO_2 fixation [4]. Therefore, how to adapt to drought stress is quite important for plant.

Responses to drought stress are so complex and different mechanisms have been developed by plants to adapt during this period [5, 6]. Plants under drought stress reveal many morphological, physiological and biochemical changes that adversely affect their growth and productivity. One of the main physiological responses is an increase in osmotic adjustment substances, such as proline. Additionally, drought responses contain increased peroxidation of lipid membranes and accumulation of reactive oxygen species (ROS). Plants developed ways to balance ROS production, many of which involve antioxidant enzyme activities [7]. ROS scavenging enzymes, including superoxide dismutase (SOD), catalase (CAT), ascorbate peroxidase (APX), and glutathione peroxidase (GPX) that minimizes the effects of oxidative stress [8]. However, to our knowledge, few studies pay close attention to the dynamic changes in physiological indexes of turfgrass under drought stress.

Perennial ryegrass (*Lolium perenne* L.) is a perennial species of the family Poaceae. It is mainly used for turf purposes, such as golf course, fairways, athletic fields, and home lawns, especially in North America and Europe areas [9, 10]. In addition, this species are drought tolerant and have potentiality in arid and semi-arid areas of Northeast China.

Moreover, rooting agent (GGR-6) is a compound plant growth regulator that can regulate plant endogenous hormone content and enzyme activity. It can promote the synthesis of biological macromolecules and the growth of plant roots, improve the survival rate of seedlings and enhance plant resistance to stress conditions [11]. Plant growth regulators with rooting effects can significantly affect plant cell proliferation [12]. Studies have shown that the application of rooting agent could improve the rooting situation of plants [13]. In the present study, perennial ryegrass was used as experimental material, and GGR-6 was irrigated in the different seedling periods. We aimed to evaluate the effect of rooting agent

on the physiological changes of this grass species under drought stress.

MATERIALS AND METHODS

The Seeds of perennial ryegrass were provided by Harbin Bifeng Grass Industry Co., Ltd. in Hei longjiang province of China. The tested drug in this experiment was GGR-6 (produced by Chinese Academy of Forestry Sciences).

The experiment was carried out in the greenhouse of Northeast Forestry University. The plastic pot of 170×150×125 mm (caliber: height: bottom diameter) was selected. Vermiculite was selected as culture substrate and weighed 430 g after sterilization under high temperature condition. After screening, the ryegrass seeds were sterilized with 1% potassium permanganate solution and dried, and then the seeds were weighed in 3.5 g/ basin, soaked for 3 hours, and watered with 300 mL water every 3 d before emergence. Weigh the basin after watering each time in order to ensure same soil moisture. The rooting agent was sprayed in batches 1 week after sowing (W1), 2 weeks after sowing (W2) and 3 weeks after sowing (W3). 300mL of rooting agent was poured every 3 d during treatment, and the exudate was poured back into the basin after 4 h. After 3 times of treatments, the growth was normal, and 100 mL Hoagland nutrient solution was applied once a week. The treatment time of each group under drought stress was shown in Table 1, and the concentration gradient of GGR-6 was set to 0 (A), 0.1g/L (B), 0.2g/L (C) and 0.3g/L (D), each treatment had 5 replicates (Table 1).

After drought stress, the content of malondialdehyde (MDA) was determined by barbituric acid sulfate (TBA) colorimetric method [14]. The superoxide dismutase (SOD) activity was determined by nitrogen blue tetrazole (NBT) method [15]. The activity of peroxidase (POD) was determined by guaiacol method [16], and the content of free proline was determined according to the method of Li et al [17], each determination was repeated 3 times.

Data Analysis. The data were analyzed by one-way ANOVA using SPSS 13.0 (SPSS Inc, Chicago, IL, USA). The means and standard errors (SE) were reported.

RESULTS

The MDA content of ryegrass leaves at 8 d, 10 d, 12 d and 15 d after drought stress was significantly higher than that of control (P<0.05). However, under W1 treatment, there was no significant difference among different concentrations of ryegrass. Under W2 and W3 treatments, the MDA content of ryegrass leaves was significantly different when the concentration of GGR-6 was 0.2 and 0.3 g, indicating that GGR-6 treatment delayed the increase in MDA content of ryegrass to varying degrees, while the application of low concentration of GGR-6 (0.1g) to ryegrass under W1 could effectively reduce the damage of membrane system in ryegrass leaves caused by drought stress (Table 2).

TABLE 1
Treatment time in each drought stress test group

Group	Initial drought stress date	Drought time
1	19 April	15 d
2	22 April	12 d
3	24 April	10 d
4	26 April	8 d
5	28 April	6 d

TABLE 2
Effects of GGR-6 on the content of MDA in perennial ryegrass seedlings under drought stress

Period	Treatment concentration	Drought days					
		0 d	6 d	8 d	10 d	12 d	15 d
W1	A	2.58±0.26c	2.62±0.49c	3.54±0.71c	4.11±0.15b	4.82±0.28b	5.87±0.49a
	B	2.60±0.42b	2.63±0.52b	4.07±0.35a	4.20±0.36a	4.46±0.46a	5.21±0.41a
	C	2.64±0.23d	2.66±0.29d	4.09±0.61c	4.17±0.50b	4.25±0.88b	5.35±0.02a
	D	2.64±0.16c	2.69±0.38c	4.30±0.20b	4.63±0.26b	4.70±0.39b	5.43±0.28a
W2	A	2.16±0.08 d	2.48±0.13d	3.91±0.16c	4.00±0.20c	4.92±0.15b	9.32±0.25a
	B	2.35±0.11d	2.40±0.10 d	3.29±0.19c	3.90±0.13b	3.58±0.22b	6.93±0.23a
	C	2.41±0.01e	2.38±0.18e	3.98±0.04d	4.38±0.02c	7.84±0.16b	11.59±1.19a
	D	2.48±0.19d	2.53±0.02d	3.75±0.04c	3.90±0.13c	4.92±0.18b	12.36±1.13a
W3	A	2.48±0.27d	2.52±0.18 d	5.12±0.21c	5.39±0.26c	6.48±0.17b	9.97±0.25a
	B	2.45±0.03d	2.74±0.20 d	5.04±0.21c	4.01±0.16b	8.58±0.19a	9.83±0.13a
	C	2.51±0.13d	2.54±0.04d	4.42±0.07c	3.29±0.19b	11.59±0.19a	12.42±0.07a
	D	2.48±0.18c	2.81±0.16c	10.21±1.01b	12.36±0.13a	14.16±1.22a	-----

Note: A, B, C, D means the concentration of 0.05 g/L, 0.1 g/L, 0.2 g/L and 0.3 g/L. The data are presented as mean ± standard error. Different lowercase letters in the same column indicate significant differences at 0.05 levels. W1, W2 and W3 indicate the treatment with GGR-6 for one week, two weeks and three weeks after sowing seeds respectively.

TABLE 3
Effects of GGR-6 on the content of proline in perennial ryegrass seedlings under drought stress

Period	Treatment concentration	Drought days					
		0 d	6 d	8 d	10 d	12 d	15 d
W1	A	52.05±3.00 d	65.68±2.14bc	76.2±0.12b	87.16±1.51a	87.21±1.30a	89.30±0.42a
	B	61.52±0.52b	62.32±1.02b	62.50±1.25b	63.26±0.24b	82.34±0.42a	83.64±1.26a
	C	60.42±0.63b	60.06±0.10b	60.00±0.60b	61.22±0.66b	89.44±1.31a	90.52±1.41a
	D	54.10±1.02c	75.05±2.14a	66.51±1.52b	56.43±1.00bc	53.32±0.53c	53.52±2.34c
W2	A	52.27±2.33d	81.36±1.13c	92.04±1.01b	94.02±0.51b	103.04±0.30a	114.83±1.14a
	B	55.05±1.08b	80.60±1.06a	80.52±0.34a	81.05±0.35a	80.43±1.02a	82.26±0.61a
	C	53.24±1.40c	62.54±3.22b	68.42±1.02b	71.12±2.11b	74.47±2.06b	108.10±2.61a
	D	52.42±0.31c	50.51±1.10c	63.07±0.32a	65.53±0.51a	62.34±0.35a	58.26±0.41b
W3	A	56.31±0.25c	79.28±0.13b	82.00±2.13b	93.29±1.51a	96.17±1.65a	95.17±1.34a
	B	64.55±1.20c	81.62±1.22b	80.64±1.01b	91.42±0.26a	96.43±1.21a	94.08±1.03a
	C	63.34±0.56 d	81.00±1.73c	94.04±1.12ab	99.55±0.63b	102.04±1.15a	93.65±2.00ab
	D	63.03±2.50 d	90.04±1.56c	102.16±1.01b	111.51±1.01ab	123.61±1.44a	-----

Note: A, B, C, D means the concentration of 0.05 g/L, 0.1 g/L, 0.2 g/L and 0.3 g/L. The data are presented as mean ± standard error. Different lowercase letters in the same column indicate significant differences at 0.05 levels. W1, W2 and W3 indicate the treatment with GGR-6 for one week, two weeks and three weeks after sowing seeds respectively.

TABLE 4
Effects of GGR-6 on the content of SOD in perennial ryegrass seedlings under drought stress

Period	Treatment concentration	Drought days					
		0 d	6 d	8 d	10 d	12 d	15 d
W1	A	153.83±12.84c	157.81±19.63c	162.36±14.28b	179.37±10.47a	173.27±14.27a	169.35±17.36b
	B	155.46±10.59d	152.05±15.44d	167.43±17.83c	192.68±16.67a	178.19±20.22b	165.01±12.85c
	C	155.46±13.04c	161.85±21.06c	189.06±11.22b	215.25±28.51a	202.08±11.51a	199.65±16.68ab
	D	148.41±17.12c	151.79±19.00c	167.73±17.15b	177.25±18.49a	176.30±19.06a	170.60±12.46a
W2	A	124.61±25.13d	134.67±19.11d	166.77±24.38c	184.25±24.57a	179.93±25.26b	176.07±16.86b
	B	137.56±15.06 d	184.36±19.33ab	198.72±14.54a	177.28±19.58b	162.55±12.37c	142.02±18.76 d
	C	132.18±15.47d	152.55±11.00b	169.02±11.35a	149.62±19.02b	146.49±10.01c	144.70±11.68c
	D	127.26±18.46ab	138.26±10.27a	110.37±11.37c	130.87±16.29a	124.16±19.27b	119.29±10.27c
W3	A	127.65±14.80e	137.24±13.63d	142.50±14.68c	172.97±12.64a	163.91±12.85ab	156.14±15.24b
	B	148.48±11.31d	153.50±17.77c	162.16±18.61b	166.80±13.17b	171.58±17.68a	180.04±19.32a
	C	124.28±10.34e	179.10±13.28b	187.73±12.72b	194.28±19.61a	150.28±15.83c	138.71±21.28 d
	D	198.77±27.23d	227.12±13.30c	241.46±26.16b	266.18±14.19a	230.06±2.54abc	-----

Note: A, B, C, D means the concentration of 0.05 g/L, 0.1 g/L, 0.2 g/L and 0.3 g/L. The data are presented as mean ± standard error. Different lowercase letters in the same column indicate significant differences at 0.05 levels. W1, W2 and W3 indicate the treatment with GGR-6 for one week, two weeks and three weeks after sowing seeds respectively.

The content of free proline in ryegrass leaves under different treatments was significantly higher than that of control ($P< 0.05$). Under W2 and W3 treatments, the content of free proline in ryegrass leaves increased at first and then decreased. The peak value was appeared on the 10 and 12 d of drought treatment, respectively. Then the value decreased with the aggravation of drought degree, but it was still significantly higher than that of the control ($P<0.05$). Under W1 treatment, the content of free proline in ryegrass leaves was significantly higher than that in the control ($P<0.05$). Among the treatments, the peak value of free proline content appeared under the concentration of 0.1 g/L and 0.2 g/L applied with GGR-6 (Table 3).

The SOD activity of ryegrass leaves treated with GGR-6 was significantly higher than that of the control under different treatments ($P<0.05$). The SOD activity of ryegrass leaves treated with GGR-6 at W1, W2 and W3 stages increased at first and then decreased, indicating that a certain degree of drought stress could induce the response of ryegrass leaves to scavenging oxygen free radicals and respond to drought stress conditions. Compared with the control, the SOD activity increased by 1.38, 1.28 and 1.33 times at W1, W2 and W3 stages, respectively. However, there was no significant difference between each group. Except that the peak value of W2 appeared on the 8 d, the peak value of the other groups appeared on the 10 day after drought stress, and then the activity of SOD decreased with the aggravation of drought stress, but it was still significantly higher than that of the control ($P<0.05$). The SOD activity of ryegrass leaves treated with low concentration (0.1 g/L and 0.2 g/L) GGR-6 in different treatments was higher than that in high concentration GGR-6 treatment group (Table 4).

The POD activity of ryegrass leaves treated with GGR-6 was significantly higher than that of the control under different treatments ($P <0. 05$). When the concentrations of GGR-6 were 0.1 g/L and 0.2 g/L, the POD activity of ryegrass leaves increased at first and then decreased, indicating that drought stress could enhance the POD activity, effectively

TABLE 5
Effects of GGR-6 on the content of POD in perennial ryegrass seedlings under drought stress

Period	Treatment concentration	Drought days					
		0 d	6 d	8 d	10 d	12 d	15 d
W1	A	195.54±12.10c	200.72±18.35c	204.52±19.12c	219.09±20.13c	291.09±22.37a	322.24±28.29a
	B	234.33±20.36c	230.72±22.67c	211.70±20.10c	416.48±33.29a	500.30±38.19a	386.51±32.19b
	C	227.34±19.16b	235.72±21.17b	230.49±22.46b	370.77±28.47a	353.51±35.26a	330.49±24.17b
	D	231.58±25.37b	232.10±20.84b	233.45±22.62b	339.18±31.73b	341.78±33.36ab	356.50±34.59a
W2	A	348.50±32.15 d	388.69±35.38 d	442.54±38.92b	488.58±47.48a	428.69±40.38bc	400.41±37.31c
	B	284.02±26.35d	362.45±34.38c	368.27±35.31c	442.54±41.53a	384.02±34.36b	381.78±35.59b
	C	300.24±28.11c	339.61±30.27c	393.90±36.29b	504.64±43.47a	339.61±27.14c	335.79±31.54c
	D	347.76±27.34c	341.67±33.25c	336.98±28.75c	348.30±29.15c	441.67±38.25b	515.50±42.52a
W3	A	276.73±22.35e	315.73±30.02d	437.79±38.05c	507.57±43.25b	660.46±51.10a	668.80±53.43a
	B	331.91±28.08e	404.53±28.18 d	442.54±35.63c	675.75±57.31a	561.53±48.52b	481.62±42.31c
	C	314.42±28.05b	355.66±36.13a	362.29±34.89a	368.57±32.58a	309.74±28.52b	301.92±27.42b
	D	318.57±26.53c	326.83±30.07c	355.52±27.46b	376.64±28.14a	379.13±27.83a	-----

Note: A, B, C, D means the concentration of 0.05 g/L, 0.1 g/L, 0.2 g/L and 0.3 g/L. The data are presented as mean ± standard error. Different lowercase letters in the same column indicate significant differences at 0.05 levels. W1, W2 and W3 indicate the treatment with GGR-6 for one week, two weeks and three weeks after sowing seeds respectively.

scavenge oxygen free radicals and prevent membrane peroxidation in ryegrass leaves. Compared with control, the activity of POD in W1, W2 and W3 increased by 1.13, 0.68 and 1.03 times, respectively, indicating that early application of GGR-6 was more helpful for ryegrass to resist leaf cell damage caused by drought stress. Except that the peak value of POD activity under W1 appeared at 12 d, the peak value of POD activity in other groups appeared on the 10 d after drought stress, and then decreased with the aggravation of drought stress, but it was still significantly higher than that of the control (P <0. 05) (Table 5).

DISCUSSION

Drought stress is considered to be one of the most serious environmental factors for plant living in the soil, especially in the northeast of China. Understanding the physiological changes is particular crucial to clarify the adaptive strategy of this species under drought stress. In addition, rooting agent (GGR-6) can effectively promote plant growth, especially the root, and also increase the resistance to stress conditions of plant. Thus, exploring the positive effect of GGR-6 on the drought tolerance of plant has great scientific significance.

In general, the much stronger the resistance of plant seedlings to drought stress, the lower the damage of membrane system under drought condition [18]. The reaction of cell membrane lipid peroxidation in the seedlings can be described by the content of MDA. As a plant growth regulator, GGR-6 can promote the growth of plants in stress and enhance the enzyme activity in plants, so as to enhance the resistance of plants to stress. In the present study, the MDA content of perennial ryegrass seedlings increased significantly under drought stress, indicating that the cell membrane damage caused by stress condition stimulated the membrane response and accumulated a large amount of reactive oxygen species, leading to an increase in membrane lipid peroxidation product, and then damaged the membrane system of the seedlings. After the application of GGR-6, the content of MDA in perennial ryegrass seedlings was significantly lower than that of the control, indicating that the interaction of different application cycles and concentrations of GGR-6 could alleviate the damage of plant somatic cell membrane under drought stress.

Due to the self-protection mechanism of plants to stress, except for accumulating a large number of reactive oxygen species on their membranes, the seedlings of plant can also maintain their metabolic balance through osmotic regulation. Proline is known to be accumulated to keep osmotic balance under stresses, such as salt stress, drought stress, and can also participate in stabilize subcellular structures and scavenge free radicals in case of plant stress [19, 20]. Under drought stress, the osmotic regulator of free proline in plants will regulate cell infiltration, prevent cell membrane dissociation, maintain the osmotic balance of plants, reduce their osmotic potential and avoid dehydration of plant seedlings [21]. In the present study, the proline content in perennial ryegrass seedlings was significantly lower than that of GGR-6 application treatment, and the proline content increased significantly with the increase of drought stress. The results showed that GGR-6 could help perennial ryegrass to actively reduce the osmotic potential and maintain cell turgor by accumulating solute under stress.

Under drought condition, plants start their reactive oxygen defense system to remove reactive oxygen species from damaged cell membranes, and the SOD and POD are the most important two enzymes in this system [22]. In this study, the contents of SOD and POD in perennial ryegrass seedlings were significantly lower than those in seedlings treated with GGR-6, and the activities of SOD and POD reached the maximum and then decreased gradually with the aggravation of drought stress. This result showed that GGR-6 affected the reactive oxygen defense

system of perennial ryegrass, and then changed the ability of plants to resist to drought stress. But with the intensification of stress, the system was gradually inhibited. In the reactive oxygen defense system of plants, SOD catalyzes superoxide anion radicals to form oxygen molecules and hydrogen peroxide in the disproportionation reaction, which reduced the toxicity of plants due to the attack of free radicals. In this study, the seedlings of perennial ryegrass treated with GGR-6 reached the maximum value under drought stress for 10 d, and then decreased gradually, indicating that this species had a certain ability to resist to drought stress.

After SOD produces oxygen molecules and hydrogen peroxide in plants through disproportionation reaction, the POD further decomposes low toxic hydrogen peroxide into water, which further alleviates the effect of drought stress on the plant stress tolerance. In the present study, the changing trend of POD activity in perennial ryegrass was similar to that of SOD activity. Drought stress significantly inhibited the membrane system, osmotic regulation system and reactive oxygen species defense system of perennial ryegrass, and the inhibitory effect of drought stress on perennial ryegrass decreased with the application of exogenous GGR-6. After application with GGR-6, the result showed that the effect of low promoting and high inhibition. Through the interactions between application cycle and concentration, the early application of middle and low concentrations of GGR-6 had a better effect on improving the drought resistance of perennial ryegrass. The results showed that GGR-6 had a more significant effect on increasing the content of endogenous hormones in the early physiological metabolism of plants subjected to drought stress.

CONCLUSION

GGR-6, as an important rooting agent, could significantly improve the ability of resisting drought stress of perennial ryegrass, and the most effective way of GGR-6 application was 0.1g /L and 0.2g/L one week after sowing seeds (W1). GGR-6 application is an effective way to increase stress tolerance of perennial ryegrass under drought condition in production practice.

ACKNOWLEDGEMENTS

This work was supported by the National Natural Science Foundation of China (31502013).

Jinyang Qi and Siddique Muhammad contributed equally to this work.

REFERENCES

[1] Bandeppa, S., Paul, S., Thakur, J.K., Chandrashekar, N., Umesh, D.K., Aggarwal, C., Asha, A.D. (2019) Antioxidant, physiological and biochemical responses of drought susceptible and drought tolerant mustard (*Brassica juncea* L) genotypes to rhizobacterial inoculation under water deficit stress. Plant Physiology and Biochemistry. 143, 19-28.

[2] Fahad, S., Bajwa, A.A., Nazir, U., Anjum, S.A., Farooq, A., Zohaib, A., Sadia, S., Nasim, W., Adkins, S., Saud, S., Ihsan, M., Alharby, H., Wu, C., Wang, D.P., Huang, J.L. (2017) Crop production under drought and heat stress: plant responses and management options. Front. Plant Sci. 8, 1147.

[3] Sun, M., Peng, F., Xiao, Y., Yu, W., Zhang, Y., Gao, H. (2019) Exogenous phosphatidylcholine treatment alleviates drought stress and maintains the integrity of root cell membranes in peach. Scientia Horticulturae. 259, 108821.

[4] Cornic, G. (2000) Drought stress inhibits photosynthesis by decreasing stomatal aperture–not by affecting ATP synthesis. Trends Plant Sci. 5(5), 187-188.

[5] Carvalho, M., Lino-Neto, T., Rosa, E., Carnide, V. (2017) Cowpea: A legume crop for a challenging environment. J. Sci. Food Agric. 97, 4273-4284.

[6] Cruz de Carvalho, M.H. (2008) Drought stress and reactive oxygen species: production, scavenging and signaling. Plant Signal. Behav. 3, 156-165.

[7] Toscano, S., Farieri, E., Ferrante, A., Romano, D. (2016) Physiological and biochemical responses in two ornamental shrubs to drought stress. Front. Plant Sci. 7, 645.

[8] Apel, K., Hirt, H. (2004) Reactive oxygen species: metabolism, oxidative stress, and signal transduction. Annu. Rev. Plant Biol. 55, 373-399.

[9] Han, K.J., Alison, M.W., Pitman, W.D., Mccormick, M.E. (2013) Contribution of field pea to winter forage production and nutritive value in the South-Central United States. Crop Sci. 53, 315–321.

[10] Pan, L., Yang, Z.F., Wang, J.P., Wang, P.X., Ma, X., Zhou, M.L., Li, J., Gang, N., Feng G.Y., Zhao, J.M., Zhang, X.Q. (2017) Comparative proteomic analyses reveal the proteome response to short-term drought in Italian ryegrass (*Lolium multiflorum*). PLoS One. 12(9).

[11] Zhang, C.M., Shi, S.L., Li, Z., Yang, F., Zhang Z.K. (2019) Effects of drought stress on the root morphology and anatomical structure of alfalfa (*Medicago sativa*) varieties with differing drought-tolerance. Acta Prataculturae Sinica. 28(05), 79-89.

[12] Qin, S.J., Tan, C.Q., Hou, W.J., Wang, L.H., Yao, J.M., Fang, X. (2014) Effect of Plant Growth Regulator GGR6 on the Physiology and Biochemistry of Saraca dives Pierre. Northern Horticulture. 22, 72-75.
[13] Lebedev, V., Arkaev, M., Dremova, M., Pozdniakov, I., Shestibratov, K. (2018) Effects of Growth Regulators and Gelling Agents on Ex Vitro Rooting of Raspberry. Plants (Basel, Switzerland). 8(1).
[14] Wang, Y., Peng, X., Salvato, F., Wang, Y., Yan, X., Zhou, Z., Lin, J. (2019) Salt-adaptive strategies in oil seed crop Ricinus communis early seedlings (cotyledon vs. true leaf) revealed from proteomics analysis. Ecotoxicology and Environmental Safety. 171, 12-25.
[15] Wang, X.K. (2006) Principles and techniques of plant physiological and biochemical experiments. Peking: China Higher Education Press, 89.
[16] Li, H.S. (2003) Principles and techniques of plant physiological and biochemical experiments. Peking: China Higher Education Press, 164-167.
[17] Li, L., Yao, Y.F., Qin, F.C., Zhang, M.L., Gao Y.H. (2016) Distribution characteristics of soil organic carbon density of different forests in Huanghuadianzi watershed. Journal of Northwest A & F University (Natural Science Edition). 44, 77.
[18] Liu, D.W., Wang, J.G., Li, L., Tan, H.J., Ma, J., Lu, S. (2015) Responses of different peanut cultivars to drought and waterlogging stress and physiological mechanism. Acta Ecologica Sinica. 35(11), 3817-3824.
[19] Funck, D.W., Baumgarten, G., L. Forlani, G. (2012) Requirement of proline synthesis during Arabidopsis reproductive development. BMC Plant Biol. 12, 191-203.
[20] Kishor, P.B.K., Sreenivasulu, N. (2014) Is proline accumulation per se correlated with stress tolerance or Is proline homoeostasis a more critical issue? Plant Cell Environment. 37, 300-311.
[21] Li, C., Li, Z.T., Yang, K.J., Xu, J.Y., Wang, Y.F., Zhao, C.J., Zhang, Y.F., Li, Z., Sun, S.H., Fu, S.J., Zhao, Y., Gu, Y.N., Fu, J., Fang, Y.J., Liu, Y., Zhang, F.M., Ma, L.F., Shi, X.X. (2015) Effects of Water Stress and Subsequent Rehydration on Physiological Characteristics of Maize (*Zea mays*) with Different Drought Tolerance. Plant Physiology Journal. 51(5), 702-708.
[22] Zhang, R.N., Zheng, Y.J., Ma, G.S., Zhang, X.H., Lu, H.D., Shi, J.T., Xue, J.Q. (2014) Effects of drought stress on photosynthetic traits and protective enzyme activity in maize seeding. Acta Ecologica Sinica. 31(5), 1303-1311.

Received: **14.11.2019**
Accepted: **19.01.2020**

CORRESPONDING AUTHOR

Jinghong Wang
No. 26 Hexing Road,
Xiangfang District, Harbin,
Heilongjiang Province – China

E-mail: yuanlin@nefu.edu.cn

© by PSP Volume 29 – No. 04A/2020 pages 2975-2981 Fresenius Environmental Bulletin

STUDY ON ENVIRONMENTAL BEHAVIOR AND DRUG-RESISTANT GENE EMISSION CHARACTERISTICS OF β-LACTAM ANTIBIOTICS IN DRUG PRODUCTION PROCESS

Jingqiong Xiao[1,*], Xiuqin Wang[1], Liming Zheng[1], Dandan Ma[2]

[1] Panjin Vocational Technical College, Panjin 124000, China
[2] China-Japan Friendship Hospital, Beijing 100029, China

ABSTRACT

In this paper, UPLC-MS/MS content determination method and β-lactam drug resistance gene detection method for simultaneous detection of five β-LAD in water were used to systematically study the environmental behaviors and drug resistance gene emission characteristics of five common β-LADs (ie amoxicillin, ampicillin, ceftazidime, cefotaxime, cefepime) in drug production process. The results showed that the bacteria selected from the system not only had a high proportion of resistant bacteria, but also had strong drug resistance, and the drug resistance genes had emission patterns. Finally, the research method established in this study was successfully applied to the detection of β-lactam concentration and drug resistance genes in the factory drainage system.

KEYWORDS:
β-LAD, UPLC-MS/MS, environmental behavior, drug resistance gene

INTRODUCTION

β-lactam antibiotic drugs (β-LAD) are among the oldest and most broad-spectrum antibacterial drugs. Its large use has led to the emergence of resistant bacteria. The main mechanism of β-LAD resistance is that strains can produce β-lactamases (ESBLs) to hydrolyze the β-lactam ring, thereby degrading β-lactam drugs [1-4]. In recent years, E. coli producing ESBLs has been reported in various environments, including poultry, dairy products, farm soils or water environments. Especially in the sewage environment, its spread increases the risk of widespread spread of drug resistance genes.

Sewage discharge from drug manufacturers is an important way for antibacterial drugs to spread to the external environment and is an important reservoir for drug-resistant bacteria [5-6]. Therefore, it is particularly important to evaluate the environment of β-LAD and its resistance genes discharged from sewage from drug manufacturers. The study on the generation of antibiotics in the environment and the study of drug resistance gene transfer are important methods to establish and control the generation and spread of drug resistance genes. This study systematically studied the resistance mechanism of E. coli through experimental tests [7-9]. This study can provide theoretical guidance for the effective prevention and treatment of E. coli disease.

In this study, LC-MS/MS method was used to detect the concentration of β-LAD in water samples by collecting water inlets, outlets and water samples at a distance of 1 km from the outlet, and to explore its behavior in the water environment. At the same time, we tested the resistance genes of β-LAD and studied the emission characteristics of drug resistance genes.

MATERIALS AND METHODS

Instruments and Reagents. (1) Main Instrument. ACQUITY UPLC-Xevo TQ Ultra Performance Liquid Chromatography-Tandem Mass Spectrometer by Waers Company; Organomation Asso-ciates nitrogen blower; MS2 vortex mixer; CT15RT high speed refrigerated centrifuge; AE-206 electronic balance; C18 solid phase extraction column (5 mL / 600 mg) by Agilen Company.

(2) Main Reagent. Amoxicillin, ampicillin, ceftazidime, cefotaxime, cefepime standard control (purity greater than 98%), all purchased from Sigma Company; chromatographic grades of pure methanol, acetonitrile and n-hexane, all purchased from Fisher Company; mueller-Hinto agar, eosin blue medium, MEE Broth medium (MEE Broth), MacConkey culture, LB liquid and solid medium, all purchased from Qingdao Gaokeyuan Haibo Biotechnology Co., Ltd.; DNA purification and recovery kit and DNA extraction kit, all purchased from Shanghai Shenggong Bioengineering Co., Ltd.; pMD18-T vector and T4 DNA ligase, both purchased from TaKaRa Company; Easy Taq DNA

polymerase, 10×PCR buffer and dNTP, all purchased from Beijing Quanjin Biotechnology Co., Ltd. The primer sequences of the E. coli bla resistance genes blaTEM, blaSHV and blaCTX-M were synthesized by Shanghai Shenggong Bioengineering Technology Service Co., Ltd.

(3) Sample Collection. 26 water samples were randomly collected at the factory inlet, outlet and 1 km from the outlet, marked and checked on the same day. Among them, 6 water samples of the water inlet, the water outlet and the outlet 1 km are used for the quantitative detection of antibiotics, and the remaining 20 water samples are used for the detection of drug resistance genes.

Quantitative Detection of Antibacterial drugs. (1) UPLC-MS/MS Analysis Method. Chromatography method: the column was Maters BEHC18 (50 mm x 2.1 mm, 1.7 μm); mobile phase A is acetonitrile and mobile phase B is 1 mL/L formate water; elution method is gradient elution (0-3 min, 5%A-95%A; 3 min-4 min, 95%A; 4 min-4.3 min, 95%A-5%A; 4.3 min-6.0 min, 5%A). The flow rate was 0.4 mL/min, the column temperature was 40 °C, and the injection volume was 10 μL.

Mass spectrometry method: Electrospray ion source (ESI+), MRM monitoring mode, ion source temperature is 150 °C, capillary voltage is 0.5 kV, atomization gas flow rate is 1 000 L/h, cone gas flow rate is 50 L/h, desolvation gas temperature is 550 °C. The parameters of each ion pair and its cone voltage and collision energy are shown in Table 1.

(2) Sample pretreatment. 10 mL of the water sample was lyophilized using a high-speed refrigerated centrifuge, and 5 mL of an acetonitrile/methanol/McIlvaine buffer (V/V/V: 60/25/15) extractant was added. The HLB solid phase extraction column was rinsed with 5 mL of acetonitrile and 10 mL of high purity water, respectively. Then, the reserve liquid was passed through the solid phase extraction column, and 5 mL of the filtrate was collected in a glass tube [10-11]. Blow at a temperature of 40 °C to a volume of less than 1 mL, transfer the liquid to a 1.5 mL centrifuge tube, and dilute to 1 mL with acetonitrile. The filtrate passing through the microporous membrane (0.22 μm) was injected through a UPLC-MS/MS to 10 μL.

(3) Methodological Verification of Antibacterial Drug Detection. Take 1 mg of amoxicillin, ampicillin, ceftazidime, cefotaxime, cefepime standard control sample, and prepare 1 mg/mL mother liquor in 10 mL volumetric flasks. One is for the preparation of the standard curve and one for the preparation of the quality control sample. The final concentration of the standard curve samples was 0.2, 1, 5, 10, 20, 50, 100, 120 ng/mL. The final limits of the high, medium and low quantitative limits of the quality control samples were 100, 50, 10, and 0.5 ng/mL, respectively. Methodological verification was carried out according to the Guiding Principles of the Chinese Pharmacopoeia. The project has a standard curve, a lower limit of quantitation, accuracy, precision, and extraction recovery.

(3) Quantitative Detection of Antibacterial Drugs. First, pre-treat the water inlet, the water outlet and the water sample 1 km away from the water outlet. The concentration is then determined using the method validation test.

Detection of Drug Resistance Genes. (1) Detection of Resistant Phenotypes. The standard E. coli ATCC 25922 strain was used as a quality control bacteria, and the test was carried out in strict accordance with the standard operating specifications of CLSI (M100-S22, 2012). Six replicates of parallel control were performed for each experiment. By analyzing the diameter of the strain inhibition loop, the results were determined and recorded as sensitive (S), resistant (R) and intermediate (I).

(2) PCR Detection of Drug Resistance Genes. The isolated DNA extracted from ESBL E. coli was used as a template according to the bacterial DNA extraction kit operating instructions. The DNA template was pre-denatured at 95 °C for 5 min, at 94 °C for 1 min, the annealing temperature was heated for 1 min, 72 °C for 1 min, 32 cycles, and finally extended at 72 °C for 10 min. The PCR products were electrophoresed on a 1% agarose gel, and the positive products were sequenced by Shanghai Shenggong Biotech Co., Ltd. to obtain the 40 genotypes of ESBL E. coli-producing resistance.

TABLE 1
Mass spectrometry parameters of β-LAD content by UPLC-MS/MS.

Drug	Qualitative ion pair ($m*z^{-1}$)	Qualitative ion pair ($m*z^{-1}$)	Cone voltage (V)	Collision Energy (V)
Amoxicillin	366.2>113.9	351.2>208.2	14	34
Ampicillin	350.2>106.1	350.2>160.2	18	20
Ceftazidime	547.1>468.2	547.1>440.2	18	20
Cefotaxime	530.3>515.2	530.3>147.1	22	22
Cefepime	481.2>86.1	481.2>166.8	16	8

RESULTS AND DISCUSSION

Quantitative Detection of Antibacterial drugs. (1) Methodological Verification. The survey items have standard curve, lower limit of quantitation, accuracy, precision and extraction recovery [11-13]. The quantitative standard curve of β-LAD was performed by weighted least squares method. The weighting factor was $1/X^2$, the linear regression determination coefficient R^2 was greater than 0.99, the RSD of each concentration calibration concentration was less than 15%, and the β-LAD was 0.5-120 ng/mL. The linear relationship is good in the concentration range. The quantitative standard curve of amoxicillin is shown in Figure 1. The quantitative standard curve and correlation coefficient of each antibacterial drug are shown in Table 2. The extraction recovery rates of high and medium concentration samples of antibacterial drugs ranged from 95.1% to 109.1%, and the coefficient of variation was 2.4% to 9.3%. The measurement results are shown in Table 3, which shows that the method has a high extraction recovery rate. Observing the intra-day accuracy and precision of quantitative detection of the lower limit concentration, low concentration, medium concentration and high concentration of each antibacterial drug and the daytime accuracy and precision, all results were less than 15%. This method has good precision and accuracy. The measurement results are shown in Table 4.

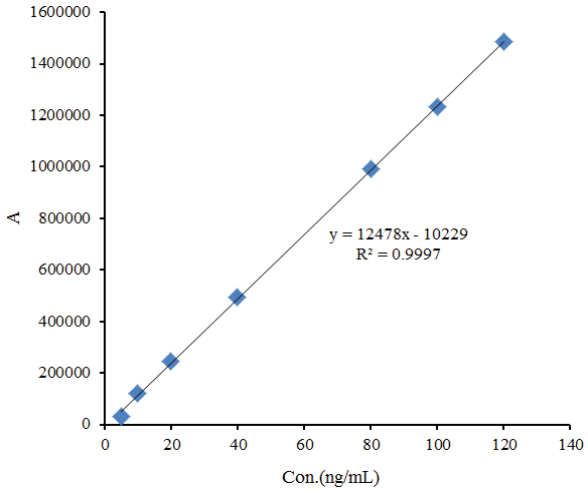

FIGURE 1
Quantitative standard curve of amoxicillin.

TABLE 2
Quantitative standard curve of β-LAD.

Drug	Standard Curve	Correlation coefficient R^2
Amoxicillin	y = 12 478x – 10 229	0.999 7
Ampicillin	y = 212 497x + 24 589	0.999 2
Ceftazidime	y = 22 853x + 65 783	0.999 6
Cefotaxime	y = 17 358x – 39 432	0.998 6
Cefepime	y = 113 645x + 68 457	0.998 9

TABLE 3
Extraction recovery of β-LAD and its lower limit (N=6).

Marked concentration Con. (ng/mL)	Extraction recovery (%)	Relative standard deviation RSD (%)	Lower limit of quantitation LLOQ (ng/mL)
100.23	103.6 ± 6.9	6.6	0.5
10.46	100.9 ± 3.9	3.9	
100.49	102.4 ± 5.7	5.7	1.5
10.53	101.4 ± 2.9	4.7	
100.35	100.1 ± 7.9	7.3	1.9
10.27	99.8 ± 4.7	9.3	
100.75	103.4 ± 5.7	2.4	0.6
10.31	102.1 ± 6.9	5.2	
100.14	99.5 ± 8.7	4.8	0.7
10.32	100.1 ± 3.6	3.8	

TABLE 4
Determination of the accuracy and precision of β-LAD in water by UPLC-MS/MS method.

Drug	Marked concentration (ng/mL)	Inter-batch (N=18) Measured Con. (ng/mL)	Accuracy (±RE%)	Percision (RSD%)	Intra-batch (N=6) Measured Con.(ng/mL)	Accuracy (±RE%)	Percision (RSD%)
Amoxicillin	LLQC	8.31 ± 2.9	0.9 ± 5.4	3.1	8.45 ± 1.6	4.4 ± 2.7	3.1
	LQC	10.19 ± 3.2	0.3 ± 3.2	3.1	10.7 ± 1.6	0.2 ± 1.4	1.5
	MQC	50.44 ± 7.9	0.6 ± 3.4	2.7	51.71 ± 9.9	2.7 ± 1.8	2.0
	HQC	99.86 ± 13.9	0.3 ± 4.0	2.7	101.68 ± 26.3	0.4 ± 2.1	2.2
Ampicillin	LLQC	8.71 ± 2.3	0.8 ± 5.7	6.3	8.75 ± 1.4	4.4 ± 2.7	2.0
	LQC	10.08 ± 5.2	0.5 ± 8.2	3.4	11.7 ± 8.6	0.2 ± 1.4	1.4
	MQC	50.74 ± 8.9	0.4 ± 3.2	6.7	51.47 ± 6.9	2.7 ± 1.8	1.8
	HQC	99.74 ± 10.2	0.4 ± 4.0	2.6	100.38 ± 25.5	0.4 ± 2.1	2.6
Ceftazidime	LLQC	7.91 ± 5.9	0.3 ± 6.1	3.4	7.75 ± 1.8	0.5 ± 8.2	1.7
	LQC	11.01 ± 6.2	0.3 ± 5.2	5.6	10.74 ± 3.4	0.4 ± 3.2	3.7
	MQC	50.21 ± 6.9	0.7 ± 3.6	7.1	50.21 ± 9.9	0.4 ± 4.0	6.8
	HQC	100.06 ± 27.2	0.5 ± 4.5	4.3	100.39 ± 31.6	0.3 ± 6.1	4.7
Cefotaxime	LLQC	8.57 ± 4.3	0.6 ± 5.7	3.4	8.85 ± 3.6	2.3 ± 6.1	6.4
	LQC	10.16 ± 7.2	0.5 ± 9.2	5.6	10.53 ± 2.9	4.6 ± 2.4	6.9
	MQC	50.64 ± 9.9	0.6 ± 3.7	9.0	51.33 ± 7.4	0.5 ± 9.2	6.1
	HQC	99.99 ± 12.2	0.7 ± 3.0	4.5	100.64 ± 17.5	0.6 ± 3.7	4.8
Cefepime	LLQC	7.98 ± 5.6	2.4 ± 1.5	6.5	8.85 ± 1.6	0.7 ± 3.0	2.4
	LQC	10.25 ± 6.8	2.3 ± 6.1	2.3	10.24 ± 1.6	2.4 ± 1.5	7.3
	MQC	51.01 ± 4.9	4.6 ± 2.4	4.9	50.56 ± 7.9	0.6 ± 5.7	5.6
	HQC	100.21 ± 16.2	5.2 ± 3.4	2.5	99.35 ± 31.1	0.5 ± 9.2	3.6

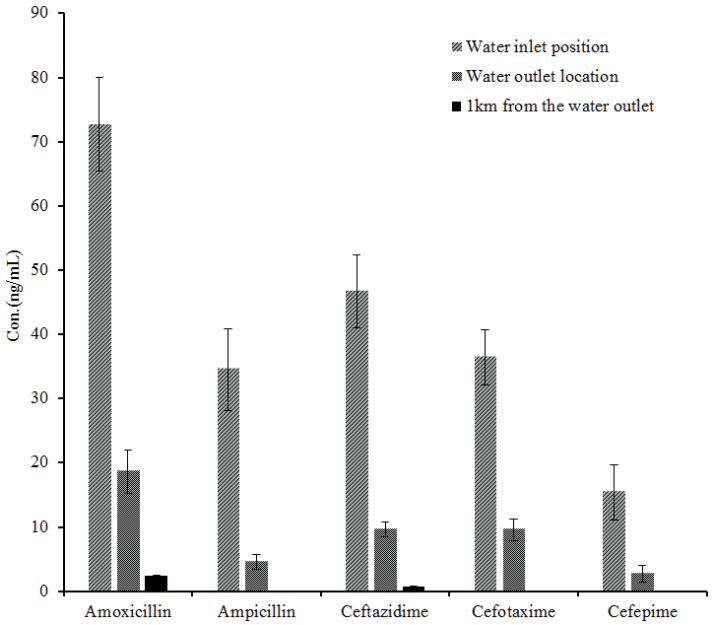

FIGURE 2
β-LAD content in the waste water (N = 6).

(2) Determination of the Concentration of Antibacterial Drugs. 78 water samples were pre-treated. The above methodology was used to verify the detection method, and the guiding principle was verified according to the analytical method of the Chinese Pharmacopoeia, and a standard curve was established for each analysis batch [14-16]. The water sample was used to measure the high-, medium-, and low-quality control samples, so that the number of quality control samples was greater than 5% of the total number of unknown samples. All the samples in this experiment were completed in 6 analytical batches. The deviation of the results of all quality control samples was less than 15%, and the R^2 of the standard curve was greater than 0.99, so the analysis was effective. The measured results are shown in Figure 2.

TABLE 5
Detection rate of bla genotype of 40 strains of ESBL-producing Escherichia coli.

Type	Bla genotypes	Percentage (%)
blaTEM	(1) blaTEM-1	72.4%
	(2) blaTEM-16	9.3%
	(3) blaTEM-33	6.1%
	(4) blaTEM-181	2.3%
	(5) blaTEM-135	9.9%
blaCTX-M	(1) blaCTX-M-35	79.6%
	(2) blaCTX-M-55	10.1%
	(3) blaCTX-M-164	10.3%
blaSHV	(1) blaSHV-6	69.3%
	(2) blaSHV-11	2.7%
	(3) blaSHV-56	4.6%
	(4) blaSHV-79	8.9%
	(5) blaSHV-40	14.5%

Detection of Drug Resistance Genes. (1) Identification Results of Isolation of ESBL-Producing Coliform Strains. Analysis by 16S rRNA PCR showed that 67 strains of E. coli were obtained from 78 water samples, of which the separation rate of the inlet was 64.5 %, the separation rate of the outlet was 43.2%, and the separation rate from the outlet was 22.6 %. Among them, 40 strains were ESBL-producing E. coli, and the isolation rate was as high as 46.7 %. The experimental results show that the collected water samples have been seriously polluted by ESBL-producing Escherichia coli [17-20]. After the sewage is treated, the ESBL-producing Escherichia coli cannot be completely eliminated, and these resistant bacteria can cause more serious infections after being discharged into the water environment through sewage.

(2) Resistance Phenotype Detection of ESBL-Producing Escherichia Coli. We tested the β-lactam resistant phenotype of 40 isolated ESBL-producing E. coli. The results showed that 40 strains of ESBL-producing Escherichia coli showed resistance to both amoxicillin and ampicillin (100% resistance). The strains resistant to ceftazidime accounted for 74.8%, the strains resistant to cefepime accounted for 41.5%, and the strains resistant to cefotaxime accounted for 1.2%.

(3) Detection of Drug Resistance Genes in ESBL-Producing Escherichia Coli Bla. The bla gene was detected in 40 ESBL-producing E. coli isolated from 78 water samples. The detection rates of blaTEM, blaSHV and blaCTX-M genes are 100%, which are resistant genotypes encoding ESBLs. Among them, blaTEM-1, blaCTX-M-35 and blaSHV-6 were the main epidemic types, and the detection rates were 72.4%, 79.6% and 69.3%, respectively. The detailed results are shown in Table 5.

CONCLUSION

This study established an LC-MS/MS method for simultaneous detection of five common β-LADs. The methodological verification results of the accuracy and precision of the method are good. We successfully applied this method to the quantitative detection of the drug concentration in the water at the factory inlet, outlet and 1 km from the outlet. The content of amoxicillin in β-LAD was the highest, followed by ceftazidime and cefotaxime. In this study, ESBL large intestine strains were isolated from the water inlet, outlet and 1 km from the outlet. The separation rate of the water inlet was 64.5 %, the separation rate of the water outlet was 43.2%, and the separation rate of 1 km from the water outlet was 22.6%. The results are consistent with the behavioral distribution of ESBL-producing strains in the factory drainage system. Resistance studies on isolated resistant Escherichia coli found that amoxicillin and ampicillin showed complete resistance, 74.8% of strains resistant to ceftazidime, 41.5% of strains resistant to cefepime, and 41.2% of strains resistant to cefotaxime. Detection of the genotypes of these resistant E. coli found that blaTEM-1, blaCTX-M-35 and blaSHV-6 are the main epidemic types. Therefore, the concentration in the β-LAD production wastewater treatment system is higher than that in the general environment, and the bacteria selected from the system not only have a high proportion of resistant bacteria, but also have strong drug resistance, and the drug resistance genes have a certain discharge law.

Environmental emissions of antimicrobial and drug resistance genes have potentially significant environmental risks. Therefore, it is necessary to effectively control the discharge of antibiotics and drug resistance genes in the production process, and set safe discharge standards for antibacterial drugs in sewage. In order to determine the emission standards for antimicrobials, it is necessary to understand the minimum antimicrobial concentration at which antimicrobial agents are selected to spread in a complex microbial environment. At present,

there are few studies on high-efficiency control technologies for antibacterial drugs and drug resistance genes. Therefore, it is very difficult to use the conventional biological treatment technology based on bacteria to degrade the antibacterial drugs, but this aspect is also the focus of future research.

ACKNOWLEDGEMENTS

The authors would like to show sincere thanks to the techniques who have contributed to this research and the authors of the references.

REFERENCES

[1] Wang, L., Kitaichi, K., Hui, C., Takagi, K., Takagi, K., Sakai, M., Yokogawa, K., Miyamoto, K., Hasegawa, T. (2000) Reversal of anticancer drug resistance by macrolide antibiotics in vitro and in Vivo. Clinical and Experimental Pharmacology and Physiology. 27(8), 587-593.

[2] He, X., Li, S., Wang, Y., Zheng, Z., Zhang, H., Jin, R., Wang, D., Wang, L., Dai, Z. (2016) Determination of antibiotic residues in fishery water environment by high performance liquid chromatography quadrupole time of flight mass spectrometry and its application. Journal of Fisheries of China. 40(4), 15-23.

[3] Zhao, F., Yang, X., Chen, F., Ruan, L., Zhang, H., Yang, Y. (2018) Transport, fate and horizontal transfer of antibiotic resistance DNA in soil and water environment. Environmental Chemistry. 37(8), 1-7.

[4] Carlier, M., Stove, V., De Waele, J., Verstraete, A. (2015) Ultrafast quantification of β-lactam antibiotics in human plasma using UPLC-MS/MS. Journal of Chromatography B. 978-979, 89-94.

[5] Huang, Z., Pan, X., Huang, B., Xu, J., Wang, M., Ren, Y. (2016) Determination of 15 β-lactam antibiotics in pork muscle by matrix solid-phase dispersion extraction (MSPD) and ultra-high pressure liquid chromatography tandem mass spectrometry. Food Control. 66, 145-150.

[6] Li, N., Feng, F., Yang, B., Jiang, P., Chu, X. (2014) Simultaneous determination of β-lactam antibiotics and β-lactamase inhibitors in bovine milk by ultra performance liquid chromatography-tandem mass spectrometry. Journal of Chromatography B. 945-946, 110-114.

[7] Zhang, X., Cai, X. (2014) Rapid simultaneous determination of 53 β-lactam antibiotics and their metabolites in milk by ultra-performance liquid chromatography coupled with triple quadrupole mass spectrometry. 32(7), 693-701.

[8] Zhang, Q., Ye, N., Gu, X., Hao, X., Liu, N. (2009) Development and application of analytical methods for analyses of β-lactam antibiotics residues. 72(5), 394-400.

[9] Noser, J., Hasler, F., Schlotterbeck, G. (2012) Bestimmung von 11 β-Lactamen in Fleisch mittels dispersiver SPE und UPLC-MS/MS. Lebensmittelchemie. 66(5), 121-123.

[10] Asgarali, A., Stubbs, K., Oliver, A., Vocadlo, D., Mark, B. (2009) Inactivation of the glycoside hydrolase NAGZ attenuates antipseudomonal -lactam resistance in pseudomonas aeruginosa. Antimicrobial Agents and Chemotherapy. 53(6), 2274-2282.

[11] Qi, Y., Zhang, L., Wang, J., Cui, R., Mo, M., Yan, G. (2010) Distribution of Drug Resistance Phenotype and Genotype in Enterococcus Faecalis Isolates from Different Animals. 30(7), 962-965.

[12] Rameshkumar, M., Vijaykanth, N., Vignesh, R., Balakrishnan, P., Solomon, S., Arunagirinathan, N. (2014) Trimethoprim sulfamethoxazole drug resistance with co resistance to extended spectrum β-lactam antibiotics among bacterial isolates from HIV patients. BMC Infectious Diseases. 14(3), 57.

[13] Fuda, C., Suvorov, M., Vakulenko, S., Mobashery, S. (2004) The basis for resistance to beta-lactam antibiotics by penicillin-binding protein 2a of methicillin-resistant staphylococcus aureus. Journal of Biological Chemistry. 279(39), 40802-40806.

[14] Kulangara, V., Nair, N., Sivasailam, A., Sasidharan, S., Kollannur, J., Syam, R. (2017) Genotypic and phenotypic β-lactam resistance and presence of PVL gene in staphylococci from dry bovine udder. Plos One. 12(11), 0187277.

[15] Buhle, B., Mrudula, P. (2016) Detection of cfxA2, cfxA3, and cfxA6 genes in beta-lactamase producing oral anaerobes. Journal of Applied Oral Science. 24(2), 142-147.

[16] Madhan, S., Kumar, K., Anand, M., Anand, A., Sudha, R., Yung-Fu, C. (2014) Detection of OXA-1 β-Lactamase Gene of Klebsiella pneumoniae from Blood Stream Infections (BSI) by conventional PCR and in-silico analysis to understand the mechanism of OXA mediated resistance. Plos One. 9(3), 91800.

[17] Xiong, Z., Zhu, D., Zhang, Y., Wang, F. (2002) Extended-spectrum β-Lactamase in Klebsiella pneumoniae and Escherichia coli isolates. National Medical Journal of China. 82(21), 1476.

[18] Nematollahi, D., Nasseri, Y., Amani, A., Fatemi, F. (2013) Kinetic and mechanistic study of drug–drug interaction between acetaminophen and β-lactam antibiotics. Progress in Reaction Kinetics and Mechanism. 38(2), 213-219.

[19] Huang, S., Pan, K., Liu, X., Xie, X., Li, H. (2015) Analysis of the drug-resistant characteristics of Klebsiella pneumoniae isolated from the respiratory tract and CTX-M ESBL Genes. Genetics and Molecular Research: GMR. 14(4), 12043-12048.
[20] Wang, C., Geng, X., Xu, Y., Chen, G., Zhao, Q., Zhou, L., Mi, Z. (2012) Study on β-lactam antibiotic resistant mechanism in pandrug-resistant Acinetobacter baumannii. Chinese Journal of Antibiotics. 37(5), 329-334.

Received: **15.11.2019**
Accepted: **21.01.2020**

CORRESPONDING AUTHOR

Jingqiong Xiao
Panjin Vocational Technical College,
Panjin 124000, China

e-mail:sunquan19101@sina.com

© by PSP Volume 29 – No. 04A/2020 pages 2982-2992 Fresenius Environmental Bulletin

EXPERIMENTAL STUDY ON DAMAGE CHARACTERISTICS OF DIRT BAND BY SHAPED CHARGE BLASTING IN COAL SEAM

Yangbo Pan*

School of Energy and Safety, Anhui University of Science and Technology, Huainan, Anhui Province 232001, China

ABSTRACT

Blasting technology is one of the effective methods to deal with the complex problems in coal mines. In order to solve the mining difficulties caused by the failure of the dirt band to be broken by the shearer in the mining process of coal seam containing dirt band, based on the ordinary deep hole blasting, a study on the damage of dirt band by shaped charge blasting for coal seam containing dirt band is carried out. In this paper, the fracture mechanics model of dirt band in shaped charge blasting is established, and the evolution law of crack and propagation law of blasting stress wave in dirt band and coal by ordinary blasting and shaped charge blasting are analyzed. By introducing the gain coefficient and the decrease coefficient of stress wave intensity in the direction of energy accumulation and non energy accumulation, separately, the calculation equations for the relationship between the range of crushing area and the stress peak value of ordinary blasting and shaped charge blasting in different directions are deduced. The mechanical properties of two identical specimens under the action of ordinary charge blasting and shaped charge blasting are systematically investigated by similar simulated experiment. The experimental data are basically in agreement with the theoretical calculation results. The research results can provide theoretical support for the weakening of dirt band by shaped charge blasting in coal seam containing dirt band.

KEYWORDS:
Coal seam, dirt band, shaped charge blasting, blasting stress wave, crack propagation, environmental damage

INTRODUCTION

With the continuous improvement of the degree of coal mining, the coal seams with better occurrence conditions are gradually becoming fewer and fewer. In China, many mining areas have entered the mining stage of complex structural coal seams. As a kind of complex structural coal seam, according to the statistics of coal occurrence in Shandong Province, the coal seams containing hard dirt bands are widely distributed [1], such as Beisu coal mine in Zoucheng, Huaheng coal mine in Xintai, Juncheng coal mine in Jining and so on. In this kind of coal mine, the hardness of the dirt band in coal seam is very high and the shearer cannot operate normally, which result in mechanical damage to shearer and low mining efficiency [2]. In order to solve the problem of mechanized mining of coal seam containing dirt band, at present, the method of using deep hole pre-splitting blasting to break dirt band in front of working face in advance has been applied in some coal mines. However, the effect of ordinary blasting is not satisfying, and the cracks develop disorderly along the radial direction of the blasting hole, which makes most of the blasting energy dissipated in coal while the blasting energy used for dirt band weakening is low. Accordingly, it is necessary to improve the blasting technique, and the shaped charge blasting technique is put forward, which can accumulate the blasting energy into the dirt band and greatly increase the crushing rate of the dirt band in coal seam in front of the working face, so as to improve mining efficiency of coal seam containing dirt band.

As for the blasting technology to solve the complex problems of coal seam and the treatment of dirt band in coal seam, many scholars have carried out a series of theoretical analyses, numerical simulations and experimental researches, and some achievements have been made. In the aspect of application of blasting technology in coal seam, the mechanism of rock cracking by blasting from the microscopic point of view was analyzed, and the parameters of shaped charge blasting were studied [3]. A series of studies on coal seam permeability improvement by shaped charge blasting in high gas and low permeability coal seam were carried out, and the mechanism of coal cracking and blasting technique were analyzed [4]. Besides, based on field experiment and numerical simulation, the mechanical characteristic of coal and the mechanism of crack propagation under the action of shaped charge blasting were discussed [5]. The dynamic mechanical characteristics of directional

fracture of rock explosion were studied by the transmitted dynamic caustics test [6]. The evolution of cracks in the direction of energy accumulation and non energy accumulation in shaped charge blasting was studied by the methods of model experiment, numerical simulation and field test [7]. The characteristics of cracks and propagation law of stress wave of coal and rock in shaped charge blasting were analyzed by designing similar simulation experiment, and the stress state of the specimens changed remarkably due to the effect of energy accumulation was pointed out [8]. The effects of ordinary blasting and shaped charge blasting on coal fracture and permeability through field experiments were investigated [9]. In the aspect of treatment of dirt band in coal seam, the field test of deep hole pre-splitting blasting weakening dirt band was analyzed, and the blasting technique was introduced [10]. The method of weakening dirt band by interval hydraulic fracturing was studied [11]. A safe and efficient mining method by analyzing the physical and mechanical characteristics of dirt band in thick coal seam containing dirt band was pointed out [12]. From here we see that there are few studies on the connection between blasting technology and dirt band weakening in coal seam at present, in addition, the similar simulated experiments on damage of dirt band and propagation law of blasting stress wave under different blasting charge methods were rarely reported.

In summary, it is important to find a reasonable way to make the dirt band in coal seam achieve ideal crushing, so as to fully realize mechanization of coal mining and improve working efficiency. In this paper, the similar simulated experimental system is used to carry out the contrast experiment of ordinary blasting and shaped charge blasting and systematically study on the mechanical properties of specimens under different blasting charge methods. The experiments provide theoretical support for weakening dirt band by shaped charge blasting technology in coal seam containing dirt band.

MATERIALS AND METHODS

Mechanism of Shaped Charge Blasting. After ordinary blasting, the stress wave and detonation gas propagate irregularly along the radial direction of the blasting hole, and the cracks generated in surrounding rocks extend outward irregularly. Through the change of charge structure, shaped charge blasting is to accumulate energy of blasting in specific direction and improve blasting damage in that direction [13]. The axisymmetric charging method is adopted and a shaped charge liner is installed on the inner wall of the cartridge shell. A cavity formed by the shaped charge liner makes the detonation products move along the direction which perpendicular to the shaped charge liner. It makes the shaped charge liner compressed, and the cavity closed rapidly to produce an impact, forming a high-pressure, high-density and high-speed gas jet, thus the blasting energy is accumulated and the energy density is increased. If the shaped charge liner is made of ductile metal, the metal jet will be formed, causing greater damage [14]. In the application of shaped charge blasting to weaken the dirt band in coal seam, it is difficult to drill and arrange the blasting holes in the dirt band when the hardness of the dirt band is large, therefore, the blasting holes are placed in the coal. In addition, in order to accumulate the blasting energy on breaking the dirt band, the direction of energy accumulation is perpendicular to the dirt band. According to explosion mechanics and fracture and damage mechanics, the rock fracture model of unidirectional shaped charge blasting is established, as shown in Figure 1.

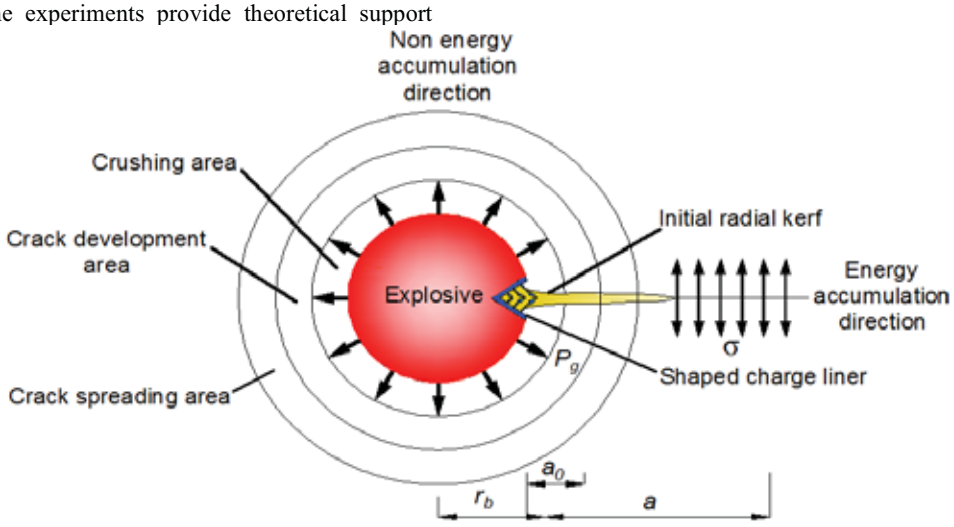

FIGURE 1
Schematic diagram of rock fracture model of unidirectional shaped charge blasting

In the model, the cracks of surrounding rock generated by stress wave are open-type cracks. According to rock fracture mechanics, the stress intensity factor (K) at the tip of open-type crack is as follow [15]:

$$K = P_g F\sqrt{\pi\left(r_b + a\right)} + \sigma\sqrt{\pi a} \qquad (1)$$

Where P_g is the pressure of detonation gas; F is the correction factor; r_b is the radius of blasting hole; a is the length of crack extension; σ is the residual tangential stress.

According to fracture mechanics, the condition of crack extension is $K > K_{IC}$. Where K_{IC} is the fracture intensity factor of rock. Combine with Eq. 1, the condition of crack initiation of rock is as below:

$$P_g > \frac{K_{IC} - \sigma\sqrt{\pi a}}{F\sqrt{\pi(r_b + a)}} \qquad (2)$$

In shaped charge blasting, as a result of the penetration effect of shaped charge jet, the initial crack will be generated in the direction of energy accumulation first, so that the high-pressure detonation gas produced by blasting will converge into the initial crack and the pressure of detonation gas drive the crack extension. According to the law of energy conservation, in the areas beyond the direction of energy accumulation, the energy of stress wave and the pressure of detonation gas decrease. Therefore, shaped charge blasting makes the blasting energy concentrated in the direction of energy accumulation, and the cracks are well developed, while in the areas beyond the direction of shaped charge go to the opposite direction.

Analysis of Propagation Law of Blasting Stress Wave in Coal Seam Containing Dirt Band. When the stress wave propagates to the interface of different media, the reflection and transmission of the stress wave will occur due to the different wave impedances of the media [16]. When the stress wave propagates from coal to dirt band after the explosive blasting in coal seam, and after passing through the interface, the transmitted wave of the stress wave enters the dirt band and causes the damage of the dirt band. According to the condition of continuous propagation of stress wave and Newton's third law, when the stress wave is incident vertically, the stress and mass point velocity on both sides of the interface between coal and dirt band are to satisfy [17]:

$$\begin{cases} \sigma_I + \sigma_R = \sigma_T \\ v_I - v_R = v_T \end{cases} \qquad (3)$$

Where σ_I , σ_R and σ_T are the stresses of incident, reflected and transmitted waves, respectively; v_I , v_R and v_T are the mass point velocities of incident, reflected and transmitted waves, respectively.

In the direction of energy accumulation, the incident stress wave enters from coal to dirt band vertically in the form of P-wave; it can be expressed as follows:

$$\begin{cases} \sigma_I = \rho_1 C_1 v_I \\ \sigma_R = \rho_1 C_1 v_R \\ \sigma_T = \rho_2 C_2 v_T \end{cases} \qquad (4)$$

Where ρ_1 and ρ_2 are the densities of coal and dirt band, respectively; C_1 and C_2 are the velocities of P-wave of coal and dirt band, respectively.

In combination with Eq. (3) and (4), it can be obtained as shown below:

$$\begin{cases} \sigma_R = \sigma_I \left(\dfrac{\rho_2 C_2 - \rho_1 C_1}{\rho_1 C_1 + \rho_2 C_2} \right) \\ \sigma_T = \sigma_I \left(\dfrac{2\rho_2 C_2}{\rho_1 C_1 + \rho_2 C_2} \right) \end{cases} \qquad (5)$$

Let R is the reflection coefficient of stress wave and $R = \dfrac{\rho_2 C_2 - \rho_1 C_1}{\rho_1 C_1 + \rho_2 C_2}$, and T is the transmission coefficient of stress wave and $T = \dfrac{2\rho_2 C_2}{\rho_1 C_1 + \rho_2 C_2}$. The relationship between R and T is as follow:

$$1 + R = T \qquad (6)$$

Because the wave impedance of dirt band is larger than that of coal, that is to say $\rho_2 C_2 > \rho_1 C_1$, it can be obtained from Eq. (6) that $R > 0$ and $T > 1$, thus the reflected wave is in the same direction as the incident wave, so that the peak value of transmitted wave is enhanced.

Under the action of blasting, the cracks in surrounding rock are the result of the interaction of stress wave and detonation gas. After blasting, the crushing area, the crack development area and the crack spreading area will be formed along the radial direction of the blasting hole outward in turn. When blasting, the mass point in the surrounding rock is in a complicated mixed tension-compression stress state with the stress wave propagating outward. The Von Mises effective stress at any point of the surrounding rock is as follow [18]:

$$\sigma_i = \frac{1}{\sqrt{2}}\left[\left(\sigma_r - \sigma_\theta\right)^2 + \left(\sigma_\theta - \sigma_z\right)^2 + \left(\sigma_z - \sigma_r\right)^2 \right]^{\frac{1}{2}} \qquad (7)$$

Where σ_r , σ_θ and σ_z are the radial, tangential and axial stresses of any point of the sur-

rounding rock, respectively, and they can be expressed as below:

$$\begin{cases} \sigma_r = P_0 \overset{\%}{r}^{-\alpha} \\ \sigma_\theta = b\sigma_r \\ \sigma_z = \mu\left(\sigma_r + \sigma_\theta\right) \end{cases} \quad (8)$$

Where P_0 is the radial impact stress that enter the blasting hole wall by decoupling charge; $\overset{\%}{r} = r / r_b$, r is the distance of a mass point in the surrounding rock from the center of the blasting hole; α is the attenuation index of stress wave; μ is the Poisson's ratio of the surrounding rock; b is the coefficient of lateral stress and $b = \mu / \left(\mu - 1\right)$. The P_0 can be shown as below:

$$P_0 = \frac{1}{8}\rho_0 D^2 \left(\frac{r_b}{r_c}\right)^6 n \quad (9)$$

Where ρ_0 is the density of explosive; D is the detonation velocity; r_c is the radius of explosive cartridge; n is the pressure increase coefficient of detonation products impacting on the blasting hole wall.

By substituting Eq. (8) into Eq. (7), it can be obtained as follow:

$$\sigma_i = \frac{1}{\sqrt{2}}\sigma_r \left[\left(1-b\right)^2 - 2\mu\left(1+b\right)^2\left(1-\mu\right) + \left(1+b^2\right)\right]^{\frac{1}{2}} \quad (10)$$

Let

$$A = \frac{1}{\sqrt{2}}\left[\left(1-b\right)^2 - 2\mu\left(1+b\right)^2\left(1-\mu\right) + \left(1+b^2\right)\right]^{\frac{1}{2}},$$

then:

$$\sigma_i = A\sigma_r \quad (11)$$

The blasting load propagates in the form of shock wave in the crushing area [19]. In the direction of energy accumulation, the shock wave will be attenuated before reaching the interface between coal and dirt band, and the attenuation law of the stress of shock wave in coal (P_1) with the propagation distance is as follow [20]:

$$P_1 = P_0 \bar{r}^{-\beta} \quad (12)$$

Where $\bar{r} = r_1 / r_b$, r_1 is the distance of a mass point in coal from the center of the blasting hole; β is the attenuation index of shock wave and $\beta = 2 + \mu_1 / \left(1+\mu_1\right)$; μ_1 is the Poisson's ratio of coal.

When the shock wave reaches the interface between coal and dirt band, the shock wave stress transmitted into the dirt band (P_2) is as below:

$$P_2 = P_1 T \quad (13)$$

It can be obtained that the attenuation law of the stress of transmitted wave (P_3) in dirt band with propagation distance is as below:

$$P_3 = P_2 \underline{r}^{-\gamma} \quad (14)$$

Where $\underline{r} = r_2 / r_b$, r_2 is the distance between a mass point in dirt band and the interface; γ is the attenuation index of transmitted wave and $\gamma = 2 + \mu_2 / \left(1+\mu_2\right)$; μ_2 is the Poisson's ratio of dirt band.

When the peak stress is greater than the dynamic compressive strength of dirt band, the dirt band will be crushed, forming the crushing area. Outside the crushing area, when the stress is greater than the dynamic tensile strength dirt band, the dirt band will be destroyed by tension, forming the crack development area. Because of the special charging method, the initial impact stresses in the direction of energy accumulation and non energy accumulation are different from that in the ordinary blasting. Therefore, the gain coefficient (C_G) of stress and the decrease coefficient of stress (C_D) are introduced in the direction of energy accumulation and the direction of non energy accumulation, respectively, and the peak value of the effective stress of the mass point in dirt band and coal in the edge of the crushing area respectively meets the following requirements:

$$\begin{cases} \sigma_{d\max} = C_G \sigma_{cd} \\ \sigma_{c\max} = C_D \sigma_{cd}^{'} \end{cases} \quad (15)$$

Where $\sigma_{d\max}$ and $\sigma_{c\max}$ are the peak value of effective stress of the mass point of dirt band in the edge of the crushing area in the direction of energy accumulation and the peak value of effective stress of mass point of coal in the edge of the crushing area in the direction of non energy accumulation respectively; σ_{cd} and $\sigma_{cd}^{'}$ are the dynamic compressive strength of dirt band and coal respectively.

In ordinary blasting, according to Eq. (12) and (15), the radius of crushing area in coal can be obtained as follow:

$$r_x = \left(\frac{\sigma_{cd}^{'}}{AP_0}\right)^{-\frac{1}{\beta}} r_b \quad (16)$$

According to Eq. (14) and (15), the radial length of the crushing area in dirt band in the vertical direction can be expressed as follow:

$$r_y = \left(\frac{\sigma_{cd}}{P_2}\right)^{-\frac{1}{\gamma}} r_b = \left(\frac{\sigma_{cd}}{AP_0 \bar{r}^{-\beta} T}\right)^{-\frac{1}{\gamma}} r_b \quad (17)$$

At this point, it is satisfied that r_1 is equal to the distance from the blast hole to the interface, so that $\bar{r}$ is a fixed value.

In shaped charge blasting, the radius of crushing area in coal in the direction of non energy accumulation can be obtained as follow:

$$r_x^{'} = \left(\frac{C_D \sigma_{cd}^{'}}{AP_0} \right)^{-\frac{1}{\beta}} r_b \tag{18}$$

In the direction of energy accumulation, the radial length of the crushing area in dirt band can be expressed as follow:

$$r_y^{'} = \left(\frac{C_G \sigma_{cd}}{P_2} \right)^{-\frac{1}{\gamma}} r_b = \left(\frac{C_G \sigma_{cd}}{AP_0 \bar{r}^{-\beta} T} \right)^{-\frac{1}{\gamma}} r_b \tag{19}$$

In combination with Eq. (16) and (18), it can be obtained as shown below:

$$\frac{r_x^{'}}{r_x} = C_D^{-\frac{1}{\beta}} \tag{20}$$

In combination with Eq. (17) and (19), it can be obtained as shown below:

$$\frac{r_y^{'}}{r_y} = C_G^{-\frac{1}{\gamma}} \tag{21}$$

In summary, under the condition of only changing blasting charge structure, compared with ordinary blasting method, the gain coefficient of stress of shaped charge blasting in the direction of energy accumulation is C_G, the length of the crushing area in the dirt band is $C_G^{-1/\gamma}$ times that of ordinary blasting; the decrease coefficient of stress in the direction of non energy accumulation is C_D, and the radius of the crushing are is $C_D^{-1/\beta}$ times that of ordinary blasting. Therefore, the similar simulated experiments are designed to verify the theoretical derivations.

Establishment of Experimental System. The similar simulated experimental system is assembled with experimental box, counter-force device, data acquisition system, et cetera. The composition of the experimental box are steel plates of 10 mm thick, and the internal space is with the geometry size of 500 mm (length) × 500 mm (width) × 600 mm (height). The counter-force device consists of a reaction steel plate of 15 mm thick and four round steels with a diameter of 20 mm, and the reaction steel plate and the bottom of the box are connected by the round steels. A steel plate will be placed on the top of the specimen and four lifting jacks will be placed above the steel plate before the beginning of the experiment. Thus, the reaction force formed by the jacks is used to load the top of the specimen, so as to achieve the effect of simulating the vertical geostress. The experimental device is shown in Figure 2.

FIGURE 2
Similar simulated experimental device

Design of the Experiments. The experiments are based on the occurrence of coal seam containing dirt band of a coal mine in Shandong Province. The average thickness of the coal seam is 1.5 m, and a layer of dirt band with an average thickness of 0.3 m which made of carbonaceous sandstone contained in the middle level of the coal seam. The blasting holes are arranged in the coal seam near to the interface between coal and dirt band and staggered up and down the dirt band layer. Two identical specimens are contrast tested respectively by ordinary blasting and shaped charge blasting. The schematic diagram of the experimental model is shown in Figure 3 (the unit marked in the figure is millimeter, similarly hereinafter).

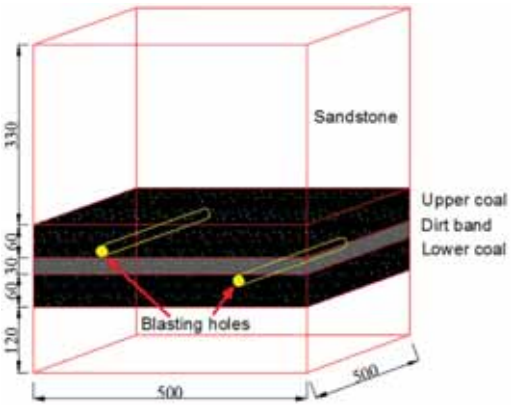

FIGURE 3
Schematic diagram of experimental model

TABLE 1
Mechanical parameters of original sandstone, coal and dirt band

Rock type	Density (g/cm^3)	Poisson's Ratio	Elasticity Modulus (GPa)	Compressive Strength (MPa)
Sandstone	2.56	0.21	25.3	62.5
Coal	1.41	0.29	4.5	10.9
Dirt band	2.68	0.22	27.4	98.8

According to the similarity law, the similar simulated materials and the original materials need to satisfy the following proportional relationship in their corresponding physical quantities: $\alpha_L = L_H / L_M$, $\alpha_\gamma = \gamma_H / \gamma_M$, $\alpha_\sigma = \alpha_L \cdot \alpha_\gamma$. Where α_L is the length scale ratio, α_γ is the density ratio, α_σ is the stress ratio (L and γ represent length and density respectively, and subscripts H and M represent original material and similar simulated material respectively). The mechanical parameters of original sandstone, coal and dirt band are shown in Table 1. According to the occurrence of the original coal seam containing dirt band, similar simulated specimens are made manually, and the similar materials included cement, sand, gypsum and mica powder. Mechanical parameters of each component of similar simulated specimen were obtained through similar proportioning test and mechanical properties test, as shown in Table 2. Base on the test results, it could be calculated that $\alpha_L = \alpha_\sigma / \alpha_\gamma \approx 10$. According to the size of the specimen, the space of 5 m × 5 m × 6 m in the original field was simulated. The finished specimen is as shown in Figure 4.

The data acquisition system is composed of dynamic strain instrument and strain gauges, and two strain gauges are arranged in each specimen. The #1(#3) strain gauge is located in the coal seam, which at the same level as the blasting hole, and it is 30 mm from the center of the blasting hole. The #2(#4) strain gauge is located in the dirt band, which on the same vertical plane as the blasting hole, and it is also 30 mm from the center of the blasting hole, namely, the distances between the two strain gauges and the center of the blasting hole are equal. The locations of the strain gauges in the contrast experiments are shown in Figure 5.

FIGURE 4
Display of the profile of finished specimen

TABLE 2
Mechanical parameters of each component of similar simulated specimen

Rock type	Density (g/cm^3)	Poisson's Ratio	Elasticity Modulus (GPa)	Compressive Strength (MPa)
Sandstone	1.72	0.21	24.9	4.22
Coal	1.58	0.29	4.5	1.22
Dirt band	1.77	0.22	27.1	6.56

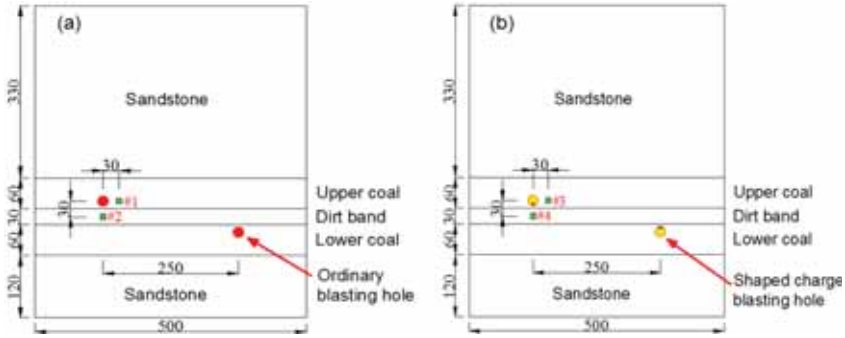

FIGURE 5
Schematic diagram of strain measurement points for specimens
Notes: (a) ordinary blasting and (b) shaped charge blasting

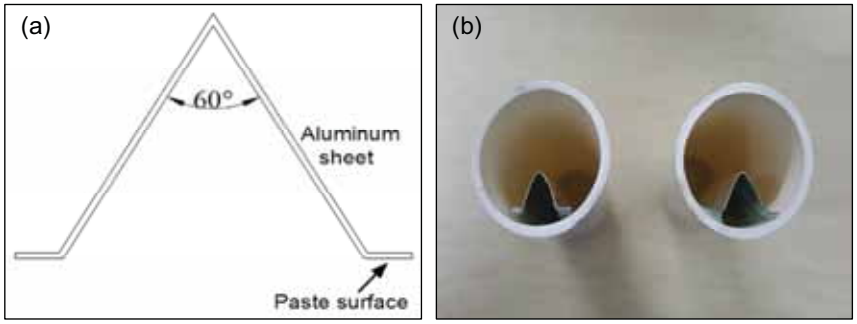

FIGURE 6
Structure of shaped charge explosive cartridge
Notes: (a) schematic diagram of shaped charge liner and (b) shaped charge explosive cartridges (explosives not loaded)

The shell of explosive cartridge is PVC pipe, and the inner diameter was 14 mm. The explosive charging density is 1050~1150 kg/m^3 and the detonation velocity is 7100~7400 m/s, and the explosive is water gel explosive and detonated by detonator. The length of the explosive cartridge is 150 mm, and the vertical distance between the center of the blasting hole and the interface between coal and dirt band is 25 mm. On the basis of ordinary explosive cartridge, a shaped charge liner is added and refitted into the shaped charge explosive cartridge. The shaped charge liner is made of aluminum sheet with thickness of 0.1 mm and the cone angle is set to 60 degrees. The edges of two sides of the aluminum sheet are slightly warped (forming paste surfaces), and pasted with the inner wall of PVC pipe, as shown in Figure 6. According to the experiment requirements, it is necessary to ensure that the difference of blasting charge methods is the only variable in the contrast experiments and keep the same in all other aspects.

RESULTS AND DISCUSSION

Before each experiment, firstly, the counterforce device and lifting jacks are used to exert pressure on the top of the specimen; secondly, open the window on the front of the box and place the explosive cartridges into the blasting holes (in the shaped charge blasting experiment, the opening direction of shaped charge liner is pointed vertically to the dirt band); thirdly, seal the holes with yellow mud, and then close the window and tighten the screws; finally, connect the detonating wires to the detonator, debug the test instruments, and then start the experiment.

Analysis of Stress Evolution. The strain values along the radial direction of the blasting hole were collected by each measuring point in two experiments, and the stress values were obtained by inversion calculation. The stress curves of each measuring point are shown in Figure 7 and Figure 8.

In the stress curve, the negative value of ordinate represents compressive stress while the positive value represents tensile stress. After blasting, the surrounding rock of the blasting hole is first crushed under the action of shock wave, and then the circumferential tensile failure occurs under the action of stress wave. Therefore, there are two stress peaks of the compressive stress and the tensile stress in the stress curve, and this stage is called dynamic load stage. Then, under the action of the air wedge produced by the expansion of a large amount of high-pressure detonation gas, the cracks develop further, causing the stress value to fluctuate up and down in a certain range, and this stage is called the static load stage. Finally, with the release of blasting energy, the change of stress tends to be stable and enters the stable stage.

From the stress curves in Figure 7, in the ordinary blasting, the stress variation in coal is monitored by #1 measuring point, and the peak value is 11.72 MPa (σ_1); the stress variation in dirt band is monitored by #2 measuring point, and the peak value is 12.78 MPa (σ_2). In the shaped charge blasting, the stress variation in the direction of non energy accumulation is monitored by #3 measuring point, and the peak value is 9.73 MPa (σ_3); the stress variation in the direction of energy accumulation is monitored by #4 measuring point, and the peak value is 18.15 MPa (σ_4).

The stress wave transmits and reflects when it passes through the interface between coal and dirt band, so that the stress which monitored at #2 measuring point is the stress of the transmitted wave entering the dirt band. According to the previous analysis, when the stress wave propagates from low wave impedance medium to high wave impedance medium, the reflected wave and the incident wave are in the same direction, so that the stress of the transmitted wave is strengthened, and the peak value of #2 measuring point is greater than that of #1 measuring point. Because the radial distances from the two measuring points to the center of the blasting hole are equal, the transmission

coefficient of stress wave could be approximately determined according to the stress peak value of #1 and #2 measuring points, and that is $T = \sigma_2 / \sigma_1 = 1.09$. The densities of coal and dirt band in specimen can be obtained from Table 2, and the P-wave velocity of coal is 1189 m/s, for dirt band, it is 1216 m/s. By substituting Eq. (5), it can be obtained that the calculated value of transmission coefficient is 1.14. Compared with the experiment result, the error is 4.6%. From Figure 8, it can be seen that the stress peak value in the direction of energy accumulation increases significantly compared with that in the direction of non energy accumulation. In the vertical direction of the blasting hole, from Figures 7(a) and 8(a), it can be seen that the stress peak value of #3 measuring point is smaller than that of #1 measuring point, and decrease coefficient of stress can be approximately considered as $C_D = \sigma_3 / \sigma_1 = 0.83$. In the horizontal direction of the blasting hole, from Figures 7(b) and 8(b), it can be seen that the stress peak value of #4 measuring point is greater than that of #2 measuring point, and the gain coefficient of stress can be approximately considered as $C_G = \sigma_4 / \sigma_2 = 1.42$.

Combined with Figures 7 and Figure 8, it can be seen that in ordinary blasting, the time interval of the static load stage is about 50~110 μs, lasting 60 μs; in shaped charge blasting, the time interval of the static load stage in the direction of energy accumulation is about 50~150 μs, lasting 100 μs, while time interval of the static load stage in the direction non energy accumulation is about 50~90 μs, lasting 40 μs. Therefore, in the direction of energy accumulation, the duration time of the static load stage is prolonged by about 40 μs compared with that of ordinary blasting, and in the direction of non energy accumulation, it is shortened by about 20 μs compared with that of ordinary blasting. It shows that shaped charge blasting not only changes the distribution of blasting stress field around the blasting hole, but also prolongs the action time of detonation gas in the direction of energy accumulation and improves the ability of crack development, however, in the direction of non energy accumulation, it is the opposite.

Analysis of Crack Evolution. After each experiment, the front steel plate of the experimental box is removed and the crack development of the specimens is obtained as shown in Figure 9.

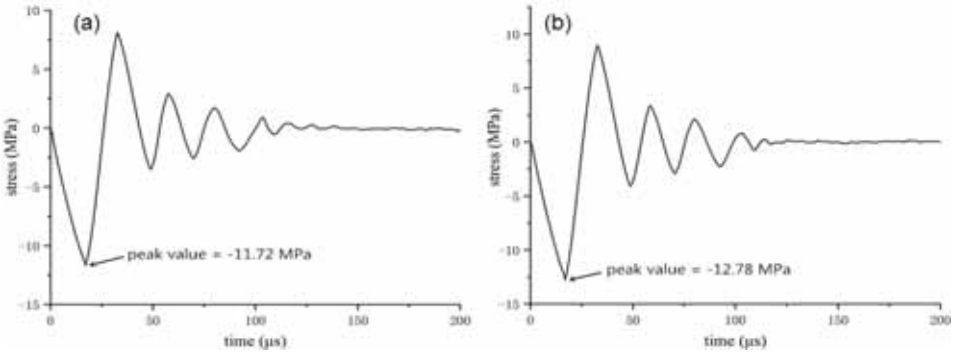

FIGURE 7
Stress curve of measuring points in ordinary blasting
Notes: (a) stress curve of #1 measuring point and (b) stress curve of #2 measuring point

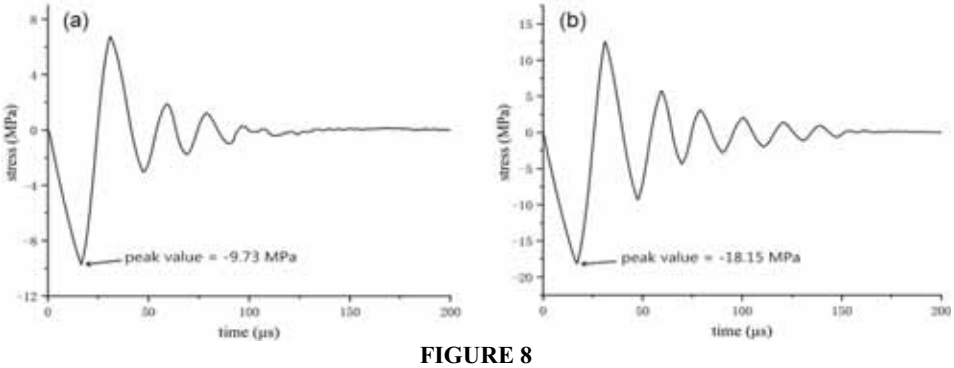

FIGURE 8
Stress curve of measuring points in shaped charge blasting
Notes: (a) stress curve of #3 measuring point and (b) stress curve of #4 measuring point

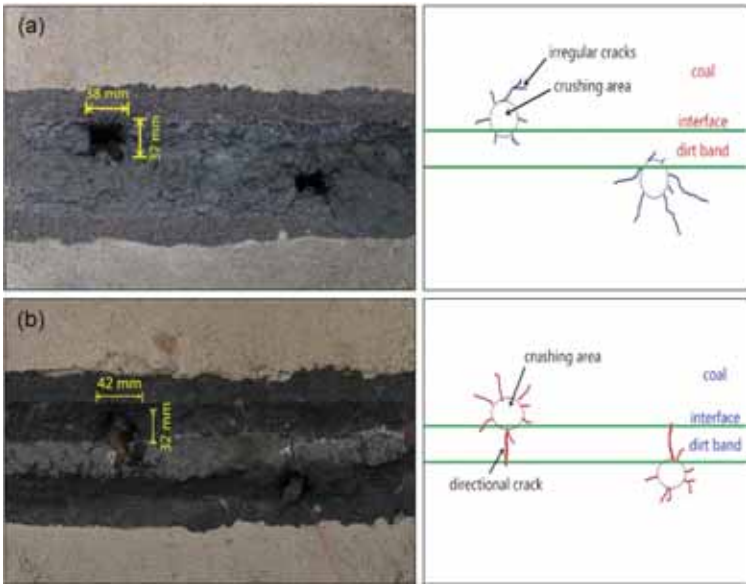

FIGURE 9
Crack development of specimens
Notes: (a) ordinary blasting experiment and (b) shaped charge blasting experiment

From Figure 9(a), it can be seen that after ordinary blasting, a larger crushing area is formed around each blasting hole. The cracks are divergent, that is irregular extension around the blasting hole, and the shape of the crushing area is approximately circular. The diameter of the crushing area in the horizontal direction is measured to be about 38 mm, and that in the vertical direction is 37 mm. However, only a few of short and narrow disordered cracks can be observed on the dirt band. From Figure 9(b), it can be seen that the shape of the crushing area has changed significantly after shaped charge blasting compared with that of ordinary blasting, and the shape of the crushing area is approximately elliptical. The direction of the long axis of the ellipse is the direction of non energy accumulation, while the direction of the short axis of the ellipse is the direction of energy accumulation. Based on the measurement, the length of crushing area in horizontal and vertical directions is 42 mm and 32 mm respectively.

Thus, it can be seen that under the action of shaped charge blasting, in the direction of energy accumulation, the range of the crushing area is reduced, while in the direction of non energy accumulation, the range of the crushing area is increased. After the explosive explosion, in the direction of energy accumulation, firstly, the high-pressure accumulated energy jet begins to penetrate the blasting hole wall, forming the directional crack; secondly, the directional crack created by the jet is much larger than the initial cracks in the other directions of the crushing area and the formation of the directional crack instantaneously creates a larger volume of sudden vacuum, so that causing an inrush of a large amount of detonation gas; finally, driven by detonation gas, the directional crack expands further, thus forming a relatively obvious main crack through the dirt band, as shown in Figure 9(b). As a result of a large amount of detonation gas rush into the directional crack, however, in the direction of non energy accumulation, the energy of detonation gas decreases, and only a small number of cracks can be formed outside the crushing area. Therefore, in Figure 7 and Figure 8, in the static load stage, the duration and stress curve amplitude of #3 measuring point are both less than #1 measuring point, while the duration and stress curve amplitude of #4 measuring points are both greater than #2 measuring point.

Because the distance between the blasting hole and the interface is relatively close, the ratio of the length of the vertical direction of the crushing area in the two experiments can be taken as the ratio of the distance between the edge of the crushing area in the dirt band and the interface. By substituting the length data of crushing area measured in the two experiments into the Eq. (20) and (21) respectively, the decrease coefficient of stress in the direction of non energy accumulation and the gain coefficient of stress in the direction of energy accumulation can be calculated, and the results are as follows:

$$C_D = \left(\frac{r_x'}{r_x}\right)^{-\beta} \approx 0.801 \quad \text{and}$$

$$C_G = \left(\frac{r_y'}{r_y}\right)^{-\gamma} \approx 1.372 \quad (22)$$

Compared with the results of stress measuring, the errors of the decrease coefficient of stress and the gain coefficient of stress calculated by theoreti-

cal equations are 3.6% and 3.5% respectively. Therefore, the experimental results are basically in agreement with the theoretical deduction.

CONCLUSIONS

(1) The rock fracture model of axisymmetric unidirectional shaped charge blasting is established, and the mechanism of shaped charge blasting in coal seam containing dirt band is analyzed. In the process of blasting, the stress wave propagates from coal to dirt band, and reflects and transmits on the interface between coal and dirt band. The transmitted stress wave acts on dirt band and causes damage to dirt band. Through theoretical deduction, the propagation law of stress wave in coal and dirt band is analyzed.

(2) The similar simulated experimental system is established, and the similar simulated experiments of the damage to dirt band are carried out for coal seam containing dirt band under the condition that blasting holes are arranged in coal seam. Through contrast experiments, it is found that the shape of crushing area of ordinary blasting is approximately circular, and the cracks expand irregularly around the blasting hole; the shape of crushing area of shaped charge blasting is approximately elliptical, and a directional crack is formed in the dirt band of the direction of energy accumulation under the combined action of accumulated energy jet and detonation gas. In the direction of non energy accumulation, the range of crushing area increases, and in the static load stage, the duration time is shortened by about 20 μs compared with that of ordinary blasting; in the direction of energy accumulation, the crushing area in the dirt band decreases, and in the static load stage, the duration time is prolonged by about 40 μs.

(3) In the shaped charge blasting, the gain coefficient of stress (C_G) is introduced in the direction of energy accumulation and the decrease coefficient of stress (C_D) is introduced in the direction of non energy accumulation, and the calculation equations are obtained by theoretical deduction, making the connection between the range of crushing area and the peak value of stress. In the experiments, the gain coefficient and decrease coefficient obtained by data acquisition system are basically consistent with those calculated by equations, thus the theoretical deduced equations are verified. Meanwhile, the pollution and damage of the method to the environment are relatively small, and it has good application value.

ACKNOWLEDGEMENTS

The author would like to show sincere thanks to those techniques who have contributed to this research and all the authors of the references.

REFERENCES

[1] Li, Y. (2011) Research and application of the high production and efficiency mining technique in thin coal seam with hard parting band face above confined aquifer. Qingdao: Shandong University of Science and Technology (Dissertation).

[2] Pu, B., Xu, Y., Wang, G., Guo, C. (2005) Studies on blasting parameter of thin coal seam contained Fe_2S nodules high production and high efficiency mining face. Coal Mining Technology. 10(1), 50-52+63.

[3] Luo, Y., Shen, Z. (2006) Application study on directional fracture controlled blasting with shaped charge in rock. Explosion and Shock Waves. 26(3), 250-255.

[4] Guo, D., Zhang, H., Lü, P., Zhang, G. (2014) Effect of fault on deep-hole cumulative blasting to improve coal bed permeability. Journal of University of Science and Technology Beijing. 36(10), 1281-1286.

[5] Guo, D., Lü, P., Pei, H., Shan, Z. (2012) Numerical simulation on crack propagation of coal bed deep-hole cumulative blasting. Journal of China Coal Society. 37(2), 274-278.

[6] Li, Q., Liang, Y, Ren, K., Zeng, J., Zhang, X. (2010) Experimental study of propagation of directional cracks with shaped charge under blasting load. Chinese Journal of Rock Mechanics and Engineering. 29(8), 1684-1689.

[7] Mu, C., Wang, H., Huang, W., Kuang, C. (2013) Increasing permeability mechanism using directional cumulative blasting in coal seams with high concentration of gas and low permeability. Rock and Soil Mechanics. 34(9), 2496-2500.

[8] Liu, J., Liu, Z., Gao, K., Ma, Y., Li, Z., Guo, L. (2014) Experimental study and application of directional focused energy blasting in deep boreholes. Chinese Journal of Rock Mechanics and Engineering. 33(12), 2490-2496.

[9] Lyu, P., Dou, X., Zhu, T., Wang, J. (2013) Application on permeability improved technology with deep borehole energy accumulation blasting in coal seam. Coal Science and Technology. 41(12), 35-38.

[10] Tao, K., Yu, F. (2012) Technology Research on crossheading deep-hole pre-splitting blasting hard dirt band. Safety in Coal Mines. 2, 55-57.

[11] Lekontsev, Y., Sazhin, P., Ushakov, S. (2012) Interval hydraulic fracturing to weaken dirt bands in coal. Journal of Mining Science. 48(3), 525-532.
[12] Pan, W., Zhao, H., Yang, S. (2011) Key technology of safety and effective mining in thick coal seams with dirt band. 2nd International Conference on Manufacturing Science and Engineering, Guilin, China.
[13] Guo, D., Song, W., Li, Z., Qin, F., Liu, X. (2009) Research on splitting technical of coal bed deep-hole cumulative blasting to improve permeability. Journal of China Coal Society. 34(8), 1086-1089.
[14] Yuan, S., Zhang, F., Ji, Z., Yang, Z. (2007) Controlled blasting theory and practice. Tian: Tianjin University Press (Dissertation).
[15] Guo, D., Shang, D., Lü, P., Wang, S., Wang, J. (2013) Experimental research of deep-hole cumulative blasting in hard roof weakening, Journal of China Coal Society, 38(7), 1149-1153.
[16] Gao, K., Liu, Z., Liu, J., Zhu, F. (2018) Propagation law and failure characteristics of blasting stress wave in structural belt coal-rock. Journal of China Coal Society. 43(1), 79-86.
[17] Dong, Y., Huang, C., Duan, Z. (2005) Analysis on the influence of multi-layered media on stress wave propagation. Chinese Journal of High Pressure Physics. 19(1), 59-65.
[18] Dai, J. (2001) Calculation of radii of the broken and cracked areas in rock by a long charge explosion. Journal of Liaoning Technology University (Natural Science). 20(2), 144-147.
[19] Lyu, P. (2014) Research on Coal Body Permeability Increase and Crack Generation Mechanism under Cumulative Blasting. Beijing: China University of Mining and Technology (Dissertation).
[20] Dai, J. (2013) Dynamic Behaviors and Blasting Theory of Rock, 2nd Edition. Metallurgical Industry Press, Beijing, China.

Received: **18.11.2019**
Accepted: **29.01.2020**

CORRESPONDING AUTHOR

Yangbo Pan
School of Energy and Safety
Anhui University of Science and Technology
Huainan, Anhui Province 232001, China

e-mail: coolpyb@qq.com

© by PSP Volume 29 – No. 04A/2020 pages 2993-3002 Fresenius Environmental Bulletin

PROPERTIES EVALUATION AND APPLICATION OF A NOVEL DRILLING FLUID WITH STRONG PLUGGING AND INHIBITION PERFORMANCE

Jianghong Jia[1,*], Zhongwen Song[2], Xiaoming Zhang[1]

[1]Drilling Technology Research Institute, Shengli Petroleum Engineering Co. Ltd, Sinopec, Dongying 257017, China
[2]Sinopec Shengli Oilfield Company Engineering Technology Management Center, Dongying 257107, China

ABSTRACT

The shale formation in the Changning area is prone to complex engineering problems such as collapse of the wellbore, falling off the block and leakage during the drilling process. The reason is that the drilling fluid cannot effectively block the micro-cracks in the formation, and it is impossible to effectively suppress the internal hydration of the shale. In this paper, from the direction of improving the plugging and inhibition ability of the drilling fluid system, the strong plugging capacity plugging agent HXSZ-1 was added to the system to improve the plugging capacity of the system. Through the synergistic action of KCl, polyamine inhibitor and silicate, the inhibition performance of the system could be further improved. The indoor evaluation showed that the system had excellent plugging ability. The reduction rate of mud cake permeability at room temperature was 68.24%, and the HTHP static filtration loss was 2.7 mL, which was equivalent to the plugging performance of oil-based drilling fluid. The secondary recovery rate of shale was as high as 96.89% with the linear expansion rate of less than 4.8%, and the anti-pollution ability was strong. The EC50 value of the system was 11500 mg/L, which was non-toxic and could meet environmental protection requirements. The field application results showed that the system had stable performance during the drilling process. The average enlargement rate of well diameter was controlled within 4%, and the drilling cycle was shortened by 20%. The purpose of excellent and fast drilling was realized, and the field application effect was good.

KEYWORDS:
Shale formation, water-based drilling fluid system, plugging capacity, inhibition capacity, environmentally friendly

INTRODUCTION

At present, shale gas exploration and development in China has been paid more attention. According to the characteristics of shale gas reservoir formation, shale gas development mainly consists of extended reach wells and cluster horizontal wells. Horizontal well drilling technology is one of the core technologies of shale gas development, which is widely used in shale gas exploration and development [1-3]. In order to increase production by hydraulic fracturing in the later stage, horizontal well sections are mostly distributed in the formation with natural fracture development and drilled along the direction of minimum horizontal in-situ stress. In the process of drilling, the filtrate of drilling fluid is very easy to invade the shale, which can lead to well loss, well collapse and other problems. At present, oil-based drilling fluid is the preferred drilling fluid system in horizontal well section of shale gas formation, but its preparation cost is high and there are environmental protection problems. Once a well loss occurs, it is difficult to deal with it, which often causes great economic losses. Therefore, it is urgent to develop high-performance water-based drilling fluid system.

In Changning area of Sichuan Province, different from other strata, there are a lot of microfractures and pores developed in shale formation, which is very easy to hydrate when encountering water [4-5]. In the process of drilling, the shale formation is prone to complex engineering problems such as collapse of the wellbore, falling off the block and leakage. Because extremely small size pores and fractures are developed in shale, shale has extremely low permeability and porosity. The transmission of pore pressure will lead to the increase of pore pressure and weaken the effective stress support of drilling fluid column. In addition, shale gas reservoir is mainly composed of hard and brittle shale, mainly illite and illite/montmorillonite [6-9]. When shale contacts with water, it is easy to have strong hydration. Strong repulsive force of hydration film will lead to deformation or peeling off of hydration interface, which will cause serious wellbore instability problem. These problems seriously restrict the wide application of water-based drilling fluid in shale gas development, so it is necessary to improve the plugging and inhibition performance of water-based drilling fluid system [10]. By adding high performance plugging agent BZ-YFT and

polyamine inhibitor BZ-YZJ, the plugging and inhibition performance of the drilling fluid system in the fauqi block of missan oilfield in Iraq has been greatly improved. The application results showed that the drilling efficiency and economic benefits of the block were good.

Starting from the structural characteristics and components of shale in Changning area, the source of downhole complexity was analyzed and the two key treatment agents (plugging agent and shale inhibitor) of drilling fluid system were optimized, thus forming a set of water-based drilling fluid suitable for Changning shale block, which had excellent plugging and inhibition ability. The field application further proved that the system had excellent performance in drilling process, which provided research ideas and technical support for the wide range promotion of water-based drilling fluid.

GEOLOGICAL CONDITIONS OF SHALE FORMATION AND METHODS.

Shale Mineral Composition Analysis. The core used in this paper was taken from Longmaxi formation shale formation in Changning, Sichuan Province. X-ray diffraction test was carried out on the core, and the results are shown in Table 1.

Table 1 shows that the illite content in this area was relatively high, with an average content of 71.17%, chlorite content of 22.58%, and illite/montmorillonite mixed layer content of 5.93%. The shale core in this area was free of montmorillonite and kaolinite. It shows that the lithology of the area was relatively brittle, and the phenomenon of falling block was easy to occur. In addition, the existence of interlayer minerals such as chlorite and illite/montmorillonite mixed layer would lead to the hydration phenomenon in shale, which was the internal cause of wellbore instability.

Microstructure Analysis of Shale. There are a lot of microfractures and pores developed in the shale formation of the target block, which are the channels for the surrounding liquid phase to invade the shale interior, thus causing the shale interior hydration and the wellbore instability [11-12]. We could observe the microstructure of the shale in this area, so as to provide data support for the optimization of plugging agents, which was very helpful for improving the plugging capacity of the system. Fig. 1 shows the micro situation of the shale in the target area.

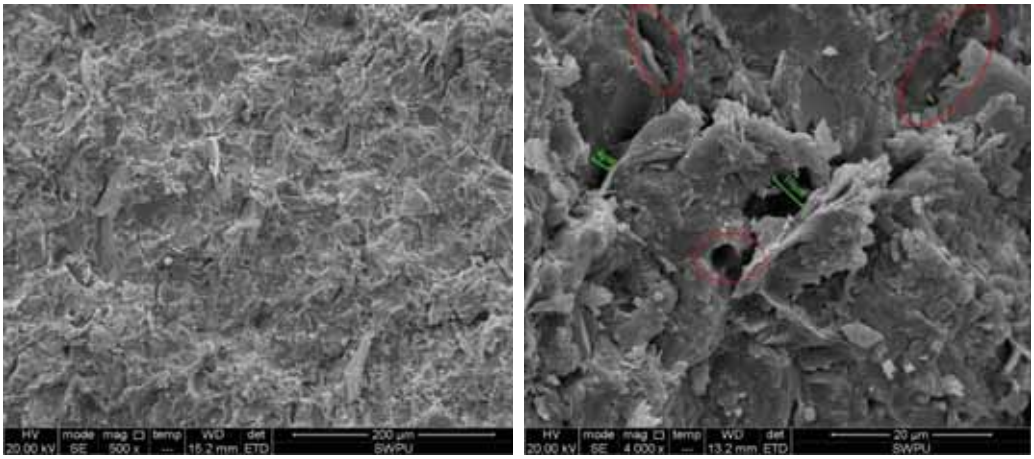

FIGURE 1
Shale core microstructure

TABLE 1
Clay mineral composition of Longmaxi shale in Changning

Label	Relative content of clay minerals（%）					Interlayer ratio(%S)
	Illite（I）	Montmorillonite（S）	I/S	Kaolinite（K）	Chlorite（C）	
1	68.5	0	8.3	0	22.3	10
2	69.4	0	8.1	0	21.8	10
3	74.1	0	4.6	0	24.4	10
4	71.5	0	7.1	0	21.6	10
5	70.7	0	6.9	0	22.3	10
6	72.6	0	4.2	0	23.3	10
7	71.7	0	2.9	0	23.9	10
8	73.8	0	5.8	0	21.1	10
9	69.3	0	6.0	0	21.2	10
10	70.1	0	5.4	0	23.9	10

TABLE 2
Permeability of shale core through gas measurement

Label	Length (cm)	Section area (cm^2)	Confining pressure (MPa)	Effective pressure (MPa)	Gas viscosity (cP)	R^2	Permeability (mD)
1	5.00	5.02	8.00	2.64	0.0189	1.00	3.67×10^{-4}
2	5.00	5.02	7.96	2.65	0.0189	1.00	3.53×10^{-4}

TABLE 3
Test results of triaxial mechanics test

Label	Confining pressure /MPa	Young modulus /GPa	Poisson's ratio	Stress value /MPa
1	25	21.7	0.33	139.7
2	25	26.2	0.19	170.6
3	25	25.4	0.24	182.4
4	25	22.1	0.25	135.1
5	25	23.6	0.26	146.2
6	25	24.5	0.30	158.6
7	25	21.6	0.27	120.9
8	25	23.8	0.23	164.7
9	25	23.2	0.31	159.4
10	25	21.5	0.33	157.9

In addition, the porosity test of shale core was carried out to analyze the development of micro fractures and pores in shale. Table 2 shows the permeability of shale core measured by experiment.

It can be seen in Fig. 1, the shale surface was dense and microfractures and pores were developed. The opening of microfractures was about 4 μm and the diameter of pores was about 10 μm. According to the data in Table 2, the shale permeability in this area was in the order of 10^{-4}. To sum up, this area was a shale stratum with dense, micro fracture and pore development.

Triaxial Stress Experiment of Shale. The triaxial mechanics test of shale core was carried out with the test temperature of 80 ℃ and the confining pressure of 25 MPa. The test results are shown in Table 3.

It can be seen from the data in Table 3, the compressive strength of shale rock in this area was high. The distribution of Young's modulus was 21.5-26.2 GPa and Poisson's ratio was 0.19-0.33. The average brittleness index of the rock in this area was about 50%, which indicated that the brittleness of the rock was strong, and the brittle failure of the wellbore was easy to occur.

Wellbore Instability Analysis and Solutions. The drilling fluid intrudes into the surrounding shale under the three main factors of positive pressure difference, micro fracture and pore development in shale formation, and the activity of drilling fluid is greater than that of surrounding shale formation [13-16]. It can be seen from the above experimental data that there were a large number of clay minerals in this area. When the invaded liquid phase contacted with clay minerals, the hydration of clay minerals would occur. In addition, due to the polarity difference of different mineral components in the rock, the hydration and expansion degree of clay minerals would be different, leading to the difference of expansion pressure. Furthermore, non-expansive minerals such as quartz and calcite surround clay minerals, which would intensify the change of swelling pressure. Based on the above actions, wellbore instability occurred [17-18].

To solve the above-mentioned wellbore instability problem, we could start from internal and external factors [19]. The internal cause was to enhance the strength of the rock by improving the cementation between the shale particles, and the external cause was to effectively inhibit the hydration of clay minerals inside the shale by adding key treatment agents to the system, forming a set of wrapping film on the outside of the rock, and preventing the invasion of external liquid phase into the interior. Through the accumulation of nano plugging agents, micro fractures and pores in the formation could be effectively sealed. The above operations were used to achieve the purpose of maintaining wellbore stability.

RESULTS AND DISCUSSION

Evaluation of Water-based Drilling Fluid System with Strong Plugging and Inhibition Performance. A set of shale water-based drilling fluid system with strong plugging and inhibition performance was designed by using the compound synergism of KCl, polyamine inhibitor and sodium silicate, the highly effective plugging effect of nano plugging agents selected through laboratory experiments, and considering the compatibility with other treating agents in the system. The formulation of shale water-based drilling fluid system was as follows: (2-3％) Sodium bentonite + (0.3-0.5％) NaOH + (5-7％) PEG + (3-5％) Plugging agent HXSZ-1 + (2-3％) Polyamine inhibitor + (2-3％) Sodium silicate + (5-7％) KCl + (3-5％) PAC-LV + (3-4％) Lubricant OEM + (0.8-1.0％) SP-80 + Barite. Next, the performance of the water-based

drilling fluid system was evaluated by laboratory experiments.

(1) Conventional Performance. Table 4 shows that the rheological parameters of the drilling fluid change little before and after aging, its performance is relatively stable, and it can resist temperature of 120 ℃.

(2) Plugging Performance. The plugging performance of the system was evaluated by simulated microfracture experiment and shale cuttings bed experiment. The specific operation was as follows [20-22].

1) Microcrack simulation experiment. ① First, prepare soil slurry for curing for 24 h, then take 8% soil slurry into the 200 ml container and mix it at 800 r/min. During the mixing process, add 40 g calcium carbonate with 1250 mesh size and 10 g calcium carbonate with 2200 mesh size. After stirring for 10 min, add 150g barite of 325 mesh size, and add 2 g polyacrylamide after stirring for 5min. After adding, adjust the rotating speed to 10000 r/min, and mix at the rotating speed for 30min, then move to the low-speed mixer to mix until the mud was evenly dispersed (About 30 minutes). ② Take a proper amount of the above-mentioned mixed mud and put it into the high-temperature and high-pressure water loss instrument, and prepare the mud cake under the conditions of 3.5 MPa and room temperature. After 30min, pour out the mud in the upper part of the instrument. The mud cake left in the instrument was the prepared mud cake. Then place the kettle body in the electric hot air dryer to heat and dry. When the water content on the mud cake surface was not much, take out the kettle body. Insert the prepared metal fine needle from one side of the filter paper until the mud cake was completely punctured, that is to say, the mud cake sewing operation was completed (Generally, when the diameter of fine metal needle was 0.25 mm and the number of jacks was 9, the permeability was similar to that of the studied formation). Put the kettle into the high-temperature and high-pressure water loss instrument, and place the new filter paper under the mud cake. Then measure the water loss of the mud cake under the same conditions above, and calculate the permeability of the mud cake at this time. ③After the determination of clean water filtration, pour out the clean water in the kettle and tie the drilling fluid to be tested to the scale line. Measure the filtration under the same test conditions, record the filtration and calculate the mud cake permeability at this time. Finally, the decline rate of mud cake permeability was calculated.

According to the above evaluation method, the plugging artificial mud cake ability of the common drilling fluid system (polymer drilling fluid system, polysulfonate drilling fluid system and oil-based drilling fluid system) and the water-based drilling fluid system for shale horizontal well were tested. The test results are shown in Table 5.

Table 5 shows that all kinds of drilling fluid systems could effectively reduce the permeability of mud cake and show good sealing effect. At room temperature, the permeability reduction rate of water-based drilling fluid system for shale horizontal well developed in laboratory was very close to that of oil-based drilling fluid used on site, which showed that the plugging performance of the system was equivalent to that of oil-based drilling fluid

2) HTHP shale bed simulation plugging experiment. The simulated plugging experiment of HTHP shale bed was carried out by using high-temperature and high-pressure water loss instrument. 30 g of shale rock cuttings (20-40 mesh) were put into the high temperature autoclave, and 50 g of shale rock cuttings (60-100 mesh) were put into it. Finally, pour the required evaluation drilling fluid into the kettle and measure the 30 min static filtration of four drilling fluid systems at 3.5MPa and 120 ℃. The experimental results are shown in Table 6.

TABLE 4
Conventional performance of water-based drilling fluid

Experimental condition	AV/(MPa·s)	PV/(MPa·s)	YP/Pa	YP/PV	$G_{10s/10min}$
Before aging	47.0	21	26	1.24	9/12
After aging	50.0	24	26	1.08	10/12

Notes: The aging condition was 120 ℃, and the aging time was 16 h.

TABLE 5
Plugging effect of various drilling fluid systems

Sample	Mud cake thickness/mm	API filtration loss /mL	Mud cake permeability/10^{-3} mD	Reduction rate of mud cake permeability /%
Clean water	4.6	13.6	1.747	—
Polymer drilling fluid system	4.4	6.3	0.774	55.70%
Polysulfonate drilling fluid system	3.8	5.6	0.594	60.00%
Indoor development of water-based drilling fluid system for shale horizontal well	4.2	3.8	0.446	74.47%
On site oil based drilling fluid system	4.0	3.0	0.335	80.82%

Notes: Concentration was the mass concentration of finished dispersion in clean water.

TABLE 6
The filtration of drilling fluid in shale bed at high-temperature and high-pressure conditions

Formula \ Time	1	7.5	15	30	Cumulative
Polymer drilling fluid system	1.8	3.9	4.4	9.5	19.6
Polysulfonate drilling fluid system	0.6	2.8	1.8	3.6	9.0
Indoor development of water-based drilling fluid system for shale horizontal well	0	0.6	1.2	1.4	3.2
On site oil based drilling fluid system	0	0.5	0.6	0.8	1.9

TABLE 7
Experimental results of shale hot-rolled dispersion

Sample	R_1/%	R_2/%	R/%
Clean water	62.43	30.81	49.35
Polysulfonate drilling fluid system	71.82	59.36	82.65
Polymer drilling fluid system	69.24	54.57	78.81
On site oil based drilling fluid system	98.87	97.65	98.77
Indoor development of water-based drilling fluid system for shale horizontal well	98.41	96.89	98.46

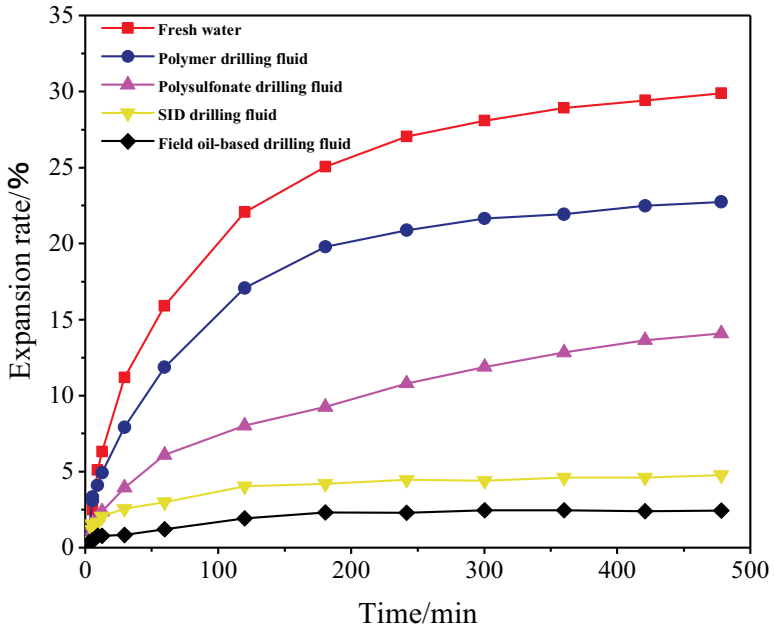

FIGURE 2
Shale linear expansion rate

Table 6 shows that the static filtration of polymer and polysulfonate drilling fluid system was 19.6 and 9.0mL respectively under the test conditions, while the static filtration of water-based drilling fluid system developed for shale horizontal well and oil-based drilling fluid used on site was 3.2 and 1.9 mL respectively. It showed that the plugging performance of water-based drilling fluid system developed in laboratory was excellent, which could be compared with that of oil-based drilling fluid.

(3) Inhibition Performance. 1) Hot-rolled dispersion experiment. Take 50g of 6-10 mesh shale cuttings from the study area and dry them in a drying oven at a temperature of (105±3) ℃, then take them out and place them in a vessel to cool them to room temperature. Then, the aged tanks containing clear water, polysulfonate drilling fluid, on-site oil-based drilling fluid, polymer drilling fluid and indoor water-based drilling fluid for shale horizontal well were respectively added with the above cooled shale cuttings, and the hot rolling operation was carried out at (80±3)℃ for 16 h. After hot rolling, the rock cuttings were recovered by 40 mesh sieve and washed by petroleum ether. After washing, the rock cuttings were placed in a drying oven and dried for 4 hours at (105±3)℃. After drying and cooling for 24h, weigh and record the data. Finally, the shale recovery rate under the

above five conditions was calculated. The results are shown in Table 7.

It can be seen from the data in Table 7 that the primary and secondary recovery rate of shale drilling fluid developed in the laboratory were far higher than that of clean water, polysulfonate drilling fluid system and polymer drilling fluid system, and were very close to the rolling recovery rate of oil-based drilling fluid used in the field. Therefore, the inhibition performance of water-based drilling fluid developed in laboratory was equivalent to that of oil-based drilling fluid.

2) Linear expansion experiment. By measuring the linear expansion rate of water-based drilling fluid filtrate in clean water and on-site oil-based drilling fluid, polysulfonate drilling fluid, polymer drilling fluid and the water-based drilling fluid developed in laboratory, the ability of different drilling fluids to inhibit shale hydration was compared. The experimental results are shown in Figure 2.

It can be seen from Fig. 2 that the expansion rate of shale in clear water, polymer drilling fluid and polysulfonate drilling fluid had changed significantly in the first 120 min, and the water-based drilling fluid for shale horizontal well developed indoors and the oil-based drilling fluid used on site basically maintained a low range. After 300 minutes, the expansion rate of shale core was stable. The expansion rate of shale in the filtrate of water-based drilling fluid and polymer drilling fluid was higher, while the expansion rate of shale in the filtrate of water-based drilling fluid developed in the laboratory was lower than that of polysulfonate drilling fluid, and it was very close to the field oil-based drilling fluid [23]. Therefore, the inhibition performance of water-based drilling fluid developed in laboratory was better than that of other two drilling fluid systems and was equivalent to that of oil-based drilling fluid system.

(4) Evaluation of Salt Resistance. In order to evaluate the anti-salt pollution performance of water-based drilling fluid for shale horizontal well, NaCl with the concentration of 4%, 7%, 10%, 13%, 15% and 18% were added into the drilling fluid respectively. Then, the rheological property and filtration reduction capacity of the drilling fluid were measured. The relationship between HTHP filtration and apparent viscosity of the drilling fluid with NaCl concentration is shown in Fig. 3.

Fig. 3 shows that the change of apparent viscosity of drilling fluid with the increase of NaCl content was not obvious. The HTHP filtrate loss of drilling fluid increased with the increase of NaCl content. When the NaCl content exceeded 13%, the HTHP filtrate loss of drilling fluid system increased significantly. Therefore, the salt resistance of drilling fluid was 13%, and the system had good salt resistance.

(5) Evaluation of Anti-Calcium Pollution Sbility. In order to evaluate the anti-calcium pollution performance of water-based drilling fluid for shale horizontal well, $CaCl_2$ with the concentration of 0.3%, 0.5%, 0.9%, 1.2% and 1.5% were added to the drilling fluid respectively. Then, the rheology and filtration reduction capacity of the drilling fluid were measured. The relationship between HTHP filtration and apparent viscosity of the drilling fluid with $CaCl_2$ concentration is shown in Fig. 4.

Fig. 4 shows that the apparent viscosity of drilling fluid first increased slightly with the increase of $CaCl_2$ addition, then decreased slowly, and the overall change trend was not obvious. With the increase of $CaCl_2$ addition, the HTHP filtration of drilling fluid first increased slowly and then increased rapidly. When the amount of $CaCl_2$ was more than 0.9%, the filtrate loss of HTHP in drilling fluid system increased significantly. Therefore, the salt resistance of drilling fluid was 0.9%, and the system had good calcium resistance.

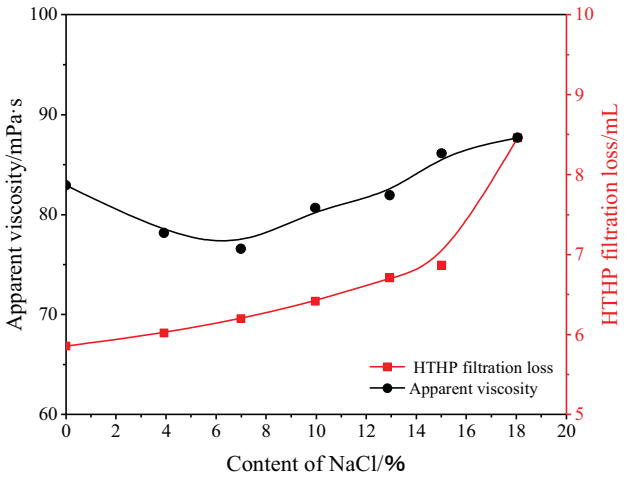

FIGURE 3
Experimental results of anti NaCl pollution performance of drilling fluid

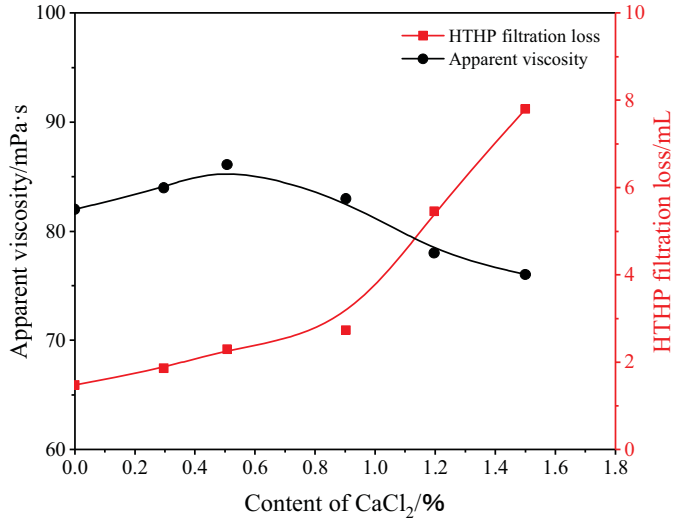

FIGURE 4
Experimental results of anti $CaCl_2$ pollution performance of drilling fluid

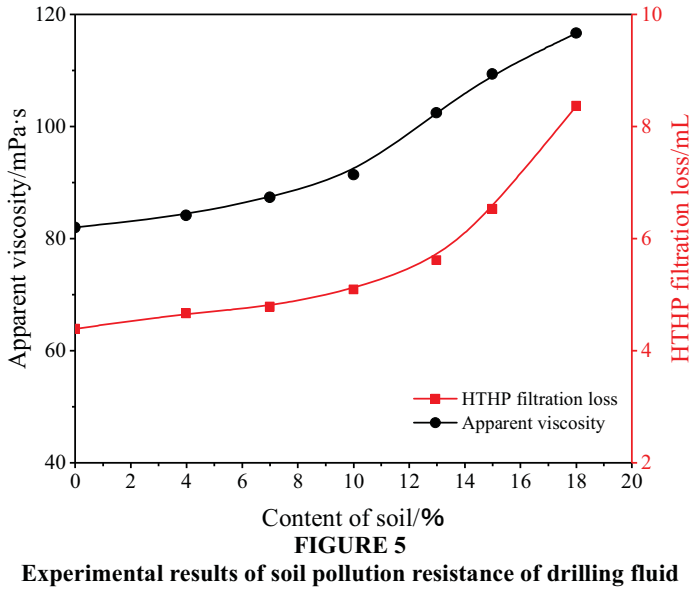

FIGURE 5
Experimental results of soil pollution resistance of drilling fluid

(6) Evaluation of Anti-Soil Pollution Resistance. In order to evaluate the anti-soil pollution performance of water-based drilling fluid for shale horizontal well, soil with the concentration of 4%, 7%, 10%, 13%, 15% and 18% were added to the drilling fluid respectively. Then, the rheological property and filtration reduction capacity of the drilling fluid were measured. The relationship between HTHP filtration and apparent viscosity of the drilling fluid with soil concentration is shown in Fig. 5.

It can be seen from Fig. 5 that the apparent viscosity and HTHP filtration of drilling fluid increased slightly first and then sharply with the increase of soil addition. When the amount of soil was more than 10%, the apparent viscosity and HTHP filtration of drilling fluid system increased significantly. Therefore, the soil resistance of drilling fluid was 10%, and the system had good soil pollution resistance.

Overall, the water-based drilling fluid system of shale horizontal well developed in the laboratory had excellent salt resistance, calcium resistance and soil pollution resistance, which could meet the performance requirements of water-based drilling fluid in the target formation [24-25].

Biological Toxicity. The biotoxicity of drilling fluid system can be determined by luminescent bacteria method [22, 26]. When EC50 value is more than 10000 mg/L, it is non-toxic. The biological toxicity test results of the three drilling fluids are shown in Table 8.

TABLE 8
Biological toxicity test results of three kinds of drilling fluids

Label	Sample	EC_{50} /mg L^{-1}	Toxicity grade
1	Polymer drilling fluid system	14500	Non-toxictity
2	Indoor development of water-based drilling fluid system	11500	Non-toxictity
3	Oil-based drilling fluid system	2000	Low toxicity

The experimental results show that the water-based drilling fluid system prepared in the laboratory was non-toxic, harmless to the environment and could meet the requirements of environmental protection.

Field Application. Well H2 is a shale gas exploration well in Changning block, with a linear distance of 1.0 km from well H1. The main drilling horizons are Xiahanjiadian formation, Shiniulan formation and Longmaxi formation. The buried depth and geological characteristics of the two wells are basically the same. Well H2 adopts three open hole structure, and the strata of Shiniulan formation and Longmaxi formation adopted the drilling fluid system with strong plugging and inhibition performance developed in laboratory. In the shale section of the target formation, there was no borehole shrinkage and bit mud inclusion, indicating that the drilling fluid had strong inhibition performance. During the drilling of Longmaxi formation in the target formation, there was no collapse and block fall in the wellbore, and the whole drilling process was smooth. Comparing well H2 with well H1, the drilling period was shortened by 20%. The results of electrical logging showed that the average well diameter expansion rate of the whole well section was 3.42%, and the target formation was 2.13%, which was 70% lower than that of H1 well. The application results showed that the drilling fluid system could greatly reduce the probability of complex accidents, at the same time, greatly improve the drilling rate, and achieve the purpose of optimal and fast drilling.

CONCLUSIONS

(1) In the target area, shale micro fracture and pore were developed with high content of clay, and hydration expansion was easy to occur. The difference of lithologic composition was easy to cause the difference of expansion pressure, and the wellbore instability was serious. To solve the wellbore instability problem, two key aspects were to improve the plugging and inhibition performance of drilling fluid system, which put forward higher requirements for the plugging and inhibition ability of water-based drilling fluid

(2) According to the indoor evaluation, the permeability reduction rate of the mud cake of the indoor development system was 74.47%, and the static filtration of HTHP was only 3.2 mL. The secondary recovery rate of shale was 96.89%, and the linear expansion rate was less than 4.8%, which showed that the system had excellent plugging and inhibition ability, and the effect was similar to that of oil-based drilling fluid. At the same time, the system had good anti-pollution performance, and non-toxictity could meet the requirements of environmental protection.

(3) The field application results showed that the developed drilling fluid system with strong plugging and inhibition performance was suitable for drilling in Changning shale block, which basically solved the problem of wellbore collapse and block falling. The average enlargement rate of well diameter was controlled within 4%, and the drilling cycle was shortened by 20%. The purpose of excellent and fast drilling was realized, and the field application effect was good.

ACKNOWLEDGEMENTS

The authors would like to express their sincere thanks to the persons who have contributed to the research and all the authors of the references.

REFERENCES

[1] Xu, J., Qiu, Z., Huang, W., Zhao, X. (2017) Preparation and performance properties of polymer latex SDNL in water-based drilling fluids for drilling troublesome shale formations. Journal of Natural Gas Science and Engineering. 37, 462-470.

[2] Yu, L., Zhang, J., Liu, B., Zhang, R., Ji, Y., Liu, C. (2017) Study and Application of Borehole Stabilization Technology in Shale Strata Containing Micro-Fractures. Petroleum Drilling Techniques. 45(3), 27-31.

[3] Ning, F., Zhang, L., Tu, Y., Jiang, G., Shi, M. (2010) Gas-hydrate formation, agglomeration and inhibition in oil-based drilling fluids for deep-water drilling. Journal of Natural Gas Chemistry. 19(3), 234-240.

[4] Liu, J., Sun, J. (2016) Effects of Drilling Fluid Activity on Hydration and Dispersion of Formation Rocks in Shale Gas Drilling in Chuan-Dian Area. Drilling Fluid & Completion Fluid. 33(2), 31-35.

[5] Bavoh, C., Yuha, Y., Tay, W., Ofei, T., Lal, B., Mukhtar, H. (2019) Experimental and modelling of the impact of quaternary ammonium salts/ionic liquid on the rheological and hydrate inhibition properties of xanthan gum water-based muds for drilling gas hydrate-bearing rocks. Journal of Petroleum Science and Engineering. 183, 106468.

[6] Saleh, T., Ibrahim, M. (2019) Advances in functionalized Nanoparticles based drilling inhibitors for oil production. Energy Reports. 5, 1293-1304.

[7] Saikia, T., Mahto, V. (2016) Experimental investigations of clathrate hydrate inhibition in water based drilling fluid using green inhibitor. Journal of Petroleum Science and Engineering. 147, 647-653.

[8] Liang, L., Xiong, J., Liu, X. (2014) Effects of hydration swelling and wettability on propagation mechanism of shale formation crack. Petroleum Geology and Experiment. 36(6), 780-786.

[9] Li, M., Liu, Z., Hu, J. (2017) Application of high density oil-based drilling fluid in shale gas horizontal wells of Changning-Weiyuan Bolck. Natural Gas Exploration and Development. 40(1), 88-92.

[10] Tang, W., Wang, C., Lin, Y., Gao, S., Han, Z., Chai, L., Zhen, J., Xue, Y., Jin, J., Chen, X. (2017) The Characteristic Analysis of Micro-nano Pore Structure in Shale Gas Formation and Its Sealing Evaluation. Science Technology and Engineering. 32-38.

[11] Shi, B., Xia, B., Lin, Y., Xu, J. (2012) CT imaging and mechanism analysis of crack development by hydration in hard-brittle shale formations. Acta Petrolei Sinica. 33(1), 137-142.

[12] Li, Z., Li, G., Yang, X., Wang, X., Liu, L., Dai, C. (2018) Study on the invasion mechanism of liquid phase into shale formation under the effect of fluid-solid coupling. Oil Drilling & Production Technology. 40(6), 720-725.

[13] Aftab, A., Ismail, A., Ibupoto, Z., Akeiber, H., Malghani, M. (2017) Nanoparticles based drilling muds a solution to drill elevated temperature wells: a review. Renewable and Sustainable Energy Reviews. 76, 1301-1313.

[14] Khodja, M., Canselier, J., Bergaya, F., Fourar, K., Khodja, M., Cohaut, N., Benmounah, A. (2010) Shale problems and water-based drilling fluid optimisation in the Hassi Messaoud Algerian oil field. Applied Clay Science. 49(4), 383-393.

[15] Zhang, X., Jiang, G., Dong, T., Wang, L., Li, X., Wang, G. (2018) An amphoteric polymer as a shale borehole stabilizer in water-based drilling fluids. Journal of Petroleum Science and Engineering. 170, 112-120.

[16] Lei, M., Huang, W., Li, N., Jia, J., Li, J., Wang, Y., Li, J. (2017) The damage mechanism of oil-based drilling fluid for tight sandstone gas reservoir and its optimization. Journal of Petroleum Science and Engineering. Journal of Petroleum Science and Engineering. 158, 616-625.

[17] Wen, H., Chen, M., Jin, Y., Wen, Z., Ye, X., Yang, S. (2014) Experimental research on brittle shale failure caused by drilling fluid activity. Oil Drilling & Production Technology. 1, 57-60.

[18] Zhang, L., Wang, S., Bao, X., Liu, F., Xiong, M., Lu, M., Jin, J., Qiao, Y. (2015) Adsorption behaviors of the two organic compounds with different polarity on cation-saturated clay minerals. Journal of Safety and Environment. 15(2), 200-204.

[19] Wang, W., Qiu, Z., Zhong, H., Huang, W., Zhao, X., Dong, B., Bao, D. (2015) Preparation and properties of thermosensitive poly (NIPAm-co-AA)/ nano-SiO_2 composite blocking agent for shale gas reservoir. Acta Petrolei Sinica. 36(3), 378-384.

[20] Barati, P., Shahbazi, K., Kamari, M., Aghajafari, A. (2017) Shale hydration inhibition characteristics and mechanism of a new amine-based additive in water-based drilling fluids. Petroleum. 3(4), 476-482.

[21] An, Y., Jiang, G., Qi, Y., Huang, X., Shi, H. (2016) High-performance shale plugging agent based on chemically modified graphene. Journal of Natural Gas Science and Engineering. 32, 347-355.

[22] Nie, Z., Zhang, Z., Luo, H., Zou, K. (2018) Key technologies for directional well drilling in high-pressure anhydrite salt layers. Natural Gas Industry B. 5(6), 598-605.

[23] Ghanbari, S., Naderifar, A. (2016) Enhancing the physical plugging behavior of colloidal silica nanoparticles using binomial size distribution. Journal of Natural Gas Science and Engineering. 30, 213-220.

[24] Saikia, T., Mahto, V., Kumar, A. (2017) Quantum dots: a new approach in thermodynamic inhibitor for the drilling of gas hydrate bearing formation. Journal of Industrial and Engineering Chemistry. 52, 89-92.

[25] Rafati, R., Smith, S., Haddad, A., Novara, R., Hamidi, H. (2017) Effect of nanoparticles on the modifications of drilling fluids properties: a review of recent advances. Journal of Petroleum Science and Engineering. 161, 61-76.

[26] Li, X., Yan, X., Kang, Y. (2017) Investigation of drill-in fluids damage and its impact on wellbore stability in Longmaxi shale reservoir. Journal of Petroleum Science and Engineering. 159, 702-709.

[27] Liu, T., Jiang, G., Zhang, P., Sun, J., Sun, H., Wang, R., Zheng, M. (2016) A new low-cost drilling fluid for drilling in natural gas hydrate-bearing sediments. Journal of Natural Gas Science and Engineering. 33, 934-941.
[28] Pei, Y., Paton, D., Knipe, R., Wu, K. (2015) A review of fault sealing behaviour and its evaluation in siliciclastic rocks. Earth-Science Reviews. 150, 121-138.

Received: **19.11.2019**
Accepted: **02.02.2020**

CORRESPONDING AUTHOR

Jianghong Jia
Drilling Technology Research Institute,
Shengli Petroleum Engineering Co. Ltd,
Sinopec, Dongying 257017, China

e-mail:, zhonghy191919@sina.com

© by PSP Volume 29 – No. 04A/2020 pages 3003-3012 Fresenius Environmental Bulletin

AFLATOXIN M_1 CONCENTRATION IN MILK AND MILK PRODUCTS FROM AYDIN PROVINCE, TURKEY

Selda Bulca*

Aydin Adnan Menderes University, Faculty of Engineering, Department of Food Engineering, 09010, Aydin, Turkey

ABSTRACT

This study's goal was to document levels of aflatoxin M_1 (AFM_1) in raw milk, UHT milk, cheese, and yoghurt produced and sold at local markets in Aydin Province, Turkey. A total of 115 samples were analyzed: 30 raw milk, 24 UHT milk, 41 cheese, and 20 yoghurt samples. AFM_1 content was determined by extracting AFM_1 from the samples, retaining aflatoxin with immunoaffinity column, eluting with methanol and acetonitrile into vials, and injecting samples into an RP-HPLC to quantify the amount by fluorescence detector. The results shown that AFM_1 was present. The numbers of contaminated samples of raw milk, UHT milk, cheese, and yogurt samples were 13 (43.3%), 14 (58.3%), 21 (51.2%), and 2 (10%), respectively. Five (16.6%) raw milk and two (8.3%) UHT milk samples had concentrations that exceeded the limits of the Turkish Food Codex (TFC). All cheese and yoghurt samples were within TFC limits. AFM_1 content in raw and UHT milk samples were significantly different from the European Commission and TFC limits of 50 ng/kg ($p<0.01$). For these samples, there were no statistically significant differences.

KEYWORDS:
Milk and Dairy Products, Aflatoxin M_1, HPLC

INTRODUCTION

Raw milk quality is very important for producing safer milk products at lower prices. There are several sources of contamination in raw milk. Toxin concentrations in raw milk must be determined before using it to produce milk byproducts. Raw milk contaminated with toxins or chemical residues should be avoided.

Aflatoxins are mycotoxins, which are toxic and carcinogenic. They are secondary metabolites mostly produced by Aspergillus species such as *Aspergillus parasiticus, Aspergillus niger*, and *Aspergillus flavus*. These metabolites are immunosuppressive, teratogenic, and mutagenic. They are classified as aflatoxin B_1 (AFB_1), AFB_2, AFG_1, and AFG_2 [1, 2]. In food and animal feed, there are 400 known forms of mycotoxins. Many scientific studies have reported that AFB_1 is formed in contaminated feed and then converted into AFM_1 in the liver. If dairy cattle are fed with AFB_1-contaminated feed (such as silage that contains the metabolic products of AFB_1), the hydroxylation of AFB_1 transforms it into AFM_1 (4-hydroxy-AFB_1) [3, 4], which is formed via the microsomal cytochrome P450-associated pathway [5]. After that, AFM_1 is secreted into milk [6] 12–24 hours after consumption contaminated feed [7]. The occurrence of AFM_1 in milk and dairy products depends on several factors such as feeding, geography, and season. When animals have been fed grass, weed, and coarse feeds, AFM_1 content is lower in summer [8, 9].

Rustom [10] claimed that for AFM_1 to decompose, heat treatment of 237–306°C was required. However, there are contradictory statements on the influence of heat on AFM_1 levels. Some researchers have reported that heating milk decreases aflatoxin content [11]. In other studies, the concentration of the toxin, spray drying, fermentation, the preparation of various dairy products, autoclaving, and other kinds of food processing procedures were unable to decrease the levels of this toxin [12, 13, 14, 15, 16].

Recently, several new techniques have been used to reduce the AFM_1 content in milk. A practical and effective method of using certain strains of lactic acid bacteria is removing AFM_1 from contaminated milk [17, 18]. In another study, *Bacillus subtilis* ANSB060 reduced the AFM_1 biodegradation product (BDP) in milk, which is contaminated with AFB_1 [19]. Azarikia et al. [20] identified high concentrations of AFB_1 and AFM_1 in breast milk samples in Iran. The estimated average daily consumption of AFM_1 by infants revealed a high risk of infant exposure to AFM_1 [20, 21].

Several studies have demonstrated that AFM_1 can bind to milk proteins, especially to hydrophobic parts of the casein fraction, which leads to high concentrations of AFM_1 in curd during cheese production [22, 23]. As a result, AFM_1 concentrations are three to four times higher in cheese than in milk [24]. Another study revealed that AFM_1 only bound with soluble proteins (whey proteins) after the binding of native caseins that were saturated with AFM_1 [25].

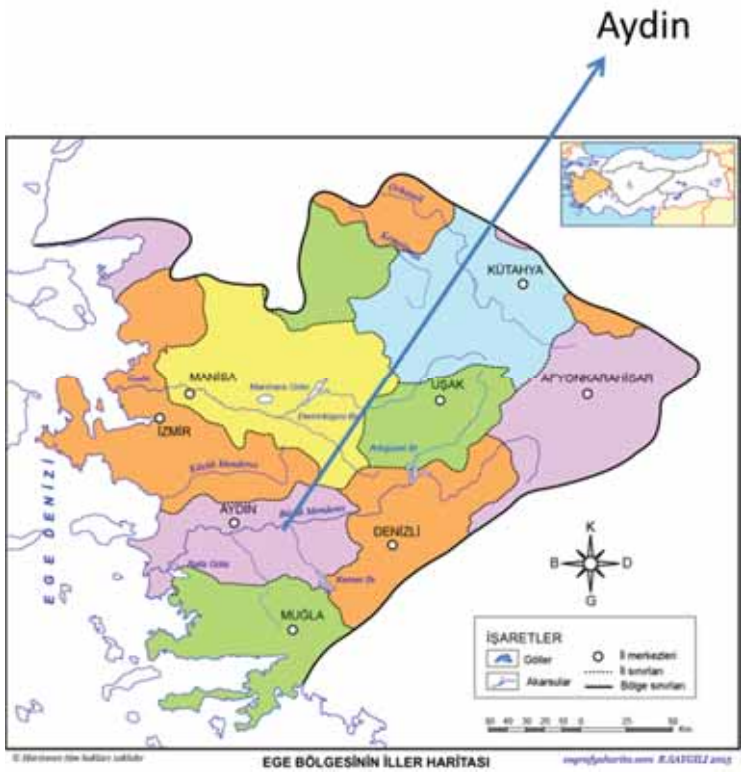

FIGURE 1
Map indicating the province in western Turkey where samples were collected.
(http://cografyaharita.com/haritalarim/4mege-bolgesi-iller-haritasi.png)

AFB_1 has more carcinogenic properties than AFM_1. Therefore, it is classified as a Group 1 carcinogen by the International Agency for Research on Cancer (IARC), meaning that it is possibly carcinogenic to people [26, 27]. AFM_1 can destroy DNA and causes problems such as chromosomal distortions, gene mutations, and cell transformation [28, 29]. Some studies have shown that AFM_1 is hepatotoxic [30].

More than sixty national governments have a legal limit for aflatoxin levels of 50 ng/l and 500 ng/kg for dairy products [13]. The EC has set a limit of 50 ng/l for AFM_1 in milk and dairy products [31]. According to the United States Food and Drug Administration (USFDA), the highest permissible level is 500 ng/l [32].

Widespread AFM_1 contamination in raw milk has been reported in countries such as Sudan, Indonesia, Kenya, Pakistan, Nigeria, Italy, Iran, and Turkey [33, 34, 35].

To determine AFM_1 content in milk, dairy products, and feeds, the most common techniques are ELISA, because it is rapid, specific, simple, sensitive, and portable [36, 37], high performance liquid chromatography (HPLC) [33, 38], thin layer chromatography (TLC) [39, 40], and liquid chromatography tandem mass spectrometry (LC-MS/MS) [41, 42].

According to TFC and EC regulations, AFM_1 should not exceed 25 ng/kg in infant and follow-on milk. According to the TFC [43], the legal AFM_1 limit is 50 ng/l in raw milk, heat-treated milk, and milk for the manufacture of milk-based products; for cheese, the limit is 250 ng/kg.

The consumption of milk and dairy products is widespread in the province of Aydin, Turkey, but the occurrence of AFM_1 has not been studied. The purpose of this study was to determine AFM_1 content in raw milk, UHT milk, cheese, and yoghurt samples produced and sold in this province. AFM_1 content was determined with HPLC and compared to the legal limits in Turkey.

MATERIALS AND METHODS

Materials. In this study, 30 raw milk samples were obtained from a local producer; 24 UHT milk, 41 cheese, and 20 yoghurt samples were purchased at local markets. Sampling locations are shown in Figure 1. Samples were stored at -20°C until the analysis, which was performed in duplicate.

TABLE 1
Incidence and levels of AFM1 in milk products reported in previous studies performed between 2010 and 2018

Samples	n	Number of AFM1 detected samples n (%)	AFM1 range (ng/l or ng/kg)	Positive mean (ng/l or ng/kg)	Country, Reference	Method of Analysis
Fresh milk	156	125 (80.1)[1]	20–3090	346.2	Pakistan, [36]	ELISA
UHT milk	214	n.g.	2.29–21.4	5.57	Croatia, [51]	ELISA
Fluid milk	84	33 (39)[2]	100–1270	720	Mexico, [37]	ELISA
Raw (fresh) milk	52	21 (40.4)[2]	9–>1000	500	Brazil, [49]	UHPLC-FL
Raw milk	530	280 (52.8)[3]	10–200	73.0	China, [50]	HPLC-MS/MS
Yoghurt	96	28 (47)[1]	4–615.8	147.1		
White cheese	119	14 (15)[1]	4–595.4	189.1	Pakistan, [33]	HPLC
Cream Cheese	150	10 (11)[1]	4–456.3	172.9		
Butter	74	17 (52)[1]	4–413.4	156.29		
Raw milk	826	23 (2.8)[1]	5.16–110.93	32.4	Kosovo, [44]	ELISA
UHT milk	69	2 (2.6)[1]	n.g.	5.10		
Raw milk	45	22 (48.9)[1]	100–3800	n.g.	India, [47]	HPLC
UHT milk	45	19 (42.2)[1]	60–700	n.g.		
Raw milk	678	382 (56.3)[1]	≤0.25–<1000	282	Serbia, [48]	ELISA
Yoghurt	21	n.g.	4.16–38.21	31.32	Qatar, [52]	ELISA
Cheese	46	39 (84.8)[1]	2.53–217.15	197.74		
Raw milk	135	20 (31.25)[1]	0.00–99.92	18.26		
--Farm	33	8 (32)[1]	0.00–97.68	29.82	Iran, [46]	ELISA
--Collection centers						
Pasteurized milk	12	2 (18.18)[1]	2.04–90.01	32.23		
Raw milk	72	17 (23.6)[1]	10–420	65	China, [45]	LC-MS/MS
UHT milk	153	31 (54.9)[1]	6–160	48	China, [53]	ELISA
Pasteurized milk	26	25 (96.2)[1]	23–154	71		
Pasteurized milk	116	31 (26.7)[4]	5.8–528.5	52.8	Iran, [15]	ELISA
UHT milk	109	19 (17.4)[4]	5.6–519.9	46.4		
Yoghurt	60	3 (5%)[1]	19.7–319.4	130.5	Iran, [54]	ELISA
Cheese	80	11 (13.8%)[1]	14.3–572.1	133.2		
UHT milk	75	23 (30.7)[2]	1000–4100	n.g.	Brazil, [55]	HPLC
--Winter Yoghurt	25	4 (18.19)[5]	21.1–137.6	36. 33	Iran, [56]	ELISA
--Summer Yoghurt	25	2 (15.38)[5]	22–65.1	17.58		
UHT milk	152	4 (2.6)[1]	n.g.	19.6	Brazil, [57]	HPLC

The values in parentheses indicate the percentage of samples
1: European Commission [58]: the maximum level of AFM_1 in liquid milk 50 ng/kg; for cheese it is 250 ng/kg
2: US FDA, Mexican, and Brazilian regulations limit AFM_1 content in milk to 500 ng/kg.
3: In China and the US, the legal limit is for milk 500 ng/l
4: ISIRI [59] (Institute of Standards and Industrial Research of Iran): limit for milk is 500 ng/l
5: ISIRI [60] (Institute of Standards and Industrial Research of Iran): limits for yoghurt is 50 ng/l
n.g.: not given

Method. All samples were evaluated for AFM_1 content with the following method: extracting the milk and milk product samples, retaining the AFM_1 by immunoaffinity column, collecting in vials by washing with methanol and acetonitrile, and finally injecting the sample into an RP-HPLC with fluorescence detector.

First, milk samples were brought to room temperature at 35°C in a water bath and the samples were centrifuged at 4000 rpm for 15 minutes. The fat layer was removed and the supernatant was collected in a separate tube and filtered through Whatman grade 4 filter paper. Fifty milliliters of filtrate was passed through an immunoaffinity column (R-Biopharm Rhone, Ltd.) and the column was washed twice with 10 ml of water. In the first stage, 1.25 ml of methanol- acetonitrile (2:3; v:v) were used and in the latter stage, 1.25 ml of water were used.

Specifications and operating conditions of the HPLC (High Performance Liquid Chromatograph, Shimadzu, Tokyo, Japan) were as follows. The system controller was an SCL-10A with an isocratic pump (LC-10AT), a fluorescence detector (RF-10AXL), a column oven (CTO-10AS), and an autosampler (SIL-10AD). An ACE 5 C18 (4.6 x 250 mm) column with a flow rate of 1.0 ml/min was used. The mobile phase was methanol-acetonitrile-water (2:3:5; v:v:v). The column temperature was adjusted to 25°C. Injection volume was 100 µl excitation was 360 nm, and emission was 430 nm.

The AFM_1 solution, with a concentration of 1000 ng/ml, was diluted to 100 ng/ml to prepare standard stock solution. Then, 500 µl AFM_1 solution was pipetted and completed to 5 ml with acetonitrile. Acetonitrile-methanol-water (3:2:5; v:v:v) was used to dilute standard solutions.

Evaluation of Data. The t-test was used to evaluate significant differences between the groups.

TABLE 2
Determination of AFM1 content in dairy products in Turkey conducted between 2008 and 2015

Samples	n	Number of samples and n (%)	AFM1 range max-min (ng/l or ng/kg)	Mean (ng/l or ng/kg)	Reference, Region	Method of Analysis
Yoghurt	80	16 (2)[1]	10–475	66.1	[71], Erzurum	ELISA
Kashar cheese	40	1 (0.4)[2]	50–700	130	[62], Turkey	ELISA
Tulum cheese	16	n.g.	50–100	70		
Dil cheese	22	n.g.	100–200	150		
Cream cheese	21	n.g.	50–160	90		
White cheese	67	5 (2.05)[2]	50–2100	280		
Raw milk	77	4 (1.64)[2]	5–410	31		
Raw milk	90	63 (70)[1]	54.4–65.5	59.9	[63], Kayseri	ELISA
Raw milk	50	n.d.	1–30	8.73	[61], Kayseri	ELISA
Yoghurt	50	7 (14)[4]	2.5–78	30.3		
Tulum cheese	20	2 (3)[4]	13–378	98.7		
White cheese	20	n.g.	15.6–154.6	72.74		
Kashar cheese	20	1 (2)[4]	12–369.5	115.3		
Kashar cheese	147	16 (11.11)[5]	15–3774	273	[38], Turkey	HPLC
UHT milk	41	3 (7.3)[1]	6.42–71.33	17.76	[67], Burdur	ELISA
Raw milk	45	16 (35.5)[6]	15.3–80	45.3	[66], Burdur	ELISA
White cheese	45	3 (6.7)[6]	55–600	199.4		
Yoghurt	45	0	50–360	176.6		
Raw milk	38	21 (55.3)[7]	0.82–125.70	56.74	[65], Şanliurfa	ELISA
UHT milk	12	3 (25)[7]	18.93–91.27	43.1		
White pickled cheese	50	5 (10)[7]	40.41–130.89	103.2		
Yoghurt	50	5 (10)[7]	40.62–72.04	55.28		
White cheese	60	12 (20)[3]	16–700	n.g.	[75], Ankara, Nevşehir, Yozgat	HPLC-FL
Raw goat milk	39	4 (10.2)[1]	2.1–866.6	n.g.	[64], Mersin	HPLC
Raw cow milk	53	39 (73.5)[1]	2.1–866.6	n.g.		
UHT milk	45	1 (2.2)[1]	1–59	n.g.		
White cheese	193	51 (26.4)[3]	52–860	284	[76], Erzurum	ELISA
--Yoghurt from Mardin	42	5 (11.9)[1]	10–101	65.7	[68], Şanliurfa, Mardin	ELISA
--Yoghurt from Sanliurfa	48	29 (60.4)[1]	10–515	174.6		
Cream cheese	100	18 (18)[3]	0–4100	330	[74], Istanbul, Izmir, Kayseri, Konya, Tekirdag	ELISA
Kashar cheese	132	36 (27.3)[7]	50–690	194	[69], Istanbul, Izmir, Konya, Tekirdag, Edirne	ELISA
UHT milk	100	31 (31)[7]	10–630	67		

1: TFC limit for yoghurt is 50 ng/kg
2: TFC limit for raw milk is 50 ng/kg and 500 ng/kg for cheese
3: TFC limit for cheese is 250 ng/kg
4. TFC limit for milk is 50 ng/l; for cheese it is 250 ng/kg; for yoghurt it is 50 ng/kg
5: TFC limit for cheese is 500 ng/kg
6: TFC limit for milk is 50 ng/l and for dairy products, 500 ng/kg
7: TFC limit for milk is 50 ng/l; for yoghurt it is 50 ng/l; for cheese it is 250 ng/kg
n.g.: not given

RESULTS AND DISCUSSIONS

Dairy products are very susceptible to AFM_1 contamination. Due to its toxicity and carcinogenic properties, the presence of AFM_1 in milk and milk products creates a human health risk, so it is important to identify its presence and concentration. Table 1 shows the prevalence of AFM_1 in milk and milk products in different countries between 2010 and 2018. Table 2 shows the presence of AFM_1 in dairy products in Turkey between 2008 and 2015.

Table 3 shows the results of the present study. AFM_1 content was undetectable in 65 of 115 samples. Of the 50 samples with AFM_1, 13 (43.3%) were raw milk, 14 (58.3%) were UHT milk, 2 (10%) were yoghurt, and 21 (51.2%) were cheese. AFM_1 contamination in 5 (16.6%) raw milk samples and in 2 (8.3%) UHT milk samples were above (50 ng/l) the TFC and EC limits but it below US regulations (500 ng/l). None of the yoghurt or cheese samples exceeded the legal limits of 50 and 250 ng/kg, respectively.

TABLE 3
Occurrence of aflatoxin M1 in milk and milk products

Milk product	n	Number of AFM1 detected samples n (%)	Range (ng/kg)	Samples over TFC and EC limit (%)	Samples over USFDA[b] limit (%)	Total mean±SD	Positive samples mean±SD
Raw milk	30	13 (43.3)	4.5–181	5 / 30 (16.6)	0 (0)	22.4 ± 49.9	51.6 ± 66.3
UHT milk	24	14 (58.3)	4–116	2 / 24 (8.3)	0 (0)	14.4 ± 29.9	24.7 ± 36.2
Yoghurt	20	2 (10)	41.25–45	0 / 20 (0)	0 (0)	4.5 ± 13.9	45 ± 7.1
Cheese	41	21 (51.2)	13.75–160	0 / 41 (0)	0 (0)	24.4 ± 33.6	47.6 ± 33.2

SD: Standard deviation
[a] Turkish Food Codex [43]: limit for AFM_1 in milk and yoghurt is 50 ng/kg, in cheese it is 250 ng/kg
[b] US FDA [32] limit for AFM_1 in milk and dairy products is 500ng/l

TABLE 4
AFM_1 content for samples (n) and percentage

Milk product	<5 ng/kg	5–50 ng/kg	51–150 ng/kg	151–250 ng/kg	>250 ng/kg
Raw milk	19 (63.3%)	6 (20%)	3 (10%)	2 (6.6%)	0
UHT milk	12 (50%)	10 (41.6%)	2 (8.3%)	0	0
Yoghurt	20 (100%)	0	0	0	0
Cheese	21 (51.2%)	16 (39%)	4 (9.75%)	1 (2.43%)	0
Total	71 (61.3%)	32 (27.8%)	10 (8.7%)	3 (2.6%)	0

Raw Milk. Table 4 shows AFM_1 content in raw milk and dairy products: 19 of 30 raw milk samples were contaminated with AFM_1 at <5 ng/kg, 6 samples at 5–50 ng/kg, 3 samples at 51–150 ng/kg, and 2 samples at 151–250 ng/kg. Contamination exceeded the TFC and EC legal limit in only 5 raw milk samples, based on t-tests that showed these samples AFM_1 content was significantly higher than 50 ng/kg ($p<0.01$).

As seen in Table 1, the lowest AFM_1 content in raw milk was published by Rama et al. [44]. Of 826 samples, only 23 (2.8%) were contaminated at 5.16–110.93 ng/l. Xiong et al. [45] reported 17 (23.6%) of 72 raw milk samples were contaminated at 10–420 ng/l in comparisons of the AFM_1 in milk from all four seasons. The highest AFM_1 content was in winter milk and there was no significant difference between milk from other seasons. Hashemi [46] reported AFM_1 contamination in 31.25% and 32% of samples from farms and collection centers, with overall levels of 0–99.92 and 0–97.68 ng/l, respectively. In India, Siddappa et al. [47] found 22 (48.9%) of 45 samples were had AFM_1 content above EC regulations with 100–3800 ng/kg; only 6 (13.3%) exceeded India's FSSAI Regulations (500 ng/l). Tomasevic et al. [48] found contamination of 25–1000 ng/l; 382 (56.3%) samples exceeded EC limits. In Pakistan, Asghar et al. [36] reported 80.1% contaminated samples with 20–3090 ng/kg and that 125 of 152 samples exceeded EC limits. Quevedo-Garza et al. [37] reported that 39% of heat-treated milk samples had AFM_1 levels above the legal limit in the US and Mexico of 500 ng/l; the overall range of their samples was 100–1270 ng/l AFM_1. In Brazil, Goncalves et al. [49] reported that 40.4% of samples exceeded the Brazilian limit of 500 ng/kg; the overall AFM_1 content range was 9–1000 ng/l. In China, 280 (52.8%) of 530 raw milk samples had AFM_1 levels of 10–200 ng/l, which is below the Chinese and US limit of 500 ng/l [50]. The lowest contamination of raw AFM_1 content was reported by Rama et al. [44] and the highest by Guo et al. [50], in which the AFM_1 contamination level set (500 ng/l) was also highest. Compared to these studies in other countries, our samples from Turkey have lower contamination levels and the number of legally contaminated samples was lower than in all published studies.

We also compared our results to other from Turkey and the TFC limit (Table 2). Ertas et al. [61] found that 0 raw milk samples exceed legal limits. However, Bakirdere et al. [62] found that 4 (5.2%) of 77 whole milk did, with an overall AFM_1 content range of 5–410 ng/l. Buldu et al. [63] reported that 63 (70%) significantly exceeded the limit. Delialioglu et al. [64] collected raw goat and raw cow milk samples in the city of Mersin. They found that 39 (73.5%) raw cow milk samples exceeded the limit but only 4 (10.2%) goat milk samples did; the overall range was 2.1–866.6 ng/l. Temamogullari and Kanici [65] reported 21 (55.3%) samples from Şanliurfa exceeded the legal limit; the overall range was 0.82–125.70 ng/l. Kocasari et al. [66] reported that 16 (35.5%) samples from Burdur exceeded the legal limit; the overall contamination range was 15.3–80 ng/l. Similarly, we found that 5 (16.6%) of 30 samples exceeded the limit in Aydin; the overall range was 4.5–181 ng/l. Compared to other studies and regions in Turkey, our results from Aydin show very low AFM_1 contamination.

UHT Milk. As shown in Table 3, 14 of 24 UHT milk samples had AFM_1; the overall range was 4–116 ng/kg. Of the 14 contaminated samples, only two exceeded TFC and EU limits (50 ng/l). In our study, AFM_1 content was significantly different from the limit of 50 ng/kg, according to a t-test ($p<0.01$).

Comparisons to other studies can be made with the data in Table 1. Bilandzic al. [51] reported that all 214 UHT milk samples were within the EC limit;

the same result was reported by Rama et al. [44]. In Brazil, Silva et al. [57] found 4 (2.6%) of 152 UHT milk samples were above the EC limit; average AFM_1 content was 19.6 ng/l. Siddappa et al. [47] reported that 19 (42.2%) of 45 samples exceeded the EC limit. Fallah [15] found that 17.4% of samples exceeded the EC limit but only 2.7% exceeded ISIRI [59] and USFDA [32] limits. In China, Zheng et al. [53], 54.9% of samples exceeded the EC limit; the overall range was 6–160 ng/l. Another study in Brazil by De Oliveira et al. [55] reported that 23 (30.7%) of 75 samples were above Brazilian legal limits; AFM_1 levels were 1000–4100 ng/l. These very high levels can cause the health problems.

In Turkey, there are fewer studies on UHT milk than other products. Temamogullari and Kanici [65] reported 3 of 12 (25%) samples exceeded the EC limit; the AFM_1 range was 18.93–91.27 ng/l. Delialioglu et al. [64] found that 1 (2.2%) of 45 UHT milk samples from Mersin was above the EC limit. Kocasari [67] analyzed 41 UHT milk samples from supermarkets and found that 3 of 41 (7.3%) were contaminated with AFM_1 levels of 6.42–71.33 ng/l. Tekinsen and Eken [69] reported 31 (31%) of 100 samples exceeded the limit. Within Turkey, AFM_1 contamination varies but overall is lower than in other countries.

Yoghurt. As indicated in Table 3, AFM_1 in yoghurt was the lowest of all dairy products, perhaps because it has lactic acid. Govaris et al. [70] showed that AFM_1 content was significantly lower in all yoghurt samples compared to milk. This could be due to a decrease in pH, the production of organic acids, or other fermentation products. In our study, 2 of 20 yoghurt samples had AFM_1 levels of 41.25–45 ng/kg; all were below the TFC limit. T-tests showed no significant differences.

As seen in Table 1, Hassan et al. [52] reported that 16 (76.1%) of 21 yoghurt samples from Qatar had AFM_1 values of 4.16–38.1 ng/kg; all samples were below the EC limit. These results are similar to ours. Takavoli et al. [56] found that 4 of 25 winter yoghurt samples (18.19%) and 2 of 25 summer yoghurt samples in Iran (15.38%) had AFM_1 levels above the legal limit of 50 ng/kg. Iqbal and Asi [33] reported that 28 (47%) of 96 yoghurt samples exceeded the EC limit; the overall range was 4–615.8 ng/kg. Another study in Iran by Rahimi [54] reported that 3 (5%) of 60 samples exceeded the limit (250 ng/kg) of both the Codex Alimentarius Commission [13] and the EC [13, 58]; the total range was 19.7–319.4 ng/l. Our results show much lower contamination rates than these studies and are not hazardous to human health.

With respect to the legal limit for AFM_1 content in yoghurt, there is different claims in the literature. Some [61, 65, 71] suggest that the acceptable level was ~50 ng/kg, while Kocasari et al. [66] claim it is 500 ng/kg. Atasever et al. [71] reports that 16 (20%) of 80 samples had AFM_1 levels of 10–475 ng/kg. Temamogullari and Kanici [65] found that 5 (10%) of 50 samples had AFM_1 levels of 40.62–72.04 ng/kg. Gurbuz and Altun [68] assessed homemade yoghurts from two different cities. In Mardin, 5 (11.9%) samples had AFM_1 values of 10–101 ng/kg, whereas in Sanliurfa, AFM_1 contamination was notably higher: 29 (60.4%) samples had values of 10–515 ng/kg. Ertas et al. [61] reported that 7 (14%) of 50 samples were above the TFC limit; the overall range was 2.5–78 ng/kg with an average of 30.3 ng/kg. Kocasarı et al. [66] reported that 20 (44.4%) of 45 samples had AFM_1 values of 50–360 ng/kg; none exceeded 500 ng/kg. In this case, it is difficult to compare the AFM_1 values with each other regarding yoghurt samples due to different claims mentioned above.

Cheese. Due to the chemical structure of AFM_1 and its closeness to casein, AFM_1 is adsorbed by casein [72]. This means that AFM_1 levels in cheese are much higher than in other dairy products. The concentration depends on cheese type, processing, and the amount of removed water [73].

In our study, 21 (51.2%) of 41 cheese samples had AFM_1 levels of 13.75–160 ng/kg but none exceeded the TFC limit of 250 ng/kg (Table 3). Twenty (48.8%) samples had less than 5 ng/kg, 16 (39%) had 5–50 ng/kg, 4 (9.75%) had 51–150 ng/kg and 1 (2.43%) had 151–250 ng/kg (Table 4). T-tests showed statistically significant differences from the TFC limit.

Unfortunately, there are not many studies of AFM_1 in cheese in other countries (Table 1). In Iran, Rahimi [54] reported 11 (13.8%) samples with levels of 14.3–572.1 ng/kg and an average of 133.2 ng/kg. Iqbal and Asi [33] reported 14 (15%) of 119 white cheese and 10 (11%) of 150 cream cheese samples exceeded the EC limit of 250 ng/kg. In Qatar, Hassan et al. [52] reported 39 (84.8%) samples had AFM_1 levels of 2.53–217.15 ng/kg.

In Turkey, there is very low AFM_1 contamination of cheese samples, for example, 2 (3%) tulum cheese samples were contaminated, 0 white cheese samples, and 1 (2%) kashar cheese sample [61]. Contamination ranges of the three varieties were 13–378, 15.6–154.6, and 12–369.5 ng/kg, respectively. Temamogullari and Kanici [65] reported that 5 (10%) samples of white pickled cheese were contaminated with AFM_1 values of 40.41–130.89 ng/kg. Tekinsen and Ucar [74] found that 18 (18%) cream cheese samples exceeded EC limits and had an average of 330 ng/kg. Tekinsen and Eken [69] reported 50–690 ng/kg in kashar cheese samples with a contamination rate of 27.3%. Koluacik et al. [75] found that 12 (20%) white cheese samples were contaminated; the overall AFM_1 range was 16–700 ng/kg. Ardic et al. [76] reported 26.4% contaminated white cheeses samples with AFM_1 levels of 52–860 ng/kg.

Bakirdere et al. [62] reported the AFM_1 content of kashar, tulum, dil, cream, and white cheese samples has ranges of 50–700, 50–100, 100–200, 50–160, 50–2100 ng/kg and averages of 130, 70, 150, 90, and 280 ng/kg, respectively. Kashar cheese analyzed by Gul and Dervisoglu [38] had AFM_1 content of 5–3774 ng/kg with an average of 273 ng/kg, which are much higher than our results. Sixteen (11.11%) samples exceeded the TFC limit (500 ng/kg).

AFM_1 contamination varies by country, city, and product. These differences could be due to measurement methods, regional and environmental factors such as humidity and temperature, and seasonal variation. Most studies found higher AFM_1 contamination in raw milk in the winter.

CONCLUSIONS

AFM_1 contamination levels in raw milk are very important because it is used to produce other milk products. Higher concentrations in raw milk leads to higher concentrations in derived milk products such as cheese, yoghurt, and UHT milks. AFM_1 concentration should be assessed with reliable, accurate, and rapid methods. Although our results show that AFM_1 was present, levels were above the TFC limit in only 7 samples (5 raw milk and 2 UHT milk) of 115 milk samples; another 7 samples had values that were much lower than published data. The AFM_1 content of yoghurt and cheese samples were within TFC limits. We can conclude that AFM_1 contamination in milk products in Aydin does not present a serious risk for human consumption. Statistical analyses revealed that raw and UHT milk samples were significantly different from the TFC limit of 50 ng/kg ($p < 0.01$). In yoghurt and cheese samples, no statistically significant differences were found.

ACKNOWLEDGEMENTS

This Project was supported by the Scientific Research Projects Coordination Unit of Aydin Adnan Menderes University (Project ZRF 12009).

REFERENCES

[1] Feddern, V., Dors, G.C., Tavarini, F.C., Mazzuco, H., Cunha Júnior, A., Krabbe, E.L., Scheuermann, G.N. (2013) Aflatoxins importance on animal nutrition. In M. Razzaghi-Abyaneh (Ed.), Aflatoxins: Recent Advances and Future Prospects (chap. 8, pp. 171-195). Rijeka: Intech.

[2] Iqbal, S.Z., Paterson, R.R.M., Bhatti, I.A., Asi, M.R. (2010) Survey of aflatoxins in chilies from Pakistan produced in rural, semi-rural and urban environments. Food Additive and Contaminants Part-B. 3(4), 268-274.

[3] Cavaliere, C., Foglia, P., Guarino, C., Marzioni, F., Nazzari, M., Samperi, R., Lagana, A. (2006) Aflatoxin M1 determination in cheese by liquid chromatography tandem mass spectrometry. Journal of Chromatography A. 1135, 135-141.

[4] WHO (2002) Evaluation of certain mycotoxins in food. Fifty-sixth report of the Joint FAO/WHO Expert Committee on Food Additives. World Health Organization Technical Report Series. 906, 1–62.

[5] Marchese, S., Polo, A., Ariano, A., Velotto, S., Costantini, S., Severino, L. (2018) Aflatoxin B1 and M1: Biological Properties and Their Involvement in Cancer Development. Toxins. 10(6), 2-19.

[6] Reddy, K.R.N., Salleh, B., Saad, B., Abbas, H.K., Abel, C.A., Shier, W.T. (2010) An overview of mycotoxin contamination in foods and its implications for human health. Toxin Reviews. 29(1), 3–26.

[7] Shundo, L., Navas, S.A., Lamardo, L.C.A., Ruvieri, V. and Sabino, M. (2009) Estimate of aflatoxin M1 exposure in milk and occurrence in Brazil. Food Control. 20, 655-657.

[8] Celik, T.H., Sarımehmetoglu, B., Kuplulu, O. (2005) Aflatoxin M1 contamination in pasteurized milk. Veterinarski Arhiv. 75, 57–65.

[9] Ghiasian, S.A., Magshood, A.H., Tirang, R., Mirhendi, S.H. (2007) Occurrence of aflatoxin M1 in raw milk during the summer and winter seasons in Hamedan, Iran. Journal of Food Safety. 27, 188-198.

[10] Rustom, I.Y.S. (1997) Aflatoxin in food and feed: Occurrence, legislation and inactivation by physical methods. Food Chemistry. 59, 57–67.

[11] Kiermeier, F., Mashaley, R. (1977) Influence of the treatment of raw milk on the aflatoxin M1 content of the products made from it. Magazine for Food Research and Technology. 164, 183-187 (in German)

[12] Badea, M., Micheli, L., Messia, M.C., Candigliota, T., Marconi, E., Mottram, T., Palleschi, G. (2004) Aflatoxin M1 determination in raw milk using a flow-injection immunoassay system. Analytica Chimica Acta. 520, 141-148.

[13] Codex Alimentarius Commission (2001) Codex Committee on Food Additives and Contaminants, 2001 (CL CX/FAC 01/20). Comments submitted on the Draft Maximum Level for Aflatoxin M1 in Milk. The Netherlands: FAO/WHO.

[14] Fallah, A.A. (2010a) Aflatoxin M1 contamination in dairy products marketed in Iran during winter and summer. Food Control. 21, 1478-1481.
[15] Fallah, A.A. (2010b) Assessment of aflatoxin M1 contamination in pasteurized and UHT milk marketed in central part of Iran. Food and Chemical Toxicology. 48, 988-991.
[16] Wiseman, D.W., Marth, E.H. (1983) Behavior of aflatoxin M1 in yogurt, buttermilk and kefir. Journal of Food Protection. 46, 115–118.
[17] Shahin, A.A.M. (2007) Removal of aflatoxin B1 from contaminated liquid media by dairy lactic acid bacteria. International Journal of Agriculture and Biology. 9, 71-75.
[18] Zinedine, A., Faid, M., Benlemlih, M. (2005) In vitro reduction of aflatoxin B1 by strains of lactic acid bacteria isolated from Moroccan sourdough bread. International Journal of Agriculture and Biology. 7, 67-70.
[19] Guo, Y., Zhang, Y., Wei, C., Ma, Q., Ji, C., Zhang, J., Zhao, L. (2019) Efficacy of Bacillus subtilis ANSB060 Biodegradation Product for the Reduction of the Milk Aflatoxin M1 Content of Dairy Cows Exposed to Aflatoxin B1. Toxins. 11, 161-171.
[20] Azarikia, M., Mahvadi, R., Nikniaz, L. (2018) Occurrence and dietary factors associated with the presence of aflatoxin B1 and M1 in breast milk of nursing mothers in Iran. Food Control. 86, 207-213.
[21] Jafari, T., Fallah, A.A., Kheiri, S., Fadaei, A., Aminia, S.A. (2017) Aflatoxin M1 in human breast milk in Shahrekord, Iran and association with dietary factors. Food Additives and Contaminants: Part B. 10, 128–136.
[22] Karaoannoglou, P., Mantis, A., Koufidis, D., Koidis, P., Trianfafillou, J. (1989) Occurrence of aflatoxin M1 in raw and pasteurized milk and in Feta and Teleme cheese samples. Milchwissenschaft. 44(12), 746-748.
[23] Lopez, C., Ramos, L., Ramadan, S., Bulacio, L., Perez, J. (2001) Distribution of aflatoxin M1 in cheese obtained from milk artificially contaminated. International Journal of Food Microbiology. 64, 211–215.
[24] Kiermeier, F., Buchner, M. (1977) Behavior of aflatoxin M1 during the ripening and storage of cheese. Magazine for Food Research and Technology.164, 87-91 (in German)
[25] Barbiroli, A., Bonomi, F., Benedetti, S., Mannino, S., Monti, L., Cattaneo, T., Iametti, S. (2007) Binding of aflatoxin M1 to different protein fractions in ovine and caprine milk. Journal of Dairy Science. 90, 532–540.
[26] IARC (International Agency for Research on Cancer) (2012) IARC Monographs on the Evaluation of Carcinogenic Risks to Humans. vol. 100F. IARC.
[27] Sugiyama, K.I., Hiraokai, H., Sugita-Konishi, Y. (2008) Aflatoxin M(1) contamination in raw bulk milk and the presence of Aflatoxin B(1) in corn supplied to dairy cattle in Japan. Journal of the Food Hygienic Society of Japan. 49(5), 352-355.
[28] Michlig, N., Signorini, M., Gaggiotti, M., Chiericatti, C., Basílico, J.C., Repetti, M.R., Beldomenico, H.R. (2016) Risk factors associated with the presence of aflatoxin M1 in raw bulk milk from Argentina. Food Control. 64, 151-156.
[29] Van Egmond, H.P. (1989) Aflatoxin M1: occurrence, toxicity, regulation. In: Van Egmond, H.P. (ed.) Mycotoxins in Dairy Products. New York. Elsevier Applied Science. 11-55.
[30] Elmali, M., Yapar, K., Kart, A., Yaman, H. (2008) Aflatoxin M1 Levels in Milk Powder Consumed in Turkey. Journal of Animal and Veterinary Advances. 7, 643-645.
[31] European Commission (2006) Commission Regulation No 1881 ⁄ 2006 of 19 December 2006. Setting maximum levels for certain contaminants in foodstuffs. Official Journal of The European Communities. 364, 5–24.
[32] US FDA. (1996) Sec. 527.400 whole milk, low fat milk, skim milk-aflatoxin M1 (CPG 7106.210). FDA Compliance Policy Guides. Washington, DC: FDA.
[33] Iqbal, S.Z., Asi, M.R. (2013) Assessment of Aflatoxin M1 in milk and milk products from Punjab, Pakistan. Food Control. 30, 235-239.
[34] Oluwafemi, F., Badmos, A.O., Kareem, S.O., Ademuyiwa, O., Kolapo, A.L. (2014) Survey of aflatoxin M1 in cows' milk from free-grazing cows in Abeokuta, Nigeria. Mycotoxin Research. 30, 207-211.
[35] Sani, A.M., Nikpooyan, H., Moshiri, R. (2010) Aflatoxin M1 contamination and antibiotic residue in milk in Khorasan province, Iran. Food and Chemical Toxicology. 48, 2130-2132.
[36] Asghar, M.A., Ahmed, A.A., Asghar, M. A. (2018) Aflatoxin M1 in fresh milk collected from local markets of Karachi, Pakistan. Food Additives and Contaminants: Part B. 11, 167–174.
[37] Quevedo-Garza, P.A., Amador-Espejo, G.G., Cantú-Martínez, P.C., Trujillo-Mesa, J.A. (2018) Aflatoxin M1 occurrence in fluid milk commercialized in Monterrey, Mexico. Journal of Food Safety. 38, e12507.
[38] Gul, O., Dervisoglu, M. (2014) Occurrence of Aflatoxin M1 in Vacuum Packed Kashar Cheeses in Turkey. International Journal of Food Properties. 17, 273–282.
[39] Shundo, L., Sabino, M. (2006) Aflatoxin M1 in milk by immunoaffinity column cleanup with TLC/HPLC determination. Brazilian Journal of Microbiology. 37, 164-167.

[40] Trucksess, M.W. (2001) Rapid analysis (thin layer chromotographic and immunochemical methods) for mycotoxins in H.P., Gilbert, J., Sabino, M. (Eds.) Mycotoxins and Phycotoxins in perspective at the turn of the millennium. Ponsen and Looyen, Wageningen, 29-40.

[41] Du, L., Wang, S., Huang, J.P., Chu, C., Li, R., Li, Q., Wang, Q., Hu, Y., Cao, J., Chen, Y., Peng, L., Yang, J. (2018) Determination of aflatoxin M1 and B1 in milk and jujube by miniaturized solid-phase extraction coupled with ultra high performance liquid chromatography and quadrupole time-of-flight tandem mass spectrometry. Journal of Separation Science. 41, 3677–3685.

[42] Wang, H., Zhou, X.J., Liu, Y.Q., Yang, H.M., Guo, Q.L. (2010) Determination xin M1 in milk by triple quadrupole liquid chromatography-tandem mass spectrometry. Food Additives and Contaminants Part A-Chemistry Analysis Control Exposure and Risk Assessment. 27, 1261-1265.

[43] Turkish Food Codex (2008) Communiqué on determining the maximum levels of certain contaminants in foodstuffs. Official Journal Number 26879 of 17 May, 3-4.

[44] Rama, A., Latifi, F., Bajraktari, D., Ramadani, N. (2015) Assessment of aflatoxin M1 levels in pasteurized and UHT milk consumed in Prishtina, Kosovo. Food Control. 57, 351-354.

[45] Xiong, J.L., Wang, Y.M., Ma, M.R., Liu, J.X. (2013) Seasonal variation of aflatoxin M1 in raw milk from the Yangtze River Delta region of China. Food Control. 34, 703-706.

[46] Hashemi, M. (2016) A survey of aflatoxin M1 in cow milk in Southern Iran. Journal of Food and Drug Analysis. 24, 888-893.

[47] Siddappa, V., Kallenahalli Nanjegowda, D., Viswanath, P. (2012) Occurrence of aflatoxin M1 in some samples of UHT, raw and pasteurized milk from Indian states of Karnataka and Tamilnadu. Food and Chemical Toxicology. 50, 4158–4162.

[48] Tomasevic, I., Petrovic, J., Jovetic, M., Raicevic, S., Milojevic, M., Miocinovic, J. (2015) Two year survey on the occurrence and seasonal variation of aflatoxin M1 in milk and milk products in Serbia. Food Control. 56, 64-70.

[49] Goncalves, L., Dalla Rosa, A., Gonzales, S.L., Feltes, M.C., Badiale-Furlong, E., Dors, G.C. (2017) Incidence of aflatoxin M1 in fresh milk from small farms. Food Science and Technology, Campinas. 37(Special issue), 11-15.

[50] Guo, L.Y., Zheng, N., Zhang, Y.D., Du, R.H., Zheng, B.Q., Wang J.Q. (2016) A survey of seasonal variations of aflatoxin M1 in raw milk in Tangshan region of China during 2012-2014. Food Control, 69, 30-35.

[51] Bilandzic, N., Bozic, D., Dokic, M., Sedac, M., Kolanovic, B.Z., Varenina, I., Tankovic, S., Cvetnic, Z. (2014) Seasonal effect on Aflatoxin M1 contamination in raw and UHT milk from Croatia. Food Control. 40, 260-264.

[52] Hassan, Z., Al-Thani, R., Atia, F.A., Almeer, S., Balmas, V., Migheli, Q., Jaoua, S., (2018) Evidence of low levels of aflatoxin M1 in milk and dairy products marketed in Qatar. Food Control. 92, 25-29.

[53] Zheng, N., Sun, P., Wang, J.Q., Zhen, Y.P., Han, R.W. Xu, X.M. (2013) Occurrence of aflatoxin M1 in UHT milk and pasteurized milk in China market. Food Control. 29, 198-201.

[54] Rahimi, E. (2014) Survey of the occurrence of aflatoxin M1 in dairy products marketed in Iran. Toxicology and Industrial Health. 30(8), 750–754.

[55] De Oliveira, C.P., Ferreira Soares, N.F., De Oliveira, T.V., Baffa Junior, J.C., Da Silva, W.A. (2013) Aflatoxin M1 occurrence in ultra high temperature (UHT) treated fluid milk from Minas Gerais/Brazil. Food Control. 30, 90-92.

[56] Takavoli, H.R., Kamkar, A., Riazipour, M., Sasan, A., Nejad, M., Hassan, R.S. (2013) Assessment of Aflatoxin M1 Levels by Enzyme-linked Immunosorbent Assay in Yoghurt Consumed in Tehran, Iran. Asian Journal of Chemistry. 25, 2836-2838.

[57] Silva, M.V., Janeiro, V., Bando, E., Machinski, M. (2015) Occurrence and estimative of aflatoxin M1 intake in UHT cow milk in Parana State, Brazil. Food Control. 53, 222-225.

[58] European Commission. (2010) Commission Regulation (EU) No 165/2010 of 26 February 2010 setting maximum levels for certain contaminations in foodstuffs as regards aflatoxins. Official Journal of the European Union. L 50, 8-11.

[59] ISIRI (2002). Institute of Standard and Industrial Research of Iran. Maximum tolerated limits of mycotoxins in foods and feeds. National Standard No. 5925

[60] ISIRI (2005) Milk and Milk Products-Raw Milk Specifications and Test Methods, Iranian National Standard 164 (2nd revision), January 2005. Institute of Standards and Industrial Research of Iran

[61] Ertas, N., Gonulalan, Z., Yildirim, Y., Karadal, F. (2011) A survey of concentration of aflatoxin M1 in dairy products marketed in Turkey. Food Control. 22, 1956-1959.

[62] Bakirdere, S., Yaroglu, T., Tirik, N., Demiröz, M., Karaca, A. (2014) Determination of trace aflatoxin M1 levels in milk and milk products consumed in Turkey by using enzyme-linked immunosorbent assay. Food and Agricultural Immunology. 25, 61-69.

[63] Buldu, H.M., Koc, N.A., Uraz, G. (2011) Aflatoxin M1 contamination in cow's milk in Kayseri (central Turkey). Turkish Journal of Veterinary and Animal Sciences. 35(2), 87-91.
[64] Delialioglu, N., Otagi, F., Ocal, D., Aslan, G., Emekdas, G. (2010) Investigation of aflatoxin M1 level in raw and market milk produced in Mersin. Microbiology Bulletin. 44, 87-91 (in Turkish)
[65] Temamogullari, F., Kanici, A. (2014) Short communication: Aflatoxin M1 in dairy products sold in Şanliurfa, Turkey. Journal of Dairy Science. 97, 162–165.
[66] Kocasari, F.S., Tasci, F., Mor, F. (2012) Survey of aflatoxin M1 in milk and dairy products consumed in Burdur, Turkey. International Journal of Dairy Technology. 65, 365-371.
[67] Kocasari, F.S. (2014) Occurrence of aflatoxin M1 in UHT milk and infant formula samples consumed in Burdur, Turkey. Environmental Monitoring Assessment. 186, 6363–6368.
[68] Gurbuz, S., Altun, S.K. (2019) Aflatoxin M1 in traditional homemade yoghurts marketed in Southeastern Turkey. Fresen. Environ. Bull. 28, 2802-2806
[69] Tekinsen, K.K., Eken, H.S. (2008) Aflatoxin M1 levels in UHT milk and kashar cheese consumed in Turkey. Food and Chemical Toxicology. 46, 3287–3289.
[70] Govaris, A., Roussi, V., Koudis, P.A., Botsoglou, N.A. (2002) Distribution and stability of aflatoxin M1 during production and storage of yoghurt. Food Additives and Contaminants. 19, 1043–1050
[71] Atasever, M.A., Atasever, M., Ozturan, K. (2011) Aflatoxin M1 levels in retail yoghurt and ayran in Erzurum in Turkey. Turkish Journal of Veterinary and Animal Sciences. 35, 59-62.
[72] Yousef, A.E., Marth, E.H. (1989) Stability and degradation of aflatoxin M1. In: Van Egmond, H.P. (ed.) Mycotoxins in dairy products. Elsevier, London, 127-161.
[73] Motawee, M.M., McMahon, D.J. (2009) Fate of Aflatoxin M1 during Manufacture and Storage of Feta Cheese. Journal of Food Science. 74, T42-T45.
[74] Tekinsen, K.K., Ucar, G. (2008) Aflatoxin M1 levels in butter and cream cheese consumed in Turkey. Food Control. 19, 27–30.
[75] Koluacik, A., Tirpanci, G., Kaptan, B. (2015) Aflatoxin M1 Determination in Traditional Küp Cheese Samples of Turkey Using Immunoaffinity Column and High-Performance Liquid Chromatography. Turkish Journal of Agriculture - Food Science and Technology. 3, 916-919
[76] Ardic, M., Karakaya, Y., Atasever, M., Adiguzel, G. (2009) Aflatoxin M1 levels of Turkish white brined cheese. Food Control. 20, 196–199.

Received: **19.11.2019**
Accepted: **24.01.2020**

CORRESPONDING AUTHOR

Selda Bulca
Aydin Adnan Menderes University,
Faculty of Engineering,
Department of Food Engineering,
09010, Aydin – Turkey

e-mail: sbulca@adu.edu.tr

© by PSP Volume 29 – No. 04A/2020 pages 3013-3025 Fresenius Environmental Bulletin

MULTIVARIATE ASSESSMENT OF WATER CHEMISTRY AND METALS IN A RIVER IMPACTED BY TANNING INDUSTRY

Usman Atique[1,2,*], Sonia Iqbal[2], Noor Khan[2], Bainazir Qazi [3], Aqeel Javeed[4], Khalid Mahmood Anjum[5], Muhammad Sultan Haider[6], Tanveer Ali Khan[3], Sajid Mahmood[2], Shahid Sherzada[2]

[1] Department of Biosciences and Biotechnology, Chungnam National University, South Korea
[2] Department of Fisheries and Aquaculture, University of Veterinary and Animal Sciences, Lahore-Pakistan
[3] Department of Zoology, University of the Punjab, Lahore, Pakistan
[4] Department of Pharmacology and Toxicology, University of Veterinary and Animal Sciences, Lahore-Pakistan
[5] Department of Wildlife and Ecology, University of Veterinary and Animal Sciences, Lahore-Pakistan
[6] Department of Zoology, University of Lahore-Pakistan

ABSTRACT

This study investigated the physicochemical water chemistry monitoring in River Sutlej impacted by the tanning industry. We performed this study for nine months at four study sites and targeted the presence of selected metals and applied multivariate analytical techniques. The results divulged that the upstream region displayed higher mean values of pH (7.77) and dissolved oxygen (5.86 mg/L). However, severe water quality degradation observed in the downstream region. The mean electrical conductivity (3.27 mS/cm), total dissolved solids (1442.7 mg/L), salinity (1.32 mg/L), total alkalinity (285.5 mg/L), hardness (195 mg/L), chlorides (912.5 mg/L) and nitrates (4.73 mg/L) recorded in downstream indicated severe water quality degradation. Similarly, the selected metals chromium (1.21 mg/L) and lead (0.83 mg/L) recorded significantly higher downstream. However, cadmium remained insignificant in both riverine zones. Most of the targeted parameters and metals studied in the river and Rohi Nullah Jamman (RNJ) either surpassed or deviated from the national surface water quality standards indicating thereby severe impact of the tanning industry. The metals concentrations revealed the array of chromium > lead > cadmium. The correlation analyses on water chemistry and metals indicated strong (r >0.70) to moderately strong (r <0.70 - >0.50) relationship. The hierarchical cluster analysis displayed metals and significant parameters originating from similar sources that could be the tanning and sewage effluents. The principal component analysis explained the 96.39% of the total variance and approximated with the results obtained by cluster analysis. The Mann Kendall Trend test indicated an increasing tendency in metals and critical water quality parameters that calls for prudent actions on water quality management. In conclusion, this study alluded to the continuously deteriorating water quality of River Sutlej that poses potential ecological and human health risks. The water quality deterioration is believed to be the result of tanning activities that could severely impact the river biodiversity.

KEYWORDS:
Water chemistry, Tanneries, Chromium, Effluents, Sutlej, Dendrogram, PCA

INTRODUCTION

River pollution and deteriorating water chemistry are amongst the most frequently discoursed environmental research topics due to imposing significance in water resource management, biodiversity and human well-being [1]. The worldwide rivers are severely affected by extreme anthropogenic activities, primarily industrial discharges [2]. Good water quality is paramount to the sustainable ecological health of the aquatic ecosystem as well as aquatic organisms reliant on lotic waters [3-6]. Since the inception of urban development and industrialization, watercourses, especially rivers, have been used as preferred dumping sites of every kind of waste and effluents [7-8]. Similarly, River Sutlej has been subjected to hazardous discharges without understanding their effects on water quality, aquatic ecosystem, and natural health and survival [9].

We describe water chemistry by the physical, chemical, biological, radiological, and aesthetic ranges of water quality aspects [3,10-12]. A sustainable aquatic environment is resilient to maintain its water quality by synchronously supporting wide-ranging biological community and meeting requirements of public health [13-14] to fulfill requirements of the present as well as future generations. Aquatic contaminants are chemicals that stay dissolved or suspended in water and cause an obnoxious environmental response of certain species leading to the extinction of specific biota [15-16]. Inversely, some of the physical and chemical factors may be so affected by pollutants when

they rise above threshold levels [16-17], which leads to massive kills in some cases (dissolved oxygen) and troubled feeding and growth in other organisms [18-19].

Water chemistry factors are considered to play a crucial role in defining the ecological health of an ecosystem [16, 20] and biotic integrity of an ecosystem [21]. Therefore, such critical alterations can be constructive in estimating source, type, and their simultaneous eco-biological health impacts on the environment [14, 22-23]. Hence knowledge of these parameters is inevitable to manage rivers sustainably and to provide proper measures [18] as well as a good measure of river eco-biological health [24].

The presence of metals is one of the critical problems in lotic ecosystems as per their harmful impacts on the ecological balance. Metals may be essential or non-essential and originate from elements having crucial implications in ecotoxicological research [25]. The heavy metals are known to be persistent in the ecosystem and have potential toxicity to aquatic life [26]. Therefore, aquatic organisms, especially fishes, are at more significant risk if metal accumulates in their vital organs [24, 27]. The tanning industry uses numerous organic and inorganic chemicals that are proven sources of toxic metals yield as well as cause pollution in surface water and sediments [22, 28]. When heavy metals such as Chromium (Cr), Cadmium (Cd), Lead (Pb), Copper (Cu), and Mercury (Hg), etc. are liberated combined with industrial and domestic effluents, they are likely to cause aquatic ecosystem deterioration and degradation of downstream waters [29]. These metals can be in two states; dissolved and particulate. However, metals are usually found to be at lower levels in the water, although they may reach higher levels in sediments as well as a higher order of food chain [30-31].

The historic waters (owing to a cross border river between India and Pakistan) of River Sutlej are of greater relevance to Kasur city. Kasur city is ranked the second-largest city among the tanning industries of Pakistan. The Government of Punjab set up a wastewater treatment plant (WWTP) in Kasur from 2000-2001 under a joint initiative with Kasur Tanneries Waste Management Association (KTWMA). The WWTP can treat approximately 13,000 of the 18,000 c^3 wastewater generated daily. This WWTP, however, does not remove metals like chromium from the generated wastewater hence, the treated water by WWTP does not meet the National Environmental Quality Standards (NEQS). Upon our extensive search, we could not find any published information and detailed documentation available relating to the Kasur tanneries and WWTP activities in the context of River Sutlej. By considering and the higher importance of River Sutlej, this study was undertaken to investigate the river water chemistry when the untreated tannery effluents mixed with city sewage enter into River Sutlej via Rohi Nullah Jamman (RNJ). We aimed at the study of selected water quality parameters, their deviations from NEQS, presence and loads of selected metals in river water. We also applied the multivariate analysis techniques (principal component analysis, hierarchical cluster analysis, Mann Kendhal Trend test) to extract the underlying information of River Sutlej water quality heavy metal dynamics.

MATERIALS AND METHODS

Study Area. The study area of the River Sutlej included four sampling stations (two upstream and two downstream regions) located close to the India-Pakistan border and a small village named Rangy Wala, district Kasur (Figure 1). The upstream and downstream regions were differentiated with reference to the confluence point of RNJ and River Sutlej. The samples were collected over nine months. The Kasur city is positioned in 55 km southeast of Lahore city. Kasur has been known for its huge tanning industry harbouring over 300 out of total 800 tanning units in Pakistan, hence ranked as the second largest town of tanneries in Pakistan. The River Sutlej has been defined as the greatest and the widest river in Pakistan before the promulgation of the 1960 Indus Waters Treaty (IWT) between India and Pakistan. Based on catch per unit effort (CPUE), it has been considered as the preeminent wild fish catch yielding river in Pakistan. Currently, it is under severe threat for multiple reasons such as the meagre water inflow from India, an increasing amount of pollutants from tanning units, untreated transport of city sewage via the RNJ. This drainage canal (RNJ) moves to the river after covering 24 km distance with total catchment area 1851.84 km^2 approximately.

RNJ is a local drain which transports the potentially hazardous effluents of Kasur tanneries to the river downstream. Most of the deterioration is happening right upon where the river enters into Pakistan territory (our study area). Despite having a 550 km of traversing length within Pakistan and basin area of 106728.23 km^2, this river is dying and deteriorating rapidly.

Water Chemistry Analyses. We collected all the surface water samples near the right bank of River Sutlej. The right bank was chosen due to the reason that the left bank faced the borderline. We collected one liter of surface water samples at three different points at each study site to ascertain the accuracy of results. We were more concerned about the downstream water samples to ensure proper mixing of the tanning discharges and river water. The pre-rinsed polyethylene containers were used to procure the water samples. Basic physicochemical parameters (pH, water temperature, dissolved

oxygen (DO), and electrical conductivity (EC)) were recorded in-situ. The water chemistry parameters requiring estimation in the lab were evaluated in the Research and Training Facilities of Department of Fisheries and Aquaculture, University of Veterinary and Animal Sciences, Ravi Campus, Pattoki using standard equipment. The details of the selected water chemistry parameters, their abbreviations, measuring units and estimation methods are given in Table 1. However, all the parameters were analyzed according to standard methods [32]. Further, we used three replicates from each water sample to achieve greater accuracy in determining water quality and the heavy metal contents.

Metal Assessments. For metal detection in water, 100 mL of the obtained water sample was measured in a pre-conditioned beaker to guarantee no contamination. Next, 5 mL of concentrated nitric acid (HNO_3) was poured into the river water sample and mixed well on a hot plate in a fume hood. The acid mixed water samples were then gently boiled to the lowest possible volume until it reached the level of complete digestion that was noticed on the appearance of a clear solution. The obtained digested samples volume was then made up to 100 mL in a volumetric flask. Before its storage for the next step of heavy metal detection and analyses, the samples were filtered using a Whatman filter [32]. The heavy metal presence and load were detected with the help of flame (a mixture of air and acetylene) atomization spectroscopy procedure, which was performed in Zeeman Atomic Absorption Spectrometer (Z-5000, Hitachi Japan). A hollow cathode lamp that was element-specific was used for each metal analysis. During the atomic atomization, 1000 mg/L stock solution for each metal was prepared as s standard solution to prepare the calibrations standards. Finally, the atomic absorption signal was measured in the form of peak area mode against a calibration curve. All the samples were taken in triplicates, and then mean values were adopted as the final value for each sample. The method detection limit (MDL) for the targeted metals of Cd, Pb, and Cr, were 0.0012, 0.0003, 0.0004 mg/L, respectively.

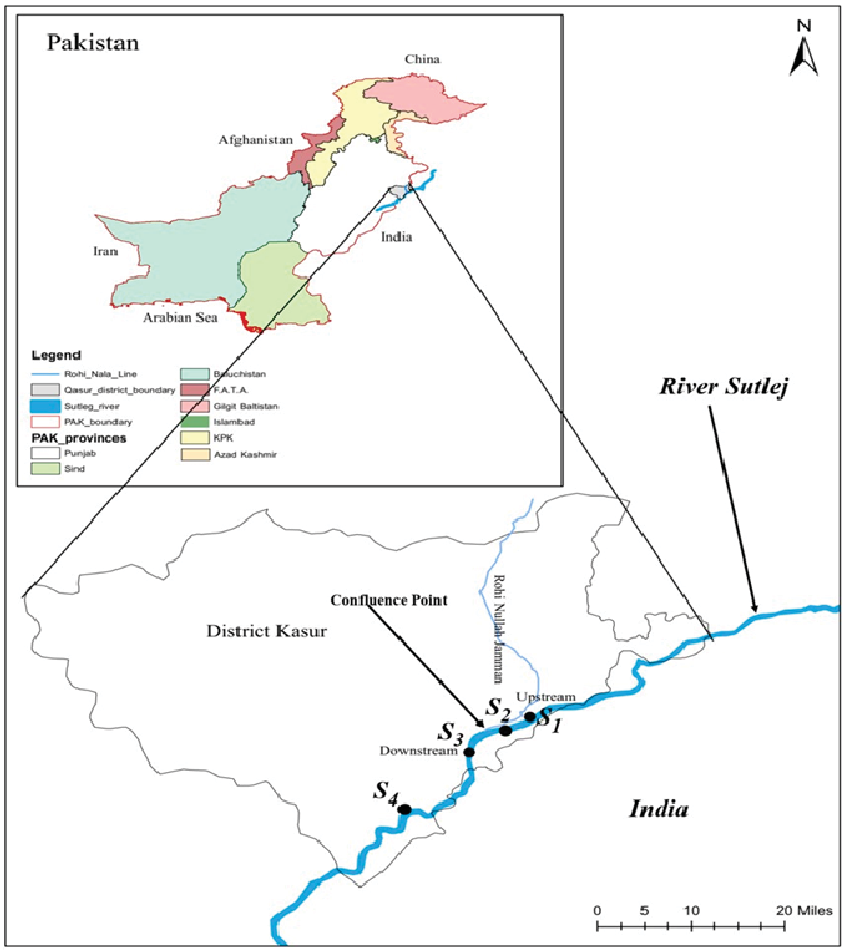

FIGURE 1
The geographical location of study sites in upstream (U_s) and downstream (D_s) stations as well as confluence point of RNJ.

TABLE 1
Selected water chemistry factors and targeted metals along with test methods

Parameter	Abbr.	Unit	Test Method
Dissolved Oxygen	DO	mg/L	DO Meter
pH	pH	-	pH Meter
Water Temperature	WT	°C	Digital Thermometry
Electrical Conductivity	EC	mS/cm	Digital Conductivity Meter
Total Dissolved Solids	TDS	mg/L	Digital Meter
Salinity	Salinity	mg/L	Salinity Meter
Chlorides	Chl.	mg/L	Argentometric
Hardness	Hard.	mg/L	EDTA titrimetric
Total Alkalinity	TA	mg/L	Titrimetric
Nitrates	NO_3-N	mg/L	Ultraviolet spectrophotometric
Chromium	Cr	mg/L	Atomic absorption spectrophotometry
Cadmium	Cd	mg/L	Atomic absorption spectrophotometry
Lead	Pb	mg/L	Atomic absorption spectrophotometry

Abbr. = Abbreviation

TABLE 2
Ranges and mean values along with t-test for upstream and downstream water chemistry parameters and targeted metals (n = 36)

Targeted Parameter / Metals	Upstream Records		Downstream Records		t value
	Range	Mean±Stan. Dev.	Range	Mean±Stan. Dev.	
DO	4.43-6.9	5.86±0.89	3.04-3.5	3.26±0.165	7.06
pH	7.08-8.59	7.77±0.74	7.58-8.82	7.78±0.74	-1.51
EC	0.24-0.31	0.27±0.027	1.2-4.8	3.27±1.40	5.23
TDS	137-168	154.5±11.29	659-1999	1442.7±598.7	5.27
Salinity	0-0.02	0.003±0.008	0-2.5	1.32± 1.019	3.16
WT	11-34.7	23±9.79	12-35.5	23.68±9.64	0.01
TA	60-111	80.5±21.99	270-294	285.5±8.57	21.27
Hardness	111-129	122±7.27	168-225	195±24.74	6.94
Chlorides	560-860	703.3±103.7	760-975	912.5±79.01	3.93
Nitrates	1.42-3.75	2.55±0.79	3.1-7	4.73±1.52	3.12
Cr	0.33 - 0.68	0.45±0.12	0.81-1.73	1.21- 0.34	2.56
Cd	0 - 0.007	0.003±0.003	0.003 - 0.02	0.01±0.007	3.34
Pb	0.22 - 0.60	0.39±0.13	0.50- 1.60	0.83±0.40	5.13

Where DO: Dissolved oxygen, EC: Electrical conductivity, TDS: Total dissolved solids, WT: Water temperature, TA: Total alkalinity, Cr: Chromium, Cd: Cadmium and Pb: Lead.

Statistical Analyses. The data thus obtained was subjected to its normality check followed by statistical analyses performed with Statistical Analysis Software (SAS Institute, v. 9.1, Cary NC) for the t-test. PAST software (Hammer 2018) was used for the multivariate analytical techniques such as correlation, principal component analysis (PCA), hierarchical cluster analysis (HCA) and Mann Kendall (MK) trend test analyses.

RESULTS AND DISCUSSION

Water Chemistry. The major water chemistry factors such as EC, TDS, Salinity, TA, hardness, chlorides as well as targeted metals excluding Cd displayed significant deviations from ideal ranges in downstream (D_s) sampling station of River Sutlej (Table 2). For instance, the DO level was significantly different (t = 7.06) and dropped in the downstream sites (3.26±0.165 mg/L). Similarly, the EC (3.27±1.40 mg/L; t = 5.23), TDS (1442.7±598.7 mg/L; t = 5.27), salinity (1.32± 1.019 mg/L; t = 3.16), TA (285.5±8.57 mg/L; t = 21.27), hardness (195±24.74 mg/L; t = 6.94), chlorides (912.5±79.11 mg/L; t = 3.93) and nitrates (4.73±1.52 mg/L; t = 3.12) indicated significant increase in the downstream sampling stations. Out of these water chemistry factors, EC, TA, TDS and salinity changes were significantly higher based on t value. Conversely, pH and the temperature difference between the upstream (U_s) and downstream (D_s) was non-significant with t value -1.51 and 0.01, respectively. It was also noticed that most of the water quality factors sharply deviated from the national water quality criteria for the propagation of fish and aquatic organisms in Pakistan freshwater bodies (Table 3)

During this study, water chemistry parameters from the four sites of River Sutlej waters were assessed for 09 months, excluding the monsoon season (June-August) to estimate the effect of tanneries-based effluents. Monsoon period was skipped purposefully because of intensive rainfall could turn into massive floods plus the unexpected release of overflowing waters by Indian authorities as it may have affected the outcomes based on the direct industrial discharges by dilution hence could have manipulated the water chemistry outcomes. In rivers and streams, certain water quality factors of

utmost significance for the survival of aquatic organisms such as fishes. Among those are counted DO, pH, water temperature, and salinity. The significant difference in DO contents, especially downstream wasters have been densely supported by several pieces of research [20,28, 33-34]. The drop in DO content may be linked to the city sewage plus industrial effluents and higher concentrations of dissolved solids [35-36].

Furthermore, deficient DO levels were revealed from the untreated effluents flowing through RNJ and later on entering into the River Sutlej leading to water chemistry degradation in the sampling stations. The pH ranged from 7.08 to 8.59 and showed a non-significant difference. Xu et al. [35] and Shalini and Sakshi [16] have reported that higher amounts of organic loads and pH in the range of 6.9–8.6 locks or hinders the element mobilization in water and sediments. pH always has a decisive role in altering the ecological environment. The pH of natural waters usually remains around seven, but the presence of certain pollutants causes it to change. It can also control the solubility of heavy metals in aquatic ecosystems [36]. Other solubilities controlling factors are temperature, redox condition and flow of water [37-38]. Moreover, seasonal fluctuations in pH levels of water may affect the interaction between hydrogen ions and heavy metal ions. Fall in pH values stimulates the separation of metal carbonate compounds with a resultant increase in the availability of free metal ions in river water [19, 39].

The electrical conductivity (EC) showed a highly significant difference between upstream and downstream. Qu et al. [40] reported equivalent results in the increase in EC records in polluted water samples. The comparison of total dissolved solids (TDS) in upstream and downstream of River Sutlej showed highly fluctuating values and a significant difference from RNJ as well. Shyamala et al. [41] recommended that higher TDS in downstream might be ascribed to the city and industrial releases. Welch [42] described that rapid TDS changes often exposed to dilution or additions in the natural waters. This linked with fluctuating water currents entering from India as well as industrial effluents. Cazemeir [43] observed the similar results of salinity in river Rhine that received industrial effluents like river Sutlej. The general tendency in the river temperature instability is linked with the atmospheric changes. According to Sweeting [13], the temperature of water changes due to the addition of industrial wastewater and may add to the thermal pollution of river water. There was a highly significant difference in TA, and in upstream were 111 mg/L and that of downstream was 294 mg/L. The TA fluctuations show considerable changes in water chemistry. Such significant changes occur with the discharge of industrial effluents. The maximum value of hardness in upstream was 129 mg/L, but for downstream, it was 225 mg/L.

Previous studies report a direct link between hardness and uptake of heavy metals in fish [7, 44]. Higher values of hardness in downstream may be linked to the run-off waters [38, 41, 45]. TDS might contribute to an increase in hardness as well. Similarly, higher nitrate levels can also add to elevated hardness. The Calcium and Magnesium chlorides are the main contributors to chlorides. Mishra et al. [46] pointed out that due to surface run-off and hardness, it results in the increased values of pH. Nitrates showed a highly significant difference, and a higher level of nitrates may cause methaemoglobinemia in fish species as well as affect the water quality [24, 47]. Barnes and Bliss [48] displayed that city sewage contributes approximately 60% of ammonium nitrogen, 39% of organic nitrogen, and less than one percent of nitrates.

TABLE 3
Mean values of water chemistry factors and targeted metals compared with national water quality standards (NWQS) for the propagation of fish and aquatic organisms

Parameters	Criteria in Pakistan	Upstream	Downstream	RNJ
DO	>5.0	5.8633	3.26	2.19
pH	6.5-8.5	7.7767	7.7767	9.8
WT	-	23.0	23.6833	29.7
EC	1.50 (dS/m)	0.275	3.2667	5.6
TDS	1000	154.5	1442.7	Out of range
Salinity	<1.0	0.00333	1.3167	2.7
Chloride	250	703.3	912.5	1123
Hardness	300	122	195	312
TA	< 20- 200	80.5	285.5	321
Nitrate	10	2.5517	4.7317	9.0
Cr	0.05	1.457	4.5545	5.5934
Cd	0.002	0.00328	0.00397	0.00411
Pb	0.01	0.3424	0.4281	0.4987

All parameters are expressed in mg/L (ppm) except pH, temperature and electrical conductivity
Where DO: Dissolved oxygen, EC: Electrical conductivity, TDS: Total dissolved solids, WT: Water temperature, TA: Total alkalinity, Cr: Chromium, Cd: Cadmium and Pb: Lead.

Heavy Metal Contents. Presence and loads of targeted metals indicated mean Cr (U_s: 0.45±0.12 – D_s: 1.21- 0.34 mg/L) and Pb (U_s: 0.39±0.13 - D_s: 0.83±0.40 mg/L) levels while mean Cd level showed a tiny increase in downstream (0.01±0.007 mg/L) as compared to upstream (0.003±0.003 mg/L) stations (Table 2). Based on the t-test, the heavy metal concentration was significantly different among the upstream and downstream waters. Chromium was found to be in the highest concentration among the selected metals in this study. The order of metals was Cr>Pb>Cd in the water samples during the study period. Table 3 previews the mean values water chemistry parameters of surface water of river Sutlej as well as the metal concentrations along with their comparison with national water quality criteria for the propagation of fish and aquatic life [49]. It gives a vivid picture of the actual state in downstream waters while comparing it with national surface water quality standards for the propagation of fish and aquatic organisms.

The most popular salts of Chromium (Cr) used in the tanning process are chromium sulfate ($Cr_2(SO_4)_3$ or $Cr_2O_{12}S_3$) and chromium oxide (Cr_2O_3). Chromium sulphate has a higher capacity to penetrate the skin under process [50-51]. The water samples contained a higher Cr level as compared to Cd and Pb, reflecting the impact and contribution of the tanning industry. It showed the river water was receiving untreated Cr effluents mixed with city sewage, which could the more prominent source of Pb and Cd. In the case of Cadmium (Cd), it was higher in the downstream and lower in upstream, although the difference was not too big. Cd is added in natural waters from agricultural run-off and other anthropogenic activities [52-54]. The level of Lead (Pb) found in this study indicated the river was polluted due to tannery effluents and city sewage draining into natural waters. The presence of metals in the river ecosystem may be linked with factors such as municipal wastewater, industrial wastewater, infiltration, and run-off water [24, 27, 55]. No matter how negligible amounts of Cd and Pb as compared with Cr, they are still very toxic in small quantities [33, 56-57]. The levels of metals present in River Sutlej are sufficient enough to make the river water unsafe to the aquatic organisms. Several studies have shown that Cr enters the river from the tanning industry discharges while Pb because of industrial waste [28, 50-51, 58]. The monthly difference in the metals loads indicated the change might be attributed to change in tanning activity and the water chemistry, particularly pH, temperature and inconsistent inflow of water.

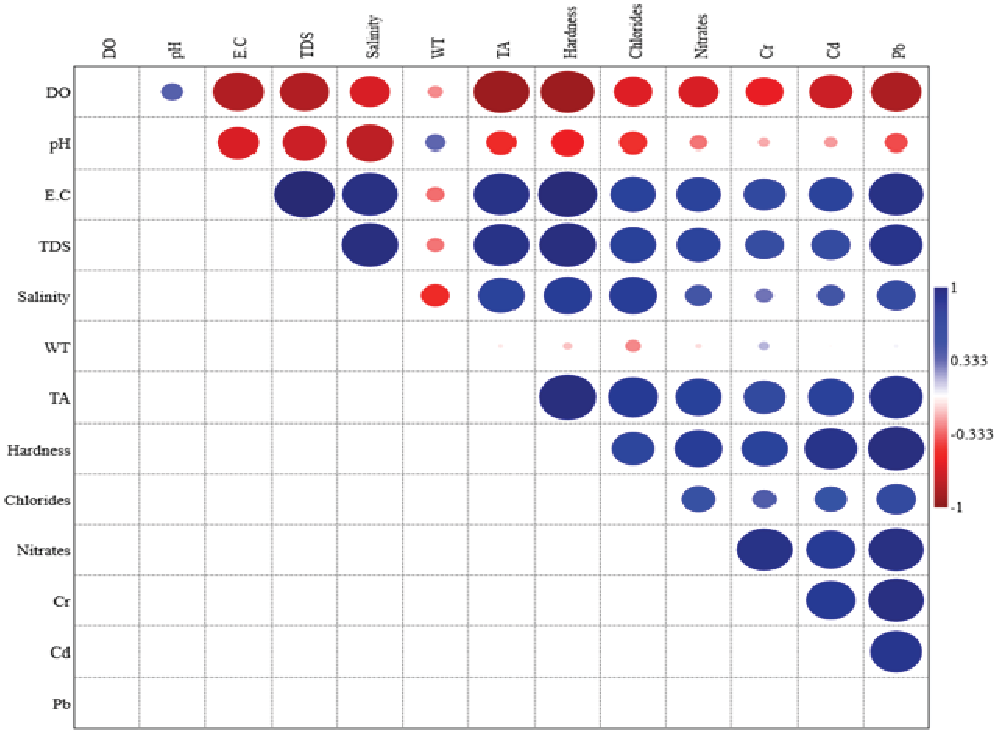

FIGURE 2
Graphical representation of Pearson's correlation analyses between water chemistry and selected metals in River Sutlej

Pearson Correlation Between Water Chemistry and Metals. The Pearson correlation analysis indicated a strong (r > 0.7) positive and negative correlation between most the water chemistry factors as well as with the selected metal contents in River Sutlej (Figure 2). The strong (r > 0.7), moderately strong (r < 0.7 - > 0.5) and weak (r <0.5 - > 0.3) correlations were designated on the basis of r coefficient values. There was strong negative correlation between DO and EC (r = -0.80), TDS (r = -0.79), TA (r = -0.88), hardness (r = -0.87), Cd (r = -0.70) and Pb (r = -0.82). However moderate negative correlation with chlorides (r = -0.61), NO_3-N (r = -0.64) and Cr (r = -0.57). EC and TDS were strongly positively correlated with each other as well as with TA, hardness, chlorides, NO_3-N, Pb and Cd. Hardness also showed a strong positive correlation with Cr, Pb, Cd, NO_3-N. The metals showed a strong positive correlation with each as well as with important water chemistry factors. Cr showed a week or moderate positive correlation with most of the parameters, which indicated that the sole contributions of Cr originated by the tanning industry.

Hierarchical Cluster Analysis (HCA). We used HCA to recognize the source and similarities between the water chemistry factors as well as metals under investigation. HCA is a prevalent data analysis technique that displays the results in the form of a tree diagram known as a dendrogram [38, 59]. The HCA presented in the diagram of a dendrogram revealed that the River Sutlej water chemistry and metals could be divided into three distinct clusters with their origin types (Figure 3). The cluster one comprised of Cr, Cd, Pb, and NO_3-N which can be ascribed to the tanning industry. A slightly longer Euclidian distance of Cd on the scale showed that the metal could have also been contributed by the other factors as well, e.g. mixed origin from city sewage and other anthropogenic activities. The second and the largest cluster comprised of EC, TDS, hardness, TA, salinity, and chlorides which showed that the water chemistry was equally affected by the industrial effluents as well as the city sewage mixed with the run-off waters. The third cluster, however, comprised of temperature, pH and DO. This cluster showed that the factors might have been affected by the tanning industry, city sewage, as well as inflow water currents entering Pakistan near Kasur city. These results have been supported by previous similar studies [12, 60-61].

Principal component analysis (PCA). Considering the intricate relationship among the water chemistry factors and metal contents, PCA was important to extract the hidden information for the proper understanding of the datasets. For this purpose, PCA has been a widely used analytical tool in water quality research. The extracted principal components (PC) provided helpful hints on the water chemistry interactions and helped to describe the source of factors and metals. The results showed that the water chemistry factor loading strengths are classified as strong, moderate, or weak as of >0.75, 0.75-0.50, and 0.50-0.30, respectively [21, 59-60, 62-63].

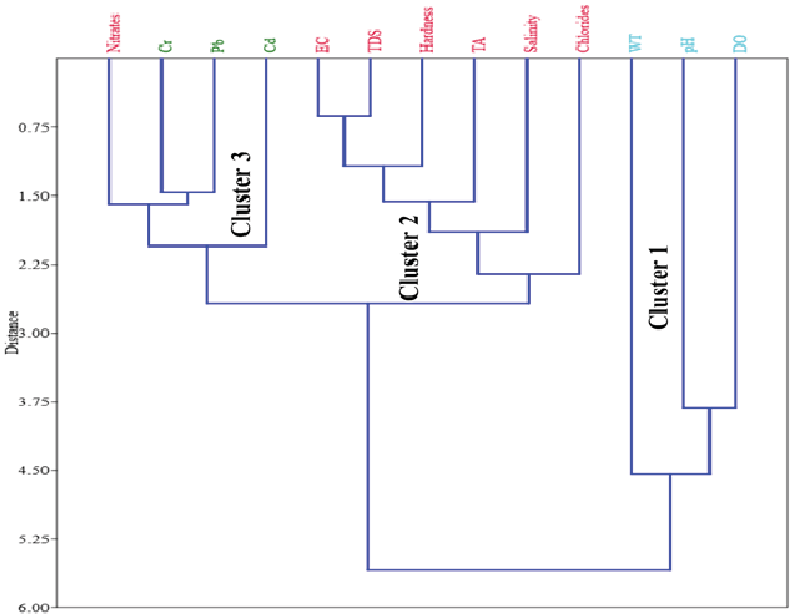

FIGURE 3

Dendrogram showing the grouping of water chemistry factors and targeted metals in River Sutlej

Where DO: Dissolved oxygen, EC: Electrical conductivity, TDS: Total dissolved solids, T: Temperature, TA: Total alkalinity, Cr: Chromium, Cd: Cadmium and Pb: Lead. Chl: Chlorides, NO3-N: Nitrates

The detailed two-dimensional loading plot of water quality parameters and metals is shown in Figure 4, whereas the loading values, along with percent variances and eigenvalues are mentioned in Table 4. The PCA yielded five distinct PCs and explained the data to 96.39 % which indicated that PCA was successful in this research. The first PC explained most of the water chemistry parameters as well as metal contents (67.33 %, eigenvalue = 8.75) However, the loading was a week in strength. The first PC (axis) explained that the tanning industry was the main factor responsible for the water quality deterioration as well as the metal contents in River Sutlej. The second PC (CV = 82.56 %, eigenvalue = 1.98) explained the factors other than the tanning industry in the form of pH, temperature, and salinity. The PC 3 explained the typical inverse relationship of DO and temperature (CV = 89.37 %, eigenvalue = 0.88). It indicates the environmental fluctuations were also at play in River Sutlej. The fourth PC showed moderately strong loadings for pH and chlorides, which indicated that the tanning industry is one of the important factors in modifying the water quality in River Sutlej.

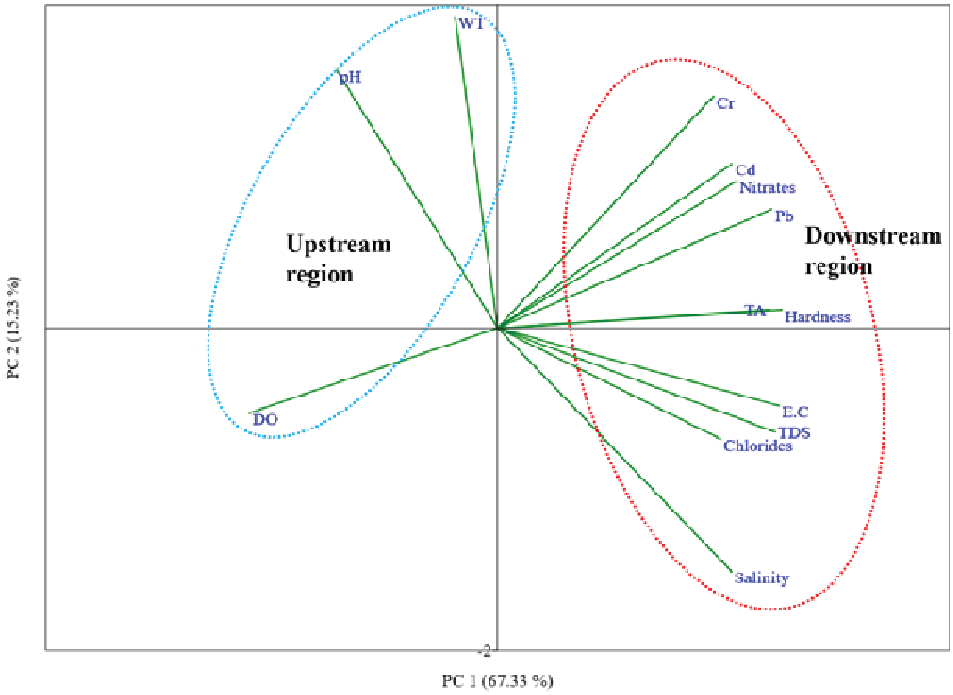

FIGURE 4
PCA loading plot of River Sutlej displaying the predominant water chemistry parameters and metals in the upstream and downstream regions

TABLE 4
PCA loading strengths of the water chemistry factors and selected metals in River Sutlej

Parameters	PC 1	PC 2	PC 3	PC 4	PC 5
DO	-0.29	-0.14	0.42	-0.10	0.34
pH	-0.19	0.42	0.15	0.67	-0.24
EC	0.33	-0.13	0.02	-0.07	-0.16
TDS	0.32	-0.17	-0.06	-0.12	-0.002
Salinity	0.27	-0.40	-0.12	0.04	-0.12
WT	-0.05	0.51	-0.69	-0.21	0.20
TA	0.32	0.030	-0.17	0.23	0.07
Hardness	0.33	0.03	-0.02	-0.01	-0.31
Chloride	0.26	-0.18	-0.14	0.58	0.58
Nitrate	0.28	0.24	0.33	-0.07	0.35
Cr	0.25	0.38	0.29	-0.25	0.23
Cd	0.27	0.27	0.23	0.10	-0.36
Pb	0.32	0.19	0.08	-0.07	0.08
Eigenvalue	8.75	1.98	0.88	0.58	0.33
% variance	67.33	15.23	6.81	4.46	2.56

Where DO: Dissolved oxygen, EC: Electrical conductivity, TDS: Total dissolved solids, WT: Water temperature, TA: Total alkalinity, Cr: Chromium, Cd: Cadmium and Pb: Lead.

TABLE 5
Mann Kendall Trend (MKT) test showing the trends of water chemistry and targeted metals in River Sutlej

Parameters	S	Z	p	Mann Kendall Trend
DO	-40	2.67	0.007	Significant decreasing trend
pH	-23	1.51	0.13	No significant trend
EC	38	2.53	0.01	Significant increasing trend
TDS	34	2.26	0.02	Significant increasing trend
Salinity	37	2.65	0.008	Significant increasing trend
WT	-4	0.20	0.84	No significant trend
TA	-4	0.20	0.84	No significant trend
Hardness	39	2.61	0.009	Significant increasing trend
Chlorides	39	2.61	0.009	Significant increasing trend
Nitrates	50	3.36	0.0007	Significant increasing trend
Cr	50	3.36	0.0007	Significant increasing trend
Cd	42	2.81	0.004	Significant increasing trend
Pb	42	2.81	0.005	Significant increasing trend

Where DO: Dissolved oxygen, EC: Electrical conductivity, TDS: Total dissolved solids, WT: Water temperature, TA: Total alkalinity, Cr: Chromium, Cd: Cadmium and Pb: Lead.

Mann-Kendall Trend (MKT) Test. MK test is a non-parametric tool used to reveal the trend in the water quality parameters. It has broader applications in trend detections procedure in hydrological time-series datasets. It has emerged as a useful tool for water resource management and organization because of its ability to extract appropriate trend information on the possibility of adjustment propensity in water chemistry. The significant trend detection in the water chemistry factors in River Sutlej gave more tremendous insights to the existing trends in critical parameters such as DO, EC, TDS, hardness, chlorides, and the heavy metals (Table 5). MKT test showed that Cr, Cd, Pb, NO_3-N, chlorides, salinity, EC, and TDS were significantly increased in the river water, which is of more significant concern. The DO showed a decreasing trend, which is very harmful to aquatic organisms. On the other hand, however, pH, temperature, and TA showed no significant trend. The increasing trend in key water chemistry parameters and the metal concentration calls for immediate attention. However, it is essential to mention that the MKT test shall always not necessarily mean that the trend will prevail because it depends on the magnitude of variables used and the anthropogenic activities in the watershed area of the water body [19-20].

CONCLUSIONS

This study targeted physicochemical water quality and the presence of selected metals, and the multivariate analytical techniques were applied to extract useful information. It points to the environmental risks posed by the second-largest tanning industry of Pakistan to a cross-border river that is already subjected to intermittent currents due to the imposed control by India on inflowing waters in River Sutlej. The results indicated that downstream water quality was severely degraded, and the reason could be linked with untreated and uncontrolled tanning effluents flowing into River Sutlej via RNJ. At the beginning of data collection, we measured all the physicochemical parameters of effluents to estimate the efficiency of the Kasur tanneries effluents treatment plant established by the Federal government. However, we noticed that there was no change in water quality factors before and after the treatment, as the treatment facility was not operational. The water chemistry factors were exceeding the limits set by national surface water quality standards for the propagation of fish and aquatic life. The watercolor was greyish-black to muddy brown with bad smell. In conclusion, this study showed that tanning industry effluents are the primary reason for water quality degradation and this practice, if not controlled, may threaten the River Sutlej aquatic ecosystem. Similarly, the fish consumers of River Sutlej are under serious health risks.

RECOMMENDATIONS

Based on obtained results, we are compelled to recommend that there is a dire need of far-reaching and strict implementation of national and international water quality standards to save the River Sutlej ecosystem as well as human beings living nearby. The tanning industry treatment plant should be made functional on a permanent basis, and its efficiency should be regularly monitored. We also recommend the installation of two new treatment plants to meet the treatment processing load. This shall be replicated in other tanning industrial cities as well. The local tanning industry lords must be directed to educate their employees about possible environmental damages, resultant threats to humans and the ecosystem, and how to mitigate potential losses to help develop a sustainable aquatic environment. The city sewage should not be mixed with industrial effluents and must be treated before it drains into the water channels.

ABBREVIATIONS

EC = Electrical conductivity
TDS = Total dissolved solids
TA = Total alkalinity
Us = Upstream
Ds = Downstream
Cr = Chromium
Pb = Lead
Cd = Cadmium
Hg = Mercury
HCA = Hierarchical cluster analysis
PCA = Principal component analysis
PC = Principal component
CV = Cumulative variance
WWTP = Wastewater treatment plant
KTWMA = Kasur Tanneries Waste Management Association
NEQS = National Environmental Quality Standards
CPUE = Catch per unit effort
IWT = Indus Waters Treaty
RNJ = RNJ
HNO_3 = Nitric acid
SAS = Statistical Analysis Software
PAST = PAleontological STatistics
MKT = Mann Kendall Trend

DECLARATIONS

Ethical Approval and Consent to Participate. Since this study does not involve human samples, therefore, this is not applicable in this case.

Ethical Approval. The Research Ethics Committee at the Department of Fisheries and Aquaculture, University of Veterinary and Animal Sciences, Lahore, Pakistan, approved this study. Further, the Office of Research, Innovation and Commercialization (ORIC), University of Veterinary and Animal Sciences, Lahore, Pakistan approved the study plan. The authors comply with the Convention on the Trade in Endangered Species of Wild Fauna and Flora and the IUCN Policy Statement on Research Involving Species at Risk of Extinction.

Competing Interests. The authors declare that they have no competing interests

Funding. This study did not receive any external funding.

Authors' Contributions. UA and SI equally participated in this research. UA and SI planned and designed the study, selected the sites, collected the data, and prepared the manuscript under the supervision of NK and AJ. KMA, MSH, and BQ helped in manuscript preparation. TAK, SM and SS helped in data analysis.

ACKNOWLEDGEMENTS

We thankfully acknowledge the Faculty of Fisheries and Wildlife, UVAS, Lahore, for providing financial support. We are also thankful to the Department of Fisheries, Kasur, for logistic help in data collection and related information.

REFERENCES

[1] Achary, M.S., Panigrahi, S., Satpathy, K.K., Prabhu, R.K. and Panigrahy, R.C. (2016) Health risk assessment and seasonal distribution of dissolved trace metals in surface waters of Kalpakkam, southwest coast of Bay of Bengal. Reg. Stud. Mar. Sci. 6, 96–108.

[2] Hering, D., Carvalho, L., Argillier, C., Beklioglu, M., Borja, A., Cardoso, A.C., Duel, H., Ferreira, T., Globevnik, L., Hanganu, J., Hellsten, S., Jeppesen, E., Kodes, V., Solheim, A.L., Noges, T., Ormerod, S., Panagopoulos, Y., Schmutz, S. and Birk, S. (2015). Managing aquatic ecosystems and water resources under multiple stress — An introduction to the MARS project. Science of the Total Environment. 503–504, 10–21.

[3] Abdul, H.M., Jaward, A., Bahram, K.M. and Abass. J.K. (2010) Evaluating Raw and treated water Quality of Tigris River within Baghdad by index Analysis. J. Water Res. Prot. 2,629-635.

[4] Haider, M.S., Ashraf, M., Azmat, H., Khalique, A., Javid, A., Atique, U., Zia, M., Iqbal, K.J., and Akram S. (2016) Nutritive evaluation of fish acid silage in *Labeo rohita* fingerlings feed. J Appl Anim Res. 44,158–164.

[5] Khan, N., Atique, U., Ashraf, M., Mustafa, A., Mughal, M.S., Rasool, F., Azmat, H., Tayyab, M and Iqbal, K.J. (2018) Effect of Various Protein Feeds on the Growth, Body Composition, Hematology and Endogenous Enzymes of Catfish (*Pangasius hypophthalmus*). Pak J Zool Suppl. Ser. 112–119.

[6] Batool, S.S., Khan, N., Atique, U., Azmat, H., Iqbal, K.J., Mughal, D.H., Ahmad, M.S., Batool, S., Munawar, S., Dogar, S., Nawaz, M. and Amjad, S. (2018) Impact of Azomite Supplemented Diets on the Growth and Body Composition of Catfish (*Pangasius hypophthalmus*). Pak J Zool Suppl. Ser.08–12.

[7] Tariq, J., Ashraf, M. and Jaffar, M. (1994) Assessment of pollution status of rivers Jehlum and Sutlej, Pakistan through trace metals in fish, sediment and water, Toxicological and Environmental Chemistry. 43 (3-4),169-174

[8] Nazeer, S., Ali, Z. and Malik, R.N. (2016) Water Quality Assessment of River Soan (Pakistan) and Source Apportionment of Pollution Sources through Receptor Modeling. Archives of Environmental Contamination and Toxicology. 71(1), 97–112.

[9] Jindal, R. and Sharma C (2011) Studies on water quality of Sutlej River around Ludhiana with reference to physicochemical parameters. Environ Monit Assess. 174, 417-425.

[10] Iqbal, S., Atique, U., Mughal, M.S., Khan, N., Haider, M.S., Iqbal, K.J., and Akmal, M. (2017) Effect of Selenium Incorporated in Feed on the Hematological Profile of Tilapia (*Oreochromis niloticus*). J Aquac Res Dev 8, 1000513.

[11] Ahsan, M.A., Satter, F., Siddique, M.A.B., Akbor, M.A., Ahmed, S., Shajahan, M. and Khan, R. (2019) Chemical and physicochemical characterization of effluents from the tanning and textile industries in Bangladesh with multivariate statistical approach. Environ. Monit. Assess. 191, 575.

[12] Atique, U. and An, K.-G. (2020). Landscape Heterogeneity Impacts Water Chemistry, Nutrient Regime, Organic Matter and Chlorophyll Dynamics in Agricultural Reservoirs. Ecol. Indic. 110, 105813

[13] Sweeting, R.A. (1994) River pollution In: Callow P, Petts GE, (Eds.) The River Handbook. Hydro biological and Ecological Principles. Oxford. Blackwell Scientific Publ. London. 23-32

[14] Adekoyeni, O. and Salako, S. (2012) Microbiological, physicochemical and mineral quality of borehole water in Ijebu Land, Ogun State, Nigeria. Int. Sci. Adv. Technol. 2(1),23-30.

[15] Hagan, G.B., Ofusu, F.G., Hayford, E.K., Osae, E.K., Oduro-Afriyie, K. (2011) Heavy metal contamination and physicochemical Assessment of the Densu River Basin in Ghana. Res. J. Environ. Earth. Sci. 3(4):385-392.

[16] Shalini, K.H. and Sakshi, G. (2016) Assessment of water quality and suitability analysis of River Ganga in Rishikesh, India. Applied Water Science. 6(4),383–392.

[17] Iqbal, S., Atique, U., Mughal, M.S., Younus, M., Rafique, M.K., Haider, M.S., Iqbal, H.S., Sherzada, S. and Khan, T.A. (2020) Selenium-Supplemented Diet Influences Histological Features of Liver and Kidney in Tilapia (*Oreochromis niloticus*). Jordan J. Biol. Sci. 13, [In Press].

[18] Singh, R.P., Nath, S., Prasad, S.C. and Verma, H. (2007) Monitoring of variation in water quality of River Ganga at Sangam in Allahabad. IJEP. 27(8), 680-688.

[19] Wijesiri, B., Liu, A., Deilami, K., He, B., Hong, N., Yang, B., Zhao, X., Ayoko, G., and Goonetilleke. A. (2019). Nutrients and metals interactions between water and sediment phases: An urban river case study. Environmental Pollution. 251, 354–362.

[20] Atique, U. and An, K.-G. (2018) Stream Health Evaluation Using a Combined Approach of Multi-Metric Chemical Pollution. Water 10, 661.

[21] Atique, U., Byungjin, L., Johee, Y. and An, K.-G. (2019) Biological Health Assessments of Lotic Waters by Biotic Integrity Indices and their Relations to. Water. 11,436.

[22] Altaf, M.M., Masood, F. and Malik, A. (2008) Impact of long term application of treated tannery effluent on the emergence of resistance traits in *Rhizobium sp*. Isolated from *Trifolium alexandrium*. Turkey J Bio. 32, 1-8.

[23] Mehboob, A., Khan, N., Atiq, U., Iqbal, K.J., Tayyab, R., Batool, S.S., Batool, H.S., Amjad, S., and Tanveer, M. (2017) Effect of Fenugreek as a Feed Additive on the Growth, Body Composition and Apparent Nutrients Digestibility of Striped Catfish *Pangasius hypophthalmus* Fry. Pak J Zool. 49, 2037–2042.

[24] Bae, D.-Y., Atique, U., Yoon, J.-H., Lim, B.-J. and An, K.-G. (2020) Ecological Risk Assessment of Urban Streams Using Fish Biomarkers of DNA Damages and Physiological Responses. Polish J Environ Stud. 29, 1–10.

[25] ALabdeh, D., Karbassi, A.R., Omidvar, B. and Sarang, A. (2019) Speciation of metals and metalloids in Anzali Wetland, Iran. Int. J. Environ. Sci. Technol. 1–14.

[26] Zafarzadeh, A., Bay, A., Fakhri, Y., Keramati, H. and Hosseini-Pouya, R. (2018) Heavy metal (Pb, Cu, Zn, and Cd) concentrations in the water and muscle of common carp (*Cyprinus carpio*) fish and associated non-carcinogenic risk assessment: alagol wetland in the Golestan, Iran. Toxin Rev. 37(2), 154–160.

[27] Moon, W.-K., Atique, U. and An, K.-G. (2020) "Ecological risk assessments and eco-toxicity analyses using chemical, biological, physiological responses, DNA damages and gene-level biomarkers in Zebrafish (*Danio rerio*) in an urban stream." Chemosphere. 239,124754.

[28] Wattoo, M.H.S., Iqbal, J., Kazi, T.G. and Jakhrani, M.A. (2009) Monitoring of Pollution Parameters in Waste Water of Tanneries in Kasur. Pakistan Journal of Biological Sciences. 3(6), 960–962.

[29] Asare, A., Asamoah, B.D. and Sanful, P.O. (2019) Assessment of Heavy Metal Contaminants Using Pollution Indices in Ankobra River at Prestea Huni-Valley District, Ghana. J. Geosci. Environ. Prot. 07, 25–35.

[30] Islam, M.S., Han, S., Ahmed, M.K. and Masunaga, S., 2014. Assessment of Trace Metal Contamination in Water and Sediment of Some Rivers in Bangladesh. J. Water Environ. Technol. 12, 109–121.
[31] Bing, H., Zhou, J., Wu, Y., Wang, X., Sun, H. and Li, R. (2016) Current state, sources, and potential risk of heavy metals in sediments of Three Gorges Reservoir, China. Environ. Pollut. 214, 485–496.
[32] APHA (1992) Standard Methods for the Examination of Water and Wastewater, American public health association publication, 18th edition, Washington DC, ISBN 0-87553-131-8, ISSN 8755-3546.
[33] Kumar, M. and Puri, A. (2012). A review of permissible limits of drinking water. Indian journal of occupational and environmental medicine, 16(1), 40–4.
[34] Ferreira, A.R.L., Sanches-Fernandes, L.F., Cortes, R.M.V. and Pacheco, F.A.L. (2017). Assessing anthropogenic impacts on riverine ecosystems using nested partial least squares regression. Science of The Total Environment, 583, 466–477.
[35] Xu, G., Li, P., Lu, K., Tantai, Z., Zhang, J., Ren, Z., Wang, X., Yu, K., Shi, P. and Cheng, Y. (2019). Seasonal changes in water quality and its main influencing factors in the Dan River basin. CATENA. 173, 131–140.
[36] Wani, K.A., Manzoor, J., Dar, A.A., Shuab, R. and Lone, R. (2020). Heavy Metal Intrusion and Accumulation in Aquatic Ecosystems, in: Fresh Water Pollution Dynamics and Remediation. Springer Singapore, Singapore. 83–104.
[37] Olías, M., Nieto, J.M., Sarmiento, A.M., Cerón, J.C. and Cánovas, C.R. (2004) Seasonal water quality variations in a river affected by acid mine drainage: The Odiel river (south west Spain). Sci. Total Environ. 333, 267-281.
[38] Atique, U. and An, K.-G. (2019) Reservoir Water Quality Assessment Based on Chemical Parameters and the Chlorophyll Dynamics in Relation to Nutrient Regime. Polish J Environ Stud 28, 1043–1061.
[39] Vardhan, K.H., Kumar, P.S. and Panda, R.C. (2019) A review on heavy metal pollution, toxicity and remedial measures: Current trends and future perspectives. J. Mol. Liq. 111197.
[40] Qu, B., Zhang, Y., Kang, S. and Sillanpää, M. (2019). Water quality in the Tibetan Plateau: Major ions and trace elements in rivers of the "Water Tower of Asia." Science of The Total Environment. 649, 571–581.
[41] Shyamala, R., Shanthi, M. and Lalitha, P. (2008) Physicochemical analysis of Borewell water samples of Telungupalayam area in Coimbatore district, Tamilnadu, India. E-J Chem. 5, 924–929.
[42] Welch, E.B. and Lindell, T. (1992) Ecological effects of wastewater. Applied Limnology and Pollutant Effects. E and F SPON. An imprint of Chapman and Hali, London. p 425.
[43] Cazemeir, W.G. (1988) Fish and their environment in large European river ecosystems, the Dutch part of river Rhine. Sciences de l'eau. 7(1), 95-114.
[44] Rauf, A., Javed, M. and Ubaidullah, M. (2009) Heavy metals levels in three major carps (*Catla catla, Labeo rohita* and *Cirrhina mrigala*) from the river Ravi, Pakistan. Pak Vet J. 29(1), 24-26.
[45] Kim, J.-J., Atique, U. and An, K.-G. (2019) Long-Term Ecological Health Assessment of a Restored Urban Stream Based on Chemical Water Quality, Physical Habitat Conditions and Biological Integrity. Water. 11,114.
[46] Mishra, P.C., Dash, M.C. and Kar, G.K. (1990) Pollution studies in river IB. Physico-chemical characteristics. In: Trivedy RK. (Ed). River pollution in India. Ashish Publishing House. 39-52 pp.
[47] Haider, M.S., Javid, A., Azmat, H., Abbas, S., Ashraf, S., Altaf, M., Atique, U., Iqbal, S., Iqbal., K.J., and Batool, M. (2018) Effect of Processed Fish Waste on Growth Rate and Digestive Enzymes Activities in *Cyprinus carpio*. Pak J Zool Suppl. Ser. 191–198.
[48] Barnes, D. and Bliss, P.J. (1983) Biological control of nitrogen in wastewater treatment. E and FN Spon Ltd. 11 Newfetter lane, London. 144 pp.
[49] National Surface Water Classification Criteria and Irrigation Water Quality Guidelines for Pakistan Report (2007) Published by WWF-Pakistan, Ferozepur Road, Lahore
[50] Bajza, Z. and Vrcek, I.V. (2001) Water quality analysis of mixtures obtained from tannery waste effluents. Ecotox Environ Safe. 50(1), 15–18.
[51] Ahsan, M.M., Shakoori, F.R. and Shakoori, A.R. (2006). Biochemical and haematological abnormalities in factory workers exposed to hexavalent chromium in tanneries of Kasur District. Pakistan Journal of Zoology. 38(3), 239–253.
[52] Jarup, L. (2003) Hazards of heavy metal contamination. British Medical Bulletin. 68, 167–182
[53] Li, S. and Zhang, Q., (2010) Risk assessment and seasonal variations of dissolved trace elements and heavy metals in the Upper Han River, China. J. Hazard. Mater. 181, 1051–1058.
[54] Javed, M. and Usmani, N. (2011) Accumulation of heavy metals in fishes: A human health concern International Journal of Environmental Sciences. 2(2), 659-670.

[55] Rahman, Z. and Singh, V.P. (2019) The relative impact of toxic heavy metals (THMs) (arsenic (As), cadmium (Cd), chromium (Cr)(VI), mercury (Hg), and lead (Pb)) on the total environment: an overview. Environ. Monit. Assess. 191, 419.
[56] Akbulut, A. and Akbulut, N.E. (2010) The study of heavy metal pollution and accumulation in water, sediment, and fish tissue in Kizilirmak River Basin in Turkey. Environmental Monitoring and Assessment. 167(1–4), 521–526.
[57] Tapia, J., Vargas-Chacoff, L., Bertran, C., Pena-Cortes, F., Hauenstein, E., Schlatter, R., Jimenez, C. and Tapia, C. (2012) Heavy metals in the liver and muscle of *Micropogonias manni* fish from Budi Lake, Araucania Region, Chile: potential risk for humans. Environ Monit Assess. 184,3141–3151.
[58] Mamat, Z., Yimit, H., Ji, R.Z.A. and Eziz, M. (2014). Source identification and hazardous risk delineation of heavy metal contamination in Yanqi basin, northwest China. Sci. Total Environ. 493, 1098–1111.
[59] Özdemir, Ö. (2016) Application of multivariate statistical methods for water quality assessment of Karasu-Sarmisakli Creeks and Kizilirmak River in Kayseri, Turkey. Polish Journal of Environmental Studies. 25 (3), 1149-1160.
[60] Holbach, A., Wang, L.J., Chen, H., Hu, W., Schleicher, N., Zheng, B. and Norra, S. (2013) Water mass interaction in the con*f*luence zone of the Daning River and the Yangtze River- a driving force for algal growth in the Three Gorges Reservoir. Environ. Sci. Pollut. Res. 20, 7027–7037.
[61] Zhong, W., Zhang, Y., Wu, Z., Yang, R., Chen, X., Yang, J. and Zhu, L. (2018) Health risk assessment of heavy metals in freshwater fish in the central and eastern North China. Ecotoxicol. Environ. Saf. 157, 343–349.
[62] Palácio, S.M., Espinoza-Quiñones, F.R.E., DePauli, A.R., Queiroz, C.B., Fabris, S.C., Fagundes-Klen, M.R., Veit, M. and Piana, P.A. (2016) Assessment of anthropogenic impacts on the water quality of Marreco River, Brazil, based on principal component analysis and toxicological assays. Water Air Soil Pollution, 227, 307.
[63] Atique, U. and An, K.-G. (2019) Water quality and Trophic state index analysis in relation to Land use patterns in Agricultural Reservoirs, in: Korea Society of Environment and Ecology Proceedings. p. 110.

Received: **21.11.2019**
Accepted: **20.01.2020**

CORRESPONDING AUTHOR

Usman Atique
Department of Biosciences and Biotechnology, Chungnam National University,
Daejeon , South Korea

e-mail: physioatique@gmail.com

© by PSP Volume 29 – No. 04A/2020 pages 3026-3032 Fresenius Environmental Bulletin

EFFECT OF WATER CONSUMPTION CHARACTERISTICS ON WATER PRODUCTION FUNCTION OF SOYBEAN IN COLD BLACK SOIL AREA

Yanyu Lin[1,2], Shujuan Yi[2,3,*], Mengxue Wang[4] ,Mingyao Wang[4],Xiaolei He[4],Xu Zhou[4]

[1] College of Civil Engineering and Water Conservancy, Heilongjiang Bayi Agricultural University, Heilongjiang Daqing 163319, China
[2] Quality Supervision and Testing Center for Agricultural Processed Products of Ministry of Agriculture (Daqing), Heilongjiang Daqing 163319, China
[3] College of Engineering, Heilongjiang Bayi Agricultural University, Heilongjiang Daqing 163319, China
[4] College of Agricultural, Heilongjiang Bayi Agricultural University, Heilongjiang Daqing 163319, China

ABSTRACT

In order to explore the water consumption characteristics of soybeans in the cold black soil area and their sensitivity to water in each growth stage, the water consumption test of soybean was carried out in the potting field of Heilongjiang *Bayi* Agricultural University in 2019. Through the barrel test, this paper adopts the comprehensive test design to analyze the variation characteristics of soybean water consumption in different growth stages, and establishes the model of soybean water production function in the area, which clarifies the water consumption regularity and the effect of water deficit on yield in each growth stage. The results showed that in the various growth stages of soybean, the water consumption from large to small was the Filling period, the knotting period, the flowering period and the seedling period. The average water consumption and water consumption modulus of each treatment in the drumming period were the highest, which were 107.8 mm and 0.45 mm respectively. The heavy variation coefficient of water consumption during the flowering period was the highest, which was 0.079. Through the *Jensen* model, the order of the sensitivity to moisture in each growth stage was calculated from flowering period to Filling period to knotting period to seedling period. It indicated that the flowering period was the most sensitive stage of soybean water requirement; the growth index of soybean was calculated to be the fastest growing rate after 100- 150 days after seedling period, and the correlation coefficient was higher in this model, so it is suitable for the area. The research results can be used to study the water demand law and the optimal allocation of water resources in the black soil region of the northeastern cold region.

KEYWORDS:
Soybean cold black soil area, water consumption characteristics, water production function

INTRODUCTION

Soybean is an important food crop and oil crop in China, and is a moisture sensitive type in legume crops [1]. The *Bei da huang jiu san* is located in the west of Heilongjiang Province. There is a shortage of water resources in the region, and there are often spring droughts and autumn droughts, resulting in unstable soybean yields [2]. Crop water consumption is not only an important part of the field water balance, but also a prerequisite for formulating planned irrigation and water supply status analyzed [3]. Under the premise of maintaining yield, crop improved water use capacity has become a research hotspot in current water-saving agriculture. Recent studies have shown that moderate water stress can help to construct a suitable plant type structure, which lays a foundation for high quality and high yield and improved water use efficiency [4]. *Chi Daocai et al*. [5] compared the effects of different degrees of water stress on water use efficiency in rice growth stages, and pointed out that the moderate water deficit interaction effect in tillering stage and milk stage can significantly improve water use efficiency. *Hou Zhiqiang et al* [6] identified the key water demand period of soybean yield by studying the drought stress in different growth stages of soybean, and analyzed the water consumption law and the influence of WUE under drought stress. *Liu et al* [7] analyzed the law of rainfall and water demand in Siping area, and proposed the appropriate irrigation water volume of soybean. According to the relationship between water and crop growth and yield, the efficiency of water to crop roots absorption and transformation and photosynthetic products to economic yield can be improved, and high yield and high water use efficiency can be achieved [8, 9].

The water production function is to describe the mathematical relationship between crop yield (grain yield or dry matter yield) and water, to establish a model of soybean water production function suitable for the region, for regional water-saving irrigation planning and systematic assessment and

for inadequate irrigation schedules. It is of great significance to develop and promote applications [10]. *AL-Jamal MS et al* [11] studied the water production function under the condition of under-irrigation of onion in *New Mexico and Lax Cruces,* and found that the functional relationship is linear and curved, respectively. *Kang Shaozhong et al* [12] passed the test. It is concluded that the degree of impact on crop yield from the period of water deficit is greater than that due to water deficit. *Rong Fengtao, Wang Yangren et al* [13-14] used the Jensen model to fit wheat, corn, cotton and other crops in Shanxi Province, and the effect was good. Liu *Changming et al* [15] used the principle of least squares method to fit the water effect and water requirement of winter wheat with less error. *Chen Xiaonan et al* [16] provided a new effective method for the calculation of crop water production function based on genetic design program. *Shen Shenzhong* [17] analyzed the water sensitivity of crops through BP neural network, and the situation was higher.

Although the above studies have reported a lot of research on crop water regulation, the climatic conditions, crop varieties, and cultivation measures in different regions are quite different. At the same time, the incidence of spring drought in the western part of Heilongjiang Province is high, which restricts the sustainable development of local agriculture. In order to change the current situation of local rainfed agriculture, it is great practical significant to study the water consumption characteristics of soybeans and the distribution of limited water resources in the region.

MATERIALS AND METHODS

Overview of the Test Area. The experiment was carried out in the potted field of Heilongjiang Bayi Agricultural University from May to September 2019. The area is a typical mid-temperate continental monsoon climate. The average annual temperature is 3.2 °C, the average annual precipitation is 450 mm, and the crop growth period is 150~170 d, frost-free period of 130 d or more. The soil to be tested was black soil, and the water holding capacity in the 1 m soil layer was 39.32%, and the soil bulk density was 1.03 g·cm-3. The basic physical and chemical properties of the tested soil were as follows, organic matter is 39.2 g·kg-1, pH is at 6.67, total nitrogen is 14.78 g·kg-1, total phosphorus (P2O5) is 14.82 g·kg-1, total potassium (K2O) is 19.51 g·kg -1. The test variety was Shannon 14.

Test Design. The test was carried out in a shelter by a barrel test. The plastic drum used was 40 cm high and 38 cm in diameter. After the black soil has screened and dried, it is placed in a bucket and the weight of the barrel is 15 kg. The bucket is filled with a plastic funnel (the length is 30 cm, the diameter is 1.5 cm) made of PVC pipe, buried 10 cm from the surface soil layer, and the funnel partially exposes the topsoil. In order to ensure uniform irrigation and avoid the topsoil, a small hole is made in the PVC pipe, and distance between holes is equal. According to the local fertilization standard, urea is at 1.0 g·barrel-1, ammonium dihydrogen phosphate is at 2.5 g·barrel-1, and potassium sulfate is at 1.5 g·barrel-1 were applied before the test. 3 holes were planted per pot, 3 seeds were planted per hole, and 1 seedling was fixed at each hole after seedlings, and 3 plants were kept in each pot. Four growth stages were set up in the experiment, and three stress levels of light drought, moderate drought, and heavy drought were set respectively. The relative water content of the soil (accounting for the percentage of water holding capacity in the field) controlled by 75%- 85%, 65% ~75%, and 55%~65%, respectively. Considering the stage of growth, the trial arranges one stage and two stages of continuous drought treatment may occur in the actual production of drought. In order

TABLE 1
Test Design Table

Treatment	Seedling period	Flowering period	Knotting period	Filling period
T1	55%-65%	85%-0mm	85%-0mm	85%-0mm
T2	75%-85%	85%-0mm	85%-0mm	85%-0mm
T3	85%-0mm	55%-65%	85%-0mm	85%-0mm
T4	85%-0mm	75%-85%	85%-0mm	85%-0mm
T5	85%-0mm	85%-0mm	55%-65%mm	85%-0mm
T6	85%-0mm	85%-0mm	75%-85%mm	85%-0mm
T7	85%-0mm	85%-0mm	85%-0mm	55%-65%
T8	85%-0mm	85%-0mm	85%-0mm	75%-85%
T9	65%-75%	65%-75%	85%-0mm	85%-0mm
T10	85%-0mm	65%-75%	65%-75%	85%-0mm
T11	85%-0mm	85%-0mm	65%-75%	65%-75%
CK	85%-0mm	85%-0mm	85%-0mm	85%-0mm

Note: "%" is the dimension of the percentage of soil water holding capacity, and "mm" is the depth dimension of the water layer.

to study the soybean water production function comprehensively, a control treatment was set at the same time, 12 treatments, and each treatment was repeated 3 times. The test design scheme is detailed in Table 1. In the water deficit adjustment stage, the irrigation level is controlled according to the treatment design level (below the lower limit, and fill to the upper limit), and the remaining stages are controlled according to the control level.

Observation Indicators and Methods. Crop Water Consumption Characteristics. Use TPIME-PICO64/32 soil moisture meter to measure 0-20 cm soil moisture content (waterless layer) at 08:00 every day to determine whether the soil moisture content reaches the lower limit, and the soil moisture content is close to or reaches the lower limit of control. The upper limit of the design is to maintain the soil moisture content between the upper and lower irrigation limits. The irrigation is required before and after irrigation, and the irrigation amount measured by the measuring cylinder. It is weighed at 08:00 every day (soil + plant), and the actual water consumption per day is calculated according to the difference between the two days before and after. Therefore, the formula for calculating the water consumption and water consumption modulus of the crop stage is as follows.

$$ETi=\Delta Wi+Ii \quad (1)$$

$$Ri= ETi/ ET\times 100\% \quad (2)$$

In the formula,

ETi———the stage water consumption, mm

ΔWi———the difference in stage water storage, mm

Ii———stage irrigation amount, mm

Ri———stage water consumption modulus, %

ET—the total amount of water consumed during the whole growth period, mm

i———In the growth stage, *i* is 1, 2, 3, and 4 respectively representing seedling period, flowering period, knotting period, and blast stage.

Establishment of Water Production Function. Many researchers have found that the *Jensen* model is the most versatile and is a commonly used static model of water production function [18- 20]. The model takes the evapotranspiration of each growth stage of the crop as a variable. This paper looks for the relationship between water deficit at different growth stages and the final yield of crops. The expression is as follows.

$$\frac{Y}{Y_{\mathrm{m}}}=\prod_{i=1}^{n}\left[\frac{ET_i}{ET_{mi}}\right]^{\lambda} \quad (3)$$

Where:

n—the number of stages during the growth period of the crop.

ETmi—the actual evapotranspiration of the crop at each growth stage, mm; that is, the water consumption of the crop under sufficient water supply conditions.

ETi—the potential evapotranspiration of the crops at each growth stage, mm.

Y—the actual yield of each growth stage of the crop, kg·hm-2;

Ym—the potential yield of crops, kg·hm-2. That is, crop yield under adequate water supply conditions.

Λ—the sensitive index of crop growth stage. The larger λ indicates that the water deficit at this stage has a greater impact on yield, and vice versa.

The test expression for the function correlation coefficient is as follows.

$$U=\sum_{m=1}^{j}\left[\left(\frac{\hat{Y}}{Y_m}\right)_j-\left(\frac{\bar{Y}}{Y_m}\right)\right]^2 \quad (4)$$

$$L_{yy}=\sum_{m=1}^{j}\left[\left(\frac{Y}{Y_m}\right)-\left(\frac{\bar{Y}}{Y_m}\right)\right]^2 \quad (5)$$

$$R=\sqrt{\frac{U}{L_{yy}}} \quad (6)$$

The relationship between the accumulated value of the water sensitivity index at each stage and the corresponding time *t* is the cumulative function of the sensitive index, and its expression is as follows.

$$z(t)=\sum_{t=0}^{t}\lambda(t) \quad (7)$$

Where: *z(t)* is the accumulated value of the water sensitivity index of each stage of the crop before the time t.

Each stage $\lambda(t)$ can be obtained by the following formula:

$$\lambda(t)=z(t_i)-z(t_{i-1}) \quad (8)$$

According to *Wang Yangren et al.*, the growth curve is used to fit the function z(t).

$$\mathrm{z}(t)=\frac{C}{1+e^{A-Bt}} \quad (9)$$

Where: *A, B, C* are all fitting parameters.

Grain Yield. After the plants are matured and harvested, the yield is measured and tested, and the plant height, number of nodes, number of pods per plant, number of grains per plant, and 100-grain weight are determined. The collected plants were placed in an oven at 120 ° C for 30 min, dried at 80 ° C to constant weight, and degranulated and weighed to calculate grain yield.

RESULTS

Water Consumption Regularity of Soybean Growth Stage. It can be seen from Figure 1 that the water consumption of each treated soybean stage shows similar changes in the same stage. The average water consumption of each treatment in the Filling period is 107.8 mm, the daily average water consumption is 3.59 mm, and the average water consumption of each treatment in the seedling period. The minimum is 48.93 mm and the average daily water consumption is 1.63 mm. The water consumption of *T7* treatment and *T8* treatment was largest, the drought stress in the grain-grain period had the greatest impact on soybean water consumption, and the variation coefficient of water consumption during the flowering period was highest, which was 0.079.

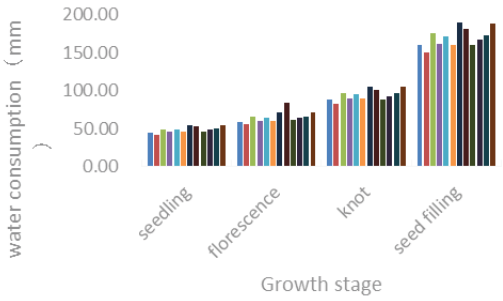

FIGURE 1
Water consumption of soybeans at various growth stages

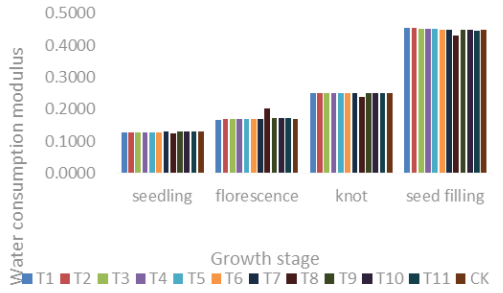

FIGURE 2
Water consumption modulus of soybean growth stages

It can be seen from Figure 2 that the water consumption modulus of the soybean in the growth stage of each treatment is the largest in the filling period, and its average value is 0.45. The seedling period is smallest, which is at 0.13. The water consumption of T7 treatment and T8 treatment is largest. It is indicated that the drought stress during the granulation period has the greatest influence on the water consumption modulus of soybean. Therefore, it can be seen from Figure 1 and Figure 2, in the various growth stages of soybean, the water consumption from large to small is the filling period, the knotting period, the flowering period, and the seedling period.

Soybean Water Production Function. Establishment and Verification of the Jensen Model. According to the water demand and yield data of each treated soybean, the sensitivity index λ and the correlation coefficient R of each growth stage can be obtained by using Equation 3 and solved by using MATLAB7.1, as shown in Table 2 and Equation 10.

TABLE 2
Sensitivity index and correlation coefficient of soybean growth stages

Fertility stage	Seedling period	flowering period	knotting period	Filling period	Correlation coefficient R
Sensitivity index	0.2458	0.4362	0.2938	0.3722	0.925

$$\frac{Y_a}{Y_m}=\left[\frac{ET_a}{ET_m}\right]_1^{0.2458}\left[\frac{ET_a}{ET_m}\right]_2^{0.4362}\left[\frac{ET_a}{ET_m}\right]_3^{0.2938}\left[\frac{ET_a}{ET_m}\right]_4^{0.3722} \quad (10)$$

It can be seen from Table 2 and Equation 7 that the four growth stages of soybean have different sensitivity to water shortage. The order of sensitive index in *Jensen* model is flowering period > Filling period > knotting period > seedling period. The model formula indicates that the value λ is larger, it means that the water deficit at this stage has a greater influence on the yield, that is, if water shortage at this stage will result in a serious reduction in production, the converse is smaller. For soybean, the flowering period is the reproductive growth stage, the growth of vegetative body reaches the peak at the end of flowering period, the metabolism is strong, and the evapotranspiration reaches the maximum. If there is water shortage or water drips in the middle stage, it will cause the flower pod to fall off a lot, directly affecting the final output. Therefore, this stage is the most sensitive stage of soybean water demand and a key stage for capturing high yields. The correlation coefficient in this model is 0.925, and the correlation is high. It is therefore suitable for the region.

Sensitive Index Cumulative Function Parameter Solving and Testing. The parameters *A, B, C* and the correlation coefficient *R* are calculated according to the formula (6) to formula (9), as shown in Table 3, the equation is shown in Equation 11, and the sensitivity index accumulation curve is shown in Figure 3.

TABLE 3
Sensitive index cumulative curve fitting parameters and test values

A	B	C	R
4.3624	0.0212	1.16	0.916

$$z(t) = \frac{1.16}{1 + e^{4.3624 - 0.0212t}}$$

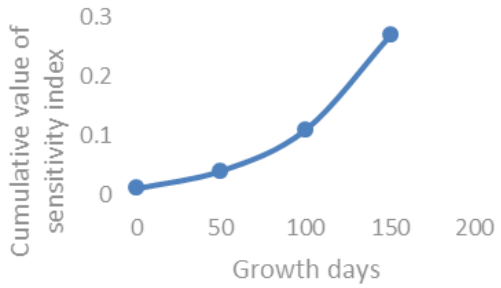

FIGURE 3
Sensitivity index accumulation curve

It can be seen from Table 3 and Figure 3 that the cumulative value of the *Jensen* model sensitivity index increases with the growth of time after the seedling period, and the growth rate is the fastest in 100- 150 days after the seedling period. The correlation coefficient in the model is 0.916, which is highly correlated, so it is suitable for the region.

DISCUSSION

Crop water consumption is not only an important part of field water balance, but also a prerequisite for formulating irrigation schedule, evaluating climate resources, and water supply. The study of crop water consumption law can clarify the difference in soybean's ability to regulate its own water loss and adapt to drought environment [21]. The results of this study showed that soybeans had the largest water consumption and water consumption modulus during the granule stage. If the drought is short of water during this period, the fruit is not full and the grain weight decreases. In the soybean granule period, the northeast soybean main producing area generally has less rainfall, which often causes autumn sag. At this time, if the granule water can be irrigated, the hydration granules can promote the yield and quality of soybean [22]. Heavy drought and light drought during flowering have the largest coefficient of variation in water consumption. It is indicated that the soybean can be rehydrated in the flowering period without affecting the normal growth of soybean. It is of great significance to study the water transport law of the crop itself, the water saving potential, the temporal and spatial evolution of multi-scale crop water by studying the soybean water production function [23].

The crop water production function is the basis for determining the optimal irrigation schedule for crops and the economic analysis of irrigation. This study uses the barrel test in the main soybean producing areas of Northeast China, and it has four stages: seedling period, flowering period, knotting period and seed filling period. They were arranged into four water stress levels: normal irrigation, light drought, moderate drought, and heavy drought. Based on the experimental data, the Jensen model and the sensitivity index cumulative function model are established. The results show that the flowering period is the most sensitive stage of soybean water demand, and it is the key stage for soybeans to capture high yield. This period of growth is the stage in which soybean evapotranspiration is the most intense, and this period requires timely and sufficient supply of water. Therefore, the crop water production function is the basis for determining the optimal irrigation schedule for crops and for conducting economic analysis of irrigation.

CONCLUSIONS

In this study, the water consumption regularity and water production function model of soybean growth stages in the northeastern cold black soil area were studied, and the following conclusions were obtained.

(1) The water consumption of each treated soybean stage showed similar changes in the same stage. The water consumption from large to small was the Filling period, the knotting period, the flowering period and the seedling period.

(2) Drought stress during the grain-grain period had the greatest impact on water consumption and water consumption modulus of soybean, and the variation coefficient of water consumption was the largest in heavy flowering and light drought during flowering period.

(3) The order of sensitive index in *Jensen* model is flowering period > filling period > knotting period > seedling period. It indicates that the flowering period is the most sensitive stage of soybean water demand. It is calculated by the sensitivity index accumulation function that the growth rate of soybean is the fastest after 100 to 150 days in the seedling period. The correlation coefficient is higher in this model, so it is suitable for the area.

ACKNOWLEDGEMENTS

Thank you for support from Sub-project of the 13th Five-Year Key R&D Project (2018YFD1000905-06), Heilongjiang Bayi Agricultural University Support Program for San Heng San Zong (TDJH201803), Talent Introduction Plan of Heilongjiang Bayi Agricultural University

(XYB201801), Postdoctor Work Station for Agricultural Processed Product Quality Supervision and Inspection Test Center (Daqing) of Ministry of Agriculture.

REFERENCES

[1] Gao, L., Liu, L., Dong, S., Zu, W. (2009) Effects of drought stress on physiological and biochemical characteristics of soybean seedling leaves. Journal of Northeast Agricultural University. 40 (8), 1-4.

[2] Zhang, R., Fu, L., Tong, B, Wu, X., Zhu, H., Sun, G. (2015) Effects of density and row spacing on agronomic traits and yield of different soybean varieties. Soybean Science. 34(1), 52-55.

[3] Cheng, Y., Ma, F., Feng, Z., Wang, Y., Fan, H., Liao, J., Han, G. (2012) Study on water consumption of spring wheat under drip irrigation. Agricultural Research in the Arid Areas. 30 (2), 112-117.

[4] Chu, G., Zhang, M., Zhu, K., Wang, Z., Yang, J. (2016) Effects of alternate wet and dry irrigation on rice yield and water use efficiency. Acta Agronomica Sinica. 42 (7), 1026-1036.

[5] Chi, D., Tong, Y., Chen, T., Zheng, J., Chen, W, Tai, E. (2016) Effects of different water stress couplings on rice yield and water productivity during multiple growth periods. Journal of Shenyang Agricultural University. 47(1), 71-77.

[6] Hou, Z., Jiang, S., Jin, J. (2018) Effects of drought stress on water consumption and water use efficiency of summer soybean in different growth stages. Journal of Irrigation and Drainage. 37 (5), 19-24.

[7] Liu, Y, Tan, J, Li, W., Liu, H. (2015) Analysis of irrigation water requirement of maize and soybean in Siping area of Jilin Province. South-to-North Water Transfer and Water Science and Technology. 13(6), 1225-1228, 1232.

[8] Meng, Z., Ban, X., Liu, A., Pang, H., Wang, H. (2006) Effects of Regulated Deficit Irrigation on Photosynthetic Physiological Characteristics of Summer Maize. Journal of Soil and Water Conservation. 20 (3), 182-186.

[9] Zhang, B., Li, F., Qi, G. (2007) Effects of Regulated Deficit Irrigation on Yield and Water Use Efficiency of Spring Wheat in Arid Environment. Chinese Journal of Eco-Agriculture. 15 (1), 58-62.

[10] Chen, Y., Kang, S. (1995) The principle of inadequate irrigation. Beijing: Water Power Press.

[11] AL-Jamal, M.S., Sammis, T.W., Ball, S., Smeal, D. (2000) Computing the crop water production function for onion. Agricultural Water Management. 46,29-41.

[12] Kang, S., Xiong, Y. (1991) Study on the method of distinguishing crop water shortage and the irrigation index. Journal of Hydraulic Engineering. (1), 34-39.

[13] Rong, F., Wang, Y. (1997) Experimental study on parameters of water production function of main crops in Shanxi Province. Journal of Hydraulic Engineering. (1),78-82.

[14] Wang, Y., Rong, F. (1997) Study on Cumulative Curve Parameters of Water Sensitivity Index. Shanxi Water Resources Science and Technology. (4),20-24.

[15] Liu, C., Zhou, C. (2005) Study on Wheat Water Production Function and Its Benefits.Geographical Research. 24 (1),1-9.

[16] Chen, X., Huang, Q., Qiu, L., Duan, C., Zhang, W. (2006) Research on crop water production function based on genetic programming. Transactions of the Chinese Society of Agricultural Engineering. 22 (3), 6-9.

[17] Shen, X., Cui, Y., Shen, H. (2001) Neural Network Method for Analysis of Crop Water Shortage Sensitivity. China Rural Water and Hydropower. (5), 12-15.

[18] Feddes, R.A., Kowalik P.J., Zaradny, H. (1978) Simulation of field water use and crop yield. Center for Agricultural Publishing and Documentation. Wageningen. Netherlands.

[19] Dierckx, J., Gilley, J.R., Feyen, J. (1988) Simulation of the soil-water dynamics and cron yields under deicit irrigation. Irrig. Sci. (9), 105-125.

[20] Wang, H. (2000) Partial least squares regression method and its application. Beijing: National Defense Industry Press.

[21] Zhao, L., Li, J., Yu, J., Sophie B. (2003) Effects of Drought Stress on Diurnal Changes of Transpiration Water Consumption of Seedlings. Journal of Beijing Forestry University. 25 (3),42-47.

[22] Jiang, H., Nie, T., Chen, P., Zhang, Z. (2018) Study on water requirement and irrigation schedule of soybean based on CROPWAT model. Water Resources and Hydropower Engineering. 49(11),211-217.

[23] Guo, Y., Wang, B., Wei, Y., Zhou, X. (2008) Experimental study on water production function of soybean in semi-arid area of western Heilongjiang Province. 27(3), 49-51.

Received: **21.11.2019**
Accepted: **20.01.2020**

CORRESPONDING AUTHOR

Shujuan Yi
College of Engineering,
Heilongjiang Bayi Agricultural University,
Heilongjiang Daqing 163319, China.

e-mail: yishujuan_2005@yeah.net

© by PSP Volume 29 – No. 04A/2020 pages 3033-3039 Fresenius Environmental Bulletin

EFFECT OF FOLIAR APPLICATION OF IRON (Fe) AND MOLIBYDENIUM (Mo) ON YIELD, PROTEIN AND NODULATION IN SOYBEAN UNDER AGRO CLIMATIC CONDITIONS OF SANLIURFA

Erdal Erbil[1], Ali Beyhan Ucak[2,*], Timucin Tas[1], Mehmet Karakus[1], Cemil Yetkin[3]

[1]GAP Agricultural Research Institute, Department of Field Crop- Sanliurfa/Turkey
[2]Siirt University, Faculty of Agriculture, Department of Biosystems Engineering - Siirt/Turkey
[3]GAP Agricultural Research Institute, Department of Plant Protect- Sanliurfa/Turkey

ABSTRACT

This study was conducted in 2017-2018 at the Gundas Research Station belong to the GAP Agricultural Research Institute in Sanliurfa/Turkey to investigate the effects of iron (Fe) and molybdenum (Mo) on soybean (*Glycine max*. L.) yield, protein and nodule formation. The study was carried out with four replications in the randomized blocks trial design. Standard NPK dose (100-50-0 kg ha^{-1}) was applied in the form of 20-20-0 compound fertilizer. Iron, one of the factors, was added in two doses (0.5 kg ha^{-1} and 1 kg ha^{-1}) in the form of iron sulphate ($FeSO_4$+$7H_2O$) and molybdenum in the form of ammonium molybdate ($(NH_4)_6Mo_2O_{24}$ $4H_2O$) was used as a liquid from the foliar spray. The results showed that application of iron and molybdenum significantly increased the grain yield, number of total and active nodules $plant^{-1}$, biomass yield, 1000 seed weight (g), total nitrogen uptake, protein content in soybean. Furthermore, it was observed that combined application of iron and molybdenum significantly produced greater crop yields and more nodulation than the only application of iron or molybdenum. It is therefore recommended that Fe and Mo may be applied to soybean in Sanliurfa for better crop yields and greater root nodulation.

KEYWORDS:
Iron, Molybdenum, Nodulation, Sanliurfa Soybean, Yield

INTRODUCTION

Soybean (*Glycine max* L.), belongs to the genus Glycine under the family *Leguminosae*. Soybean, the most important food source of East Asian countries, is the only legume among five sacred products (paddy, wheat, barley, millet and soybean) mostly consumed and cultivated for 5000 years. The composition of the seeds is 40-44% protein, 18-24% fat, 20% carbohydrate, 5% mineral substances and 1% lecithin. Being the rich source of protein it is also called "poor man's meat". Since the protein found in soybean seeds contains highly valuable amino acids like histidine, leucine, isoleucine and lysine making its nutritional value quite high. Soybean is also known as the vitamin B store. For this reason, soybean foods, digestion facilitated and increased bone development in children has been determined [1]. Soybean's oil is abundant in Ca, Fe, Zn minerals and A, B1, B2, C, D, E, K vitamins [2]. Under present scenario, rapid soybean expansion took place at global level due to by-product (soybean cake) after oil extraction.

It is used in the production of soap, wax, insulating materials, protein derivatives and printing inks. Soybean's meal contains a lower proportion of crude cellulose compared to other oilseeds meal. Due to its high fat and protein content and easy digestibility in animal feeds, it is the most preferred feed raw material in bovine, poultry and seafood. USA, Brazil, Argentina, China and India are the big producers of soybean. In Turkey, soybean was cultivated on an area of 24 thousand hectares in 2017-18. It is noted that in the Cukurova region, where 95% of the local soybean crop is planted, soybeans have to compete with wheat, corn and cotton [3].

The growth and development of soybean plants is highly affected by the environmental conditions, and the photoperiod responses vary by variety [4]. According to the photoperiods of soybean varieties are classified in 12 different growth groups towards the poles, starting from the north of the equator. Generally defined as short-day plants, soybean produces a higher number of flowers in long-day conditions, but the flower shrub rate is increasing [5].

Soybean is a plant that has the ability to fix environmental nitrogen by *Bradyrhizobium japonicum* bacteria present on its roots' nodules [6]. Inoculation of soybean seeds with this bacteria, enhances the capability of host plant in fixation. Thus, it meets a part of the nitrogen that it needs, and leaves a nitrogen-rich field to the plant to be planted after it.

Because micro nutrient elements are indispensable for plants. Iron (Fe) is an important component of cells, proteins and enzymes in plants[7, 8]. Iron deficiency decreases the amount of other pigments such as carotene, xanthine and lutein besides chlorophyll a and b [9]. Molybdenum (Mo) is the micronutrient required for growth and development of plants from the soil. Molybdenum is required to produce the nitrogenase (nitrate reductase) enzyme [10]. This enzyme is the microelement that directly affects N_2 fixation [11, 12]. Plants only containing enough molybdenum and iron can produce the nitrogenase enzyme. Many researchers have reported the important effect of micro-elements on legumes [13, 14, 15, 16]. Iron and molybdenum play an important role in legume production due to their effects on nitrogen fixation and ultimately on the growth and development.

Present research is designed to study, the effects of iron (Fe) and molybdenum (Mo) on soybean nodulation and yield through foliar application of different concentrations.

MATERIAL AND METHODS

A field experiment was carried out to determine the effect of iron and molybdenum on nodulation and yield of the Soybean at Gundas Research Station of the Directorate of GAP Agricultural Research Institute Sanliurfa, Turkey during 2017 and 2018. Soybean cultivar used in this experiment was Gapsoy 16 (is 3.2 maturity group and flower colour is White) registered by GAP Agricultural Research Institute (GAPTAEM) in 2016. Gundas Research Station (latitude 36° 44' N, longitude 36° 48' ' E) is situated at 374 m above sea level [17]. The sandy clay soil with pH 7.8 and organic matter of 1.1% but rich in potassium downstream of all profiles.

The average of air temperature during the vegetation period of June-October period was 28.9 °C, the maximum average subsoil temperature was 32.1°C in 2017 and the average temperature was 29.2°C and 34.2 °C in 2018, respectively. Average relative humidity during the vegetation period was 43.6% and 43.3% in 2017 and 2018, respectively. There was no rainfall in the second crop soybean vegetation period in Sanliurfa province

.

TABLE 1
Some soil properties of the experiment area [18]

Soil depth (cm)	EC (ds/m)	Lime (%)	pH	Phosphorus (kg/da)	Potassium (kg/da)	Organic Matter (%)	Water Saturation (%)
0-30	0.71	18.6	7.9	5.43	273.6	1.13	57
30-60	0.69	17.9	7.8	5.45	270.2	1.12	59
60-90	0.67	17.3	7.8	5.51	269.2	1.13	60
Texture	Sand (%)	Clay (%)	Silt (%)				
	37	40	23				

TABLE 2
Weather data for the years 2017-2018 and average of long time Gundas Akcakale district [19]

Mounts	Years	Average Air Temp. (°C)	Average Max.Air Temp. (°C)	Average Min.Air Temp (°C)	Average Relative Humidity (%)	Precipitation (mm)
June	2017	29.8	38.4	16.7	29.6	1.8
	2018	29.6	42.0	18.9	39.2	0.2
	Avg.*	28.4	36.1	18.3	38.8	1.3
July	2017	33.1	42.8	21.4	33.6	-
	2018	34.4	43.0	20.9	32.7	-
	Avg.*	31.5	39.8	21.4	38.8	0.6
August	2017	33.0	43.1	22.1	35.5	1.2
	2018	32.1	43.0	21.2	40.9	1.1
	Avg.*	30.5	39.2	20.7	42.0	0.1
September	2017	26.5	40.4	18.7	45.1	0.2
	2018	29.7	39.3	14.7	39.6	1.3
	Avg.*	25.8	34.9	16.4	44.7	1.2
October	2017	22.2	33.0	12.7	56.6	13.6
	2018	20.6	30.4	12.9	54.9	3.4
	Avg.*	19.4	26.9	14.6	51.8	19.3
November	2017	12.7	24.3	6.8	60.1	18.2
	2018	13.7	20.1	5.6	65.1	19.6
	Avg.*	12.0	18.5	6.7	64.1	28.1
December	2017	5.5	20.0	0.5	82.1	16.4
	2018	10.2	14.6	1.3	77.6	26.9
	Avg.*	7.5	12.1	2.3	73.7	44.5

* Average of long years

Field trials were carried out with 3 replications according to Randomized Complete Block Design (RCBD). In both years, trials were carried out in the middle of June (14.06.2017 and 16.06.2018). Land was prepared with twice cultivation with common cultivator. Under the light of soil analysis report, fertilizers amounting 10 kg of N and 5 kg of P were applied as ammonium sulphate and triple super phosphate sources, respectively at the time of sowing. Each plot was consist of 4 rows with row to row distance of 70 cm and row length was 5m. The net plot size in this way was 2.8m × 5m = 14m2. After the sprinkling, the average 6 times of the irrigation was done to meet the delta of water treatments were comprised of two doses (0.5kg ha-1 and 1kg ha-1) of iron in the form of FeSO4.7H2O and two doses (0.05 and 0.10 kg ha-1) of molybdenum applied in the form of ammonium molybdate (NH4.6Mo2O24). 4H2O). These were used as liquid solution foliar spray. Treatments were comprised of Control (U1), 0.5 kg Fe ha -1 (U2), 1.0 kg Fe ha-1 (U3), 0.05 kg Mo ha-1 (U4), 0.10 kg Mo ha-1 (U5), 0.5 kg Fe ha-1 + kg 0.05 Moha-1 (U6), 0.5 Fe kg ha-1 + 0.10 Mo kg ha-1 (U7), 1.0 Fe kg ha-1+ 0.05 kg Mo ha-1 (U8) and 1.0 Fe kg ha-1 + 0.10 kg Mo ha-1 (U9). In two year trials, soybean harvest was performed manually in October. Ten plants randomly selected from each plot were used to record data six quantitative traits (the number of active nodules, biomass yield, grain yield, 1000-seed weight, total nitrogen and total protein). After harvesting grain yield was converted into t ha-1. Grain yield is calculated on a 13% moisture basis The data obtained were subjected to variance analysis by using JMP 5.1 package program at 5% of the significance tests. Statistically different groups were determined by OEF (LSD) test [20].

Measurement of Morphological and Physiological Parameters. Number of Active Nodules. In order to determine the number of active nodules, 10 plants were randomly selected from each plot and their roots were removed and the nodules were counted at R3 (Pod formation). For nodule counting, the plants were washed with tap water after carefully removing them from the soil and the roots were removed from the soil. The roots were then washed with purified water and dried with drying paper. Nodules were separated from the roots and then sliced into two parts by a sharp knife. Internal colour was observed to determine the active nodules. Nodules coloured pink-red (because of Leghaemoglobin protein) were classified as active while white into inactive.

Biomass Yield (kg ha^{-1}). Randomly 10 plants were selected from each plot at harvesting. At harvesting plant from each treatment plot was sun drying and the biomass/straw was weighted by electronic scale and then converted to kg per hector by the following formula [21].

$$\text{Biomass yield } (\text{kg ha}^{-1}) = \frac{\text{Biomass yield } (g) \times 10000}{\text{Area} \times 1000} \quad (1)$$

1000-Seed Weight (g). One hundred seeds were randomly collected from each plot with 4 replicates and average value was calculated. Then the average value multiplied by 10 to get weight of 1000 grains.

Seed yield (kg ha^{-1}). The whole plot was harvested and plants were thrashed to determine seed yield. The yield was then converted to hectare

$$\text{Seed yield } (kg\ ha^{-1}) = \frac{\text{Harvested seed of the plot } (kg)}{\text{Area of the plot } (m^2)} \times 10000 \quad (2)$$

Total Nitrogen (N). Fresh leaves from each application were washed with tap water, then with purified water, and dried on drying paper. It was then kept in oven at 80 °C for 48 hours. Similarly the harvested seeds were ground at 13% moisture and the total nitrogen amounts of Nitrogen in both the samples were determined by micro-Kjeldahl analysis method [22].

Total Protein (%). The nitrogen readings from the samples recorded severe multiplied by 6.25 constant and the total amount of protein was calculated in % [23].

RESULTS AND DISCUSSION

Number of Active Nodules. The number of active nodules per plant is affected by Fe and Mo. According to the results presented in Table 3. Fe and Mo both alone and in combined applications, it was observed that the formation of nodules in soybean was significant ($p < 0.01$). The maximum number of active nodules in was, 26 and 29 for the year 2017 and 2018, respectively where 1 kg Fe and 0.5 kg Mo (U_8) were applied. While the lowest number of nodules 2 and 3, were observed in control plot (U_1) in the experiments, years i.e. 2017 and 2018. The results showed that Fe and Mo elements had an important role in nodular nodulation and N_2 fixation [24]. He reported that 1.0 kg ha^{-1} applied caused 97% more nodule formation than control. Furthermore, [25] reported that Mo application significantly increased the nodule weight compared to the control and that the highest nodule weight was obtained from 0.8 kg ha^{-1} Mo application. The results were consistent with the findings of the investigators observed that similar results were obtained from [26] in other legumes.

TABLE 3
The mean values of number of nodules, biomass yields and seed yield and groups according to LSD test in soybean cultivar examined in the study

Treatments	Number of Active Nodules		Biomass Yield (kg ha $^{-1}$)		Grain Yield (kg ha^{-1})	
	2017**	2018**	2017**	2018**	2017**	2018**
Control (U_1)	2 e	3 g	1470.24 efg	1450.74 h	2276.85 g	2256.54 h
0.5 kg Fe ha $^{-1}$ (U_2)	11 d	12 f	2520.71 def	2518.96 g	2535.52 f	2506.71 g
1.0 kg Fe ha $^{-1}$ (U_3)	16 c	18 d	3551.88 cde	3569.13 ef	2515.59 f	2434.53 fg
0.05 kg Mo ha $^{-1}$ (U_4)	12 d	13 ef	3730.25 b	3799.51 de	3119.87 cde	3014.31 def
0.10 kg Mo ha $^{-1}$ (U_5)	15 c	14 e	3831.68 a	3846.93 d	3333.33 bc	3419.27 bc
0.5 kg Fe ha $^{-1}$ + 0.05 kg Mo ha $^{-1}$ (U_6)	18 bc	20 bc	4621.79 b	4820.54 b	3307.59 bc	3214.53 cde
0.5 kg Fe ha $^{-1}$ + 0.10 kg Mo ha $^{-1}$ (U_7)	19 bc	21 bc	4420.45 bc	4488.65 c	3697.86 a	3718.16 a
1.0 kg Fe ha $^{-1}$ + 0.05 kg Mo ha $^{-1}$ (U_8)	26 a	29 a	4850.69 a	4949.94 a	3356.62 b	3428.05 bc
1.0 kg Fe ha $^{-1}$ + 0.10 kg Mo ha $^{-1}$ (U_9)	21 b	22 b	4551.51 bc	4621.11 bc	3199.118 b-e	3137.36 def
LSD	1.80	3.89	8.85	9.06	22.07	23.80
Cv (%)	1.10	2.44	3.97	4.07	4.96	5.30

** (*p<0.01*)

TABLE 4
The mean values of thousand grain weight, total nitrogen groups and total protein and groups according to LSD test in soybean cultivar examined in the study

Treatments	1000-seed weight (g)		Total Nitrogen of Grains (kg ha^{-1})		Total Protein of Grains (%)	
	2017**	2018**	2017**	2018**	2017**	2018**
Control (U_1)	142.45 g	142.65 g	5.692 f	5.654 g	35.58 e	35.34 e
0.5 kg Fe ha $^{-1}$ (U_2)	144.16 fg	144.41 fg	5.883 e	5.987 e	36.77 e	37.42 de
1.0 kg Fe ha $^{-1}$ (U_3)	152.71 def	151.96 def	5.913 d	5.832 f	36.96 e	36.45 e
0.05 kg Mo ha $^{-1}$ (U_4)	152.61 def	151.61 def	6.091 cbd	5.926 de	38.07 bcde	37.04 de
0.10 kg Mo ha $^{-1}$ (U_5)	147.24 efg	145.74 fg	6.030 cde	6.209 bc	37.69 cde	38.81 bc
0.5 kg Fe ha $^{-1}$ + 0.05 kg Mo ha $^{-1}$ (U_6)	162.79 c	162.54 c	6.294 ab	6.328 ab	39.34ab	39.55 ab
0.5 kg Fe ha $^{-1}$ + 0.10 kg Mo ha $^{-1}$ (U_7)	155.88 cde	156.13 cde	6.310 ab	6.294 b	39.44 ab	39.34 b
1.0 kg Fe ha $^{-1}$ + 0.05 kg Mo ha $^{-1}$ (U_8)	183.68 a	184.93 a	6.472 a	6.36 ab	40.45 a	39.75 ab
1.0 kg Fe ha $^{-1}$ + 0.10 kg Mo ha $^{-1}$ (U_9)	173.25 b	173.51 b	6.302 ab	6.497 a	39.39 ab	40.61 a
LSD	8.85	9.06	0.27	0.23	1.56	1.15
Cv (%)	4.02	4.11	1.21	1.13	2.90	2.70

** (*p<0.01)*

Biomass Yield (kg ha^{-1}). Biomass yields are significantly (*p<0.01*) affected by the application of Fe and Mo, (Table 3). The highest biomass yield was obtained in both years (2017 and 2018) (4850.69 and 4949.94 kg ha $^{-1}$, respectively). Where 1.0 kg Fe ha $^{-1}$, 0.05 kg Mo ha $^{-1}$ (U_8) were applied followed by (4620.74 kg ha-1 and 4621.79 in 2017) U_7 where 0.5 kg Fe ha $^{-1}$, 0.05 kg Mo ha $^{-1}$ were applied group. While the lowest biomass 1470.24 and 1450.74 kg ha^{-1} in 2017 and 2018, respectively were recorded in the control (U_1). Similar effects of Fe and Mo were observed in the study of [27].

Grain Yield (kg ha^{-1}). Table 3 also shows significant (p<0.01) effect of both Fe and Mo on grain yield is statistically significant. The highest grain yield (3697.86 and 3718.16 kg ha-1 for the years 2017&2018, respectively) were obtained where 0.5 kg Fe ha-1 + 0.10 kg Mo ha-1 (U7).This may be due to the low level of both the micronutrients in test's area soil. Both these two micronutrients have symbiotic relationship nitrogen fixation. But increase in doses of these both have negative impact on grain yield, Table 3. Similar results were determined by [28, 29, 30, 26]. who that application of micro elements through foliar application contributed to yield by increasing the number of seeds per plant. However, contrary to findings, [31] reported increase in yield by 46% over control on applying 1.0 kg of Mo ha^{-1}.

1000-Seed Weight (g). The data showing the effects of iron and molybdenum applications on the weight of one thousand grains of soybean are shown in Table-4. The results for both years were found statistically significant (p<0.01). In 2017 and 2018, the highest 1000 grains weights (183.68 and 184.93 g, respectively) where 1.0 kg Fe ha-1 + 0.05 kg Mo ha-1 (U8) were applied, while the lowest values of 142.45 and 142.65 g, were recorded in the control application for both years.. When the results are evaluated, it is estimated that the test field is poor in iron and molybdenum concentrations. [32], reported that only the size of the seed is not related to the efficiency, but the total number of grains per plant are worth important. [33] also reported that grain weight and grain numbers of the plant are closely related to yield, but grain weight could be phenotypically an unbalanced character. This study showed that there is a positive relationship between seed weight and yield.

Total Nitrogen (kg ha^{-1}). Total nitrogen (kg ha^{-1}) of soybean seeds was determined through Kjeldahl method and results are shown in Table-4. Statistically significant ($p<0.01$) response of both micronutrients was observed in in terms of nitrogen content. Maximum nitrogen content (6.472 kg ha^{-1}) was in 2017 obtained where 1.0 kg Fe ha^{-1} + 0.05 kg Mo ha^{-1} (U_8) while in 2018, 6.497 kg ha^{-1} nitrogen was recorded where 1.0 kg Fe ha^{-1} + Mo 0.10 kg ha^{-1} (U_9) Fe and Mo symbiotic nitrogen fixation is known to support the formation of the essential component of the enzyme nitrogenase [34]. [35] Reported that the application of Mo increased the nitrogenase activity (82.44 H mol C_2H_4 / plant / hr) over the application of 1.5 kg Mo ha^{-1} application. Similar results were observed by [36].

Total Protein (%). Likewise, results were recorded in case of Total Protein (%) as were for Total N kg ha^{-1}. The Table-4 showed protein (%) ranges from 35.3 to 40.61 and the highest protein content was obtained from 1.0 kg Fe ha-^{1} + 0.05 kg Mo ha^{-1} (U_8) in 2017, while in 2018, 40.61% N was observed in U_9 (1.0 kg Fe ha $^{-1}$ + 0.10 kg Mo ha $^{-1}$. [37] Reported that foliar applied iron and molybdenum at a concentration of 4 ppm on 60 days after planting gave the highest nitrogenase activity and nitrogen fixation ultimately the highest protein content of seed.

CONCLUSIONS

Micronutrients play a vital role in the growth and yield of legumes crops, it is therefore proved from our investigations that foliar application of iron and molybdenum significantly improved yield and nodulation of soybean. It was observed that foliar application of iron and molybdenum have significant effects on grain yield and protein contents of seed. The dose 1.0 kg Fe ha^{-1} + 0.05 kg Mo ha-1 (U_8) have the best results. Further studies with microelement applications are needed to improve the yield and quality parameters and nodulation of legumes especially soybean.

ACKNOWLEDGEMENTS

The authors thank to Siirt University Scientific Research Projects Department and Sanlıurfa GAP Agricultural Research Institute for their financial support and to Fresenius Environmental Bulletin Journal for their technical supports.

REFERENCES

[1] Yetgin, S.G. (2008). Determination of yield and important plant characteristics of some soybean varieties and genotypes grown as a main crop in the Cukurova region. Cukurova University, Institute of Natural and Applied Science Field Crops Department, Master's Thesis Adana. 56p (in Turkish).

[2] Arıoglu, H.H. (2007). Oil seed Plants Growth and Breeding Lecture Books No:A-70, Cukurova University Faculty of Agriculture Offset Workshop, 204 s., Adana. (in Turkish)

[3] Anonymous, 2019. Turkey Oilseeds and Products Annual Report 2019

[4] Zhang, L., Wang, R. and J. D. Hesketh. (2001). Effects of Photoperiod on Growth and Development of Soybean Floral Bud in Different Maturity. Agronomy Journal. 93, 944-948.

[5] Arıoglu, H.H. (2000). Oil seed Plants Growth and Breeding. Cukurova University, Faculty of Agriculture, Department of Field Crops Lecture Notes. Cukurova University, Faculty of Agriculture Offset Workshop II. Edition S:40. (in Turkish)

[6] Sogut, T. (2005). The Effect of Inoculation and Nitrogen Application on Yield and Yield Components of Soybean Cultivars. Akdeniz University Mediterranean Agricultural Science. 18(2), 213-218. (in Turkish)

[7] Katyal, J.C and Randhawa, N.S. (1983). Micronutrient. F.A.O. Fertilizer and Plant Nutrition. Bulletin No. 7. United Nation.

[8] Kerkeb, L. and Connolly, E. (2006). Iron transport and metabolism in plants. J. Gent. Eng. 27, 119-140.

[9] Kacar, B. and Katkat, V. (2009). Plant Nutrition. Nobel Publications, Ankara, 659 p. (in Turkish)

[10] Kriem, H.M., Abdel-Mottaleb, M.A., El-Fouly, M.M, Nofal, O.A. (1991). Response of Soybean to Micronutrient Foliar Fertilization of Different Formulations under Two Soil Conditions. I. Yield Responses Egypt. J. Physiol. Sci. 15(1,2), 131-140.

[11] Durrant, M.C. (2001). Controlled Protonation of Iron-Molybdenum Cofactor by Nitrogenase: a Structural and Theoretical analysis. Department of Biological Chemistry, John Innes Centre, Norwich Research Park, Colney, Norwich NR4 7UH, U. K.

[12] Ferreira, A.C., Araujo, G.A., Cardoso, A.A., Fontes, P.C.R., Vieira, C., Araujo, G.A. (2002). Influence of Seed Molybdenum Contents and its Foliar Application on the Mineral Composition of Bean Leaves and Seeds. Revista Ceres. 49, 284, 443-452; 18 ref

[13] Akkuş, E. (2009) The effect of different doses molybdenum applied to nitrogen content of chickpea (*Cicer arietinum* L.) Canakkale Onsekiz Mart University Graduate School of Science and Engineering Chair for Soil Thesis of Master of Science Canakkale, 48p. (in Turkish)

[14] Bhuiyan, M.M.H., Rahman, M.M., Afroze, F., Sutradhar, G.N.C and Bhutyan, M.S.I. (2008). Effect of Phosphorus, Molybdenum and Rhizobium Inoculation on Growth and Nodulation on Mung bean. Journal of Soil and Nature. 2(2), 25-30.

[15] Dogan, K. (2007). Effects of Bacteria Inoculation and Iron Application on Nodulation, Biomass and Grain Yield in Peanut. Cukurova University, Institute of Natural and Applied Science Field Crops Department, PhD Thesis, Adana, 192p (in Turkish)

[16] Verma L.P., Ram P.C and Maurya B.R. (1988). Response of Chickpea to Phosphorus and Molybdenum in Alluvium of Eastern Uttar Pradesh. Inter chickpea Newsletter. 18, 31-33

[17] Erbil, E. (2013). Determination of Yield and Quality Characters of Winter and Spring Sugar Beet Varieties for Sanliurfa Region. Harran University, Graduate School of Natural and Applied Sciences, Master Thesis, Sanliurfa, 72p. (in Turkish)

[18] Anonymous, 2018a. GAP Agricultural Research Institute Annual -2012, Publication No:165, Sanliurfa, 41-42p. (in Turkish)

[19] Anonymous, 2018b. Climatic Data. Sanliurfa Meteorology Regional Directorate Datas, Sanliurfa. (in Turkish)

[20] Der, G. and Everitt, B.S. (2002). A Handbook of Statistical Analyses Using SAS. Second Edition. CRC Press LLC, 2000 N.W. Corporate Blvd., Boca Raton, Florida 3431. USA.

[21] Kolay, B. (2007). Effects of Different Soil Tillage Methods on Second Crop Soybean Yield and Some Soil Properties at Diyarbakır Conditions. Harran University, Graduate School of Natural and Applied Sciences, Master Thesis, Sanlıurfa, 66p. (in Turkish)

[22] Mulvaney R.L and Brown H.M. (1996). A soil organic nitrogen fraction that reduce the need for nitrogen fertilization. Soil Sci. Soc. Am. J. 65, 1164-1172.

[23] Akyıldız, R. (1984). Feed Information Laboratory Guide, 213 Ankara University, Faculty of Agriculture Publications: 895, Ankara. (in Turkish

[24] Zaman, A.K.M.M., Alam, M.S., Roy, B. and Beg, A.H. (1996). Effect of B and Mo Application on Mungbean. Bangladesh J. Agril. Res. 21(1), 118-124.

[25] Aghatise, V.O. and Tayo, T.O. (1994). Response of Soybean to Molybdenum Application in Nigeria. Indian J. Agric. Sci. 64 (4), 597-603.

[26] Elballa, M.M.A., El-amin, A.H.B., Elamin, E.A., Elsheikh, E.A.E. (2004). Interactive Effects of Cultivars, Foliar Application of Micronutrients and Rhizobium Inoculation on Snap Bean (*Phaseolus vulgaris* L.) Performance. U of K J Agric Sci. 12(3). Available online at: http://staffcv.uofk.edu/agriculture/shayatti/downloads/43.pdf

[27] Durrant, M.C. (2001). Controlled Protonation of Iron-Molybdenum Cofactor by Nitrogenase: a Structural and Theoretical Analysis. Department of Biological Chemistry, John Innes Centre, Norwich Research Park, Colney, Norwich NR4 7UH, U. K.

[28] Bertie, M., Vrataric M. and Vukadinovic, M. 1991. Three-year Investigation of Foliar Application of Micronutrients and Side Dressing Treatment with Nitrogen in Soybean Crop Sci. 21, 9-14

[29] Rahman, M.M., Bhuiyan, M.M.H., Sutradhar, G.N.C., Rahman, M.M., Paul, A.K. (2008). Effect of Phosphorus, Molybdenum and Rhizobium Inoculation on Yield and Yield Attributes of Mungbean. Int. J. Sustain. Crop Prod. 3, 26-33.

[30] Heidarian, A. R., Kord, H., Mostafavi, K., Lak, A.P., Mashhadi, F.A. (2011). Investigating Fe and Zn Foliar Application on Yield and its Components of Soybean (*Glycine max* (L) Merr.) at Different Growth Stages. J. Agric. Biotech. Sustain. Dev. 3, 189-197.

[31] Kalia, B.D. and Sharma, C.M. (1989). Effect of Micronutrients on Yield of Soybean. Ind. J. Agron. 33(2), 199-200

[32] Morrison, M.J., Voldeng, H.D., and Cober, E.R. (2000). Agronomic Changes from 58 years of Genetic Improvement of Short-Season Soybean Cultivars in Canada. Agronomy Journal. 92(4), 780-784.

[33] Egli, D.B., Leggett, J.E. and Wood, J.M. (1978) Influence of Soybean Seed Size and Position on the Rate and Duration of Filling. Agronomy Journal. 70(1),127-130.

[34] Nasar, J and Zahir, S. (2017). Effect of Iron and Molybdenum on Yield and Nodulation of Lentil. ARPN Journal of Agricultural and Biological Science. 12, 332-339.

[35] Solaiman, A.R.M. (1999). Effects of *Bradyrhizobium japonicum* Inoculation and Molybdenum on Soybean. Bangladesh J. Bot. 28(2), 181-183.

[36] Civelek, T. (2006). The effects of leaf nutrient with iron applications on yield and yield components with important quality characters in some soybean [*Glycine max*. (L.) Merrill] cultivars. Ondokuz Mayıs University. Graduate School of Natural and Applied Sciences, Master Thesis, Samsun, 66s. (in Turkish)
[37] Chhonkar, A.K. and Chandel, A.S. (1991). Effect of Iron and Molybdenum on Nitrogenase Activity and Nitrogen Fixation in Soybean Grown in Alluvial Soil of North India. Indian Jour. Agron. 36 (Supp.), 124- 128. 8s.

Received: **25.11.2019**
Accepted: **03.02.2020**

CORRESPONDING AUTHOR

Ali Beyhan Ucak
Siirt University, Faculty of Agriculture,
Department of Biosystems Engineering
Siirt – Turkey

e-mail: abucak@siirt.edu.tr

© by PSP Volume 29 – No. 04A/2020 pages 3040-3047 Fresenius Environmental Bulletin

SEDIMENTARY FACIES MODEL IN THE SOUTHWESTERN PART OF THE QAIDAM BASIN, CHINA

Bing Hao[1,*], Xinyuan Ma[2], Qingfeng Zhang[2], Jianhua Zhong[1], Ningliang Sun[1]

[1]School of Geoscience, China University of Petroleum (East China), Qingdao 266580, China
[2]PetroChina Coalbed Methane Company Limited, Xinzhou 036600, China

ABSTRACT

The sedimentary characteristics of the southwestern part of the Qaidam Basin are complex. So far, the sedimentary facies types and sedimentary models in the region are still controversial. In this paper, we use the rich core data, logging data, mineral test data and regional sedimentary tectonic background in the region to study the sedimentary model of the area. The results show that the lower segment of the Xiaganchaigou Formation (E_3^1) is mainly the western source, followed by the northwest and southwest sources; the Shangganchaigou Formation (N_1) is mainly the western source, followed by the northwest and southwest sources; The Xiayoushashan Formation (N_2^1) is mainly the western source, followed by the northwest and southwest sources. The Xiayoushashan Formation (N_2^1) is formed in the underwater environment under weak reduction-weak oxidation conditions; the Shangganchaigou Formation (N_1) is formed in the weak hydrodynamic environment under weak reduction conditions; and the Lower Ganchaigou Formation (E_3^1) is formed in a strong hydrodynamic environment under oxidizing conditions. Finally, the sedimentary facies model of YJ No. 2 Oilfield was established. The YJ No. 2 oilfield developed a braided river and lake sedimentary system. The E_3^1 reservoir is mainly a sedimentary system of the delta plain distributary channel, the E_3^2 develops a lacustrine sedimentary system, the N_1 reservoir develops a braided river sedimentary system, and the N_2^1 reservoir mainly develops a braided river sedimentary system.

KEYWORDS:
Qaidam Basin, core, logging data, mineral testing, sedimentary facies model

INTRODUCTION

China is rich in tight oil resources [1-8]. Tight oil is one of the most exploitable natural resources in China [9-11]. China's Qaidam Basin is also rich in tight oil resources, but the current level of exploration is relatively low [12-13]. The sedimentary and tectonic features of the southwestern part of the Qaidam Basin are complex. The trap in the area is an anticline that is complicated by faults. The small fault block makes the oil layer have multiple, scattered and miscellaneous distribution characteristics. The oil field is a typical high-abundance, same-deposited complex fault block oilfield. Within the structural range, the secondary fault is extremely developed, and the oil-water relationship is complex, so its development is also difficult. So far, the sedimentary facies types and sedimentary models in the region are highly controversial. At the same time, due to geological conditions and factors such as injection and production systems and mining methods during mining, the distribution of underground oil and water has become more complicated [14-16]. Because the research on sedimentary models in the region is very weak, it restricts the fine development of oil fields. Therefore, in this paper, we use the rich core data, well logging data and mineral test data of the region to conduct a detailed study of the sedimentary model of the region. This study can provide a reference for the detailed evaluation of complex reservoirs in this region.

GEOLOGICAL BACKGROUND AND METHODS

Geological Background. The YJ No.2 area in the southwestern part of the Qaidam Basin is a complex fault anticline structure oilfield. After years of exploration, the oil field consists of three reservoirs N_2^1, N_1 and E_3^1. The oil geological reserves are 2 138.04×10^4 t and the oil-bearing area is 2.25 km^2 (Figure 1).

Within the oilfield, it is a saline-alkaline marshland with an elevation of 2 855 m above sea level and a flat ground with a height difference of less than 10 m. The climate in this area is cold and dry, with an average annual temperature of 1.4 °C (the highest temperature is 28.6 °C, the lowest temperature is -29.5 °C), and the depth of the frozen soil is about 2 m. The annual average rainfall is 47.1 mm, and the annual evaporation is as high as 2 795.3 mm. The maximum wind speed is 26 m/s, the annual average wind is 5.1, the winds above 8 can reach 108 days, and the wind season is 3-4 months and September-October. The frost period is long,

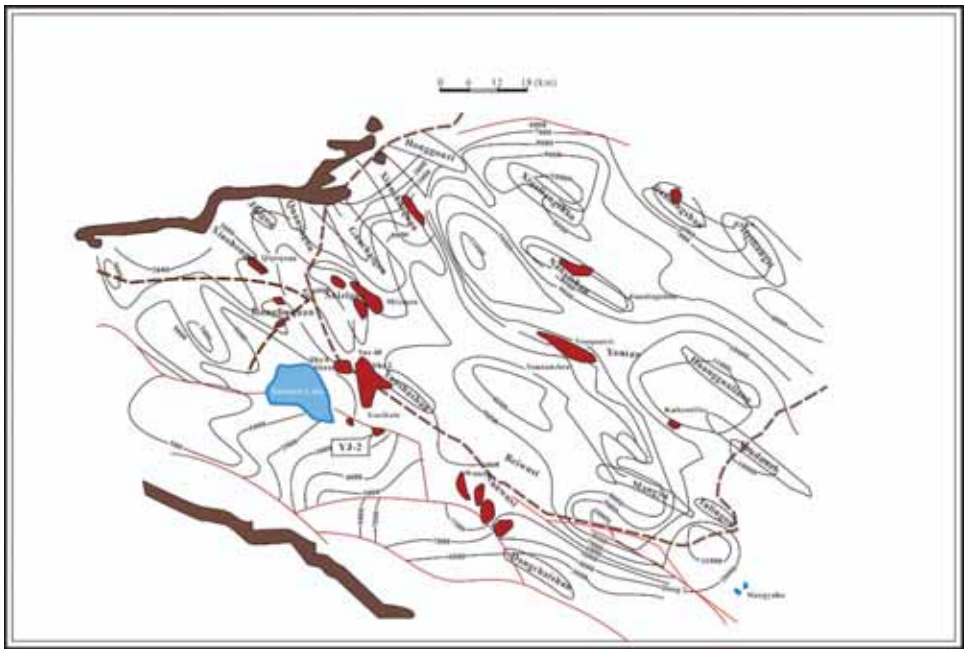

FIGURE 1
Regional location of YJ No. 2 Oilfield in Qaidam Basin

TABLE 1
Strata unit of YJ No. 2 Oilfield.

Layer System	Series	Formation	Segment	Code	Evolutionary stage		Structural cycle
Quaternary	Pleistocene	Qigequan	/	Q_{1+2}	Fold rise period	Delta frontal subfacies and river facies.	Late Himalayan cycle
		Shizigou	/	N_2^3			
Neogene	Pliocene	Shangyoushashan	/	N_2^2	Large depression period	Lake sediment deposition, delta front subfacies deposition.	
		Xiayoushashan	/	N_2^1			
	Miocene	Shangganchaigou	/	N_1			
	Oligocene	Xiaganchaigou	Upper	E_3^2			
			Lower	E_3^1	Fault depression transitional stage	The river floods the plain facies and the delta plain subfacies.	Early Himalayan cycle
Paleogene	Ancient Eocene	Lulehe	/	E_{1+2}			

and the temperature difference between day and night in winter and summer is large.

According to the drilling, logging, seismic data and previous research results, the results of stratigraphic division in the study area are shown in Table 1. The target layer of this study is Xiayoushashan Formation (N_2^1), Shangganchaigou Formation (N_1) and Xiaganchaigou Formation (E_3^1).

Methodology. Accurate stratigraphic contrast and division is the foundation of all research work [17-18]. The reasonable comparison and division of strata is an important procedure in the reservoir description from single well evaluation to multi-well evaluation. It is also the basis for describing the reservoir morphology and the spatial distribution characteristics of its parameters [19]. The stratigraphic correlation should be guided by seismic stratigraphy, logging geology, and reservoir geology theory [20]. According to the "regional standard layer", select "stable mark layer" to control, and combined with "auxiliary mark layer" to carry out "equal time body" repeated comparison, and then we can achieve a unified layer within a certain range.

In this paper, based on lithology and biofossils, we use the stable marker layer (standard layer) as the control, and use the logging curve as a means to carry out the fine contrast and division of formation of 355 wells in the work area according to the shape of the logging curve reflected by the sedimentary cycle. By adopting the method of "sedimentary cycle comparison, hierarchical control", the sedimentary cycles of each stage are corresponding to each other. Thereby effectively controlling the sandstone group and the small layer and improving the correctness of the comparison.

RESULTS AND DISCUSSION

The sedimentary environment and sedimentary facies determine the rock type, rock structure and vertical and horizontal combination of the reservoir. It is also an important factor in causing reservoir heterogeneity and controlling the distribution of remaining oil [21]. Through sedimentary microfacies analysis, the heterogeneity of the reservoir can be explained from the deposition mechanism, and the distribution of remaining oil can be predicted. To this end, based on the comparison of the YJ No. 2 stratigraphic division, we carried out a detailed study of the sedimentary microfacies of the key small layers.

Regional Sedimentary Background. The eastern high point structure of YJ 2 is a tertiary structure in the western depression of the Qaidam Basin in Qinghai Province. The development and evolution of this area is controlled by tectonic activities. Since the Tertiary, the Qaidam Basin can be divided into three evolutionary stages: (1) Paleogene and Eocene (E_{1+2})-Eocene (E_3^1). The topography of the Paleogene and Eocene (E_{1+2}) is relatively flat, and the YJ 2 area is mainly developed by river floodplain. In the early Oligocene (E_3^1), the decontamination occurred, and the delta plain sub-facies developed in the east high point of YJ 2; (2) In the late Oligocene (E_3^2)-Middle Pliocene (N_2^2) large-scale depression period, the tectonic movement was strong, and the delta front facies deposition was developed in the east high point of YJ 2. In the late Oligocene to the early Miocene, the lake water completely invaded the area. At this time, the lakeside facies sendiments developed. The center of the lake basin is in the east of the east high point of YJ No. 2, and the lake water gradually withdraws from the area in the late Miocene, and the delta front subfacies deposits. (3) In the late Pliocene (N_2^3)-Quaternary (Q), delta front subfacies and river facies develop.

Source Direction. Heavy minerals are effective means of discriminating the direction and partition of the source [22]. The sedimentary age is relatively new and is less affected by changes in temperature and depth. Accurate and reliable results can be obtained using the heavy mineral method. The heavy mineral samples from the core wells were analyzed for analysis around the study block. Statistics show that heavy minerals with relatively high content are zircon, tourmaline, garnet, magnetite, epidote, hornblende, vermiculite and ilmenite. The source of the block is inferred by stabilizing the distribution of mineral (zircon) and unstable minerals (hornblende) (Figure 2 - Figure 3).

It can be seen from the statistics of heavy minerals that the plane distribution of heavy minerals has a certain regularity, and the content of stable minerals increases from low to high as the transport distance increases (Figure 4). This indicates that the lower segment of the Xiaganchaigou Formation (E_3^1) is mainly the western source, followed by the northwest and southwest sources.

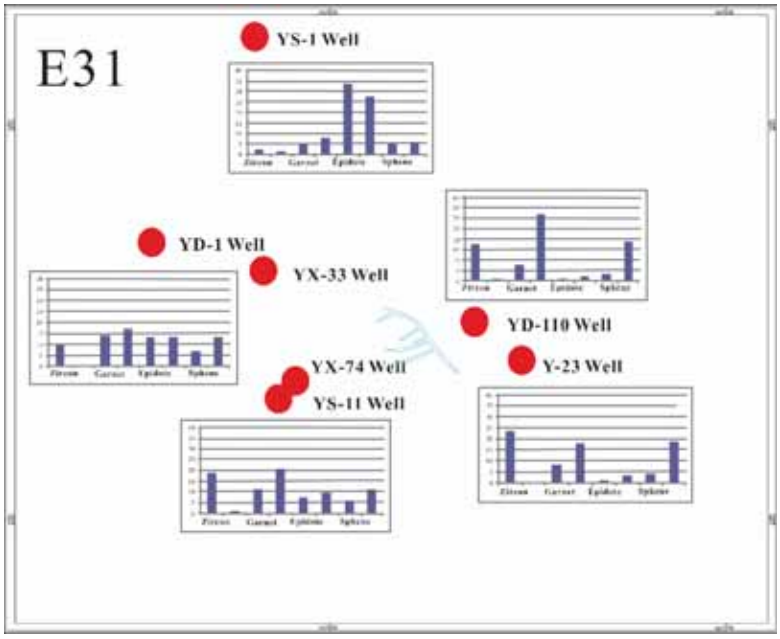

FIGURE 2
Distribution of heavy mineral content in the surrounding wells of YJ No. 2 oil field (E_3^1)

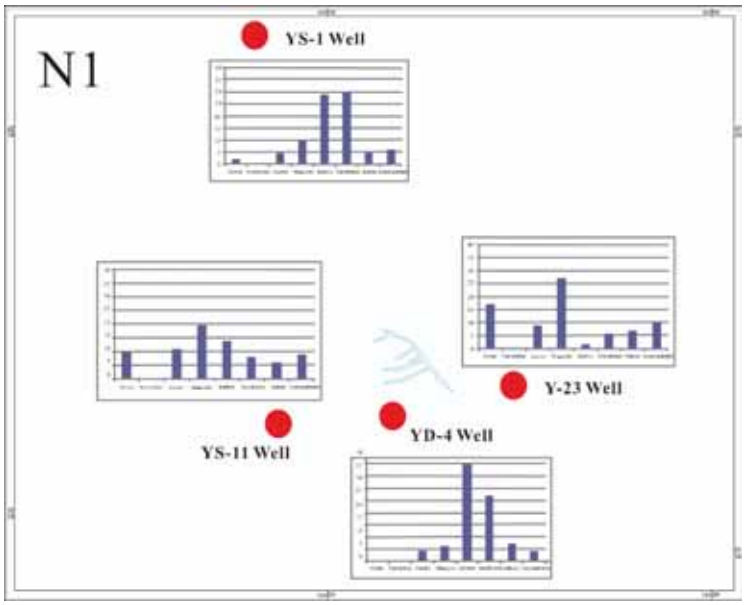

FIGURE 3
Distribution of heavy mineral content in the surrounding wells of YJ No. 2 oil field (N_1)

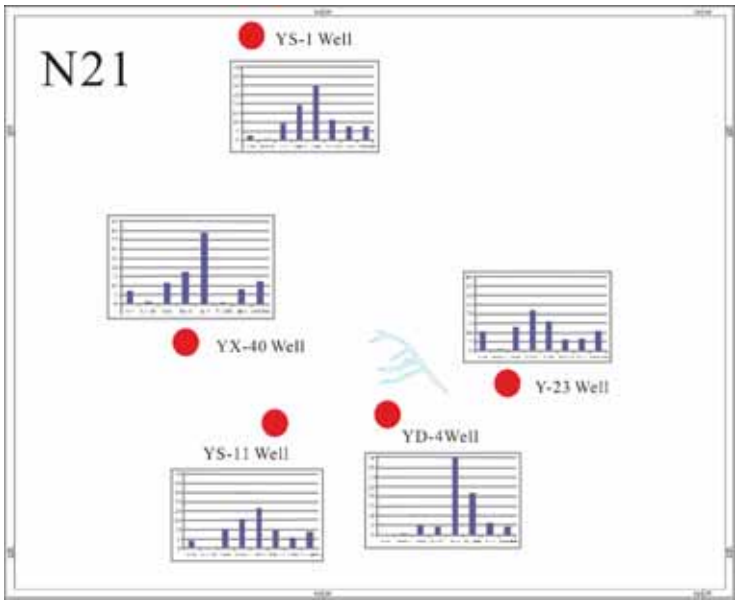

FIGURE 4
Distribution of heavy mineral content in the surrounding wells of YJ No. 2 oil field (N_2^1)

The average content of stable mineral zircons in the Yueshen 11 and Yuedi 4 wells in the western part of the Upper Ganchaigou Formation (N_1) was 9.8% and 0.3%, respectively, while that of the Yue 23 well in the east was 17.3%. The average content of unstable mineral hornblende in the Yueshen 11 and Yuedi 4 wells in the west was 7.8% and 26.8%, respectively, while that in the eastern Yue 23 well was 5.5%. This indicates that the Shangganchaigou Formation (N_1) is mainly a western source, followed by a northwest and southwest sources.

The average content of stable mineral zircon in the wells of Yueshen 11 and Yuedi 4 in the Xiayoushashan Formation (N_2^1) was 4% and 0.2%, respectively, while that of the Yue 23 well in the east was 10.8%. The average content of unstable mineral hornblende in the Yueshen 11 and Yuedi 4 wells in the west was 10% and 21.6%, respectively, while that in the eastern Yue 23 well was 5.8%. In summary, the Xiayoushashan Formation (N_2^1) is mainly western source, followed by northwest and southwest provenance.

Sedimentary Environment and Sedimentary facies markers. Sedimentary facies mark mainly include paleontological signs, core marks, electrical signs, particle size analysis and other signs. By establishing the sedimentary facies marks of typical wells and typical intervals, the foundation for sedimentary model research is laid.

(1) Paleontology Sign. The sedimentary environment is a combination of natural and geographical conditions, including water depth, water medium conditions, paleoclimate environment and other factors. All living things always adapt to the surrounding environment to survive, and certain environments control certain biological species and combinations. Therefore, different biological combinations reflect different ecological environments accordingly.

The color of sediments in the Xiayoushashan Formation (N_2^1) is dominated by red and grey, and Xiaomeixing fossils are visible, which is reflected as an underwater deposition under weak reducing-weak oxidative deposition conditions. The upper part of the Shangganchaigou Formation (N_1) is dominated by brown-red mudstone, with fine sandstone and pebbly sandstone. The local layer contains the caudate fossils, and the lower part is dominated by gray, dark gray mudstone and gray mudstone. It is reflected as an underwater deposition under a weakly reduced depositional environment. The upper part of the Xiaganchaigou Formation (E_3^2) is dominated by gray and dark gray mudstones, and visible fossils such as the multi-lateral true star mediator. The lower part of the Xiaganchaigou Formation (E_3^1) is mainly composed of brown-red, brown mudstone and sandy mudstone in the oxidizing environment. It is reflected as a water deposit under oxidative deposition conditions.

(2) Lithological Characteristics. According to the core data and the logging statistics, the mudstones in the N_1-N_2^1 and E_3^1 formations account for 40-45%, the siltstones account for 25-30%, and the fine sandstones and conglomerates account for 10-20%. The lithology of the E31 formation is thicker than that of the N1-N21 formation. In particular, the content of conglomerate in the lower stratum of E31 is relatively high. According to the observation of the core of Yue II264 well, the sandstone contains large conglomerate, which is poorly ground, reflecting the strong hydrodynamic rapid accumulation characteristics.

(3) Sedimentary Structure. Core observations show that the sedimentary structure of the target layer is rich. The E_3^1 stratum of the YJ No. 2 east high point oilfield has structures such as collapse and disturbance, and has block-like bedding and interlaced bedding (Figure 5). Oblique layering and small interlaced bedding are observed in fine sandstone, unequal grain sandstone and medium-fine sandstone. It reflects a strong hydrodynamic environment of river facies deposition.

(a) Massive bedding in 1806.1 m, Well YJ-264 (b) Cross bedding in 1771.2 m, Well YJ-12

FIGURE 5
Sedimentary structure and bedding of E_3^1 stratum in YJ No. 2 Oilfield

(a) Horizontal bedding in 1214-1218.5 m, Well YJ-12 (b) Cave structure with solution pores in 1368.4-1374.8 m, Well YJ-71

FIGURE 6
Sedimentary structure and bedding of N_1 stratum in YJ No. 2 Oilfield

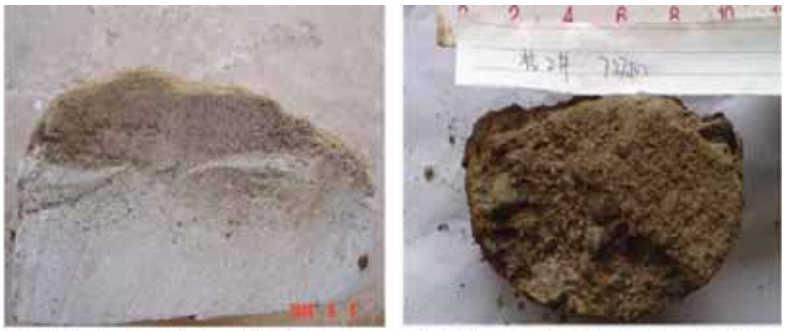

(a) Massive bedding in 800-804 m, Well YJ-155 (b) Massive bedding 727.5 m, Well YJ-155

FIGURE 7
Sedimentary structure and bedding of N_2^1 stratum in YJ No. 2 Oilfield

The N_1 formation has structures such as dissolved pores, caves, and wormholes (Figure 6). The horizontal bedding is relatively developed in silty mudstone, argillaceous siltstone and siltstone. Horizontal bedding often occurs in the form of gradient bedding and rhythm bedding, reflecting the relatively quiet weak hydrodynamic depositional environment of the water.

The N_2^1 Formation has horizontal bedding, staggered bedding and massive bedding (Figure 7). The hydrodynamic depositional environment is between the E_3^1 and the lower N_1.

(4) Logging Facies Characteristics. The natural potential and resistivity curve patterns of this area can be divided into five types of curve combinations: (1) positive trapezoid and box shape, which are combination of positive cycle and composite cycle. It corresponds to the micro-facies sedimentary characteristics of the distributary channel and the delta front of the delta plain; (2) inverted trapezoidal or thick finger shape, which is a combination of reverse cycle and composite cycle. It deposits on the sedimentary microfacies corresponding to the estuary dam of the delta front; (3) thin finger and thorn shape, which is a composite spiral and a non-uniform thorn-like interbed. It corresponds to the matte sand microfacies of the delta front and the beach dam microfacies of the shore shallow lake; (4) sawtooth morphology, which corresponds to the natural dyke microfacies of the study area; (5) straight or small zigzag, which is a logging response characteristic of muddy deposits. It corresponds to the diversion plain microfacies of the delta plain, the sub-facies of the delta front, and the micro-facies between the sub-streams and the shallow lakes.

Sedimentary model. Based on the above-mentioned regional sedimentary background, sedimentary environment analysis, source analysis, combined with lithofacies, grain size characteristics and sedimentary structural features, we established the sedimentary facies model of YJ No. 2 oilfield (Figure 8).

Through the comparative study of sedimentary characteristics, the YJ-2 east high point oilfield developed a braided river and lake sedimentary system. Among them, the E_3^1 reservoir is mainly the sedimentary system of the delta plain distributary channel, the E_3^2 develops the lacustrine sedimentary system, the N_1 reservoir develops the braided river sedimentary system, and the N_2^1 reservoir mainly develops the braided river sedimentary system.

Combined with the lithological characteristics and sedimentary structure of each sedimentary system, the N_2^1, N_1, E_3^1 and E_3^2 strata of the YJ-2 east high point oilfield can be divided into three sub-facies: the delta plain, the delta front and the lake.

(1) The lakeshore subfacies are mainly developed in E_3^2, mainly for underwater sedimentation. The sediments are darker in color, and the lithology is mainly mudstone, argillaceous siltstone and siltstone. The horizontal bedding and wavy bedding are developed.

(2) The delta front subfacies are the underwater part of the delta and are the combined zones of rivers, lakes and waters. The delta front subfacies of the YJ 2 area are mainly distributed in the upper part of N_1 and the N_2^1 stratum, with the main features of underwater sedimentation and interbedded water. The color of the sediment is red and gray, and the development of the sand layer is concentrated. The horizontal bedding, wavy bedding and cross-layering are developed.

(3) The delta plain subfacies are the onshore parts of the delta deposits. In the YJ 2 area, it is mainly distributed in the middle and lower strata of E_3^1. The stratum is mainly composed of water deposits and a small amount of underwater sediments. The color of the sediment is mainly brown red or dark red. The sandstone has coarser grain size and less sand body. It has blocky bedding and cross-layering.

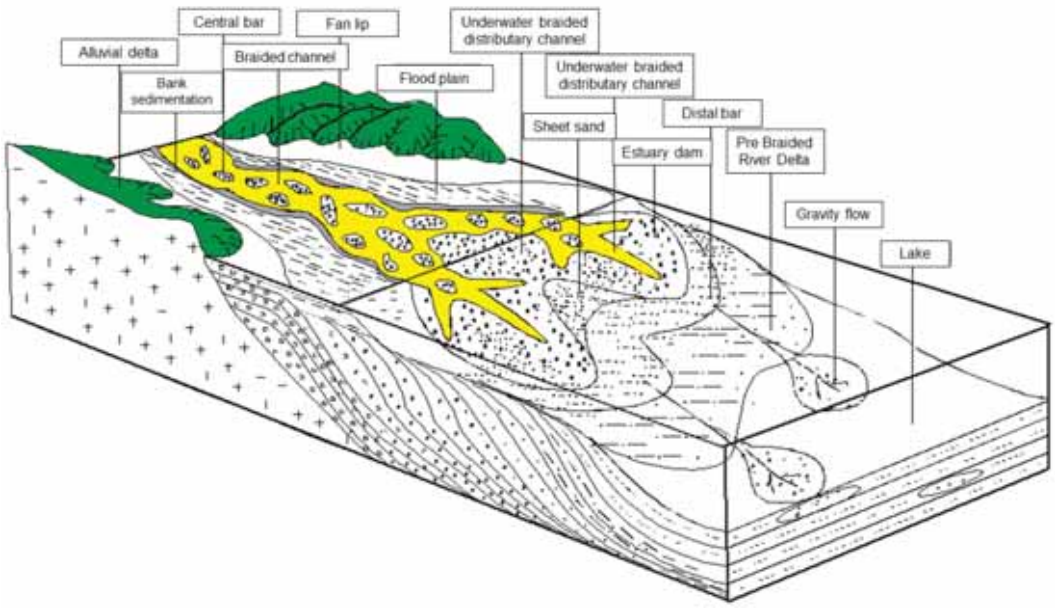

FIGURE 8
Sedimentary model of YJ No. 2 Oilfield

CONCLUSIONS

(1) In this paper, we use the rich core data, logging data, mineral test data and regional sedimentary tectonic background in the region to study the sedimentary model of the area.

(2) The lower segment of the Xiaganchaigou Formation (E_3^1) is mainly the western source, followed by the northwest and southwest sources; the Shangganchaigou Formation (N_1) is mainly the western source, followed by the northwest and southwest sources; The Xiayoushashan Formation (N_2^1) is mainly the western source, followed by the northwest and southwest sources.

(3) The Xiayoushashan Formation (N_2^1) is formed in the underwater environment under weak reduction-weak oxidation conditions; the Shangganchaigou Formation (N_1) is formed in the weak hydrodynamic environment under weak reduction conditions; and the Lower Ganchaigou Formation (E_3^1) is formed in a strong hydrodynamic environment under oxidizing conditions.

(4) The sedimentary facies model of YJ No. 2 Oilfield was established. The YJ No. 2 oilfield developed a braided river and lake sedimentary system. The E_3^1 reservoir is mainly a sedimentary system of the delta plain distributary channel, the E_3^2 develops a lacustrine sedimentary system, the N_1 reservoir develops a braided river sedimentary system, and the N_2^1 reservoir mainly develops a braided river sedimentary system.

ACKNOWLEDGEMENTS

This work was financially supported by the National Natural Science Fundation of China (No. 41172093).

REFERENCES

[1] Li, X. (2012) Genesis of formation water and oil migration in Dongying depression. Petroleum Geology and Recovery Efficiency. 19(3), 18-21.

[2] Allan, J., Creaney, S. (1991) Oil families of the Western Canada Basin. Bulletin of Canadian Petroleum Geology. 39, 107−122.

[3] Peters, K. (1986) Guidelines for evaluating petroleum pyrolysis. AAPG Bulletin. 70, 318-329.

[4] Chang, X., Wang, Y., Shi, B., Xu, Y. (2019) Charging of Carboniferous volcanic reservoirs in the eastern Chepaizi uplift, Junggar Basin (northwestern China) constrained by oil geochemistry and fluid inclusion. AAPG Bulletin. 103, 1-14.

[5] Hakimi, M., Abdullah, W., Shalaby, M. (2010) Source rock characterization and oil generating potential of the Jurassic Madbi formation, onshore East Shabowah oilfields, Republic of Yemen. Organic Geochemistry. 41, 513-521.

[6] Klemme, H., Ulmishek, G. (1991) Effective petroleum source rocks of the world: Stratigraphic distribution and controlling depositional factors. AAPG Bulletin. 75(12), 1809-1851.
[7] Xu, D., Zhou, J., Wang, H. (2010) Chemical characteristics of formation water significant to oil reservoir in Dongying Formation, Nanpu Sag, Bohai Bay Basin. Petroleum Geology and Experiment. 32(3), 285-289.
[8] Lasaga, A., Luttge, A. (2001) Variation of crystal dissolution rate based on a dissolution step wave model. Science. 291(5512), 2400-2404.
[9] Antonio, C., Andreas, L. (2004) Mineralogical approaches to fundamental crystal dissolution kinetics. American Mineralogist. 89(4), 527-540.
[10] Davisson, M., Criss, R. (1996) Na - Ca - Cl relations in Basinal fluids, Geochimica et CosmochimicaActa. 60(15), 2743-2752.
[11] Fisher, J., Boles, J. (1990) Water-rock interaction in Tertiary sandstones, San Joaquin Basin, California, USA: Diagenetic controls on water composition. Chemical Geology. 82, 83-101.
[12] Peters, K., Walters, C., Moldowan, J. (2005) The biomarker guide (Volume 2): Biomarkers and isotopes in petroleum exploration and earth history. Cambridge: Cambridge University Press.
[13] Horita, J., Zimmermann, H., Holland, H. (2002) Chemical evolution of seawater during the pHanerozoic: Implication from the record of marine evaporites. Geochimica et Cosmochimica Acta. 66(21), 3733-3756.
[14] Zhu, R., Lou, Z., Yun, L. (2008) Occurrence and distribution of formation water in the Ordovician reservoirs of the Tahe Oilfield. Chinese Journal of Geology. 43(2), 228-237.
[15] Liu, Y., Hu, W., Cao, J., Wang, X., Tang, Q. (2018) Diagenetic constraints on the heterogeneity of tight sandstone reservoirs: A case study on the Upper Triassic Xujiahe Formation in the Sichuan Basin, southwest China. Marine Petroleum Geology. 92, 650-669.
[16] Yin, S., Lv, D., Ding, W. (2018) New method for assessing microfracture stress sensitivity in tight sandstone reservoirs based on acoustic experiments. International Journal of Geomechanics. 18(4), 1-16.
[17] Kharaka, Y., Law, L., Carothers, W. (1986) Role of organic species dissvolved in formation water from sedimentary basins in mineral diagenesis. In: Gautier D L.Role of Organic Matter in Sediment Diagenesis. Soc. Econ. Paleontol. Mineral. Spec. Publ. 38, 111-122.
[18] Connolly, C., Walter, L., Baadsgaard, H., Longstaffe, F. (1990) Origin and evolution of formation waters, Alberta Basin, Western Canada Sedimentary Basin. Applied Geochemistry. 5, 375-413.
[19] Yin, S., Han, C., Wu, Z., Li, Q. (2019) Developmental characteristics, influencing factors and prediction of fractures for a tight gas sandstone in a gentle structural area of the Ordos Basin, China. Journal of Natural Gas Science and Engineering. 72, 1-14.
[20] Li, Y., Chang, X., Yin, W., Sun, T., Song, T. (2017) Quantitative impact of diagenesis on reservoir quality of the Triassic Chang 6 tight oil sandstones, Zhenjing area, Ordos Basin, China. Marine Petroleum Geology. 86, 1014-1028.
[21] Knauth, L., Beeunas, M. (1986) Isotope geochemistry of fluid inclusions in Permian halite with implications for the isotopic history of ocean water and origin of saline formation waters. Geochimicaet Cosmochimica Acta. 50, 419-433.
[22] Peters, K., Moldowan, J. (1993) Guide for the application of biological markets. New Jersey: Prentice-Hall.

Received: **25.11.2019**
Accepted: **20.01.2020**

CORRESPONDING AUTHOR

Bing Hao
School of Geoscience,
China University of Petroleum (East China),
Qingdao 266580, China

e-mail: 312034461@qq.com

© by PSP Volume 29 – No. 04A/2020 pages 3048-3055 Fresenius Environmental Bulletin

VEGAN *VS.* MEAT: CATEGORIZATION OF PLATE WASTE IN RESTAURANTS

Neven Voca[1,*], Eda Puntaric[2], Jona Suric[1], Dunja Kunjko[1]

[1]Faculty of Agriculture University of Zagreb, Svetosimunska cesta 25, Zagreb, Croatia
[2]Ministry of Environment and Energy, Radnicka cesta 80, Zagreb, Croatia

ABSTRACT

The purpose of the paper was to determine the quantity and composition of plate waste left over after the guests had consumed their meals in a restaurant that serves only vegan meals and in restaurant that serves dishes including food of animal origin. Both restaurants are located in Zagreb (Croatia) and the sample size was 500 plates. After meal consumption, each component was weighed separately. Subsequently, in-depth interviews were conducted with restaurant staff members. Out of the 500 plates served in the vegan restaurant, 377 were empty after the guests had finished their consumption. The remaining 123 plates contained 6,951 g of plate waste. In the restaurant that serves meals containing meat, 264 out of the 500 serving plates remained empty. The remaining 236 plates contained 20,966 g of plate waste. In addition, it was assessed whether the size of the portion caused an increase in amount of food waste. Namely, when portion size was larger than 410 g more plate waste was generated, but at the same time also more food was eaten. The results and research methodology could act as a useful guide for decreasing plate waste in restaurants and invoke a possible change of eating habits.

KEYWORDS:
Food waste, plate waste, restaurant, in-depth interviews, portion size

INTRODUCTION

Food production is one of the main factors related to environmental impacts in the European Union (EU). The environmental impact of food production and consumption is worsened when food is wasted rather than consumed. When food is wasted, then all associated activities and emissions created in the food supply chain are in vain [1]. The United Nations' Food and Agriculture Organization [2] estimates that the world produces about 1.4 billion tons of food waste each year. The amount of food waste that is thrown every year is enough to feed about 2 billion people.

Reducing food waste would help in the path towards a more sustainable global food system [3]. It is important to explain definitions such as food loss, food waste and plate waste. Food loss is wastage of food from production to retail and consumer phases. This includes losses from harvesting, handling, storage, packing or transportation of food [2,4]. Food waste is a term that designates edible and healthy food that is lost from the food production chain [5]. Food waste can be divided into several categories such as edible/inedible food waste or avoidable/unavoidable food waste [1]. Research has showed that food waste made in restaurants can be classified into several categories or areas depending on where the waste is generated. Categories are storage losses, preparation losses, service losses, leftovers and plate waste. The term "Plate waste" designates all edible waste that has remained on the plate after the end of the meal, or in other words, plate waste represents food that is served but not eaten [6]. Plate waste is often measured in order to get information on how customers are satisfied with the food they ate. This information can prove to be helpful when planning the menu or to make changes to the existing menu. Plate waste in hospitals can also show patient food adequacy and meal provision efficiency. Plate waste measured in hospitals can be 2 to 3 times higher than food waste measured in restaurants, schools, kindergartens or canteens. To estimate plate waste, there are two basic measurement methods. These are weighing method and estimation method [7].

Some scientists divide measuring plate waste methods into direct and indirect methods depending on whether the plate waste is weighed or evaluated. Regardless of the existence of both the "direct method" and "weighing method" terms, weighing plate waste is the most accurate and most commonly used method. The weighing method includes collecting plate waste and weighing total mass, or each individual food component can be measured individually. Although the weighing method is the most accurate and commonly used, it requires significant resources and time and can therefore be difficult to perform without interrupting normal work of the food facility [3,7]. Therefore, the visual assessment methods are becoming ever more popu-

lar because of their simplicity of implementation and cost efficiency [8]. Visual estimation uses a scale to measure approximately what proportion of food is left based on different grading scales for plate waste. Compared to the weighing method, the visual evaluation method requires less time and space. The negative aspects of the visual assessment method are observer affinities and subjective attitudes. The results of plate waste estimation are most often displayed as the percentage by weight of served food that has remained undisturbed. In some studies, the results are presented in terms of money value of plate waste [7,8].

The European Commission has set a target presented in the document The Roadmap to a Resource Efficient Europe [9], according to which the EU waste disposal should be reduced by 50% by 2020. In accordance with the aforementioned, the government of the Republic of Croatia has set the Waste Management Plan of the Republic of Croatia for the 2017-2022 periods. In this document, the government of the Republic of Croatia has introduced a series of measures that may lead to reduction of food waste [10]. In order to reduce the amount of food waste, it is necessary to work on improving the system for collecting and processing food waste data. There is still no uniform data collection system. Currently, reliable data are missing, especially data on the quantity and type of food waste from the service sector in the Republic of Croatia.

Anthropologists often emphasize that eating habits are most challenging to change. Nonetheless, over the past hundred years, eating habits have changed significantly. The reason for this is industrialization, urbanization, the revolution in production, storage, transport, distribution and consumption of food, as well as the desire for a healthier way of life. Precisely because of the adoption of healthier eating habits, the consumption of carbohydrates *per capita* has decreased, while the consumption of milk, fruit and vegetables increased. Thus, there is an increasing number of people who do not eat meat and/or generally food of animal origin such as cheese, eggs, milk, meat, etc. Research in Europe in 2018 revealed that the greatest contribution to general impacts on food waste resulted from meat products [1,11]. That is why the vegan and vegetarian diet is considered more environmentally friendly, and it was the reason why we decided to compare the amount and composition of food waste in a restaurant offering meals of animal origin versus a vegetarian restaurant.

It is also important to emphasize that when it comes to plate waste, the decisions that people make are crucial. Although people may not be aware of this, their choices and the food they (not) consume directly affect the environment. Additional information to people and a change in diet could benefit both the health of the population and the environment [12].

This study aimed to determine the quantity and composition of plate waste left over after food consumption in two restaurants in Zagreb, Croatia. Food waste was measured in two different restaurants, i.e. in one restaurant facility, only vegan meals are served, while the other restaurant facility serves foods that include meals of animal origin. From the results obtained, observing each category of waste separately, it was determined which type of food made the largest component of plate waste. Furthermore, the aim of the study was to determine whether the vegan restaurant produced less plate waste than the restaurant that serves animal-derived dishes.

MATERIALS AND METHODS

Due to the protection of data and privacy and for the sake of simplicity, the restaurant facility which serves only vegan meals is designated as “Restaurant A” and the other restaurant facility which serves foods that include meals of animal origin is designated as “'Restaurant B”. Both restaurants are located in Zagreb (Croatia) and the sample size in both restaurants was 500 plates.

In Restaurant A, two chefs and two assistant chefs are employed. They make about 100 meals *per* day. The initial plate weight was known in Restaurant A because of the norms that were made before. This means that the initial plate weight was known at this restaurant without the need for weighing. In Restaurant B, there are seven people working in the kitchen, of which three are chefs and three assistant chefs, and one person is a pizza master. The average daily number of meals made in Restaurant B is between 100 and 150. The restaurant offers a range of three different daily meals, which vary depending on the day of the week, pizzas and meals on request. Restaurant B is located in the immediate vicinity of the city industrial zone and most common guests are employees from the surrounding companies who come to dine during their lunch breaks.

A direct method of weighing plate waste that remained on the plate after consumption was used in this study in both restaurants. After the customers were done eating, each component left over was weighed separately on the kitchen digital scale. If the plate was returned after consumption to the kitchen completely empty, the amount of plate waste was recorded as zero but these results were also taken into account in the research. After weighing plate waste from 500 plates, all the measurements were entered in tables with predefined waste categories to help determine the composition and the average amount of plate waste as easily as possible. If more food components have been left

on the plate after the customer was finished eating their meal, each component was weighted separately. All the food left on the plate after consumption was weighed on a digital scale, its amounts were recorded in the waste tables, and then the food was thrown away.

Tables defined by these categories allow easier and more efficient classification of plate waste for further data processing. The category of grain products included falafels, pasta, tortillas, vegetable pies (fritters) and lasagne. Category of processed beans included hummus and puree made of lentils and pumpkin. Category of lettuces and salad includes all vegetables served as salad - green salad, cabbage, tomatoes and other. Unavoidable waste includes bones and skin from meat and fish bone together with the heads. Grain products included couscous, buckwheat, bulgur, barley and similar food.

After weighing plate waste in-depth interviews were conducted with certain members of the restaurant staff. The researchers talked to the main chef and procurement manager at both restaurants. All the respondents who participated in the in-depth interviews were asked the same questions.

RESULTS AND DISCUSSION

Out of the 500 plates served in Restaurant A, 377 remained empty after the restaurant guests had finished their consumption. On the remaining 123 plates containing plate waste, the total measured amount of plate waste was 6,951 g. The mean amount of waste *per* plate in a sample of 123 plates returned with a certain amount of food was 56.51 g. Considering that in this study the total sample was 500 plates *per* restaurant, the mean amount of food waste *per* plate (if all plates were taken into account) was 13.90 g. The amount of plate waste after the end of consumption varied depending on the type of food. The largest amount of plate waste in Restaurant A consisted of grain products (without bread) with a total quantity of 2,162 g or 31% of the total amount of plate waste, followed by the waste of rice (1,118 g). The smallest amount of plate waste in Restaurant A consisted of vegan mayonnaise with the amount of 4 g (0.06 %) (Table 1). Statistical processing of plate waste from Restaurant A is shown in Table 2.

In Restaurant B, out of the 500 plates served, 264 remained empty after the restaurant guests had finished their consumption. On the remaining 236 plates containing plate waste, the total measured amount of plate waste was 20,966 g. The mean amount of food waste *per* plate in a sample of 236 plates returned with a certain amount of leftovers was 88.84 g, but the mean amount of waste *per* plate was 41.93 g when all 500 plates were taken into account. In Restaurant B, the largest amount of plate waste referred to potatoes with a total quantity of 7,352 g or 35% of the total amount of plate waste. It is interesting to note that one category in restaurant B had more waste than all the categories in restaurant A combined. The next category of food that produced a lot of plate waste was unavoidable waste. This category includes skin and bones of meat or fish. Total quantity of unavoidable waste was 4,311 g. The category of unavoidable waste was followed by the amount of fish (2,911 g) and meat (1,989 g) waste. Only 8.5% of total food waste referred to the category of vegetable waste with 1,284 g. Unlike Restaurant A, which is vegan, rice ranked sixth in restaurant B with 1,027 g, followed by the grain/wheat products (868 g), bread (522 g), stewed vegetables (492 g), and lettuces and salad with the smallest amount of 210 g (1%) (Table 3).

The last column in Table 4 shows how many plates represented each waste category. This means that in addition to having the most potato waste, it is also the most common food on the plate. Specifically, potatoes were also found on almost 50% of the food waste plates.

TABLE 1
The amount and composition of plate waste in the Restaurant A

Type of waste	Quantity (g)	%
Grain products	2,162	31.10
Rice	1,118	16.08
Stewed vegetables	1,054	15.16
Other vegetables	643	9.25
Lettuces and salad	624	8.98
Beans products	569	8.19
Bread	472	6.79
Cakes	191	2.75
Potato	114	1.64
Vegan mayonnaise	4	0.06
Total:	**6,951**	**100**

TABLE 2
Statistical analysis of data from Restaurant A

Type of waste	Average (g)	Standard deviation	Minimum (g)	Maximum (g)	Number of plates with this waste
Grain products	17.58	48.90	8	287	34
Rice	9.09	36.03	14	320	19
Stewed vegetables	8.57	29.22	12	242	19
Other vegetables	5.23	22.44	3	175	13
Lettuces and salad	5.07	15.88	3	109	23
Beans products	4.63	17.86	5	160	16
Bread	3.84	12.53	11	79	16
Cakes	1.55	11.99	5	131	7
Potato	0.93	7.55	8	79	3
Vegan mayonnaise	0.03	0.36	4	4	1

TABLE 3
The amount and composition of plate waste in restaurant B

Type of waste	Quantity (g)	%
Potato	7,352	35.07
Unavoidable waste	4,311	20.56
Fish/squid	2,911	13.88
Meat	1,989	9.49
Vegetables	1,284	6.12
Rice	1,027	4.90
Grain products	868	4.14
Bread	522	2.49
Stewed vegetables	492	2.35
Lettuces and salad	210	1.00
Total:	**20,966**	**100**

TABLE 4
Statistical analysis of data from Restaurant B

Type of waste	Average (g)	Standard deviation	Minimum (g)	Maximum (g)	Number of plates with this waste
Potato	31.19	47.38	4	257	115
Unavoidable waste	18.42	39.31	15	200	56
Fish/squid	11.72	42.72	4	410	52
Meat	8.5	23.83	2	172	47
Vegetables	5.49	23.86	9	225	20
Rice	4.39	21.27	6	186	15
Grain products	3.71	17.27	7	160	14
Bread	2.23	17.19	26	228	7
Stewed Vegetables	2.10	11.76	15	135	11
Lettuces and salad	0.89	8.06	15	104	4

TABLE 5
Comparison of data obtained from Restaurant A and Restaurant B

	Restaurant A	Restaurant B
Type of restaurant	vegan	meaty
Number of empty plates	377	264
Number of plates with waste	123	236
Total amount of waste	6,951 g	20,966 g
Mean value of food waste per plate (500 plates)	13.90 g	41.93 g
Annual amount of plate waste	361.45 kg	1,090.23 kg

When comparing the amount of plate waste generated in Restaurant A and Restaurant B, it is evident that threefold lower amounts of waste were produced in Restaurant A that serves only vegan foods (Table 5).

The data obtained in this study are hardly comparable with the research conducted to date because there is not much information so far on the amount of food/plate waste from restaurants that do not serve meat dishes (vegan and vegetarian restaurants and the like). The results obtained in this study are different from those reported by Ferreira (2013) [13], where the average amount of food waste was 200 g per plate. Similar results were obtained by Silvennoinen (2015) [14] in Finland, where the quantity of wasted food *per* portion in workplace canteens was 189 g per portion. A study on the amount of food waste was also conducted in China in 4 cities, where the average amount of food waste per capita per meal was calculated to be 93 g in 2015 [4]. Taking these researches into account, the amount of plate waste in the restaurants from Zagreb was much smaller when compared to different facilities that provide food around the world.

TABLE 6
Comparing the portion size and increase of amount of waste in Restaurant A and Restaurant B

	Restaurant A	Restaurant B
Number of plates where the portion was less than 410 g:	41	61
The average portion quantity when the portion is less than 410 g:	375.61 g	377.25 g
Total plate waste where the portion was less than 410 g:	2,228 g	5,302 g
The average amount of plate waste where the portion was less than 410 g:	54.34 g	86.92 f
Percentage of plate waste where the portion was less than 410 g:	14.47%	23.04%
Number of plates where the portion was more than 410 g:	82	175
The average portion quantity when the portion is more than 410 g:	509.63 g	553.20 g
Total plate waste where the portion was more than 410 g:	4,723 g	15,664 g
The average amount of plate waste where the portion was more than 410 g:	57.60 g	89.51 g
Percentage of plate waste where the portion was more than 410 g:	11.30%	16.18%

Considering the composition of plate waste, there also are differences. In the vegan restaurant, most of the plate waste consisted of grain products, whereas in Restaurant B, most of plate waste consisted of potatoes. The results obtained in Restaurant B are similar to the results of a survey conducted in Sweden, where school students mostly left potatoes, rice and pasta [15]. In another study conducted in China, the results were completely different in terms of waste composition. Vegetables contributed most to plate waste (29%), followed by rice (14%), seafood (11%), wheat (10%), and pork (8%) [4]. These data clearly illustrate the problem of data comparison because each restaurant serves different type of foods and the results obtained are difficult to compare. This is especially apparent when comparing different dishes and consumer habits and socio-demographic characteristics [16].

A study conducted in Canada investigated whether the portion size influenced the amount of waste [6]. They found that increasing the portion size in turn increases the percentage of waste. The results also suggested that there was an obvious 'step' at about 410 g, because researchers conclude that plates greater than approximately 400 to 410 g were unlikely to generate zero waste. This result does not suggest, therefore, that meals should simply be reduced. It is more likely that the amount of about 410 g or above is too large a quantity for some consumers and they simply cannot eat everything on the plate [6]. The results obtained in Restaurant A and Restaurant B was divided into more or less than 410-gram-sized portions. In the first half of the Table 6 are results of portions less than 410 g followed by results where the portions weighed more than 410 g.

This data analysis confirmed the results from a Canada study [6], where the amount of plate waste increased with the increase in portion. It can be concluded that when the portion is larger (more than 410 g), more total waste is generated. In Restaurant A, for example, when the portion was less than 410 g, a total of 2,228 g of waste was generated. When the portion was larger than 410 g, twice as much waste was generated (4,723 g). The results of research conducted for this paper have not confirmed the fact that increasing the portion size increases the percentage of waste. On the contrary, the percentage of plate waste where the portion was larger than 410 g was lower compared to the percentage of plate waste where the portion was less than 410 g. In Restaurant B, for example, the percentage of plate waste was higher (23.04%) when the portion was less than 410 g. In portions larger than 410 g, the percentage of waste on the plate was 16.18%. Similar results were also obtained in the vegan restaurant (Table 4). It can be concluded that more food is eaten when the portion is larger. This conclusion could be interesting to nutritionists and physicians considering the growing proportion of obese people all over the world.

When it comes to increased energy intake through food, it is interesting to point out the observations of Macdiarmid (2013) [12] where the focus was made on Green House Gas Emissions (GHGE) and climate change. In that study, two suggestions were made to reduce GHGE. The first was to reduce the intake of meat and dairy products, while the second was to reduce the excessive consumption of food. This would mean consuming only as much energy as it is necessary to maintain a healthy body weight. Accepting these suggestions restaurants could have both health and environmental benefits. Following these tips, it can be concluded that eating in meat-free restaurant (like Vegan Restaurant A) would be more environmentally friendly.

The results obtained in this study may be explained or at least clarified by analysing opinions and beliefs of the restaurant employees where data were collected. In-depth interviews were conducted in Restaurant A and Restaurant B. Respondents were asked about kitchen waste, service losses, and other food waste and plate waste issues. All the respondents in both restaurants emphasised food quality as an essential factor. Groceries bought at a discount spoil faster. Automatically, more food is thrown away and discount saving is actually questionable. On the other hand, less food is thrown if high-quality groceries are acquired, especially the ones that have quality certificates. Respondents in both restaurants first use groceries that have a near expiration date. No large stock is made. Groceries are purchased as needed and it is not the reason why food is being thrown away. The amount of food thrown away due to expiration date was insignificant in its amount. If food is thrown away due to

the expiration date, it is mostly fresh food (vegetables) in Restaurant B and hummus in Restaurant A. The respondents stated that they were mindful concerning the amount of supplies being ordered. If too much is cooked or if all the cooked food is not sold/consumed by the end of the working day in the vegan restaurant, the restaurant workers often share the food leftover among themselves. In Restaurant B, stewed vegetables, soups and the like are stored for another day or some foods are frozen. For example, grain food if not used is usually frozen and later used to make other kinds of meals. In Restaurant B, the food that is not eaten is frozen, shocked, or vacuumed if possible. The food that can be used for another day is stored in cooling chambers. According to the restaurant manager at the vegan restaurant, vegan mayonnaise is the largest part of their plate waste. The reason is not known. The restaurant manager assumes that the reason may be because vegan mayonnaise tastes differently from the 'typical mayonnaise' because it is made without eggs and with soy milk.

The restaurant manager in Restaurant B believes that side dish is their biggest leftover. The manager feels that the reason is that guests prefer to eat meat and that the side dish on the plate is too large in quantity. According to the data collected in this research, the restaurant manager in Restaurant B is right because potatoes were the biggest part of plate waste. This fact is also confirmed by the results of a research from Switzerland, which showed that meat and fish rarely become waste [15]. When asked the question: In your opinion, are portions in your restaurant too large and is that the possible cause why food stays uneaten, in both Restaurant A and Restaurant B respondents answered that the portions might be too large and gave reasons as to why food is left on the plate and why food is eventually thrown away. The Restaurant B chef further noted that the portions might be too large but that they could not be reduced because of the price. Employees in the same restaurant said that when the amount of side dish was reduced, the guests expressed their discontent. The chefs in both restaurants and the manager in Restaurant B believe that one of the reasons for food being left on the plate is because the food is not visually eye pleasing. The head of the vegan restaurant did not agree with the above because he did not believe that serving meals that were not visually eye pleasing was the reason for waste disposal. Restaurant managers and chefs in both restaurants answered positively the question whether they were willing to get informed and learn new skills in order to reduce the amount of waste. In order to prevent the formation of waste when purchasing groceries, it is advisable to check what the actual consumption of food is when compared to the quantities that are ordered. It is recommended to establish a precise storage and stock inventory to avoid food getting spoiled due to oversupply. Furthermore, by purchasing local products, one contributes to the reduction of adverse environmental impacts due to transport of goods.

The first step in the process of preventing the emergence of food/plate waste requires identification of the type and amount of waste generated by the business. This means that research such as this one should be carried out by every restaurant that wants to reduce the amount of plate/food waste. It is suggested that organic waste is separated from the rest of the waste during one week in a separate vessel. It is important that the week in which the measurement is carried out is representative (it is important to select a week that will adequately display business throughout the year). For example, it is not advisable to measure food waste during the week in which some exceptional events take place (for example, New Year's Eve). As an example of our research, the annual amount of plate waste in the vegan restaurant (Restaurant A) would be about 361,452 g, whereas in Restaurant B it would be 1,090,232 g (Table 5). As stated earlier, the results obtained by measuring plate waste in restaurants can help the restaurant staff change or adjust the menu or otherwise develop a policy that will strive for a smaller amount of food /plate waste. If despite the above-mentioned the facility prepares too much food that cannot be sold, it is advisable that the food is shared by the restaurant staff. It is also advisable to educate and train restaurant workers (primarily waiters) to ask guests if they want to take home food they have not eaten, so that they can later eat it at home (doggy bag). One another option is to donate the food that is leftover.

With the information received through conversation with restaurant staff, one can conclude that employees in both restaurants take care when it comes to food quality, food storage, the atmosphere in the restaurant, and finally the amount of food that is thrown away. Taking this professional and responsible approach into account, these restaurants may have a smaller amount of plate waste compared to other restaurants around the world where such or similar research was conducted.

Although the employees in this research are rationally handling the food in this study, certain information is also needed for the users of the food that is served. Recently, people have been thinking more and more about the impact of human existence on the environment and its threat. This is confirmed by a survey conducted in 2001 where 62% of adults in Australia stated they were concerned about environmental issues. Nevertheless, people are not sufficiently informed about the environmental impact of food waste and the environmental impact of food generally. Macdiarmid (2013) [12] found out that out of a sample of 3,000 adults in the UK, only 15% of respondents would be willing to change their diet for environmental benefits. The same survey pointed out that only 22% of respond-

ents thought it were possible to make positive shifts towards environmental benefits with a reduction in meat consumption. Health and nutrition professionals are in a position to improve consumer awareness of the link between food, health and the environment [17]. Keeping in mind that according to the data from this research, less wastes occurring in a vegan restaurant and that plant-based diets have less environmental impact, more research is needed to confirm the above said in more detail. But it could be concluded that a diet that does not include meat is less damaging to the environment and that kind of diet should be encouraged. The above said also indicates that consumers can make nutritional choices that can improve current and future environmental situation as well as improve their health [18].

Finally, when talking about plate waste in general, one needs to keep in mind other factors that can influence the amount of plate waste such as age, gender or consumer habits. Education, socio-economic status of consumers, environment during meals, as well as the reason for meal (business lunch, meal with friends or family, etc.) and various other reasons can influence the amount of plate waste [19].

While this paper does not address disposal of food waste directly, it is important to emphasise that food waste has a certain potential for further usage and that the worst possible option for disposal of plate waste is disposal at landfills. When providing restaurant services, it is mainly non-hazardous waste that is produced. If it cannot be reused in the restaurant facility itself, it is necessary that it is collected separately and stored and handed over to a licensed waste management company. Mostly, all kinds of non-hazardous waste generated in restaurant facilities can be reused. The main types of waste generated by the providing restaurant services are food waste, packaging waste (paper and paper cardboard, plastic, metal, textile), wood and waste paper. Food waste can be sent to further exploitation or recovery such as anaerobic digestion, composting, energy recovery, etc. Anaerobic digestion can produce biogas that can be used as a source of energy, while digestive can be used as a substitute for mineral fertilizers and soil quality improvement. Many studies have been carried out exploring different ways of managing food waste and their impact on the environment.

In some countries, disposing of food waste at landfills is forbidden and other ways of managing this type of waste are explored. In the South Korean research, the entire life cycle of production was monitored until final disposal [20]. This again supports the fact that disposal at the landfill is the most unfavourable way of food waste disposal. There is also a problem with disposal of food waste in Singapore because the local landfill (Semakau Island) does not accept organic waste, so a large part of biodegradable waste from food is sent to incinerators [21].

Another way of encouraging an environmentally acceptable way of managing food waste is to adjust prices respectively to reduce costs. This method has been conducted in Berkeley, California, USA. Business owners in Berkeley are stimulated to compost instead of sending food waste to the landfill because the cost for hauling compost bins is by 20% lower than the cost of transportation of trash cans to the landfill [22]. In this way, the food that is thrown away could be managed in a well-defined and environmentally satisfactory manner. The quantities of waste landfilled would be reduced and brought closer to the targets imposed by the European Commission in order to reduce EU waste disposal by 50% by 2020. More importantly, the negative impact on the environment would be reduced.

CONCLUSIONS

Although the survey sample was relatively small, this is a good start in determining the amount of plate waste generated in the service sector in Croatia, especially if one considers the fact that there are currently no reliable data on the food/plate waste produced in the service sector. The results obtained by this research could provide the basis and be a stepping stone for comparison with future research on the topic. Although in the researched restaurants, the amount of waste that is left over is lower compared to other similar research, the results obtained can help restaurant staff find out where the biggest losses are being made and what type of food is mostly thrown away. Consequently, it would be possible to change or adjust the menu or otherwise develop a policy that will strive for an even smaller production of plate waste.

With this study, the hypothesis that less waste is generated in a vegan restaurant than in restaurants that serve animal-derived dishes was confirmed. It also determined the quantity and composition of plate waste leftover after quests had finished their meals in two restaurants in Zagreb, Croatia. In the vegan restaurant (Restaurant A), most of the plate waste consisted of grain products, whereas in Restaurant B most of plate waste consisted of potatoes. It was also noticed that when the portion size exceeded 410 g, more plate waste was generated, but at the same time more food was consumed when the portions were larger than 410 g.

Additional research on this topic is certainly needed, but in the desire for eco-advancement, it could be suggested that people need more information, education and change of mindset, which will later lead to a change in diet in a more rational and environmentally friendly way.

REFERENCES

[1] Scherhaufer, S., Moates, G., Hartikainen, H., Waldron, K., Obersteiner, G. (2018) Environmental impacts of food waste in Europe. Waste Manage. 77, 98-113.

[2] FAO. World's food waste could feed 2 billion people, available at: https://www.worldvision.org/hunger-news-stories/food-waste (accessed 9. March 2019) (2019).

[3] Derqui, B., Fernandez, V. (2017) The opportunity of tracking food waste in school canteens: guidelines for self-assessment. Waste Manage. 69, 431-444.

[4] Wang, L., Gang, L., Liu, X., Liu, Y., Gao, J., Zhou, B., Gao, S., Cheng, S. (2017) The weight of unfinished plate: a survey based characterization of restaurant food waste in Chinese cities. Waste Manage. 66, 3-12.

[5] Laso, J., Margallo, M., Garcia-Herrero, I., Fullana, P., Bala, A., Gazulla, C. (2018) Combined application of Life Cycle Assessment and linear programming to evaluate food waste-to-food strategies: seeking for answers in the nexus approach. Waste Manage. 80, 186-197.

[6] Von Massow, M., McAdams, B. (2015) Table scraps: an evaluation of plate waste in restaurants. JFBR. 18(4), 437-453.

[7] Willams, P., Walton, K. (2011) Plate waste in hospitals and strategies for change. E-SPEN. E Spen Eur E J Clin Nutr Metab. e235-e241.

[8] Hanks, A.S., Wansink, B., Just, D.R. (2014) Reliability and accuracy of real-time visualization techniques for measuring school cafeteria tray waste: validating the quarter-waste method. J Acad Nutr Diet. 114 (3), 470-474.

[9] European Commission. The Roadmap to a Resource Efficient Europe, available at: http://ec.europa.eu/environment/resource_efficiency/about/roadmap/index_en.htm (accessed 28. March.2019) (2011).

[10] Official Gazette. Waste Management Plan of the Republic of Croatia for the Period 2017-2022. Republic of Croatia, Ministry of Environment and Energy (2017):

[11] Arganini, C., Saba, A., Comitto, R., Virgili, F., Turrini, A. (2012) Gender Differences in Food Choice and Dietary Intake in Modern Western Societies. Public Health – Social and Behavioral Health, Prof. Jay Maddock (Ed.), InTech, Available from: https://www.intechopen.com/books/public-health-social-and-behavioral-health/gender-differences-in-food-choice-and-dietary-intake-in-modern-western-societies (accessed 19. July.2019).

[12] Macdiarmid, J.I. (2013) Is a healthy diet an environmentally sustainable diet?, Nutrition Society. 72, 13-20.

[13] Ferreira, M., Martins, M.L., Rocha, A. (2013) Food waste as an index of food service quality. Br Food J. 115(11), 1628-1637.

[14] Silvennoinen, K., Heikkilä, L., Katajajuuri, J.M., Reinikainen, A. (2015) Food waste volume and origin: Case studies in the Finnish food service sector. Waste Manage. 46, 140-145.

[15] Engstörm, R., Carlsson-Kanyama, A. (2014) Food Losses in Food Service Institutions. Example from Sweden, Food Policy. 29, 203-213.

[16] Porpino, G., Wansink, B., Cheek, K. (2015) Saving food in restaurants: half-sized portions out perform persuasion on mitigating waste. J Nutri Educ Behav. 47(4), S46.

[17] Lea, E. (2005) Food, health, the environment and consumers. Nutrition and Dietetics, 62, 21-25.

[18] Franchetti, M. (2013) Economic and environment analysis of four different configurations of anaerobic digestion for food waste to energy conversion using LCA for: a food service provider case study. J Environ Manage. 23, 42-48.

[19] Ilakovac, B., Ilickovic, M., Voca, N. (2018) Food waste drivers in Croatian households. J Cent Eur Argic. 19(3), 698-709.

[20] Kim, M.H., Song, Y.E., Song, H.B., Kim, J.W., Hwang, S.J. (2011) Evaluation of food waste disposal options by LCC analysis from the perspective of global warming. Waste Manage. 31, 2112-2120.

[21] Hsien, H.K., Teik, Z.L., Reginald, B.H.T. (2010) Food waste conversion options in Singapore: environmental impacts based on an LCA perspective. Sci Total Environ. 408, 1367-1373.

[22] Sakaguchi, L., Pak, N., Potts, M.D. (2018) Tackling the issue of food waste in restaurants: options for measurement method, reduction and behavioral change. J Clean Prod. 77, 430-436.

Received: **28.11.2019**
Accepted: **10.02.2020**

CORRESPONDING AUTHOR

Neven Voca
Faculty of Agriculture
University of Zagreb,
Svetosimunska 25, Zagreb, Croatia

e-mail: nvoca@agr.hr

© by PSP Volume 29 – No. 04A/2020 pages 3056-3071 Fresenius Environmental Bulletin

DETERMINATION OF DIOXINS/FURANS IN HUMAN GALLBLADDER STONES AND GALLBLADDER TISSUES AS INDICATOR FOR ENVIRONMENTAL CONTAMINATIONS

Sharif Arar[1], Samer Awaideh[2], Mohammed H Kailani[1], Mahmoud Alawi[1,*]

[1] School of Science, Department of Chemistry, University of Jordan, Amman, 11942, Jordan
[2] Faculty of Science, Department of Chemistry, Al Isra University, Amman-11622, Jordan

ABSTRACT

The levels of 17 congeners of Polychlorinated dibenzo-*p*-dioxins (PCDDs) and polychlorinated dibenzofurans (PCDFs) in human gallbladder tissue and gallbladder stone samples gathered from patients of the "Jordan university hospital" in the period between February 2016 and April 2016, were analyzed. All samples were extracted, cleaned-up, and analyzed using GC-EI/MS. The total mean concentration of dioxins/furans in gallbladder tissues and stone samples were 1.62 µg/kg and 2.30 µg/kg, respectively. In all samples most of dioxin/furans congeners were not detected. Octachlorodibenzo-*p*-dioxin was the most abundant congener with average concentrations of 1.19 µg/kg in gallbladder tissue samples and of 1.64 µg/kg in gallbladder stone samples. The TEQ values for PCDDs/Fs in all samples were found in the range of 0.40 to 124.9 ng TEQ/kg for gallbladder tissue samples and 15.7 - 135.9 ng TEQ/kg for gallbladder stone samples. The distribution coefficient for dioxins/furans were calculated between gallbladder stones and gallbladder tissue in each sample. The distribution coefficients, ($Kd = C_{stone}/C_{tissue}$) for dioxins/ furans were found in the range 0.88 to 2.06. The variations in Kd depend mainly on the type of gallbladder stone and on the fat content of the gallbladder tissue (obesity) of the patient. The results of this study show that both gallbladder stones and gallbladder tissues can be used as a good indicator for body pollution especially if the stone was of pure cholesterol type. The concentrations we found in this study are much higher than what Muto [29] found, nevertheless there was no deaths among the donors of the 39 samples in our study. It is also attention drawing that the congeners 1,2,3,6,7,8-hexachlorodibenzino-p-dioxin and 1,2,3,4,6,7,8-heptaclorodibenzo-*p*-dioxin are present at high frequency, numerically 97.4% and 100% respectively.

KEYWORDS:
Dioxins/Furans, Gallbladder tissues, Gallbladder stones, Pollution, Toxicity equivalency (TEQ), Jordan

INTRODUCTION

Dioxins and Furans. Polychlorinated dibenzo-*p*-dioxins (PCDDs) and polychlorinated dibenzofurans (PCDFs) are planar tricyclic compounds, that exhibit comparable toxicities and properties [1-4]. PCDDs and PCDFs are semi-volatile and toxicologically significant trace organic contaminants [5]. They are introduced into the environment through various sources and accumulate in human tissues [6]. The importance of studying the bioaccumulation of these compounds come from their high toxicity, their transport pathway between air, water and food [1, 5].

According to Fiedler [7], the number of PCDDs congeners is 75 and those of PCDFs is 135 depending on the positions of chlorine atoms on the aromatic rings, with wide variations in the physiochemical properties between the congeners. Generally, these compounds are insoluble in water and lipophilic. Dioxins and furans are unintentionally produced through high temperature processes. They have no commercial applications and easily introduced to the environment due to their lipophilic behavior and ~~its~~ transportation ability.

The sources of dioxins and furans are chemical processes which associated with the production of trace amounts of dioxins/furans as byproducts including the manufacturing of PCBs and OCPs. The other sources are uncompleted combustion processes such as chemical waste, hospital waste, coal and peat; landfill gas combustion, crematoria, and cement manufacture [7].

From all dioxin and furan congeners, only 17 of them have shown significant potential toxicity, and bio-accumulation ability [2, 8]. 2,3,7,8-tetrachlorodibenzo-*p*-dioxin (TCDD) has been reported to be the most toxic dioxin congener [3, 8], and the strongest carcinogenic agent [3, 9], where 2,3,7,8-TCDF is about 10% as toxic as TCDD.

These compounds have high ability to transport for long distance, are highly lipophilic, have high penetration ability, high resistance against metabolism and easily deposited onto surfaces of water, soil and plants. So, they exist in all environmental compartments.

Gallbladder and Gallbladder Stones. According to the Florida Medical Center "Gallbladder is a small pear-shaped sac that sits in the upper abdomen on the right side, just under the ribcage [10]. It is about 7 cm in length and its main function is to store and concentrate the bile, a yellow -brown digestive enzyme produced by the liver [11].

Bile contains cholesterol and bile salts. After a meal the gallbladder contracts and bile passes down the bile duct to enter the duodenum, the beginning of the small bowel. If too much cholesterol accumulates in the bile it crystallizes out as stones, either by itself, or mixed with bile pigments. This can form a sludgy gravel or stones as big as chestnuts. The only way out for the stones is to travel down the bile duct into the bowel. If they are too big they will get stuck and cause severe pain and a number of other problems [11].

There are several factors that predispose to gallstones. They tend to run in families and are twice as common in women. Being overweight can also contribute. As quoted from Gastroenterological Society of Australia "Gallstones are a common problem as we age, with an estimated prevalence of 25–30% in Australians over the age of 50 years" [12]. Gallstones are a common clinical finding in the Western populations. The prevalence rates in European adults is 10–15%, while in African and Asian populations prevalence is 3–5 % [13-14]. In the United States, the prevalence rates range from 5% to 27%. In American Indians, gallstone disease is found in 30% of male and 64% of female [14-15]. The prevalence of gallstones is rising day by day in Pakistani population [16-17]. Gallstones types are classified according to the cholesterol content to pure cholesterol stones which are constitutes around 90% cholesterol, pigment stones constitutes around 90% bilirubin and mixed composition stones, which are constitute of varying percentages of cholesterol, bilirubin and other substances such as calcium carbonate, calcium phosphate and calcium palmitate [14, 18, 19].

Literature Review. Saqib, et al. [14], studied the recognition of various gallstones in the patients attending surgical OPD (Outpatient Department) by biochemical analysis of gallstones. The study was done in ISRA' hospital in Hyderabad /Pakistan during 18 months on sixty-nine patients. They found that the frequencies in different age groups were as follows: 11.60% for the age group 15-24 years, 24.64% for 25-34 years, 53.63% for 35-44 years, 8.69% for 45-54 years and 1.45% for 55-64 years. The frequencies ratio between males to females was 1: 2.45 and the frequencies of stone types were 55.07% for cholesterol stones, 28.99% for pigment stones and 15.94% for mixed stones.

Kitamura, et al. [20], studied the concentration of 20 dioxin/furans congeners in 27 autopsy cases. They found a total TEQ values in the bile of 43.2 ± 30.9 pg TEQ/g lipid, where the concentration of 1,2,3,4,6,7,8-heptachloro-*p*-dibenzodioxin was the highest.

Up till now there is no research work dealing with dioxins/furans in gallbladder tissues and gallbladder stones. This will be the first study on this field.

Aims of the Present Work. This study aims to determine the concentrations of Polychlorinated dibenzo-*p*-dioxins (PCDDs) and polychlorinated dibenzofurans (PCDFs) in gallbladder tissues and gallbladder stones in samples gathered from the Jordan hospital in Amman-Jordan as indicator for human body pollution and to calculate the toxicity risk in (ng TEQ/ g sample) concentration for PCCD/Fs in both gallbladder tissues and stones.

Then to make a comparison between the PCDDs/Fs concentrations in gallbladder tissues and their concentrations in the gallbladder stones to determine which of them is the most favorable site of bioaccumulation and to calculate the distribution coefficient of PCDDsd/Fs congeners between gallbladder tissues and gallbladder stones. Study if these POPs can be one of the agents that contribute to the formation of dysplasia in the human tissues by studying its concentrations in the available samples that have dysplasia which are tow samples only.

MATERIALS AND METHODS

Chemicals and Solvents. Solvents used were as follows: n-hexane of 97% purity, and toluene of 98% purity were purchased from Tedia (USA); ethanol absolute of 99% purity, n-nonane of 98.7% purity, and isooctane of 98.7% purity were purchased from Riedel deHaën (Hannover/ Germany); dichloromethane of 97% purity and petroleum ether (40-60 ºC) of 95% purity was purchased from Carlo-Erba (Italy); acetone of 99% purity was purchase from GCC (UK). Chemicals used for the extraction and clean-up were purchased as follows: Silica gel 60, 0.063–0.200 mm (70–230 mesh) from Merck (Germany), anhydrous sodium sulfate extra pure was purchased from Fluka (Switzerland) and Florisil® 0.15–0.25 mm (60– 100 mesh) from Merck (Germany) [6].

Standards and Internal Standards. EPA method 1613 stock solution of PCDDs/PCDFs and internal standard for PCDDs/PCDFs (1,2,3,4-tetrachloro [$^{13}C_{12}$] dibenzo-*p*-dioxin), 200 ng/mL, were purchased from Willington Laboratory (Canada) [6].

Apparatus. The instrument used for the determination of PCDDs/PCDFs was as mentioned in Alawi, et al. [6].

TABLE 1
Participants information

Participants No.	Cancer patient (Yes / No)	Sex	Age (year)	BMI * ($kg\ m^{-2}$)	Address	Smoking
S-01	No	F	46	18.40	Hai Nazzal	No
S-02	No	F	36	34.50	Irbid	No
S-03	No	F	31	30.62	Sweileh	No
S-04	No	F	24	34.50	Um Alheeran	No
S-05	No	M	55	19.95	Wadi Alsair	Yes
S-06	No	F	52	17.90	Hai Nazzal	No
S-07	No	F	33	17.87	Tabarbore	No
S-08	No	F	45	17.72	Sweileh	Yes
S-09	No	M	52	33.16	Ain Albasha	Yes
S-10	No	M	74	23.50	Tla'a Ali	Yes
S-11	No	F	54	23.00	Alunzhah	No
S-12	No	F	44	35.02	Aljwaidah	No
S-13	No	F	28	17.41	Albaqa'a	No
S-14	No	F	24	39.52	Alsalt	No
S-15	No	M	70	33.27	Hainazzal	Yes
S-16	No	F	47	17.39	Jarash	No
S-17	No	F	57	17.00	South Shounah	No
S-18	No	F	28	19.70	Marj AlHamam	No
S-19	Dysplasia	F	40	36.01	Jabal AlHusein	No
S-20	No	F	75	17.00	Marka	No
S-21	No	M	76	18.61	Algeezah	No
S-22	No	F	59	24.05	North Marka	No
S-23	No	F	39	23.50	Abu Alanda	Yes
S-24	No	F	60	22.90	Aljbaihah	No
S-25	No	F	49	21.00	Dahiat Alrasheed	No
S-26	No	F	40	21.72	Aqaba	Yes
S-27	No	F	52	18.66	Ain Albasha	No
S-28	No	F	29	35.00	Alzarqa	No
S-29	No	M	43	16.91	Ajloun	Yes
S-30	Dysplasia	M	61	37.62	Albaqa'a	No
S-31	No	F	44	16.97	Amman-Tariq	No
S-32	No	M	21	18.83	Madaba	No
S-33	No	M	21	16.50	Dabooq	No
S-34	No	F	24	19.50	Shafabadran	No
S-35	No	F	56	39.20	Ala'shrafiah	No
S-36	No	F	52	16.32	Marka	No
S-37	No	F	28	21.67	Al-abdali	No
S-38	No	F	31	15.88	Ajloun	Yes
S-39	No	F	77	16.50	Al Bnaiat	No

*Body Mass Index (BMI) = Body weight / $(Body\ height)^2$

SAMPLING AND SAMPLE PREPARATION

Sample Collection. A total of thirty nine samples of each fresh gallbladder tissues and gallbladder stones were collected with collaboration with the Institutional Review Board (IRB) in the Jordan University Hospital (JUH) - surgery department and histology laboratory in the period from February 2016 to April 2016.

All samples were stored at – 20 °C until analysis. Sample data sheets with questionnaire were filled for each patient; the summary of information for all samples is listed in Table 1.

Sample Extraction and Clean-up. One gram of each homogenized gallbladder tissue sample or gallbladder stone sample was weighed into a Soxhlet thimble, spiked with 200 µL IS (100 ppb) and then extracted in a Soxhlet apparatus with 200 mL toluene for 16 h. The extracts were reduced to ca. 2 mL using the rotary evaporator at 30 °C and 140 mbar [6]. The cleanup of the extracts was conducted according to Hagenmaier [21] method, on three columns as follows:

Macro Alumina Column. A glass column (25x1.6 cm) was filled with 20 g dry (500 °C, 6h) alumina B (Super I) and 10 g Na_2SO_4 then washed with 100 ml of n-hexane. Sample residues from the extraction step were dissolved in 10 ml n-hexane and added to the column, using Pasteur pipette. The column was then eluted with 80 ml n-hexane, 100 ml n-hexane/ dichloromethane (98:2) and 180 ml n-hexane/dichloromethane (1:1), successively. The third (last) fraction which contains PCDD/Fs was collected and evaporated to few milliliters at 40 °C and 280 mbar (the vacuum is to be reduced stepwise).

Mixed Silica Gel Column. A glass column (25x1.6 cm) was filled from bottom to top with 2.0 g of dry (220 °C, 6h) silica, 5 g basic silica gel mixed with 1 M NaOH (30% w/w), 2.0 g dry silica gel, 10 g acidic silica gel mixed with concentrated H_2SO_4 (40% w/w), 2.0 g dry silica gel and finally

10 g anhydrous Na_2SO_4. The column was washed with 100 ml n-hexane. Sample residues from the previous column cleanup step were dissolved in 10-20 ml n-hexane and transferred to the column using Pasteur pipette. The column was then eluted with 250 ml n-hexane. The eluates were evaporated to few milliliters at 30 °C and 240 mbar.

Mini Alumina Column. A glass column (25x0.8 cm) was filled with 4 g of basic alumina B (Super I) and 2.5 g of anhydrous Na_2SO_4. The column was washed with 10 ml n-hexane. The residues from previous column cleanup step were dissolved in 2-2.5 ml n-hexane and transferred to the column using Pasteur pipette. The column was eluted with 25 ml n-hexane/ dichloromethane (98:2) and 30 ml n-hexane/ dichloromethane (1:1), successively. The second (last) fraction was collected and evaporated to few milliliters then transferred to a pear shaped flask using n-hexane and re-evaporated almost to dryness at 30 °C and 240 mbar. The last few drops of the solvent were evaporated using a gentle nitrogen stream. 200 µL n-nonane were added to re-dissolve the residue, and transferred to micro-insert which placed in a small vial and closed until GC analysis.

GC/MS ANALYTICAL METHOD

GC and GC Conditions. As mentioned in Alawi, et al. [6].

* GC model: Agilent 6890 series II, with autosampler injector 7683 series
* Injector: 280 °C, 1 µL/splitless
* Columns: TRB-5MS, 30m× 0.25 mm i.d. × 0.25 µm film thickness
* Carrier gas: helium grade 5.0 (99.999%), 8 psi
* Flow rate: 1.0 mL/min
* Temperature programs: 150 °C (1 min)→200 °C, 12 °C/min→235 °C, 3 °C/min (8 min) → 310°C (8 min).

Mass Detector (MSD) Conditions. As mentioned in Alawi, et al. [6].

- Model: Agilent 5973 N, quadruple at 150 °C, electron impact ionization, 70 eV at 230 °C
- 280 °C (auxiliary)
- Tuning substance: perfluorotributylamine (PFTBA)
-Tuning masses: 69, 219, and 502 m/z
-Acquisition mode: total ion chromatogram (TIC)
-Data analysis: MSD Chemstation software

METHOD VALIDATION

Detection limits and limits of quantitation. The results show that for all studied PCDDs/PCDFs the LOD were between 0.02 and 0.03 µg/L; the LOQ were between 0.08 and 0.10 µg/L; the MDL were between 0.02 and 0.03 µg/kg fat and the MLOQ were between 0.08 and 0.16 µg/kg fat.

Instrument precision. The precision of the instrument was measured through the injection of three standard solutions of different concentrations. High concentration: (20 ng/ml) for tet-PCDDs/Fs, (100 ng/ml) for penta, hexa, hepta-PCDDs/Fs and (200 ng/ml) for oct-PCDDs/Fs; then medium concentration: (10 ng/ml) for tetra-PCDDs/Fs, (50 ng/ml) for penta, hexa, hepta-PCDDs/Fs and (100 ng/ml) for octa-PCDDs/Fs and low concentration: (5 ng/ml) for tetra-PCDDs/Fs, (25 ng/ml) for penta, hexa, hepta-PCDDs/Fs and (50 ng/ml) for octa-PCDDs/Fs. Each solution was injected three times. Tables 2, 3, and 4 show the calculated concentrations for the three injections, the average, standard deviation (SD) and the coefficients of variation (CV). The coefficients of variation (CV) were

TABLE 2
Instrument precision using high concentrations of standard solution mixture of PCDDs/PCDFs

No.	Congener	R.T (min)	Calculated concentration (ng mL^{-1})					
			Trial 1	Trial 2	Trial 3	Average	SD	CV(%)
1	2,3,7,8-Tetrachlorodibenzofuran	18.06	21.6	24.5	22.6	22.9	1.48	6.45
2	2,3,7,8-Tetrachlorodibenzeno-p-dioxin	18.378	22.0	23.4	26.6	24.0	2.35	9.81
3	1,2,3,7,8-Pentachlorodibenzofuran	19.98	118	116	118	117.3	1.15	0.98
4	2,3,4,7,8-Pentachlorodibenzofuran	20.41	117	115	117	116.3	1.15	0.99
5	1,2,3,7,8-Pentachlorodibenzo-p-dioxin	20.62	115	119	115	116.3	2.31	1.99
6	1,2,3,4,7,8-Hexachlorodibenzofuran	22.53	93	100	95	96.0	3.61	3.76
7	1,2,3,6,7,8-Hexachlorodibenzofuran	22.63	90	95	90	91.7	2.89	3.15
8	2,3,4,6,7,8-Hexachlorodibenzofuran	23.12	105	112	105	107.3	4.04	3.77
9	1,2,3,7,8,9-Hexachlorodibenzofuran	23.26	103	115	109	109.0	6.00	5.50
10	1,2,3,4,7,8-Hexachlorodibenzo-p-dioxin	23.35	97	115	97	103.0	10.39	10.09
11	1,2,3,6,7,8-Hexachlorodibenzo-p-dioxin	23.67	113	100	116	109.7	8.50	7.76
12	1,2,3,7,8,9-Hexachlorodibenzo-p-dioxin	23.89	107	95	107	103.0	6.93	6.73
13	1,2,3,4,6,7,8-Heptachlorodibenzofuran	25.84	98	103	98	99.7	2.89	2.90
14	1,2,3,4,6,7,8-Heptachlorodibenzo-p-dioxin	27.27	93	112	93	99.3	10.97	11.04
15	1,2,3,4,7,8,9-Heptachlorodibenzofuran	27.85	111	109	115	111.67	3.06	2.74
16	Octachlorodibenzo-p-dioxin	32.86	212	241	235	229.3	15.31	6.67
17	Octachlorodibenzofuran	32.99	225	214	232	223.7	9.07	4.06

TABLE 3
Instrument precision using medium concentrations of standard solution mixture of PCDDs/Fs

No.	Congener	R.T (min)	Calculated concentration (ng mL^{-1})					
			Trial 1	Trial 2	Trial 3	Average	SD	CV(%)
1	2,3,7,8-Tetrachlorodibenzofuran	18.06	9.8	10.2	10.2	10.1	0.24	2.41
2	2,3,7,8-Tetrachlorodibenzeno-p-dioxin	18.378	11.2	11.9	10.5	11.2	0.70	6.25
3	1,2,3,7,8-Pentachlorodibenzofuran	19.98	48	51	49	49.3	1.53	3.10
4	2,3,4,7,8-Pentachlorodibenzofuran	20.41	53	49	48	50.0	2.65	5.29
5	1,2,3,7,8-Pentachlorodibenzo-p-dioxin	20.62	52	48	47	49.0	2.65	5.40
6	1,2,3,4,7,8-Hexachlorodibenzofuran	22.53	43	47	48	46.0	2.65	5.75
7	1,2,3,6,7,8-Hexachlorodibenzofuran	22.63	42	44	44	43.3	1.15	2.66
8	2,3,4,6,7,8-Hexachlorodibenzofuran	23.12	47	48	42	45.7	3.21	7.04
9	1,2,3,7,8,9-Hexachlorodibenzofuran	23.26	44	42	46	44.0	2.00	4.55
10	1,2,3,4,7,8-Hexachlorodibenzo-p-dioxin	23.35	54	52	51	52.3	1.53	2.92
11	1,2,3,6,7,8-Hexachlorodibenzo-p-dioxin	23.67	46	45	45	45.3	0.58	1.27
12	1,2,3,7,8,9-Hexachlorodibenzo-p-dioxin	23.89	45	44	48	45.7	2.08	4.56
13	1,2,3,4,6,7,8-Heptachlorodibenzofuran	25.84	52	53	55	53.3	1.53	2.86
14	1,2,3,4,6,7,8-Heptachlorodibenzo-p-dioxin	27.27	51	42	44	45.7	4.73	10.35
15	1,2,3,4,7,8,9-Heptachlorodibenzofuran	27.85	48	52	51	50.3	2.08	4.14
16	Octachlorodibenzo-p-dioxin	32.86	99	97	96	97.3	1.53	1.57
17	Octachlorodibenzofuran	32.99	109	115	105	109.7	5.03	4.59

TABLE 4
Instrument precision using low concentrations of standard solution mixture of PCDDs/PCDFs

No.	Congener	R.T (min)	Calculated concentration (ng mL^{-1})					
			Trial 1	Trial 2	Trial 3	Average	SD	CV(%)
1	2,3,7,8-Tetrachlorodibenzofuran	18.06	4.4	4.2	5.3	4.6	0.59	12.65
2	2,3,7,8-Tetrachlorodibenzeno-p-dioxin	18.378	5.2	5.6	4.9	5.2	0.35	6.71
3	1,2,3,7,8-Pentachlorodibenzofuran	19.98	26	27	24	25.7	1.53	5.95
4	2,3,4,7,8-Pentachlorodibenzofuran	20.41	22	24	22	22.7	1.15	5.09
5	1,2,3,7,8-Pentachlorodibenzo-p-dioxin	20.62	24	21	26	23.7	2.52	10.63
6	1,2,3,4,7,8-Hexachlorodibenzofuran	22.53	29	28	27	28.0	1.00	3.57
7	1,2,3,6,7,8-Hexachlorodibenzofuran	22.63	26	23	22	23.7	2.08	8.80
8	2,3,4,6,7,8-Hexachlorodibenzofuran	23.12	27	25	29	27.0	2.00	7.41
9	1,2,3,7,8,9-Hexachlorodibenzofuran	23.26	26	24	25	25.0	1.00	4.00
10	1,2,3,4,7,8-Hexachlorodibenzo-p-dioxin	23.35	23	21	22	22.0	1.00	4.55
11	1,2,3,6,7,8-Hexachlorodibenzo-p-dioxin	23.67	26	26	27	26.3	0.58	2.19
12	1,2,3,7,8,9-Hexachlorodibenzo-p-dioxin	23.89	24	21	23	22.7	1.53	6.74
13	1,2,3,4,6,7,8-Heptachlorodibenzofuran	25.84	22	22	21	21.7	0.58	2.66
14	1,2,3,4,6,7,8-Heptachlorodibenzo-p-dioxin	27.27	24	25	21	23.3	2.08	8.92
15	1,2,3,4,7,8,9-Heptachlorodibenzofuran	27.85	26	25	23	24.7	1.53	6.19
16	Octachlorodibenzo-p-dioxin	32.86	55	54	51	53.3	2.08	3.90
17	Octachlorodibenzofuran	32.99	56	52	51	53.0	2.65	4.99

TABLE 5
PCDDs/Fs recoveries and method precision (CV %) for gallbladder tissue blanks spiked with high concentration standard solution mixture

No.	Congener	Average Concentration Found (N=3) ($\bar{x} \pm s$)	Average recovery %	CV(%)
	Spiked concentration: 20 ng g^{-1}			
1.	2,3,7,8-Tetrachlorodibenzofuran	21.23 ± 0.60	106	2.84
2.	2,3,7,8-Tetrachlorodibenzeno-p-dioxin	21.57 ± 0.25	108	1.17
	Spiked concentration: 100 ng g^{-1}			
3.	1,2,3,7,8-Pentachlorodibenzofuran	102.43 ± 1.91	102	1.87
4.	2,3,4,7,8-Pentachlorodibenzofuran	101.77 ± 1.37	102	1.34
5.	1,2,3,7,8-Pentachlorodibenzo-p-dioxin	102.43 ± 1.91	102	1.87
6.	1,2,3,4,7,8-Hexachlorodibenzofuran	99.43 ± 1.25	99	1.26
7.	1,2,3,6,7,8-Hexachlorodibenzofuran	100.10 ± 1.01	100	1.01
8.	2,3,4,6,7,8-Hexachlorodibenzofuran	95.77 ± 4.20	96	4.39
9.	1,2,3,7,8,9-Hexachlorodibenzofuran	97.77 ± 2.66	98	2.72
10.	1,2,3,4,7,8-Hexachlorodibenzo-p-dioxin	93.77 ± 5.85	94	6.24
11.	1,2,3,6,7,8-Hexachlorodibenzo-p-dioxin	96.43 ± 3.39	96	3.51
12.	1,2,3,7,8,9-Hexachlorodibenzo-p-dioxin	95.10 ± 4.53	95	4.76
13.	1,2,3,4,6,7,8-Heptachlorodibenzofuran	94.43 ± 5.1	94	5.41
14.	1,2,3,4,6,7,8-Heptachlorodibenzo-p-dioxin	97.10 ± 2.82	97	2.90
15.	1,2,3,4,7,8,9-Heptachlorodibenzofuran	102.77 ± 2.36	103	2.30
	Spiked concentration: 200 ng g^{-1}			
16.	Octachlorodibenzo-p-dioxin	202.67 ± 3.51	101	1.73
17.	Octachlorodibenzofuran	203.00 ± 2.65	102	1.30

found to be less than the accepted limit value for trace analysis (CV< 15%) [22].

Recoveries. Nine portions each of one gram sheep gallbladder tissue were used as blank samples representing the human gallbladder tissues and nine portions each of one gram weight of a mixture of sand mixed with cholesterol compound (sigma, 99%) were used as blank samples representing the human gallbladder stones.

Each of the nine blank samples was spiked with the one of the PCDDs/Fs standard solution mixtures to give the concentrations in three levels high, medium and low concentration.

The high concentration level was as follows: (20 ng/ml) for tetra-PCDDs/Fs, (100 ng/ml) for penta, hexa, hepta-PCDDs/Fs and (200 ng/ml) for octa-PCDDs/Fs. The medium concentration level

TABLE 6
PCDDs/Fs recoveries and method precision (CV %) for gallbladder stone blanks spiked with high concentration standard solution mixture

No.	Congener	Average Concentration Found (N=3) ($\bar{x} \pm s$)	Average recovery %	CV(%)
	Spiked concentration: 20 ng g^{-1}			
1.	2,3,7,8-Tetrachlorodibenzofuran	20.63 ± 0.65	103	3.15
2.	2,3,7,8-Tetrachlorodibenzeno-p-dioxin	20.97 ± 0.85	105	4.83
	Spiked concentration: 100 ng g^{-1}			
3.	1,2,3,7,8-Pentachlorodibenzofuran	103.00 ± 1.00	103	0.97
4.	2,3,4,7,8-Pentachlorodibenzofuran	102.33 ± 0.58	102	0.56
5.	1,2,3,7,8-Pentachlorodibenzo-p-dioxin	103.00 ± 1.00	103	0.97
6.	1,2,3,4,7,8-Hexachlorodibenzofuran	100.00 ± 2.00	100	2.00
7.	1,2,3,6,7,8-Hexachlorodibenzofuran	100.67 ± 1.53	101	1.52
8.	2,3,4,6,7,8-Hexachlorodibenzofuran	96.33 ± 5.13	96	5.33
9.	1,2,3,7,8,9-Hexachlorodibenzofuran	98.33 ± 3.51	98	3.57
10.	1,2,3,4,7,8-Hexachlorodibenzo-p-dioxin	94.33 ± 6.81	94	7.22
11.	1,2,3,6,7,8-Hexachlorodibenzo-p-dioxin	97.00 ± 4.36	97	4.49
12.	1,2,3,7,8,9-Hexachlorodibenzo-p-dioxin	95.67 ± 5.51	96	5.76
13.	1,2,3,4,6,7,8-Heptachlorodibenzofuran	95.00 ± 6.08	95	6.40
14.	1,2,3,4,6,7,8-Heptachlorodibenzo-p-dioxin	97.67 ± 3.79	98	3.88
15.	1,2,3,4,7,8,9-Heptachlorodibenzofuran	103.33 ± 1.53	103	1.48
	Spiked concentration: 200 ng g^{-1}			
16.	Octachlorodibenzo-p-dioxin	201.33 ± 2.08	101	1.03
17.	Octachlorodibenzofuran	201.67 ± 0.58	101	0.29

TABLE 7
PCDDs/Fs recoveries and method precision (CV %) for gallbladder tissue blanks spiked with medium concentration standard solution mixture

No.	Congener	Average Concentration Found (N=3) ($\bar{x} \pm s$)	Average recovery %	CV(%)
	Spiked concentration: 10 ng/g			
1.	2,3,7,8-Tetrachlorodibenzofuran	10.73 ± 0.15	107	1.42
2.	2,3,7,8-Tetrachlorodibenzeno-p-dioxin	10.80 ± 0.62	108	5.78
	Spiked concentration: 50 ng/g			
3.	1,2,3,7,8-Pentachlorodibenzofuran	53.33 ± 1.15	107	2.17
4.	2,3,4,7,8-Pentachlorodibenzofuran	52.00 ± 2.65	104	5.09
5.	1,2,3,7,8-Pentachlorodibenzo-p-dioxin	48.33 ± 6.03	97	12.47
6.	1,2,3,4,7,8-Hexachlorodibenzofuran	48.00 ± 6.00	96	12.50
7.	1,2,3,6,7,8-Hexachlorodibenzofuran	52.00 ± 2.65	104	5.09
8.	2,3,4,6,7,8-Hexachlorodibenzofuran	49.00 ± 4.36	98	8.90
9.	1,2,3,7,8,9-Hexachlorodibenzofuran	50.00 ± 3.61	100	7.21
10.	1,2,3,4,7,8-Hexachlorodibenzo-p-dioxin	47.00 ± 6.56	94	13.95
11.	1,2,3,6,7,8-Hexachlorodibenzo-p-dioxin	47.33 ± 5.86	95	12.38
12.	1,2,3,7,8,9-Hexachlorodibenzo-p-dioxin	47.67 ± 6.03	95	12.65
13.	1,2,3,4,6,7,8-Heptachlorodibenzofuran	48.33 ± 4.93	97	10.21
14.	1,2,3,4,6,7,8-Heptachlorodibenzo-p-dioxin	47.00 ± 6.08	94	12.94
15.	1,2,3,4,7,8,9-Heptachlorodibenzofuran	55.67 ± 2.08	111	3.74
	Spiked concentration: 100 ng/g			
16.	Octachlorodibenzo-p-dioxin	108.33 ± 3.06	108	2.82
17.	Octachlorodibenzofuran	101.67 ± 6.43	102	6.32

TABLE 8
PCDDs/Fs recoveries and method precision (CV %) for gallbladder stone blanks spiked with high concentration standard solution mixture

No.	Congener	Average Concentration Found (N=3) ($\overline{x} \pm s$)	Average recovery %	CV(%)
	Spiked concentration: 10 ng g^{-1}			
1.	2,3,7,8-Tetrachlorodibenzofuran	10.70 ± 0.20	107	1.87
2.	2,3,7,8-Tetrachlorodibenzeno-p-dioxin	10.77 ± 0.64	108	5.97
	Spiked concentration: 50 ng g^{-1}			
3.	1,2,3,7,8-Pentachlorodibenzofuran	52.33 ± 1.53	105	2.92
4.	2,3,4,7,8-Pentachlorodibenzofuran	51.00 ± 2.00	102	3.92
5.	1,2,3,7,8-Pentachlorodibenzo-p-dioxin	47.33 ± 4.73	95	9.98
6.	1,2,3,4,7,8-Hexachlorodibenzofuran	47.00 ± 4.58	94	9.75
7.	1,2,3,6,7,8-Hexachlorodibenzofuran	51.00 ± 2.00	102	3.92
8.	2,3,4,6,7,8-Hexachlorodibenzofuran	48.00 ± 2.65	96	5.51
9.	1,2,3,7,8,9-Hexachlorodibenzofuran	49.00 ± 2.00	98	4.08
10.	1,2,3,4,7,8-Hexachlorodibenzo-p-dioxin	46.00 ± 5.00	92	10.87
11.	1,2,3,6,7,8-Hexachlorodibenzo-p-dioxin	46.33 ± 4.16	93	8.99
12.	1,2,3,7,8,9-Hexachlorodibenzo-p-dioxin	46.67 ± 4.51	93	9.66
13.	1,2,3,4,6,7,8-Heptachlorodibenzofuran	47.33 ± 3.21	95	6.79
14.	1,2,3,4,6,7,8-Heptachlorodibenzo-p-dioxin	46.00 ± 4.36	92	9.48
15.	1,2,3,4,7,8,9-Heptachlorodibenzofuran	54.67 ± 3.51	109	6.42
	Spiked concentration: 200 ng g^{-1}			
16.	Octachlorodibenzo-p-dioxin	106.67 ± 3.79	107	3.55
17.	Octachlorodibenzofuran	100.00 ± 3.61	100	3.61

was as follows: (10 ng/ml) for tetra-PCDDs/Fs, (50 ng/ml) for penta, hexa, hepta-PCDDs/Fs and (100 ng/ml) for octa-PCDDs/Fs and the low concentration level was as follows: (5 ng/ml) for tetra-PCDDs/Fs, (25 ng/ml) for penta, hexa, hepta-PCDDs/Fs and (50 ng/ml) for octa-PCDDs/Fs. This process was done for three samples. All spiked samples were mixed thoroughly, extracted, cleaned-up and analyzed according to the above mentioned method. The recoveries were done in triplicate at different time. The average recoveries were calculated. The results are shown in Tables 5, 6, 7, 8, 9 and 10. All recoveries were found to be within the acceptable range for analysis of (80-120%) [22].

RESULTS

General. Thirty nine of each gallbladder tissues and gallbladder stones have been investigated for PCDDs/Fs). The average age for normal persons was 48 years (range from 21 to 77). The body mass index (BMI) was ranged from 15.88 to 39.52. The samples were chosen by convenience, and there was no statistically representative survey design used to select sampled persons. As such, no inference to the population of sick or healthy people can be made with confidence at this stage.

TABLE 9
PCDDs/Fs recoveries and method precision (CV %) for gallbladder tissue blanks spiked with low concentration standard solution mixture

No.	Congener	Average Concentration Found (N=3) ($\overline{x} \pm s$)	Average recovery %	CV(%)
	Spiked concentration: 5 ng g^{-1}			
1.	2,3,7,8-Tetrachlorodibenzofuran	4.67 ± 0.38	93	8.11
2.	2,3,7,8-Tetrachlorodibenzeno-p-dioxin	5.23 ± 0.15	105	2.92
	Spiked concentration: 25 ng g^{-1}			
3.	1,2,3,7,8-Pentachlorodibenzofuran	24.00 ± 2.65	96	11.02
4.	2,3,4,7,8-Pentachlorodibenzofuran	22.00 ± 2.65	88	12.03
5.	1,2,3,7,8-Pentachlorodibenzo-p-dioxin	23.33 ± 1.53	93	6.55
6.	1,2,3,4,7,8-Hexachlorodibenzofuran	23.67 ± 2.31	95	9.76
7.	1,2,3,6,7,8-Hexachlorodibenzofuran	24.00 ± 1.00	96	4.17
8.	2,3,4,6,7,8-Hexachlorodibenzofuran	22.67 ± 2.52	91	11.10
9.	1,2,3,7,8,9-Hexachlorodibenzofuran	23.67 ± 1.53	95	6.45
10.	1,2,3,4,7,8-Hexachlorodibenzo-p-dioxin	23.67 ± 3.21	95	13.58
11.	1,2,3,6,7,8-Hexachlorodibenzo-p-dioxin	23.33 ± 1.53	93	6.55
12.	1,2,3,7,8,9-Hexachlorodibenzo-p-dioxin	24.00 ± 1.73	96	7.22
13.	1,2,3,4,6,7,8-Heptachlorodibenzofuran	23.00 ± 2.00	92	8.70
14.	1,2,3,4,6,7,8-Heptachlorodibenzo-p-dioxin	24.67 ± 0.58	99	2.34
15.	1,2,3,4,7,8,9-Heptachlorodibenzofuran	25.67 ± 1.15	103	4.50
	Spiked concentration: 50 ng g^{-1}			
16.	Octachlorodibenzo-p-dioxin	43.67 ± 1.53	87	3.50
17.	Octachlorodibenzofuran	48.33 ± 5.51	97	11.39

TABLE 10
PCDDs/Fs recoveries and method precision (CV %) for gallbladder stone blanks spiked with high concentration standard solution mixture

No.	Congener	Average Concentration Found (N=3) ($\bar{x} \pm s$)	Average recovery %	CV(%)
	Spiked concentration: 5 ng g^{-1}			
1.	2,3,7,8-Tetrachlorodibenzofuran	4.63 ± 0.32	93	6.94
2.	2,3,7,8-Tetrachlorodibenzeno-p-dioxin	5.20 ± 0.20	104	3.85
	Spiked concentration: 25ng g^{-1}			
3.	1,2,3,7,8-Pentachlorodibenzofuran	23.67 ± 2.52	95	10.63
4.	2,3,4,7,8-Pentachlorodibenzofuran	21.67 ± 2.08	87	9.61
5.	1,2,3,7,8-Pentachlorodibenzo-p-dioxin	23.00 ± 1.00	92	4.35
6.	1,2,3,4,7,8-Hexachlorodibenzofuran	23.33 ± 2.08	93	8.92
7.	1,2,3,6,7,8-Hexachlorodibenzofuran	23.67 ± 0.58	95	2.44
8.	2,3,4,6,7,8-Hexachlorodibenzofuran	22.33 ± 2.08	89	9.32
9.	1,2,3,7,8,9-Hexachlorodibenzofuran	23.33 ± 1.15	93	4.95
10.	1,2,3,4,7,8-Hexachlorodibenzo-p-dioxin	23.33 ± 3.06	93	13.09
11.	1,2,3,6,7,8-Hexachlorodibenzo-p-dioxin	23.00 ± 1.00	92	4.35
12.	1,2,3,7,8,9-Hexachlorodibenzo-p-dioxin	23.67 ± 1.53	95	6.45
13.	1,2,3,4,6,7,8-Heptachlorodibenzofuran	22.67 ±1.53	91	6.74
14.	1,2,3,4,6,7,8-Heptachlorodibenzo-p-dioxin	24.33 ± 0.58	97	2.37
15.	1,2,3,4,7,8,9-Heptachlorodibenzofuran	25.33 ± 1.53	101	6.03
	Spiked concentration: 50 ng g^{-1}			
16.	Octachlorodibenzo-p-dioxin	47.33 ± 2.08	95	4.40
17.	Octachlorodibenzofuran	50.33 ± 2.08	101	4.14

Concentration of PCDDs/Fs in Gallbladder tissue and Gallbladder Stone Samples. For each sample three processes were performed: weighing, Soxhlet extraction and clean-up. The final extract was injected onto the GCMS column three times. A standard solution mixture of the 17 PCDDs/Fs congeners was injected every batch of samples (8 – 10 samples) to produce a chromatogram used for the calculation of the Relative Peak Area (RPA) for each standard compound ($RPA_{standard}$). In the same way, RPA for each compound in the unknown chromatogram ($RPA_{unknown}$) was compared with ($RPA_{standard}$) to find the concentration of (X) compound in the unknown sample, as shown in the following equation:

Conc. of (X) in unknown sample = Conc. of (X) in standard x (RPAunknown / RPAstandard)

Table 11 shows the analytical results of the gallbladder tissue samples presented as average ± standard deviation ($\bar{x} \pm s$) for each compound.

Tables 12 shows the analytical results of the gallbladder stone samples presented as average ± standard deviation ($\bar{x} \pm s$) for each compound.

Toxicity equivalencies were calculated for all samples by converting the concentrations to the ng TEQ/kg samples as follows:

TEQ (ng TEQ/kg) = Conc. of unknown sample µg/kg tissues TEF

The sum of toxicity equivalence concentrations are shown in the bottom of Table 11 for gallbladder tissue samples.

The sum of toxicity equivalence concentrations are shown in the bottom of Table 12 for gallbladder stone samples.

DISCUSSION

Octachlorodibenzo-*p*-dioxin has eight chlorine atoms which make it highest lipophilic in comparison with other PCDDs/Fs and it has a high abundance in the environment so it has the highest average concentrations in all samples in both tissues and stones which are 1134.49 µg/kg and 1645.39 µg/kg respectively. Eight PCDDs/Fs congeners have zero concentrations or less than the detection limit.

The TEQ values for each PCDDs/Fs congener in each gallbladder tissue and stone sample were calculated and the sums are presented in Tables 11 and 12 for tissues and stones respectively and summarized in Figures 1 and 2 for tissues samples and Figures 3 and 4 for the stones samples. The sum of TEQ of each PCDDs/Fs congener show that highest toxic PCDDs/Fs congeners in gallbladder tissues and stones were 1,2,3,7,8-pentachlorodibenzo-*p*-dioxin, 1,2,3,6,7,8-hexachlorodibenzo-*p*-dioxin and 1,2,3,7,8,9-hexachlorodibenzo-*p*-dioxin due to their high concentration and high Toxicity Equivalency Factors (TEF).

A comparison between the average concentration of each PCDDs/Fs in gallbladder tissue samples and gallbladder stone samples is presented in Figure 5. Most of the detected PCDDs/Fs congeners show an accumulation in the gallbladder stones more than in the gallbladder tissue samples.

The equilibrium in concentrations of PCDDs/Fs congeners between the gallbladder tissues and gallbladder stones can be represented by

the distribution coefficient Kd which can be calculated by dividing the total concentration of PCDDs/Fs congeners in all gallstone samples by the total concentration in the gallbladder tissue samples as shown in the following equation:

Kd = ∑concentration in stone / ∑ concentration in gallbladder stones.

The results are presented in Table 13 and Figure 6 which shows that the Kd values ranged between 0.86 for 1,2,3,4,7,8-Hexachlorodibenzo-*p*-dioxin and 2.96 for 1,2,3,4,6,7,8-Heptachlorodibenzofuran This slight variation is due to the chemical structure of each congener which determine its lipophilic character and its ability to bind stronger to the fat or to the cholesterol. The type of gallbladder stone which determine its cholesterol content while the obesity which determine the percent of fat in the gallbladder tissue sample.

TABLE 11
Concentration of PCDDs/Fs (µg kg^{-1} tissue) in gallbladder tissue samples (G-1 - G-13)

	Average Concentration (µg kg^{-1} tissue ($\bar{x} \pm s$)												
Congener Nr.*(TEF)**	G-1	G-2	G-3	G-4	G-5	G-6	G-7	G-8	G-9	G-10	G-11	G-12	G-13
1 (0.1)	< MDL***	87.2 ± 5.2	< MDL	45.7 ± 5.0	49.4 ± 6.7	< MDL	44.3 ± 5.5	68.6 ± 8.2	< MDL	35.4 ± 3.5	35.0 ± 1.7	46.4 ± 5.2	48.9 ± 4.8
2 (1.0)	< MDL	< MDL	< MDL	< MDL	< MDL	< MDL	< MDL	< MDL	< MDL	< MDL	< MDL	< MDL	< MDL
3 (0.03)	< MDL	< MDL	< MDL	< MDL	< MDL	< MDL	< MDL	< MDL	< MDL	< MDL	< MDL	< MDL	< MDL
4 (0.3)	< MDL	< MDL	< MDL	< MDL	< MDL	< MDL	< MDL	< MDL	< MDL	< MDL	< MDL	< MDL	< MDL
5 (1.0)	< MDL	< MDL	< MDL	< MDL	< MDL	< MDL	< MDL	< MDL	28.8 ±1.7	< MDL	< MDL	< MDL	49.7 ± 3.4
6 (0.1)	< MDL	< MDL	< MDL	< MDL	< MDL	< MDL	< MDL	< MDL	29.5 ± 1.4	< MDL	< MDL	< MDL	< MDL
7 (0.1)	< MDL	< MDL	< MDL	< MDL	< MDL	< MDL	< MDL	< MDL	< MDL	< MDL	< MDL	< MDL	< MDL
8 (0.1)	< MDL	< MDL	< MDL	< MDL	< MDL	< MDL	< MDL	< MDL	< MDL	< MDL	< MDL	< MDL	< MDL
9 (0.1)	< MDL	< MDL	< MDL	< MDL	< MDL	< MDL	< MDL	< MDL	< MDL	< MDL	< MDL	< MDL	< MDL
10 (0.1)	< MDL	42.7 ± 4.7	< MDL	< MDL	< MDL	35.7 ± 4.4	< MDL	49.3 ± 1.7	26.9 ± 3.0	< MDL	< MDL	< MDL	27.9 ± 3.7
11 (0.1)	< MDL	101.8 ± 5.4	104.1 ± 14.1	94.3 ± 5.3	304.5 ± 35.8	80.9 ± 6.3	< MDL	238.7 ± 23.4	< MDL	206.3 ± 24.4	111.2 ± 10.4	229.1 ± 21.7	243.6 ± 26.3
12 (0.1)	< MDL	52.3 ± 2.6	157.6 ± 12.6	178.7 ± 21.9	132.6 ± 6.4	61.2 ± 3.6	79.8 ± 10.7	30.9 ± 4.1	59.7 ± 5.9	48.5 ± 6.2	54.6 ± 7.7	< MDL	50.1 ± 3.2
13 (0.01)	< MDL	132.7 ± 8.0	55.8 ± 4.5	< MDL	60.6 ± 7.9	120.7 ± 5.4	83.6 ± 7.6	113.7 ± 10.3	35.4 ± 1.6	31.9 ± 1.9	< MDL	< MDL	< MDL
14 (0.01)	< MDL	386.1 ± 39.2	328.9 ± 40.4	132.5 ± 13.8	336.1 ± 41.1	194.7 ± 26.5	88.4 ± 6.1	120.4 ± 9.1	76.6 ± 6.4	283.9 ± 17.8	93.9 ± 8.8	341.0 ± 30.5	113.3 ± 13.3
15 (0.01)	< MDL	< MDL	< MDL	< MDL	< MDL	< MDL	< MDL	< MDL	< MDL	< MDL	< MDL	< MDL	< MDL
16 (0.0003)	289 ± 19.5	252..4 ± 30.1	1428.5 ± 108.9	3294.3 ± 200.3	1224.9 ± 166.2	292.5 ± 33.0	144.1 ± 18.8	489.8 ± 24.9	1896.2 ± 207.5	1607.2 ± 179.4	1720.5 ± 185.6	1884.0 ± 246.2	462.8 ± 23.7
17 (0.0003)	< MDL	< MDL	< MDL	< MDL	< MDL	< MDL	< MDL	< MDL	< MDL	< MDL	< MDL	< MDL	< MDL
∑PCDDs/Fs	289.0	1046.2	2074.8	3745.6	2135.5	785.6	440.2	1111.3	2153.0	2213.2	2015.1	2500.5	1000.3
∑TEQs ng TEQ/kg	0.4	33.6	30.4	34.2	55.1	21.0	14.2	41.2	42.1	32.7	21.5	31.5	88.4

* Congener numbers as in Table 2; ** TEF = Toxicity Equivalency Factor *** MDL = method detection limit

TABLE 12
Concentration of PCDDs/Fs (µg kg^{-1} tissue) in gallbladder stone samples (S-1 - S-13)

	Average Concentration (µg kg^{-1} tissue ($\bar{x} \pm s$)												
Congener Nr.* (TEF**)	S-1	S-2	S-3	S-4	S-5	S-6	S-7	S-8	S-9	S-10	S-11	S-12	S-13
1 (0.1)	67.3 ± 5.4	53.5 ± 5.6	26.2 ± 1.4	60.2 ± 2.1	< MDL	35.7 ± 4.4	28.4 ± 1.3	< MDL	84.8 ± 4.7	33.25 ± 1.4	32.1 ± 1.6	14.9 ± 0.5	35.5 ± 4.4
2 (1.0)	< MDL***	< MDL	< MDL	< MDL	< MDL	< MDL	< MDL	< MDL	< MDL	< MDL	< MDL	< MDL	< MDL
3 (0.03)	< MDL	< MDL	< MDL	< MDL	< MDL	< MDL	< MDL	< MDL	< MDL	< MDL	< MDL	< MDL	< MDL
4 (0.3)	< MDL	< MDL	< MDL	< MDL	< MDL	< MDL	< MDL	< MDL	< MDL	< MDL	< MDL	< MDL	< MDL
5 (1.0)	< MDL	65.7 ±5.0	< MDL	< MDL	59.3 ± 6.8	60.0 ± 3.9	47.8 ± 5.7	< MDL	< MDL	< MDL	< MDL	51.8 ± 6.0	< MDL
6 (0.1)	< MDL	< MDL	< MDL	< MDL	< MDL	38.8 ± 1.3	< MDL	< MDL	< MDL	< MDL	< MDL	< MDL	< MDL
7 (0.1)	< MDL	< MDL	< MDL	< MDL	< MDL	< MDL	< MDL	< MDL	< MDL	< MDL	< MDL	< MDL	< MDL
8 (0.1)	< MDL	< MDL	< MDL	< MDL	< MDL	< MDL	< MDL	< MDL	< MDL	< MDL	< MDL	< MDL	< MDL
9 (0.1)	< MDL	< MDL	< MDL	< MDL	< MDL	< MDL	< MDL	< MDL	< MDL	< MDL	< MDL	< MDL	< MDL
10 (0.1)	< MDL	< MDL	< MDL	< MDL	< MDL	< MDL	< MDL	28.8 ± 3.3	< MDL	54.82 ± 1.8	< MDL	< MDL	< MDL
11 (0.1)	54.1 ± 11.5	108.7 ± 8.9	282.7 ± 28.3	215.1 ± 20.1	42.5 ± 4.9	64. 8± 6.3	< MDL	33.0 ± 1.6	207.1 ± 18.5	99.8 ± 6.6	< MD	< MDL	46.8 ± 3.1
12 (0.1)	58.6 ± 6.4	258.7 ± 22.8	66.7 ± 7.9	99.6 ± 8.4	196.8 ± 8.9	182.6 ± 20.1	281.4 ± 33.3	244.9 ± 14.2	74.2 ± 2.3	61.13 ± 5.1	114.7 ± 13.7	278.4 ± 18.2	40.2 ± 3.6
13 (0.01)	109.4 ± 8.1	232.3 ± 25.5	217.9 ± 24.8	151.2 ± 15.7	90.1 ± 8.9	132.2 ± 10.0	140.8 ± 15.8	241.1 ± 24.5	78.5 ± 4.7	193.8 ± 6.8	321.9 ± 22.9	104.1 ± 10.2	74.7 ± 6.2
14 (0.01)	107.4 ± 10.0	295.4 ± 11.0	327.3 ± 36.7	127.9 ± 10.3	180.8 ± 18.1	104.9 ± 7.9	166.7 ± 6.6	106.9 ± 9.9	472.6 ± 30.2	260.4 ± 19.4	54.0 ± 6.5	213.2 ± 21.3	238.6 ± 17.2
15 (0.01)	< MDL	< MDL	< MDL	< MDL	< MDL	< MDL	< MDL	< MDL	< MDL	< MDL	< MDL	< MDL	< MDL
16 (0.0003)	1652.0 ± 133.0	2354.8 ± 215.5	1332.2 ± 150.3	1039.5 ± 54.4	1574.5± 93.2	1057.1 ± 38.4	1827.3 ± 139.8	663.9 ± 75.6	1628.7 ± 69.6	1333.6 ± 79.1	1603.9 ± 55.8	2485.9 ± 333.9	1107.0 ±
17 (0.0003)	< MDL	< MDL	< MDL	< MDL	< MDL	< MDL	< MDL	< MDL	< MDL	< MDL	< MDL	< MDL	< MDL
∑PCDDs/Fs	2048.8	3369.0	2253.6	1693.5	2143.9	1676.3	2492.4	1318.6	2617.3	2036.7	2126.4	3133.4	1542.8
∑TEQs ng TEQ/kg	20.7	113.7	18.0	21.2	86.4	94.9	82.4	34.4	42.6	29.8	18.9	85.0	15.7

* Congener numbers as in Table 2; ** TEF = Toxicity Equivalency Factor; *** MDL = method detection limit

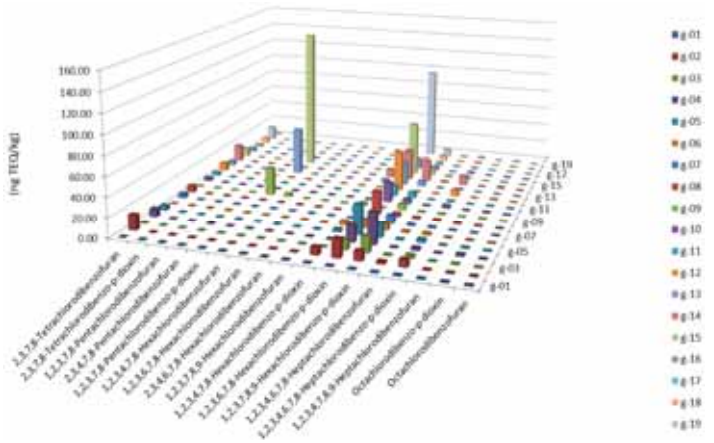

FIGURE 1
TEQ of PCDDs/Fs (ng TEQ kg^{-1}) in gallbladder tissues for samples (G-1 to G-20)

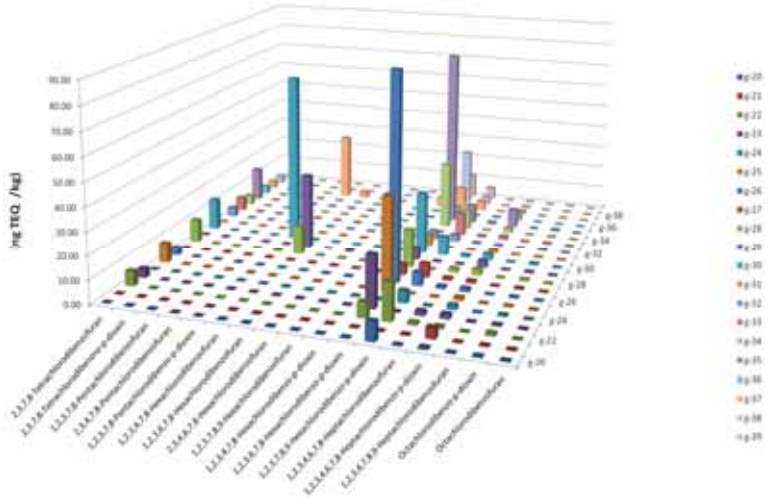

FIGURE 2
TEQ of PCDDs/Fs (ng TEQ kg^{-1}) in gallbladder tissues for samples (G-20 to G-39)

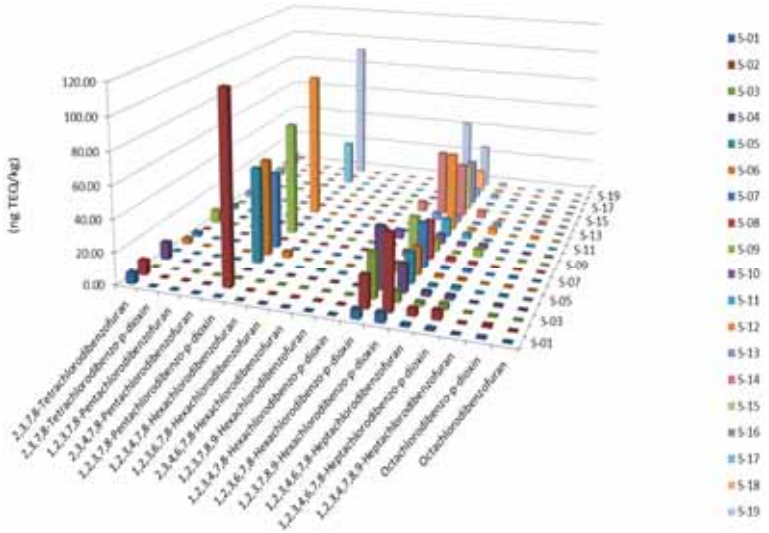

FIGURE 3
TEQ of PCDDs/Fs (ng TEQ kg^{-1}) in gallbladder stone for samples (S-1 to S -20)

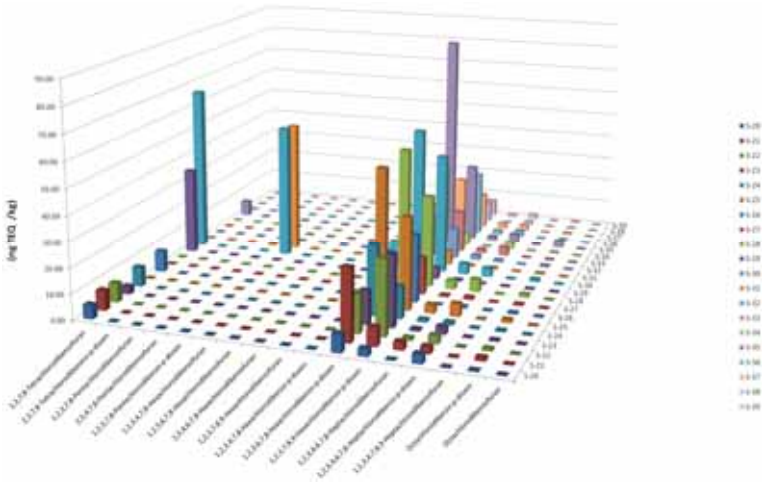

FIGURE 4
TEQ of PCDDs/Fs (ng TEQ kg^{-1}) in gallbladder stone for samples (S-20 to S-39)

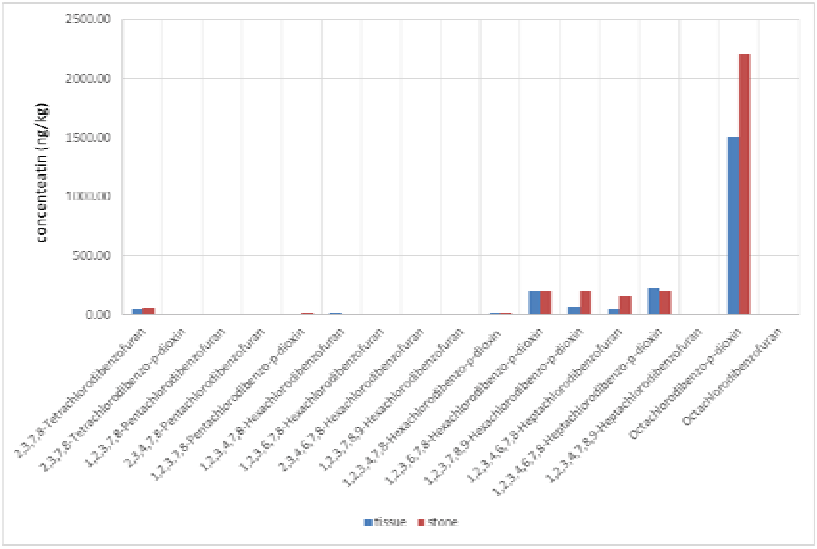

FIGURE 5
Comparison of the average concentration of each PCDDs/Fs (µg kg^{-1}) in the gallbladder tissues (blue) and gallbladder stones (red).

TABLE 13
Distribution coefficient (Kd) of PCDDs/Fs in gallbladders tissue and stone

No.	PCDDs/Fs congener	∑ PCDDs/Fs in gallbladder stone	∑ PCDDs/Fs in gallbladder tissues	Kd
1.	2,3,7,8-Tetrachlorodibenzofuran	2270.88	1417.40	1.60
2.	2,3,7,8-Tetrachlorodibenzeno-p-dioxin	0.00	0.00	0.00
3.	1,2,3,7,8-Pentachlorodibenzofuran	0.00	0.01	0.00
4.	2,3,4,7,8-Pentachlorodibenzofuran	0.00	0.00	0.00
5.	1,2,3,7,8-Pentachlorodibenzino-p-dioxin	520.23	231.61	2.25
6.	1,2,3,4,7,8-Hexachlorodibenzofuran	38.83	456.27	0.09
7.	1,2,3,6,7,8-Hexachlorodibenzofuran	0.00	0.00	0.00
8.	2,3,4,6,7,8-Hexachlorodibenzofuran	0.00	0.00	0.00
9.	1,2,3,7,8,9-Hexachlorodibenzofuran	0.00	0.00	0.00
10.	1,2,3,4,7,8-Hexachlorodibenzino-p-dioxin	365.52	423.80	0.86
11.	1,2,3,6,7,8-Hexachlorodibenzino-p-dioxin	5612.77	5887.61	0.95
12.	1,2,3,7,8,9-Hexachlorodibenzino-p-dioxin	5709.82	1992.58	2.87
13.	1,2,3,4,6,7,8-Heptachlorodibenzofuran	4785.65	1617.93	2.96
14.	1,2,3,4,6,7,8-Heptachlorodibenzino-p-dioxin	6278.03	6803.77	0.92
15.	1,2,3,4,7,8,9-Heptachlorodibenzofuran	0.00	0.00	0.00
16.	Octachlorodibenzino-p-dioxin	64170.04	44245.23	1.45
17.	Octachlorodibenzofuran	0.00	0.00	0.00

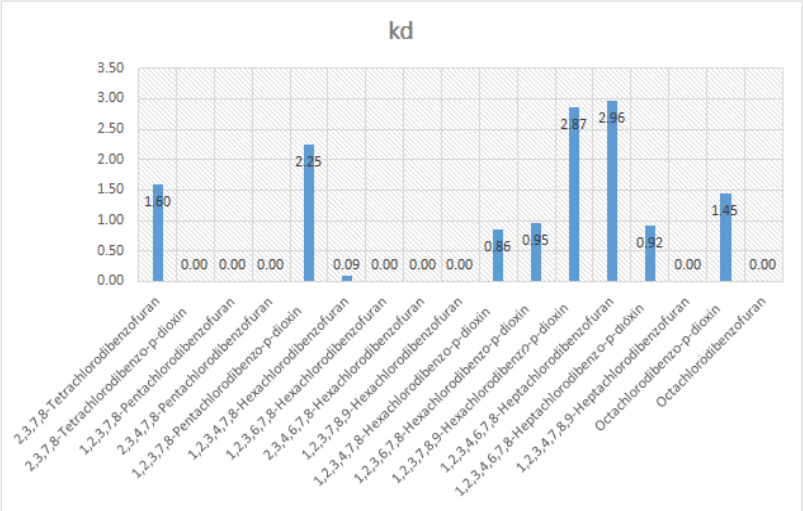

FIGURE 6
Distribution coefficient (K_d) values of PCDDs/Fs between gallbladder stones and gallbladder tissues

TABLE 14
Classification of samples according BMI and the concentrations of PCBs in each class

Group of BMI (kg m^{-2})	Symbol	Samples in each class	Average Concentration in gallbladder Tissue samples (μg kg^{-1})	Average Concentration in gallbladder Stone samples (μg kg^{-1})	Average Concentration in all samples (μg kg^{-1})
0 - 18.5	L (low)	1,6,7,8,13,16,17,20,21,29,31, 33,36,38,39	1838	1730	3568
18.5 -25	M (medium)	5,10,11,18,22,23,24,25,26,27, 32,34,37	1786	2192	3978
> 25	H (high)	2,3,4,9,12,14,15,19,28,30,35	2391	3111	5502

To study the factors which affect the concentrations of PCDDs/Fs in the 39 samples of gallbladder tissues and gallbladder stones, many correlations trails between the concentrations and many factors were done and showed that there was no significant correlation between the concentration with age, sex, living place, smoking and healthy state. But it shows a significant correlation with obesity which is represented by the body mass index (BMI).

The samples were classified to three groups depending on their BMI as shown in Table 14. The average concentrations of PCDDs/Fs in gallbladder tissues, stones and in both tissues and stones (total)

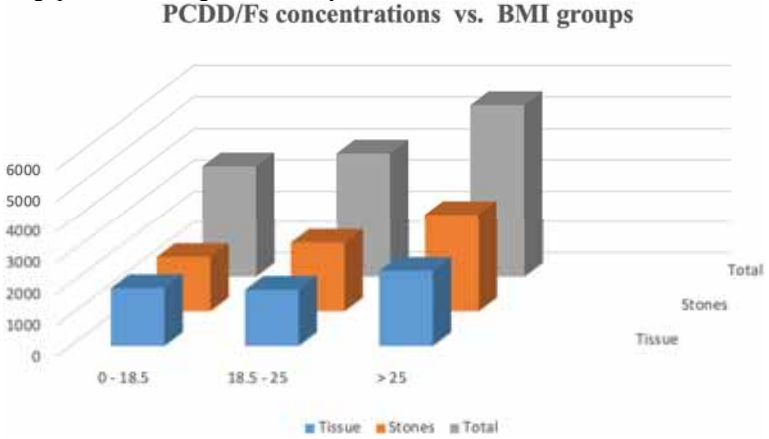

FIGURE 7
Average concentration of PCDDs/Fs in gallbladder stones, tissues and for both versus BMI groups

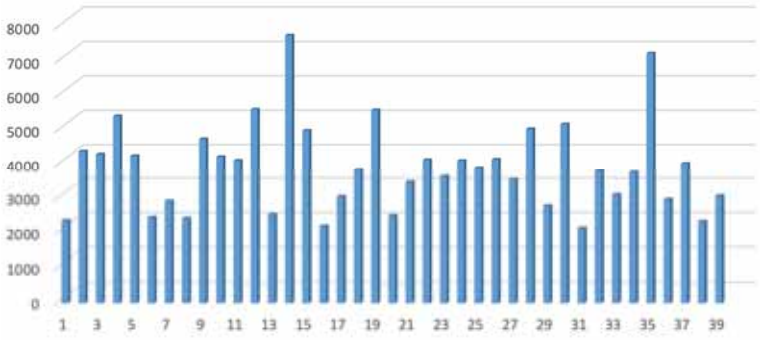

FIGURE 8
Total concentrations (ng/kg) in both gallbladder tissues and stones of all PCDDs/Fs congeners in each sample.

TABLE 15
Comparison between the results (ng kg^{-1} tissue) of this study and the findings of others [25]

Congeners found	Gallbladder Tissue			Gallbladder Stones			Results of Muto *et al.*, 1991		
	Mean	Range	Frequency	Mean	Range	Frequency	Mean	Range	Cause of Death
1,2,3,7,8-Pentachlorodi-benzo-*p*-dioxin	46.3	28.8 – 82.7	12%	52.3	29.2 – 65.7	20.5%	11.0 4.6	1.8 – 41.8 -	-- Hepatoma
1,2,3,6,7,8-Hexachlorodi-benzo-*p*-dioxin	203.7	31.0 – 892.9	93.3%	157	31.0 – 473.5	93.3%	1.5 2.3	0 – 1.5 -	- Hepatoma
1,2,3,4,6,7,8-Heptachlorodi-benzo-*p*-dioxin	178.3	30.1 - 533	97.4	252	29.0 – 2262.4	84.6%	99.6 90.3 79.5	- - 20.7 – 108 - -	Hepatoma Cancer Goiter Hepatoma
Octachlorodi-benzo-*p*-dioxin	1075.1	117.5 – 1896.2	100%	1646.9	424.6 – 4229.5	100%	132 81.8 101 225	24.8 – 225 - - - - - -	Cancer Goiter Hepatoma Hepatoma Cancer Goiter

for each group were calculated, and the correlation with BMI is shown in Figures 7.

The total concentrations of all PCDDs/Fs in gallbladder tissues and stones in each sample were calculated and shown in Figure 8 which shows high concentrations in the samples 14, 19, 30 and 35. Of these, samples 19 and 30 were diagnosed as a dysplasia cases (the presence of cells of an abnormal type within a tissue, which may signify a stage preceding the development of cancer), so these compounds can affect the cells and change their nature and then can be carcinogenic [23-24].

In the literature, there is very limited number of publications deals with PCDDs/Fs in gallbladder tissues, and nothing about gallbladder stones. Muto et al. [25] studied the tissue distribution of 2,3,7,8-chlorine substituted dibenzo-*p*-dioxins in 11 patients who died of cancer. The concentrations of some PCDDs/Fs he found in gallbladder tissues are summarized in Table 15 and compared to the findings of this study. Table 15 shows that the concentrations found in this study are much higher than what Muto and his research group [29] found, nevertheless there was no deaths among the donors of the 39 samples. It is also attention drawing that the congeners 1,2,3,6,7,8-hexachlorodibenzino-*p*-dioxin and 1,2,3,4,6,7,8-heptachlorodibenzo-*p*-dioxin are present at high frequency, numerically 97.4% and 100% respectively.

CONCLUSIONS

[1] All PCDDs/Fs that exist in the gallbladder tissue can exist in the gallbladder stone too which mean both gallbladder stones and gallbladder tissues can be good indicator for PCDDs/Fs exposure.

[2] Distribution coefficients of PCCDs/Fs between gallbladder tissues and gallbladder stones are close to one, and its deviation from one depend on the amounts of cholesterol in stone and the amounts of fat in tissue.

[3] Significant correlation between body mass index (BMI) and concentration of PCDDs/Fs take place in both gallbladder tissues and gallbladder stones, so that as BMI increase the concentrations of PCDDs/Fs also increase due to the increasing in the bioaccumulation tendency.

[4] Dysplasia correlated to the concentrations of PCDDs/Fs, the higher the concentration, the higher is the probability to have dysplasia which means these pollutants can be one of the most factors that induce the formation of dysplasia or cancer.

ACKNOWLEDGEMENTS

The authors would like to thank the Deanship for academic research at the University of Jordan for the financial support.

All procedures performed in studies involving human participants were in accordance with the ethical standards of the institutional and/or national research committee and with the 1964 Helsinki declaration and its later amendments or comparable ethical standards.

REFERENCES

[1] Shahawi, M.S., Hamza, A., Bashammakh, A.S., Al-Saggaf, W.T. (2010) An overview on the accumulation, distribution, transformations, toxicity and analytical methods for the monitoring of persistent organic pollutants. Talanta. 80, 1587 - 1597.

[2] Ritter, L., Solomon, K.R., Forget, J.A. (1995) Review of selected persistent organic pollutants. The International Programme on Chemical Safety (IPCS), Geneva, Switzerland.

[3] Andersen, M., Mills, J., Gargas, M., Kedderis, L., Birnbaum, L.S., Neubert, D., Greenlee, W. (1993) Modeling receptor-mediated processes with dioxin: Implications for pharmacokinetics and risk assessment. Risk Analysis. 13(1), 25-36.

[4] Moussaoui, Y., Tuduri, L., Kerchich, Y., Meklati, B.Y., Eppe, G. (2012) Atmospheric concentrations of PCDD/Fs, dl-PCBs and some pesticides in northern Algeria using passive air sampling. Chemosphere. 88, 270 – 277.

[5] Lohmann, R., Jones, K.C. (1998) Dioxins and furans in air and deposition: a review of level levels, behavior and processes. Science of the Total Environment. 219, 53 – 81.

[6] Alawi, M., Masad, M., Al-Hussaini, M. (2018) Comparative study of persistent organic pollutants (POPs) (chlorinated pesticides, PCBs, and dioxins/furans) concentrations in cancer-affected human organs with those of healthy organs. Environ Monit Assess. 190, 470.

[7] Fiedler, H. (1993) The handbook of environmental chemistry. Persistent organic pollutants.3rd ed. Chapter 1. Springer-Verlag, Berlin / Heidelberg.

[8] Pereira, MS. (2004) Polychlorinated dibenzo-*p*- dioxins (PADD), dibenzofurans (PCDF) and polychlorinated biphenyls (PCB): main sources, environmental, behavior and risk to man and biota. Quim Nova. 27(6), 934 - 943.

[9] Mahnke, K. (1997) "Investigations on the foration and distribution of organic pollutants (PCDD/Fs, PCBs and PAHs) in the tropics and subtropics" , PhD Thesis, Organic Chemistry Institute, Eberhard-Karls Universität Tübingen, Germany[in German].

[10] Recognizing the Symptoms of a Gallbladder Attack. Florida Medical Center. June, 26, 2015. https://www.floridamedicalclinic.com/blog/recognizing-the-symptoms-of-a-gallbladder-attack

[11] Housset, C., Chrétien, Y., Debray, D., Chignard, N. (2016) Functions of the Gallbladder. Comprehensive Physiology. 6: 1549 – 1577.

[12] Crawford, M. (2013) Biliary Pain: Work up and management in general practice Australian Family Physician. 42(7), 458-461

[13] Kratzer, W., Mason, R.A., Kachele, V. (1999) Prevalence of gallstones in sonographic surveys worldwide. Journal of Clinical Ultra sound. 27, 1–7.

[14] Saqib, A., Shaikh, S.S., Sodhar, J.M. (2014) GALL STONES; Frequencies of gall stones in the patients attending surgical OPD at Isra Hospital Hyderabad. The Professional Med J. 21(2), 386-390.

[15] Everhart, J.E., Yeh, F., Lee, E.T., Hill, M.C., Fabsitz, R., Howard, B.V., Welty, T.K. (2002) Prevalence of gallbladder disease in American Indian populations: Findings from the strong Heart Study. Hepatology. 35(6), 1507-12.

[16] Channa, N.A., Khand, F.D., Bhanger, M.I., Leghari, M.H. (2004) Surgical incidence of cholelithiasis in Hyderabad and adjoining areas (Pakistan). Pakistan Journal of Medical Science. 20(1), 13 – 7.

[17] Khand, F.D. (1997) Cholelithiasis in Southern Sindh (Pakistan): Incidence and composition of gallstones. Specialist. 13, 263 – 70.

[18] Beckingham, I.J. (2001) Gallstone disease. British Medical Journal. 322, 91- 4.

[19] Channa, N.A. (2008) Gallstone disease: A review. Pak Armed Forces Med J. 2.

[20] Kitamura, K., Nagao, M., Yamada, T., Sunaga, M., Hata, J., Watanaba, S. (2001) Dioxin in bile in relation to those in human liver and blood. J. Toxicol. Sci. 65(5), 327 – 336.
[21] Hagenmaier, H. (1987) The final report to the research and investigation plan, burden of the environment with Dioxins. Environment Ministry Baden-Wuertemberg. Ed Tübingen, Germany [in German].
[22] Gonzalez, A., Herrador, M., Asuero, A.G. (2010) Intra-laboratory assessment of method accuracy (trueness and precision) by using validation standards. Talanta. 82, 1995-1998.
[23] Genuis, S.J., Kiln, K.L. (2015) Toxicant exposure and bioaccumulation: A common and potentially reversible cause of cognitive dysfunction and dementia. Behavioral Neurology. 2015, Article ID 620143, 10 p.
[24] Williams, G.M. (1983) Genotoxic and epigenetic carcinogens: their identification and significance. Annals of the New York Academy of Sciences. 407(1), 328 – 333.
[25] Muto, H., Shinada, M., Abe, T., Takizawa, Y. (1991) The tissue distribution of 2,3,7,8- chlorine substituted-*p*-dioxins in humans who died of cancer. Life Science. 48(17), 1645–1657.

Received: **30.11.2019**
Accepted: **26.01.2020**

CORRESPONDING AUTHOR

Mahmoud Alawi
School of Science,
Department of Chemistry,
University of Jordan,
Amman, 11942 – Jordan

E-mail: alawima@ju.edu.jo

© by PSP Volume 29 – No. 04A/2020 pages 3072-3083 Fresenius Environmental Bulletin

EXPERIMENTAL STUDY ON RESISTIVITY CHARACTERISTICS OF PURPLE SOIL IN DRYING SHRINKAGE PROCESS IN THREE GORGES RESERVOIR AREA, CHINA

Zhengcheng Wang[1], Xin Tang[2,*], Haitao Mao[1,3], Jiwei Shen[1], Tingqiang Zhou[1]

[1]College of Civil Engineering, Chongqing Three Gorges University, Chongqing 404100, China
[2]Key Laboratory of Coalbed Methane Resources and Reservoir Formation Process, Ministry of Education, China University of Mining and Technology, Jiangsu Xuzhou, 221008, China
[3]Institute of Water Conservancy and Hydroelectric Power, Wuhan University, Wuhan 430072, China

ABSTRACT

Purple soil is widely distributed in the Three Gorges Reservoir area, and its resistivity can represent the basic parameters of soil conductivity. In recent years, due to the frequent occurrence of arid climate, soil moisture evaporation and soil shrinkage and deformation have been caused. We conducted a series of indoor drying experiments to explore the resistivity characteristics of the purple soil during shrinkage. The test results show that: (1) The changes in soil mass and water content during the dry shrinkage process can be divided into rapid evaporation and deceleration rate stage. The soil mass and water content in the early drying period decrease rapidly, and then the decline rate slows down. (2) The change in the axial / transverse shrinkage rate of the soil can also be divided into a rapid shrinkage stage and a deceleration rate stage, and the slope of the curve in the rapid shrinkage phase is larger. (3) AC resistivity decreases with the increase of current frequency, water content, and zinc content. With the development of drying, tensile stress is generated in the soil, which promotes contraction and deformation of the soil. (4) The conductive path of soil is divided into the first conductive path (soil and water), the second conductive path (water), the third conductive path (soil). The main reason for the lack of cracks in the soil is due to the large thickness of Vaseline and the soil. The research results can provide theoretical support for the determination of soil resistivity under dry shrinkage conditions.

KEYWORDS:
Purple soil, resistivity, water content, drying shrinkage, current frequency

INTRODUCTION

Purple soil is widely distributed in the Three Gorges Reservoir area [1]. Its electrical resistivity is a basic parameter for expressing soil conductivity, and it can reflect the basic physical properties of land conductivity to a certain extent. The important method to study soil microstructure, physical and mechanical properties, sand liquefaction, and soil pollution characteristics is resistivity test, which has important theoretical significance and application value [2-3]. In recent years, the influencing factors and correlations of soil resistivity have become hot topics of research. Scholars at home and abroad have mainly carried out a lot of research work on soil microstructure, physical and mechanical properties, soil pollution, etc[4]. YOON Gil Lim and other studies show that the soil resistivity is closely related to soil parameters, such as salt content, clay content, water content, plasticity index, sensitivity, gravity, shear strength and porosity[5]. Long Michael and others believe that the soil resistivity is most significantly affected by the salt content of pore fluid[6]. Friedman SP and others proposed that the resistivity of soil is affected by factors such as soil particle morphology environment and so on [7].

In recent years, due to the impact of global climate change, extreme arid climates have occurred frequently, and the soil will shrink and deform under drought conditions. Scholars have also carried out related research on resistivity characteristics during soil shrinkage. Luo Xiaowei and others studied the change law of the resistance value during the initial saturation of the soil sample during the drying process[8]. It was concluded that the resistance value of the soil body slowly decreased and then increased slowly during the initial stage of drying and evaporation. The resistance value has a tendency to increase suddenly. Jones G and others can monitor the development of fractures in the later stage, and measure the resistivity of the soil and detect the location of fractures by means of resistivity tomography (ERT) technology[9]. L.

Mol and others resistivity tomography (ERT) technology explored the movement of capillary water in cracks and pores during the drying of sandstone[10]. Gareth Jones and others applied resistivity tomography (ERT) technology to flood dikes in order to detect the crack development of the dam. Studies have shown that the smaller the electrode spacing, the higher[11].

In summary, scholars have mainly explored the influencing factors of soil resistivity, including soil moisture content and heavy metal content. In addition, resistivity tomography (ERT) technology is mainly used to monitor the occurrence and development of cracks in rock and soil, providing technical support for dam seepage control and rock and soil slope reinforcement. However, the research on the resistivity characteristics of the dry shrinkage process of the purple soil in the Three Gorges Reservoir area (without cracks) is rare, and a lot of research work is still needed. Therefore, in order to further explore the resistivity characteristics of the purple soil in the shrinkage process of the Three Gorges Reservoir area, this article takes the purple soil in the Three Gorges Reservoir area as the research object, combines the basic soil test in the laboratory, and uses the two-electrode method to conduct a resistivity test and discuss the soil quality, soil water content, soil shrinkage, resistivity change in time series.

MATERIALS AND METHODS

Soil Sampling and Characterization. The test raw material is purple soil (Figure 1), which is taken from the bank slope of the Yangtze River. The slope angle of the slope measured by geological compass is 38º, and the tendency is SW152º. The purple soil particles are angular, flaky, or fine powder.

FIGURE 1
Undisturbed purple soil

Due to the large inclination of the mudstone slope, no signs of vegetation and farming were seen on the slope, there were no human settlements and obvious roads nearby, and the probability of human disturbance was low. The color of the purple soil is purple, and it is easy to disintegrate in water. After the screening test, coarse soil particles with a particle size larger than 4.75 mm were discarded, and purple soil particles with a particle size smaller than this were the object of this study. The particle grading curve of test soil is shown in Figure 2.

The liquid-plastic limit of soil samples was determined by means of the SYS digital liquid-plastic limit tester. The water content was determined by drying method:

$$w = \frac{20 - (38.96 - 20)}{38.96 - 20} = 5.5\% \quad (1)$$

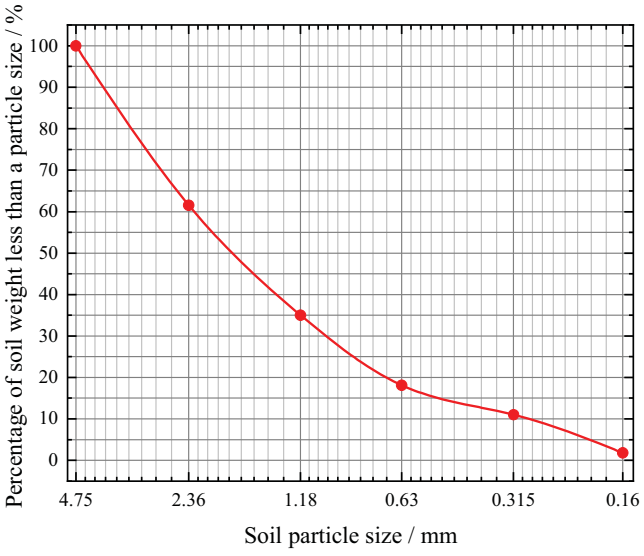

FIGURE 2
The grading curve of test soil

TABLE 1
Basic properties of original purple soil

Water content / %	Dry density / (g·cm^{-3})	Relative density	pH	Liquid limit	Total soil Zn / mg·kg^{-1}
5.5	1.32	2.646	6.2	32.8%	78

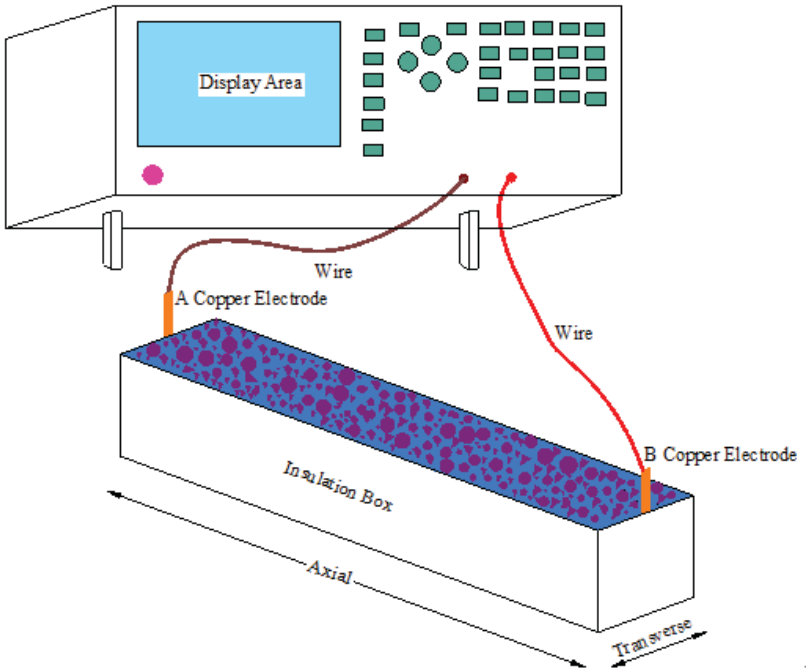

FIGURE 3
Test device diagram of alternating current resistivity of purple soil

The cone liquid limiter is used to determine the liquid limit of the soil sample which equal to 32.8%. And the dry density(1.32g/cm^3) can be determined through tests. The relative density Gs of the soil sample was measured by the pycnometer method:

$$G_s = \frac{m_d}{m_{bw} + m_d - m_{bws}} G_{wT} = 2.464 \quad (2)$$

The pH value was measured by a soil pH tester; the total Zn content in the soil sample was determined to be 78 mg/kg^{-1} by using Hitachi Z-5000, NaOH melting method, atomic absorption spectrophotometry. The basic properties of purple soil are listed in Table 1.

Experiment Device. In this paper, the two-electrode method was used to carry out the purple soil resistivity test. The test device is shown in Figure 3.

In this experiment, a custom-shaped strip-shaped insulation box was used. The material was polymethyl methacrylate, and its inner length, inner width, and inner height were 20.00, 4.00, and 4.00 cm, respectively. The purple soil is placed in the box, and a rectangular copper electrode sheet is arranged at each end, the size is the same as the internal section of the insulation box, and the distance between the electrodes A and B is l_{AB} = 20cm, which is used to contact the purple soil and propagate current. Connect the LCR digital bridge through the wire to test the impedance R of the purple soil [12].

Material Preparation. The incompletely weathered stones and other debris in the purple soil were screened out and dried in an oven at a drying temperature of 105 °C and a drying time of 24 h. The dried purple soil was placed in a bag seal. The Communiqué of the First National Survey of Pollution Sources shows that livestock and poultry farming and aquaculture are the largest sources of zinc, at 4756.94 and 105.63 t, respectively. There are animal husbandry and aquaculture bases around the study area. Farm manure, the soil in this area is susceptible to zinc pollution. Therefore, this article takes zinc pollution as an example to analyze the effect of heavy metal pollution on the resistivity of purple soil.

Sample preparation and packing: (1) Based on the test soil sample liquid limit w_L = 32.7%, set the initial moisture content of the purple soil to 28% (saturated state). (2) Preparation of contaminated soil: according to soil environmental quality stand-

ards, set 8 kinds of zinc content c, which are 0 (not added as a control group), 20, 40, 80, 160, 320, 640 mg·kg^{-1}; The specific setting method is as follows: According to the set mix ratio, add zinc sulfate solution and distilled water to the purple soil, mix it evenly and then install a sealed bag to prevent the influence of moisture in the air. (3) Put the electrode sheet in the insulation box, and weigh the masses 143.1, 143.3, 142.9, 144.1, 142.8, 143.8, 143.5, and 143.3g, respectively, to calculate the mass of soil in the insulation box. (4) The prepared soil sample is packed into the box with the help of a geo-knife, and the soil is compacted by vibration, and the gas in the pores of the soil is excluded, and the surface of the soil is smoothed. The prepared soil sample is shown in Figure 4.

FIGURE 4
Prepared purple soil sample

Experiment Process. (1) Determine of the current frequency f. Some studies have shown that when the AC resistivity of soil is measured, the measurement results within a frequency of 1000 Hz are not much different [13]. In this paper, 100Hz is selected as the basic frequency of the purple soil resistivity test, and subsequent experiments are conducted to further explore the resistivity characteristics of the purple soil during the dry shrinkage process with different metal contents.

(2) Apply Vaseline to the side and bottom of the insulation box, install copper electrode pads, select purple soil with water content w = 28%, zinc content c = 0 ~ 640 mg·kg^{-1}, and install it into the insulation box.

(3) Measure of soil mass. The measurement period on August 21 is from 11:00 to 23:00, and the measurement is performed every 3 hours, for a total of 5 times. The measurement period from August 22 to August 27 is from 5:00 to 23:00, with an interval of 3 It is measured once every hour for a total of seven times. The measurement period from August 28 to August 29 is from 5:00 to 23:00, and it is measured every six hours for a total of four times. The measurement time on August 30 is 11:00.

(4) Measure of the impedance value R. The two-electrode method was used to measure the soil electrical impedance at different times, and the measurement time points were consistent with step 2.

(5) Measure soil shrinkage. The axial and lateral shrinkage values of the soil were measured with a vernier caliper. The measurement time node was 11:00 from August 21st to August 30th, and the shrinkage rate was further calculated.

(6) Substituting the impedance value R into equation (1), the AC resistivity ρ of the purple soil is calculated.

$$\rho = R\frac{A}{L} \tag{3}$$

Where ρ is the AC resistivity of the purple soil, Ω·m; is the contact area between the copper electrode sheet and the soil body, m^2; In the calculation process, the distance L between the electrode pieces and the contact area A between the copper electrode piece and the soil body are gradually reduced as the soil body shrinks.

RESULTS AND DISCUSSION

Temperature Change During Drying Process. An electronic thermometer was used to measure the laboratory temperature during the experiment. The temperature change curve during the soil shrinkage test is shown in Figure 5. It can be seen from the figure that the temperature fluctuates between 24 and 40 °C, and the fluctuation range is large. The maximum temperature difference is 16 °C and the average temperature is 32.5 °C. Existing studies have shown that soil resistivity is significantly affected by temperature and will decrease when temperature rises. Soil resistivity results measured at different temperatures need to be corrected to a certain reference temperature [14].

In order to reduce the influence of temperature on the resistivity of purple soil, the test results of resistivity at different times are uniformly modified to resistivity ρ_{18} (hereinafter referred to as resistivity) at 18°C. The temperature correction formula is the formula.

$$\rho_{18} = \left[1+\alpha(T-18)\right]\rho \tag{4}$$

Where T is the experimental temperature, it is the AC resistivity of purple soil, ρ_{18} is the resistivity at 18°C, and α is the experimental constant 0. 025ºC^{-1}.

Soil Mass and Moisture Content During Drying Process. Figure 6 shows the change curve of soil mass during drying. As the drying time increases, the liquid water between the pores of the solid particles evaporates and the mass of the sample decreases. The evaporation of purple soil can be divided into two stages, the rapid evaporation stage (5:00, August 21, 2019 ~ 5:00, August 27, 2019) and the deceleration rate evaporation stage (5:00,

August 27, 2019 ~ 11:00, August 30, 2019). It is not difficult to see that in the rapid evaporation stage, the zinc content c=0 mg·kg^{-1} corresponds to the fastest decline in soil mass, and the zinc content c = 640 mg·kg^{-1} corresponds to the slowest decline in soil mass. In addition, the decrease in the rapid evaporation stage is significantly higher than that in the deceleration rate evaporation stage. Taking the zinc content c = 80 mg·kg^{-1} as an example, the stage-1 and stage-2 decrease by 108.4 and 9.2g, respectively, and the decreases are 17.46% and 1.8%. From the beginning to the end of the experiment, the zinc content c = 0 ~ 640 mg·kg^{-1} corresponds to a decrease in soil mass from 620.9 to 621 g to 501.5 to 506.1 g, a decrease of 18.49% to 19%.

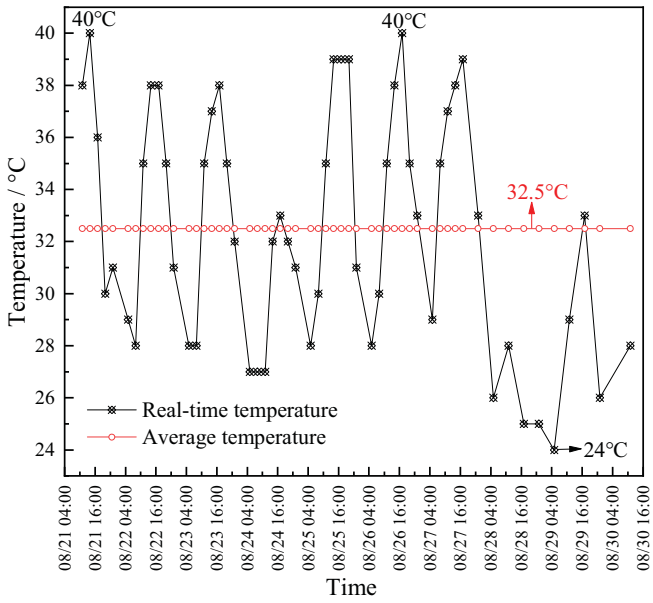

FIGURE 5
Variation of environment temperature during drying process

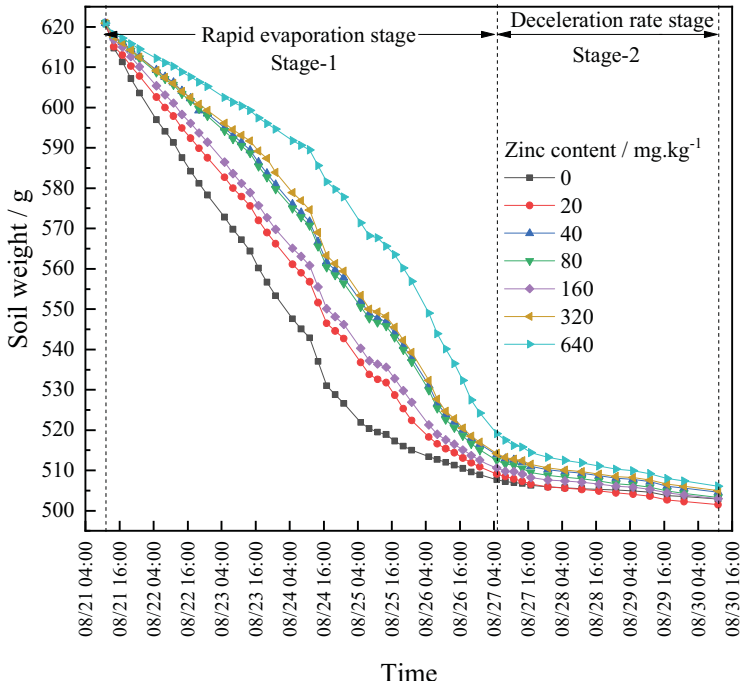

FIGURE 6
Change curves of soil mass

Based on the mass of the soil, the mass of the insulating box and the electrode pad, and the initial moisture content of the soil, the moisture content of the soil at each time point is calculated. the change laws of water content and soil mass are similar, and will not be described in detail.

Soil Shrinkage During Drying Process. The lateral shrinkage and axial shrinkage of the soil were measured at each time node, and the equation (5) was taken to calculate the shrinkage of the soil.

$$\eta = \frac{l_1 - l_2}{l_1} \times 100\% \tag{5}$$

Where η is the shrinkage rate, l_1 is the length before the soil body shrinks, and l_2 is the length after the soil body shrinks. The change curve of purple soil shrinkage is shown in Figure 7.

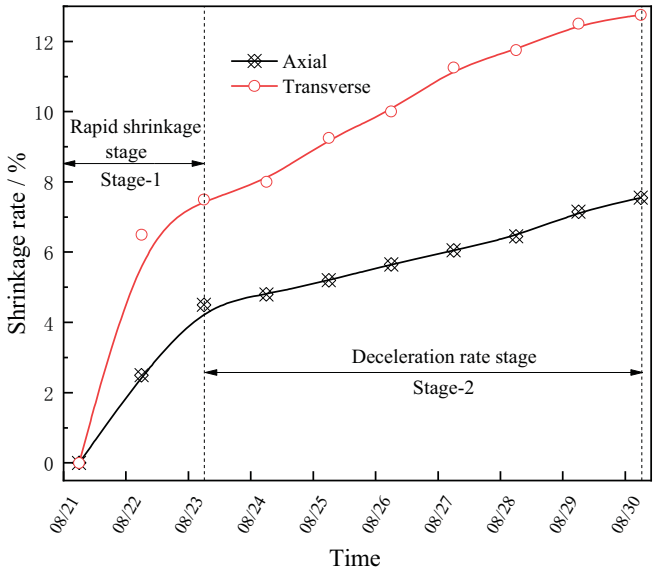

FIGURE 7
Change curves of purple soil shrinkage rate

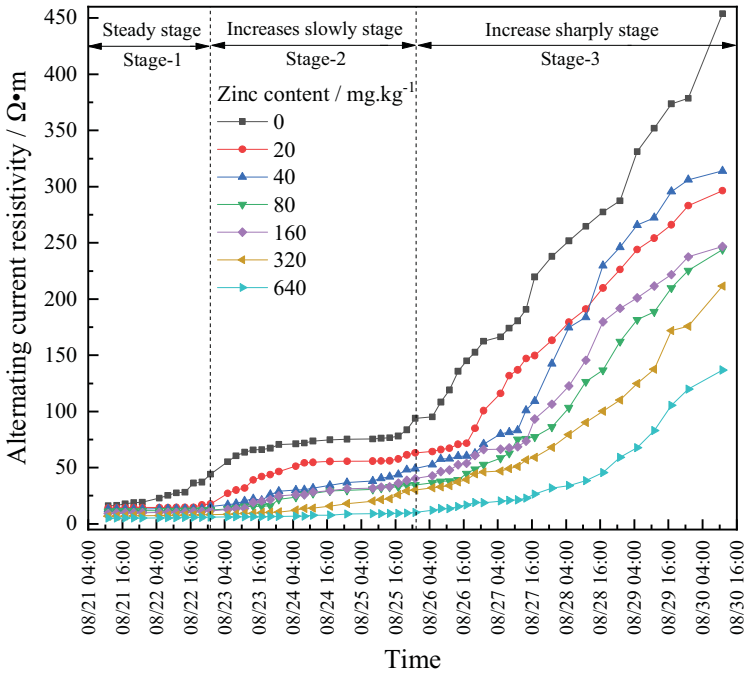

FIGURE 8
Change curves of alternating current resistivity

In the experiment, an image monitoring system was used to obtain photos of soil samples shrinking at different times. It was observed that the experiment began at 9 hours, the soil contracted axially, and a certain gap was created between the electrode sheet and the insulation box. At the beginning of the experiment, the soil contracted laterally and isolated from the insulation box.

It can be concluded from Figure 7 that the axial and transverse shrinkage of the soil body is 0 to 1.51, 0 to 0.51 cm, and the axial shrinkage is significantly higher than the transverse. The axial and transverse shrinkage rates of purple soil are 0% to 7.55% and 0% to 12.755%, and the transverse shrinkage rates are larger. The soil shrinkage process can be divided into two stages: the rapid shrinkage stage (11:00, August 21, 2019 ~ 11:00, August 23, 2019) and the deceleration rate stage (11:00, August 23, 2019 ~ 11:00, August 30, 2019), the slope of the curve for stage-1 is significantly higher than that for stage-2.

Variation of Soil Resistivity During Drying Process. The soil resistance values measured at different time nodes are converted into resistivity for analysis. The specific results are shown in Figure 8.

Analysis of Figure 8 shows that the resistivity of the samples increases with the increase of the drying time in the time sequence, and can be divided into three phases: the steady stage (11:00, August 21, 2019 ~ 23:00, August 22, 2019), increase slowly stage (5:00, August 23, 2019 ~ 23:00, August 25, 2019) and increase sharply stage (5: 00 August 26, 2019 ~ 23:00, August 30, 2019). The slope of the resistivity curve is smaller in the initial stage, and then gradually increases. In the gradual phase (stage-1), only the curve with c = 0 ~ 640 mg·kg^{-1} fluctuated greatly, with an increase of 174.87%; the other curves changed gently (c = 20 ~ 640 mg·kg^{-1}) with an increase of 11.76% to 28.37%. In the increase slowly stage (stage-2), the resistivity gradually increases in time sequence, with an increase of 66.93% to 249.07%. In the increase sharply stage (stage-3), the resistivity at each zinc content increased significantly, with an increase of 360.88% to 1032.54%. From the beginning to the end of the experiment, the zinc content c = 0 ~ 640 mg·kg^{-1} increased the resistivity ofs the soil by 2016.3% ~ 3073.61%. The soil sample did not crack during the experiment, so it did not increase sharply at a certain time. The reason why the soil body only shrunk and did not crack will be further analyzed later.

With the help of the AC test impedance value, the effects of electrochemical effects and electrokinetic phenomena can be effectively avoided, and the experimental errors can be greatly reduced. However, the current frequency has a great influence on the resistivity test, and the existing research results have not yet reached a corresponding conclusion. The influence of the current frequency on the resistivity is worth exploring. When the water content in the experiment is w = 28%, the soil sample has just been made (11:00, August 21, 2019). The AC resistivity at different current frequencies f is measured experimentally. ρ, its change curve is shown in Figure 9.

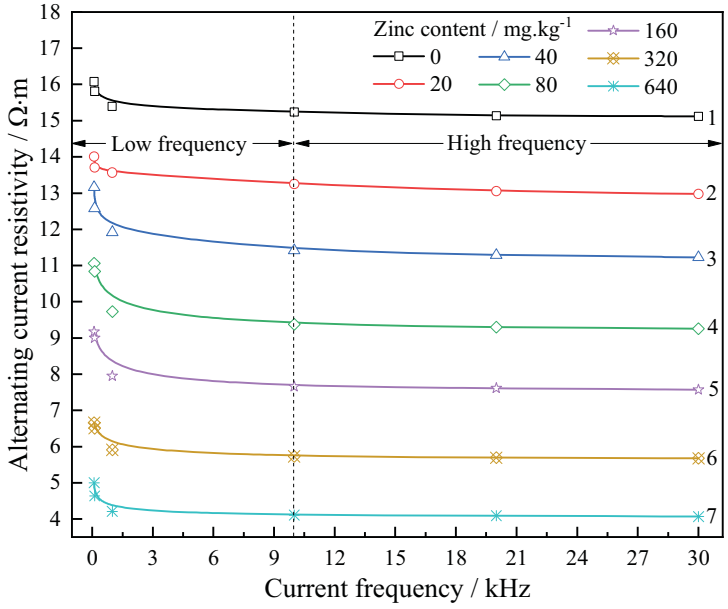

FIGURE 9
Change curves of alternating current resistivity with current frequency

It can be obtained from Figure 9 that the change laws of the curves are similar. The AC resistivity ρ decreases with the increase of the current frequency f. The initial decrease rate is faster and then gradually stabilizes. The reason is that the electrical impedance of water increases with frequency. The decrease of the resistivity of purple soil will decrease with the increase of current frequency. Taking curve 4 (zinc content c = 80 mg·kg^{-1}) as an example, the AC resistivity gradually decreased from 11.06 Ω·m to 9.25 Ω·m, a decrease of 16.37%; in the low frequency band (f = 0.1 ~ 10 kHz), the current frequency is reduced by 99%, the average slope of the curve is k = -0.17; in the high frequency band (f = 10 ~ 30 kHz), the current frequency is reduced by 66.67%, the average slope of the curve is k = -0.006, and the curve is low The average slope of the frequency band is significantly higher than that of the high frequency band. It can be seen that the resistivity ρ is greatly affected by the AC frequency f in the low frequency band, and is relatively small in the high frequency band.

With the progress of the experiment, the water content between the pores of the purple soil particles gradually increased, resulting in a gradual decrease in the water content (which has been specifically analyzed in Figure 7), which in turn affected the soil resistivity. In order to find out the influence of soil moisture content on resistivity, the curve of soil resistivity versus moisture content is shown in Figure 10.

Analysis of Figure 10 shows that the change laws of the curves are similar. The AC resistivity gradually increases with the decrease of the water content w and can be divided into four stages: the influence stable stage-1 (w = 22% ~ 28%), the influence expansion stage (w = 17% ~ 22%), the influence stable stage-2 (w = 6% ~ 17%) and the influence increase sharply stage (w = 3.39% ~ 4.33%). The changes of each curve are relatively gentle in the influence stable stage-1 and the influence stable stage-2, the resistivity increase rate increases during the impact expansion phase, and the resistivity increases sharply during the impact surge phase. Taking zinc content c = 80 mg·kg^{-1} as an example, when the water content is reduced from 28% to 22.08%, the AC resistivity increases from 11.06Ω·m to 14.07Ω·m, an increase of 27.2%; When the water content was reduced from 21.73% to 17.65%, the AC resistivity increased from 15.49Ω·m to 27.14Ω·m, an increase of 75.19%; when the water content was reduced from 15.53% to 6.19%, the AC resistivity changed from 29.18Ω·m increased to 52.74Ω·m, an increase of 80.77%; when the water content was reduced from 5.65% to 3.76%, the AC resistivity increased from 58.48Ω·m to 244.09Ω·m, an increase of 317.36%.

In addition to the current frequency f and water content w affecting the AC resistivity of purple soil, the zinc content also has an effect. In order to ascertain the effect of the zinc content c on the AC resistivity, the variation curve of the soil AC resistivity is shown in Figure 11. It can be obtained from Figure 11 that the change laws of the curves are similar. The AC resistivity gradually decreases with the increase of the zinc content. It can be divided into two stages: the decrease sharply stage and decrease slowly stage. The reduction speed of stage-1 is significantly higher than stage-2. Taking the purple soil at the time point of 23:00, 2019/08/22 as an example, when the zinc content c increased from 0 mg·kg^{-1} to 20 mg·kg^{-1}, the AC resistivity ρ changed from 44.18Ω·m. It decreases to 15.34 Ω·m with a decrease of 65.29%; when the zinc content c increases from 40 mg·kg^{-1} to 640 mg·kg^{-1}, it increases 15 times, and the AC resistivity ρ decreases from 15.34Ω·m. As small as 5.97Ω·m, the decrease is 61.1%; the reason for the analysis is that after the zinc content increases, the conductive ion content in the water increases, which is conducive to conduction and reduces the resistivity.

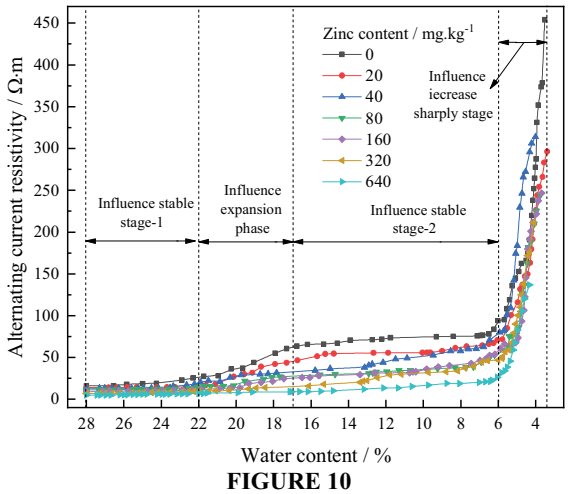

FIGURE 10
Change curves of alternating current resistivity with water content

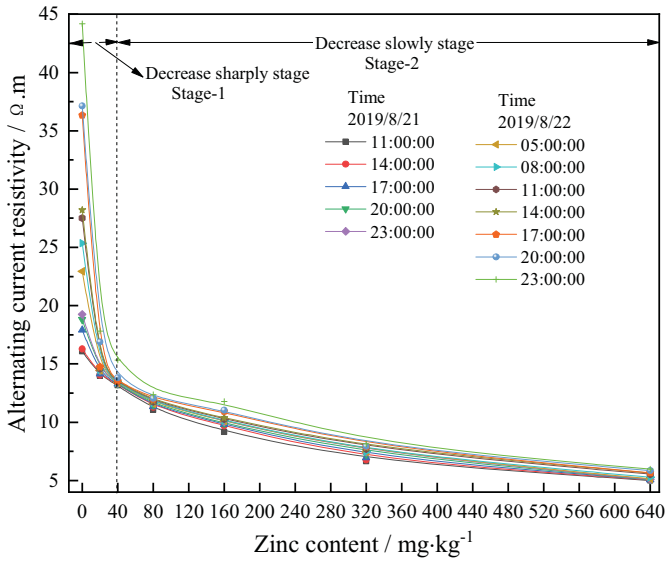

FIGURE 11
Change curves of alternating current resistivity with current frequency and zinc content

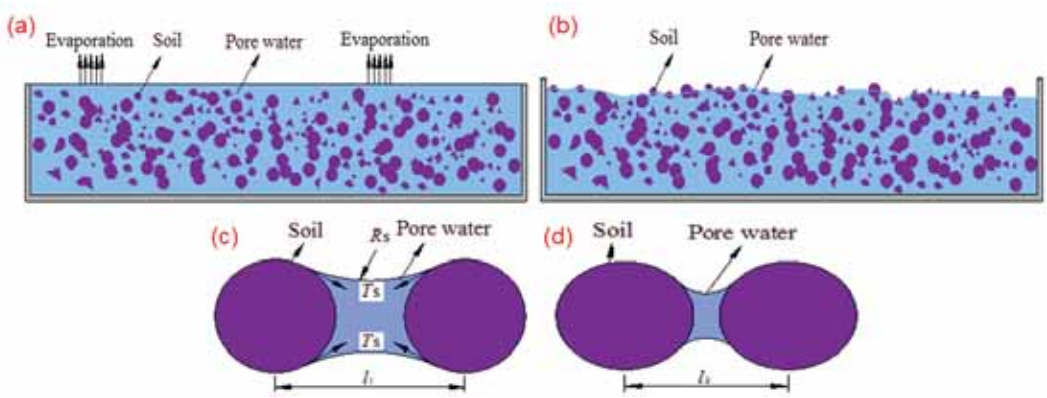

FIGURE 12
The diagram of purple soil
Notices: (a) Saturated, (b) Water evaporation, (c) Capillary effect, (d) Decrease of distance between soil particles

Principle Analysis. (1) Dry Shrinkage Principle. The shrinking process of purple soil is shown in Figure 12.

When the initially saturated mud-like purple soil sample is dried and evaporated, the soil water will continuously evaporate from the sample surface and be lost (Figures 12 (a, b)). Due to the capillary action between the soil pores, the pores Water forms a meniscus between soil particles, that is, a shrink film, and there is a surface tension on the surface of the shrink film (Figure 12 (c)) [15]. According to the theory of unsaturated soil mechanics, the matrix suction in the soil is the difference between the pore gas pressure and the pore water pressure. The relationship between the matrix suction and the surface tension of the shrinkage film is as follows:

$$u_m = u_a - u_w = \frac{2T_s \cos\theta}{r} = \frac{2T_s}{R_s} \quad (6)$$

In the formula, u_m is the matrix suction in kPa; u_a is the pore gas pressure in kPa; u_m is the pore water pressure in kPa; T_s is the surface tension of the shrink film in kPa; r is the radius of the capillary; θ is the capillary water Contact angle; R_s is the radius of curvature of the shrink film.

During the drying process, the water in the lower soil is continuously migrated to the surface to maintain evaporation. The evaporation of water causes the pore water pressure to decrease, which in turn causes the matrix suction to increase [16], and generates tensile stress in the soil. The soil pores are reduced, and the soil particles are closer to each other (Figure 12 (d)). Macroscopically, the soil is axially and laterally contracted.

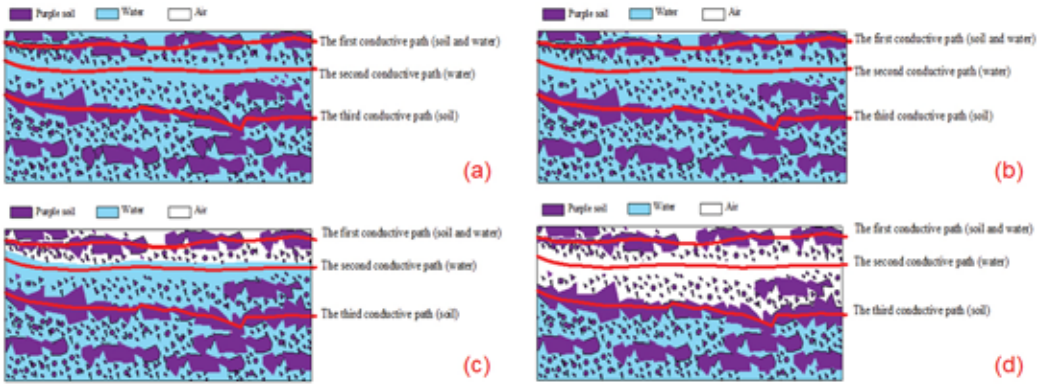

FIGURE 13
Conduction diagram of purple soil
Notices: (a) initial stage, (b) steady stage, (c) increase slowly stage, (d) increase sharply stage.

Principle of Soil Conduction. The schematic diagram of purple soil conductivity is shown in Figure 13.

The conductive path of the purple soil sample is divided into three types: the first conductive paths (the conductive medium is soil and water), the second conductive paths (all conductive media are water), the third conductive paths (all conductive media are soil). At the initial stage (Figure 13 (a)), the soil is saturated, the water content of the soil is high, the liquid phase in the pores is fully connected, and all three types of paths can conduct electricity. At this time, the soil resistivity is the smallest. As the surface moisture of the sample evaporates, the moisture content of the soil decreases, and all resistivities are flat (Figure 13 (b)). This is mainly because the hydration film on the surface of clay particles becomes thinner due to the decrease of the water content, the electrical conductivity of the electric double layer is enhanced, and the contact area between the clay particles is increased, which in turn leads to the enhanced conductivity of the clay minerals. The pores are filled with conductive pore water. With further evaporation of the water, especially from saturation to unsaturated, the pores between the particles are replaced by more air, and the resistance value of the soil sample gradually increases (Figure 13 (c)); at this time as the water in the first conductive paths is replaced by air, the resistivity is bound to increase. When the water content of the sample continues to decrease, the resistivity increases rapidly (Figure 13(d)); this is mainly because after the water content of the sample reaches the critical water content, an effective continuous conductive water film cannot be formed between the soil particles; At this time, the conductive water medium in the first and second conductive paths is replaced by air, so the resistance is significantly increased.

Discussion. (1) Soil Samples are not Cracked. A large number of studies have shown that as the soil gradually shrinks, corresponding cracks will occur in the soil [17-18], but the soil did not crack in this experiment, and the reason will be discussed in the following. The purple soil mass showed overall shrinkage during the drying process, and the shrinkage area was mainly reflected at the edge of the soil mass without cracks.

Friction between soil layers is an important prerequisite for restricting the development of fractures. During the evaporation process, if the shrinkage and deformation of the soil are limited, then the soil particles cannot be close to each other. As the evaporation loss continues, the shrinking film curvature radius continues to decrease, and the matrix suction continues to increase, so the tensile stress continues to increase and cannot Release and stress concentration occurs. When the internal tensile stress of the soil mass exceeds the tensile strength of the soil mass, cracks will be generated, and the energy accumulated by the tensile stress will be released. If there is a significant friction at the interface of the soil layer, it will inevitably limit the shrinkage and deformation of the soil, and then affect the tensile stress concentration and crack development process. Under the condition of the same thickness of the soil, the greater the interface roughness, the stronger the limit on the shrinkage and deformation of the soil layer, so the faster the tensile stress concentration, the shorter the time required to reach the tensile strength and cracking of the soil. However, in this experiment, the surface of the insulation box is smooth and flat, and petroleum jelly is applied around it (with typical lubrication characteristics). At this time, a relatively ideal and smooth interface is formed, so there is only minimal friction at the soil layer interface, and the soil shrinkage is not restricted No soil stress concentration can occur, and no soil cracking conditions are available.

Soil thickness has a significant impact on crack development. When the tensile stress generated during the dry shrinkage of the soil is greater than the tensile strength of the soil, tensile cracks

will be generated in the soil. The expression of tensile stress is as follows

$$\sigma = \frac{f(\mu) \times L}{d} \quad (7)$$

In the formula, σ is the tensile stress; d is the thickness of the soil; $f(\mu)$ is a function of the friction coefficient, which depends on the roughness of the interface; L is the length of the action. It is not difficult to see from formula (5) that the thicker the soil, the greater the tensile force required for the soil layer to crack. Under the same rough interface conditions, the greater the thickness of the soil, the more difficult it is to develop cracks. Because the thickness of the soil layer is large and the friction between the soil layer interfaces is very small in the experiment, only a small tensile stress can be generated inside the soil body, which cannot exceed the tensile strength of the soil body, so there is no crack development.

(2) Soil Samples are Long Strips. Polarization is really easy to occur near the electrode sheet, which has a great influence on the measurement of resistivity. The entire conduction process can be regarded as two transition sections that are prone to polarization and are connected in series with the normal section. The current conduction sequence is: transition section A, normal section, and transition section B. The transition section is located at both ends of the soil sample and directly contacts the copper electrode pads. The normal section is located in the middle section of the soil sample. Therefore, the soil sample to be measured should be made into a long strip to reduce the error caused by the polarization effect on the resistivity measurement.

CONCLUSIONS

(1) In order to reduce the influence of temperature on the soil resistivity test, the soil resistivity results should be corrected to a certain reference temperature. The change curve of soil mass and moisture content during the drying shrinkage process can be divided into rapid evaporation phase and deceleration rate phase. The soil mass and moisture content decrease rapidly during the initial drying period, and then gradually decrease. From the beginning to the end of the experiment, the soil mass decreased by 18.49% ~ 19%.

(2) The change of soil shrinkage rate can be divided into the rapid evaporation stage and the deceleration rate evaporation stage. The slope of the curve in the rapid evaporation stage is significantly higher than that in the deceleration evaporation stage. In addition, the axial shrinkage (0% to 7.55%) is lower than that in the transverse direction (0% to 12.755%).

(3) The change of the resistivity of the soil can be divided into the steady stage, increase slowly stage and increase sharply stage, and the increase rates of each phase are 11.76 to 174.87%, 66.93% to 249.07%, 360.88% to 1032.54%. The slope of the resistivity curve is smaller in the initial stage, and then gradually increases.

(4) The AC resistivity decreases with the increase of the current frequency. The initial reduction rate is faster, and then gradually stabilizes. The AC resistivity gradually increases with decreasing water content and can be divided into the influence stable stage-1, the influence expansion stage, the influence stable stage-2 and the influence increase sharply stage. The AC resistivity gradually decreases with the increase of zinc content, and can be divided into a decrease sharply stage and a decrease slowly stage. The curve slope corresponding to the rapid decrease phase is significantly higher than the deceleration phase.

(5) During the drying process, the pore water pressure decreases, which in turn leads to an increase in the suction of the matrix, and generates tensile stress in the soil, bringing the soil particles closer to each other, and macroscopically showing the soil shrinking. There are three types of conductive paths in soil: the first conductive paths (soil and water), the second conductive paths (water), the third conductive paths (soil). When the conductive medium is replaced by air, the resistivity of the soil increases.

(6) Vaseline painted on the interface between the insulation box and the soil weakens the friction effect, and the large thickness of the soil weakens the internal tensile stress, so that no cracks develop during the shrinkage of the soil. The long strip of soil can reduce the polarization effect and improve the test accuracy of resistivity.

ACKNOWLEDGEMENTS

This research was financially supported by Chongqing Natural Science Foundation (cstc2018jcyjA; cstc2019jcyj-msxm1330; cstc2019jscx-tjsbX0015; cstc2019jcyj-msxm1865) and the Technological Research Program of Chongqing Municipal Education Commission (No. KJQN201901202; No. KJQN201901209; No.KJQN201901240) and Funded by the Research Fund of Key Laboratory of Coalbed Methane Resources and Reservoir Formation Process, Ministry of Education, China University of Mining and Technology (No.2019-002).

REFERENCES

[1] Hu, Z., Gao, M., Xie, D., Wang, Z., Zhang, K., Jin, H. (2015). On contents of Cu and Zn in different parent materials of purple soil and pollution assessment in the Three Gores Reservoir area. Journal of Southwest China Normal University (Natural Science Edition). 40(3), 112-119.

[2] Mitchell, J., Arulanandan, K. (1968). Closure of "Electrical Dispersion in Relation to Soil Structure". Journal of Soil Mechanics and Foundation Division. 94(2), 447-471.

[3] Smith, S., Arulanandan, K. (1981). Relationship of electrical dispersion to soil properties. Journal of Geotechnical Engineering. Division, ASCE. 107(5), 591-604.

[4] Fukue, M., Minato, T., Horibe, H.,Taya, N. (1999). The microstructure of clay given by resistivity measurements. Engineering Geology. 54(1/2), 43-53.

[5] Yoon, G., Oh, M., Park, J. (2002). Laboratory study of landfill leachate effect on resistivity in unsaturated soil using cone penetrometer. Environmental Geology. 43(1), 18-28.

[6] Long, M., Donohue, S., L'heureux, J., Solberg, I. (2012) .Relationship between electrical resistivity and basic geotechnical parameters for marine clays. Canadian Geotechnical Journal. 49(10), 1158-1168.

[7] Friedman, S. (2005). Soil properties influencing apparent electrical conductivity: a review. Computers and Electronics in Agriculture. 46(1), 45-70.

[8] Luo, X., Zhang, K., Tang, C., Zeng, H., Wang, Y ., Tan, Z. (2018). Monitoring of soil desiccation cracking process using electrical resistivity tomography. Geological Journal of China Universities. 24(06), 939-946.

[9] Jones, G., Zielinski, M., Sentenac, P. (2012). Mapping desiccation fissures using 3-D electrical resistivity tomography. Journal of Applied Geophysics. 84(12), 39-51.

[10] Mol, L., Viles H. (2013) .Exposing drying patterns: using electrical resistivity tomography to monitor capillary rise in sandstone under varying drying conditions. Environmental Earth Sciences. 68(6), 1647-1659.

[11] Gareth, J., Philippe, S., Marcin, Z. (2014) .Desiccation cracking detection using 2-D and 3-D Electrical Resistivity Tomography: Validation on a flood embankment. Journal of Applied Geophysics. 106(04), 196-211.

[12] Dong, X., Kin, Y.,Woo, H., Park, H., Park, J. (2013). Application of a newly developed column test device to analyze seawater transport in sandy soils. Environmental Earth Sciences. 70(5), 2397-2404.

[13] Zhou, M., Wang, J., Huang, S., Dong, P., Zhang, L., Yao, W. (2011) .Experimental investigation on influencing factors in soil resistivity measurement. Rock and Soil Mechanics. 32(11), 3269-3275.

[14] Zhou, M., Wang, J., Fan, X., Huang, S., Dou, P,. Wang, Y. (2012). Temperature correction model for soil electrical resistivity in Pearl River Delta. High Voltage Engineering. 38(03), 623-631.

[15] Bronswijk, J. (1988) Modeling of water balance, cracking and subsidence of clay soils. Journal of Hydrology. 97(3),199-212.

[16] Wilson, G., Frfdlund, D., Barbour, S. (1997) The effect of soil suction on evaporative fluxes from soil surfaces. Canadian Geotechnical Journal. 34,145-155.

[17] Sadhukhan, S., Prehl, J., Blaudeck, P., Hoffmann, K., Dutta, T., Tarafdar, S. (2008) .Desiccation of a clay film: Cracking versus peeling. The European Physical Journal E - Soft Matter. 27(4),391-395.

[18] Konrad, J., Ayad, R. (1997) .Desiccation of a sensitive clay: field experimental observations. Canadian Geotechnical Journal. 34(6), 929-942.

Received: **03.12.2019**
Accepted: **30.01.2020**

CORRESPONDING AUTHOR

Xin Tang
Key Laboratory of Coalbed Methane Resources and Reservoir Formation Process,
Ministry of Education,
China University of Mining and Technology,
Jiangsu Xuzhou, 221008, China.

e-mail: tangxin191909@sina.com

© by PSP Volume 29 – No. 04A/2020 pages 3084-3090 Fresenius Environmental Bulletin

A NOVEL NON-UNIFORM CLUSTERING ALGORITHM FOR WIRELESS SENSOR NETWORKS BASED ON ECOLOGICAL ENVIRONMENT MONITORING REQUIREMENTS

Yan Li*

Jingdezhen Ceramic Institute, Jingdezhen 333403, China

ABSTRACT

Various sensor nodes in a wireless sensor network (WSN) can communicate in a self-organizing mode to achieve real-time monitoring and real-time transmission. WSN has been widely used in military, agricultural, industrial, medical services and other fields. The purpose of the environmental monitoring system is to control the surrounding environment in real time, provide basic data for environmental control, judge the quality of the environment, analyze the types of pollutants, and finally provide the big data required for environmental protection methods. The traditional environment detection wireless sensor network system usually needs to initialize the sensor network. Generally speaking, this kind of sensor has some limitations such as the accuracy cannot meet the monitoring requirements of a comprehensive system. The sensor network monitoring range is small and there are monitoring blind spots. What's worse, the fault tolerance performance of the network system is not good. This paper mainly proposes a new wireless sensor network non-uniform clustering algorithm, which is used to alleviate the problem of holes in the network energy of wireless sensors. This algorithm comprehensively analyzes the remaining energy of the nodes, the distance between the nodes and the base station, and the distance between the neighbor nodes during the selection of the cluster head. This algorithm mainly uses the time competition mechanism to select the nodes of the cluster head. The new method research in this paper can provide a good reference for the application of wireless sensor network systems in ecological environment monitoring.

KEYWORDS:
Ecological environment, real-time monitoring, wireless sensor network, non-uniform clustering, algorithm analysis

INTRODUCTION

In recent years, micro-electro-mechanical technology, integrated circuits and wireless communication network technologies have developed rapidly. The development and progress of these technologies have led to the mass production of multi-functional miniature wireless sensors with lower cost and lower power consumption, thereby promoting the applications in the actual production and life [1-3]. The wireless sensor network technology has obtained extremely wide application prospects, such as: space detection, defense military, industry and agriculture, medical care, smart home, emergency rescue, etc., and has been introduced into the field of dynamic environmental monitoring, which has caused great concern. Especially in the global process of advocating the establishment of a sustainable ecological environment and society, the importance of environmental monitoring has become increasingly prominent [4-6]. The applications in the field of environmental detection include marine animal and plant living environment monitoring, plant growing environment monitoring, animal growth environment monitoring, volcanic eruption monitoring, urban road environment monitoring, and so on. For example, in livestock farms, it can be used to collect various environmental parameters in the farm environment, and control the breeding environment based on the feedback [7]. In large-scale farmland irrigation areas or nursery farms, soil moisture and air temperature and humidity can be monitored to control irrigation. In addition, we can collect the various environmental parameters of nursery farms to control nursery environment.

Compared with traditional environmental monitoring technologies, wireless sensor networks can use their miniature wireless sensor nodes to detect and sense environmental information, and quickly deploy and monitor the study areas. It is suitable for the monitored environment with harsh environment and has strong signal-to-noise ratio and fault tolerance. In addition, it can use distributed information to process a large amount of collected data, and intelligently process and analyze the data, greatly improving the precision of data information [8-9]. It can be seen that the application advantages of wireless sensor networks in the field of environmental monitoring mainly include [10-12]: (1) It can greatly improve the efficiency of network activities and grasp real-time information

efficiently and timely, and then provide a reference for the allocation of limited resources; (2) The network has a strong security and storage capabilities. This network can be used to aggregate, classify and store data in different areas and types in a timely manner, thereby forming a valuable big data system. (3) The wireless transmission mode, compared to conventional mode, is more efficient, and the loss is small, which saves a lot of hardware maintenance costs. The effective development and application of wireless sensor network technology can greatly improve the efficiency and quality of environmental detection, and at the same time, can form valuable big data resources in a timely and effective manner.

After many years of exploration and research in wireless sensor networks, many non-uniform clustering algorithms for wireless sensor networks have been generated, but there are certain disadvantages in these algorithms. This paper proposes a new non-uniform clustering algorithm for wireless sensor networks which can ultimately improve the promotion and application of wireless sensor network technology.

METHODS AND BASIC THEORY

Overview and analysis of non-uniform clustering algorithms in wireless sensor networks. A wireless sensor network is composed of a large number of sensor nodes, and its energy consumption is relatively low, and it can also achieve a certain data transmission effect (Figure 1).

The nodes of a wireless sensor network are mainly used for monitoring a specific area. The node sends the monitored data to the base station through the corresponding wireless transmission methods, and then analyzes and processes the data. However, the nodes of the wireless sensor network are unevenly distributed. In this way, the energy consumption of some nodes will be relatively fast, causing the corresponding nodes to die prematurely, which has a great impact on the service life of the entire network [13-14].

The clustering of wireless sensor network nodes can effectively reduce their node energy consumption. The LEACH algorithm is the most classic type of adaptive clustering routing algorithm. This algorithm mainly uses a certain periodic random selection of cluster heads and periodic replacement of cluster heads to reduce the energy consumption of its nodes, but the single-hop transmission of this algorithm limits the expansion of wireless sensor networks, which is not good for the practical application and promotion. Besides, the cluster head nodes use single hops to communicate directly with the base station, which also results in the fast energy consumption of the cluster head being far away from the base station, affecting its life cycle.

In order to solve the shortcomings of the LEACH algorithm, many researchers have also continuously developed many algorithms, such as DEBUC algorithm, EBUCA algorithm, etc. However, among these many algorithms, there are still some shortcomings in the selection of cluster heads. This article mainly proposes a new non-uniform clustering algorithm, namely the WUCH algorithm. In this algorithm, based on the comprehensive consideration of the remaining energy of the network nodes, the distance between the network nodes and the base station, and the distance between the nodes in the cluster and the cluster head is selected. The network is divided into non-uniform clusters, and then the dual cluster head nodes are selected in a relatively large cluster. The main cluster head is mainly responsible for collecting monitoring data. The nodes of the main cluster head must have higher energy than the remaining energy of the secondary cluster head who are responsible for data fusion and transmitting. This algorithm optimizes the cluster head routing, reducing the energy consumption of the nodes effectively.

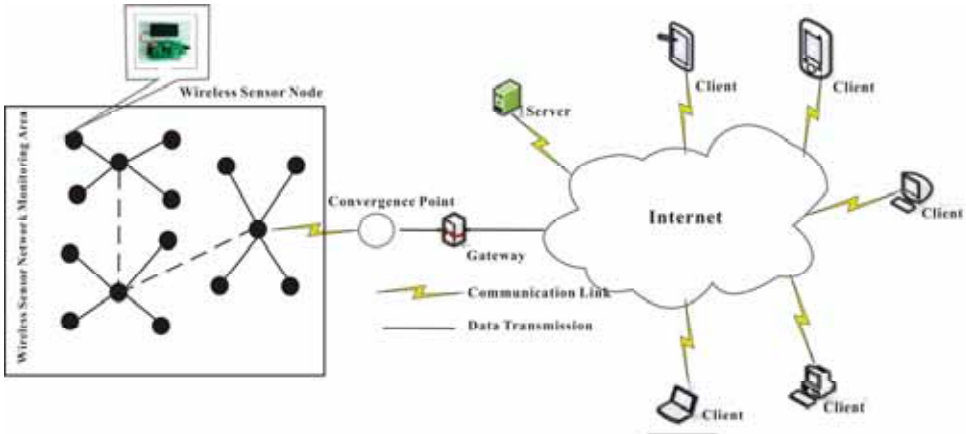

FIGURE 1
Basic composition of wireless sensor network system

Network Model. The wireless sensor network model needs to have certain properties. For example, the base station is not inside its sensor area, and the nodes of each network can also transmit information to each other. At the same time, the nodes are randomly distributed inside the area. For N nodes, the set of nodes is expressed as N = {N_1, N_2… N_n}, and the network nodes can use the signal strength transmitted by other nodes to calculate the approximate distance between the sending node and itself effectively. In addition, the network node transceiver can enter the sleep mode if it does not send and receive data [15].

Energy model. In the wireless sensor network data transmission, the energy consumed by its nodes is too large to be consumed by other functional nodes. In the capability model established in this paper, the energy consumption of the data it sends is expressed as:

$$E_{TX}(l,d) = \begin{cases} lE_{elec} + l\varepsilon_{fs}d^2, d < d_c \\ lE_{elec} + l\varepsilon_{fs}d^4, d \geq d_c \end{cases} \quad (1)$$

$$d_c = \sqrt{\varepsilon_{fs}/\varepsilon_{mp}} \quad (2)$$

In the above formula, l is the length of the data sent by the node, E_{elec} is the circuit energy consumed by each bit of data sent and received by the node, and d is the distance between the sending node and the receiving node. When $d < d_c$, the energy consumption of its network mainly uses the free space model. When $d \geq d_c$, the energy consumption of the network mainly uses the multipath attenuation model. ε_{fs} and ε_{mp} are the power consumption of the free space and multipath attenuation models, respectively [16].

RESULTS AND DISCUSSION

WUCH algorithm calculation. After the deployment of wireless sensor network nodes is completed, a strong signal is sent at the base station. All nodes in the network can receive the signal from the base station, and each node then calculates the distance from node to base station based on the strength of the signal it receives to prepare for the selection of cluster head nodes in the next stage. Both the WUCH routing protocol and the LEACH algorithm use a periodic operation mode [17-18]. Each round includes the establishment of the corresponding cluster head and data transmission. The time competition mechanism is mainly used in the selection of the cluster head nodes. For some large-scale clustering, the corresponding secondary cluster head node is generally selected to reduce the burden on its main cluster head node.

In the data transmission, the remaining energy of its cluster head nodes, the distance between the cluster head nodes and the base station, and the amount of data transmitted by the cluster head nodes are used as its weights, and then the corresponding weights are used to establish and improve optimal transmission Path to extend the life of its network. Figure 2 is a schematic diagram of the WUCH protocol. The area with unequal circles in the Figure 2 indicates that non-uniform clustering is achieved according to the WUCH algorithm. The black dots represent the main cluster head and the gray dots represent the secondary cluster head. The arrows and black lines between them indicate the data transmission path between the cluster heads [6, 12].

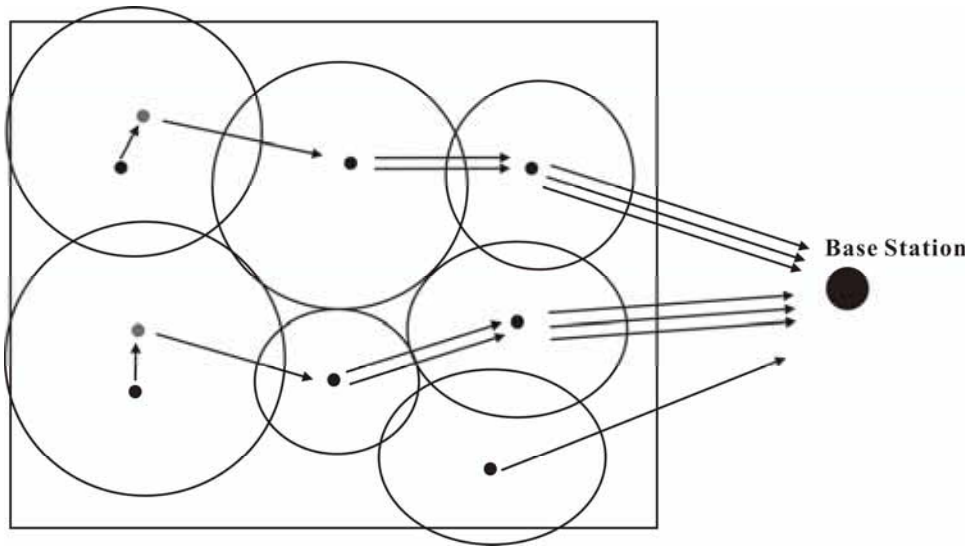

FIGURE 2
Schematic diagram of WUCH protocol

(1) Cluster Head Selection. The WUCH routing protocol is an algorithm that uses the corresponding distributed time competition to select cluster heads. During the selection of cluster heads, the remaining energy of the nodes, the distance between the nodes in the cluster, and the nodes and base stations are considered. If only one cluster head node is generated for each cluster, for some cluster head nodes with a relatively large range, the energy consumption will be large and sharply increased due to the amount of data processed and transmitted. However, regardless of its size, if the corresponding primary and secondary cluster heads are generated in its clusters, it will inevitably lead to waste of energy. For smaller clusters, it is not necessary to choose the secondary cluster head [19]. This is because in a relatively small cluster, the secondary cluster head will generate excess energy consumption, which will not achieve the purpose of node energy saving. This article chooses to set the corresponding threshold based on its cluster size, the remaining energy of the node, the amount of data transmitted, and the distance between the node and the base station. Once the secondary cluster head generates a weight greater than its threshold, the cluster can generate the corresponding secondary cluster head.

After the WSN selects the corresponding candidate cluster head node, its ordinary nodes will enter the dormant state until the election of its cluster head is completed, thereby saving energy consumption. Each candidate cluster head node is broadcasted. After the message of Prepare_Message (I_D, R_c, E_i), the candidate cluster head node will update the information table of its neighbors after receiving the message of Prepare_Message (I_D, R_c, E_i). The competition radius of the node is expressed as:

$$R_i = \left(1 - \alpha \frac{E_i}{E_{max}} - \beta \frac{d_{max} - d_i}{d_{max} - d_{min}}\right) R_c^0 \quad (3)$$

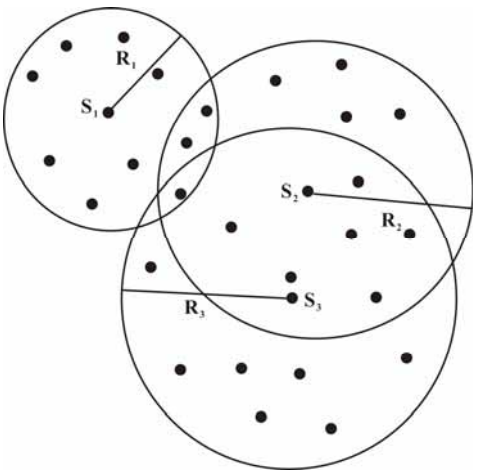

FIGURE 3
Cluster head competition diagram

The wireless sensor network selects the corresponding cluster-head nodes through the WUCH protocol. No other cluster-head nodes are allowed within the radius of the cluster-head node selection. S_2 in Figure 3 is mainly the corresponding cluster head node selected by the WUCH protocol in the network. Because S_2 is selected earlier than S_3, so S_3 cannot select the corresponding cluster head node, and because S1 is not in the election radius of S_2, therefore, S_1 can be selected as the corresponding cluster head node [18].

The average remaining energy of a node is calculated based on the remaining energy of the neighbor nodes in the neighbor table as:

$$E_{ave} = \left(\sum_{i=1}^{d_u} e_i\right)/\mathrm{du} \quad (4)$$

Then, the WUCH protocol uses its timing broadcast method to perform cluster head selection, and then calculates the approximate distance Di between the cluster head and the base station based on the received signal strength of the cluster head. After that, the average distance of the corresponding node according to the distance between the neighbor node in the neighbor table and the node was calculated:

$$d_{ave} = \left(\sum_{i=1}^{d_u} e_i\right)/\mathrm{du} \quad (5)$$

Then, the clustering is constructed according to the competition time, and the cluster head is selected first. For general-scale clustering, its main cluster head needs to select its second cluster head based on the remaining nodes and their distances and the remaining energy of the nodes. For some large clusters, in addition to selecting the corresponding second cluster head, the corresponding secondary cluster head also needs to be selected. Compared with other algorithms, the proposed algorithm saves more energy. After the node receives the cluster head selection message from the base station, the time for sending the cluster head competition message is:

$$t = \chi \frac{E_{avg}}{e_i} \frac{d_i}{d_{max}} \frac{d_{avg}}{d_{avg} + \delta} T_{ch} \quad (6)$$

In the above formula, χ is a random value taken between [0,1], T_{ch} is the time required to run for the cluster head in advance, e_i is the residual energy of the node, and δ is the adjustment factor of the parameter. The competition time t of the cluster head is defined according to the remaining energy of its nodes, the distance to the base station, and the distance between neighbor nodes and nodes. The larger the t, the smaller the probability that it will act as a cluster head node, which effectively improves the rationality of the selection of cluster head nodes. The selection function T of the secondary cluster head is expressed as:

$$T = \varepsilon \frac{E_{res}}{E_{max}} \frac{S}{n^2} \quad (7)$$

In the above formula, ε is a certain parameter, n is the number of network cluster nodes, S is the amount of transmission information collected by

the nodes in the cluster, and Eres is the remaining energy.

(2) Data Transmission Path. After the clustering and selection of the cluster head through the network, the data collected by its nodes will be transmitted towards the base station by means of multi-hop minimum spanning tree routing. It is necessary to first abstract the cluster of the network as a point and then connect with the neighbor points to form the corresponding connected graph with weights G = (V, E). Where, V is the cluster head node and the base station set, E is the weight between the cluster heads, and the formula for calculating the weight is:

$$w_{ij} = a\frac{d_{ij}}{e_i} + b\frac{d_{ij}}{e_j} + (1-a-b)\rho \qquad (8)$$

In the above formula, w_{ij} is the abstract connection weight between cluster heads i and j, d_{ij} is the distance between cluster heads i and j, e_i and e_j are the remaining energy of cluster heads i and j, respectively, and ρ is the density of cluster nodes, a and b are artificially adjustable parameters. It is known from equation (8) that if we consider the distance between cluster heads, the remaining energy of the cluster heads, and the cluster size, the calculated weight will be even more reasonable.

The inter-cluster routing process of the WUCH algorithm is as follows:

When the transmitted data cluster head/sub-cluster head is selected according to the above cluster head, the distance between the recording cluster head and the base station is D_i. When $D_i < D_0$, the node of the cluster head is calculated according to the above formula (8). The weight w between the cluster head and the base station is sent to the base station directly when $w < w_0$. In its directed connection graph $G = (V, E)$, the cluster head of data transmitted to its base station needs to be grouped into set V_1, and its cluster head and base station edges are grouped into set E_1. Each cluster head that transmits data sends W_MSG information to the surroundings while others cannot send data directly to the cluster head. The node at the cluster head calculates the distance between the two cluster head nodes according to the strength of the W_MSG information received. The distance d_{ij}, the remaining energy, the size of the cluster, and the edge weight w_{ij} of the connection between the two cluster heads are calculated according to formula (8). Then select the smallest edge of the w_{ij} between its two cluster heads, and then group the two cluster heads of this edge into the set V_1, and classify its edges into the set E_1. Repeat the above steps 4 until the set $V_1 = V$, then the elements in E_1 constitute the smallest spanning tree. After the construction of the smallest spanning tree is completed, the transmitting node adjusts its transmitting power so that it can reach the node of the next hop neighbor [20].

Algorithm Analysis and Experimental Simulation. (1) Complexity Analysis of WUCH Algorithm. In the stage of generating the cluster head candidate of WSN, the (N × T) number of candidate cluster head nodes generated by the network are running for election, and each candidate cluster head node needs to broadcast a Prepare_Message message, so a total of (N × T) pieces of information can be generated. During the competition of the cluster head, if it is assumed that a total of K corresponding candidate cluster head nodes are selected as the main cluster head, it will transmit a total of K FinalHead_Message messages. When a node is selected, ordinary nodes send out (N -K) messages in total. The average number of total WSN messages is N × T + K + NK = N × T + N, and the complexity of the message is O(N).

(2) Experimental Simulation. This paper uses OMNET4.0 simulation software to compare the new algorithm, EBUCA algorithm and EEUC algorithm. The experimental parameters are shown in Table 1. The sensor nodes are randomly distributed, and the fusion data energy of the cluster points can be ignored. Figure 4 is a comparison of the remaining energy of the nodes in the network.

TABLE 1
The main parameters and values for the test

Parameters	Value
Area/ m^2	10000
Nodes number	400
Location of base station	(50,50)
data package/ bit	600
Nodes initial energy/ J	0.5
ε_{mp}/ $(pJ(bitm^4)^{-1})$	0.0013
ε_{fs}/ $(pJ(bitm^2)^{-1})$	10
E_{elec}/ $nJbit^{-1}$	50
d_0/ m	45
D_0/ m	20

According to Figure 4, with the increase of the number of network running rounds, the WUCH algorithm effectively delays node death compared with the other two algorithms. In order to reduce the burden of collecting and transmitting data on larger cluster head nodes, the data transmission path considered the node density, the remaining energy of the cluster head node, and the distance between the cluster head node and the base station during the construction of its data transmission phase. According to Figure 5, as the number of wireless sensor network running rounds increases, the energy variance of the WUCH algorithm network nodes is smaller than that of the other two algorithms. This is mainly due to the WUCH protocol in the cluster head selection stage. Various factors have been comprehensively considered in the stage of data transmission and data transmission.

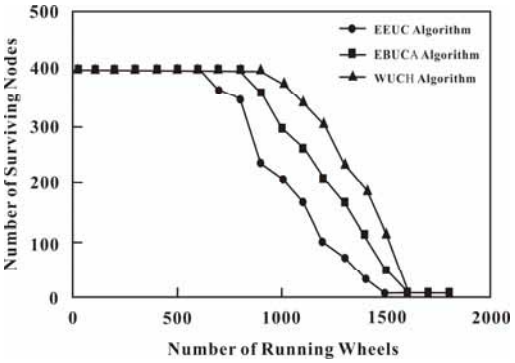

FIGURE 4
Statistics of node survivals in the network

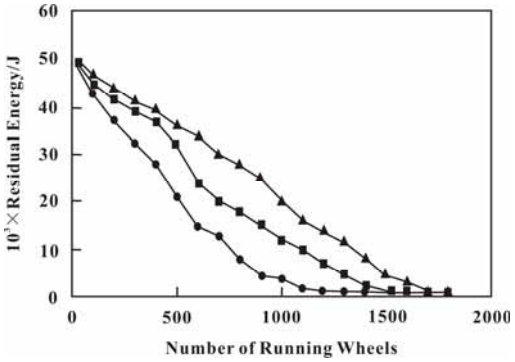

FIGURE 5
Comparison of residual energy of nodes in network

CONCLUSIONS

A new wireless sensor network non-uniform clustering algorithm (WUCH algorithm) is developed for the ecological environment monitoring. The new non-uniform clustering algorithm considers the remaining energy of the nodes, the distance between the nodes and the base station, and the distance between the neighbor nodes to select the cluster head. Compared with the other algorithms such as EBUCA algorithm and EEUC algorithm, the new algorithm effectively delays node death and has smaller energy variance. This research can provide a reliable theoretical basis for the application of wireless sensor network in the field of environmental monitoring.

ACKNOWLEDGEMENTS

The authors would like to thank all the techniques who have offered help for this research, the platform of the research institute, and the authors of all the references.

REFERENCES

[1] Chang, X., Zhang, D. (2016) A New Non-Uniform Clustering Algorithm for Wireless Sensor Networks. Journal of Jilin University (Science Edition). 54(6), 1388-1394.
[2] Wu, Z., Zhao, M., Deng, Y. (2016) New Uneven Double Cluster Head Clustering Algorithm for WSN-PUDCH Algorithm. Chinese Journal of Sensors and Actuators. 37(12), 2612-2616.
[3] Yang, X., Wang, R., Peng, L. (2015) Hybrid multi-hop routing algorithm of effective energy-hole avoidance for wireless sensor networks. Journal of Computer Applications. 35(7), 1815-1819.
[4] Li, H., Li, M. (2019) Study on optimization of WSN routing in granary temperature and humidity monitoring system. Cereal and Feed Industry. 3, 24-27.
[5] Du, J., Ma, L., Yang, J. (2017) Research on Wireless Multimedia Sensor Networks ant Colony Routing Algorithm Based on QoS and Clustering. Computer Measurement and Control. 25(2), 196-200+207.
[6] Thanigaivelu, K., Murugan, K. (2012) Grid-based clustering with dual cluster heads to alleviate energy hole problem for non-uniform node distribution in wireless sensor networks. International Journal of Mobile Network Design and Innovation. 4(1), 3.
[7] Selvakennedy, S., Sinnappan, S. (2005) A configurable time-controlled clustering algorithm for wireless sensor networks. International Workshop on Heterogenous Wireless Sensor Networks IEEE Computer Society. 2(2), 368-372.
[8] Hong, G., Tang, B., Pei, Y. (2012) Clustering Routing Arithmetic Based on Minimum Energy Consumption Path. Computer Simulation. 29(10), 177-180.
[9] Peng, Y., Wang, J. (2010) A Monitoring System for Eco-environment in Orchard. Journal of Anhui Agricultural Sciences. 38(9), 4923-4924.
[10] Wang, Z., Sun, S., Xu, B. (2014) An uneven clustering algorithm for WSNs based on time delay mechanism. Transducer and Microsystem Technologies. 33(4), 146-149.
[11] Dai, Z., Yan, C., Wu, Z. (2016) An uneven clustering algorithm for WSNs based on time delay mechanism. Transducer and Microsystem Technologies. 29(12), 1912-1918.
[12] He, Y., Zeng, C., Li, H., Chen, Q. (2014) Clustering Routing Algorithm Based on DIJKSTRA for Wireless Sensor Networks. Computer Measurement and Control. 22(9), 2867-2869+2892.

[13] Chen, S., Han, J., Jiang, W. (2014) Application Research on Uneven Clustering Algorithm in Low-redundancy WSN. Computer Engineering. 40(8), 10-14.
[14] Gong, P. (2010) Progress in recent environmental applications of wireless sensor networks. Journal of Remote Sensing. 14(2), 387-395.
[15] Nokhanji, N., Hanapi, Z., Subramaniam, S., Mohamed, M. (2015) An energy aware distributed clustering algorithm using fuzzy logic for wireless sensor networks with non-uniform node distribution. Wireless Personal Communications. 84(1), 395-419.
[16] Shin, H., Moh, S., Chung, I. (2011) A Balanced Clustering Algorithm for Non-uniformly Deployed Sensor Networks. IEEE Ninth International Conference on Dependable, Autonomic and Secure Computing, DASC 2011, 12-14 December 2011, Sydney, Australia. IEEE.
[17] Zaeri, N., Habib, S. (2011) Optimization of non-uniform sensing coverage for wireless sensor networks. Advanced Materials Research. 230-232, 605-609.
[18] Wang, N., Liu, X. (2012) Study on Wireless Sensor Network Data Fusion Technology in Monitoring Forest Ecological Environment. Forest Engineering. 28(4), 85-88.
[19] He, W., Xu, D. (2017) Improved uneven cluster routing algorithm for wireless sensor network. Computer Engineering and Applications. 53(24), 136-141+270.
[20] Lu, X., Wang, Y., Wang, H., Xu, B. (2013) Energy-balanced Unequal Clustering Algorithm in Wireless Sensor Network. 40(5), 78-81.

Received: **07.12.2019**
Accepted: **26.01.2020**

CORRESPONDING AUTHOR

Yan Li
Jingdezhen Ceramic Institute,
Jingdezhen 333403, China

e-mail: gtzgur@163.com

© by PSP Volume 29 – No. 04A/2020 pages 3091-3101 Fresenius Environmental Bulletin

GEOLOGICAL MODELING AND STABILITY ANALYSIS OF HORIZONTAL WALL IN TYPICAL SHALE GAS BLOCKS-TAKING WEI 202 BLOCK FOR EXAMPLE

Qihua Ran*

Shale Gas Exploration and Development Department, CNPC Chuanqing Drilling Engineering Company Limited, Chengdu 610051, China

ABSTRACT

At present, tight shale gas has become a hot spot for oil and gas exploration and development in China. The Sichuan Basin is rich in shale gas reserves and has significant commercial exploitation value. At present, the Changning-Weiyuan shale gas exploration and development test zone has been formed. As the main production unit of Weiyuan shale gas, the geological conditions of Wei 202 block are complex, which brings great challenges to engineering technology. The Longmaxi Formation shale stratum in Wei 202 block is ancient and has undergone multi-stage tectonic movements. The problems of burial depth, large stress difference, strong reservoir heterogeneity, and well wall instability are prominent. Based on the current on-site shale gas development test data and the classic models related to geological modeling, the geological attribute model of Wei 202 block is established. On this basis, the stability analysis of the borehole wall before drilling was performed in combination with the real well, and a suitable safe drilling fluid density window was derived. The research results of this paper have reliable reference significance for the efficient and safe drilling of horizontal sections of shale gas wells in Wei 202 block.

KEYWORDS:
Shale gas, geological model, borehole stability, horizontal section, drilling fluid

INTRODUCTION

China has rich reserves of shale gas, with recoverable resources of $25 \times 10^{12}m^3$, of which the recoverable resources of shale gas in the Sichuan Basin can reach $4.4 \times 10^{12}m^3$. The efficient development of these resources will reduce the external dependence of natural gas and ensure national energy security [1-3]. At the same time, as the main production unit of the Weiyuan shale gas, the Wei 202 block has complex geological conditions and outstanding engineering technology challenges. The Longmaxi Formation shale stratum is ancient and has undergone multi-stage tectonic movements. The problems of strong homogeneity and instability of the well wall pose certain challenges to current drilling and completion [4-6]. Therefore, based on the characteristics of shale gas reservoirs in this area, it is necessary to study and form a targeted geological model for Wei 202 block to effectively control the wall instability and provide strong technical support for the superior fast drilling in Wei 202 block.

Researchers in geological modeling and borehole stability direction have done a lot of work. Zhang et al. [7], based on logging-while-drilling (LWD) data, established three-dimensional geological models at different drilling times by updating previous geological models. The dynamic update of the geological model can effectively obtain the spatial distribution of the reservoir, discover the structure changes in a timely manner, thereby modifying the wellbore trajectory originally designed, adjusting the drilling trajectory through geological guidance, and drilling the oil layer in the best way. His model can increase the effectiveness of horizontal intervals. Combining well logging, geological and seismic data, and logging-while-drilling data, the method is successfully applied to drilling in the Guanjiabao Oilfield. Multi-level modeling methods are used to constrain geological conditions to ensure the accuracy and reliability of the model. Wang et al. [8] studied and proposed the modeling method of sedimentary facies coupled petrophysical type based on T reservoir in Zagros Basin. Based on geological research, this method established a sedimentary facies model through well-seismic joints, and then establishes a three-dimensional distribution model of porosity and petrophysical type based on sedimentary facies control. After that, based on the mathematical model of porosity and permeability under the control of petrophysical type and saturation degree, a deterministic modeling method is used to establish a three-dimensional distribution model of permeability and saturation. The effects of permeability anisotropy parallel to the bedding plane and perpendicular was considered to the bedding plane [9-10], and established a pore pressure distribution and seepage stress model under anisotropic seepage. Combining the effects of anisotropic seepage and bedding plane, the equivalent collapse density (ECD) around the

horizontal wellbore was studied. The ECD considering the weakness of the bedding plane is much higher than the ECD without considering the weakening of the bedding plane, and the shape of the area where the surrounding rocks are relatively easy to collapse is similar to two pairs of cat ears [11-13]. If a hole is drilled in a direction close to the minimum ground stress, the point where the ECD reaches its maximum value tends to move from the well wall to the internal rock. The higher the anisotropic permeability, the more obvious the phenomenon. Yuan et al. [14] developed a new prediction method to calculate in-situ stress in shale formations. Due to the non-uniformity of mechanical properties and permeability, the pore pressure near the borehole is not uniform in the radial and tangential directions. Therefore, after the formation is drained, the stress state around the wellbore will change with time. In addition, based on the experimental results, the failure criterion was verified and used to determine the strength of the Silurian shale in the Sichuan Basin, including the long-term strength of gas shale. Based on this, a new on-site stress prediction model is used to analyze the stability of the horizontal wellbore [15-18]. The results show that if the conventional model is used incorrectly in shale gas reservoirs, the collapse pressure will be underestimated. When the inclination angle is 45°, the collapse pressure of the horizontal well is the largest. If the borehole is exposed for a period of time, the critical mud weight should be continuously increased to prevent the borehole from collapsing.

The above studies are mainly based on laboratory experiments and mathematical modeling to study the modeling of geological bodies and the stability of borehole walls. Due to the complexity, uncertainty, and incomplete information of geological data and its applications, it is very difficult to guarantee the accuracy of geological modeling results and the accuracy of borehole stability evaluation. Based on the field data and the classic models related to geological modeling, this paper establishes the geological attribute model of Wei 202 block and conducts a horizontal comparative analysis. At the same time, it gives the drilling operations in this block to avoid well wall instability.

MATERIALS AND METHODS

A complete geomechanical model is composed of five main parts, namely the overburden pressure S_v, the maximum horizontal principal stress S_{Hmax} and the minimum horizontal principal stress S_{hmin}, the pore pressure and rock mechanical properties, including the uniaxial compressive strength (UCS) of the rock, internal friction coefficient (μ), Young's modulus (E), Poisson's ratio (v), and Biot coefficient (α).

Vertical Principal Stress.

$$S_v = \int_{dw}^{z} \rho(z)\, g dz \tag{1}$$

Among them:

S_v: vertical / overlay stratum stress, MPa; ρ(z): total formation density, g/cm^3; g: acceleration of gravity, m/s^2; z: depth, m.

The equation includes all matter (rock and fluid) from the surface to the target point (z). On the premise that the density curve data is complete, the density overlying relationship can be used to obtain the overlying formation pressure value from the surface to an arbitrary depth (z) and the overlying formation pressure gradient in the longitudinal direction. Establish a pseudo-density curve for the depth section with missing density data. Based on the existing logging density data, fit the relationship between acoustic velocity and -density (such as the relationship between Gardner and Bellotti) [19-20], and use the acoustic data to establish the pseudo-density curve. In the interval without any logging data, use the existing data to fit the density information of the missing section of the data, and finally use the "measured density" and "pseudo-density" methods to calculate the overburden pressure.

Maximum and Minimum Horizontal Principal Stress. Use the "constant strain coefficient" method to estimate the S_{hmin} and S_{Hmax} values derived from logging:

$$S_{h\min} = \frac{\nu}{1-\nu} S_v + \frac{1-2\nu}{1-\nu} \alpha P_p + \frac{E_{sta}}{1-\nu^2} \varepsilon_h + \frac{\nu E}{1-\nu^2} \varepsilon_H \tag{2}$$

$$S_{H\max} = \frac{\nu}{1-\nu} S_v + \frac{1-2\nu}{1-\nu} \alpha P_p + \frac{E_{sta}}{1-\nu^2} \varepsilon_H + \frac{\nu E}{1-\nu^2} \varepsilon_h \tag{3}$$

Among them:

μ: static Poisson's ratio, dimensionless; α: Biot coefficient, dimensionless; ε_h、ε_H: tectonic strain in S_{hmin} and S_{Hmax} directions.

The magnitude and direction of the principal stress constitute a stress tensor, which interacts with pore pressure and rock strength, causing problems such as wall collapse, drilling fluid loss, and formation sand formation during drilling [21]. Wall collapse is a section of a well where shear collapse occurs. During the drilling process, the lower-density mud replaced the rock, disturbing the original in-situ stress field and causing stress concentration around the borehole wall. During vertical well drilling, the hoop compressive stress acting around the borehole wall is greatest in the S_{hmin} direction. If the resulting hoop compressive stress exceeds the compressive strength of the formation, the wall of the well will undergo shear failure, and the rock will collapse from the wall of the well. The side collapse direction is parallel to the S_{hmin} direction in the vertical well. In areas where the overlying formation pressure is the principal stress, in vertical wells, continuous wall

collapse will be in the direction of the minimum horizontal principal stress, forming symmetrical vertical features on both sides of the borehole. In addition, in the direction perpendicular to the wall collapse and parallel to the S_{Hmax} (in a vertical well) direction, drilling-induced tensile fractures will occur. A necessary condition for producing well-induced tension fractures is that the hoop stress at the S_{Hmax} direction around the wellbore is less than or equal to zero.

Pore Pressure. Some methods based on logging techniques, such as normal compaction trend analysis, are used to predict pore pressure in the study area. However, due to the presence of thick carbonate formations and the influence of complex tectonic evolution, the pore pressure from the above method has a certain deviation from the true value. The parameters predicted by the pore pressure model need to be comprehensively calibrated using various data, including collating and analyzing drilling events and knowledge of adjacent wells, regional pressure data, related geological information, and verification of geomechanical models. According to the well testing and drilling experience in this study area, it is known that there is overburden overpressure in the target strata of the Longmaxi shale formation. There is no evidence of reservoir failure in this study area. Because the total organic content, hydrocarbon generation, and reservoir characteristics are different in different aspects, the pore pressure in Longmaxi shale formations will also be quite different.

Pore pressure prediction based on the Eaton resistivity method and the sonic method [22-23]. When using the resistivity method, the Eaton index is 1.3, and when using the sonic method, the Eaton index is 3.4.

Eaton resistivity method:

$$P_f = OBG - \left(\left(OBG - P_n \right) \cdot \left(\frac{R_o}{R_n} \right) \cdot m \right) \quad (4)$$

Eaton Sonic Method:

$$P_f = OBG - \left(\left(OBG - P_n \right) \cdot \left(\frac{dT_n}{dT_o} \right) \cdot n \right) \quad (5)$$

Among them:

P_f: pore pressure gradient, dimensionless; OBG: overlay pressure gradient, dimensionless; P_n: normal pore pressure gradient, dimensionless; R_o: measured resistivity, Ω; R_n: normal formation resistivity, Ω; dT_n: sound wave velocity in normal compacted formation, from normal compaction trend line, km/s; dT_o: measured acoustic velocity of the formation, km/s; m, n: corresponding to Eaton index, dimensionless.

Rock Mechanical Properties. Rock mechanical properties reflect the characteristics of mechanical response of underground rocks due to changes in stress. Analysis of rock mechanical properties, such as uniaxial compressive strength (UCS), internal friction coefficient (μ), Young's modulus (E), Poisson's ratio (ν), etc., are important research contents for geomechanical model. These rock mechanical characteristics can be obtained by performing triaxial compression tests on core samples at the same depth and different ambient pressures. The modulus of elasticity (Young's modulus and Poisson's ratio) can be calculated from stress-strain measurements in the axial and radial directions. For the samples with shear failure in the experiment, various analysis can be performed by Mohr's circle method to obtain different rock mechanical parameters.

The following equations were used to estimate the dynamic Young's modulus (E_{dyn}), dynamic Poisson's ratio (ν_d), and internal friction coefficient (IF) based on the acoustic data [24-25]:

$$E_{dyn} = Den \cdot V_s^2 \cdot \frac{3V_p^2 - 4V_s^2}{V_p^2 - V_s^2} \quad (6)$$

Among them:

V_p: longitudinal wave sound velocity, km/s; V_s: shear wave sound velocity, km/s; Den: formation density, kg/m^3.

The conversion relationship between static Young's modulus and dynamic Young's modulus is: $E_{sta} = 0.6E_{dyn}$.

Calculate the internal friction coefficient using the improved Lal-V_p equation:

(1) Shale, siltstone and limestone:

$$IF = \tan\left(\alpha \sin\left(\frac{V_p - 1}{V_p + 1} \right) \right) \quad (7)$$

(2) Dolomites:

$$IF = \tan\left(\frac{18.532 \cdot pow\left(V_p, 0.5148 \right) \cdot \pi}{180} \right) \quad (8)$$

Based on the logging data, a continuous rock mechanical parameter profile of a single well is established. The most common method for calculating rock mechanical strength from log data is to use empirical formulas between uniaxial compressive strength (UCS) and log data or other reservoir information. The laboratory rock strength test is used to calibrate the empirical formula, making the empirical formula suitable for the geological characteristics of the study area.

The shale uniaxial compressive strength (UCS) uses an empirical formula:

$$UCS = 0.00135 \cdot E_{sta}^{1.0908} \quad (9)$$

Limestone uniaxial compressive strength (UCS) was calculated using the improved Militzer-DT equation:

$$UCS = \left(\frac{7682}{DTCO} \right)^{1.82} \quad (10)$$

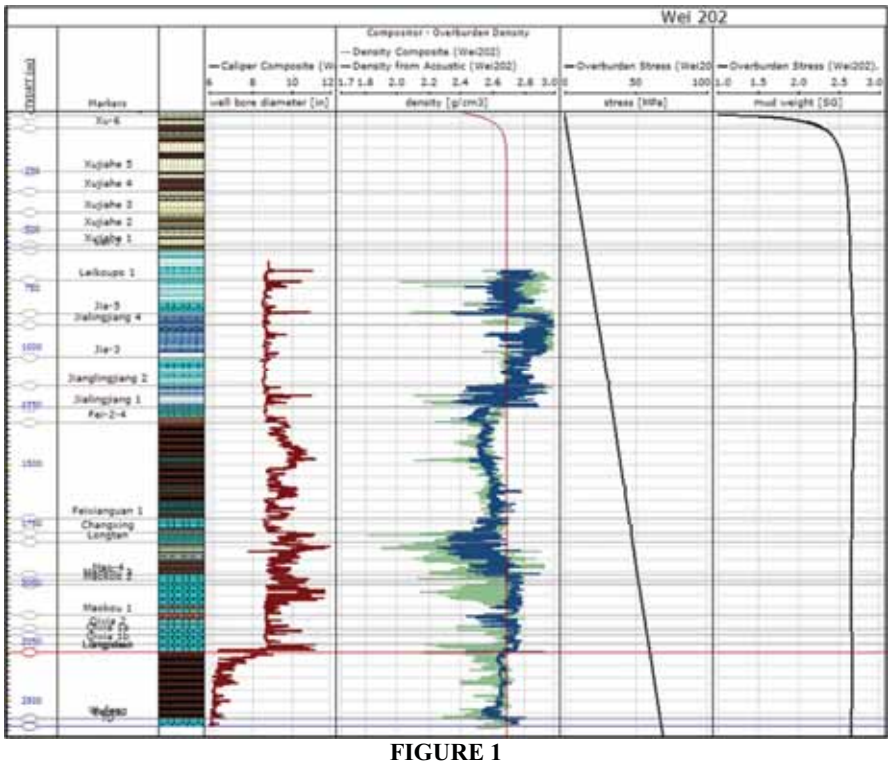

FIGURE 1
Calculation results of overlying formation pressure in Wei 202

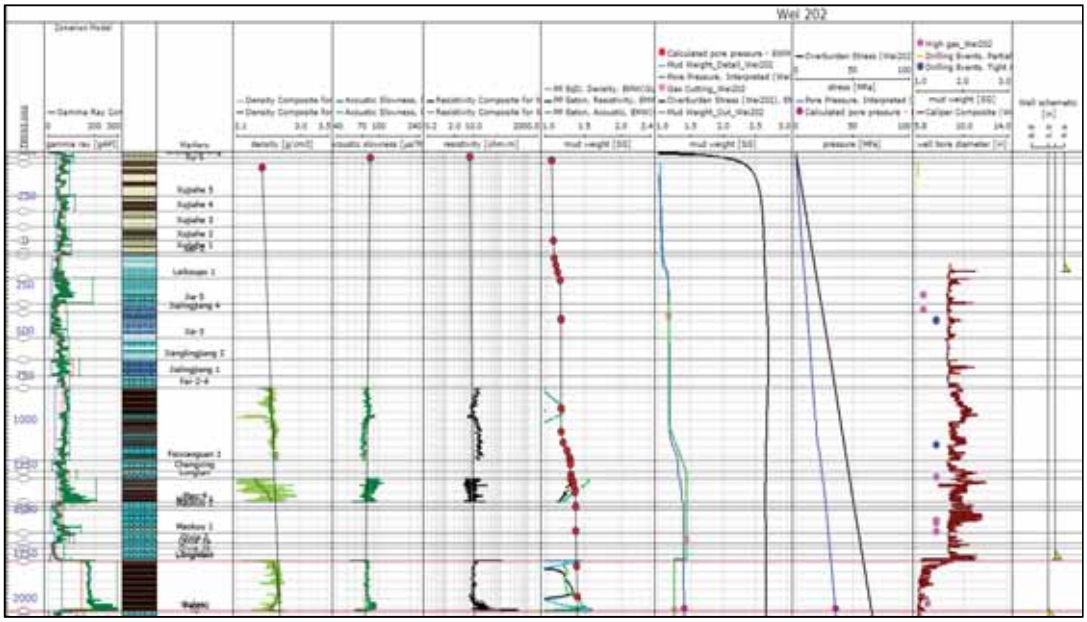

FIGURE 2
Analysis results of pore pressure in Wei 202

The uniaxial compressive strength (UCS) of the dolomite is calculated using the E-Dolomite equation [26]:

$$UCS = 64 \cdot E_{sta}^{0.34} \tag{11}$$

The uniaxial compressive strength (UCS) of sandstone is calculated using the modified McNally equation:

$$UCS = 111099 \cdot e^{(-0.37 \cdot DTCO)} \tag{12}$$

UCS: uniaxial compressive strength, psi; *DTCO*: μs/ft.

RESULTS

Case Verification. Based on the vertical principal stress, maximum horizontal principal stress, minimum horizontal principal stress, pore pressure calculation model and related mechanical parameters of the rock established previously, the relevant logging data of Wei 202 block well was used to calculate the geological parameters of Wei 202 block.

Further analysis of the overlying formation pressure in Wei 202 block shows that the variables between the overlying formations are relatively small, indicating that the horizontal trend of formation density in the study area is relatively stable. The overlying formation pressure coefficient of Longmaxi Formation ranges from 2.66 to 2.67 SG (Figure 1).

The pore pressure modeling and calculation results of Well Wei 202 are shown in Figure 2.

At the top of the Xu 6 Member formation, the hydrostatic pressure was close to the overpressure. The overpressure increased from this depth, and the pressure coefficient reached 1.4SG near the drilling depth. During drilling, multiple drilling events such as overflow and gas invasion were observed to verify certain pore pressure characteristics.

Figure 3, Figure 4 and Table 1 show the comparison of Longmaxi stratum rock strength. The rock strength of shale reservoirs is large, and the average uniaxial compressive strength (UCS) in Longmaxi shale is about 87-115 MPa.

Analysis of Borehole Wall Stability Based on Actual Engineering Data. Drilling in the horizontal well section of Wei 202 block is a problem in this block. In order to better support drilling operations, based on the geomechanical model constructed above, stability analysis of the horizontal well sections of Well 202H19-5 and Well 202H19-7 was carried out.

(1) Well Wei 202H19-5. Figure 5 and Figure 6 show the results of wellbore stability analysis of Well 202H19-5. The specific gravity of mud in each wellbore section is controlled by the collapse pressure, pore pressure and fracture pressure of the wellbore. The upper limit of the mud's specific gravity should consider the S_{hmin} of the shale. During the drilling process, the ECD value is also controlled by S_{hmin}. In deeper intervals and Longmaxi shale intervals, although some areas with weak compressive properties will affect the correct selection of appropriate mud proportions, pore pressure is still the most important factor in selecting reasonable mud proportions [27]. By analyzing and predicting the conditions of borehole wall instability and borehole collapse in this well. The optimized geomechanical model and recommended mud gravity were used to predict the instability of the wellbore. The prediction results show that the collapse angle of the horizontal well drilling section is less than 30 degrees, and the vertical well is less than 90 degrees. If the wellbore cleanliness is maintained during drilling, we need to use the reasonable drilling fluid types to minimize the reaction between shale reservoirs and drilling fluids. The recommended mud density can ensure the safe drilling of the wellbore trajectory.

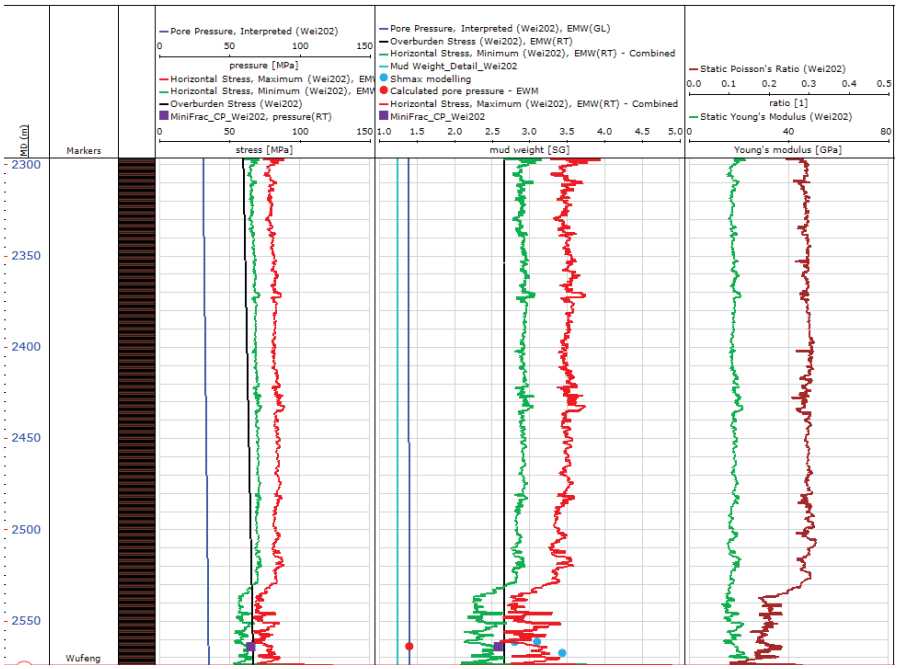

FIGURE 3
Modeling of the minimum horizontal principal stress in Wei 202

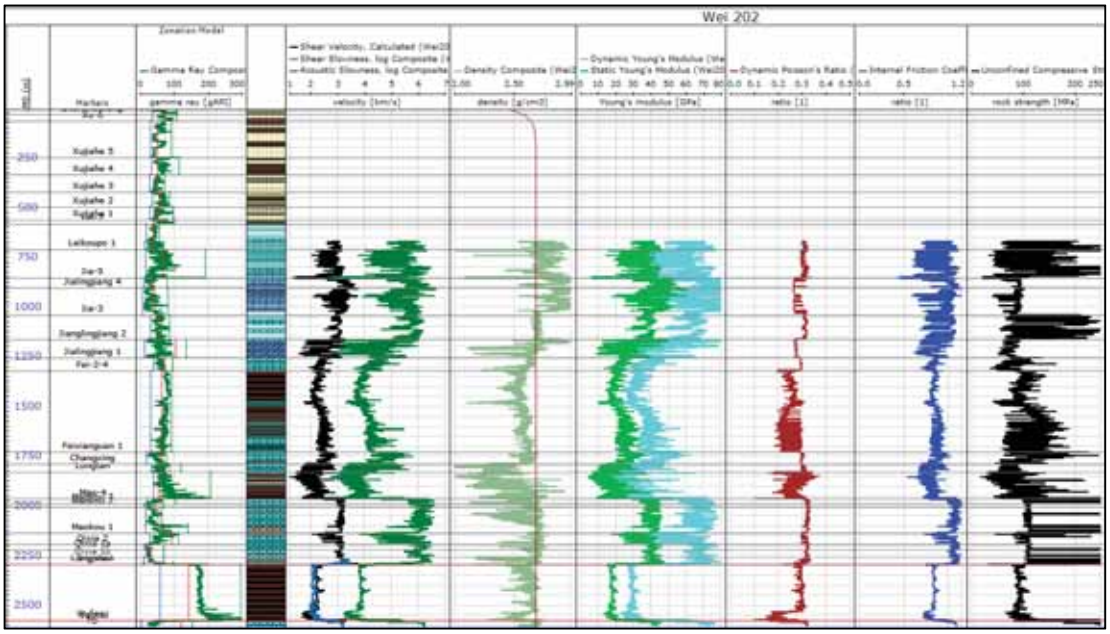

FIGURE 4
Rock mechanics modeling results of Wei 202

TABLE 1
Uniaxial compressive strength test results of Wei 202

Well name	Minimum UCS/MPa	Average UCS/MPa	P10 UCS/MPa	P90 UCS/MPa
Wei 202	59	92	82	101

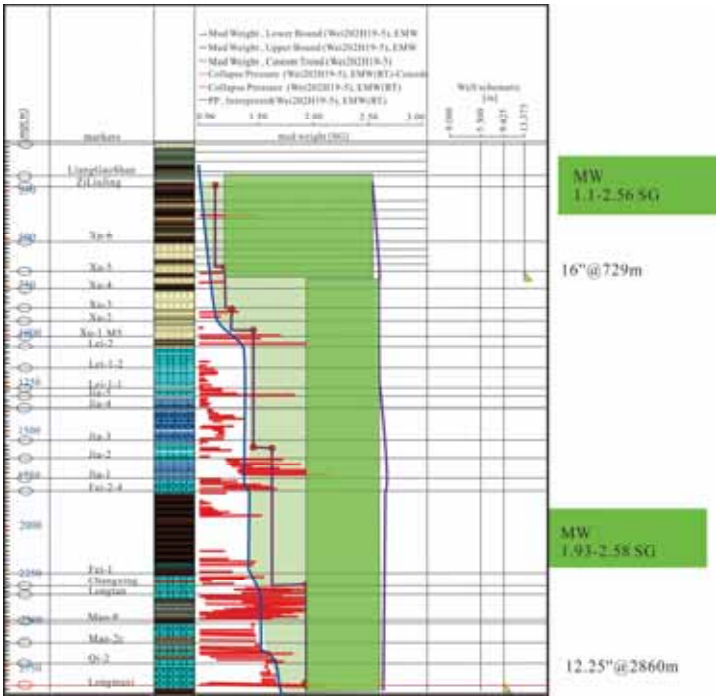

FIGURE 5
Prediction of the safety mud window of the first two sections of Well Wei 202H19-5

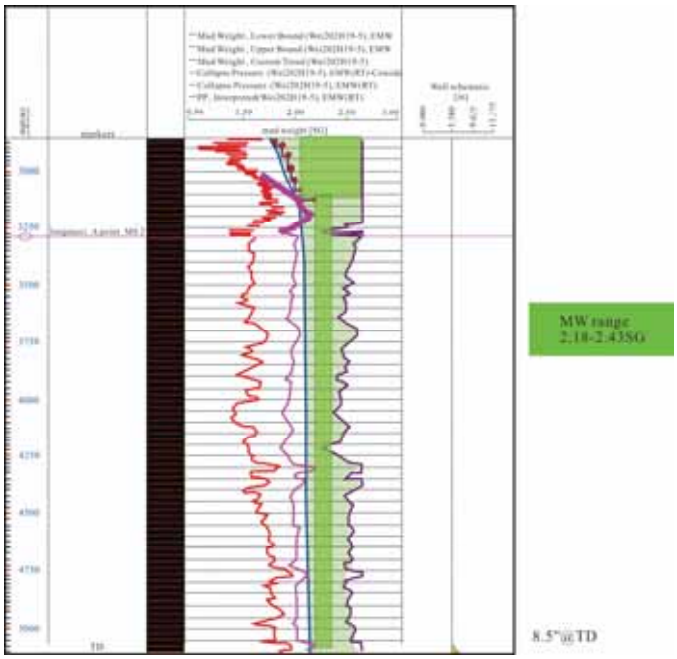

FIGURE 6
Prediction of the safety mud window in the third section of Well Wei 202H19-5

Based on wellbore stability analysis of Well 202H19-5. For formations above Jia2, it is recommended that the minimum mud specific gravity should be 1.1-1.45SG to reduce formation collapse. The Jialu-Liangshan Formation is recommended to have a minimum mud specific gravity of 1.85-1.93 SG to reduce formation collapse (Table 2). For the Jia2 Member and Longtan Formation, it is recommended to increase the mud density to effectively provide well wall stability. Controlled by the maximum predicted pore pressure of the Longmaxi reservoir, the study concluded that the weak bedding existing in shale gas reservoirs may cause rupture of related bedding. In order to prevent bedding failure, it is recommended that the minimum mud specific gravity should be increased to 1.9- 2.05SG (Table 3). This means that if the stability of weak rocks is to be maintained, the mud ratio is more important than the pore pressure. Because the mud specific gravity safety window is very small in the horizontal section of a horizontal well, the management of ECD is extremely important. If the initiation pressure is considered as the upper limit of the mud window, the range of mud specific gravity variation in the horizontal section will increase. If good borehole cleanliness is maintained during drilling, reasonable drilling fluid types are used, and the reaction between shale reservoirs and drilling fluids is minimized, the recommended mud density should ensure safe drilling of the wellbore trajectory [28-29].

(2) Well Wei 202H19-7. Figure 7 and Figure 8 show the results of wellbore stability analysis for Well Wei 202H19-7. The specific gravity of mud in each wellbore section is controlled by the collapse pressure, pore pressure and fracture pressure of the wellbore. The upper limit of mud specific gravity should consider the rock fracture pressure gradient when the S_{hmin} intact formation of shale is formed. During the drilling process, the ECD value is also controlled by S_{hmin}. In the shallow depth section, the collapse pressure controls the mud specific gravity. In deeper intervals and Longmaxi shale intervals, although some areas with weak compressive properties will affect the correct selection of the appropriate mud proportion, pore pressure is still the most important factor in selecting a reasonable mud proportion.

TABLE 2
Recommended minimum specific gravity of mud of the first two sections in Well Wei 202H19-5

Depth/m	The specific gravity of mud /SG
To729	1.1
729-1000	1.45
1000-1600	1.45
1600-2300	1.63
2300-2860	1.93

TABLE 3
Recommended minimum specific gravity of mud of the third section in Well Wei 202H19-5

Depth/m	The specific gravity of mud /SG
2860-2900	1.9
2900-3000	1.95
3000-3070	2.05
3070-TD	2.18-2.23

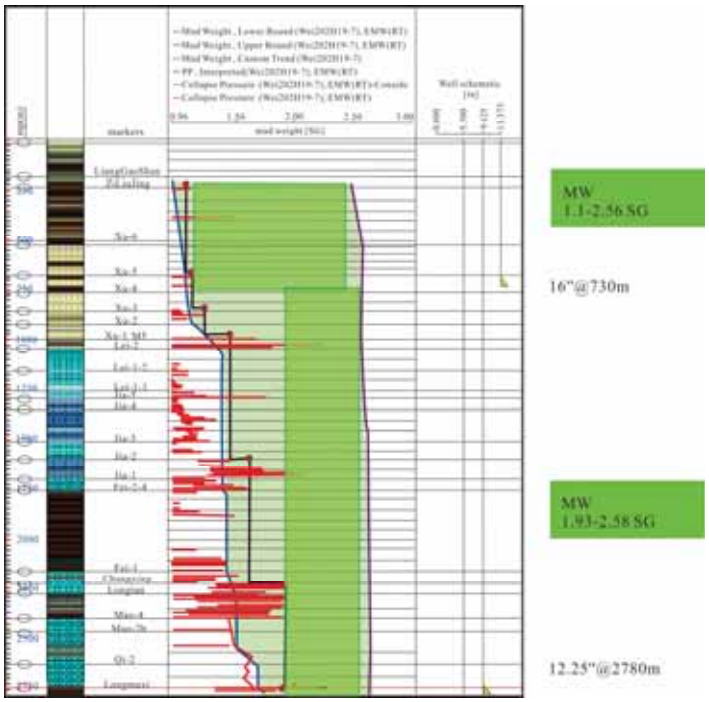

FIGURE 7
Prediction of the safety mud window of the first two sections Well Wei 202H19-7

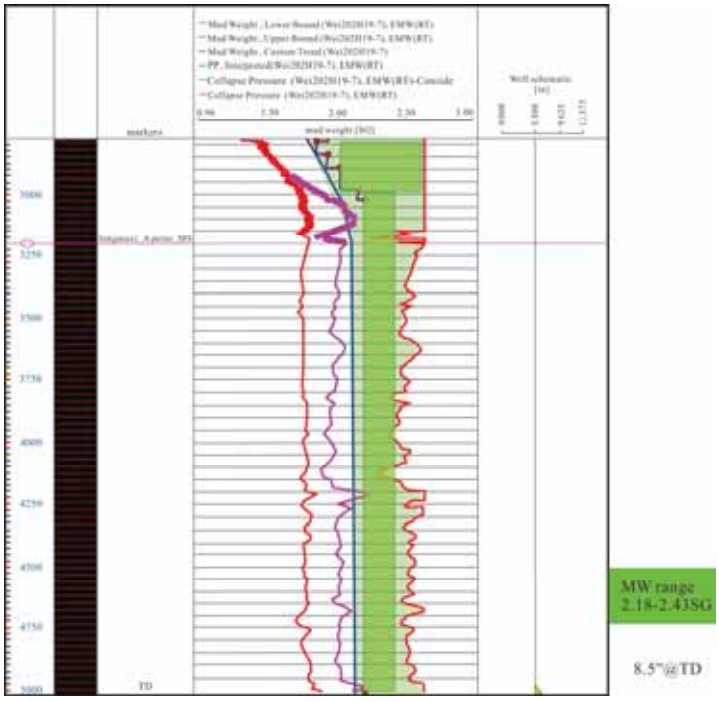

FIGURE 8
Prediction of safety mud window of the third section in Wei 202H19-7

By analyzing and predicting the conditions of borehole wall instability and borehole collapse in this well. The optimized geomechanical model and the recommended mud gravity were used to predict the instability of the wellbore. The prediction results show that most of the collapse angles of the vertical well section are less than 90 degrees, and the horizontal wells are less than 30 degrees. If wellbore cleanliness is maintained during drilling and the reaction between shale reservoirs and drilling fluids is

minimized, the recommended mud density can ensure safe drilling of the wellbore trajectory.

For formations above Jia 2, it is recommended that the minimum mud specific gravity should be 1.1-1.45 SG to reduce formation collapse. For the Jiajia-Liangshan Formation, the minimum mud specific gravity needs to be 1.85-1.93 SG to reduce formation collapse (Table 4). For Jia2 and Longtan formations, it is recommended to increase mud to effectively provide the stability of the borehole wall. The study concluded that the weak bedding existing in the shale gas reservoir may cause the rupture of the relevant bedding. In order to prevent the bedding failure, it is recommended that the mud specific gravity range of the inclined well section is 1.9-2.05 SG, the minimum mud specific gravity of the horizontal well section is 2.18-2.23SG (Table 5). This means that if the stability of weak rocks is to be maintained, the mud ratio is more important than the pore pressure. Because the mud gravity safety window is very small in the horizontal section of a horizontal well, the management of ECD is extremely important. If good borehole cleanliness is maintained during drilling, reasonable drilling fluid types are used, and the reaction between shale reservoirs and drilling fluids is minimized, the recommended mud density should ensure safe drilling of the wellbore trajectory.

TABLE 4
Recommended minimum specific gravity of mud of the first two sections in Well Wei 202H19-7

Depth/m	The specific gravity of mud /SG
To730	1.1
730-950	1.45
950-1600	1.45
1600-2200	1.63
2200-2780	1.93

TABLE 5
Recommended minimum specific gravity of mud of the third section in Well Wei 202H19-7

Depth/m	The specific gravity of mud /SG
2780-2840	1.9
2840-2900	1.95
2900-3000	2.05
3000-TD	2.18-2.23

CONCLUSIONS

(1) The reservoir section of Wei 202 pre-drilling model is estimated to be a strike-slip stress mechanism, and the upper and lower formations are reverse fault in-situ stress mechanisms. However, due to the influence of the ultra-high pressure, the three principal stresses in the Longmaxi Formation are very similar, which may lead to a transitional forward fault mechanism or a reverse fault mechanism at a certain depth.

(2) From the surface to 1000mTVD, the pore pressure is the hydrostatic pressure. High pressure appears from the Xujia River Formation. After that, the overpressure gradually increases with the depth, and the increase rate varies in different regions. The formation pressure of the Longmaxi reservoir section in Wei 202 block reaches 1.56SG, and the rocks generally appear very hard. The rock strength of the Longmaxi reservoir section is 87-115MPa.

(3) The geomechanical model of Wei 202 has been verified by drilling and imaging data of adjacent wells. This model can be used for optimization of well design and wall stability analysis of new wells in the block. Different formation drilling directions have different effects on borehole stability. For horizontal wells with drilling direction and S_{Hmax} direction, higher mud specific gravity is required. In the Longmaxi Formation, the azimuth has a greater impact on the collapse pressure, and the specific gravity of the mud required to drill a high-angle well in the S_{Hmax} direction is slightly lower.

ACKNOWLEDGEMENTS

This research was financially supported by the Key Science and Technology Project of the Sichuan Province, China (No. 2015SZ0003).

REFERENCES

[1] Xie, J. (2017) Rapid shale gas development accelerated by the progress in key technologies: a case study of the Changning-Weiyuan National shale gas demonstration zone. Natural Gas Industry. 37(12), 1-10.

[2] Ma, X., Xie, J. (2018) The progress and prospects of shale gas exploration and exploitation in southern Sichuan Basin, NW China. Petroleum Exploration and Development. 45(1), 161-169.

[3] Xie, J. (2018) Practices and achievements of the Changning–Weiyuan shale gas National demonstration project construction. Natural Gas Industry. 38(2), 1-7.

[4] Gutman, E., Haddad, J., Bergman, R. (2005) Stability of thin-walled high-pressure cylindrical pipes with non-circular cross-section and variable wall thickness subjected to non-homogeneous corrosion. Thin-Walled Structures. 43(1), 23-32.

[5] Safari-Beidokhti, M., Hashemi, A. (2016) Condensate blockage effects in well test analysis of dual-porosity/dual-permeability, naturally fractured gas condensate reservoirs: A simulation approach. Journal of Petroleum Exploration and Production Technology. 6(4), 729-742.

[6] Park, Y., Sung, W., Kim, S. (2002) Development of a fem reservoir model equipped with an effective permeability tensor and its application to naturally fractured reservoirs. Energy Sources. 24(6), 1531-542.
[7] Zhang, W., Lin, C., Zhou, M., Wang, H. (2010) Application of geological model dynamic updating method in Guanjiapu Oilfield, Dagang. Petroleum Exploration and Development. 37(2), 220-225.
[8] Wang, M., Duan, T., Du, X., Lian, P., Li, Y., Zhang, W. (2018) Geological modeling method based on sedimentary facies coupled rock type for porous carbonate reservoirs. Petroleum Geology and Experiment. 40(2), 253-259.
[9] Yin, S., Lv, D., Ding, W. (2018) New method for assessing microfracture stress sensitivity in tight sandstone reservoirs based on acoustic experiments. International Journal of Geomechanics. 18(4), 1-16.
[10] Meng, M., Qiu, Z. (2018) Experiment study of mechanical properties and microstructures of bituminous coals influenced by supercritical carbon dioxide. Fuel. 219, 223-238.
[11] Meng, M., Baldino, S., Miska, S., Takach, N. (2019) Wellbore Stability in Naturally Fractured Formations Featuring Dual-Porosity/Single-Permeability and Finite Radial Fluid Discharge. Journal of Petroleum Science and Engineering. 174, 790-803.
[12] Jia, P., Cheng, L., Huang, S., Wu, Y. (2016) A semi-analytical model for the flow behavior of naturally fractured formations with multi-scale fracture networks. Journal of Hydrology. 537, 208-220.
[13] Ding, Y., Luo, P., Liu, X., Liang, L. (2018) Wellbore stability model for horizontal wells in shale formations with multiple planes of weakness. Journal of Natural Gas Science and Engineering. 52, 334-347.
[14] Yuan, J., Deng, J., Tan, Q., Yu, B., Jin, X. (2013) Borehole stability analysis of horizontal drilling in shale gas reservoirs. Rock Mechanics and Rock Engineering. 46(5), 1157-1164.
[15] Liu, Y., Qiu, Z., Zhong, H., Nie, Z., Li, J., Huang, W., Zhao, X. (2019) Bitumen Recovery from Crude Bitumen Samples from Halfaya Oilfield by Single and Composite Solvents-Process, Parameters, and Mechanism. Materials. 12(17), 2656.
[16] Liu, Y., Qiu, Z., Nie, Z., Li, J., Zhong, H., Huang, W., Zhao, X. (2019) Numerical Simulation and Analysis of the Bitumen Intrusion Mechanism Based on Density Difference Between Bitumen and Drilling Fluid in Halfaya Oilfield, Iraq. Fresen. Environ. Bull. 28, 8275-8281.
[17] Biryukov, D., Kuchuk, F. (2015) Pressure transient behavior of horizontal wells intersecting multiple hydraulic fractures in naturally fractured reservoirs. Transport in Porous Media. 110(3), 369-408.
[18] Corkum, A., Damjanac, B., Lam, T. (2018) Variation of horizontal in situ stress with depth for long-term performance evaluation of the deep geological repository project access shaft. International Journal of Rock Mechanics and Mining Sciences. 107, 75-85.
[19] Liu, H. (2008) The relation between density and P-wave velocity of rocks in Jiyang Depression. Petroleum Geology and Recovery Efficiency. 15(6), 26-28.
[20] Deng, J., Lin, H., Hu, L., Chen, Z., Yuan, J., Liu, Z. (2013) Variations of In-situ Stress and Wellbore Stability for Kingfisher Block Through the Fault. Science and Technology Review. 31(23), 53-56.
[21] Yang, Z., Wu, B., Wang, Y. (2012) Application of Eaton Method in Predict the Formation Pore Pressure of M Oilfield. Journal of Oil and Gas Technology. 9, 181-182.
[22] Birchwood, R., Noeth, S. (2012) Horizontal stress contrast in the shallow marine sediments of the Gulf of Mexico sites Walker Ridge 313 and Atwater Valley 13 and 14 - Geological observations, effects on wellbore stability, and implications for drilling. Marine and Petroleum Geology. 34(1), 186-208.
[23] Delgado, J., Garrido, J., Lenti, L., Lopez-Casado, C., Martino, S., Sierra, F. (2015) Unconventional pseudostatic stability analysis of the Diezma landslide (Granada, Spain) based on a high-resolution engineering-geological model. Engineering Geology. 184, 81-95.
[24] Gentzis, T., Deisman, N., Chalaturnyk, R. (2009) A method to predict geomechanical properties and model well stability in horizontal boreholes. International Journal of Coal Geology. 78(2), 149-160.
[25] Wu, X. (2019) Key Technologies for Evaluation and Development of High Productivity Zone in Weiyuan Shale Gas Field, Sichuan Basin. Petroleum Drilling Techniques. 47(4), 1-9.
[26] Ma, C., Zhang, X., Li, S. (2017) 3D geological modeling of effective shale-gas reservoirs: Taking Wei 202H2 platform of Weiyuan Area as an example. Fault-Block Oil and Gas Field. 24(4), 495-499.
[27] Liang, C., Chen, M., Jin, Y., Lu, Y. (2014) Wellbore stability model for shale gas reservoir considering the coupling of multi-weakness planes and porous flow. Journal of Natural Gas Science and Engineering. 21, 364-378.

[28] Xu, P., He, Z., Wen, X., Lei, F., Hu, C. (2010) The Relationship between Compressional Wave Velocity and Density of Carbonate Reservoirs. Journal of Oil and Gas Technology. 6, 391-394.
[29] Zang, Y., Wang, R., Wang, Z., Zhang, R., He, Y. (2012) Evaluation of Uncertainties for Pore-pressure Taking Eaton Method as an Example. Journal of Southwest Petroleum University (Science and Technology Edition). 34(4), 55-61.

Received: **09.12.2019**
Accepted: **27.01.2020**

CORRESPONDING AUTHOR

Qihua Ran
Shale Gas Exploration and Development Department,
CNPC Chuanqing Drilling Engineering Company Limited,
Chengdu 610051 – China

e-mail: yangchunpetro01@163.com

© by PSP Volume 29 – No. 04A/2020 pages 3102-3109 Fresenius Environmental Bulletin

RELATIONSHIP BETWEEN HOPELESSNESS AND SELF-ESTEEM OF PREGNANT WOMEN: A CROSS-SECTIONAL STUDY IN SOUTH EASTERN TURKEY

Ilknur Yesilcinar[1,*], Derya Yanik[2], Sahide Akbulut[2]

[1]Izmir Katip Celebi University, Health Science Faculty, Nursing Department, Obstetrics and Gynecology Nursing
[2]Batman University, Health School, Nursing Department

ABSTRACT

This study aimed to determine relationship between hopelessness and self-esteem of pregnant women.

This descriptive cross-sectional study was conducted between February and June 2019 at the maternity and children hospital of a province, located in south-east region of Turkey. 128 pregnant women in the third trimester, who applied to the hospital in order to receive antenatal care, constituted the sample. "Sociodemographic data form", "Rosenberg self-esteem scale" and "Beck hopelessness scale" were used for data collection. Statistical significance was set at $p<0.05$.

Mean age of the participants was 27.99±5.89 and mean gestational week was 34.67±6.44. Mean total scores obtained from the Rosenberg Self-Esteem and Beck Hopelessness scales were 0.97±0.47 and 4.92±4.02, respectively. We found a statistically significant relationship between the education level of the pregnant women and mean score obtained from the Beck hopelessness scale ($p<0.05$). We also found a weak and positive relationship between self-esteem and hopelessness levels of the participants (r: 0.251, p: 0.005).

This study found that self-esteem levels of the participants decreased as their hopelessness levels increased. Besides, pregnant women with lower education level had higher hopelessness levels. The feeling of hopelessness during the pregnancy had a negative impact on self-perception, which, in turn, creates problems for the pregnant mother to fulfill their roles of motherhood. Consequently, we may suggest that the attempts to increase education levels of women may help them to demonstrate healthy lifestyle behaviors.

KEYWORDS:
Pregnancy, hopelessness, self-esteem, nursing

INTRODUCTION

Pregnancy, which starts with fertilization and ends with childbirth, creates important psychological and emotional changes for pregnant women [1,2,3]. Physical changes in their bodies and uncertainty about the antenatal and postnatal periods creates anxiety and excitement, which, in some cases, may lead to psychosocial problems for pregnant women [3]. Due to this reason, pregnancy is considered as a natural crisis to which women may find it hard to adapt [2]. Adaptation to the physical and psychological changes caused by pregnancy is influenced by the previous experiences of pregnant women and their ability to cope with stress. Pregnancy may result in higher self-esteem. However, negative expectations about the future, unplanned or unwanted pregnancies and low self-esteem may lead to a feeling of hopelessness and decrease in self-confidence, which, in turn, may decrease hopes about the future [1,2,4]. Hopelessness may be defined as a psychological situation in which, the individual assigns negative characteristics to him/herself, has negative expectations from the future and considers negative developments as an unchangeable part of his/her life [5]. Although prenatal period is considered by most women as a positive life experience since the period mostly ends with childbirth, health problems during the prenatal period, problems related with social support, physical and emotional burden of pregnancy and hormonal change during the prenatal period may have negative effects on emotional status of pregnant women [2,3]. Although hopelessness is widespread among the women with recurrent pregnancy loss or health problems during prenatal period and the couples with infertility problems, it may be affected by socio-demographic characteristics of pregnant women and the emotional effects of pregnancy on women [1,5,6]. Social and psychological problems during the prenatal period increases prenatal complications and have negative impacts on both the mother and the newborn during both the prenatal and postnatal periods [7,8]. Due to this reason, hopelessness levels of the women with healthy pregnancy should be evaluated. The review

of the literature reveals that no study has been conducted to evaluate the hopelessness levels of women with healthy pregnancy.

Self-esteem of pregnant women plays a crucial role to solve psychosocial problems and cope with difficulties. Self-esteem, which may be defined as the value that an individual assigns him/herself, helps the individual to evaluate him/herself and accept his/her weaknesses and strengths [9]. Lower self-esteem may result with lower self-confidence, risky sexual intercourse, adolescent pregnancy, depression and hopelessness [4-6,10-12]. Existing studies found that the level of self-esteem is influenced by factors, including, educational and socioeconomic levels and family type of pregnant women, spouse support, having consanguineous marriage and planning status of pregnancy [3,6,13].

Self-esteem and hope for the future should be encouraged in order to maintain a healthy psychological status during the prenatal and postnatal periods, prevent prenatal complications and encourage positive health behaviors [14]. According to data provided by Turkish Statistical Institute (TUIK), Turkey's total fertility rate was 1.99 in 2018. Provincial fertility rate, which ranged between 1.3 and 4.13, was lower in provinces in Western Anatolia, which were characterized by higher socio-economic development levels [15,16]. Fertility rate of the province that this study was conducted, was 3.17, which is well above the Turkish fertility rate in 2018 [15,16]. Due to this reason, we believe that high fertility rate in the province may influence self-esteem and hopelessness levels of the pregnant women. There is a considerable number of studies on psychosocial problems during the prenatal period. However, we have not found any studies that analyzed the self-esteem and hopelessness levels of women with healthy pregnancy. This study aims to determine the self-esteem and hopelessness levels of pregnant women.

MATERIALS AND METHODS

This descriptive cross-sectional study was conducted between February and June 2019 at a maternity and children hospital, which was located in a south-eastern province of Turkey. Without calculating sample size, we asked 186 pregnant women, who applied to the hospital to receive antenatal care and met the inclusion criteria, to participate in the research. 128 pregnant women that agreed to participate constituted the sample of the study.

Inclusion Criteria. Women that met the following criteria were included to the study:

- Had cognitive capacity to answer the questions,
- Could speak Turkish,
- Did not have any psychiatric disorders,
- In third trimester
- Volunteered to participate to the research.

Data Collection. We used "Sociodemographic Data Form", "Rosenberg Self-esteem Scale" and "Beck Hopelessness Scale" for data collection. After obtaining their informed consent, the principal investigator conducted face-to-face interviews with the participants. The principal investigator read the data collection questionnaires and recorded the responses of the participants. Data collection per participant took approximately 15 minutes.

Sociodemographic Data Form. This form was prepared by the researchers by using the relevant literature [3,6,9,13]. The form consisted of 14 questions on sociodemographic and obstetric characteristics of the participants.

Rosenberg Self-esteem Scale (RSS): RSS was developed by Morris Rosenberg in 1963 [17]. The first ten items of the scale, which has 12 subscales and 63 items in total, is used to measure global self-worth. The scale, which has five positive and five negative items, is rated on a four-point Likert type scale, with higher scores indicating lower self-esteem levels. Total score ranges between zero and six and a total score of 0-1 indicates high, 2-4 moderate and 5-6 low self-esteem. Reliability and validity of the Turkish version of the scale was evaluated by Çuhadaroğlu [18].

Beck Hopelessness Scale (BHS). BHS was developed by Beck et al (1971) [19] in order to evaluate the level of hopelessness. Validity of the Turkish version of the scale was tested by Durak and Palabıyıkoğlu (1994) [20]. The scale, which measures the pessimism about the future, has 20 items. Total score ranges between 0 and 20 with higher scores indicating higher hopelessness [20].

Ethical Considerations. We obtained written permission from Batman Regional State Hospital Ethical Board (No. 131, dated 28.01.2019). We also obtained written and verbal informed consent from the participants. Authors declare that the procedures were followed according to the regulations established by the research and ethics committee and to the Helsinki Declaration of the World Medical Association.

Data Analysis. We used IBM SPSS Statistics 26.0 statistical software for data analysis. Descriptive statistics (frequency, percentage, mean and standard deviation), T-test, Mann-Whitney U test, Kruskal-Wallis test and one-dimensional correlation analysis were used for statistical evaluation of collected data. Statistical significance was set at $p<0.05$ for all data.

TABLE 1
Socio-Demographic and Obstetric Characteristics of Participants

Characteristics	n=128	
	$\bar{X}$	±SS
Age	27.99	±5.89
Gestational Week	34.67	±6.44
	n	%
Age Group		
19-34	109	85.2
35-46	19	14.8
Education Level		
Illiterate	36	28.2
Primary and Secondary	59	46.1
High School	20	15.6
University and higher	13	10.2
Employment		
Employed	11	8.6
Unemployed	117	91.4
Income		
Low	38	29.7
Moderate	75	58.6
High	15	11.7
Number of Previous Pregnancies (Min: 1-Max: 11)		
1	32	25.0
2-3	55	43.0
4 and higher	41	32.0
Consanguineous Marriage		
Yes	43	33.6
No	85	66.4
Miscarriage		
Yes	46	35.9
No	82	64.1

TABLE 2
Comparison of the sociodemographic and obstetric characteristics of the participants with their mean total RSS and BHS scores

Characteristics	n	Mean BHS Score ($\bar{X}$ ± SS)	Mean RSS score ($\bar{X}$ ± SS)
Age			
18-34	109	4.77±3.68	0.97±0.47
35-46	19	5.78±5.58	0.97±0.49
Z, p*		-0.558, 0.577	-0.213, 0.831
Socio-Economic Level			
Low	38	5.84±4.61	0.92±0.44
Moderate	75	4.68±3.84	0.99±0.48
High	15	3.71±2.72	1.01±0.50
F, p		3.919, 0.141	0.631, 0.729
Number of previous pregnancies			
1	32	4.06±3.04	0.96±0.52
2-3	55	4.64±3.44	1.00±0.44
4 and higher	41	5.92±5.18	0.95±0.49
F, p		2.013, 0.266	0.409, 0.815
Education Level			
Illiterate	36	5.44±4.90	1.00±0.49
Primary and Secondary	59	5.26±3.57	1.01±0.52
High School	20	4.70±4.14	0.83±0.32
University and above	13	2.38±1.70	0.93±0.35
F, p		10.899, 0.018	1.694, 0.638
Consanguineous Marriage			
Yes	43	6.00±4.83	1.05±0.50
No	85	4.38±3.44	0.93±0.45
Z, p		-1.695, 0.090	-1.266, 0.206

* p values for F test are given for comparison of three or more groups and p values for Z test are used for comparison of two groups.

RESULTS

Mean age of the 128 participant pregnant women was 27.99±5.89 and the mean gestational week was 34.67±6.44. 28.2% of the participants was illiterate whereas 46.1% was graduate of primary school. 91.4% was unemployed and 58.6% had moderate income levels. Mean number of pre-

vious pregnancies was 3.14±2.20 and 43.0% of the participants had 2-3 children. 33.6% had consanguineous marriage and 35.9% had history of miscarriage. Table 1 shows the sociodemographic and obstetric characteristics of the participant pregnant women.

Mean total RSS and BHS scores of the participants were 0.97±0.47 and 4.92±4.02, respectively. Table 2 compares some of the sociodemographic and obstetric characteristics of the participants with their mean total RSS and BHS scores. We did not find any statistically significant relationship between the mean total RSS and BHS scores of the participants and their age, socio-economic level, number of previous pregnancy and consanguineous marriage (p>0.05). However, we found a statistically significant relationship between the education levels of the participants and mean total score obtained from BHS (F: 10.899, p: 0.018). The finding suggests that hopelessness levels of the participants that had an education level of university or above were statistically significantly lower than the rest of the participants. On the other hand, we did not find any statistically significant relationship between the education level and RSS scores of the participants (p>0.05).

Table 3 compares some of the sociodemographic and obstetric characteristics of the participants with the scores obtained from the three factors of the BHS. We did not find any statistically significant relationship between mean BHS factor scores, age and the number of previous pregnancies of the participants (p>0.05). However, we found a statistically significant relationship between the socio-economic levels of the participants and mean scores obtained from the "feelings about the future" and "expectations" factors of the BHS (F: 10.224, p: 0.006). Participants with lower socio-economic levels obtained higher scores from the "feelings about the future" and "expectations" factors, indicating negative feelings and expectations about the future. Besides, we found a statistically significant relationship between the education levels of the participants and the scores obtained from the "loss of motivation" factor of the BHS (F: 12.728, p: 0.005). Loss of motivation was lower for the participants that had an education level of university or above. Finally, we found a statistically significant relationship between having consanguineous marriage and the score obtained from the "expectation" factor (Z:-2.003, p: 0.045). Pregnant women that had consanguineous marriage had lower expectation levels.

TABLE 3
Comparison of the sociodemographic and obstetric characteristics of the participants with the scores obtained from the three factors of the BHS

Characteristics	n	Feelings about the future ($\overline{X}$ ± SS)	Loss of motivation ($\overline{X}$ ± SS)	Expectations ($\overline{X}$ ± SS)
Age				
18-34	109	0.68±1.12	2.41±1.93	1.66±1.40
35-46	19	1.21±1.68	2.78±2.46	1.78±1.84
Z, p*		-1.380, 0.168	-0.432, 0.666	-0.221, 0.825
Socio-Economic Level				
Low	38	1.26±1.50	2.60±2.23	1.97±1.53
Moderate	75	0.55±1.07	2.50±1.94	1.60±1.50
High	15	0.53±0.83	1.92±1.77	1.40±1.05
F, p		10.224, 0.006	0.832, 0.660	2.483, 0.289
Number of previous pregnancies				
1	32	0.35±0.70	2.22±1.56	1.48±1.48
2-3	55	0.78±1.14	2.31±1.84	1.58±1.38
4 and higher	41	1.05±1.56	2.80±2.48	1.97±1.62
F, p		4.275,0.118	0.291, 0.865	2.098, 0.350
Education Level				
Illiterate	36	0.91±1.55	2.61±2.28	1.91±1.44
Primary and Elementary	59	0.75±1.06	2.73±2.00	1.74±1.46
High School	20	0.75±1.33	2.45±1.79	1.50±1.57
University and above	13	0.38±0.65	0.92±0.49	1.07±1.38
F, p		1.297, 0.730	12.728, 0.005	4.776, 0.189
Consanguineous Marriage				
Yes	43	1.09±1.63	2.85±2.32	2.00±1.48
No	85	0.59±0.93	2.37±1.82	1.52±1.45
Z, p		-0.947, 0.344	-1.203, 0.229	-2.003, 0.045

* p values for F test are given for comparison of three or more groups and p values for Z test are used for comparison of two groups.

TABLE 4
Correlation between RSS, BHS and factors

Scale	RSS	
	r	p
BHS	0.251*	0.005
Feelings about the future	0.191**	0.032
Loss of motivation	0.260*	0.003
Expectations	0.169	0.057

*Correlation is significant at the 0.01 level (2-tailed).
**Correlation is significant at the 0.05 level (2-tailed).

TABLE 5
Relationship between the scores obtained from the RSS, BHS and its factors according to the number of previous pregnancies and the age of participants

Scale	Number of Pregnancy		**Age**	
	r	p	**r**	**p**
RSS	0.004	0.962	-0.040	0.652
BHS	0.314*	<0.001	0.119	0.186
Feelings about the future	0.312*	<0.001	0.202	0.017**
Loss of motivation	0.249*	0.003	0.067	0.457
Expectations	0.234*	0.008	0.048	0.592

*Correlation is significant at the 0.01 level (2-tailed).
**Correlation is significant at the 0.05 level (2-tailed).

Table 4 displays the relationship between the total RSS score, total BHS score and the scores obtained from the three factors of the BHS. The table shows a weak, positive (r: 0.251) and statistically significant (p: 0.005) relationship between the self-esteem and hopelessness levels of the pregnant women. Total RSS scores of the participants increase as their total BHS scores increase. Higher scores obtained from the RSS indicate lower self-esteem (Keskin and Babacan-Gümüş, 2014). We also found a weak, positive (r: 0.191) and statistically significant (p: 0.032) relationship between the RSS score and the scores obtained from the "feelings about the future" and "expectations" factors of the BHS. As the self-esteem levels of the pregnant women increased, their hopelessness about the future and expectations also increased. Finally, we found a weak, positive (r: 0.260) and statistically significant (p: 0.003) relationship between the RSS scores and the score obtained from the "loss of motivation" factor of the BHS. The finding indicates that "loss of motivation" levels of the participants increased as their self-esteem levels decreased.

Table 5 shows a statistically significant relationship between the number of previous pregnancies and the scores obtained from the BHS and its three factors. The finding indicates that hopelessness and loss of motivation levels of the participants increase as the number of previous pregnancies increase. Besides, increase in the number of previous pregnancies is associated with negative feelings and expectations about the future. Finally, we found no statistically significant relationship between the age of the participants and the scores obtained from the RSS, BHS and its three factors.

DISCUSSION

Self-Esteem. Individuals' self-perception may have an impact on their self-esteem. Pregnancy is one the situation that may affect the self-perception and self-esteem. Because of this, some of the individual properties such as educational level may positive affect on self-esteem [11]. In our study we found no significant relationship between the self-esteem and education levels of the participants, but some of the existing studies note that self-esteem levels were lower for pregnant women with lower education levels [13,21]. We may relate the absence of the relationship between education and self-esteem levels in our study to the widespread belief in the region of our study that "woman is valuable as long as she is fertile". Due to such a belief, being a pregnant woman is considered as dignified, which, in turn, increases self-esteem levels of the participants. As a result of this belief, self-esteem levels of the participants in this study was considerably high. The study of Maçola et al. (2010) on 127 pregnant women found that women with unplanned pregnancy had lower self-esteem levels [13]. Unlike this study, we found no significant relationship between self-esteem and having unplanned pregnancy.

We found no significant relationship between the number of previous pregnancies and self-esteem levels. Our findings are consistent with some of the studies in the literature [13,21]. Besides, we did not find any significant relationship between consanguineous marriage and self-esteem levels. A study on 150 pregnant women that live in a province at the western region of Turkey found that self-esteem levels of the participants that had consanguineous marriage was lower [21]. We may explain this

difference with reference to regional differences about the perception of consanguineous marriage in Turkey. Consanguineous marriage is widespread and considered as a normal practice in eastern regions of Turkey, including the province that this study was conducted [14,15]. The percentage of consanguineous marriage in our study is 33.6%, whereas the percentage in the study of Babacan Gümüş et al. (2011), which was conducted in western Marmara region, was 9.3% [21]. Furthermore, statistical data provided by the TUIK shows that the percentage of consanguineous marriage in south-eastern region of Turkey, including the province that our study was conducted, was 42.6% whereas the percentage for the western Marmara region was 8.2% in 2016 [14,15]. Due to this regional difference, we did not find any significant relationship between consanguineous marriage and self-esteem levels.

Hopelessness. We found that hopelessness level of the pregnant women with lower education levels was significantly high. Another study on Turkish pregnant women found no relationship between education and hopelessness levels [5]. Higher hopelessness levels of the participants of our study may be explained with reference to the low education and socio-economic levels of the women and the traditional cultural values, which are hard to be changed in the region of our study.

Hopelessness levels of the participants of our study increased as their number of previous pregnancies increased. The study of Keskin and Babacan Gümüş (2014) found that hopelessness levels of infertile women increased as the duration of infertility treatment increased [5]. These two different findings show that childlessness and having a high number of children lead to higher levels of hopelessness. Society may consider having children as an indicator of being a family [22]. Thus, childlessness may be considered as a deficit in the family and an indicator of inadequate parents. On the other hand, although having children increases self-esteem levels of the women, having a high number of children puts further burden on pregnant women, which, in turn, increases their hopelessness levels. Having lots of children increases not only self-esteem but also hopelessness levels of the women in south-eastern region of Turkey due to increased burden of childcare.

This study found that self-esteem levels of the participants decreased as their hopelessness levels increased. A study on 141 women, who received infertility treatment, found a relationship between self-esteem and hopelessness levels [5]. As the self-esteem of the participants in our study decreased, negative feelings about the future and the loss of motivation increased. Similarly, a study on infertile women found a moderate relationship between "feelings about the future" and "loss of motivation" factors of the BHS and self-esteem levels of the participants [5]. Two studies on different samples of healthy pregnant and infertile women had similar findings on the relationship between hopelessness and self-esteem. Hopelessness of the women with healthy pregnancy in our study may be explained with reference to the sociodemographic characteristics of our participants, who live in south-eastern region of Turkey. Our findings on the increase of hopelessness levels, loss of motivations, pessimism about the future expectations and negative feelings about the future parallel to the increase in the number of previous pregnancies supports our argument.

We found that hopelessness of the participants increased as their self-esteem levels decreased. There is a limited number of studies that deals with self-esteem and hopelessness levels of pregnant women [4,5]. Other studies analyzed the hopelessness levels of women with special problems, such as infertile women [5,21], adolescents [4,6] and women with postpartum depression [7,11] and women who diagnosed with cervical cancer [23]. We did not find any studies on women with healthy pregnancy or having a high number of children. We believe that this study may contribute to the literature by filling this deficit.

LIMITATIONS

The number of participants in this study was limited due to the cultural values, language problems between the researchers and the participants and the reluctance of the pregnant women to take part in the research. Findings of this study reflect the characteristics of the region that the study was conducted and may not be generalized to the whole Turkish population.

CONCLUSIONS

Negative mindscapes, such as hopelessness, which are results of personal experiences, influence self-evaluation of the individuals. Due to this reason, hopelessness may have an impact on healthy life behaviors [4]. This study found that low education level and higher number of previous pregnancies had an impact on hopelessness level of the participants. Based on these findings, we may suggest that regulations to increase education level of women living in the region, where the study was conducted, should be enacted and family planning counseling services should be enhanced. Further research that evaluates the factors, which may have an impact on self-esteem and hopelessness levels of women with healthy pregnancy, should be undertaken.

REFERENCES

[1] Gümüş, A.B., Çevik, N., Hyusni, S.H., Biçen, Ş., Keskin, G., Malak, A.T. (2011) Characteristics Associated with Self_esteem and Body Image in Pregnancy. Anatol J Clin Investig. 5(1), 7-14.

[2] Kumcağız, H. (2012). Pregnant women, body image and self-esteem according to the examination of some of the variables. International Journal of Human Sciences. 9(2), 691-703.

[3] Aksay, Y., Yıldırım G.B., Saygın, N., Körükçü, Ö. (2017) Is There any Effect of Psychosocial Health of Pregnant Women on Birth Preference? Gümüşhane University Journal Of Health Sciences. 6(4), 138-145.

[4] Fedorowicz, A.R., Hellerstedt, W.L., Schreiner, P.J., and Bolland, J.M. (2014). Associations of adolescent hopelessness and self-worth with pregnancy attempts and pregnancy desire. American Journal of Public Health. 104(8).

[5] Keskin, G., Babacan Gumus, A. (2014) Infertility: An examination hopelessness perspective. Journal of Psychiatric Nursing. 5(1), 9–16.

[6] Babington, L.M., Malone, L., Kelley, B.R. (2015). Perceived social support, self esteem, and pregnancy status among Dominican adolescents. Applied Nursing Research. 28, 121–126.

[7] Kettunen, P., Koistinen, E., and Hintikka, J. (2014). Is postpartum depression a homogenous disorder: time of onset, severity, symptoms and hopelessness in relation to the course of depression. BMC Pregnancy and Childbirth, 14:402. Retrieved from http://www.biomedcentral.com/1471-2393/ 14/ 402

[8] Siegel, R.S., Brandon, A.R. (2014). Adolescents, Pregnancy and Mental Health. Pediatr Adolesc Gynecol. 27, 138-150

[9] Lee E.J. (2015). The effect of positive group psychotherapy on self-esteem and state anger among adolescents at Korean immigrant churches. Archives of Psychiatric Nursing. 29, 108–13.

[10] Ethier K.A., Kershaw, T.S., Lewis, J.B., Milan, S., Niccolai, L.M. (2006). Self- esteem, emotional distress and sexual behavior among adolescent females: Inter-relationships and temporal effects. Journal of Adolescent Health. 38, 268 –276.

[11] Franck, E., Vanderhasselt, M.A., Goubert, L., Loeys, T. , Temmerman, M., Raedt, R. (2016). The role of self-esteem instability in the development of postnatal depression: A prospective study testing a diathesis-stress account. J. Behav. Ther. and Exp. Psychiat. 50, 15-22.

[12] Zubair, U.B., Mahjabeen S. (2017). Assessment of self esteem and affecting socio- demographic factors among pregnant women of a developing country. Journal Of Pakistan Psychiatric Society. 14(4),21-24.

[13] Maçola, L., Vale I.N. (2010). Carmona EV. Assessment of self-esteem in pregnant women using Rosenberg's Self-Esteem Scale. Rev Esc Enferm USP. 44(3), 569-76.

[14] Jeannette R. Ickovics, Elizabeth Reed , Urania Magriples , Claire Westdahl ,Sharon Schindler Rising and Trace S. Kershaw (2011). Effects of group prenatal care on psychosocial risk in pregnancy: Results from a randomised controlled trial. Psychology and Health. 26(2), 235-250.

[15] http://www.tuik.gov.tr/PreTablo.do?alt_id=1068. Access Date: 16.10.2019

[16] https://biruni.tuik.gov.tr/medas/?kn=113&locale=tr. Access Date: 16.10.2019

[17] Rosenberg, M. (1965). Society and the adolescent self-image. Princeton, NJ: Princeton University Press.

[18] Çuhadaroğlu F. (1986) Self-Esteem in Adolescents. Unpublished Master Dissertation, Hacettepe University, Ankara.

[19] Beck AT, Weissman A., Lester D., Trexler L (1971) The measurement of pessimism. The Hopelessness Scale. Journal of Consulting and Clinical Psychology. 12 (6), 861-865.

[20] Durak, A., Palabıyıkoğlu, R. (2006). Validity of Beck Hopelessness Scale. Kriz Journal. 2(2), 311-319.

[21] Babacan Gumus, A., Cevik, N., Hataf Hyusni, S., Bicen, Ş., Keskin, G., and Tuna Malak, A. (2011). Characteristics Associated With Self-Esteem and. Anatol J Clin Investig. 5(1), 7–14.

[22] Demirel Guler ZC, Guler AE, Kinci MF, Akturk E. (2019) Does parity and labor influence anxiety levels of pregnant women? Perinatal Journal. 27(1), 43–48.

[23] Gümüş, A.B., Çam, O. (2011). Relationships Between Early Diagnosis Attitudes In Cervical Cancer Of Women And Levels Of Self-Esteem, Body Perception And Hopelessness. Nobel Medicus. 7(3), 46-52.

Received: **10.12.2019**
Accepted: **29.01.2020**

CORRESPONDING AUTHOR

Ilknur Yesilcinar
Health Sciences Faculty,
Nursing Department,
Obstetrics and Gynecology Nursing ,
Izmir Katip Celebi University
35620 Cigli – Izmir

e-mail: iyesilcinar14@gmail.com

© by PSP Volume 29 – No. 04A/2020 pages 3110-3117 Fresenius Environmental Bulletin

IMPACT OF DYNAMIC FAULT DAMAGE TO CAPROCK ON OIL AND GAS RECOVERY OF TIGHT SANDSTONE

Yu Zhu*

Hua Zhong Agricultural University and College of Engineering, Hubei, Wuhan 430070, China

ABSTRACT

In order to improve the oil and gas exploration efficiency and recovery rate, the effect of the dynamic failure of the fault to the caprock on the oil and gas recovery of tight sandstone was studied. The influence of faults on oil and gas accumulation is analyzed in four parts: fault conductance, fault plugging, fault enrichment, and the effect of faults on the overall distribution of oil and gas. Based on the analysis results, the impact of faults on the damage of tight sandstone oil and gas reservoirs, and the damage scope and mechanism of dynamic damage of faults to caprock on tight sandstone oil and gas reservoirs were revealed. A model is constructed to realize the impact of dynamic failure of faults to the caprock on tight sandstone oil and gas recovery. The model is used to test a depression area with fault as the main structural type to verify the reliability of the model. Experimental results show that the evaluation model has high accuracy and robustness, and the application of the model in this paper can improve the efficiency of oil and gas exploration and the recovery rate.

KEYWORDS:
Fault, caprock, dynamic failure, tight sandstone, oil and gas recovery rate

INTRODUCTION

The overall demand for oil and natural gas is developing in an increasing trend. However, due to the increasing demand for the exploration and development, conventional oil and gas fields that are easier to explore have gradually been discovered. In the future, oil and gas exploration targets will shift to deeper basins with more complex geological conditions. Tight sandstone oil and gas reservoir contains a very large resource potential and will occupy a very important position in future oil and gas exploration. Currently, many important discoveries have effectively revealed the oil and gas potential in the deep layers of sedimentary basins. In recent years, exploration practice has proved that the development structure of relatively classic tight sandstone oil and gas reservoirs in China is relatively complicated. Especially in the multi-stage structure, the dynamic damage degree of faults to the caprock has a very critical controlling effect on tight sandstone oil and gas recovery. This effect will also cause the overall distribution of tight sandstone reservoirs to show a complex and changeable trend [1-3].

In fact, there are some differences from the typical tight sandstones at home and abroad. There are many types of tight sandstone oil and gas reservoirs in the deep layers of the depression, and their interruption layers are very common. Relevant issues such as the control effect of very widely distributed faults on different types of tight sandstone oil and gas, the mechanism by which faults control tight sandstone oil and gas, and the evaluation of the impact of faults on tight sandstone oil and gas recovery are still needed to be solved [4-5]. These issues are of great significance to the exploration of tight sandstone oil and gas. The practical results of deep oil and gas exploration show that the lack of scientific and reasonable theoretical guidance and evaluation methods for widely developed tight sandstone oil and gas reservoirs will lead to ambiguous exploration directions. Faults can not only provide a channel for oil and gas transfer, but also serve as a shielding surface for oil and gas. Therefore, the impact of faults on oil and gas recovery in tight sandstone is two-sided. However, the traditional evaluation theory of tight sandstone oil and gas accumulation cannot only fully describe the tight sandstone oil and gas accumulation under complex geological conditions, but also cannot describe the related factors of oil and gas recovery [6].

In summary, the analysis of oil and gas accumulation in tight sandstone under relatively complex tectonic environments and the efficient evaluation of oil and gas recovery in tight sandstone are of great significance and value to the exploration and development. The impact of the dynamic failure of the fault to the caprock on tight sandstone oil and gas recovery is studied. The failure mode is mainly used for the calculation to evaluate its impact on tight sandstone oil and gas recovery. The innovation of this paper is to use the combination of schematic diagrams and relevant test data to focus on refining the impact of late-developed faults on continuous tight sandstone reservoirs, improve the

impact evaluation model constructed, and strive to provide theoretical basis and constructive guidance.

MATERIALS AND METHODS

Impact of Faults on Hydrocarbon Accumulation. Practice has shown that [7], the channel and transmission system for the secondary transfer of oil and gas will directly affect the direction and the path of oil and gas transfer. Under normal circumstances, the overall migration of oil and gas at the fault depression location is mainly vertical, and secondary lateral. Among them, the various horizons and regional transfer modes also have certain differences. The interior of the basin is mainly lateral, and the boundary fault area is mainly vertical. Taking the Shaojia depression area as an example, the channel used for the secondary transfer of oil and gas in the depression area is a transmission network designed and constructed based on faults, fractures, and conductive layers. At the same time, its relationship with the overall space-time distribution of the source rock layer to the trap can control the formation and distribution of oil and gas reservoirs. Taking the Shaojia depression area as an example, the overall development of the sandstone transport layer in this area is not very high, and the overall connectivity of the limestone is not significant. It can be seen that faults and unconformities play a key role in the process of oil and gas transfer and accumulation in this area.

(1) Fault Conductance. Taking the Shaojia depression area as an example, faults have a relatively high overall development degree. The fault with significant fault distance, long active time, and large extended distance is one of the main channels for oil and gas transportation and transfer. The Sikou Sag in this area is the main oil supply area, and after the first transfer of produced oil and gas, the large-scale secondary transfer channel is mainly faults and regional unconformities. The oil and gas will be transmitted along the fault vertically. The unconformity encountered by the oil and gas along the vertical transmission of the fault will cause a lateral transmission to form a zigzag in the space, and finally form a composite oil and gas reservoir.

(2) Blockage of Faults. There is a certain correlation between fault plugging and its own nature, and this correlation is a function of time and space. At the temporal level, fault activity is dominated by opening and fault dormancy is dominated by blocking. At the spatial level, fault plugging will be affected by the overall permeability of the upper and lower plates to the ground plane. When the permeable formations are docked, there is no plugging situation, otherwise there will be a plugging situation [8-9]. Thick mudstone active faults, due to muddy smearing, will improve their plugging characteristics. For example, the ancient buried hill reservoir has a high performance in sealing the fault when it is docked with thick mudstones. However, it has a relatively low performance when it is docked with sandstones. In this area, the connectivity of the sandstones on both sides of the general caprock fault is significantly lower, showing good plugging properties, which is beneficial for the accumulation of oil and gas.

(3) Fault Enrichment. The fault will connect the relatively independent source rock and reservoir to a relatively large oil and gas reservoir system, so that scattered oil and gas will accumulate according to faults and fractures.

(4) The Effect of Faults on the Overall Distribution of Oil and Gas. Once the fault cuts through the formation, oil and gas on both sides of the fault can converge to the fault and further transfer. The fault-disconnected horizons can determine the direction of oil and gas transmission to a certain extent, and can also have an important impact on the distribution of oil and gas space [10-11]. The higher the fault disconnection level, the higher the hydrocarbon accumulation and accumulation level.

Impact Mechanism of Dynamic Failure of Faults to Caprock on Tight Sandstone Reservoirs. According to the above contents combined with related research, the overall distribution of tight sandstone reservoirs will be affected by the lower limit of buoyancy. Macroscopically, the lower limit of buoyancy where the dynamics of oil and gas transfer are equal to the transfer resistance [12-16]. Microscopically, there is a critical pore throat radius that controls the boundary of continuous tight sandstone reservoirs: within the reservoir, the pore throat radius of tight sandstone reservoirs is smaller than the critical pore throat radius. Under the molecular expansion forces, oil and gas are transferred and accumulated at the bottom, and at the same time, the formation water is systematically driven to gradually to the higher part, thereby forming a continuous tight sandstone oil and gas reservoir. When the reservoir pore throat radius is equal to the critical pore throat radius, a transition will be formed, where is the lower limit of buoyancy. When the pore throat radius of the reservoir is larger than the critical pore throat radius, oil and gas will gradually shift to a high point under the influence of buoyancy, and a continuous dense sandstone oil and gas reservoir cannot be formed, as shown in Figure 1 (a).

The force balance equation that has a decisive effect on the maximum distribution area of tight sandstone reservoirs is [17-18]:

$$P_e = P_w + P_c \quad (1)$$

Hydrostatic pressure is calculated as:

$$P_w = \rho_w g H \quad (2)$$

The formula for capillary pressure is:

$$P_c = 2\sigma \frac{\cos\theta}{r} \quad (3)$$

The gas expansion force is calculated as:

$$P_e = Z\rho_g \frac{RT}{M} \quad (4)$$

Based on the force balance equation, the critical pore throat radius calculation formula can be obtained:

$$r = \frac{2\sigma\cos\theta}{Z\rho_g RT / M - \rho_w g H} \quad (5)$$

In the above expression, σ represents the interfacial tension of water, θ is the wetting contact angle, H is the number of pressure points, g is the gas saturation, Z is the compression coefficient of the gas, ρ_g is the gas density, ρ_w is the water density, R is the gas constant, and M is the molar mass. T represents thermodynamic temperature.

It is assumed that faults are developed at the lower limit of buoyancy in the late stage. The fault-associated fractures will definitely increase the pore throat radius at this location to break the oil-gas force balance in this part. Oil and gas reservoirs are shrinking. At the same time, new reservoir accumulation boundaries are constructed based on force equilibrium conditions, as shown in Figure 1 (b). Therefore, the damage effect of late-developed faults on the lower limit of buoyancy is mainly reflected in the microcosm of the critical pore throat radius.

Based on the relevant test data, comparing the pore throat radius of fracture samples with the pore throat radius of samples without fractures, it can be seen that the diameter distribution range of pore throats of tight sandstone is 0.03μm to 2μm [19-20]. The width of the crack is usually 10μm to 40μm. The pore throat radius at the tight reservoir location increased by 0.5 to 51 times, as shown in Figure 2. Fractures at the late developmental location near the boundary of tight sandstone reservoirs will damage the balance of the lower limit force of buoyancy to a certain extent, thus causing continuous tight sandstone reservoirs to be damaged.

Based on the correlation of mercury intrusion data and core analysis data, the correlation between the porosity and permeability of the samples with fractures and samples without fractures can be understood. The ratio between the porosity of fractured samples and the porosity of samples without fractures Φ_1/Φ_2 is roughly 1: 1.5, indicating that the overall contribution of fractures to tight porosity is relatively small. However, the ratio between the permeability of fractured samples and the permeability of samples without fractures K_1/K_2 is approximately 10 to 1000, indicating that the role of fractures in permeability is significant which is shown in Figure 3. To sum up, during the late development of the lower limit of buoyancy for fault development, the permeability of the adjacent layer which is close to the lower limit is destroyed.

Evaluation of Oil and Gas Recovery in Faulted Tight Sandstone. Based on the above-mentioned analysis of the control indicators of the damage caused by the late fault to the lower limit of buoyancy and the mechanism of the failure of the fault on the tight sandstone reservoirs, a model for evaluating the oil and gas recovery of tight sandstone by the dynamic failure of faults to the caprocks is established.

Taking a certain stratum as an example, the scale of the fault is different, that is, the fault distance is different. The ratio between the permeability of the fault zone and the tight sandstone permeability varies with the distance from the fault surface. For the same fault, the closest distance to the fault, that is, without considering the fault core, the permeability of the fault to the tight sandstone improves the most. When the distance to the fault increases, the effect of the fault on the permeability improvement of the sandstone is weakening [21-23].

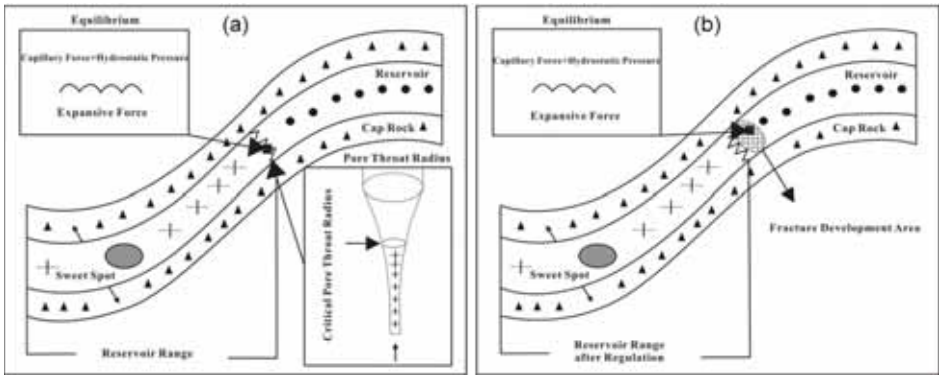

FIGURE 1
Theoretical schematic diagram of the failure of late developed faults to tight sandstone reservoirs.

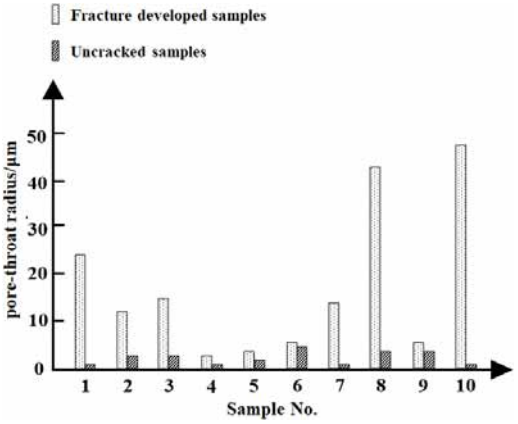

FIGURE 2
Schematic diagram of pore throat radius of cracked and non-cracked samples.

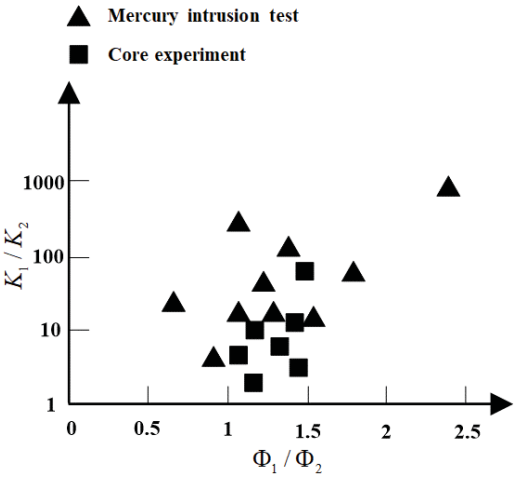

FIGURE 3
Comparison of porosity and permeability of cracked and non-cracked samples.

Quantitative evaluation model of the lower limit buoyancy damage of the fault zone constructed is shown in formula (6):

$$D = a \times \ln\left(\frac{K_1}{K_2}\right) \quad (6)$$

In the formula, D represents the distance from the fault, and α represents a constant.

Based on the evaluation model, it can be known that for a certain location of the fault, when the fault distance is a certain value, the fault destruction range can be judged based on equation (6).

In detail, when the distance from the fault surface is increasing, and the ratio between the permeability of the fault zone and the tight sandstone permeability is 1, indicating that the permeability of the fault zone is the same as that of the tight sandstone. The fault zone has no significant effect on improving the permeability of tight reservoirs. At this time, the corresponding distance from the fault is the range of failure caused by the lower limit of the buoyancy of the fault, which is shown in Figure 4.

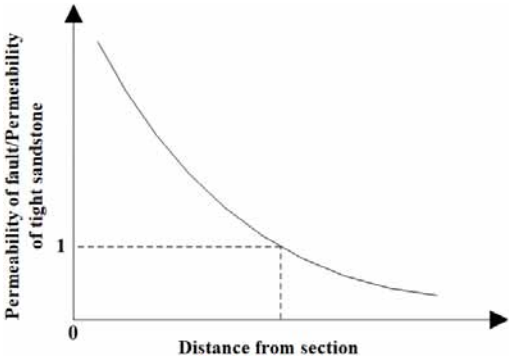

FIGURE 4
Evaluation model of the damage range caused by faults on the lower limit of buoyancy.

The effect of the dynamic failure of the fault to the caprock on the oil and gas recovery of tight sandstone is essentially the destruction of the lower limit of buoyancy. According to statistical analysis, it can be seen that the damage caused by faults to the lower limit of buoyancy has a certain scope. At the same time, the scope of damage is mainly controlled by fault distances. The larger the distance, the greater the extent of damage to the fault tight sandstone reservoir. After the development of late faults, the faults have caused damage to the force balance at the lower limit of buoyancy. Microscopically, the radius of the pore throat of tight sandstone reservoirs has been increased [24-25]. Macroscopically, the overall permeability of tight sandstone reservoirs has been increased. The loss of oil and gas and the shrinkage of oil and gas reservoirs will affect the recovery factor accordingly. Based on the correlation between the ratio of fault zone permeability and tight sandstone permeability under varying distances from the fault, a quantitative evaluation model is constructed, and the range from the core of the fault zone to the fault zone permeability and tight sandstone permeability is also approximately equivalent.

RESULTS AND DISCUSSION

The validity of the above evaluation model is verified by using a depression area with a fault as the main structural type as an experimental area.

Fault System in the Experimental Area. The existence of faults is an important and main structural type in the experimental area, which includes controlling the basement fault zone at the depression boundary and the internal fault zone generated during the development of the depression. The study area started from the Cenozoic and the distri-

bution of the fault plane was very complicated, which could be divided into near east-west, north-east and north-south directions. Fault characteristics are mainly manifested in the following aspects:

(1) There were significant differences in the degree of fault development, the pelvic margin was strong while the abdomen is weak. A large-scale base fault developed in the northern margin of the study area, and a large-scale concealed fault developed in the Pre-Tertiary in the eastern fault. A small-scale secondary fault developed in the depression. (2) Fault activities are intermittent and inherited. (3) Faults have a single characteristic in nature. Within the study area, all near-west, northwest faults, and small-east-north faults in the caprock range in some areas are tensile normal faults. (4) In the distribution, faults show two characteristics of division and direction. The distribution area of the main fault is the sag edge, and the distribution area of the secondary faults is mainly in the area of some low bulges and depressions. In the study area, some faults show strike-slip phenomenon due to the effect of tension and twist. The remaining faults are generally basin-dipping. The secondary faults in the area near the low bulge have a tendency to diverge to the northeast. (5) Some faults are closely related to magmatic activities.

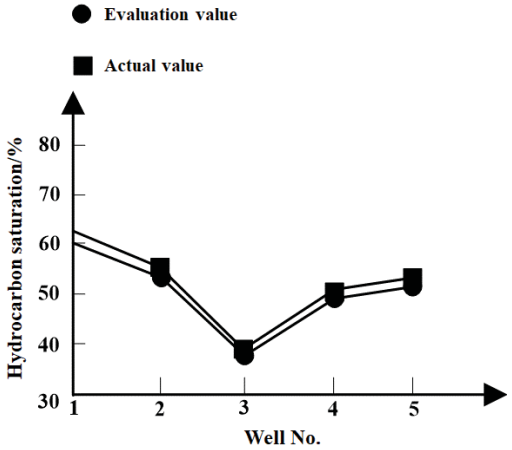

FIGURE 5
Comparison between evaluation results and actual data.

Analysis of Experimental Results. Based on the evaluation of fault control, the differences in the evolution and distribution of faults in different areas of the experimental area are integrated. In view of the dynamic failure of faults to the caprock in the experimental area, this model is used to evaluate the damage of tight sandstone reservoirs and recovery factors.

(1) Consistency of Hydrocarbon Saturation. Combined with a set of experimental data randomly selected from the 30-year history of oil and gas exploration from the Shaojia depression area, there will be 5 exploration wells numbered 1-5 and the data from these five wells are used for the oil and gas saturation evaluation. Compare the evaluation results with real drilling data in the PSCAD platform. The results obtained are shown in Figure 5.

It can be seen from the analysis of Figure 5 that the actual measurement data and the evaluation data can be compared, and the evaluation results and the actual results are approximately consistent. It can be shown that the model built can efficiently evaluate the impact of the dynamic failure of the fault to the caprock on the tight sandstone reservoirs and recovery factors. This is due to that the built evaluation model takes into account the larger the fault distance [26-27]. The larger the fault scale, the larger the fault zone width, the larger the scope of damage to fault tight sandstone reservoirs.

(2) Periodic Evaluation. The model in this paper is compared with the traditional evaluation method represented by [6], and the comparison index is the effective source rock mass size in the three stages of the fault in the Shaojia depression area. These three stages are the immature stage, the low-maturity stage, and the mature stage. Comparing the evaluation results of the oil production efficiency of these three stages, the results are shown in Figure 6.

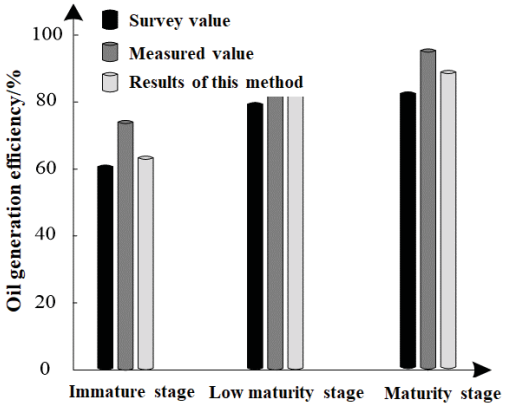

FIGURE 6
Comparison of evaluation results of oil production efficiency.

It can be seen from Figure 6 that the oil production efficiency of the fault is continuously increasing from the immature stage to the low-maturity stage to the mature stage, and one of the measured values is above 60%, indicating that this fault has a good oil production effect. Compared with the results in [6, 28-29], it can be seen that the proposed method has a better evaluation effect and is closer to the measured value. This indicates that the model in this paper can determine that the fault has caused damage to the lower limit buoyancy position force balance after the development of the

late fault. The overall permeability of tight sandstone reservoirs is increased, which results in the loss of oil and gas and the shrinkage of oil and gas reservoirs. In addition, the recovery factor will be affected accordingly. The above analysis shows that the evaluation model is more stable and highly accurate.

(3) Factors Affecting Oil and Gas Recovery. Based on the distance from the fault surface, the model used in this paper is used to judge the degree of influence of the various influencing factors of the fault to the caprock on oil and gas recovery. The current judgment results are shown in Figure 7.

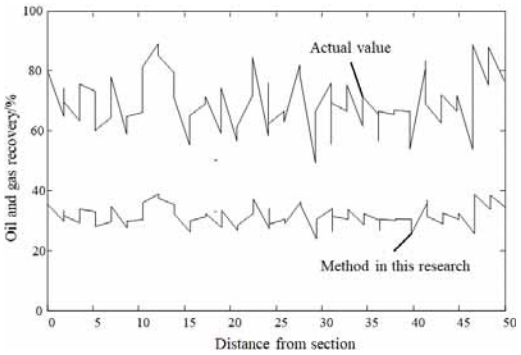

FIGURE 7
The degree of influence of various factors on oil and gas recovery.

It can be seen from Figure 7 that at different distances from the end face, the degree of oil and gas recovery is consistent with the curve of actual oil and gas recovery, which proves the conclusion of this paper: fault activity has intermittent and inherited characteristics and is affected by magmatic activity. The validity of the model can be used in the practical application of tight sandstone oil and gas exploration and recovery.

CONCLUSIONS

(1) The faults are intermittent and inherited and these faults are closely related to magmatic activities. For the hydrocarbon saturation evaluation, the data from the proposed model is very close to the actual measurement data.

(2) For the oil production efficiency, compared with the previous model, the proposed method has a better evaluation effect and is closer to the measured value. This model can efficiently evaluate tight sandstone oil and gas reservoirs and recovery factors under fault dynamic damage, and can provide reliable support for research and development in this field.

ACKNOWLEDGEMENTS

The authors would like to show sincere thanks to those persons who have helped this research and all the authors of the references.

REFERENCES

[1] Du, J., Chang, D., Tang, J., Zhang, Y., Li, Q. (2017) Research on the Upper Paleozoic Hydrocarbon Exploration Direction and Target Area in southern North China. Special Oil and Gas Reservoirs. 24(6), 23-27.

[2] Xia, L., Liu, Z., Liu, J., Lu, C., Li, Y., Sun, D. (2016) Research on the dynamic evaluation method for oil-bearing degree of low-permeability and tight sandstone reservoirs: A case from the Yanchang formation of south Ordos basin. Journal of China University of Mining and Technology. 45(6), 1193-1203.

[3] Xiong, N., Ding, W., Yin, S., Wang, R., Cao, X. (2016) Method of Calculating Tight Sandstone Reservoir Permeability by Creating Dynamic Permeability Chart Based on Formation Rock Conductivity. Science Technology and Engineering. 16(21), 20-26.

[4] Zhong, J., Liu, C., Wu, J., Zhang, S., Yang, G. (2018) Symbiotic accumulation characteristics of coal measure gas in Linxing Block, eastern Ordos Basin. Journal of China Coal Society. 43(6), 1517-1525.

[5] Wang, F., Ma, C., An, C. (2016) Gas exploration prospects of the Upper Paleozoic in Tongxu area, southern North China Basin. Lithologic Reservoirs. 28(2), 33-40.

[6] Meng, Y., Cui, C., Zhang, F., Meng, F., Hu, A., Zhao, Z., Xu, C., Qu, G. (2016) A Prediction of Tight Sandstone Types under Abnormally Low Pressure in the Southern Part of the West Sag of the Liaohe Depression. Bulletin of Mineralogy, Petrology and Geochemistry. 35(4), 701-709.

[7] Yan, M., Zhang, Y. (2016) The Effect of Authigenic Illite on the Relatively High-quality Reservoir of Compact Sandstone in the 4th Member of the Quantou Formation in the Da'an Oilfield. Bulletin of Mineralogy, Petrology and Geochemistry. 35(4), 692-700.

[8] Zhao, D., Xu, H., Wang, L., Tang, D., Meng, S., Li, L. (2016) Characteristics and genesis of tight sandstone reservoir of Shanxi Formation in Linxing Area, Ordos Basin. Lithologic Reservoirs. 28(4), 51-58.

[9] Shang, T., Cao, H., Guo, Y., Wu, H., Qiang, J., Wu, Y., Gao, F., Luo, T. (2017) Microscopic pore structure characteristics and its effects on reservoir quality:A case study from Shanxi formation of upper Paleozoic in Yanchang exploration area in Ordos Basin. Journal of Northwest University (Natural Science Edition). 47(6), 877-886.

[10] Kang, H., Lin, C., Li, H., Wang, K. (2016) Reservoir characteristics and favorable zone prediction of tight sandstone gas of the Ahe Formation in Yinan area, Kuqa Depression. Petroleum Geology and Experiment. 38(2), 162-169.

[11] Wang, K., Zhang, H., Zhang, R., Wang, J., Dai, J., Yang, X. (2016) Characteristics and influencing factors of ultra-deep tight sandstone reservoir structural fracture: a case study of Keshen-2 gas field, Tarim Basin. Acta Petrolei Sinica. 37(6), 715-727.

[12] Li, W., Dong, Y., Guo, A., Liu, X., Zhou, D. (2013) Chronology and tectonic significance of Cenozoic faults in the Liupanshan Arcuate Tectonic Belt at the northeastern margin of the Qinghai–Tibet Plateau. Journal of Asian Earth Sciences. 73, 103-113.

[13] Cheng, J., Sun, X., Gong, Z., Feng, G., Jian, Z. (2013) Numerical simulations of water-inrush induced by fault activation during deep coal mining based on fluid-solid coupling interaction. Disaster Advances. 6(11), 10-14.

[14] Meng, F., Zhou, H., Wang, Z., Zhang, L., Kong, L., Li, S., Zhang, C., Hu, S. (2017) Experimental study of factors affecting fault slip rockbursts in deeply buried hard rock tunnels. Bulletin of Engineering Geology and the Environment. 76(3), 1167-1182.

[15] Ren, D., Sun, W., Huang, H., Liu, D., Qu, X., Lei, Q. (2016) Formation Mechanism of Chang 6 Tight Sandstone Reservoir in Jiyuan Oilfield,Ordos Basin. Editorial Committee of Earth Science-Journal of China University of Geosciences. 41(10), 1735-1744.

[16] Zhang, J. (2016) Main Controlling Factors of Oilliness Property of Tight Sandstone Reservoir within Source Rock in Continental Depression Basin: A case of Gaotaizi oil reservoir in Qijia sag of central depression area in northern Songliao Basin. Acta Sedimentologica Sinica. 34(5), 991-1002.

[17] Chen, M., Qin, Y., Wang, J., Chen, S., Fang, S. (2016) Seismic identification method for tight sandstone reservoir based on isochronous phased inversion. Oil Geophysical Prospecting. 51(4), 782-791.

[18] Qin, X., Huang, W., Lü, A., Zhou, N. (2017) Identification of State Equation and Process Optimization for the Condensation Simulation of Oil Vapor Recovery With Water Content. Acta Petrolei Sinica. 33(5), 998-1006.

[19] Liu, J., Sun, J. (2017) Water Base Drilling Fluid Technology for Horizontal Shale Gas Drilling in Sichuan and Yunnan. Drilling Fluid and Completion Fluid. 34(2), 9-14.

[20] Gao, L., Han, Z., Han, Y., Han, C., Wei, F. (2013) Controlling of cements and physical property of sandstone by fault as observed in well Xia503 of Huimin Sag, Linnan Sub-Depression. Science China Earth Sciences. 56(11), 1942-1952.

[21] Liu, Y., Hu, W., Cao, J., Wang, X., Tang, Q., Wu, H., Kang, X. (2017) Diagenetic constraints on the heterogeneity of tight sandstone reservoirs: A case study on the Upper Triassic Xujiahe Formation in the Sichuan Basin, southwest China. Marine and Petroleum Geology. 92, 650-669.

[22] Lu, X., Rong, Y., Li, X., Wu, F. (2017) Construction of injection-production well pattern in fractured-vuggy carbonate reservoir and its development significance: A case study from Tahe oilfield in Tarim Basin. Oil and Gas Geology. 38(4), 658-664.

[23] Hosseini-Nasab, S., Zitha, P. (2017) Investigation of certain physical–chemical features of oil recovery by an optimized alkali–surfactant–foam (ASF) system. Colloid and Polymer Science. 295(10), 1-14.

[24] Huang, X., Li, T., Gao, H., Zhao, J., Wang, C. (2019) Comparison of SO_2 with CO_2 for Enhancing Shale-hydrocarbon Recovery using Low-field Nuclear Magnetic Resonance. Fuel. 245, 563-569.

[25] Huang, X., Li, T., Gao, H., Zhao, J., Wang, C. (2019) Comparison of SO_2 with CO_2 for Enhancing Shale-hydrocarbon Recovery using Low-field Nuclear Magnetic Resonance. Fuel. 245, 563-569.

[26] Wang, G., Chang, X., Yin, W., Li, Y., Song, T. (2017) Impact of diagenesis on reservoir quality and heterogeneity of the Upper Triassic Chang 8 tight oil sandstones in the Zhenjing Area, Ordos Basin, China. Marine and Petroleum Geology. 83, 84-96.

[27] Yang, R., Fan, A., Van Loon, A., Han, Z., Wang, X. (2014) Depositional and diagenetic controls on sandstone reservoirs with low porosity and low permeability in the eastern Sulige gas field, China. Acta Geologica Sinica - English Edition. 88(5), 1513-1534.

[28] Xu, C., Zou, W., Yang, Y., Duan, Y. (2017) Status and prospects of exploration and exploitation of the deep oil and gas resources onshore China. Natural Gas Geoscience. 28(8), 1139-1153.

[29] Jia, A., Wang, G., Meng, D., Guo, Z. (2018) Well pattern infilling strategy to enhance oil recovery of giant low-permeability tight gasfield: a case study of Sulige gasfield, Ordos Basin. Acta Petrolei Sinica. 39(7), 802-813.

Received: **12.12.2019**
Accepted: **28.01.2020**

CORRESPONDING AUTHOR

Yu Zhu
Hua Zhong Agricultural University and College of Engineering,
Hubei, Wuhan 430070, China

e-mail: lizhonguniv01@126.com

© by PSP Volume 29 – No. 04A/2020 pages 3118-3125 Fresenius Environmental Bulletin

EXPERIMENTAL STUDY OF ENVIRONMENTAL-FRIENDLY MODIFIED CELLULOSE AS RHEOLOGY MODIFIER IN CLAY-FREE WATER-BASED DRILLING FLUIDS

Junyi Liu*

Drilling Technology Research Institute of SINOPEC Shengli Oilfield Service Corporation, Dongying 257100, China

ABSTRACT

This research demonstrates the effectiveness of environmental-friendly modified cellulose to replace synthetic polymer as the rheology modifier in enhancing the environmental-friendly performance of clay-free water-based drilling fluids. This paper first introduces the long-chain hydrophobic groups into hydroxyethyl cellulose (HEC) molecules to synthesize the hydrophobically modified hydroxyethyl cellulose (HMHEC). The evaluation results indicate that after the HMHEC concentration exceeds its critical associating concentration (CAC), HMHEC exhibits excellent viscosity, salt and shear resistance due to hydrophobic modification. Compared with the synthetic polymer PAM, HMHEC presents better environmental-friendly performance, with the EC_{50} value being 60000mg/L and the BOD_5/COD_{Cr} ratio being 18.21%. Furthermore, this paper performs rheological and filtration measurements to investigate the feasibility or compatibility of HMHEC as the rheology modifier for clay-free water-based drilling fluids. The results demonstrate that HMHEC has better rheological behavior, higher temperature stability and greater salt resistance than PAM and XC, and that it can be an environmental-friendly alternative to conventional rheology modifier in clay-free water-based drilling fluids.

KEYWORDS:
Environmental-friendly, modified cellulose, hydrophobically associating, drilling fluid, rheology modifier

INTRODUCTION

With the promotion of oil and gas development around the world, the exploration scope has gradually expanded to environmentally sensitive or ecologically fragile areas, such as ocean, coastal wetlands and farmlands, where all environmental pollution should be eliminated to ensure the coordinated development of environment and petroleum exploration [1-2]. Drilling fluids play irreplaceable roles in the drilling operations for oil and gas development, including balancing formation pressure, maintaining wellbore stability, cooling and lubricating drilling pipes and bits, transporting drill cuttings and avoiding formation damages [3]. By fluid media, drilling fluids are generally divided into four types: water-based, oil-based, synthetic-based and gas drilling fluids. Water-based drilling fluid (WBM) has been most widely adopted in drilling operations because of its low cost and environmental-friendliness [4]. However, this kind of fluids produce waste WBM, which is becoming one of the main pollutants in the petroleum industry. Statistics show that more than 12 million tons of waste WBM would be produced in China per year. Such waste water-based drilling fluids are generally considered as dangerous solid wastes because they are highly hazardous to the environment and difficult for harmless treatment [5]. Recent studies have concluded that one of the best ways to improve the environmental performance of drilling fluids is to replace the synthetic polymer additives with environmental-friendly cellulose-based or starch-based ones to decrease the biological toxicity and increase the biodegradability of waste water-based drilling fluids.

In recent years, clay-free water-based drilling fluids have been successively developed based on the optimization of the functional polymers to replace or partially replace bentonite [6]. Such clay-free water-based drilling fluids are easier to control, with lower density and better rheological property than the conventional bentonite water-based drilling fluids, thus improving the efficiency of rock breaking and rate of penetration in drilling operations. Moreover, clay-free water-based drilling fluids can also effectively prevent reservoir damages, such as clay particle plugging and water locks, which is beneficial to increasing the oil or gas productivity [7].

The rheological behaviors of clay-free water-based drilling fluids are mainly adjusted by functional polymers or rheology modifiers [8], as they reduce the clay or solid content dispersed in the drilling fluids without reducing the suspension or transportation capacity of the fluids. There are two types of rheology modifiers that are most widely used in the clay-free water-based drilling fluids - synthetic polymers represented by polyacrylamide (PAM) and

biopolymers represented by xanthan gum (XC). The latter, a microbial high molecular polysaccharide, has a strong viscosifying ability in water-based drilling fluids with excellent salt resistance and shear thinning performance. However, xanthan gum is prone to thermal oxidative degradation due to backbone oxidization and fractionation at high temperature even with a small amount of oxygen [9]. Therefore, polyacrylamide (PAM) has been widely applied as the viscosifier and filtration reducer in water-based drilling fluids. This substance also exhibits an excellent encapsulating inhibition ability, which can improve the shale wellbore stability. But due to its high biological toxicity and low biodegradability, polyacrylamide (PAM) cannot meet the environmental-friendliness requirement of the clay-free water-based drilling fluids. What is more, polyacrylamide (PAM) is susceptible to oxidative or shearing degradation, especially under high temperature, high salt concentration or high shear rate, resulting in a sharp drop in solution viscosity, which in turn leads to a significant reduction in the drilling fluid performance [10].

To improve the performance and adaptability of rheology modifiers in harsh conditions, the concept of hydrophobic modification has become a research hotspot in recent years. Hydrophobically modified water-soluble polymers (HMWSP) refer to a new type of polymers obtained by introducing a very small amount of hydrophobic groups (with a molar fraction of less than 2%) to the conventional water-soluble polymer backbone. Compared with conventional water-soluble polymers, HMWSP exhibits interesting rheological and solution properties, which have attracted much attention in the petroleum industry because of its unique properties, including its viscosifying ability, recoverable shear thinning performance and salt resistance [11]. As currently reported, several different types of HMWSP [12-13], including the hydrophobically modified polyacrylamide, ethoxylated urethane and acrylamide-styrene block copolymer, have been studied. Currently, the petroleum industry has demands for environmentally friendly materials, and therefore, natural polymers, such as cellulose and starch, may be an alternative suitable for the water-based drilling fluids. The hydroxyethyl cellulose (HEC), a nonionic hydrophilic polysaccharide or cellulose derivative, is commonly used as a viscosifier and filtration reducer in the water-based drilling fluids, and can be classified as an environmentally friendly polymer. To enhance the viscosity and temperature and salt resistance, the hydrophobically modified hydroxyethyl cellulose (HMHEC) has also been synthesized and mainly used in chemical or polymer flooding to enhance oil recovery, but the potential of HMHEC being applied in drilling fluids has not been further investigated so far [14].

In the present study, environmental-friendly modified cellulose is introduced as the rheology modifier in the clay-free water-based drilling fluids. Firstly, this paper synthesizes a kind of hydrophobically modified hydroxyethyl cellulose (HMHEC) through both hydrophobic modification and polymeric chain modification. Then it characterizes and discusses the viscosity of the newly-synthesized HMHEC, conducts experimental evaluation on its rheological and filtration performance and environmental-friendliness, and studies its feasibility or compatibility as a rheology modifier for clay-free water-based drilling fluids.

MATERIALS AND METHODS

Experimental Materials. (1) Chemical Agents. Hydroxyethyl cellulose (HEC) and 1-bromododecane (98%), the two core chemical reagents to synthesize the hydrophobically modified hydroxyethyl cellulose (HMHEC), were obtained from Shanghai Aladdin Biochemical Technology Co. Ltd. (Shanghai, China) and used without further purification. Isopropanol (IPA), hexane, acetone, acetic acid, sodium hydroxide (NaOH), hydrochloric acid (HCl), sodium chloride (NaCl), AR grade, were all purchased from Sinopharm Chemical Reagent Co. Ltd (Shanghai, China) and used as received. Distilled water was used throughout the experiments.

(2) Drilling Fluid Additives. The clay-free water-based drilling fluid tested was prepared using standard commercial additives. The conventional rheology modifiers - acrylamide polymers (PAM) and xanthan gum (XC) - were provided by Shengli Petroleum Engineering Co., Ltd. (Dongying, China). The fluid loss reducer - the low-viscosity polyanionic celluloses (LV-PAC) - was provided by Shandong Deshunyuan Petroleum Technology Co., Ltd. (Dongying, China). Polyamine inhibitor (AP-1), rigid sealing agent (QS-2) and polymeric alcohol (JLX) were provided by Shandong Shida Chuangxin Technology Co., Ltd. (Dongying, China). Sodium chloride (NaCl) of industrial grade was purchased from Shengli Chemical Co. Ltd (Dongying, China). All the drilling fluid additives above were used as received without further purification.

Synthesis of HMHEC. Hydrophobically modified hydroxyethyl cellulose (HMHEC) was synthesized through the Williamson etherification reaction of the active hydroxyl groups on the molecular chain of hydroxyethyl cellulose (HEC) with alkyl halide, which introduced the long-chain hydrophobic alkane into the hydrophilic molecular chain of hydroxyethyl cellulose (HEC). The synthesis reaction was performed in a 250 mL round-bottom flask with three-necks that was equipped with a mechanical stirrer. Firstly, hydroxyethyl cellulose (9.0 wt%) and isopropanol were successively added into the flask and stirred for 30 min. Then, the NaOH aqueous solution

(3.0 wt%) was added dropwise while the solution was being stirred intensely. After the dropwise addition of NaOH solution, the stirring speed was appropriately lowered. The reaction system was charged with nitrogen gas and then sealed under nitrogen for 24h at room temperature, which allowed hydroxyethyl cellulose (HEC) to be fully swelling and activated. Secondly, the flask was immersed into a thermostat water bath at 80 ºC, and added with 1-bromododecane (3.3 wt%) dropwise and then sealed under nitrogen again for 5h. After the reaction ended, the flask was rapidly cooled with running water, and the reaction product was washed with hexane twice and then with acetone three times respectively. After being soaked in acetone for 5h, the reaction product was adjusted to a pH value of 7~8 with acetic acid. The neutralized reaction product was washed with acetone three times again, and filtrated after being soaked in acetone for another 5h. The solid reaction product was finally obtained for further use after being dried at 40~45 °C for 5h under vacuum condition.

The new-synthesized HMHEC was characterized by Fourier transforms infrared spectroscopy (FT-IR) and gravimetric analysis (TGA). The FT-IR spectra were recorded by NEXUS 670 FT-IR spectrometer (Thermo Nicolet Corporation, USA) and scanned from 4000 to 400 cm-1. The mixture of HMHEC samples and potassium bromide (KBr) was pressed into pellets for FT-IR analysis.

Viscosity Measurement of HMHEC Solutions. The HMHEC stock solutions were prepared as follows for further use: HMHEC was dissolved in distilled water and continuously stirred for 6.0h, and then aged for 24h at room temperature. The concentrations of HMHEC stock solutions were 500mg/L, 1000mg/L, 2000mg/L, 4000mg/L, 6000mg/L, 8000mg/L and 10000mg/L, respectively. The HEC solutions with the same concentrations were also prepared for comparison.

The influencing factors to the viscosity of the HMHEC solutions, such as HMHEC concentration, shear rate, and salt, were investigated quantitatively based on the variation of apparent viscosity. The apparent viscosity of the HMHEC solutions was measured using the DV-II rotor viscometer (Brookfield, USA), normally at a shear rate of 6 s^{-1} at 25 °C except in the shear rate and temperature effect experiments. The effect of shear rate on the apparent viscosity of the HMHEC solutions was investigated in the shear rate range of 6 s^{-1} to 100 s^{-1} at 25 °C.

Environmental Friendliness Evaluation. The environmental-friendliness of HMHEC, XC and PAM as rheology modifiers was evaluated through biological toxicity and biodegradability tests. The half-maximal effective concentration (EC50) was adopted as the evaluation parameter of biological toxicity, and the biological toxicity tests were conducted with the Microtox Model 500 Biological Toxicity Tester (SDI Corporation, USA) by the luminescent bacteria method. The ratio of biochemical oxygen demand (BOD) to chemical oxygen demand (COD) was adopted as the evaluation parameter of biodegradability, and the biodegradability tests were conducted with the Biochemical Oxygen Demand Tester (JUCHUANG, China) by the air pressure difference method and the Chemical Oxygen Demand Tester (XINGHUAN, China) by the rapid digestion spectrophotometry method.

Compatibility Tests. The clay-free water-based drilling fluids were prepared according to the API Recommended Practice for Standard Procedure for Field Testing Water-based Drilling Fluids (API RP 13B-1). The clay-free water-based drilling fluids tested were prepared using standard commercial additives, with the formulation listed in Table 1. In order to simulate the downhole environment, the CFWBMs were hot rolled using a rolling oven (Haitongda, China) at the desired temperature for 16h.

The compatibility or applicability of HMHEC in clay-free water-based drilling fluids was investigated based on the comparison of rheological and filtration behaviors. The fluids were vigorously stirred for 20min at 10000r/min before each measurement. To characterize the properties of drilling fluids based on industrial practice, the rheological behaviors of the water-based drilling fluids were measured at a fixed rate of 600 and 300 r/min according to the API Recommended Practice for Standard Procedure for Field Testing Water-based Drilling Fluids (API RP 13B-1), using a model ZNN-D6 viscometer. The initial and 10min gel strengths - Gelin and Gel10min - were recorded as the half-maximal dial readings at a fixed rate of 3r/min after being undisturbed for 10 s and 10 min, respectively. The filtration performance was also measured using the ZNS-2A filtration apparatus at room temperature for 7.5 min, (Eq.1-Eq.4).

TABLE 1
Formulation of tested clay-free WBMs

Additives	Mass Fraction % (m/v)			Additives	Mass Fraction % (m/v)		
	WBM-1	WBM-2	WBM-3		WBM-1	WBM-2	WBM-3
HMHEC	0.5	-	-	AP-1	1.0	1.0	1.0
XC	-	0.5	-	QS-2	2.5	2.5	2.5
PAM	-	-	0.3	JLX	2.0	2.0	2.0
PAC-LV	1.5	1.5	1.5	NaCl	5.0	5.0	5.0

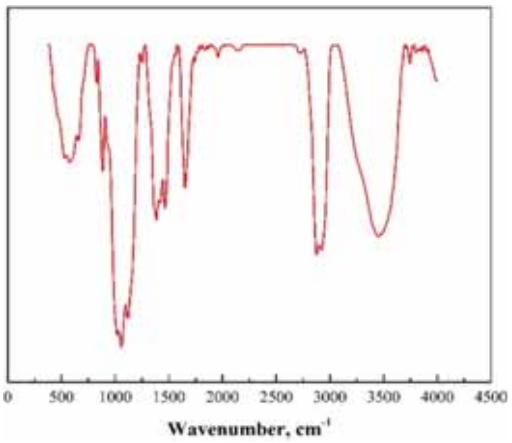

FIGURE 1
FT-IR spectrum of HEC.

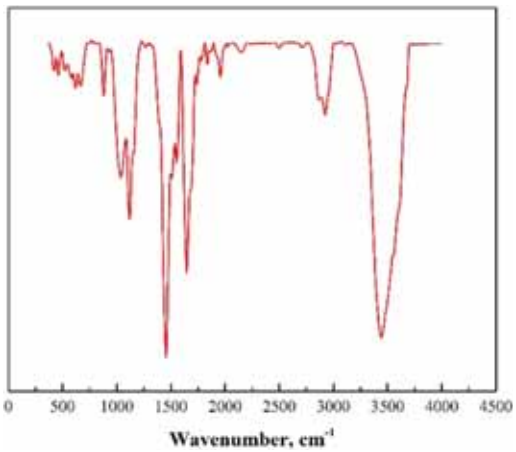

FIGURE 2
FT-IR spectrum of HMHEC.

Apparent viscosity (AV) = φ_{600}/2 (mPa·s) (1)
Plastic viscosity (PV) = φ_{600}-φ_{300} (mPa·s) (2)
Yield point (YP) = (φ_{300}-PV)/2 (Pa) (3)
API filtration ($API\ FL$) = 2×FL_{ZNS} (mL) (4)

where, AV is the apparent viscosity, mPa·s; PV is the plastic viscosity, mPa·s; YP is the yield point, Pa; φ600 and φ300 are dial readings at 600 and 300r/min respectively; R is the ratio of yield point to plastic viscosity, Pa/ mPa·s; API FL is the API filtration volume, mL; FLZNS is filtration volume measured with the ZNS-2A filtration apparatus, mL.

RESULTS AND DISCUSSION

Characterization of HMHEC. The FT-IR spectra of HEC and HMHEC were illustrated in Figure1 and Figure2, respectively. It can be seen that there exist significant differences in the absorption bands at 1375 cm^{-1} and 1450 cm^{-1} of the FT-IR spectra of HEC and HMHEC. The absorption bands at 1375 cm^{-1} and 1450 cm^{-1} were corresponding to the symmetrical bending vibration and asymmetric bending vibration peaks of methyl (-CH_3) and methylene (-CH_2-) groups, and the peak increase also reflected the alkane content increase in the molecule structure of HEC. It can be confirmed from the above discussion that HMHEC was obtained by introducing the long-chain alkane groups (-$C_{12}H_{25}$) into the macromolecular chain of HEC.

Viscosity of HMHEC. Effect of HMHEC Concentration. The effect of concentration on the apparent viscosity of the HMHEC solution was investigated, and the experimental results are shown in Figure 3. It can be seen that the apparent viscosity of the HMHEC solution increased monotonically with the increase of the HMHEC concentration. When the concentration of the HMHEC solution was lower than 4000mg/L, there was no significant difference in the apparent viscosity between the HMHEC and HEC solutions. However, when the concentration of HMHEC increased to 4000mg/L, the apparent viscosity sharply increased to 2040mPa·s, while the apparent viscosity of the HEC solution was only around 100mPa·s at the same concentration. It can be seen that the apparent viscosity of the HMHEC solution is more than 20 times that of the HEC solution at this concentration, reflecting an excellent viscosifying ability. With the further increase of the HMHEC concentration, the apparent viscosity of the HMHEC solution rapidly increased. When the HMHEC concentration finally reached 10000mg/L, the apparent viscosity of the HMHEC solution was nearly 60000 mPa·s, while that of the HEC solution at the same concentration was only around 200 mPa·s.

What is worth discussing is that the critical associating concentration (CAC) of the HMHEC solution was corresponding to the sharp increase of the apparent viscosity. Due to the introduction of the long-chain alkane groups (-$C_{12}H_{25}$) into the macromolecular chain of HMHEC, the hydrophobic groups tend to associate together in the aqueous solution to form intramolecular or intermolecular associations, mainly depending on the HMHEC concentration [15]. As discussed above, for a relatively low concentration of HMHEC, the intramolecular associations between the hydrophilic and hydrophobic groups of a single HMHEC macromolecular chain take up the main position, and the macromolecular chain tends to curl or shrink, leading to a similar viscosity with HEC. But when HMHEC reached its critical associating concentration, the intermolecular associations between the hydrophilic and hydrophobic groups of different HMHEC macromolecular chains take the place of the intramolecular associations and occupy the main position, forming a reversible physical cross-linking network with a supramolecular structure throughout the solution, which in turn significantly increases the hydrodynamic volume of the HMHEC macromolecules and enhances the viscosifying ability of the HMHEC aqueous solution [16].

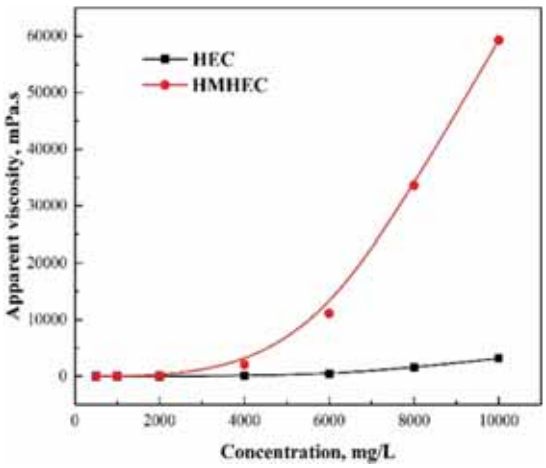

FIGURE 3
Relationship between apparent viscosity and concentration of HMHEC and HEC solution.

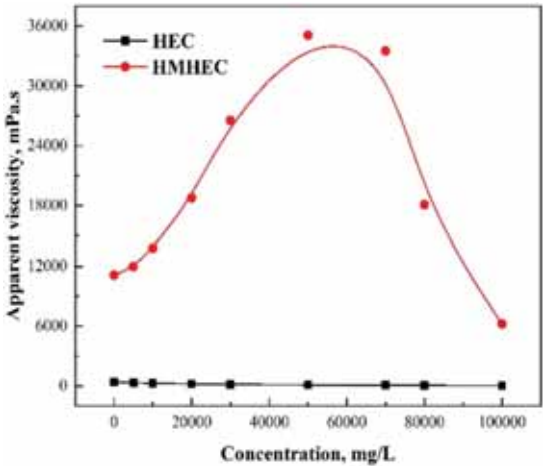

FIGURE 4
Relationship between apparent viscosity and salt concentration of HMHEC and HEC solution.

Effect of Salt. Several experimental researches have proved that the main disadvantage of polyacrylamide (PAM) as a rheology modifier is its high sensitivity to salt [17], such as sodium chloride (NaCl), which is widely used to improve the inhibitive performance of WBMs. Now with the introduction of the hydrophobic alkane group (-$C_{12}H_{25}$), the hydrophobic association makes it possible to improve the salt resistance of HMHEC.

Figure 4 presents the relationships between the apparent viscosity of the HMHEC and HEC solutions (6000mg/L) and the NaCl concentration. It shows that the apparent viscosity of the HEC solution decreased monotonically with the increase of the NaCl concentration. However, the apparent viscosity variation trend of the HMHEC solution was quite different from that of the HEC solution at the same NaCl concentration. The apparent viscosity of the HMHEC solution firstly increased when the NaCl concentration was lower than 30000mg/L; and then it decreased gradually when the NaCl concentration exceeded 30000mg/L. When the NaCl concentration reached 100000mg/L, the apparent viscosity was still about 6200 mPa·s, indicating a good salt resistance.

The experimental results in Figure 4 prove that the addition of electrolytes enhanced the polarity of the BHEC solution, and the hydrophobic groups tended to associate to form hydrophobic microdomains, thus forming a more complete and extensive physical cross-linking network with a supramolecular structure and a correspondingly increasing hydrodynamic volume, which was consistent with the increase in the apparent viscosity of the HMHEC solution when the NaCl concentration was lower than 30000mg/L. But with the further increase of the NaCl concentration, the excessive electrolytes made the hydrophobic association too strong, leading to the associative phase separation, and a little part of HMHEC precipitated out of the aqueous solution, which was consistent with the decrease in the apparent viscosity of the HMHEC solution when the NaCl concentration exceeded 30000mg/L.

Effect of Shear Rate. The effect of shear rate on the apparent viscosity of the HMHEC and HEC solutions with the concentration of 60000mg/L was investigated at 25 °C, and the apparent viscosity of the HMHEC solution was observed within the increase and decrease cycle range of the shear rate from 6s^{-1} to 100s^{-1}.

It can be seen from Figure 5 that the apparent viscosity of the HMHEC solution significantly decreased with the increase of the shear rate. With the shear rate reaching 50 s-1 or higher, the apparent viscosity of the HMHEC solution tended to be stable at about 3000 mPa·s. However, with the decrease of the shear rate, the apparent viscosity of the HMHEC solution gradually increased and basically restored or returned to the initial values, indicating the much better shear resistance and shear thinning performance of HMHEC than those of PAM. Previous results showed that after continuous shearing at 60 s-1 for two minutes, the apparent viscosity of the PAM solution could not return to the initial value like that of HMHEC and only maintained about 20% of the initial value [18].

Figure 6 presents the apparent viscosity variation trends of the HEC solution with the increase and decrease of the shear rate. Unlike the apparent viscosity variation trends of the HMHEC solution, that of the HEC solution was nearly the same when the shear rate either increased or decreased. Due to the lack of the long-chain hydrophobic alkane group, the supramolecular aggregates cannot be formed through the hydrophobic association reaction.

The most interesting phenomenon is that the apparent viscosity of the HMHEC solution when the shear rate decreased from 60s^{-1} to 30s^{-1} was even higher than that of the HMHEC solution when the

shear rate increased from $30s^{-1}$ to $60s^{-1}$. This was because under the strong shearing force, the original hydrophobic association structure of HMHEC was inevitably damaged and the HMHEC macromolecules tended to further stretch, and when the shear rate began to decrease, a more complete hydrophobic association structure would rebuild, resulting in much higher apparent viscosity. Moreover, when the shear rate further decreased to lower than 30-1, the apparent viscosity of the HMHEC solution became slightly lower than the initial value. The results and discussions above prove that after the HMHEC concentration exceeds its critical associating concentration, the intermolecular association leads to the formation of supramolecular aggregates. The hydrophobic association process is a reversible reaction (Figure 7), and it can be disassociated under certain circumstances, such as under a high shear rate.

Comparison of Environmental-Friendliness. According to the classification criteria for biological toxicity and biodegradability of drilling fluid additives [19-20], it is considered as "not biologically toxic" when the EC_{50} value is higher than 30000mg/L and "biologically toxic" when the EC_{50} value is lower than 30000mg/L; it is considered as "easy to biodegrade" when the BOD_5/COD_{Cr} ratio is higher than 10%, and "difficult to biodegrade" when the BOD_5/COD_{Cr} ratio is lower than 10%.

Table 2 displays the biological toxicity and biodegradability test results. It can be seen that polyacrylamide (PAM) is considered as biologically toxic and difficult to biodegrade, and it cannot meet the environmental-friendliness requirements of the clay-free water-based drilling fluids. However, the newly-synthesized HMHEC presents excellent environmental-friendliness, with the EC_{50} value being 60000mg/L (not biologically toxic) and the BOD_5/COD_{Cr} ratio being 18.21% (easy to biodegrade), so it can be introduced as an environmental-friendly additive to water-based drilling fluids. Moreover, xanthan gum (XC) is also considered as an environmental-friendly additive that is not biologically toxic and easy to biodegrade, but it cannot maintain its properties stable under high temperature conditions due to its own molecular structure and physical & chemical properties.

Compatibility of HMHEC in Clay-Free WBMs. It can be clearly seen from Table 3 that due to the poor thermal stability, XC could only be used as a rheology modifier in the clay-free water-based drilling fluid when the bottomhole temperature was around 120 °C and that after being hot-rolled at 150 °C for 16h, it had little effect in adjusting the rheological and filtration performance. The viscosifying effect of PAM was greatly affected in the brine environment because of its high sensitivity to salt. However, when using the HMHEC as the rheology modifier, WBM-1 exhibited excellent rheological and filtration performance after being hot-rolled at both 120 °C and 150 °C for 16h, indicating superior rheology modification and high temperature resistance. Moreover, WBM-1 also had a larger ratio of yield point to plastic viscosity than WBM-2 and WBM-3, which demonstrates that using HMHEC as the rheology modifier is beneficial to improving the shear thinning performance and further improving the suspension or transportation capacity of the clay-free water-based drilling fluid. Therefore, the newly-synthesized HMHEC can be an alternative to the conventional or standard rheology modifiers in clay-free water-based drilling fluids.

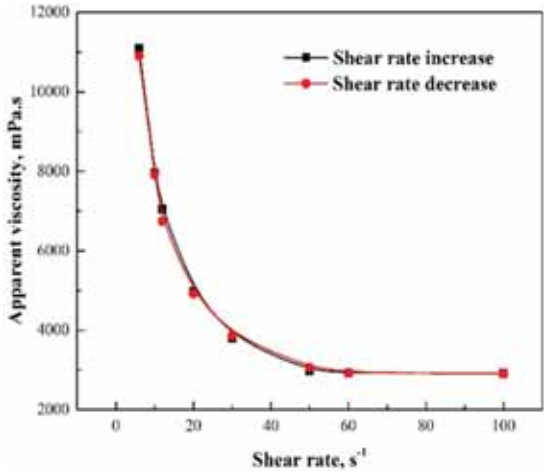

FIGURE 5
Relationship between apparent viscosity and shear rate of HMHEC solution.

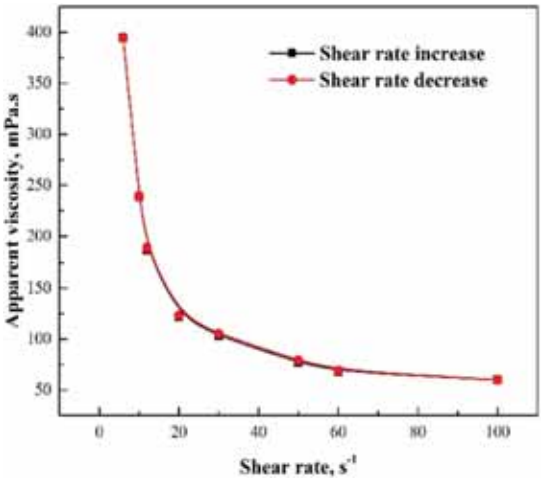

FIGURE 6
Relationship between apparent viscosity and shear rate of HEC solution.

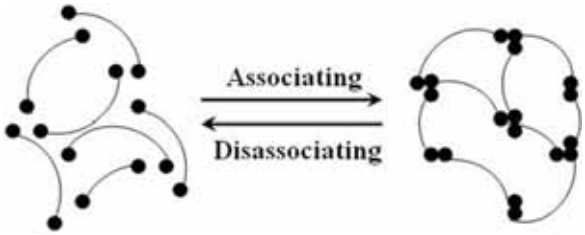

FIGURE 7
Reversible process of intermolecular association.

TABLE 2
Biological toxicity and biodegradability test results

Data	EC_{50}/(mg/L)	Biological Toxicity	BOD_5/COD_{Cr}/%	Biodegradability
HMHEC	60000	no biologically toxic	18.21	easily biodegrade
PAM	23000	biologically toxic	7.85	difficultly biodegrade
XC	80000	no biologically toxic	26.13	easily biodegrade

TABLE 3
Rheological and filtration properties of drilling fluids

Data	WBM-1		WBM-2		WBM-3	
	120 °C	150 °C	120 °C	150 °C	120 °C	150 °C
600 rpm	57.0	51.0	61.0	30.0	43.0	35.0
300 rpm	38.0	33.5	41.0	17.5	26.0	21.0
10 s	11.0	9.0	10.0	3.0	3.0	2.0
10 min	16.0	15.0	15.0	4.0	4.0	3.0
AV (mPa.s)	28.5	25.5	30.5	15.0	21.5	17.5
PV (mPa.s)	19.0	17.5	20.0	12.5	17.0	14.0
Y (Pa)	9.5	8.0	10.5	2.5	4.5	3.5
R (Pa/mPa.s)	0.50	0.46	0.53	0.20	0.26	0.25
FL_{API} (mL)	3.6	4.8	3.8	14.6	7.6	16.8
Gel_{in} (Pa)	5.5	4.5	5.0	1.5	1.5	1.0
Gel_{10min} (Pa)	8.0	7.5	7.5	2.0	2.0	1.5

CONCLUSIONS

This study first synthesized the hydrophobically modified hydroxyethyl cellulose (HMHEC), and then investigated and discussed its viscosity and environmental-friendliness and its feasibility or compatibility as a rheology modifier in enhancing the rheological and filtration performance of clay-free water-based drilling fluids.

Firstly, HMHEC exhibits excellent viscosity after its concentration exceeded its critical associating concentration (CEC). Thanks to hydrophobic modification, HMHEC has better salt resistance. What is more, due to the unique shear resistance, HMHEC maintains satisfactory shear thinning performance for clay-free water-based drilling fluids. Secondly, HMHEC displays much better environmental-friendliness than the conventional rheology modifier PAM, so it is considered as an environmental-friendly additive to water-based drilling fluids. Finally, the results of rheological and filtration measurements demonstrate that HMHEC has superior rheological behaviors, high temperature stability, salt resistance, and less fluid loss volume, and that it can be an alternative to the conventional rheology modifiers PAM and XC in clay-free water-based drilling fluids.

ACKNOWLEDGEMENTS

We would like to thank the financial support from the National Science and Technology Major Project of China (2016ZX05040-005).

REFERENCES

[1] Zhang, Y., Su, G., Zheng, L., Liu, D., Guo, Z., Wei, P. (2019) The environmental friendliness of fuzzy-ball drilling fluids during their entire life-cycles for fragile ecosystems in coalbed methane well plants. Journal of Hazardous Materials. 364, 396-405.

[2] Liu, J., Guo, B., Li, G., Wang, B., Chai, J. (2019) Synthesis and performance of environmental-friendly starch-based filtrate reducers for water-based drilling fluids. Fresen. Environ. Bull. 28, 5618-5623.

[3] Liu, J., Qiu, Z., Huang, W. (2015) Novel latex particles and aluminum complexes as potential shale stabilizers in water-based drilling fluids. Journal of Petroleum Science and Engineering. 135, 433-441.

[4] Zhao, X., Qiu, Z., Wang, M., Huang, W., Zhang, S. (2018) Performance evaluation of a highly inhibitive water-based drilling fluid for ultralow temperature wells. Journal of Energy Resources Technology. 140(1), 012906.
[5] Zha, X., Liao, X., Zhao, X., Liu, F., He, A., Xiong, W. (2018) Turning Waste drilling fluids into a new, sustainable soil resources for landscaping. Ecological Engineering. 121, 130-136.
[6] Werner, B., Myrseth, V., Saasen, A. (2017) Viscoelastic properties of drilling fluids and their influence on cuttings transport. Journal of Petroleum Science and Engineering. 156, 845-851.
[7] Su, Z., Wang, R., Liu, J., Chen, E. (2019) Filtration reduction mechanism of environmental-friendly compound modified starch in water-based drilling fluids. Fresen. Environ. Bull. 28, 8227-8243.
[8] Ahmad, H., Kamal, M., Al-Harthi, M. (2018) High molecular weight copolymers as rheology modifier and fluid loss additive for water-based drilling fluids. Journal of Molecular Liquids. 252, 133-143.
[9] Petri, D. (2014) Xanthan Gum: A versatile biopolymer for biomedical and technological applications. Journal of Applied Polymer Science. 132(23), 38-47.
[10] Vipulanandan, C., Mohammed, A. (2014) Hyperbolic rheological model with shear stress limit for acrylamide polymer modified bentonite drilling muds. Journal of Petroleum Science and Engineering. 122, 38-47.
[11] Wever, D., Picchioni, F., Broekhuis, A. (2011) Polymers for enhanced oil recovery: A paradigm for structure-property relationship in aqueous solution. Progress in Polymer Science. 36(11), 1558-1628.
[12] Liu, R., Pu, W., Sheng, J., Du, D. (2017) Star-like hydrophobically associative polyacrylamide for enhanced oil recovery: comprehensive properties in harsh reservoir conditions. Journal of the Taiwan Institute of Chemical Engineers. 80: 639-649.
[13] Taylor, K., Nasr-El-Din, H. (1998) Water-soluble hydrophobically associating polymers for improved oil recovery: A literature review. Journal of Petroleum Science and Engineering. 19, 265-280.
[14] Bai, Y., Shang, X., Zeng, Z., Zhao, X. (2018) Experimental study on hydrophobically associating hydroxyethyl cellulose flooding system for enhanced oil recovery. Energy and Fuels. 32(6), 6713-6725.
[15] Sharma, V., Haward, S., Serdy, J., Keshavarz, B., Soderlund, A., Threlfall-Holmes, P., McKinley, G. (2015) The rheology of aqueous solutions of ethyl hydroxy-ethyl cellulose (EHEC) and its hydrophobically modified analogue (hmEHEC): extensional flow response in capillary break-up, jetting (ROJER) and in a cross-slot extensional rheometer. Soft Matter. 11(16), 3251-3270.
[16] Yang, Z., Gao, Y., Li, C., Yue, Q., Liu, B. (2010) Synthesis and characterization of hydrophobically associating cationic polyacrylamide. Chemical Engineering Journal. 161(1-2), 27-33.
[17] Hu, S., Zhang, L., Cao, X., Guo, L., Zhu, Y., Zhang, L., Zhao, S. (2015) Influence of crude oil components on interfacial dilational properties of hydrophobically modified polyacrylamide. Energy and Fuels. 29(3), 1564-1573.
[18] Vittadello, S., Biggs, S. (1998) Shear history effects in associative thicker solutions. Macromolecules. 31(22), 7691-7697.
[19] Liu, J. (2018) New research progress on high performance environmental friendly water-based drilling fluid technology. Advances in Fine Petrochemicals. 19(6), 29-34.
[20] Polo, A., Tobajas M., Sanchis, S., Mohedano, A., Rodriguez, J.J. (2011) Comparison of experimental methods for determination of toxicity and biodegradability of xenobiotic compounds. Biodegradation. 22(4), 751-761.

Received: **15.12.2019**
Accepted: **31.01.2020**

CORRESPONDING AUTHOR

Junyi Liu,
Drilling Technology Research Institute of SINOPEC
Shengli Oilfield Service Corporation,
Dongying 257100 – China

e-mail: danielliu1988@126.com

© by PSP Volume 29 – No. 04A/2020 pages 3126-3133 Fresenius Environmental Bulletin

COMPREHENSIVE EVALUATION AND ANALYSIS OF BIODIVERSITY IN SOUTHERN GUIZHOU PROVINCE, CHINA

Lulu Liu[1], Quanqin Shao[2,*]

[1]School of Architecture and Civil Engineering, Chengdu University, Chengdu 610106, China
[2]Institute of Geographic Sciences and Natural Resources Research, CAS, Beijing 100101, China

ABSTRACT

The southern region of Guizhou Province is a typical karst mountainous region in China. The ecological environment is fragile and biodiversity is extremely vulnerable. Based on the previous research results and the actual physical and geographical conditions and biodiversity characteristics of southern Guizhou, a biodiversity evaluation index system with 9 primary indicators and 25 secondary indicators was designed, including species number, endemic species, endangered species, important resource species, diversity of ecosystem types, protected area coverage, alien species invasion, vegetation damage, and the integrity of the vertical spectrum of the vegetation. Based on the actual physical geographic conditions and collected data, the comprehensive evaluation of the biodiversity in the southern area of Guizhou Province was carried out using six primary indicators in counties (districts, cities) scale. The evaluation results show that the areas with better biodiversity are mainly concentrated in the lower mountainous areas in the southeast, and the areas with poorer biodiversity are mainly concentrated in the west with more severe rocky desertification. Libo County of the Qiannan Prefecture has the best biodiversity while Zhenfeng County of the Qianxinan Prefecture has the worst biodiversity. On the whole, the biodiversity of the southern Guizhou Province is good.. The counties with a “mediocre” review accounted for the highest proportion, reaching 41.67%, followed by “good” and “excellent”, accounting for 33.33% and 13.89% of the total counties, respectively. There were no counties with a “poor” biodiversity evaluation.

KEYWORDS:
Ecological environment, biodiversity, comprehensive evaluation index system, Karst, southern Guizhou

INTRODUCTION

Biodiversity refers to variability in living organisms from all sources, including terrestrial, marine and other aquatic ecosystems and the ecological complexes they form, etc [1]. Diversity, which is a sign of maintaining the safety of human living environment [2], has direct, indirect and potential values, and is very important for ecosystem services and human welfare [3]. However, nowadays, the loss of biodiversity is faster than ever, and it has threatened the survival itself [4].

Biodiversity monitoring and evaluation is an important basis for objectively understanding the status of biodiversity and its changing trends, and carrying out biodiversity protection. The focus and difficulty is the establishment of a comprehensive evaluation index system [5-6]. Since the 1990s, both home and abroad gradually paid attention to the study of biodiversity evaluation indicators. The Convention on Biological Diversity, adopted at the seventh meeting of the Intergovernmental Negotiating Committee initiated by the United Nations Environment Programme in 1992, continuously emphasizes "predicting, preventing, and eliminating at the source of the causes of reduced or lost biodiversity", and put forward specific requirements for parties to conduct biodiversity monitoring and assessment [6].

Some countries and regions such as Germany, the United Kingdom, and South Africa [7-9] have established national biodiversity monitoring and evaluation systems. China actively implements the Convention on Biological Diversity, and at the same time, based on different ecosystems, many scholars did discussion and research on biodiversity evaluation indicators of different types and different scales, such as Qian Yingqian and Ma Keping who discussed biodiversity measurement indicators [10]. Zhang et al. [11] proposed a wetland ecosystem evaluation indicator system. According to the biodiversity hotspot methodology and the characteristics of the biodiversity assessment index system, Xu et al. [4] proposed a biodiversity assessment index system suitable for China. In 2012, in order to grasp and understand the status, spatial distribution and changing trends of biodiversity nationwide and everywhere,

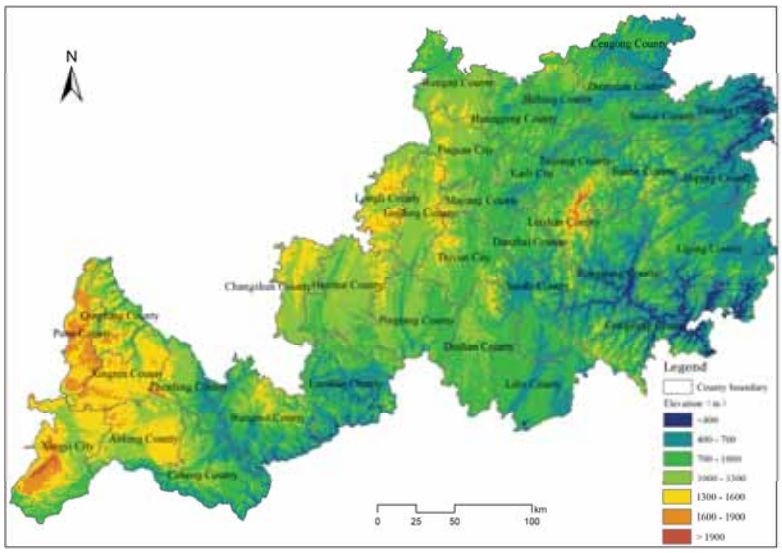

FIGURE 1
The elevation of the study area.

the Ministry of Environmental Protection of China issued the "Regional Biodiversity Evaluation Standards". However, due to the lack of biodiversity monitoring data, most of China's current biodiversity assessments are based on provinces (cities, districts) as units, and fewer biodiversity assessments have been carried on the county-level.

Guizhou Province is a typical karst mountainous region in China. It is located on the eastern side of the Qinghai-Tibet Plateau and on the eastern slope of the Yunnan-Guizhou Plateau, and its surface is rugged and broken. The climate in Guizhou is in the transition zone from the humid subtropical monsoon climate in the eastern subtropical zone to the semi-humid climate in the western subtropical zone. Coupled with the widespread distribution and strong development of karst, it has created good conditions for the life and reproduction of wild animals and plants with different ecological characteristics and exhibits high biodiversity. Therefore, the entire region of Guizhou Province has been included in the biodiversity protection priority area-the mountainous and hilly areas in the western and central and southern parts of China with the special protection of China's unique subtropical evergreen broad-leaved forests and karst forests and other natural vegetations [12]. South Guizhou Province, Qiandongnan Miao and Dong Autonomous Prefecture (refers as Qiandongnan Prefecture below), Qiannan Buyi and Miao Autonomous Prefecture (refers as Qiannan Prefecture below), and Qianxinan Buyi and Miao Autonomous Prefecture (refers as Qianxinan Prefecture) are karst areas with concentrated subtropical evergreen broad-leaved forest distribution. However, the region is highly vulnerable to ecological damage, and it is difficult to recover once damaged. Based on the previous research results and the actual physical and geographical conditions and biodiversity characteristics of southern Guizhou, a comprehensive biodiversity evaluation index system is designed in this paper. Based on remote sensing and geographic information system technology, biodiversity comprehensive assessment of the three prefectures in southern Guizhou is carried out using county as the evaluation unit. This can help to master the status of biodiversity systematically and provide a reference for the future development of local biodiversity conservation.

MATERIALS AND METHODS

Qianxinan, Qiannan, and Qiandongnan Prefectures are located in the east longitude 104° 35′-109° 35′ and the north latitude 24° 38′-27°31′. They govern 36 counties (cities) with a total area of 77100 square kilometers, accounting for 41.6% of the total area of Guizhou Province. The terrain in the territory is generally high in the west and low in the east, with mountains, canyons, hills, valley plains, and mountain basins interlaced. The landform is deeply controlled by the geological structure, showing a characteristic of high mountains and steep slopes, obvious height differences between valleys, and strong cutting (Figure 1). This region belongs to subtropical humid monsoon climate zone, the average annual temperature in this area is 16.2 °C, and the average annual rainfall is 1183mm. The May-September precipitation accounts for about 80% of the total precipitation in the whole year. The zonal vegetation in this area is subtropical evergreen broad-leaved forest. Due to the undulating terrain and obvious climate differences, the types of vegetation vary greatly, having tropical rain forest, subtropical humid and

semi-humid evergreen broad-leaved forest, evergreen broad-leaved and deciduous broad-leaved forests, mountain coniferous, broad-leaved mixed forest, coniferous forest, thicket, meadow and other diverse vegetation types and their ecosystems, as well as karst-specific cave ecosystems.

Evaluation System. (1) Evaluation Index Selection principles. 1) Scientific principles. The selection of indicators should be based on a thorough understanding of biodiversity and in-depth research, which can objectively, truthfully and scientifically reflect the basic characteristics of biodiversity and the status of protection. 2) Principle of representativeness. The selected indicators should directly reflect the essential characteristics of biodiversity and have high representativeness. At the same time, they should be concise and comprehensive. 3) Applicability principle. There are differences in the status of biodiversity in different regions and different types of ecosystems, so the selection of evaluation indicators needs to consider their differences.

(2) Evaluation Index System. In large-scale biodiversity assessment, comprehensive and multi-index evaluation of ecosystems is required [13-14], but often only the related species and landscapes can be involved in the measurement [15-16]. In the seventh session of the Conference of the Parties to the Convention on Biological Diversity [17], protected area coverage was used as an indicator to significantly reduce the rate of biodiversity loss before 2010. Therefore, in this study, the ratio of the area of nature reserves, forest parks and scenic spots to the administrative area is taken as one of the indicators, and its number is also considered. At the same time, according to the study of Xu et al. [4], the important species resources such as medicinal resources, germplasm resources, etc. should also be used as an important indicator to evaluate biodiversity. In the evaluation of ecosystem diversity, combining the natural geographical conditions and biodiversity characteristics of the three prefectures in southern Guizhou Province, this study believes that their unique ecosystem types and the ratio of natural ecosystems area including natural wetlands, natural forests, and natural grasslands to land area of each county should be considered simultaneously.

Therefore, based on the 2012 Regional Biodiversity Evaluation Standards issued by the Ministry of Environmental Protection, the Convention on Biological Diversity, and the research results of domestic scholars [4-5, 18-21], nine primary indicators and 25 secondary indicators were designed, include: 1) Species number: refers to the number of vascular plant and higher animal species recorded in the area being evaluated, and is used to characterize the diversity of higher species. 2) Endemic species: refers to the number of endemic species in the assessed area, divided into two levels: endemic to the world and endemic to China. 3) Endangered species: This study evaluates biodiversity by assessing the species number of different endangered levels in the region, divided into three levels: endangered, rare, and gradually endangered. Other rare and endangered species are also considered. 4) Important resource species: including germplasm resources and medicinal resources. 5) Diversity of ecosystem types: including the number of unique ecosystems, such as karst forest ecosystems; the area ratio of natural ecosystems, that is, the ratio of the area of natural woodlands, natural grasslands, and natural wetlands to the land area; the diversity of forest ecosystem structures, classified by dominant species. 6) Coverage of protected area: The number of nature reserves, forest parks, and scenic spots and their area ratio to the total area of the county. The product of the area ratio and the number is considered in this calculation. 7) Invasiveness of alien species: refers to the ratio of the number of alien invasive species to the total number of native wild mammals, birds, reptiles, amphibians, freshwater and vascular plants in the evaluated area, which is used to characterize the extent of interference by invasive species. 8) Vegetation damage: The percentage of vegetation damage in the assessment area. 9) The completeness of the vertical layer spectrum of vegetation: refers to the completeness of the vertical layered structure of the vegetation community in the evaluated area, and is used to indicate the stability of the ecosystem.

Evaluation Index Weight. The vegetation vertical layer spectrum has more than 5 (including 5) vegetation distribution layers in all counties (cities, districts) of Guizhou Province. Therefore, this evaluation index is not considered in the evaluation process [20]. Vegetation damage and invasiveness of alien species indicators were not included in the calculation due to lack of data. Therefore, the six primary indicators selected in this assessment are: species number, endemic species number, endangered species, important resource species, diversity of ecosystem types, and protected area coverage.

Based on the research by Xue et al. [4], Wan et al. [5], and regional biodiversity evaluation standards [1], and combined with the natural geographical conditions and biodiversity characteristics of the three prefectures in southern Guizhou Province, the study sets the scores and weights of the six evaluation indicators can be seen in Table 1.

Calculation Method of Comprehensive Biodiversity Evaluation Index. The normalization method of the evaluation index is:

Normalized evaluation index (*BI*) = evaluation index before normalization × normalization coefficient.

Normalization coefficient = $100/A_{maximum}$.

$A_{maximum}$- refers to the maximum value before normalization of an indicator.

TABLE 1
Weight values of the assessment indicators

Primary indicators	Secondary indicators	Assign-ment	Weight	Weight set by Xue et al [4].	Weight set by Wan et al. [5]
Species number	--	--	0.18	0.18	0.5
Endemic species	endemic to the world	100	0.1	0.1	0.15
	endemic to China	50			
Endangered species	endangered	100	0.12	0.12	--
	rare	60			--
	gradually endangered	30			--
	rare and endangered species	50			--
Important resource species	medicinal resources	100	0.1	0.1	--
	germplasm resources	100			--
Diversity of ecosystem types	unique ecosystems	100	0.22	--	--
	natural ecosystems	80		--	--
	the diversity of forest eco-system structures	60		0.22	0.15
Protected coverage area	World Natural Heritage	100	0.12	0.13	--
	National Nature Reserve	80			--
	Provincial Nature Reserve	50			--
	State Nature Reserve	30			--
	County Nature Reserve	20			--
	National Forest Park	100	0.09		--
	Provincial Forest Park	80			--
	State Forest Park	60			--
	County Forest Park	20			--
	National Scenic Area	100	0.07	--	--
	Provincial Scenic Area	80		--	--
Invasiveness of alien species	Alien species invasion	--		0.05	0.1
Vegetation damage	Vegetation damage	--		0.1	--
The completeness of the vertical layer spectrum of vegetation	Vegetation vertical horizons integrity	--		--	0.1

Calculation formula of comprehensive biodiversity evaluation index is:

$$BI = \sum_{i=1}^{n} p_i * [(\sum_{j=1}^{m} q_{ij} * f_{ij}) * (\frac{100}{MAX(\sum_{j=1}^{m} q_{ij} * f_{ij})})] \quad (1)$$

Among them: *BI* is the indicator of biodiversity, p_i is the weight of each indicator, i = 1, 2, ... 6, n is the total number of indicators 6, q_{ij} is the score of each secondary index in each indicator, and f_{ij} is the value of secondary indicator, m is the number of secondary indicators of the primary evaluation indicator.

Data and Parameters. Through the collection of local government data in the study area, supplemented by network data collection and literature retrieval, the related information such as the number of species, important resource species, rare and endangered plant species, endemic species, and nature reserves, forest parks, and scenic areas in southern Guizhou were obtained.

For ecosystem diversity, forest ecosystem structure diversity uses forest inventory data to make statistics based on dominant species attributes. At the same time, the natural ecosystems include natural forest resources in forest inventory data and natural grasslands and natural wetlands in the second national land survey data. Due to the lack of specific data on the four indicators of species numbers, the endangered species, endemic species and important resources in each county, state-level data are used for calculation. Endangered species only consider plants due to data problems, adopting the number of endangered, rare and gradually endangered species recorded in the "Chinese Red Book of Plants", supplemented by other rare or endangered species recorded in the "China List of Rare and Endangered Protected Plants", "National Key Protected Wild Plant List (First batch)", "List of Key Protected Tree Species in Guizhou Province" and "the Convention on International Trade in Endangered Species of Wild Fauna and Flora" [18-19].

RESULTS

Spatial Distribution and Area Statistics of Natural Ecosystems. Qianxinan, Qiannan and Qiandongnan Prefecture are rich in natural ecological resources, covering an area of 24,642.42 km^2, accounting for 33.61% of the total land area, and are of high quality with the natural forest resources accounting for 96.68% of the area of all natural ecosystems. The spatial distribution of natural ecosystems is relatively uniform with the central counties being slightly better than the eastern and western counties (Figure 2).

Qiannan Prefecture has the largest natural ecosystem area and the highest proportion. The area of natural ecosystem in Qiandongnan Prefecture is higher than that in Qianxinan Prefecture, but it has the lowest proportion. In terms of counties (cities), Wangmo County in Qianxinan Prefecture has the highest proportion of natural ecosystems, reaching

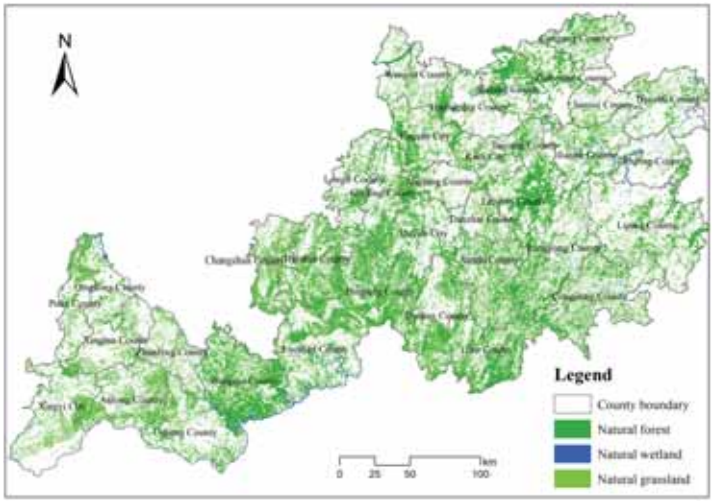

FIGURE 2
Spatial distribution of natural ecosystems in counties in three prefectures in southern Guizhou.

TABLE 2
Areas and proportions of natural ecosystems in counties (cities) in three prefectures in southern Guizhou Province

Prefectures	Counties (cities or districts)	Natural resources area/km^2	Area ratio /%	Prefecturs	Counties (cities or districts)	Natural resources area/km^2	Area ratio /%	Prefecturs	Counties (cities or districts)	Natural resources area/km^2	Area ratio /%
Qiandongnan	Kaili	421.02	32.24	Qiannan	Duyun	782.98	34.31	Qianxinan	Xingyi	608.07	20.68
	Huangpin	305.39	18.33		Fuquan	618.99	36.61		Xingren	385.95	21.58
	Shibing	676.62	43.46		Libo	1244.49	50.91		Pu'an	419.59	29.24
	Sansui	195.95	18.83		Guiding	588.82	36.37		Qinglong	310.17	23.44
	Zhenyuan	510.50	27.09		Weng'an	447.20	22.92		Zhenfeng	341.50	22.51
	Cengong	469.32	31.73		Dushan	1048.07	42.80		Wangmo	1745.63	58.06
	Tianzhu	459.71	21.08		Pingtang	1580.20	55.91		Ceheng	704.50	27.10
	Jinping	283.91	17.65		Luodian	1022.95	34.00		Anlong	767.41	34.29
	Jianhe	619.03	28.70		Changshun	592.84	38.39	--	--	--	--
	Taijiang	482.62	44.56		Longli	384.53	25.39	--	--	--	--
	Liping	1034.74	23.33		Huishui	1111.47	44.92	--	--	--	--
	Rongjiang	1245.61	37.60		Sandu	1006.94	42.49	--	--	--	--
	Congjiang	1114.21	34.58	-	--	--	--	--	--	--	--
	Leishan	533.93	44.53	-	--	--	--	--	--	--	--
	Majiang	315.93	26.00	-	--	--	--	--	--	--	--
	Danzhai	261.61	27.85	-	--	--	--	--	--	--	--
Subtotal		8930.10	29.49	-	--	10429.50	39.85	--	--	5282.82	31.35
Total						24642.42					

58.06%, which can provide a good habitat environment for more animals, followed by Pingtang County and Libo in Qiannan Prefecture. The proportions of natural ecosystem area of these two counties are 55.91% and 50.91%, respectively. Jinping County in Qiandongnan Prefecture has the lowest proportion of natural ecosystem area, only 17.65% (Table 2).

Evaluation Results. Through the above methods, the comprehensive biodiversity evaluation index of the three prefectures in southern Guizhou Province is calculated. As shown in Figure 3 and Figure 4, the evaluation results objectively reflect the status of biodiversity in each county.

From the spatial distribution map of the comprehensive biodiversity assessment index, it can be seen that the biodiversity status of the three prefectures in southern Guizhou gradually deteriorated from east to west. On the whole, Libo County in Qiannan Prefecture has the best biodiversity status, followed by Leishan County, and the worst is Zhenfeng County in Qianxinan Prefecture.

In Qiandongnan Prefecture, Leishan County is the best in terms of biodiversity. It has the Leigong Mountain National Nature Reserve and Forest Park. It has rich species and large natural ecosystems area. The worst is Sansui County.

In Qiannan Prefecture, Libo County has the best biodiversity. It has a unique karst forest ecosystem, which is a world natural heritage site, and is

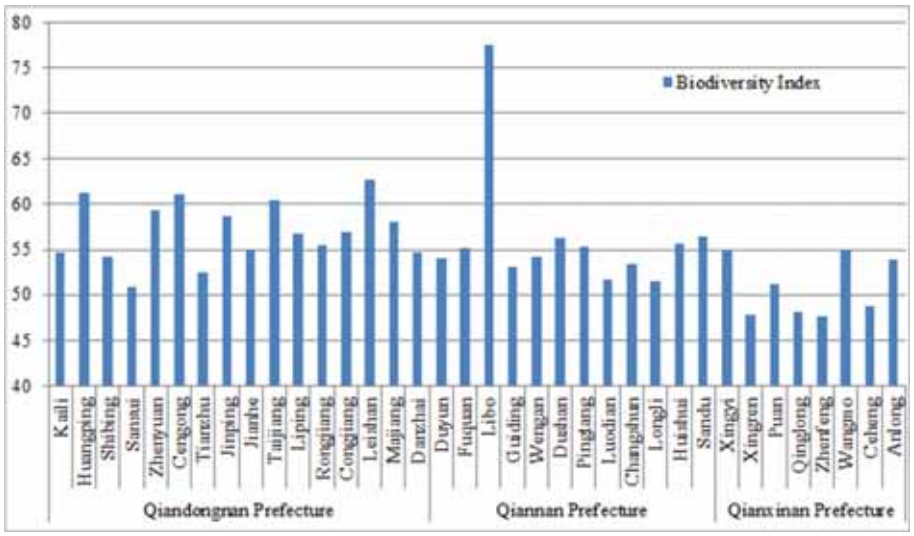

FIGURE 3
Biodiversity comprehensive assessment indexes of every county.

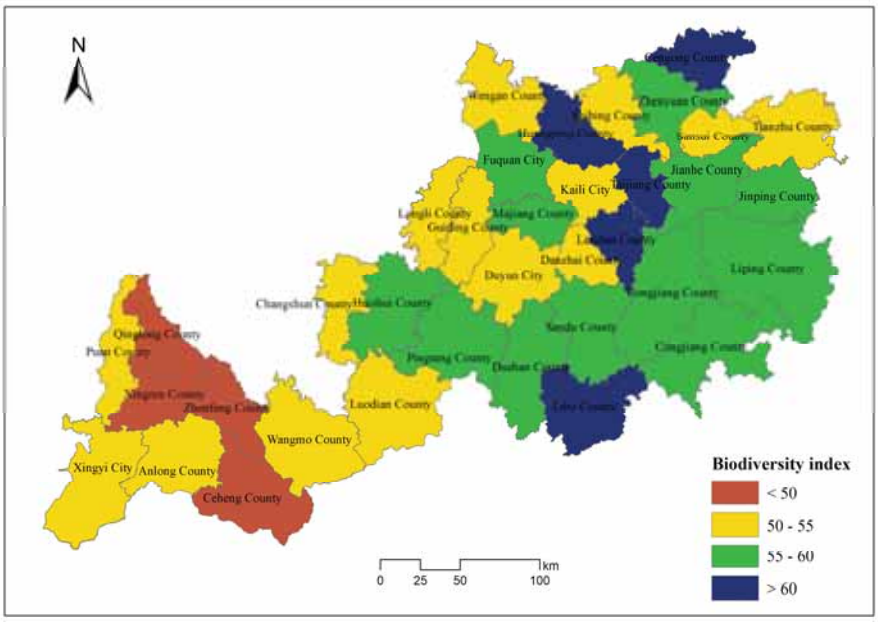

FIGURE 4
The spatial distribution of biodiversity comprehensive assessment indexes of every county.

TABLE 3
The level of biodiversity

Level	BI index	Biodiversity status
Poor	BI<45	Poor species, few ecosystem types, fragile, small protected area, extremely low biodiversity
Relative poor	45≤BI<50	Relative few species, relative few ecosystem types, low protected area levels, and relative poor overall biodiversity
Mediocre	50≤BI<55	Rich in species, rich in biodiversity in some areas, and general level of biodiversity
Good	55≤BI<60	Rich in species, many types of ecosystems, and high biodiversity in some areas
Excellent	60≤BI	The species is highly abundant, the ecosystem is rich and diverse, stable, the protected area is large and high, and the overall biodiversity is rich

known as "Emerald on Earth Belt". Endemic genera and species are abundant, and the ecosystem type is rich and diverse. The worst are Longli County and Luodian County. In the Qianxinan Prefecture, Wangmo County has the best biodiversity, and it has a large area of natural forests. The worst is Zhenfeng County, because of its severe rocky desertification and poor species.

Based on the comprehensive biodiversity assessment index, the biodiversity assessment results of the three prefectures in the south of Guizhou Province are divided into five levels: excellent, good, mediocre, relative poor, and poor.

There was no counties show the "poor" evaluation results. There are 4 counties with "relative poor" evaluation results, accounting for 11.11% of the total counties, all of which are located in the Qianxinan Prefecture, including Zhenfeng County, Xingren County, Qinglong County and Ceheng County. There were 15 counties with "mediocre" evaluation results, accounting for 41.67% of the total counties, including Sansui County, Pu'an County, Longli County, Luodian County, Tianzhu County, Guiding County, Changshun County, Anlong County, Duyun City, Weng'an County, Shibing County, Kaili City, Danzhai County, Xingyi City, Wangmo County. There are 12 counties with "good" evaluation results, accounting for 33.33% of the total counties, mainly distributed in Qiannan and Qiandongnan Prefecture, including Jianhe County, Fuquan City, Pingtang County, Rongjiang County, Huishui County, Dushan County, Sandu County, Liping County, Congjiang County, Majiang County, Jinping County, Zhenyuan County. There were 5 counties with "excellent" evaluation results, accounting for 13.89% of the total counties, including Taijiang County, Cengong County, Huangping County, Leishan County and Libo County.

CONCLUSIONS

(1) From the perspective of spatial distribution, the areas with better biodiversity status in the southern part of Guizhou are mainly concentrated in lower mountainous areas in the southeast. The trend of worsening is from east to west, among which Libo County in Qiannan Prefecture is the best, and Zhenfeng County in Qianxinan Prefecture is the worst.

(2) The biodiversity in southern Guizhou is relatively good. The percentage of counties with a mediocre" review result is the highest, reaching 41.67%, followed by "good" and "excellent", accounting for 33.33% and 13.89% of the total counties, respectively.

(3) Biodiversity is mainly affected by two factors, including natural factors and human factors. Although some of the indicators selected in this study are not accurate enough due to data problems, they can still reveal the relative differences in biodiversity in southern Guizhou and provide a reference for the future development of local biodiversity conservation.

ACKNOWLEDGEMENTS

This work was financially supported by the Natural Science Foundation of the Education Department of Sichuan Province, China (No. 18ZA0125).

REFERENCES

[1] Ministry of Environmental Protection (China) (2012) National Environmental Protection Standard of the People's Republic of China. Regional Biodiversity Assessment Standard.
[2] Yuan, G., Chen, L., Cheng, Y. (2010) Study of Investigation and Evaluation about Biology Diversity of Xinjiang. Environmental Protection of Xinjiang. 1, 1-6.
[3] World Resources Institute (2005) Millennium Ecosystem Assessment. Ecosystem and Human Wellbeing: Biodiversity Synthesis. Washington DC.
[4] Xue, X., Wang, S., Ma, K. (2006) Index system of biodiversity assessment. The 7th National Symposium on Biodiversity Conservation and Sustainable Utilization. 9, 28-36.
[5] Wan, B., Xu, H., Ding, H., Liu, Z., Wang, J. (2007) Methodology of comprehensive biodiversity assessment. Biodiversity Science. 1, 97-106.
[6] Li, G., Wu, X., Luo, Z., Li, J. (2011) Establishing an indicator system for biodiversity assessment in China. Biodiversity Science. 5, 497-504.
[7] BFN (Federal Agency for Nature Conservation) (2008) Policy related Indicators: Measure the Effectiveness of the German National Strategy on Biological Diversity. Berlin, Germany.
[8] DEAT (Department of Environmental Affairs and Tourism, Republic of South Africa) (2009) South Africa's Fourth National Report to the Convention on Biological Diversity.
[9] Defra (Department for Environment, Food and Rural Affairs) (2009) Biodiversity Indicators in Your Pocket 2009: Measuring Progress towards Halting Biodiversity Loss. London, UK.
[10] Qian, Y. (1994) Principles and methods of biodiversity research. Beijing: China Science and Technology Press.
[11] Zhang, Z., Zhang, J., Li, Y., Wang, X., Zhang, J. (1999) Study on Ecological Evaluation Index System for Wetland. Agro-Environmental Protection. 18(6), 283-285.

[12] Ministry of Environmental Protection (China) (2010) China's Biodiversity Conservation Strategy and Action Plan (2011-2030).
[13] Sole, R., Manrubia, S., Benton, M., Kauffman, S., Bak, P. (1999) Criticality and scaling in evolutionary ecology. Trends in Ecology and Evolution. 14(4), 156-159.
[14] Ayensu, E., Claasen, D., Collins, M. (1999) International Ecosystem Assessment. Science. 286, 685- 686.
[15] Zhao, H., Ji, L. (2003) Biodiversity assessment at broad scale. Biodiversity Science. 11(1), 78-85.
[16] Yoccoz, N., Nichols, J., Boulinier, T. (2001) Monitoring of biological diversity in space and time. Trends in Ecology and Evolution. 16(8), 446-453.
[17] Calvignac-Spencer, S., Merkel, K., Kutzner, N., Kühl, H., Boesch, C., Kappeler, P., Metzger, S., Schubert, G., Leendertz, F. (2013) Carrion fly-derived DNA as a tool for comprehensive and cost-effective assessment of mammalian biodiversity. Molecular Ecology. 22(4), 915-924.
[18] Zhang, H. (2009) Study on the Geographical Distribution of Rare and Endangered Plants in Guizhou. Seed. 28(06), 68-72.
[19] Chen, W., Xiong, X., Zheng, Y., Jin, X. (2018) Floristic analysis of the seed plants from Yandang Mountain of Yueqing, Zhejiang. Journal of Zhejiang University (Science Edition). 45(1), 118-126.
[20] Zhao, W., Wu, K., Su, W., Lu, L. (2011) Comprehensive Assessment and Analysis of Bio-diversity in Guizhou Province. Bulletin of Soil and Water Conservation. 31(3), 171-174.
[21] Zhu, W., Fan, J., Wang, Y., Shen, X., Tian, B., Wei, Z. (2009) Assessment of biodiversity conservation importance in the upper reaches of the Yangtze River: by taking county area as the basic assessment unit. Acta Ecologica Sinica. 29(5), 2603-2611.

Received: **15.12.2019**
Accepted: **27.01.2020**

CORRESPONDING AUTHOR

Quanqin Shao
Institute of Geographic Sciences and
Natural Resources Research,
CAS, Beijing 100101 – China

e-mail: shaoqq@lreis.ac.cn

© by PSP Volume 29 – No. 04A/2020 pages 3134-3143 Fresenius Environmental Bulletin

EXPERIMENTAL STUDY ON THE FLOW CHARACTERISTICS OF JET IMPINGEMENT IN MICRO-SCALE ENVIRONMENT

Jie Zheng[1,*], Yarong Zhang[2], Yihua Dou[1]

[1]School of Mechanical Engineering, Xi'an Shiyou University, Xi'an, Shaanxi 710065, P.R. China
[2]School of Science, Xi'an University of Architecture and Technology, Xi'an, Shaanxi 710055, P.R China

ABSTRACT

Micro-scale cooling structures can significantly improve the heat resistance of turbine blades so that they can still operate effectively in high-temperature environments. In order to achieve the optimal cooling effect of gas turbine blades with the minimum cooling air quantity, experimental and numerical simulations of jet impingement channel flow in a micro-scale composite cooling structure were carried out innovatively in this study. The diameters of shock hole and film hole were taken as 0.3-0.5mm, and the impact distance was between 2.0-3.0. The value of Reynolds number was 1000-10000, and Knudsen number was according to the real engine working conditions. The flow situations of different structure micro-scale shock channels were compared and analyzed. The results show that the flow coefficient increased with the increase of Reynolds number, but its growth trend slowed down with the increase of Reynolds number, and finally tended towards to a constant. For the same value of Reynolds number, the flow coefficient increased with the increase of pore diameter and the hole spacing, but the impact distance had no obvious effect on the flow coefficient. Moreover, the flow coefficient was fitted out and the results of the calculation were in good agreement with the experimental results, which could be used in an actual engineering environment.

KEYWORDS:
Micro-scale, environment, optimal cooling effect, simulation, working condition, flow coefficient

INTRODUCTION

The gas temperature in front of the turbine is far high when the aeroengine is running, and which is much higher than the heat-resistant limit of engine [1]. The high thrust weight ratio of the high-temperature parts of a first-stage aeroengine, especially the high-pressure turbine guide vanes and moving vanes, adopt a convective shock film compound cooling structure for a traditional scale. The demand of the cold air is high, and if the new structure is not adopted, it will be difficult to reduce or not reduce the cold air [2-4]. Under the condition of dosage, cooling efficiency will continue to be improved. At present, the cooling technology based on the traditional scale has been unable to meet the requirements of greatly increasing the working environment temperature of high-temperature components, and the micro-scale structure has a very high heat transfer rate. There are not many research studies on the micro-scale cooling structure of gas turbine blades around the world. Studies have mainly focused on the micro-/nano-scale field [5, 6], but the micro-scale structure has a very high heat transfer rate [7]. Integrating the micro-scale cooling technology into the development process of a gas turbine can provide an effective technical way to solve the bottleneck of the cooling capacity of turbine blades.

In 1981, Tuckerman et al. found through experimental research that the heat exchange rate of microchannels was very high. Because of the high heat exchange rate, a large number of studies on the flow and heat exchange of microchannels have been carried out [8]. The flow and heat transfer characteristics of an impinging jet is investigated in two major stages [9]. Three-dimensional numerical study is conducted to investigate the heat transfer characteristics for the flow impingement cooling in the narrow passage based on cooling technology of turbine blade [10]. Wang et al. reviewed the flow and heat transfer of an air-precooled engine and microchannel in detail, especially the application prospect of a microchannel in an aeroengine, which is an effective way to improve the engine efficiency [11]. Guo et al. studied the influence of scale on the flow and heat transfer of microchannels. They believed that the assumption of fluid continuity still held when the scale of the general microchannels was small. The difference between the performance of micro-scale and conventional scale in flow and heat transfers is mainly due to the influence of specific conditions on the mechanism of convection and heat transfer, especially the influence of the specific channel shape and size on the flow and heat transfers. The response mechanism needs further study [12]. In addition, the heat transfer characteristics of the microchannel fluids were analyzed by studying the heat transfer mechanism of micro-scale simple structures [13-15].

Samad et al. analyzed and studied the design optimization of a micro-scale structure in a turbomachinery air system [16]. Lorenzini et al. studied the flow characteristics of compressible fluid with different roughness in a microchannel with a diameter of 26-508μm, and they found that there was a large difference between the flow characteristics and the macro-scale under different flow conditions [17]. Guo et al. has been devoted to the study of micro-scale flow and heat transfer [18, 19]. Ma studied and measured the pressure distribution in a microchannel under the conditions of micro-scale flow and found that the pressure loss distribution in the microchannel was no longer linear [20]. By studying the role of *Knudsen* numbers in micro-scale similar flow characteristics, Xu et al. found that under the condition of continuous medium flow, different *Knudsen* numbers still had an influence on the flow results. Therefore, in order to get more accurate results in similar experiments, it was necessary to ensure that the similar magnifier and micro-scale original *Knudsen* numbers were the same [21]. Zheng et al. used experiments to verify the role of a *Knudsen* number in the study of micro-scale similar flow characteristics [22].

Therefore, we described the limited channel jet impingement unit cooling structure in the leading edge and the middle chord area of a turbine blade in a real environment. In this study, the flow resistance characteristics were obtained for different geometries and aerodynamic conditions through experiments and numerical simulation. The influence law of the geometry and aerodynamic parameters on the flow characteristics was determined. The experimental correlation was arranged, and the basis for the cooling structure design was provided. The analysis method could provide the evaluation method for the application environment of the existing data in the cross-scale cooling structure.

MATERIALS AND METHODS

Experimental Design. Figure 1 shows the impact cooling structure of the micro-scale restricted channel in the chordal region of the turbine blade. The geometry changes of the test piece included four parameters: the impact pore diameter, outlet pore diameter, pore spacing, and impact distance. Among these parameters, the impact hole and the outlet hole were staggered, and the impact hole and the outlet hole had the same hole diameter. In different calculation models, the outlet hole diameter was 0.3mm, 0.4mm, and 0.5 mm. The hole spacings of the impact hole were 5 and 10, and the impact distances were 2.0, 2.5, and 3.0.

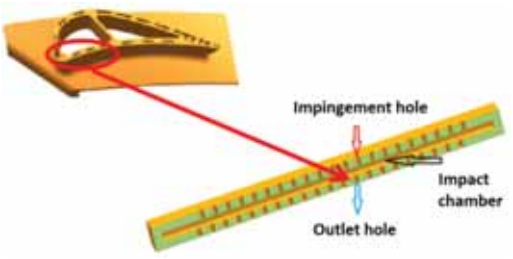

FIGURE 1
Schematic diagram of the test coupon

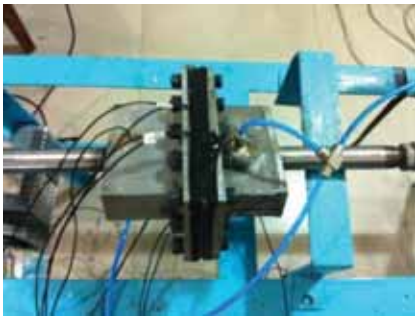

FIGURE 2
Air tight test

The experimental section consisted of six parts: The front cavity, the impact hole heat insulation plate, the copper test piece, the heating steel strip, the heat insulation outlet hole plate, and the rear cavity. Figure 2 is the schematic of the air tightness measurement of the assembled test section. When the flange plate was fixed tightly by bolts, a high-pressure gas was applied. When the pressure exceeded 120% of the maximum pressure of the test condition, air leakage and a pressure drop were detected. If not, it was proven that the air tightness was good.

TABLE 1
Schematic diagram of the hole diameter

Theoretical diameter	D=0.3mm	D=0.4mm	D=0.5
Measurement diagram			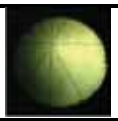
Measured diameter	0.306mm	0.396mm	0.501mm

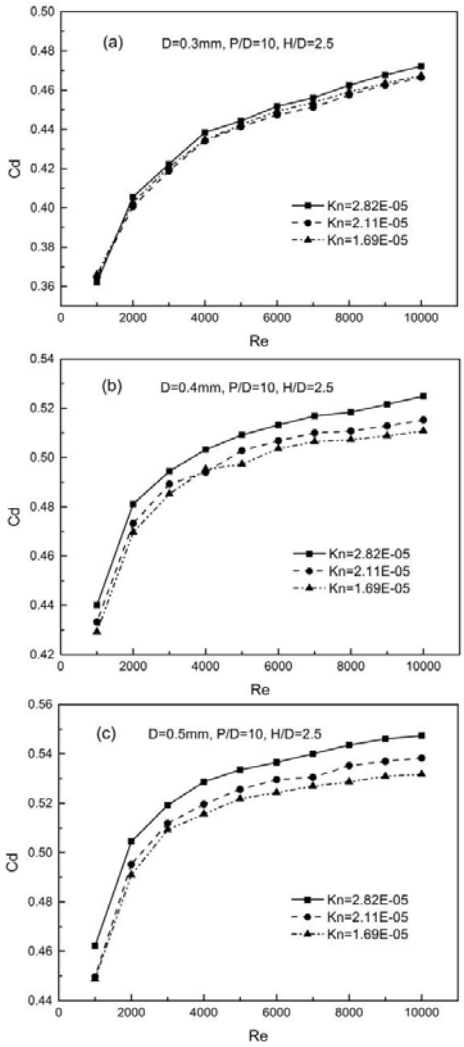

FIGURE 3
Variation of flow coefficient with *Re* number at different *Kn*

Measurement Parameters. Based on the measurement results in Table 1, it can be seen that the roundness of hole processing was very good, and the theoretical diameter was essentially the same. In this measurement, six holes were randomly selected from the test piece for measurement.

Experimental Condition. In order to study the flow characteristics for the real structure of the engine, the real working conditions of turbine blade impact hole inlet of an aeroengine were assumed to be 2.4 MPa and 800 K. In order to simulate the real size of the engine, according to the equation for *Knudsen* value (K_b is 1.38×10^{-23}, effective diameter of an air molecule σ is 3.5×10^{-10} m), for the same scale, it was necessary to ensure that the ratio of the temperature and pressure was the same. In experiments, the temperature of the airflow was 300 K. Then, according to the formula, the pressure in the experiment was 0.9 MPa. That is to say, it was ensured that the *Knudsen* was consistent with the real engine. When the hole diameter is 0.3 mm, 0.4 mm, and 0.5 mm, the *Knudsen* values were 2.82×10^{-5}, 2.11×10^{-5} and 1.69×10^{-5}, respectively. In addition, different apertures, the hole spaces, and the impact distances were studied respectively. Each experiment piece studied at three different *Knudsen* number, for a total of 540 working conditions.

Discharge Coefficient. The flow coefficient represents the flow loss and flow capacity, which is equal to the ratio of actual flow m_r and the theoretical flow m_i per unit time [23].

$$C_D = \frac{m_r}{m_i} \tag{1}$$

m_i is calculated by continuous equation and Bernoulli equation under isentropic condition:

$$C_d = \frac{m_r}{AP_i^*\left(\frac{P_i^*}{P_0}\right)^{-\frac{k+1}{2k}}\sqrt{\frac{2k}{(k-1)R_gT}\left[\left(\frac{P_i^*}{P_0}\right)^{-\frac{k-1}{k}}-1\right]}} \tag{2}$$

In which, A is the cross-sectional area of the impact hole. D is the diameter of the impact hole. P_i^* is the total pressure in the front cavity of the test section. P_0 is the static pressure at rear chamber. m_r is the mass flow measured by the mass flow control meter after the experimental section. T is the temperature of the cooling gas. K is the adiabatic coefficient of gas, 1.4. Rg is the gas constant, 286.7J/(kg · K).

RESULTS

The Influence of *Kn* on the Flow Characteristics. Figure 3 shows the change of the flow coefficient with *Re* number of the micro-confined jet impingement cooling structure for different *Kn*.

It can be seen that the change of *Kn* number had little effect on the flow coefficient when the *Re* number was less than 3000. However, with the increase of *Re* number, that is, when the *Re* number was greater than 3000 and when *Kn* is 2.82E-05 for the same *Re* number, the flow coefficient was significantly higher than that for the other two kn. With the increase of *Re* number, the influence of *Kn* number on the flow coefficient was gradually obvious. From the trend in Figure 3, it can be observed that for the same *Re* number, the corresponding flow coefficient increased with the increase of *Kn* number. When the *Kn* number was small, the fluid was closer to the continuous range, and the influence of *Kn* number on the flow coefficient was not obvious. Otherwise, when the *Kn* number was large, changing the *Kn* number had a great influence on

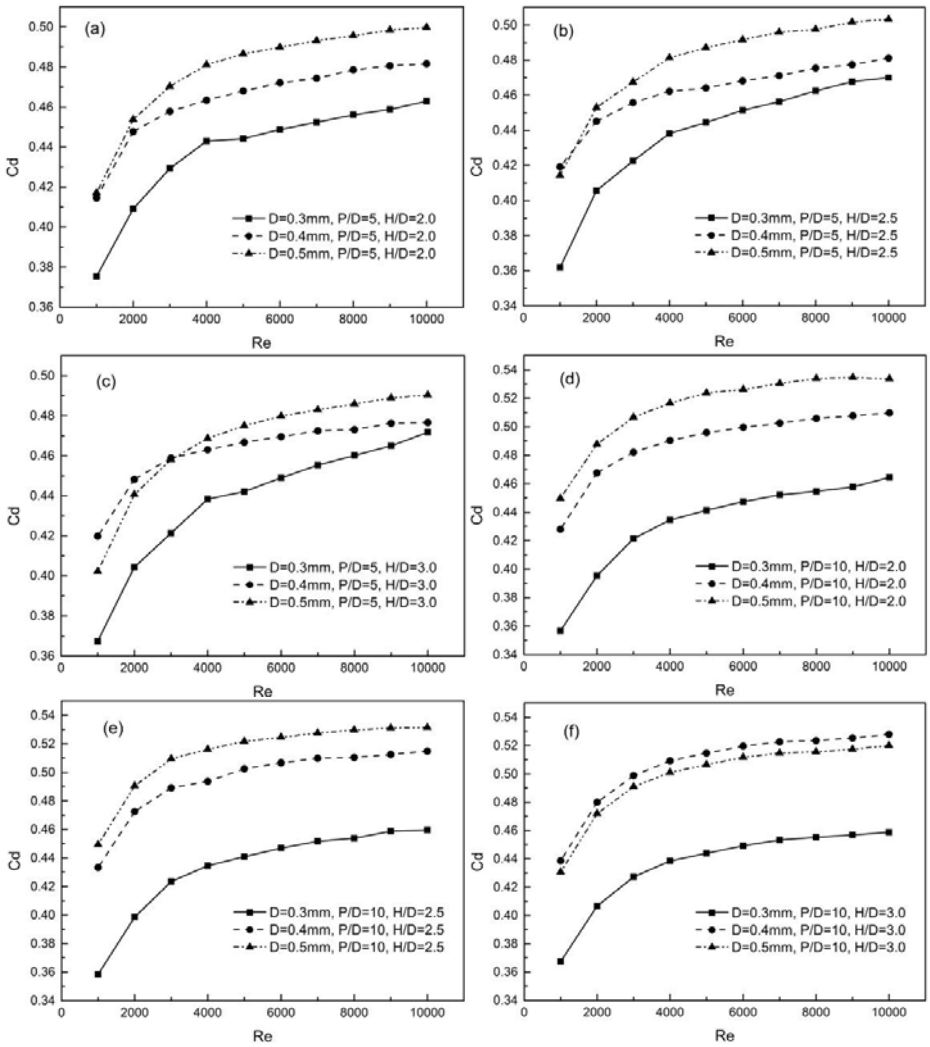

FIGURE 4
Variation of flow coefficient with *Re* number at different pore sizes

the flow coefficient. It shows that the influence of the dimensionless criterion number *Kn* relative to the scale on the calculation results could not be ignored in the numerical simulation of the micro-scale structures with a large *Re* number and a large *Kn* number [24].

Moreover, the same law can be seen from the difference of the streamline diagram. When the aperture was 0.4 mm, the hole spacing was 5D, the impact distance was 2D, and the Reynolds number was 6000. A vortex formed near the outlet wall, which hindered the flow. The size and strength of the vortex directly affected the flow coefficient of the hole. It can be seen from the comparison of the streamline diagrams in Figure 3 that with the increase of Knudsen number, the vortex center gradually became close to the wall, the vortex range was gradually reduced, and the flow obstruction of the vortex near the outlet hole was gradually reduced. With the increase of Knudsen number, the flow coefficient gradually increased and the flow situation gradually improved. Therefore, in order to ensure the accuracy of the flow of the limited impact structure under real engine conditions, it was necessary to ensure that the Knudsen number was consistent with the real conditions.

The Influence of Pore Size on the Flow Characteristics. Figure 4 shows the influence of the pore diameter on the distribution of the flow coefficient with the change of the Reynolds number in the impact channel. It can be observed that the flow coefficient changed regularly with the change of the pore diameter. For the same Reynolds number, the flow coefficient increased with the increase of the pore diameter, and it can be observed that the flow coefficient increased with the increase of the Reynolds number. When the Reynolds number was less than 3000, the growth rate of the flow coefficient was larger. When the Reynolds number was greater than

3000, the growth rate of the flow coefficient decreased gradually and the flow coefficient tended to be gentle. When the hole spacing was 10, it can be seen from Figure 5 (d-f) that the flow coefficient of the hole diameter was 0.5 mm, which was close to that of the hole diameter 0.4 mm. The flow coefficient of the hole diameter of 0.4 mm was much higher than that of the hole diameter of 0.3 mm at the same Reynolds number. It can be seen that the flow coefficient of the small hole diameter was much smaller than that of the large hole diameter with the decrease of the hole diameter. Compared with the two kinds of impact distances, when the hole spacing was 5, it can be seen that the distribution of the flow coefficient was more uniform with the increase of the impact distance and more uniform with the increase of the hole diameter.

In the traditional large-scale cooling structure, the flow state was obviously affected by the impact aperture. Whether the flow state had the same law in the small-scale cooling structure is worthy of further discussion. In order to better observe the flow field structure and master the flow rule of the cooling gas in the limited impact cooling channel, a three-dimensional streamline diagram of the fluid domain was given when the aperture was 0.4 mm, the spacing was 5D and 2.5D, as shown in Figure 5.

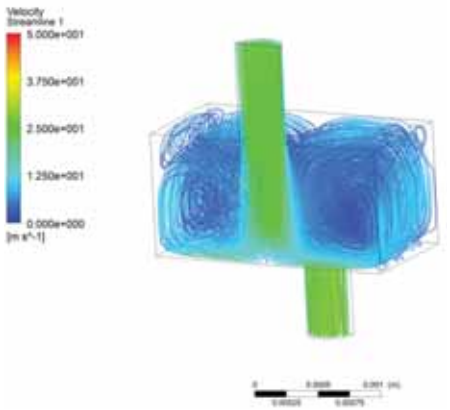

FIGURE 5
Impingement chamber of the three-dimensional streamlines

It can be seen that the cooling fluid flowed from the impact hole at a high speed and entered the impact cavity at a greatly reduced speed. After hitting the impact target, two symmetrical vortices rolled up towards the wall directions of both sides of the impact cavity. The two vortices were small in the beginning. Then the vortices spiraled along the X direction to the outlet direction and gradually became larger. When they reached the outlet hole, the structure of the symmetrical vortices was much larger than the initial structure. Because of the jet and the suction of the outlet hole, the center of the vortices moved up from the jet hole to the outlet hole. Because the flow was limited by the wall of the impinging cavity, a small vortex opposite to the symmetrical vortex in the center of the cavity was produced at the corner of the impinging cavity. With the change of the pore size, the flow pattern of the fluid in the impingement chamber did not change much, but the position and development trend of the vortex structure were different.

Effect of the Hole Spacing on the Flow Characteristics. Figure 6 shows the distribution of the flow coefficient with the Reynolds number in the impact channel for different hole spacings. It can be observed that the hole diameter changed regularly with the flow coefficient, and the flow coefficient generally increased with the increase of the Reynolds number. It can be observed that for the same hole diameter and the same impact distance, the flow coefficient with the hole spacing of 5 was smaller than that with the hole spacing of 10. It can also be seen that when the impact distance was large, the difference in the flow coefficient for different hole spacings was relatively large, but when the impact distance was small, the influence of different hole spacings was gradually weakened. Because of the increase of the hole spacing, the area of the impinging jet cavity increased, so the fluid contact area increased under the same conditions and the flow loss was increased based on the hole spacing. For the same Reynolds number, the flow loss of the hole spacings of 5 and 10 was just the difference between the two flow coefficients. It can be seen that the difference increased with the increase of the hole diameter.

Figure 7 shows the streamline and velocity nephogram at the center section with different hole spacings when *Re* is 5000, D is 0.3 mm and H/D is 2. It can be seen that the cooling airflow speed was the largest in the impact hole, and the flow speed dropped sharply after entering the impact cavity due to the greatly increased flow space. After the cooling gas flowed down the impinging hole, it hit the impinging target surface and reached a lower velocity near the impinging stagnation point directly below the impinging hole. Then the cooling gas rolled up and moved to the exit hole in a spiraling and symmetrical direction along the X-axis. In this process, the airflow accelerated gradually and the fluid velocity near the impact target surface was significantly higher than that in the upper part of the impact chamber. The vortex that formed on the wall of the outlet hole was a great hindrance to the flow of the cooling gas. The cooling gas velocity near the vortex center was very small, and the heat transfer capacity was poor. As the pressure of cooling gas decreased after expansion, the gas velocity in the outlet hole increased compared with that in the impact hole. By comparing the cooling structure for 10D and 5D, it can be seen that the cooling structure with 10D had a large low-speed flow area. Except for the area near

the impact hole and the outlet hole, the air-conditioning flow velocity in other places was very low. Because the low-speed area with 10D was relatively large and the existence of the low-speed area weakened the heat exchange effect in its area, one of the effective means for improving the heat exchange effect was to reduce the flow process of an area of low fluid velocity. Compared with 10D and 5D, the central position of the vortex in the impact cavity was close to the outlet hole. The vortices near the wall of the outlet hole with the 10D structure were smaller than that with 5D, and the average velocity of the cooling gas in the outlet hole also increased.

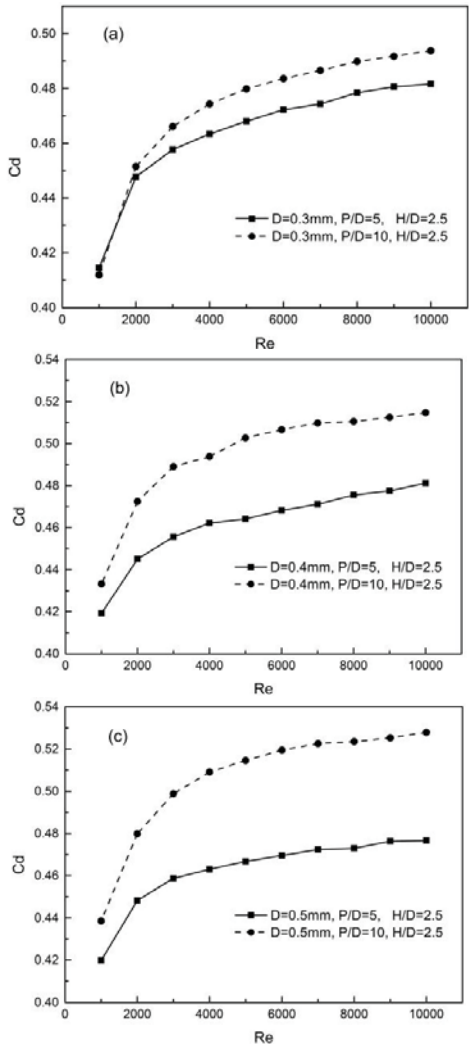

FIGURE 6
Variation of flow coefficient with *Re* number at different hole spacings
(a. D=0.3mm; b. D=0.4mm; c. D=0.5mm)

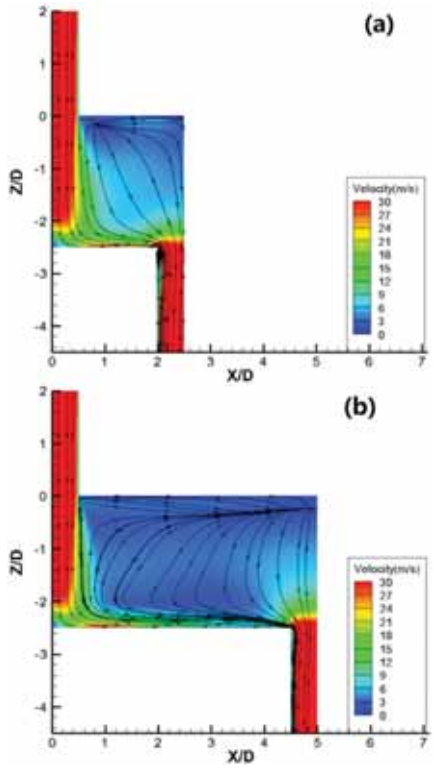

FIGURE 7
Streamlines and velocity contouring at section Y=0 when different pitch of holes
(a. P=5D; b. P=10D)

Influence of the Impact Distance on the Flow Characteristics. Figure 8 is the distribution diagram of the impact distance's influence on the channel flow coefficient with the change of the Reynolds number. It can be observed from the diagram that the flow coefficient generally increased with the increase of Reynolds number. For the same Reynolds number, the impact distance's change had little influence on the flow coefficient. According to the basic law, the flow coefficient increased with the increase of the Reynolds number. Figure 8(d) shows the flow coefficient changes with Reynolds number when the hole spacing was 10 and the hole diameter was 0.4mm. It can be seen that the flow coefficient decreased with the increase of the impact distance, but Figure 8(e) shows that the flow coefficient changed with the Reynolds number when the hole spacing was 5 and 0.5 mm. It can also be observed that the flow coefficient of the impact distance of 3 was higher than that of the other two impact distances. However, Figure 8(a) (b) (c) (f) shows that the influence of the impact distance on the flow coefficient was very small, so it could be considered that the impact distance on the flow coefficient could be ignored when the impact distance was 2-3 in the micro-scale. With the premise of convenient processing, the recommended impact distance was 3.

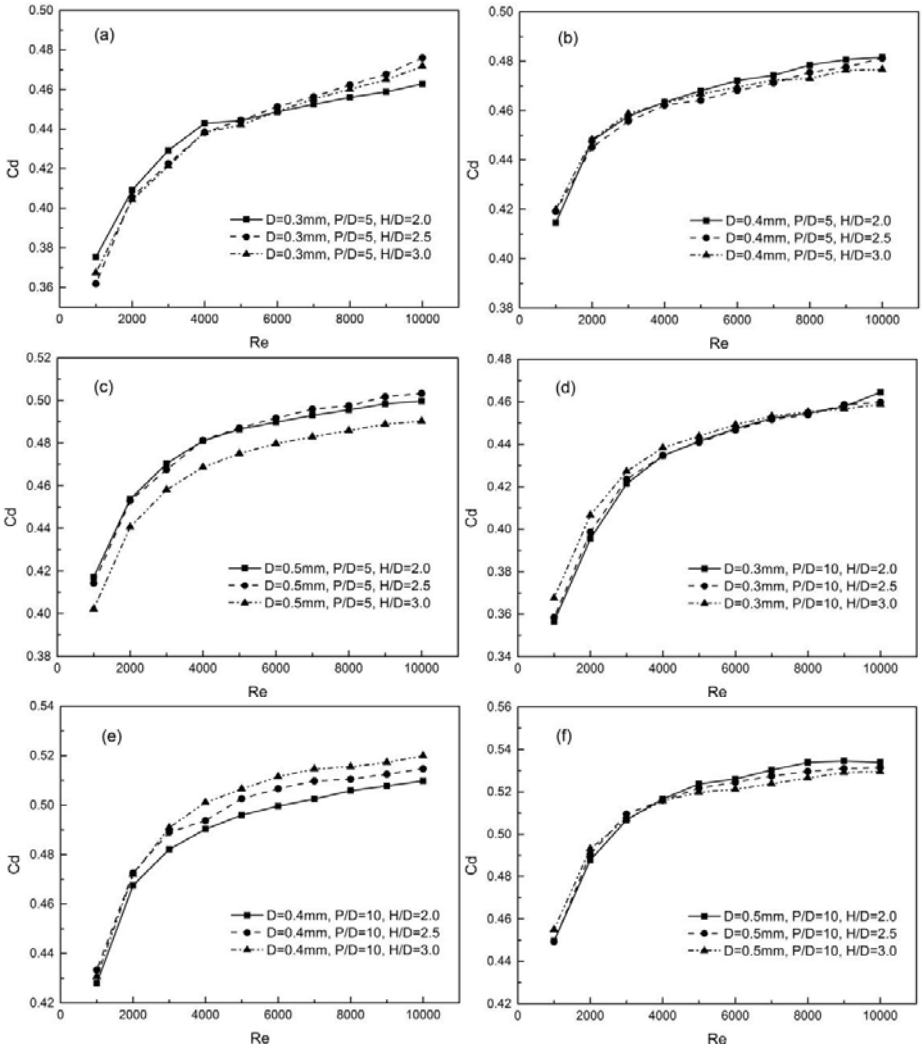

FIGURE 8
Variation of flow coefficient with *Re* number at different impingement distances

Figure 9 shows the streamline and velocity cloud diagrams at the section Y = 0 for the hole diameter is 0.3 mm, *Re* is 5000 and the impact distance is 2.0, 2.5, and 3.0 respectively. It can be seen that the cooling airflow speed was the largest in the impact hole and the flow speed dropped sharply after entering the impact cavity due to the greatly increased flow space. After the cooling gas was ejected from the impinging hole, it hit the impinging target surface and reached a lower velocity near the impinging stagnation point directly below the impinging hole. Then the cooling air rolled up and moves to the exit hole in a spiraling and symmetrical direction along the X-axis. In this process, the airflow accelerated gradually, and the fluid velocity near the impact target surface was significantly higher than that in the upper part of the impact chamber. The vortex that formed on the wall of the outlet hole had a great effect on the cooling gas flow, and the cooling gas velocity near the vortex center was very small. As the pressure of the cooling gas decreased after expansion, the gas velocity in the outlet hole increased compared with that in the impact hole. Compared with the cooling structure with the impact distance of 2.0, 2.5, and 3.0, the change of the velocity field caused by the change of hole spacing was not very obvious. The peak value of the velocity and the structure of the flow field had no sgnificant changes, and the size of vortex at the outlet hole was similar. Therefore, it could bie predicted that the change of the impact distance had little impact on the flow coefficient. However, the impact velocity of the impinging jet into the cavity decreased with the increase of the impact distance. At the same time, based on the 9(a) and 9(c) velocity nephograms, it can be observed that the area of the high-speed fluid flowing into the impinging hole of the impact structure with 2 was larger than that of the high-speed fluid with 3.

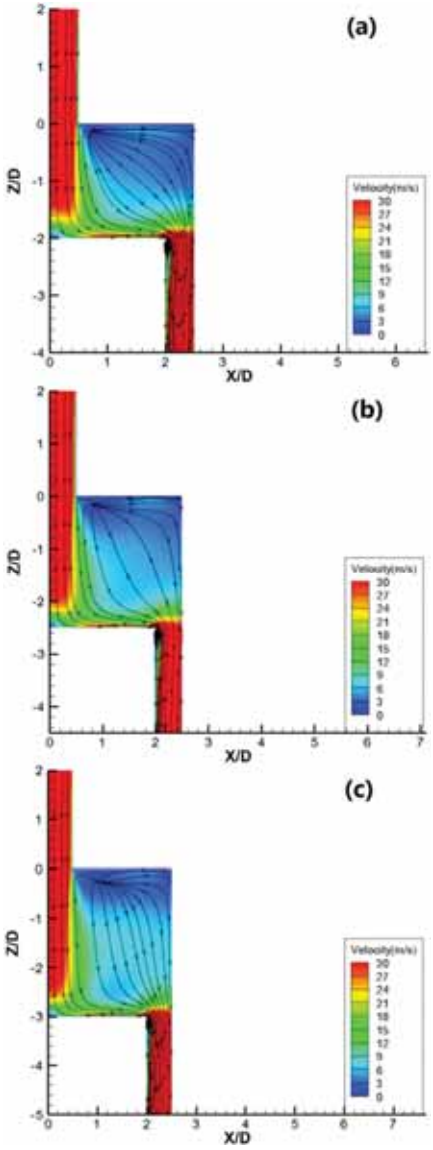

FIGURE 9
Streamlines and velocity contouring at section Y=0 when different impingement distances
(a. D=0.3mm, H/D=2; b. D=0.3mm, H/D=2.5; c. D=0.3mm, H/D=3.0)

Fitting of the Empirical Relationship of the Discharge Coefficient. In order to provide a basis and analysis method for the cooling structure design and thermal analysis, the empirical relationship was fitted:

$$C_d = 0.193720Kn^{0.006701}\,\mathrm{Re}^{0.081220}\left(\frac{P}{D}\right)^{0.1130520}\left(\frac{H}{D}\right)^{0.033638} \quad (3)$$

Among them, C_d is flow coefficient. *Re* is Reynolds number. *P/D* is the ratio of spacing of impact holes to hole diameter. *H/D* is the ratio of impact distance to hole diameter.

The comparison between the experimental data of the flow coefficient for different structures and the results of the fitting formula can be found in Figure 11. The results calculated by the fitting formula were generally consistent with the laws of the experimental results, and the numerical differences were relatively small. Therefore, the fitting formula could be applied to actual engineering to evaluate the flow resistance characteristics of such limited impact channels.

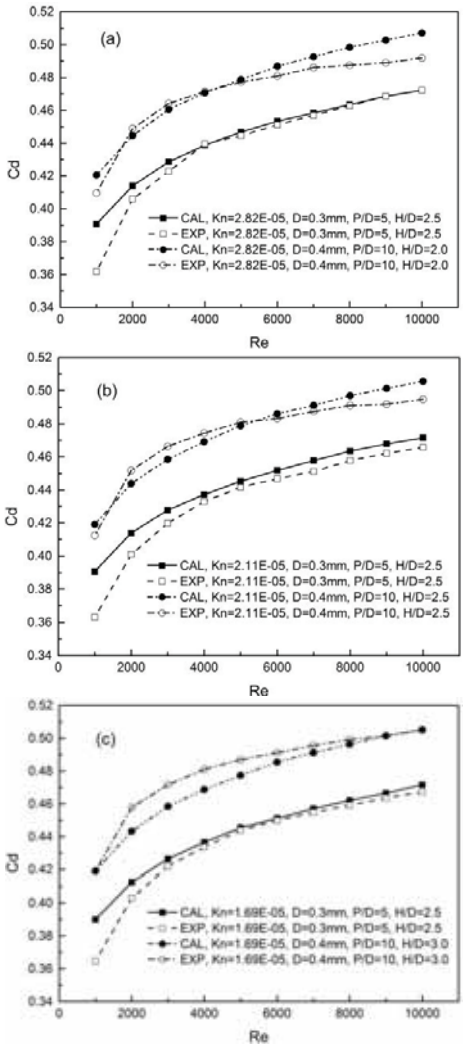

FIGURE 10
Comparison of measured and predicted C_d

CONCLUSIONS

The flow characteristics of the micro-scale limited impact cooling structure of a real aeroengine with different parameters were studied, and the flow characteristics of a micro-scale limited impact cooling structure were analyzed. The main conclusions are as follows: (1) The flow coefficient increased

with the increase of Reynolds number, but its trend slowed down with the increase of the Reynolds number, and finally tended towards a constant. (2) For the same Reynolds number, the flow coefficient increased with the increase of the pore diameter. It could be observed that the flow coefficient increased with the increase of the Reynolds number. When the Reynolds number was smaller, the growth rate of the flow coefficient became smaller, and the flow coefficient tended to be flat. (3) When the impact distance was 2.0-3.0, the influence on the flow coefficient was not obvious. (4) For the same hole diameter and impact distance, the flow coefficient of the hole spacing 5 was smaller than that of the hole spacing 10. When the impact distance was large, the difference in flow coefficient for different hole spacing was obvious, but when the impact distance was small, the influence for different hole spacing was not significant.

ACKNOWLEDGEMENTS

This project was supported by the Natural Science Foundation of Shaan Xi Province in 2019 (No.2019JQ-825) and (No.2019JQ-755) and the Natural Science Foundation of Shaanxi Provincial Department of Education in 2019 (19JK0462).

We thank LetPub (www.letpub.com) for its linguistic assistance during the preparation of this manuscript.

REFERENCES

[1] Karabulut, K. (2019) Heat Transfer Improvement Study of Electronic Component Surfaces Using Air Jet Impingement. Journal of Computational Electronics. 18, 1259-1271.

[2] Vershinin, V.E., Polkovnikov, F.I. (2019) Numerical Investigation of the Influence of Bluff Body's Shape on Flow Characteristics in Vortex Flowmeters. Autom Remote Control. 80, 1368-1373.

[3] Feng, G., Hu, S.Y., Li, Z., Jiang, H.N., Zhang, Y.T., Xu, G., Wang, Z., Kang, L.X. (2016) Distribution of Methane Enrichment Zone in Abandoned Coal Mine and Methane Drainage by Surface Vertical Boreholes: a Case Study from China. Journal of Natural Gas Science and Engineering. 34, 767-778.

[4] Tao, Z., Li, L.W., Zhu, J.Q., Hu, X.Z., Wang, L.Y., Qiu, L. (2019) Numerical Investigation on Flow and Heat Transfer Characteristics of Supercritical RP-3 in Inclined Pipe. Chinese Journal of Aeronautics. 5(7), 7-16.

[5] Cheng, P. (2013) Foreword to Special Issue on Micro/Nanoscale Heat and Mass Transfer. ASME J. Heat Transfer. 135(9), 301-305.

[6] Maranzana, G., Perry, I., Maillet, D. (2004) Mini- and Micro-Channels: Influence of Axial Conduction in the Walls. International Journal of Heat and Mass Transfer. 47(17), 3993-4004.

[7] Zheng, J., Zhu, H.R., Guo, T. (2015) Experimental Study on Heat Transfer Characteristics of Micro Scale Impingement Cooling Channel. Journal of Propulsion Technology. 36(1), 82-88.

[8] Tuckerman, D.B., Pease, R.F.W. (1981) High performance heat sinking for VLSI. Electron Device Letters, IEEE. 2(5), 126-129.

[9] Kim, K.S. (1993) An experimental study on the flow and heat transfer characteristics of an impinging jet. KSME Journal. 7, 258-271.

[10] Sun, R.P., Zhu, W.B., Chen, H., Chen, C.J. (2011) Numerical Study on Flow and Heat Transfer Characteristics of Jet Impingement Cooling. Applied Mechanics and Materials. 148, 680-683.

[11] Wang, Y., Wang, Z.G. (2016) A Review of Flow and Heat Transfer in Air Precooled Engine and Microchannel. Journal of Astronautics. 1, 11-20.

[12] Guo, Z.Y., Li, Z.X. (2003) Size Effect on Single-Phase Channel Flow and Heat Transfer at Microscale. International Journal of Heat and Fluid Flow. 24(3), 284-298.

[13] Morini, G.L. (2005) Viscous Heating in Liquid Flows in Micro-Channels. International Journal of Heat and Mass Transfer. 48(17), 3637-3647.

[14] Mathew, B., Hegab, H. (2008) Effectiveness of Parallel Flow Micro-channel Heat Exchangers with External Heat Transfer and Internal Heat Generation. ASME Journal of Heat Transfer. 2008, 175-184.

[15] Cole, K.D., Cetin, B., Brettmann, L. (2014) Microchannel Heat Transfer with Slip Flow and Wall Effects. Journal of Thermophysics and Heat Transfer. 28(3), 455-462.

[16] Samad, A., Kim, K.Y. (2009) Surrogate Based Optimization Techniques for Aerodynamic Design of Turbomachinery. International Journal of Fluid Machinery and Systems. 2(2), 179-188.

[17] Lorenzini, M., Morini, G.L., Salvigni, S.L. (2010) Transitional and Turbulent Friction Factors for Gas Flows in Smooth and Rough Microtubes. International Journal of Thermal Sciences. 49(2), 248-255.

[18] Guo, Z.Y. (2010) The Frontier of International Heat Transfer Research Micro Scale Heat Transfer. Advances in Mechanics. 30(1), 1-6.

[19] Guo, Z.Y., Li, Z.X. (2003) Size Effect on Single-phase Channel Flow and Heat Transfer at Microscale. International Journal of Heat and Fluid Flow. 24(2), 284-298.

[20] Ma, J. (2004) Experimental Study of Low Reynolds Number Flow in Micro-channels. Master thesis. Nanjing University of Aeronautics and Astronautics, Nanjing, China. 46-58.

[21] Xu, Y.Z., Zhu, H.R., Zheng, J. (2013) The Role of Knudsen Number in the Study of Micro Scale Similar Flow Characteristics. Journal of Aerospace Power. 28(8), 1752-1758.
[22] Zheng, J., Zhu, H.R., Guo, T. (2014) Experimental Study on the Influence of Knudsen Number on the Characteristics of Microscale Similar Flow. Journal of Aerospace Power. 29(8), 1782-1788.
[23] Lee, S.W., Lee, J.S., Ro, S.T. (1994) Experimental Study on the Flow Characteristics of Streamwise Inclined Jets in Crossflow on Flat Plate. Journal of Turbomachinery. 116(1), 283-292.
[24] Abdelmotalib, H.M., Im, I.T. (2019) Simulation study of the effect of the restitution coefficient on interphase heat transfer processes and flow characteristics in a fluidized bed. Numerical Heat Transfer, Part A: Applications. 75(12), 1102-1108.

Received: **19.12.2019**
Accepted: **30.01.2020**

CORRESPONDING AUTHOR

Jie Zheng
School of Mechanical Engineering,
Xi'an Shiyou University,
Xi'an, Shaanxi 710065 – P.R. China

e-mail: jackzheng1@126.com

© by PSP Volume 29 – No. 04A/2020 pages 3144-3153 Fresenius Environmental Bulletin

A NOVEL CONCURRENT RISK IDENTIFICATION AND ANALYSIS METHOD FOR EQUIPMENT FAILURE BY COMBINING PETRI NET REASONING AND AN EXTENDED FMEA USING FOR SAFE OIL AND GAS STORAGE AND TRANSPORTATION ENVIRONMENT

Meng Zhang[1,*], Wei Liang[1], Weijun Li[2], Yanfen Yang[3]

[1]College of Safety and Ocean Engineering, China University of Petroleum, Beijing 102249, China
[2]College of Mining and Safety Engineering, Shandong University of Science and Technology, Qingdao 266590, China
[3]College of Machinery and Electronic Engineering, Guangdong University of Petrochemical Technology, Maoming Guangdong, 525000, China

ABSTRACT

Expert experience and knowledge can provide unstructured and non-detectable fault data for equipment safety management. Therefore, knowledge-based risk analysis is integral compared with signal-based and quantitative data-driven equipment risk analysis methods. Petri net is an intuitive and dynamic knowledge representation and risk reasoning tool. The concurrent risks are particularly focused during reasoning process by proposing a backward-forward reasoning strategy. First, equipment components failure is described as production rules based on expert knowledge. Then Petri net is presented to depict complex cause-effect relationships among components graphically. Furthermore, concurrent risk reachability tree modeling method is presented to trace risk propagation paths. To identify potential concurrent risks, concurrent forward reachability set is first defined for risk reachability tree. In this paper, the method was applied to a reciprocating compressor failure risk identification case. Through concurrent risk analysis, an extended Failure Mode and Effects Analysis (FMEA) for the reciprocating compressor can be conducted. The results show that the proposed method can reveal not only evident risks but also potential risks. Therefore, it can provide the basis for the equipment preventive maintenance and risk management and maintaining safe oil and gas storage and transportation environment.

KEYWORDS:
Oil and gas storage and transportation environment, risk identification, risk analysis, concurrent risk, Petri net reasoning, extended FMEA

INTRODUCTION

As a conventional energy, oil plays an important role in the development of the global economy. The petroleum industry poses a huge threat to the environment. Based on American Petroleum Institute (API) reports, even small leaks from pinholes that were undetected for a long time can cause significant soil and water pollution [1-3]. Not only can oil spills cause accidents, but also natural gas. Integrity failure of the natural gas transportation system can cause natural gas to leak to the surface. This can cause widespread damage to people, property and the environment [4-5]. How to control the failure of equipment in the petroleum industry has become an important issue in environmental protection. Reciprocating compressors play an important role in petroleum industries. In natural gas transportation system, reciprocating compressors are used to pressurize and transport gas. Compressor failures may cause major accidents like gas leakage, fire, or explosion. The integrity of reciprocating compressors requires effective evaluation and maintenance. Risk analysis is an effective tool to identify the abnormal status and provide a basis for maintenance. For reciprocating compressor fault diagnosis, signal-based and quantitative data-driven methods have been the dominant ones in recent years [6-8]. The reasons may be the rapid development of inspection equipment, signal processing technology, and big data acquisition. In contrast, fewer attentions have been paid to qualitative knowledge-based reciprocating compressor fault diagnosis. Consequently, the information stored in experts' brains cannot be utilized. Besides, complex relationships between implicit causes and compressor failures cannot be totally represented by variables or signals. Therefore, qualitative knowledge-based methods should be applied for reciprocating compressor fault diagnosis. On the basis of historical data and experience, knowledge-based fault diagnosis opens a new era for equipment risk analysis [9].

Two common qualitative (or symbolic) knowledge-based fault diagnosis methods are expert system and fault tree analysis. In an expert system, expert knowledge is represented by if-then production rules [10, 11]. However, it often lacks the ability of reasoning, especially for the complex system. On the other hand, fault tree analysis provides an intuitive way to represent the logic structures among fault causes [12-14], but the well-known tree-like structure cannot depict complex relationships.

The net theory provides a tool to solve these problems. One of the most powerful tools of net modeling is Petri net. Petri net was first proposed to deal with information in a computer system [15]. Like most graphical methods, Petri net provides an intuitive way to represent knowledge, but it uses network structure to represent complex relationships among nodes rather than tree-like structures. Besides, Petri net has the ability of path marking and dynamic reasoning. All of these advantages make it have broad applications in many fields, such as power system [16, 17], emergency response [18], traffic safety control [19], manufacturing systems [20], hazard analysis [21], and so on. It should be pointed out that Petri net has a history of origin relationship with safety-related applications [22, 23].

In our work, Petri net (PN) is used to represent rules and simulate risk propagation paths for reciprocating compressor fault diagnosis. Petri net offers the advantages of dynamic knowledge representation and concurrent reasoning [24]. Concurrent risks exist in reciprocating compressor fault. For example, gas impurities may cause potential damage to the piston ring, cylinder, and piston rod overheated concurrently. But not all these components have evident or detectable fault symptoms. Those unobservable faults may not cause immediate failures, but it does not signify that there are no potential risks [25, 26]. Those potential fault propagation paths should be identified to reduce uncertain risk. To address this problem, a concurrent risk-based reasoning Petri net is proposed to analyze risk reachability of reciprocating compressor fault. Based on concurrent risk analysis, an extended Failure Mode and Effects Analysis (FMEA) will be conducted for the reciprocating compressor.

The remaining content is structured as follows. Graphical model representation and risk reasoning with Petri net are presented in Section 2. In Section 3, fault diagnosis rules of the reciprocating compressor are summarized based on expert knowledge, as well as concurrent risk reachability analysis and FMEA. The conclusions are discussed in Section 4.

MATERIALS AND METHODS

Petri Net Model Representation. A general Petri net consists of places, transitions, arcs, and tokens. Generally, places represent system static states, transitions represent the events that change system states, arcs mean input or output relationships, and tokens represent resources. While for fault diagnosis, the definition and scope of Petri net are different from the general Petri net [19, 27]. Petri net in fault diagnosis field has the following features:

(1) For fault diagnosis, the tokens in places represent state rather than resources, therefore the number of tokens means nothing. In other words, the number of tokens is either 1 or 0. In addition, no conflict problems in fault diagnosis Petri net.

(2) Transitions of tokens represent the dynamic propagation of risk. Tokens from input places to output places are in the form of derivation instead of flows. It means that the states of those tokens in input places do not change.

(3) Since the net structures represent cause-and-effect relationships, there is no self-loop problem. Accordingly, the fault diagnosis Petri net is Pure Petri net [17]. For convenience, Pure Petri net is collectively referred to as Petri net.

To sum up, in fault diagnosis Petri net, places represent fault proposition, transitions represent fault diagnosis rules, arcs represent cause-and-effect

TABLE 1
Petri net basic symbols and their definitions in fault diagnosis

Symbols	Meanings	Definitions in fault diagnosis
○	Places	Places are divided into three types according to their different locations, which respectively are initial places, terminate places, and intermediate places. For fault diagnosis, initial places are root causes, terminate places are equipment failures, and intermediate places are components failures.
•	Tokens	If the fault diagnosis proposition is true, there is a token in the place. Otherwise, no token is put into the place.
▬	Transitions	If a diagnosis rule is true, the corresponding transition occurs and token derives to the next place. Otherwise, the transition does not occur and token does not derive.
↝	Arcs	The arrow of an arc points to the same direction with system state changes. Each arc represents a possible risk propagation path.

relationships, and tokens represent that the fault propositions are true. Basic symbols and their detail definitions in fault diagnosis Petri net are listed in Table 1.

According to the definitions of Petri net, we performed structure modeling combining rule-based knowledge. Assume that there are three fault diagnosis rules, which respectively are if A then D, if B then D, if C then D. In this case, A, B, C are possible causes for failure consequence D. The corresponding Petri net can be described as Figure 1.

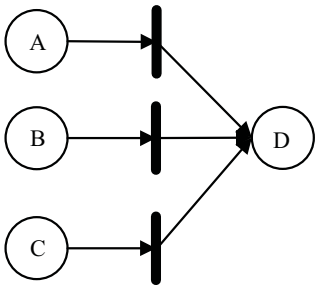

FIGURE 1
A simple Petri net model based on rules

Concurrent Risk Analysis. Generally, there are three strategies in qualitative fault inference or reasoning process, which respectively are forward reasoning, backward reasoning, and hybrid reasoning. Forward reasoning follows the direction of arcs to find consequences of failures. Backward reasoning finds possible causes against the direction of arcs.

Hybrid reasoning combines the advantages of the former two reasoning strategies. Especially, backward-forward reasoning can provide tools for concurrent risk analysis. After converting rules into Petri network, our goal is to analyze the causes and consequences of failure events. Generally, the events adjacent to failure events are direct causes and consequences. However, the most dangerous scenario is that potential risks are under the surface. Therefore, we develop a backward-forward reasoning strategy to dig those indirect causes and consequences, i.e., concurrent risk. The reasoning process is shown in Figure 2.

RESULTS

Fault Diagnosis Rules and Graphical Representation. According to Iceberg Theory, most causes of reciprocating compressor failure are implicit. A reciprocating compressor is a complex system, which is composed of components like a piston, crankshaft, crosshead, etc. Any component malfunction might cause the entire system shutdown. Besides, poor operating conditions, for example, impurities in the air, make the fault rate of reciprocating compressor relatively high. With the long-term use of a reciprocating compressor, experience and lessons have been accumulated. By representing the extensive experience with rules, data in experts' mind can be captured. Therefore, we interviewed field specialists who had experienced reciprocating compressor failure accidents. Six types of component failure were identified, which are crankshaft wear, piston ring wear, cylinder overheated, piston rod overheated, crosshead overheated, and valve plate wear. Production rules were summarized using the following format: IF (implicit causes) THEN (component malfunction).

The possible causes of reciprocating compressor failure are summarized in terms of component malfunctions, listed in Table 2. Note that the possible causes are incomplete because not any failure was or will be experienced. For the convenience of modeling in the following section, we also proceed to code for each proposition.

According to modeling principles, the fault diagnosis rules in Table 1 can be depicted by the Petri net, as is shown in Figure 4. We assume that the observed fault is "cylinder overheated", then a token is marked in place P16.

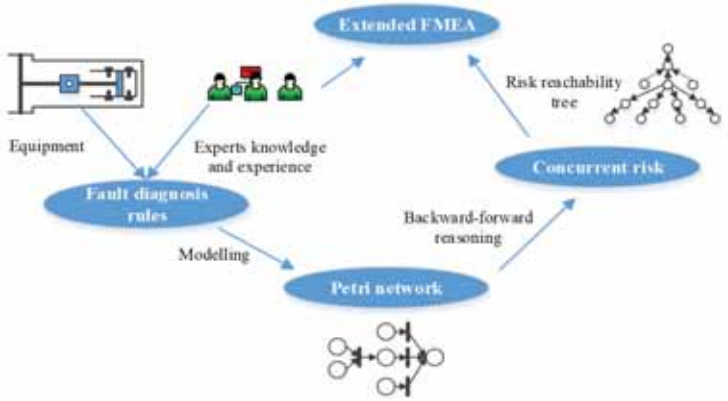

FIGURE 2
Backward-forward reasoning process

TABLE 2
Possible fault propagation paths to reciprocating compressor failure

Code	Reciprocating compressor failure	Code	Component failure	Code	Basic causes
P20	Abnormal state of reciprocating compressor	P14	Crankshaft wear	P1	Small clearance of bush
				P2	Crankshaft deformation
				P3	Foundation Sinking
				P6	Insufficient lubrication
		P15	Piston ring wear	P4	Not homocentric with cylinder
				P5	Rough inner wall of cylinder
				P8	Gas impurities
				P6	Insufficient lubrication
		P16	Cylinder overheated	P7	Insufficient cooling
				P6	Insufficient lubrication
				P8	Gas impurities
		P17	Piston rod overheated	P6	Insufficient lubrication
				P9	Rough piston rod surface
				P10	Small fitting clearance of packing
				P8	Gas impurities
		P18	Crosshead overheated	P11	Big clearance with crosshead guide
				P8	Gas impurities
				P6	Insufficient lubrication
		P19	Valve plate wear	P8	Gas impurities
				P12	Too much oil in cylinder
				P13	Bolts looseness

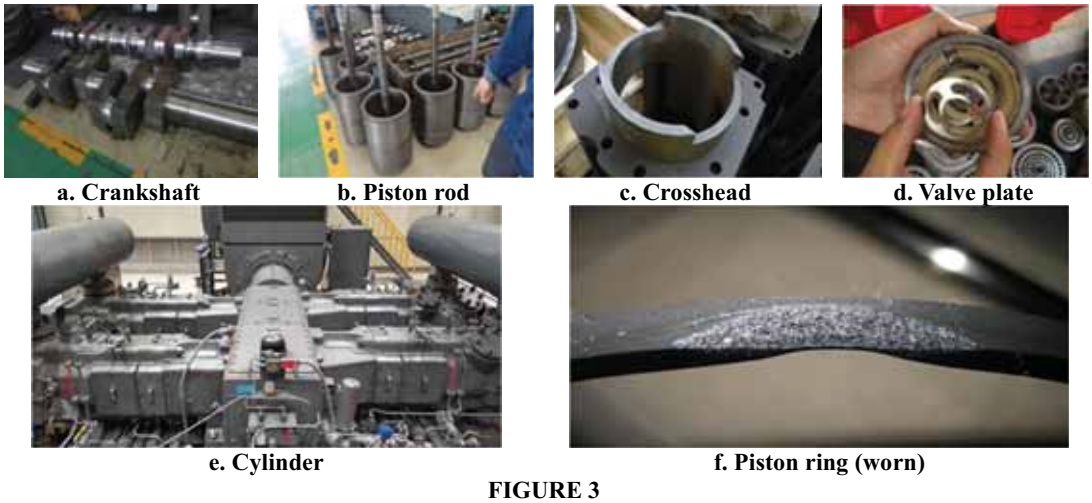

a. Crankshaft **b. Piston rod** **c. Crosshead** **d. Valve plate**

e. Cylinder **f. Piston ring (worn)**

FIGURE 3
Possible failure components of reciprocating compressor

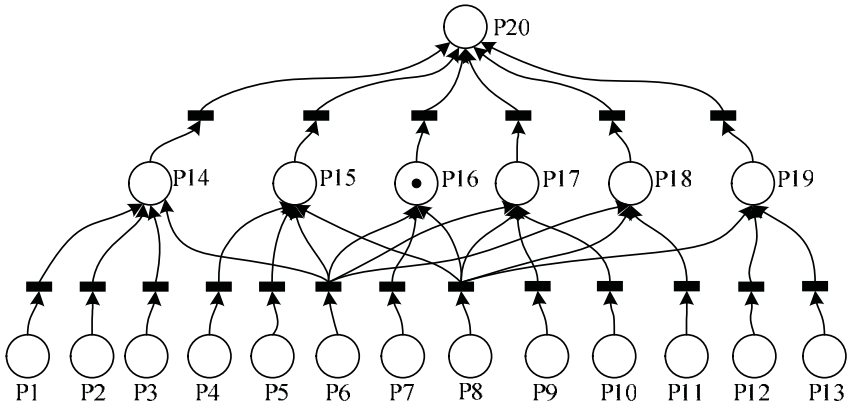

FIGURE 4
Petri net model of compressor fault diagnosis rules

As mentioned above, assume "cylinder overheated" fault is observed or detected. According to Petri net backward reasoning rules, there are three possible risk propagation paths leading to P16, which respectively are P6→P16, P7→P16, and P8→P16. In one troubleshooting task, assume that both cooling system and lubrication system worked properly. In other words, P6→P16 and P7→P16 are impossible paths. Then the possible cause is gas impurities (P8). Therefore, the token in P16 could be derived from P8. This process is the backward reasoning, as is shown in Figure 5.

However, this is not the end of a complete fault diagnosis process. In practice, many malfunctions could be caused by gas impurities. But not all these malfunctions or failures are evident or detected. Therefore, forward reasoning is needed to identify more risk propagation paths, as shown in Figure 6. Start from P8, there are five paths, which are P8→P15, P8→P16, P8→P17, P8→P18, and P8→P19. Consequently, apart from cylinder overheated, the other possible faults are piston ring wear, piston rod overheated, crosshead overheated, and valve plate wear. This can provide the basis for the preventive maintenance of reciprocating compressor (Figure 6).

Concurrent Risk Reachability Tree. Reachability is one of the most important properties of Petri net. For fault diagnosis, reachability refers in particular to risk reachability. According to backward-forward reasoning strategy, reachability sets are given for all the intermediate places. Due to the different reasoning directions, three kinds of reachability sets are defined, which are forward reachability set (FRS), backward reachability set (BRS), and concurrent forward reachability set (CFRS). In our case, FRS represents the consequences of intermediate places risk, BRS means causes of intermediate places risk, and CFRS represents the latent risk. Reachability sets of all the intermediate places are listed in Table 3.

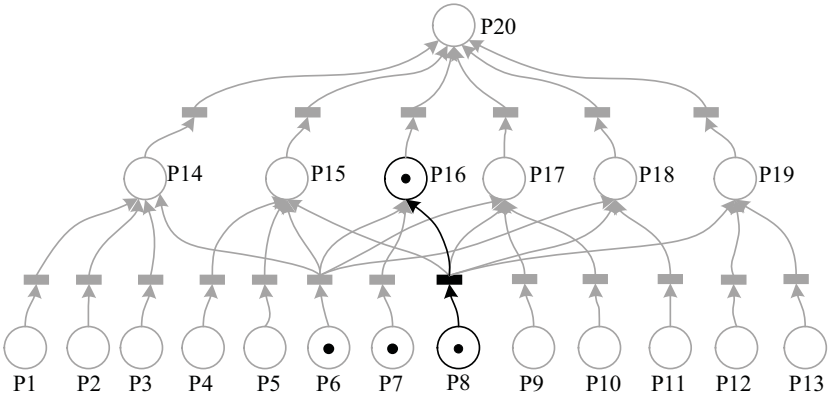

FIGURE 5
Backward reasoning of compressor failure Petri net

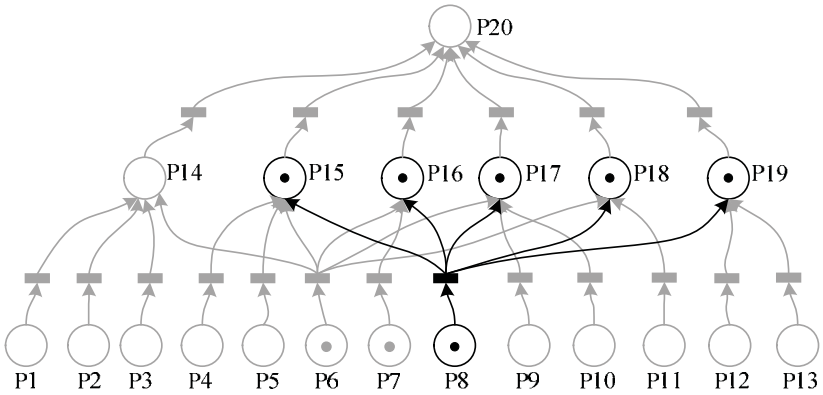

FIGURE 6
Forward reasoning of compressor failure Petri net

TABLE 3
Reachability Set of intermediate places

Places	FRS	BRS		CFRS
P14	{P20}	{P1, P2, P3, P6}	P1	Ø
			P2	Ø
			P3	Ø
			P6	{P15, P16, P17, P18, P20}
P15	{P20}	{P4, P5, P6, P8}	P4	Ø
			P5	Ø
			P6	{P14, P16, P17, P18, P20}
			P8	{ P16, P17, P18, P19, P20}
P16	{P20}	{P6, P7, P8}	P6	{P14, P15, P17, P18, P20}
			P7	Ø
			P8	{P15, P17, P18, P19, P20}
P17	{P20}	{P6, P8, P9, P10}	P6	{P14, P15, P16, P18, P20}
			P8	{P15, P16, P18, P19, P20}
			P9	Ø
			P10	Ø
P18	{P20}	{P6, P8, P11}	P6	{P14, P15, P16, P17, P20}
			P8	{P15, P16, P17, P19, P20}
			P11	Ø
P19	{P20}	{P8, P12, P13}	P8	{P15, P16, P17, P18, P20}
			P12	Ø
			P13	Ø

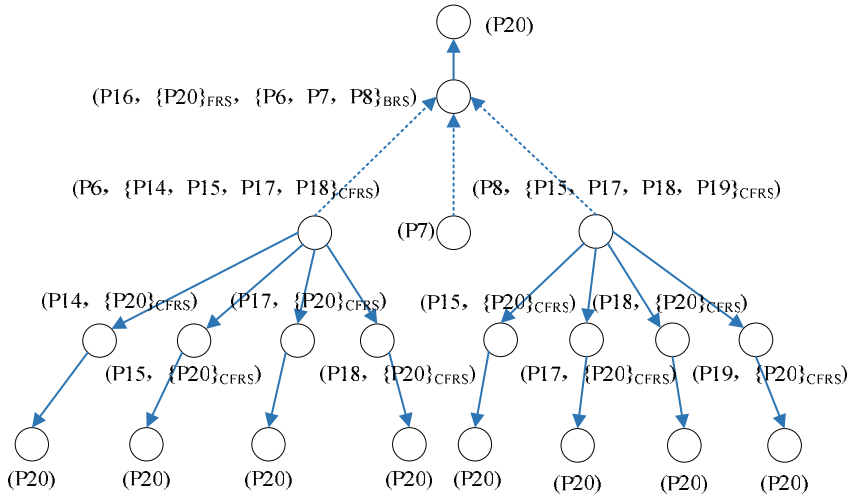

FIGURE 7
Risk reachability tree of intermediate place P16

Reachability tree can be established based on reachability sets. It is an effective dynamic analysis tool of Petri net. Each branch of reachability tree represents a possible risk propagation path. The state of the place to be analyzed is expressed by a triple, which is composed of place, forward reasoning set of the place, and backward reasoning set of the place. We used P16 as an example to demonstrate the analysis process. First, the state of P16 can be expressed by a triple (P16, $\{P20\}_{FRS}$, $\{P6, P7, P8\}_{BRS}$). Then construct connecting lines between these relevant places. If the reasoning process has the same direction with risk propagation, full lines are used, otherwise, dotted lines are used. From Table 3, we can see that {P6, P7, P8} is the backward reachability set of P16. Hence, dotted lines are drawn. Take P6, P7, and P8 as starting point to proceed concurrent forward reasoning process, respectively. Since the concurrent forward set of P7 is Ø, no branch is derived from P7. The concurrent forward set of P6 is {P14, P15, P16, P18, P20} and P14, P15, P16, and P18 are immediately reachable. So there are four branches from P6. The concurrent forward sets of P14, P15, P16, and P18 are {P20} and the concurrent forward set of P7 is Ø. Consequently, the reachability tree is expanded, shown in Figure7.

TABLE 4
Extended FMEA of reciprocating compressor

Component failure mode	Causes	Effects	Safety management and maintenance strategies
Crankshaft wear	Small clearance of bush	Reciprocating compressor failure	Reinstall or replace the bush
	Crankshaft deformation	Reciprocating compressor failure	Replace the crankshaft
	Foundation Sinking	Reciprocating compressor failure	Adjust foundation
	Insufficient lubrication	Piston ring wear Cylinder overheated Piston rod overheated Crosshead overheated Reciprocating compressor failure	Increase lubrication volume Keep lubrication pressure steady Observe or detect if there are cylinder overheated, piston rod overheated, crosshead overheated or piston ring wear
Piston ring wear	Not homocentric with cylinder	Reciprocating compressor failure	Adjust and ensure centering
	Rough inner wall of cylinder	Reciprocating compressor failure	Repair or replace cylinder
	Gas impurities	Cylinder overheated Piston rod overheated Crosshead overheated Valve plate wear Reciprocating compressor failure	Repair or replace inlet filter Observe or detect if there are cylinder overheated, piston rod overheated, crosshead overheated or valve plate wear
	Insufficient lubrication	Crankshaft wear Cylinder overheated Piston rod overheated Crosshead overheated Reciprocating compressor failure	Increase lubrication volume Keep lubrication pressure steady Observe or detect if there are cylinder overheated, piston rod overheated, crosshead overheated or crankshaft wear
Cylinder overheated	Insufficient lubrication	Crankshaft wear Piston ring wear Piston rod overheated Crosshead overheated Reciprocating compressor failure	Increase lubrication volume Keep lubrication pressure steady Observe or detect if there are piston rod overheated, Piston ring wear, crosshead overheated or crankshaft wear
	Insufficient cooling	Reciprocating compressor failure	Increase cooling water flow
	Gas impurities	Piston ring wear Piston rod overheated Crosshead overheated Valve plate wear Reciprocating compressor failure	Repair or replace inlet filter Observe or detect if there are piston rod overheated, Piston ring wear, crosshead overheated or valve plate wear
Piston rod overheated	Insufficient lubrication	Crankshaft wear Piston ring wear Cylinder overheated Crosshead overheated Reciprocating compressor failure	Increase lubrication volume Keep lubrication pressure steady Observe or detect if there are piston ring wear, crankshaft wear, cylinder overheated, or crosshead overheated
	Gas impurities	Piston ring wear Cylinder overheated Piston rod overheated Crosshead overheated Valve plate wear Reciprocating compressor failure	Repair or replace inlet filter Observe or detect if there are piston ring wear, cylinder overheated, valve plate wear, crosshead overheated, or piston rod overheated
	Rough piston rod surface	Reciprocating compressor failure	Grind or replace piston rod
	Small fitting clearance of packing	Reciprocating compressor failure	Replace packing
Crosshead overheated	Insufficient lubrication	Crankshaft wear Piston ring wear Cylinder overheated Piston rod overheated Reciprocating compressor failure	Increase lubrication volume Keep lubrication pressure steady Observe or detect if there are crankshaft wear, piston ring wear, cylinder overheated, or piston rod overheated
	Gas impurities	Piston ring wear Cylinder overheated Piston rod overheated Valve plate wear Reciprocating compressor failure	Repair or replace inlet filter Observe or detect if there are piston ring wear, cylinder overheated, valve plate wear, or piston rod overheated
	Big clearance with crosshead guide	Reciprocating compressor failure	Maintenance and adjust clearance
Valve plate wear	Gas impurities	Piston ring wear Cylinder overheated Piston rod overheated Crosshead overheated Reciprocating compressor failure	Repair or replace inlet filter Observe or detect if there are piston ring wear, cylinder overheated, piston rod overheated, or crosshead overheated
	Too much oil in cylinder	Reciprocating compressor failure	Decrease lubrication volume
	Bolts looseness	Reciprocating compressor failure	Tightening bolts

From Figure 7, it can be concluded that not only evident risks but also latent risks are traced in risk reachability tree. The relationships between the overheated cylinder and the abnormal state of the reciprocating compressor are more complicated than what can be directly detected. Concurrent risk-based reasoning Petri net makes latent risk propagation transparent and thus can help equipment managers and operators to identify more hidden risks.

Extended FMEA Based on Concurrent Risk Analysis. As an effective equipment risk analysis tool, FMEA has the advantages of convenience and operability comparing with other methods [28, 29] It decomposes a system into several components and separately evaluates each component according to expert knowledge. However, those complex cause-consequence relationships hidden in expert knowledge cannot be identified in FMEA. As we stated above, potential risk propagation paths are revealed through concurrent risk reachability tree. Therefore, the Petri net modeling and reasoning method we proposed can compensate it. Table 4 presented the extended FMEA of the reciprocating compressor.

By comparing Table 2 and Table 4, it can be seen that more potential effects can be identified in the extended FMEA. Accordingly, more safety management and maintenance strategies are developed. Therefore, we can conclude that Petri net modeling helps concurrent risk reasoning, provides deeper risk propagation paths, and further enriches the knowledge base.

Discussion. As can be seen from the above, there are usually more than one cause of equipment failure. When analyzing security issues, traditional security analysis methods may not effectively analyze all concurrent failures. This article presents a method of combining Petri net reasoning and an extended FMEA (PN-FMEA). An example of applying this method was proposed to perform concurrent risk analysis and identification of the reciprocating compressors. In this paper, the authors utilized expert knowledge to define the failure behavior of the components of a reciprocating compressor system. Afterward, the Petri net (PN) was used to model the cause-effect relationships among component failures based on the rules defined earlier. The PN model was subsequently used to trace the risk propagation path via a reachability tree modeling. Finally, FMEA was derived through concurrent risk analysis. Compared to other event-based safety analysis methods, traditional FMEA can obtain more accurate and detailed qualitative and quantitative results. However, FMEA considers a single failure mode, the risk analysis for multiple concurrency failure modes is considered less. Petri net facilitates the reasoning of concurrent risks, provides a deeper risk propagation path, and further enriches the knowledge base. In the process of safety analysis using the PN-FMEA method, the advantages of the two analysis methods can be combined to further analyze the system safety, especially for the concurrency failure. From the perspective of security, the security of reciprocating compressor system has been improved.

CONCLUSIONS

(1) A reciprocating compressor is composed of many interrelated components. Any component malfunction may cause reciprocating compressor failure. But not any component has evident or detectable symptoms. In fact, those risks, which are not evident, are the most dangerous. A concurrent risk reasoning method is proposed to qualitatively analyze reciprocating compressor risks based on fault diagnosis knowledge.

(2) Knowledge representation rules in fault diagnosis Petri net is presented. It can be seen from the net map that complex relationships exist in reciprocating compressor fault diagnosis knowledge. Concurrent risks are revealed by backward-forward reasoning strategy. An illustrative example of cylinder overheated fault caused by gas impurities is presented. Through backward-forward reasoning process, piston ring wear, piston rod overheated, crosshead overheated, and valve plate wear are also possible risks even though not all of them can be observed or detected. Furthermore, Concurrent risk reachability tree is depicted to trace risk propagation paths. It can be seen from the risk reachability tree that the risk of a reciprocating compressor is much more higher considering latent risks. Based on concurrent risk analysis, the extended FMEA provides detailed equipment management and preventive maintenance strategies for the reciprocating compressor.

(3) The fault diagnosis Petri net provides a modeling method to represent complex equipment fault diagnosis knowledge. It should be noted that only qualitative analysis is conducted mainly because that the failure probability of varies from equipment to equipment. The analysis method presented can provide the basis for the equipment management and preventive maintenance. We believe this modeling and reasoning method can also be applied to other equipment fault diagnosis and risk analyses.

ACKNOWLEDGEMENTS

This paper was supported by the Science Foundation of the China University of Petroleum, Beijing (No. 2462015YO0406).

REFERENCES

[1] Zheng, D., Xu, H., Wang, J., Sun, J., Zhao, K., Li, C., Shi, L., Tang, L. (2017) Key evaluation techniques in the process of gas reservoir being converted into underground gas storage. Pet. Explor. Dev. 44, 840-849.

[2] Bott, I., De Souza, L., Texeira, J., Rios, P. (2005) High-strength steel development for pipelines: A Brazilian Perspective. Metallurgical and Materials Transactions A (Physical Metallurgy and, Materials Science). 36(2), 443-454.

[3] Feng, Q., Dai, L. (2016) Revelation of Pipeline Accidents. China Building Materials Press: Beijing, China. 5.

[4] Cheng, Y., Yang, L. (2009) A Fuzzy Petri Nets approach for railway traffic control in case of abnormality: Evidence from Taiwan railway system. Expert Syst. Appl. 36(4), 8040-8048.

[5] Chung, L., Chang, C. (2011) Petri-net models for comprehensive hazard analysis of MOCVD processes. Comput. Chem. Eng. 35(2), 356-371.

[6] Cicek, K., Celik, M. (2013) Application of failure modes and effects analysis to main engine crankcase explosion failure on-board ship. Safety Sci. 51(1), 6-10.

[7] Dai, X., Gao, Z. (2013) From model, signal to knowledge: A data-driven perspective of fault detection and diagnosis. IEEE Trans. Ind. Inf. 9(4), 2226-2238.

[8] Dotoli, M., Fanti, M., Mangini, A., Ukovich, W. (2011) Identification of the unobservable behaviour of industrial automation systems by Petri nets. Control Eng. Pract. 19(9), 958-966.

[9] Duan, Y., Zhao, J., Chen, J., Bai, G. (2016) A Risk Matrix Analysis Method Based on Potential Risk Influence: A Case Study on Cryogenic Liquid Hydrogen Filling System. Process Saf. Environ. 102, 277-287.

[10] Filippetti, F., Franceschini, G., Tassoni, C., Vas, P. (2000) Recent developments of induction motor drives fault diagnosis using AI techniques. IEEE Trans. Ind. Electron. 47(5), 994-1004.

[11] Gao, M., Wu, Z., Zhou, M. (2000) A Petri net-based formal reasoning algorithm for fuzzy production rule-based systems. IEEE International Conference on Systems, Man, and Cybernetics. 4, 3093-3097.

[12] Gao, Z., Cecati, C., Ding, S. (2015) A survey of fault diagnosis and fault-tolerant techniques—Part I: Fault diagnosis with model-based and signal-based approaches. IEEE Trans. Ind. Electron. 62(6), 3757-3767.

[13] Li, W., Cao, Q., He, M., Sun, Y. (2018) Industrial non-routine operation process risk assessment using job safety analysis (JSA) and a revised Petri net. Process Saf. Environ. 117, 533-538.

[14] Kumamoto, H., Ikenchi, K., Inoue, K., Henley, E. (1984) Application of expert system techniques to fault diagnosis. Chem. Eng. J. 29(1), 1-9.

[15] Leveson, N., Stolzy, J. (1987) Safety analysis using Petri nets. IEEE T. Software Eng. 13(3), 386-397.

[16] Li, X., Lara-Rosano, F. (2000) Adaptive fuzzy Petri nets for dynamic knowledge representation and inference. Expert Syst. Appl. 19(3), 235-241.

[17] Pan, Y., Liao, B., Yang, C., Tian, M. (2014) Modeling and Design of One Real Eight-Phase Traffic Light Control System Using Pure Petri Nets. In: Proceedings of the 2nd International Conference on Intelligent Technologies and Engineering Systems. 899-905.

[18] Qi, G., Tsai, W. T., Hong, Y., Wang, W., Hou, G., Zhu, Z. (2016) Fault-Diagnosis for Reciprocating Compressors Using Big Data. 2016 IEEE Second International Conference on Big Data Computing Service and Applications (BigDataService). 72-81.

[19] Szücs, A., Gerzson, M., Hangos, K. (1996) An intelligent diagnostic system based on Petri nets. Comput. Chem. Eng. 20, 635-640.

[20] Uzam, M. (2002) An optimal deadlock prevention policy for flexible manufacturing systems using Petri net models with resources and the theory of regions. Int. J. Adv. Manuf. Tech. 19(3), 192-208.

[21] Vernez, D., Buchs, D., Pierrehumbert, G. (2003) Perspectives in the use of coloured Petri nets for risk analysis and accident modelling. Safety Sci. 41(5), 445-463.

[22] Ramming, F. (1977) Petri-net based description, analysis and simulation of concurrent processes. ACM SIGDA Newsletter. 7(2), 15-27.

[23] Wang, B., Sechilariu, M., Locment, F. (2013) Power flow Petri Net modelling for building integrated multi-source power system with smart grid interaction. Math. Comput. Simulat. 91, 119-133.

[24] Wang, R., Zheng, W., Liang, C., Tang, T. (2016) An integrated hazard identification method based on the hierarchical Colored Petri Net. Safety Sci. 88, 166-179.

[25] Zhang, Y., Zhang, Y., Wen, F., Chung, C., Tseng, C., Zhang, X., Zeng, F., Yuan, Y. (2016) A fuzzy Petri net based approach for fault diagnosis in power systems considering temporal constraints. Int. J. Elec. Power. 78, 215-224.

[26] Zhou, M. (1998) Modeling, analysis, simulation, scheduling, and control of semiconductor manufacturing systems: A Petri net approach. IEEE T. Semiconduct. M. 11(3), 333-357.

[27] Zhong, M., Shi, C., Fu, T., He, L., Shi, J. (2010) Study in performance analysis of China Urban Emergency Response System based on Petri net. Safety Sci. 48(6), 755-762.

[28] Zhou, J. (2013) Petri net modeling for the emergency response to chemical accidents. J. Loss Prev. Process Ind. 26(4), 766-770.
[29] Zhou, Q., Thai, V. (2016) Fuzzy and grey theories in failure mode and effect analysis for tanker equipment failure prediction. Safety Sci. 83, 74-79.

Received: **20.12.2019**
Accepted: **29.01.2020**

CORRESPONDING AUTHOR

Meng Zhang
College of Safety and Ocean Engineering
China University of Petroleum
Beijng 102249 – China

e-mail: yangzhi2105@126.com

© by PSP Volume 29 – No. 04A/2020 pages 3154-3165 Fresenius Environmental Bulletin

RESEARCH ON A NOVEL LASER DETECTION METHOD FOR CASING DAMAGE OF CNG GAS STORAGE WELL AND FIELD TRIAL

Liansheng Qin[1], Jian Du[1,*], Shiyong Cao[2], Han Liu[3]

[1]School of Mechanical Engineering, Southwest Petroleum University, Chengdu 610500, China
[2]Sichuan Zhongman Electrical Engineering and Technology Co. Ltd., Chengdu 610500, China
[3]Southwest Branch, CNPC Logging Co. Ltd., Chongqing 401147, China

ABSTRACT

Aiming at the casing damage detection of CNG gas storage wells, this paper proposes a CNG gas storage well casing damage detection method based on the principle of laser ranging. Based on this detection method, the experimental prototype of the measurement device is completed, and the supporting software is also developed. The detection system can detect the size of the inner wall damage and the location of the damage in real time. After debugging the developed testing device, based on the indoor simulation experiment platform, the joint detection of the indoor 7-inch casing and the 9-inch casing and the full-circumference simulated damage indoor inspection of the casing were performed. After analyzing the obtained detection results from the experiment, it can be known that the new detection device has higher detection accuracy with the error less than 5%, showing that the detection results are reliable. Based on the indoor simulation experiment, a field experiment was carried out using a 7-inch casing in a teaching experimental well. The confirmatory experimental results show that the casing damage detection device developed in this paper can complete the detection of simulated casing damage, and the detection results have reached the expected target, which has certain practical value. In addition, it also proves that the laser detection method can be applied to casing damage detection. The feasibility and correctness of the detection provides a certain research basis for the further development of the laser method in the field of casing damage detection.

KEY WORDS:
CNG gas storage well, laser, triangle method, damage detection, simulation platform, detection device

INTRODUCTION

In recent years, as people's awareness of environmental protection continues to increase, clean energy has attracted more and more attention. As a result, the domestic energy structure has changed a lot, and it has gradually developed towards a green and low-carbon direction. Natural gas as a kind of green and highly efficient energy sources are taking an increasingly larger share in China's energy consumption structure [1-2]. Compared with traditional coal, gasoline, diesel and other fuels, the Compressed Natural Gas (CNG) as fuel emits fewer pollutants and is more energy-saving and environmentally friendly. Therefore, more and more buses and taxis in China have successively adopted natural gas as a fuel for power. Natural gas fuel has also shown a good development trend due to its obvious advantages [3]. CNG gas stations are an indispensable part of urban infrastructure construction in western countries.

CNG gas storage stations mainly include several methods for storing CNG, such as underground gas storage wells, high-pressure gas storage cylinders, and buried gas storage pipe sections. The above-mentioned various gas storage methods also have aspects of construction methods, construction costs, hazard effects, and maintenance. Each has its pros and cons [4-5]. However, the method of storing CNG in underground gas storage wells has become the most common gas storage method (around 80% of the total) in gas storage stations due to its advantages such as large gas storage capacity, high space utilization rate, and small change in wellbore affected by temperature [6-7]. At present, the number of domestic gas storage wells is growing rapidly. According to incomplete statistics, there are currently tens of thousands of gas storage wells in the country [8-9].

The casing materials used in CNG underground gas storage wells are mostly metal materials. During long-term use, the inner wall of the wellbore is prone to corrosion because of moisture and corrosive gases. Corrosion occurs from the surface of the metal, and in most cases, it also causes various cracks, large areas of depression, or thinning along with changes in the shape. Once the casing has serious corrosion defects, it will easily cause the wellbore to rupture and leak, which will cause serious safety problems. Therefore, many gas

storage wells with long service life need to be tested in accordance with relevant national standards. However, currently, there are few special detection instruments for the casing damage of CNG underground gas storage wells, and the detection technology is not mature enough, which has brought certain difficulties to the inspection work. Because the casing of a gas storage well has the characteristics of buried cementing, which can be classified as a downhole casing. Therefore, the study of casing damage detection methods for CNG wells can use the downhole casing detection technology.

At present, research techniques for the casing damage in gas storage wells at home and abroad mainly include ultrasonic detection [10-14], eddy current detection [15-18], magnetic flux leakage detection [19-21] and other methods, supplemented by downhole television technology [22]. For example, Zhang et al. and others, based on the principle of magnetic flux leakage detection, optimized the excitation structure of the magnetic flux leakage indoor detection device of the gas storage well by finite element analysis [2]. Jian et al. and others studied the ultrasonic wall thickness detection system based on the water intrusion method, but needs to be improved in terms of detection accuracy and coverage of the well wall [8]. Luo et al. and others, based on the ultrasonic detection principle of seamless steel pipes, designed an ultrasonic detection system for gas storage wells to achieve various types of defects at different angles [23].

The above methods can obtain casing damage information to a certain extent. But these various methods have limitations in detecting small defects, high missed detection rate and high false detection rate. Based on the analysis of the existing technology, this article attempts to apply the laser to detect the casing damage based on the working conditions of CNG gas storage wells, and develops an indoor casing damage detection device to increase the precision and accuracy of the measurement. The new device can be used to explore the minor damage which to provide a basis for future research on practical equipment.

MATERIALS AND METHODS

According to the needs of actual research, this article takes laser triangulation as the theoretical basis, and takes the content of API-SPEC-5CT "Sleeve and Tubing" specification as well as API-RP-5A5-2005 "On-site inspection method for new casing, tubing and flat end drill pipe" as the standard and basis for the design and research work to explore the experimental detection device for the damage of the inner wall of CNG gas storage casing. The detection device mainly includes three parts: mechanical part, measurement and control part and detection information analysis part.

The mechanical part includes a lifting system for vertically lowering and lifting the detection device in the casing under the experimental platform and the field environment to ensure that the detection device is centered and stable in the casing and obtain a good measurement effect. Body structure equipped with measurement and control circuits such as sensors. The measurement and control part are the core part of the casing damage detection device. It is composed of a detection unit, a data conversion unit and a control unit. It is a key part of signal measurement, data transmission and display, including a sensor group, a single-chip microcomputer and an application circuit. The analysis unit uses the software platform to screen, analyze the collected signals and data, draw the inner wall curve of the casing, and finally obtain the test results.

Principle of Triangulation. With the continuous improvement of a series of photodetectors and laser technologies such as CCD and PSD, laser triangulation has shown strong vitality and accuracy in the fields of minute displacement, object contours and related precision detection. The triangulation method uses a laser beam to irradiate a measured object to generate a light spot. A position sensitive device is placed on the focal plane, and the light reflected or scattered by the surface of the object passes through the lens to image the light spot on the focal plane. When the external contour of an object is scanned with a light beam or the object moves, the spot position will change accordingly, and the image near the focal plane will change accordingly. The image contour of the object or its displacement can be obtained through the image sensor device CCD the amount. The principle of the above-mentioned laser triangulation distance measurement is shown in Figure 1.

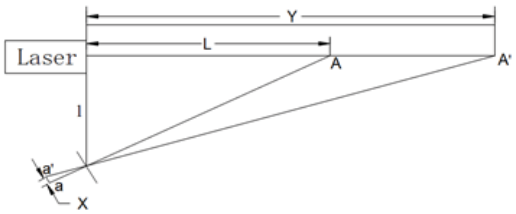

FIGURE 1
Schematic diagram of triangulation method.

Let the laser light shine perpendicularly on the surface of the object. Point A in the Figure 1 reflected on the CCD light sensitive surface is point a, and point A′ is reflected on the light sensitive surface of CCD as a′. At the same time, the corresponding light spot image position X on the photosensitive device also changes. According to the Newtonian object image relationship and the triangular relationship formula shown in Figure 1, the relationship between the two is [24-25]:

$$Y = \frac{X(f\sqrt{L^2 + l^2} - l^2) - flL}{XL - fl} \quad (1)$$

$$X = \frac{fl(L - Y)}{f\sqrt{L^2 + l^2} - l^2 - LY} \quad (2)$$

Where: Y is the measured distance; F is the focal length of the imaging system; l is the baseline length, which is the distance from the laser emission port to the center of the imaging system; L is the reference distance, generally the distance corresponding to the center of the photosensitive surface receiver (the length is known); X is the distance between the measured distance and the known distance of the image point on the photosensitive receiver.

Laser Detection Scheme Design. CNG gas storage well casing damage detection device measurement and control part are the core content of the entire detection device and instrument research. Its main task is to detect the casing damage through laser ranging sensors, and summarize the data and transmit it to the ground to form casing damage. The raw data would provide the subsequent parameter processing. However, because the sensor uses a point-to-point measurement method which means that the measurement area covered by one sensor is one point. This situation will cause the small actual measurement coverage of the sensor [26]. Therefore, multiple sensors need to work in a certain arrangement to form a sensor array to complete the circumferential comprehensive detection of the casing wall. In the design, the laser sensors are arranged in a layered array.

In this study, we expect to design a laser detection probe to detect the damage to the inner wall of the casing of CNG gas wells, and use a computer terminal to realize the real-time measurement and monitoring. Therefore, the laser probe should include the mechanical unit (centering unit, probe structure design), measurement and control unit, and analysis software. Among them, the measurement and control unit are the core unit of the probe design. It should use a single-chip microcomputer as the central controller. The casing damage is detected by a high-precision laser sensor. The measured distance signals are processed by the single-chip microcomputer and transmitted to the computer through a cable for data analysis. The schematic diagram of the measurement and control scheme of the laser detection system is shown in Figure 2.

The laser detection probe needs to realize real-time downhole measurement. Therefore, it is necessary to design the multi-channel laser sensor, the displacement encoder, the single-chip microcomputer, and the centralizer as a whole. To make better use of the downhole space, the sensors and circuits, the peripheral installation shapes of each part should be uniform round which are consistent with the shape of the space inside the sleeve. Therefore, the structural design diagram of the detection system is shown in Figure 3.

Software Process Design of Laser Detection System. After the detection system completes the self-test, the user logs in, executes the interface data, and starts to collect the depth and pipe wall data. The system completes the data acquisition process at a certain interval. The data is processed in the computer to form a curve (horizontal - vertical) are displayed on the interface at the same time. At the same time of data collection, users can zoom in on the curve, and perform the online measurement and analysis on the enlarged graph line. When the test is completed, the data and curve information are saved, and the software exits. The software process design is shown in Figure 4.

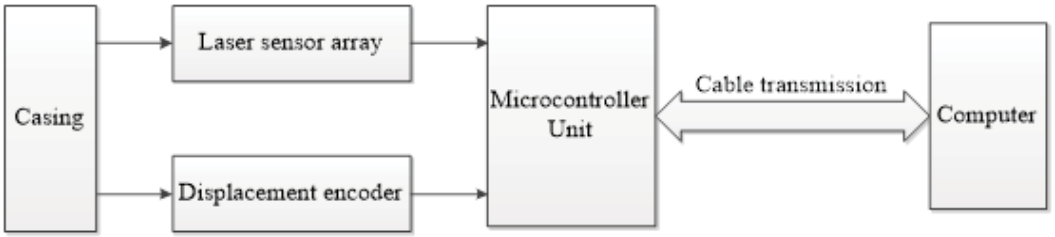

FIGURE 2
Schematic diagram of the measurement and control scheme of the laser detection system.

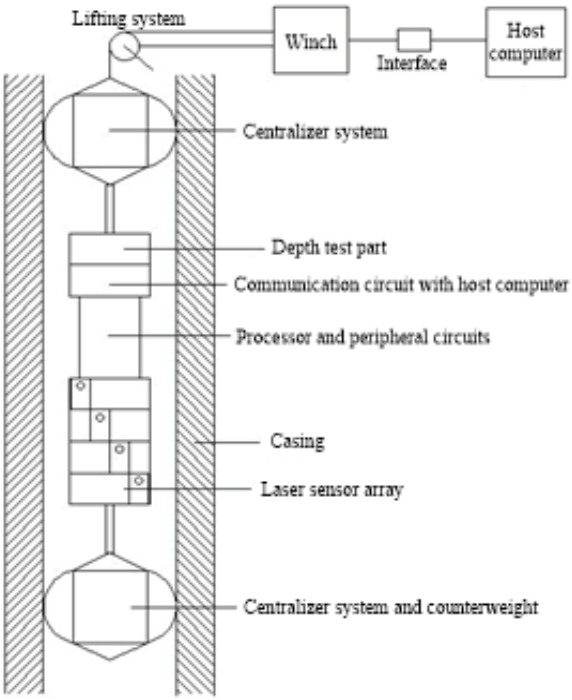

FIGURE 3
Schematic design of the detection system structure.

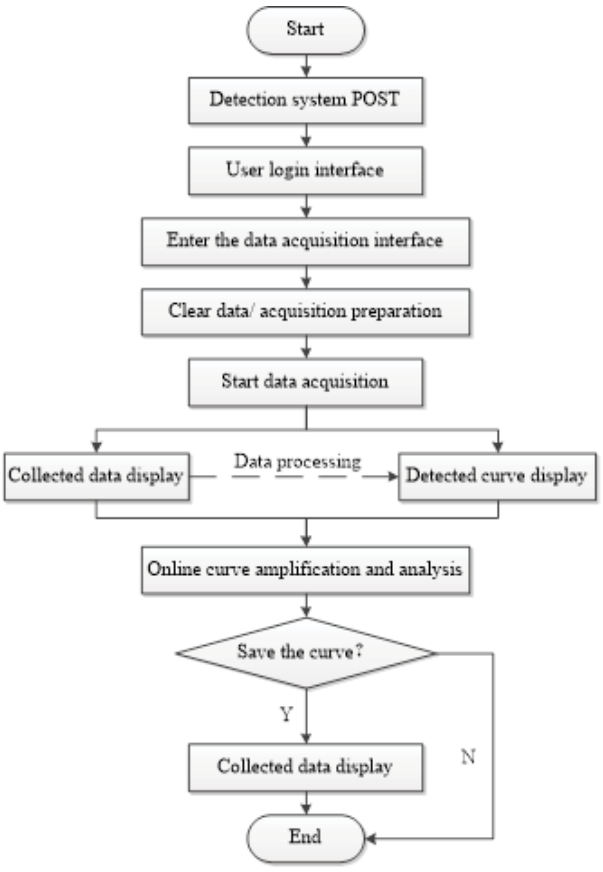

FIGURE 4
Software process design.

RESULTS AND DISCUSSION

Based on the measurement principle of the detection device and the software design of the detection design scheme, the mechanical components, measurement and control parts, communication links and software debugging are completed. To determine the feasibility and reliability of the detection device, before the formal launch of relevant experiments, this paper also calibrates the laser sensor that undertakes direct parameter distance measurement and the wheel displacement measurement sensor that bears the depth of the equipment in the detection device. The following series of experiments were completed.

Coupling Indoor Testing Experiment. The testing device after debugging and calibration is shown in Figure 5 (a). The sensor group in the figure is composed of 8 laser sensors. This device is applied to the casing damage detection simulation platform to simulate the casing damage detection experiment. The experimental platform is shown in the Figure 5 (b). The casing damage simulation experiment platform includes 7-inch and 9-inch simulated casing damage pipe sections (both with couplings), pipe section fixing straps, and pipe section support and stabilization devices (loading the pipe sections to the 90-degree vertical position and maintaining stability or horizontal position unloading), which mainly serves as an external experimental place for the indoor testing device to simulate the experiment and the downhole casing environment. The casing used in the actual production of various sizes can be fixed on the platform, and the simulated casing can be placed at different angles and shapes for different drilling trajectories according to specific needs, further closer to the real working conditions.

In the experiment, laboratory coupling tests were first performed on 7-inch and 9-inch sleeves, as shown in Figure 6 (a) and Figure 6 (b).

The upper computer is used to receive the detection signal. After the detected data of the 8 channels is processed by the software, it is stored in the background database and the corresponding detection signal curve is drawn. Figure 7 shows the coupling test curve of the 7-inch sleeve in the laboratory.

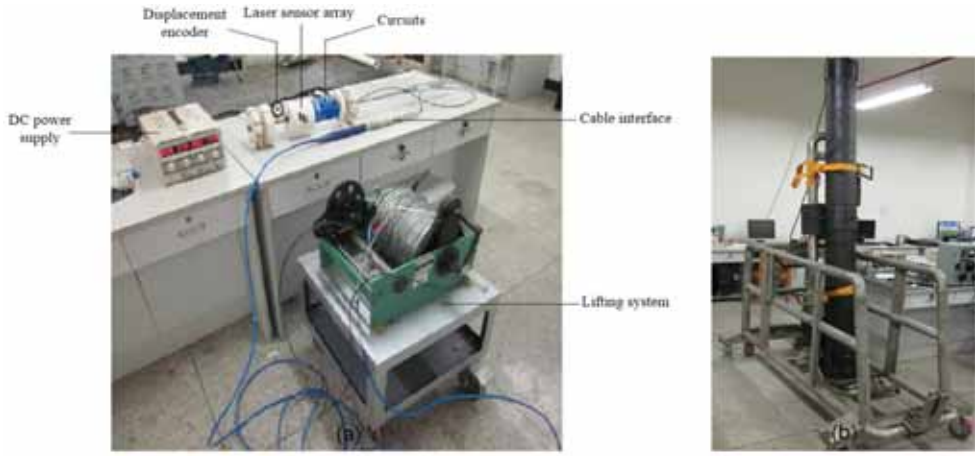

FIGURE 5
Detection device and experimental platform.
Notes: (a) Detection device, (b) Experimental platform.

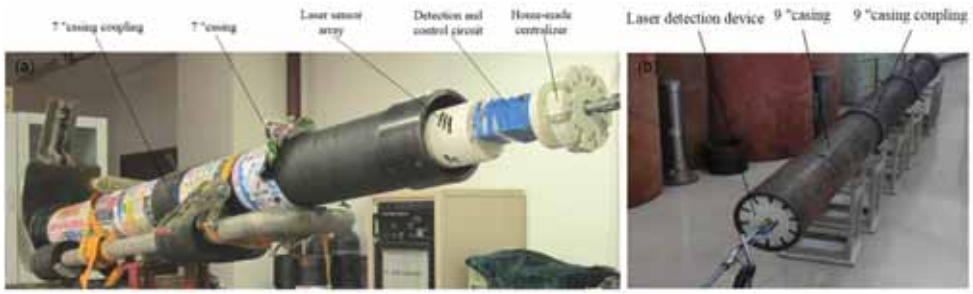

FIGURE 6
Casing coupling detection experiment.
Notes: (a) 7-inch casing coupling experiment, (b) 9-inch casing coupling experiment.

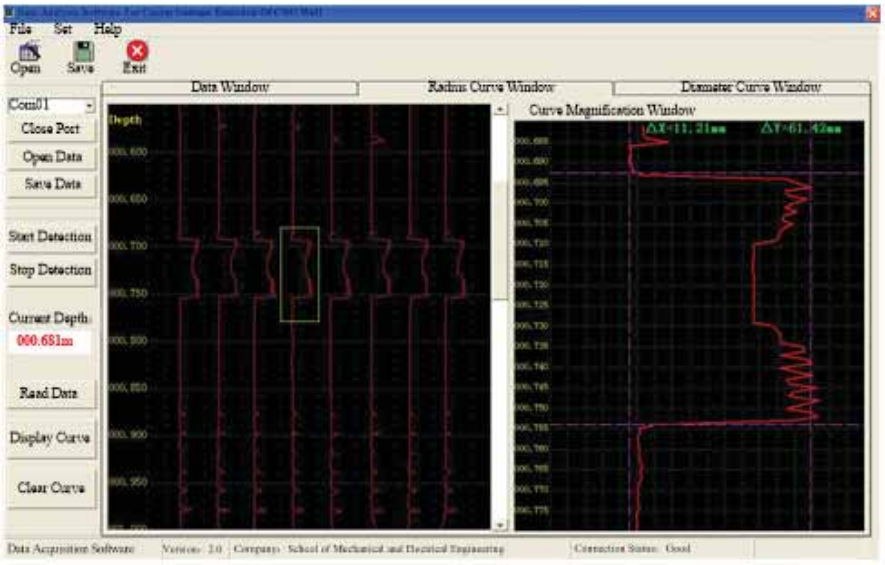

FIGURE 7
Indoor 7-inch casing coupling detection curve.

TABLE 1
7-inch sleeve coupling parameters measurement

Coupling Information	Measurements	Actual value
The length of the coupling（mm）	61.42	63.7
The depth of the coupling（mm）	11.21	11.5
Number of teeth in the upper part of the buckle	3~4	4
Number of teeth in the Lower part of the buckle	6	6

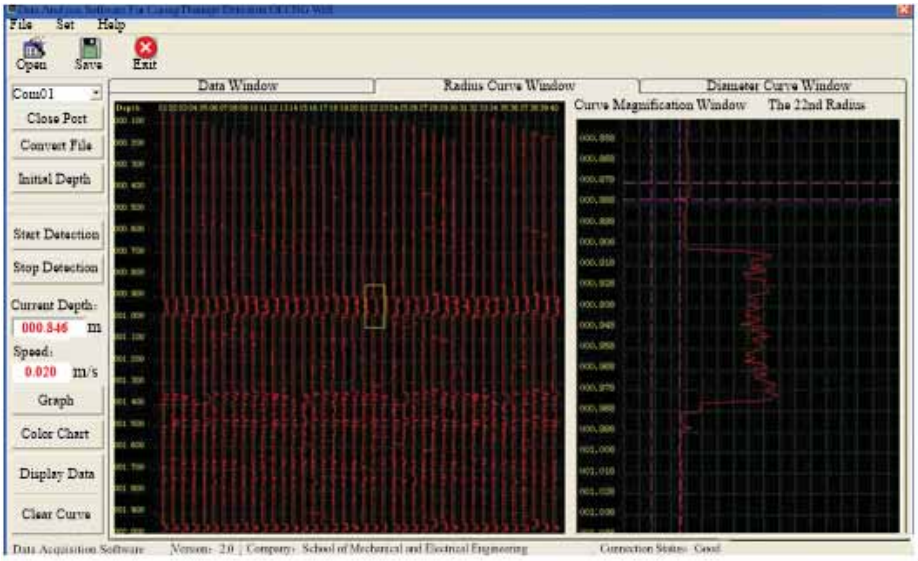

FIGURE 8
Indoor 9-inch casing coupling test curve.

The experimental data reflects the detection results of this part of the ferrule that is not buckled in the middle (that is, the ends of the coupling are buckled into the sleeve, and the middle part is not buckled). In the Figure 8, the left window is the detection signal curve of the multi-channel laser sensor and the right window is a partial enlarged view of the coupling selected in a certain detection signal curve. The current depth at the left edge shows the depth corresponding to the local detection position which is measured by a wheel encoder. It can be seen from the left window in the Figure

9 that the shape of the detection signal curve is the same at the coupling while the right window shows the approximate shape and size of the selected coupling. The upper and lower saw tooth shape curve parts in the Figure 9 show a wire buckle that is not buckled into the sleeve. The parameters of this coupling are shown in Table 1.

In the Table 1, multiple measurements are taken with a micrometer and the average value from these measurements can be regarded as the actual value. Because there is a certain degree of difficulty in measuring the data in the casing, it is easy to cause errors and affect the accuracy of the measurement. Therefore, it is more appropriate to take the first place of the reading data after the decimal point. The length of the coupling refers to the length of the coupling corresponding to the gap at the joint between the two sections of casing. The depth of the coupling is the sum of the wall thickness of the casing and the depth of the coupling thread. Compare the measured value with the actual value, and the measurement errors of the length and depth of the coupling at this section are 3.6% and 2.5%, respectively. The in-lab coupling test curve for a 9-inch sleeve is shown in Figure 8.

It can be known from Figure 8 that the enlarged curve of the part of the 9-inch casing coupling that does not enter the casing in the laboratory has good consistency with the 7-inch casing coupling, and there is no flat part in the middle of the 9-inch casing coupling.

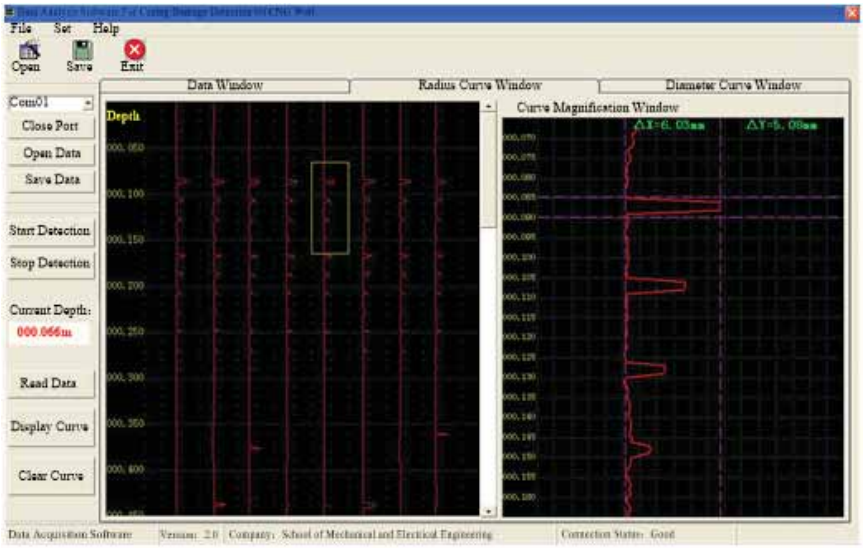

FIGURE 9
Results of the first damage detection.

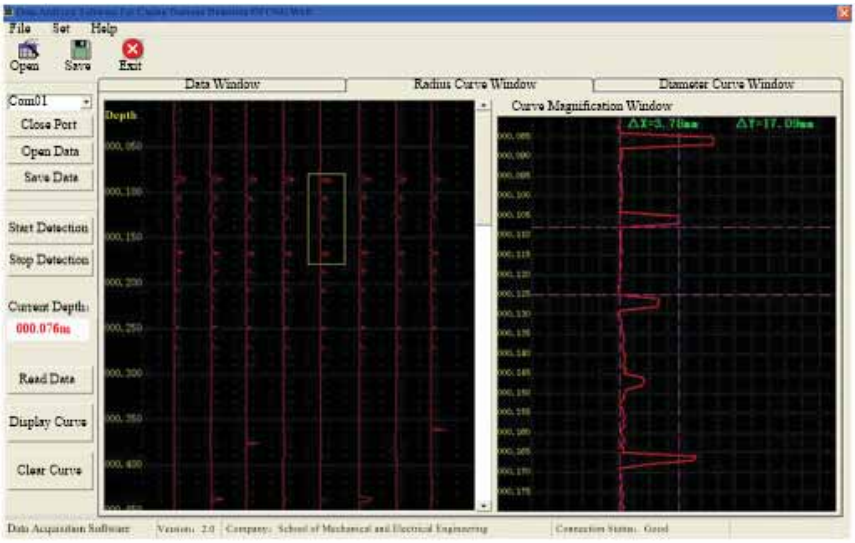

FIGURE 10
Results of the second damage detection.

Laboratory Test of Full Circumferential Damage. The full circumferential damage test of the casing is still performed on the indoor simulation experiment platform for 7-inch casing and 9-inch casing, respectively. The upper computer receives the detection signal, and after processing the 8 channels of data, it is stored in the background database and the corresponding detection signal curve is drawn. Due to the limited space, only a set of test results of simulated damage in a 7-inch cannula is used as an example for analysis. The width of the first damage (ie, the length of the defect extending in the axial direction of the casing) and the depth inspection results are shown in Figure 9. It can be seen from Figure 9 that the width of the first damage is 6.03 mm and the depth is 5.08 mm.

The depth detection result of the second damage is shown in Figure 10. It can be seen from Figure 10 that the depth detection value of the second damage is 3.78 mm.

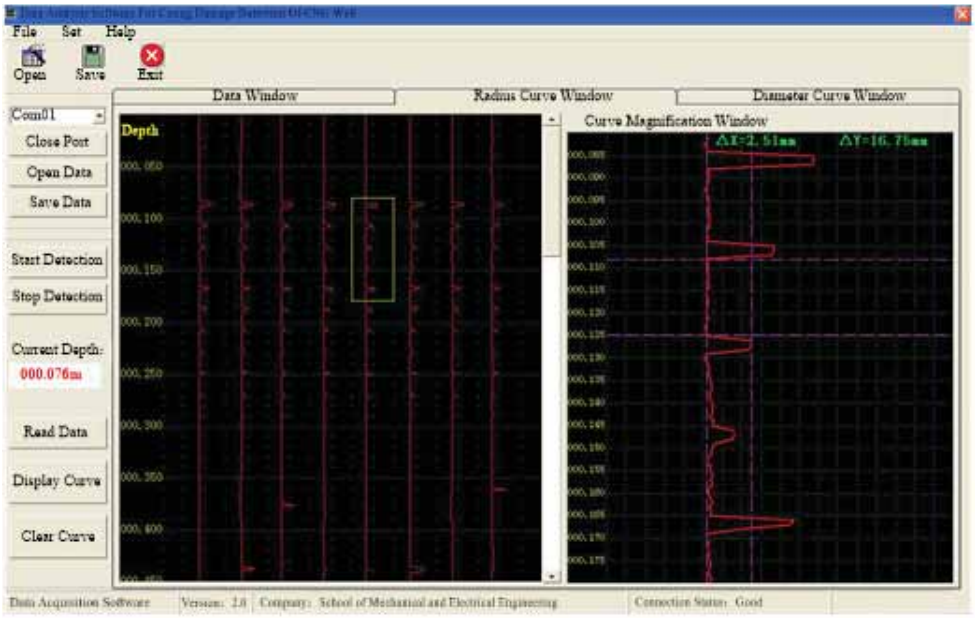

FIGURE 11
Results of the third damage detection.

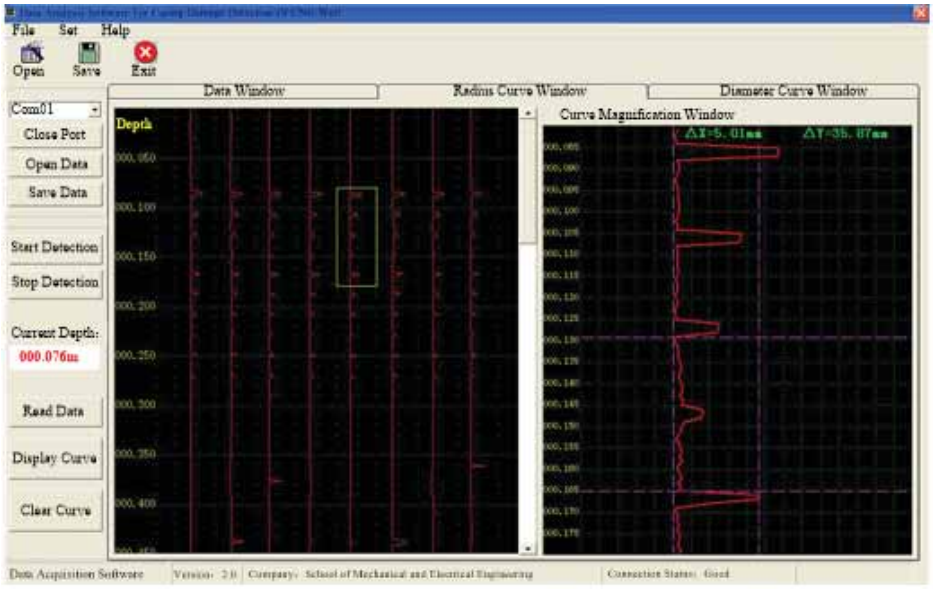

FIGURE 12
Results of the fourth damage detection.

The depth detection result of the third damage is shown in Figure 11. It can be seen from Figure 11 that the depth detection value of the second damage is 2.51 mm.

The depth detection result of the fourth damage is shown in Figure 12. It can be seen from Figure 12 that the depth detection value of the second damage is 5.01 mm.

According to the drawn detection curve, in addition to the specific size of the damage, the distance between two adjacent damage can also be measured. The detection results of the distance between the first and second damage are shown in Figure 13. The distance between the first two damage is 15.91 mm. Similarly, the distance between the second and third damage can be measured to be 17.09mm and the distance between the third and fourth damage is 35.87mm.

Since the accurate actual value can be obtained from the mechanical drawing of the simulated damaged casing, the test result is compared with the actual value list, and the measurement error is calculated, as shown in Table 2. It can be known from Table 2 that the measured errors are small with values below 5%, showing that the high detection accuracy and good detection effect.

Field Test Experiment. The field experiment was completed in a teaching experimental well of Southwest Petroleum University, and the experimental casing was a 7-inch pipeline. Before the experiment, the 7-inch casing of this experimental well was visually inspected. There was rust inside the pipeline and no obvious defects were found. The casing was connected through a coupling. The signal line of the detection device communicates with the upper computer through the aviation head via the lifting system, which can perform real-time online detection and offline data display and analysis. The field downhole experiment is shown in Figure 14.

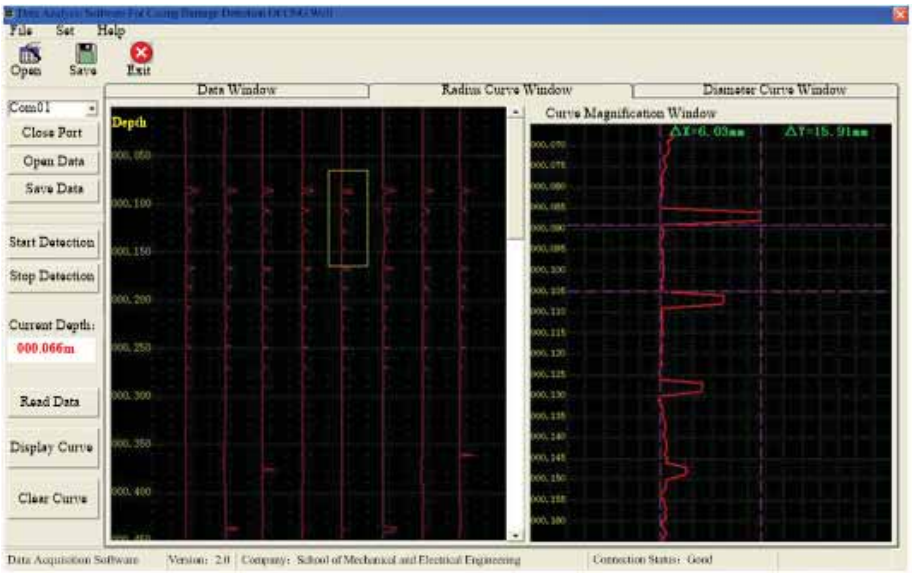

FIGURE 13
Distance detection results between the first and second damage.

TABLE 2
Analysis table

/	Measurements (mm)	Actual value Measured (mm)	Error (%)
First damage depth × width	6.03×5.08	6.2×5.0	2.7×1.6
Second damage depth	3.78	3.7	2.2
Third damage depth	2.51	2.4	4.6
Fourth damage depth	5.01	5.1	1.8
Distance between the first and second damage	15.91	16.0	0.6
Distance between the second and third damage	17.09	17.2	0.6
Distance between the third and fourth damage	35.87	35.7	0.5

FIGURE 14
Field test experiment chart.

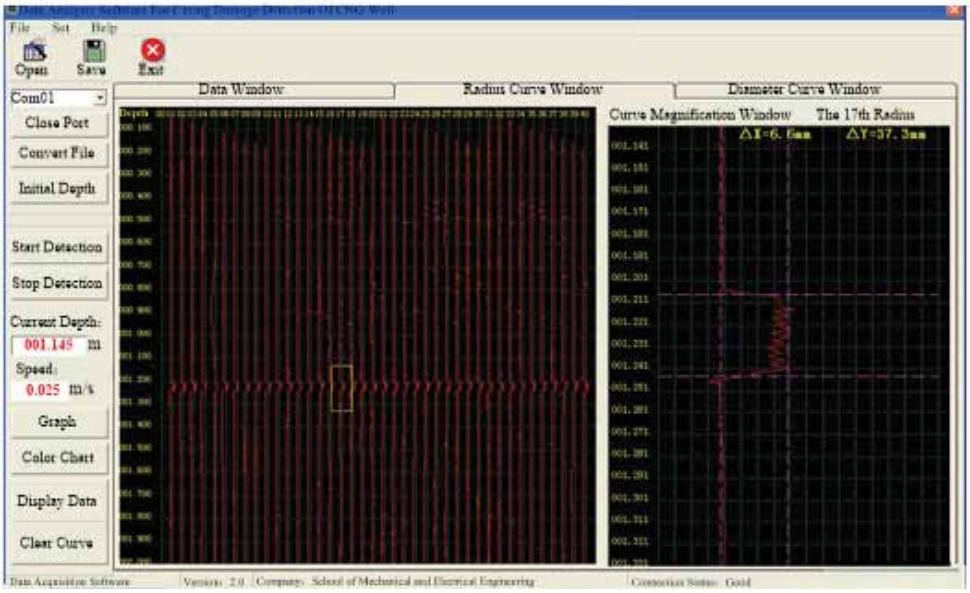

FIGURE 15
Curve of laser detection results of field casing.

The curve of the detection results of the 40 lasers of the detection device is shown in Figure 15.

According to the analysis of the test data, it can be known that the laser detection device runs normally in the actual detection, and the casing damage (coupling position) is detected accurately, which is consistent with the actual situation of the 7-inch casing in the experimental well with high accuracy.

CONCLUSIONS

(1) Based on the principle of laser triangulation ranging in this paper, an experimental laser detection device for the CNG gas well casing damage was developed.

(2) Based on the indoor simulation experiment platform, the coupling detection of the indoor 7-inch casing and the 9-inch casing and the laboratory test of the full circumferential damage of the casing were respectively performed. After analysis of the obtained test results, it can be known that the detection device detects high accuracy and reliable results with the error value below 5%.

(3) On the basis of the indoor simulation experiment, a field experiment was carried out using a testing device developed on the basis of a 7-inch casing of a teaching experimental well. The experimental results show that the detection device operates normally and can accurately detect the damage of the inner wall of the field casing.

ACKNOWLEDGEMENTS

The authors would like to show their sincere thanks to the relevant techniques who have helped this research and the authors of the references.

REFERENCES

[1] Zhu, Q., Huang, H., He, T. (2006) Discussion on the Safety Technology of Several Problems about CNG Station. 25(1), 14-16+22.

[2] Zhang, Z. (2019) Research on magnetic flux leakage detection technology of gas storage well. Daqing: Northeast Petroleum University (Dissertation).

[3] Lin, Y. (2015) Development of detection system for underground gas storage well. Nanchang: Nanchang Hangkong University (Dissertation).

[4] Feng, F. (2013) Technical and Economic Comparison of Storage Methods of CNG Gas Station. Shanghai Gas. 6, 16-17+22.

[5] Zhu, L. (2011) Comparison and analysis of two ways of gas storage in CNG gas station. Inner Mongulia Petrochemical Industry. 20, 56-58.

[6] Zhao, L. (2014) Safety analysis of underground gas storage well in CNG station. Xi'an: Xi'an Shiyou University (Dissertation).

[7] Xie, S., Xia, Z., Shi, H., Cheng, J., Wang, R., Luo, Q. (2019) The Development of Defect Calibration Sample Tube on Compressed Natural Gas Underground Gas Storage Well. Nondestructive Testing. 41(1), 53-57.

[8] Jian, H. (2017) Research on ultrasonic testing technology of compressed natural gas storage well wall thickness. Nanjing: Nanjing University of Aeronautics and Astronautics (Dissertation).

[9] Duan, Z., Shi, K., Li, B., Liu, H., Chen, Y., Duan, H. (2016) Analysis of Cases in Periodical Inspection of In-service Gas Storage Wells. China Special Equipment Safety. 32(7), 25-29.

[10] Lie, S., Zhang, Y., Wang, L. (2015) Damage detection in compressed natural gas (CNG) cylinders based on auxiliary mass induced frequency shift. Experimental Mechanics. 55(3), 487-498.

[11] Wang, R., Shi, H., Xia, Z., Cheng, J., Xie, S., Luo, L. (2018) Study on uniform corrosion of casing in CNG gas storage well by ultrasonic phased array test. Safety Technology of Special Equipment. 5, 47-49.

[12] Cegla, F., Huthwaite, P., Lowe, M. (2013) Inspection vs structural health monitoring: manual ultrasonic thickness measurements compared to monitoring with permanently installed sensors. The Journal of the Acoustical Society of America. 134(5), 4132.

[13] Shih, J., Kobayashi, M., Jen, C. (2010) Flexible metallic ultrasonic transducers for structural health monitoring of pipes at high temperatures. IEEE Transactions on Ultrasonics Ferroelectrics and Frequency Control. 57(9), 2103-2110.

[14] Particular, I., Field, I. (2014) In-line ultrasonic monitoring for sediments stuck on inner wall of a polyvinyl chloride pipe. The Scientific World Journal. 2, 731621.

[15] Du, J., Duan, B., Zhang, W., Chou, Z., Zhao, Y., Lu, S. (2012) Research on CNG Gas Storage Well Casing Damage Detection Based on Remote Field Eddy Current Technology. Nondestructive Testing. 34(2), 41-44.

[16] Zhao, Y., Huang, C., Song, Z., Yu, C., Liang, S., Luo, X., Qing, A. (2019) A digital metamaterial of arbitrary base based on voltage tunable liquid crystal. IEEE Access. 7, 79671-79676.

[17] Zhao, Y., Qing, A., Meng, Y., Song, Z., Lin, C. (2018) Dual-band circular polarizer based on simultaneous anisotropy and chirality in planar metamaterial. Scientific Reports. 8, 1729.

[18] Goldstein, A., Kalganov, S. (2000) Eddy-current nondestructive testing of long cylindrical components using spatial magnetic field components of different frequencies. Russian Journal of Nondestructive Testing. 36(5), 360-365.

[19] Min, K., Geun, H., Ho, C., Soo, P. (2018) Determination scheme for accurate defect depth in underground pipeline inspection by using magnetic flux leakage sensors. IEEE Transactions on Magnetics. 1-5.

[20] Feng, J., Li, F., Lu, S., Liu, J. (2017) Fast reconstruction of defect profiles from magnetic flux leakage measurements using a RBFNN based error adjustment methodology. IET Science Measurement and Technology. 11(3), 262-269.

[21] Liu, D. (2009) Experimental study on magnetic flux leakage detection of underground gas storage well. Wuhan: Huazhong University of Science and Technology (Dissertation).

[22] Fuentes, R., Dwyer-Joyce, R., Marshall, M., Wheals, J., Cross, E. (2020) Detection of subsurface damage in wind turbine bearings using acoustic emissions and probabilistic modelling. Renewable Energy. 147, 776-797.

[23] Luo, L., Xia, Z., Shi, H., Cheng, J. (2019) Design of ultrasonic testing system for underground gas storage well. Nondestructive Testing. 41(1), 69-72.

[24] Cravetchi, I., Taschuk, M., Rieger, G., Tsui, Y., Fedosejevs, R. (2003) Spectrochemical microanalysis of aluminum alloys by laser-induced breakdown spectroscopy: identification of precipitates. Applied Optics. 42(30), 6138.

[25] Paone, N., Scalise, L., Stavrakakis, G., Pouliezos, A. (1999) Fault detection for quality control of household appliances by non-invasive laser doppler technique and likelihood classifier. Measurement. 25(4), 237-247.

[26] Feng, X., Zhang, X., Sun, C., Motamedi, M., Ansari, F. (2014) Stationary wavelet transform method for distributed detection of damage by fiber-optic sensors. Journal of Engineering Mechanics. 140(4), 04013004.

Received: **22.12.2019**
Accepted: **27.01.2020**

CORRESPONDING AUTHOR

Jian Du
School of Mechanical Engineering,
Southwest Petroleum University,
Chengdu 610500, China

e-mail: chuanglei2019@126.com

© by PSP Volume 29 – No. 04A/2020 pages 3166-3172 Fresenius Environmental Bulletin

RESEARCH ON THE PREDICTION OF DIRECTIONAL WELL SAFE DENSITY WINDOW AND THE INFLUENCES OF FORMATION PARAMETERS

Peng Huang, Zhiqiang Huang*

School of Petroleum Engineering, Yangtze University, Wuhan, Hubei 430100, China

ABSTRACT

The prediction of the safety density window of the directional well is the basis for correctly designing a safe drilling fluid density, ensuring the stability of the well wall, and reducing downhole accidents caused by leaks and collapses. The safety density window of the directional well is mainly affected by formation pore pressure, rupture pressure and collapse pressure. In order to accurately predict the safety density window of the directional well, based on the porous elastic stress model, a mathematical model for the calculation the directional well formation pore pressure, formation rupture pressure, and formation collapse pressure using the log data was established. The safety density window of the directional well was developed using Visual Basic. The prediction software uses the field data of a well in Shengli Oilfield as an example to draw the three major pressure profile curves. The application results meet the site requirements. Through the single factor analysis, the change law of the safety density window with the parameters is studied, which provides a reference for the site construction.

KEYWORDS:
Directional well, logging parameters, safety density window, formation parameters, influence law

INTRODUCTION

During the drilling of directional wells, with the development of oil and gas towards deep formations and deep water, it is more and more common to drill into narrow safety density windows. There are two main cases of narrow safety windows [1-3]: The loss is greater than or equal to the difference between the rupture pressure and the maximum value of the pore pressure and collapse pressure and the second is that the formation rupture pressure is lower than the formation pore pressure or collapse pressure. When directional wells encounter a narrow safety density window, drilling operation often leads to leaks and even some other complex issues [4-6]. The accurate prediction of the density window has important guiding significance for the reasonable deployment of drilling fluids on site and ensuring the smooth drilling.

The current methods for predicting pore pressure include effective depth method, Eaton method [7-9], effective stress method, etc. The calculation models of rupture pressure mainly include Eaton method, Huang Rongzun method, Stephen method Holbrook method, etc. The prediction model for the collapse pressure is mainly based on the Mohr-Coulomb criterion [10-12]. This article is based on the theory of stratigraphic compaction. The prediction of formation pore pressure is calculated by Eaton method. Starting from the stress analysis of directional well wall surrounding rock, a calculation model of directional well wall collapse pressure and rupture pressure in cylindrical coordinates is established. By using the logging data, a mathematical model for predicting the safety density window of the directional well using logging data is obtained and the software for predicting the safety density window of directional wells was developed using Visual Basic programming software language. Based on field calculations, three major formation pressure profiles and equivalent density profiles were drawn, and the prediction results met the site requirements. The influence of the change of a single formation parameter on the safety density window of directional wells is statistically analyzed, which provides a reference for the prediction analysis and field application of the safety density window of directional wells.

METHODS AND TYPICAL MODELS

During the drilling of directional wells, reasonable drilling fluid density should ensure that no downhole complex accidents such as blowouts, overflows, collapses, shrinkages, and leaks occur, and the drilling fluid density should be between the lower and upper limits of the safety density window. When calculating the drilling fluid safety density window, the safety density window of the

directional well is mainly controlled by formation pore pressure, rupture pressure and collapse pressure. The lower limit is usually specified as the maximum value of the collapse pressure equivalent density and the pore pressure equivalent density and the upper limit is based on the maximum rupture pressure equivalent density calculated from failure criteria. The calculation of the three major pressure prediction models involves the calculation of formation rock mechanical parameters under in-situ stress.

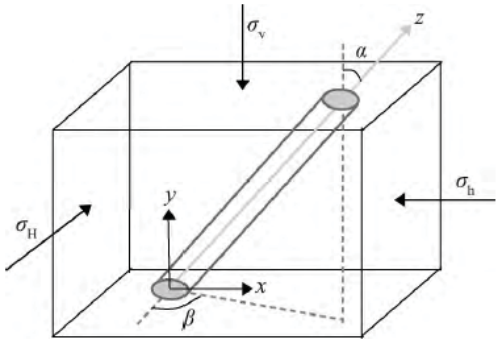

FIGURE 1
The diagram of borehole position and in-situ stress of directional well.

Density Window Prediction Model. The safe density window prediction model is based on the three major pressure prediction models. Currently, the well logging calculation methods commonly used in formation pore pressure include equivalent depth method, Eaton method and effective stress method. The equivalent depth method is suitable for the area which is just surveyed while the effective stress method is cumbersome to calculate. Therefore, the Eaton method is used to calculate the formation pore pressure in this paper. The Eaton method comprehensively considers the role of other high-pressure formation mechanisms in addition to compaction. The coefficients in the formula include the pressure formation mechanism and the overpressure preservation. The basic formula of the pressure estimation formula for the hydrodynamics of sand and mudstone is as follows:

$$\Delta t_n = \Delta t_0 e^{aH} \quad (1)$$

$$P_p = P_0 - (P_0 - P_n) \times \left(\Delta t_n / \Delta t \right)^e \quad (2)$$

Where Δt_n is the time difference of sound waves on the normal trend line, μs/m; Δt_0 is the intercept of the normal compaction trend line, μs/m; a is the compaction coefficient which is the slope of the normal compaction trend line; P_n is hydrostatic pressure, MPa; Δt is the actual acoustic time difference of the formation, μs/m ; e is the Eaton index, and the Eaton index e is obtained from the measured formation pore pressure data.

During the drilling of directional wells, the original stress balance of the formation will be broken, and the formation stress near the wellbore will change within a certain range, affecting the stability of the well wall. Figure 1 is the relationship between directional wellbore position and ground stress.

For directional well formation fracture pressure prediction, the prediction model is established in a cylindrical coordinate system, ψ is the well inclination angle, β is the azimuth angle, and the stress distribution on the well wall in the cylindrical coordinate system is:

$$\begin{cases} \sigma_{rr} = P_w \\ \sigma_{\theta\theta} = (\sigma_x + \sigma_y) - 2(\sigma_x - \sigma_y) \cdot \cos 2\theta - 4 \cdot \tau_{xy} \sin 2\theta - P_w \\ \sigma_{zz} = \sigma_z - 2\nu(\sigma_x - \sigma_y) \cdot \cos 2\theta - 4\nu\tau_{xy} \cdot \sin 2\theta \\ \tau_{\theta z} = 2 \cdot (\tau_{yz} \cos\theta - \tau_{xz} \sin\theta) \\ \tau_{r\theta} = \tau_{rz} = 0 \end{cases} \quad (3)$$

In the above formula, σ_{rr}, the radial normal stress is one of the three-way principal stress. The other two principal stresses can be given by the plane principal stress solution formula:

$$\begin{cases} \sigma_1 = \sigma_r = P_w \\ \sigma_{2,3} = \frac{1}{2}(\sigma_{\theta\theta} + \sigma_{zz}) \pm \frac{1}{2}\left[(\sigma_{\theta\theta} - \sigma_{zz})^2 + 4\tau_{\theta z}^2 \right]^{1/2} \end{cases} \quad (4)$$

According to the maximum tensile stress failure criterion:

$$\sigma_3 = -\sigma_t \quad (5)$$

When calculating formation rupture pressure, it is necessary to ensure that the wall of the well at different well angles is not fractured, and the minimum wellbore pressure at this location is obtained, that is, the formation rupture pressure at this plane. When ψ and β are both zero, the formula for the formation rupture pressure of vertical wells is obtained, which is the Hamison natural fracture pressure prediction formula.

With the decrease of the directional wellbore pressure, the radial stress gradually changes from compressive to tensile. When the rock fracture occurs, the formation collapses, and the drilling fluid column pressure in the well is the formation collapse pressure. The effective stress principle is:

$$\overline{\sigma_{ij}} = \sigma_{ij} - \alpha P_p \delta_{ij} \quad (6)$$

The key to establishing the calculation model of formation rupture pressure and collapse pressure is to choose the appropriate strength yield criterion. At present, the prediction models of collapse pressure at home and abroad are mainly based on

the Mohr-Coulomb criterion. According to the Mohr-Coulomb criterion, the ultimate stress state form of rock equilibrium is obtained by triangulation [13-16]:

$$\begin{cases} \overline{\sigma_{\max}} = \overline{\sigma_{\min}} \tan^{-2}\left(45° - \frac{\phi}{2}\right) \\ + 2c \tan\left(45° - \frac{\phi}{2}\right) \\ \overline{\sigma_{\max}} = \max\left(\overline{\sigma_1}, \overline{\sigma_2}, \overline{\sigma_3}\right) \\ \overline{\sigma_{\min}} = \min\left(\overline{\sigma_1}, \overline{\sigma_2}, \overline{\sigma_3}\right) \end{cases} \quad (7)$$

When the shear stress increases beyond this state, the rock is destroyed. The wellbore pressure obtained at this time is the formation collapse pressure. When calculating the formation collapse pressure, it must be ensured that the rock at the wall of the well can be maintained at different angles θ. At the same time, when both ψ and β are zero, the formula for the formation collapse pressure of the vertical well is obtained.

Stratum Parameter Calculation Method. The formation parameters in the above model can be obtained directly or indirectly through well logging data, and the natural gamma value, P-wave time difference, and formation density can be directly obtained from the well logging data. These parameters can be used to calculate formation clay content, porosity, shear wave time difference, Poisson's ratio, and elastic modulus [17-20]:

$$SH = \frac{GR - GR_{\min}}{GR_{\max} - GR_{\min}} \quad (8)$$

$$V_{cl} = \frac{2^{GCUR \cdot SH} - 1}{2^{GCUR} - 1} \quad (9)$$

$$\phi = \frac{1}{x} \bullet \left(1 - \frac{T_m}{T}\right) \quad (10)$$

In the formula, *SH* is the relative value of natural gamma; V_{cl} is the shale content, decimal; GCUR is the empirical coefficient related to the age of the formation, the new formation is 3.7 and the old formation is 2; φ is the porosity; T is the acoustic time difference of the rock formation; T_m is the acoustic time difference of the skeleton; x is a constant value of 1.6 for sandstone, 1.76 for carbonate, and 2.0 for dolomite.

The dynamic Poisson's ratio and dynamic elastic modulus of rocks can be calculated from the sonic time difference log data and density log data. The calculation formula is:

$$\nu_d = \frac{\Delta t_s^2 - 2\Delta t_p^2}{2\left(\Delta t_s^2 - \Delta t_p^2\right)} \quad (11)$$

$$E_d = \frac{\rho\left(3\Delta t_s^{\ 2} - 4\Delta t_p^{\ 2}\right)}{\Delta t_s^{\ 2}\left(\Delta t_s^{\ 2} - \Delta t_p^{\ 2}\right)} \times 10^6 \quad (12)$$

Where ρ is the bulk density of the formation rock, g/cm^3; V_p is the P-wave wave velocity, km/s; ν_d is the dynamic Poisson's ratio, dimensionless; Δt_p is the P-wave time difference, $\mu s/m$; Δt_s is the S-wave time difference, $\mu s/m$; E_d is the dynamic elastic modulus, GPa.

Because the formation pressure prediction is derived from mechanics, the elastic parameters should be static parameters while the formation elastic parameters calculated from sonic logging data are dynamic parameters. Thus, the dynamic and static parameter conversions must be performed [21-22]:

$$E_s = 0.6435E_d + 4.396 \quad (13)$$

$$\nu_s = 0.1268 + 0.25\nu_d \quad (14)$$

E_s is the static elastic modulus, GPa; ν_s is the static Poisson's ratio, dimensionless.

Rock strength mainly includes uniaxial compressive strength, tensile strength, rock cohesion, maximum and minimum horizontal stresses. These parameters can be calculated from log data. After comprehensively considered after investigation, rock compressive strength, tensile strength, rock viscosity and cohesion are calculated from the method proposed, while Huang's model is used for the calculation of the maximum and minimum horizontal principal stresses [23-24].

RESULTS AND DISCUSSION

Example Application. In order to input logging data more conveniently and output various calculation results intuitively, the prediction application software for safety density window using above-mentioned method was developed. The software uses Visual Basic language code when compiling which is easy to understand and can run in Windows XP / Win7 / Win8 / Win10 and other environments. The program uses an interactive interface and is easy to operate, ensuring that the software has a wide applicability. This software can use well logging data to calculate formation rock mechanical parameters, in-situ stress, and formation three-pressure profile, and can predict safety density window of the drilling fluid during directional well drilling, which can effectively guide field construction. With the help of the developed application software, the density window of a well in the Shengli Oilfield is forecasted. The well is a fractured shale reservoir. Table 1 is the log

data of this well section, which mainly includes parameters such as depth and P-wave time difference. Table 2 shows the drilling construction parameters, the well inclination angle is 35° and the azimuth angle is 14°. Logging data are imported to draw three pressure profiles and equivalent density profiles, as shown in Figure 2. The predicted safety density window is 1.75-1.88 g/cm^3. Compared with the actual designed drilling fluid density, the upper limit is lowered while the lower limit is almost unchanged. The density window is narrowed, and the prediction results can provide guidance for on-site construction. It is of great significance for the prediction of the safety density window of directional wells and safe drilling.

TABLE 1
The logging data

DEPTH	GR	CAL	SP	AC	CN
3200.000	67.100	21.891	17.662	214.616	0.142
3200.125	69.801	21.956	17.792	218.355	0.167
……	……	……	……	……	……
3325.750	56.820	10.008	39.000	247.948	0.251
3325.875	56.820	10.008	39.000	247.948	0.241

TABLE 2
The drilling parameters

Depth/m	Inclination angle /°	Azimuth angle /°	Drilling fluid density g/cm^3
3305.76	35	14	1.77-1.95
3330	35	14	1.77-1.95

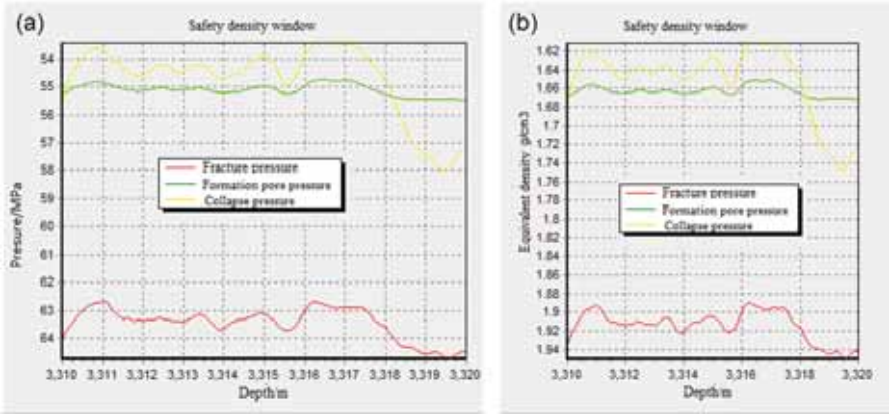

FIGURE 2
The profile curves of the pressures and equivalent density.
Notes: (a) The profile curves of the pressures, (b) The profile curves of the equivalent density.

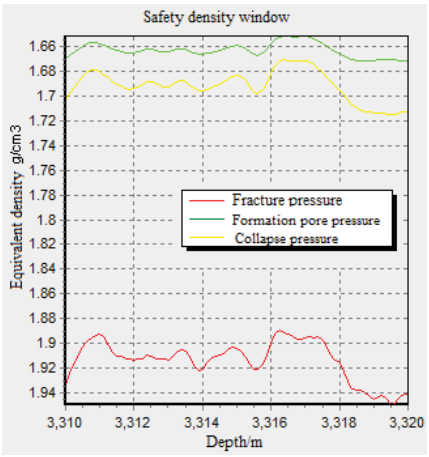

FIGURE 3
The profile curves of equivalent density.

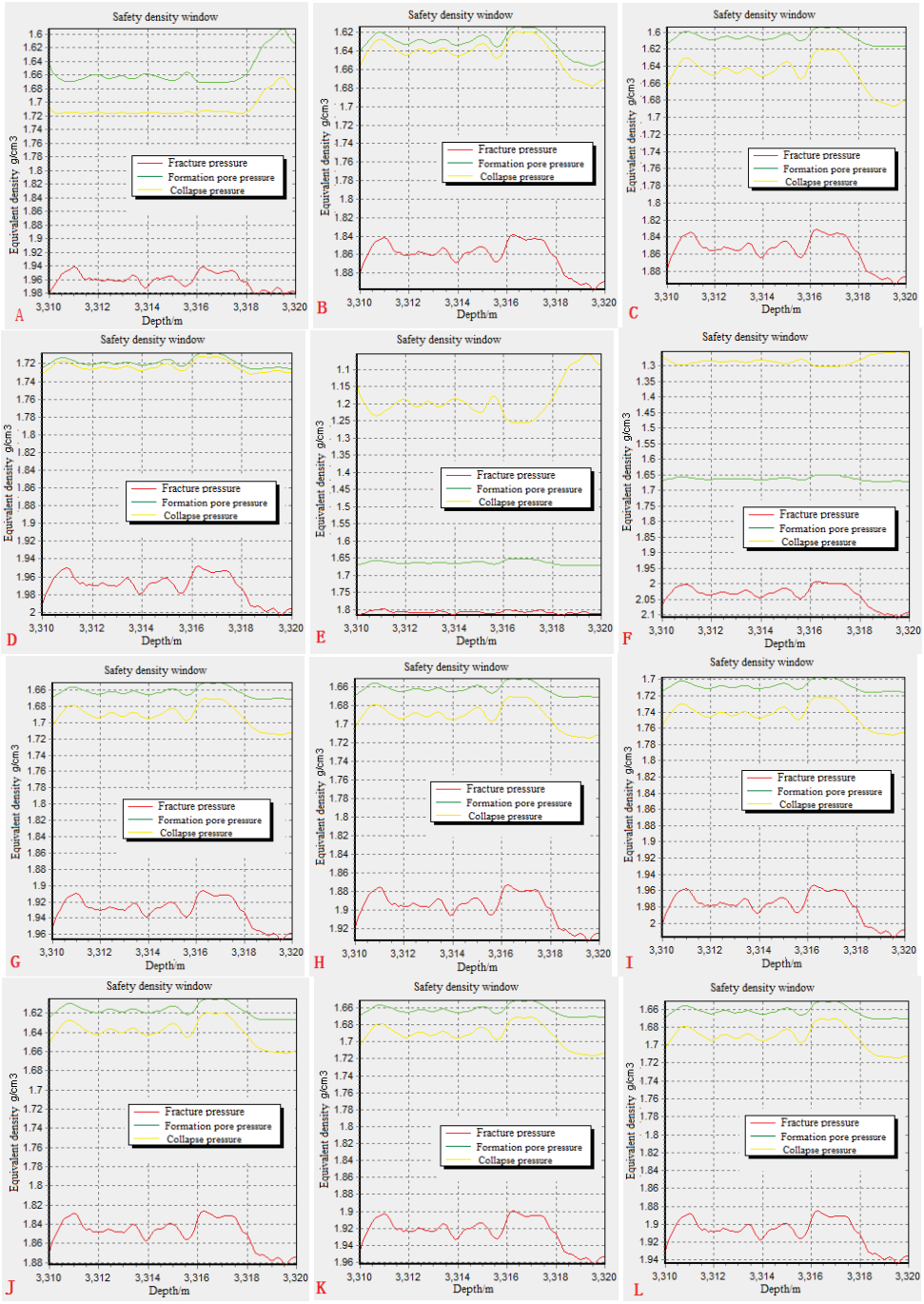

FIGURE 4

The change rule of the density window with the formation parameters.

Notes: (A) Compared with Figure 2, the drawn safety density window if the longitudinal wave time difference is reduced by 50 μs/m; (B) Compared with Figure 2, the drawn safety density window if the longitudinal wave time difference is increased by 50 μs/m; (C) Compared with Figure 2, the drawn safety density window if the formation density is reduced by 0.1 g/cm^3; (D) Compared with Figure 2, the drawn safety density window if the formation density is increased by 0.1 g/cm^3; (E) Compared with Figure 2, the drawn safety density window if the Poisson ratio is decreased by 0.05; (F) Compared with Figure 2, the drawn safety density window if the Poisson ratio is increased by 0.05; (G) Compared with Figure 2, the drawn safe density window if the elastic modulus is reduced by 1 GPa; (H) Compared with Figure 2, the drawn safety density window if the elastic modulus is increased by 1 GPa; (I) Compared with Figure 2, the drawn safety density window if the porosity is decreased by 0.05; (J) Compared with Figure 2, the drawn safety density window if the porosity is increased by 0.05; (K) Compared with Figure 2, the drawn safety density window if the clay content is reduced by 0.1; (L) Compared with Figure 2, the safety density window if the mud content is increased by 0.1.

TABLE 3
Analysis on various factors

Formation parameters	Safety density window g/cm³	Formation parameters	Safety density window g/cm³
Original data	1.75-1.88		
Longitudinal wave time difference -10μs/m	1.80-1.90	Elastic modulus +1GPa	1.75-1.86
Longitudinal wave time difference +10μs/m	1.72-1.87	Porosity -0.05	1.80-1.95
Formation density -0.05g/cm³	1.66-1.86	Porosity +0.05	1.70-1.82
Formation density +0.05g/cm³	1.86-1.92	Clay content -0.2	1.75-1.91
Elastic modulus -1GPa	1.75-1.90	Clay content +0.2	1.75-1.86

Analysis of Density Window Changes. Take this well section as an example to analyze the change law of the safety density window with a single formation parameter. The main study is the P-wave time difference, formation density, elastic modulus, porosity, and clay content. The single factor analysis method is used to study the effect of the changes of a single formation parameter on the width of the security density window. The density window prediction curve of the original contrast is shown in Figure 3 and the analysis results are shown in Table 3. Figure 4 shows the safety density window after changing a specific formation parameter.

The range of the safety density window calculated after statistically changing a single factor is shown in Table 3. The analysis shows that the influence of the parameters on the width of the safety density window are different. As the time difference of the acoustic wave increases, the safety density window moves down. As the density increases, the safety density window moves up. As the elastic modulus of the formation increases, the safety density window becomes narrower (the lower limit remains unchanged and the upper limit decreases). As as the porosity increases, the safety density window moves down as a whole and as the clay content increases, the safety density window becomes narrower (the lower limit remains the same and the upper limit decreases).

CONCLUSIONS

(1) A mathematical model for accurately predicting the formation's three pressure profiles using well logging data is established to provide support for the prediction of the safety density window of directional wells.

(2) The reliability of the safety density window prediction model of the directional well is proved by field application example. Based on this, the safety density window prediction analysis software of the directional well is developed in Visual Basic language to provide guidance for field applications.

(3) The change law of the safety density window with the parameters is obtained through a single factor analysis: as the time difference of the acoustic wave increases, the safety density window moves down as a whole and as the formation density increases, the safety density window moves up as a whole. With the increase of the elastic modulus of the formation, the safety density window becomes narrower (the lower limit remains unchanged, and the upper limit decreases). As the porosity increases, the safety density window moves down as a whole and as the clay content increases, the safety density window becomes narrower (the lower limit remains the same and the upper limit decreases).

ACKNOWLEDGEMENTS

The authors would like to show sincere thanks to the relevant techniques who have helped this research and the authors of the references.

REFERENCES

[1] Liu, Z., Xia, H., Chen, P. (2005) Calculating Three-Formation Pressure of Carbonate Rock Using Logging Data. Drilling and Production Technology. 28(1), 18-21.

[2] Cheng, Y., Xu, T. (1999) Determination and Application of the Safe Mud Density Window. Petroleum Drilling Techniques. 27(3), 16-18.

[3] Sheng, Y., Guan, Z., Xu, Y., Wang, Q., Zhang, B. (2017) Discussion on uncertainty analysis method for wellbore stability. Fault-Block Oil and Gas Field. 24(1), 12-16.

[4] Jia, L., Huang, X., Guo, Z. (2017) Comparative analysis of intermediate principal stress strength criterion of wellbore stability. Fault-Block Oil and Gas Field. 31(5), 15-18.

[5] Yan, C., Xie, Y., Deng, J., Wei, B., Zhu, H. (2013) A method of determining the safe upper limit of drilling fluid density. Natural Gas Industry. 24(1), 5-9.

[6] Holbrook, P. (1989) A New Method for Predicting Fracture Propagation Pressure From MWD or Wireline Log Data. SPE 165487.

[7] Yang, Z., Wu, B., Wang, Y. (2012) Prediction of formation pore pressure in M Oilfield by Eaton method. Journal of Oil and Gas Technology. 4(9), 181-187.
[8] Eaton, B. (1969) Fracture gradient prediction and its application in oilfield operations. Journal of Petroleum Technology. 21(10), 1353-1360.
[9] Eaton, B. (1997) Fracture gradient prediction for the new generation. World Oil. 218(10), 93-100.
[10] Atashbari, V. (2012) Pore Pressure Prediction in Carbonate Reservoirs. Latin American and Caribbean Petroleum Engineering Conference. SPE 150835.
[11] Stephen, R. (2006) Wellbore Stability Assessment for Highly Inclined Wells Using Limited Rock-Mechanics Data, SPE 99644.
[12] Stephen, R. (1982) Prediction of fracture pressure for wildcat wells. Journal of Petroleum Technology. 34(4), 863-872.
[13] Lou, Y., Zhuang, J., Huang, R. (1989) Study on the correlation of dynamic and static elastic parameters of rock and its application in petroleum engineering. Journal of Petroleum Technology. 11(2), 69-69.
[14] Li, P., Li, P., Cao, L. (2010) Theoretical Study on Collapse Pressure Calculating Equation of Deviated Wellbore. Journal of Shanghai University of Engineering Science. 24(1), 1-4.
[15] Zhou, D., Yang, H., Li, J., Wang, X., Wang, H., Xue, Y. (2017) A test method for the in-situ stress of salt rock. Oil and Gas Storage and Transportation. 36(12), 1385-1390.
[16] Lu, Y., Chen, M., Yuan, J., Jin, Y., Teng, X. (2013) Borehole instability mechanism of a deviated well in anisotropic formations. Acta Petrolei Sinica. 34(3), 563-568.
[17] Zhang, X. (2008) Study on Optimization Design of construction parameters of high pressure gravel filling in loose sandstone. Dongying: China University of Petroleum (East China) (Dissertation).
[18] Li, M., Lian, Z., Chen, S. (2009) Rock mechanical parametric experiments and the research of formation fracture pressure prediction. 31(5), 15-18.
[19] Zhou, Y., Yang, X., Fang, S., Wang, K. (2010) An analysis of the difficulties in narrow window drilling and technical solutions. China Petroleum Machinery. 38(4), 1-7.
[20] Yang, X., Zhou, Y., Fang, S., Wang, K. (2010) Strategy Analysis of Narrow Window Drilling Technology and Practice. Oil Field Equipment. 39(8), 7-11.
[21] Ma, T., Tang, T., Chen, P., Chen, C., Sun, S., Liu, Y. (2019) Prediction of fracture pressure of wellbore for anisotropic formations. Journal of China University of Petroleum (Edition of Natural Science). 43(3), 80-89.
[22] Shi, X., Cheng, Y., Yuan, Z., Mei, W. (2012) The Prediction of Fracture Pressure for the Deviated Wells and the Analysis of Relating Parameters. Science Technology and Engineering. 12(31), 8205-8209.
[23] Lyu, Y., Chow, T., Wang, J. (2018) Numerical prediction of thermal performance of liquid-flow window in different climates with anti-freeze. Energy. 157, 412-423.
[24] Wu, S., Zhang, L., Fan, J., Zhang, X., Zhou, Y., Wang, D. (2018) Prediction analysis of downhole tubing leakage location for offshore gas production wells. Measurement. 127, 546-553.
[25] Ma, T., Zhang, Q., Chen, P., Yang, C., Zhao, J. (2017) Fracture pressure model for inclined wells in layered formations with anisotropic rock strengths. Journal of Petroleum Science and Engineering. 149, 393-408.
[26] Meng, M., Baldino, S., Miska, S., Takach, N. (2018) Wellbore stability in naturally fractured formations featuring dual-porosity/single-permeability and finite radial fluid discharge. Journal of Petroleum Science and Engineering. 174, 790-803.

Received: **24.12.2019**
Accepted: **25.01.2020**

CORRESPONDING AUTHOR

Zhiqiang Huang
School of Petroleum Engineering,
Yangtze University,
Wuhan, Hubei 430100, China

e-mail: hzq6565@126.com

© by PSP Volume 29 – No. 04A/2020 pages 3173-3183 Fresenius Environmental Bulletin

INFLUENCE OF DISPLACEMENT VELOCITY ON THE EFFECT OF THE ENHANCED OIL RECOVERY OF BINARY COMPOSITE FLOODING IN LONG CORE

Yuting Pan, Zhiquan Zhang*

School of Petroleum Engineering, Yangtze University, Hubei, Wuhan 430100, China

ABSTRACT

In recent years, basic research and field tests on the application of chemical composite flooding technology have made great progress. The ultra-low interfacial tension of the composite flooding system can improve the oil washing efficiency and the viscosity can be enlarged to expand the volume and improve the heterogeneity. However, the low interfacial tension system will exacerbate interlayer heterogeneity after breakthrough in the formation, which is mainly affected by the injection rate of the composite system. Aiming at the common polymer/surfactant binary system, a three-pipe parallel heterogeneous long core with a big permeability difference was used to investigate the influence of injection speed on the oil displacement effect of the composite system. Three injection speeds (1m/d, 2m/d and 5m/d) were used in the experiment and the water flooding speed remains the same at 2m/d. The experimental results show that the increase of the injection rate and the increase of the injection pressure of the binary composite system will help to improve the recovery factor within a certain range. However, when the injection speed is too high, the channelling of the high permeability layer will be intensified, the heterogeneity will be strengthened, and the effect of improving the recovery factor will be reduced. When the injection speed is 1m/d, the best recovery enhancement effect can be obtained, which is 18.09%. The enhanced recovery efficiency mainly affects the medium and high permeability layers.

KEYWORDS:
Binary composite flooding, long core, heterogeneity, injection speed, enhanced oil recovery

INTRODUCTION

Chemical flooding technology is widely used in China, especially in oilfields such as Daqing and Shengli and it is now China's main oil recovery technology [1]. Polymer flooding mainly uses the viscoelasticity of polymers. The purpose of enhancing oil recovery is to increase the volume and oil displacement efficiency. The range of oil recovery enhancement is generally about 10%. Because the polymer does not have a strong oil-washing ability with low interfacial tension, and the polymer solution has a poor regulation and displacement effect on the high-permeability layer, a further enhanced recovery factor replacement technology is required after polymer flooding [2-5]. Polymer/surfactant binary composite flooding technology has unique advantages. It combines the characteristics of polymers and surfactants, which can simultaneously expand the volume and improve the efficiency of oil washing.

Han et al. [6] proved that the binary composite flooding can improve the recovery factor by 14.3% on the basis of polymer flooding, which is second only to 17.2% of the ternary composite flooding. The alkali-containing ternary system can increase the recovery factor by 3% ~ 5% compared with the binary system, but the binary composite system is more environmentally friendly and can reduce the problems such as the treatment of the produced fluid [7-9]. After the polymer flooding, the heterogeneity of the reservoir further intensified. By identifying and analyzing the remaining oil, the stronger the heterogeneity of the reservoir, the greater the difference in utilization of the low-permeability layer [10-12]. The polymer/surfactant binary system can enter the hypertonic layer, aggregate and disperse oil droplets to form an oil wall through the action of ultra-low interfacial tension. While improving the washing efficiency of the dominant channel, it can increase the percolation resistance and further expand the spread volume which could improve the use of low-permeability areas [13].

Polymer/surfactant binary composite flooding is mainly affected by injection parameters [14-17], which is the focus of scholars at home and abroad. Ming et al. [18] used response surface method to establish a binary composite flooding injection and production parameter optimization method. They used slug size, polymer mass concentration and slug injection speed as the main control factors of the binary composite flooding to optimize the composite flooding injection-production parameters with a polymer concentration of 2418 mg/L, a slug size of 0.22 times the pore volume, and a slug injec-

tion rate of 0.06 PV/a. Zhang et al. [19] established a binary composite flooding injection and production optimization model with the economic net present value as an optimization objective function, taking into account the mine injection capacity and formation conditions as constraints, and optimized the injection parameters. Bao et al. [20] investigated the effects of polymer solution concentration, surfactant content, and slug size on oil displacement efficiency through laboratory experiments and obtained the optimal injection parameters for binary systems such as the polymer solution concentrations of 1400 to 1600 mg / L, surfactant content of 0.2% to 0.3% and slug sizes of 0.5 to 0.7PV.

The research of polymer/surfactant binary system injection factors mostly focuses on the system concentration and injection amount, while the research on the injection speed of the system is rarely studied. Wang et al. [21-23] used the numerical simulation method to optimize the combination of binary composite flooding and optimized the design of the main development factors affecting the development effect of composite flooding, including injection timing, injection volume, injection production rate and injection production ratio. It believes that the increase in injection speed is conducive to improving development results and economic benefits, but it is limited by the oilfield injection capacity. Xia et al. [24] established a typical numerical simulation model of polymer-viscosity reducing composite flooding based on mathematical statistics principles and reservoir numerical simulation methods. The limit injection speed of the target block was optimized to be 0.1064 PV/a which is similar to the actual injection of 0.11 PV/a at the mine site.

The above studies on the injection speed of the binary composite system to improve the recovery factor have all adopted numerical simulation methods which lack the experimental data support. In this paper, through indoor core displacement experiments, a three-pipe parallel heterogeneous long core with a big permeability difference was used to explore the effect of injection speed on the displacement of the composite system.

MATERIALS AND METHODS

Experimental Materials. The experimental water is simulated saltwater with a mineralization degree of 10000 mg/L and the experimental oil is a compound simulated oil with a viscosity of 31 mPa·s at 53 °C. The experimental polymer is a common intermediate polymer HX-2 with a molecular weight of 10 million. The surfactant is a compound of petroleum sulfonate type surfactant with an effective concentration of 50%. The polymer/surfactant binary system has a polymer concentration of 1500mg/L and a surfactant concentration of 0.4wt%. The experimental cores are artificial square long cores with gas permeability of 400mD, 1200mD, and 2500mD, respectively. The core size was 4.5 × 4.5 × 30cm and displacement experiments were performed using a square holder.

In addition, during the experiment, electronic balances, electronic stirrers, ISCO constant speed pumps, and thermostats are required. Chemicals (sodium chloride, anhydrous calcium chloride, magnesium chloride hexahydrate, etc.) are of analytical grade.

Experimental Methods. This paper mainly involves heterogeneous flooding experiments. The interlayer heterogeneity is simulated by paralleling the three cores. The production rate and recovery of the three cores under different conditions are obtained by changing the injection speed. The effect of injection speed on heterogeneous reservoir development is obtained through comparative analysis. The experiment adopts the form of combined injection and split mining. The injection speed of the water flooding is 2m/d, the injection speed of the polymer/surfactant binary system is 1m/d, 2m/d, and 5m/d, and the subsequent water flooding speed is 2m/d. The specific experimental scheme and parameters are shown in Table 1.

TABLE 1
Experimental design table

Number	Gas Permeability/mD	Modeling/cm^3	Size	Porosity%	Pore Volume /cm^3	Oil Saturation/%	Injection Velocity/mL/min
1	400			23.5	142.8	70.4	
2	1200			24.5	148.8	68.5	1m/d
3	2500			24.0	145.8	66.8	
4	400			22.7	137.9	61.1	
5	1200	607.5		23.5	142.8	68.2	2m/d
6	2500			23.5	142.8	64.6	
8	400			22.7	137.9	65.9	
8	1200			23.7	144.0	64.4	5m/d
9	2500			24.0	145.8	65.3	

The specific experimental procedures are as follows: (1) Pre-model preparation: The cores of different permeability layers are respectively evacuated and saturated with water to calculate the pore volume, porosity of each permeability layer and the total pore volume and porosity of the model; (2) Water permeability: Test the effective permeability of cores in different layers; (3) Saturated oil: Saturate oil treatment of cores in different layers, calculate the oil saturation of each permeability layer and the total oil saturation of the model; (4) Water flooding: According to the connection experiment process in Figure 1, the method of cage injection and separation is used to inject formation water at a set speed until the pressure of each layer stabilizes and reaches a high water-containing state. Record the pressure, oil production, and water production of each permeable layer during the process, and draw the single layer and the comprehensive recovery degree and water content curve; (5) Polymer/surfactant binary flooding: The speed (1m/d, 2m/d, 5m/d) is used into the binary system to displace 1PV. Record the pressure, oil production, water production of each permeable layer, and draw the single layer and the comprehensive recovery degree and water content curve; (6) Reinjection of subsequent water: At the set speed, reinject subsequent water. Record the pressure, oil production, and water production of each permeable layer, and draw the single layer and comprehensive recovery degree and water content curve.

Through comparative experiments of different binary system injection speeds, experimental parameters such as pressure, oil production, and water production of each permeable layer were obtained during the experiment. By analyzing the pressure change law, flow rate, and recovery efficiency of different permeable layers, the impact of injection speed on the effect of enhanced oil recovery in heterogeneous reservoirs was evaluated.

RESULTS AND DISCUSSION

Influence of Displacement Speed on Injection Pressure. Displacement differential pressure is the key technical parameter to improve the recovery factor. The increase of displacement pressure helps the displacement agent to enter the unaffected medium-low permeability layer and effectively use the remaining oil. An increase in injection speed will inevitably lead to an increase in displacement differential pressure. The injection pressure curve at three injection speeds is shown in Figure 2.

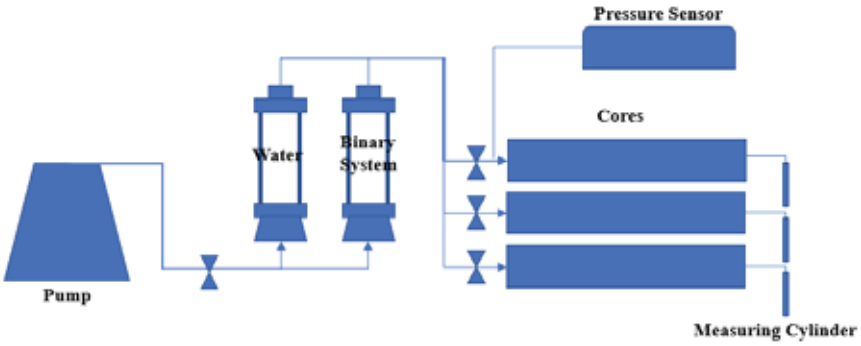

FIGURE 1
Experimental flowchart.

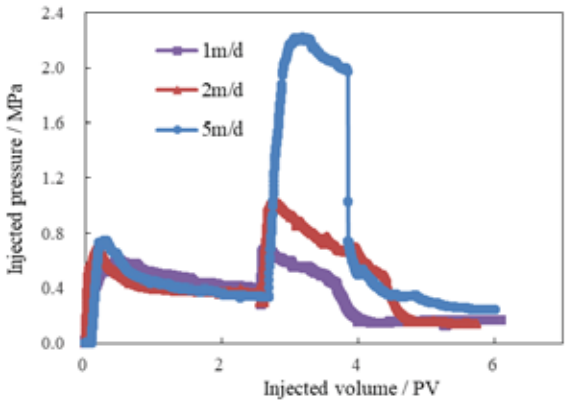

FIGURE 2
Injection pressure curves for three injection speeds.

It can be seen from Figure 2 that the conditions of the three sets of experiments in the water flooding stage are all the same. The injection pressure rises rapidly and then decreases slowly. After the injection volume reaches 1 PV, it remains basically constant and stabilizes at about 0.4 MPa. In the binary flooding stage, due to the high viscosity effect of the injection system, the seepage resistance is increased, and the injection pressure is increased compared to the water flooding. In the subsequent water flooding phase, the injection pressure rapidly decreased, and the long-term erosion of the high-velocity binary system exacerbated the heterogeneity of the reservoir. At the same time, a small amount of retained binary system reduced the oil-water interfacial tension, which led to a reduction in displacement resistance and reduced the subsequent water flooding injection pressure which is less than water flooding pressure.

In the binary flooding stage, the injection speed has a significant effect on the injection pressure [25-27]. There is also a process in which the pressure rapidly rises to the maximum and then slowly drops in the binary flooding stage. The rising phase is the result of the polymer/surfactant binary composite flooding in the high permeability layer which can build displacement resistance and coalesce the oil wall. When the oil wall is mined, the pressure begins to decrease. When the injection speed is 1m/d, the maximum injection pressure is 0.63MPa, which is 1.5 times the end pressure of water flooding. When the injection speed is 2m/d, the maximum injection pressure is 1.04MPa, which is 2.5 times the water flood end pressure. The maximum injection pressure at 5 m/ d is 2.22 MPa, which is 4.5 times the end pressure of water flooding. It can be seen that the injection pressure increases linearly with the increase of the injection speed, as shown in Figure 3. The injection pressure can be optimized according to the injection speed. Combined with the field, the pressure of injecting chemicals should be 2-3 times the pressure of water flooding, so the injection speed should be controlled within 1-2.5m/d.

By comprehensively analyzing the pressure changes of the three groups of experiments, it can be found that after increasing the injection speed of the binary system, the injection pressure linearly increases, which is consistent with the theory.

Impact of Displacement Rate on Enhanced Oil Recovery. The effect of improving the recovery factor of the binary compound flooding is the ultimate indicator of concern in this experiment [26]. Within a certain range, the increase in displacement differential pressure will expand the spread volume and improve the recovery factor effect. The increase of displacement pressure caused by the increase of injection rate has a negative effect on improving oil recovery. The recovery and comprehensive recovery curves for each layer at three injection rates are shown in Figure 4.

By comparing the recovery degree of each permeable layer in Figure 4 and the comprehensive recovery degree of the model, the difference in oil displacement effect of each displacement method can be explained. In the water flooding stage, due to the difference in permeability between layers, channeling phenomenon occurs in the injected water, and the production of the high-permeability layer is the largest. The comprehensive recovery of water flooding in the three groups of experiments is about 49% with parallel contrast. The water flooding recovery is high, but there is still a large amount of remaining oil. After transferring the binary system, on one hand, the oil washing efficiency of each permeable layer is improved and on the other hand, the thickening effect of the polymer and the role of the surfactant to peel off the oil film can converge the oil wall to reduce the effect of channeling, making the low-permeability layer more affected, so that the extraction degree of each permeability layer is improved [28-30]. In the subsequent water flooding stage, the extent of recovery of each layer was reduced, mainly because the subsequent water lost the viscosity-enhancing effect, and the residual effect of the binary system reducing the oil-water interface tension will make the injected water and water channeling more serious, and the remaining oil that can be used is reduced.

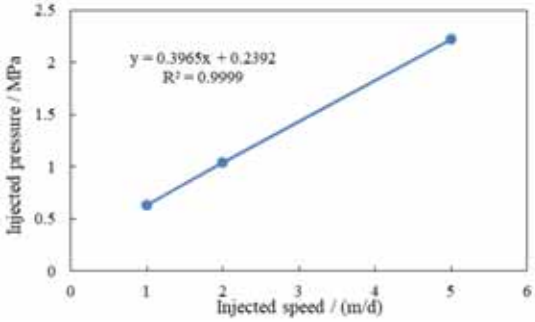

FIGURE 3
Fitting curve of injection speed and injection pressure.

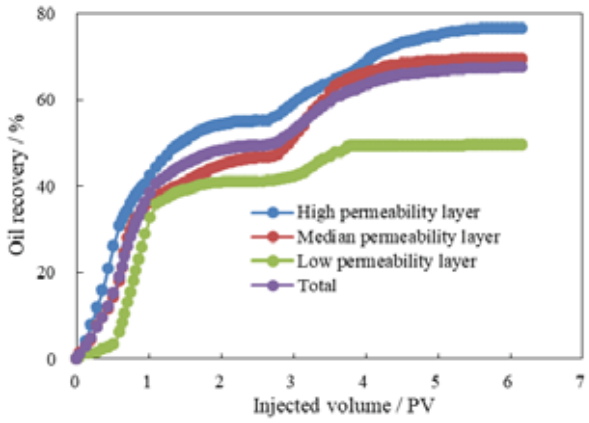

(a) 1 m/d

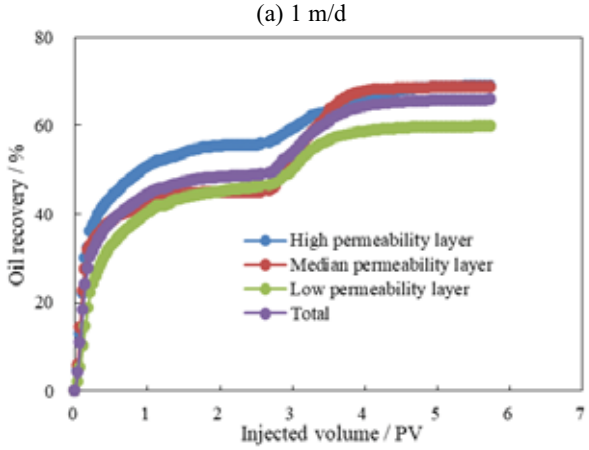

(b) 2 m/d

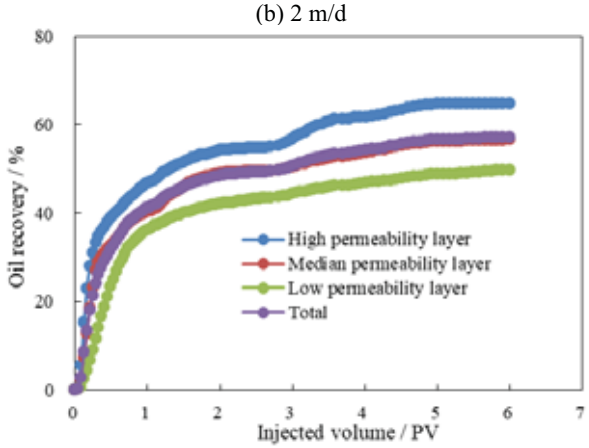

(c) 5 m/d

FIGURE 4
Recovery curves of three injection rates.

The binary flooding stage is the main period for enhanced recovery by chemical compound flooding, and the recovery enhancement values of each layer at three injection speed are shown in Figure 5. It can be found that when the injection speed is 1m/d, the effect of improving the recovery factor is the best, which is 18.09%. When the injection speed is increased from 1m/d to 2m/d, the increase in injection pressure forces the binary composite system to enter the low-to-medium permeability layer, and the remaining oil in the medium-permeability layer can be further stripped and coalesced by the binary system to increase the displacement resistance. The medium and low permeability layer can get the maximum utilization. At the same time, the intake of the binary system in the high-permeability layer is reduced, and the oil-washing ability of the high-permeability layer is

reduced, which leads to the enhanced recovery of the high-permeability layer below 1 m/d.

When the injection speed is further increased to 5m/d, the enhanced recovery factor is greatly reduced, and the comprehensive enhanced recovery factor is only 7.74%, which mainly contributes to the high permeability layer. This is mainly because the increase of the injection speed has limited improvement in heterogeneous liquid absorption. The high permeability layer is always the dominant channel, while the excessive injection speed causes the channel of the high permeability layer to be further strengthened [31-33]. Moreover, too high injection pressure also leads to the formation of water channeling channels in the low-permeability layer, which makes it difficult to expand the volume in a single layer. At the same time, the injection speed is too fast, which makes it difficult to exert the role of the surfactant. The binary system is too ineffective to circulate in the high water-containing channels, and it is difficult to contact the residual oil.

Influence of Displacement Speed on Production Parameters. It can be seen that although the increase of the injection speed will increase the displacement pressure, it cannot effectively expand the spread volume, which is mainly related to the formation of channeling flow. Increasing the displacement differential pressure will have a positive impact on enhanced oil recovery, but the fluid needs to have enough opportunity to enter the uncovered areas rather than channeling along the high permeability layer. Therefore, the diversion rate and water content of each layer are important indicators for evaluating the effect of heterogeneous improvement of the reservoir in real time.

The split rate curves at three injection speeds are shown in Figure 6. It can be seen that, corresponding to the analysis results of the recovery curve, the maximum percolation rate of the high-permeability layer in the water flooding stage is about 80%. When the binary system is injected, the flow rate of the heterogeneous reservoir is improved, and the percolation rate of the high-permeability layer is reduced. The shunt rate of the low-permeability layer increased. In the subsequent water flooding stage, the recovery shunt rate of the displacement agent fluid deteriorated again, and the hypertonic layer returned to the situation of high shunt rate and high dominant channel. Due to the strong heterogeneity of the reservoir, the shunt rate of the low-permeability layer is always low, maintaining below 10%. On one hand, it indicates that there is a large amount of remaining oil in the low-permeability layer to be exploited, and further replacement technology is needed to expand the affected volume; on the other hand, it also explains that the low-permeability layer has a limited degree of application in the binary flooding to improve the recovery efficiency. The effect of improving the recovery factor mainly comes from the medium and high permeability layers.

The injection speed of the binary compound flooding stage has a significant impact on the improvement of the shunt rate. When the injection speed is 1 m/d, the shunt rate of the high permeability layer decreases from 73% to 63%, and almost all of it acts on the medium permeability layer. When the injection speed increases at 2 m/d, the shunt rate of the high-permeability layer was reduced from 74% to 53%. At the same time, it was obvious that the shunt rate of the low-permeability layer had increased from 5% to 10%. The shunt rate had doubled, and the profile improvement effect was also doubled. When the injection speed is further increased to 5m/d, the diversion rate of the high permeability layer increased from 73% to 80%. Corresponding to the recovery analysis result, more injection systems pass through the high permeability layer. On one hand, the spread of the low-permeability layer is reduced, on the other hand, the use of residual oil in the high-permeability layer is weakened, and the effect of improving the recovery factor is the worst.

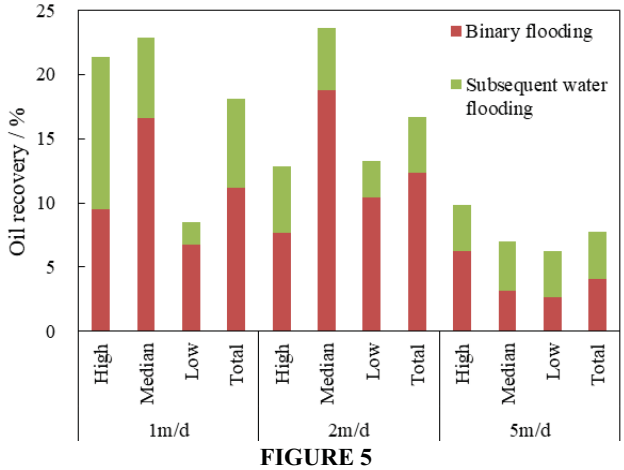

FIGURE 5
Enhanced oil recovery at three injection rates.

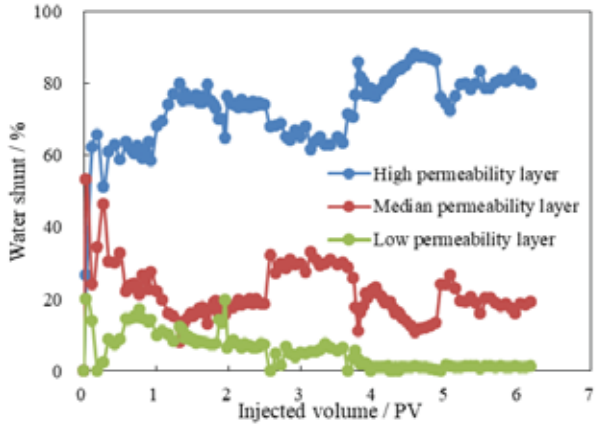

(a) 1 m/d

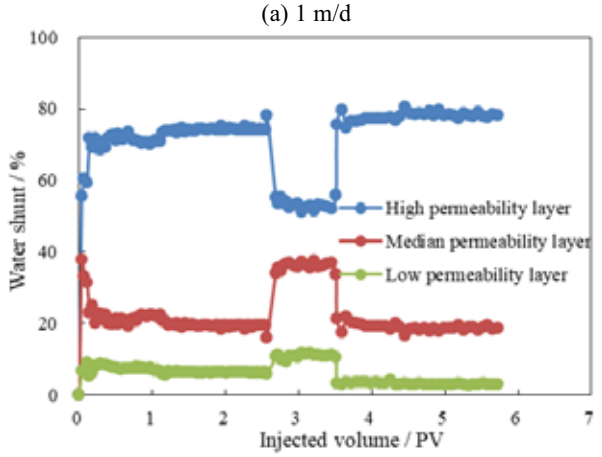

(b) 2 m/d

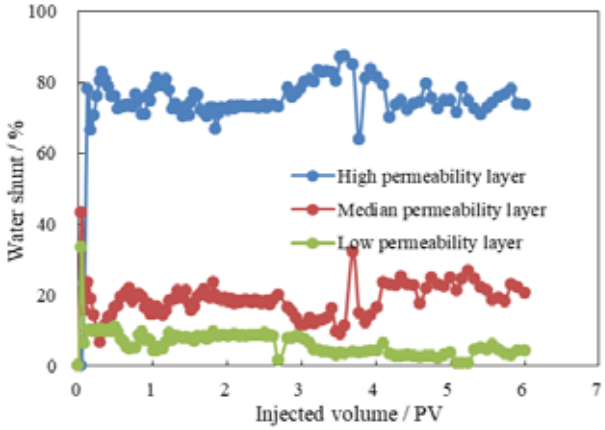

(c) 5 m/d

FIGURE 6
Flow rate curves at three injection speeds.

Comprehensive analysis of the three sets of experimental results shows that the polymer/surfactant binary system injection rate is vulgar when the injection rate is 1m/d and 2m/d. The shunt rate of the hypertonic layer decreases, and the shunt rate of the medium permeability layer increases by about 10% which can play the effect of improving the percolation of the high permeability layer. However, when the injection speed is increased to 5m/d, the flow rate of the high permeability layer is increased, and the flow rate of the low-permeability layer is decreased. It shows that increasing the binary injection rate will aggravate the interlayer contradiction and make the channeling phenomenon of the high permeability layer more serious.

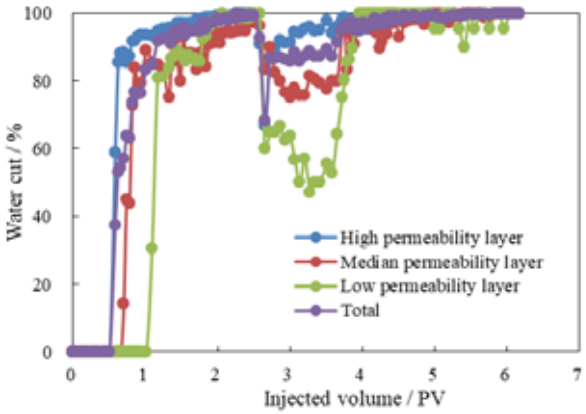

(a) 1 m/d

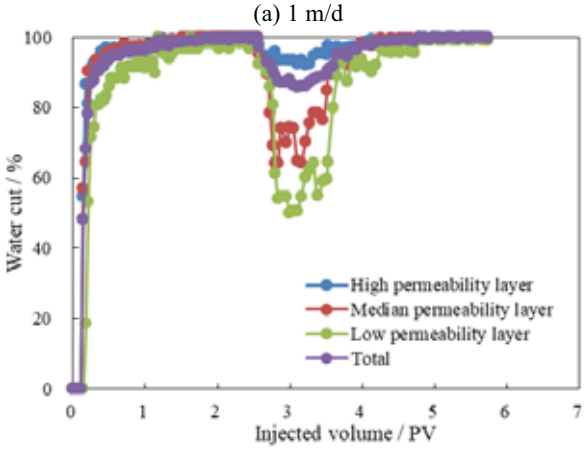

(b) 2 m/d

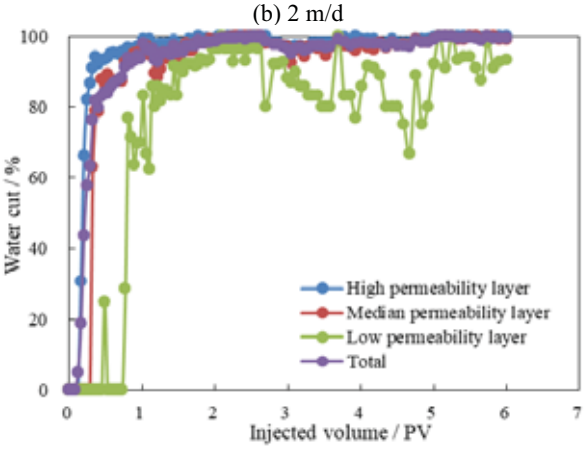

(c) 5 m/d

FIGURE 7
Moisture content curves at three injection rates.

In the same way, the moisture content curves at three injection speeds can be analyzed, and the results are the same. The flow rate curves at three injection speeds are shown in Figure 7. It can be seen from the figure that when the injection speeds are 1m/d and 2m/d, there is a significant decrease in water content in the binary composite flooding stage of each layer. The reduction of the low permeability layer is the most obvious. The binary system can play a better role after entering the system, and the effect of improving the recovery factor is obvious. However, because of the lower splitting rate, its impact on the comprehensive water content is small. When the injection rate is 1m/d, the lowest moisture content of the medium and low-permeability layer is 60.14% and 50.67%, respectively indicating the best recovery efficiency. When the injection speed is 5m/d, the moisture content of

the medium-permeability layer hardly decreases, and it is always maintained above 95%. The moisture content of the low-permeability layer fluctuates and decreases slightly. After increasing the injection speed of the binary system, although some of the remaining oil can be used, due to the further intensification of inter-layer contradictions, it is difficult to spread more to the low-permeability layer, resulting in poor water content reduction effect.

The above results are corresponding and supportive to each other, which proves that when the binary system is injected at a low speed, it can effectively play the role of expanding the volumetric agent's oil washing efficiency of the binary system, improve the profile, control water and oil, and greatly improve the recovery factor.

CONCLUSIONS

(1) As the injection speed of the polymer/surfactant binary system increases, the effect of increasing the recovery degree gradually decreases. When the speed is 1m/d, 2m/d, and 5m/d, the comprehensive recovery efficiency of composite flooding is 18.09%, 16.69%, and 7.74%, respectively. The smaller the injection rate, the better the effect of improving the recovery factor.

(2) The injection pressure of polymer/surfactant binary system increases linearly with the injection speed. When the injection speed is 1m/d-2.5m/d, the displacement differential pressure can be guaranteed to be 2-3 times the value from the water flooding, which is conducive to on-site injection.

(3) The increase of the injection rate of the polymer/surfactant binary system will increase the channel strength of the hypertonic layer to a certain extent, increase the shunt rate of the hypertonic layer, and reduce the water content reduction effect of each layer. To ensure that the binary system improves the recovery efficiency, the experiment shows that the injection speed value should be less than 2.5m/d.

(4) When the polymer/surfactant binary system is injected at a high speed, although the injection pressure is increased, the phenomenon of channeling in the high-permeability layer is more serious, which exacerbates the contradiction between layers and leads to a lower degree of final recovery. For this experiment, the injection speed of the binary system is best chosen at 1m/d.

ACKOWLEDGEMENTS

The authors would like to express sincere thanks to the relevant techniques who have contributed to this research and all the authors of the references.

REFERENCES

[1] He, J., Liao, G., Wang, Z. (2012) Oilfield development strategy and replacement techniques. Acta Petrolei Sinica. 3(3), 519-525.

[2] Zhao, F., Wang, Y., Dai, C., Ren, S., Jiao, C. (2006) Techniques of enhanced oil recovery after polymer flooding. Journal of China University of Petroleum (Edition of Natural Science). 30(1), 86-89+101.

[3] Ruschau, G. (1997) Considerations for Polymers In Enhanced Oil Recovery Operations. SPE 97086.

[4] Ojukwu, C., Onyekonwu, M., Ogolo, N., Ubani, C. (2013) Alkaline Surfactant Polymer (Local) Enhanced Oil Recovery: An Experimental Approach. SPE 167529-MS.

[5] Wylde, J., Slayer, J., Barbu, V. (2013) Polymeric and Alkali-Surfactant Polymer Enhanced Oil Recovery Chemical Treatment: Chemistry and Strategies Required After Breakthrough into the Process. SPE 164078-MS.

[6] Han, P., Su, W., Lin, H., Gao, S., Cao, R., Li, Y. (2011) Comparative evaluation on EOR of different chemical flooding after polymer flooding. Journal of Xi'an Shiyou University (Natural Science). 26(5), 44-48+92+115-116.

[7] Denney, D. (2008) Pump-Scaling Issues in ASP Flooding in Daqing Oil Field. SPE 0108-0050-JPT.

[8] Korrani, A., Sepehrnoori, K., Delshad, M. (2016) Significance of Geochemistry in Alkaline/Surfactant/Polymer (ASP) Flooding. SPE 179563-MS.

[9] Zhao, C., Zhao, Q., Me, S. (2006) A Correlation of Weak and Strong Base ASP Flooding Processes. Xinjiang Petroleum Geology. 27(6), 728-730.

[10] Lu, X., Gao, Z., Zhao, X., Yan, W., Wang, W. (1996) Distribution regularities of remaining oil in heterogeneous reservoirs after polymer flooding. Acta Petrolei Sinica. 4, 55-61.

[11] Xu, Q. (2019) Distribution characteristics of the micro-remained oil after ASP flooding in Daqing Oilfield. Petroleum Geology & Oilfield Development in Daqing. 38(4), 110-116.

[12] Wu, Z. (2017) Experimental Research and Potential Evaluation about Remaining Oil Distribution after Water Flooding in Heterogeneous Reservoir. Science Technology and Engineering. 17(15), 57-64.

[13] Sun, Z., Lu, X., Sun, X., Zhou, Y. (2018) Research on the Influence Factors of Weak-Base Ternary Compound System on Oil Incremental Effect and Its Action Mechanism. Journal of Petrochemical Universities. 31(1), 35-42.

[14] Chen, W., Lu, X., Yu, T., Xiao, C. (2010) Experimental study of injection parameters optimization of surfactant/polymer flooding. Special Oil and Gas Reservoirs. 17(5), 96-99+133.

[15] Jiang, G., Liu, J., Zhang, J., Xie, L., Dong, J. (2014) Optimization of injection parameters for polymer / surfactant flooding in Dagang oilfield. Petroleum Geology and Engineering. 28(4), 144-146.

[16] Hocine, S., Magnan, A., Degre, G., Rousseau, N., Rousseau, D. (2014) Alkaline-Free Surfactant Polymer Process for Heavy Oil. SPE 169697-MS.

[17] Oyemade, S. (2010) Alkaline - Surfactant - Polymer Flood (ASP): Single Well Chemical Tracer Tests - Design, Implementation and Performance. SPE 130042-MS.

[18] Ming, Y. (2017) Optimization method of the injection-production parameters for SP flooding based on the response surface methodology-A case study of Ng41-51 submember in the west of the 7th block of Gudong oilfield. Petroleum Geology and Recovery Efficiency. 24(3), 91-97.

[19] Zhang, F. (2018) Optimization method of injection and production parameters for polymer/surfactant binary flooding. Journal of China University of Petroleum (Edition of Natural Science). 42(5), 98-104.

[20] Bao, L., Zou, H., Liang, B., Xia, Y., Zhao, H. (2013) Parameter Optimization for Injection of Surfactant-polymer Composite Flooding System. Advances in Fine Petrochemicals. 14(1), 20-22+41.

[21] Xu, Y., Lu, M. (2011) Microbially enhanced oil recovery at simulated reservoir conditions by use of engineered bacteria. Journal of Petroleum Science and Engineering. 78(2), 233-238.

[22] Chang, X., Wang, G., Guo, H., Cui, J., Wang, T. (2016) A case study of crude oil alteration in a clastic reservoir by waterflooding. Journal of Petroleum Science and Engineering. 146, 380-391.

[23] Wang, J. (2019) Study on Optimization Design of combined flooding parameters after polymer flooding. Chemical Engineering and Equipment. 1, 99-101.

[24] Xia, X. (2018) A method of calculating injection rate limit for polymer/viscosity reducer combination flooding. Petroleum Geology and Recovery Efficiency. 25(6), 89-95.

[25] Yin, S., Zhao, J., Wu, Z., Ding, W. (2018) Strain energy density distribution of a tight gas sandstone reservoir in a low-amplitude tectonic zone and its effect on gas well productivity: A 3D FEM study. Journal of Petroleum Science and Engineering. 170(6), 1-16.

[26] Huang, X., Li, T., Gao, H., Zhao, J., Wang, C. (2019) Comparison of SO_2 with CO_2 for Enhancing Shale-hydrocarbon Recovery using Low-field Nuclear Magnetic Resonance. Fuel. 245, 563-569.

[27] Huang, X., Li, A., Li, X., Liu, Y. (2019) Influence of Typical Core Minerals on Tight Oil Recovery during CO_2 Flooding using NMR Technique. Energy & Fuels. 33(8), 7147-7154.

[28] Xia, Z., Liu, J., Ni, J., Zhang, T., Shi, X., Wu, Y. (2016) Structure, evolution and regional tectonic implications of the Queshan metamorphic core complex in eastern Jiaodong Peninsula of China. Science China Earth Sciences. 59(5), 997-1013.

[29] Ni, J., Liu, J., Tang, X., Yang, H., Xia, Z., Guo, Q. (2013) The Wulian metamorphic core complex: A newly discovered metamorphic core complex along the Sulu orogenic belt, eastern China. Journal of Earth Science. 24, 297-313.

[30] Yu, H., Yuan, J., Guo, W., Cheng, J., Hu, Q. (2008) A preliminary laboratory experiment on coalbed methane displacement with carbon dioxide injection. International Journal of Coal Geology. 73(2), 156-166.

[31] Pu, W., Zhao, S., Lu, X., Yuan, C., Wang, S., Tang, Y., Zhang, L., Li, R. (2016) The effect of oil properties on oil recovery in dilute surfactant flooding. Petroleum Science and Technology. 34(8), 759-764.

[32] Liu, H., Zhang, Y., Li, Y., Hou, J., Liu, Y. (2016) Influence on emulsification in binary flooding of oil displacement effect. Journal of Dispersion Science and Technology. 37(1), 89-96.

[33] Rostami, P., Sharifi, M., Aminshahidy, B., Fahimpour, J. (2019) The effect of nanoparticles on wettability alteration for enhanced oil recovery: Micromodel experimental studies and CFD simulation. Petroleum Science. 16, 859-873.

Received: **25.12.2019**
Accepted: **31.01.2020**

CORRESPONDING AUTHOR

Zhiquan Zhang
School of Petroleum Engineering,
Yangtze University,
Hubei, Wuhan 430100, China

e-mail: 2492402704@qq.com

© by PSP Volume 29 – No. 04A/2020 pages 3184-3192 Fresenius Environmental Bulletin

ANALYSIS ON THE INFLUENCING FACTORS OF MODERN FORESTRY DEVELOPMENT IN RECLAMATION AREA BASED ON ECOLOGICAL SECURITY--TAKING HEILONGJIANG PROVINCE AS AN EXAMPLE

Wanjing Dong[1], Dapeng Jiang[2], Hongbo Li [2], Yingli Huang[1,*]

[1]School of Economics and Management, Northeast Forestry University, Harbin, Heilongjiang Province, 150036, China
[2]School of Mechanical and Electrical Engineering, Northeast Forestry University, Harbin, Heilongjiang, 150036, China

ABSTRACT

The evaluation system of the modern forestry development in reclamation area based on ecological security was established based on the evaluation index system and combing the characteristics of modern forestry development in reclamation area. The core indicators of the factors which influencing the modern forestry development in reclamation area of Heilongjiang Province were analyzed from four aspects: forestry resources, ecological security, industrial development and security system, using the principal components analysis. It is found that the proportion of shelterbelt area, farmland forest net rate in reclamation area, the ratio of secondary and tertiary industrial structure of forestry, and the proportion of forestry scientific and technological personnel are the most influential factors on each subsystem. Based on the above analysis, some suggestions were made in the paper, such as putting forward policy support to establish ecological protection system; exploring new ways to expand the area of forestry; continuously improving the competitive advantage of the industry by developing forestry industry in combination with the actual situation of agriculture and forestry; establishing the Industry-University-Research collaborative service system and other suggestions. This research has a good guiding significance for improving the sustainable ecological security maintenance system of the modern forestry, and finally forming a systematic green forest environment.

KEYWORDS:
Heilongjiang Province, reclamation area, modern forestry, principal component analysis, ecological security

INTRODUCTION

Located in the economic center of Northeast Asia, with high degree of modernization and comprehensive production capacity and being the largest cultivated land of China, Heilongjiang Reclamation Area is the China's important commodity grain base and grain strategic reserve base in China. Not only the basis of the development capability of modern agriculture of the forestry in Heilongjiang Reclamation Area is continuously improving, but also the carrier and indicator the ecological civilization of this area is building, under the background of the implementation of ecological civilization construction and rural revitalization strategy. To put the development and the buildings into practice, modern forestry development and construction in Heilongjiang Reclamation Area must have a specific measurement standard.

The modern forestry evaluation research system undertook by the State Forestry Administration in 2007 is a relatively systematic evaluation system in the national level [1]. Based on different research perspectives, scholars have made empirical analysis on the construction of modern forestry evaluation index system for different regions and different development periods. From the systematic perspective, some scholars have constructed the modern forestry comprehensive index system, economic index system, environmental index system, scientific and technological index system and social index system to study the framework of modern forestry index system [2]; and from the connotation of modern forestry development, 3 first-level indexes, namely, forest ecological system, forestry industry system and forest culture system, and 13 second-level indexes evaluating the modern forestry development were established [3]. By using the method of fuzzy evaluation, the four first-level modules of forestry ecology, industry, ecological culture and basic support of the index system and 41 secondary indexes to evaluate the development level of modern forestry in Xinyang City were constructed [4].

The above researches provide enlightenment on how to construct the index system construction, the index selection and research methods and other aspects of the system. But most of the existing papers all made the research form the national point of view, and there exists few empirical studies on the evaluation of modern forestry development of the specific Heilongjiang reclamation area. The modern forestry

evaluation index is a nested, complex and dynamic system. The establishment of a scientific evaluation index system can not only reflect the status of modern forestry construction and industrial development objectively and comprehensively, but also promote the sustainable development of modern forestry [5].

Based on the research of many other scholars and the actual situations of the modern forestry construction and development in Heilongjiang reclamation area (Figure 1), the evaluation index system of modern forestry development in Heilongjiang reclamation was built from the four aspects: forestry resources, forestry ecological security, forestry industry and modern forestry development guarantee, with the aim of pursuing the sustainable development of modern forestry in Heilongjiang reclamation area which is of great importance and significance to promote the construction of ecological civilization in reclamation area and ensure the safety of food production.

MATERIALS AND METHODS

Concept of Modern Forestry in Reclamation Area. Modern forestry is a dynamic and developing concept. Experts in different periods have different understanding of the connotation of modern forestry. In 1989, Frankling et al. and other scholars defined modern forestry as "forests which are built based on the principles of forest ecology and landscape ecology, with the goal of realizing the unity of economic value, ecological value and social value of forests, which can not only produce timber and other forest products, but also sustainably exert various ecological benefits and societies, such as protecting biodiversity and improving ecological environment." Efficient forestry" [6].

Domestic scholars put forward modern forestry concept, which reflects the basic connotation of modern forestry knowledge system [7], considering that modern forestry is system which is of highly efficient and pursuing not only multiple functions of forests but also the sustainable forestry development mode to meet the changing social needs. It is a complex system which consists ecological, economic and social benefits from multivariate and multi-level [8-9]. It is also a forest resources which not only requires the whole society widely involving in the protection and cultivation of forest resources by making full use of the technologies and science, but also a forestry that can meet the growing ecological, economic and social needs of mankind by efficiently utilizing the multiple functions and multiple values of forests [10].

To sum up, modern forestry in reclamation area refers to the forestry which realizing the coordinated development of three major benefits of reclamation area forestry through scientific management mode, by relying on modern agricultural management system which based on the modern scientific and technological development, and combing the particularity of reclamation area forestry and the connotation of general modern forestry development.

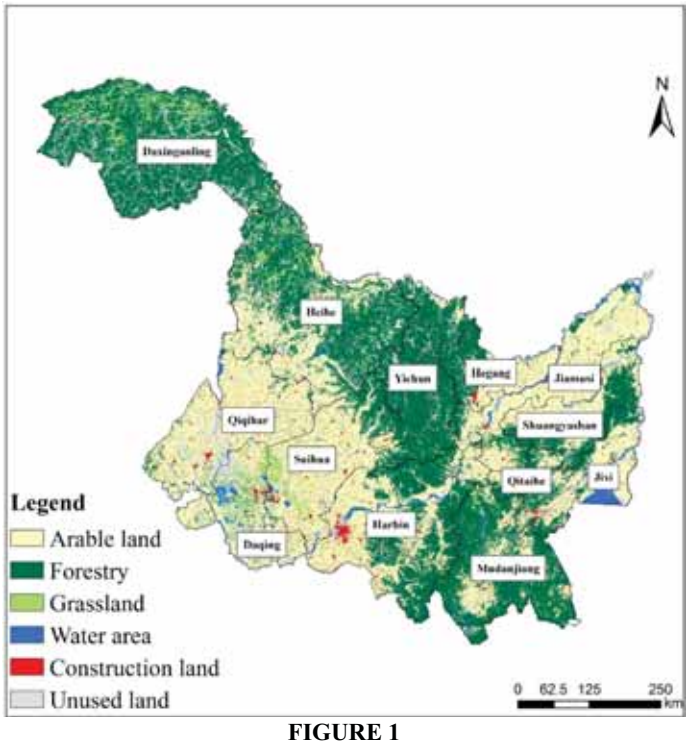

FIGURE 1
Geographic Information System Map of Heilongjiang Province in 2018

TABLE 1
Evaluation Index System of Modern Forestry in Reclamation Areas

First level index	Second level index	Expression
Forestry Resources system	Forest coverage (%) x_{11}	Forest area/administrative area * 100%
	Forest stock per unit area (m^3/hm^2) x_2	Forest stock/forest area
	Proportion of shelterbelt area (%) x_{13}	Shelterbelt area/administrative area * 100%
	Per capita forest land occupation (m^2) x_{14}	Forestland area/total population of Administrative Region
	Proportion of tending area of young and middle-aged forests (%) x_{15}	Medium and young age forest area/administrative area * 100%
Forestry ecological security system	Urban Greening Coverage (%) x_{21}	Vertical projection area/administrative area of greening plants *100%
	Area proportion of nature reserves (%) x_{22}	Area of Nature Reserve/Administrative Region *100%
	Forest net rate of farmland in reclamation area (%) x_{23}	Farmland Shelterbelt Area/Farmland Area*100%
	Control rate of forest diseases, pests and rodents (%) x_{24}	The occurrence area of forest diseases/insect pests and rodents *100% of the forest area
	Soil erosion control rate (%) x_{25}	Controlled area/soil erosion area * 100%
Forestry industry development system	Percentage of total forestry output value (%) x_{31}	Gross Output Value of Forestry Industry/Gross Output Value of Administrative Region *100%
	Industrial Structure Ratio of Forestry II and III (%) x_{32}	Gross Output Value of Secondary and Third Forestry Industries/Gross Output Value of Forestry Industries *100%
	Wood output per unit forest area (m^3/hm^2) x_{33}	Wood yield/forest area
	Yield of fresh and dry fruits per unit economic forest area (t/hm^2) x_{34}	Dry and Fresh Fruit Yield/Land Area of Administrative Region
	Sales volume of woody forest products (m^3) x_{35}	Statistical value
	Output value of non-wood forest products (Yuan) x_{36}	Statistical value
	Forestry output value per unit forest area (Yuan/m^2) x_{37}	Gross Output Value of Forestry Industry/Forest Area
	Regional per capita forestry output value (Yuan /person) x_{38}	Gross Output Value of Forestry Industry/Total Population of Administrative Regions
	Contribution Rate of Forestry Employment (%) x_{39}	Total number of forestry industry practitioners/total number of age-appropriate employment in Administrative Region *100%
	Per capita forestry income of workers as a proportion of total income (%) x_{310}	Per capita forestry disposable income per farm worker per capita/total disposable income per farm worker per capita per capita per year x 100%
Forestry development guarantee system	Cost-benefit ratio x_{41}	Gross Output Value of Forestry Industry/Completed Investment of Forestry in Place *100%
	Study Rate of Forestry Colleges and Universities (%) x_{42}	Number of Students in Forestry Specialized Schools/Total Number of Students in Secondary Schools
	The proportion of forestry science and technology personnel (%) x_{43}	Number of Forestry Science and Technology Personnel * Total Number of Industry Science and Technology Personnel in Administrative Region * 100%
	Forestry Science and Technology Progress Rate (%) x_{44}	Growth Rate of Forestry Gross Output - Growth Rate of Forestry Output Produced by New Input
	Contribution Rate of Forestry Science and Technology (%) x_{45}	Forestry Science and Technology Progress Rate/Growth Rate of Forestry Gross Output Value

Index Selection. There must have a specific measurement standard for the process of modern forestry development when the forestry changing from traditional forestry to forestry construction in the new period [11]. The purpose of constructing the framework of comprehensive evaluation system is to establish the quantitative standard of modern forestry in reclamation area.

Under the premise of ensuring the sustainable development of modern forestry in the reclamation area, the evaluation system designed by the comprehensive scholars [12-19], in accordance with the principles of science, operability, system city and importance, combined with the modernity of the district. The characteristics of forestry development, the evaluation index system of modern forestry development in the urban area, which taking forestry resources, forestry ecological security, forestry industry development and forestry development guarantee as the first-level indicators, and forest coverage, plain farmland forest network rate, forestry secondary and tertiary industry structure ratio, forestry employment contribution rate, forestry science and technology progress rate and as the 25 secondary indicators, was constructed (Table 1).

Research Method. In this paper, on the basis of other scholars' research, the modern forestry evaluation index system is classified, and the principal component analysis method is used to analyze the representative influence factors of various indicators. This explains the changes of different impact factors for the development of modern forestry in Heilongjiang Province.

TABLE 2
Characteristic values and variance contribution rate of forestry resource indicator system

Principal Component	Eigenvalues	Contribution rate/%	Accumulated contribution rate/%
1	0.416	51.091	51.091
2	0.284	34.929	86.020
3	0.084	10.313	96.333
4	0.030	3.667	100.000

The basic method of data analysis was as follows [20]:

Firstly, suppose there are n samples and p indicators. And the original data is $X=(xij)n \times p$. In order to eliminate the influence of the original data dimension and magnitude, the original variable matrix X is normalized, and the result is still X;

Secondly, the correlation coefficient matrix R is calculated and the result is $R=[r_{ij}]_{p\times p}$;

Thirdly, the eigenvalues and eigenvectors of the matrix, the contribution rate, the cumulative contribution rate are calculated, and the related information of the principal component are determined. By multiplying with the transformation matrix T into a diagonal matrix, $T'RT$, the elements $\lambda_1, \lambda_2 \ldots \lambda_p$ on the diagonal are the p eigenvalues of R, and the columns T of the transformation T are $T_j=(t_{1j} \ldots t_{pj})'$ is a feature vector corresponding to the feature value;

In the fourth step, the principal component would be selected. If the cumulative variance contribution rate of the first k principal components reaches *85%,* the first k principal components are selected: $Z_j=T'Y=t_{1j}Y_1+\ldots+t_{pj}Y_p$, $j= 1$、2、…、k, where *Y1, Y2, ... Yp* are standardized indicator vectors;

Finally, the comprehensive evaluation function Z is constructed. The principal component values of the indicators in each system are calculated by substituting the standardized data of each evaluation index in 2007-2016 into the expressions of each principal component.

Where the coefficient of the principal component Z_j is $\omega_j=\lambda_j/\sum_{j=1}^{k}\lambda_j$, j=1, 2…k, $F=\omega_1Z_1+\omega_2Z_2+\ldots+\omega_KZ_K$, and $W=(\omega_1, \omega_2 \ldots \omega_K)'$, and $Z=T'Y$, then $F=\omega_1Z_1+\omega_2Z_2+\ldots+\omega_KZ_K=W'Z=W'T'Y=(TW)'Y$.

Data Sources. All the statistics are from the China Forestry Statistical Yearbook, Heilongjiang Statistical Yearbook, Heilongjiang Reclamation Statistical Yearbook and Heilongjiang Reclamation Annual Bulletin form the year 2007 to 2016. And the indicator data is further calculated based on these statistics.

RESULTS

Forestry resource indicator system. Forestry resources are the foundation of modern forestry development. The forest coverage rate, forest area per unit area and shelter forest area ratio were selected to reflect the richness and quality of forestry resources in Heilongjiang Province. What's more, the per capita possession of forest land and the proportion of medium and young forest nurturing areas are important indicators reflecting the sustainability of forest management in the reclamation area. The Sklearn, the third-party library, is called to standardize the evaluation indicators by using Python, and then the principal component analysis is performed on the standardized variables.

In general, the criterion for extracting the number of principal components is 75 to 85% of the cumulative information extraction, that is, when the accumulated extracted information exceeds 85%, it indicates that the number of components at this time can satisfy the information requirement of principal component analysis [21].

The first three principal components are extracted, and the information extraction reaches 96.333 (>85%), which meets the needs of subsequent analysis, from the perspective of the component extraction of the forestry resource indicator system (Table 2).

The principal components Z_{11}, Z_{12}, and Z_{13} are represented by a linear combination of five index vectors, and the eigenvectors of each principal component are obtained. According to the feature vector, the principal component is represented by a linear combination of five vectors:

$$Z_{11} = -0.395x_{11} - 0.607x_{12} - 0.475x_{13} + 0.361x_{14} + 0.364x_{15} \quad (1)$$

$$Z_{12} = -0.784x_{11} + 0.267x_{12} + 0.404x_{13} - 0.525x_{14} - 0.411x_{15} \quad (2)$$

$$Z_{12}=0.322x_{11}-0.392x_{12}+0.118x_{13}-0.507x_{14}-0.687x_{15} \quad (3)$$

It can be seen that the first principal component mainly represents the forest volume per unit area and the proportion of the shelter forest area since the coefficients of x_{12} and x_{13} are relatively high. And the second principal component mainly represents the proportion of the per capita possession of forest land and the area of the young and middle-aged forests for the coefficients of x_{11} and x_{14} are relatively high; and the third principal component mainly represents forest coverage since x_{15} has the largest relative coefficient.

In order to further analyze the role of each indicator in the forestry resource system, the weight of each principal component is obtained by using the eigenvalues in the principal component establishment process. By substituting the feature root weight

into the comprehensive evaluation function model, a linear model for comprehensively evaluating the principal components of forestry resources can be obtained:

$$Z_{1\ comprehensive} = -0.360x_{11}-0.209x_{12}- 0.073x_{13} + 0.285x_{14} + 0.026x_{15} \quad (4)$$

It can be seen from the impact of these indicators on the reclamation of forest resources that the proportion of protective forest reclamation area of greatest impact on modern forestry resources. It also can be seen from the actual construction of the "Three North" shelterbelt project in the reclamation area that the forestry area in the reclamation area is increasing, the forest stock volume and forest coverage rate are increasing year by year, and the total forestry resources are increasing year by year. The quantity, quality and stability of forest land resources are the basis of modern forestry construction. The forest land resources could be used rationally for tending afforestation, this would directly affect the overall pattern and changes of forest resources, and thus determining the level of development of modern forestry.

Forestry Ecological Security Indicator System. The fundamental purpose of the development of modern forestry is the ecological construction. The urban greening rate and the farmland forest network rate in the reclamation area were selected to reflect the urban ecological environment and the construction of the agricultural and forestry forests; the proportion of the nature reserves, the prevention and control rate of forest pests and rodents and the rate of soil erosion control were selected to reflect the level of the ecological protection and ecology governess of the reclamation area. In the same way, the principal component analysis of the five indicators of the forestry ecological security index system is carried out, and the variance of the forestry ecological security index system is calculated (Table 3). When the number of extracted principal components reaches 3, the variance contribution rate reaches 94.093 (>85%), which satisfies the principal component analysis requirements.

And the linear combinations of the three principal components of the forestry ecological security indicator system are:

$$Z_{21} = -0.567x_{21} +0.426x_{22} +0.492x_{23}-0.277\ x_{24}+ 0.423x_{25} \quad (5)$$

$$Z_{22}=-0.306x_{21}-0.582x_{22}+0.288x_{23}-0.498x_{24}-0.486x_{25} \quad (6)$$

$$Z_{23}=0.095x_{21}+0.688x_{22}+0.027x_{23}-0.162x_{24}-0.701x_{25} \quad (7)$$

Apparently, the first principal component mainly represents the urban green coverage rate and the farmland forest network rate, for the coefficient of x_{21} and x_{23} in the first principal component is relatively high; in the second principal component, the x_{22} and x_{24} coefficients are relatively high, which is to say that this principal component mainly represents the area specific gravity of the nature reserve and the prevention rate of forest pests and diseases. The coefficient of x_{23} in the third principal component is the largest, which means that this component represents the rate of soil erosion control.

The weight of each principal component is obtained by using the feature values in the principal component establishment process. The linear model for comprehensively evaluating the main components of forestry ecological security can be obtained by substituting the feature root weight into the comprehensive evaluation function model,

$$Z_{2\ comprehensive} = - 0.215x_{21} + 0.109x_{22}+ 0.198x_{23} - 0.167x_{24} + 0.019x_{25} \quad (8)$$

It can be seen from the coefficient of comprehensive principle component of forestry ecological security, the modern forestry ecological construction in the reclamation area should not only focus on the construction of nature reserves, pest control and soil erosion control, highlighting the effectiveness of farmland protection, but also shouldering ecological security and agricultural production. Safety is a double responsibility.

Forestry Industry Indicator System. The development of modern forestry industry in Heilongjiang Reclamation is in a process of shifting from traditional forestry to efficient, technology-intensive forestry. The amount of forest output per unit of forest area, the yield of dry and fresh fruit per unit of economic forest area, the sales volume of woody forest products, the output value of non-wood forest products and the forestry output value per unit of forest area reflect the level of economic benefits and intensive management of forestry products.

The per capita forestry output value, the contribution rate of forestry employment and the per capita forestry income of employees accounted for the total income ratio, which reflected the impact of industrial development on the employment income of people in the region.

TABLE 3
Characteristic values and variance contribution rate of forestry ecological security indicator system

Principal Component	Eigenvalues	Contribution rate/%	Accumulated contribution rate/%
1	0.320	57.052	57.052
2	0.134	23.931	80.984
3	0.073	13.109	94.092
4	0.033	5.908	100.000

TABLE 4
Characteristics of the eigenvalue and variance contribution rate of the forestry industry indicator system

Principal Component	Eigenvalues	Contribution rate/%	Accumulated contribution rate/%
1	0.562	57.142	57.142
2	0.236	23.983	81.126
3	0.083	8.392	89.517
4	0.055	5.600	95.117
5	0.048	4.883	100.000

TABLE 5
Characteristic values and variance contribution rate of modern forestry development support indicator system

Principal Component	Eigenvalues	Contribution rate/%	Accumulated contribution rate/%
1	0.310	57.562	57.562
2	0.088	16.412	73.975
3	0.072	13.446	87.420
4	0.070	12.58	100.000

The principal component analysis was carried out on the 10 indicators of the forestry industry indicator system, and the variance of the forestry industry indicator system was extracted by calculation (Table 4). When the number of extracted principal components reaches 3, the variance contribution rate reaches 89.517 (>85%), which satisfies the principal component analysis requirements. The linear combinations of the three principal components of the forestry ecological security indicator system are:

$$Z_{31} = 0.322x_{31} + 0.416x_{32}+0.167x_{33}- 0.050x_{34}+ 0.271x_{35}- 0.410x_{36} + 0.447x_{37} + 0.447x_{38}-0.224x_{39} +0.040x_{310} \quad (9)$$

$$Z_{32}=-0.189x_{31}-0.191x_{32}-0.504x_{33}+0.375x_{34}-0.429x_{35} - 0.149x_{36} + 0.102x_{37} + 0.126x_{38}-0.548x_{39}-0.017x_{310} \quad (10)$$

$$Z_{33}=-0.094x_{31}+0.177x_{32}+0.211x_{33}-0.535x_{34}-0.172x_{35} - 0.176x_{36} + 0.048x_{37} + 0.043x_{38}-0.242x_{39}-0.711x_{310} \quad (11)$$

The first principal component represents the proportion of total forestry output value, the ratio of forestry secondary and tertiary industries, the output value of non-timber forest products, the forestry output value per forest area, and the per capita forestry output value of the region, because the coefficients of the components, x_{31}, x_{32}, x_{36}, x_{37} x_{38}, are relatively high. The second principal component mainly represents the amount of forest output per unit of forest area, the sales volume of woody forest products, and the contribution rate of forestry employment for the coefficient of this component, x_{33}, x_{35}, and x_{39} are pretty high. The coefficient of x_{34} and x_{310} in the third principal component is relatively large, which represents the ratio of dry and fresh fruit yield per unit of economic forest area and the per capita forestry income of workers to the total income. The weight of each principal component was calculated using the feature values in the principal component establishment process.

A linear model for comprehensively evaluating the main components of the forestry industry can be obtained by substituting the feature root weight into the comprehensive evaluation function model.

$$Z_{3\ \text{comprehensive}} = 0.128x_{31} + 0.293x_{32}-0.008x_{33} +0.072x_{34} + 0.037x_{35} +0.181x_{36} +0.279x_{37}+0.285x_{38} -0.276x_{39}-0.040x_{310} \quad (12)$$

As it can be seen from the analysis of the principle components of the forestry industry that the first principal component reflects the structural transformation and updating of the forestry industry, the diversified development of the secondary and tertiary industries, and the first principle also reflects the economic contribution of modern forestry development to society; the second principal component indicates that the modern forestry industry's production and marketing integration drives employment development; the third principal component indicates the development of a three-dimensional operation of agroforestry, improving the comprehensive utilization rate and output rate of forest land, and promoting farmers to get rid of poverty and increase income.

The ranking of the influencing factors of the integrated principal component reflects the rapid development of the forestry industry in Heilongjiang Reclamation Area, and the composite industry has obvious advantages in the future to come.

Forestry Development Support Index System. The benefit ratio of forestry production and investment is selected to reflect the financial security of modern forestry development; the attendance rate of forestry colleges and the ratio of forestry science and technology personnel were selected to reflect the reserve and application of modern forestry science and technology talents; the rate of forestry science and technology advancement and the contribution rate of forestry science and technology were selected to reflect the proportion of resources and benefits

that have been increased in the entire forestry economy by using forestry science and technology to transform traditional forestry in modern forestry construction.

Principal component analysis was carried out on the five indicators of the modern forestry development support index system, and the variance of the modern forestry development support index system was calculated (Table 5). When the number of extracted principal components reaches 3, the variance contribution rate reaches 87.420 (>85%), which satisfies the principal component analysis requirements. The linear combination of the three principal components of the modern forestry development support indicator system is:

$$Z_{41}= 0.488x_{41} - 0.549x_{42} - 0.429x_{43} + 0.321x_{44}+ 0.417x_{45} \quad (13)$$

$$Z_{42}=-0.223x_{41}-0.009x_{42}-0.769x_{43}-0.592x_{44}-0.087x_{45} \quad (14)$$

$$Z_{43}=-0.592x_{41}-0.266x_{42}-0.250x_{43}+0.608x_{44}-0.382x_{45} \quad (15)$$

Obviously, the first principal component has a relatively large coefficient of x_{42} and x_{45}, which means the principal component mainly represents the attendance rate of forestry colleges and the contribution rate of forestry science and technology. The second principal component has a relatively large x_{43} coefficient, which means the principal component mainly represents the proportion of forestry science and technology personnel.

The coefficients of x_{41} and x_{44} in the third principal component are relatively large, representing the ratio of production to investment and the rate of advancement in forestry science and technology. In the same way, the weight of each principal component is obtained by using the feature values in the principal component establishment process. By substituting the feature root weight into the comprehensive evaluation function model, a linear model for comprehensive evaluation of the main components of forestry development support can be obtained:

$$Z_{4\ \text{Comprehensive}} = 0.089x_{41} - 0.190x_{42}-0.219x_{43} + 0.091x_{44}+ 0.094x_{45} \quad (16)$$

The distinguishing feature of modern forestry from traditional forestry is the investment in science and technology. The results show that forestry personnel training and technological achievements into forestry is closely linked, which is, increasing the number of science and technology talent and accelerating the conversion of scientific and technological achievements provide a strong guarantee for the development of modern forestry reclamation and forestry industry investment provides economic security for scientific and technological progress and the development of modern forestry.

DISCUSSIONS

(1) Establishing Ecological Protection System Through National Policy and Actively Exploring New Ways to Expand the Area of Barracks. It can be seen from the above analysis, shelter construction has a significant impact on the ecological construction of modern forestry reclamation, modern agricultural production and business activities. Under the premise of limited land area, it is recommended to focus on afforestation and tending work, actively create economic forests with protective benefits and economic benefits, make full use of peasant courtyards, street vacant land, and farmers' own land to increase urban forest coverage.

At the same time, local forestry production should be included in the implementation scope of relevant agricultural policies, and when relevant departments at all levels formulate policies for benefiting farmers, thus creating conditions for farmers to participate in modern forestry construction. For example, the protection of forest land can be set like the demarcation of basic farmland, under the premise of ensuring basic farmland land and basic forest land, the afforestation policy for farmers to fully open their own land could be given.

(2) Developing Agriculture and Forestry According to the Actual Situation, and Continuously improve the Competitive Advantage of Industry. To achieve the outcome of economic development, income incensement and get rid of poverty in modern forestry construction in the urban area, the premise of ecological security and food security in the construction process must be ensured.

It can be seen from the proportion of forestry secondary and tertiary industries in the above research that the forestry industry structure needs to be upgrade and optimized. The forestry industry indicator system reflects the need to jump out of the timber industry, expand the business field to the non-wood forestry industry, give full play to the multiple functional benefits of forestry, and realize the development direction of multi-directional and multi-industry operations. The brand building of the forestry industry should be actively established to increase brand attractiveness and influence, enhance product value, realize the development of characteristic cultural industries, and promote the integration and development of tourism industry and cultural industry.

(3) Industry-University-Research Collaborative Service System Should Be Established. Modern forestry construction depends highly on scientific and technological progress. Therefore, the cooperation of industry, university and research institutes could be carried out, relying on the comprehensive practice bases of agricultural and forestry expert workstations and agricultural and forestry colleges.

The forestry science and technology extension system should be improved. For example, forestry technology can be applied to production and management activities through the establishment of forestry professional cooperatives; technical researches such as compound management, breeding improvement and forest product processing should be carried out to solve the technical problems encountered in forestry production and management in a scientific way, and provide scientific and technological support for the development of modern forestry in the region.

CONCLUSIONS

(1) The influential impact ability of each factor on modern forestry development in Heilongjiang reclamation area on forestry resources is as follows: the proportion of shelter forest area, forest coverage, per capita forest area, forest stock per unit area, and the proportion of tending area of young and middle-aged forests.

(2) The order of the factors which effect the forestry industry in a most influential way are as follows: the ratio of secondary and tertiary industrial structure, the per capita forestry output value, the per unit forest area forestry output value, the contribution rate of forestry employment, the output value of non-woody forest products, the proportion of total forestry output value, the output of dry and fresh fruits per unit economic forest area, the sales volume of woody forest products, the per capita forestry income of workers and the per unit forest area forest area and wood yield.

(3) The order of the effects of various indicators of forestry ecological security system on ecological security is the proportion of forestry science and technology personnel, the rate of forestry colleges, the contribution rate of forestry science and technology, the rate of forestry science and technology, and the ratio of investment and investment.

ACKNOWLEDGEMENTS

The authors would like to show thanks to those persons who have contributed to this work and the authors of all the references.

REFERENCES

[1] Zhang, J. (2013) Research Group of Modern Forestry Statistical Evaluation Research. Research on Modern Forestry Statistical Evaluation. China National Conditions. 10, 59-61.

[2] Lu, L., Wen, Z. (1997) Study on the framework of modern forestry indicator system. World Forestry Research. 06, 65-71.

[3] Guo, H., Chen, W. (2013) Study on the Design of Modern Forestry Evaluation Index System in China. Journal of Anhui Agricultural Sciences. 41(13), 5791-5793.

[4] Xie, Z. (2010) Evaluation of the development level of modern forestry in Xinyang City. Dissertation. Changsha: Central South University of Forestry and Technology.

[5] Yu, B., Liu, Z. (2009) The Reform of Current Forestry Statistical Indicator System. Forestry Economics. 08, 49-52.

[6] Franklin, J. (1989) Toward a new forestry. American Forests. 11-12, 37-44.

[7] Franklin, J. (1989) The new forestry. Journal of Sail and Water Conservation. 44(6), 549.

[8] Zhang, J. (1998) Research on Building Modern Forestry with Chinese Characteristics. Forest Resources Management. 04, 13-22.

[9] Horn, R., Vossbrink, J., Becker, S. (2004) Modern forestry vehicles and their impacts on soil physical properties. Soil and Tillage Research. 79(2), 207-219.

[10] Xu, L. (1999) A review of modern forestry theory research. Jiangxi Forestry Science and Technology. 05, 39-45.

[11] Vossbrink, J., Horn, R. (2004) Modern forestry vehicles and their impact on soil physical properties. European Journal of Forest Research. 123(4), 259-267.

[12] Zhao, H., Zhao, W. (2018) Research on Clustering Analysis of Forestry Modernization Development Level in Yunnan Province. Forestry Economy. 40 (01), 92-97.

[13] Liu, Y., Xie, Y., Zhu, L. (2016) Construction and Empirical Analysis of Forestry Modernization Evaluation Index System in Yunnan Province. Forestry Economics. 36(02), 103-108.

[14] Liao, C., Liu, Y. (2009) Analysis of Evaluation Indexes of Modern Forestry. China Science and Technology Wealth. 04, 112.

[15] Xu, S. (2009) Research on Modern Forestry Evaluation Index System. Hubei Forestry Science and Technology. 02, 43-47.

[16] Ren, Y., Liu, Z., Zhao, Y., Zhang, X. (2008) Evaluation Index System and Evaluation Method of Forestry Modernization Development Process in Erdos City. Inner Mongolia Forestry Science and Technology. 02, 48-53+62.

[17] Xu, W., Kong, X., Bao, Q. (2018) Research on Regional Differences and Dynamic Evolution of China's Forestry Modernization Level. Forestry Economic Issues. 38(04), 86-90+111.

[18] Eszter, T. (2016) Modern resource use and its impact in karst areas - agriculture, forestry and grazing. Zeitschrift für Geomorphologie Supplementary Issues. 60(2), 175-198.

[19] Appuhn, K. (2000) Inventing nature: forests, forestry, and state power in renaissance Venice. The Journal of Modern History. 72(4), 861-889.

[20] Zhang, X., Gu, F. (2019) Evaluation of soil fertility using principal component analysis. Journal of Northeast Forestry University. 02, 47-49.
[21] Li, J., Zhang, B., Lv, J. (2015) Study on the dominant factors of forest ecosystem services based on adaptive management horizon-Taking the forest ecological function zone of the Xing'an Mountains as an example. Forestry Economics. 35(02), 109-117.

Received: **25.12.2019**
Accepted: **01.02.2020**

CORRESPONDING AUTHOR

Yingli Huang
School of Economics and Management,
Northeast Forestry University,
Harbin, Heilongjiang Province, 150040 – China

e-mail: feigq167486@126.com

© by PSP Volume 29 – No. 04A/2020 pages 3193-3200 Fresenius Environmental Bulletin

IMPACT FORCE CALCULATION OF CHAIN DRIVE AND MODEL ANALYSIS OF FLEXIBLE GRAPHITE SHEET BASED ON THE CONCEPT OF NOISE REDUCTION AND ENERGY SAVING

Wei Jiang[1,2,*], Wei Li[1], Congwang Bao[2]

[1]School of Mechatronic Engineering, China University of Mining and Technology, Xuzhou 221116, China
[2]School of Mining and Civil Engineering, Liupanshui Normal University, Liupanshui 553004, China

ABSTRACT

Chain drive is a transmission method that transmits the motion and power of the active sprocket with a special tooth shape to the driven sprocket through the chain. It can work in harsh environmental conditions and they are widely used. However, currently widely used roller chain transmissions have significant problems such as poor stability, large running resistance, noise pollution, large energy consumption, and high maintenance costs. Therefore, based on the concept of energy saving and environmental protection, it is necessary to carry out energy-saving and environmentally friendly chain drive related technology research. In this paper, the Hertz stress formula is used to theoretically analyze the chain drive system of a mill's heat-removing graphite plate rolling mill. Then the meshing impact force of the chain drive system at a speed of 150r / min is calculated. The finite element analysis software ANASYS Workbench was used to perform modal analysis on four different specifications of graphite plates, and then the natural frequencies and mode shapes were obtained. It was found that the natural frequency of graphite plates decreased with decreasing thickness. The graphite plate natural frequency is compared with the roller rotation frequency, and the critical speed of the roller is calculated when rolling four kinds of graphite plates, which provides guidance for the selection of the roller speed in production. The research on this technology can provide a certain amount of technical support for the development of energy-saving and environmentally friendly chain transmissions.

KEYWORDS:
Chain drive, energy saving and environmental protection, graphite plate, finite element, natural frequency, modal analysis

INTRODUCTION

Chain drive is a kind of non-conjugate meshing drive with intermediate flexible parts. It has both the characteristics of gear drive and belt drive, such as accurate transmission ratio, large transmission force, high efficiency, long life, reliable use, convenient maintenance, and low cost [1-3] (Figure 1). Especially under the conditions of large center distance, constant speed ratio, multi-shaft transmission, open environment transmission with severe environment, transmission with large impact vibration, low-speed transmission with large load, and high-speed transmission with good lubrication, chain transmission brings obvious technical and economic benefits. During the operation of the chain, there is a large friction (mainly sliding friction) between the roller and the sleeve moving along the track, which results in a large running resistance of the chain [4-5]. At this time, in order to effectively reduce the frictional resistance of the chain movement, a method of dripping a suitable lubricant between the roller and the sleeve is often used, but the lubricant cannot be completely removed effectively, and it will cause certain oil pollution to the equipment. In addition, this type of chain transmission structure cannot be completely effectively sealed. Under severe working conditions, the lubricating oil cannot achieve the ideal lubricating effect. Instead, it will increase the frictional resistance to a certain extent, increase energy consumption, and bring noise pollution [6-8].

Due to the polygonal effect of the chain transmission, the pitch line of the traditional toothed chain and the sprocket's graduation circle alternately tangent, and the position of the centerline of the tight side chain changes periodically (Figure 2). At the same time, the linear speed of the toothed chain and the angular speed of the driven sprocket will also change cyclically, and this change will have a greater impact on the chain drive, which mainly transfers motion, and impairs the synchronization and uniformity of the drive. This is also one of the main reasons that lead to a larger whole building and noise during the operation of the chain drive [9-12].

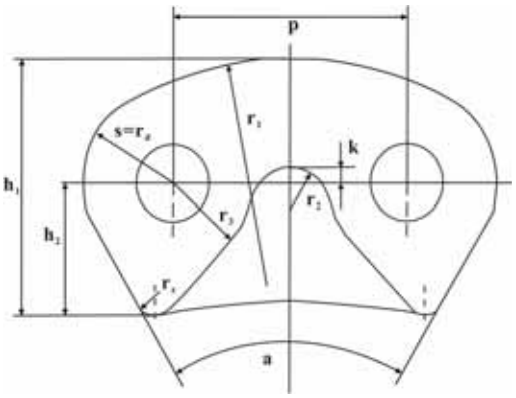

FIGURE 1
Basic shape of a typical outer toothed link plate.

The theoretical analysis and calculation of the impact meshing force in the chain transmission process is an important content of the chain transmission dynamics research, and it is also the basis for strength analysis and design. Relevant scholars have theoretically analyzed the meshing impact between rollers [13-14], and experimentally tested its impact noise. ADAMS was used to simulate and analyze the impact force and angular velocity of the chain transmission [15]. Finite element analysis software was adopted to simulate the impact force of the chain drive, and compared with the theoretical results, it was found that the experimental value was 25% to 30% larger than the theoretical value [16-17].

At present, with the development of high-tech technology, the core components of machinery and equipment are gradually moving towards integration, miniaturization, and high power. The problem of heat dissipation during mechanical operation has become one of the bottlenecks restricting the development of the industry [18-20]. If the heat dissipation of the electronic device is poor, it will easily lead to high temperature and failure of the mechanical equipment, which seriously affects the product life and brings large economic losses. Therefore, effective heat dissipation design for mechanical core electronic equipment is the key to improving product reliability, which mainly includes good heat dissipation materials, reasonable heat dissipation methods, and product manufacturing processes [21-22]. The optimized design of the heat dissipation system mainly focuses on the heat dissipation effect under extreme harsh working conditions. At the same time, it should also have good durability, standardization and low cost. Graphite plate is a material with high thermal conductivity (Figure 3), which is widely used in heat dissipation of mining machines. At home and abroad, the research on graphite plate is mostly about its internal structure and manufacturing process while not many kinetic analyses have been performed. The modal analysis can find out its natural frequency, which can provide guidance for improving the rolling quality.

MATERIALS AND METHODS

The transmission method of the rolling mill of a graphite plate rolling plant adopts chain transmission, as shown in Figure 4.

The Hertz stress formula is used to theoretically analyze the chain drive system of a rolling mill in a graphite slab rolling mill of a certain mining machine, and then calculate the meshing impact force of the chain drive system at a speed of 150r/min. The finite element analysis software ANASYS Workbench was used to perform modal analysis on four different specifications of graphite plates, and the natural frequencies and mode shapes were obtained. The mode shapes were analyzed briefly, and it was found that the natural frequency of graphite plates decreased with decreasing thickness. The graphite plate natural frequency is compared with the roller rotation frequency, and the critical speed of the roller is calculated when rolling four kinds of graphite plates, which provides guidance for the selection of the roller speed in production.

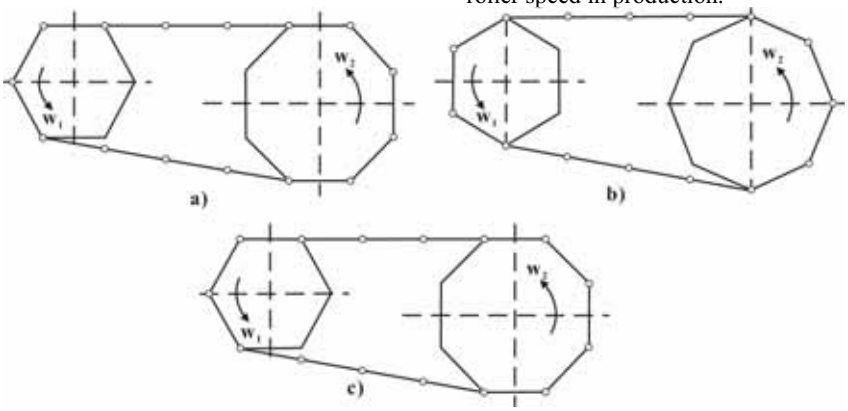

FIGURE 2
Schematic diagram of the polygon effect of chain transmission.

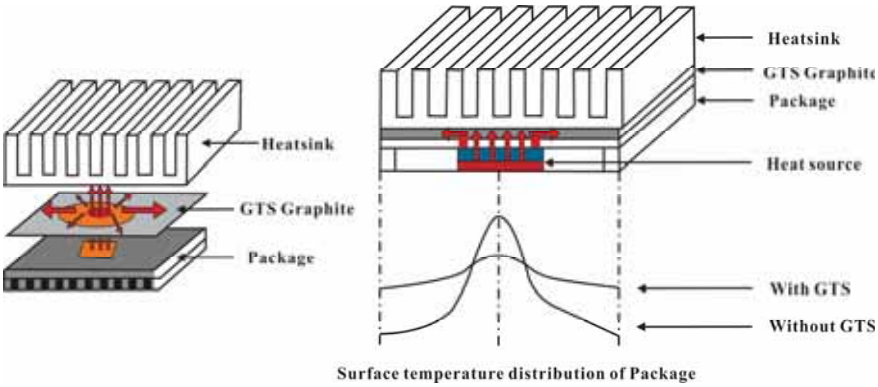

FIGURE 3
Schematic diagram of thermal diffusion of a typical GTS graphite heat sink.

RESULTS

Chain Drive Impact Force Calculation. (1) Theoretical Analysis. The impact force in the chain transmission process depends on its effective impact mass, relative impact speed, contact stiffness between the roller and gear teeth, and contact damping [23-24]. The impact is now equivalent to the following process: A roller of equivalent mass m impacts with the sprocket gear teeth at a certain impact angle at the meshing point at a relative speed v, as shown in Figure 5.

FIGURE 4
Transmission Part of Graphite Milling Machine.

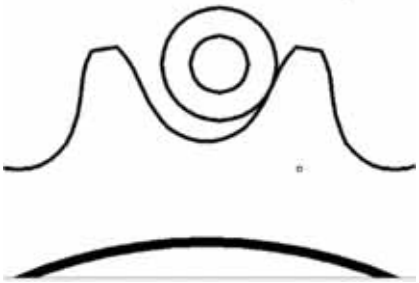

FIGURE 5
Impact Diagram

It was believed that if the equivalent mass is taken as the mass of one chain link, the error produced will not exceed 5% [5, 25], so the equivalent impact mass can be taken as the mass of one chain link. The contact between the roller and the sprocket under the impact load can be regarded as the contact between the parallel cylinder and the concave cylindrical surface under the pressure. In order to calculate the contact stiffness k, the width 2b of the contact area and the contact deformation depths h_1, h_2 need to be obtained. According to Hertz stress formula:

$$b = \left[\frac{2P\frac{1-\mu_1^2}{E_1}+\frac{1-\mu_2^2}{E_2}}{\pi l\left(\frac{1}{\rho_1}-\frac{1}{\rho_2}\right)}\right]^{\frac{1}{2}} \quad (1)$$

$$h_1 = \rho_1 - \sqrt{\rho_1^2 - b^2} \quad (2)$$

$$h_2 = \rho_2 - \sqrt{\rho_2^2 - b^2} \quad (3)$$

The contact stiffness can be obtained by:

$$k = \frac{P}{h_1+h_2} \quad (4)$$

Where E_1 and E_2 are the elastic moduli of the chain and the rollers, respectively; μ_1 and μ_2 are the Poisson's ratios of the chain and the rollers, respectively; ρ_1, ρ_2 are the radius of curvature of the roller and the impact of the roller and the sprocket, respectively; l is the tooth width; P is the unit pressure and the size are 1N.

The roller and gear teeth are lubricated with normal production, and the damping coefficient is 0.1. When the roller and gear teeth impact, the dynamic equation is:

$$m\ddot{x} + c\dot{x} + kx = 0 \quad (5)$$

Where m is the equivalent impact mass, and the calculation method is as follows:

$$m = \frac{qp}{1000} \quad (6)$$

Where q is the weight per meter of the chain; p is the pitch.

Equation (4) satisfies the initial conditions:

$$\begin{cases} x(0) = 0 \\ \dot{x}(0) = v_1 sin\eta \end{cases} \quad (7)$$

Where v_1 is the relative impact velocity and its magnitude is:

$$v_1 = 2r\omega \sin\left(\frac{\pi}{2}\right) \quad (8)$$

In the equation, r is the radius of the sprocket; ω is the angular velocity of the sprocket; z is the number of teeth.

Solving the differential equation (4) gives:

$$x = \frac{e^{-\xi\omega_2 t}}{\omega_1} v_1 sin\eta . sinw_2 t \quad (9)$$

Where, $\xi = \frac{c}{2\sqrt{mk}}$; $\omega_1 = \omega_2\sqrt{1-\xi^2}$; $\omega_2 = \sqrt{\frac{k}{m}}$; $\eta = 35° + \frac{240}{z}$.

In a meshing cycle, the impact force is:

$$F(t) = k\frac{e^{-\xi\omega_2 t}}{\omega_1} v_1 sin\eta . sinw_2 t \quad (10)$$

Its period is:

$$t = \frac{\pi}{\omega_1} \quad (11)$$

(2) Chain Impact Force of Rolling Mill. The specifications of the chain used in the graphite plate rolling mill of this plant are shown in Table 1, and the specifications of the sprocket are shown in Table 2.

TABLE1
Standard of Chain

ISO Chain number	Roller diameter /mm	Pitch p/mm	Weight per meter /kg	Texture
20A-2	19.05	31.75	7.8	45 steel

TABLE 2
Standard of Sprocket

Number of teeth	Tooth circle diameter /mm	Pitch *p*/mm	Tooth width /mm	Texture
21	228	31.75	17	45 steel

FIGURE 6
Three-Dimensional Model of Chain Wheel

The curvature radius of the roller is 9.525mm. The curvature radius at the impact of the gear teeth is not specified in the national standard. The author uses the parameterization module in the 3D modeling software Pro/E to establish a 3D model of the sprocket, as shown in Figure 6. The radius of curvature at the impact point was measured using the built-in measurement function, which was 24.8626mm. The elastic modulus of No. 45 steel is 2.1 × 105N/mm^2, and its Poisson ratio is 0.3. The speed of the sprocket is 150r/min, which is 15.708rad/s.

Bringing the above data into the above equation, the various data required by equation (9) can be obtained, and the process is not described in detail. The magnitude of the impact force in a cycle is [26]:

$$F(t) = 1008.766\sin(10532.75t)\, e^{-0.2019t} \quad (12)$$

Use Excel to calculate the meshing impact force in one cycle and draw a schematic diagram, as shown in Figure 7. It can be known from Figure 7 that the period of the impact force is about 0.0003s, and the amplitude reaches about 0.0015s with the value of about 1008N. There is an unavoidable installation gap of the rolling mill rolls, so the rolls will vibrate under the impact of the chain, which will seriously affect the rolling of the graphite sheet.

Modal Analysis of Graphite Plate. (1) Basic Theory of Modal Analysis. Modal analysis is the most basic dynamic analysis and the basis of other dynamic analysis. Modal analysis can help determine the natural frequency and mode shape of the structure, thereby avoiding resonance in the structure design [6, 27]. Suppose the structure is discretely divided into n-degree-of-freedom systems after finite element partitioning. The dynamic equilibrium equation of the system is [9]:

$$[M]\{\ddot{x}\} + [C]\{\dot{x}\} + [K]\{x\} = \{F(t)\} \quad (13)$$

[M], [C], and [K] are mass matrix, stiffness matrix, and damping matrix, respectively; {x}, F(t) are node displacement vector and load vector, respectively.

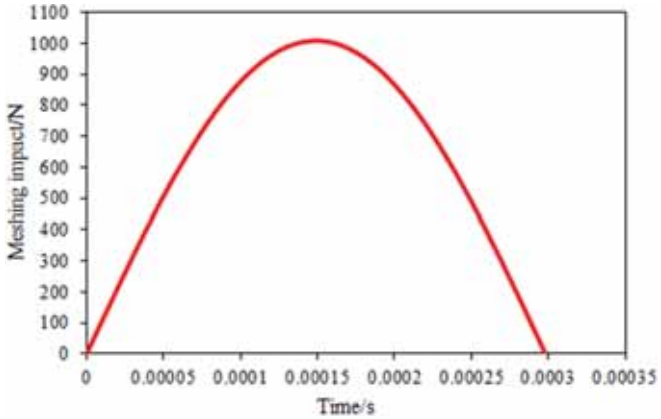

FIGURE7
Impact Force Diagram

Calculating the natural frequency and mode shape of a structure is the basic content of dynamic analysis. Computational experience indicates that the damping of many engineering structures has a small effect on the frequency and mode shape of the structure and can be ignored. Therefore, the equation of undamped vibration is obtained from (13):

$$[M]\{\ddot{x}\} + [K]\{x\} = 0 \quad (14)$$

In free vibration, it is assumed that each node makes simple harmonic vibration, and its displacement is expressed as:

$$\{x\} = \{X\}\sin(\omega t + \varphi) \quad (15)$$

In the equation, {X} is the mode vector of each node; ω is the natural frequency corresponding to the mode shape; φ is the phase angle.

Substituting (15) into (14) gives:

$$([K] - \omega^2[M])\{X\} = 0 \quad (16)$$

Therefore, the simple resonance of equation (14) becomes a problem of finding generalized eigenvalues. The generalized eigenvalue ω^2 is the natural frequency of the structure, and the generalized eigenvector is the corresponding mode shape. The modal analysis problem is transformed into the eigenvalue solution.

(2) Modal Analysis of Mining Machine's Thermal Graphite Sheet. In actual production, the length of the graphite plate of the mining machine can reach tens of meters, and the thickness of conventional products is 0.2~1.2mm. It can also be produced according to customer's special requirements and performance indicators. The mechanical performance parameters of the mining machine's cooling graphite plate do not have a uniform value in the current market. Some mechanical parameters of the graphite plate of the mining machine produced by the company are shown in Table 3.

TABLE 3
Mechanical properties of Graphite Paper

Density /kg/m^3	Young's modulus/GPa	Poisson's ratio
1530	15	0.34

A three-dimensional model of flexible graphite plate was established using the three-dimensional modeling software PRO/E, and then the three-dimensional model was imported into the finite element analysis software ANSYS Workbench. The graphite plate material in Table 3 was given to divide the finite element mesh. Set both ends of the graphite plate to Fix Support, which is a fixed constraint, and then perform a modal analysis. The graphite plate finite element model is shown in Figure 8.

In the process of modal analysis, the first few modes of vibration play a major role in vibration. Thus, only the first four modes of mode are extracted here [8]. Although the sizes of graphite plates of different specifications are different, the mode shapes should have the same trend of displacement change, and the natural frequencies and maximum displacements of each order of graphite plates of different specifications are not equal [28-29].

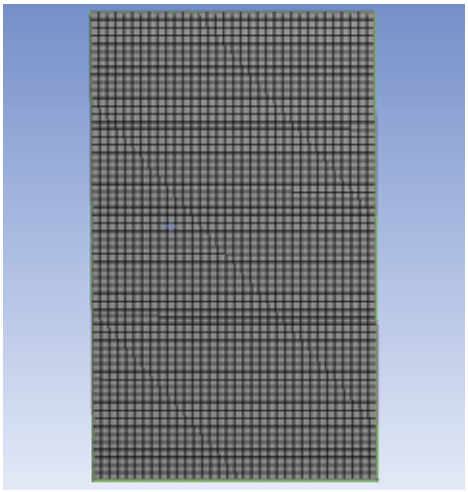

FIGURE 8
FEM of Graphite Paper

First, the first four-order mode shapes of a graphite plate with a length of 700 mm, a width of 400 mm, and a thickness of 0.4 mm are analyzed. The first four-mode modes are shown in Figure 9. In addition, the maximum displacements and natural frequencies of the first fourth-order mode shapes of graphite plates with the same length but different widths and thicknesses are calculated, as shown in Table 4.

TABLE 4
Graphite Sheet Frequency—Displacement Relationship

Specification /mm	Project	First-order mode	Second-order mode	Third-order mode	Fourth-order mode
700×400×0.4	Natural frequency /Hz	2.767	4.116	7.636	9.684
	Maximum displacement /mm	131.46	206.06	132.96	198.77
700×400×0.3	Natural frequency /Hz	2.075	3.087	5.728	7.264
	Maximum displacement /mm	151.81	237.95	153.51	229.52
700×300×0.4	Natural frequency /Hz	2.756	4.881	7.599	10.969
	Maximum displacement /mm	148.36	235.39	149.06	228.61
700×300×0.3	Natural frequency /Hz	2.068	3.662	5.701	8.228
	Maximum displacement /mm	171.32	271.82	172.11	263.98

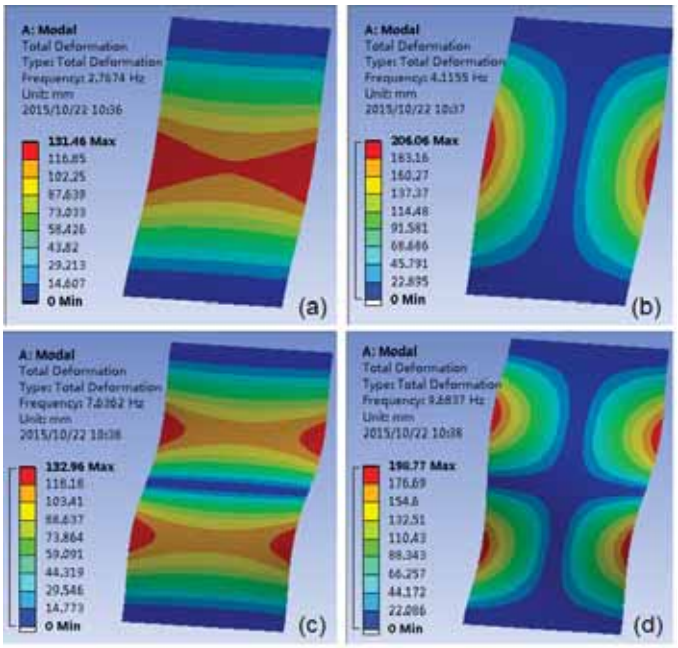

FIGURE 9
Graphite Sheet Vibration Modes
Notes: (a) First-order mode, (b) Second-order mode, (c) Third-order mode (d) Fourth-order mode.

It can be seen from Figure 9 that the first-order mode shape of the graphite plate shows a large displacement at the center of the graphite plate parallel to the width, and the displacement gradually decreases toward the two ends along the length direction. The second-order mode shows the largest displacement occurrence at the middle portion of the graphite plate, and the radiation to the middle decreases along the width direction [30-32]. In the third-order mode, the graphite plate appears wavy vibration, and the maximum displacement occurs at one-fifth of the total length of the graphite plate from both sides of the graphite plate, except for the two ends of the graphite plate. The maximum displacement of the graphite plate in the fourth-order mode appears at one-fifth of the total length of the graphite plate from both ends of the graphite plate, and the radiation to the middle decreases along the width direction. The displacements of the first four modes of the graphite plate are symmetrically distributed. It can be known from Table 4 that graphite plates of different specifications correspond to different natural frequencies, and the relationship between the natural frequency and thickness of graphite paper is significant, but the relationship with the width is not significant [33]. The maximum displacement in the vibration of graphite paper not only becomes larger as the thickness decreases, but also has a significant relationship with its width. This shows that the smaller the thickness and width of the graphite plate, the more difficult it is to control its vibration.

Roller Critical Speed. During the rolling process of the graphite plate of the mining machine, the roller is the direct vibration source of the graphite plate vibration. When the rotation frequency of the roller is close to the natural frequency of the graphite plate, it will cause the graphite plate and the roller to resonate [34-35]. Therefore, the rotation frequency of the roller must be far from the natural frequency of the flexible graphite plate, otherwise the graphite plate and the roller shaft will resonate, leading to the degradation of the graphite plate quality. The rotation frequency of the roll shaft is calculated as shown below [36]:

$$f = \frac{n}{60} \tag{17}$$

In the equation: f is the rotation frequency of the roller shaft, Hz; n is the Roller shaft speed, r/min. The rotation speed of the roller shaft is 150r/min. According to equation (17), the rotation frequency is 2.5Hz, which is close to the natural frequency of the four graphite plates, which will cause the graphite plate to resonate with the roller shaft and seriously affect its quality. It even could cause the graphite plate to break. During the rolling process, it is necessary to find the critical speed of the roller and keep the actual rolling speed away from the critical speed. Table 5 lists the critical speeds of the rollers during the rolling process of the graphite sheets of the above four specifications.

It can be known from Table 5 that the critical speed decreases as the thickness of the graphite plate decreases. In order to avoid the critical speed during rolling, the speed of the roller must be reduced.

TABLE 5
Critical Speed of Roller

Specification /mm	1st order frequency /Hz	Critical speed of roller /(r/min)
700×400×0.4	2.767	166.02
700×400×0.3	2.075	124.5
700×300×0.4	2.756	165.36
700×300×0.3	2.068	124.08

CONCLUSIONS

(1) Using Hertz formula to calculate the meshing impact force of a chain drive system of a graphite plate rolling mill under the condition that the sprocket speed is 150 r/min, the impact force amplitude is to be about 1010N. The finite element analysis software ANSYS Workbench was used to perform modal analysis on four different specifications of the mining machine's heat dissipation graphite plate, and the first four order natural frequencies were obtained. The first order natural frequencies were: 2.767 Hz, 2.075 Hz, 2.756 Hz, 2.068 Hz, respectively.

(2) The study obtained the critical speed of the rollers when rolling the graphite plates of the four types of mining machines. In order to ensure the rolling of the graphite plates, the speed of the rollers must be reduced to keep them away from the critical speed. This research provides a reference for the vibration study of chain transmission and the structural improvement of the graphite machine's heat-dissipating graphite plate rolling mill, which ultimately helps to achieve the energy-saving and noise-reduction effect of mechanical equipment.

ACKNOWLEDGEMENTS

This work was financially supported by the Project of Science and Technology Department of Guizhou Province, China (No. LH-2015-7623), the Fund of Liupanshui Normal University, China (No. LPSSYKYJJ201414), and the Project of Education Department of Guizhou Province, China (No. KY-2017-026)

REFERENCES

[1] Wang, K., Liu, S., Havek, S., Chen, F. (1992) On the impact intensity of vibrating axially moving roller chains. Journal of Vibration and Acoustics. 114(3), 397-403.

[2] Liu, S., Wang, K., Havek, S., Trethewey, M., Chen, F. (1997) A global-local inter-grated study of roller chain meshing dynamics. Journal of Sound and Vibration. 203(1), 41-46.

[3] Ni, J., Li, W. (2015) Simulation analysis of chain transmission mechanism based on ADAMS and Pro-E. Journal of Chinese Agricultural Mechanization. 36(1), 242-245.

[4] Xu, L., Yang, Y., Liu, J. (2012) Theoretical Analysis and Finite Element Simulation of the Meshing Impact of Roller Chain Drive. Journal of Tianjin University. 43(2), 132-137.

[5] Xue, Y. (2006) Research on the meshing theory and application of double meshing tooth chain drive. Dissertation. Jinan: Shandong University.

[6] Mao, X., Xu, Z., Zhao, M. (2013) The Research of the Heat Dissipation Performance for Graphite Plate and Graphite Plates with Metal Film. Energy Conservation Technology. 31(3), 217-220.

[7] Matsumoto, R., Okabe, Y. (2016) Highly electrically conductive and air-stable metal chloride ternary graphite intercalation compounds with $AlCl_3$-$FeCl_3$ and $AlCl_3$-$CuCl_2$ prepared from flexible graphite sheets. Synthetic Metals. 222, 351-355.

[8] Matsumoto, R., Arakawa, M., Yoshida, H., Akuzawa, N. (2012) Alkali-metal-graphite intercalation compounds prepared from flexible graphite sheets exhibiting high air stability and electrical conductivity. Synthetic Metals. 162(23), 2149-2154.

[9] Pereira, C., Ambrósio, J., Ramalho, A. (2015) Dynamics of chain drives using a generalized revolute clearance joint formulation. Mechanism and Machine Theory. 92, 64-85.

[10] Fuglede, N., Thomsen, J. (2016) Kinematic and dynamic modeling and approximate analysis of a roller chain drive. Journal of Sound and Vibration. 366, 447-470.

[11] Chew, M. (1985) Inertia effects of a roller-chain on impact intensity. Journal of Mechanisms, Transmissions, and Automation in Design. 107(1), 123-130.

[12] Xu, J. (2012) ANSYS 12.0 workbench numerical simulation technology. Beijing: China Water and Power Press.

[13] Zhang, D. (2011) Structural analysis and optimal design of single beam double hook gantry crane. Dissertation. Xi'an: Chang'an University.

[14] Li, C., Yang, J., Zhang, J. (2014) Study on Shearing Force and Vibration of Steel Strip. Machinery Design and Manufacture. 7, 142-144.

[15] De Tomas, C., Suarez-Martinez, I., Marks, N. (2016) Graphitization of amorphous carbons: A comparative study of interatomic potentials. Carbon. 109, 681-693.

[16] Sun, K., Qiu, Y., Zhang, L. (2019) Preserving Flake Size in an African Flake Graphite Ore Beneficiation Using a Modified Grinding and Pre-Screening Process. Minerals. 7(7), 115.

[17] Khurana, V., Kaur, M., Kumar, S., Gupta, D., Goswamy, J. (2019) Multifunctional graphitic tracks on flexible polymer sheet as strain, acoustic vibration and human motion sensor. Measurement. 146, 9-14.
[18] Nagaraju, S., Mohan, R. (2018) Lightweight flexible graphite sheet for high-performance electromagnetic interference shielding. Materials Letters. 233, 59-62.
[19] Rika, M. (2014) Investigation of the high, stable electrical conductivity in graphite intercalation compounds prepared from flexible graphite sheets. Synthetic Metals. 198, 107-112.
[20] Shi, X., Yang, B. (2006) Temperature Field and Mode Analysis of Flat Plate with Thermal Environment of Transient Heating. Computer Aided Engineering. 15, 15-18.
[21] Bai, J., Li, J., Sun, A. (2019) Modal analysis and size determination of damping test sample for vibration damping composite plate. China Metallurgy. 29(2), 45-49.
[22] Ge, Z., Li, A., Ma, L., Chen, H. (2018) Research of Modal Analysis and Dynamic Characteristics for Turbine Rotor. Turbine Technology. 60(6), 435-438.
[23] Wang, Y., Xiang, Y., Sun, R., Li, K. (2018) Engine Room and Floor Modal Analysis and Structural Optimization of a Pickup Truck. Agricultural Equipment and Vehicle Engineering. 56(6), 74-77.
[24] Zhang, Z., Ying, H., Liu, J., Yang, J., Li, L. (2009) Vibration Characteristics of a New Air Bearing Rotor System During Startup. Journal Of Vibration, Measurement and Diagnosis. 29(2), 159-161.
[25] Liu, Z., Jiang, R., Li, X., Ju, Z., Chen, D. (2012) Design and Casting Test of Ultrasonic Radiator with Different Materials. Hot Working Technology. 41(9), 1-4+8.
[26] Kobayashi, M., Toda, H., Takeuchi, A., Uesugi, K., Suzuki, Y. (2012) Three-dimensional evaluation of the compression and recovery behavior in a flexible graphite sheet by synchrotron radiation microtomography. Materials Characterization. 69, 52-62.
[27] HoChtl, F., Hein, M., Klug, S., Sennera, V. (2012) On the effect of chain stay impact on the structural safety of CFRP structures in mountain biking. Procedia Engineering. 34, 664-669.
[28] Pinna, C., Demartini, M., Tonelli, F., Terzi, S. (2018) How Soft Drink Supply Chains drive sustainability: Key Performance Indicators (KPIs) identification. Procedia CIRP. 72, 862-867.
[29] Lindahl, N., Midtvedt, D., Svensson, J., Nerushev, O., Lindvall, N., Isacsson, A., Campbell, E. (2012) Determination of the bending rigidity of graphene via electrostatic actuation of buckled membranes. Nano Letters. 12(7), 3526-3531.
[30] Xu, W., Wang, L., Jiang, J. (2014) Vibration of graphene monolayer based on strain gradient finite element method. Chinese Journal of Solid Mechanics. 35(5), 441-450.
[31] Li, Z., Zhu, T. (2016) Continuum modeling of thermal transport in superlattices and layered materials for new energy materials. Acta Physica Sinica. 65(11), 1-9.
[32] Li, C., Xiao, J., Guo, T., Fan, S., Jin, W. (2015) Large Deflection Mechanical Characteristics of Graphene Films. Journal of Mechanical Engineering. 6, 87-92.
[33] Xiao, J., Dong, P., Guo, C. (2001) Study and practice on producing high grade graphite products by using vibrating mill. Coal Technology. 20(5), 58-59.
[34] Wang, L. (2015) Design and Dynamic Characteristic Analysis of New Tooth Roller Chain Drive. Journal of Mechanical Transmission. 39(1), 92-95+110.
[35] Fan, P., Kou, B., Li, Z. (2014) Simulation research on meshing impact of chain drive based on ADAMS. Mining and Processing Equipment. 12, 113-116.
[36] Zhang, J., Hu, S. (2017) Chain Conveying System Analysis and Simulation of 30t/h Aluminum Ingot Continuous Casting Machine. Machine Building and Automation. 46(3), 100-102.

Received: **27.12.2019**
Accepted: **31.01.2020**

CORRESPONDING AUTHOR

Wei Jiang
School of Mechatronic Engineering,
China University of Mining and Technology,
Xuzhou 221116 – China

e-mail: 474972786@qq.com

© by PSP Volume 29 – No. 04A/2020 pages 3201-3211 Fresenius Environmental Bulletin

STUDY ON WATERFLOODING MODEL OF FRACTURED GLUTENITE RESERVOIR - TAKING THE LOWER WUERHE FORMATION IN THE EIGHTH AREA OF KARAMAY OILFIELD AS AN EXAMPLE

Yangzhi Shi[1,2], Weifeng Li[1,2,*], Xiaojing Wang[3], Jie Zhang[3]

[1]Key Laboratory of Exploration Technologies for Oil and Gas Resources, Ministry of Education, Yangtze University, Wuhan 430100, China
[2]School of Geosciences, Yangtze University, Wuhan 430100, China
[3]Xinjiang Oilfield Exploration and Development Research Institute, Karamay 834000, China

ABSTRACT

The lower Wuerhe Formation reservoir in the eighth area of Karamay Oilfield is a fractured thick conglomerate reservoir with low-porosity and ultra-low permeability. The development of this reservoir has always encountered problems such as inconsistency of injection and production, and ineffectiveness of water in oil wells. Fractures have a great impact on oil well development. Based on geological research, by starting from the fracture development degree of a single well and its corresponding water seeing with the combination of the corresponding relationship between injection and production of typical well patterns in fractured and non-fractured areas, the author established three water flooding modes: longitudinal water flooding, mixed water flooding and flat-water flooding. The research shows that the fracture development area is dominated by longitudinal water flooding and oil wells are liable to form fracture water channeling. The medium fracture development zone is dominated by plane water flooding, supplemented by vertical water flooding, that is, mixed water flooding, and oil wells have obvious results. The areas with no fractures developed shows the a planar waterflood, but the oil wells are relatively slow to take effect. The research results can provide a basis for the improvement of subsequent injection-production correspondence.

KEYWORDS:
Fractured reservoir, glutenite, water flooding model, lower Wuerhe Formation, Karamay oilfield

INTRODUCTION

The Lower Wuerhe Formation glutenite reservoir in the eighth area of Karamay Oilfield is one of the most potential blocks in the northwestern margin of the Junggar Basin with relatively large geological reserves [1-3]. Since the reservoir was developed by water injection in 1979, during the four infill adjustments, the problems of reduced injection-production correspondence and large reservoir decline have become more serious, and the effect of water injection development has not been significantly improved. Based on the control of faults and sedimentary favorable facies belts [4-7], it is considered that the difference in microscopic pore structure of the reservoir is the key factor affecting the reservoirs in the study area [8]. The reservoirs are mainly connected by fractures, and water injection is mainly propagated along the east-west fracture. From the perspective of the seepage mechanism, some scholars have clearly identified water flooding and oil recovery as the main technology for the development of the study area [9-10]. More and more scholars have gradually realized that the different sedimentary genesis of sand bodies is the main factor that affects reservoir connectivity and reservoir injection-production correspondence, and the development of fractures greatly affects the connectivity of reservoirs [11-13]. However, these studies did not analyze the water flooding model of the reservoir under the above geological conditions in detail. Therefore, based on the analysis of glutenite reservoirs, combining the longitudinal and planar distribution of fractures, the characteristics of water seepage and water flooding in typical fractured and non-fractured areas needs to be explored [14], and finally water flooding mode for fractured glutenite reservoirs needs to be established which can be used to guide the later adjustment of water flooding strategy and waterflooding development of similar reservoirs.

RESEARCH AREA AND METHODS

The reservoir of the Lower Wuerhe Formation in the eighth area is located in the lower plate of the southern Baijiantan fault of the Yuanke-Wuniyan fault in the northwestern margin of the Junggar Basin (Figure 1). The conglomerate deposits are divided into 5 sections P_2w_5、P_2w_4、P_2w_3、P_2w_2

and P_2w_1 from bottom to top. The reservoir has strong heterogeneity with porosity of 11.0% and horizontal permeability of 1.2mD. The fractures are relatively developed in this reservoir. The effective fractures in this reservoir are mainly high-angle fractures and straight split fractures, which indicates that this reservoir is a typical fractured reservoir with low porosity and ultra-low permeability.

Geological Features. (1) Characteristics of Glutenite Reservoirs. In the study area, a set of sedimentary system of fan-regressive fan delta is developed, and its lithology is mainly conglomerate. According to different genetic types, glutenite is divided into three types: traction flow glutenite, transition flow glutenite, and gravity flow glutenite.

The physical properties and oil-bearing properties of sand bodies with different causes are quite different [15-16]. By analyzing the porosity and permeability of 1494 samples, the average porosity of sandstone is 11.85%, and the average permeability is 0.44mD. The porosity of traction flow conglomerate is 11.31%, and the average permeability is 11.78mD. %. The average porosity of transitional glutenite is 9.31%, and the average permeability is 0.15mD. The average porosity of gravity flow glutenite is 8.21%, and the average permeability is 0.01mD. In addition, from the perspective of oiliness, the traction conglomerate core has significantly higher oil content than other lithologies, followed by transitional flow, and gravity flow glutenite has the worst oil content (Figure 2).

In summary, traction flow glutenite has the best physical properties and oil content. Its content of impurities and interstitial material is less than that of transition type glutenite and gravity flow glutenite. Gravity flow glutenite has the worst physical properties and oil-bearing properties, as well as the highest content of impurities and interstitials. From the perspective of pore types, the proportion of residual intergranular pores is also low in traction flow glutenite to transitional type glutenite and gravitational flow glutenite. Under the circumstances, gravity flow glutenite can be regarded as non-reservoir. Therefore, different lithologies are the fundamental factors that determine the differences of reservoirs.

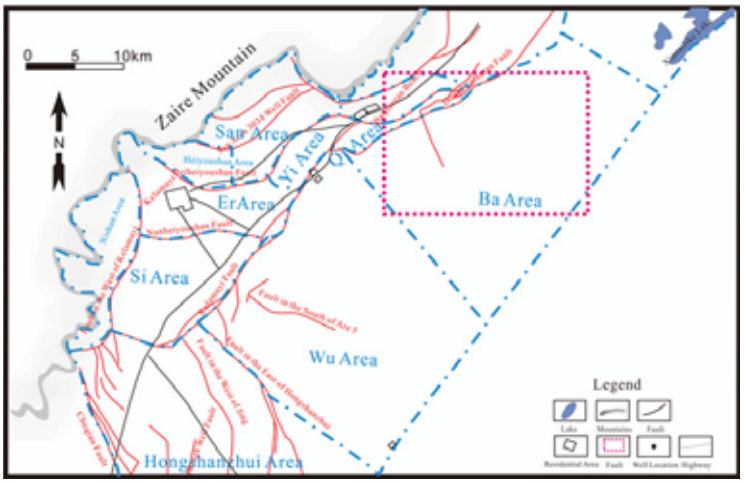

FIGURE 1
Geographical map of the eight districts of Karamay Oilfield

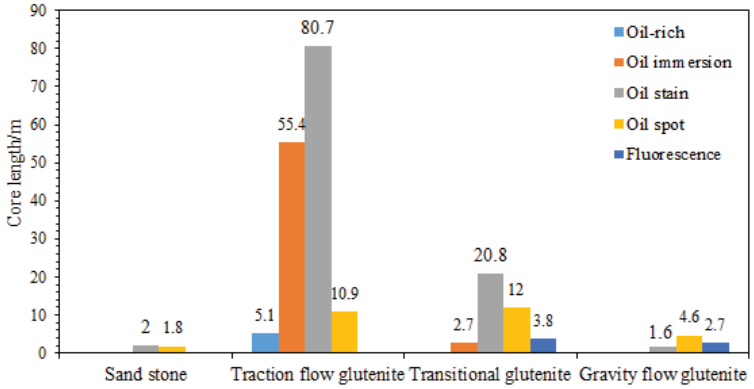

FIGURE 2
Relationship between lithology and oil-bearing properties of the Wuerhe Formation in the eighth area

(2) Characteristics and Distribution of Fractures. From the perspective of fracture types and occurrences of core development, natural fractures in the Lower Wuerhe Formation are relatively developed, mainly structural high-angle fractures and straight split fractures related to tectonic stress [17-18]. Based on core observation, combined with imaging logging and conventional logging analysis, the longitudinal fractures in the study area are mainly developed in P_2w_5, P_2w_4 and P_2w_3. Fractures are hardly developed in P_2w_2 and P_2w_1. In the plane, the fractures are mainly concentrated parallel to the west and faults in the northwest have a strip-shaped distribution.

In order to clarify the degree of fracture development and its effect on water flooding, fractures are divided into three types according to the ratio of the length of the fracture's longitudinal extension to the thickness of the stratum: (1) well developed fractures: the fracture section of the well accounts for more than 1/3 of the layer thickness; (2) Moderately developed fractures: Fracture sections account for 1/10-1/3 of the layer thickness; (3) non-developed fractures: no fractures or well fracture sections account for less than 1/10 of the layer thickness. According to the definition of fracture development degree, the corresponding fracture development degree of oil wells in the whole area was classified, and the planar distribution characteristics of fracture development degree were clarified (Figure 3).

Methods. In this study, we combined the fractures derived from the loggings and the water injection and production data of the wells to study the waterflooding model of fractured glutenite reservoir.

RESULTS AND DISCUSSION

Relationship Between Fracture Characteristics and Water Seepage in a Single Well. For conventional reservoirs, during the process of water injection development, only the traction flow glutenite or transitional flow glutenite will show a better injection-production correspondence and form a better development [19-21]. In fractured reservoirs, due to the degree of fracture development, the water seepage characteristics are quite different, and the mechanism is not clear. Therefore, the relationship between water well and water efficiency of oil wells corresponding to different fracture development levels is analyzed.

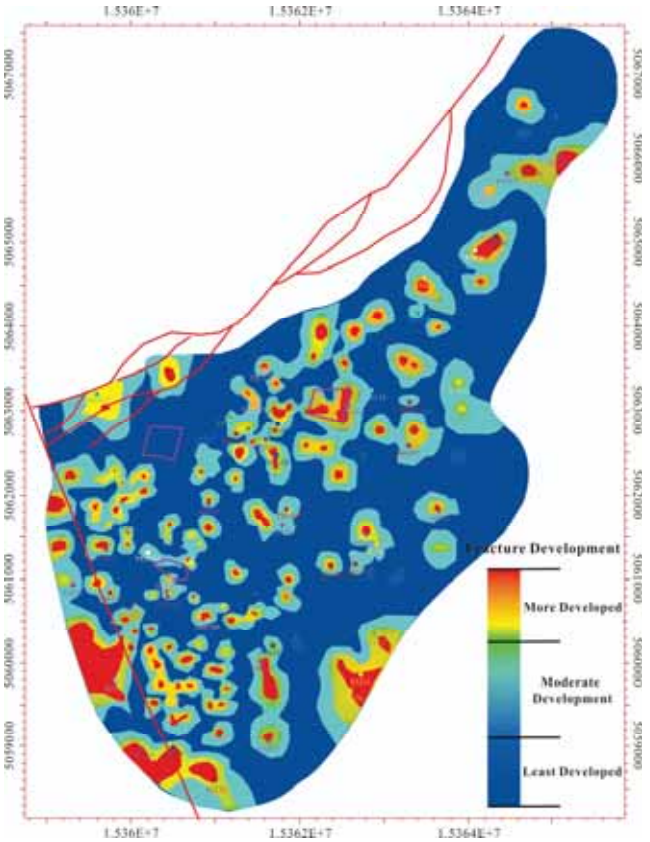

FIGURE 3
Plane distribution of fracture development in oil wells in the study area

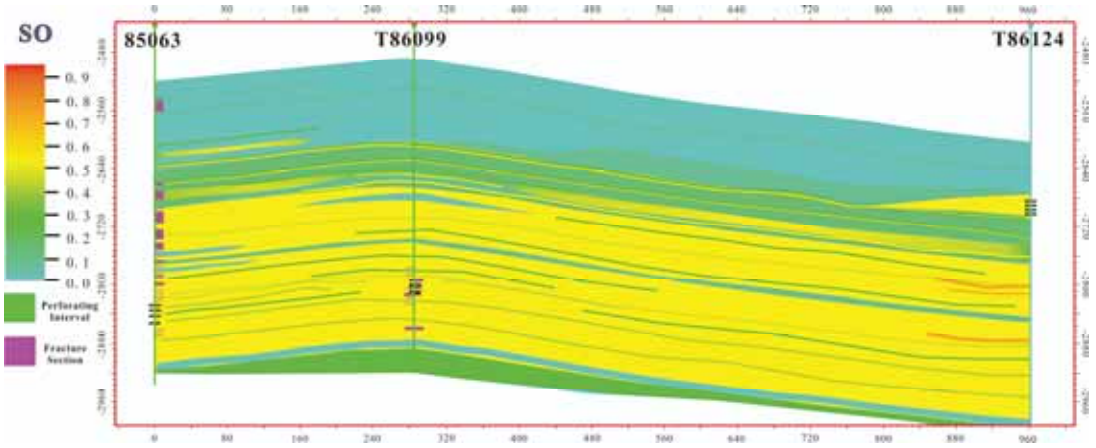

FIGURE 4
Typical wells with single fractures

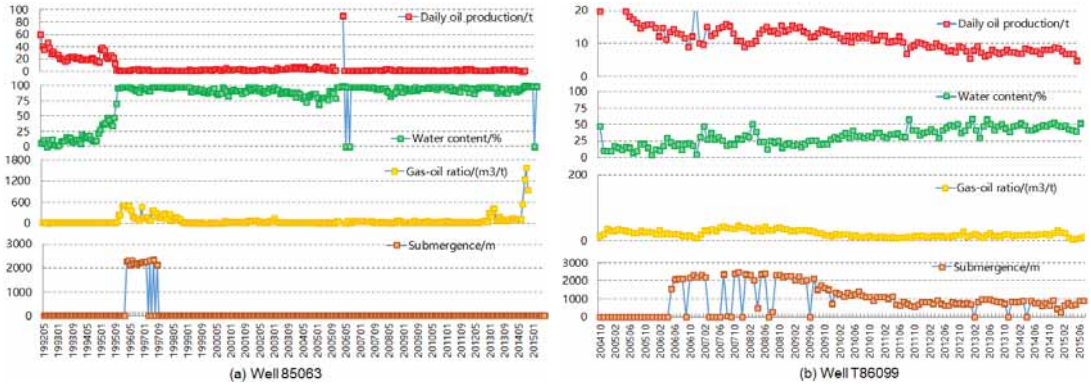

FIGURE 5
Comprehensive dynamic curve of test well

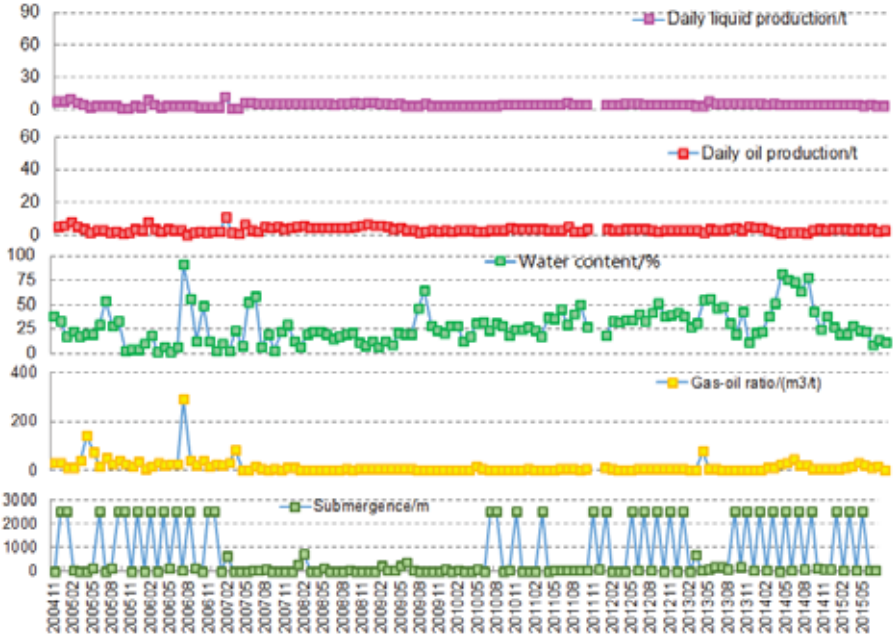

FIGURE 6
Comprehensive dynamic curve of test well T86124

As shown in Figure 4, three typical wells were selected. fractures well developed in Well 85063 and moderately developed fractures in Well T86099. There were no fractures in Well T86124. Reservoir well sections were dominated by traction flow conglomerate and transitional flow conglomerate.

The fracture of Well 85063 is developed. After the oil well was put into production, the oil production decreased rapidly, and the water cut rose rapidly until it was flooded, showing the fracture channeling characteristics (Figure 5(a)). Well T86099 has moderately developed fractures (Figure 5(b)). Soon after the oil well was put into production, the water injection effect of nearby wells was seen. The oil production of oil wells rebounded and remained stable, and the oil production was high. The water content was moderate, and the performance of water injection was better. (Figure 6).

Well T86124 does not develop fractures. After the oil well is put into production, the oil production is stable, but the fluid production level and oil production level are low, indicating that the oil well has seen the water injection effect of nearby wells, but the effect is weak or slow, and the performance of water injection is affected by weak water injection (Figure 6).

By analyzing all the wells in the area, it can be seen that oil wells with well-developed fractures are characterized by water channeling characteristics of fractures that do not see water, and oil wells with moderately developed fractures are characterized by good water seeing characteristics [22-23]. For the oil wells with no fractures, although water injection effects can be seen, the oil wells have weak effectiveness.

Water Flooding Characteristics of Typical Well Groups. The reservoir well sections are mainly traction flow glutenite and transitional flow glutenite. A single well with different fractures shows large difference in water development and effectiveness. On this basis, we need continue to explore the water flooding in different levels of fracture development.

(1) Water Flooding Characteristics in Fractured Areas. In the anti-nine-point well pattern system centered on Well 8630A, fractures in most wells are relatively developed while fractures in T86100 are not developed (Figure 7, Figure 8).

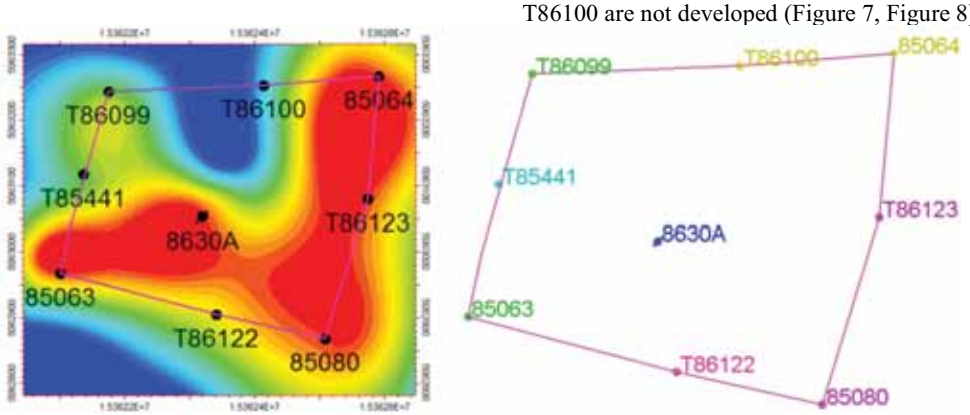

FIGURE 7
Fracture development degree and well location map of fractured well group.

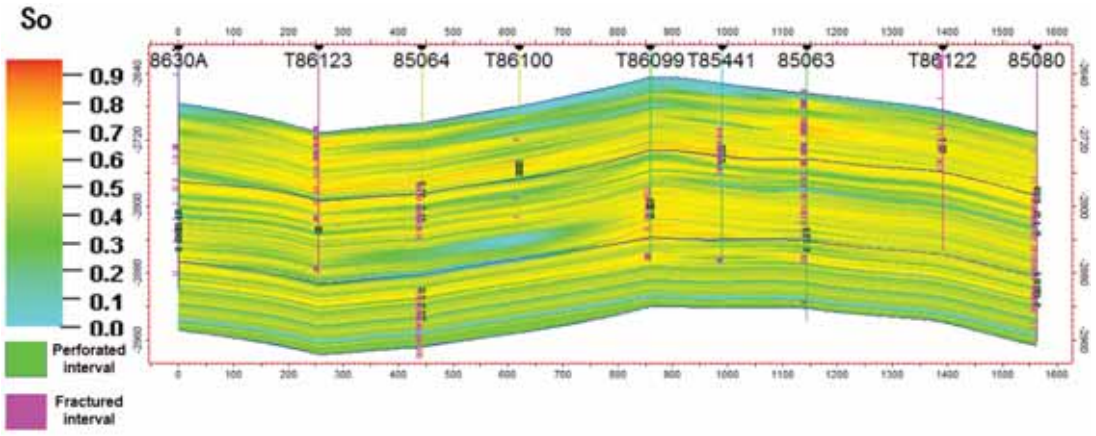

FIGURE 8
Cross-section of fractured well group.

The data of Well 85064, T86123, 85080, T86122, and 85063 all show ineffective water and fracture water channeling characteristics. Well T86099, T86100, and T85441 show water injection effects, forming a good injection-production correspondence relationship. The Well 85080 and its corresponding injection Well 8630A and 8517 are mainly traction flow glutenite and transitional flow glutenite. They have good injection-production connectivity and show longitudinal water flooding. However, after the oil production increases, it quickly falls back, the water content rises, and the fractures water channeling is obvious (Figure 9).

(2) Water Flooding Characteristics in the Area with Moderately Developed Fractures. The reverse-slope seven-point well pattern system centered on Well 8638A shows that fractures are moderately developed in general (Figure 10, Figure 11).

Among the 6 oil wells in this well group, the Well 85075, 85075, T86763, T85574, TD86761, T85554 and T85495 all show dynamic performance and good water injection effects. A good injection-production correspondence relationship has been formed. Well T85554 and its corresponding injection well, T85554, are mainly traction flow conglomerate, with good injection-production correspondence, which are represented by plane water flooding and longitudinal water flooding (Figure 12).

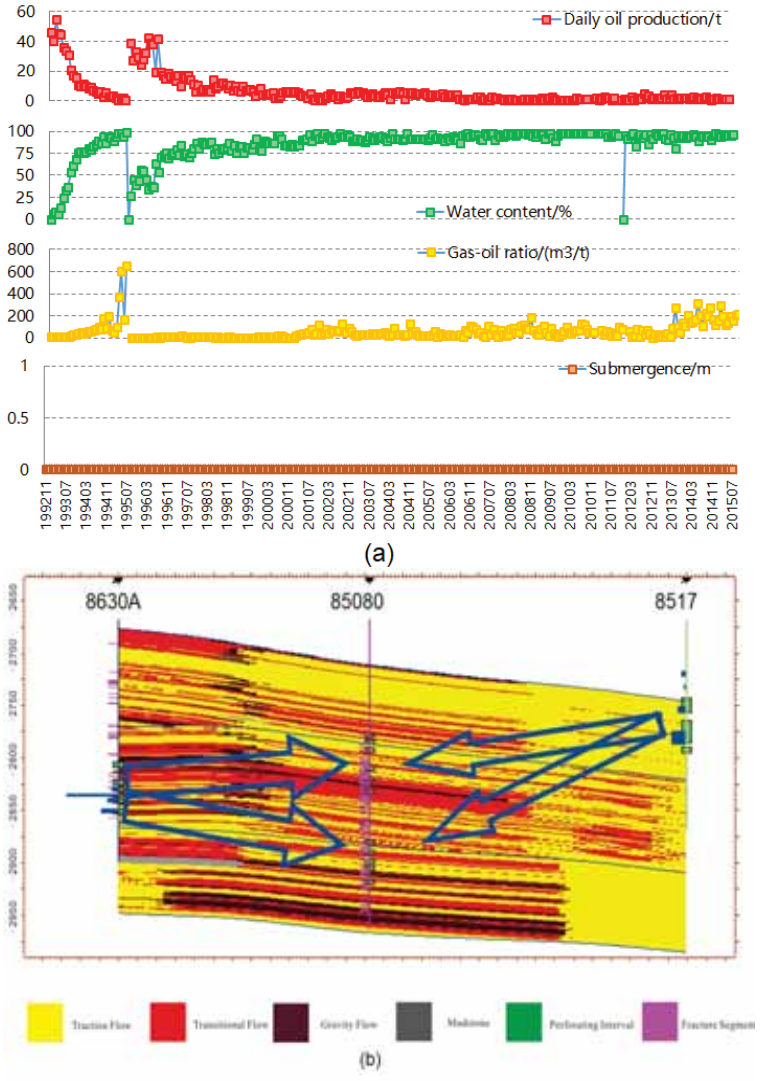

FIGURE 9
Comprehensive dynamic curve, injection-production corresponding well profile and water drive direction of well 85080.
Notes: (a) Comprehensive dynamic curve, (b) injection-production corresponding well profile and water drive direction

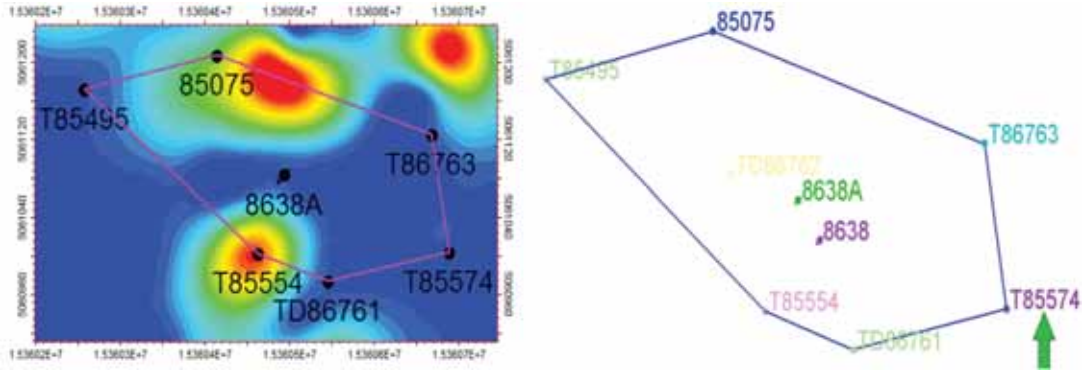

FIGURE 10
Fracture development degree and well location map.

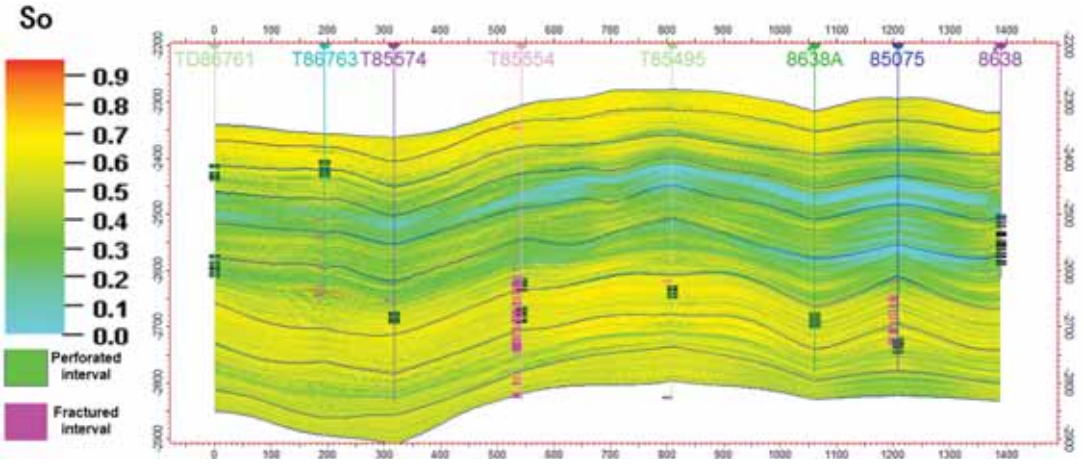

FIGURE 11
Cross-well section of a moderately developed fractured well group.

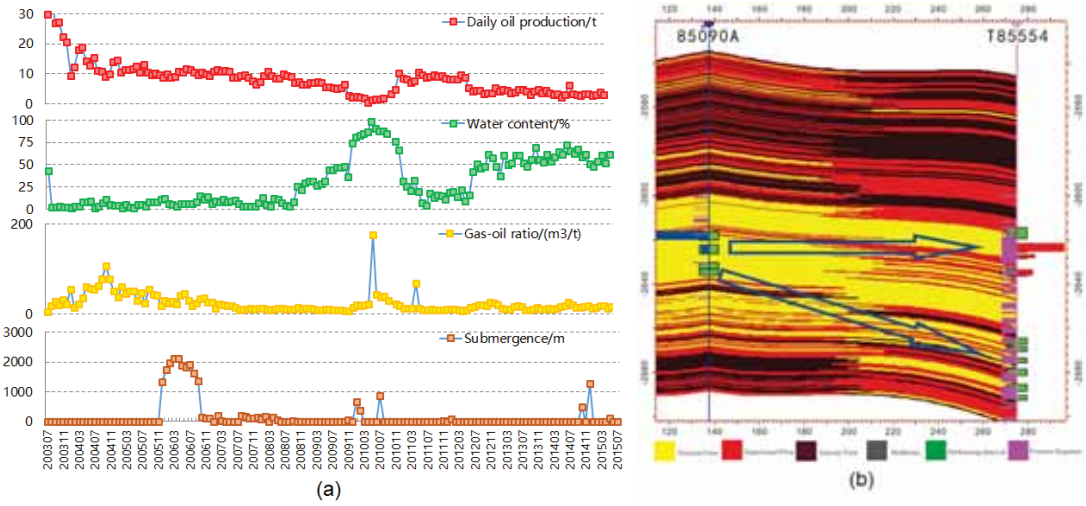

FIGURE 12
Comprehensive dynamic curve, injection-production corresponding well profile and water drive direction of Well T85554.

Notes: (a) Comprehensive dynamic curve, (b) injection-production corresponding well profile and water drive direction.

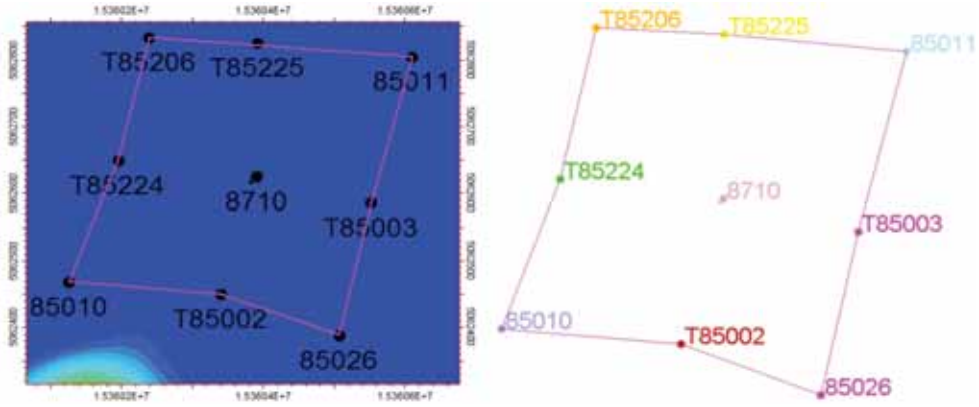

FIGURE 13
Fracture development degree and well location map of fracture non-developed well group.

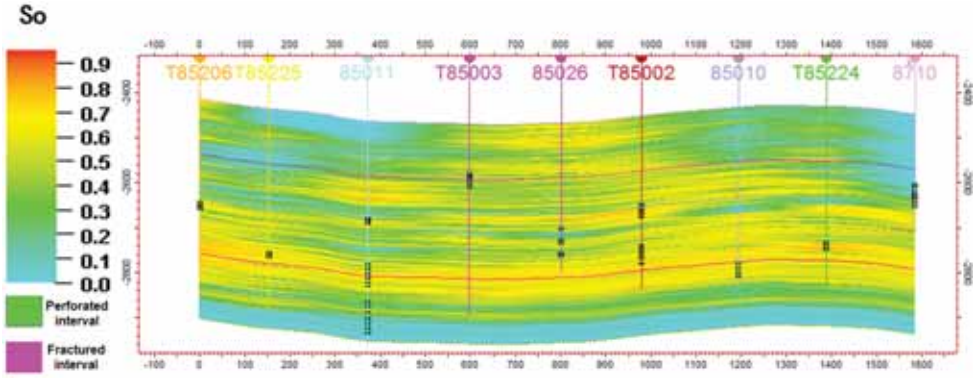

FIGURE 14
Cross-well section of fracture non-developed well group.

(3) Characteristics of Water Flooding in Unfractured Areas. In the anti-nine-point well pattern system centered on Well 8710, there are no fractures in the single well in the well group (Figure 13 and Figure 14).

Of the 8 oil wells in this well group, Well T85206, T85225, 85011, T85003, T85022, and T85224 showed no water injection response, that is, the oil well did not receive the water injection effect from the water injection well, showing low production and low water content. Well 85026 and 85010 show dynamic performance but no water, but the fluid volume and oil volume of the oil well are low, and the water cut is low. Even if the oil well has a water injection response, the effect is very slow [24-25]. Although it can form a good injection-production correspondence relationship, the oil well is not effective. The Well 85010 and its corresponding injection well T86028 both mainly develop traction flow conglomerate, which corresponds to injection and production and shows effective plane water flooding (Figure 15).

In summary, the fracture development area generally exhibits a longitudinal water flooding pattern, that is, the fracture development area is prone to form longitudinal water flooding, and it is not easy to form an effective injection-production response [26-28]. Oil well performance is mostly characterized by fracture water channeling characteristics. The injection-production correspondence is not suitable for water injection development. The area of moderately developed fractures is dominated by plane water flooding as a whole, supplemented by longitudinal water flooding, that is, mixed water flooding mode. The oil wells in the well groups have all seen good water injection effects, indicating that there are certain fractures in the reservoir, which is conducive to establishing the correspondence between oil and water well injection and production, and improving the water injection development effect of the reservoir [29-33]. The non-developed fracture area generally shows a plane water flooding pattern, and the injection-production correspondence of oil-water wells is good. However, due to the lack of necessary fracture communication, oil wells see slow water-injection effects, which delays the effectiveness of injection-production correspondence. The effect of water injection in this type of reservoir is mainly controlled by the origin of the sand body. Such zones can form a relatively perfect injection-production correspondence, but the oil wells have a slower effect and can be used for water injection development.

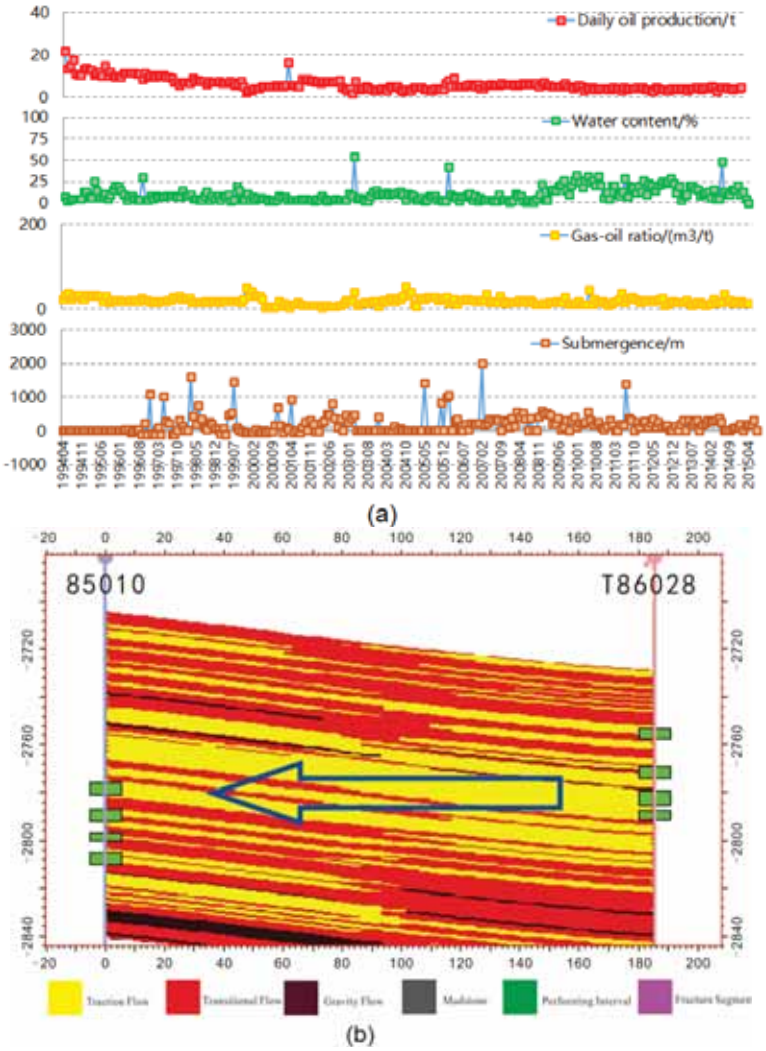

FIGURE 15
Comprehensive dynamic curve, injection-production corresponding well profile and water drive direction of well 85010.

Notes: (a) Comprehensive dynamic curve, (b) injection-production corresponding well profile and water drive direction.

CONCLUSIONS

(1) The lithology of different genesis has great differences in porosity, permeability, and oiliness. According to the different genesis of lithology, the Lower Wuerhe Formation glutenite reservoir in the eight districts can be divided into traction flow glutenite, transitional flow gluten and gravity flow glutenite. Traction flow glutenite has the best in physical properties and oil content while gravity flow glutenite is the worst. The development of fractures in the study area is mainly concentrated in faults parallel to the west and northwest, showing a strip-shaped distribution.

(2) Through the analysis of typical single wells and well groups, it is found that single wells and well groups with fractures are prone to water channeling. Single wells and well groups with moderate fractures show good water injection and effective water seeing characteristics. Single wells and well groups with non-developed fractures show weak results.

(3) For the fractured glutenite reservoirs of the Upper Wuerhe Formation in the eighth district, three types of water flooding modes have been established. The water flooding mode of the fracture development areas is a longitudinal water flooding mode. The area with moderate fractures is a mixed waterflood mode with plane waterflood as the main type. The area where fractures are not developed, that is, the area mainly dominated by reservoir matrix pore seepage, and the water flooding mode is a flat water flooding mode.

ACKNOWLEDGEMENTS

The authors would like to show thanks to the techniques who have helped this research and the authors of the references.

REFERENCES

[1] Yuan, S., Qiu, Z., Zhang, Y., Deng, S., Li, T, Zeng, Y. (2014) Probe into Xiawuerhe Reservoir controlling factors in No. eight area of Kalamay Oilfield. Xinjiang Oil and Gas. 10(01), 7-9+18+5.

[2] Mei, H., Chen, Y., Gong, F., Chen, K., Liu, M., Hu,Z., Ji, X., Mi, M. (2014) Analysis of reservoir control factors for Xiawuerhe formation of Permian in northwestern margin of Junggar Basin. Journal of Xi'an University of Science and Technology. 34(04), 420-425.

[3] Li, X., Xiao, C., Yuan, S., Xu, H., Dong, X., Hou, W. (2015) Study of percolation mechanism of extra lower-permeability conglomerate reservoir-taking Wuerhe reservoir of NO.8 district of Karamay oil field as an example. Xinjiang Oil and Gas. 11(1), 37-41.

[4] Ding, Z., Liu, Y., Zhang, Y., Ao, K. (2012) A quantitative 3D physical simulation method of waterflooding in fractured reservoirs. Petroleum Science and Technology. 30(12), 1250-1261.

[5] Li, M., Lv, D., Kou, G., Li, Z., Xia, H. (2012) Analysis of Waterflooding Dash Characteristics of Fractured Reservoir with Low Permeability. Journal of Jianghan Petroleum University of Staff and Workers. 25(02), 1-3+7.

[6] Zekri, A., Reyadh, A. (2003) Microbial and waterflooding of fractured carbonate rocks: an experimental approach. Liquid Fuels Technology. 21(1-2), 315-331.

[7] Mazo, A., Khamidullin, M., Potashev, K. (2016) Waterflooding simulation of reservoir containing horizontal well stimulated by multistage hydraulic fracturing. IOP Conference Series: Materials Science and Engineering. 158(1), 012053.

[8] Pang, D. (2015) Sedimentary genesis of sand-conglomerate reservoir and its control effect on reservoir properties: A case study of the lower Urho Formation in Ma 2 well block of Mahu Depression. Lithologic Reservoirs. 27(05), 149-154.

[9] Zhao, H., Li, W., Zhu, Y., Wang, X., Han, D., Ren, T., Feng, X. (2017) Characteristics of sandy conglomerates reservoir and corresponding relation of injection and production: Take the lower Wuerhe formation of permian in the 8th area of Karamay oilfield as an example. China Sciencepaper. 12(09), 1070-1078.

[10] Huang, X., Li, T., Gao, H., Zhao, J., Wang, C. (2019) Comparison of SO2 with CO2 for Enhancing Shale-hydrocarbon Recovery using Low-field Nuclear Magnetic Resonance. Fuel. 245, 563-569.

[11] Huang, X., Li, A., Li, X., Liu, Y. (2019) Influence of Typical Core Minerals on Tight Oil Recovery during CO_2 Flooding using NMR Technique. Energy and Fuels. 33(8), 7147-7154.

[12] Yin, G., Xu, H., Zhang, G., Tao, W., Zhang, B. (2011) Fractures Characteristics of Conglomerate Reservoirs and Their Influence on Development Effectiveness: A Case Study of the Urho Reservoir of NO.8 District of Karamay Oil Field. Science and Technology Review. 29(15), 46-51.

[13] Wang, L. (2005) Research on Development Technology Of Low-Permeability Reservoirs In Wangguang and Huangchang Oilfield. Beijing: China University of Geosciences (Dissertation).

[14] Yuan, X. (2016) Research of Conglomerate Reservoir Characteristics of Triassic Baikouquan Formation in Mabei Slope. Jingzhou: Yangtze University (Dissertation).

[15] Ghasemi, M., Astutik, W., Alavian, S., Whitson, C., Suicmez, V. (2018) Experimental and numerical investigation of tertiary-CO_2 flooding in a fractured chalk reservoir. Journal of Petroleum Science and Engineering. 164, 485-500.

[16] Ghasemi, M., Astutik, W., Alavian, S., Whitson, C., Suicmez, V. (2018) Impact of pressure on tertiary-CO_2 flooding in a fractured chalk reservoir. Journal of Petroleum Science and Engineering. 167, 406-417.

[17] Alhuraishawy, A., Sun, X., Bai, B., Wei, M., Imqam, A. (2018) Areal sweep efficiency improvement by integrating preformed particle gel and low salinity water flooding in fractured reservoirs. Fuel. 221, 380-392.

[18] Harimi, B., Masihi, M., Mirzaei-Paiaman, A., Hamidpour, E. (2018) Experimental study of dynamic imbibition during water flooding of naturally fractured reservoirs. Journal of Petroleum Science and Engineering. 174, 1-13.

[19] Gao, D., Ye, J., Wang, T., Zhao, L., Pan, S., Sun, Z. (2018) An independent fracturing water-flooding development method for shallow low-permeability thin oil layers in multi-layer sandstone reservoirs. Journal of Petroleum Science and Engineering. 167, 877-889.

[20] Wang, H., Liu, X., Gai, C. (2014) A new method to improve waterflood effect analysis in Karamay Glutenite Reservoir. Applied Mechanics and Materials. 641-642, 458-461.

[21] Yuan, D., Hou, J., Song, Z., Wang, Y., Luo, M., Zheng, Z. (2015) Residual oil distribution characteristic of fractured-cavity carbonate reservoir after water flooding and enhanced oil recovery by N_2 flooding of fractured-cavity carbonate reservoir. Journal of Petroleum Science and Engineering. 129, 15-22.
[22] Yin, S., Zhao, J., Wu, Z., Ding, W. (2018) Strain energy density distribution of a tight gas sandstone reservoir in a low-amplitude tectonic zone and its effect on gas well productivity: A 3D FEM study. Journal of Petroleum Science and Engineering. 170(6), 1-16.
[23] Gu, S., Liu, Y., Chen, Z., Ma, C. (2014) A method for evaluation of water flooding performance in fractured reservoirs. Journal of Petroleum Science and Engineering. 120, 130-140.
[24] Alhuraishawy, A., Bai, B., Imqam, A., Wei, M. (2018) Experimental study of combining low salinity water flooding and preformed particle gel to enhance oil recovery for fractured carbonate reservoirs. 214, 342-350.
[25] Ghasemi, M., Suicmez, V. (2019) Upscaling of CO_2 injection in a fractured oil reservoir. Journal of Natural Gas Science and Engineering. 63, 70-84.
[26] Kakati, A., Sangwai, J. (2018) Wettability alteration of mineral surface during low-salinity water flooding: role of salt type, pure alkanes, and model oils containing polar components. Energy and Fuels. 32(3), 3127-3137.
[27] Arimi, S., Gandomkar, A. (2019) Influence of electrical surface charges on thermodynamics of wettability during low salinity water flooding on limestone reservoirs. Journal of Molecular Liquids. 277, 132-141.
[28] Liu, H., Pang, J., Yu, X. (2012) A Mathematical Model for Natural Fracture Evolution in Water-flooding Oil Reservoir. Energy Procedia. 16, 1348-1356.
[29] Jiao, F. (2019) Practice and knowledge of volumetric development of deep fractured-vuggy carbonate reservoirs in Tarim Basin, NW China. Petroleum Exploration and Development. 46(3), 576-582.
[30] Sheng, G., Su, Y., Wang, W. (2019) A new fractal approach for describing induced-fracture porosity/permeability/compressibility in stimulated unconventional reservoirs. Journal of Petroleum Science and Engineering. 179, 855-866.
[31] Sheng, G., Zhao, H., Su, Y., Javadpour, F., Wang, C., Zhou, Y., Liu, J., Wang, H. (2020) An analytical model to couple gas storage and transport capacity in organic matter with noncircular pores. 268, 117288.
[32] Wang, J., Liu, H., Ning, Z., Zhang, H., Hong, C. (2014) Experiments on water flooding in fractured-vuggy cells in fractured-vuggy reservoirs. Petroleum Exploration and Development. 41(1), 74-81.
[33] Zhang, Y., Gao, M., You, Q., Fan, H., Li, W., Liu, Y., Fang, J., Zhao, G., Jin, Z., Dai, C. (2019). Smart mobility control agent for enhanced oil recovery during co2 flooding in ultra-low permeability reservoirs. Fuel. 241, 442-450.

Received: **29.12.2019**
Accepted: **30.01.2020**

CORRESPONDING AUTHOR

Weifeng Li
Key Laboratory of Exploration Technologies for Oil and Gas Resources,
Ministry of Education, Yangtze University,
Wuhan 430100, China

e-mail: 969070520@qq.com

© by PSP Volume 29 – No. 04A/2020 pages 3212-3222 Fresenius Environmental Bulletin

MICROPORE STRUCTURE CHARACTERISTICS OF TIGHT OIL RESERVOIRS IN THE YANCHANG FORMATION IN THE ORDOS BASIN, CHINA

Tianjin Zhang[1], Gang Zhang[2,*], Lushe Zhang[3]

[1]College of Petrol and Environmental Engineering, Yan'an University, Yan'an 716000, China
[2]Yan Chang Petroleum. Co.Ltd., ,DinBian Oilfield, Yulin 718600, China
[3]Yan Chang Petroleum. Co.Ltd., ,ZiChang Oilfield, Yan'an 717399, China

ABSTRACT

Pore structure is an important factor affecting the reserve and recovery of tight reservoir. In this paper, taking shale samples from the Triassic Chang 7 Member in the Ordos Basin as examples, the porosity, pore type, and pore size distribution of tight oil reservoirs were studied using scanning electron microscopy, high-pressure mercury tests, and CO_2 and N_2 adsorption methods. The key factors affecting the pore structure of shale were discussed. The results show that the porosity of the Late Triassic shale in the Ordos region is 1.30-13.37%, with an average of 4.56%. The types of shale micropores are intergranular pores, organic pores and intragranular pores. Organic pores are the main type of pores. The shale mainly has micropores (<2 nm) and mesopores (2-50 nm). The total shale surface area accounts for 94.3% of the total specific surface area, and its pore size is mainly distributed in three intervals: 0.4-0.7 nm, 3-10 nm, and > 50 nm. Shale pore structure is affected by shale organic carbon content, organic matter maturity, and mineral content. As shale porosity and pore volume increase, its maturity R_o increases and clay mineral content increases, but shale porosity and pore volume gradually decrease.

KEYWORDS:
Tight oil reservoir, pore structure, pore type, pore size distribution, Late Triassic, Ordos Basin

INTRODUCTION

Tight oil is oil and natural gas mainly found in tight sandstone and shale. The shale of the Yanchang Formation in the Ordos Basin is rich in tight oil [1]. Shale pore structure is an important factor affecting oil storage capacity and oil production [2-4]. Researchers around the world have done a lot of work on reservoir tightness, pore classification, and reservoir evaluation [5-9], but the classification scheme of reservoir tight pores has not been unified. Vallbaum et al. [10] proposed a simple shale pore classification scheme and classified shale pores into intergranular pores, intragranular pores and organic pores. Patwardhan et al. [11-12] separated the micropores and nanopores with a pore size of 0.75 μm in the study of North American Barnett shale pores. Zou et al. [13] systematically studied the shale nanoscale pore system by using field emission scanning electron microscope and nano-CT reconstruction technology. Ma et al. [13] pointed out that the smaller the pore diameter of the reservoir, the larger the specific surface area, and the stronger the ability to adsorb gas. Yang et al. [14] found a large amount of shale oil in the Yanchang Formation shale in southern Sichuan Basin. Previous studies [15-19] have shown that quantitative characterization of shale micro- and nano-scale pore structures is very important for assessing tight oil recovery.

The Ordos Basin is one of the important areas for the investigation and evaluation of the continental tight oil resources in northern China. In this area, the organic carbon content of the Late Triassic shale is high, and the type of organic matter is mainly type II. It is an over-mature organic shale with a wide distribution [20-21]. At present, many scholars are studying the pore characteristics of the Late Triassic shale in the Ordos Basin [22-24], but the research level is still very low. In this paper, taking shale samples from the Triassic Chang 7 Formation in the Ordos Basin as examples, the porosity, pore type, and pore size distribution of tight oil reservoirs were studied using scanning electron microscopy, high-pressure mercury tests, and CO_2 and N_2 adsorption methods. This research can provide scientific basis for the exploration and development of tight oil.

MATERIALS AND METHODS

The Ordos Basin is located at the southwestern end of the North China platform (Figure 1). In the early Paleozoic, terrestrial sediments such as carbonates, sandstones, mudstones and shales were mainly developed in the Ordos Basin. The thickness of the Chang 7 Member shale is about 30-110 m.

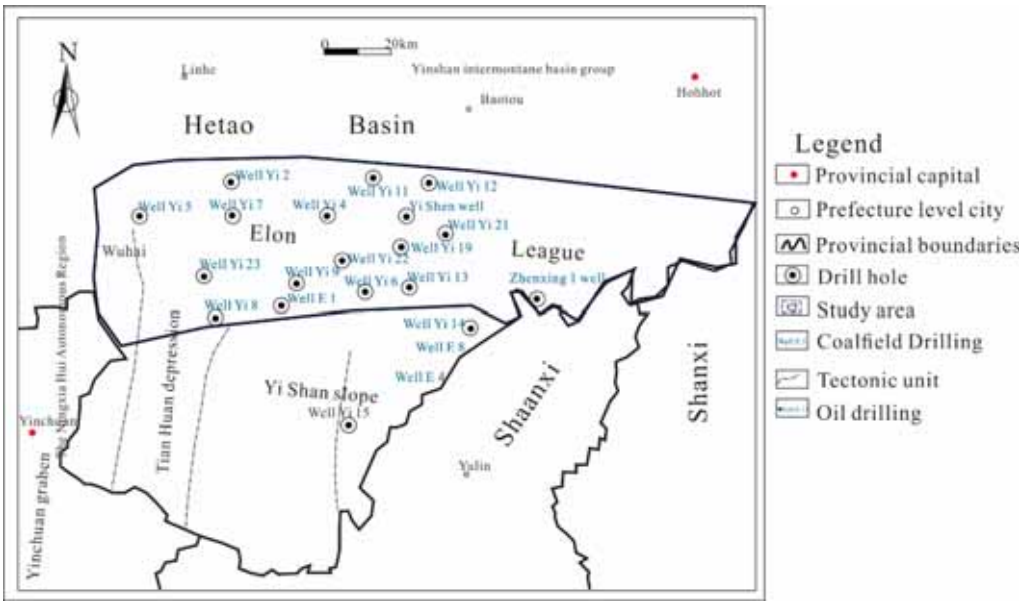

FIGURE 1
Location of Ordos Basin and distribution of drilling wells.

TABLE 1
Geochemical characteristics of the Late Triassic shale samples in the Ordos Basin.

No.	Interval	TOC (%)	R_o (%)	Whole rock mineral component content (%)							Brittle mineral content (%)
				Quartz	Feldspar	Calcite	Dolomite	Clay	Pyrite	Other	
Q5-1	T_3y	3.55	2.97	42.45	6.37	10.20	2.50	34.91	3.56	Microscale	61.52
Q5-2	T_3y	3.13	2.92	46.4	6.79	9.18	4.02	29.39	3.80	0.42	66.40
Q5-3	T_3y	2.19	2.89	33.47	10.2	3.99	0.55	49.32	2.46	Microscale	48.22
Q5-4	T_3y	0.85	2.79	29.94	6.48	3.21	1.52	57.25	1.32	0.28	41.15
Q5-5	T_3y	0.70	2.85	25.6	7.50	4.64	1.55	59.53	1.18	Microscale	39.29
Q5-6	T_3y	0.80	2.89	26.66	5.37	8.74	2.49	55.85	0.89	Microscale	43.26
Q4-1	T_3y	6.19	3.90	36.58	22.4	Microscale	5.45	29.01	5.60	1	64.39
Q4-2	T_3y	6.99	/	44.56	15.2	Microscale	6.34	28.92	4.49	0.48	66.11
Q4-3	T_3y	5.39	/	39.63	19.4	0.54	Microscale	32.37	3.99	4.1	59.54
Q4-4	T_3y	4.24	3.67	30.26	19.9	Microscale	1.83	42.36	4.44	1.23	51.97
Q4-5	T_3y	5.99	3.45	40.47	9.42	Microscale	Microscale	44.05	5.18	0.87	49.90
M-2	T_3y	6.80	2.43	49.20	6.43	Microscale	Microscale	36.63	2.90	4.81	55.67
M-3	T_3y	8.65	/	64.99	4.33	Microscale	Microscale	25.5	5.18	Microscale	69.32
M-5	T_3y	4.23	2.28	32.80	1.81	Microscale	Microscale	43.36	10.39	11.64	34.61
M-6	T_3y	2.09	/	54.78	1.31	Microscale	Microscale	43.53	Microscale	0.37	56.10
M-8	T_3y	5.60	/	46.89	2.67	Microscale	0.61	49.39	Microscale	0.44	50.17
M-9	T_3y	6.58	/	45.59	4.80	Microscale	0.82	48.48	Microscale	0.31	51.21
M-10	T_3y	4.87	2.31	58.97	2.07	Microscale	Microscale	35.83	2.97	0.16	61.04
M-11	T_3y	4.07	2.62	26.00	37.09	15.08	Microscale	14.99	Microscale	6.84	78.17
M-13	T_3y	6.25	/	54.86	5.42	0.91	0.36	34.77	3.68	Microscale	61.55
M-14	T_3y	2.15	2.41	51.86	1.00	Microscale	Microscale	45.92	0.44	0.79	52.86
M-15	T_3y	22.55	2.55	66.52	6.29	Microscale	Microscale	27.18	Microscale	Microscale	72.82
S-1	T_3y	15.8	2.35	38.83	2.14	Microscale	Microscale	56.93	0.65	1.44	40.97
S-2	T_3y	13.9	2.77	58.92	7.21	Microscale	Microscale	32.76	Microscale	1.11	66.13
S-3	T_3y	15.2	/	51.99	2.37	Microscale	Microscale	44.09	0.33	1.23	54.36
L-1	T_3y	9.42	2.44	64.04	8.06	Microscale	Microscale	23.61	4.30	Microscale	72.10

Notes: "R_o" indicates the measured terrestrial vitrinite reflectance value; "/" indicates that it is not detected; mineral component content data is obtained by X-ray diffraction analysis, and "microscale" indicates that the content is less than 0.1%.

The samples were collected from downhole cores (wells Q4 and Q5) and outcrop profiles (S, M, L profiles) in the Ordos Basin (Table 1). As shown in Table 1, the organic carbon content of the Chang 7 Member sandstone is 2.09-22.5%, and the maturity R_o is 2.28-3.90%. The mineral composition is mainly quartz, feldspar, clay, calcite and pyrite. The brittle mineral content is 34.61 - 78.17%, and the clay mineral content is 14.99 - 56.93%.

In this paper, scanning electron microscope (SEM) observations, high-pressure mercury injection tests, and CO_2 and N_2 adsorption experiments were performed. Scanning electron microscope analysis uses the Tescan VEGA II scanning elec-

tron microscope. In high-resolution mode, the maximum magnification is 100 000 times and the resolution is 3.0 nm / 30 kv. The He-Hg method was used to measure porosity on a QKY-ZN type porosity analyzer. The high-pressure mercury injection experiment was performed using Poremaster GT60 full-automatic porosity analyzer (mercury analyzer). The pore size measurement range is 0.0036 to 950 μm, and the pore size distribution of large pores (> 50 nm) is obtained using the Warborn equation. CO_2 and N_2 adsorption experiments were performed on Conta's NOVA4200e specific surface area and porosity analyzer. The specific surface area measurement range was greater than 0.01 m^2/g, and the pore size measurement range was 0.35 to 200 nm. The DFT model was used to calculate the mesopore pore volume, specific surface area and pore size distribution.

RESULTS AND DISCUSSION

Porosity Characteristics. Porosity is a general indicator of the degree of pore development, and the number of pores determines the amount of oil and gas in the reservoir. When the reservoir is dense, shale porosity is very important [25-26]. But as shale porosity increased from 0.5% to 4.2%, the free hydrocarbon content increased sharply from 5% to 50%.

The porosity distribution of the Late Triassic shale in the Ordos Basin ranges from 1.30% to 13.37%, with an average of 4.56%. Figure 2 shows that the porosity of the Chang 7 Member sandstone is mainly distributed between 1% and 7%, with an average of 5.3%. Among them, 2.5% are samples with porosity less than 1%, and 53.8% are samples with porosity distribution between 1-4%. Overall, the porosity of the Chang 7 Member sandstone is very low.

Micro-pore Type Characteristics. Scanning electron microscope (SEM) observations showed that various types of micron-sized pores existed in the Chang 7 shale samples in the Ordos area. Micropore types mainly include intra-particle pores and organic pores. Among the intergranular pores, intergranular pores and organic pores are the most developed, and they provide the main storage space for tight oils.

Intra-particle pores refer to the pores inside the shale mineral particles. Scanning electron microscopy has shown that transgranular pores are one of the most common pore types in the Late Triassic shale in the Ordos Basin. These pores are mainly distributed in detrital mineral crystals, such as quartz, feldspar and calcite, and usually appear as dissolved pores (Figure 3a).

Organic matter pores are pores formed in shale organic matter. Organic pores in the Late Triassic shale were relatively developed in the Ordos region. The pore types are mainly organic pores (Figure 3b) and diatom fossil pores (Figure 3c). In terms of pore characteristics, a large number of organic pores were observed under a microscope. It is a stomata formed during the production of organic hydrocarbons or other biological algae communities [9, 14]. The cross section of organic pores is irregular [7]. Compared with the organic pores of North American Barnet shale, the pore distribution of the Late Triassic shale in the Ordos area is wider.

Intergranular pores are pores between shale mineral particles or crystals. The Late Triassic shale in the Ordos Basin contains residual primary pores (Figure 3d), inter-mineral crystalline pores (Figure 3e) and mineral cast film pores (Figure 3f).

In addition, micro-fractures developed in the Late Triassic shale in the Ordos Basin. Microfractures are conducive to the storage and seepage of tight oil and are an important part of shale pore system [27].

In general, the shale of the Chang 7 Member of the Late Triassic in the Ordos Basin developed micro-pores of different genetic types. Micron-nanometer pores are widely distributed. Intergranular pores and organic pores are more developed and have better pore connectivity.

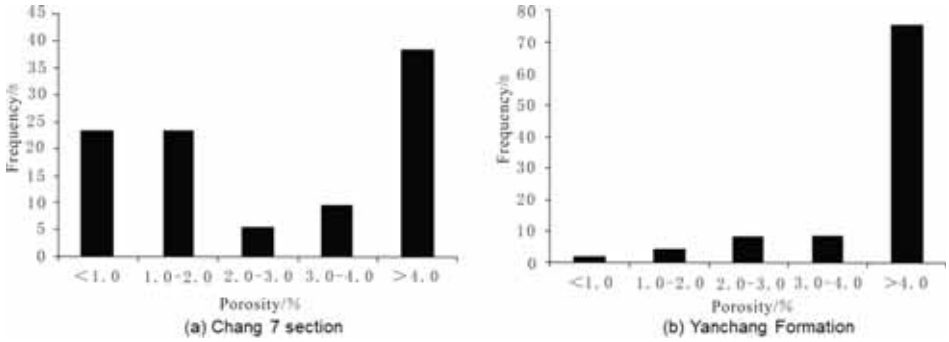

FIGURE 2
Histogram of porosity distribution of Late Triassic shale samples in Ordos Basin.

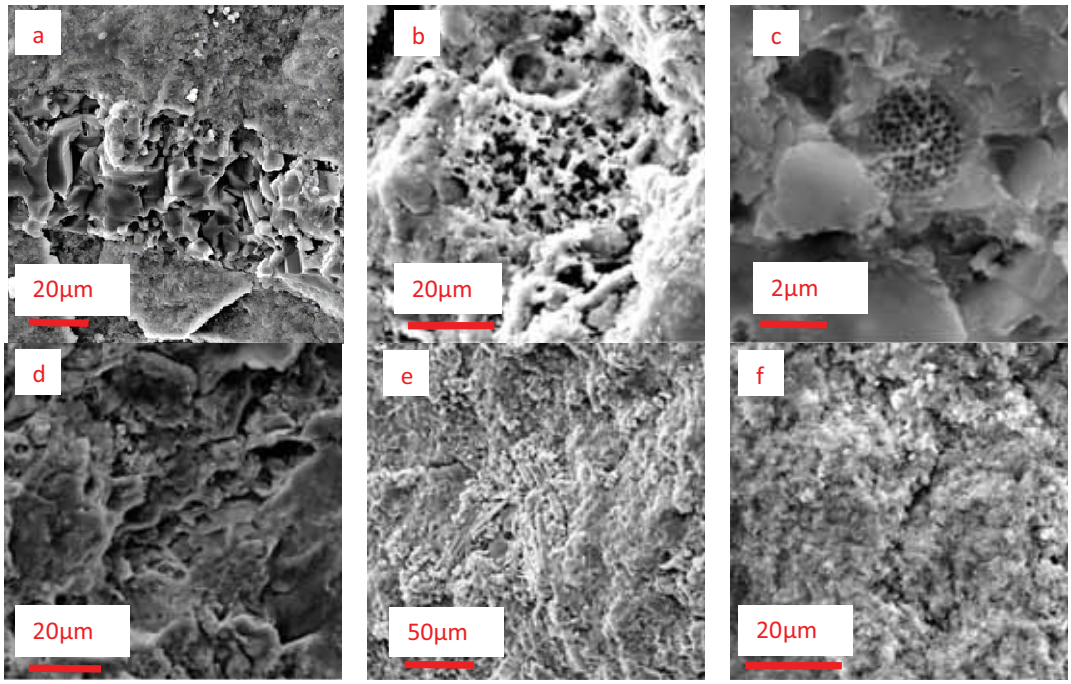

FIGURE 3

Scanning electron microscopy image of micro-pores of Late Triassic shale samples in Ordos Basin.

Notes: (a)-mineral pores, T3*c* shale, M-4; (b)-organic pores, T3*c* shale, S-1; (c)-diatom fossil pores, T3*c* shale, M-10; (d)-residual primary pores and clay mineral interlayer pores, T3*c* shale, Q4-4; (e)-mineral intercrystalline pores, T3*y* shale, Q5-1; (f)-mineral cast film pores, T3*c* shale, M-11.

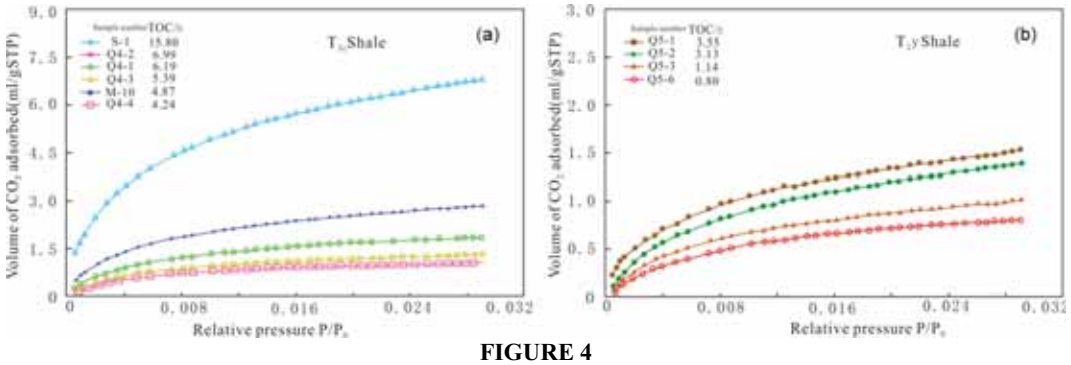

FIGURE 4

CO_2 adsorption-desorption curve of late Triassic shale samples in Ordos Basin.

Pore Structure Characteristics. The distribution characteristics of micropores (<2 nm) were determined by CO_2 adsorption method, the distribution characteristics of mesopores (2-50 nm) were determined by N_2 adsorption method, and the distribution of macropores (> 50 nm) was determined by high pressure mercury injection tests. In this way, the pore structure and pore size distribution characteristics of the shale are obtained.

According to the International Theoretical and Applied Chemistry (IUPAC) classification method, the type of CO_2 adsorption / desorption curves of shale samples can be determined (Figure 4). The results show that there are open micropores smaller than 2 nm. Because the CO_2 adsorption and desorption processes are performed at relatively low pressures, there is no capillary condensation. And the desorption curve matches the adsorption curve.

The N_2 adsorption and desorption curves of shale samples (Figure 5) indicate that the types of adsorption and desorption curves of shale samples are similar to the IV isotherms [28]. When the adsorption relative pressure (P/P_o) is less than 0.5, the N_2 adsorption curve will appear slightly concave, and this is the gas monolayer adsorption process. Near the relative pressure ($P/P_o = 0.5$), there will be an inflection point of the N_2 adsorption curve. At the boundary between single-layer gas adsorption and multi-layer gas adsorption, the gas adsorption amount begins to increase. When the relative pressure (P/P_o)> 0.5, the N_2 adsorption curve becomes slightly convex, indicating the presence of meso-

pores and macropores. When the relative pressure is 0.50, the desorption curve drops sharply, indicating that there are ink bottle-like pores with large pore space in the shale. When the relative pressure is less than 0.45, the adsorption force decreases.

Due to the shape of the hysteresis loop produced by the experimental sample, the pore structure type of shale does not correspond to the adsorption / desorption curve of a specific pore structure type. Compared with the type of hysteresis loop, the type of hysteresis loop in the Late Triassic shale sample of the Ordos Basin is type B hysteresis loop, which are considered to have type A and type E hysteresis loops Characteristics. Therefore, the pore structure of this sample should include parallel slit pores, open tubular pores, and ink bottle-like pores.

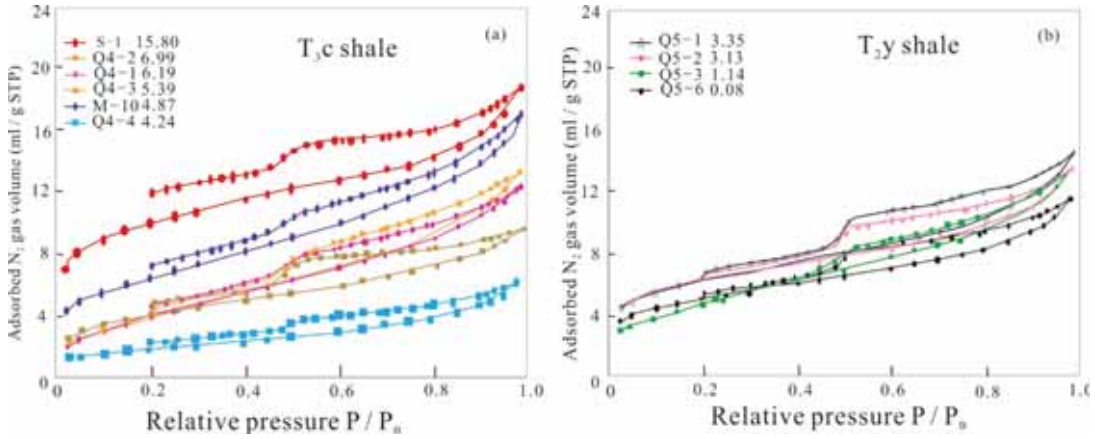

FIGURE 5
N_2 adsorption-desorption curve of late Triassic shale samples in Ordos Basin.

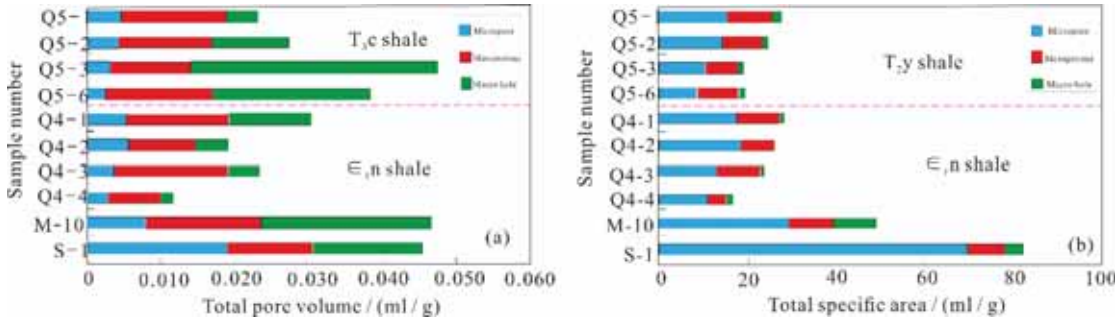

FIGURE 6
Pore volume and specific surface area distribution of the Late Triassic shale in the Ordos Basin.

TABLE 2
Pore structure data of late Triassic shale samples in Ordos Basin.

No.	Average pore Size (nm)	Total pore volume (10^{-3}ml/g)	Total specific surface area (m^2/g)	Micropore (<2nm)		Mesopore (2~50nm)		Macropore (>50nm)	
				Pore volume (10^{-3}ml/g)	Specific surface area (m^2/g)	Pore volume (10^{-3}ml/g)	Specific surface area (m^2/g)	Pore volume (10^{-3}ml/g)	Specific surface area (m^2/g)
Q5-1	4.14	22.82	26.87	4.72	15.67	14.10	10.31	22.90	9.74
Q5-2	3.77	27.15	24.26	4.25	14.15	12.70	9.46	14.70	3.87
Q5-3	4.12	47.66	18.96	3.16	10.41	10.90	7.81	10.80	0.01
Q5-6	4.88	38.35	19.09	2.55	8.47	14.40	9.59	4.40	0.01
Q4-1	5.14	29.99	28.19	5.09	18.22	14.10	9.96	4.20	0.05
Q4-2	4.12	19.00	26.54	5.40	18.88	9.20	7.65	1.50	1.21
Q4-3	5.45	23.52	24.36	3.72	13.54	15.60	10.76	4.00	0.89
Q4-4	5.80	11.46	17.09	2.86	11.09	7.10	4.80	10.20	0.66
M-10	4.49	46.60	49.26	8.00	29.50	15.70	10.02	33.60	0.74
S-1	3.26	45.26	82.42	18.96	70.28	11.60	8.27	21.40	1.03

As shown in Table 2 and Figure 6, the micro and mesopores of the Late Triassic shale in the Ordos Basin constitute a tight oil storage space. The sum of these two specific surface areas accounts for 94.3% of the total specific surface area of the shale. The total pore volume accounts for 59.1% of the total shale pore volume. The specific surface area is mainly provided by micropores and mesopores. The average surface area of the micropores accounts for 66.3% of the total specific surface area. The average mesopore specific surface area accounts for 28.0% of the total specific surface area, and the macropore specific surface area accounts for only 5.7%.

Studies show that there is a specific relationship between pore volume and specific surface area of the Late Triassic shale. The pore volume of micropores and mesopores has a good positive correlation with the specific surface area. The correlation between total pore volume and total specific surface area, macropore volume, and specific surface area is small (Figure 7). Within a specific pore size range, the smaller the pore size, the greater the gas adsorption capacity and the greater the gas storage capacity. Some scholars have reported [12-14] that the pore size is negatively related to the specific surface area. Nano-sized pores with smaller pore sizes have stronger adsorption capabilities. Therefore, we believe that high-density oil exists in the shale pore structure.

Based on the results of CO_2 and N_2 adsorption experiments, we analyzed the pore size distribution of micropores and mesopores in the Late Triassic shale in the Ordos area, and compared it with the North American shale. It can be determined that the distribution of micropores and mesopores in the Late Triassic shale in the Ordos area is different from that in North America (Figure 8). From the peak position, the main peak of the Late Triassic shale micropores in the Ordos region is located at 0.4-0.7 nm, and the main peak of the North American shale micropores is located at 0.7-1.0 nm. The mesopore pore size distribution is completely different. In the Late Triassic, the peak of shale pore volume in the Ordos region was at the 3-10 nm pore size, while the shale pore volume in North America did not change with the change of pore size. For the average pore volume, the Ordos Late Triassic shale is roughly equivalent to the North American shale. The average pore volume of the Ordos Late Triassic shale is 0.003 9 ml/g, and the average pore volume of the six sets of North American shales is 0.004 0 ml/g. In terms of average pore diameter, the average pore diameter of the Late Triassic shale in Ordos region is 4.52 nm, and the average pore diameter of the Chang 7 member shale is 4.23 nm. North American shale has a slightly larger average pore size, which is 4.00 nm.

According to the results of high-pressure mercury intrusion experiments, the pore size distribution of large pores in the Late Triassic shale in the Ordos area was obtained. Figure 9 shows that the mercury intrusion amount is small in the range of 50-0.05 μm. When the pore diameter exceeds 50 μm, the amount of mercury introduced sharply increases, indicating that the macropore diameter of the Late Triassic shale samples in the Ordos region is 50-200 μm.

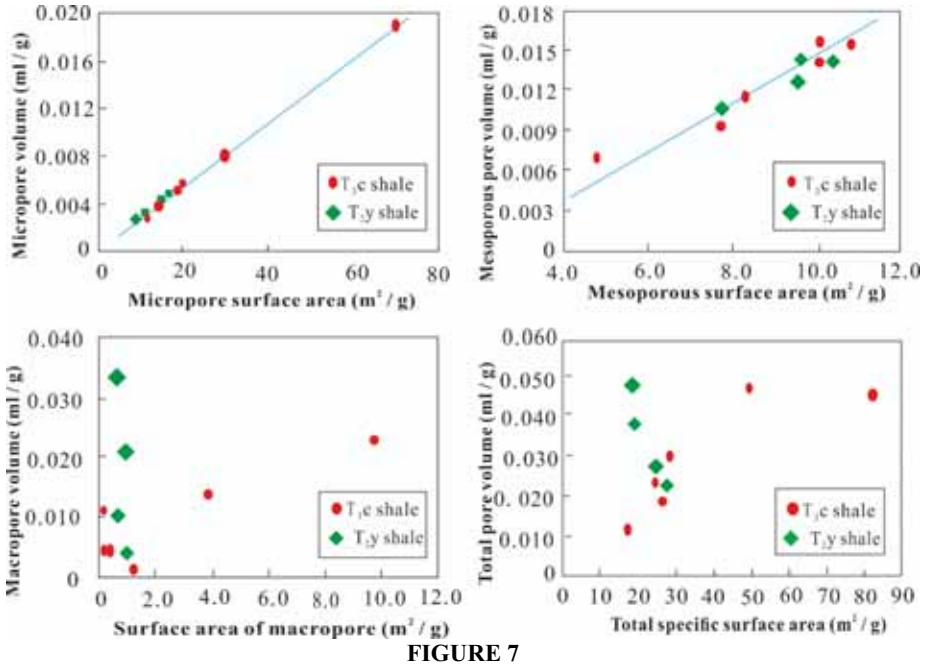

FIGURE 7
Relationship between pore volume and specific surface area of Late Triassic shale in Ordos Basin.

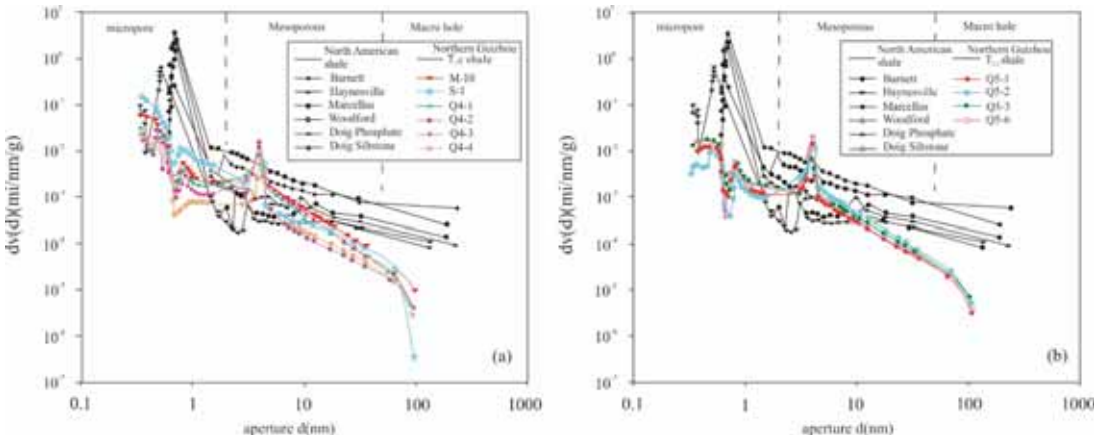

FIGURE 8
Comparison of the pore size distribution of micropores and mesopores in the Late Triassic shale in the Ordos Basin with North American shales.

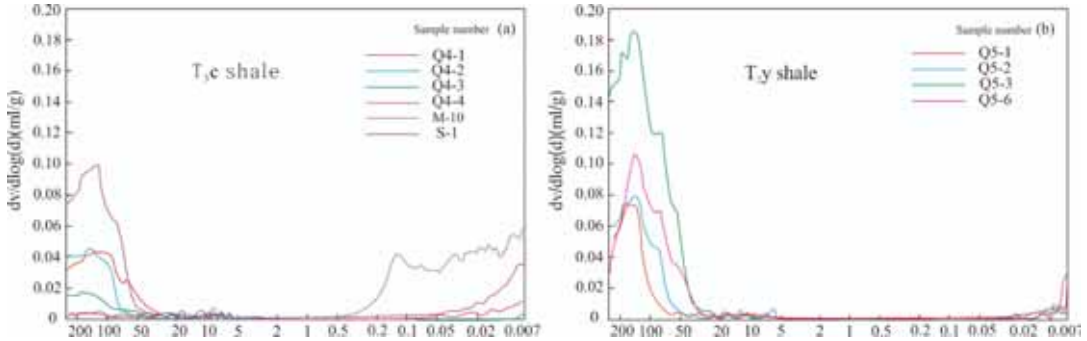

FIGURE 9
Macropore pore size distribution curve of Late Triassic shale in Ordos Basin.

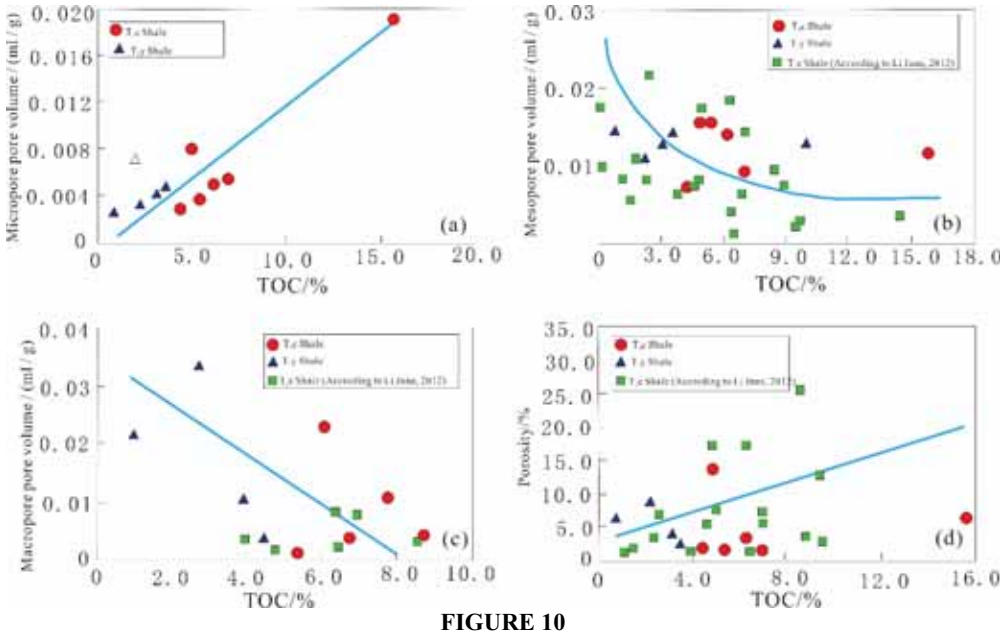

FIGURE 10
Relationship between pore volume, porosity and organic carbon content in the Late Triassic shale in Ordos Basin.

Main Factors Affecting the Pore Structure. Organic carbon content is one of the inherent factors controlling shale pore development. Higher organic carbon content is helpful for pore development. The results show that the porosity of shale is mainly formed by hydrocarbon generation [29-30]. If the mass percentage of organic shale is 7%, its volume percentage is 14%, and the conversion increases the pore space of the rock by 4.9%.

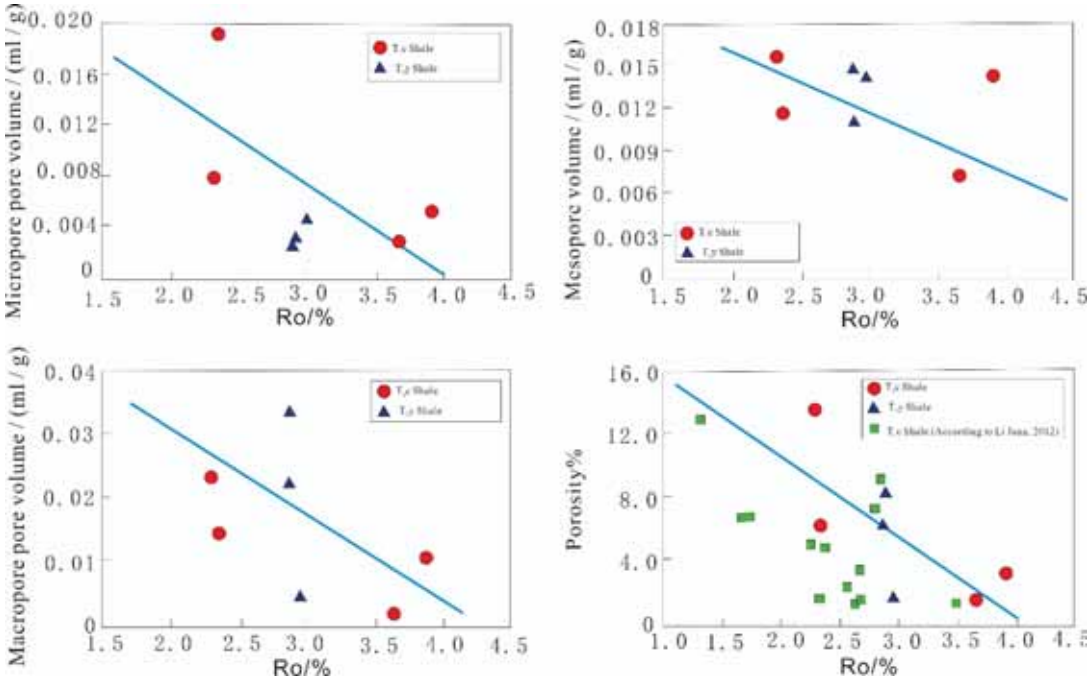

FIGURE 11
Relationship between pore volume and maturity Ro of Late Triassic shale in Ordos Basin.

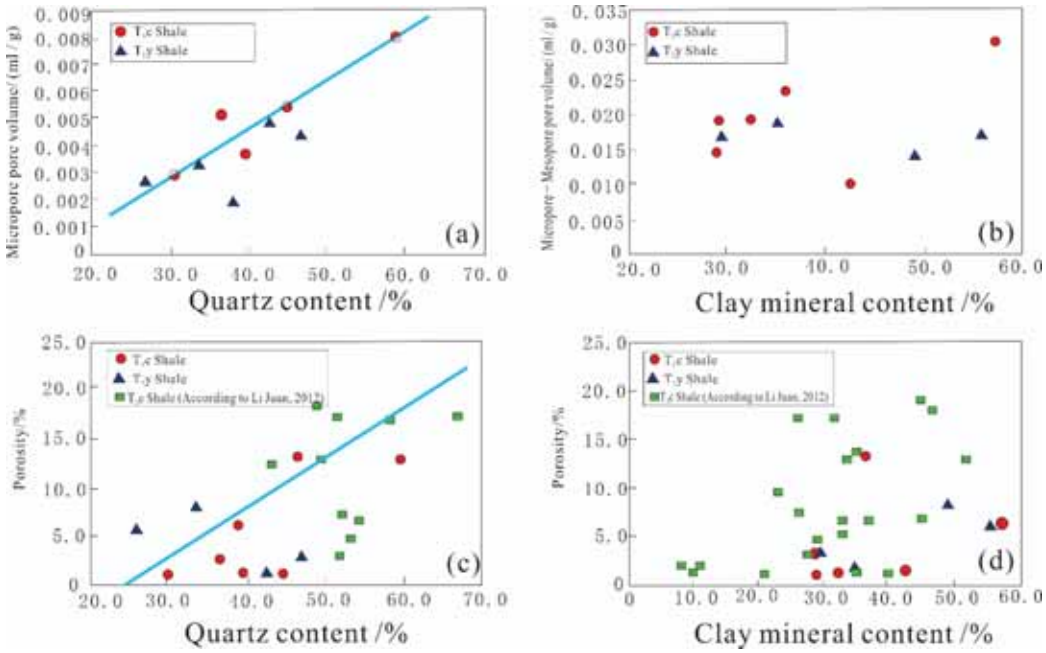

FIGURE 12
Relationship between pore volume and mineral component content of Late Triassic shale in Ordos Basin.

There is a constant relationship between the porosity of the Late Triassic shale and the volume of micropores, mesopores, and macropores, and organic carbon content (TOC) in the Ordos area (Figure 10). The pore volume decreases with increasing organic carbon content. The pore volume of large pores was negatively correlated with TOC. And the porosity increases with the pore volume. Chen et al. [17] pointed out that the organic carbon content in shale is the main intrinsic factor controlling the nanopore volume and specific surface area of tight oil reservoirs. There was a significant positive correlation between pore volume and organic carbon content.

Organic matter maturity Ro is an important factor influencing shale pore development. In the Late Triassic shale, the porosity and pore volume of micropores, mesopores, and macropores in the Ordos Basin decreased with increasing maturity Ro (Figure 11). Zhang et al. [30] also pointed out that as the maturity R_o increases, shale porosity decreases. The Late Triassic shale maturity in Ordos region is generally high (R_o is greater than 2%, and the higher reaches more than 3%), and it is in an overmaturity stage. As the maturity Ro increases, the decrease in shale porosity is not due to the decrease in the pore volume of specific pore sizes. It is caused by the simultaneous reduction of the pore volume of the entire micropore, mesopore and macropore.

In the Late Triassic shale of the Ordos Basin, the microporosity has a positive correlation with the quartz content. The porosity of micropores and mesopores has a positive correlation with clay minerals. The correlation between mineral components is unclear (Figure 12). As the quartz content increases, the pore volume of the shale increases accordingly. With the increase of clay mineral content, the pore volume of micropores and mesopores in shale changes discontinuously. This may be due to the complexity of the clay mineral composition.

CONCLUSIONS

(1) The porosity of the Late Triassic shale in the Ordos region is 1.30-13.37%, with an average of 4.56%. The types of shale micropores are intergranular pores, organic pores and intragranular pores. Organic pores are the main type of pores. The shale mainly has micropores (<2 nm) and mesopores (2-50 nm).

(2) The total shale surface area accounts for 94.3% of the total specific surface area, and its pore size is mainly distributed in three intervals: 0.4-0.7 nm, 3-10 nm, and > 50 nm.

(3) Shale pore structure is affected by shale organic carbon content, organic matter maturity, and mineral content. As shale porosity and pore volume increase, its maturity R_o increases and clay mineral content increases, but shale porosity and pore volume gradually decrease.

ACKNOWLEDGEMENTS

This work was financially supported by the Yan' an Science and Technology Bureau Project: Study on Key Technique to Enhance Oil Recovery and Its Demonstration and Popularization, China (No. 2017WZZ-01-02) and the 2018 National University Student Innovation and Entrepreneurship Training Project, China (No. D2018117).

REFERENCES

[1] Mc, M., Upton, G. (2018) Local labor market shocks and residential mortgage payments: Evidence from shale oil and gas booms. Resource and Energy Economics. 53(1), 105-113.

[2] Wang, S., Song, Z., Cao, T., Song, X. (2013) The methane sorption capacity of Paleozoic shales from the Sichuan Basin, China. Marine and Petroleum Geology. 44(3), 112-119.

[3] Luo, X., Guo, Q., Zhang, D., Zhou, H., Yang, Q. (2018) Simulation, exergy analysis and optimization of a shale oil hydrogenation process for clean fuels production. Applied Thermal Engineering. 140, 102-111.

[4] Li, Y., Sun, W., Liu, X., Zhang, D., Wang, Y., Liu, Z. (2018) Study of the relationship between fractures and highly productive shale gas zones, Longmaxi Formation, Jiaoshiba area in eastern Sichuan. Petroleum Science. 15(3), 498-509.

[5] Wang, W., Lin, C., Zheng, M., Lu, S., Wang, M., Zhang, T. (2018) Enrichment patterns and resource prospects of tight oil and shale oil: A Case Study of the Second Member of Kongdian Formation in the Cangdong Sag, Huanghua Depression. 47(2), 332-344.

[6] Kim, C., Jang, H., Lee, J. (2015) Experimental investigation on the characteristics of gas diffusion in shale gas reservoir using porosity and permeability of nanopore scale. Journal of Petroleum Science and Engineering. 133, 226-237.

[7] Yan, W., Qi, Y., Zhen, G., Gang, G., Gang, C. (2018) Investigation of oleate diethylamine epichlorohydrin copolymer as a clay swelling inhibitor for shale oil/gas exploration. Petroleum Chemistry. 58(3), 245-249.

[8] Wang, Y., Dong, D., Li, J., Wang, S., Li, X., Wang, L. (2012) Characteristics of shale gas reservoirs in the Lower Machiliu Formation of the Lower Silurian, southern Sichuan. Acta Petrologica Sinica. 33(4), 551-561.

[9] Dai, S., Gong, Y., Wang, F., Hu, P. (2019) Diagenesis evolution of tight sandstones in Chang 8 Member of Upper Triassic in the Xiasiwan area, Ordos Basin, China. Fresen. Environ. Bull. 28, 6275-6281.

[10] Vallbaum, R., Muoni, T., Soone, J. (2018) Effect of a shale oil based additive on the properties of biodiesel fuel. Solid Fuel Chemistry. 52(1), 44-52.

[11] Patwardhan, S., Famoori, F., Gunaji, R., Govindarajan, S. (2014) Simulation and mathematical modeling of stimulated shale gas reservoirs. Industrial and Engineering Chemistry Research. 53(51), 19788-19805.

[12] Romadenkina, S., Yu, A., Zeml, Y., Pankratov, I. (2019) Removal of sulfur-containing compounds from gas obtained by the pyrolysis of oil shale. Solid Fuel Chemistry. 53(3), 156-158.

[13] Ma, J. (2016) Chapter 4 - pore-scale characterization of gas flow properties in shale bydigital core analysis. Unconventional Oil and Gas Resources Handbook. 127-150.

[14] Yang, C., Zhang, J., Tang, X. (2013). Microscopic pore types and its impact on the storage and permeability of continental shale gas, Ordos Basin. Earth Science Frontiers. 20(4), 240-250.

[15] Wang, G., Chang, X., Yin, W., Li, Y., Song, T. (2017) Impact of diagenesis on reservoir quality and heterogeneity of the Upper Triassic Chang 8 tight oil sandstones in the Zhenjing Area, Ordos Basin, China. Marine and Petroleum Geology. 83, 84-96.

[16] Wang, G., Hao, F., Chang, X., Lan, C., Li, P., Zou, H. (2017) Quantitative analyses of porosity evolution in tight grainstones: A case study of the Triassic Feixianguan Formation in the Jiannan gas field, Sichuan Basin, China. Marine and Petroleum Geology. 86, 259-267.

[17] Chen, S., Xia, X., Qin, Y., Fu, C., Hu, L. (2013) Classification of pore structures in shale gas reservoir at the Longmaxi Formation in the south of Sichuan Basin. Journal of China Coal Society. 38(5), 760-765.

[18] Wei, S., Liu, Z., Ren, D., Xiong, W., Wang, X. (2019) Reservoir Study and Sequence Division of Shahezi Formation in Songliao Basin, China. Fresen. Environ. Bull. 28, 7469-7476.

[19] Zhu, H., Ju, Y., Yu, Q., Cheng, H., Le, Z. (2018) Impact of tectonism on pore type and pore structure evolution in organic-rich shale: Implications for gas storage and migration pathways in naturally deformed rocks. Fuel. 228, 272-289.

[20] Liang, W., Fu, Y., Li, J., Sima, L., Wu, Q., Jin, W. (2016) Mineral and pore structure characteristics of gas shale in Longmaxi Formation: A case study of Jiaoshiba Gas Field in the southern Sichuan Basin, China. Arabian Journal of Geosciences. 9(19), 733-741.

[21] Feng, X., Ao, W., Xuan, T. (2018) Characteristics of pore development and its main controlling factors of continental shale gas reservoirs: A case study of Chang 7 Member in Ordos Basin. Journal of Jilin University. 48(3), 678-692.

[22] Khangar, R., Singh, H. (2017) Organo petro graphic and pore facets of permian shale beds of Jharia Basin with implications to shale gas reservoir. Journal of Earth Science. 5, 658-669.

[23] Li, Y., Chang, X., Yin, W., Sun, T., Song, T. (2017) Quantitative impact of diagenesis on reservoir quality of the Triassic Chang 6 tight oil sandstones, Zhenjing Area, Ordos Basin, China. Marine and Petroleum Geology. 86, 1014-1028.

[24] Yang, Y., Qiu, L., Cao, Y., Chen, C., Lei, D., Wan, M. (2017) Reservoir quality and diagenesis of the Permian Lucaogou Formation tight carbonates in Jimsar Sag, Junggar Basin, west China. Journal of Earth Science. 28(6), 1032-1046.

[25] Yang, R., Jin, Z., Van Loon, A., Han, Z., Fan, A. (2017) Climatic and tectonic controls of lacustrine hyperpycnite origination in the late Triassic Ordos Basin, central China: Implications for unconventional petroleum development. AAPG Bulletin. 101(01), 95-117.

[26] Wang, Q., Shen, C., Chen, Q., Zhang, L., Hong, L. (2015) Pore characteristics and gas released by crush methods of Wufeng-Longmaxi shale in the northwest of Hubei province, China. Acta Geologica Sinica. 89(s1), 93-96.

[27] Sun, Y., Shuai, Z., Qiang, L., Liu, S., Jing, H. (2018) Thermoelectric coupling analysis of high-voltage breakdown industrial frequency pyrolysis in Fuyu oil shale. International Journal of Thermal Sciences. 130(10), 19-27.

[28] Lapidus, L., Yu, N., Beilina, D., Khudyakov, F., Zhagfarov, V., Ilyasov, N. (2018) Complex processing of oil shale from the Volga Basin. Solid Fuel Chemistry. 52(2), 62-69.

[29] Cunbao, L., Viet, T., Chau, H., Ping, X., Zdenek, P. (2018) Recent advances in mechanics of fracking and new results on 2D simulation of crack branching in anisotropic gas or oil shale. Acta Mechanica. 229(12), 1-18.

[30] Zhang, H., Xu, J., Zhao, P. (2018) Geological characteristics and exploration potential of oil and gas in the northeast area of China. Geology in China. 45(2), 260-273.

Received: **30.12.2019**
Accepted: **21.01.2020**

CORRESPONDING AUTHOR

Gang Zhang
Dingbian Oilfield,
Yanchang Petroleum Co.Ltd.,
Yulin 718600, China

e-mail: 2994156585@qq.com

© by PSP Volume 29 – No. 04A/2020 pages 3223-3229 Fresenius Environmental Bulletin

DESIGN AND IMPLEMENTATION OF A NOVEL ENVIRONMENTAL FRIENDLY CHATBOT BASED ON VSM AND RASPBERRY PI WITH ENVIRONMENTAL PROTECTION KNOWLEDGE

Linyan Ouyang[1,2,*], Xi Luo[1], Linsheng Xiong[1]

[1]College of Artificial Intelligence, Yango University, Fuzhou 350015, China
[2]Spatial Data Mining and Application Engineering Research Center of Fujian Province University, Fuzhou 350015, China

ABSTRACT

In the continuous development of the Internet, the amount of information storage is getting larger and larger. People's standards for information demand are getting higher and higher. In the face of a large amount of data in the Internet, fast and accurate data acquisition has become the most urgent demand at present. At the same time, with the deepening of environmental awareness in all walks of life, the contradiction between the shortcomings of traditional energy and the requirements of environmental protection becomes more and more obvious. New clean energy has many advantages such as cleanness, high efficiency and renewability, which has gradually become the main trend of environmental energy development. Therefore, based on the development principle of green environmental protection economy, environmental protection new energy can be combined with the design of intelligent robot, so as to finally design a special clean and environmental protection robot. According to the principle of the construction of Q&A System, it used octopus to collect environmental protection knowledge, build library, and use the Vector Space Model (VSM) for text similarity calculation. Raspberry Pi was used to develop hardware, and ultimately a voice chatbot about environmental protection knowledge had been achieved. It can answer the problems of environmental protection knowledge, and make environmental knowledge and environmental protection concept deeply rooted in the hearts of the people. It is a contribution to environmental causes.

KEYWORDS:
Q&A System, environmental protection, clean power system, VSM Algorithm, Raspberry Pi, Chatbot

INTRODUCTION

Development and Status of Chatbot. With the continuous progress of the Internet, people have a higher and higher demand for information retrieval. They hope to obtain more accurate data information in the retrieval method, instead of the data obtained from the webpage link [1-3]. Although search engine is very convenient, but the user in the search process, need to exclude advertising and irrelevant information. the whole process needs to spend a lot of time, and may not be able to quickly get the answer information. It is necessary to provide users with a more accurate, efficient, convenient and humanized information retrieval method, while intelligent chatbots can solve this problem for people [4-5].

Since ancient times, in the research process of intelligent robot technology, some teams have spent a long time to research, and the research process is conducive to the development of man-machine interaction [6-8]. After years of growth, through the development and progress of natural language processing, big data analysis, machine learning and other technologies, now intelligent robots have realized basic chat and dialogue functions. In recent years, China has also made great progress in the research of intelligent robots. Some universities, like Tsinghua University, Institute of Computing Technology Chinese Academy of Sciences and Harbin Institute of Technology, have made outstanding achievements in their research fields [9]. In the domestic Taobao mall, the customer service chatbot can chat with customers, so that customers can get commodity information, transaction information and other data information; The Apple mobile phone developed by foreign apple company has its own intelligent robot Siri. The robot can be awakened by the wake-up command and then talk with us. During the conversation, the alarm clock data, weather conditions, calls, SMS and other functions can be checked. The realization of intelligent robot can enable users to get the information they want in the process of dialogue, so as to meet the requirements of users to obtain accurate information.

This project collected data of Environmental Protection Knowledge by octopus, established knowledge question-and-answer database, used vector space model (VSM) to calculate text similarity, Choose Raspberry Pi 3 generation of type B + to and python programming to control voice recognition

and voice synthesis. The chatbot finished to answer the questions about Environmental Protection Knowledge for people.

MATERIALS AND METHODS

Q&A System. Q&A System is the most promising system in the field of Artificial Intelligence and Natural Language Processing. It is also the core principle of chatbot. The running process of Q&A System is mainly divided into three processes: question analysis, information retrieval and answer extraction [8, 10-11]. The process of problem analysis is to analyze the questions raised by users, the process of information retrieval is to quickly locate the questions raised by users into the database, and the process of answer extraction is to check the final answer from the corresponding database. The running process of Q&A System is mainly divided into three processes: question analysis, information retrieval and answer extraction.

Vector Space Model (VSM). Vector space model (VSM) is a relatively simple text similarity algorithm in recent years. By viewing a more complete article as a document. For document D (T_1, $T_2 \ldots T_n$) will have a weight W representing the degree of importance, and $D = D$ (W_1, $W_2 \ldots W_n$) [9].

The calculation principle of VSM algorithm is that every entry T_1, $T_2 \ldots T_n$ is regarded as a coordinate system, and the document is regarded as A and B. Mathematical knowledge is used to calculate the Angle value of cosine, namely the text-similarity value Sim (D_1, D_2), which is used to measure the degree of correlation between document D_1 and D_2 [12-13]. The calculation formula is shown in Formula 1.

$$Sim(D_1, D_2) = \cos\theta = \frac{\sum_{k=1}^{n} W_{1k} * W_{2k}}{\sqrt{(\sum_{k=1}^{n} W_{1k}^2)(\sum_{k=1}^{n} W_{2k}^2)}} \quad (1)$$

W_{1k} and W_{2k} represent weights in document D_1 and D_2 respectively, $1 <= k <= N$.

Principle of TF-IDF Algorithm. TF-IDF algorithm is used to count for word frequency, TF is the Word frequency, it refers to the ratio of the number of a word's occurrences in a document to the total number of times. IDF is the reverse document frequency. It is defined as IDF=log (N/N_k) [10]. In the TF-IDF algorithm, the weight "w" is calculated based on the values of TF and IDF, and formula 2 is obtained by sorting.

$$w_{ik} = \frac{tf_{ik} * \log\left(N/n_k\right)}{\sqrt{\sum_{k=1}^{n}\left(tf_{ik} * \log\left(N/n_k\right)\right)^2}} \quad (2)$$

Raspberry PI Development Board. Raspberry Pi is a hardware product for programming. Its internal system environment is developed based on Linux system. Raspberry PI is a microcomputer motherboard based on ARM, the main internal system resources mainly MicroSD card for memory system of hard disk, motherboard configuration around the four USB interface can choose for peripherals, including used to connect to the sound card, mouse, USB camera and an Ethernet interface for Internet access and data transmission. At the same time, it also has the video signal output interface and HDMI video output interface.

RESULTS

Chatbot Design. (1) Design of Automatic Question and Answer Module. The principle of Q&A System is mainly embodied in the three processes of question analysis, information retrieval and answer extraction. The problem analysis process is to analyze the questions raised by users, use the Chinese academy of sciences' word segmentation tool NLPIR to analyze the questions, extract keywords, and get the core of the problem through the analysis of keywords [14-15]. The information retrieval process is to use the VSM algorithm to obtain the maximum Sim value for the post-word segmentation problem, use the Sim value to find the problem closest to the database, and quickly locate it in the corresponding database. The answer extraction process is to find the final answer according to the ID corresponding to the closest question. The block diagram of the Q&A module is shown in Figure 1.

For example, the user puts forward "What are the advantages of using air purifier". Through word segmentation tool, the corresponding word segmentation result is "What/are/the/advantages/of/using/air purifier". The keyword extraction situation is "air purifier" and "advantages". According to the keywords, we know the user wants to get the information of air purifier. It can be quickly located to the route table, to improve the retrieval rate. VSM algorithm and TF-IDF algorithm are used for information retrieval. The Sim value obtained by VSM algorithm was used for sorting, to find the question closest to the user's question in the question-and-answer database, and to extract the corresponding answer.

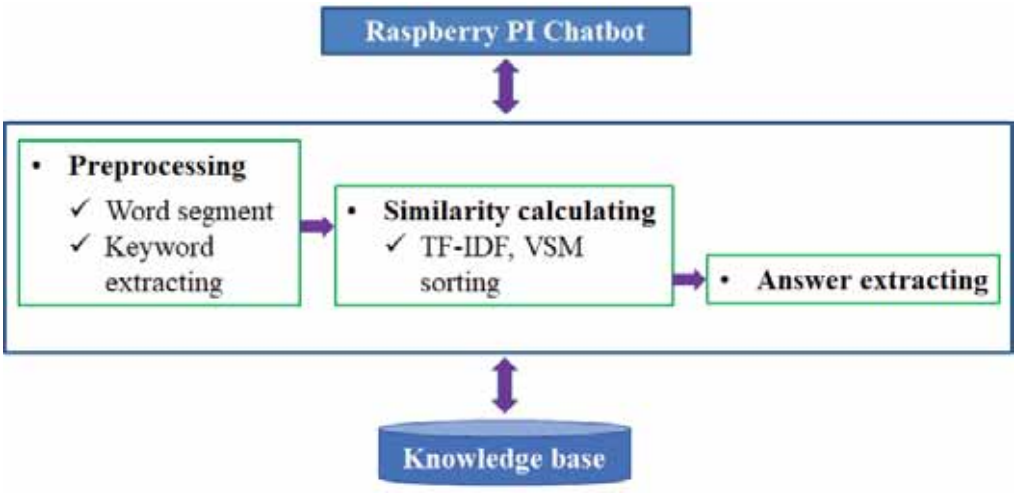

FIGURE 1
Block diagram of automatic Q&A module

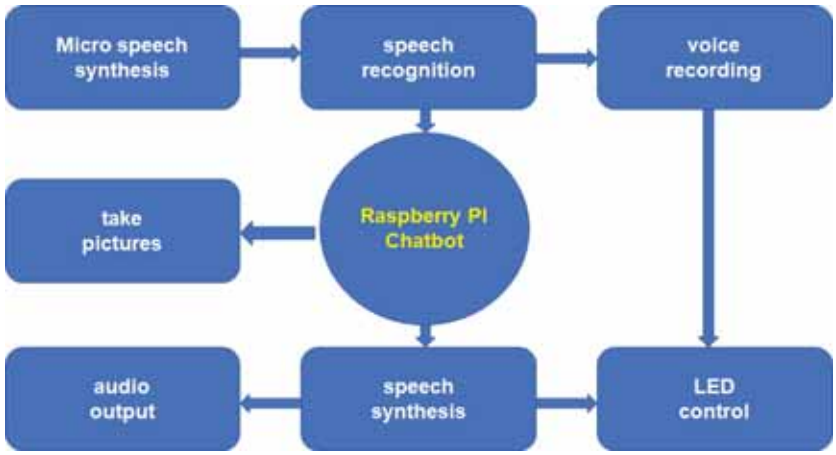

FIGURE 2
Hardware structure diagram of voice chatbot

(2) Hardware Module Design. Raspberry Pi was used to control the chatbot. It can support the python language development. It added the wireless network card on the plate and bluetooth adapter module makes development easier, and the project schedule can advance. The image and VNC visual interface provided by the system is easier to combine with human-computer interaction and programming environment [16-17]. Built-in board and audio output IO choice are more likely to achieve the objective function of the serial port.

Since the development board of Raspberry Pi has no input interface but only one audio output interface, it needs to simulate an input interface in development. However, due to the design of other sound CARDS that need to be driven, and the signal-to-noise ratio is higher than this sound card in design, 7.1 sound card is chosen. Add a sound card configuration so that audio can be saved, and set up a save recording function to save the audio data. There is no voice input interface on the development board of Raspberry pi. In order to meet the selection of interface availability, add the configuration of sound card, so that the audio can be saved. In addition, the recording function is established to save the audio data.

The hardware module of voice chatbot is mainly composed of nine modules: main control module, the configuration of sound card and input module of microphone, recording module, audio output module, speech synthesis, and speech recognition module, knowledge question-answering module, LED lamp module and binocular camera module [18]. The Hardware structure diagram of voice chatbot is shown in Figure 2.

Clean Power System. The power system is the necessary component for the normal and efficient operation of the robot. Commonly used lithium batteries and other power supplies usually have many disadvantages, such as low efficiency, strong pollu-

tion and non-reusable. As the main focus of sustainable clean energy, solar energy has the advantages of high energy efficiency, clean and renewable. In general, the solar energy storage battery can meet the normal needs of the robot operation, but in case of continuous cold and humid weather conditions, the photoelectric conversion efficiency may be low, the power supply cannot be sustained and the power shortage may occur. Therefore, a set of Ni MH rechargeable battery made of hydrogen storage alloy is preferred as a backup battery.

Realization of Chatbot. (1) Data Collection and Storage. Using artificial collection and octopus, the basic knowledge base was built. For all kinds of environmental protection knowledge, not only the manual construction, but also the octopus network environmental protection knowledge collection. Fundamental questions, water, electricity, air, garbage classification, household appliances and other common environmental protection knowledge collection and analysis, and data cleaning, environmental protection knowledge storage in the database, to build environmental protection knowledge Q&A database.

Due to the differences in language expression between different users, the same word may be different [19]. Say "what role does the environmental protection", "what's the meaning of" environmental protection, these words actually express the same meaning, if not handled, from algorithm to calculate their differences are relatively large in the process, as a result, in order to improve the compatibility problem, enhance the accuracy in the answer, in the knowledge base is specially set up a synonym table, such as "environmental protection" is synonymous with "environmental protection", "role" and "meaning" are synonymous. When the user asks a question, the synonyms of the question are extracted and replaced, and then the similarity is compared.

(2) Realization of Automatic Question and Answer Module. Background core VSM algorithm module includes query answer module, question retrieval module, text preprocessing module and user interaction data processing module.

1) User's interactive data processing: including data reception and data return. If the user asks "what garbage does the fish bone belong to", the system will receive the data of this problem and use it for the next processing; When the answer is "fish bones are wet garbage," the answer data is returned to the user.

2) Text preprocessing: including word segmentation and keyword extraction. Word segmentation tool is used to process the transformed data and extract keywords to obtain the core of the problem. The Chinese word segmentation system "NLPIR" of the Chinese academy of sciences was adopted for word segmentation of questions in the library and user questions, such as "what garbage do fish bones belong to? Go to the synonym list to see if any synonyms exist, and if so, perform the basic word substitution, and calculate the values of TF, IDF, and w.

3) Problem retrieving: including similarity comparison and correlation value sorting. The similarity between the post-segmentation problem and the data in the database is compared to find the maximum Sim value. Through VSM algorithm, user problems are compared with data in the database for similarity, their Sim values are calculated, and the largest Sim value is found by sorting.

4) Answer extracting: including database matching and answer search. By matching the ID corresponding to the maximum Sim value to the database query to find the corresponding answer.

(3) Hardware Module Structure Implementation. The hardware module of voice chatbot is mainly composed of nine modules: main control module, configuration of sound card and input module of microphone, recording module, audio output module, speech synthesis and speech recognition module, knowledge question-answering module, LED lamp module and binocular camera module.

The main control module is the control center of the whole intelligent voice chatbot system. According to the written programming program of the system, the main control module sends the corresponding control instructions, so that the corresponding input module, output module, as well as the speech recognition and synthesis module, execute the corresponding actions and complete the basic voice dialogue function [20-21]. The recording function module mainly detects and distinguishes the audio of the chat user to judge whether the input state of the voice is normal. Q&A database is responsible for the content reply of the whole voice chat conversation. The workflow is shown in Figure 3.

1) Voice Recognition and Voice Synthesis. By calling Baidu's speech recognition API, the sound2text() function was used to identify and translate the recording files. According to the recognition interface's matching algorithm of due similarity, the speech recognition was converted into the text with the highest corresponding similarity.

The main implementation step of speech synthesis is to call API interface and send it to the corresponding knowledge, a database according to the recognized text, so as to match the most appropriate answer text. Then the text2sound() method in the speech synthesis module is called to synthesize the corresponding tone speech and then output and play it. The process is shown in Figure 4.

2) Binocular Camera. In order to make the chatbot more intelligent, this project uses binocular

cameras to realize the chatbot's "eye" with photography and video recording functions. By programming the software to control the command of taking photos or photographing, the main module will complete the function of taking photos or photographing after receiving the corresponding command. The user can access the video file through the Raspberry PI IP address.

3) LED Flash Effect. To make the chatbot more intelligent, this project also adds the control of LED lights, so that the chatbot "teeth" can achieve the effect of LED lights flashing. When the user speaks, the main thread executes the record_ sound function, and calls the loop() function concurrently to achieve the effect of running horse lamp. When the robot speaks, it executes the function play_ sound and calls ledHL() function to achieve the scintillation effect.

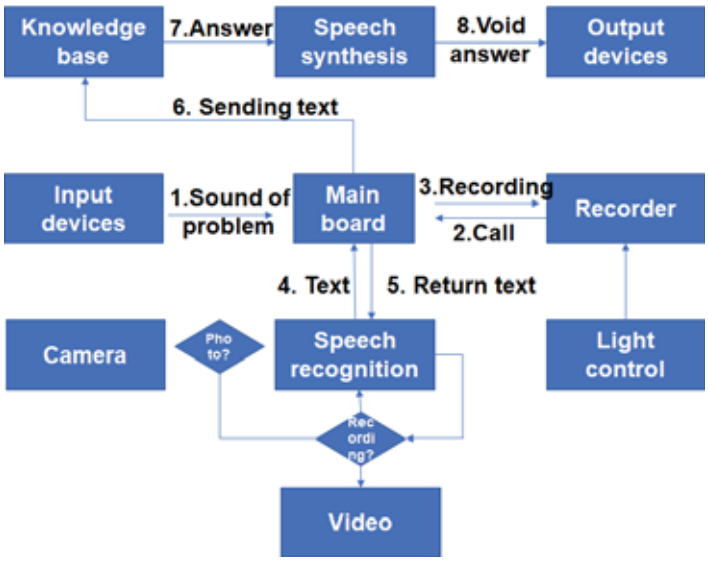

FIGURE 3
The workflow of Q&A database

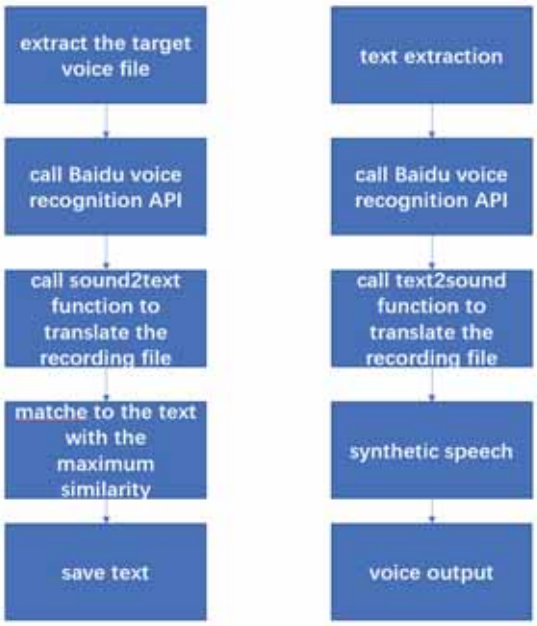

FIGURE 4
Voice recognition and voice synthesis

Chatbot Test. The chat function test mainly tests the chat data and analyzes the accuracy. It is mainly tested from two aspects: pickup effect, answer accuracy. Scientists research shows that the average person when you talk in decibels of 40-60 decibels, and the man's voice between 100 Hz - 1000 Hz frequency range, because of the difference of male and female, different tones for pickup effect is different. And in the normal quiet environment and the slightly noisy environment or very noisy environment, different speaking distance and corresponding to different speaking frequency, the corresponding pickup is also very big difference, and in the acquisition effect, because of the distance, the acquisition error and other phenomena. Table 1 to Table 3 are tests of the chatbot's sound card.

TABLE 1
Comparison table of sound card acquisition effect under quiet environment

Distance from the microphone (m)	Decibel	Acquisition effect
20m	55	Very poor
10m	55	Poor
5m	55	General
2m	55	Good

TABLE 2
Comparison table of sound card acquisition effect under slightly noisy environment

Distance from the microphone (m)	Decibel	Acquisition effect
12m	85	very poor
8m	70	poor
5m	65	general
1m	55	good

TABLE 3
Comparison table of sound card acquisition effect under noisy environment

Distance from the microphone (m)	Decibel	Acquisition effect
2m	98	none
1m	74	none
0.5m	68	very poor
0.1m	55	poor

Compared with the pickup effect, in a quiet environment, the position of voice chat robot is kept at 2 meters, and the pickup effect is best at 55 db. In the noisy environment, the position of the voice chat robot was kept at 1 meter, and the sound frequency was the best at 55 db. In the noisier environment, the position of the voice chat robot remained at 0.1 meters, and the sound frequency was the best at 55 db.

The chatbot's accuracy in answering questions was also an important part of the test. Accuracy is the percentage of the number of questions answered correctly. Several types of questions in the question-and-answer database are tested. Each type of question was asked for 200 times, and the accuracy was shown in the Table 4.

TABLE 4
Accuracy of answers to various questions

Type of problem	Accuracy rate
Fundamental questions	0.78
Water	0.85
Electricity	0.87
Air	0.81
Garbage classification	0.75
Household appliances	0.89
Others	0.68

After testing, the voice chatbot can realize man-machine dialogue, the accuracy rate is about 80 percent. The accuracy rate of the chatbot in answering questions is also affected by the picking up and recognition factors. In a quiet environment, the position of the voice chatbot are kept at 2 meters, and the sound frequency is the best at 55 decibels, so the recognition effect is relatively good. If the environment is relatively noisy, the recognition degree decreases, and the accuracy decreases.

CONCLUSIONS

Intelligent voice chatbot take the Python programming language, it uses hardware circuit connection and programming of the two-way control software code, with Raspberry as operating system and operation environment, using VSM algorithm to identify corresponding data, according maximum to find the answer, for the user. The whole process enables users to quickly get information through chat, which saves the time of searching data with Baidu and brings convenience to users. In addition, the robot has an excellent composite clean energy guarantee system, which can effectively reduce the environmental pollution and achieve the effect of energy conservation and environmental protection. Furthermore, the robot is integrated with the dual-eye camera module and LED light control module, which realizes the camera photography and camera control through voice recognition, enabling the chatbot to have extended functions. The LED light realizes the effect of flashing and "running horse light", making the chatbot image more vivid and interesting. Users can ask questions to the intelligent chatbot to enjoy the consulting service of environmental protection knowledge.

ACKNOWLEDGEMENTS

This work was financially supported by the Scientific Research Project for Middle-Aged and Young

People of Education Department of Fujian Province, China (No. JT180731).

REFERENCES

[1] Zhou, L. (2018) Research and implementation of key technologies of internet-based Q&A System. Dissertation. Xi 'an: Software Engineering, Northwest University.
[2] Li, Z., Li, S. (2017) Overview of web-based Q&A system. Computer Science. 44(6), 1-7.
[3] Feng, S. (2016) Status and development of chatbot Q&A system. Robot Technology and Application. 4, 34-36.
[4] Dai, Y., Liu, G. (2008) Overview of intelligent robot technology. Computer Science and Application. 8(6), 918-929.
[5] Garza-Reyes, J., Torres Romero, J., Govindan, K., Cherrafi, A., Ramanathan, U. (2018) A PDCA-based approach to environmental value stream mapping (E-VSM). Journal of Cleaner Production. 180, 335-348.
[6] Bustard, D., Sterritt, R., Taleb-Bendiab, A., Laws, A. (2006) Autonomic system design based on the integrated use of SSM and VSM. Artificial Intelligence Review. 25(4), 313-327.
[7] Guo, Q. (2008) The Similarity Computing of Documents Based on VSM. Computer Software and Applications, 2008. COMPSAC '08. 32nd Annual IEEE International. IEEE.
[8] Liang, X., Wang, D., Huang, M. (2010) Improved Sentence Similarity Algorithm based on VSM and its application in Question Answering System. IEEE International Conference on Intelligent Computing and Intelligent Systems. IEEE.
[9] Wu, Y., Wu, W., Li, Z., Zhou, M. (2016) Response selection with topic clues for retrieval-based chatbots. Neurocomputing. 316, 251-261.
[10] García-Valls, M., Ampuero-Calleja, J., Ferreira, L. (2017) Integration of Data Distribution Service and Raspberry Pi. In Book: Green, Pervasive, and Cloud Computing. 10232, 490-504.
[11] Sunehra, D., Goud, V. (2016) Attendance recording and consolidation system using Arduino and Raspberry Pi. 2016 International conference on Signal Processing, Communication, Power and Embedded System (SCOPES). IEEE.
[12] Liu, K., Zhao, J., He, S. (2015) Question Answering over Knowledge Bases. IEEE Intelligent Systems. 30(5), 26-35.
[13] Cai, L. (2018) Research on text content screening method based on spatial vector model. Dissertation. Chengdu: Control Science and Engineering, University of Electronic Science and Technology of China.
[14] Jin, Z. (2015) Chinese microblog topic detection and research based on the improved TF-IDF algorithm. Dissertation. Beijing: Computer Science and Technology, Beijing Institute of Technology.
[15] Manalu, S., Moniaga, J., Hadipurnawan, D., Sahidi, F., Kesselman, M. (2017) OBD- II and raspberry pi technology to diagnose car's machine current condition: Study literature. Library Hi Tech News. 34(10), 15-21.
[16] Tiwari, R., Singh, D. (2018) Vehicle control using raspberry PI and image processing. In Book: Intelligent Communication, Control and Devices. 624, 219-227.
[17] Liu, Q. (2016) Discussion on the application of computer artificial intelligence recognition technology. Journal of Science and Technology. 4, 121-122.
[18] Kang, H., Li, Y., Teng, G., Fan, X., He, X. (2004) Research on natural language IR system based on genetic algorithm and VSM. International Conference on Machine Learning and Cybernetics. IEEE.
[19] Ropero, J., Ariel, G., Carrasco, A., Carlos, L. (2012) A fuzzy logic intelligent agent for information extraction: introducing a new fuzzy logic-based term weighting scheme. Expert Systems with Applications. 39(4), 4567-4581.
[20] Bagheri, S., Asadi, A., Kinsner, W., Sepehri, N. (2016) Ferroelectric random access memory (FRAM) fatigue test with Arduino and Raspberry Pi. 2016 IEEE International Conference on Electro Information Technology (EIT). IEEE.
[21] Sharma, J., Anbarasu, M., Chakraborty, C., Shanmugasundaram, M. (2017) Iris movement based wheel chair control using raspberry pi. IOP Conference Series: Materials Science and Engineering. 263, 052049.

Received: **02.01.2020**
Accepted: **30.01.2020**

CORRESPONDING AUTHOR

Linyan Ouyang
College of Artificial Intelligence,
Yango University,
Fuzhou 350015 – China

e-mail: jiabaoyu63@sina.com

© by PSP Volume 29 – No. 04A/2020 pages 3230-3239 Fresenius Environmental Bulletin

NITROGEN REMOVAL IN DITCH WETLAND SYSTEMS: EFFECTS OF HYDRAULIC RETENTION TIME (HRT) AND SPATIAL CONFIGURATION

Wenjing Wang, Zifang Chi*, Ying Yin

Key Lab of Groundwater Resources and Environment, Ministry of Education, Jilin University, Changchun 130021, China

ABSTRACT

The two ditch wetland systems coupling substrate dam with constructed wetland, with different spatial configurations of substrate dam (20 and 0 cm distances, DW1 and DW2), were built to study nitrogen removal of the sewage under different HRTs (0.5d, 1d, 2d). The results showed that the gravel+zeolite and gravel+ceramsite were preferred to ammonia nitrogen adsorption. The removals of COD, nitrate nitrogen and total nitrogen appeared an increasing trend as the increase of pollutant loads, while ammonia nitrogen showed an increasing first and then decreasing trend. COD and nitrate nitrogen removals were stable at around 85% and 97%, ammonia nitrogen removal remained at about 40%, and the total nitrogen finally was stable at more than 70%. Continuous results showed that COD, ammonia nitrogen, nitrate nitrogen and total nitrogen removal presented the downward trend, and the performance of DW1 was superior to the DW2 under the condition of HRT 0.5d, suggesting that the physical-chemical function might play a major role. The removal of ammonia nitrogen was effectively enhanced with the increase of HRT (2d), and the performance of DW2 is higher than the DW1. The ammonia nitrogen, nitrate nitrogen and total nitrogen removal stood at 33%, 98% and 65% in DW2, respectively.

KEYWORDS:
Ditch wetland, HRT, spatial configuration, nitrogen removal

INTRODUCTION

Man-made ditch was the artificial channel excavated for drainage and irrigation. As the corridor of drained and irrigated water, it can improve soil structure, promote crop growth, and improve crop output. The artificial ditch can also play its ecological environment effect to improve the whole ecological environment [1]. Ditch wetland had a good retention effect on various forms of nitrogen and phosphorus [2, 3], and could reduce effectively the potential toxic effects of pollutants in the agricultural drainage ditch system [4, 5], and avoid the delocalization caused by ditch irrigation [6]. Ditch wetlands had the capacity to remove and purify non-point source pollutants from agricultural drainage by sediment retention, plant absorption and microorganism decomposition [7].

Under the influence of crop and environmental conditions, the fate of nitrogen fertilizer was a comprehensive manifestation of the transformation and movement of nitrogen in soil [8]. The loss of farmland nitrogen was the main contributor of agricultural non-point source pollutants, such as the loss of nitrate leaching [9, 10] and surface runoff [11-13]. The problem of environmental pollution caused by nitrogen loss in farmland was becoming more and more serious, which posed a serious threat to the sustainable development of modern agriculture and social economy [14-16]. Northeast China was an important grain core producing area and the largest commodity grain production base, and the application of excessive nitrogen fertilizer caused nitrogen (such as ammonia nitrogen and nitrate nitrogen) pollution to enter the surrounding receiving water body, which could cause eutrophication [17-19]. Although drainage ditches can play a role in pollutant purification to some extent, there was the problem of low treatment efficiency [20-24].

Therefore, the development of new constructed wetland technology had an important practical significance. The aim of the study was to investigate the effects of different hydraulic retention time (HRT) and spatial configuration of substrate dam on nitrogen removal for two ditch wetland systems coupling substrate dam with constructed wetland, which was expected to provide technical support for the operation and promotion of the ditch wetland system.

MATERIALS AND METHODS

Experimental Device. The two ditch wetland systems coupling substrate dam with constructed wetland were applied (Fig. 1). The device size was 100cm in length, 15cm in width, 35cm in depth,

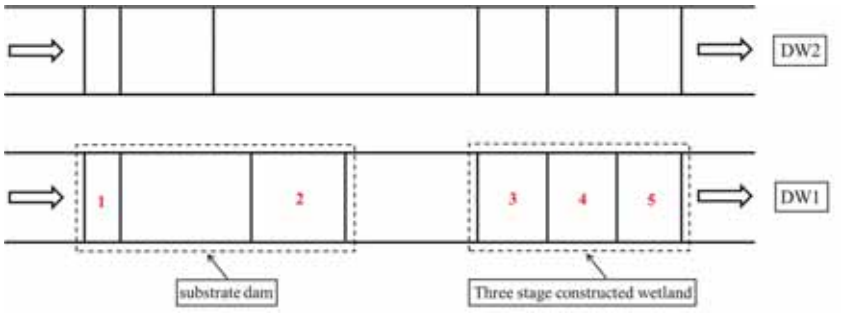

FIGURE 1
Schematic diagram of the ditch system coupling substrate dam with constructed wetland

TABLE 1
Characteristics of the simulated wastewater

COD mass concentration (mg/L)	NH_4^+-N mass concentration (mg/L)	NO_3^--N mass concentration (mg/L)	TN mass concentration (mg/L)	TP mass concentration (mg/L)	pH	temperature (°C)
50～300	5～30	5～30	10～60	8	7	25

TABLE 2
Test indicators, Test indicators and instruments of water samples

Test indicators	Test indicators	Test instruments
COD	Potassium dichromate method	-
NH_4^+-N	Nessler reagent spectrophotometry	automated discrete analyzer SMART CHEM 200
NO_3^--N	Ultraviolet spectrophotometry	automated discrete analyzer
TN	Alkaline potassium persulfate digestion ultraviolet spectrophotometric method	automated discrete analyzer

and the depth of substrate was 30cm and the effective water depth was 30cm. The experimental device was composed of substrate dam and constructed wetland. Among them, the first level substrate dam was SS interception dam (No. 1, width 5cm), the second level matrix dam was ammonia nitrogen interception dam (No. 2, width 15cm), and there was no plant cultivation. The constructed wetland was composed of three wetland units (No.: 3-4-5), all of which were 10cm wide, and *Canna indica* was planted above. In this experiment, two ditch wetland systems coupling substrate dam with constructed wetland (DW1 and DW2) were set up. In DW1, the distance between the first level substrate dam and the second level matrix dam was 20cm, while the two substrate dams were connected in DW2. The orders of substrates in DW1 and DW2 from left to right (1-2-3-4-5) were gravel, gravel+zeolite, slag, volcanic rock, gravel and gravel, gravel+ceramsite, slag, volcanic rock and gravel, respectively. The particle sizes of ceramsite, slag, volcanic rock and gravel were 5~6 mm, 30~50 mm, 20~30 mm and 20~30 mm, respectively. The water flow entered from the left side and discharged from the right side.

Experimental Design and Analysis Methods. Simulated wastewater was used and mainly made up of sodium acetate, potassium nitrate, ammonium chloride and potassium dihydrogen phosphate. The quality of simulated wastewater was illustrated in Table 1.

A series of flask-shaking tests in this study were carried out to select a combined matrix filler with high efficiency of ammonia nitrogen adsorption and easy to hang biofilm. The effluent concentrations and removal efficiencies of DW1 and DW2 were investigated under different HRTs (0.5d, 1d and 2d). The continuous influent mode was adopted by peristaltic pump and the sampling period was 24h. COD, ammonia nitrogen, nitrate nitrogen, total nitrogen in water samples were monitored. The methods and instruments were summarized in Table 2 [25, 26].

RESULTS AND DISCUSSION

Screening High Efficiency Ammonia Nitrogen Adsorption Substrates. The influences of eight fillers (gravel, zeolite, vermiculite, slag, ceramsite, volcanic rock, sponge iron and biochar) on ammonia nitrogen adsorption were studied by static simulation test. It can be seen that vermiculite and gravel had good adsorption effect on ammonia nitrogen, and zeolite, volcanic rock, ceramsite and slag took the second level, while sponge iron and biochar were poor (Fig. 2). Furthermore, Langmuir adsorption isotherm and Freundlich adsorption

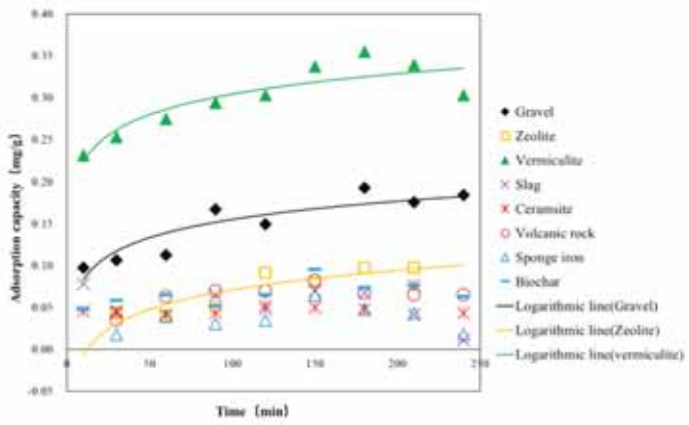

FIGURE 2
The adsorption kinetics of ammonia nitrogen under different substrates

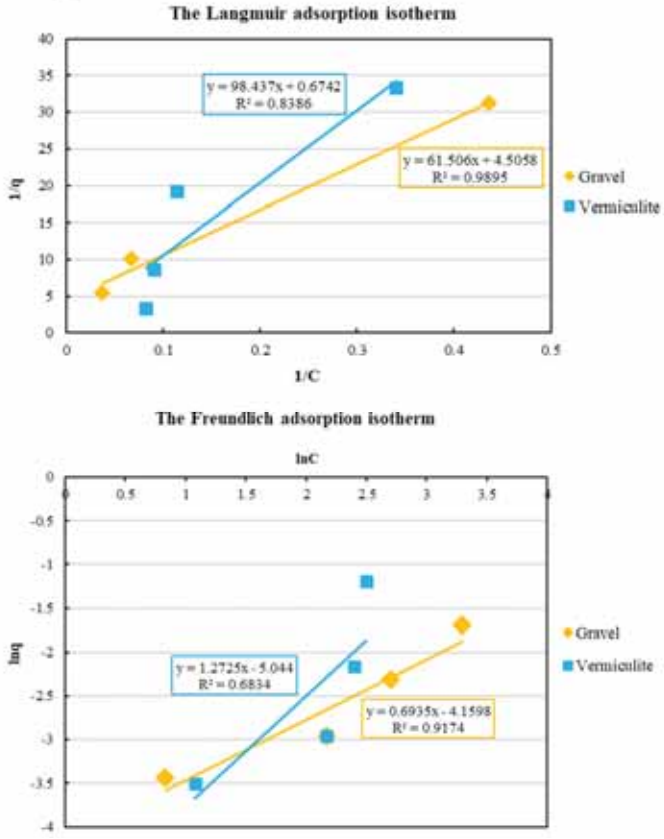

FIGURE 3
The Langmuir and Freundlich adsorption isotherms on the vermiculite and gravel

isotherm were used to simulate the adsorption data of vermiculite and gravel, and the results were shown in Fig. 3. It can be seen that the adsorption isotherm equations of Langmuir and Freundlich better described the adsorption behavior of ammonia nitrogen on gravel, and the correlation coefficient (R^2) of the equations were greater than 0.9, so the adsorption mechanism could be described as the monolayer adsorption process on the uneven surface, and the maximum adsorption capacity of ammonia nitrogen was 0.22mg/g. Some studies showed that zeolite had better adsorption capacity for ammonia nitrogen, while the adsorption capacity of zeolite for ammonia nitrogen was lower than that of gravel in this study, which might be related to the difference of substrate particle size and chemical composition [27, 28]. Vermiculite could be described by Langmuir adsorption isotherm (R^2 > 0.8), and the maximum adsorption capacity was as high as 1.48 mg/g. Nie et al. [29] showed that

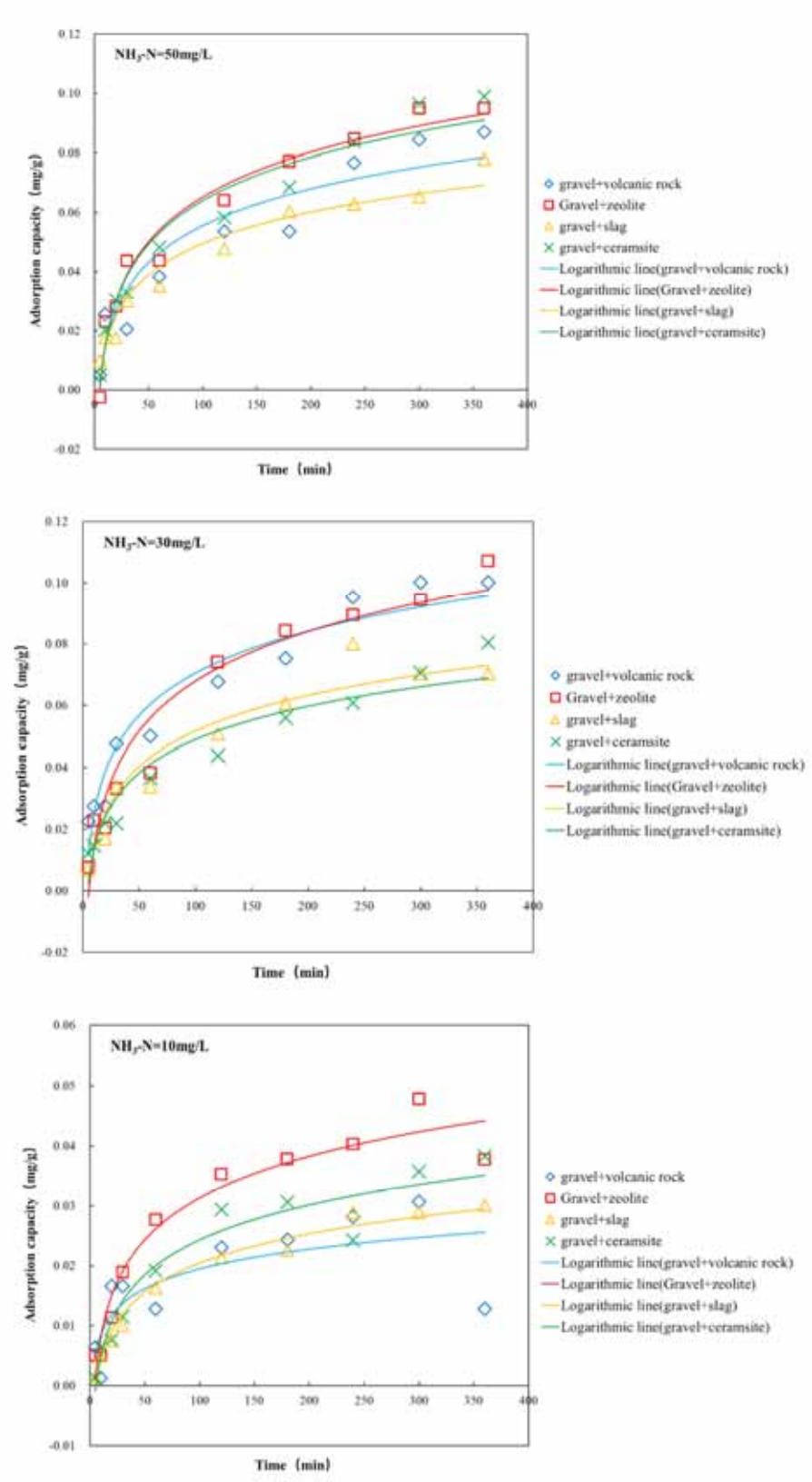

FIGURE 4
The adsorption kinetics of ammonia nitrogen under combined substrates

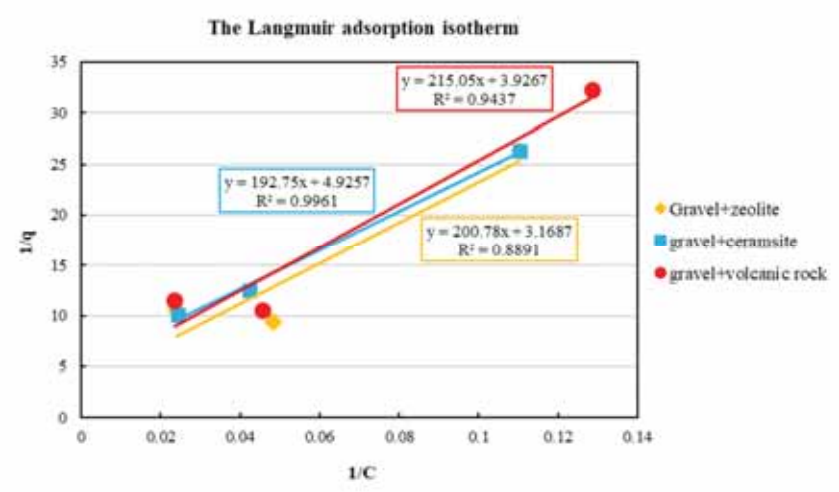

FIGURE 5
The Langmuir adsorption isotherm on the combined substrates

vermiculite had good adsorption performance for ammonia nitrogen. However, vermiculite was not used as engineering filler because it was fragile and easy to float. Therefore, gravel with relatively large adsorption capacity and fast adsorption rate was selected as engineering filler.

Optimization of High Efficiency Adsorption/easy Hang Biofilm Combined Substrate. Considering the important role of biofilm in wetland processes, the combination of gravel and easy hang membrane filler were optimized. It can be seen from the results that the adsorption sequence of ammonia nitrogen under different initial concentrations were: gravel+zeolite > gravel+ceramsite > gravel+volcanic rock > gravel+slag (Fig. 4), and the average adsorption rates were 0.02125, 0.02100, 0.01925 and 0.01575 mg/g/h, respectively. In addition, the Langmuir adsorption isotherm equation was used to fit the ammonia nitrogen adsorption data of gravel+zeolite, gravel+ceramsite and gravel+volcanic rock, and the maximum adsorption capacities were 0.3157, 0.2030 and 0.2547 mg/g, respectively (Fig. 5). Some studies found that the adsorption performance of the combined substrate for ammonia nitrogen was higher than that of the single substrate [30]. Therefore, gravel+zeolite and gravel+ceramsite were selected as the fillers of the substrate dam, which possessed with fast adsorption rate, large adsorption capacity and easy hang biofilm.

Start-up of Ditch Wetland Systems Coupling Substrate Dam with Constructed Wetland. The increasing load (five stages) was adopted gradually to realize the start-up of the ditch wetland systems (Fig. 6). As a whole, the removal rates of nitrate nitrogen, total nitrogen and COD appeared an increasing trend with the addition of inoculated sludge and pollutant load, while ammonia nitrogen showed an increasing first and then decreasing trend. In stage I, the influent concentrations were COD 50mg/L, ammonia nitrogen 8 mg/L and nitrate nitrogen 8 mg/L, respectively. It could be seen from the results that COD, ammonia nitrogen and nitrate nitrogen were removed to a certain extent due to the substrate adsorption. In stage II, the activated sludge was properly inoculated to improve the microbial denitrification process on the constant pollutant load. We could see that the removal rates of COD and nitrate nitrogen showed an increasing trend, and the removal rates of ammonia nitrogen presented a fluctuating trend after a short period of domestication (Fig. 6). In stage III, the influent load was increased to COD 100mg/L, ammonia nitrogen 10mg/L, nitrate nitrogen 10mg/L. The removal rates of COD and nitrate nitrogen gradually increased and remained stable, and the removal of ammonia nitrogen slightly decreased, which was probably due to the competition of heterotrophic microorganisms. In stages IV and V, the influent load were further increased to COD 150 and 200mg/L, ammonia nitrogen 15 and 20mg/L, nitrate nitrogen 15 and 20mg/L. The removal efficiency of COD and nitrate nitrogen remained stable at about 85% and 97%, and the removal efficiency of ammonia nitrogen still had a downward trend, but remained at about 40%. At the same time, the variation trend of total nitrogen was basically the same as that of nitrate nitrogen, and the removal rate was stable at above 70%. Nitrification and denitrification of microorganisms were the key denitrification ways of wetland system. Sufficient carbon source and nitrate nitrogen in wastewater can improve effectively the denitrification capacity of the system, but there was the certain inhibition on autotrophic nitrifying bacteria [31, 32]. In summary, the enrichment and domestication of denitrifying microorganisms in ditch wetland systems were realized by gradual increasing the load in 32 days, and

the systems had the potential of high efficiency nitrification and denitrification.

Effect of Different HRTs on Denitrification Performance of the Ditch Wetland System. It could be seen from Fig. 7 that when HRT=0.5d, COD concentration in the influent was 300mg/L, ammonia nitrogen concentration was 30 mg/L, and nitrate nitrogen concentration was 30 mg/L, the removal rates of COD, ammonia nitrogen, nitrate nitrogen and total nitrogen presents the downward trend after more than 20 days continuous operation. Among them, the removal efficiency of COD decreased significantly from 60% to 20%, which might be due to the shorter contact time between sewage and biofilm, and the insufficient degradation of pollutants. The removal efficiency of ammonia nitrogen was reduced from 20% to 10%, and DW1 was better than DW2. This may be due to the fact that the shorter HRT and the fast flow rate lead to the weakening of microbial action to some extent. It also proved directly the conclusion from batch tests that zeolite in DW1 had better ammonia nitrogen adsorption capacity. The nitrate nitrogen removal also showed a decreasing trend and decreased from 97% to 50%. In addition, the removal rate of total nitrogen gradually decreased from 60% to about 30%. The performance of DW1 was better than that of DW2 under the condition of short HRT (0.5d), in which physicochemical effect may play a major role.

When HRT was increased from 0.5d to 1d, the removal rates of COD, ammonia nitrogen, nitrate nitrogen and total nitrogen were improved to some extent. As shown in Fig. 8, the removal rate of COD showed an increasing trend and finally stabilized at about 85%, and the ammonia nitrogen removal stabilized at about 15%. And nitrate nitrogen concentration had a certain fluctuation and the removal rate was stable at about 98%. In addition, the total nitrogen removal increased from 30% (HRT=0.5d) to about 60%. With the increase of HRT, the removal performance of DW2 was slightly better than that of DW1, but it was not significant. Thus, the extension of HRT could effectively strengthen the removal of COD, suggesting that the increase of the effective contact time between pollutants and microorganisms could improve the removal efficiency [33].

When HRT was increased to 2d, the removal rate of COD was stable at about 80% after 20 days of continuous operation (Fig. 9). And ammonia nitrogen removal had been effectively enhanced with the increase of HRT, which in both were higher than 25%. The removal rate of DW2 was higher than that of DW1, and it finally stabilized at about 33%. This phenomenon showed that the extension of HRT can improve the ammonia nitrogen removal which could lead to more thorough nitrification

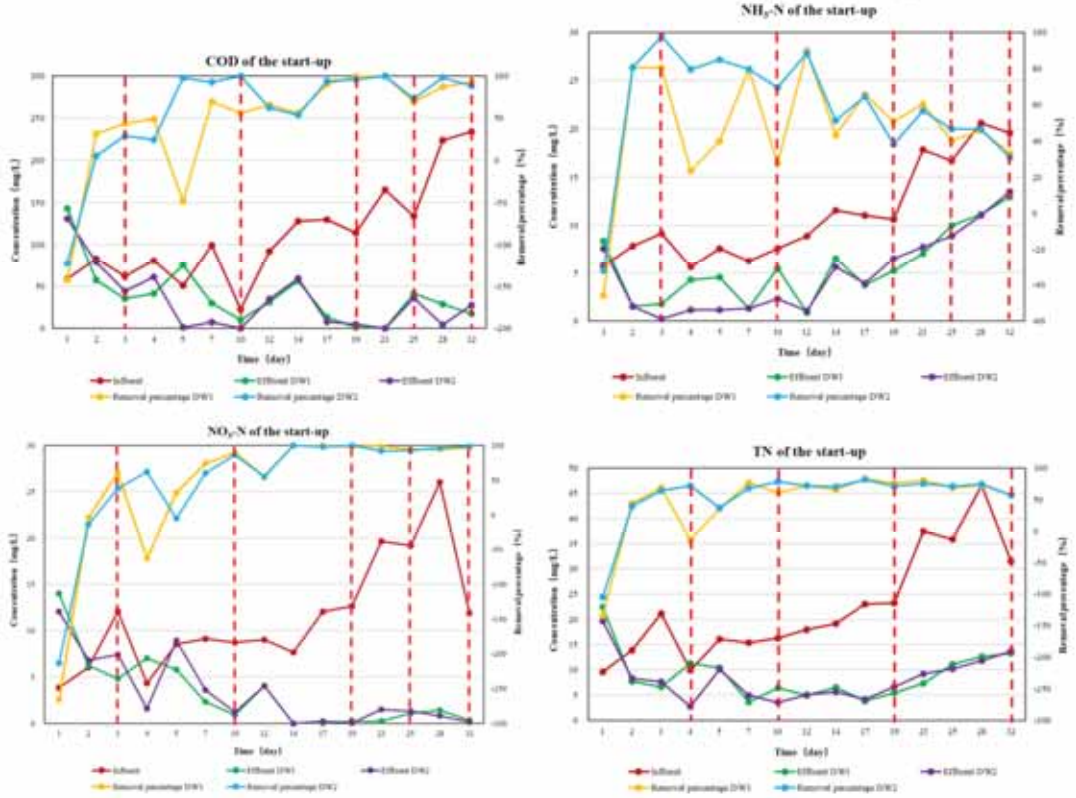

FIGURE 6
The concentration and removal rate of COD and nitrogen species during the start-up phases

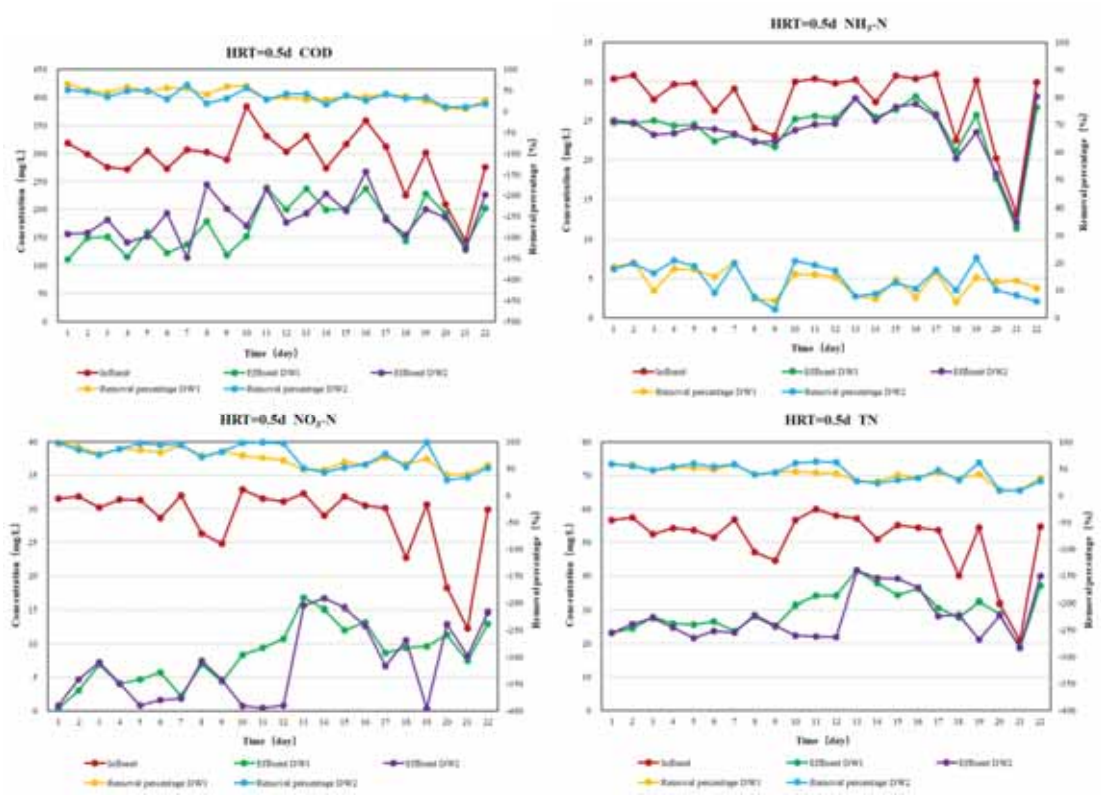

FIGURE 7
The concentration and removal rate of COD and nitrogen species under HRT=0.5d

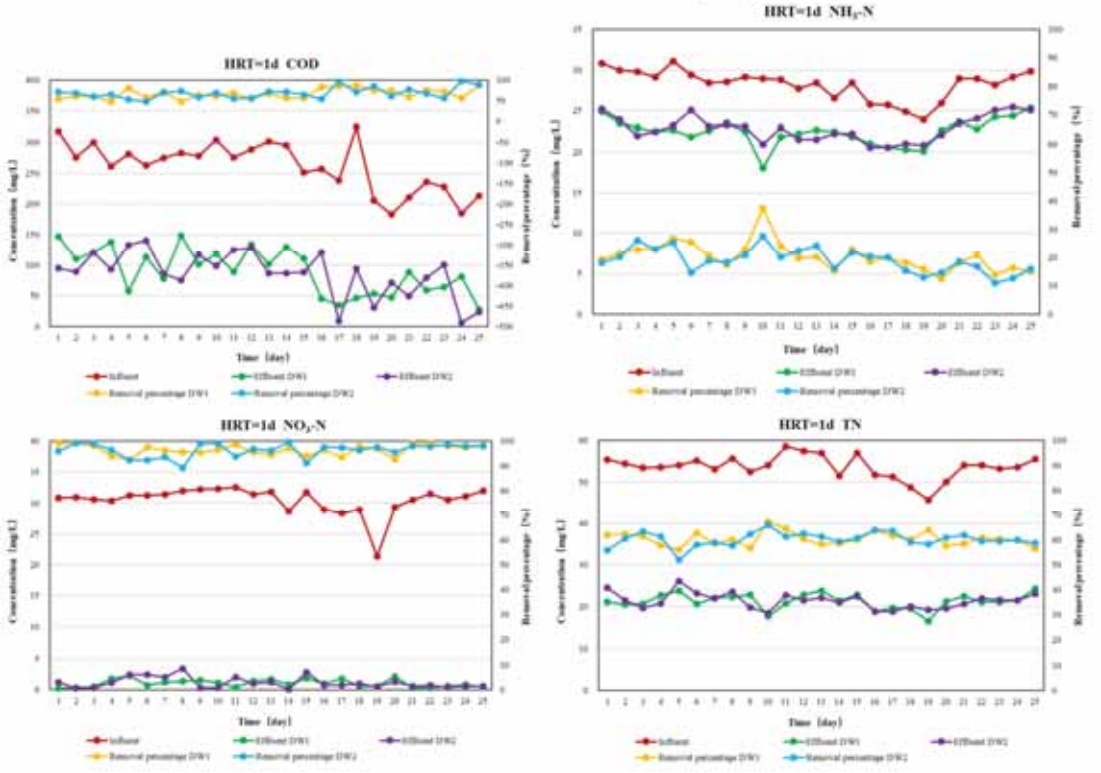

FIGURE 8
The concentration and removal rate of COD and nitrogen species under HRT=1d

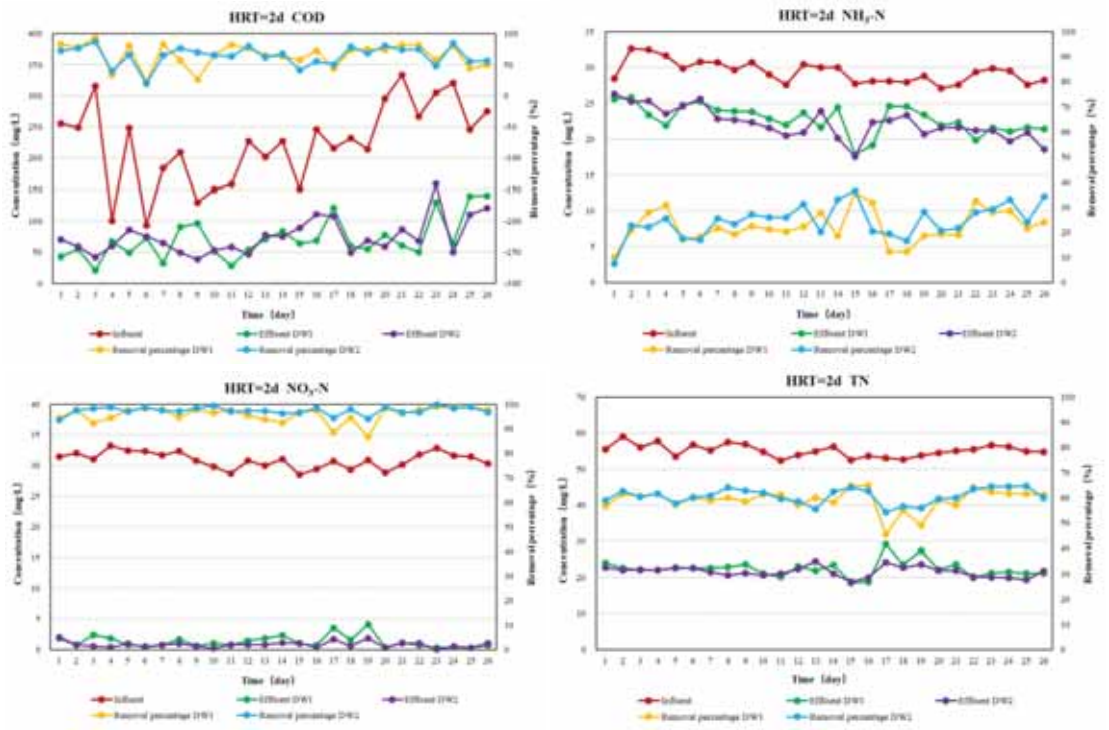

FIGURE 9
The concentration and removal rate of COD and nitrogen species under HRT=2d

process [34]. In addition, the nitrate nitrogen removal were relatively stable for two ditch wetland systems, both of which were stabilized at above 98%. The removal efficiency of total nitrogen in DW2 was better than that of DW1, and it reached about 65% which might be related to good microbial nitrification. Some studies showed that total nitrogen removal was positively correlated with HRT, and the extension of HRT could improve nitrogen removal [35]. Therefore, the extending HRT within a certain range could effectively improve the purification efficiency of the ditch system. The enhancement effect of reoxygenation based on the open water area in DW1 was less than the effect of nitrification by the ceramsite biofilm in DW2. DW2 mode had stronger nitrogen removal potential, especially nitrification potential, which could be used as an alternative mode for subsequent engineering application (HRT=2d). At the same time, the reoxygenation of increasing the open water area could only be used as an auxiliary measure.

CONCLUSIONS

Gravel+zeolite and gravel+ceramsite were the preferred matrix fillers for ammonia nitrogen removal. The enrichment and domestication of the functional microflora in DW1 and DW2 were realized by gradual increasing the load on 32 days. The nitrogen removal showed a downward trend under the condition of short HRT (0.5d), and the performance of DW1 was better than that of DW2. With the increase of HRT (2d), the removal efficiency in DW2 was higher than that of DW1, in which good nitrification led to its stronger nitrogen removal potential. The enhancement effect of reoxygenation based on the open water area between the substrate dams in DW1 was less than the effect of nitrification by the ceramsite biofilm in DW2. Reoxygenation of the open water area could only be used as an auxiliary measure to improve the denitrification performance of ditch wetland.

ACKNOWLEDGEMENTS

The work was supported by the National Natural Science Foundation of China (Nos. 41977158 and 41772244) and the National Key R&D Program of China (NO. 2018YFD0800904).

REFERENCES

[1] Xi, M., Lu, X., Liu, H. (2005) Effects of man-made ditch on eco-environment: A research review. Chinese Journal of Ecology. 24(12), 1471-1476.

[2] Yin, C., Lan, Z., Yan, W. (1995) Retention of allochthonous nutrients by ecotones of Baiyangdian Lake. Chinese Journal of Applied Ecology. 6(1), 76-80.
[3] Qu, X., Jia, H., Zhang, H., Li, X., Li, P. (2000) Preliminary study on purification function of reed wetland for nutrients from land sources. Chinese Journal of Applied Ecology. 11(2), 270-272.
[4] Bouldin, J.L., Milam, C.D., Farris, J.L., Moore, M. T., Smith Jr, S., Cooper, C.M. (2004) Evaluating toxicity of Asana XL (esfenvalerate) amendments in agricultural ditch mesocosms. Chemosphere. 56(7), 677-683.
[5] Louchart, X., Voltz, M., Coulouma, G., Andrieux, P. (2004) Oryzalin fate and transport in runoff water in Mediterranean vineyards. Chemosphere. 57(8), 921-930.
[6] Causapé, J., Quílez, D., Aragüés, R. (2004) Assessment of irrigation and environmental quality at the hydrological basin level: I. Irrigation quality. Agricultural Water Management. 70(3), 195-209.
[7] Jiang, C., Cui, G., Fan, X., Zhang, Y. (2004) Purification Capacity of Ditch Wetland to Agricultural Non-point Pollutants. Environmental Science. 25(2), 125-128.
[8] Li, S., Li, J. (2001) Research progress on losses of fertilizer nitrogen. Agricultural Environmental Protection. 20(5), 377-379.
[9] Wang, J.Y., Wang, S.J., Chen, Y. (1994) Study on leaching loss of nitrogen in ricefields by using large undisturbed monolith lysimenters. Pedosphere. 4(1), 87-92.
[10] Owens, L.B., Edwards, W.M., Van Keuren, R.W. (1999) Nitrate leaching from grassed lysimeters treated with ammonium nitrate or slow-release nitrogen fertilizer. Journal of Environmental Quality. 28, 1810-1816.
[11] Sharpley, A.N., Simth, S.J., Naney, J.W. (1987) Environmental impact of agricultural nitrogen and phosphorus use. J. Agric. Food Chem. 35, 812-817.
[12] David, M.B., Gentry, L.E., Kovacic, D.A., Smith, K.M. (1997) Nitrogen balance in and export from agricultural watershed. Journal of Environmental Quality. 26, 1038-1048.
[13] Eghball, B., Gilley, J.E. (1999) Phosphorus and nitrogen in runoff following beef cattle manure or compost application. Journal of Environmental Quality. 28, 1201-1210.
[14] Zak, D., Kronvang, B., Carstensen, M.V., Hoffmann, C.C., Kjeldgaard, A., Larsen, S.E., Audet, J., Egemose, S., Jorgensen, C.A., Feuerbach, P., Gertz, F., Jensen, H.S. (2018) Nitrogen and phosphorus removal from agricultural runoff in integrated buffer zones. Environmental Science and Technology. 52(11), 6508-6517.
[15] Moeder, M., Carranza-Diaz, O., López-Angulo, G., Vega-Aviña, R., Chávez-Durán, F.A., Jomaa, S., Winkler, U., Schrader, S., Reemtsma, T., Delgado-Vargas, F. (2017) Potential of vegetated ditches to manage organic pollutants derived from agricultural runoff and domestic sewage: A case study in Sinaloa (Mexico). Science of The Total Environment. 598(15), 1106-1115.
[16] Yang, Y., Chen, Y., Zhang, X.L., Ongley, E., Zhao, L. (2012) Methodology for agricultural and rural NPS pollution in a typical county of the North China Plain. Environmental Pollution. 168, 170-176.
[17] Sun, C., Zhou, H., Chen, L., Shen, Z., Wang, H., Liu, H. (2018) Pollution grade assessment of nitrogen leaching from farmland fertilizer in three northeastern provinces. Journal of Agricultural Resources and Environment. 35(5), 405-411.
[18] Zhang, W., Wu, S., Ji, H., Kolbe, H. (2004) Estimation of Agricultural Non-Point Source Pollution in China and the Alleviating Strategies I. Estimation of Agricultural Non-Point Source Pollution in China in Early 21 Century. Scientia Agricultura Sinica. 37(7), 1008-1017.
[19] National Bureau of Statistics. (2007) Bulletin of the First National Census on Pollution Source. http://www.stats.gov.cn/tjgb/qttjgb/qgqttjgb/t20100211_402621161.htm.
[20] Ma, F., Xing, S., Xu, Y., Gong, J., Tian, Y., Ma, Y.H. (2019) Temporal and Spatial Distribution and Output Characteristics of Nitrogen and Phosphorus in Farmland Drainage Ditch in Polder Area around Chaohu Lake. Guangdong Agricultural Sciences. 2019(5), 67-73.
[21] Bracewell, S., Verdonschot, R.C.M., Schäfer, R.B., Bush, A., Lapen, D. R., Van den Brink, P. J. (2019) Qualifying the effects of single and multiple stressors on the food web structure of Dutch drainage ditches using a literature review and conceptual models. Science of The Total Environment. 684, 727-740.
[22] Wang, Y., Wang, J., Li, W., Bo, L., Yang, L. (2010) Initial Exploration of Mechanism of Ecological Ditch Intercepting Nitrogen and Phosphorus in Drainage from Farmland. Journal of Ecology and Rural Environment. 26(6), 586-590.
[23] Yang, L.Z., Zhou, X.P., Wang, J.G., Wang, D.J., Shi, W.M., Shi, L.X. (2005) Ecological ditch system with interception function and its effects on controlling farmland non-point pollution. Chinese Journal of Ecology. 24(11), 1371-1374.

[24] Kröger, R., Cooper, C.M., Moore, M.T. (2008) A preliminary study of an alternative controlled drainage strategy in surface drainage ditches: Low-grade weirs. Agricultural Water Management. 95(6), 678-684.
[25] Li, H., Yan, B., Cheng, L., Zhou, Q., Zhu, H., Wang, L., Ou, Y. (2016) Effect of Effluent Recirculation on the Nitrogen and Phosphorus Removal in Horizontal Baffle Subsurface Flow Constructed Wetland under Effluent Reflux. Wetland Science. 14(6), 860-865.
[26] Li, H., Yan, B., Li, H., Xu, X., (2018) Distribution Characteristics of Nitrogen and Phosphorus in Soils of Typical Saltwater-freshwater Interface Wetlands of the Yellow River Delta. Wetland Science. 16(5), 679-683.
[27] Chen, L.L., Zhang, C.J., Li, P., Li, X.R., Dong, R.Z., Zhao, T.K. (2012) Study on ammonia nitrogen adsorption characteristics of different substrates in constructed wetland. Ecology and Environmental Sciences. 21(3), 518-523.
[28] Wang, W., Hu, F., Kong, L. (2016) Adsorption Capacity of Substrates of Denitrification and Dephosphorization in Constructed Wetlands and Their Influencing Factors. Wetland Science. 14(1), 122-128.
[29] Nie, F., Wu, X., Hu, Y. (2003) NH_4-N Removal Capacity of Vermiculite Stuffing in Constructed Wetland. Urban Environment and Urban Ecology. 16(6), 280-282.
[30] Zhao, D., Zhang, S., Zhao, S., Zhao, Y., Tian, W., Liu, J. (2018) Screening of ammonia nitrogen removal schemes from construct wetland matrix and dynamic analysis of influencing factors. Journal of Water Resources and Water Engineering. 29(4), 121-126.
[31] Zhao, L., Shao, X., Wu, M., Jiang, X.S., Lu, L.Y. (2018) Effects of Different Substrates and Particle Sizes on Wastewater Purification. Environmental Science. 39(9), 1-8.
[32] Li, H., Chi, Z., Yan, B., Cheng, L., Li, J. (2017) An innovative wood-chip-framework substrate used as slow-release carbon source to treat high-strength nitrogen wastewater. Journal of Environmental Sciences. 51, 275-283.
[33] Liu, Z., Shao, X., Hou, R., Chen, Y. (2018) Effect of HRT on Nitrogen and Phosphorus Removal in Integrated Domestic Sewage Treatment Device. Technology of Water Treatment. 44(4), 95-97.
[34] Cheng, L., Li, H., Yan, B. (2016) The Nitrogen and Phosphorus Removal Efficiency of Horizontal Baffle Subsurface Flow Constructed Wetland without Plants. Wetland Science. 14(2), 219-225.
[35] Xu, J., He, S., Wu, S., Huang, J., Zhou, W., Chen, X. (2016) Effects of HRT and water temperature on nitrogen removal in autotrophic gravel filter. Chemosphere. 147, 203-209.

Received: **02.01.2020**
Accepted: **29.01.2020**

CORRESPONDING AUTHOR

Zifang Chi
Key Lab of Groundwater Resources and Environment, Ministry of Education,
Jilin University,
Changchun 130021 – China

e-mail: chizifang@jlu.edu.cn

© by PSP Volume 29 – No. 04A/2020 pages 3240-3253 Fresenius Environmental Bulletin

PRACTICES OF COASTAL ZONE MANAGEMENT OF THE JORDANIAN GULF OF AQABA BY MAPPING SPATIAL CONVERGENCE OF SEAFRONT HUMAN ACTIVITIES AND THEIR POTENTIAL IMPACT ON THE MARINE ENVIRONMENT

Ala'aldin Alrowwad[1], Ali Al Sawalmih[2,3,*], Riyad Manasrah[4], Mohammed Rasheed[5], Maysoon Kteifan[2], Aiman Soleiman[6], Zeinab Arabeyyat[4], Ahmad M. Al-Saad[7], Samantha Barnett[2]

[1]School of Business, The University of Jordan, Aqaba 77110, Jordan
[2]Marine Science Station (MSS), The University of Jordan and Yarmouk University, Aqaba 77110, Jordan
[3]Max-Planck Institute for Colloids and Interfaces (MPIKG), 14476 Potsdam, Germany
[4]Faculty of Basic & Marine Sciences, The University of Jordan, Aqaba 77110, Jordan
[5]Chemistry Department, The University of Jordan, Amman 11942, Jordan
[6]Aqaba Special Economic Zone Authority (ASEZA), Aqaba 77110, Jordan
[7]Dept. of Physics, Jordan University for Science and Technology (JUST), Irbid, Jordan

ABSTRACT

This study aims to present the practices of coastal zone management of the Jordanian coastline in the Gulf of Aqaba by mapping and analyzing the business sectors along the Jordanian coastline and their corresponding potential impact on marine environment. Geographic Information System (GIS) tools were applied in order to illustrate the spatial convergence of current human activities along the coastal zone region. Although the Jordanian Gulf of Aqaba looks increasingly overused due to the relatively limited shoreline (~27km), it is almost managed due to successful spatial clustering of coastal sectors, which resulted that human activities, mostly tourism and industrial terminals, is continuing to grow, without remarkable conflict with one another. Conserving space for nature, e.g., the Aqaba Marine Park and potential new marine protected areas, may not conflicts with marine shipping in a big extent, after translocating Aqaba Port to the southernmost area. The results of the study present an overview of the coastal management of the Jordanian coast of the Gulf of Aqaba and aim to depict possible impact of existing human activities with ecosystem components. This study also shows the development of an effective coastal management in the Jordanian coastline, as an element of integrated coastal-use management that calls for sustainable development.

KEYWORDS:
Coastal management, business coastal sectors, Gulf of Aqaba, marine environment, human uses, conflicts, GIS mapping

INTRODUCTION

The coastal land-based sea-front human activities along the Jordanian shoreline in the Gulf of Aqaba (including industrial and touristic) have undergone remarkable change in terms of shape and disposition due to both natural and anthropogenic interference [1, 2]. The Jordanian shoreline in the Gulf of Aqaba is only 27 km long and is the only maritime gateway of Jordan, with many human activities having claimed the short shoreline in the last 50 years [3-5]. The Jordanian shoreline has become a strategic international asset, with major industrial facilities, shipping activities, and rapidly expanding tourism which may cause severe disturbance and damage to the coastal and marine ecosystems [3].

Though a relatively small body of water, the Gulf of Aqaba hosts an extraordinary diversity of corals and related marine life, with approximately 50% of the Gulf's shoreline being fringed with coral reefs. Understandably, there are concerns that poorly regulated coastal development may transform the ecology in many in these coastal and marine areas, particularly popular nearshore diving areas [6]. These nearshore coral reefs provide essential habitat and energy not only for the biodiversity directly on these reef zones, but their presence and functionality facilitate the existence of numerous other reef-associated species in the region [7, 8].

The current threats to coral life identified in the Gulf of Aqaba region include the transboundary movement of pollutants, phosphate deposition from ship-loading operations, frequent small to moderate oil spills, and thermal pollution from coastal industries. These threats may severely erode coral life, particularly in the Gulf's intensively developed southern that overlap spatially with vulnerable and endangered habitats and species [2, 9-11]. In order to

promote the conservation of marine areas, ASEZA has established a marine protected area, the Aqaba Marine Park, along 7 km of shoreline on the eastern side of the Gulf of Aqaba [12, 13]. One major threat for marine ecology from human activities is littering which occurs in densely populated coastal areas especially public beaches and ferry terminals due to irresponsible behavior from many visitors. Predominate litter types include disposal of cigarette butts, food wrappers, cups, plastic bottles, and beverage cans [14-19]. On the other hand, chemical dust can be transported to seawater by wind at industrial terminals and at the main port area the deposition of chemicals into the aquatic environment during handling and loading operations are also a concern [20]. Big ships and boats at terminals and ports in addition to diving sites in front of the public beach may cause physical damage of marine ecology [21-24]. Another risk on marine ecology from sea-front human activities is the drainage of chemically- and physically-polluted water to coastal water, like saline discharges from desalination plants [25], thermal water from coastal cooling units, effluents from export/import terminals containing colloidal, suspended or dissolved matter, discharged washing/rinsing water and littering of variety of drinks at public beach [26-28]. The threat of hydrocarbons or oil pollution from boats and ships occurs mainly in ports, terminals, and to a lesser extent at marinas at the resorts [29].

In order to balance competing demands on the marine environment, limit ecosystems' degradation, and avoid conflicts among human activities and between human activities and the marine environment, a variety of policies from global to local level under the broad concept of sea use management have arisen and have led to the development of the Sea Use Planning or Marine Spatial Planning (MSP) initiative [30]. MSP is a tool for making informed and coordinated decisions to balance demands for development with the need to protect marine ecosystems, and to achieve social and economic objectives in an open and planned way [31, 32]. ASEZA, the Aqaba Special Economic Zone Authority, was established in 2001 to attract and facilitate sustainable investment in Aqaba in the areas of industry, port development, tourism, infrastructure, utilities and services and is mainly responsible for planning and zoning and administrative of the sea side of the coastal zone [33]. It also has the legislative power to act as the authority that is responsible for the sea use planning and management in integrated fashion.

ASEZA is investing great efforts for maintaining the balance between the economic developments and the integrity as well as the sustainable exploitation of the coastal resources. This challenge has manifested itself in the currently multi-sectorial coastal areas uses which has been overwhelmed by the size and capacity of activities that ranges from the very simple use of the coastal area to the most complex industrial and maritime, as well as to the supper high end scale sea resorts. The 2001-2020 ASEZ General Use Master Plan which was adopted by ASEZA in 2003 is considered by the as a comprehensive vision that defines long-term development strategies for the growth of ASEZ. This Plan establishes goals and policies to sustain coordinated development throughout the area with respect to land use, zoning, density, circulation, utilities, environmental protection, and design guidelines to simplify and streamline the planning approval process.

Within the zoning plan for coastal sectors along the Jordanian coast in the Gulf of Aqaba, ports and terminals were clustered in the southernmost area, by translocating the main port of Aqaba by ASEZA to the southern area. The port relocation and development were established and biodiversity protection was ensured by successfully translocating over 7,000 coral reef colonies from the site of the new Aqaba Port to the Aqaba Marine Park (AMP), with survival rates of transplanted colonies exceeding 85 per cent [34]. Port Services to be developed at the South Port will include: general cargo, grain, bulk liquids including ammonia, vegetable oil, LPG, and bulk salts including phosphate, in addition to oil.

The spatial policy which was adopted by ASEZA in developing the master plan was based on the philosophy of maximum and optimal use of the lands in the zone. This was interpreted in giving "services divisions" scenarios where 50% of development is for tourism-oriented projects and services, while 7% was allocated for Heavy Industries, 13% for light industries and 30 % for services and ports operation. The planning and zoning and administrative responsibility of the sea side of the coastal zone is lying under the jurisdiction of the ASEZA, the legislative power to act as the authority that is responsible for the sea use planning and management in integrated fashion. [13].

This study aims to collect and map the appropriate information related to existing land-based sea-front business sectors of human uses in the Jordanian Gulf of Aqaba and analyze their occupancy of the coastal line, to allow the identification of possible conflicts and compatibilities between these offshore marine uses and conservation features focusing particularly on those introduced by the existing development in the area. It also focuses on the potential environmental challenges facing the Gulf of Aqaba which can proposes an approach to future coastal management in the development process, based on reducing conflicts among uses, reduce conflicts between uses and nature conservation, promote compatible uses where appropriate, and encourage sustainable development in and around the Gulf of Aqaba.

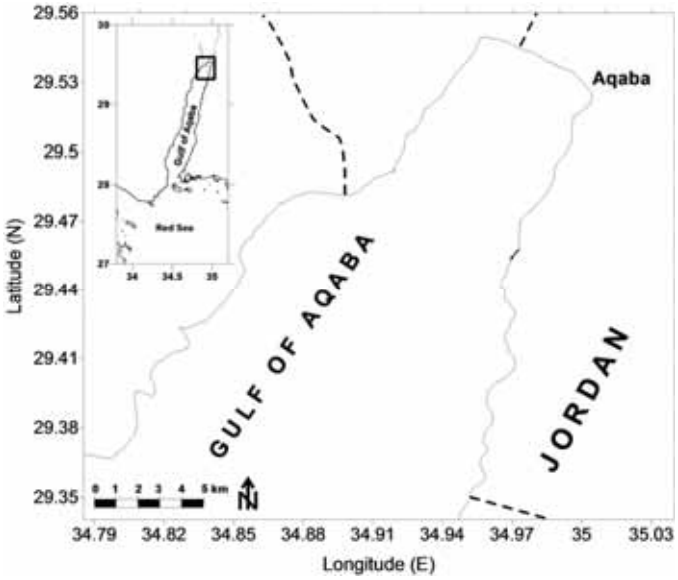

FIGURE 1
The Jordanian coast of the Gulf of Aqaba

MATERIALS AND METHODS

The study area includes the coastal area of the Jordanian Gulf of Aqaba (Figure 1) in the southern part of Jordan, where several human activities take place, among which tourism and terminals are the most important, while other offshore activities may also occur in the future.

This study considers mapping of human activities along the Jordanian coast of the Gulf of Aqaba and tends to identify the spatial patterns of their potential impact on the coastal environment within the case study area. Shapes and borderlines of the coastal facilities were conducted using Google Earth®. Data collection was conducted using various sources from the scientific literature and technical reports. Maps were created using the GIS mapping tool QGIS® in order to depict the offshore overlapping uses of the marine space and the potential environmental impact on marine life.

The most important human activities that take place within the boundaries of the case study area was categorized into three land-based sea-front types of sectors:

A: Tourism/Recreation, B: Ports/Terminals, and C: Services. Tourism/Recreation Sectors are facilities that are mainly offered to the use of humans. We divide this group into sectors based on their corresponding activities as follows: A1: Resort: a facility with combination of residential area, hotels, shopping, swimming pools, beach club and marina, and targeted by frequent tourists, A2: Private resorts: a private property on the coast, A3: Hotels/chalets: mainly used for lodge and sport activities, targeted mostly by tourists. A4: Public Beach: a shoreline that is opened for locals and tourists, so it is mostly crowdy. A5: Marina: Harbor for Settlement of boats and yachts for cruising purposes, and finally A6 which represents shoreline that is currently has no distinct use.

B: Ports/Terminals, an access to navigable water where ships/ferries load or unload. This type of sectors includes the following: B1: Ferry Terminal: harbor for conveying passengers and goods B2: Industrial terminals: terminals for loading specific chemical products like: fertilizers, potash, phosphate, in addition to terminals for the receiving, and storing liquified gas and oil. B3: Container Terminals: exporting and receiving containers, B4: Main Port: exporting and receiving cargo, RO-RO, bulk, retail and other goods. B5: Power Station, which is a sea-front station that uses seawater for cooling.

C: Services includes every facility that is marine related authority, like: C1: Security (navy, border security, etc.), C2: Harbor, C3: Research, C4: others. In addition to the above sectors, there are sea-based activities like diving, fishing, and cruising.

Each sector mentioned above and based to its function, has specific properties that interact with the marine environment through sea water. The potential threats to marine life that may occur by the sea-front sectors are as follows: littering which include materials that degrade slowly in the sea, which includes also microplastics, chemicals, physical damage to marine habitat and coral reef, drainage of chemical/thermal waste, and finally the oil pollution by hydrocarbons.

Based on the type of the coastal use of the Jordanian shoreline, the corresponding major potential impacts on marine ecology and seawater quality were determined, namely, littering, chemicals that are being leaked through loading and handling at ports, physical damage of marine habitat due to anchoring or direct proximity to the corals in diving

and snorkeling, drainage of chemically- and physically polluted water which liker saline water, cooling water and any chemical liquids that may be discharged at public beach, and oil/hydrocarbons pollution from leakage or boats. Seawater can be considered as the medium of transport of pollutants and through which the pollution can reach the marine life. Table 1 represents the level of threat of each group of sectors on the marine environment and biodiversity, especially coral reef, that was identified based on the function of each sectors, as high (black), medium (grey), and low (white).

RESULTS AND DISCUSSIONS

The study area of the Jordanian shoreline in the Gulf of Aqaba hosts a considerable number of land-based sea-front human activities, A: Tourism/Recreation, B: Ports/Terminals, and C: Services, and their corresponding shoreline length are listed in Table 2. Figure 2 represents a map of the Gulf of Aqaba illustrating the spatial convergence of coastal sectors along the shoreline and suggests successful zoning plan and clustering of sectors based on their type of service, and ensures absence of interactions or possible conflicts among overlapping human activities. The zoning resembles northern and middle touristic clusters of sectors and middle and southern industrial/terminal zones [13]. ASEZA has identified spatially explicit management actions to lead to the desired spatial vision for the use of the coast, as zoning scheme is developed to support the implementation of a master plan comprised of a General Land-use Plan, Sea-use Plan, Environmental Sensitivity Plan, and a General Transportation Plan, which focus on zoning and clustering of human activities in the area [6].

ASEZA has developed a master plan for Aqaba city in 2001 in which the old main port land use has been altered to be dedicated for touristic uses and relocated all ports operations to the far southern area in addition to the existing middle terminal area. This zoning process aims toward allowing more space for natural growth of economical and touristic development of the city. The relocation of the Main Port has established a logistically served port supported by industries in order to increase the handling volumes, enhance the handling and storage efficiency and reduce the cost in addition to improving the environmental conditions of the city and developing the southern zone in accordance with Master plan's objectives [13].

Figure 3 shows the occupancy length of the coast by each type of coastal sector. Shoreline used by tourism and recreation sectors represent 66% of the total shoreline, whereas 29% of the shoreline is dedicated to ports and terminals sectors and the rest (5%) for authority services. This result reveals that the Jordanian coastline is mainly dedicated for tourism and recreation use.

Maps in Figure 4 illustrates spatial mapping of all sectors in each type, while their length and percentage of the coastline that is occupied by each sector are shown in Figure 5. From the total shoreline length that is being used by the tourism/recreation sector (app. 17.9 km), public beach represents 43% of the total tourism use, while 34% used by resorts (A1+A2), 11% for hotels/chalets, and the rest for marina and others. The total coastal line length that is being used for ports/terminal sectors is 7832 m, from which 50% is used by industrial terminals, 23% for the main port, 18% for the container terminal, and the rest for transport/ferries terminal and power station.

TABLE 1
The level of threat of each sector on the marine environment and biodiversity

		Littering	Chemical Dust	Physical Damage	Drainage	Oil Pollution
A: Tourism/ Recreation	A1: Resorts					
	A2: Private resorts					
	A3: Hotels/chalets					
	A4: Public Beach					
	A5: Marina					
	A6: Unused					
B: Ports/ Terminals	B1: Ferry Terminal					
	B2: Industrial Terminals					
	B3: Container Terminals					
	B4: Main Port					
	B5: Power Station					
C: Services	C1: Security					
	C2: Harbor					
	C3: Research					
	C4: Others					

(white: low, grey: medium, black: high)

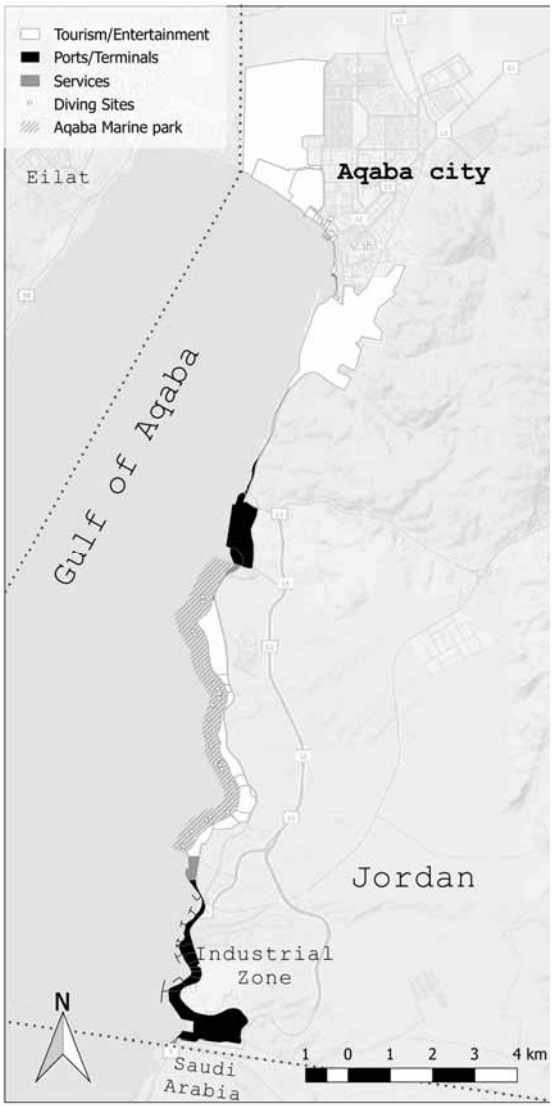

FIGURE 2
Map shows all sectors existing along the Jordanian coastline of the Gulf of Aqaba

TABLE 2
The shoreline length and area of coastal corporations on the Jordanian Gulf of Aqaba

	Sector	length (m)
A: Tourism/ Recreation	A1: Resorts	4686
	A2: Private resorts	1340
	A3: Hotels/chalets	1946
	A4: Public Beach	7678
	A5: Marina	1153
	A6: Unused	1092
	Sum	17895
B: Ports/ Terminals	B1: Ferry Terminal	413
	B2: Industrial terminals	3887
	B3: Container Terminals	1422
	B4: Main Port	1762
	B5: Thermal water	348
	Sum	7832
C: Services	C1: Security	633
	C2: Harbor	250
	C3: Research	403
	C4: Others	240
	Sum	1526

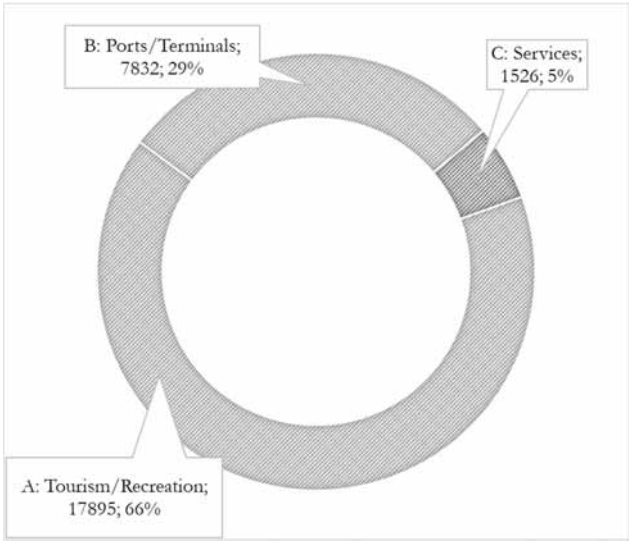

FIGURE 3
Coastal length all groups

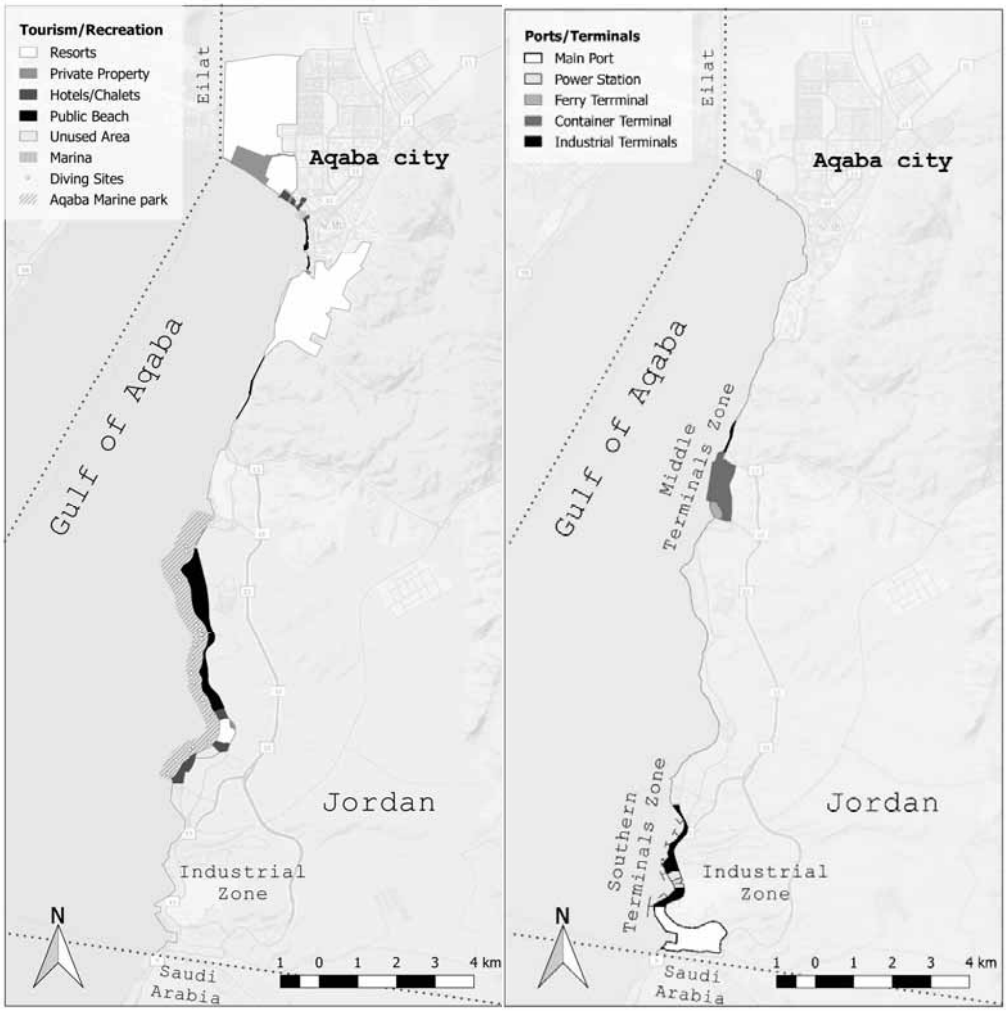

FIGURE 4
Maps shows sectors of Tourism/recreation (left) and Ports/Terminals (right)

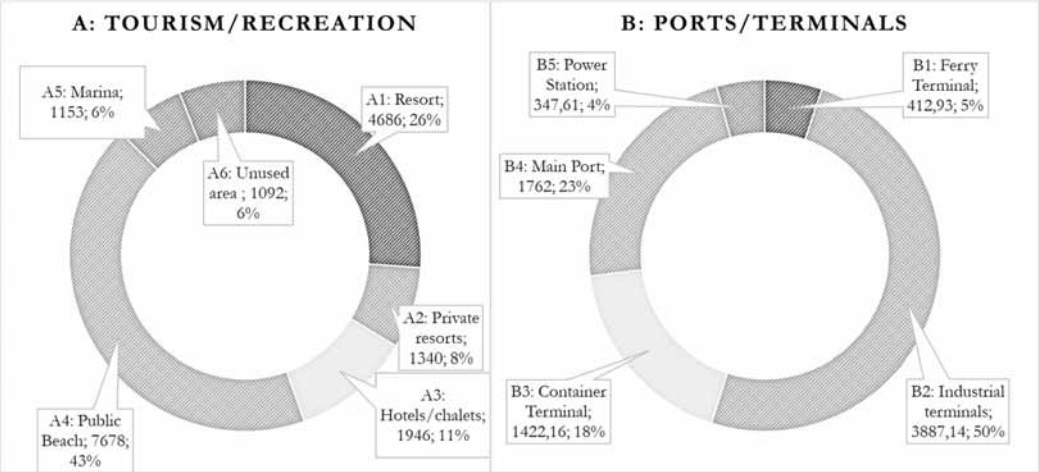

FIGURE 5
Coastal length of sectors A, and B

Besides having the tourism/recreation sectors almost two-third of the total coastal length, the public beach with free access opportunities to the Jordanian coast has remarkably approximately 29% of the total coastal length, indicating successful planning that comes in accordance with socio-economic participation for public tourism in Aqaba and Jordan, adding to that beaches that are attached to the hotels, chalets, and resorts.

Resorts in Aqaba represent major investments, like Ayla Oasis, Saraya Aqaba, Marsa Zayed, and Talabay. Ayla Oasis is a project that includes a variety of up-market hotels, unique residential communities, a golf course and a town center that encompasses a marina, retail units, cafes, entertainment and recreational facilities and the project has created new bay and lagoons along 17 km of seafront. In order to maintain reasonable water quality in their marina and lagoons, Ayla and other resorts in Aqaba complies with ASEZA regulations for marine environment protection [35].

Figure 4 shows also that ports/terminals facilities are clustered with two coastal zones: middle zone and southern zone. The middle zone comprises of Cement/Grain Joint Terminal, Passenger Terminal, and Aqaba Container Terminal. The southern terminal zone contains the following: Oil Export Terminal, LPG Oil Terminal, LNG Terminal, Phosphate Export Port, Potash Export Port, and Aqaba New Port.

Based on the impact assessment for each sector and its corresponding level of threat to the marine environment (Table 1), a spatial map for each sector was generated (see Figure 6). Levels of threat were given: High, Medium, and Low estimates based on the function and role of each coastal sector. Littering and physical damage were identified as the main threats along the tourism/recreational shoreline, while oil pollution, chemical dust and waste, are predominately related to the industrial ports and terminals sectors.

The calculated shoreline length affected by and exposed to each threat is represented in Table 3 and in the doughnut charts in Figure 7. Only 30% of the shoreline is highly threatened by littering, which is mainly originated from public beach and ferry terminal, while 21% of the shoreline is highly threatened by chemicals that come from industrial terminals, 61% of the shoreline marine habitat is exposed to physical damage that is may be caused by diving and snorkeling activities along the public beach, and anchoring along the terminals. The risk of oil/hydrocarbons pollution present in 32% of the shoreline which occurs mainly in terminals and in less extent at the marina and public beach from tourism boats. Drainage of chemically- and physically-polluted water may exist at industrial terminals as well as at public beaches in less extent.

Based on above analysis, 56% of the Jordanian coast in the Gulf of Aqaba can be considered as littering-free although 66% of the shoreline length is mainly used by tourism sectors. This is due to that resorts, hotels, and coastal private properties have strict regulations for littering and waste disposal and is mostly attended by well-behaved tourists. Having the Terminals/Ports using 29% of the Jordanian shoreline, makes it less exposed to chemical waste that may occur during handling of exported/imported cargo, which is considered to be under control due to high level of monitoring applied on these terminals with regard to leaking, and mitigation measures that is being undertaken for prevention of such accidents.

However, pollution with hydrocarbons and drainage of polluted water into the coastal water are hardly unavoidable because of the intense use of shipping and touristic boats along the coast and operations of washing, rinsing, and littering of liquids that may occur along this wide area of the shoreline.

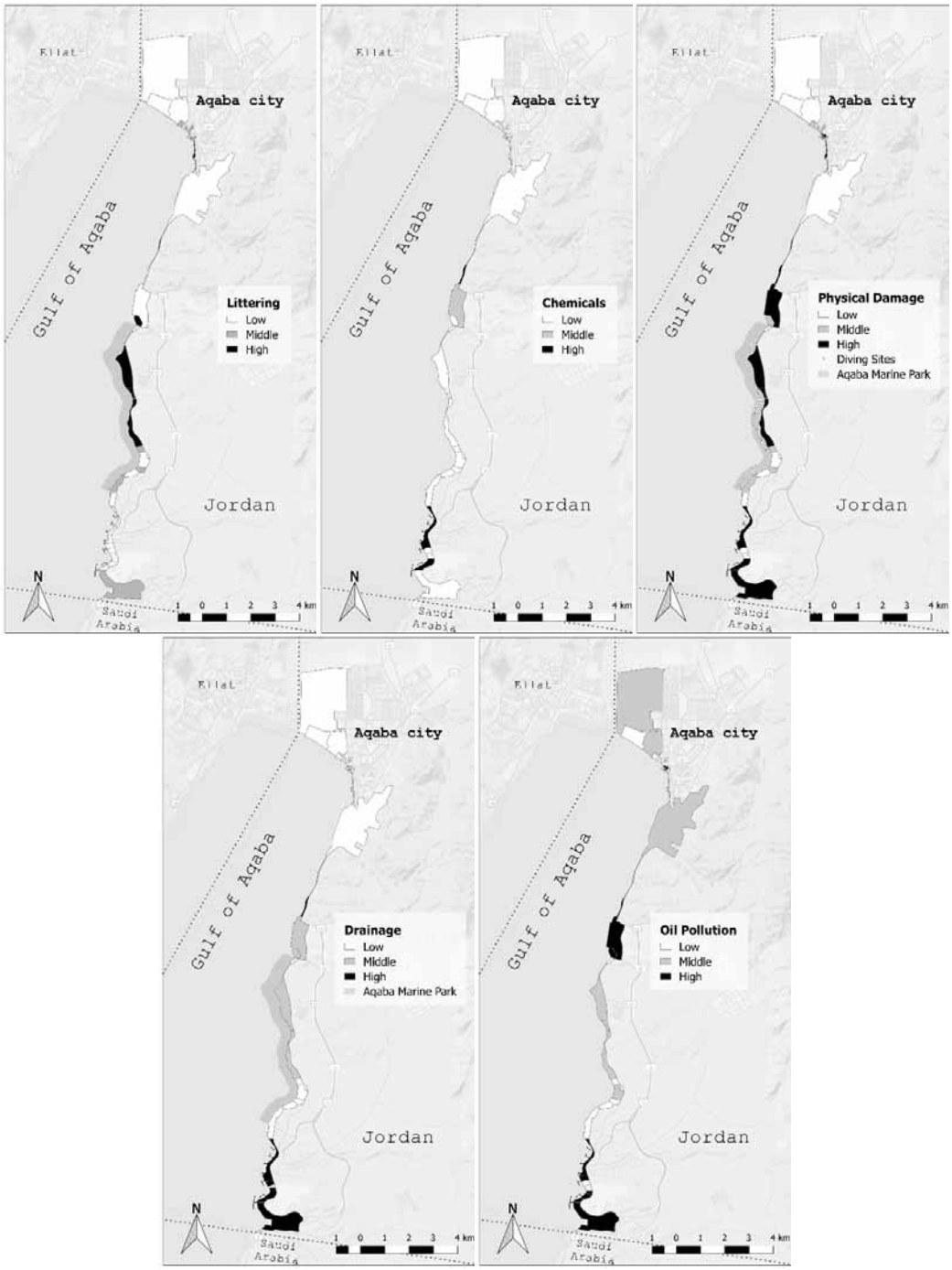

FIGURE 6
Map represents the spatial convergence of the threats on the marine environment

TABLE 3
The coastal length (m) exposed to each anthropogenic threat based on the levels: H for high, M for medium, and L for low.

Threatened coastal length/ Threat level	Littering	Chemical Dust	Physical Damage	Drainage	Oil Pollution
H	8091	5649	17325	5997	8887
M	3958	1422	2359	10253	12364
L	15204	20182	8991	11003	6252

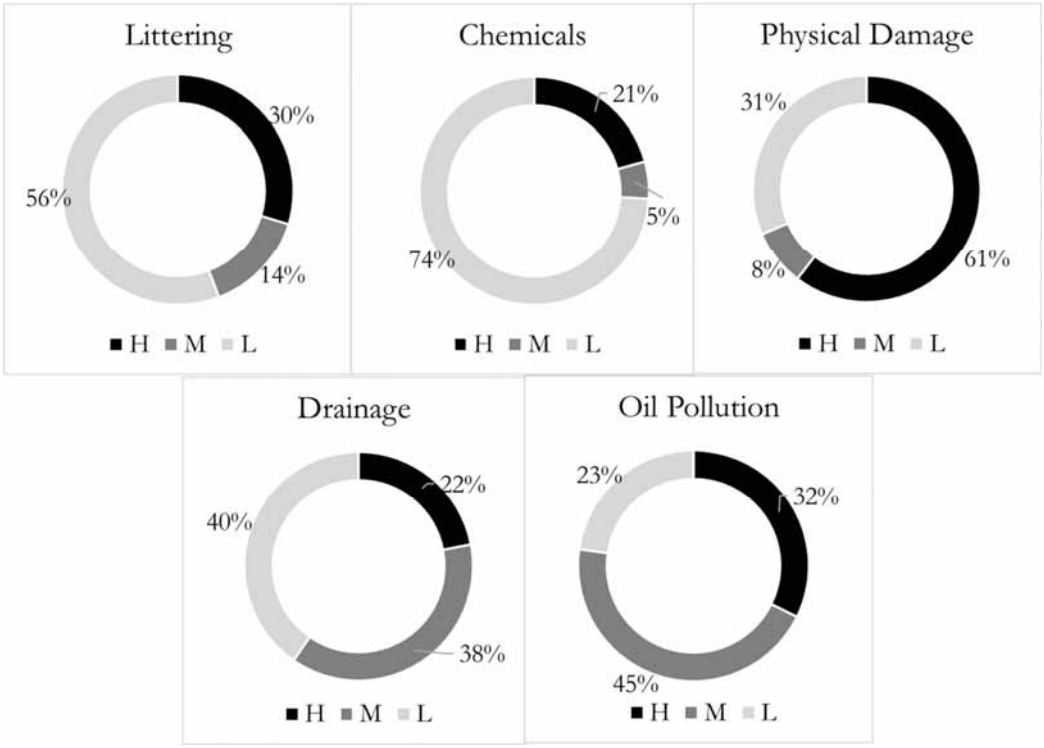

FIGURE 7
Doughnut representation for the threat level of human activities and its corresponding coastal length, for littering chemical dust, physical damage, drainage, and oil pollution.
H: high, M: medium, L: low

It was reported that coastal and marine tourism in the Gulf of Aqaba involves distinct land-based facilities/activities and sea-based facilities/activities especially in the northern and middle coast with entanglement with and ingestion of marine litter items, which harm to a wide range of marine biota [36-38]. Littering is the main source of microplastics that are available for ingestion by a wide range of organisms and propagated over trophic levels of the marine food web [39]. However, their contamination of associated chemicals in marine organisms causes harm to ecosystems and human health [40, 41].

On the other hand, marine and coastal tourism activities that involve boat anchors, snorkeling and diving cause physical damage to coral reefs in the Gulf of Aqaba, particularly at public beaches, diving sites, and terminals that see significant boat and ship traffic, which may lead to decline in fish and coral populations, and diving in the southern coast [42]. Tourist activities, both land- and ship-based in the Gulf of Aqaba have been reported to cause habitat damage, particularly in breakage of corals by divers and snorkelers, trampling of intertidal areas, and anchor damage to corals [21-24]. For better protection of coral reef, ASEZA has assigned several diving sites along the Aqaba Marine Park (AMP) in order to harmonize between tourism and environment in a sustainable way.

The increasing numbers of divers and tourists visiting the reef areas have caused great damage to the corals in many parts of the Gulf of Aqaba and the number of tourists is still increasing Eighteen dive centers in Aqaba operate 20,000 to 30,000 dives per year along the 1.2 km of coral reef area. In addition, fifty-five glass-bottom boats cruise the same area every day, making about 8000 cruises per year. Furthermore, the diving clubs arrange diving courses for more than 20,000 training dives in the same area every year.

Port handling of dry bulk cargo may produce dust that is transported to the sea surface and dilute with seawater [20]. Most dry bulk commodities are prone to spillage and dust pollution, posing environmental problems to the marine ecosystem and seawater and are confronted with critical ship-to shore transfer problems, which are far more complex than those involving ship loading or unloading of containers [43, 44]. Blowing of dust at seawater leads to an increase in the level of suspended solids that reduces sunlight penetration and the clarity of coastal waters and restricts the growth of light-dependent plants and animals like corals, in addition to the concentration of organic matter [2]. For example, the dust generated from the physical handling of the Potash- and Phosphate-based fertilizer cargoes is generally harmful to the marine environment. Fertilizers dry bulk cargoes have high concentrations of organic

material and nutrients, with high biological oxygen demands, which makes nutrient enrichment (eutrophication) in seawater often associated with coral reef decline and harmful algae blooms [45].

According to official reports, 3.5 to 6.4 million tons of raw phosphate are exported through the Gulf of Aqaba. Phosphate dust generated during ship loadings considered a serious environmental problem in Aqaba due to the environmental effects of the dust include reduction in water clarity, reduction in light penetration rate, and slow coral growth rates. Other possible effects are higher levels of dissolved phosphate nutrients, and other toxic heavy metals such as As and Zn. Phosphate loading and unloading terminal have been relocated from the north main port to the south industrial zone. This shall eliminate the phosphate dust impact on the city of Aqaba and the nearby coral reef communities. Moreover, some accidental spills could take place during loading of fertilizer product onto ships, and unloading of raw Sulphur and Ammonia from ships berthing at the industrial port in the vicinity of the industrial complex pose a risk to the environment. The 30,000-ton onsite Ammonia storage tank (cooled Ammonia at — 32°C) is another health and environmental hazard.

The potash storage capacity of the Aqaba Potash Company (APC) in Aqaba was recently expanded from 160,000 tons to 260,000 tons. The Aqaba facilities are among the most efficient and modern in the Potash industry. The reclaiming system ensures physical uniformity, guarantees reduced segregation and prevents caking. Deducing, oil treatment and new screening units are installed to remove any fine particles and to reduce dust emissions during loading vessels at rates up to 1000 tons/hr.

The Jordan Phosphate Mines Company/Industrial Complex (JPMC-IC) produces 740,000 tons of Di- Ammonium Phosphate (DAD) and 270,000 tons of phosphoric acid annually. Chlorinated cooling water is released from the factory into the Gulf at a rate of 20,000 m3 per hour, at a discharge point located 150m from shore at a depth of 27m. The cooling water is about 3°C above ambient sea water temperature.

Despite the large dilution capacity of seawater, coastal discharged water mixed with different chemical and physical characteristics of seawater that comes from possibly discharged liquid bulks at terminals and public beach may cause adverse ecological impacts, particularly in the vicinity of the outfalls, which makes any potential risk of such drainage crucial for marine life [46].

The Aqaba Thermal Power Plant (TPP) is located in the south-western border of Jordan, approximately 22 km south of the town of Aqaba and 1 km from the beach. The TPP, which is a 260MW station uses seawater for cooling purposes, has been registered as a clean development mechanism (CDM) project in (UNFCCC) on 2008. This qualifies the TPP to sell carbon reduction emissions (CERs) in the international market to countries granting considerable benefits to Jordan. At present some 38,000 m3 of cooling water are discharged into the Gulf from an outlet 20m below the surface and 200m from shore. The temperature is about 3°C above ambient water temperature.

Pollution by oil and hydrocarbons spills from small watercraft reduce water column quality and the substrate as habitat for fish species and their prey, increasing the levels of toxicity for both pelagic and benthic species which occurs often in marinas and harbors, which suffer from poor water circulation [47]. Spills may be dispersed into the water column, which is difficult to be quantified due inability to separate pollution from boating from that of storm drains in the vicinity [48]. A measure of the impact of marinas can be obtained by a study of hydrocarbons in their sediments [49].

More than 2300 ships use the port of Aqaba each year. In addition, tankers with a capacity of 100,000- 150,000 tons of crude oil arrive at Eilat oil terminal every week, unloading about 3.5 million tons of oil per year. Accidental oil spills could have disastrous effects on coral reef ecosystems in the Gulf. There are currently several efforts to create and implement effective strategies and action plans for combating small to medium-sized oil spills.

CONCLUSIONS

This study gives emphasis on the identification of human uses and ecosystem components of the Jordanian coast in the Gulf of Aqaba, highlighting the possible conflicts and compatibilities between these uses and conservation features. According to the aforementioned information it has become clear that although ports and tourism development in the study area would cause potential conflicts with the existing marine ecosystem and more specifically with corals and biodiversity, having them clustered in a planned way allows the allocation of space in a more effective, efficient and equitable manner. However, a thorough investigation of the impacts of the human use on the marine ecosystem was conducted aiming to minimize them under the “blue growth” concept.

Synthesis of the spatial overlap between human uses and ecosystem components constitute an important input for an effective coastal management. Since the overarching goal of the coastal management is to accomplish the social and economic objectives and simultaneously protect marine ecosystems, it is evident that the sustainable development of human activity is interdependent on the sustainability of existing ones that are distributed at the same place, and at the same time it should safeguard the provision of ecosystem goods and services.

ASEZA has taken several measures that aim to maintain the sustainability by zoning the industrial

and touristic sectors as well as establishing the Aqaba Marine Park in form of clusters in order to minimize the adverse impacts of human activities on the marine ecosystem and protect the coral reef in the coast of Aqaba. Moreover, in the framework of the sea use plan that is adopted by ASEZA, wider access for the general public to the beach was recorded to be in accordance with the recreational requirements by the community and public. These strategies have proven the effectiveness of the sea use management that is being undertaken by authorities in Aqaba. In the view of this study, zoning of sea-front human use of the Jordanian coast of the Gulf of Aqaba is a model for best practice in successful coastal management which permits multiple human activities, while simultaneously providing a high level of protection for specific areas.

A strong set of polices for planning and management of coastal environment and its resources are very essential for the success of Integrated Coastal Zone Management ICZM. The legal framework for the establishment of ASEZA has supported the necessary policy for an effective coastal management system. Regulation No. 21 of 2001 for the Environmental Protection Regulations of ASEZA constitutes a strong regulatory basis and ensures pollution control and environmental impact assessment. A zero-discharge policy to sea has accordingly been adopted; large development projects within ASEZA's mandate which can may have potential negative environmental impacts are all subjected to detailed environment impact assessments. This unique environmental condition without direct source point of pollution give chance to protect the coral reef and marine protected area.

ASEZA is committed with scientific agencies in Aqaba has conducted a National Monitoring Program along the Jordanian Gulf that keeps the Gulf tracked with any possible change in the water quality, fish and benthic communities. In addition, most industrial and tourist activities along the Gulf is obligated by ASEZA to do their own monitoring activities to follow any possible environmental changes in their own properties.

Monitoring of the coastal environment in Jordan has been systematically conducted since the mid-1990s. The strong driver behind this has been well coordinated and collaborative efforts between International Organizations, the Jordanian Government, Scientific Institutions and the Private Sector. The Gulf of Aqaba Environmental Action Plan (GAEAP), a fruit of collaboration between the Aqaba Region Authority (ARA), Jordan and the World Bank, has given considerable emphasis to the environmental protection of the Gulf of Aqaba and to monitoring its environmental quality (World Bank, 1993). The Marine Science Station of the University of Jordan and Yarmouk University (MSS) as the only national research center specialized in marine sciences then has benefited from most of the International support. A World Bank GEF Project; the Aqaba Marine Peace Park (1996-1999) provided considerable financial support for enhancement of the MSS equipment. The Red Sea Program (1997-2003) funded by the German Government provided substantial capacity in terms of equipment and human resources.

Immediately after completion of the Aqaba Marine Peace Park Project and as one of the commitments on Jordan a long term monitoring program has been established implemented by the MSS and funded by the ARA, then continued to be funded by the Aqaba Special Economic Zone Authority (ASEZA) as one of ASEZA obligations by Law # 32 of the Year 2000 through which ASEZA has been established.

Numerous MERC USAID Projects and European Projects realized since 2000 have lent considerable support to the coastal and marine monitoring efforts in Jordan.

Parallel with starting the GEF World Bank Marine Peace Park Project the Private Sector started its first systematic monitoring program. The Jordanian Phosphate Mines Company signed an agreement with the MSS to conduct coastal monitoring at the Industrial Complex in 1996, which is still in effect. With ASEZA Law #32 of the year 2000 and the Environmental Protection Act in the Aqaba Special Economic Zone Authority # 21 for the year 2001 in place numerous monitoring programs appeared as requirements of Environmental Impact Assessment Studies (EIAs) of coastal investment initiatives.

The Jordanian National Monitoring Program of the coastal environment presents a suite of water quality, bottom sediments and coastal habitats monitoring. The monitoring sites take account of Tourist Areas, Fishermen Ports, Shipping Ports, the Marine Park Area and the Industrial Area. Water monitoring includes coastal stations of depths about 10m, where the samples are collected at the surface; and an offshore station where samples are collected at specified depths down to the bottom. The coastal habitats monitoring includes records of bottom cover coral reef or seagrass beds and their health conditions as well as fish abundance and diversity at eight coastal stations at the beginning, which were increased to ten stations since 2008.

In the scope of its role to preserve the marine ecosystems in the Gulf and to ensure a sustainable balance between the marine ecosystem and the ongoing human development in the region, the Aqaba Special Economic Zone Authority (ASEZA) funded the initiation and maintenance of the National Monitoring Program (NMP) at the Gulf of Aqaba. The NMP is an independent government-funded program hosted by the Marine Science Station (MSS) in Aqaba, where it enjoys technical and scientific support. The overarching goal of the NMP at the Gulf of Aq-

aba is to provide a long-term scientific data base encompassing the marine ecosystems at the Jordanian northern head of the Gulf of Aqaba in order to facilitate the formation of scientific recommendations for measures to be taken, providing well-monitored coastal zone, which requires reporting the "state of health" of the marine ecosystem and warn of impending problems [50].

REFERENCES

[1] Al-Rousan, S., Al-Taani, A.A. and Rashdan, M. (2016) Effects of pollution on the geochemical properties of marine sediments across the fringing reef of Aqaba, Red Sea. Marine Pollution Bulletin. 110(1), 546-554.

[2] Al-Sawalmih, A., Al-Horani, F.A. and Al-Rousan, S. (2017) Elemental Analysis of the Coral Stylophora Pistillata Incubated Along the Jordanian Coast of the Gulf of Aqaba. Fresen. Environ. Bull. 26, 3029-3036.

[3] Al-Rousan, S., Al-Shloul, R., Al-Horani, F., and Abu-Hilal, A. (2012) Heavy metals signature of human activities recorded in coral skeletons along the Jordanian coast of the Gulf of Aqaba, Red Sea. Environmental Earth Sciences. 67(7), 2003-2013.

[4] Kotb, M.M.A. (2016) Coral translocation and farming as mitigation and conservation measures for coastal development in the Red Sea: Aqaba case study, Jordan. Environmental Earth Sciences. 75(5).

[5] Badran, M.I. and Foster, P. (1998) Environmental quality of the Jordanian coastal waters of the Gulf of Aqaba, Red Sea. Aquatic Ecosystem Health and Management. 1(1), 75-89.

[6] U.N.E.P. (2006) Promoting awareness and enabling a policy framework for environment and development integration in the Mediterranean with focus on Integrated Coastal Zone Management, Policy Brief Reducing Conflicts in the Jordanian Gulf of Aqaba.

[7] Komyakova, V., Munday, P.L., Jones G.P. (2013) Relative Importance of Coral Cover, Habitat Complexity and Diversity in Determining the Structure of Reef Fish Communities. Plos One. 8(12).

[8] Penin, L., Michonneau, F., Baird, A.H., Connolly, S.R., Pratchett, M.S., Kayal, M., and Adjeroud, M. (2010) Early post-settlement mortality and the structure of coral assemblages. Marine Ecology Progress Series. 408, 55-64.

[9] Aljbour, S.M., Al-Horani, F.A. and Kunzmann, A. (2018) Metabolic and oxidative stress responses of the jellyfish Cassiopea to pollution in the Gulf of Aqaba, Jordan. Marine Pollution Bulletin. 130, 271-278.

[10] Barakat, S.A., Al-Rousan, S. and Al-Trabeen, M.S. (2015) Use of scleractinian corals to indicate marine pollution in the northern Gulf of Aqaba, Jordan. Environmental Monitoring and Assessment. 187(2).

[11] Kteifan, M., Wahsha, M. and Al-Horani, F.A. (2017) Assessing stress response of Stylophora pistillata towards oil and phosphate pollution in the Gulf of Aqaba, using molecular and biochemical markers. Chemistry and Ecology. 33(4), 281-294.

[12] Al-Zibdah, M. (2013) The Aqaba Marine Protected Area -- Integration of Marine Science and Resource Management in the Gulf of Aqaba-Red Sea.

[13] U.N.D.P. (2014) Jordan ICZM Country Report 2014: Towards Sustainable Coastal Zone Development. United Nations Development Programme, UNDP.

[14] Bergmann, M., Gutow, L. and Klages, M. (2015) Marine anthropogenic litter. Springer.

[15] Gladstone, W., Curley, B. and Shokri, M.R. (2013) Environmental impacts of tourism in the Gulf and the Red Sea. Marine Pollution Bulletin. 72(2), 375-388.

[16] Eremina, T., Ershova, A., Martin, G., and Shilin, M. (2018) Marine litter monitoring: review for the Gulf of Finland coast. 2018 Ieee/Oes Baltic International Symposium (Baltic).

[17] Fauziah, S.H., Liyana, I.A., and Agamuthu, P. (2015) Plastic debris in the coastal environment: The invincible threat? Abundance of buried plastic debris on Malaysian beaches. Waste Management and Research. 33(9), 812-821.

[18] Kitto, M.R. and Sambhu, C. (2012) Litter Pollution on the Coastline of Obhur, Kingdom of Saudi Arabia. Arab Gulf Journal of Scientific Research. 30(2-3), 112-119.

[19] Nelms, S.E., Coombes, C., Foster, L.C., Galloway, T.S., Godley, B.J., Lindeque, P.K., and Witt, M.J. (2017) Marine anthropogenic litter on British beaches: A 10-year nationwide assessment using citizen science data. Science of the Total Environment. 579, 1399-1409.

[20] Grote, M., Mazurek, N., Gräbsch, C., Zeilinger, J., Le Floch, S., Wahrendorf, D.-S. and Höfer, T. (2016) Dry bulk cargo shipping — An overlooked threat to the marine environment? Marine Pollution Bulletin. 110(1), 511-519.

[21] Abidin, S.Z.Z. and Mohamed, B. (2014) A Review of SCUBA Diving Impacts and Implication for Coral Reefs Conservation and Tourism Management. 4th International Conference on Tourism Research (4ictr). 12.

[22] Giglio, V.J., Ternes, M.L.F., Mendes, T.C., Cordeiro, C.A.M.M. and Ferreira, C.E.L. (2017) Anchoring damages to benthic organisms in a subtropical scuba dive hotspot. Journal of Coastal Conservation. 21(2), 311-316.

[23] Lyons, P.J., Arboleda, E., Benkwitt, C.E., Davis, B., Gleason, M., Howe, C., Mathe, J., Middleton, J., Sikowitz, N., Untersteggaber, L. and Villalobos, S. (2015) The effect of recreational SCUBA divers on the structural complexity and benthic assemblage of a Caribbean coral reef. Biodiversity and Conservation. 24(14), 3491-3504.

[24] Muhidin, Yulianda, F. and Zamani, N.P. (2017) Impact of Snorkeling and Diving to Coral Reef Ecosystem. Journal Ilmu Dan Teknologi Kelautan Tropis. 9(1), 315-326.

[25] Roberts, D.A., Johnston, E.L. and Knott, N.A. (2010) Impacts of desalination plant discharges on the marine environment: A critical review of published studies. Water Research. 44(18), 5117-5128.

[26] Finkl, C.W. and Krupa, S.L. (2003) Environmental impacts of coastal-plain activities on sandy beach systems: Hazards, perception and mitigation. Journal of Coastal Research. 35, 132-150.

[27] Kocasoy, G., Mutlu, H.I. and Alagoz, B.A.Z. (2008) Prevention of marine environment pollution at the tourism regions by the application of a simple method for the domestic wastewater. Desalination. 226(1-3), 21-37.

[28] Zappala, G., Bonamano, S., Madonia, A., Caruso, G. and Marcelli, M. (2012) Microbiological risk assessment in a coastal marine environment through the use of mathematical models. Water Pollution Xi. 164, 3-14.

[29] Cook, M.C., May, A., Kohl, L., Van Biesen, G., Parrish, C.C. and Morrill, P.L. (2018) The Potential Impact of Hydrocarbons on Mussels in Port au Port Bay, Newfoundland. Emerging Pollutants and Their Effects on Marine Ecosystems. 81p. 1-+.

[30] Kokkali, A., Vassilopoulou, V., Issaris, Y., Kavadas, S., Karris, G., Fric, J. and Panayotidis, P. (2014) Using Geographic Information Systems (GIS) to map human activities and ecosystem components as the basis for effective Marine Spatial Planning (MSP), in 12th International Conference on Protection and Restoration of the Environment. 2014: (PRE XII) Skiathos Island, Greece.

[31] Micheli, F., Halpern, B.S., Walbridge, S., Ciriaco, S., Ferretti, F., Fraschetti, S., Lewison, R., Nykjaer, L. and Rosenberg, A.A. (2013) Cumulative Human Impacts on Mediterranean and Black Sea Marine Ecosystems: Assessing Current Pressures and Opportunities. PLoS ONE. 8(12).

[32] Ehler, C.N., Douvere, F. (2009) Marine Spatial Planning: a step-by-step approach toward ecosystem-based management. Intergovernmental Oceanographic Commission and Man and the Biosphere Programme, in Intergovernmental Oceangraphic Commission Manuals and Guides. Unesco, Paris, France.

[33] A.S.E.Z.A. (2015) Industrial Investment opportunities, Aqaba Special Economic Zone. Aqaba Development Corporation.

[34] Kotb, M., M Alouran, N., A Awali, A. and Hararah, M. (2015) Coral Translocation: Mitigating Adverse Impact of Development along the Aqaba Coastline/Jordan. Biomedical and Pharmacology Journal. 8, 91-101.

[35] Manasrah, R. (2015) Physical Properties and Exchange System of Seawater in Ayla Lagoons in the Northern Gulf of Aqaba, Red Sea. Fresen. Environ. Bull. 24, 1232-1249.

[36] Abu-Hilal, A. and Al-Najjar, T. (2009) Marine litter in coral reef areas along the Jordan Gulf of Aqaba, Red Sea. Journal of Environmental Management. 90(2), 1043-1049.

[37] Abu-Hilal, A.H. and Al-Najjar, T.H. (2009) Plastic pellets on the beaches of the northern Gulf of Aqaba, Red Sea. Aquatic Ecosystem Health and Management. 12(4), 461-470.

[38] Abu-Hilal, A.H. and Al-Najjar, T. (2004) Litter pollution on the Jordanian shores of the Gulf of Aqaba (Red Sea). Marine Environmental Research. 58(1), 39-63.

[39] Setala, O., Fleming-Lehtinen, V. and Lehtiniemi, M. (2014) Ingestion and transfer of microplastics in the planktonic food web. Environmental Pollution. 185, 77-83.

[40] Browne, M.A., Niven, S.J., Galloway, T.S., Rowland, S.J., and Thompson, R.C. (2013) Microplastic Moves Pollutants and Additives to Worms, Reducing Functions Linked to Health and Biodiversity. Current Biology. 23(23), 2388-2392.

[41] Van Cauwenberghe, L. and Janssen, C.R. (2014) Microplastics in bivalves cultured for human consumption. Environmental Pollution. 193, 65-70.

[42] Al-Horani, F.A., Al-Rousan, S.A., Al-Zibdeh, M. and Khalaf, M.A. (2006) The status of coral reefs on the Jordanian coast of the Gulf of Aqaba, Red Sea. Zoology in the Middle East. 38(1), 99-110.

[43] Knatz, G. (2013) Looking Beyond Cargo and Cruise Ships: Promoting Academic Marine Research and Clean Technologies as an Economic Development Strategy for Ports. Coastal Management. 41(4), 314-326.

[44] Jagerman, D. and Altiok, T. (2003) Vessel arrival process and queueing in marine ports handling bulk materials. Queueing Systems. 45(3), 223-243.

[45] Armon, R.H. and Hänninen, O. (2015) Environmental Indicators. Springer Netherlands.
[46] Tayeb, A., Chellali, M.R., Hamou, A. and Debbah, S. (2015) Impact of urban and industrial effluents on the coastal marine environment in Oran, Algeria. Marine Pollution Bulletin. 98(1-2), 281-288.
[47] van Bernem, C., Wesnigk, J.B., Wunderlich , M., Adamm S. and Callies, U. (2008) Oil pollution in marine ecosystems - Policy, fate, effects and response. In Environmental Crises (eds.), 101-139.
[48] California, U.o. (1998) Environmental impacts of pleasure craft oil spills. University of California.
[49] Voudrias, E.A. and Smith, C.L. (1986) Hydrocarbon pollution from marinas in estuarine sediments. Estuarine, Coastal and Shelf Science. 22(3), 271-284.
[50] Marine Science Station-Aqaba (2018) Appraisal Report of the National Monitoring Program of the Jordanian Coast of the Gulf of Aqaba. Aqaba Special Economic Zone Authority (ASEZA).

Received: **04.01.2020**
Accepted: **20.01.2020**

CORRESPONDING AUTHOR

Ali Al Sawalmih
Marine Science Station (MSS),
The University of Jordan and Yarmouk University,
Aqaba 77110 – Jordan

e-mail: a.sawalmih@ju.edu.jo

© by PSP Volume 29 – No. 04A/2020 pages 3254-3260 Fresenius Environmental Bulletin

OCCURRENCE OF UNCONVENTIONAL NATURAL GAS IN COAL-BEARING STRATA IN ORDOS BASIN, CHINA

Zhanjun Chen[1,*], Yidong Yuan[1,2], Xiulan Zhu[1], Yanni Liu[3]

[1]School of Energy Engineering, Longdong University, Qingyang 745000, China
[2]Department of Geology, Northwest University, Xi'an 710069, China
[3]Research Institute of Exploration and Development of Changqing Oilfield, PetroChina, Xi'an 710018, China

ABSTRACT

The Carboniferous-Permian coal-bearing strata of the Ordos Basin are one of China's major coalbed methane/shale gas and tight sandstone gas reservoirs. Based on the geochemistry of argillaceous shale, coal seam and tight sandstone, this paper systematically analyzes the physical properties of the reservoir, gas content characteristics, gas isotopes, unconventional natural gas and other data to analyze the occurrence characteristics of unconventional natural gas. Studies show that shales rich in coal and organic matter are source rocks of non-traditional natural gas systems, and the organic matter is in a stage of high supersaturation. In terms of reservoir, shale porosity is the lowest and sandstone reservoir has highest permeability, which is an order of magnitude higher than that of mudstones and coal seams. The gas in the mudstone shale occurs mainly in parallel with the formation. In terms of gas content, the average shale gas content is 3.53m^3 per ton of formation, sandstone is 5.04m^3, and the total gas content per ton in coal seams is 22.39m^3. All gas reservoirs in the Taiyuan and Shanxi formations are coal-type gas reservoirs. The isotopic data mainly shows two characteristics: the carbon isotope values of the same type of gas reservoirs are relatively similar while the methane and ethane carbon isotopes of the two gas reservoirs shows a certain difference. In the local scope, different types of gas reservoirs adjacent to each other cannot achieve free gas exchange in the vertical direction.

KEYWORDS:
Coal-bearing strata, unconventional gas system, occurrence characteristics, gas isotope

INTRODUCTION

Advances in horizontal wells and fracturing technologies have enabled large-scale commercial development of unconventional natural gas such as shale gas, coalbed methane and tight sandstone gas [1]. The Ordos Basin has abundant unconventional natural gas resources. The Sugli tight sandstone gas field and Dani tight sandstone gas field in this basin are being used commercially [2-3]. Exploration and development have achieved good results [4-8]. The tight sandstone gas, coalbed gas and shale gas in the Ordos Basin are concentrated in the Upper Paleozoic, indicating that there is an overlapping relationship in space.

Gas-bearing systems include shale gas, coalbed gas, and tight sandstone gas reservoirs, while shale gas reservoirs are self-generating, self-storing, and self-sealing [9-10]. The accumulation pattern of coalbed methane reservoirs is also self-generating and self-storing [11], but the capping conditions are one of the main controlling factors for coalbed methane enrichment [12]. Methane is mainly stored in coalbed gas reservoirs in an adsorbed state. Compared with coalbed methane and shale gas, in other tight sandstone gas reservoirs, tight sandstone gas reservoirs have relatively good permeability, and the gas is mainly free [13]. Considering the spatial overlap of three gas reservoirs in a coal-bearing formation, many scholars have proposed the concept of joint exploration and production of unexplored natural gas in coal measures reservoirs [14-16]. Based on basic geological data, this study analyzes the physical properties of shale, coal, and sandstone reservoirs as well as the geochemistry of natural gas isotopes and explores the generation of coal-bearing formation gas and the interaction between the three gas reservoirs.

MATERIALS AND METHODS

Geological Background. The study area is in the northern part of the Yishan slope in the Ordos Basin (Figure 1). The Carboniferous-Permian buried depth is 3000 ~ 4000m. The study area is rich in tight sandstone gas, shale gas, and coalbed methane resources. The Upper Paleozoic coal-bearing strata are mainly concentrated in the Taiyuan and Shanxi formations. It is a set of sea-land interactive facies sedimentary strata. The coal seams, shales, and sandstones are vertical stacked. The thickness of coal seam is 6-20m and the thickness of the dark mudstone is 40-120m.

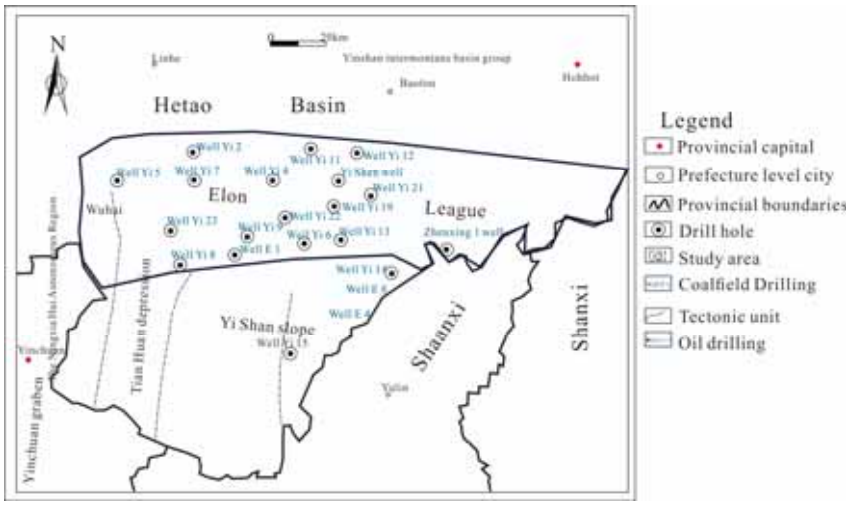

FIGURE 1
Location and structural division of the study area.

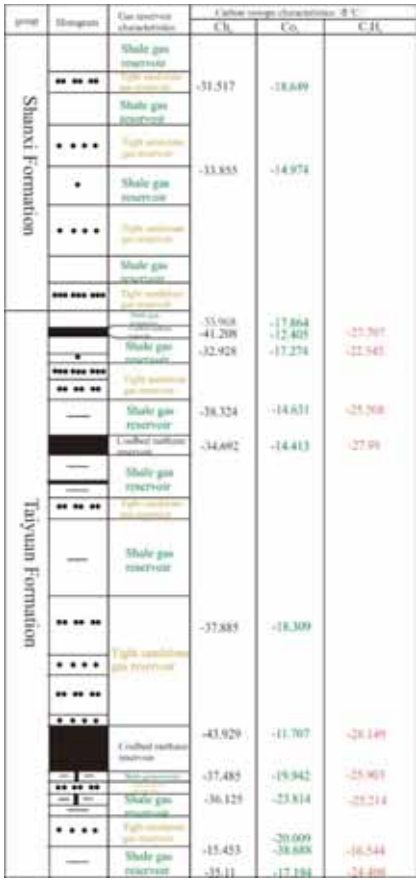

FIGURE 2
Drilling columnar, geochemical, and physical properties of the target layer in the study area.

The borehole columns and geochemical and physical properties of the Taiyuan and Shanxi formations in the study area were plotted in Figure 2. For the Taiyuan Formation, the TOC content in the bottom is lower than the top. Above the Taiyuan Formation, the organic matter content gradually decreased. The porosity in the reservoir gradually changes from the bottom to the upper part.

Methods. (1) Experimental Analysis of Mercury Intrusion. The mercury intrusion method measures the amount of mercury entering degassed solids at different static pressures. The pore diameter, pore size distribution, cumulative pore volume, pore volume distribution, cumulative pore specific surface area, and specific surface area distribution under the corresponding pressure are obtained through the Washburn equation [17-18]. These data could reveal the pore structure of the sample.

The experiment uses a MICRO MERITICS INSTRUMENT company's 9510 mercury intrusion micropore tester. The working pressure of the instrument is from 0.0035 to 206.843MPa. The resolution of this instrument is 0.1mm. The volume of the powder dilatometer is 5.1669cm, and the computer presents a control point measurement. 108 pressure points are selected ($0.1655 \leq P \leq 206.843$MPa) and each point has a stabilization time of 5s. The test volume of each sample is about 3g. The pure shale was crushed to about 5mm and then put in the oven at 70 ~ 80 °C for 12h. After that, these powders were put into the dilatometer to evacuate to $P < 6.67$Pa for testing.

(2) TOC Test. The TOC test expresses the comprehensive index of the total organic matter in the rock reservoir by the carbon content. TOC can be used directly to express the total amount of organic matter. Therefore, it is used as an important reference index for evaluating the content of organic matter in oil and gas reservoirs [19]. The CS organic carbon analyzer of Jiangsu Institute of Geology and Mineral Resources was selected to carry out the test work. The rock samples were pulverized to less than

100 mesh, and the carbon content of inorganic minerals in the rocks was removed by acid treatment. The converted CO_2 content is used to calculate the organic carbon content in the rock.

RESULTS

Space Grid Characteristics of Coal-Bearing Strata in Taiyuan-Shanxi Formation. The tight sandstones, shales and coal seams of the Taiyuan Formation and Shanxi Formation in the northern part of the Yishan slope in Ordos are good gas injection intervals. The thickness of each lithological section of the gas-bearing system of the Shanxi Formation is relatively small, generally 5-20m. The shale formation is next to the tight sandstone formation and the coal seam.

Geochemical Characteristics of Source rocks of Taiyuan-Shanxi Gas-Bearing System. The source rocks of the gas-bearing systems of the Taiyuan and Shanxi formations in the study area are coal seams and dark mud shales. The total thickness of the dark mud shales is 51.9 m, and the total thickness of coal seam is 9.1 m. The TOC value of argillaceous shale was measured from 0.04% to 7.33%, with an average of 1.64%. Types of organic matter in coal and shale belong to type III kerogen and have high potential for gas generation. The vitrinite reflectance in coal and shale is between 1.6% and 1.9%, which is at a mature stage, indicating that a large amount of hydrocarbon gas will be generated in the geological history.

In the natural gas system of the Taiyuan-Shanxi Formation, the gas sources of the three gas reservoirs are the dark mud shales and coal seams of the Taiyuan and Shanxi formations [20-21]. We compared the thickness ratio and the TOC ratio of coal seam and black mud shale to calculate the relative content of black mud shale gas and coal bed gas in the target layer (Table 1). The average organic carbon content of the coal seam is 40 times that of the shale, and its thickness is 1/5.7 of the dark mud shale. The proportion of organic matter in the original coal seam is 87.5% and in shale accounts for only 12.5%. The evolution of organic matter in coal is similar to that of shale. Therefore, the gas generation accounted for 87.5% of the original gas and the black mud shale accounted for only 12.5%. It can be assumed that it is a gas-generating layer.

Physical Properties of Coal-Bearing Gas-Bearing Systems. In the Taiyuan-Shanxi gas bearing system, the corresponding reservoirs for tight sandstone gas reservoirs, coalbed gas reservoirs, and shale gas reservoirs are tight sandstone, coal, and shale gas reservoirs. Among them, tight sandstone has the highest porosity and belongs to coal seams. The porosity is 1.00-6.79% with the average value of 3.17%, and the shale porosity is the smallest, only 0.51-1.51% with the average value of 1.02%.

The target shale layer in the study area is relatively dense, and its pores are mainly concentrated in the range of less than 100 nm to more than 10000 nm (Figure 3). Pores are mainly pores with high methane adsorption capacity. Organic pores larger than 10000 nm are mainly grain boundary pores. The former is easily converted to methane gas by adsorption, and the latter is converted to methane gas in free manner. Within this range, the pore structure of the reservoir can promote the existence of gas through adsorption (Figure 4).

TABLE 1
Proportion of organic carbon and gas generation in coal and shale in source rocks

Lithology	Thickness	TOC	Average TOC	Proportion of the TOC in source rocks	Gas generation ratio
Coal seams	9.1m	55.8~81.5%	65.50%	87.5%	87.5%
Dark mud shales	51.9m	0.04~7.33%	1.64%	12.5%	12.5%

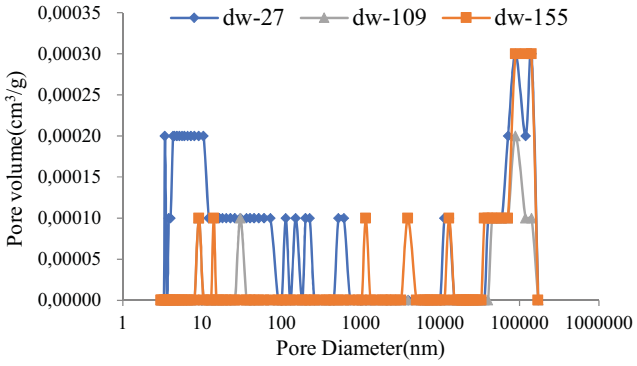

FIGURE 3
Characteristics of pore-pore size distribution of shale.

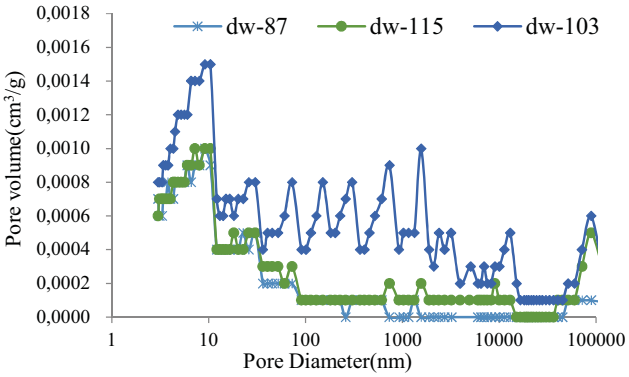

FIGURE 4
Characteristics of pore-pore size distribution of coal.

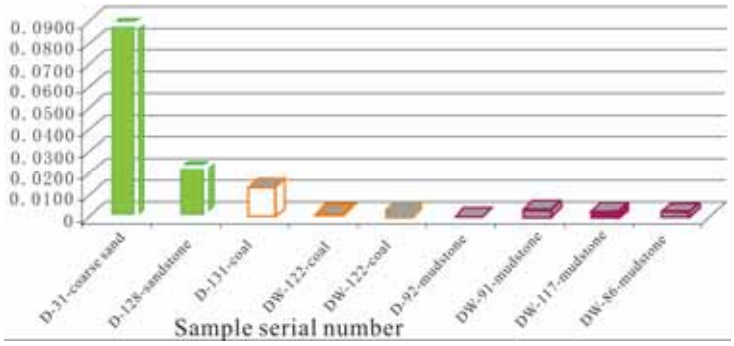

FIGURE 5
Distribution characteristics of the permeability of sandstone, coal, and shale.

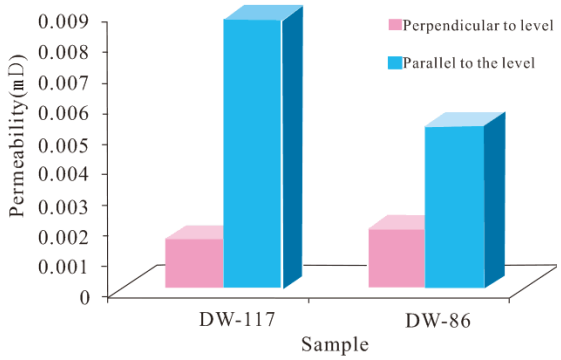

FIGURE 6
Comparison of mudstone permeability perpendicular to the stratum and permeability parallel to the stratum.

The sandstone permeability of each reservoir in the Taiyuan Shanxi Formation is the largest, ranging from 0.23 to 0.89 md, with an average of 0.056 md. Coal seam permeability is between 0.0014 and 0.0138 md, with an average of 0.0060 md. Shale has the smallest permeability ranging from 0.000061 to 0.008750 md. The average permeability of sandstone is an order of magnitude higher than the average permeability of mudstone and coal seams. The average permeability of coal seams is about twice that of mud shale (Figure 5). At the same time, it should be noted that the mud shale permeability value parallel to the formation is much larger than the vertical formation permeability (Figure 6).

In conventional gas storage formations for hydrocarbon generation, the types of reservoir pores and the state of gas generation are different. Tight sandstone is mainly composed of inorganic pores, and gas exists mainly in free state [22]. Coal seams are mainly organic pores with adsorbed natural gas. The shale reservoir contains organic and inorganic pores, each of which has a certain proportion of adsorbed gas and free gas. All unconventional natural

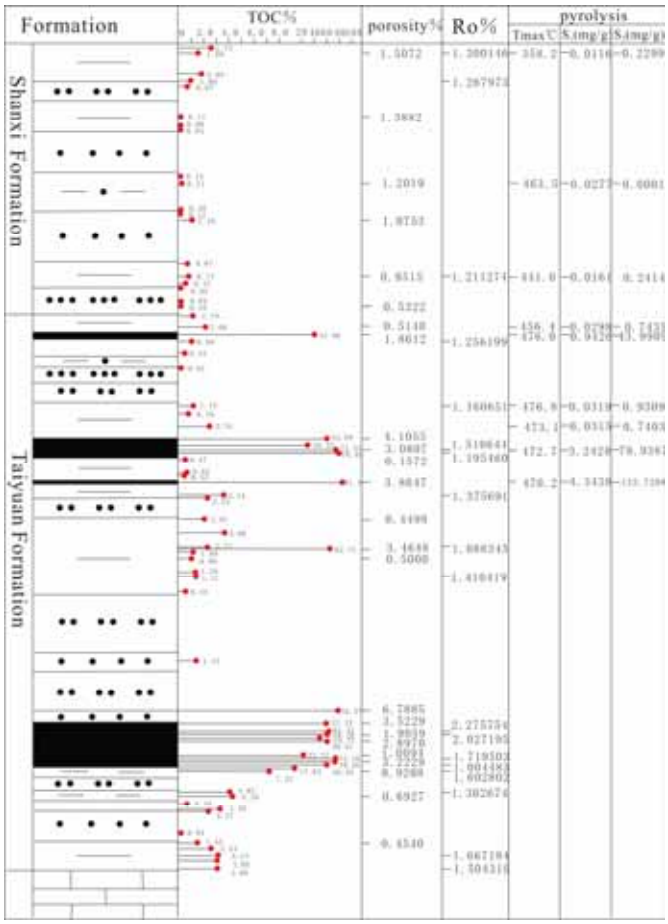

FIGURE 7
Overlapping characteristics and gas isotope characteristics of Taiyuan-Shanxi Formation coal gas reservoirs.

gas reservoirs in the coal series have the characteristics of "low porosity and low permeability", and the mechanism of gas evolution and permeability is more complicated. Throughout the system, the porosity and permeability of sandstone are much larger than coal seams. It is mainly free gas, which moves relatively easily. Coal seams are mainly composed of nano-scale pores and have a high content of adsorbed gas, so the pressure must be released during the mining process to desorb the adsorbed gas. Shale permeability is very low, with vertical permeability lower than horizontal permeability, which acts as a seal in the system. The free gas can be transported through natural or artificial channels. The adsorbed gas can be depressurized and desorbed for transport transfer.

Gas-Bearing Characteristics of the Ordos Coal-Bearing Gas-Bearing System. On-site analysis was performed on 22 mudstone shale samples, 4 coal samples, and 11 sandstone samples in Well E1 in the study area, and the lost gas and total gas content (excluding residual gas) were calculated according to relevant standards. The gas content of mud shale is 1.22 ~ 6.97m^3/t, with an average of 3.35m^3/t. The gas content of mudstone shale has a large correlation with the content of organic matter. The gas content of carbonaceous mudstone shale is 2.08 ~ 5.11m^3/t, with an average of 4.19m^3/t, much larger than the average gas content of ordinary dark mud shale. The total gas content in the sandstone is 1.88 ~ 12.37m^3/t, with an average of 5.04m^3/t. The total gas content in the coal seam is 19.54 ~ 26.07m^3/t, with an average of 22.39m^3/t, which is much larger than the gas content of sandstone and mudstone (Figure 7).

From the isotope data of each gas reservoir, the ethane isotopes of tight sandstone gas, coalbed methane and shale gas all exceed -28 ‰, belonging to coal gas [18]. The methane/carbon dioxide/ethane carbon isotope values of three gas reservoirs at different distances in the western Taiyuan Formation are similar, mainly in two characteristics with some differences: Carbon isotope values in gas reservoirs are relatively similar, indicating that methane and ethane C isotopes in coalbed methane are lighter, while carbon dioxide in carbon dioxide is heavier [23-24]. The carbon isotopes of methane and ethane

are heavier in shale gas, while the carbon isotopes of carbon dioxide are lighter. In natural gas, methane and carbon dioxide in tight sandstone gas reservoirs may originate from shale and coal seams. The carbon isotopes of methane and ethane in two adjacent gas reservoirs are different. The gas storage tanks cannot achieve free gas exchange, each gas storage tank forms an independent small gas-containing system, indicating that the gas storage tanks are completely independent of each other [25]. The carbon isotopes in gas-bearing intervals are similar, indicating that during the history of geology, shale gas, coal-bed gas, and tight sandstone gas combined the gas-bearing systems during the formation of reservoirs. It should also be noted that there is an isotope inversion phenomenon in the shale gas reservoir at the bottom of the Taiyuan Formation: the carbon isotope of methane is -15.45 ‰, and the carbon isotope of ethane is -16.544 ‰, with high production. This indicates that shale rates may be formed in the gas storage.

Comprehensive gas isotope information can infer the physical properties of tight sandstone, shale and coal reservoirs. Due to the ultra-low permeability exhibited by vertical shales, gas communication between different gas reservoirs is blocked. At this stage, all types of vertically adjacent gas reservoirs have no free gas exchange, and in large planar areas, the gas can move on a plane parallel to the fault or rupture zone [26]. Vertical gas exchange and movement of each gas storage tank can be performed anywhere. In the coal series unconventional natural gas system, coal seams and mud shales are source rocks. Among them, coal seam gas and shale gas are mainly self-generating and self-storing. Tight sandstone gas is a mixed source formed by coal seam and shale transfer. According to the thickness and average gas content of each gas storage tank in the system, the total gas content of the three gas storage formations can be calculated, but the difficulty of gas transportation depends on the type. Most importantly, sandstone gas transport is smoothest, and mud shale permeability are small, and fracturing and destruction are required. When considering the coal countermeasure system as a whole, the system is almost self-generating and self-protecting, but the connections between reservoirs in the system are poor.

CONCLUSIONS

(1) The single-layer thickness of each rock layer of the Taiyuan-Shanxi gas-bearing system in the Yishan slope of the Ordos Basin is generally small, ranging from 5-20m, and the shale layer is adjacent to the tight space sandstone and coal seams. The total thickness of the dark mud shale in the western Taiyuan Mountains of the study area is 51.9m, the total thickness of the coal seam is 9.1m. The TOC value of the shale is 0.04-7.33% with the average value of 1.64%. The vitrinite reflectance value is 1.6-1.9% indicating the maturity is high. Among the two source rocks, the coal seam is the main natural gas layer, accounting for 87.5% of the total natural gas production.

(2) Tight sandstone has the highest porosity in gas-bearing systems in coal-bearing formations, followed by coal beds, and shale has the lowest porosity. Sandstone has the highest permeability, several orders of magnitude higher than mudstone shale and coal seams. The average permeability of coal seams is about twice that of mudstone.

(3) In terms of gas content, the average gas content of mud shale is 3.35m^3/t, the total gas content of sandstone is 5.04m^3/t, and the total gas content of coal seam is 22.39m^3/t, which is much larger than that of sandstone and mudstone. Each gas reservoir in the coal area of the study area belongs to a coal-type gas reservoir with two main characteristics. The carbon isotope values of the same type of gas reservoirs are relatively similar. The difference is that different types of adjacent gas storage cannot achieve the free exchange of vertical gas.

ACKNOWLEDGEMENTS

This work was financially supported by the Key Projects of China National Natural Science Foundation (No. 41630312) and the China National Key R & D Program (No. 2017YFC0603106).

REFERENCES

[1] Jia, C., Zheng, M., Zhang, Y. (2014) Four Important Theoretical Issues of Unconventional Petroleum Geology. Acta Petrolei Sinica. 35(01), 1-10.

[2] Yang, H., Liu, X. (2014) Progress of Paleozoic Coal-Derived Gas Exploration in Ordos Basin. Petroleum Exploration and Development. 41(02), 129-137.

[3] Li, J., Tang, S., Zhang, S., Li, L., Wei, J., Xi, Z., Sun, K. (2017) Characterization of unconventional reservoirs and continuous accumulations of natural gas in the Carboniferous-Permian strata, Mid-Eastern Qinshui Basin, China. Journal of Natural Gas Science and Engineering. 49, 298-316.

[4] Hackley, P., Guevara, E., Hentz, T., Hook, R. (2009) Thermal maturity and organic composition of Pennsylvanian coals and carbonaceous shales, North-Central Texas: Implications for coalbed gas potential. International Journal of Coal Geology. 77(3-4), 294-309.

[5] Humez, P., Mayer, B., Ing, J., Nightingale, M., Taylor, S. (2015) Occurrence and origin of methane in groundwater in Alberta (Canada): gas geochemical and isotopic approaches. Science of The Total Environment. 541(4), 1253-1268.

[6] Yang, H., Fu, J., Liu, X. (2012) Accumulation Conditions and Exploration and Development of Tight Gas in the Upper Paleozoic of the Ordos Basin. Petroleum Exploration and Development. 39(03), 295-303.
[7] Li, G., Zhang, H. (2013) The Origin Mechanism of Coalbed Methane in the Eastern of Ordos Basin. Science China: Earth Science. 43(08), 1359-1364.
[8] Feng, S., Ye, J., Zhang, S. (2002) Coalbed Methane Resources in the Ordos Basin and its Development Potential. Geological Bulletin of China. 21(10), 658-662.
[9] Jie, M. (2014) Prospects in Coalbed Methane Gas Exploration and Production in the Eastern Ordos Basin. Natural Gas Industry. 30(06), 1-6.
[10] Yan, D., Huang, W., Li, A. (2013) Preliminary Analysis of Marine-Continental Transitional Shale Gas Accumulation Conditions and Favorable Areas in the Upper Paleozoic Ordos Basin. Journal of Northeast Petroleum University. 37(05), 1-9.
[11] Wang, S., Li, D., Li, J. (2011) Exploration Potential of Shale Gas in the Ordos Basin. Natural Gas Industry. 31(12), 40-46.
[12] Dai, J., Qi, H., Song, Y. (1985) On the Indicators for Identifying Gas from Oil and Gas from Coal Measure. Acta Petrole Sinica. 2, 31-38.
[13] Gai, H., Xiao, X. (2013) Mechanism and Application of Carbon Isotope Reversal of Shale Gas. Journal of China Coal Society. 38(05), 827-833.
[14] Zhang, J., Jin, Z., Yuan, M. (2004) Reservoiring Mechanism of Shale Gas and Its Distribution. Natural Gas Industry. 24(07), 15-18.
[15] Zhou, C., Dong, D., Wang, S. (2010) Geological Characteristics, Formation Mechanism and Resource Potential of Shale Gas in China. Petroleum Exploration and Development. 37(06), 641-653.
[16] Curtis, J. (2002) Fractured Shale-Gas Systems. AAPG Bulletin. 86(11), 1921-1976.
[17] Domokos, G., Mckavneyb, R., Gilfillanb, S., Stuarta, F. (2017) Fingerprinting coal-derived gases from the UK. Chemical Geology. 480, 75-85.
[18] Mallants, D., Jeffrey, R., Zhang, X., Wu, B., Kear, J., Chen, Z., Wu, B., Bekele, E., Raiber, M., Apte, S., Gray, B. (2018) Review of plausible chemical migration pathways in Australian coal seam gas basins. International Journal of Coal Geology. 195, 280-303.
[19] Fu, X. (2007) Coalbed Methane Geology. Xuzhou: China University of Mining and Technology Press.
[20] Sang, S., Fan, B., Qin, Y. (1999) Conditions of Sealing and Accumulation in Coalbed Gas. Oil and Gas Geology. 20(02), 8-11.
[21] Li, J., Guo, B., Zheng, M. (2014) Main Types, Geological Features and Resource Potential of Tight Sandstone Gas in China. Natural Gas Geoscience. 23(04), 607-615.
[22] Gao, W., Tian, W., Qin, W. (2014) Geological Optimization of Coalbed Methane and Shale Gas Co-Exploration and Concurrent Production in Guizhou Province. Fault-Block Oil and Gas Field. 21(01), 36-38.
[23] Bustin, A., Bustin, R. (2016) Total gas-in-place, gas composition and reservoir properties of coal of the Mannville coal measures, Central Alberta. International Journal of Coal Geology. 153, 127-143.
[24] Torres, L., Yadav, O., Khan, E. (2016) A review on risk assessment techniques for hydraulic fracturing water and produced water management implemented in onshore unconventional oil and gas production. Science of The Total Environment. 539, 478-493.
[25] Qin, Y., Liang, J., Shen, J. (2014) Gas Logging Shows and Gas Reservoirs Types in Tight Sandstone and Shale from Southern Qinshui Basin. Journal of China Coal Society. 39(08), 1559-1565.
[26] Ju, Y., Yan, Z., Li, C. (2011) The Similarities and Differences of Enrichment Characteristics and Mining Technology of Coalbed Methane and Shale Gas in China. CBM Symposium. 32(16), 75-91.

Received: **07.01.2020**
Accepted: **30.01.2020**

CORRESPONDING AUTHOR

Zhanjun Chen
School of Energy Engineering,
Longdong University,
Qingyang 745000 – China

e-mail: wangxifeng5115@sina.com

© by PSP Volume 29 – No. 04A/2020 pages 3261-3268 Fresenius Environmental Bulletin

EXPERIMENTAL STUDY ON OPTIMAL CO_2 FLOODING PRESSURE BEFORE AND AFTER FRACTURING IN HEAVY OIL RESERVOIRS

Le Qu[1,2,3,4,*], Tiantai Li[1,5], Rongjun Zhang[1,6], Zhipeng Miao[6], Hui Gao[1,6], Qing Guo[7]

[1] Post-Doctoral Contribution Center, College of Petroleum Engineering, Xi'an Shiyou University, Xi'an, Shaanxi 710065, China
[2] The Key Laboratory of Accumulation and Development of the Continental Shale Gas in Shaanxi Province, Xi'an, Shaanxi 710075, China
[3] State Key Laboratory of Oil and Gas Reservoir Geology and Exploitation（Chengdu University of Technology）,Chengdu, Sichuan 610059, China
[4] Post-Doctoral Research Station of Oil and Gas Engineering, China University of Petroleum, Beijing 102249, China
[5] Shaanxi Cooperative Innovation Center of Unconventional Oil and Gas Exploration and Development (Xi'an Shiyou University), Xi'an, Shaanxi 710065, China
[6] Xi'an Key Laboratory of Tight oil (Shale oil) Development (Xi'an Shiyou University), Xi'an, Shaanxi 710065, China
[7] Changqing Branch of Geophysical Research Institute,BGP,CNPC, Xi'an, Shaanxi, 710021,China

ABSTRACT

Low-permeability heavy oil reservoirs have the characteristics of low reservoir permeability, high crude oil viscosity, and poor flow coefficient. In the conventional single gas injection development process, the mechanism of dissolved gas flooding and miscible flooding can reduce the seepage resistance of porous media to a certain extent. However, the low permeability properties of the reservoir often limit the ultimate recovery. In this paper, from the perspective of reservoir reconstruction, tight sandstone reservoir cores are selected for gas flooding experimental evaluation before and after fracturing. Four groups of gas injection pressure values of 16.3 MPa, 18.0 MPa, 20.0 MPa, and 22.0 MPa are set to evaluate the porosity and permeability, variation, recovery factor and recovery degree under different gas injection PV numbers before and after fracturing. The experimental results show that there is an obvious start-up pressure gradient in the process of gas injection and flooding of heavy oil in tight sandstones before fracturing. The recovery rates of gas injection after fracturing are higher than before fracturing. After increasing the injection pressure, the recovery rate tends to decrease. As the corresponding gas injection pressure is 24 MPa, the recovery factor per unit gas injection PV is the highest. The experimental research in this paper shows that in the process of gas injection development in low-permeability heavy oil reservoirs, on the basis of reservoir reconstruction, an appropriate increase in gas injection pressure value can achieve a higher recovery degree.

KEYWORDS:
Heavy oil reservoir, fracturing reform, CO_2 dissolution and displacement, low-permeability, experimental research

INTRODUCTION

Heavy oil reservoirs are rich in geological reserves, and the proven geological reserves are currently higher than those of conventional oil and gas [1-2]. However, unlike conventional reservoirs, heavy oils have high viscosity and high density due to the large amount of asphaltenes and heavy oil components dissolved in the heavy oil. During the conventional pressure reduction development, when the reservoir pressure drops below the bubble point pressure, a large amount of dissolved gas overflows, the viscosity of heavy oil rises sharply, and the seepage resistance increases greatly. Although water injection can maintain the reservoir pressure above the bubble point pressure to a certain extent, heavy oil is a displaced phase with a low fluidity. Fingering is easily induced during the two-phase seepage process, resulting in low ultimate recovery [3-4]. In view of the high viscosity characteristics of heavy oil, CO_2 gas can be dissolved in heavy oil to reduce the viscosity of the heavy oil. In addition, the swelling effect of CO_2 gas after the injection into the heavy oil reservoir is obvious, which improves the ultimate recovery of heavy oil extraction. In addition, CO_2 seals can effectively delay the greenhouse effect. So far, there are many researches on the technology of developing heavy oil reservoirs for CO_2 injection at home and abroad [5-6]. In 1963, Welker et al. [7] studied the dissolution of CO_2 in ground degassed crude oil. It was shown that increasing the pressure can increase the amount of CO_2 dissolution, and the volume expansion of crude oil will also increase. In 1981, Miller et al. [8] studied the dissolution process of CO_2 in heavy oil, and the results showed that increasing the temperature would reduce the amount of CO_2 dissolved in heavy oil, but the viscosity of crude oil would not decrease. In 1983, Sankur et al. [9] carried out a comparative study of the CO_2 injection technology

and the CO_2 stimulation technology to improve the recovery factor in heavy oil reservoirs. The results show that the effect of CO_2 injection is better, while increasing the CO_2 injection pressure can improve the recovery factor of the displacement process of heavy oil. In 1986, Jha et al. [10] studied the effects of heavy oil development by water flooding, CO_2 injection flooding, and pure CO_2 gas flooding through laboratory experiments. The results show that pure CO_2 flooding can achieve the best development results. In 1992, Mungan et al. [11] made a comparative study on the effects of CO_2 dissolution and viscosity reduction in heavy oils, and the results showed that the effects were similar. In 1998, Srivastava et al. [12] conducted an indoor miscible flooding experimental study on the asphaltene aggregation phenomenon in the process of CO_2 injection to improve the recovery factor in Weyburn reservoir. The experimental results show that as the CO_2 saturation in the heavy oil increases, the phenomenon of the asphalt qualitative sedimentation has intensified. In 2007, Papadimitriou et al. [13] carried out an indoor core flooding heavy oil experiment. The experimental results show that as the CO_2 injection pressure increases, the amount of asphaltene accumulation increases and the permeability of the porous medium decreases. In 2012, Huang et al. [14] studied the experiment of CO_2 displacement of heavy oil in the core of long rocks. The experimental results show that asphaltene accumulation can occur at the gas injection inlet. The actual reservoir development process may cause the blocking situation of the seepage channels near the wellbore. In 2017, Jiang et al. [15] carried out fracturing reform and development in view of the poor fluidity of low-permeability heavy oil reservoirs. Laboratory experiments and field applications have shown that the oil production capacity and development status of the reservoirs have improved after fracturing reforms.

During the development of CO_2 injection in heavy oil reservoirs, although CO_2 swelling and viscosity reduction can increase the production of heavy oil to a certain extent [16-17], as the CO_2 injection pressure increases, the gas easily breaks through prematurely to form gas channeling The dominant percolation channel reduces the CO_2 spread coefficient during displacement and affects heavy oil production [18]. This article conducts indoor core displacement experiments for the development of heavy oil reservoirs. The reservoir is modified by fracturing to evaluate the ultimate recovery of the displaced heavy oil under different gas injection pressures before and after fracturing, and to optimize the development of heavy oil reservoir by CO_2 injection process.

MATERIALS AND METHODS

Formation of Heavy Oil. During the indoor simulation experiment, in order to increase the degree of fit of the indoor simulation experiment, the heavy oil used this time was taken from the W152 low-permeability heavy oil reservoir in Shengli Oilfield. The parameters of the formation heavy oil after surface degassing and dehydration are shown in the Table 1. The viscosity of the heavy oil sample used in this experiment is 12282 mPa·s. The mole fraction of asphaltenes is 21.7%, the mole fraction of wax is 24.4%, the freezing point is 32 °C, and the characteristics of heavy oil are typical heavy oil with high asphalt content and high waxy content.

Experimental Core Preparation. The porosity distribution of Block W152 is 10.9 ~ 18.3%, and the air permeability is 0.5 ~ 50.6 md. The core used in this indoor simulation experiment was obtained by core processing of the onsite wellbore in Block W152. It was prepared into eight segments by the laboratory's own line cutting equipment. The cores are all perpendicular to the bedding direction, with a core diameter of 25mm and a core length of 80mm. In order to compare the gas injection flooding experiments before and after fracturing, the fracturing experiments were performed on sample #5, #6, #7, and #8. Considering that the axial fracturing process can better reflect the formation fractures and the fracture closure is relatively complete during the axial fracturing process, the fracture will not penetrate both ends of the core to avoid the formation of high-permeability channels in the core [19-20]. The specific steps of this axial fracturing process are as follows: (1) Sweep the core prepared by wire cutting under high pressure gas and number it. (2) Cover the experimental core completely with raw tape, and then place the core in the core holder. (3) Raise the core to increase the confining pressure and simulate the formation stress conditions.

(4) Block one end of the core holder and inject the fracturing fluid through the advection pump at the other end. When the pressure in the core holder shows a large and instantaneous pressure drop, indicating that the core fracture is complete.

Then, the permeability testing equipment was used to test the permeability data before and after fracturing. The statistical data are shown in Table 2.

The hydraulic fracturing treatments for the numbers # 5, # 6, # 7, and # 8 were performed this time, and the results showed that the core permeability data increased significantly after fracturing, and the reservoir reconstruction effect was good.

TABLE 1
Properties of heavy oil after degassing

Temperature/°C	Density/(g·cm^{-3})	Viscosity/(mPa·s)	Asphaltenes/%	Wax/%	Pour point/°C
50	0.97	12282	21.7	24.4	32

TABLE 2
Porosity and permeability before and after core fracturing

Fracturing			Without fracture		
Core	Porosity (%)	Permeability (md)	Core	Porosity (%)	Permeability (md)
#1	12.4	2.43	#5	20.2	76.21
#2	11.8	2.01	#6	19.8	68.85
#3	11.9	2.15	#7	20.0	73.22
#4	11.7	1.97	#8	18.1	53.48

Gas Injection Flooding Experiment Before and After Fracturing. This experimental process is divided into the following seven steps: (1) Place the cores that have been dried and stored in the core holder and test the airtightness of the pipeline along the displacement. (2) Pipeline the core holder and carry the vacuum processing test with the negative pressure value -0.09MPa for 4h. (3) Open the incubator, set the system temperature value to 70 °C. (4) Set the back pressure valve value to 16MPa and the advection pump flow rate to 0.2ml/min, displace the formation water in the intermediate container to the core holder until the water production rate at the outlet end is constant at 0.2ml/min. (5) Set the flow rate of the advection pump at 0.2ml/min, displace the water phase in the core until the water is no longer produced at the outlet end. Close the advection pump and close the inlet and outlet valves of the lithologic holder. (6) Put the core in the core holder for 24 hours before the gas injection and flooding experiments were performed. (7) Set the different gas injection pressures and corresponding outlet back pressure values according to the core number to conduct the flooding experiments and record the gas seeing time at the outlet end of the flooding process and the recovery process, the relationship between the degree of change over time and the end of the displacement rate. The specific experimental flow chart of this displacement experiment is shown in Figure 1.

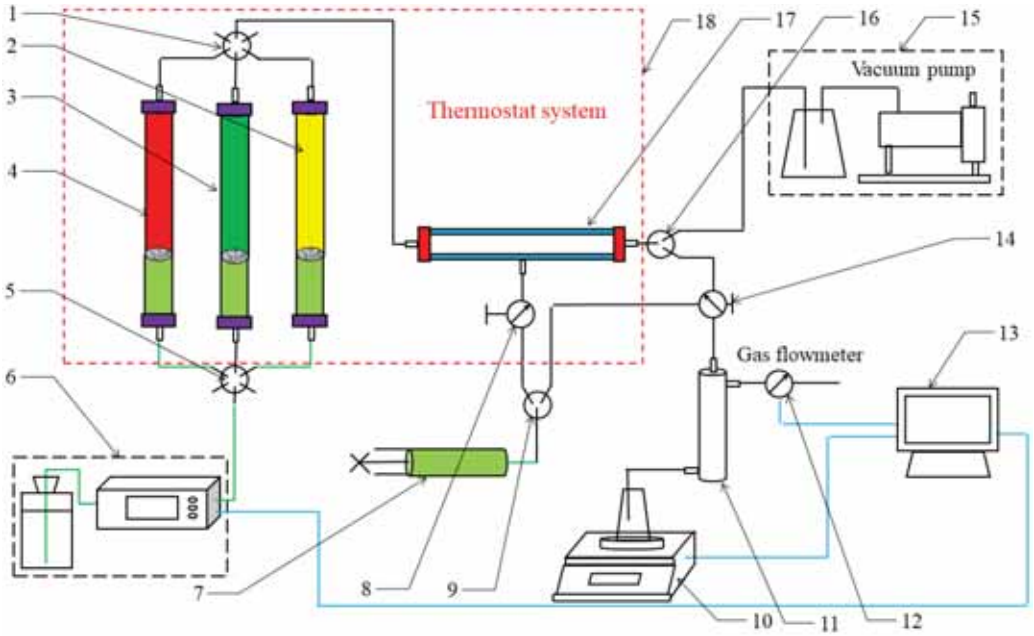

FIGURE 1
Schematic of the experimental apparatus

Notes: 1-Six-way shut-off valve; 2- CO_2 piston cylinder; 3-Water piston cylinder; 4-Heavy oil piston cylinder;5- Six-way shut-off valve; 6- Advection pump; 7-Hand pump; 8-Ring pressure valve; 9-Three-way shut-off valve; 10- Electronic balance instrument; 11- Gas-liquid separation device; 12-Gas Flowmeter; 13-Computer; 14- Back pressure valve; 15- Vacuum pump; 16-Three-way shut-off valve; 17- Core holder; 18- Temperature control system.

TABLE 3
Gas injection pressures and production pressure during different experiment

Fracturing			Without fracturing		
Core	Injection pressure (MPa)	Back pressure (%)	Core	Injection pressure (MPa)	Back pressure (%)
#1	16.3	16.0	#5	16.3	16.0
#2	20.0	16.0	#6	20.0	16.0
#3	24.0	16.0	#7	24.0	16.0
#4	28.0	16.0	#8	28.0	16.0

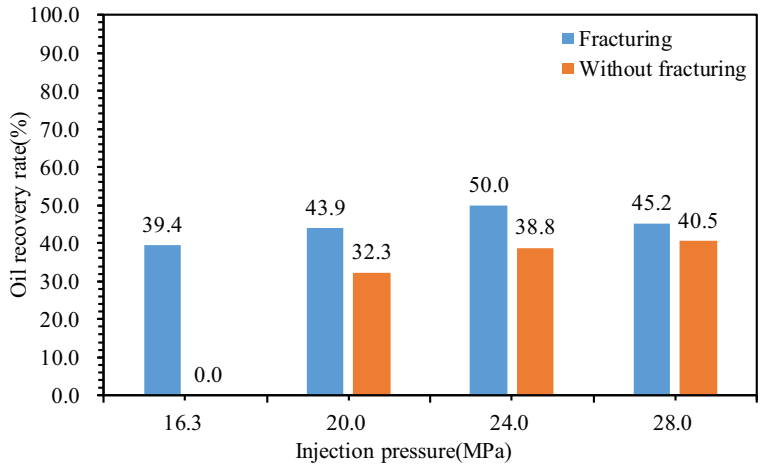

FIGURE 2
Recovery at different gas injection pressures.

RESULTS AND DISCUSSION

Fracture Effect Analysis. There are eight groups of CO_2 flooding experiments, including four groups of unfractured core displacement experiments and four groups of fractured core displacement experiments. By increasing the pressure at the injection end to increase the displacement pressure difference, the strength of the dissolution, viscosity reduction and swelling displacement process during the CO_2 flooding process is changed, and different development effects are obtained.

Analyzing the data in Table 3, during the CO_2 flooding process before and after this fracturing, the back pressure was set at 16 MPa, which is consistent with the true reservoir pressure. After that, the change of the ultimate recovery factor of eight groups of cores is calculated, and the corresponding data is plotted according to the change of the gas injection pressure value. The data graph is shown in Figure 2.

The data in Figure 2 show that at the same gas injection pressure, the core can obtain a greater degree of recovery during the CO_2 flooding process after fracturing treatment, which is explained by the increase in the percolation channel during the fracturing process. In the two-phase percolation process, the relative permeability of each phase is increased, the two-phase common flow range is widened, the residual oil saturation is reduced, and the ultimate recovery is increased [21-22]. At the same time, the final recovery value of the experiment in #1 is zero, which is interpreted as that the permeability value is low and the starting pressure gradient is large before the core is not fractured. When the low pressure difference is driven, the heavy oil in the lithological porous medium fails to occur seepage, which in turn causes the final recovery factor to be zero.

Analysis of CO_2 Flooding Process After Fracturing. During gas injection development in heavy oil reservoirs, a certain amount of gas injection can reduce the viscosity of heavy oil through dissolution. However, as the gas injection volume continues to increase, the two-phase displacement process uses gas as the displacement phase, and the fluidity is much lower. In the displaced phase, the gas breakthrough in the later stage of gas injection forms a dominant channel, reducing the gas injection and recovery rate. During the CO_2 flooding development process, the recovery degree and gas-oil production ratio at different gas injection PV numbers were counted. The detailed data are shown in Figure 3.

Analysis of the entire gas injection flooding process, the degree of recovery gradually increased, which can be divided into three stages: Stage 1, gas dissolution stage (0 ~ 0.15PV), in this process, the injected CO_2gas dissolve the heavy oil at the inlet end. The viscosity of the heavy oil at the inlet is reduced, and the composition of the heavy oil near the outlet is basically unchanged, which results in the initial heavy oil production rate at the initial

outlet is relatively low, and the dissolved gas content in the heavy oil is displaced by the outlet. Stage 2, the dissolved gas flooding stage (0.15 ~ 0.65PV). In this process, CO_2 is dissolved in the heavy oil in the porous medium, the viscosity of the heavy oil in the percolation channel is reduced, and the combined effects of viscosity reduction and swelling displacement during CO_2 injection are reduced. At the same time, the output rate of heavy oil at the outlet end increases, and at the same time, the dissolved gas content at the outlet end increases; Stage 3, the gas breakthrough phase (0.65PV ~ 1.0PV), at this time the dissolved gas in the heavy oil is saturated, and CO_2 gas is injected. Considering that the CO_2 gas as the displaced phase has a low fluidity, when the gas at the outlet end breaks through, a gas-dominant percolation channel is quickly formed in the porous core, causing the incremental increase in production to slow down to become stable, and the gas-oil production ratio rises rapidly.

Analysis of CO_2 Flooding Time After Fracturing. For the development of heavy oil reservoirs during gas injection, during the later stage of gas injection and displacement, the production gas-oil ratio is extremely high, that is, gas injection development has entered the gas breakthrough stage defined in this paper, although continuous gas injection can still increase the recovery efficiency to a certain extent, but the gas injection development efficiency at this stage is low [23]. After the fracturing, the four groups of cores are injected with CO_2 to drive the breakthrough stage of the gas breakthrough and the extent of production is increased. The statistics are plotted in Figure 4.

The data in Figure 4 shows that during the later stage of CO_2 flooding, as the gas injection pressure increases, the duration of stage 3 decreases, the incremental increase in production in stage 3 decreases. Under lower injection pressures, the maximum increase in production degree is 1.8%. Although reducing the injection pressure can increase the final recovery of stage 3, considering the effects of the duration of the CO_2 flooding and the low efficiency of stage 3 CO_2 flooding, the injection pressure of CO_2 flooding cannot be too low.

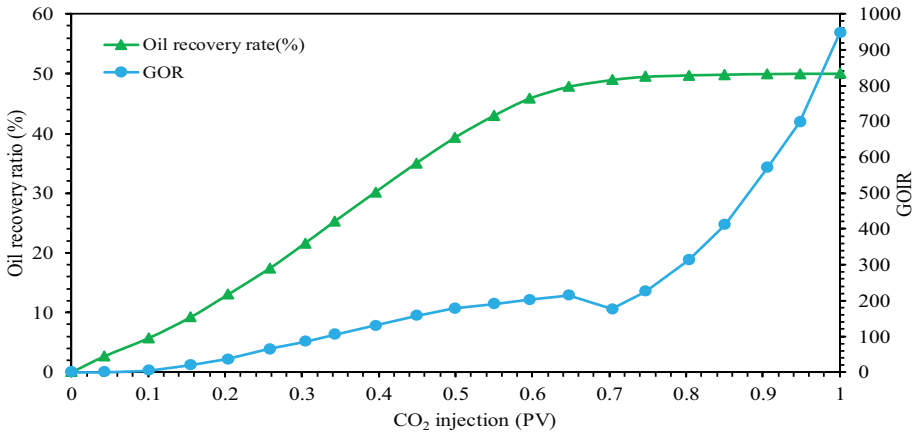

FIGURE 3
Change of recovery rate and GOR at different gas injection PV numbers (take # 7 as an example).

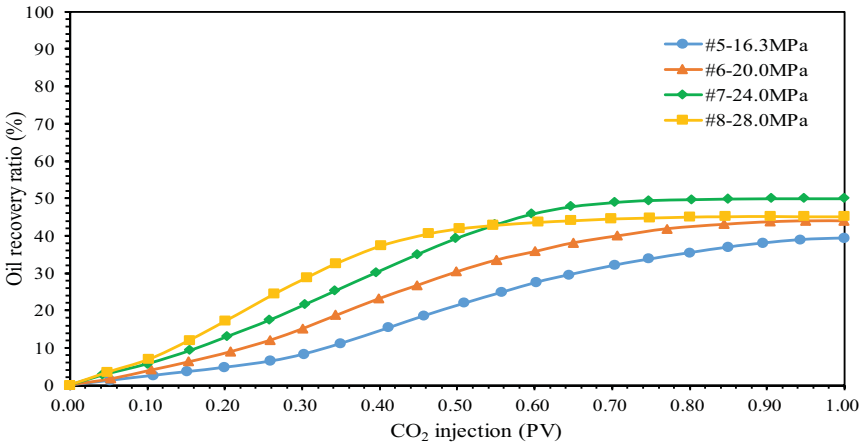

FIGURE 4
Duration of each core and increment of extraction degree in stage 3.

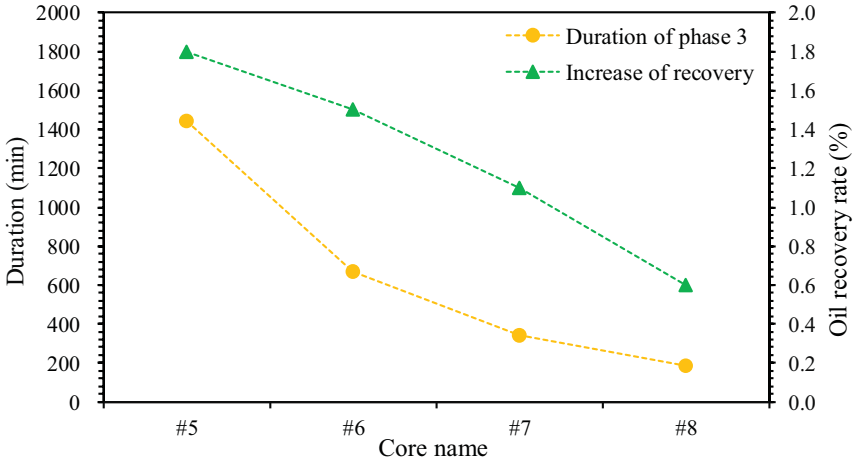

FIGURE 5
Variation of gas production rate with the number of injected PVs.

Optimal Gas Injection Pressure. The gas injection flooding experiments at different pressures were performed on cores after fracturing. The changes in CO_2 injection volume during CO_2 flooding were recorded, and the changes in recovery degree during CO_2 flooding were recorded. A total of four core data of #5, #6, #7, and #8 were counted and plotted into the data shown in Figure 5.

The data in Figure 5 shows that during the CO_2 injection flooding process, the recovery degree gradually increased with the increase in the number of injected PVs. At the same time, the increase rate of recovery degree conformed to the three-stage characteristic, that is, the increase of the recovery degree in the initial gas dissolution process is slow, and the recovery of dissolved gas flooding in the middle period increases rapidly, and then the increase of recovery in the later stage of gas breakthrough slows down to stabilize [24-25]. The analysis of the degree of recovery under different gas injection pressures shows that for stage 1, as the gas injection pressure increases, the duration of this phase decreases, which is interpreted as the increasing of the gas injection pressure can accelerate the gas dissolution process, thereby shortening the gas dissolution stage. For stage 2, with the increase of the gas injection pressure, the increase in the extraction rate at this stage gradually increases, which is explained that without changing the free properties of the seepage channel, a higher injection pressure can strengthen the dissolution and viscosity reduction and swelling, leading to an increase in the degree of production of heavy oil. For stage 3, with the increase of gas injection pressure, the increase in the degree of recovery gradually decreases after gas breakthrough. It is explained that the percolation in the porous medium at this stage is two-phase percolation, and the increase in the relative permeability of the gas phase caused by the greater displacement pressure is obvious. The advantages of gas-phase percolation have been further expanded, resulting in a faster appearance of the dominant channel, which in turn resulting a gradual decrease in the recovery factor [26-29]. The final recovery factor under different gas injection pressures this time shows that the final recovery factor does not increase with the increase of gas injection pressure, but there is an optimal gas injection pressure value that makes the final recovery factor the largest. The optimal gas injection pressure is 24 MPa, which means that when the gas injection pressure is low, the gas injection dissolution and viscosity reduction process and swelling displacement process are weak. When the gas injection pressure is too high, the gas as the displacement phase will burst into the outlet too quickly, and then a gas channeling dominant percolation channel will be formed, reducing the spread coefficient of the gas injection displacement process, and then reducing the final recovery factor.

CONCLUSIONS

(1) The experimental results show that, before fracturing, with the increase of gas injection pressure, the ultimate heavy oil recovery rate gradually increases, and at the same time, there is a starting pressure for CO_2 flooding in low permeability reservoirs to displace heavy oil.

(2) Through fracturing the core, the results show that both the porosity and permeability of the core have increased significantly compared to the unfractured core. After fracturing, the ultimate recovery rate increased to a certain extent, which was manifested by the improvement of the porous media seepage channels in the core after fracturing transformation. At the same time, with the increase of gas injection fracturing, the recovery rate of fracturing transformation decreased.

(3) After analyzing the four groups of CO_2 flooding experiments in the core after fracturing and reforming, the recovery rate of the initial gas dissolution phase increased slowly, and as the gas injection pressure increased, the duration of the dissolved gas flooding phase gradually decreased (Stage 1). For stage 2, the degree of production has increased significantly, and with the increase of gas injection pressure, the rate of production has gradually accelerated. In the later stage of gas breakthrough, the degree of production gradually stabilizes to no longer change, and with the increase of gas injection pressure, the production degree of increase gradually decreases (Stage 3). The maximum value of the final recovery factor is calculated to be 50.0% based on the three-stage recovery value, which indicates that the final recovery factor increases first and then decreases as the gas injection pressure increases. The optimal injection pressure value for the indoor displacement experiment after fracturing is 24 MPa.

ACKNOWLEDGEMENTS

This work was financially supported by Open Fund(PLC20190702) of State Key Laboratory of Oil and Gas Reservoir Geology and Exploitation（Chengdu University of Technology）, the National Natural Science Foundation of China (No. 51774236), the National Science and Technology Major Project of China (No. 2017ZX05069004), the Natural Science Basic Research Plan in Shaanxi Province of China (No. 2019JQ-407), and the Open Fund of The Key Laboratory of Accumulation and Development of the Continental Shale Gas in Shaanxi Province, China (No. YJSYZX19SKF 0001).

REFERENCES

[1] Chen, Z. (2018) Technology and practice of heavy oil development in Liaohe Oilfield. Petrochemical Industry Technology. (1), 44.

[2] Wang, F., Mou, Z., Liu, P. (2017) Experiment and numerical simulation on mechanism of CO2 assisted mining in super heavy oil reservoirs. Petroleum Geology and Recovery Efficiency. 24(6), 86-91.

[3] Ren, F., Sun, H., Hu, C. (2012) Heavy oil development technology and practices in Liaohe oilfield. Special Oil and Gas Reservoirs. 19(1), 1-8+135.

[4] Xi, C., Guan, W., Jiang, Y., Liang, J., Zhou, Y., Wu, J., Wang, X., Cheng, H., Huang, J., Wang, B. (2013) Numerical simulation of fire flooding for heavy oil reservoirs after steam injection: a case study on Block H1 of Xinjiang oilfield. Petroleum Exploration and Development. 40(6), 766-773.

[5] Hu, W., Lv, C., Wang, R., Yang, Y., Xin, W. (2017) Mechanism of CO_2 immiscible flooding and distribution of remaining oil in water drive oil reservoir. Petroleum Geology and Recovery Efficiency. 24(5), 99-105.

[6] Hamouda, A., Chukwudeme, E., Mirza, D. (2009) Investigating the effect of CO_2 flooding on asphaltenes oil recovery and reservoir wettability. Energy and Fuels. 23(2), 1118-1127.

[7] Welker, J. (1963) Physical properties of carbonated oils. Journal of Petroleum Technology. 15(08), 873-876.

[8] Miller, J., Jones, R. (1981) A laboratory study to determine physical characteristics of heavy oil after CO_2 saturation. In SPE/DOE Enhanced Oil Recovery Symposium. Society of Petroleum Engineers.

[9] Sankur, V., Emanuel, A. (1983) A laboratory study of heavy oil recovery with CO_2 injection. In SPE California Regional Meeting. Society of Petroleum Engineers.

[10] Jha, K. (1986) A laboratory study of heavy oil recovery with carbon dioxide. Journal of Canadian Petroleum Technology. 25(02), 54-63.

[11] Mungan, N. (1992) Carbon dioxide flooding as an enhanced oil recovery process. Journal of Canadian Petroleum Technology. 31(09), 13-15.

[12] Srivastava, R., Huang, S., Dyer, S., Mourits, F. (1995) Quantification of asphaltene flocculation during miscible co_2 flooding in the Weyburn reservoir. Journal of Canadian Petroleum Technology. 34(08), 31-41.

[13] Papadimitriou, N., Romanos, G., Charalambopoulou, G., Kainourgiakis, M., Katsaros, F., Stubos, A. (2007) Experimental investigation of asphaltene deposition mechanism during oil flow in core samples. Journal of Petroleum Science and Engineering. 57(3-4), 281-293.

[14] Huang, L., Jia, Y., Quan, Y., Sun, L. (2012) The long core experiment and numerical simulation research on asphaltic oil with co_2 flooding. Journal of Southwest Petroleum University (Science and Technology Edition). 34(4), 135-140.

[15] Jiang, H., Liu, Z., Yuan, S., Tian, X., Zhang, D. (2017) Fracturing treatment of water-sensitive low-permeability heavy oil thin-layer reservoir. Journal of Xinjiang University (Natural Science Edition). 34(3), 299-302.

[16] Guo, X. (2019) Study on microscopic migration characteristics of heavy oil by CO_2 flooding at high temperature and high pressure. Petroleum Geology and Recovery Efficiency. 26(3), 99-104.
[17] Hao, M., Song, Y. (2010) Research status of CO_2 – EOR. Drilling Production Technology. 33(4), 59-63.
[18] Yang, S., Hang, D., Sun, R., Lv, W., Wu, M., Deng, H. (2009) CO_2 extraction for crude oil and its effect on crude oil viscosity. Journal of China University of Petroleum. 4, 85-88.
[19] Yang, J., Fu, Y., Zeng, L., Peng, J., Chen, X. (2011) Study on experimental techniques of rock direction in tight sandstone reservoir. Drilling and Production Technology. 21 (5), 63-65.
[20] Li, Q., Kang, Y., Luo, P. (2006) Multi-scale effect in tight sandstone gas reservoir and production mechanism. Natural Gas Industry. 26(2), 111-113.
[21] Li, Y., Pu, W., Wei, B., Chen, Y., Bai, B. (2018) The feasibility of CO_2 and N_2 injection for the Tahe fracture-cavity carbonate extra-heavy oil reservoir: An Experimental Study. Fuel. 226, 598-606.
[22] Huang, X., Li, T., Gao, H., Zhao, J., Wang, C. (2019) Comparison of SO_2 with CO_2 for Enhancing Shale-hydrocarbon Recovery using Low-field Nuclear Magnetic Resonance. Fuel. 245, 563-569.
[23] Huang, X., Li, A., Li, X., Liu, Y. (2019) Influence of Typical Core Minerals on Tight Oil Recovery during CO_2 Flooding using NMR Technique. Energy and Fuels. 33(8), 7147-7154.
[24] Ghasemi, M., Astutik, W., Alavian, S., Whitson, C., Suicmez, V. (2018) Impact of pressure on tertiary-CO_2 flooding in a fractured chalk reservoir. Journal of Petroleum Science and Engineering. 167, 406-417.
[25] Ghasemi, M., Suicmez, V. (2019) Upscaling of CO_2 injection in a fractured oil reservoir. Journal of Natural Gas Science and Engineering. 63, 70-84.
[26] Ren, G., Nguyen, Q., Lau, H. (2018) Laboratory investigation of oil recovery by CO_2 foam in a fractured carbonate reservoir using CO_2-Soluble surfactants. Journal of Petroleum Science and Engineering. 169, 277-296.
[27] Sheng, G., Su, Y., Wang, W. (2019) A new fractal approach for describing induced-fracture porosity/permeability/compressibility in stimulated unconventional reservoirs. Journal of Petroleum Science and Engineering. 179, 855-866.
[28] Sheng, G., Zhao, H., Su, Y., Javadpour, F., Wang, C., Zhou, Y., Liu, J., Wang, H. (2020) An analytical model to couple gas storage and transport capacity in organic matter with noncircular pores. 268, 117288.
[29] Ghasemi, M., Astutik, W., Alavian, S., Whitson, C., Suicmez, V. (2018) Experimental and numerical investigation of tertiary-CO_2 flooding in a fractured chalk reservoir. Journal of Petroleum Science and Engineering. 164, 485-500.

Received: **09.01.2020**
Accepted: **12.02.2020**

CORRESPONDING AUTHOR

Le Qu
Post-Doctoral Contribution Center,
College of Petroleum Engineering,
Xi'an Shiyou University,
Xi'an, Shaanxi 710065, China

e-mail: qule@xsyu.edu.cn

© by PSP Volume 29 – No. 04A/2020 pages 3269-3278 Fresenius Environmental Bulletin

ACCURATE PREDICTION OF EXTERNAL CORROSION RATE OF BURIED PIPELINE BASED ON KPCA-MABC-SVR MODEL USING IN OIL AND GAS GATHERING AND TRANSPORTING SYSTEM

Hui Xu[1,*], Shipeng Wang[2], Min Yan[1], Zhixiu Liu[3], Rongrong Xie[1]

[1]Shaanxi Key Laboratory of Advanced Stimulation Technology for Oil & Gas Reservoirs, College of Petroleum Engineering, Xi'an Shiyou University, Xi'an, Shaanxi 710065, China
[2]Chinagas Holdings Limited, Shenzhen, Guangdong 518033, China
[3]QingYang Vocational College of Technology, Qingyang, Gansu 745000, China

ABSTRACT

Buried pipelines are an indispensable part in the process of oil and gas gathering and transportation. Due to the increase in service time and harsh working environment, the pipelines are prone to various corrosion effects and damage, and then oil and gas leaks cause serious environmental pollution. Aiming at the problem of external corrosion rate of buried pipelines, this study first analyzes the influencing factors of external corrosion of pipelines, and analyzes the KPCA (Kernel Principal Component Analysis) algorithm, MABC (Improved Artificial Bee Colony) algorithm, and SVR (Support Vector Machine Regression) algorithm separately. After that, the construction method of the KPCA-MABC-SVR model is proposed. Then the KPCA algorithm is used to reduce the dimension of the factors affecting the external corrosion rate of the pipeline. The MABC algorithm is used to optimize the parameters of the SVR algorithm. The 64 sets of data are used to the SVR model. Training was performed to predict the external corrosion rate data of the remaining 12 groups of pipelines, and the prediction results were compared with KPCA-ABC-SVR model, KPCA-BP neural network model and KPCA-BAS-GRNN model in the literature to prove the new model (KPCA-MABC-SVR model) that we developed in this study. The research shows that the integrity of the anticorrosion layer outside the pipeline, the effectiveness of cathodic protection, and the soil pH are the main factors affecting the external corrosion of the pipeline. The average absolute error of the prediction of the external corrosion rate of the pipeline using the KPCA-MABC-SVR combined model is 3.0385%, and the training time is 4.76s, and both data are shorter than other models. The research results show that using the KPCA-MABC-SVR model to predict the external corrosion rate of the pipeline has a relatively small error and the model training time is relatively small. Therefore, the KPCA-MABC-SVR model has a strong ability to predict the external corrosion rate of the pipeline.

KEYWORDS:
Oil and gas gathering and transporting system, environmental pollution, KPCA-MABC-SVR model, buried pipeline, external corrosion rate, influencing factors

INTRODUCTION

At present, some of our pipelines have been in operation for more than 10 years. Although pipelines have adopted certain external anticorrosive measures, as time goes by, external anticorrosive measures will inevitably cause damage, which will cause severe external corrosion of the pipelines [1-2]. According to national standards, pipeline inspection is required after a certain period of time which is a good measure to find major defects in pipelines. However, due to economic and other factors, pipeline inspections cannot be performed every year [3-4]. If pipeline corrosion rates can be predicted, guidance can be improved for pipeline protection. Therefore, it is of great significance to predict the external corrosion rate of pipelines.

In recent years, domestic and foreign scholars have conducted in-depth research on the problem of external corrosion of pipelines, and have achieved certain research results. For example, Bi et al. [5] used the PCA algorithm to study the influencing factors of the external corrosion rate of oil pipelines in order to discover the important factors that cause the external corrosion rate of the pipeline. Jain et al. [6] predicted the external corrosion rate of the pipeline by establishing a neural network model, but in the process of research, no in-depth analysis of the relevant factors of the external corrosion rate of the pipeline was carried out. At the same time, because the neural network model has a relatively large dependence on the amount of data, the prediction result is relatively poor. Luo et al. [7] used KPCA algorithm to optimize the influencing factors affecting the external corrosion rate of the pipeline, used BAS algorithm to optimize the parameters of the GRNN algorithm, and finally used the GRNN model to learn and predict the external corrosion rate

data of the pipeline. However, The GRNN model is also a kind of neural network model. Due to the limitation of the amount of data, the prediction error is relatively large. Comprehensive analysis can find that relatively little data on the external corrosion rate of pipelines and related influencing factors is a major problem restricting further development in this direction.

Aiming at the problems in the current research, this research proposed a method for predicting the external corrosion rate of the pipeline using the KPCA-MABC-SVR model. First, the SVR model is a learning prediction algorithm suitable for small sample problems, so it can be used outside the pipeline. The field of corrosion rate prediction has been applied, but the model needs to optimize some parameters in the process of use. Therefore, this study proposed the MABC (Improved Artificial Bee Colony) algorithm to optimize parameters. Before making predictions, first the factors affecting the external corrosion rate of the pipeline are reduced in dimension. While ensuring the accuracy of the prediction results, the model training time is reduced to a certain extent. Using the KPCA-MABC-SVR model to predict the external corrosion rate of the pipeline can provide guidance and suggestions for pipeline maintenance and external protection work.

MATERIALS AND METHODS

Analysis of Influencing Factors on External Corrosion Rate of Buried Pipeline. For buried pipelines, protection measures such as shade protection and external corrosion protection are generally used. The existence of these protection measures greatly reduces the corrosion rate. However, no corrosion protection measures can completely avoid pipeline corrosion problems, which can only reduce the corrosion rate of pipes [8]. On the other hand, if the protection measures of the pipeline are problematic and affected by the soil environment, the corrosion rate of the pipeline will be further increased [9]. Comprehensive analysis shows that the problem of external corrosion of pipelines is mainly affected by the soil environment and the degree of protection measures.

The soil environmental factors that cause external corrosion of pipelines can be divided into seven aspects, which are the content of microorganisms, water content, pH, porosity, oxygen content, electrical resistivity, and salt content. These factors will affect pipeline corrosion alone. In addition, there will be a certain relationship between each other. For example, when the porosity of the soil environment where the pipeline is located is relatively large, the oxygen content and moisture content of the soil will be increased to a certain extent. When the pipeline is in an acidic environment under the influence of oxygen, the corrosion rate will be further accelerated [10-13]. Therefore, the influence of soil environment on pipeline corrosion is relatively complicated, which is also the main reason why it is difficult to perform simple mathematical calculations on the corrosion rate outside the pipeline.

The so-called pipeline protection measures mainly include two aspects, namely the integrity of the outer anti-corrosion layer of the pipeline and the effectiveness of the overcast current. When the outer anti-corrosion layer of the pipeline causes damage, the pipeline will be directly affected by the soil environment. At the same time, galvanic cells are likely to be formed in different parts of the pipeline, which will further accelerate the corrosion rate of the pipeline at the damaged part of the outer anticorrosive layer [14]. The failure of the current which is likely to occur will accelerate the corrosion rate outside the pipeline. In fact, after a long period of operation, some pipelines have experienced serious damage to the outer anticorrosive layer and cathode failure.

Through the above analysis, it can be found that the factors that affect the external corrosion of the pipeline can be divided into nine aspects, that is, the content of microorganisms in the soil, water content, pH, porosity, oxygen content, resistivity, salt content, external corrosion protection, the integrity of the layer and the effective of the protective current. In the process of predicting the corrosion rate outside the pipeline, theoretically, these nine factors need to be considered. However, in order to reduce the complexity of the prediction model and reduce the model training time, it is necessary to reduce the dimension of the influencing factors.

KPCA-MABC-SVR Model Theory. (1) KPCA Algorithm Theory. The KPCA (Kernel Principal Component Analysis) algorithm is a data dimensionality reduction method evolved from the traditional PCA (Principal Component Analysis). Unlike the PCA algorithm, the process of applying the KPCA algorithm is mainly through non-linear mapping. The related influence factor data is transformed into the feature space, and then the relevant data is processed in the feature space. Relatively speaking, this type of data dimensionality reduction method has strong nonlinear processing ability [15]. The basic principle of the KPCA algorithm is:

First, suppose that all data can be combined into a data set $X = \{x_1, x_2, \cdots x_n\}$, $x_i \in R^p, i = 1, \cdots n$, where, R^p represents the input space of these data, and p represents the dimensions of these data. In the process of data mapping, special mapping functions ϕ will be used to process, and then $R_p \to F, x \to X$. At the same time, $\sum_{i=1}^{M} \phi(x_i) = 0$ will be satisfied. At this time, the

covariance matrix of these data is obtained. The covariance matrix is as follows:

$$C = \frac{1}{m}\sum_{i=1}^{m}\phi(x_i)\phi(x_j)^T \quad (1)$$

Solve the eigenvalues of the covariance matrix λ and the eigenvectors corresponding to each eigenvalue$v$. Assuming that the calculated eigenvalues satisfy $0 \le \lambda_1 \le \lambda_2 \le \cdots \le \lambda_n$, the eigenvectors corresponding to these eigenvalues are represented by $v_1, v_2, \cdots, v_n$. At this time, we can get:

$$v_r = \sum_{i=1}^{n}\alpha_r^i\phi(x_i) \quad (2)$$

Substituting the above two formulas into the formula $\phi(x_i)\cdot Cv = \lambda(\phi(x_i)\cdot v)$, suppose$K = (k_{ij})_{n\times n} = \phi(x_i)\cdot\phi(x_j)$ $(i, j = 1, 2, \cdots n)$, and then $K\alpha = n\lambda\alpha$ can be obtained, where K is the kernel matrix in the KPCA algorithm, $n\lambda_i$ is the eigenvalue of the kernel matrix, the feature vector is $\alpha_1, \alpha_2, \cdots, \alpha_n$. First, take the first $m(m < n)$ of these eigenvalues and the corresponding feature is $\alpha_1, \alpha_2, \cdots, \alpha_m$. The vector $\alpha_r = \left\{\alpha_r^1, \alpha_r^2, \cdots, \alpha_r^m\right\}$ $(r = 1, 2, \cdots, m)$ is assumed at this time, $\phi(x_i)$ can be projected in the feature space at this time:

$$g_r(x_j) = \sum_{i=1}^{n}\alpha_r^i[\phi(x_i)\cdot\phi(x_j)] \quad (3)$$

On the other hand, it is difficult to meet the basic conditions $\sum_{i=1}^{M}\phi(x_i) = 0$, so we need to transform $\phi(x_i)$. First, suppose:

$$\tilde{\phi}(x_i) = \phi(x_i) - \frac{1}{m}\sum_{j=1}^{m}\phi(x_j), i = 1, 2, \cdots, m \quad (4)$$

Then we can get:

$$K_{ij} = (\tilde{\phi}(x_i)\cdot\tilde{\phi}(x_j)) = K_{ij} - \frac{1}{m}\sum_{p=1}^{m}K_{ip} - \frac{1}{m}\sum_{q=1}^{m}K_{qj} + \frac{1}{m^2}\sum_{p,q=1}^{m}K_{pq} \quad (5)$$

Finally, according to the actual situation, several principal component factors with relatively high contribution rate can be selected from the above formula (3) to replace all the principal components for further research [16].

(2) SVR Model Algorithm Theory. The SVR algorithm is the support vector machine regression algorithm. This kind of algorithm can transform the original data into a high-dimensional space, that is, convert a non-linear problem into a linearized problem in a high-dimensional space [17]. In the process of using this algorithm, the purpose of risk minimization can be achieved, and at the same time, training samples with the smallest generalization error can be obtained, so the generalization ability of this algorithm is relatively good [18-19].

For non-linear problems, suppose the data set used for model training is $\{(x_i, y_i)|i = 1, 2, \cdots, n\}$. In this data set, x_i is the input vector represented by the vector has a dimensional structure D, y_i is the output vector and has n groups. The relationship between them can be expressed using the following formula:

$$f(x) = w^T\varphi(x) + b \quad (6)$$

In the above formulas: $f(x)$ is the predicted value; w is weight vector, $\varphi(x)$ is mapping function; b is the threshold value. The SVR algorithm mainly searches for w and b in order to achieve the purpose of minimizing risk. These two parameters can be determined mainly by introducing a secondary planning method. In the process of solving the non-linear problem, two relaxation variables $\xi_i \ge 0$, $\xi^*_i \ge 0$, need to be introduced. The main purpose of introducing relaxation variables is to determine the deviation between the actual value of the data point and the ideal value. If all the training data can be linearized with a certain accuracy fitting, the quadratic programming equations introduced at this time and the constraint equations are as follows:

$$\min R(w, \xi_i, \xi^*_i) = \frac{1}{2}\|w\|^2 + C\sum_{p=1}^{P}(\xi_i + \xi^*_i) \quad (7)$$

$$\text{Subject to} \begin{cases} y_i - w\varphi(x_i) - b \le \varepsilon + \xi_i \\ w\varphi(x_i) + b - y_i \le \varepsilon + \xi^*_i \\ \xi_i \ge 0, \xi^*_i \ge 0 \end{cases} \quad (8)$$

In the above formula: C-Penalty factor; ε-Precision. The quadratic programming problem in the above formula can be solved by introducing the Lagrange equation. The two multipliers of the Lagrange equation are α_i and α_i^*. After the Lagrange equation is introduced, the quadratic programming equation can be transformed into:

$$\max W(\alpha_i, \alpha_i^*) = -\frac{1}{2}\sum_{i,j=1}^{n}(\alpha_i^* - \alpha_i)(\alpha_j^* - \alpha_j)(x_i, x_j) + \sum_{i=1}^{n}y_i(\alpha_i^* - \alpha_i) - \varepsilon\sum_{i=1}^{n}(\alpha_i^* + \alpha_i) \quad (9)$$

$$\text{Subject to} \sum_{i=1}^{n}(\alpha_i - \alpha_i^*) = 0$$

$$(0 \le \alpha_i, \alpha_i^* \le C) \quad (10)$$

In the above formula: x_i, x_j-training sample data; y_i-return value of training sample data; α_j, α_j^*-multiplier. You can finally get the regression function:

$$f(x)=\sum_{i=1}^{n}(\alpha_i-\alpha_i^*)(x_i\square x)+b \quad (11)$$

If the regression problem is a non-linear problem, we need to transform the input data into a high-dimensional space and solve it in a high-dimensional space. At this time, we need to introduce a kernel function $K(x_i\cdot x)=\varphi(x_i)\cdot\varphi(x)$. In the kernel function, $\varphi(x_i)$ represents the mapping in the high-dimensional space of x_i, The regression function expression equation at this time is:

$$f(x)=\sum_{i=1}^{n}(\alpha_i-\alpha_i^*)K(x_i\square x)+b \quad (12)$$

At present, the most common kernel function RBF function is:

$$K(x_i\square x)=\exp(-g\left\|x-x_i\right\|^2) \quad (13)$$

In the above formula: g is the parameter of the kernel function. After analyzing the SVR intelligent algorithm, it was found that in the process of using this prediction algorithm, in order to obtain accurate prediction results, it is necessary to first determine the values of the penalty factor *C* and the parameter of the kernel function *g*. These two values can be obtained by using MABC (Improved artificial bee colony algorithm).

(3) MABC Algorithm Theory. The artificial bee colony algorithm (ABC algorithm) is an optimization algorithm developed based on the honey-picking behavior of bees. Although this algorithm has the advantage of high accuracy in the process of use, it is very easy to fall into a local optimum. For this problem, in this research, the artificial bee colony algorithm is improved. The improved artificial bee colony algorithm (MABC algorithm) will reasonably rank the fitness of the honey sources. After finding the honey source with the highest fitness, the optimal solution will be performed [20-21]. The specific application steps of the MABC algorithm are:

1) Assume that the population of nectar powder is *NP*, the number of nectar sources is *FN*=*NP*/2, the maximum number of searches during the search process is Limit, the number of search cycles is Maxcycle, and the dimension of the nectar source is *D*=2.

2) The honey source is randomly generated, and its initial position is assumed to be x_{ij}:

$$x_{ij}=x_{j\min}+\text{rand}(0,1)(x_{j\max}-x_{j\min}) \quad (14)$$

Around the honey source i, the leading bee can produce new honey sources v_{ij}:

$$v_{ij}=x_{ij}+\theta(x_{ij}-x_{kj}) \quad (15)$$

In the above formula: i-honey source; j-random number in interval [1, D]; $x_{j\max}$ and $x_{j\min}$ are upper and lower limit of search space; k-random honey source different from honey source i; θ-disturbance amplitude, random number in [-1, 1].

3) Compare the fitness of v_{ij} and the fitness of x_{ij}, leaving a high fitness nectar.

4) Determine the nectar source selected by the following bee according to the following probability calculation formula, and then update the nectar source in the same way as the lead bee.

$$p_i=\frac{\text{fit}_i}{\sum_{i=1}^{FN}\text{fit}_i} \quad (16)$$

In the above formula: p_i-the probability of selecting a honey source; fit_i-the fitness of the honey source.

5) If the iteration of the honey source exceeds the preset number of iterations at this time, but there is no improvement, then the honey source is abandoned for searching.

6) Repeat the above steps until the preset number of cycles is completed.

(4) KPCA-MABC-SVR Model Establishment. The flowchart of the KPCA-MABC-SVR model is shown in Figure 1 below. First, the obtained pipeline corrosion rate and influencing factor data are divided into two groups, which are a training data set and a test data set, in which the training data set contains 64 sets of data and the test data set contains 12 sets of data. Then we build a KPCA-MABC-SVR model in MATLAB software, input the training data set into the model for training, predict the corrosion rate of the test data set, and compare the prediction result with the actual corrosion rate to calculate the relative error. The prediction accuracy of the KPCA-MABC-SVR model is compared with the KPCA-ABC-SVR model, the KPCA-BP neural network model and the KPCA-BAS-GRNN model [7].

RESULTS AND DISCUSSION

Data Source. The QX oil pipeline is located in the northwestern region of China. The pipeline has been running continuously for more than 10 years. After a general survey of the pipeline, it was found that although the pipeline has taken external anticorrosion and cathodic protection measures, there are problems of external anticorrosion damage and overcast protection. In May 2017, the staff used an ultrasonic thickness gauge to measure the wall thickness of the pipeline at 76 locations along the pipeline. In May 2018, the staff again used an ultrasonic thickness gauge to measure the wall thickness of the pipeline at 76 locations along the pipeline.

Due to the integrity of the inner anticorrosion layer taken on the inner wall of the pipeline, and the crude oil itself attached to the inner wall can play a good protection role, therefore, The wall thickness of 64 locations from May 2017 to May 2018 can be regarded as the corrosion rate of the outer wall of the pipe. At the same time, the staff also sampled the soil at 76 locations, tested the soil microbial content, pH and other seven indicators. The validity and integrity of the external anticorrosion were checked, and some of the test results are shown in Table 1 (the external anticorrosion layer is complete defined as 1, the external anticorrosion layer is damaged defined as 0; the overcast protection is effective defined as 1, and the overcast protection is non-effective defined as 0).

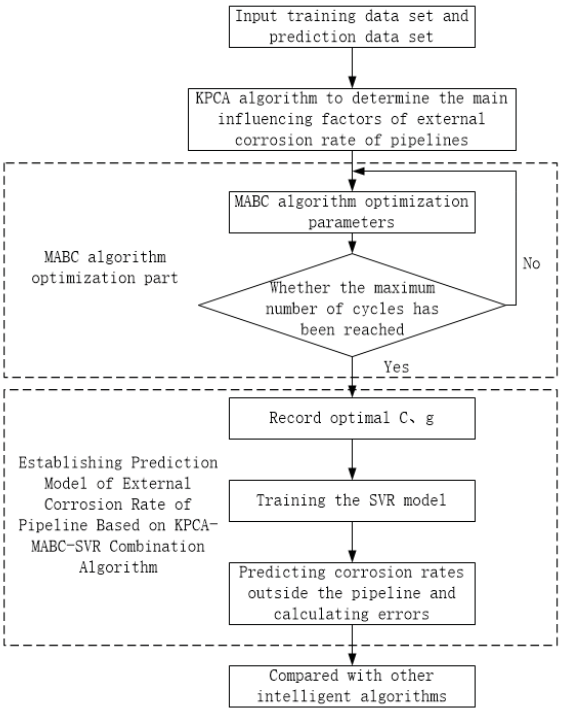

FIGURE 1
KPCA-MABC-SVR model flowchart.

TABLE 1
Test results of external corrosion rate and related influencing factors on some locations of QX oil pipelines

Samples	Pipe corrosion rate ($mm \cdot a^{-1}$)	Microbial content (10^8 pcs/g)	Water content (%)	pH value	Porosity (%)
1	0.05	56.39	4.279	6.5	18.80
2	0.11	24.52	4.036	6.4	16.18
3	0.25	18.20	5.782	6.5	16.22
4	0.09	8.69	3.279	6.7	15.66
5	0.14	14.67	6.489	6.6	15.09
6	0.08	55.30	8.019	6.6	18.71
7	0.15	10.83	5.276	6.8	17.07
8	0.02	52.84	5.387	6.5	16.12
9	0.16	39.01	4.222	6.7	16.47
10	0.11	35.08	8.245	6.6	18.72
Samples	Oxygen content (%)	Soil resistivity (Ω·m)	Salt content (%)	Outer coating integrity	Cathodic protection effectiveness
1	13.98	63.8	0.05	1	0
2	13.19	74.6	0.08	1	0
3	15.49	71.4	0.14	0	0
4	14.51	91.2	0.17	0	0
5	11.65	95.5	0.19	0	1
6	11.01	100.2	0.30	1	1
7	14.04	99.6	0.21	1	1
8	10.89	110.5	0.15	1	1
9	11.11	91.7	0.09	1	0
10	10.57	88.6	0.15	0	0

TABLE 2
Data normalization results

Samples	Pipe corrosion rate	Microbial content	Water content	pH value	Porosity	Oxygen content	Soil resistivity	Salt content	Outer coating integrity	Cathodic protection effectiveness
1	-0.5473	-0.0770	-0.5201	-0.0177	-0.5473	-0.3915	--0.2862	-0.5469	-0.4893	-0.1372
2	-0.6395	-0.0077	-0.6163	0.0151	-0.6396	-0.3778	-0.3916	-0.6388	-0.5142	-0.5052
3	-0.5586	-0.2164	-0.5453	0.1185	-0.5586	-0.2387	-0.3162	-0.5574	-0.4917	-0.4804
4	-0.5214	-0.1617	-0.5078	-0.2439	-0.5213	-0.2053	-0.2977	-0.5210	-0.5008	-0.4988
5	-0.4989	-0.2481	-0.4892	-0.2566	-0.4987	-0.3403	-0.3114	-0.4976	-0.5446	-0.4867
6	-0.5209	-0.1909	-0.5063	-0.0318	-0.5209	-0.4389	-0.4828	-0.5188	-0.5271	-0.5418
7	-0.4810	-0.2518	-0.4677	-0.3036	-0.4806	-0.4193	-0.4581	-0.4806	-0.6332	-0.5002
8	-0.5254	-0.3455	-0.5062	0.1515	-0.5253	-0.3389	-0.4433	-0.5229	-0.5475	-0.5189
9	-0.5034	-0.1617	-0.4880	0.1590	-0.5033	-0.3614	-0.4703	-0.5002	-0.5017	-0.4689
10	-0.5468	-0.2805	-0.4988	0.3929	-0.5467	-0.4121	-0.4502	-0.5454	-0.4884	-0.5146

TABLE 3
KPCA algorithm analysis results

Principal component name	Outer coating integrity	Soil resistivity	Oxygen content	Cathodic protection effectiveness	pH value	Water content	Microbial content	Porosity	Salt content
Eigenvalues	8.8149	0.4612	0.2719	0.1725	0.1207	0.08	0.0376	0.0219	0.0155
Difference	8.3538	0.1893	0.0994	0.0519	0.0407	0.0424	0.0157	0.0065	0.0116
Contribution rate	68.7319	12.6116	8.7189	3.7252	2.2066	1.8001	1.3761	0.6193	0.2103
Cumulative contribution rate	68.7319	81.3435	90.0624	93.7876	95.9942	97.7943	99.1704	99.7897	100

Analysis of KPCA Processing Results. After analyzing Table 1, it is found that the dimensions of various influencing factors are different. In order to perform KPCA analysis, the data needs to be standardized first, and the results after normalization are shown in Table 2. After standardized processing, it can be input into the KPCA model to analyze the contribution rate of each influencing factor to the external corrosion rate of the pipeline. The analysis results are shown in Table 3.

After analyzing Table 3, it is found that three factors, including the integrity of the outer preservative layer, the electrical resistivity of the soil, and the oxygen content of the soil are important factors that affect the external corrosion rate of the pipeline. The cumulative contribution of the five factors including the integrity of the outer preservative layer, the electrical resistivity of the soil, the oxygen content of the soil, the effectiveness of the cathodic protection, and the pH of the soil to the external corrosion rate of the pipeline exceeds 95%. In order to ensure the accuracy of the external corrosion rate prediction of the pipeline using the KPCA-MABC-SVR model, in this study, five influencing factors whose cumulative contribution rate exceeded 95% were selected as the influencing factors for the external corrosion rate study of the pipeline.

Analysis of Prediction Results. The MABC-SVR model was constructed in MATLAB software. A training data set consisting of 64 sets of data was input into the model. First, the parameters C and g of the SVR model were optimized. The optimization results showed that the best penalty factor C of the SVR model was 46.2853 and the optimal kernel function parameter g is 5.2642. After the optimal parameters are known, the SVR model is trained using 64 sets of data, the corrosion rate of 12 sets of test data sets is predicted, and the prediction results are de-normalized. Finally, the KPCA-MABC-SVR model is obtained. The predicted external corrosion rate of the pipeline is shown in Figure 2, and the relative error of the predicted result is shown in Figure 3. After analyzing these two figures, it was found that the external corrosion rate predicted by the KPCA-MABC-SVR model is very close to the actual external corrosion rate, and the maximum prediction error is not more than 6%, which proves that the method proposed in this study has strong prediction accuracy.

Comparison of Multiple Prediction Algorithms. In order to further study the advanced nature of the KPCA-MABC-SVR model proposed in this article, we use the same data to train the KPCA-ABC-SVR model, KPCA-BP neural network model, and the KPCA-BAS-GRNN model in the literature to predict the remaining 12 sets of data, calculate the relative error and average relative error of the prediction results, and measure the time required for model training and prediction. The calculation and measurement results are shown in Table 4. The prediction results and actual corrosion rates of the four models are shown below. The comparison is shown in Figure 4, and the relative error change is shown in Figure 5. After analyzing Table 4, Figure 4, and Figure 5, it was found that compared with the KPCA-ABC-SVR model, KPCA-BP neural network model, and KPCA-BAS-GRNN model, the average relative error of the prediction results of the KPCA-MABC-SVR model is the smallest, only 3.0385%. At the same time, the time required for model training and prediction is only 4.76s, which proves that this model has a strong advancement in the prediction of the corrosion rate outside the pipeline.

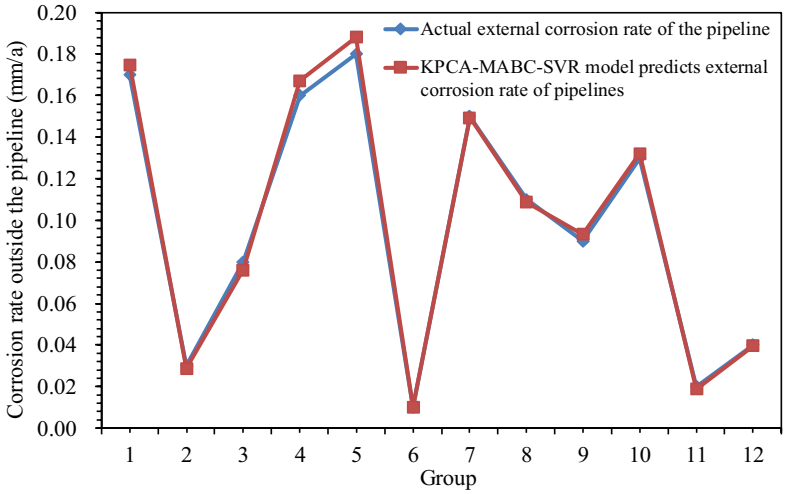

FIGURE 2
Comparison of predicted results and actual external corrosion rate of the pipeline.

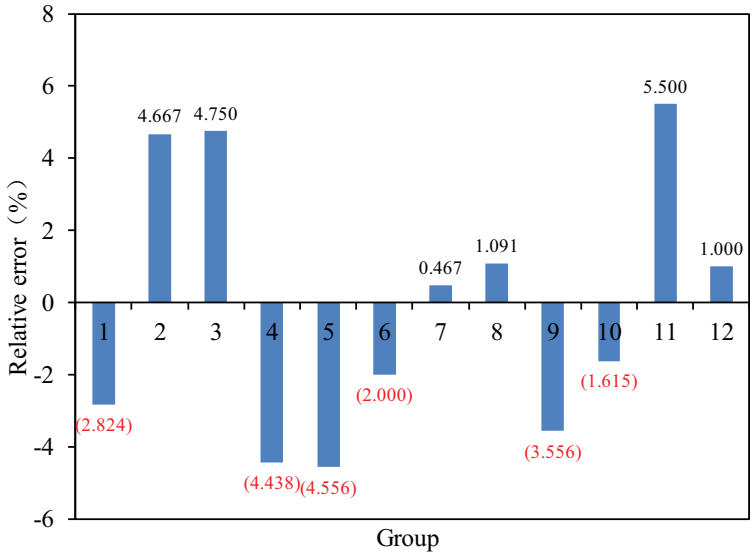

FIGURE 3
Relatively poor change of prediction results.

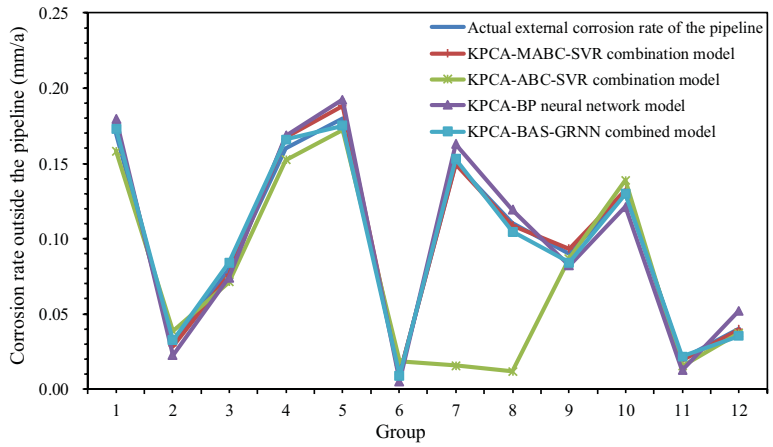

FIGURE 4
Comparison of prediction results of the four models with actual corrosion rates.

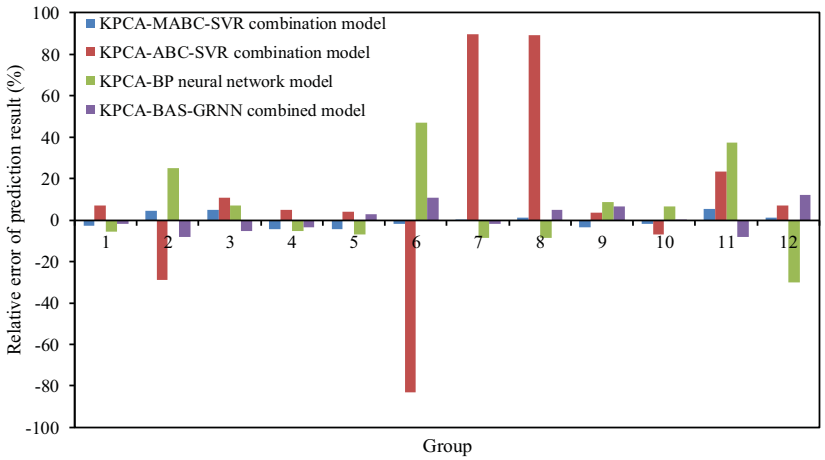

FIGURE 5
Relative errors of prediction results of the four models.

TABLE 4
Comparison of four model methods

Serial number	Actual external corrosion rate of pipeline (mm / a)	KPCA-MABC-SVR combination model		KPCA-ABC-SVR combination model		KPCA-BP neural network model		KPCA-BAS-GRNN combined model	
		Forecast result (mm / a)	Relative error (%)	Forecast result (mm / a)	Relative error (%)	Forecast result (mm / a)	Relative error (%)	Forecast result (mm / a)	Relative error (%)
1	0.17	0.1748	-2.8235%	0.1583	6.8824%	0.1798	-5.7647%	0.1732	-1.8824%
2	0.03	0.0286	4.6667%	0.0386	-28.6667%	0.0225	25.0000%	0.0324	-8.0000%
3	0.08	0.0762	4.7500%	0.0712	11.0000%	0.0743	7.1250%	0.0841	-5.1250%
4	0.16	0.1671	-4.4375%	0.1524	4.7500%	0.1683	-5.1875%	0.1658	-3.6250%
5	0.18	0.1882	-4.5556%	0.1723	4.2778%	0.1924	-6.8889%	0.1751	2.7222%
6	0.01	0.0102	-2.0000%	0.0183	-83.0000%	0.0053	47.0000%	0.0089	11.0000%
7	0.15	0.1493	0.4667%	0.0156	89.6000%	0.1628	-8.5333%	0.1529	-1.9333%
8	0.11	0.1088	1.0909%	0.0118	89.2727%	0.1193	-8.4545%	0.1047	4.8182%
9	0.09	0.0932	-3.5556%	0.0869	3.4444%	0.0821	8.7778%	0.0842	6.4444%
10	0.13	0.1321	-1.6154%	0.1389	-6.8462%	0.1212	6.7692%	0.1296	0.3077%
11	0.02	0.0189	5.5000%	0.0153	23.5000%	0.0125	37.5000%	0.0216	-8.0000%
12	0.04	0.0396	1.0000%	0.0372	7.0000%	0.0521	-30.2500%	0.0352	12.0000%
Mean absolute error (%)		3.0385%		29.8487%		16.4376%		5.4882%	
Model training prediction time		4.76s		6.85s		15.68s		8.52s	

CONCLUSIONS

(1) Because the corrosion rate of the outer wall of the pipeline is affected by a variety of factors, it is difficult to calculate and predict the external corrosion rate of the pipeline by summarizing mathematical formulas while using intelligent algorithms to predict is a more advanced way. Among all the factors influencing the external corrosion rate of the pipeline, the integrity of the outer anticorrosion layer, the electrical resistivity of the soil and the oxygen content of the soil have a relatively large effect on the external corrosion rate of the pipeline while the effect of the porosity of the soil and the oxygen content on the external corrosion rate is relatively small.

(2) KPCA algorithm is the upgraded version of the PCA algorithm which has more advantages in the application process. The SVR algorithm is an algorithm suitable for small sample training and prediction problems. For the prediction of the corrosion rate outside the pipeline, the amount of real data obtained is relatively small, which makes the traditional neural network model cannot be widely used in this field. The SVR algorithm is suitable for the small sample problem of prediction of the corrosion rate outside the pipeline. The MABC algorithm is an upgraded version of the ABC algorithm, which overcomes the shortcomings of the ABC algorithm and can reasonably optimize the parameters of the SVR algorithm.

(3) After using the KPCA-MABC-SVR model to predict the external corrosion rate of the pipeline, it was found that the prediction result of this model is very close to the actual external corrosion rate, and the maximum prediction error is not more than 6%, which proves that the method has strong prediction accuracy. By comparing the prediction results of the KPCA-MABC-SVR model with the prediction results of the KPCA-ABC-SVR model, the KPCA-BP neural network model, and the KPCA-BAS-GRNN model, it is found that KPCA - MABC-SVR model has the smallest average relative error of prediction results, only 3.0385%. At the same time, the time required for model training and prediction is only 4.76s, which proves that this model has a very important role in the prediction of the corrosion rate outside the pipeline. This study can provide a reliable reference for related research on buried pipeline corrosion damage, and then effectively reduce the risk of oil and gas leakage pollution.

REFERENCES

[1] Zhang, C., Shen, L., Guo, H., Du, M., Tai, Z. (2011) Research Progress of External Corrosion of Buried Oil and Gas Pipelines and Anticorrosion Technology. Contemporary Chemical Industry. 40(02), 202-205.

[2] Li, M., Wang, X., Qiao, G., Liu, S., Chen, T. (2015) Practice of Direct Evaluation of External Corrosion of Natural Gas Transmission Pipeline. Materials Protection. 48 (08), 70-73 + 76 + 9.

[3] Jiang, Y., Wu, M., Chen, X., Wang, W., Xie, F., Wu, G., Peng, Z. (2010) Analysis and Evaluation of External Corrosion Factors of Pipelines Based on Factor Analysis. Oil and Gas Storage and Transportation. 29(08), 605-608+556.

[4] Tao, W., Yang, Z., Wu, X., Hu, C., Yan, M., Yu, C., Xu, J., Sun, C. (2017) Comprehensive detection and evaluation method for external corrosion of old pipelines in oil and gas fields. Corrosion Science and Protection Technology. 29(02), 188-194.

[5] Bi, A., Luo, Z., Wang, X., Sun, Y. (2018) Study on Deterioration Wiener Process of Metal Pipeline Based on Soil Corrosion Principal Components. Materials Protection. 51(01), 37-42.

[6] Jain, S., Sanchez, A., Guan, S., Wu, S. (2015) Probabilistic assessment of external corrosion rates in buried oil and gas pipelines. International Corrosion Conference Series. 21(01), 71-78.

[7] Luo, Z., Yao, M., Luo, J., Wang, X. (2018) Prediction of External Corrosion Rate of Buried Pipeline Based on KPCA-BAS-GRNN. Surface Technology. 47(11), 173-180.

[8] Yuan, G. (2011) Corrosion and Prediction of Oil and Gas Pipelines. Dalian: Dalian University of Technology (Dissertation).

[9] He, F. (2016) Corrosion characteristics and control measures of gathering pipeline network in the old area of western Sichuan gas field. Chengdu: Southwest Petroleum University (Dissertation).

[10] Feng, J. (2018) Corrosion of buried steel pipes in Daqing Oilfield. Total Corrosion Control. 32(07), 79-81

[11] Metcalfe, R., Pearce, B. (2018) Stress corrosion cracking of a copper elbow fitting. Engineering Failure Analysis. 90(02), 197-201.

[12] Chen, Y., Li, L., Li, D., Chen, Y., Yu, X. (2015) Research on External Corrosion Mechanism of Oilfield Buried Metal Pipelines. Corrosion and Protection. 36(11), 1009-1013+1020.

[13] Wang, W., Shen, S. (2007) Analysis of Accident Tree Caused by External Corrosion of Buried Pipelines. Corrosion and Protection. 28(11), 587-589.

[14] Chen, J. (2011) Direct Evaluation Technology for External Corrosion of Pipelines. Oil and Gas Storage and Transportation. 30(07), 523-527+471-472.
[15] Luttrell, R., Vogt, F. (2008) Accelerating kernel principal component analysis (KPCA) by utilizing two-dimensional wavelet compression: applications to spectroscopic imaging. Journal of Chemometrics. 22(9), 510-521.
[16] Gomez, C., Ivan, A., Olivieri, D. (2015) A KPCA spatio-temporal differential geometric trajectory cloud classifier for recognizing human actions in a CBVR system. Expert Systems with Applications. 42(13), 5472-5490.
[17] Matsuda, K., Musashi, T., Watanabe, M. (2017) An Examination of a Priority Control Algorithm for a SVR Considering Reactive Power of a SVC in a Distribution Network. IEEJ Transactions on Power and Energy. 137(6), 419-425.
[18] Matsuda, K., Futakami, T., Horikoshi, K., Seto, T., Watanabe, M., Murakoshi, J. (2012) A decision method for ldc parameters of a SVR and voltage control algorithm using measurement data of a distribution system. IEEJ Transactions on Power and Energy. 132(132), 701-708.
[19] Brugger, D., Rosenstiel, W., Bogdan, M. (2011) Online SVR training by solving the primal optimization problem. Journal of Signal Processing Systems. 65(3), 391-402.
[20] Xu, W. (2012) Research on Optimal Population Structure of Improved Bee Swarm Algorithm. Journal of Taiyuan University of Science and Technology. 33(01), 10-14.
[21] Wang, S., Liu, H., Gao, K. (2018) Multi-group artificial bee colony algorithm applied to function optimization problems. Journal of Zhengzhou University (Engineering Science). 39(06), 30-35.

Received: **12.01.2020**
Accepted: **29.01.2020**

CORRESPONDING AUTHOR

Hui Xu
Shaanxi Key Laboratory of Advanced Stimulation Technology for Oil and Gas Reservoirs,
College of Petroleum Engineering,
Xi'an Shiyou University,
Xi'an, Shaanxi 710065, China

e -mail: 2564532926@qq.com

© by PSP Volume 29 – No. 04A/2020 pages 3279-3286 Fresenius Environmental Bulletin

EFFECTS OF SALICYLIC ACID APPLICATION ON WRKY GENE IN PEPPER (*CAPSICUM ANNUUM* L.) SEEDLING

Mohammed Ahmed Ahmed[1], Muhemet Zeki Karipcin[1,*], Fikret Yasar[2]

[1] Siirt University Faculty of Agriculture, Siirt, Turkey
[2] Van Yuzuncu Yıl University Faculty of Agriculture, Van, Turkey

ABSTRACT

This project was developed to investigate the contribution of salicylic acid to development of pepper seedlings grown in low temperature (0 ^{0}C) conditions. The research was carried out in the controlled plant growing cabinet in the research-investigation area of the Department of Horticulture, Faculty of Agriculture, Siirt University. As a vegetable material, Urartu F1 pepper type (capia) which is used in greenhouse cultivation has been used. As a dose of different salicylic acid; 0.01 and 0.05 mmol doses were applied. The dose of 0 mmol salicylic acid was used as control group. Application frequency; It was applied 1 time, 2 times and 3 times.

3 different cold application times were also investigated; 24 hours, 48 hours and 72 hours. The experiment was designed in randomized plots and 3 replications. In the pepper seedlings the effect of the seedlings on the WRKY genes were investigated. Considering the administration of both salicylic acids, it was found that 0.05 mmol dose had a clearer and more understanding response to the expression of WRKY gene.

KEYWORDS:
Low temperature, salicylic acid, pepper, WRKY genes.

INTRODUCTION

Low temperatures (LT) diminish the biosynthetic action of plants; LT bring out aggravation in essential capacities and productivity and may dispense lasting wounds that at long last achieve death. The survival limit of a plant species or variety in a particular environment is determined by as far as possible to which its metabolic procedures keep on working under low-temperature stress and by its cold resistance, the two of which are attributes of its ecophysiological constitution [1]. Low-temperatures to promote the accumulation of endogenous free Salicylic acid (SA) in grape berry and wheat [2-3-4]. In winter wheat leaves grown at low temperatures, when sprayed with salicylic acid, the influence of external factors decreased and also the decreased freezing injury [5]. Improves the cold resistance of the plants of tomatoes and beans, when soaked their seeds in the solution of aspirin or SA solution at a concentration of 0.1–0.5 mM before agriculture [6]. Chilling damage in freshly harvested green bell pepper (*Capsicum annuum* L.) was reduced by SA and methyl [7] increase in response to low-temperature pressure in rice to express alternative oxidase (AOX) [8]. The treatment of salicylic acid is effective in relieving damage to the cooling, which is one of the most serious post-harvest losses in peach fruit. Curiously, the combination of ultrasonic and ultrasound treatment greatly inhibited the chilling injury of peach fruits compared to SA treatment alone [9]. The utilization of low centralizations of SA to tomato fruits products reduced the chilling damage and the occurrence of rot amid low-temperature stockpiling [10]. But high concentrations of salicylic acid may cause cell death or exposure to abiotic stresses, in general, may lead low concentrations of salicylic acid may enhance antioxidant capacity in plants [11]. SA was seen to lessen leaf zone (optional leaf), root development, and in addition protein and chlorophyll (a+b) sum parallel to an expansion in its focus in grain plants which were produced from grain seeds sprouted in SA arrangements of fluctuating fixations and developed in SA-containing milieu [12]. Ecological anxiety adversely influences the elements of the plasma layer which can be measured as the level of lipid peroxidation. The measure of malondialdehyde (MDA) mirrors the level of lipid peroxidation. Concentrate on the impact of SA in connection to oxidative anxiety demonstrates that the level of MDA in leaves stayed unaltered [13], diminished [14] in a relationship with poisonous worry in connection to different SA focuses. The situation being what it is, the target of the present investigation is to inspect the physiological and some biochemical impacts of low and high centralizations of salicylic corrosive which manufactures protection against biotic and abiotic worry in plants, on pepper seedlings without some different anxiety factor. To reduce the tolerability of plants for salinity the external application of SA was used extensively [15]. To increase the state of abiotic stress,

SA interferes with various physiological responses such as lipid oxidation-reduction, oxidative system regulation, ion prohibiting, osmotic adjustments and kinases synthesis [16]. SA is one of the substances similar to hormone and its role is important in the direction the physiological process like ion uptake and transport, stress tolerance as well as membrane permeability and photosynthesis [17]. The treatment of gloxinia with a concentration of 20 mg/L of SA resulted in a significant increase in the pepper area, while the concentration of 10 mg /L increased the number of leaves, the spraying of plants Jaafari (*Tagetes erecta*), by SA led to a moral increase in the soft and dry walnut and roots length [18]. SA is a natural phenolic and is widely available in the plant kingdom. It is characterized as an internal growth organization. It is proven that it regulates many physiological processes of the plant under stress conditions such as photosynthesis, breathing, nutrient absorption, opening and closing of holes, and improves plant tolerance for salinity by increasing non-enzymatic antioxidants such as superoxide enzyme dismutase, catalase enzyme, and peroxidase enzyme [19]. It has attracted the attention of researchers in the past few years, the active role for plant growth hormone salicylic acid in improving plant tolerance for environmental stresses and different biological stresses through its effect on the internal content of the plant from plant hormones [20]. The treatment of plants with salicylic acid is one of the projects and solutions to reduce the impact of the drought phenomenon of drought and semi-drought areas in the world to increase plant resistance to dry stress conditions [21]. Scientific research has indicated that spraying plants with low concentrations of salicylic acid it can stimulate endure of vital and abiotic stresses such as cold and drought tolerance high temperature and resistance to fungal, bacterial and viral diseases [22].

Pepper (*Capsicum annuum* L.) an individual from the *Solanaceae* family, is an imperative harvest, its organic products being the second overall consumable vegetables and phenomenal wellsprings of numerous fundamental supplements for people, particularly vitamin C, Magnesium, β-carotene, Iron, potassium, vitamin B and calcium. Moreover, some pepper cultivars contain huge amounts of capsaicinoids, a gathering of sharp phenolic-determined mixes with solid physiological and pharmacological properties [23]. Sweet pepper (*Capsicum annuum*, L) is known as a most loved and broad vegetable yield over the world, its fruit wealthy in cancer prevention agents, vitamins, and minerals for human eating routine and sound [24]. Along these lines, the developing worldwide request of pepper natural products suggests a few methodologies to expand edit generation and organic product quality through particular horticultural treatment hones [25] or elevating the examination to enhance the plant protection from ecological burdens.

Plants have various active defense mechanisms to protect themselves from biotic and abiotic stresses. The common feature of plant defense properties is the transcriptional activation of a number of genes on treatment with biotic and abiotic markers. [26-27]. It has been found that WRKY's members is involved in the defense of various stress situations, aging, embryoogenesis, trichome development with seed coat, arrangement of biosynthetic functions and regulation of different physiological processes specific to plants such as hormone signals [28-29]. WRKY genes are also involved in defense against pathogens such as fungi, bacteria and viruses [30-31]. These responses to pathogen attack require large-scale transcriptional repetition and new programming. The transcription factor, such as the WRKY genes, requires teams [32-33]. A large number of WRKY proteins have been identified in responses to pathogen attack or stress conditions and plant internal hormone signaling [34-35]. Due to their involvement in transcriptional programming during plant immune responses, the WRKY family is one of the most influential trans active elements in the last decade [36]. Recent findings suggest that WRKY genes have a role in the signal path between jasmonic asid and salicylic asid [36]. WRKY transcription factors are encoded by multiple genes, for example Arabidopsis has at least 72 and 100 members [37] also rice (*Oryza sativa*) [38]. WRKY proteins probably have regulatory functions in plant defense responses to pathogen infection; pathogen infection or improvement with SA has been shown to induce rapid identification of WRKY genes [39-40-41-42-43-44]. WRKY proteins show that they play an important role in the differential regulation of their genes during the activation of plant defense initiatives.

The experiment was designed to study the effect of different concentrations of salicylic acid on resistance to low temperature. The aim of this study to find out the answer to these questions;

- To determine whether the negative effects of low temperatures on pepper plants are eliminated with salicylic acid.
- Determination of the possibilities of growing hot peppers in low temperature vegetables.
- Determination of the most suitable salicylic acid doses.
- To observe the effects of salicylic acid applications on different low temperature periods.

Application of salicylic acid in pepper seedlings and studying the effects of pepper seedlings on gene expression constitute the specificity of this study.

TABLE 1
The features of Urartu F1

Variety	Fruit Weight	Growing Season	Period of Maturity	Disease Resistance HR
Urartu F1	100-120gr	Winter in green-house	Late	Tm0 (TMV, ToMV, PMMoV)

FIGURE 1
Putting the pepper seedlings on the cooling device (Refrigerator).

MATERIALS AND METHODS

Plant Materials. In this experiment, pepper (*Capsicum annuum*) was used as plant material. Urartu F1 pepper variety which could be grown in the greenhouse was used as pepper variety. Pepper is grown at large area and needs a high temperature for flowering and fertilization. Urartu F1 has capita form and is grown in greenhouse in the winter. Capita peppers are rich in ascorbic acid and carotene. Grill it or just eat it raw. The Capita pepper is a delicacy of different southern cousins the features of Urartu F1 is given (Table 1).

A plant growing cabinet was used for growing seedlings (Figure 1) the seeds were sown which (month) ago from low-temperature applications. For seedling a shaded seedling, the tunnel was used.

The Chemicals Materials. Salicylic acid was used as the chemical material for the resistance of pepper seedlings to low temperature (Figure 2). Polysorbate 20 is a hydrophilic nonionic surfactant generally used as emulsifiers, dispersing agent and solubilizer [45].

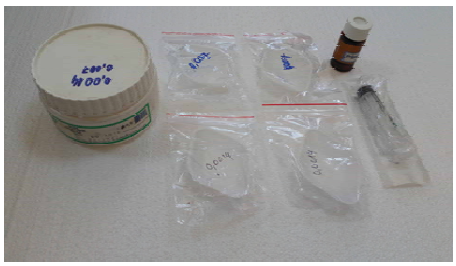

FIGURE 2
The chemicals materials

Methods. Salicylic Acid Application and Applications' Frequencies;Three different treatments 0.01 mmol, 0.05 mmol, and 0 mmol salicylic acid applicated. Salicylic acid was 1, 2 and 3 times applicated for each dose. For control groups only distilled water was applicated each time. Polysorbate (Twin 20) was also used very very small quantity for adhesive. With small needles, very thin holes were opened in the leaves, making salicylic acid penetration easier (Figure 3.).

FIGURE 3
Opening holes on leaves.

Temperature and Temperature Durations. 0 ^{0}C was the application temperature for the seedlings to find out the effect of salicylic acid at low temperature. All seedlings were exposed to the cold application for 24, 48 and 72 hours. The temperature was measured with a maximum/minimum thermometer (Figure 4.).

FIGURE 4
Maximum/minimum thermometer.

Measurement of Gene Expression Level in Salicylic Acid Treated Tissues. RNA isolation will be carried out by taking samples of pepper seedlings which have been applied with salicylic acid. cDNA synthesis from isolated total RNA will be performed. The following q-RT PCR steps will be followed to measure the level of the WRKY gene:

Analysis of Gene Expression in Salicylic Acid-Treated Tissues with qRT-PCR. After converting Total RNA into cDNA, the expression level of the WRKY gene, which is thought to be different between the leaf tissues of the pepper seedlings which salicylic acid was applied, was demonstrated by q-RT-PCR. Primary3 program was used for primers belonging to WRKY gene. For the analysis of the data, the 'threshold Pf (Ct) value was taken and the Pfaffl's model was used. Thermo piko-real device and SYBR Green I Master Mix kit (Roche kat. No: 04707516001) were used. qRT-PCR experiments were performed in three replicates. At first, the amount of RNA in each sample was normalized using 18S rRNA primers (X16077.1). Sequences of these primers were 18S rRNA İleri 5'-TTTGACTCAACACGGGGAAA-3'and 18S rRNA Geri 5'-CAGACAA ATCGCTCCACCAA-3. 18 µl was distributed to each of the wells determined according to the experimental plan from the prepared mixture. 'Plate' was covered with special bonding gelatin and placed on the q-RT-PCR. The results of q-RT-PCR were analyzed by 2 - 2Ct method.

Experimental Design. The experimental design used was a Randomized Complete Parcel Design (RCPD) with factorial. The treatment in each experiment had three replicates. Where was statistically analyze the data and compared means using "LSD"s Multiple Range Test at 0.05 and 0.01 levels.

RESULTS AND DISCUSSIONS

Salicylic acid (SA) is an intrinsic plant growth regulator that constitutes the corresponding response in many growth-development pathways in plants and thus affects plant growth and development [46]. Graphic 1 and Graphic 2 show how the changes in the gene level depend on the time of cold stress in salicylic acid applied pepper genotypes. As shown in Graphic 1, leaf samples were taken after 24, 48 and 72 hours to measure the expression level of WRKY gene.

As a result of the analysis, it was found that the expression level of WRKY gene increased with the application of salicylic acid. This increase was highest in the first 24 hours exposed to cold stress, while gene expression decreased gradually in 48 and 72 hours (Graphic 1 and 2). In many more studies, the expression of WRKY gene was found to be increased in the presence of salicylic acid. For example, in a study conducted on Arabidopsis, Of the 72 Arabidopsis WRKY genes, 49 were found to be regulated differently after treatment with a bacterial pathogen or avirulent strain of SA [47]. WRKY proteins are a group of transcription factors that appear as a gene superfamily in plants and play important roles in the regulation of defense response pathways in plants. WRKY proteins also play a role in other plant-specific functions such as trichome development and biosynthesis of secondary metabolites [48].

As shown in (Graphic 1 and 2) leaf samples were taken after 24, 48 and 72 hours to measure the expression level of the WRKY gene.

As a result of the analysis, it was found that the expression level of WRKY gene increased with the application of salicylic acid.

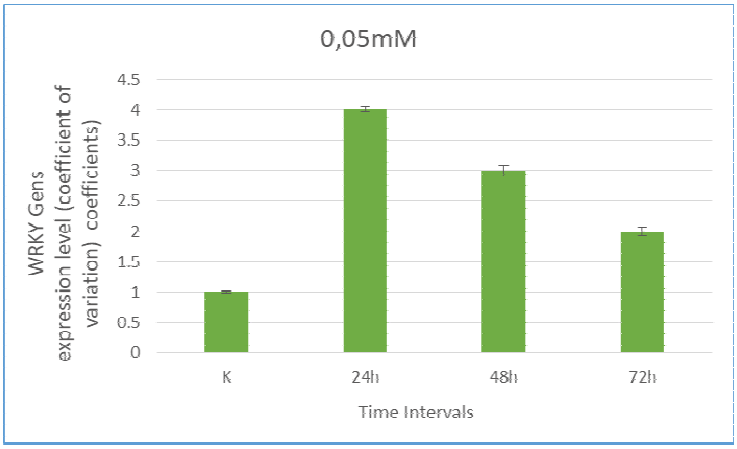

GRAPHIC 1
Determination of the level of expression of WRKY gene in real-time polymerase chain reaction (PCR) at 0.05 mmol salicylic pepper.

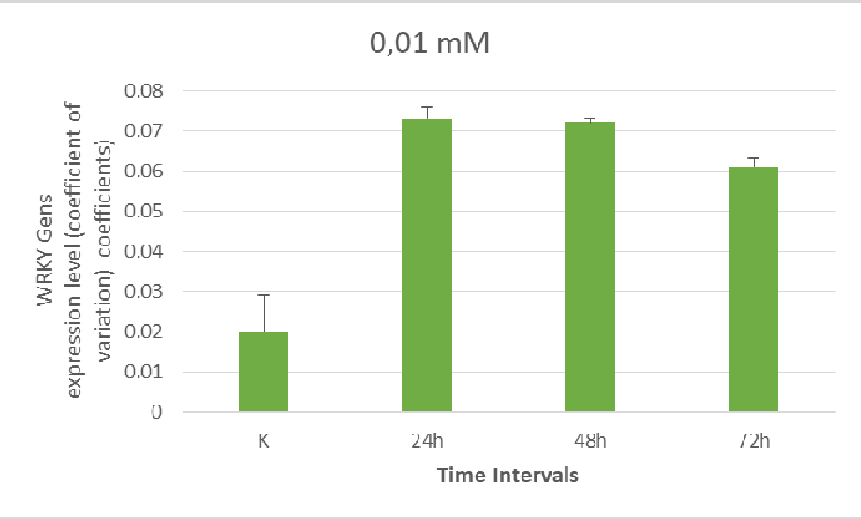

GRAPHIC 2
Determination of the level of expression of WRKY gene in real-time (PCR) at 0.01 mmol salicylic pepper.

This increase was highest for the first 24 hours exposed to cold stress, while gene expression was gradually decreased at 48 and 72 hours, but this decrease was not very sharp compared to 0.05 mmol application. Determined expression level of WRKY genes is close to each other. Considering the administration of both salicylic acids, it was found that the pepper plant has a clearer and more understanding response to the expression of WRKY gene in the application of 0.05 mmol SA (Graphic 1).

In Arabidopsis, the onset of Systemic acquired resistance (SAR) is initiated by the accumulation of the signal molecule, salicylic acid.

Salicylic acid promotes nuclear translocation of transcription cofactor regulatory protein NPR1 (Non-expressıon of pathogenesıs-related genes1) to activate most genes needed for disease resistance [49-50]. The expression of regulatory protein NPR1 has been shown to be under the regulation of WRKY transcription factors [51]. In another study, the WRKY59 gene was identified to be the direct target of SA-dependent defense and NPR1 [49]. WRKY59 also plays an important role in sustainable defense [32]. WRKY proteins, a group of DNA binding transcription factors, are involved in a number of plant processes, including in plant responses to biotic and abiotic stresses [52]. Infections involving many pathogens in viruses [51-53], bacteria [52] and coomycetes [54] are known to induce many WRKY genes.

CONCLUSIONS

Furthermore, when the application of 0.01 mmol and 0.05 mmol SA was evaluated for the expression of the WRKY gene of the pepper plant, it was found that the application of 0.05 mmol SA yielded very clear and observable results.

Vegetables grown in seasons without sufficient temperature values are expected to be low temperature resistant or tolerant, and both tolerant and resistant to the use of regulators that run WRKY proteins such as salicylic acid appear to be the right way to produce products naturally. According to this study, we may recommolend the use of 0.05 mmol salicylic acid.

Compliance with Ethical Standards. This study was funded by Siirt University Scientific Research Projects Council (Project number: SİÜBAP-2018 SİÜFEB-21)

Conflict of Interest . The authors declare that they have no conflict of interest.

ACKNOWLEDGEMENTS

The authors would like to thank Siirt University Scientific Research Projects (Project number: SİÜBAP-2018 SİÜFEB-21) Council.

REFERENCES

[1] Larcher, W. (1968). Die Temperaturresistenz also Konstitutionsmerkmal der Pflanzen. Dtsch Akad Landwirtschaftswiss, Tagungsbericht. 100, 7–21

[2] Scott, I.M., Clarke, S.M., Wood, J.E., Mur, L.A. (2004). Salicylate accumulation inhibits growth at chilling temperature in Arabidopsis. Plant Physiology. 135 (2), 1040-1049

[3] Wan, S.B., Tian, L., Tian, R.R., Zhan, Q.H. (2009). Involvement of phospholipase D in the low-temperature acclimation-induced thermotolerance in grape berry. Plant Physiology and Biochemistry. 47(6), 504-510

[4] Kosova, K., Prasil, I.T., Vitamvas, P., Dobrev, P., Motyka, V., Flokova, K. (2012). Complex phytohormone responses during the cold acclimation of two wheat cultivars differing in cold tolerance, winter Samanta, and spring Sandra. Journal of Plant Physiology. 169 (6), 567-576

[5] Taşgin, E., Atící, Ö. Nalbantoğlu, B. (2003). Effects of salicylic acid and cold on freezing tolerance in winter wheat leaves. Plant Growth Regulation. 41(3), 231-236

[6] Senaratna, T., Touchell, D., Bunn, E., Dixon, K. (2000). Acetyl salicylic acid (aspirin) and salicylic acid induce multiple stress tolerance in bean and tomato plants. Plant Growth Regulation. 30, 157–161

[7] Fung, R.W., Wang, C.Y., Smith, D.L., Gross, K.C., Tian, M. (2004). MeSA and MeJA increase steady-state transcript levels of alternative oxidase and resistance against chilling injury in sweet peppers (Capsicum annuum L.). Plant Science. 166 (3), 711-719

[8] Ito, Y., Saisho, D., Nakazono, M., Tsutsumi, N., Hirai, A. (1997). Transcript levels of tandem-arranged alternative oxidase genes in rice are increased by low temperature. Gene. 203, 121-129

[9] Yang, Z., Cao, S., Zheng, Y., Jiang, Y. (2012). Combined salicyclic acid and ultrasound treatments for reducing the chilling injury on peach fruit. Journal of agricultural and food chemistry. 60 (5), 1209-1212

[10] Ding, C.K., Wang, C.Y., Gross, K.C., Smith, D.L. (2002). Jasmonate and salicylate induce the expression of pathogenesis-related-protein genes and increase resistance to chilling injury in tomato fruit. Planta. 214, 895–901

[11] Hara, M., Furukawa, J., Sato, A., Mizoguchi, T., Miura, K. (2012). Abiotic stress and role of salicylic acid in plants. In Abiotic Stress Responses in Plants, Eds A. Parviz and M. N. V. Prasad (New York, NY: Springer). 235–251

[12] Ananieva, E.A., Alexieva, V.S., Popova, L.P. (2002). Treatment with salicylic acid decreases the effects of paraquat on photosynthesis. Journal of Plant Physiology. 159, 685-693

[13] Gautam, S., and Singh, P.K. (2009). Salicylic acid-induced salinity tolerance in corn grown under NaCl stress. Acta Physiological Plant. 31, 1185-1190

[14] Krantev, A., Yordanova, R., Janda, T., Szalai, G., Popova, L. (2008). Treatment with salicylic acid decreases the effect of cadmium on photosynthesis in maize plants. Journal of Plant Physiology. 165 (9), 920-931

[15] Jayakannan, M., Bose, J., Babourina, O., Rengel, Z. Shabala, S. (2015). Salicylic acid in plant salinity stress signalling and tolerance. Plant Growth Regulation. 76 (1), 25-40

[16] Jayakannan, M., Bose, J., Babourina, O., Rengel, Z., Shabala, S. (2013). Salicylic acid improves salinity tolerance in Arabidopsis by restoring membrane potential and preventing salt-induced K+ loss via a GORK channel. Journal of Experimental Botany. 64 (8), 2255-2268

[17] Noreen, S., Ashraf, M., Hussain, M., Jamil, A. (2009). Exogenous application of salicylic acid enhances antioxidative capacity in salt stressed sunflower (Helianthus annuus L.) plants. Pakistan Journal of Botany. 41 (1), 473-479

[18] Jabbar, A.K.A., Saeed, M. (2017). Effect of the date of the developing summolit earring and paper spraying of salicylic acid in the growth and flowering of the Jaafari plant Tagetes erecta L. Double Eagle. Technical Journal. 30 (3), A21-A31

[19] Tufail, A., Arfan, M., Gurmani, A.R., Khan, A.B., Bano, A. (2013). Salicylic acid-induced salinity tolerance in maize (Zea mays). Pakistan Journal of Botany. 45 (1), 75-82

[20] Naji, D.B. (2013). Evaluation of some citrus assets to tolerate salinity outside the living body. Master Thesis. Faculty of Agriculture Kufa. The Republic of Iraq.

[21] Aldesuquy, H.S., Baka, Z.A., Abbas, M.A., Alazab, N.T. (2014). Faba bean can adapt to chocolate spot disease by pretreatment with shikimic and salicylic acids through osmotic adjustment, solutes allocation and leaf turgidity. Journal of Stress Physiology and Biochemistry. 10 (1), 230-243

[22] Al-Hamdani, S.A., Al-Obeidi, Z.H., Al-Bayati, Y.Y. (2017). The effect of shading and spraying salicylic acid in 2-hoids tomato recipes by using verticai way of training method. Diyala Agricultural Sciences Journal. 9 (2), 222-230

[23] Topuz, A., and Ozdemir, F. (2007). Assessment of carotenoids, capsaicinoids and ascorbic acid composition of some selected pepper cultivars grown in Turkey. Journal of Food Composition and Analysis. 20, 596–602

[24] Mateos, R. M. (2006). Pepper Antioxidants: Biochemical and Molecular Study of the Fruit Ripening and the Response to Abiotic Stress. Ph.D. Thesis, University of Granada, Spain, ISBN 84-338-3868-7

[25] Pascual, I., Azcona, I., Aguirreolea, J., Morales, F., Corpas, F. J., Palma, J. M. (2010). Growth, yield, and fruit quality of pepper plants amended with two sanitized sewage sludges. Journal of Agricultural and Food Chemistry. 58(11), 6951-6959

[26] Yang, Y., Qi, M., Mei, C. (2004). By aging as well as biotic and abiotic stress. The Plant Journal. 40 (6), 909-919
[27] Rushton, P.J., & Somssich, I.E. (1998). Transcriptional control of plant genes responsive to pathogens. Current Opinion in Plant Biology.1(4), 311-315
[28] Rushton, P.J., Somssich, I.E., Ringler, P., Shen, Q.J. (2010). WRKY transcription factors. Trends in Plant Science. 15(5), 247-258
[29] Zhang, H., L. Ma, M. Turner, Xu, H., Zheng, X., Dong, Y., Jiang, S. (2004). Salicylic acid enhances the biocontrol efficacy of Rhodotorula glutinis against postharvest Rhizopus rot of strawberries and the possible mechanisms involved. Food Chemistry. 122 (3), 577-583
[30] Fan, X., Guo, Q., Xu, P., Gong, Y., Shu, H., Yang, Y., & Shen, X. (2015). Transcriptome-wide identification of salt-responsive members of the WRKY gene family in Gossypium aridum. PLoS One. 10(5), e0126148
[31] Park, S. W., Liu, P. P., Forouhar, F., Volt, A. C., Tong, L., Tietjen, K., Klessig, D. F. (2009). Use of a synthetic salicylic acid analog to investigate the roles of methyl salicylate and its esterases in plant disease resistance. Journal of Biological Chemistry
[32] Eulgem, T. (2005). Regulation of the Arabidopsis defense transcriptome. Trends in Plant Science. 10 (2), 71-78
[33] Naoumkina, M.A., He, X., Dixon, R.A. (2008). Elicitor-induced transcription factors for metabolic reprogramming of secondary metabolism in Medicago truncatula. BMC Plant Biology. 8(1), 132
[34] Li, W. Godzik, A. (2006). Cd-hit: a fast program for clustering and comparing large sets of protein or nucleotide sequences. Bioinformatics. 22(13), 1658-1659
[35] Marchive, C., Léon, C., Kappel, C., Coutos-Thévenot, P., Corio-Costet, M. F., Delrot, S., Lauvergeat, V. (2013). Over-expression of VvWRKY1 in grapevines induces expression of jasmonic acid pathway-related genes and confers higher tolerance to the downy mildew. PLoS One. 8(1), e54185
[36] Miao, Y. and Zentgraf, U. (2010). A HECT E3 ubiquitin ligase negatively regulates Arabidopsis leaf senescence through degradation of the transcription factor WRKY53. The Plant Journal. 63(2), 179-188
[37] Dong, J., Chen, C., Chen, Z. (2003). Expression profiles of the Arabidopsis WRKY gene superfamily during plant defense response. Plant Mol Biological. 51,21–37
[38] Wu, K.L., Guo, Z.J., Wang, H.H., Li, J. (2005). The WRKY family of transcription factors in rice and Arabidopsis and their origins. DNA Research. 12(1), 9-26
[39] Rushton, D.L., Tripathi, P., Rabara, R.C., Lin, J., Ringler, P., Boken, A. K., Langum T. J., Smidt, L., Boomsma D. D., Emme, N. J., Chen, X., Finer J. J., Shen, Q. J., Rushton P. J. (2012). WRKY transcription factors: key components in abscisic acid signalling. Plant Biotechnology Journal. 10(1), 2-11
[40] Eulgem, T. and Somssich, I.E. (2007). Networks of WRKY transcription factors in defense signaling. Current Opinion in Plant Biology. 10(4), 366-371
[41] Yu, D., Chen, C., Chen, Z. (2001). Evidence for an important role of WRKY DNA binding proteins in the regulation of NPR1 gene expression. The Plant Cell. 13(7), 1527-1540
[42] Dellagi, A., Heilbronn, J., Avrova, A. O., Montesano, M., Palva, E. T., Stewart, H. E., Toth, I. K., Cooke, D. E., Lyon, G. D., Birch, P. R. (2000). A potato gene encoding a WRKY-like transcription factor is induced in interactions with Erwinia carotovora subsp. atroseptica and Phytophthora infestans and is coregulated with class I endochitinase expression. Molecular Plant-microbe Interactions. 13(10), 1092-1101
[43] Hara, M., Furukawa, J., Sato, A., Mizoguchi, T., and Miura, K. (2012). Abiotic stress and role of salicylic acid in plants. In Abiotic Stress Responses in Plants, Eds A. Parviz and M. N. V. Prasad (New York, NY: Springer). 235–251
[44] Lee, H.R., Kim, K.T., Kim, H.J., Han, J.H., Kim, J.H., Yeom, S.I., Kim, H. J., Kang, W. H., Park, S. W., Bae, I. H., Lee, S., Cho, J., Oh, D., Kim, B. D. (2011). QTL analysis of fruit length using rRAMP, WRKY, and AFLP markers in chili pepper. Horticulture, Environment and Biotechnology. 52(6), 602-613
[45] Zielinski, M., Burke, L.A., Samokhvalov, A. (2015). Selective activation of C= C bond in sustainable phenolic compounds from lignin via photooxidation: experiment and density functional theory calculations. Photochemistry and Photobiology. 91 (6), 1332-1339
[46] Hayat, Q., Hayat, S., Irfan, M., Ahmad, A. (2010). Effect of exogenous salicylic acid under changing environment: a review. Environmental and Experimental Botany. 68(1), 14-25
[47] Dong, J., Chen, C., Chen, Z. (2003). Expression profiles of the Arabidopsis WRKY gene superfamily during plant defense response. Plant Mol Biological. 51,21–37

[48] Ramiro, D., Jalloul, A., Petitot, A.S., De Sá, M.F.G., Maluf, M.P., Fernandez, D. (2010). Identification of coffee WRKY transcription factor genes and expression profiling in resistance responses to pathogens. Tree Genetics and Genomes. 6 (5), 767-781

[49] Wang, D., Amornsiripanitch, N., Dong, X. (2006). A genomic approach to identify regulatory nodes in the transcriptional network of systemic acquired resistance in plants. PLOS Pathogens. 2(11), e123.

[50] Kinkema, M., Fan, W., Dong, X. (2000). Nuclear localization of NPR_1 is required for activation of PR gene expression. The Plant Cell. 12 (12), 2339-2350

[51] Yu, T. and Zheng, X. D. (2006). Salicylic acid enhances the biocontrol efficacy of the antagonist Cryptococcus laurenti in apple fruit. Joutnal Plant Growth Regulation. 25, 166-174

[52] Eulgem, T., Rushton, P.J., Robatzek, S., Somssich, I.E. (2000). The WRKY superfamily of plant transcription factors. Trends in Plant Science. 5(5), 199-206

[53] Yang, Z., Cao, S., Zheng, Y., Jiang, Y. (2012). Combined salicyclic acid and ultrasound treatments for reducing the chilling injury on peach fruit. Journal of Agricultural and Food Chemistry. 60 (5), 1209-1212

[54] Dellagi, A., Heilbronn, J., Avrova, A. O., Montesano, M., Palva, E.T., Stewart, H.E., ... & Birch, P.R. (2000). A potato gene encoding a WRKY-like transcription factor is induced in interactions with Erwinia carotovora subsp. atroseptica and Phytophthora infestans and is coregulated with class I endochitinase expression. Molecular Plant-microbe Interactions. 13(10), 1092-1101

Received: **13.04.2019**
Accepted: **29.01.2020**

CORRESPONDING AUTHOR

Muhemet Zeki Karipcin
Siirt University
Agricultural Faculty
Department of Horticulture

e-mail: zkaripcin@siirt.edu.tr

© by PSP Volume 29 – No. 4A/2019 pages 3287-3299 Fresenius Environmental Bulletin

MODELING AND COMPUTER SIMULATION OF DRAINAGE, EVAPORATION, AND RUNOFF (DEAR) FROM BARE SOILS

Mehmet Aydin[1,*], Baran Aydin[2], Veysel Polat[3]

[1]Emeritus, Mustafa Kemal University, Department of Soil Science and Plant Nutrition, Antakya, Turkey.
[2]Adana Alparslan Turkes Science and Technology University, Department of Civil Engineering, Adana, Turkey.
[3]Cukurova University, Vocational School of Adana, Turkey.

ABSTRACT

An improved model and its computer program for Drainage, Evaporation and Runoff (DEaR) from bare soils are presented. The model, which is the successor of the model originally known as E-DiGOR, adequately represents the physical processes important in estimating actual soil evaporation, soil water storage, direct surface runoff, infiltrated rainfall, and subsurface flow. The model is useful for quantifying these components of soil water balance with a few parameters, and for the descriptions and predictions of the past, present and future dynamics if climate data are available. Although the physical credibility of the model is quite high, a consistent set of values suitable for the calculations is required. The input variables of the computer program are climate data (sunshine duration, air-temperature, relative humidity, wind speed, and precipitation) and environmental data/soil properties (albedo, psychrometric constant, latitude, fraction of radiation, height for resistance, tortuosity, average diffusivity for drying soil, volumetric water content at field capacity, air-dry water content, threshold potential, reset threshold, profile depth, initial water content of the profile, porosity, slope gradient, and ratio of saturated hydraulic conductivity to maximum rainfall intensity) to account for specific soil-climate combinations. The computer program developed is a useful tool for a fast and precise simulation, and consists of three modules. The computer program has been developed as a MATLAB™ application. The software can be obtained upon request.

KEYWORDS:
Computer program, drainage, E-DiGOR model, runoff, soil evaporation, soil-water storage

INTRODUCTION

Quantification of soil hydrological components is of major importance in the assessment of water balance especially under the bare-field conditions [1-4]. Instead of working with an in-situ measurement method, many researchers prefer using a simulation model for estimating the rates of the components. However, the models are structured based on simplifications of the real systems, although soil is a very complex environment [5]. For example, evaporation from a bare soil surface is a complex process and the link between the atmosphere and soil surface in the water cycle; and it is also a key issue in the hydrologic processes which are linked to water fluxes in the soil [6-8]. On the other hand, many models have been developed to represent the rainfall-runoff processes [9-14]. In surface runoff studies, data collection and process knowledge mostly originate from the plot scale [15-16], although models often operate at the catchment scale [17-18]. At the plot scale, surface runoff depends on the surface characteristics (gradient and soil properties), rainfall intensity and the antecedent soil water conditions [19]. The role of initial soil water content in runoff generation was emphasized by several authors [20-23].

Changes in the soil water content greatly deal with evaporation; however, the calculation of actual soil evaporation poses a serious challenge. Therefore, a model referred to as the Aydin equation was tested by Aydin et al. [24] in order to estimate the actual soil evaporation under different environmental conditions: A sandy soil column-experiment in a drying chamber and a study with the same sand medium in a greenhouse had been conducted at Arid Land Research Center, Tottori University (Japan) to test the performance of the model. Additionally, field experiments had been carried out on two clay soils in a semi-arid region of Turkey. It was concluded that the model was capable of estimating actual evaporation from bare soils as a function of matric potential measured at the 1 cm soil depth accurately. However, the objective measurements of soil water potential near the surface of the soil profile were difficult, especially for drier upper layer. In order to overcome of this difficulty, a simplified model for predicting soil water potential at the top surface layer had been described by Aydin and Uygur [25]. Later on, Aydin et al. [26] tested the combination of Aydin and Aydin-Uygur

models to predict quantitative changes in evaporation from soils in the Mediterranean climatic region of Turkey in response to the projections of a regional climate model developed in Japan. The authors concluded that the combined model had appeared useful in estimating actual evaporation from bare soils, with only a few parameters. Concurrently, a new model with the acronym E-DiGOR was developed by Aydin [27] to predict soil evaporation, drainage, and water storage based on the physical features. Daily potential evaporation from bare soils was calculated using the Penman–Monteith equation with a surface resistance of zero, and actual soil evaporation was computed with the Aydin equation. Deep drainage was simply calculated from the mass balance, taking field capacity into account. In order to assess the performance of the model mainly for drainage estimations, a micro-lysimeter experiment had been carried out under field conditions. The experimental terrain was nearly flat, with no appreciable slope. The experimental data had supported the model hypothesis, thus rendering the model useful in estimating soil evaporation, drainage and water storage in an interactive way. It was concluded that the next logical step in model improvement would be the inclusion of runoff module for sloping lands and development of a software giving rise to a versatile and functional implementation of the E-DiGOR model. The model had also been validated by Onder et al. [28], Kurt [29], and Aydin et al. [30, 31] under the conditions of different countries. Over the last decade, Aydin and Polat [32] supplied a computer program without the runoff module for the functional implementation of the model described above. That software had been developed as a Delphi application, written in Object Pascal including two sub-runs. With time, Aydin [33] devised a new model for predicting runoff losses and thus improved the E-DiGOR model, since soil evaporation, drainage, soil-water storage, and runoff are strongly interdependent. In addition, Aydin et al. [5] verified the last version of E-DiGOR model under the conditions of South Korea. More recently, Aydin et al. [34, 35] and Kapur et al. [36] have applied the E-DiGOR model as a complementary tool in their research. It is worthy to note that the model attracted special attention at global scale; for example, the first paper describing the equation of actual soil evaporation [Ecological Modelling 182 (1): 91-105, 2005] has been cited 88 times, so far.

The DEaR (Drainage, Evaporation and Runoff) model presented here is an improved version of the E-DiGOR with a new title which better reflects the signs of the computed variables. Although the model can be used successfully, the volume of involved calculations is considerably high. The goal of developing this computer program is therefore to ensure a functional implementation of the DEaR model and to accurately and easily calculate the hydrological components of bare soils.

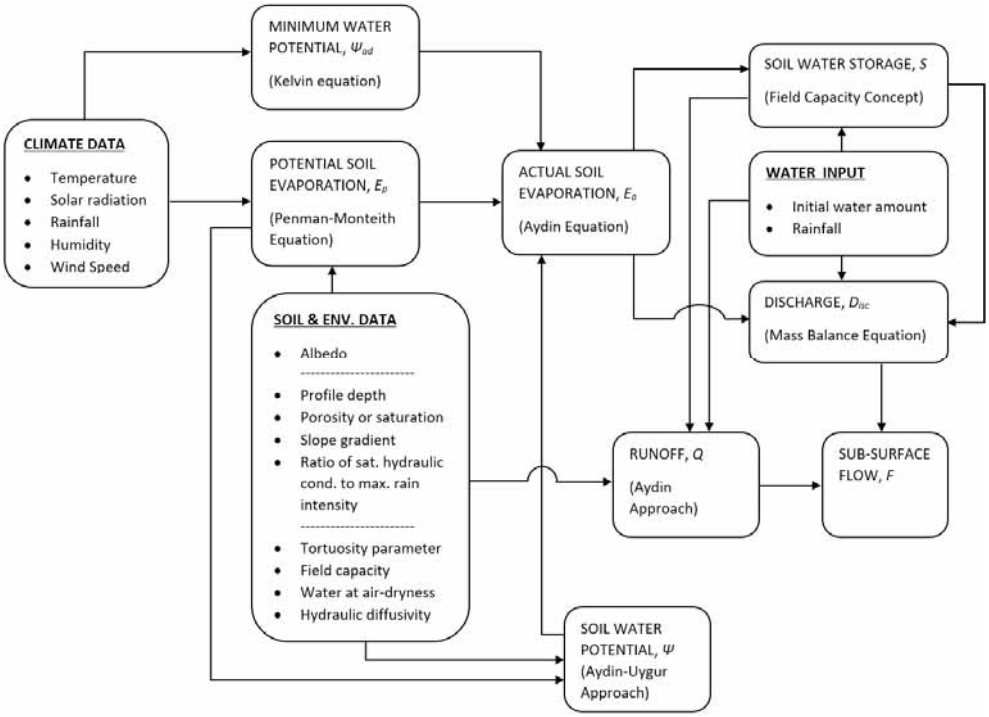

FIGURE 1
Schematic definition of DEaR model (altered from Aydin [27]).

MATERIALS AND METHODS

Theory of the Model. The theory of the processes simulated by DEaR software was extensively described by Aydin [27, 33] and Aydin et al. [5]. For completeness of the present study, the main mathematical expressions of the model are revisited and rearranged here. A relational diagram of the processes considered is illustrated in Figure 1.

Net radiation is an important variable in modeling studies of land-surface processes and soil water balance. For general purposes, net radiation is computed as the sum of net short wave radiation and net long wave radiation [37, 38]. When sunshine data are available, net radiation can be expressed as [37]:

$$R_n = (1-\beta)(a+b\frac{n}{N})R_a - 2.25\times10^{-9}(0.9\frac{n}{N}+0.1)(0.34-0.14\sqrt{e_d})(T^4_{kx}+T^4_{kn}) \quad (1)$$

where R_n is net radiation (MJ m^{-2} day^{-1}), β is albedo or reflection coefficient of the surface ($\beta \cong 0.15$ for bare soils), a is fraction of extraterrestrial radiation on overcast days and changes between 0.18 and 0.25, b is coefficient of relative sunshine and changes between 0.50 and 55 for an average climate, ($a+b$) is thus fraction of radiation on clear days (≈ 0.75), n is bright sunshine hours per day, N is total day-length (hours), R_a is extraterrestrial radiation (MJ m^{-2} day^{-1}), e_d is actual vapor pressure (kPa), T_{kx} is maximum daily air temperature (K), and T_{kn} is minimum daily air temperature (K). Similarly, net radiation is commonly predicted from incoming solar radiation (R_s) when solar radiation is measured in the meteorological stations with various radiometers and pyranometers (for further calculations, please see [37]).

On the other hand, soil heat flux density can be estimated using a heat balance of the soil profile. For daily temperature fluctuations (effective soil depth 0.18 m), the equation is [37]:

$$G_s = 0.38(T^{(j)} - T^{(j-1)}) \quad (2)$$

here G_s is soil heat flux (MJ m^{-2} day^{-1}), $T^{(j)}$ is mean daily air temperature (ºC) on day j, $T^{(j-1)}$ is mean daily air temperature (ºC) of the preceding day.

Potential soil evaporation is commonly computed using the classic Penman-Monteith equation, with a surface resistance of zero [24, 37, 39], although the model requires a large number of climatic parameters [40]. The Penman-Monteith equation can be simplified to estimate the potential evaporation from a bare soil surface for a 24-hour time step by assuming a standardized height for wind-speed, temperature, and humidity measurements at 2.0 m [34, 35]:

$$E_p = \frac{\Delta(R_n - G_s) + 0.1248\rho c_p u_2 e_s (1-\frac{H}{100})}{\lambda(\Delta+\gamma)} \quad (3)$$

where E_p is the potential soil evaporation (mm day^{-1}), Δ is the slope of saturated vapor pressure-temperature curve (kPaºC^{-1}), R_n is the net radiation (MJ m^{-2} day^{-1}), G_s is the soil heat flux (MJ m^{-2} day^{-1}), ρ is the air density (kg m^{-3}), c_p is the specific heat of air (kJ kg^{-1}ºC^{-1}=1.013), u_2 is the wind-speed (m s^{-1}) at 2.0 m height, e_s is the saturation vapor pressure (kPa), H is relative humidity (%), λ is the latent heat of vaporization (MJ kg^{-1}), γ is the psychrometric constant (kPaºC^{-1}).

Then, the actual soil evaporation can be calculated by the Aydin equation [24, 41]:

$$E_a = \frac{Log|\psi| - Log|\psi_{ad}|}{Log|\psi_{tp}| - Log|\psi_{ad}|}E_p \quad (4)$$

If $|\psi| \le |\psi_{tp}|$ then $E_a = E_p$ or $E_a/E_p = 1$

For $|\psi| \ge |\psi_{ad}|$, $E_a = 0$.

Remember that $E_p \ge 0$.

where E_a and E_p are actual and potential evaporation rates (mm day^{-1}), respectively; $|\psi_{tp}|$ is the absolute value of soil water potential (matric potential) at which actual evaporation starts to drop below potential one (cm of water), $|\psi_{ad}|$ is the absolute value of soil water potential at air-dryness (cm), and $|\psi|$ is the absolute value of soil water potential at the surface layer (cm).

Although the Aydin equation appeared to be useful, the objective measurement of soil water potential near the surface of the profile was difficult, especially at drier upper layer. In order to overcome this difficulty, the following equation can be used for estimating the soil water potential at the top surface layer [26]:

$$\psi = -\left[\frac{(1/\alpha)(10\sum E_p)^3}{2(\theta_{fc}-\theta_{ad})(D_{av}t/\pi)^{1/2}}\right] \quad (5)$$

where ψ is soil water potential (cm of water) at the top surface layer, α is a soil specific parameter (cm) related to flow path tortuosity in the soil, ΣE_p is cumulative potential soil evaporation (cm), θ_{fc} and θ_{ad} are volumetric water content (cm^3 cm^{-3}) at field capacity and air-dryness, respectively, D_{av} is average hydraulic diffusivity (cm^2 day^{-1}) deter-

mined experimentally, t is time (day) and π is 3.1416.

In very dry range (in which the flow is entirely vapor), either resistance models or a Fickian equation should be used [42] to estimate water transport through the slow process of moisture diffusion. Minimum water potential at a dry soil surface can be derived from the Kelvin equation [24, 27, 43]:

$$\psi_{ad} = \frac{R_g T}{mg} \ln H_r \quad (6)$$

where ψ_{ad} is the water potential for air-dry conditions (cm of water), T is the absolute temperature (K), g is the acceleration due to gravity (981 cm s^{-2}), m is the molecular weight of water (0.01802 kg mol^{-1}), H_r is the relative humidity of the air (fraction), and R_g is the universal gas constant (8.3143x10^4 kg cm^2 s^{-2} mol^{-1} K^{-1}).

In practice, soil water storage between the soil surface (0) and a given depth (z) is calculated by integrating water content of individual soil layers:

$$S = \int_0^z \theta dz \quad (7)$$

where S is soil water storage with dimension of length (mm) allowing to compare it with precipitation or evaporation and to facilitate the calculations, θ is volumetric water content (cm^3 cm^{-3}) of the individual soil layers, and z is the depth of soil zone (mm) considered [27]. Similar definitions hold for initial water amount ($\int_0^z \theta_i dz$). Remember that $S \le \theta_{fc} Z$. Here, Z is profile depth considered and θ_{fc} is average-volumetric water content at field capacity.

Drainage term used by Aydin [27] for nearly level soils has been adopted as discharge for sloping land when soil water content exceeds the field capacity. Discharge is simply calculated by the mass balance. The cumulative discharge until the day j can be expressed as follows:

$$\left[\sum Disc\right]^{(j)} = \int_0^z \theta_i dz + \left[\sum P\right]^{(j)} - \left[\sum E_a\right]^{(j)} - S^{(j)} \quad (8)$$

where ΣD_{isc} is cumulative discharge (mm) including runoff and subsurface flow out of the storage depth from the first day of simulation period, ΣP is cumulative rainfall (mm), and ΣE_a is cumulative actual soil evaporation (mm). Thus, from the differences between the consecutive days, discharge rates (D_{isc}, having units mm day^{-1}) can be easily calculated, if any:

$$Disc^{(j)} = \left[\sum Disc\right]^{(j)} - \left[\sum Disc\right]^{(j-1)} \quad (9)$$

A new approach which requires rainfall depth-intensity, slope steepness, soil water deficit and saturated hydraulic conductivity data, is used for estimating runoff (surface flow) from bare soils [33]:

$$Q = P \times \{1/2 \times [\log\sqrt{S_p} + \exp(-D_s / P)]\}^{(Ks/\mathrm{Im})} \quad (10)$$

where Q is the direct surface runoff [44] or rainfall excess in dimension length (mm or mm day^{-1}) allowing to facilitate comparisons among precipitation, percolation, storage and evaporation; P is rainfall (mm), S_p is slope steepness (%), K_s is saturated hydraulic conductivity (mm h^{-1}), I_m is maximum intensity of rainfall (mm h^{-1}) and D_s is deficit of saturation (mm) which means saturated water amount minus the antecedent water amount. If $Q > Disc$, then $Q = Disc$.

Infiltrated rainfall represents rain-water uptake by soil [45]. A simplified approach is implemented to derive the portion of rainfall infiltrating (U, having units mm) into soil [5]:

$$U = P - Q \quad (11)$$

On rainy days, the subsurface flow rates (F, having units mm day^{-1}) including vertical movement (percolation) and lateral flow (interflow) through the profile can be simply accounted [5], if any, as:

$$F = Disc - Q \quad (12)$$

Description of the DEaR Software. The computer program has been developed as a MATLAB™ (R2019a) application, which is a registered trademark of Mathworks Inc., on a 64-bit Windows® 10 professional-platform. The minimum system requirements for MATLAB™ are at least 2.6 GB of hard disk drive and a 4 GB RAM.

The input variables of the computer program are climate data (sunshine duration, air-temperature, relative humidity, wind speed, and precipitation) and environmental data/soil properties (albedo, psychrometric constant, latitude, fraction of radiation, height for resistance, tortuosity, average diffusivity for drying soil, volumetric water content at field capacity, air-dry water content, threshold potential, reset threshold, profile depth, initial water content of the profile, porosity, slope gradient, and the ratio of saturated hydraulic conductivity to maximum rainfall intensity). The input data are prepared in the form of two excel files (Tables 1 and 2, and Figure 2).

The MATLAB™ program consists of three modules. The first module calculates net radiation (R_n), soil heat flux (G_s), and potential soil evaporation (E_p) (Figure 3a). The second module computes actual soil evaporation (E_a), soil water storage (S), and discharge (D_{isc}) which is the sum of runoff and subsurface flow (Figure 3b), while the third module calculates runoff (Q), infiltrated rainfall (U), and subsurface flow (F) as the sum of percolation and interflow through the soil profile (Figure 3c). The outputs of each module can be saved in the excel format separately or all together (Figure 4, Table 3).

TABLE 1
An example of the excel-input file for Soil & Env Data

Albedo	Psychrometer constant	Latitude	Fraction of extraterrestrial radiation	Coefficient of relative sunshine	Height for resistance	Tortuosity	Field Capacity	Air-dry water	Diffusivity	Threshold Potential	Profile depth	Initial water: $Zx\theta_i$	Reset Threshold	Porosity	Slope	K_s/I_m
β	γ	ϕ	a	b	h_c (m)	α	θ_{fc} (v/v)	θ_{ad} (v/v)	(cm^2/day)	ψ_{tp} (cm)	(mm)	(mm)	-	(v/v)	(%)	-
0.150	0.067 0	36.590	0.180	0.550	0.0010	1.10	0.310	0.050	95 0	-60 0	900 0	275 0	0.10	0.520	9 0	1.00

TABLE 2
An example of the excel-input file for Climate Data

Date dd.mm.yyyy	DoY J	Actual Sunshine (hours)	Air temperature ($^{\circ}$C)	Relative humidity (%)	Wind speed μ_2 (m/s)	Rainfall (mm)
1.1. 2018	1	6.5	11.7	83.8	1.0	14.7
2.1. 2018	2	6.5	10.6	64.9	0.8	0.0
3.1. 2018	3	0.2	11.2	80.8	1.4	0.0
4.1. 2018	4	0.0	10.1	98.6	2.2	64.1
5.1. 2018	5	0.0	11.0	79.9	2.0	44.2
6.1. 2018	6	5.5	13.3	70.5	0.9	2.4
	0	0	0	0	0	0

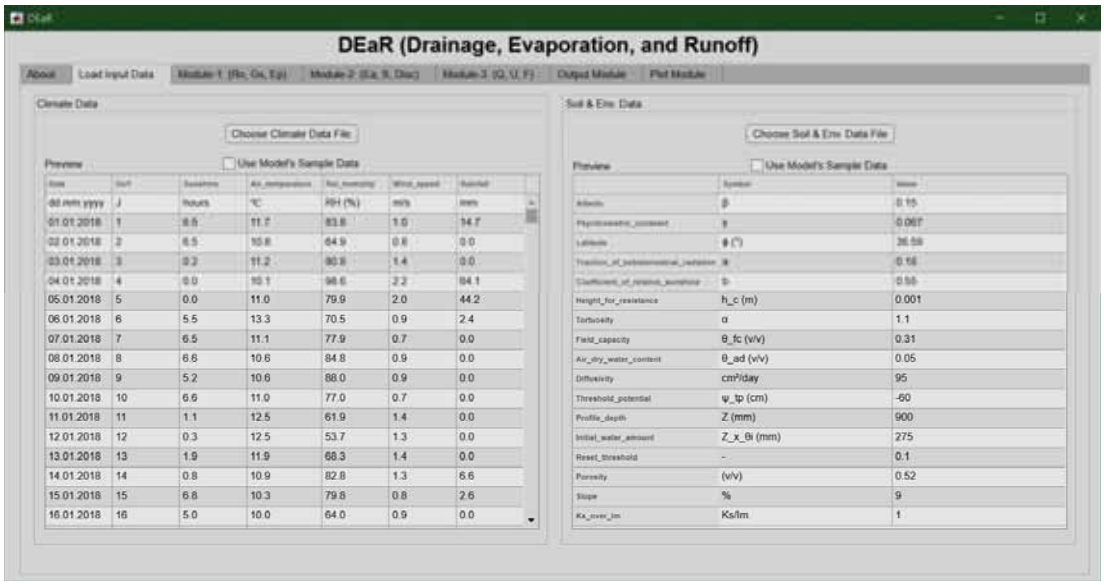

FIGURE 2
Menu screen for loading input (climate, soil & environmental) data from excel files.

Data Source. Study site –Adana (36°59′ N, 35°18′ E)– is located in a semi-arid environment of Turkey. A typical Mediterranean climate prevails in the study area. About 87% of precipitation occurs during the period of November to May [46]. Daily climate data were obtained from Adana Meteorological Station for the period of 2014-2018. Water balance components of a clay soil with an average slope of 9% were simulated. Daily computations of bare soil evaporation, soil water storage, direct surface runoff and subsurface flow (if any) were carried out for a period of 5 years. In this study, it was assumed that no impervious barrier existed throughout a profile depth up to 90 cm. Volumetric water content at field capacity and saturation (or porosity) were measured as 0.31 and 0.52 cm^3 cm^{-3}, respectively. Other soil parameters for the model calibration were compiled from literature [26, 27, 32, 37, 47, 48].

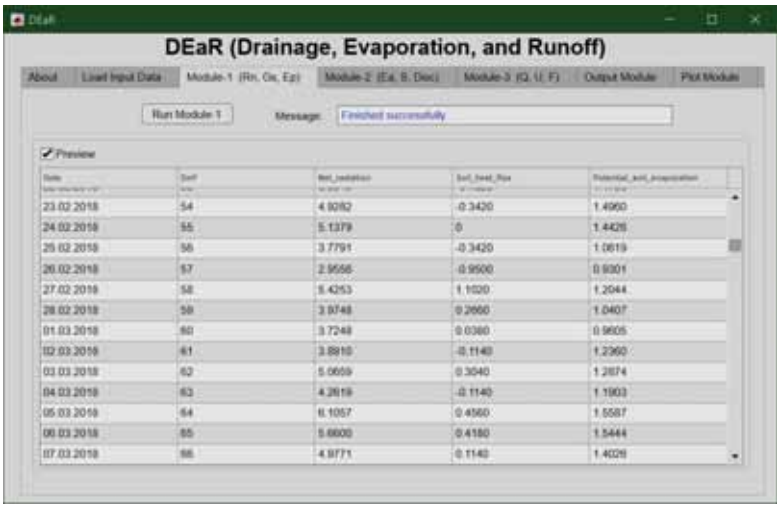

(a)

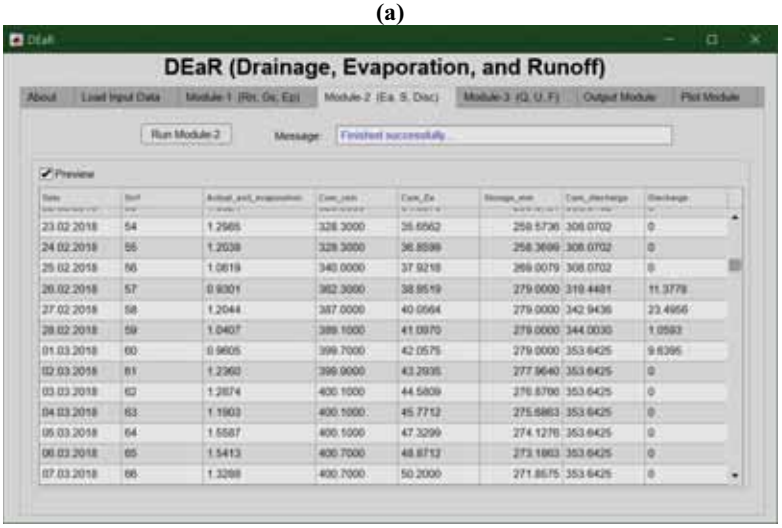

(b)

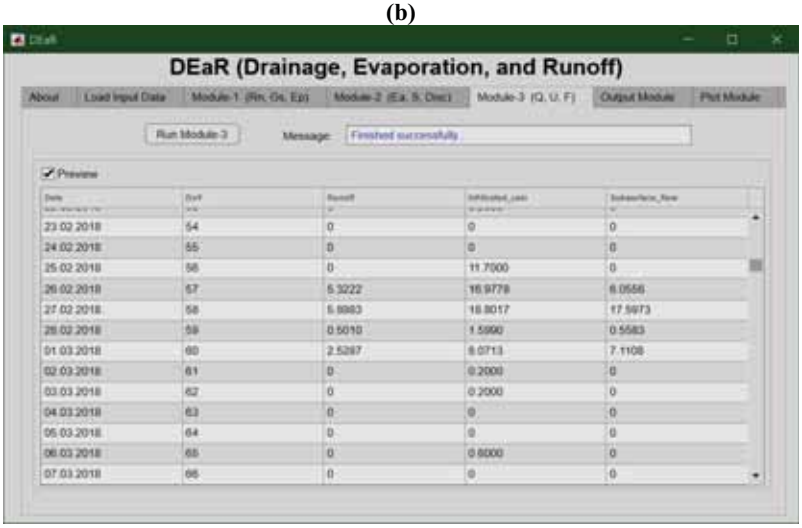

(c)

FIGURE 3
Menu options for calculation of the components.

TABLE 3
An example for the output file of the DEaR program

Date	DoY	Net radiation (R_n)	Soil heat flux (G_s)	Potential soil evaporation (E_p)	Actual soil evapora-tion (E_a)	Cumula-tive rainfall	Cumula-tive E_a	Storage	Cumula-tive discharge	Dis-charge	Runoff	Infil-trated rain	Subsur-face flow
dd.mm .yyyy	J	(MJ/m²/ day)	(MJ/m²/ day)	(mm/day)	(mm/day)	(mm)	(mm)	(mm)	(mm)	(mm/ day)	(mm)	(mm)	(mm/ day)
15.02. 2018	46	3.268	0.608	0.837	0.837	327.7	26.450	268.180	312.070	0	0	0.7	0
16.02. 2018	47	2.818	0.608	1.120	1.120	327.7	27.570	267.060	312.070	0	0	0	0
17.02. 2018	48	2.799	0	1.252	1.252	327.7	28.822	265.808	312.070	0	0	0	0
18.02. 2018	49	3.490	-0.266	1.336	1.336	328.1	30.157	264.873	312.070	0	0	0.4	0
19.02. 2018	50	3.605	-0.836	1.345	1.335	328.1	31.492	263.538	312.070	0	0	0	0
20.02. 2018	51	3.262	0.570	0.829	0.801	328.1	32.294	262.736	312.070	0	0	0	0
21.02. 2018	52	3.021	0.342	1.068	1.002	328.1	33.295	261.734	312.070	0	0	0	0
22.02. 2018	53	3.355	-0.152	1.170	1.062	328.3	34.358	260.872	312.070	0	0	0.2	0
23.02. 2018	54	4.928	-0.342	1.496	1.299	328.3	35.656	259.574	312.070	0	0	0	0
24.02. 2018	55	5.138	0	1.443	1.204	328.3	36.860	258.370	312.070	0	0	0	0
25.02. 2018	56	3.779	-0.342	1.062	1.062	340.0	37.922	269.008	312.070	0	0	11.7	0
26.02. 2018	57	2.956	-0.950	0.930	0.930	362.3	38.852	279.000	323.448	11.378	5.322	16.978	6.056
27.02. 2018	58	5.425	1.102	1.204	1.204	387.0	40.056	279.000	346.944	23.496	5.898	18.802	17.597
28.02. 2018	59	3.975	0.266	1.041	1.041	389.1	41.097	279.000	348.003	1.059	0.501	1.599	0.558
01.03. 2018	60	3.725	0.038	0.960	0.960	399.7	42.057	279.000	357.643	9.640	2.529	8.071	7.111
02.03. 2018	61	3.891	-0.114	1.236	1.236	399.9	43.294	277.964	357.643	0	0	0.2	0
03.03. 2018	62	5.066	0.304	1.287	1.287	400.1	44.581	276.877	357.643	0	0	0.2	0
04.03. 2018	63	4.262	-0.114	1.190	1.190	400.1	45.771	275.686	357.643	0	0	0	0
05.03. 2018	64	6.106	0.456	1.559	1.559	400.1	47.330	274.128	357.643	0	0	0	0
06.03. 2018	65	5.660	0.418	1.544	1.541	400.7	48.871	273.186	357.643	0	0	0.6	0
07.03. 2018	66	4.977	0.114	1.403	1.329	400.7	50.200	271.857	357.643	0	0	0	0
08.03. 2018	67	5.795	0.342	1.598	1.438	400.7	51.638	270.420	357.643	0	0	0	0
09.03. 2018	68	5.464	-0.152	1.794	1.548	401.5	53.186	269.672	357.643	0	0	0.8	0
10.03. 2018	69	6.612	-0.760	2.046	1.662	401.5	54.848	268.010	357.643	0	0	0	0
11.03. 2018	70	5.791	-0.190	1.607	1.237	401.5	56.085	266.773	357.643	0	0	0	0
12.03. 2018	71	6.176	0.570	1.568	1.171	401.5	57.256	265.601	357.643	0	0	0	0
13.03. 2018	72	5.384	0.076	1.501	1.083	401.5	58.339	264.519	357.643	0	0	0	0
14.03. 2018	73	5.619	-0.038	1.618	1.136	401.5	59.474	263.383	357.643	0	0	0	0
15.03. 2018	74	6.180	-0.418	1.840	1.243	401.8	60.717	262.440	357.643	0	0	0.3	0

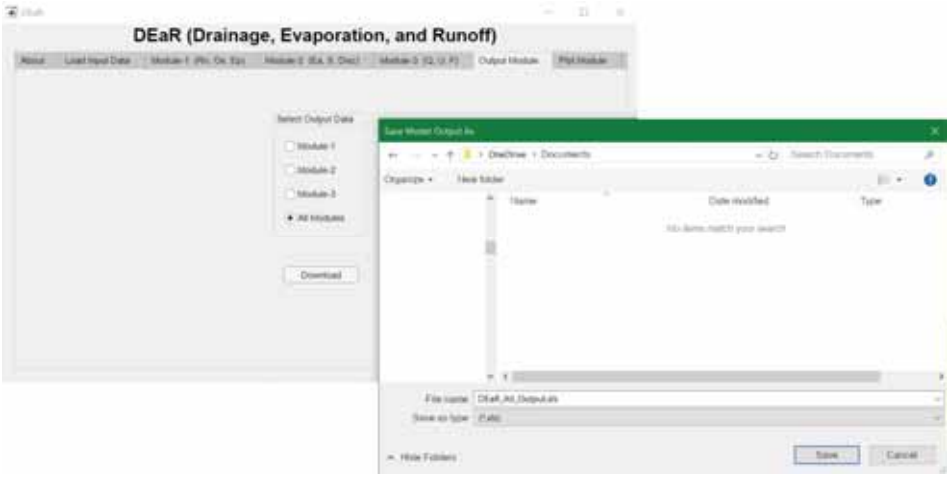

FIGURE 4
Menu options for generation of outputs in the form of excel file.

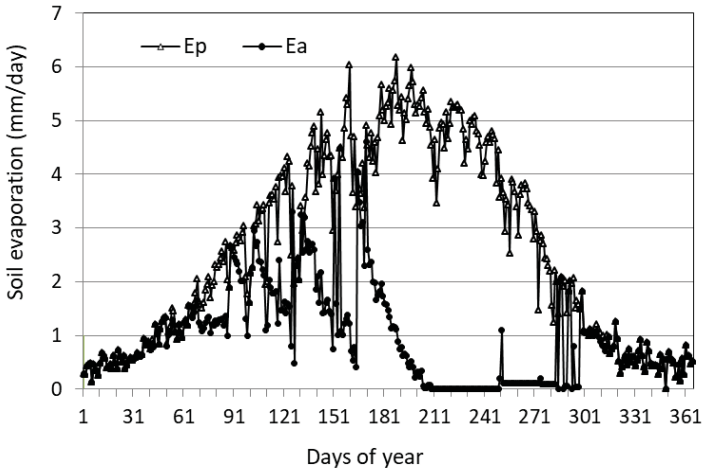

FIGURE 5
Comparison of potential (E_p) and actual (E_a) evaporations from bare soil for the year 2018.

RESULTS

The DEaR model outputs are calculated on daily basis for any study period. However, the first module must continue the calculations until the end of simulation period since it provides some data to the second sub-run. Otherwise, the second module may generate floating point error or fail to run, and consequently, the report file may be empty or may have missing data. Similarly, the second sub-routine supplies the necessary data to the third sub-program.

Simulations of the water balance components were conducted daily for each of the years during the period of 2014 to 2018. The cumulative values of the variables were calculated from the first Julian day of the study year. Potential soil evaporation (E_p), actual soil evaporation (E_a), and soil water storage (S) revealed similar patterns among the years. Graphical illustration of daily values for the entire period required an extensive space. In this respect, daily changes of some variables in Adana are given only for the year 2018 in the examples. The values of E_p and E_a were similar to the long-term data of the study area [26]; E_p rates were lower during the winter season because of the lesser evaporative demand of the atmosphere. However, E_a rates were mainly found to be a function of the amount and timing of rainfall, and presumably soil wetness [48] in addition to atmospheric evaporative demand (Figure 5). Similarly, S amounts were very low from July to October. During much of the rainy seasons, soil water storage was at or close to field capacity (Figure 6).

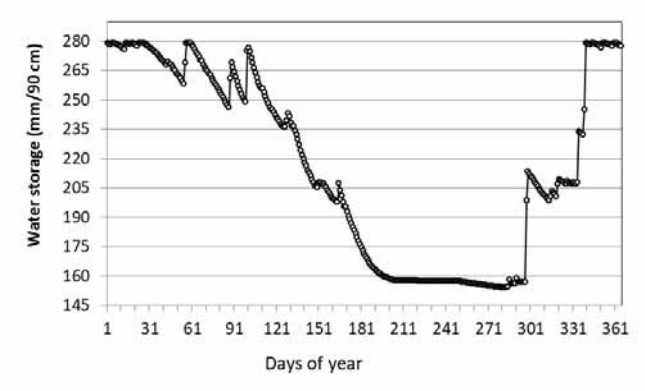

FIGURE 6
Daily changes in soil water storage (*S*) in the soil profile for the year 2018.

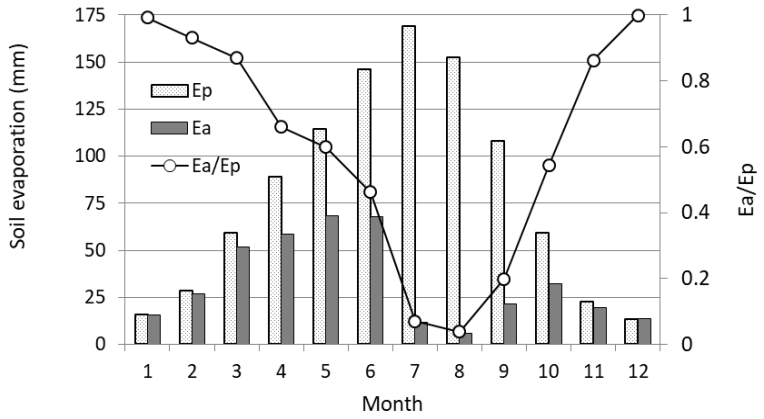

FIGURE 7
Monthly average potential (E_p) and actual (E_a) evaporations over five years along with the ratio of E_a/E_p.

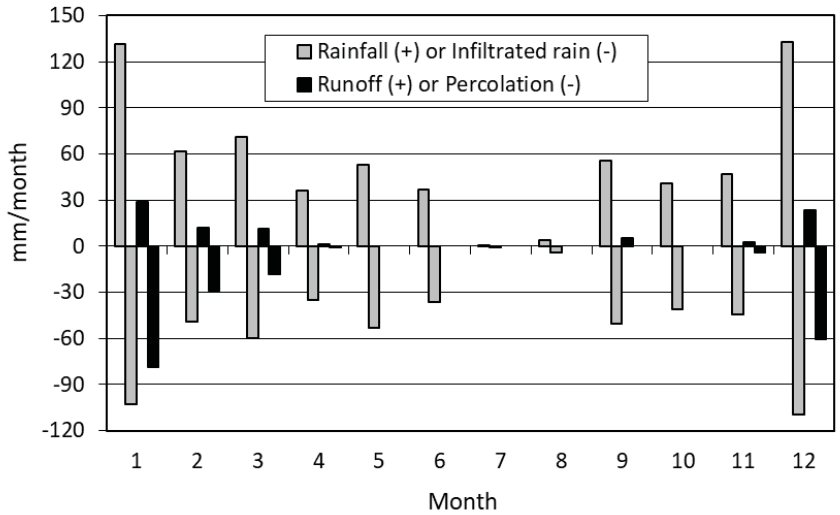

FIGURE 8
Monthly average changes in rainfall (*P*), infiltrated rain (*U*), runoff (*Q*), and drainage or deep percolation (*F*) over five years.

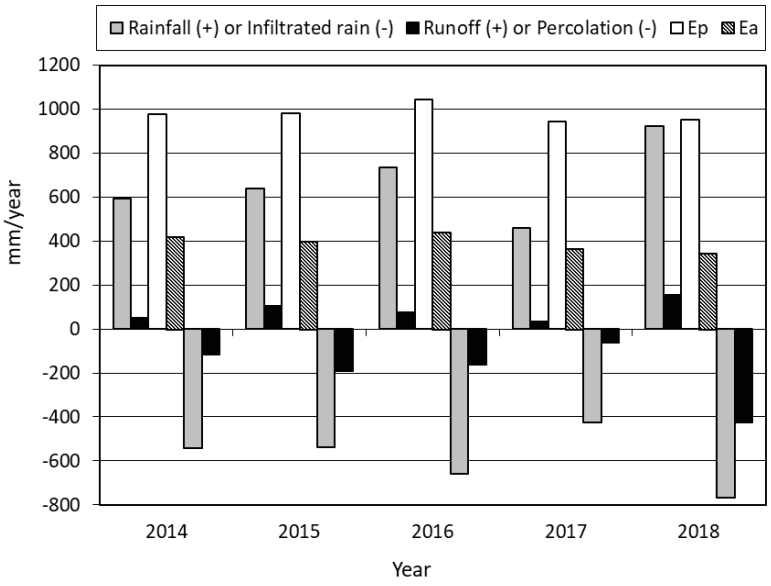

FIGURE 9
Yearly comparisons of rainfall (*P*), infiltrated rain (*U*), runoff (*Q*), percolation (*F*), potential (E_p) and actual (E_a) soil evaporations.

Monthly variations of E_p and E_a, as the average of five years, are given in Figure 7. It is very well known that potential evaporation is mainly related to the evaporative power of the atmosphere. However, the actual evaporation from bare soils depends not only on the atmospheric conditions but also on the soil properties, particularly soil wetness [5]. The ratio of actual to potential soil evaporation (E_a/E_p) is closely related to soil water content.

Changes in infiltrated rain, runoff, and percolation (that is actually subsurface flow contenting interflow) along with rainfall as the five-year average are shown in Figure 8. Excess surface runoff occurred throughout the rainy months; remarkably in December and January. Drainage or percolation occurred during rainy months starting from December to March, with a peak in January. These outputs are consistent with the results of Aydin [27] for Adana. The drainage was affected by rainfall and increased with a higher amount of infiltrated rain and presumably soil water content.

Yearly variations of rainfall, infiltrated rain, runoff, percolation, potential and actual soil evaporations for a period of five years are depicted in Figure 9. Soil hydrological components are strongly interdependent. Similar runoff trends in the same region have been reported by Celik [49]. These results may be promising in terms of prevention of water losses through runoff, evaporation, and drainage from bare soils and adoption of an effective management strategy for soil water, particularly, in rainfed-areas.

DISCUSSION

In a changing climate, researchers may face the challenge of water scarcity and efficient use of water available in the soil profile for plant growth especially in arid and semi-arid regions which comprise almost 40% of the world's land surface [50]. In this regard, quantifying the components of water balance in the assessment of soil water management under fallow conditions still poses a challenge [32]. Nevertheless, the DEaR model, which was derived from E-DiGOR, can be simultaneously employed for the simulation of water balance components and commonly used in rainfed-areas worldwide regardless of scale, because the model provides descriptions of water balance components at the scale of a single farm plot (as a matter of fact, the model simulates the components at point scale; then the homogeneous conditions are assumed over a plot field by scaling up that point situation). As discussed by Brutsaert [48], beside the soil water potential or soil water content, the instantaneous evaporation process from a drying soil must be affected by such additional factors as gravity, thermal gradients and vapor transfer, and storage in the soil. Moreover, by virtue of the alternate wetting and drying in the near surface soil profile during the diurnal cycle, the complications of hysteresis must also come into play [24, 48]. The main advantage of the DEaR model is to calculate actual soil evaporation, soil water storage, direct surface runoff, infiltrated rainfall, and subsurface flow in an interactive way. Since rainfall-runoff models are poorly responsive to potential evaporation [51], the computed actual soil evaporation is used as an input to

soil water balance to obtain a realistic estimation of the antecedent soil water storage [33]. As reported previously, the evaporation module of the model could derive soil evaporation successfully from soil water potential [24, 52]. It is based on energy fluxes and soil properties, and experimental data are used to define a threshold separating the potential-rate and falling-rate stages of evaporation [53, 54].

The outputs of the model will not only improve our understanding of the physical processes controlling soil water losses but also provide valuable information of risk assessment and management for soil and water resources. For example, once the soil was fully charged with water or soil water content reached field capacity, the rate of actual soil evaporation was equal or closer to that of the potential one. This means that soil water content has the greatest effect on actual evaporation, and consequently subsurface flow and surface runoff production [5]. These results may set the basis for prevention of water losses through evaporation, runoff and drainage from bare soils and adoption of an effective management strategy for soil water, particularly, under fallow conditions [32]. On the other hand, Kurt [29] highlighted that the model could also be used in the groves of olive trees.

As stated by Aydin et al. [5], the primary disadvantage of the DEaR model is that it cannot provide flow and transport dynamics in individual soil layers, since it acts as a single-layer model. Meanwhile, Brutsaert [48] emphasized that in many situations the soil layer contributing to evaporation is fairly shallow and only a few tens of centimeters thick. In addition, the model does not consider the effect of slope on soil evaporation, as most models do. However, there is no single tool to be applied to all processes.

In conclusion, the DEaR model adequately represents the physical processes important in estimating actual soil evaporation, runoff and subsurface flow from bare soils as well as water amount in the soil profile. In other words, the model can be used to successfully quantify the water balance components of bare soils under the absence of a shallow water table. At this point, upward capillary fluxes from (or the contribution of) water table and the hysteresis effects are not taken into consideration. The results, without any validation, may not allow to draw clear-cut conclusions here; however, the credibility of the original model has been demonstrated by different researchers explicitly, using laboratory –and field– based measurements in a wide range of environments as stated before. The outputs of the computer program developed here not only improve our understanding of water transport processes, but also provide useful information to adapt a strategy for soil-water conservation.

Software availability. It is planned to donate the computer program of the DEaR model to relevant non-profit organizations. The software can be provided upon request. It is free of charge, including databases for a region of choice for a period of one year. However, the program source codes cannot be supplied.

REFERENCES

[1] Agam, N., Berliner, P.R., Zangvil, A. and Ben-Dor, E. (2004) Soil water evaporation during the dry season in an arid zone. J. Geophys. Res.-Atmos. 109, 16103.

[2] Bittelli, M., Ventura, F., Campbell, G.S., Snyder, R.L., Gallegati, F. and Pisa, P.R. (2008) Coupling of heat, water vapor, and liquid water fluxes to compute evaporation in bare soils. J. Hydrol. 362(3-4), 191-205.

[3] Allen, R.G. (2011) Skin layer evaporation to account for small precipitation events-An enhancement to the FAO-56 evaporation model. Agr. Water Manage. 99(1), 8-18.

[4] Xiao, X., Horton, R., Sauer, T.J., Heitman, J.L. and Ren, T. (2011) Cumulative soil water evaporation as a function of depth and time. Vadose Zone J. 10(3), 1016-1022.

[5] Aydin, M., Jung, Y.-S., Yang, J.-E. and Lee, H.-il. (2014) Long-term water balance of a bare soil with slope in Chuncheon, South Korea. Turk. J. Agric. For. 38(1), 80-90.

[6] Alvenas, G. and Jansson, P.E. (1997) Model for evaporation, moisture and temperature of bare soil: calibration and sensitivity analysis. Agric. Forest Meteorol. 88, 47-56.

[7] Romano, E. and Giudici, M. (2009) On the use of meteorological data to assess the evaporation from a bare soil. J. Hydrol. 372(1-4), 30-40.

[8] Vanderborght, J., Graf, A., Steenpass, C., Scharnagl, B., Prolingheuer, N., Herbst, M., Franssen, H.J.H. and Vereecken, H. (2010) Within-field variability of bare soil evaporation derived from Eddy Covariance measurements. Vadose Zone J. 9(4), 943-954.

[9] Renard, K.G., Foster, G.R., Weesies, G.A., McCool, D.K. and Yoder, D.C. (1997) Predicting Soil Erosion by Water: A guide to conservation planning with the Revised Universal Soil Loss Equation (RUSLE). Agriculture Handbook, 703. USDA, Washington DC.

[10] Croke, B., Cleridou, N., Kolovos, A., Vardavas, I. and Papamastorakis, J. (2000) Water resources in the desertification-threatened Messara Valley of Crete: estimation of the annual water budget using a rainfall-runoff model. Environ. Modell. Softw. 15, 387-402.

[11] van Dijk, A.I.J.M., Meesters, A.G.C.A., Schellekens, J. and Bruijnzeel, L.A. (2005) A two-parameter exponential rainfall depth-intensity distribution applied to runoff and erosion modelling. J. Hydrol. 300, 155–171.
[12] Yoo, C. and Park, J. (2008) Rainfall-runoff analysis based on competing linear impulse responses: decomposition of rainfall-runoff processes. Hydrol. Process. 22, 660-669.
[13] Hwang, M.H., Maeng, S.J., Lee, S.J., Lee B.S. and Koh, I.H. (2009) Discharge characteristics at the control point for rainfall runoff model application. Irrig. Drain. 58, 429-444.
[14] Kim, M.-K., Flanagan, D.C., Frankenberger, J.R. and Meyer, C.R. (2009) Impact of precipitation changes on runoff and soil erosion in Korea using CLIGEN and WEPP. J. Soil Water Conserv. 64(2), 154-162.
[15] Kirkby, M.J. (2001) From plot to continent: reconciling fine and coarse scale erosion models. In: Stott, D.E., Mohtar, R.H. and Steinhardt, G.C. (Eds.), Sustaining the Global Farm, 10th International Soil Conservation Organization Meeting, May 24–29, 1999, Purdue University and the USDA-ARS National Soil Erosion Research Laboratory, pp. 860-870.
[16] Haggard, B.E., Moore Jr., P.A. and Brye, K.R. (2005) Effect of slope on runoff from a small variable slope box-plot. J. Env. Hydr. 13, 1-8.
[17] Morgan, R.P.C., Quinton, J.N., Smith, R.E., Govers, G., Poesen, J.W.A., Auerswald, K., Chisci, G., Torri, D. and Styczen, M.E. (1998) The European soil erosion model (EUROSEM): a dynamic approach for predicting sediment transport from fields and small catchments. Earth Surf. Process. 23, 527-544.
[18] Cerdan, O., Le Bissonnais, Y., Govers, G., Lecomte, V., van Oost, K., Couturier, A., King, C. and Dubreuil, N. (2004) Scale effect on runoff from experimental plots to catchments in agricultural areas in Normandy. J. Hydrol. 299, 4-14.
[19] Eilers, V.H.M., Carter, R.C. and Rushton, K.R. (2007) A single layer soil water balance model for estimating deep drainage (potential recharge): an application to cropped land in semi-arid North-east Nigeria. Geoderma 140, 119-131.
[20] Karnieli, A. and Ben-Asher, J. (1993) A daily runoff simulation in semiarid watersheds based on soil water deficit. J. Hydrol. 149, 9-25.
[21] Fitzjohn, C., Ternan, J.L. and Williams, A.G. (1998) Soil moisture variability in a semi-arid gully catchment: implications for runoff and erosion control. Catena 32, 55-70.
[22] Descroix, L., Nouvelot, J.-F. and Vauclin, M. (2002) Evaluation of an antecedent precipitation index to model runoff yield in the western Sierra Madre (North-west Mexico). J. Hydrol. 263, 114-130.
[23] Castillo, V.M., Gomez-Plaza, A. and Martinez-Mena, M. (2003) The role of antecedent soil water content in the runoff response of semiarid catchments: a simulation approach. J. Hydrol. 284, 114–130.
[24] Aydin, M., Yang, S.L., Kurt, N. and Yano, T. (2005) Test of a simple model for estimating evaporation from bare soils in different environments. Ecol. Model. 182(1), 91-105.
[25] Aydin, M. and Uygur, V. (2006) A model for estimating soil water potential of bare fields. Proceedings of 18th International Soil Meeting (ISM) on Soils Sustaining Life on Earth, Managing Soil and Technology, Sanliurfa-Turkey, Volume 1, pp. 477-480, ISBN: 975-96629-3-0.
[26] Aydin, M., Yano, T., Evrendilek, F. and Uygur, V. (2008) Implications of climate change for evaporation from bare soils in a Mediterranean environment. Environ. Monit. Assess. 140, 123-130.
[27] Aydin, M. (2008) A model for evaporation and drainage investigations at ground of ordinary rainfed-areas. Ecol. Model. 217(1-2), 148-156.
[28] Onder, D., Aydin, M. and Onder, S. (2009) Estimation of actual soil evaporation using E-DiGOR model in different parts of Turkey. Afr. J. Agric. Res. 4(5), 505-510.
[29] Kurt, N. (2011) Monitoring of Soil Water Budget Using E-DiGOR Model in Olive Producing Area. Ph.D. Thesis, Mustafa Kemal University, Hatay, Turkey (in Turkish).
[30] Aydin, M., Jung, Y.-S., Yang, J.-E., Lee, H.-il. and Kim, K.-D. (2012) Simulation of soil hydrological components in Chuncheon over 30 years using E-DiGOR model. Korean J. Soil Sci. Fert. 45(4), 484-491.
[31] Aydin, M., Vithanage, M., Mowjood, M.I.M., Jung, Y.-S., Yang, J.-E., Ok, Y.S., Kim, S.C. and Dissanayake, C.B. (2012). Estimation of evaporation and drainage losses from two bare soils in Sri Lanka. Eurasian J. Soil Sci. 1, 1-9.
[32] Aydin, M., and Polat, V. (2010) A computer program for E-DiGOR model. International Soil Science Congress on Management of Natural Resources to Sustain Soil Health and Quality, 26–28 May 2010, Samsun, Turkey, Book of Proceedings, pp. 9-16, ISBN: 978-975-7636-72-4.
[33] Aydin, M. (2012) Improvements in E-DiGOR model: quantifying the water balance components of bare soils. KNU J. Agric. Life Env. Sci. 24(2), 68-71.
[34] Aydin, M., Jung, Y.-S., Yang, J.-E., Kim, S.-J. and Kim, K.-D. (2015) Sensitivity of soil evaporation and reference evapotranspiration to climatic variables in South Korea. Turk. J. Agric. For. 39(6), 652-662.

[35] Aydin, M., Watanabe, T. and Kapur, S. (2019) Sensitivity of Reference Evapotranspiration and Soil Evaporation to Climate Change in the Eastern Mediterranean Region (Chapter 14). In: Watanabe et al. (Eds.), Climate Change Impacts on Basin Agro-ecosystems. Springer APESS (Volume 18). 295-315.
[36] Kapur, B., Aydin, M., Yano, T., Koc, M. and Barutcular, C. (2019) Interactive Effects of Elevated CO_2 and Climate Change on Wheat Production in the Mediterranean Region (Chapter 12). In: Watanabe et al. (Eds.), Climate Change Impacts on Basin Agro-ecosystems. Springer APESS (Volume 18). 245-268.
[37] Allen, R.G., Smith, M., Perrier, A. and Pereira, L.S. (1994) An update for the definition of reference evapotranspiration. ICID Bull. 43(2), 92 pp.
[38] Wu, B., Liu, S., Zhu, W., Yan, N., Xing, Q. and Tan, S. (2017) An improved approach for estimating daily net radiation over the Heihe River Basin. Sensors 17(1), 86.
[39] Wallace, J.S., Jackson, N.A. and Ong, C.K. (1999) Modelling soil evaporation in an agroforestry system in Kenya. Agric. Forest Meteorol. 94, 189-202.
[40] Karaca, C., Buyuktas, D., Bastug, R., Aydinsakir, K. and Buyuktas, K. (2018) Comparing seven different reference evapotranspiration equations with Penman-Monteith for Antalya, Turkey. Fresenius Env. Bull. 27, 9500-9508.
[41] Bellot, J. and Chirino, E. (2013) Hydrobal: An eco-hydrological modelling approach for assessing water balances in different vegetation types in semi-arid areas. Ecol. Model. 266, 30-41.
[42] Konukcu, F. (2007) Modification of the Penman method for computing bare soil evaporation. Hydrol. Process. 21(26), 3627-3634.
[43] Brown, R.W. and Oosterhuis, D.M. (1992) Measuring plant and soil water potentials with thermocouple psychrometers: some concerns. Agron. J. 84, 78-86.
[44] Kim, N.W. and Lee, J. (2008) Temporally weighted average curve number method for daily runoff simulation. Hydrol. Process. 22, 4936-4948.
[45] Rubin, J. (1966) Theory of rainfall uptake by soils initially drier than their field capacity and its applications. Water Resour. Res. 2(4), 739-749.
[46] Yano, T., Aydin, M. and Haraguchi, T. (2007) Impact of climate change on irrigation demand and crop growth in a Mediterranean environment of Turkey. Sensors 7, 2297-2315.
[47] Aydin, M. and Kececioglu, S.F. (2010) Sensitivity analysis of evaporation module of E-DiGOR model. Turk. J. Agric. For. 34, 497-507.
[48] Brutsaert, W. (2014) Daily evaporation from drying soil: Universal parameterization with similarity. Water Resour. Res. (50), 3206-3215.
[49] Celik, I. (1998) A Study on the Applicability of Some Natural Plant Species for Erosion Control in the Cukurova Region. Ph.D. Thesis, Cukurova University, Adana, Turkey (in Turkish).
[50] Aydin, M. (1995) Water: Key ingredient in Turkish farming. Forum for Applied Research and Public Policy (A Quarterly Journal of the University of Tennessee, USA) 10(4), 68-70.
[51] Oudin, L., Hervieu, F., Michel, C., Perrin, C., Andreassian, V., Anctil, F. and Loumagne, C. (2005) Which potential evapotranspiration input for a lumped rainfall-runoff model? Part 2– Towards a simple and efficient potential evapotranspiration model for rainfall-runoff modelling. J. Hydrol. 303, 290-306.
[52] Falge, E., Reth, S., Bruggemann, N., Butterbach-Bahl, K., Goldberg, V., Oltchev, A., Schaaf, S., Spindler, G., Stiller, B., Queck, R., Kostner, B. and Bernhofer, C. (2005) Comparison of surface energy exchange models with eddy flux data in forest and grassland ecosystems of Germany. Ecol. Model. 188, 174-216.
[53] Romano, E. and Giudici, M. (2007) Experimental and modeling study of the soil-atmosphere interaction and unsaturated water flow to estimate the recharge of a phreatic aquifer. J. Hydrol. Eng. 12(6), 573-584.
[54] Quevedo, D.-I. and Frances, F. (2008) A conceptual dynamic vegetation-soil model for arid and semiarid zones. Hydrol. Earth Syst. Sci. 12, 1175-1187.

Received: **17.09.2019**
Accepted: **09.02.2020**

CORRESPONDING AUTHOR

Mehmet Aydin
Emeritus, Mustafa Kemal University,
Department of Soil Science and Plant Nutrition,
Antakya, Turkey.

e-mail: maydin08@yahoo.com

© by PSP Volume 29 – No. 04A/2020 pages 3300-3307 Fresenius Environmental Bulletin

NOTICE

LANDSCAPE DESIGN OF THE URBAN BUS STATION BASED ON THE URBAN CHARACTERISTICS AND ECOLOGICAL ENVIRONMENT OF SMART CITY, CHINA

Chunyan Li*

Pingdingshan University, Pingdingshan, Henan 467000, China

ABSTRACT

Now China is in an important decisive stage for building a moderately prosperous society in all respects. With the acceleration of urbanization, people have higher requirements for urban work, travel and living environment. The overall construction of smart city should be comprehensive. With the global attention to the concept of ecological environment, the construction process of China's smart city should also be based on the construction of a systematic and comprehensive ecological environment. In order to combine greening, sculpture, architecture, modern technology and other diversified elements with urban bus station that will enrich the connotation of urban landscape and show the brand-new spirit and cultural outlook of the city, this paper will preliminarily analyze the basic form of urban bus station from the perspective of landscape meaning, and study the content of urban bus station landscaping. On this basis, the optimized path of urban bus station landscape design is emphatically explored for reference.

KEYWORDS:
Ecological environment, smart city, bus station, landscape design, comprehensive

INTRODUCTION

At present, the majority of residents still travel by bus excluding in Beijing, Shanghai, Guangzhou, Shenzhen and other economically developed cities. As the traffic site with carrying large passenger traffic bus station is the important transport hub of the city. Because in actual operation it is fast, high efficient, cheap, and can carry large passenger traffic, etc. The design of the bus station is obviously limited in the traditional yard design as an independent municipal facility. Especially the overall landscape design is neglected, and the green planting design is relatively single, and the overall service function and station is lack of overall consideration [1-3]. In the early 19th century, German geobotanist and geographer explained the term of landscape as "the overall characteristic of a region". It is pointed out that landscape problem should be regarded as the core problem in geography and the gradual evolution of primitive landscape to human cultural landscape should be explored [4-5]. Russian scholar Berge carried forward this view and formed a new school of landscape geography research. He believed that landscape was the city of biological and non-biological phenomena and was the intersection and integration between ecology and geography. At present, it is generally believed that landscape is the general name of the complex including land and ground building space, and is the result of the changes of human life and natural activities over the years [6].

In order to beautify the public transportation sites, to combine the landscape design and the urban transit site, to organically combine the plant, road, station, public facilities and all kinds of architecture through the landscape design, the space layout as well as a series of optimizing reform measures, to realize the effect of landscape design of public transport station, at the same time guaranteeing the transportation service function of the bus stops, meeting the commuters' leisure need has become an important content of a modern city bus stops' design and build.

METHODS AND THE BASIC FORM OF URBAN BUS STATION

Basic Requirements for Ecological Environment of Smart City. In the process of human development, we must seek the coordinated development of ecological environment and social economy. The ecological environment is the basis of social and economic development, which greatly affects [7-9]. Social economy plays an active role in the ecological environment, promoting or hindering the ecological environment. The ecological environment is a resource as well as an asset, which is a potential development advantage and benefit. When the carrying capacity of the ecological environment is greater, the social and economic development

will also be positively affected (Figure 1). The environment depend on the development of social economy. And the low-carbon circulation of the social and economic development of the ring promotes the sustainability of the ecological environment. On the contrary, it will aggravate the degree of damage to the ecological environment [10-13].At present, there are several problems in the construc-effective utilization and protection of the ecological

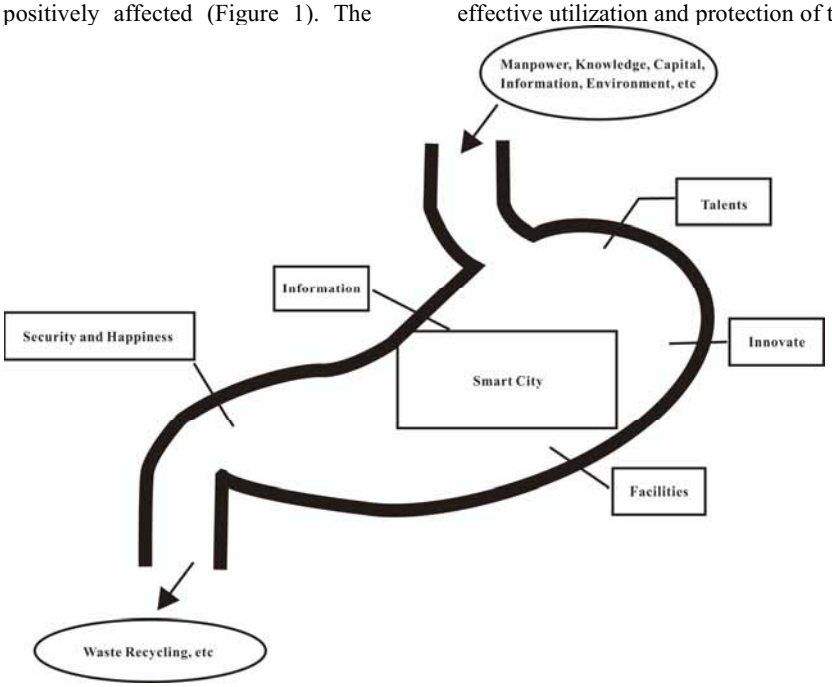

FIGURE 1
The ideal constitution of smart city

TABLE 1
Evaluation index system of urban ecological environment in key ecological functional areas

First-grade Index	Second-grade Index	Order Number
Natural Ecological Environment/*A*	Population density	A_1
	Forest coverage	A_2
	Public green area per capita	A_3
	Conservation rate of rare and endangered species	A_4
	Excellent rate of ambient air quality	A_5
	Average value of regional ambient noise	A_6
	Water resources per capita	A_7
	Standard rate of drinking water source	A_8
Environmental Resource Protection/*B*	Soil erosion area	B_1
	Urban domestic sewage treatment rate	B_2
	Harmless treatment rate of domestic waste	B_3
	Comprehensive utilization rate of industrial solid waste	B_4
	Planting area of organic, green and pollution-free products in main agricultural products	B_5
Capacity of ecological environment management/*C*	Proportion of environmental protection investment in GDP	C_1
	Popularization rate of ecological civilization publicity and education	C_2
	Public satisfaction with ecological environment	C_3

tion of urban ecological environment in China: (1) the development of ecological environment and social economy is slow; (2) the level of coordinated development of ecological environment and social economy is generally not coordinated; (3) the level of coordinated development of ecological environment and social economy is quite different [14-15]. Among them, how to fully and effectively solve the traffic problem is the necessary prerequisite for building a smart city (Table 1). At present, the public transportation system is still the main component of urban transportation in China, which accounts for a large proportion. Therefore, it is necessary to carry out systematic research on the optimal design of public transportation station landscape based on the urban characteristics and the concept of ecological environment, which is of great significance for building a sustainable and green smart city [16-18].

At present, there are no unified standards for the classification of urban bus hubs at home and abroad. And the station scale depends on the annual maximum passenger flow of a day and the passenger flow during peak hours. China mainly divides the station scale into the following four levels, and puts forward relevant suggestions for the allocation and planning of some public facilities, as shown in Table 2.

Regular stops at bus stations include the following types.

Island Type Station. most of the stops are located in the island, which has good applicability in the design of a large number of bus lines' stations and a compact stop. The plane structure is shown in Figure 2. Island station can effectively save land use area and improve land utilization rate, but passengers sometimes need to cross the lane to change buses, which is likely to cause traffic congestion and accidents.

Platform Station. When there are many and relatively complex lines, the corresponding stopover station is usually set on a separate platform, which is usually more common in the long-distance bus station setting. The plane structure is shown in Figure 3. The inclined platform can be used to improve vehicle control performance, but passengers need to cross the lane to change other tools, which has potential risks.

TABLE 2
China light rail station classification and suggestions for supporting facilities

Station Scale	The passenger flow during peak hours. (10,000 people/h)	Daily passenger flow (10,000 people /d)	Bicycle parking area (m^2)	Ticket window Bird type platform	Side platform
Small site	≤0.5	≤5	＞60	1～2	2
Medium site	0.5～2	5～20	＞240	2～3	2～4
Large site	2～10	20～100	＞480	3～4	3～4
Mega site	＞10	＞100	＞2000	＞8	＞10

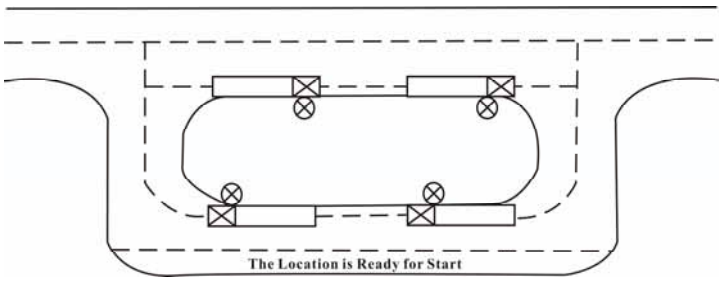

FIGURE 2
Island type station

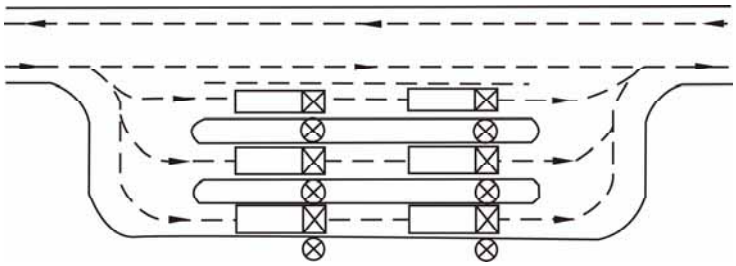

FIGURE 3
Platform station

Combination Station. In practical application, two or more combination modes are usually adopted. In the public station transportation, each bus station with important hub function is usually a mixed stop for taxi, bus and other parking tools, so other layout design and plan need to be considered.

Special Station. in the design of stations, multiple combination modes can be adopted to divide multi-layer station into integrated stations that combine rail transit stations with large buildings and entertainment malls. The plane structure of the two special complex stations is shown in Figure 4 and Figure 5. The underground in Figure 5 is the rail transit station, and the bus stops on the ground. Commercial entertainment buildings can be set up on the ground station to improve the utilization rate of the limited space of the station.

Connect with the Road Network. The transportation efficiency of bus station is closely related to its connection with the road traffic network. When setting up bus station, it is necessary to avoid the collision between bus entrance and exit path and other vehicles and passerby. In some special cases, special lanes can be set up for bus operation, such as express bus, to ensure the continuity and timeliness of bus daily operation [19]. In addition, when planning the bus stop, the entrance and exit of the station should be added as far as possible to ensure the vehicle can enter and leave from multiple directions.

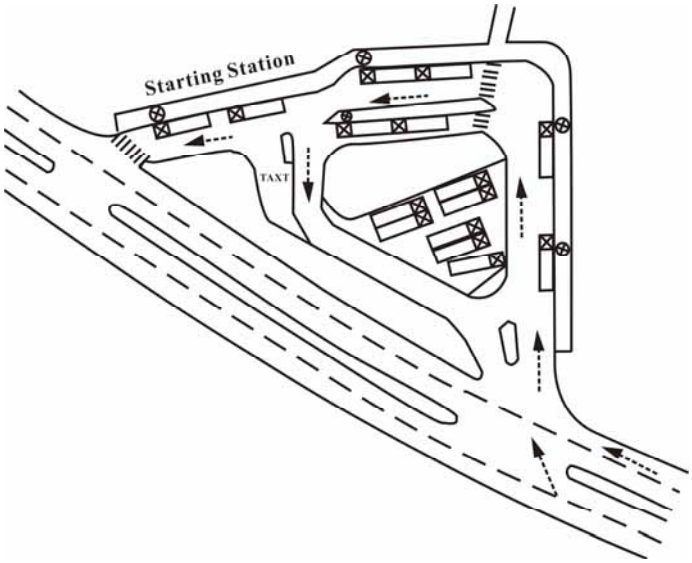

FIGURE 4
Special station of platform and island

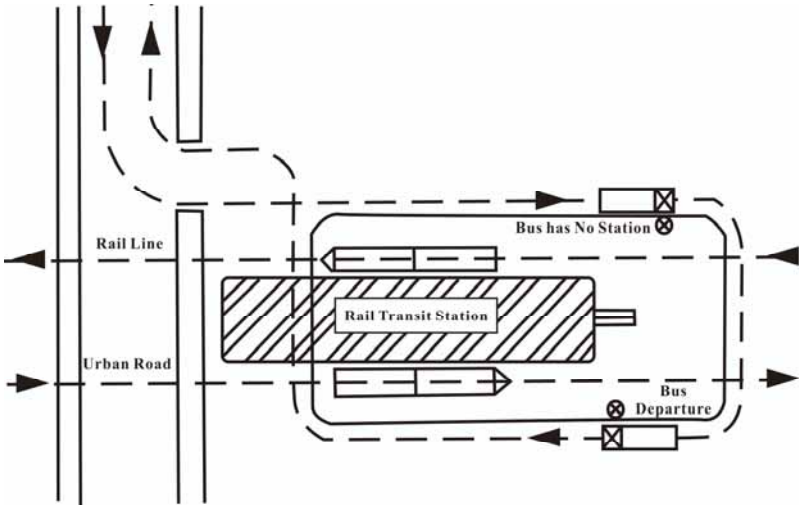

FIGURE 5
Transfer station of rail transit and bus

RESULTS AND DISCUSSION

Landscaping Site Building. Architectural landscape design is the basic architectural content in the landscape design of bus stations. People can directly recognize the visual perception of the space structure of bus stations and identify bus stations according to the characteristics of architectural landscape texture and color [20].

(1) Form is the visual rendering of building structure and the carrier of the function of the bus stops. The extrinsic manifestation of a site is mainly composed of simple geometric elements such as dot, line, face. Form includes the relationship between the material quality of space dimension, the relationship between the morphological structure, and the relations between movement situation, rhythm and cadence, scale relation, etc. It is the important means of identifying objects.

(2) At the same time, in the design of site architecture, designers must pay attention to reflecting the beauty of buildings through texture, so as to promote people to experience the comfort and safety performance of materials by material colors and tactility, and improve the space environment of bus stations. For example, the construction materials and elevated rail materials of Shanghai bus station are mostly made of reinforced concrete, the top of the station is made of semi-open cantilever steel frame, and the rain shed is made of stretch film or light steel plate. Making use of the thick texture of concrete appearance can give person with solemn, steady, safe psychological feeling. The steel structure with meticulous sense can give person with relaxed, fine psychological tendency.

(3) As a basic visual element in landscape design, color can endow the external features enjoyed by buildings, giving people a unique and intuitive visual experience, and color can trigger people's emotional association through visual images of people's behaviors and psychology with purity, lightness and hue. Shenzhen seaside boulevard, for example, with total length of 9.65 km, the building, canopy and supporting facilities of their bus stations are with blue and green. Echoed with the green garden and coastal landscape on the avenue, they create the best ecological effect, and form a clear level of urban green landscape and unique tropical scenery, and reflect the site's three-dimensional landscape characteristics.

Landscaping Site Building. Road landscape is the main channel connecting the entrance and exit of bus stations. When designing road landscape, we should pay attention to integrate landscape environment control with surrounding ecological system, urban culture, ecological aesthetics and landscape tour design [21-22]. With the progress and development of science and technology, governments are clearly aware of the importance of "harmony between man and nature". Human beings must do their best to protect our living environment while accepting the beautiful things like mountains, forests, rivers, lakes and animals that nature gives us. Therefore, more and more municipal infrastructure design and construction begin to incorporate the natural environmental protection factors into the landscape design. Due to relatively high traffic flow, most roads are paved with asphalt and concrete, giving people a dull and monotonous feeling. At the same time, during the hot summer days, a large amount of light energy and heat will be reflected, which will affect the working and living environment of the users of surrounding buildings. So, in the transit site connected road design, the designers need to be good at using green between road and site links. By planting flowers and trees, the ideal environmental protection effect is achieved that combines the bus stops and natural system. At the same time, the green belt plays a positive role in clean air, reducing noise and reducing temperature, so as to improve the urban road ecological environment. Taking the pedestrian green belt in Los Angeles as an example, it fully introduces the concept of "ecological design" in the road design connected with the bus station. In planting different kinds of vegetation and trees in the same community, they adhere to the ecological principle of "adapting to local conditions" and "mutual benefit", and use ecological landscape to beautify the road landscape of public transportation stations. At the same time, the psychological and behavioral characteristics and walking safety of pedestrians are considered in the design. In the middle of the bus stop, the stops are close to the edge of the green belt of the express lane, with a length about 30m, and the paved ground with a width of 1-2m is reserved in the parking area (Figure 6) [23-24]. Tall and luxuriant deciduous trees are planted, which can effectively play the role of shading passengers in summer.

FIGURE 6
Ideal bus stop thumbnail based on the concept of green landscape

Optimization of Detailed Landscape Configuration. Rest area is the key link in the design of bus stops. In this aspect, the design usually integrates the avenue, flowers, plants and fountains with the rest area of the station, and uses the avenue and various flowers and plants to separate the roadway, so as to create an ideal rest place for passengers, and set up simple garden facilities for pedestrians to rest, including benches and shade shelters [25]. For example, the layout types of the avenue mainly include the following three types:

(1) It is necessary to set up an avenue in the middle of the connection. There are bus stops on both sides of the avenue and a green belt in the middle for recreational use by pedestrians. This king of design has obvious symmetry and can play the role of lane separator. It has good applicability in the design of the bus station with small passenger flow, but it is not suitable to set too many entrances and exits.

(2) To set up an avenue on one side of the street to reduce the frequency of traffic and pedestrian crossing, so as to enable pedestrians to reach the avenue directly through the sidewalk, so as to improve the traffic safety of pedestrians.

(3) An avenue is arranged on both sides of the street to make the avenue adjacent to the sidewalk. That makes it safe and convenient for pedestrians to reach the avenue, and gives full play to the effect of the avenue on reducing noise and dust of urban road traffic which improves the sense of symmetry of urban street design. This scheme is suitable for wide roads with free space. Usually, the avenue can be equipped with supporting architectural items, such as flower beds, chairs for pedestrians to rest, flower stands, publicity display spaces and fountains etc., as well as small children's amusement parks to enhance the leisure and entertainment effect.

In addition, it is necessary to follow the principles of "integrity", "practicability" and "economy" to fully consider the construction and subsequent maintenance costs of landscape architecture and vegetation. For example, Jingdezhen adopted the ceramic exterior street lamp with local characteristics in the green belt design near the bus stop, appropriately enlarging the lamp body, so that the street lamp can be integrated with the surrounding environment. The Venetian hotel in Las Vegas, USA, has adopted European-style street lighting installation on the surrounding road, which makes visitors feel as if they are in Venice city that enhances the local tourist characteristics. Some provincial capitals in central China, such as Taiyuan and Zhengzhou, have adopted environment-friendly street lamps with the dual energy-saving effects of solar power generation and wind power generation in the construction of new bus stations and surrounding roads to implement the concept of green development.

The Optimization of Site Traffic Organization. The landscape design of the traffic station must be based on the concept of convenient service, and create convenient conditions for pedestrians to travel by bus. The rapid development of China's economy and the acceleration of urbanization have led to the doubling of traffic pressure in urban central areas. Although urban rail transit has achieved unprecedented development in recent years, bus is still the main mode of routine travel. In order to provide more high-end services for passengers in urban central areas, it is necessary to improve and optimize the traffic organization of bus stations, shorten the waiting time of vehicles in stations, simplify the traffic environment and improve the operation efficiency of transportation networks.

(1) When designing the landscape of the site, the location of the site must be reasonably arranged. According to different types of buses and demands of the bus, appropriate bus stops should be selected. For example, compared with the direct route stations, the harbor - style bus stations can effectively save the road resources and improve the phenomenon of traffic reading. Therefore, the harbor - style bus stations should be selected as far as possible if the road conditions permit. At the same time, in site selection, it is necessary to avoid contact with intersections, sidewalks and other non-bus vehicles to alleviate traffic congestion.

(2) With the help of diversified means, the number of bus information sources are increased and the effect of information transmission are enhanced. At present, the information content of bus stations mainly includes guideposts, bus stop signs, transfer guides and bus stops. In order to increase the number of information sources, the location identification of the bus station can be added at the intersection of the nearby community and the heavy traffic, providing the required information for passengers. At the same time, modern information technology is used to equip stations with electronic screens and dynamic reporting stations, so as to increase necessary bus transfer information. Especially in large cities with complex routes, such as Beijing, Shanghai, Guangzhou and so on, it is necessary to reduce the public display space of bus stop information occupied by advertisement column and provide more comprehensive public transport services for tourists. For example, Beijing Tiantongyuan express bus station and Hangzhou new express bus station use satellite positioning system to transmit wireless information data, and all stations are equipped with electronic scroll screens to provide passengers with bus arrival and transfer information and improve the overall service function of the transportation station.

CONCLUSIONS

To sum up, green, environment friendly and sustainable development have become important concepts to be followed in the construction and design of China's urbanization infrastructure. This paper mainly elaborates the main content of urban bus station landscape design from the aspects of architectural landscape, road landscape, landscape sketch and traffic organization optimization of public transportation stations based on the ecological environment concept. It provides a reference for the improvement and optimization of the landscape design of bus stations, provides more complete public transport services for pedestrians, and promotes the long-term progress and development of smart cities.

ACKNOWLEDGEMENTS

The author would like to show sincere thanks to those persons who have helped this research and all the authors of the references.

REFERENCES

[1] Wei, L., Chen, X. (2017) Coupling research between urban performance and ecological environment based on smart development: A case study of Harbin-Changchun city group. Scientia Geographica Sinica. 37(7), 1032-1039.

[2] Wang, D. (2013) Study of green building design based on micro-project in correlate urban ecological environment. Applied Mechanics and Materials. 329, 51-55.

[3] Sun, B., Yu, D. (2018) Study on Jinan urban construction planning based on the protection of karst landscape. Journal of Groundwater Science and Engineering. 6(04), 41-53.

[4] Bi, L. (2016) Research of Urban Lake Ring landscape planning and design--Case Study of Niushan Lake Tech-Eco City. 2016 International Conference on Engineering and Technology Innovations. 113-121.

[5] Zou, Y. (2016) Study on informatization and systematic design strategy of bus waiting facilities - A case study of Dalian. Industrial Design. 11, 78-80.

[6] Liang, S. (2016) A case study of Xinzhou bus terminal on urban transport hub design. Shanxi Architecture. 42(10), 24-25.

[7] Chen, X., Jiang, M. (2017) Technical approach to creative programming in urban public space dynamic landscape design. Packaging Engineering. 6, 149-153.

[8] Liu, Q., Qian, Z. (2016) Classification planning guidelines for north American urban TOD rail stations. Urban Planning. 346(3), 63-70.

[9] Barakat, A., Ayad, H., El-Sayed, Z. (2017) Urban design in favor of human thermal comfort for hot arid climate using advanced simulation methods. AEJ - Alexandria Engineering Journal. 56(4), 533-543.

[10] Yigitcanlar, T., Lee, S. (2014) Korean ubiquitous-eco-city: a smart-sustainable urban form or a branding hoax? Technological Forecasting and Social Change. 89, 100-114.

[11] Audirac, I. (2017) Shrinking cities: An unfit term for American urban policy? Cities. 75, 12-19.

[12] Wang, Z., Zhao, Y., Hou, J. (2017) Suggestions on urban park herbal design based on landscape preference research. Chinese Garden. 9, 33-39.

[13] Bai, Z., Cao, J. (2017) Design and development of GIS query system for urban public transportation. Mapping Science. 42(4), 86-90.

[14] Qi, L. (2016) Landscape design around rail transit stations. Residential Property. 1, 76.

[15] Duan, T. (2017) Urban design strategy research based on the concept of sponge city: A case study of Renbei district in Chengdu. Journal of Landscape Research. 9(06), 52-55.

[16] Dang, X., Zhang, D., Zhou, R. (2013) The probe into the multi-objective landscape design of urban river based on ecological security - with the planning of the Weihe River landscape zone in Xi'an-Xianyang as an example. Advanced Materials Research. 671-674, 2796-2801.

[17] Xia, L. (2011) Discussion about the ecology landscape pattern design of riverside hilly urban water system based on corridor theory. International Conference on Information Science and Engineering. IEEE.

[18] Francesco, P., Marcos, L., Sotirios, P. (2019) Understanding Smart Cities: Innovation ecosystems, technological advancements, and societal challenges. Technological Forecasting and Social Change. 142, 1-14.

[19] Khaled, A. (2017) Rethinking Dubai's urbanism: Generating sustainable form-based urban design strategies for an integrated neighborhood. Cities. 60, 353-366.

[20] Leem, Y., Lee, S., Yoon, J. (2014) Linking data and converging systems for smarter urban services: two cases of U-City service in Korea. Procedia Environmental Sciences. 22, 89-100.

[21] Acar, C., Sari, D. (2010) Evaluation of plant species in urban residential landscapes based on their characteristics for landscape preferences: A sample of Trabzon City. Ekoloji. 19(74), 173-180.

[22] Zhu, Q. (2013) The urban environment design based on the combination of ecological and cultural expressions. Applied Mechanics and Materials. 357-360, 1984-1987.
[23] Lin, B. (2014) Planning and design for constructed wetlands based on the ecological landscape. Applied Mechanics and Materials. 584-586, 662-667.
[24] Wu, J., Zhang, L., Peng, J., Feng, Z., He, S. (2013) The integrated recognition of the source area of the urban ecological security pattern in Shenzhen. Acta Ecologica Sinica. 33(13), 4125-4133.
[25] Zhang, D., Li, F., Wang, R. (2011) Optimization of urban land structure based on ecological green equivalent: A case study in Ningguo City, China. Acta Ecologica Sinica. 31(20), 6242-6250.

Received: **05.12.2019**
Accepted: **01.02.2020**

CORRESPONDING AUTHOR

Chunyan Li
Pingdingshan University,
Pingdingshan, Henan 467000, China

e-mail: chaoxi125430795@163.com

© by PSP Volume 29 – No. 04A/2020 pages 3308-3314 Fresenius Environmental Bulletin

NOTICE

STUDY ON NEW ENVIRONMENTAL PROTECTION LAW AND CONSTRUCTION STRATEGY OF ECOLOGICAL COMPENSATION SYSTEM

Qingpo Wei*

School of Law, Capital University of Economics and Business, Beijing 100070, China

ABSTRACT

This study was intended to estimate the changes in ecosystem service values (ESVs) as well as other related data such as statistical data. New environmental protection law and construction strategy of ecological compensation system is studied. The results showed that among the ESVs, the values of climate regulation (CL), water regulation (WA) and waste treatment (WT) were the highest. In combination with the new environmental protection law, which encourages the development of environmental protection industry, emphasizes the government's supervision and management responsibility, guarantees environmental protection information disclosure and public participation, and establishes a sound environmental monitoring system, the scientific compensation scope and compensation standards need to protect ecological integrity. To eliminate the "one size fits all" approach, through the intersection of law, economics and environmental science, divide the types of ecological compensation, and clarify accounting methods and indicator systems.

KEYWORDS:
Ecosystem function, Ecosystem service value, New Environmental Protection Law, Ecological Compensation

INTRODUCTION

Although efforts to conserve natural resources have a long history, only relatively recently have governments implemented relatively effective laws and regulations to control some forms of air, water and soil pollution [1]. Key components of such laws include clearly stated goals and objectives, numerical discharge and ambient criteria based on acute and chronic toxicity tests, funding and technologies for reducing point and diffuse sources of pollution, rigorous discharge and ambient monitoring programs, large data storage and retrieval programs, and reporting that is interpretable by the general public and suitable for publication in scientific journals. Equally important components of pollution control and mitigation are engaged and active citizens, media, regulatory agencies, legislative bodies, and judiciaries as well as some sort of widely adopted conservation ethic [2, 3]. Historically, rigorous air, water and soil pollution controls have not been implemented until after a political unit or nation experiences serious and widespread pollution, i.e., some sort of crisis arising from industrialization, urbanization, and largely uncontrolled pollution or environmental and biological contamination [4].

China's industrialization and urbanization have generated undesirable environmental consequences. Having recognized the substantial adverse social and ecological impacts of economic and population growth, over the past three years China has developed and reinforced its environmental regulations by passing three key statutes [5]. First, revised and enacted on 1 January 2015, the new Environmental Protection Law (EPL) has become the most progressive and stringent law in the history of environmental protection in China [6]. It details harsher penalties for environmental offences such as daily fines, contains provisions for tackling pollution, enshrines the public's environmental right-to-know, establishes a framework for environmental public-interest ligation, and increases accountability of local governments and law-enforcement agencies. The new EPL also provides a much clearer framework and guidelines for improved environment governance in China than what previously existed. Another key component of the EPL is a chapter on information disclosure and public participation that addresses improving data collecting and reporting measures including principles, scope, content, methods and procedures, and supervision of environmental information disclosure including that for enterprises. Second, the newly revised Atmospheric Pollution Prevention and Control Law took effect in early 2016, emphasizing addressing the sources, total discharge, and density of pollutants [7]. Third, the State Council issued three ten-point action plans for tackling air, water and soil pollution in 2013, 2015 and 2016, respectively, to implement the new laws and regulations.

China's 13 th Five-Year Plan for Economic and Social Development (2016–2020) increases the independence of provincial environmental protection departments (EPDs) from local governments and

unifies monitoring and inspection programs at the national level. Under this reform, city/county environmental enforcement and monitoring agencies will be restructured to report directly to provincial EPDs rather than the governments at the same levels [8]. These reforms will be phased in on a pilot basis in 17 provinces/autonomous regions and completed nationwide in 2018 [9]. The laws and regulations and their subsequent environmental management program reforms outlined in the 13th Five-Year Plan represent a paradigm change from an ineffective pollution control system to one based on environmental quality goals and standards.

Ecological compensation has been used as a direct and effective protection tool to change uncompensated externalities into economic incentives to conserve the ecosystems [10-12]. Now, ecological compensation has been applied to some environmental management schemes, such as land compensation, forests compensation, biodiversity conservation [13-17]. Ecological compensation has been widely recognized by many countries [18]. At present, the research on ecological compensation mainly focuses on the conceptual framework, compensation standard, compensation effect and evaluation.

In this paper, we discussed and promoted one approach to constitute and consummate the ecological compensation mechanism, in order to fulfill a win-win situation between environmental protection and economic development. Construction strategy of ecological compensation system is studied.

MATERIALS AND METHODS

Data Acquisition. Statistical data: statistical data included the average monthly rainfall (1980–2018), average monthly temperature (1980–2018), average monthly evaporation (1980–2018), average monthly wind speed (1980–2018), average monthly relative humidity (1980–2018), and number of days on which wind-blown sand speeds are ≥ 10 m/s (1980–2018). Statistical data were collected from the Surface Annual Value Annual Data (1980–2018) by the Chinese Meteorological Science Data Sharing Service (http://data.cma.cn/site/index.html), and according to the latitude and longitude information of each meteorological site, we use the kriging spatial interpolation method of ArcGIS to convert the meteorological statistics into raster images of the meteorological data of the study area.

RESULTS AND DISCUSSION

The first-level ecological space management zone mainly covers ecosystem types with high ESV values, including forestland and wetland. The ecological space management of the region needs to be strict and appropriately increase the ESVs (Figures 1-3).

The first-level ecological space management system is meant to protect and optimize ecosystem function. It does not allow any construction development and activities, and this designation can strictly protect the authenticity of the ecological environment, ensure that existing forest area does not decrease, and strengthen the self sustaining ability of an ecosystem. The zone requires implementation of the strictest control measures, such as prohibiting any construction development that is not related to ecological safety or any other activities that may destroy the ecological environment.

The establishment and improvement of the ecological protection compensation system by the state is a highlight of the new environmental protection law. How to implement the ecological compensation mechanism through specific laws, regulations and policy measures, and to study and solve specific problems in operation is the future legislative direction and fundamental. The scope of scientific compensation and compensation standards need to be based on the principle of protecting ecological integrity, to eliminate the "one size fits all" approach, and to clearly define the types of ecological compensation, accounting methods and indicator systems.

In accordance with the provisions of Article 31 of the New Environmental Protection Law, the state will increase the financial transfer payments to ecologically protected areas, and guide the people's governments in the beneficiary areas and ecological protection areas to make ecological protection compensation through consultation or in accordance with market rules. In addition to the state financial allocation, the collection of ecological security insurance, the collection of forest resources ecological compensation fees to beneficiaries, the ecological fundraising of forest resources, the issuance of ecological lottery and the BOT (Build, Operate, Transfer) financing methods are all effective ways to raise funds.

In the second-level ecological space management zones, there are fewer types of ecosystems that cover high ESV, and more types of ecosystems are concentrated in croplands (Figures 4-6). The second-level ecological space management system aims to maintain and control the area, which includes rehabilitating the ecological environment, reducing the ecological sensitivity level and the occurrence of ecological problems (such as soil erosion and land desertification), maintaining the current level of the environment, and strictly controlling the status quo of urban construction development. It has been suggested to set urban expansion boundaries, which limit any unplanned expansion of the urban and industrial space. Governmental policies related to implementing monitoring and policing of the planning of regional land development. For any proposed land development, the conditions must be within the guidelines.

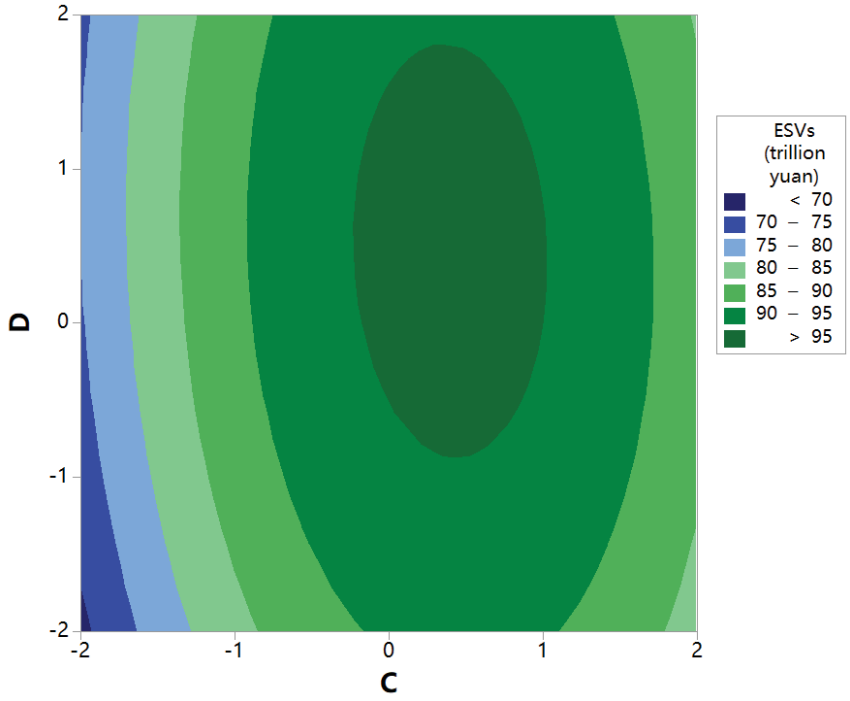

FIGURE 1
Contour Plot of ESVs (trillion yuan) vs D, C

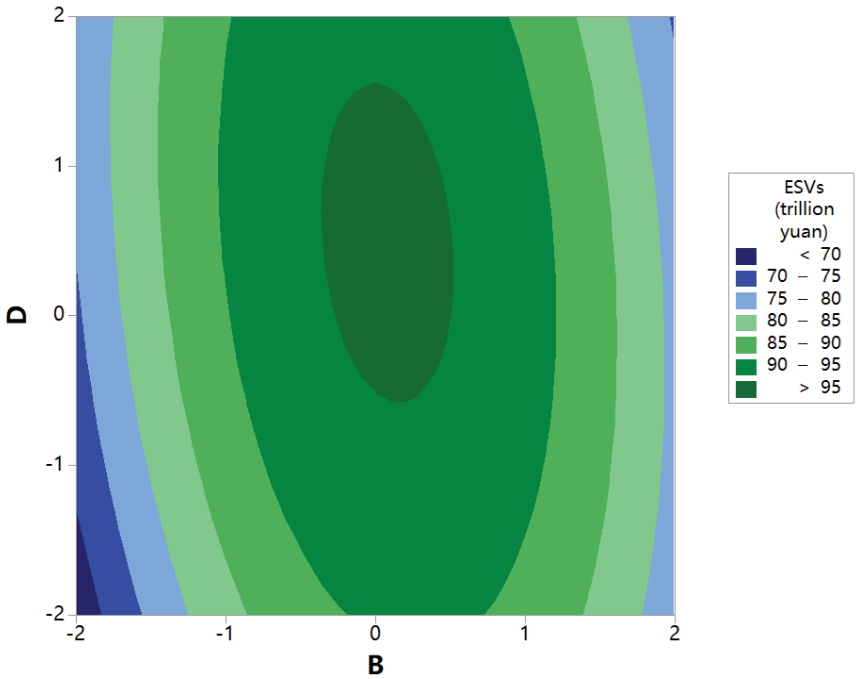

FIGURE 2
Contour Plot of ESVs (trillion yuan) vs D, B

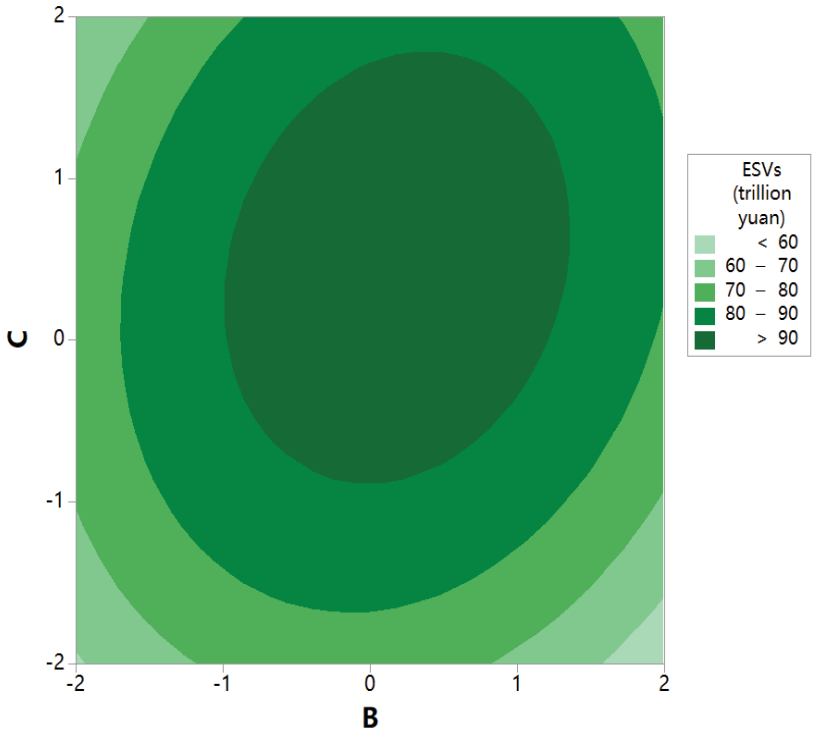

FIGURE 3
Contour Plot of ESVs (trillion yuan) vs C, B

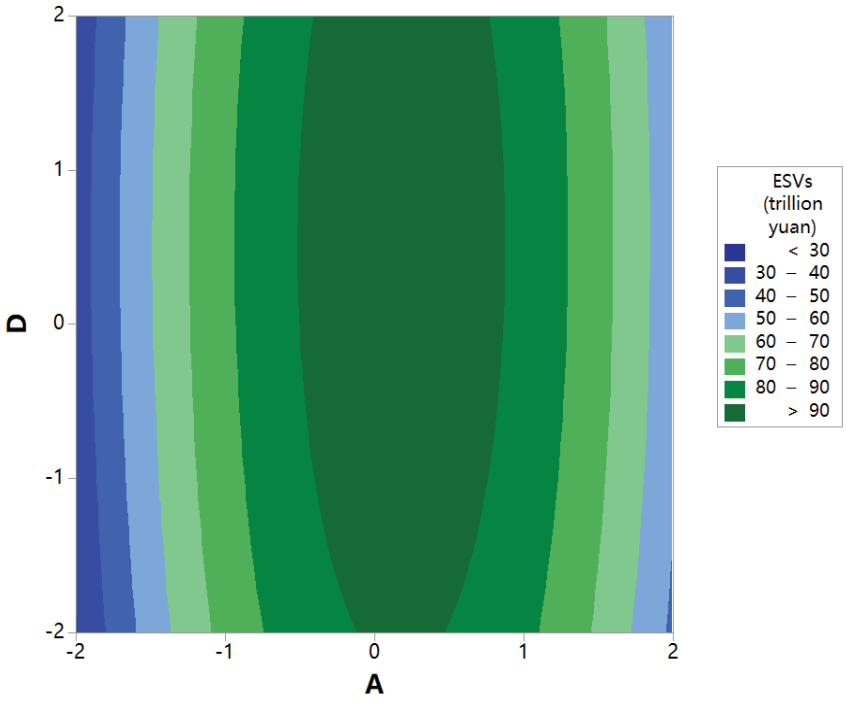

FIGURE 4
Contour Plot of ESVs (trillion yuan) vs D, A

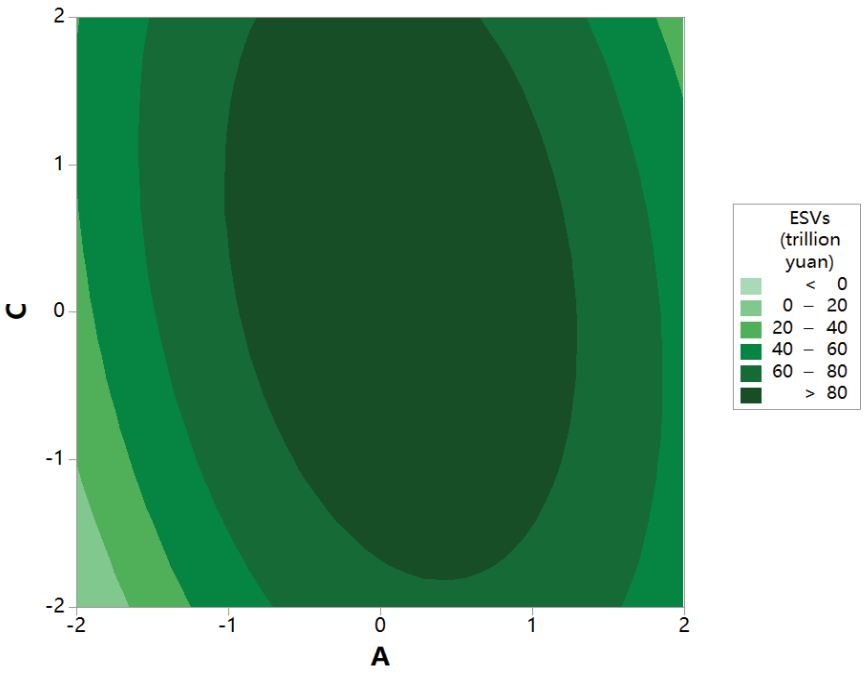

FIGURE 5
Contour Plot of ESVs (trillion yuan) vs C, A

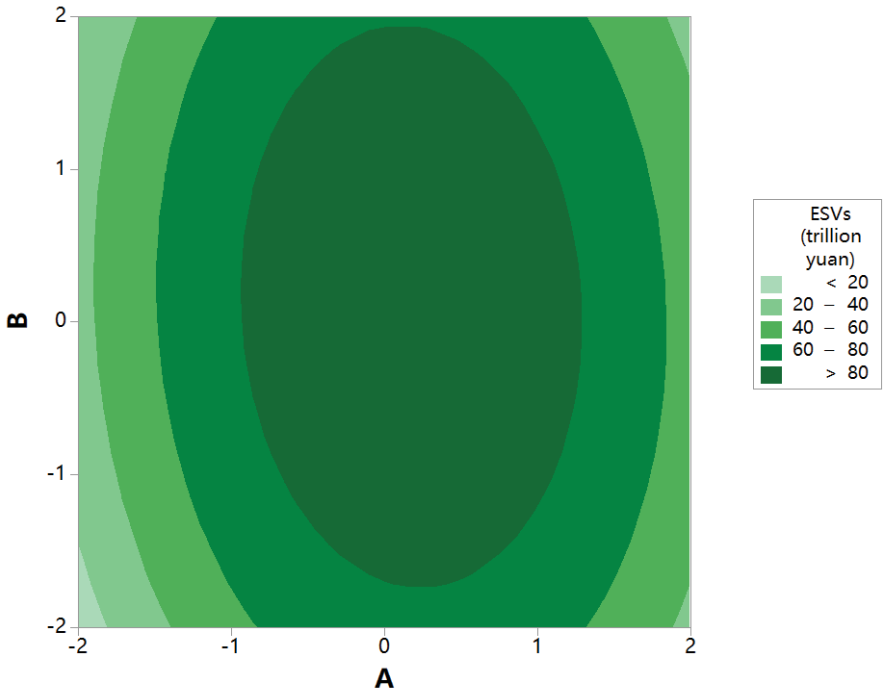

FIGURE 6
Contour Plot of ESVs (trillion yuan) vs B, A

The new environmental protection law has further increased the responsibility of local governments and environmental protection departments. The local government and its environmental protection department shall be responsible for environmental quality and emergencies; the environmental protection department of the higher-level people's government may impose penalties on the offenders at lower levels; the principal responsible person who violates the law and causes serious consequences shall be resigned. In the construction of the ecological protection compensation system, the strict management and supervision system is the fundamental guarantee for the compensation fund to be implemented, to play its role, and to realize the value goal.

CONCLUSIONS

This study was intended to estimate the changes in ecosystem service values (ESVs) as well as other related data such as statistical data. New environmental protection law and construction strategy of ecological compensation system is studied. The results showed that among the ESVs, the values of climate regulation (CL), water regulation (WA) and waste treatment (WT) were the highest.

The new environmental protection law confirms the establishment and improvement of the ecological protection compensation system in the form of the Basic Law on Environmental Protection, clarifies the legal status of the ecological compensation system, and lays the framework and foundation for the construction of China's ecological compensation system. However, the narrow compensation range, single and too low compensation standards, limited compensation funds channels, inefficient supervision and management, and fuzzy distribution of powers and responsibilities are all urgent problems to be solved in the improvement of China's ecological protection compensation system. In combination with the new environmental protection law, which encourages the development of environmental protection industry, emphasizes the government's supervision and management responsibility, guarantees environmental protection information disclosure and public participation, and establishes a sound environmental monitoring system, the scientific compensation scope and compensation standards need to protect ecological integrity. To eliminate the "one size fits all" approach, through the intersection of law, economics and environmental science, divide the types of ecological compensation, and clarify accounting methods and indicator systems.

ACKNOWLEDGEMENTS

This work was supported by Chinese Law Society 2018 Ministerial Law Research Project: Research on Interaction and Integration of Carbon Reduction Tools and Energy Policies, NO. CLS(2018) D151, Beijing Municipal Social Science Foundation "Research on the Legal Protection System of Green Finance Development under the Belt and Road Initiative" (No. 17FXC018). Research Fund Project for Newly-joined.

REFERENCES

[1] Wulf, A. (2015) The Invention of Nature: Alexander von Humboldt's New World. Knopf, New York, NY.
[2] Hughes, R.M. (2014) Fisheries ethics, or what do you want to do with your scientific knowledge in addition to earning a living. Fisheries. 39, 195–196.
[3] Wood, M.C. (2013) Nature's Trust: Environmental Law for a New Ecological Age. CU Press, New York, NY.
[4] Hughes, R.M. (1999) Conservation of Natural Resources. In: Alexander, D.E., Fairbridge, R.W. (Eds.) Encyclopedia of Environmental Science. Kluwer.
[5] Limburg, K.E., Hughes, R.M., Jackson, D.C., Czech, B. (2011) Population increase, economic growth, and fish conservation: Collision course or savvy stewardship? Fisheries. 36, 27-35.
[6] Zhang, B., Cao, C. (2015) Four gaps in China's new environmental law. Nature. 517, 433-434.
[7] Zhang, B., Cao, C., Hughes, R.M., Davis, W.S. (2017) China's new environmental protection regulatory regime: Effects and gaps. Journal of Environmental Management. 187, 464-469.
[8] Zhang, B. (2016) Supervise Chinese Environment Policy. Nature. 534, 179-180.
[9] Finamore, B. (2016) Tackling Pollution in China's 13th Five Year Plan: Emphasis on Enforcement. NRDC.
[10] Kangas, J., Ollikainen, M. (2019) Economic Insights in Ecological Compensations: Market Analysis with an Empirical Application to the Finnish Economy. Ecological Economics. 159, 54-67.
[11] Yu, B., Xu, L. (2016) Review of ecological compensation in hydropower development. Renewable and Sustainable Energy Reviews. 55, 729-738.
[12] Zhang, J., Zhang, J., Liang, Y., Li, N., Liu, Z. (2005) An analysis of touristic ecological footprint and eco-compensation of Jiuzhaigou in 2002. Journal of Natural Resources. 20, 735-744.

[13] Liu, J. (2006) Viewing the structure relationship among ecotourism stakeholders from the perspective of systematology. Tourism Tribune. 21, 17-21.
[14] Seroa da Motta, R., Ortiz, R.A. (2018) Costs and perceptions conditioning willingness to accept payments for ecosystem services in a Brazilian case. Ecological Economics. 147, 333-342.
[15] Zhang, Y.J., Wei, Y.M. (2010) An overview of current research on EU ETS: Evidence from its operating mechanism and economic effect. Applied Energy. 87, 1804-1814.
[16] Guan, X., Liu, W., Chen, M. (2016) Study on the ecological compensation standard for river basin water environment based on total pollutants control. Ecological Indicators. 69, 446-452.
[17] Yu, B., Xu, L., Wang, X. (2016) Ecological compensation for hydropower resettlement in a Reservoir wetland based on welfare change in Tibet, China. Ecological Engineering. 96, 128-136.
[18] Olli, V., Pertti, V. (2001) China's 8 challenges to water resources management in the first quarter of the 21st Century. Geomorphology, 41, 93-104.

Received: **20.10.2019**
Accepted: **26.01.2020**

CORRESPONDING AUTHOR

Qingpo Wei
School of Law,
Capital University of Economics and Business
Beijing 100070 – China

e-mail: maigood889@sina.com

AUTHOR INDEX

A

Adamska, A.	2632	Amjad, A.	2818
Ahmed, M. A.	3279	Anjum, K. M.	3013
Akbulut, S.	3102	Arabaci, G.	2646
Akinci, I. Y.	2683	Arabeyyat, Z.	3240
Al Sawalmih, A.	3240	Arar, S.	3056
Alawi, M.	3056	Arslan, M.	2670
Ali, A.	2818	Atique, U.	3013
Ali, M.	2818	Awaideh, S.	3056
Ali, S.	2818	Aydin, B.	3287
Alrowwad, A.	3240	Aydin, M.	3287
Al-Saad, A. M.	3240		

B

Bahar, B.	2897	Borowiak, K.	2632
Balas, L.	2725	Boyacioglu, O.	2746
Bao, C.	3193	Bozdogan, N. Y.	2802
Barnett, S.	3240	Bu, J.	2960
Barpete, S.	2698	Budka, A.	2632
Bayhan, B.	2626	Bugdayci, K. E.	2683
Bayraktar, Z.	2951	Bulca, S.	3003
Borkoyev, B.	2809		

C

Cao, S.	3154	Chen, X.	2886
Cesko, C.	2646	Chen, Z.	3254
Cetin, I.	2766	Cheng, J.	2858
Cevik, E. E.	2662	Chi, Z.	3230

D

Daglioglu, N.	2802	Djurdjevic, V.	2758
Dai, J.	2960	Dong, W.	3184
Dede, G.	2739	Dong, Y.	2942
Delik, A.	2784	Dou, Y.	3134
Deng, J.	2932	Du, J.	3154
Dincer, S.	2784	Duru, A. A.	2766
Dis, M. O.	2778	Duskov, L.	2758

E

Engin, S.	2691	Erturk, U.	2809
Erbil, E.	3033	Esgici, R.	2772
Erdogdu, M.	2678		

F

Fadiloglu, E. E.	2711	Filipovic, D.	2758
Fang, L.	2834	Firat, K.	2691

G

Gao, H.	3261	Gulsun, B.	2653
Gao, S.	2858	Guo, Q.	3261
Gao, X.	2752	Guo, Y.	2925
Ge, S.	2886	Gupta, P.	2698
Gedikli, M.	2739	Guzel, E.	2802

H
Haider, M. S. 3013
Hao, B. 3040
He, C. 2891
He, X. 3026
Huang, P. 3166
Huang, Q. 2869
Huang, Y. 3184
Huang, Z. 2886, 3166

I
Ilic, Z. S. 2615
Inan, A. 2725
Iqbal, S. 3013
Iwaniuk, P. 2719

J
Janicka, E. 2632
Javeed, A. 3013
Jia, J. 2993
Jiang, D. 3184
Jiang, W. 3193
Jin, L. 2879
Jing, D. 2886

K
Kailani, M. H. 3056
Kanclerz, J. 2632
Kaplan, C. 2917
Karabulut, H. A. 2951
Karademir, D. 2639
Karakus, M. 3033
Karipcin, M. Z. 3279
Khan, N. 3013
Khan, T. A. 3013
Khawar, K. M. 2698
Kir, H. 2843
Koc, K. H. 2639
Kong, X. 2891
Kteifan, M. 3240
Kumar, S. 2698
Kunjko, D. 3048
Kurnaz, M. A. 2662
Kurtoglu, I. Z. 2951

L
Li, C. 3300
Li, H. 3184
Li, N. 2858
Li, T. 3261
Li, W. 3144, 3193, 3201
Li, X. 2908, 2932
Li, Y. 2732, 2752, 3084
Li, Z. 2834, 2932
Liang, W. 3144
Liao, J. 2932
Libront, A. 2632
Lin, J. 2969
Lin, Y. 3026
Lisiak, M. 2632
Liu, H. 2932, 3154
Liu, J. 3118
Liu, L. 3126
Liu, Y. 3254
Liu, Z. 3269
Lozowicka, B. 2719
Lu, H. 2858
Luo, X. 3223

M
Ma, D. 2975
Ma, X. 3040
Mahmood, S. 3013
Manasrah, R. 3240
Mao, H. 3072
Miao, Y. 2834
Miao, Z. 3261
Mic, P. 2653
Muhammad, S. 2969

N
Ni, B. 2925

O
Oguz, F. K. 2683
Oguz, M. N. 2683
Oktelik, F. B. 2670
Ouyang, L. 3223
Ozcan, S. 2698
Ozen, F. 2823
Ozkan, E. 2670
Ozseker, P. E. 2802
Ozyiğit, I. I. 2809

P
Pan, Y. 2982, 3173
Pang, H. 2960
Peng, P. 2732
Polat, V. 3287
Puntaric, E. 3048

Q
Qazi, B. 3013
Qi, J. 2969
Qin, L. 3154
Qin, Z. 2869
Qu, L. 3261

R
Ran, Q. 3091
Rasheed, M. 3240
Ren, G. 2925
Rong, W. 2932

S
Saka, S. 2691
Saliyeva, K. 2809
Sartaj, A. 2818
Saygi, H. 2626
Severoglu, Z. 2809
Shang, X. 2925
Shao, Q. 3126
Shen, J. 3072
Shen, M. 2858
Sherzada, S. 3013
Shi, X. 2732
Shi, Y. 3201
Sirat, A. 2897
Solak, A. O. 2809
Soleiman, A. 3240
Song, Z. 2993
Stankovic-Popic, M. 2615
Sun, H. 2752
Sun, L. 2752
Sun, N. 3040
Sunbul, A. B. 2739
Sunic, L. 2615
Suric, J. 3048

T
Tang, X. 3072
Tas, T. 3033
Tian, J. 2969
Topkara, E. T. 2626
Trajkovic, R. 2615
Turker, A. U. 2670

U
Ucak, A. B. 3033
Unsal, M. 2778
Uslu, F. M. 2784
Usluoglu, A. 2646
Uyguralp, I. C. 2683

V
Voca, N. 3048

W
Wang, B. 2908
Wang, C. 2869
Wang, H. 2908
Wang, J. 2925, 2969
Wang, L. 2879
Wang, M. 3026
Wang, S. 3269
Wang, W. 3230
Wang, X. 2975, 3201
Wang, Z. 3072
Wei, Q. 3308

X
Xi, A. 2932
Xiao, J. 2975
Xie, R. 3269
Xiong, L. 3223
Xu, H. 3269

Y

Yagci, A. E. 2778
Yan, M. 3269
Yan, X. 2891
Yang, L. 2886
Yang, Y. 2732, 2925, 3144
Yang, Z. 2732
Yanik, D. 3102
Yasar, F. 3279
Yesilcinar, I. 3102
Yetkin, C. 3033
Yi, S. 3026
Yigittekin, E. S. 2784
Yildirim, A. B. 2670
Yin, T. 2869
Yin, Y. 3230
Yu, Y. 2960
Yuan, Y. 3254
Yucel, S. 2809
Yuksek, T. 2951

Z

Zhang, G. 3212
Zhang, J. 2850, 3201
Zhang, L. 3212
Zhang, M. 3144
Zhang, Q. 3040
Zhang, R. 3261
Zhang, S. 2908
Zhang, T. 3212
Zhang, X. 2993
Zhang, Y. 2834, 3134
Zhang, Z. 3173
Zhao, Z. 2752
Zheng, J. 3134
Zheng, L. 2975
Zheng, T. 2792
Zheng, Y. 2707
Zhong, J. 3040
Zhou, L. 2850
Zhou, T. 3072
Zhou, X. 3026
Zhu, H. 2891
Zhu, X. 3254
Zhu, Y. 2707, 3110
Zi, X. 2960

SUBJECT INDEX

A

Additive 2766
Aflatoxin 2818
Aflatoxin M_1 3003
AgBr 2732
agriculture 2758
algorithm analysis 3084
Alkaloid 2670
alpha-hederin 2746
Amateur Fishing Competition 2626
Antibiotic resistance. 2784
anti-browning 2646
Apericot kernel 2818
Ascomycota 2678

B

Bacillus subtilis 2711
β-LAD 2975
binary composite flooding 3173
biodiversity 2678, 3126
Biomonitoring 2802
Biopreservation 2711
Black seed essential oil 2746
blade edge 2772
blasting stress wave 2982
borehole stability 3091
Brine discharges 2725
buried pipeline 3269
bus station 3300
business coastal sectors 3240

C

calcium 2683
caprock 3110
Carassius gibelio 2626
catalase 2615
Central Sichuan 2925
Chain drive 3193
Chatbot 3223
Chestnut 2917
Chromium 3013
clean power system 3223
climate change 2758
CNG gas storage well 3154
CO_2 dissolution and displacement 3261
Coagulants 2834
Coal Mines 2850
coal seam 2982
Coal-bearing strata 3254
Coastal management 3240
cold storage 2711
Collaborative platform 2879
colon cancer 2746
comprehensive 3300
comprehensive evaluation index system 3126
Computer program 3287
concurrent risk 3144
conflicts 3240
Contamination level 2818
core 3040
CORMIX 2725
cotton 2772
crack propagation 2982
Crispr 2.1 Locus 2784
crucian carp 2858
Crude protein 2843
Cryopreservation 2691
Cukurova Region 2802
current frequency 3072
cutting force 2772
Cuttlefish bone 2683

D

damage detection 3154
database 2869
Datong River 2908
DDMY 2843
Deep water sedimentation slope 2932
Dendrogram 3013
Denolder 2626
Density 2891
desalination 2725
detection device 3154
diesel engine 2960
diesel particulate filter 2960
Dioxins/Furans 3056
directional well 3166
dirt band 2982
distribution 2917
Distribution of Particle Size 2886
Ditch wetland 3230
drainage 3287
drilling fluid 3091, 3118
Drought stress 2969
drug resistance gene 2975
drying shrinkage 3072
Dust 2886
dynamic failure 3110

E

Earthworm meal 2951
Ecological Compensation 3308
ecological environment 3084, 3126, 3300
ecological security 3184
Ecosystem function 3308
Ecosystem service value 3308
E-DiGOR model 3287
Effluents 3013
egg quality 2683
energy consumption analysis 2792
energy saving and environmental protection 3193
enhanced oil recovery 3173
enrichment law 2932
environment 2662, 3134
environmental behavior 2975
environmental damage 2982
environmental education 2662
environmental impact assessment 2632
environmental pollution 3269
environmental problems 2662
environmental protection 3223
environmental sensitivity 2662
Environmental-friendly 3118
environmentally friendly 2993
Escherichia coli 2784
EU Legislation 2639
experimental research 3261
extended FMEA 3144
external corrosion rate 3269

F

Fatty acids 2809
fault 3110
Feed 2897
finite element 3193
fish nutrition 2951
fishmeal 2951
flood area model 2908
flood disaster 2908
flow coefficient 3134
food waste 3048
Forage turnip 2766
forest 2758
formation parameters 3166
Fractional inhibitory concentration index (FICI) 2719
fractured reservoir 3201
fracturing reform 3261
fresh farmed sea bass 2711
Fungicides 2719
fuzzy PROMETHEE 2653
fuzzy sets 2653

G

galanthamine 2670
Gallbladder stones 3056
Gallbladder tissues 3056
gas isotope 3254
Gaussian model 2879
g-C_3N_4 2732
Gediz Delta 2823
Genetic Algorithms 2778
geochemical parameter 2942
geological model 3091
GEP 2778
GGR-6 2969
Gilgit-Baltistan 2818
Gilthead Sea Bream 2691
GIS mapping 3240
GIS technology 2869
glutenite 3201
Gökpınar Dam Pond 2626
graphite plate 3193
Grass pea 2698
Green 2850
green towns 2792
growth performance 2951
growth trend 2792
Gulf of Aqaba 3240

H

Hair 2802
Heavy metals 2752
heavy oil reservoir 3261
Heilongjiang Province 3184
hepatic enzyme activity 2858
heterogeneity 3173
High Pressure Mist Spray 2886
histological change 2858
hopelessness 3102
horizontal section 3091
HPLC 3003
HRT 3230
human uses 3240
hydrophobically associating 3118

I

improved Δlog *R* method 2942
In vitro flowering 2698
in-depth interviews 3048
influence law 3166
influencing factors 3269
inhibition 2646
inhibition capacity 2993
injection speed 3173
Intelligent planning 2879
Invasive fish 2626
Iron 3033

J
Jordan 3056

K
Karamay oilfield 3201
Karst 3126
knife 2772
KPCA-MABC-SVR model 3269
Kyrgyzstan 2809

L
landfill cap layer 2739
landscape design 3300
Landscape visual attractiveness 2632
laser 3154
Late Triassic 3212
Lathyrus sativus L. 2698
laying quail 2683
lettuce 2615
Leucojum aestivum 2670
logging data 3040
logging parameters 3166
long core 3173
low temperature 3279
lower Wuerhe Formation 3201
low-permeability 3261
Low-turbidity 2834
lycorine 2670

M
malting barley 2897
marine environment 3240
Materials selection 2653
MDA 2969
metal 2646
Microbiological properties 2766
microfungi 2678
Micro-scale 3134
Middle Permian 2925
Milk and Dairy Products 3003
mineral testing 3040
Minimal inhibitory concentration (MIC) 2719
modal analysis 3193
modern forestry 3184
modified cellulose 3118
Molybdenum 3033
Motility 2691
multi criteria decision making 2653
Multiphase Flow 2886

N
natural frequency 3193
near-field dilution 2725
New Environmental Protection Law 3308
new host 2678
new record 2678
Nitrogen absorption 2891
nitrogen removal 3230
Nodal junction 2698
Nodulation 3033
non-uniform clustering 3084
Numerical Simulation 2886
nursing 3102
Nut traits 2809

O
object-oriented classification. 2823
Occupational accident and occupational diseases 2639
Occupational health and safety 2639
occurrence characteristics 3254
ODAP 2698
oil and gas gathering and transporting system 3269
oil and gas recovery rate 3110
Oil and gas storage and transportation environment 3144
Oncorhynchus mykiss 2951
Online monitoring 2707
optimal cooling effect 3134
Ordos Basin 2932, 3212
organic acid 2615
organic components 2942
orthophoto 2823

P

Partial discharge 2707
Particle filtering 2879
PCA 3013
pepper 3279
perennial ryegrass 2969
performance 2683
Pesticide 2802
Petri net reasoning 3144
phase differentiation 2932
photocatalytic degradation 2732
Phytopathogenic fungi 2719
plate waste 3048
plugging capacity 2993
Pollution 3056
Pollution assessment 2752
Polyphenol oxidase (PPO) 2646
population development,Turkey 2917
pore size distribution 3212
pore structure 3212
pore type 3212
portion size 3048
Pregnancy 3102
pressure drop 2960
princess tree 2646
principal component analysis 3184
proline 2969
prospective science teachers 2662
prostate cancer 2746
Prussian carp 2626
public buildings 2792
purple soil 3072

Q

Q&A System 3223
Qaidam Basin 3040
Quality 2711, 2843
quality traits 2897

R

radish 2615
Rainfall-Runoff 2778
Raska Administrative District 2758
Raspberry Pi 3223
ration preparation 2951
real-time monitoring 3084
reclamation area 3184
Recycling sludge 2834
regeneration schedule 2960
Regression analysis 2792
Removal efficiency 2834
Republic of Serbia 2758
reservoir characteristics 2925, 2932
resistivity 3072
restaurant 3048
reuse 2739
rGO 2732
rheology modifier 3118
risk analysis 3144
Risk assessment 2758, 2908
risk identification 3144
runoff 3287
Rural landscape 2879

S

safety density window 3166
Safety Production 2850
salicylic acid 3279
Samsun Bay 2725
Sanliurfa Soybean 3033
scenic perception 2632
sedimentary facies model 3040
seed germination 2615
self-esteem 3102
sequence division 2925
sewage sludge 2739
shale formation 2993
Shale gas 3091
shale oil reservoir 2942
shaped charge blasting 2982
Silage 2766
simulation 3134
simulation platform 3154
smart city 3300
Soil 2752
soil evaporation 3287
Soil pollution 2615
soil-water storage 3287
soot loading 2960
Source approximation 2752
southern Guizhou 3126
Sowing date 2891
soybean cold black soil area 3026
spatial configuration 3230
Sperm 2691
stalk 2772
Storm 2778
stratigraphy 2925
Sub-Tropical 2778
summer snowflake 2670
Sustainable packaging 2653
Sutlej 3013
Synanthedon vespiformis 2917

T
Tanneries 3013
tetracycline 2732
thymoquinone 2746
thyroid hormone 2858
tight oil reservoir 3212
tight sandstone 3110
torrential rain 2908
Toxicity equivalency (TEQ) 3056
Transformer 2707
triangle method 3154
Turkey Furniture Industry 2639

U
UCG 2850
unconventional gas system 3254
UPLC-MS/MS 2975
urban rainfall 2869

V
Volatile fatty acids 2766
VSM Algorithm 3223
Vulnerability 2758

W
Walnut 2809
Waste foundry sand 2739
Water chemistry 3013
water consumption characteristics 3026
water content 3072
water flooding model 3201
water production function 3026
water-based drilling fluid system 2993
waterlogging simulation 2869
Wavelet-based denoising 2707
Wetland 2823
Wheat 2891
wireless sensor network 3084
Work environment 2639
working condition 3134
WRKY genes. 3279

Y
Yield 2891, 2897, 3033
yield components 2897

Z
Zea mays L. Yield 2843
zinc 2746

1, 2, 3,….., 0
2,2’,4,4’- tetrabromodiphenyl ether 2858

FEB – GUIDE FOR AUTHORS

General

FEB accepts original papers, review articles, short communications, research abstracts from the entire sphere of environmental-chemistry,-biology,-microbiology,- technology, -biotechnology and-management, furthermore, about residue analysis/ and ecotoxicology of contaminants.

Acceptance or no acceptance of a contribution will be decided, as in the case of other scientific journals, by a board of reviewers. Papers are processed with the understanding that they have not been published before (except in form of an abstract or as a part of a published lecture, review or thesis);that they are not under consideration for publication elsewhere; that their publication has been approved by all co-authors, if any, as well as- tacitly or explicitly- by the responsible authorities at the institute where the work has been carried out and that, if accepted, it will not be published elsewhere in the same form, in either the same or another language, without the consent of the copyright holders.

Language

Papers must be written in English. Spelling may either follow American (Webster) or British (Oxford) usage but must be consistent. Authors who are less familiar with the English language should seek assistance from proficient colleagues in order to produce manuscripts that are grammatically and linguistically correct.

Size of manuscript

Review articles should not exceed 30 typewritten pages. In addition up to 5 figures may be included.

Original papers must not exceed 14 typewritten pages. In addition up to 5 figures may be included.

Short-Communications should be limited to 4 typewritten pages plus not more than 1 illustration.

Short descriptions of the authors, presentation of their groups and their research activities (with photo) should together not exceed I typewritten page. Short research abstracts should report in a few brief sentences (one-fourth to one page) particularly significant findings. Short articles by relative newcomers to the chemical innovation arena highlight the key elements of their Master and PhD-works in about I page.

Book Reviews are normally written in-house, but suggestions for books to review are welcome.

Preparation of manuscript

Dear authors,

FEB is available both as printed journal and as online journal on the web. You can now e-mail your manuscripts with an attached file. Save both time and money. To avoid any problems handling your text please follow the instructions given below:

When preparing your manuscripts have the formula K/SS (Keep It Simple and Stupid) in mind. Most word processing programs such as MS-Word offer a lot of features. Some of them can do serious harm to our layout. So please do not insert hyperlinks and/or automatic cross-references, tables of contents, references, footnotes, etc.

1. Please use the standard format features of your word processor (such as standard.dot for MS Word).
2. Please do not insert automatisms or secret link-ups between your text and your figures or tables. These features will drive our graphic department sometimes mad.
3. Please only use two fonts for text or tables "Times New Roman" and for graphical presentations "Arial".
4. Stylesheets, text, tables and graphics in shade of grey
5. Turn on the automatic language detection in English (American or British)
6. Please - check your files for viruses before you send them to us!!

Manuscripts should be uploaded on our website prt-parlar.de

Thank you very much!

STRUCTURE OF THE MANUSCRIPT

Title page: The first page of the manuscript should contain the following items in the sequence given: A concise title of the paper (no abbreviations). The names of all authors with at least one first name spelled out for every author. The names of Universities with Faculty, City and Country of all authors.

Abstracts: The second page of the manuscript should start with an abstract that summarizes briefly the contents of the paper (except short communications). Its length should not exceed 150-200 words. The abstract should be as informative as possible. An extended repetition of the paper's title is not considered to be an abstract.

Keywords: Below the Summary up to 6 key words have to be provided which will assist indexers in cross-indexing your article.

Introduction: This should define the problem and, if possible, the frame of existing knowledge. Please ensure that people not working in that particular field will be able to understand the intention. The word length of the introduction should be 150 to 300 words.

Materials and methods:
Please be as precise as possible to enable other scientists to repeat the work.

Results: Only material pertinent to the subject must be included. Data must not be repeated in figures and tables.

Acknowledgements: Acknowledgements of financial support, advice or other kind of assistance should be given at the end of the text under the heading "Acknowledgements". The names of funding organisations should be written in full.

References: Responsibility for the accuracy of references rests with the authors. References are to be limited in number to those absolutely necessary. References should appear in numerical order in brackets and in order of their citation in the text. They should be grouped at the end of the paper in numerical order of appearance. Abbreviated titles of periodicals are to be used according to Chemical or Biological Abstracts, but names of lesser known journals should be typed in full. References should be styled and punctuated according to the following examples:

ORIGINAL PAPERS:
l. Author, N.N. and Author, N.N. (Year) Full title of the article. Journal and Volume, first and last page.
BOOK OR PROCEEDING:
2. Author, N.N. and Author, N.N. (Year) Title of the contribution. In: Title of the book or proceeding. Volume (Edition of klitor-s, ed-s) Publisher, City, first and last page

DOCTORAL THESIS:
3. Author, N.N. (Year) Title of the thesis, University and Faculty, City

UNPUBLISHED WORK:
Papers that are unpublished but have been submitted to a journal may be cited with the journal's name followed by "in press". However, this practice is acceptable only if the author has at least received galley proofs of his paper. In all other cases reference must be made to “unpublished work" or "personal communication".

Discussion and Conclusion: This part should interpret the results in reference to the problem outlined in the introduction and of related observations by the author/s or others. Implications for further studies or application may be discussed. A conclusion should be added if results and discussion are combined.

Corresponding author: The name of the corresponding author with complete postal address

Reprints:
1 - 4 pp.: 200,- EURO + postage/handling
5 - 8 pp.: 250,- EURO + postage/ handling
More than 8pp: 350,- EURO +postage/ handling.
The prices are based upon the number of pages in our journal layout (not on the page numbers of the submitted manuscript).
Postage/ Handling: The current freight rate is Germany 10 €, Europe 18 €, International 30 €.
VAT: In certain circumstances (if no VAT registration number exists) we may be obliged to charge 7% VAT on sales to other EU member countries.MESAEP and SECOTOX members get a further discountof 20% (postage/ handling full).